351956

UNLIMITED

AGARD-CP-598

S 55
12/6

AGARD-CP-598

# AGARD

ADVISORY GROUP FOR AEROSPACE RESEARCH & DEVELOPMENT

7 RUE ANCELLE, 92200 NEUILLY-SUR-SEINE, FRANCE

**AGARD CONFERENCE PROCEEDINGS 598**

# Advanced Non-Intrusive Instrumentation for Propulsion Engines

(l'Instrumentation non-invasive avancée pour les propulseurs)

*Papers presented at the Propulsion and Energetics Panel (PEP) 90th Symposium, held in Brussels, Belgium, 20-24 October 1997.*

Processed / Not Processed by DIMS

.....signed .....date

NOT FOR DESTRUCTION

**NORTH ATLANTIC TREATY ORGANIZATION**

Published May 1998

*Distribution and Availability on Back Cover*

UNLIMITED

(554PP) S 58/19/6

AGARD-CP-598

# AGARD

ADVISORY GROUP FOR AEROSPACE RESEARCH & DEVELOPMENT
7 RUE ANCELLE, 92200 NEUILLY-SUR-SEINE, FRANCE

**AGARD CONFERENCE PROCEEDINGS 598**

# Advanced Non-Intrusive Instrumentation for Propulsion Engines

(l'Instrumentation non-invasive avancée pour les propulseurs)

Papers presented at the Propulsion and Energetics Panel (PEP) 90th Symposium, held in Brussels, Belgium, 20-24 October 1997.

North Atlantic Treaty Organization
*Organisation du Traité de l'Atlantique Nord*

# The Mission of AGARD*

According to its Charter, the mission of AGARD is to bring together the leading personalities of the NATO nations in the fields of science and technology relating to aerospace for the following purposes:

— Recommending effective ways for the member nations to use their research and development capabilities for the common benefit of the NATO community;

— Providing scientific and technical advice and assistance to the Military Committee in the field of aerospace research and development (with particular regard to its military application);

— Continuously stimulating advances in the aerospace sciences relevant to strengthening the common defence posture;

— Improving the co-operation among member nations in aerospace research and development;

— Exchange of scientific and technical information;

— Providing assistance to member nations for the purpose of increasing their scientific and technical potential;

— Rendering scientific and technical assistance, as requested, to other NATO bodies and to member nations in connection with research and development problems in the aerospace field.

The highest authority within AGARD is the National Delegates Board consisting of officially appointed senior representatives from each member nation. The mission of AGARD is carried out through the Panels which are composed of experts appointed by the National Delegates, the Consultant and Exchange Programme and the Aerospace Applications Studies Programme. The results of AGARD work are reported to the member nations and the NATO Authorities through the AGARD series of publications of which this is one.

Participation in AGARD activities is by invitation only and is normally limited to citizens of the NATO nations.

* AGARD merged with the Defence Research Group of NATO (DRG) on 1 January 1998 to form the Research and Technology Organization (RTO) of NATO. However, both AGARD and DRG will continue to issue publications under their own names in respect of work performed in 1997.

The content of this publication has been reproduced
directly from material supplied by AGARD or the authors.

*Printed on recycled paper*

Published May 1998

Copyright © AGARD 1998
All Rights Reserved

ISBN 92-836-0055-X

*Printed by Canada Communication Group Inc.*
*(A St. Joseph Corporation Company)*
*45 Sacré-Cœur Blvd., Hull (Québec), Canada K1A 0S7*

# Advanced Non-Intrusive Instrumentation for Propulsion Engines

## (AGARD CP-598)

## Executive Summary

The ability to measure and monitor key internal gas and structural characteristics is crucial to improving performance, operability, durability and economy of engines. Non-intrusive measurement techniques provide this capability and thus are a key technology to maintaining and upgrading NATO's defence capabilities. This forum for communication between engine manufacturers, researchers and developers and users has already proved that there are many technologies fit for routine application and many are maturing. Future development work must continue to aim at robust technologies apt for application by non-specialists and it was found that this is already a well established attitude in development and industry. The need to keep this up was reinforced and directions to be followed evolved from the presentation and discussions. The technologies presented, at different stages of development, as well as the future outlook proved that this field contributes and will continue to contribute greatly to NATO's air, land and sea powers.

# L'instrumentation non invasive avancée pour les propulseurs

## (AGARD CP-598)

## Synthèse

La capacité de mesurer et de contrôler les caractéristiques des gaz et des structures internes clés des moteurs d'avion est fondamentale pour améliorer les performances, l'exploitabilité, la longévité et la rentabilité. Les techniques de mesure non intrusives offrent cette possibilité et représentent, par conséquent, une technologie essentielle pour le maintien et la mise à niveau des moyens de défense de l'OTAN. Ce forum, qui a permis des échanges entre motoristes, chercheurs, concepteurs et utilisateurs, a prouvé qu'il existe déjà bon nombre de technologies susceptibles de trouver des applications courantes et d'autres encore arrivant à maturité. Les travaux de développement futurs devraient privilégier des technologies sûres, pouvant être mises en application par des non-spécialistes, ce qui est déjà la pratique courante dans le secteur du développement comme dans l'industrie. L'accent a été mis sur le souhait de maintenir cette situation, et les présentations et les discussions qui les ont suivies ont permis d'identifier les voies à suivre. Les technologies présentées, aux différents stades de leur développement, ont fourni la preuve que cet aspect joue déjà et continuera de jouer un rôle important dans l'évolution des forces armées de l'OTAN.

# Contents


| | Page |
|---|---|
| **Executive Summary** | iii |
| **Synthèse** | iv |
| **Theme/Thème** | x |
| **Propulsion and Energetics Panel** | xi |
| **Recent Publications of PEP** | xii |

| | Reference |
|---|---|
| **Technical Evaluation Report**<br>by R. Ainsworth | T |
| **Research and Development In the Business Environment of the 21st Century**<br>by K. Benson | K |
| **SESSION I: LASER POINT MEASUREMENTS - PART 1** | |
| **On the Aerothermochemistry of Recirculating Premixed Flames with and without Swirl**<br>by D. Duarte and M.V. Heitor | 1 |
| **The Simultaneous Measurements of Velocity, Pressure, Temperature and Heat Release in an Oscillating Flame**<br>by E.C. Fernandes and M.V. Heitor | 2 |
| **Laser Two-Focus Flow Field Investigation within a High-Speed High-Pressure Centrifugal Compressor**<br>by I. Trébinjac and I. Claudin | 3 |
| **3-D LDA Measurements in an Annular Cascade for Studying Tip Clearance Effects**<br>by A. Doukelis, K. Mathioudakis, M. Founti and K. Papailiou | 4 |
| **Investigation of the Spray Dynamics of Aeroengine Fuel Injectors under Atmospheric and Simulated Pressure Conditions**<br>by T. Behrendt and C. Hassa | 5 |
| **Laser Two Focus Anemometry (L2F-3D) for Three-Dimensional Flow Analysis in an Axial Compressor**<br>by A. Vouillarmet and S. Charpenel | 6 |
| **SESSION II: ABSORPTION AND INFRARED TECHNIQUES** | |
| **Non-Intrusive Measurement Technique For Propulsion Engines**<br>by M.F. Mulligan and J.D. MacLeod | 7 |
| **Application of FTIR Spectroscopy to Measurement of Gas Turbine Engine Exhaust Emissions**<br>by M. Hilton and A.H. Lettington | 8 |

**DIAL Measurements on a Gas Turbine Exhaust** 9
by C. Wilson, K. Brundish, J.T.M. Moncrieff and A.G. Wootton

**UV Absorption Measurements of Nitric Oxide Compared to Probe Sampling Data for Measurements in a Turbine Engine Exhaust at Simulated Altitude Conditions** 10
by R.P. Howard

SESSION III: LASER POINT MEASUREMENTS - Part 2

**Paper 11 withdrawn**

**Laser-2-Focus Measurements on a Turbine Cascade With Leading Edge Film Cooling** 12
by S. Ardey, L. Fottner, M. Beversdorff and H. Weyer

**Application of 3D-Laser Two Focus Velocimetry in Turbomachine Investigations** 13
by M. Beversdorff, L. Matziol and C. Blaha

**Characterization of Gas Turbine Combustion Chambers with Single Pulse CARS Thermometery** 14
by R. Lückerath, V. Bergmann and W. Stricker

**CARS Diagnostics on Model Gas Turbine Combustor Rigs** 15
by J.D. Black and S.S. Wiseall

**Recent Developments in the Application of Laser Doppler Anemometry to Compressor Rigs** 16
by J.D. Edmonds, D. Harvey and S.S. Wiseall

SESSION IV: PAINTS - SURFACE SENSORS

**PSP - Intensity and Lifetime Measurements for Steady and Nonsteady Flow** 17
by R.H. Engler and Chr. Klein

**Optical Measurements of Surface Pressure and Temperature in Turbomachinery** 18
by K. Navarra, L. Goss, J. Jordan, D. Rabe, J. Gord and D. Car

**Rotor Blade Pressure Measurement in a Rotating Machinery Using Pressure and Temperature Sensitive Paints** 19
by S. Torgerson, T. Liu and J. Sullivan

**Use of Liquid Crystal Techniques to Measure Film Cooling Heat Transfer and Effectiveness** 20
by S.M. Guo, C.C. Lai, J.H. Jeong, T.V. Jones, M.L.G. Oldfield, G.D. Lock and A.J. Rawlinson

**Surface Temperature Measurement in Turbines** 21
by C. Bird, J.E. Mutton, R. Shepherd, M.D.W. Smith and H.M.L. Watson

**Effective Spectral Emissivity Measurements of Superalloys and YSZ Thermal Barrier Coating at High Temperatures Using a 1.6 μm Single Wavelength Pyrometer** 22
by S. Alaruri, L. Bianchini and A. Brewingston

SESSION V: LASER INDUCED FLUORESCENCE

**Development and Application of Laser Induced Incandescence (LII) as a Diagnostic for Soot Particulate Measurements** 23
by D.R. Snelling, G.J. Smallwood, I.G. Campbell, J.E. Medlock and Ö.L. Gülder

**Application de la fluorescence de l'iode induite par laser aux mesures de pression, température et vitesse** 24
by X. Lefebvre and B. Leporcq

**Development of Planar Laser Induced Fluorescence for Fuel: Application to Gas Turbine Combustion** 25
by D.A. Greenhalgh, D.J. Bryce, R.D. Lockett and S.C. Harding

**High-Temperature Surface Measurements of Turbine Engine Components Using Thermographic Phosphors** 26
by S. Alaruri and A. Brewington

**Optical Instrumentation for Temperature and Velocity Measurements in Rig Turbines** 27
by I. Ceyhan, E.M. d'Hoop, G.R. Guenette, A.H. Epstein and P.J. Bryanston-Cross

**Application of Laser-Induced Fluorescence (LIP) to Liquid-Propellant Rocket Engine Testing** 28
by C.W. Brasier, J.A. Drakes and M.A. Simmons

**Paper 29 withdrawn**

SESSION VI: MECHANICAL

**Meeting the Advanced Instrumentation Needs of the Integrated High Performance Turbine Engine Technology and High Cycle Fatigue Programs** 30
by W.A. Stange

**Optical Blade Vibration Measurement at MTU** 31
by M. Zielinski and G. Ziller

**Turbomachinery Blade Tip Measurement Techniques** 32
by S. Heath, T. Slater, L. Mansfield and P. Loftus

**Vibrational Analysis of Engine Components Using Neural-Net Processing and Electronic Holography** 33
by A.J. Decker, E.B. Fite, O. Mehmed and S.A. Thorpe

**Mesure non-intrusive de la vitesse de régression d'un matériau énergétique (Non-Intrusive Measurement of an Energetic Material Regression Rate)** 34
by F. Cauty

**Solid Rocket Propellant Behaviour During Static Firing Test Using Real Time X Ray Radioscopy** 35
by J.M. Tauzia and P. Lamarque

**Developments in High Energy X-Ray Radiography of Running Engines** 36
by M.J. Allen and J.D. Rogers

SESSION VII: FILMS

**Measurement of Unsteady Wake-Boundary Layer Interaction Using Hot Films** 37
by Z. Gete and R.L. Evans

**Measurements With Surface Mounted Hot-Film Sensors on Boundary Layer Transition in Wake Disturbed Flow** 38
by V. Haueisen, T. Schröder and D.K. Hennecke

**Paper 39 withdrawn**

**Time Resolved Measurements of Turbine Blade Flow Phenomena** 40
by T.E. Diller, W.F. Ng and J.A. Schetz

**Overcoats for the Improved Performance of PdCr High Temperature Thin Film Strain Gages** 41
by O.J. Gregory, S.E. Dyer and J.D. Cooke

**High Temperature - Thin Film Strain Gages Based on Alloys of Indium Tin Oxide** 42
by O.J. Gregory, J.D. Cooke and J.M. Bienkiewicz

**Paper 43 withdrawn**

SESSION VIII: LASER PLANAR MEASUREMENTS - PART 1

**Optical Diagnostics for Cryogenic Liquid Propellants Combustion** 44
by L. Vingert, M. Habiballah, P. Gicquel, E. Brisson, S. Candel, G. Herding, R. Snyder, P. Scouflaire, C. Rolon, D. Stepowski, A. Cessou, R. Bazile, P. Colin, S. Guerre, M. Péalat, F. Grisch and P. Bouchardy

**A Quantitative 2D Density Measuring System using UV Rayleigh Scattering at an Atmospheric Wind Tunnel** 45
by C. Jakiel, K. Fielder and O. Sieber

**Particle Image Velocimetry Measurements from the Stator-Rotor Interaction Region of a High Pressure Transonic Turbine Stage at the DERA Isentropic Light Piston Facility** 46
by K.S. Chana, N. Healey and P.J. Bryanston-Cross

SESSION IX: LASER PLANAR MEASUREMENTS - PART 2

**The Unsteady Structure of Simulated Turbine Film Cooling Flows from PIV** 47
by R.B. Rivir, S.P. Gogineni, L.P. Goss and D.J. Pestian

**Using the Laser Light Sheet Technique in Combustion Research** 48
by P. Voigt and R. Schodl

**Application of Two-Color Digital PIV for Turbomachinery Flows** 49
by S. Gogineni, J. Estevadeordal, B. Sarka, L. Goss and W. Copenhaver

**Recent Progress in Whole-Field Non-Intrusive Measurements of 3-D Velocity Vectors and Particle Size** 50
by C.S. Moraitis, D. Tisserant and F.A.E. Breugelmans

**Demonstration of PIV in a Transonic Compressor** 51
by M.P. Wernet

**Applications of Three Dimensional Doppler Global Velocimetry to Turbomachinery and Wind Tunnel Flows** 52
by I. Roehle and R. Schodl

# Theme

Improving the performance, operability, durability and economy of propulsion engines is vital to maintaining NATO's air defense capabilities. Advances in propulsion will provide future generations of aircraft and missiles with extended range, greater pay load capability, and improved lethality performance. This will require radical changes in many aspects of engine technology such as much higher temperatures, higher tip speeds, new metal/composite/ceramic materials together with radical changes in design philosophy. Implementing the advanced technologies will require amongst other prerequisites the ability to measure and to monitor key internal gas and structural characteristics.

PEP conducted a technical symposium of Advanced Instrumentation for Aero Engine Components in May, 1986. Since that time significant progress has been made e.g. in vibration analysis and surface pressure measurements for rotating turbine blade components, in temperature measurements and many other areas. Techniques having potential application to operational systems have been developed and need to be widely applied.

This symposium will address non-intrusive optical vibration measurement and analysis, neutron diffraction and laser speckle interferometry; temperature measurements of the new materials such as ceramics and composites, addressing amongst other things imbedded sensors; coherent anti-stokes Raman spectroscopy, laser anemometry, holography, pressure sensitive paint and others; highly advanced concepts such as smart structures, gas path laser-induced-fluorescence, super lattice strain sensors.

The Symposium will offer a premier opportunity for propulsion experts from the NATO Nations to discuss and improve technologies from various facilities across NATO and elsewhere putting them to wide application in the defense propulsion sector as well as in civil use. The Symposium will provide a synergistic boost for NATO, in affordability, mobility, flexibility and operational reliability. There is no other event which would serve the focused exchange in the foreseeable future.

# Thème

L'amélioration des performances, de l'exploitation, de la durée et de la rentabilité des propulseurs est indispensable au maintien des moyens de défense aérienne de l'OTAN. Les avancées prévues en matière de propulsion permettront de disposer d'aéronefs et de missiles de portée et de charge utile accrues avec des performances améliorées en léthalité. Ceci nécessitera des changements radicaux au niveau des technologies de propulsion tels que, par exemple, des températures beaucoup plus élevées, des vitesses en bout d'aube plus élevées, des nouveaux matériaux métalliques/composites/céramiques, ainsi que la réorientation en profondeur des principes de conception. La mise en œuvre des technologies avancées nécessitera, entre autres, la possibilité de pouvoir disposer, au préalable, de la capacité de mesurer et de contrôler certaines caractéristiques internes fondamentales des écoulements et des structures.

Le Panel PEP a organisé un symposium sur l'instrumentation avancée pour les composants des moteurs d'avion en mai 1986. Depuis lors, des progrès considérables ont été réalisés, par exemple dans l'analyse des vibrations et du contrôle des pressions superficielles pour les aubes de turbine, ainsi que dans les mesures de températures et dans bien d'autres domaines. Certaines techniques qui ont été développées et qui ont des applications potentielles aux systèmes opérationnels mériteraient une large diffusion.

Ce symposium examinera les méthodes d'instrumentation employées dans quatre domaines:

— la mesure des vibrations et des contraintes, y compris les méthodes optiques non-invasives de mesure de l'analyse des vibrations, la diffraction des neutrons et l'interférométrie à granularité laser;

— les mesures de température effectuées sur de nouveaux matériaux tels que les céramiques et les composites, couvrant entre autres, les senseurs intégrés;

— la mesure des écoulements gazeux aux températures élevées, y compris la spectroscopie Raman cohérente anti-Stokes, l'anémométrie laser, l'holographie et les peintures sensibles à la pression;

— des concepts hautement avancés tels que les structures intelligentes, la fluorescence induite par laser et les capteurs extensométriques pour les très grands maillages.

Ce symposium représente une occasion exceptionnelle pour les experts en propulsion des pays membres de l'OTAN de se réunir afin de discuter des technologies mises en œuvre dans les différentes installations de l'Alliance et autres, en vue de leur amélioration avant de proposer des applications plus larges dans les secteurs de propulsion civils et militaires. La synergie créée par le symposium doit permettre à l'OTAN de réaliser des avancées considérables en termes de mobilité, de coûts de possession, de flexibilité et de fiabilité opérationnelle. A notre connaissance, il n'y a aucune manifestation qui soit organisée autre que ce symposium, qui puisse offrir de tels échanges, dans un avenir prévisible.

# Propulsion and Energetics Panel


Chairman: Prof Dr. D. K. HENNECKE
Fachgebiet Gasturbinen und Flugantriebe
Technische Hochschule Darmstadt
Petersenstrasse 30
64287 DARMSTADT, Germany

Deputy Chairman: Prof. R. S. FLETCHER
Deputy Vice Chancellor
Cranfield Institute of Technology
Cranfield, BEDFORD MK43 0AL, United Kingdom

**PROGRAMME COMMITTEE**

Prof F.A.E. BREUGELMANS (Chairman)
Head Turbomachinery Department
Assistant Director
Von Karman Institute for Fluid Dynamics
Chaussée de Waterloo, 72
1640 Rhode Saint Genese, Belgium

Lt. Col. Ing. M. de Matos G. CHAMBEL
CLAFA/DMA
Av. Vasconcelos
Alfragide
2700 Amadora, Portugal

Dr. F. CULICK
California Institute of Technology
205 Guggenheim
Mail Stop 205-45, Pasadena, CA 91125, USA

Dr. R. L. EVANS
Mechanical Engineering
University of British Columbia
2324 Main Mall
Vancouver, B.C. V6T 1W5, Canada

Mr. K. R. GARWOOD
Rolls Royce plc
P.O. Box 3
Mail Drop OS6
Filton, Bristol BS12 7QE, UK

Major E. GUNES
1 nci Hava Ikmal Bakum Merkezi
26030 Eskisehir, Turkey

Mr. R. J. HILL
Chief of Technology
WL/POT, Building 18, 1950 Fifth Street
Wright Patterson AFB, OH 45433 7251, USA

Prof Dr. P. KOTSIOPOULOS
Hellenic Air Force Academy
Chair of Propulsion Systems
Dekelia, Attiki, Greece

Prof F. LEBOEUF
Directeur Scientifique à l'Ecole Centrale de Lyon
ECL- 36 avenue Guy de Collongue
69131 Ecully Cedex, France

Dr. G. MEAUZE
Coordinateur Turbomachine
ONERA, BP 72
92322 Chatillon Cedex

Dr. C. RUSSO
Director of Aeronautics
NASA Lewis Research Center, MS 3-8
21000 Brookpark Road, Cleveland, OH 44135, USA

Mr. I. SOLLIEN
Norwegian Defence Research Est., (FFI)
P.O. 25
N-2007 Kjeller, Norway

Prof. G. TORELLA
Accademia Aeronautica
Dipartimento di Scienze Applicate al Volo
80078 Pozzuoli (Napoli), Italy

Prof. H. WEYER
Direktor
Institut fuer Antriebstechnik
Postfach 90 60 58
D-51140 Köln, Germany

HOST NATION COORDINATOR
Prof. F.A.E. BREUGELMANS

PANEL EXECUTIVE OFFICE

From Europe
PEP, AGARD-OTAN
7, rue Ancelle
92200 Neuilly-sur-Seine, France

From US & Canada
PEP, AGARD-NATO
PSC 116
APO AE 09777

Tel.: 33 (1) 55 61 22 87/85- Telefax: 33 (1) 55 61 22 98/99

# Recent Publications of the Propulsion and Energetics Panel

CONFERENCE PROCEEDINGS (CP)

**Interior Ballistics of Guns**
AGARD CP 392, January 1986

**Advanced Instrumentation for Aero Engine Components**
AGARD CP 399, November 1986

**Engine Response to Distorted Inflow Conditions**
AGARD CP 400, March 1987

**Transonic and Supersonic Phenomena in Turbomachines**
AGARD CP 401, March 1987

**Advanced Technology for Aero Engine Components**
AGARD CP 421, September 1987

**Combustion and Fuels in Gas Turbine Engines**
AGARD CP 422, June 1988

**Engine Condition Monitoring — Technology and Experience**
AGARD CP 448, October 1988

**Application of Advanced Material for Turbomachinery and Rocket Propulsion**
AGARD CP 449, March 1989

**Combustion Instabilities in Liquid-Fuelled Propulsion Systems**
AGARD CP 450, April 1989

**Aircraft Fire Safety**
AGARD CP 467, October 1989

**Unsteady Aerodynamic Phenomena in Turbomachines**
AGARD CP 468, February 1990

**Secondary Flows in Turbomachines**
AGARD CP 469, February 1990

**Hypersonic Combined Cycle Propulsion**
AGARD CP 479, December 1990

**Low Temperature Environment Operations of Turboengines (Design and User's Problems)**
AGARD CP 480, May 1991

**CFD Techniques for Propulsion Applications**
AGARD CP 510, February 1992

**Insensitive Munitions**
AGARD CP 511, July 1992

**Combat Aircraft Noise**
AGARD CP 512, April 1992

**Airbreathing Propulsion for Missiles and Projectiles**
AGARD CP 526, September 1992

**Heat Transfer and Cooling in Gas Turbines**
AGARD CP 527, February 1993

**Fuels and Combustion Technology for Advanced Aircraft Engines**
AGARD CP 536, September 1993

**Technology Requirements for Small Gas Turbines**
AGARD CP 537, March 1994

**Erosion, Corrosion and Foreign Object Damage Effects in Gas Turbines**
AGARD CP 558, February 1995

**Environmental Aspects of Rocket and Gun Propulsion**
AGARD CP 559, February 1995

**Loss Mechanisms and Unsteady Flows in Turbomachines**
AGARD CP 571, January 1996

**Advanced Aero-Engine Concepts and Controls**
AGARD CP 572, June 1996

**Service Life of Solid Rocket Propellants**
AGARD CP 586, May 1997

**Aircraft Fire Safety**
AGARD CP 587, September 1997

**Future Aerospace Technology in the Service of the Alliance: Sustained Hypersonic Flight**
(In) AGARD CP 600 Vol. 3, December 1997

**ADVISORY REPORTS (AR)**

**The Uniform Engine Test Programme** *(Results of Working Group 15)*
AGARD AR 248, February 1990

**Test Cases for Computation of Internal Flows in Aero Engine Components** *(Results of Working Group 18)*
AGARD AR 275, July 1990

**Test Cases for Engine Life Assessment Technology** *(Results of Working Group 20)*
AGARD AR 308, September 1992

**Terminology and Assessment Methods of Solid Propellant Rocket Exhaust Signatures** *(Results of Working Group 21)*
AGARD AR 287, February 1993

**Guide to the Measurement of the Transient Performance of Aircraft Turbine Engines and Components** *(Results of Working Group 23)*
AGARD AR 320, March 1994

**Experimental and Analytical Methods for the Determination of Connected — Pipe Ramjet and Ducted Rocket Internal Performance** *(Results of Working Group 22)*
AGARD AR 323, July 1994

**Recommended Practices for the Assessment of the Effects of Atmospheric Water Ingestion on the Performance and Operability of Gas Turbine Engines** *(Results of Working Group 24)*
AGARD AR 332, September 1995

**Structural Analysis and Failure Prediction of Solid Propellant Grains** *(Results of Working Group 25)*
AGARD AR 350, December 1997

**CFD Validation for Propulsion System Components** *(Results of Working Group 26)*
AGARD AR 355, May 1998

**LECTURE SERIES (LS)**

**Design Methods Used in Solid Rocket Motors**
AGARD LS 150 (Revised), April 1988

**Blading Design for Axial Turbomachines**
AGARD LS 167, June 1989

**Comparative Engine Performance Measurements**
AGARD LS 169, May 1990

**Combustion of Solid Propellants**
AGARD LS 180, July 1991

**Steady and Transient Performance Prediction of Gas Turbine Engines**
AGARD LS 183, May 1992

**Rocket Motor Plume Technology**
AGARD LS 188, June 1993

**Research and Development of Ram/Scramjets and Turboramjets in Russia**
AGARD LS 194, December 1993

**Turbomachinery Design Using CFD**
AGARD LS 195, May 1994

**Mathematical Models of Gas Turbine Engines and their Components**
AGARD LS 198, December 1994

**AGARDOGRAPHS (AG)**

**Measurement Uncertainty within the Uniform Engine Test Programme**
AGARD AG 307, May 1989

**Hazard Studies for Solid Propellant Rocket Motors**
AGARD AG 316, September 1990

**Advanced Methods for Cascade Testing**
AGARD AG 328, August 1993

**REPORTS (R)**

**Application of Modified Loss and Deviation Correlations to Transonik Axial Compressors**
AGARD R 745, June 1990

**Rotorcraft Drivetrain Life Safety and Reliability**
AGARD R 775, June 1990

**Propulsion and Energy Issues for the 21st Century**
AGARD R 824, March 1997

**Impact Study on the use of JET A Fuel in Military Aircraft during Operations in Europe**
AGARD R 801, January 1997

**The Single Fuel Concept and Operation Desert Shield/Storm**
AGARD R 810, January 1997 (*NATO Unclassified*)

**Active Combustion Control for Propulsion Systems**
AGARD R 820, September 1997

Technical Evaluation Report

90th Symposium of the Propulsion and Energetics Panel of AGARD on the topic of Advanced Non-Intrusive Instrumentation for Propulsion Engines

***Dr. R.W. Ainsworth***
***Oxford University***
***Department of Engineering Science***
***Park Road***
***Oxford, 0X1 3PZ, UK***

# 1. Summary

The objectives of holding this symposium were clearly met, in terms of assembling a large number of high quality papers for presentation to an appropriate audience on a wide range of advanced non-intrusive instrumentation techniques for use in propulsion engines. This perhaps was not surprising since over ten years had elapsed since the last such forum. The committee were to be congratulated for their efforts in producing such a relevant programme. The conclusions which I drew were as follows:

1. There has been very significant progress made in advanced non-intrusive measurement techniques for use in propulsion engines in the last ten years in terms of furtherance of knowledge.

2. There has been an impressive amount of guidance from the applications, and thus the research programmes have a great degree of relevance to future R & D programmes in propulsion system technology, and the way in which this will interact with military planning.

3. This massive progress has been made possible by the high degree of enthusiasm and commitment of the research community, who are clearly motivated by their work. Every means should be made of maintaining this commitment.

4. All the work reported at this symposium is relevant to the stated goals.

5. There have been many real and significant successes reported of particular relevance to the ultimate application. There were also some failures, and a degree of realism is required in understanding that it is impossible to make progess without this aspect.

Consequently, I would recommend:

1. A continuation of the process of rendering the measurement techniques fit for routine application, by for example concentrating on the robustness of the technology, such that application by the non-specialist continues to expand.

2. A continuation of the development of new ideas, such as high bandwidth whole-field measurements to determine turbulence structures for flow modellers.

3. Devotion of effort to ensure that new ideas are taken towards maturing technology.

4. To maintain a careful watching role over the eventual application, to ensure that research and development work continue to be entirely relevant to the needs of propulsion technology.

5. To ensure that the necessary feedback mechanism is in place, in terms of enabling the researchers to be sure that they are working on relevant techology (targeting).

This symposium has provided a most valuable feedback forum to ensure not only that the engine manufacturers and developers are aware of the state of development of the various advanced techniques, but also that the technique researchers and developers themselves see where the priority areas lie in terms of the applications. I can quite categorically state that no other suitable forum exists in such an apposite context. Therefore, I strongly recommend that, in order for this healthy research and development area, which is so relevant to the extension of propulsion capabilities to continue to flourish, the highest priority should be given to ensuring that in the new NATO RTO organisation, an equivalent forum is established with some urgency

## 2. Introduction

The subject for this 90th and final Symposium of the Propulsion and Energetics Panel of AGARD was that of Advanced Non-Intrusive Instrumentation for Propulsion Engines. In the past the activities of the Propulsion and Energetics Panel has encompassed all aspects of aerospace propulsion such as turbojets, turboshaft engines, ramjets, and solid and liquid propellant rockets. The theme of this symposium was cast in terms of the importance of improving performance, operability, economy and durability of propulsion engines in order to maintain NATO's air defence capabilities. In order to implement with some degree of confidence advanced methodologies and technologies to achieve these goals, it is evident that the ability to measure and monitor key internal gas and structural characteristics must be required. This is where Non-Intrusive Instrumentation might be expected to play a large and increasingly important role.

The symposium was organised in such a way as to solicit papers in the following four areas:

vibration and strain measurements
temperature measurements of new materials
gas flow measurements, particularly at higher temperatures
highly advanced techniques, such as laser-induced-fluorescence,

and in general succeeded greatly in attracting high quality papers covering very advanced techniques, which are set out in more detail below. There is no doubt that a highly active and motivated research community has busied itself in producing many tools which are of direct use to the propulsion system manufacturers. Naturally, these tools are at different stages of development, and these stages of development are discussed in the following text.

## 3. Evaluation

The degree of sophistication of the techniques on display was most marked, and the progess over the last ten years has been rapid. However, equally impressive was the number of times that presenters talked about the need to make their technology robust, and as easily applicable in difficult circumstances as possible. It seems that there has been a great concentration on this aspect of technology, which must be of comfort to the propulsion system manufacturers and users.

I would like to categorise the significance of the symposium in the way in which it has addressed its objectives by looking at the contents in three different ways, or indeed perhaps by posing three questions. Firstly, how widespread amongst the NATO community are these developments? Secondly, which branches of propulsion system technology are being exposed to the techniques? Thirdly, are there projects at all stages of development (as befits a healthy programme area) in terms of new technologies, maturing technologies, and production technologies capable of widespread application by non-specialists?

The first is easily answered. In geographic terms, there was indeed widespread use amongst the NATO community of non-intrusive techniques to monitor the performance of propulsion engines. The geographic distribution of the number of papers presented by each country was as follows: U.S.A. 16; U.K. 10; Germany 10; France 6; Canada 3; Portugal 2; Greece 1; Belgium 1. In addition, there were representatives from the following countries at the meeting: Netherlands; Spain; Italy; Turkey.

For the second question, I examined the component parts of propulsion systems, to see which technologies were being applied in each area, with a view to determining whether there was a good spread of applications. In looking at this, it is perhaps worth being tediously detailed to record the results, which I present in tabular form:

**Aerothermal**

| | |
|---|---|
| Combustors (13 papers): | UV absorption; Infra-Red Spectroscopy (IRS); Coherent Anti-Raman Spectroscopy (CARS); Rayleigh scattering; Fourier Transform Infra-Red Spectroscopy (FTIRS); Laser Doppler Anemometry (LDA); 3D PDA; Laser Induced Incandescence (LII); Planar Laser Induced Fluorescence (PLIF); Laser Induced Iodine Fluorescence (LIIF); DIAL. |
| Turbines (13 papers): | 3D LDA; Laser two Focus anemometry (L2F); Liquid crystals (LX); Thermographic Phosphors (TGP); Theremocouples (T/C); Thermal Paints (TP); UV Rayleigh scattering; Particle Image Velocimetry (PIV); Laser Induced Fluorescence (LIF); Hot Film Gauges (HFG); This film gauges (TFG); Pressure Sensors (PS); Two Colour Digital PIV (2CDPIV); Shadowgraph and interferometry. |
| Compressors (8 papers): and fans | L2F; L2F- 3D; LDA; Pressure Sensitive Paints (PSP); Temperature Sensitive Paints (TSP); 2CDPIV; PIV. |
| General (3 papers): | Pyrometry; 3D PIV; Doppler Global Velocimetry (DGV). |
| Rockets (1 paper): | LIF. |

**Structural**

| | |
|---|---|
| Compressors and rocket fuel | Tip measurement; Holography; Ultrasound; X-ray; High temperature strain gauges. |

The conclusion from this was that there was a good spread of instrumentation techniques being applied to all important technology areas.

In answering the third question as a diagnosis of the health of the programme area, I endeavoured to split the technology developments into three areas: new technology; medium maturity techniques; and highly productionised techniques capable of operation by non-specialists. My thesis was that in order to maintain a competitive position technically, components in all three categories were required. Naturally, these divisions are somewhat artificial, and it is difficult to be entirely categorical about some techniques: ie they straddle the borders between categorisations. Again, I present this in tabular form:

| | |
|---|---|
| New techniques: | DGV; PSP; UV Rayleigh scattering. |
| Medium maturity: | PIV in compressible flows (high speed); Spectroscopic methods; 3D laser techniques. |
| Productionised: techniques. | LDA; L2F; 2D laser techniques in general; PIV in lower speed flows; some spectroscopic techniques. |

I was particularly impressed to find such a concentration on making sure that techniques could be applied in a robust manner in difficult environments. The specialist had addressed the problem of making his technique accessible to the non-specialist. I found that there were indeed technologies at all stages of development, so the prospect of paucity of tools in the future is diminished. I believe that the research community in this area is healthy, has good guidance from application requirements, and is characterised by a high degree of enthusiasm.

In addition to these formal classifications given above, I would like to add here a breakdown for the technical enthusiast in terms of (a) difficult/heroic/valiant work; (b) classic work; and (c) encouraging work. I would put the work on L2F in a centrifugal compressor, UV Rayleigh scattering for density measurement, and 3D-PIV into the first category. Into the second category, I would select the work on Pressure Sensitive Paint from Purdue, and the use of hot film sensors for separation detection in LP turbines. Finally, into the third, I would feel very encouraged by the work on PIV in transonic flows, particularly the attention which has been paid to making the technique robust.

A detailed paper-by-paper summary follows.

Paper 1

On the Aerotherochemistry of Recirculating Premixed Flames with and without Swirl

This paper describes the recent progress in the analysis of the nature of turbulent premixed flames stabilised behind a baffle. Laser based techniques were used for velocity and temperature measurement. It was shown that the swirl attenuated the turbulent heat transfer rate, due to the decrease of temperature across the reacting zone. The experimental technique was based on a combination of laser Doppler velocimetry techniques, combined with a Rayleigh scattering detection system. These techniques were used to produce simultaneous measurements of time-resolved velocity and temperature in the near wake of premixed recirculating flames.

Paper 2

The Simultaneous Measurement of Velocity, Pressure, Temperature and Heat Release in a Oscillating Flame

This paper describes the detailed physics of the flow in a pulsed premixed turbulent flame, obtained by analysing experimental results. Time-resolved measurements of velocity, temperature, pressure and light emission were obtained. This is of interest to the field of low NOx combustors. Increasing the rate of turbulent mixing offers the possibility of reducing NOx emissions. There is a drive to explain the coupling between pressure oscillations and heat release in combustion, hence the need to look at the microscopic physical process. This is the first time that such a detailed time resolved spatial distribution of phase averaged radicals has been obtained.

Paper 3

Flow Field Investigation within a High Speed High Pressure Centrifugal Compressor

Detailed L2F measurements were reported within the small, highly curved impeller passage of a high-speed high-pressure centrifugal compressor. The results were shown to be in good agreement with the expected analytical results in the potential flow entrance region. A good explanation was proposed of the vortical mechanisms within the blade passages, which was substantiated by the experimental results. It was thought in particular that the tip clearance flows had a major influence on the location of low momentum fluid.

Paper 4

3-D LDA Measurements in an Annular Cascade for Studying Tip Clearance Effects

The context of this paper was the paucity of information available in terms of detailed 3-D compressible flow field measurements inside turbomachines. Consequently, developments are required to apply a 3-D LDA measurement system to the tip clearance flow within an annular cascade. Sample measurements were compared with a conventional 5-hole probe in terms of pitch angle, yaw angle and velocity. The agreement with the first two was very good, whilst the latter was slightly disappointing. This was thought to be due to slightly different

atmospheric conditions. On a practical point, good details are given in the paper on the technology employed to address the problems of window fouling.

Paper 5

Investigation of the Spray Dynamics of Aeroengine Fuel Injectors under Atmospheric and Simulated Pressure Conditions

The thrust of this paper was to study the two phase flowfield in the near-field of a fuel injector operating at atmospheric and simulated engine conditions, using a commercial 3D Phase Doppler Anemometer (PDA). In particular, a new algorithm was developed for calculating injected mass flux from three components of velocity. A local enrichment of the spray due to reduced dispersion was identified, and this was thought to influence NOx emissions and soot production.

Paper 6

Laser Two Focus Anemometry (L2F-3D) for Three-Dimensional Flow Analysis in an Axial Compressor

Emphasis is given to the requirement of understanding the three dimensional nature of the flow in highly loaded , high speed turbomachines, and the consequent need to employ L2F-3D anemometry. The paper presents a statistical calculation method for first and second order moments of the velocity data derived from the 3D-L2F system. Validation of the analysis was undertaken with reference to measurements made in a free jet. Finally the system was applied to the tip leakage flow in a highly loaded compressor. The basic problem lies in the non simultaneous measurement of the three components of velocity, and the postulated analytical method makes progress with the application of this technique.

Paper 7

Non-Intrusive Measurement Technique for Propulsion Engines

A method of using combined gas and metal thermal patterns in the infrared radiation spectrum was used to evaluate gas path patterns to help in diagnosing faults at early stages of deterioration. The method had been used successfully to detect faulty fuel nozzles and combustors. It was shown that the infra-red system allowed the mapping of the whole thermal field at the turbine exit, much superior to single point measurements which can be misleading.

Paper 8

Application of FTIR Spectroscopy to Measurement of Gas Turbine Engine Exhaust Emissions

Fourier Transform Infrared spectroscopy raises the spectre of real time multicomponent gas analysis with the possibility of in-flight continuous monitoring of pollutant levels. This paper describes recent non-intrusive single ended passive measurements of gas temperature and concentration in the exhaust plume of a Rolls-Royce Avon engine, specifically in the 1m free space between the jet pipe nozzle and the detuner entrance. Emphasis was placed on the remote siting of the spectrometer to avoid vibration, viewing down a 16cm aperture reflective telescope. In this application, the system was shown to identify the spectral lines of CO and $CO_2$, and to measure their intensities. Gas temperatures were calculated from saturated $CO_2$ band radiance; good agreement with the thermocouples was achieved demonstrating the validity of the technique. Two distinct technology changes, use of the telescope, and use of an Insb detector, had both contributed to improved measurements over earlier variants. The future looks glowing for this technology in comparison with gas sampling, with IR spectroscopy remotely monitoring a number of chemical compounds simultaneously.

Paper 9

DIAL Measurements on a Gas Turbine Exhaust

This paper examines the application of the technique of DIAL (Differential Absorption of LIDAR (Laser Induced Distance Ranging)) as a non-intrusive measurement of emissions from a gas turbine. A tuneable laser source gives LIDAR both range and spectroscopic capabilities, with attenuation, in comparison with a reference beam, giving the number of molecules of the target species. The objective of the test programme was to establish the applicability of DIAL as a technique for plume emission measurement. The conclusion was that useful measurements could indeed be made, being within 25 % of intrusive probe measurements. Future objective: to try to understand plume chemistry.

Paper 10

UV Absorption Measurements of Nitric Oxide Compared to Probe Sampling Data for Measurements in a Turbine Exhaust at Simulated Altitude Conditions

The investigators were interested in gaining an insight into exhaust emission variation as a function of combustor parameters and altitude at standard day conditions. This paper details the NO-UV absorption techniques available, comparing the results with probe sampled data.

Paper 12

Laser 2-D Focus Measurements on a Turbine Cascade with Leading Edge Film Cooling

The fluid mechanics for the flow around the leading edge of a turbine blade with film cooling ejection are very complex. In this paper 2D and 3D Laser two Focus measurements were especially selected to probe the flow volumes very close to the blade walls. The systems were applied to a three blade large scale cascade, and the paper focuses mainly on the results obtained rather than the measurement technology. Impressive details of the flow were presented.

Paper 13

Application of 3D-Laser Two Focus Velocimetry in Turbomachine Investigations

A transonic single stage compressor was commissioned with a view to enabling public access to L2F measurements made in engine representative conditions. In this investigation a newly developed 3D-L2F velocimeter was applied to this rig. A special feature was the design of seeding probes, placed upstream of the measurement volume to increase particle count rates and thus to reduce experiment run time. Some secondary flow vectors were presented.

Paper 14

Characterisation of Gas Turbine Combustion Chambers with Single Pulse CARS Thermometry

Three different combustion chambers were investigated using a mobile single pulse CARS (Coherent Anti-Roman Spectroscopy) system. Specifically, mean temperature and describing statistics were obtained with an accuracy of up to ± 7%. Details of the physics of the flow in the three different combustors are discussed in the light of the measurements made.

Paper 15

CARS Diagnostics on Model Gas Turbine Combustor Rigs

This paper incorporates a general review of CARS technology, as currently used in Rolls-Royce, discusses its limitations, and outlines future strategy. According to the paper, the technique is the only non-intrusive technique to have provided temperature information with liquid fuelled combustion rigs. The drawbacks were also discussed: the fact that it is a point-wise technique; and the time taken to extract temperatures from spectra. The possibility of real-time processing using neural networks was raised. An impressive agreement between measurement and CFD was demonstrated, though the measurements failed to match the predicted highest temperatures.

Paper 16
Recent Developments in the Application of Laser Doppler Anemometry to Compressor Rigs

The paper discusses the application of LDA to a transonic fan rig, the choice of LDA rather than L2F being driven by rig running costs. One of the objectives of the work was to engineer a system which could be applied to a rig in one day. A 5 axis computer controlled traverse system allowed, for example, the ability to input a CFD grid for measurement positions The measurements presented, taken from the transonic fan, demonstrated that the objectives had been met.

Paper 18

Optical Measurements of Surface Pressure and Temperature in Turbomachinery

Pressure sensitive paint has been employed in large scale wind tunnel experiments in the US for approximately ten years. The technique uses molecular spectroscopy, in terms of monitoring the emitted radiation, when a surface coated in the particular paint is illuminated with a UV light source. Intensity of radiation is related to oxygen partial pressure. This paper demonstrates the use of both pressure and temperature sensitive paints in a transonic compressor. Some problems were encountered with camera (detector) performance.

Paper 19

Rotor Blade Pressure Measurements in Rotating Machinery Using Pressure and Temperature Sensitive Paints

This presentation gave a very clear exposition of the background and application of pressure and temperature sensitive paints. Time response performance was addressed, together with pressure/temperature sensitivity, roughness effects, photodegradation, shear etc. The concept of using two fluorescent molecules in one binder matrix was outlined. A transonic aerofoil application of the technique clearly showed shock positions, and comparisons with pressure tap data was good. Results were clearly demonstrated from the Purdue Axial Fan facility, and comparison with CFD was shown to be reasonable. Temperature dependence of pressure sensitive paint was still seen to be an issue.

Paper 20

Use of Liquid Crystal Techniques to Measure Film Cooling Heat Transfer and Effectiveness

This paper outlines a transient experimental technique using double wideband liquid crystals applied to the surface of a nozzle guide vane with film cooling. This technique was used to measure the heat transfer coefficient and the cooling effectiveness at engine representative Mach and Reynolds numbers.

Paper 21

Surface Temperature Measurement in Turbines

The paper discusses the importance of establishing the surface temperature of components in gas turbines, to allow component life to be established accurately, and to valid the computational models. Three techniques are reviewed: thermal paints; thin film thermocouple; and thermographic phosphors. In the case of the first technique, emphasis was placed on digital and automated analysis. In the second, the advantages of surface rather than embedded thermocouples were outlined. In the third, the potential for measurements to be made on rotating blades was expounded.

Paper 22

Effective Spectral Emissivity Measurements of Superalloys and YSZ Thermal Barrier Coating at High Temperatures Using a 1.6 micron Single Wavelength Pyrometer

The paper drew attention to the fact that single wavelength infra-red pyrometers were often used for measuring the surface temperatures of gas turbine components non-intrusively, but that inferring surface temperature from spectral radiance without knowing emissivity is problematic. The spectral effective emissivities of five materials were presented.

Paper 23

Development and Application of Laser Induced Incandescence (LII) as a Diagnostic for Soot Particulate Measurements

This paper addresses the use of a Nd:YAG laser as the pulsed light source for the diagnostic technique of Laser Induced Incandescence. The experimental approach was described together with theoretical (numerical) modelling of the expected signal variations with time and particle size. Preliminary experiments were conducted in order to demonstrate the feasibility of ultimately applying LII to a gas turbine combustor, in a confined bluff-body stabilised turbulent diffusion flame.

Paper 25

Development of Planar Laser Induced Fluorescence for Fuel: Application to Gas Turbine Combustion

The objective of this work was the provision of high resolution instantaneous two-dimensional images of liquid and vapour fuel concentration in operating turbine combustors, using Planar Laser Induced Fluorescence, a technique developed during the early 1990s. The technique is demonstrated in three measurement configurations. The first was a simple gas-gas jet mixing experiment where acetone at 2% by volume was introduced into a nitrogen jet. Impressive comparisons with accepted theory were made. The second was a double annular conventional combustor where mineral oil was seeded with PPO and naphthalene. Individual fuel injector performance was visible. In the third application, a lean pre-vapourised pre-mixed combustor, imaging of both the liquid and vapour phases was performed, together with different boiling-point fractions. The technique can now be applied to gas turbine combustors.

Paper 26

High Temperature Surface Measurements of Turbine Engine Components Using Thermographic Phosphors

A technique using rare earth thermographic phosphors applied to the surfaces of turbine components and energised with radiation from a laser in order to ascertain surface temperature was described. The main advantage of this LIF technique in comparison with pyrometry was seen to be insensitivity to reflected radiation from other parts and from particles. Basically, the phosphor has a decay time which is a function of temperature.

Paper 27

Optical Instrumentation for Temperature and Velocity Measurements in Rig Turbines

The need for robustness in developing an engineering utility approach to practical measurements of velocity, gas and temperature in transonic compressor and turbine rigs was emphasized. Constraints which were faced included optical access, contaminants, vibration, temperature and safety. PIV was selected for velocity measurement and $0_2$ LIF for temperature measurement. The conclusion of the PIV work was that it was practical technique for transonic turbomachines, and good data was available for comparison with CFD. The $0^2$ LIF proved less successful in the transonic flow context, though measurements at low velocities were possible. The author was categoric that previously published broadband PLIF work based around $0_2$ emission for temperature measurement in supersonic flows was totally erroneous in the 300-500 K range.

Paper 28

Application of Laser-Induced Fluorescence to Liquid-Propellant Rocket Engine Testing

This paper describes the use of LIF in rocket engine combustion exhausts to determine flow property information. During the combustion of the fuel, atomic sodium is released, yielding an ideal tracer of the disposition of the fuel in the flow, by providing an intensity signal when fluorescing on excitation from a laser. As the frequency of the laser is adjusted, and data recorded, the shape of the spectral line at each spatial point in the flow (as a function of frequency) is determined, together with the spectral shift. The shape yields temperature, the shift velocity. A number of applications were given with the LIF technique providing good data. Future work will concentrate on reducing the complexity to make a routinely useable system.

Paper 30

Meeting the Advanced Instrumentation Needs of the Integrated High Performance Turbine Engine Technology and High Cycle Fatigue Programs

This paper encompassed a broad review of current research aimed at improving engine structure instrumentation capabilities.

Paper 31

Optical Blade Vibration Measurement at M.T.U.

In this paper, success was demonstrated of an optical blade vibration measurement system, in terms of comparisons made on surging compressors by this method and by conventional strain gauges. Future work will improve reliability, move to automatic operation, increase the efficiency of analysis algorithms, and perform on-line analysis.

Paper 32

Turbomachinery Blade Tip Measurement Techniques

The paper discussed two blade tip measurement techniques: blade tip clearance and blade tip timing. Tip clearance measurement was achieved using FM Capacitance probes, and extensions of up to 7m between the driving unit and the probe tip have eased installation problems. A review of tip-timing methods was presented. It was stated that tip-timing had become an accepted vibration measurement technique, reducing significantly the number of strain gauge measurement points.

Paper 33

Vibrational Analysis of Engine Components Using Neural-Net Processing and Electronic Holography

There is a perceived need for a non-interference inspection procedure to detect structural damage in aero-engine blades, particularly those subjected to high vibration stress amplitudes and frequencies. This paper discusses the use of neural networks to map vibration characteristics obtained from two holograms into a map related to bending strain distribution, which in itself is very sensitive to component damage.

Paper 34

Non-Intrusive Measurements of an Energetic Material Regression Rate

A range of solid propellant burning rate problems were studied using ultrasound techniques. The aim was to produce an industrial NDT tool aimed at the solid propellant manufacturers. Pressure and temperature effects on wave propagation had to be taken into account. Future work would look to improve the coupling between thermo-ablative/erosive codes in dealing with issues of wave reflection.

Paper 35

Solid Rocket Propellant Behaviour during Static Firing Tests using Real Time X-ray Radioscopy

In an application similar to the previous paper, i.e. where there is a need to monitor the behaviour of solid rocket propellant material during ignition and subsequent burning, propellant behaviour was monitored using real time X-ray equipment. Examples of the system in use were given, and results compared twith computer simulation.

Paper 36

Developments in High Energy X-ray Radiography of Running Engines

X-ray radiography has been used for a number of years to investigate the movement of components and changes in their dimensions in the industrial context of, for example, operating aero-engines. This paper describes the development of an Electronic Radiography imaging system, allowing long sequences of high resolution images to be obtained and component movement tracked to sub-pixel accuracy.

Paper 37

Measurement of Unsteady Wake-Boundary Layer Interaction using Hot Films

In this simulation of the interaction between wakes (as might be found in turbomachines) and boundary layers, hot wire anemometry and glue on hot-film sensors were used to diagnose the flow-field. The fluctuating shear stress was measured using the hot-film sensors, which consisted of a 0.1 x 0.9mm Nickel film deposited on a 0.05mm thick insulating foil. The experimental results conclusively showed that the mean skin friction in the case of periodically disturbed boundary layers should not be estimated using steady flow skin friction measurements.

Paper 44

Optical Diagnostics for Cryogenic Liquid Propellants Combustion

The thrust of this investigation was aimed at understanding the physical processes occuring in the combustion of liquid oxygen with gaseous hydrogen. A facility was constructed to study these processes, using the jet flame issuing from a single co-axial injector. The optical methods used included high speed cinematography, light emission from OH radicals, laser induced fluorescence of OH and $O_2$, and elastic scattering from the liquid oxygen jet.

Paper 45

A Quantitative 2D Density Measuring System Using UV Rayleigh Scattering in an Atmospheric Wind Tunnel

In this investigation, Rayleigh scattering was the physical process utilised in an optical system designed to measure density. Measurements were carried out in an atmospheric wind tunnel turbine cascade, using a geometry typical of transonic turbine blades. A laser working in the deep UV region of the spectrum enabled higher Rayleigh scattering signals to be acquired than those working in the visible range. The emitted light was imaged by an intensified CCD. Care has to be taken that Mie scattering from larger particles is neglected correctly. Good results of density measurements with a Mach number of 1 at cascade exit were exhibited.

Paper 46

Particle Image Velocimetry Measurements from the Stator-Rotor Interaction Region of a High Pressure Transonic Turbine Stage at the DERA Isentropic Light Piston Facility

The first PIV measurements to be made in a rotating transonic turbine facility were presented, and compared with CFD predictions. The measurements were made in the stator passage and also in the difficult stator-rotor gap. Digital cameras, together with fibre-optic and rigid optics light delivery systems were used. Polystyrene particles of 0.45μm diameter, suspended in water, were used to seed the flow, at a density of 2 particle-pairs per cubic mm.

Paper 47

The Unsteady Structure of Simulated Turbine Film Cooling Flows from PIV

An ambitious, elaborate and productive experiment was described in which a two colour double-pulsed PIV system was used to investigate turbine film-cooling flows with high free stream turbulence and simulated wake passing. Very detailed conclusions were possible, with information on the structure of film cooling flows in terms of, for example, jet spread, shear layer growth and shear layer frequency.

Paper 48

Using the Laser Light Sheet Technique in Combustion Research

Useful practical details in association with a laser based two-dimensional Mie scattering technique for concentration measurements inside isothermal mixing fields were discussed. Issues addressed included light sheet generation, unwanted reflection suppression, the optimum particle diameter and polarisation.

Paper 49

Application of two-colour Digital PIV for Turbomachinery Flows

This paper aims to evaluate the potential of digital two colour PIV for application in turbomachinery flows. A simple unshrouded fan and a larger shrouded fan were the test vehicles. Valuable lessons were learnt on issues such as seeding, optical access and synchronization of the digital camera with the blade position.

Paper 38

Measurements with Surface Mounted Hot-film Sensors on Boundary Layer Transition in Wake-disturbed Flow

In a classic investigation, boundary layer flows were investigated around a cylinder with undisturbed, periodically disturbed, and steadily disturbed flows. Both surface mounted hot-films and hot-wire anemometry were used to investigate the flow-field. The investigation focused on the use of hot-films to diagnose separation and transition behaviour, demonstrating a most valuable diagnostic with both high spatial and temporal resolutions. The investigators carried their work forward to an LP turbine application, where in detailed interpretation of their results, they were able to identify for example the existence of an oscillating separation bubble. Thus the work can be shown directly to feed into the design and development of state-of-the-art low pressure turbine blading.

Paper 39

Evaluation of Thin-Film Heat Flux Sensors with High Frequency Response Characteristics

Paper not presented.

Paper 40

Time Resolved Measurements of Turbine Blade Flow Phenomena

A transonic blow-down turbine cascade facility capable of operation at engine Reynolds number, Mach number and temperature ratios, for investigating time-dependent flow phenomena was described. Three sources of unsteadiness in engines were modelled separately: shock movement, wakes and free-stream turbulence. Upstream shocks were provided by a novel shock tube and shaper, capable of providing shocks at pre-set timings and of pre-set strengths. Fast response pressure sensors and heat flux meters were used to monitor time-varying phenomena. A video was shown which had been constructed from individual shadowgraphs, assembled into an animation of the dynamic behaviour.

Paper 41

Overcoats for the Improved Performance of PdCr High Temperature Thin Film Gauges

The goal of this work was to improve the stability of PdCr thin film strain gauges under dynamic strain conditions at elevated temperatures. This material is seen as the leading candidate material for high temperature strain gauges. Ultimately, these improvements were demonstrated in the electrical response of these films at high temperatures.

Paper 42

High Temperature - Thin Film Strain Gauges based on Alloys of Indium Tin Oxide

This paper describes the investigation of a semi-conductor oxide film (indium tin oxide) as the material for active strain elements in high temperature thin film strain gauges (temperature up to 1050°C).

Paper 43

Use of Skin Friction Gauges in the French PREPHA programme

Withdrawn

Paper 50

A novel and valiant attempt has been made to obtain 3-D velocity information in a seeded flow-field using an optical/digital processing technique involving holography (holographic particle records). The extraction of the velocity field information was based on the digital processing of the optical Fourier transformation of the particle-field image. Synthetic particle field images were processed satisfactorily, but for real flows optical noise and the size of the seeding material caused difficulties. In particular, the size of the particle diffraction-halo has limited the number of "visible" fringes. Further work is required and underway.

Paper 51

Demonstration of PIV in a Transonic Compressor

This paper encompasses a review of existing PIV knowledge, discusses light sheet generation and delivery, seeding issues, image acquisition and processing, and demonstrates current 2D capabilities in a single stage axial compressor. High quality detailed results are given, and the need to move to 3D PIV is expressed.

Paper 52

Applications of Three Dimensional Doppler Global Velocimetry to Turbomachinery and Wind Tunnel Flows

The novel technique of DGV was discussed and applied to three investigations: the flow-field of a swirl spray nozzle in a cylindrical casing; the wake region of a car; a model of the intake of a fighter aircraft. This is potentially a very important technique for determining "whole field" velocity in that it may offer advantages over PIV. A number of international teams are working on it.

# 4. Conclusions and Recommendations

My conclusions are as follows:

1. There has been very significant progress made in advanced non-intrusive measurement techniques for use in propulsion engines in the last ten years in terms of furtherance of knowledge.

2. There has been an impressive amount of guidance from the applications, and thus the research programmes have a great degree of relevance to future R & D programmes in propulsion system technology and the way in which this will interact with military planning.

3. This massive progress has been made possible by the high degree of enthusiasm and commitment of the research community, who are clearly motivated by their work. Every means should be made of maintaining this commitment.

4. All the work reported at this symposium is relevant to the stated goals.

5. There have been many real and significant successes reported of particular relevance to the ultimate application. There were also some failures, and a degree of realism is required in understanding that it is impossible to make progess without this aspect.

Consequently, I would recommend:

1. A continuation of the process of rendering the measurement techniques fit for routine application, by for example concentrating on the robustness of the technology, such that application by the non-specialist continues to expand.

2. A continuation of the development of new ideas, such as high bandwidth whole-field measurements to determine turbulence structures for flow modellers.

3. Devotion of effort to ensure that new ideas are taken towards maturing technology.

4. To maintain a careful watching role over the eventual applications, to ensure that research and development work continue to be entirely relevant to the needs of propulsion technology.

5. To ensure that the necessary feedback mechanism is in place, in terms of enabling the researchers to be sure that they are working on relevant techology (targeting).

This symposium has provided a most valuable feedback forum to ensure not only that the engine manufacturers and developers are aware of the state of development of the various advanced techniques, but also that the technique researchers and developers themselves see where the priority areas lie in terms of the applications. I can quite categorically state that no other suitable forum exists in such an apposite context. Therefore, I strongly recommend that, in order for this healthy research and development area, which is so relevant to the extension of propulsion capabilities, to continue to flourish, the highest priority should be given to ensuring that in the new NATO RTO organisation, an equivalent forum is established with some urgency.

# Research and Development In the Business Environment of the 21st Century

**Kenneth B. Benson**
**Manager, Instrumentation Engineering**
**Pratt & Whitney**
**400 Main Street**
**East Hartford, CT 06108, USA**

## 1. SUMMARY

The beginning 21st century will provide as significantly different world than what we experienced during the last half of the 20th century. Politics, business and technology how they relate, how they inter-react and how they depend on each other is going through significant and irreversible transition.

The known fixed enemy of yesterday who was dealt with in terms of mega-tons, Star Wars and global reach, has transitioned into limited incursions, minimal collateral damage, and no casualties. The world of commerce has changed from multiple producers, large budgets, national competition and super technology to the world of single producers, decreasing budgets, international cooperation and time to market. Today a company, a university or a government agency can be a customer, colleague and competitor all at the same time.

The research and development community is being forced to come out from under the shade of technology for technology sake and into the bright light of an changing eco-political environment. Not only does the researcher have to understand this strange and sometime alien world but they have to make these changes work for them to increase the technology base, and ensure an environment that will attract the next generation of scientists and engineers.

By having an action plan and realizing that these changes will not be reversed but in fact will accelerate, strategies can be developed that will incentivize the support of basic research and provide quicker transition of technology to the market place.

## 2. INTRODUCTION

Research and development, and specifically basic research, has changed fundamentally and irrevocably from the era following World War II. The linear research model that progressed from basic research to applied research, and then to development as defined by Vannevar Bush, President Truman's science advisor(1) in 1945 is no longer valid. The political and economic forces today are so much different than 10 years ago, much less 50 years ago. Yet the call can be heard from many circles that research moves in a strict stepwise fashion from fundamental work to development. Bush wrote for Truman, "Basic research is performed without thought of practical ends."

Like most myths the linear model is appealingly simple. The research process today is actually a complex feedback model. This is in part driven by the time compression from basic understanding to things in the market place. Now a lot of research is done concurrently with the production to save money and time.

The scientist, the engineer, the researcher has to understand this changing world. Government, industry and universities are changing the mix on who does basic research.

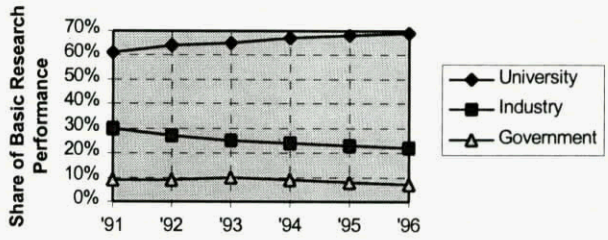


Figure 1. **Who Does Basic Research**

The research and development expenditures are also decreasing.

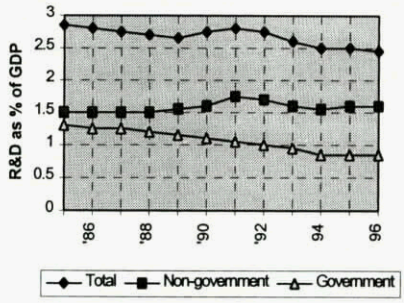


Figure 2. **National R&D Expenditures**

We can be frustrated by the changes in the government, industry or academic policy; feel that we are victims; wonder where the young bright talent has gone or why the lab is being closed. OR we can understand the changes, make them work for us, make the public aware and be an integral part of the business.

This paper will focus on our changing world and offer an action plan for the future of research.

## 3. TODAY'S ENVIRONMENT

Research on all quarters is under attack. The national legislature see the social needs overshadowing the national security explanation that fueled the research process through the Cold War. It has been said that today science is somewhere between the stepchild and the superstar. Researchers must now

*Paper presented at an AGARD PEP Symposium on "Advanced Non-Intrusive Instrumentation for Propulsion Engines", held in Brussels, Belgium, 20-24 October 1997, and published in CP-598.*

be able to relate their work to the list of social problems because these have replaced the treats of the Cold War as a reason for funding.

The business community is faced with intense competition for the shrinking government markets for defense related equipment. The commercial markets are challenged similarly with "reduced time to market" pressures, costs of high technology commodities such as computers, laboratory sensors and materials and quality issue on products that are expected to meet or exceed customer expectations.

Businesses are taking an integrated management approach to maximize the return on investments in technology. Today this means integrating different functional perspectives within the company, integrating supplier and customer perspectives with the internal technology perspective and integrating partner companies' business systems in the context of alliances.

The universities have been a haven for the researcher/teacher. Drawing in the best and the brightest with the well published, world recognized professors and supported by a state-of-the-art laboratory. All this was supported by grants or contracts form government, industry or endowment sources. Today all this has changed. Industry in the U.S., in general, is not likely to increase support of basic research without significant, yet to be identified, incentives. Successful companies will likely continue and even increase funding of basic research efforts as they find new ways to quickly integrate the new - and potentially profitable - knowledge across all levels of their organization. University-based research, at least in the U.S., is at most risk over the next five to ten years. Government support for basic research continues to erode in real dollars. However industrial support for directed basic research in universities could very well increase as a low-risk way of generating new knowledge.

The threats that NATO addresses today are very different than they were for the first 40 years of its existence. Looking at the AGAR mission statement and how the NATO community has changed in faces and geography. The admission for the central European countries that were once part of the Warsaw Pact has added new dimensions and opportunities for NATO. The "common defense posture" has changed from nuclear deterrence and large army engagements, to local conflicts, with ill-defined combatants and rapid response requirements.

The military requirements have to be articulated and absorbed by the research community to ensure they meet NATO and national objectives. New platforms incorporating stealth, that are unmanned and have a multi-role will be demanded.

The consolidation of aerospace and defense business continues globally at an increasing rate. You can be dealing with a company that in the same day is a competitor, customer and colleague. (Aviation Week article)

## 4. WHAT'S IMPORTANT

The words you hear from industry today are "Cost - Quality - Schedule." Proprietary technology is less of a differentiator. Being able to commercialize the technology is the compelling driver. The reason is this: as the more competitive companies demonstrate they can meet these challenges, the performance bar is raised yet again.

A survey by Ladish Co., Inc.(2) shows that competitiveness is the single most important objective of 108 European and U.S. aerospace industry executives that purchase more than $3 billion of finished materials annually.

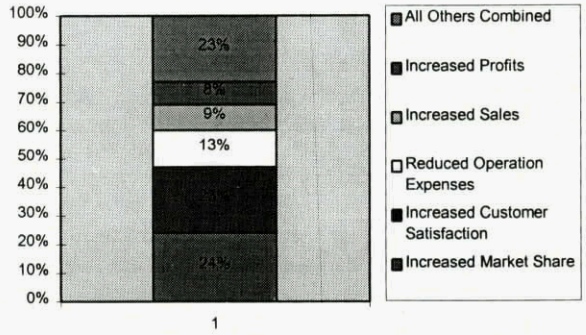


Figure 3. **Most Important Company Objective**

How they plan to achieve these results is even more revealing.

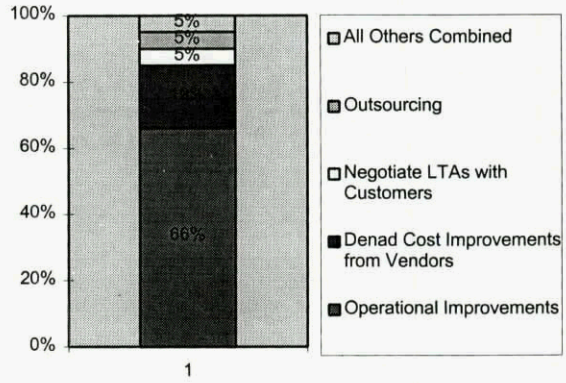


Figure 4. **Preferred Strategy for Sustaining a Competitive Company**

Many companies are adopting lean production strategies. The preferred strategy by 76% of the respondents is redesigning their business processes for greater operational efficiency. The goal is to reduce cycle time. Nearly as many (73%) indicated their companies are pursuing a program of continuous improvements.

The research has to understand these changes and take advantage of the strategic direction changes to ensure their technologies can be commercialized rather than treat commercialization as a purely intuitive, creative process.

If you look at leaders vs. laggards in commercialization you see leading companies:(3)

- Commercialize two or three times the number of new products and processes as do their competitors of comparable size.

- Incorporate two to three times as many technologies in their products.

- Bring their product to market in less than half the time.

- Compete in twice as many products and geographic markets.

The good companies view commercialization as a highly-disciplined system.

Part of the discipline is the introduction of the Integrated Product Development (IPD) process. This process can take different forms and fits but the function remains an integrated, cohesive process that changes from a technical focus to a business focus.

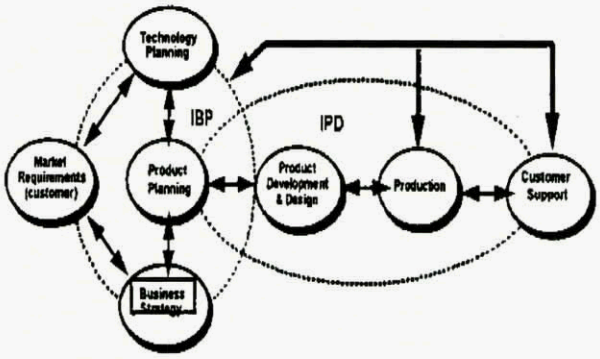


Figure 5. **The Enterprise Model**

The visions are realized through:

- Focusing on process
- Common objectives
- Continued evolution

To bring new products to market quicker the lead time has to be reduced.

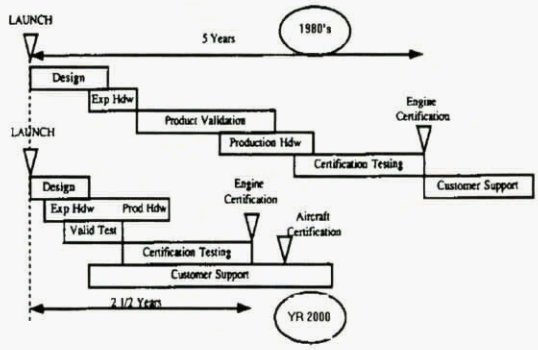


Figure 6. **Reduced Product Introduction Lead-Time**

The focus is on process. The focus is on teams. The focus is on communication. If you as a researcher, scientist or engineer do not understand, are unwilling to join or fail to contribute to the new process your project, your influence and your career will disappear.

## 5. ACTION PLAN

5.1 Understand Your Enterprise

Listen to what your leadership is saying. What are the most enterprise objectives? Is there a strategic plan with defined goals? How is the organization structured and where do you fit in? Understand the language, understand the financial accounting. Plan how to take advantage of the change and influence the change. Be part of the decision making process.

5.2 Explain to the Public

Scientists and engineers must make it part of their mission to explain their work to the public. The speed and accessibility of the public to electronic communication is doubling every 18 months. Web site, cable television, national newspapers all drive public opinion. Effort is needed to interest more students in science careers, educate voter and justify research and development funding to government, industry and academia policy makers. Principle engineers and scientists should be trained to explain their research out of the parochial confines of the scientific community.

We also have to listen and respond to the social and community needs. By being part of the community and an advocate of technology benefits for public good the scientists and engineers can help shape the direction of funding, policy and politics.

5.3 Be Part of the Team

Integrated Product Development, customer focus, technology readiness are all terms used today in describing industry and government initiatives. Know the language that's being used today. Enterprise models, productivity initiatives, process improvements, Kaizen events, process improvements are all the

current buzz words that should "involve" the research community.
Most industrial, scientific and defense communities are developing "road maps"(4) to implement policies and strategies being established for the YR 2000 and beyond. Be sure you are part of the team that is establishing and implementing these road maps.

Represent yourself as part of the team. Present your ideas, concerns and solutions in context of the team mission. Be able to debate the issues without the appearance of being self-serving.

5.4 Keep an Eye on Trends
Where will the technology I know be applied five, ten or twenty years from now?? We should ask this question of ourselves every time we read the newspaper or watch the evening news. How we answer that question can have profound effects on what we will be doing; how we ensure the success of our careers; what business we will be in and where we call home.

Who would have thought 15 years ago that the U.S. nuclear power industry would be considered by many today as a "fading industry." Or that today's P.C. would have as much computing power as the large 1980 mainframe.

New platforms are coming about. The "pilotless" airplane, stronger, agile, cheaper and more deadly than today's fighter may engage the enemy in future wars. As an example, NASA has established the "Three Pillars of Success"(5). Be aware of the goals of these programs. How do you fit in? Or how do you compete? Technology selection is more critical today than in the past. The cost of a false solution or delay in execution can doom an otherwise worthy initiative.

5.5 Maintain Focus
Social needs have overshadowed the national security explanation that fueled the research process through the Cold War. Funding for weapons system has turned into funding for the environment. University-based research, in the U.S. at least, is most at risk over the next five to ten years with the shift from government funding to industrial support. Know who has the deep pockets and what their agendas are. Then design how you can ensure their success. Concentrate on the "vital few." The vital few are the technology investments that provide the breakthrough, the enabling or the cost reduction required for the enterprise. The project value should be assessed on the strategic fit, technical feasibility and financial impact. Focus on the vital few. These will have the most impact and will be valued most by the organization.

5.6 Maintain Flexibility
The rule of survival in a changing environment is "flexibility." The alibi of "we've never done it that way" or "that's not my job" will rapidly make you a person on the outside looking in and exploring alternate career paths. The attitude that has to be demonstrated is "how can I contribute," not "why are they doing this to me." The changes our world is going through are not pre-ordained or being made through divine guidance. They are being driven by the market and the politics of the world. The changes are being executed by people like you and I. There will be mistakes, false starts and redirections. Frustrations will be plentiful and tempers will be frayed. The key success will be understanding, patience, a sense of urgency, and a dose of humor. Flexibility will provide the leadership trait that will encourage the people working with you, support the people that employ you and ensure you remain part of the decision making process.

## 6. CONCLUSION
We are entering the most exciting time of our lives -- the future. Not only is it a new century but a new millennium. The science we have yet to discover is all around us: A cheap, clean and recyclable form of energy; materials that have a strength-to-weight and manufacturability greater than anything we have today; food that is abundant, nutritious and tastes good; freedom from disease, pestilence and want. All of these are noble goals. And all of these will be discovered in the next century. We each have an opportunity to share in their discoveries. We cannot tie our hands by being fixed in paradigms that no longer are valid. The research and development community are where the solutions will come from. Be part of the decision making process!!!

## 7. REFERENCES

(1) Vannevar Bush "Science - The Endless Frontier," 1945.

(2) Velocci, Anthony L. "Survey Underscore Shift in Management Emphasis," Aviation Week and Space Technology, June 9, 1997.

(3) Nevens, Mike; Summe, Greg; Uttal, Bro "Commercializing Technology: What the Best Companies Do," Harvard Business Review, May-June 1990.

(4) Achieving Aeronautics Leadership: Aeronautics Strategic Enterprise Plan 1995 - 2000; Office of Aeronautics, NASA, Washington, DC, April 1995.

(5) Maintaining U.S. Leadership in Aeronautic: Scenario-Based Strategic Planning for NASA's Aeronautic Enterprise, National Research Council, Washington, DC, January 1997.

# ON THE AEROTHERMOCHEMISTRY OF RECIRCULATING PREMIXED FLAMES WITH AND WITHOUT SWIRL

by

D. Duarte, P. Ferrão and M. V. Heitor

Department of Mechanical Engineering

Instituto Superior Técnico

Av. Rovisco Pais

1096 Lisboa Codex

Portugal

## ABSTRACT

This paper describes recent progress in the analysis of the nature of turbulent premixed flames stabilised behind an axisymmetric baffle, which are of fundamental interest in the development of new and cleaner propulsion combustion systems. The work includes the use of laser-based diagnostics for velocity and temperature measurements, which are extended to the analysis of turbulence statistics, including the energy spectrum and typical length scales in a reacting shear layer. The results provided experimental evidence of the extension of the flamelet regime beyond the Klimov-Wiliams criterion. Arguments based on the shape of the weighted joint probability distributions of axial velocity and temperature fluctuations show that the counter-gradient nature of heat flux is derived from large departures from the local mean values.

The influence of swirl in strongly sheared disc-stabilised flames is analysed and the results obtained show that swirl attenuates the rate of turbulent heat transfer due to the decrease of the temperature gradients across the reacting zone, but does not alter the existence of a large zone of flame characterised by non-gradient scalar fluxes.

## 1. INTRODUCTION

In the past many attempts have been performed to extend the knowledge on laminar flames and non-reacting fluid mechanics, to turbulent combustion, but turbulent mixing in flames is altered by the accompanying heat release and can, as consequence, be qualitatively different from that occurring in non-reacting flows. Examples include counter-gradient diffusion, e.g. Libby and Bray (1981), Bray et al. (1985), in either confined non-premixed swirling flames, Takagi et al. (1985), or in unconfined premixed flames, Heitor et al. (1987), Ferrão and Heitor (1995).

Although turbulent flames are characteristic of most of the practical burning devices, their physical structure cannot be regarded as completely understood at the present. As pointed out by Borghi (1985), the detailed study of the fine scale fluctuating structure of turbulent flames is very difficult to investigate experimentally and, consequently, theoretical studies based on physical assumptions suffer from lack of validation. This is the main motivation of the work reported in this paper.

In previous papers we have discussed the occurrence of non-gradient scalar fluxes in turbulent recirculating premixed flames stabilised downstream of baffles, which appear to be particularly influenced by the magnitude of the mean pressure gradients associated with the streamline curvature and are associated with the acceleration of gases across the flame front, Heitor et al (1987), Ferrão and Heitor (1995), Duarte et al. (1996). Most of the analysis which has been presented in flames with practical interest (eg. Takagi et al., 1985, Takagi and Okamoto, 1987, Fernandes et al. 1994) may be considered to represent reacting regimes statistically equivalent to distributed reaction zones and/or well-stirred

*Paper presented at an AGARD PEP Symposium on "Advanced Non-Intrusive Instrumentation for Propulsion Engines", held in Brussels, Belgium, 20-24 October 1997, and published in CP-598.*

flames, but the extent to which the time-resolved nature of the flames affect their propagation remains to be understood. Also, the experimental evidence of the transition between the various combustion regimes remains to be shown, for flames of practical relevance.

As noted by Poinsot et al. (1996), the time-averaged integral scales are unable to represent the multiscale nature of the interaction process between the combustion process and the turbulent flow field. In fact, the turbulent flow features a complex combination of vortices with scales ranging from the integral scale to the Kolmogorov scale. Each of these may be characterised by a length scale and a velocity fluctuation. To describe turbulence/combustion interactions, one has to take into account the existence of these various scales in the flow and, accordingly, build a spectral diagram for each point of the integral combustion diagram. The experimental validation of the combustion regimes and the related difference on the flame structure requires in-flame measurement of length scales and the associated turbulent intensities, which is the main motivation of the present paper. The work includes the analysis of counter gradient diffusion of turbulent heat flux, as reported by Ferrão and Heitor (1995), and correlates its concurrence in practical flames with the shape of weighted joint probability density functions of axial velocity and temperature fluctuations, as described by Hardalupas et al. (1996). The ultimate objective is to provide new insight into the nature of turbulent premixed flames and to provide new data for model development. The practical implication in the context of combustion devices is that the retardation of mixing, which is associated with the occurrence of counter-gradient heat flux, may be technically desirable.

It is important to make clear that in our previous works the occurrence of counter-gradient heat flux has been identified from the analysis of the terms in the conservation equations of the scalar fluxes, which clearly identify the reacting shear layer as the zone where the interaction between the mean pressure gradients and density fluctuations are important (e.g., Ferrão and Heitor, 1995).

This paper shows that even in the regions of the reacting shear layer where there is no evidence of counter-gradient diffusion, the underlying driving mechanism remains important and, therefore, the so-called second moment closures must be used to calculate the flame. To achieve this objective, the method of analysis is that previously used by Cheng and Ng (1985) and, more recently, by Hardalupas et al. (1996) making use of quadrant analysis.

The next section describes the experimental method and gives details of the extension to which laser-based techniques can be used in premixed flames diagnostics. The third and fourth sections present and discuss sample results obtained for non-swirling flames and swirling flames respectively, and the last section provides the main conclusions of the work.

## 2 . THE EXPERIMENTAL METHOD

The laser Doppler velocimeter was based on the green light (514.5 nm) of the laser and was operated in the dual-beam, forward scatter mode with sensitivity to the flow direction provided by a rotating diffraction grating. The calculated dimensions of the measuring volume at $e^{-2}$ were 606 μm and 44 μm. The Rayleigh scattering system was operated from the blue line (488 nm) of the same laser source, which was vertically polarised and made to pass through a 5: 1 beam expander. The light converged in a beam waist of 50 μm diameter, and was collected at 90° from the laser beam direction, through a slit of 1 mm. The collected light was filtered by a 1 nm interference filter and passed through a polariser in order to increase the signal-to-noise ratio. A calibration procedure was implemented in order to compensate for number density dependence on the chemical composition. The uncertainty on the average temperature was quantified as 4%.

The signal was amplified and low pass filtered at 10KHz before digitalisation. The temporal resolution of the system depends on the integration time associated with this filter, which is quantified to be 50μs. This value, associated with the typical flow velocities, give rise to path lengths of about 1mm and, therefore, smaller than the integral length scales in the reaction shear layer. The resolution of the system was confirmed by the measured temperature distributions, which include instantaneous values close to either adiabatic or room temperature, confirming that the system is capable of resolving the temperature fluctuations associated with the premixed flames analysed in this work.

The details associated with the accuracy of the experimental method used, and in particular of the laser Rayleigh scattering, has been discussed by Caldas et al. (1997) and is not reported here.

For the measurements of spatial velocity correlations, the laser light source was operated in multiline and the LRS optical system was replaced by a second dual-beam laser velocimeter mounted on a positioning system which allows the displacement of the control volume of this system relative to that described before, figure 1 b). This second LDV was based on the green light (514.5 nm) of the laser and operated in backscatter mode, with sensitivity to the flow direction provided by a bragg cell. Two interference filters of 1 nm bandwith were used in each optical collection systems, in order to avoid optical interference between the two systems.

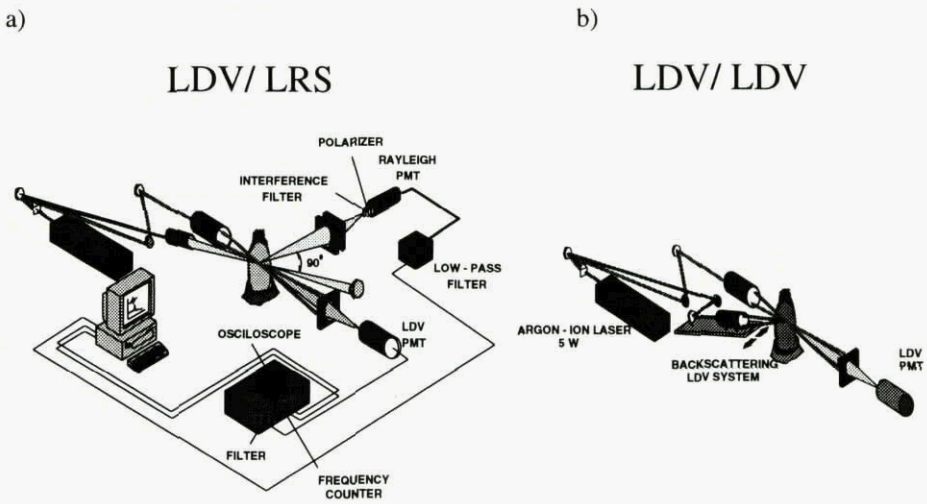


Fig. 1 – Schematic diagram of the instrumentation used: a) Combined LDV/Rayleigh scattering system; b) Velocity correlations measurement.

Two frequency counters (DANTEC, model 55L96) were used to process the Doppler signals and a maximum coincidence time of 1μs was used to decide upon the simultaneity of the measurements. Each measurement was based in a population of N=6144 valid simultaneous velocity time series.

Correlation measurements at small separations can be expected to be influenced by the spatial resolution of the system. However, this does not noticeably affect the determination of the integral length scales, which are the purpose of the present work. The consequence of the limited spatial resolution is that the velocity correlation measured for nominally zero separation is never equal to unity. In practice, this is mainly because the measuring values are bigger than the smaller scales of the flow.

The experimental procedure included the measurement of the axial velocity fluctuations with the two LDV systems, respectively $u_1$ and $u_2$, at each measuring location, r which was followed by successive displacement, $\zeta$, of the backscatter system up to a maximum distance of 17 mm. This procedure allowed the measurement of the lateral velocity correlation coefficient, $g(r, \zeta)$, for a location r, defined as:

$$g(r,\zeta) = \frac{1}{(N-1)} \frac{\widetilde{u''_1}(r)\widetilde{u''_2}(r+\zeta)}{\sqrt{\widetilde{u''^2_1}(\zeta)}\sqrt{\widetilde{u''^2_2}(r+\zeta)}}$$

were $u''_1$, represents the turbulent velocity fluctuations of $u_1$ .

For the results reported here, the velocity correlations obtained were divided by the value measured at zero separation, which was generally about 0.7.

## 3 . CHARACTERISATION OF THE NON-SWIRLING FLAMES

The experiments reported in this section were conducted in unconfined non-swirling premixed flames of air and propane, stabilised on a disk with D=56 mm in diameter, which is located at the exit section of a contraction with 80mm in diameter.

The annular bulk velocity is in the range $10 < U_o(m/s) < 42$, resulting in a Reynolds number, based on a disk diameter, up to $1.5 \times 10^5$. The equivalence ratio was varied between 0.53 and 1, although most of the results characterised in this paper correspond to lean flames, with $\phi = 0.55$. Table 1 characterises the three mean experimental conditions used, which are identified as flame A, B and C.

Table 1 - Characterisation of the experimental conditions.

| Flame | $U_o$ (m/s) | Re | $\phi$ | $S_L$ (cm/s) | $l_F$ (mm) |
|---|---|---|---|---|---|
| A | 10 | 35 700 | 0.64 | 12 | 0.6 |
| B | 20 | 71 400 | 0.64 | 12 | 0.6 |
| C | 42 | 150 000 | 0.64 | 12 | 0.6 |

The analysis and discussion of the experimental results presented in this section is divided in three parts. The first characterises the main features of the typical flame studied and the measurements of the lateral velocity correlation coefficient and the evaluation of the integral scales along the flame. The values obtained are used to define the combustion regime representative of the flame, which is compared to theoretical considerations. The last section summarises the main mechanisms inherent to the turbulent transport of kinetic energy and heat fluxes in the flames considered.

### 3.1 – Experimental Characterisation of the Flame Studied

The most salient features of the mean flow characteristics can be inferred from the measured velocity vectors and isocontours of mean temperature represented in figure 2, for flame C. The results are similar to those found in other baffle-stabilised recirculating flames, in that they exhibit a recirculation region extending up to $L_R/D = 2.23$, where the fluid has a large and fairly uniform mean temperature, surrounded by an annular region of highly sheared fluid where gradients of mean temperature are large. The length of the recirculation zone decreases as the Reynolds number is decreased, with the rear stagnation point located at $L_R/D=1.8$ for $Re=0.7X10^5$ (Flame B).

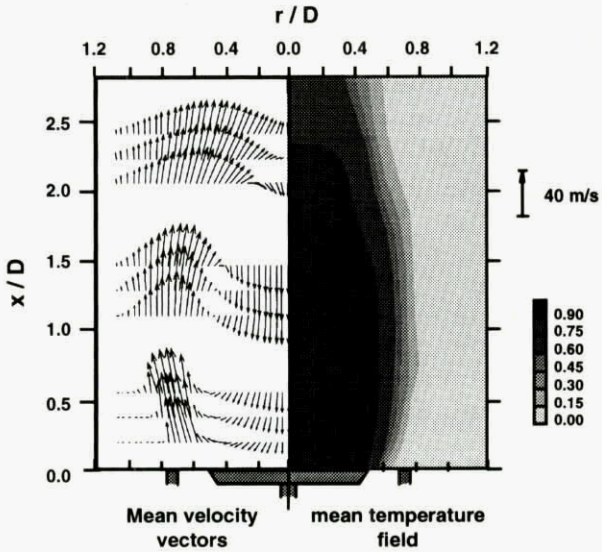


Fig. 2 - Distribution of mean velocity vectors and isotherms along a vertical plane of symmetry for flame C.

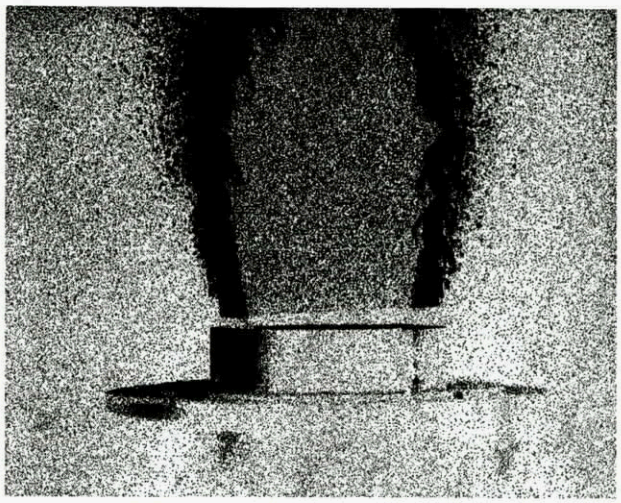

Fig. 3 - Instantaneous flame (B) visualisation during a 9 ns Nd-yag laser pulse.

The isotherms are highly curved for the three conditions studied and reveal non-planar flames oblique to the oncoming reactants. For these conditions, the analysis of the photography of figure 3 shows that reaction occurs along a thin shear layer located between the locus of maximum axial velocity and the locus of the mean separation streamline, which is curved along its length. This curvature varies with the Reynolds number considered and imposes mean velocity effects on the turbulence field in a way which depends on the level of interaction between the gradients of mean pressure typical of the present flames and the associated density fluctuations.

Analysis has shown that along the reacting shear layer turbulence is mainly generated by the interaction between shear strain and shear stress, giving rise to a strongly anisotropic turbulent field with comparatively large axial velocity fluctuations. As the stagnation region is approached, the cross-stream turbulent components increase as a result of the increased importance of the interaction between normal strains and normal stresses in the conservation of turbulent kinetic energy as in other recirculating flows with free stagnation points.

The detailed velocity and scalar characteristics obtained along the present flames are presented elsewhere. Here, attention is focused on the zone which characterises the maximum width of the recirculation zone of the flames considered and Figure 4 shows the temporal distributions of Eulerian time correlations for characteristic points across the reacting shear layer for the flames studied.

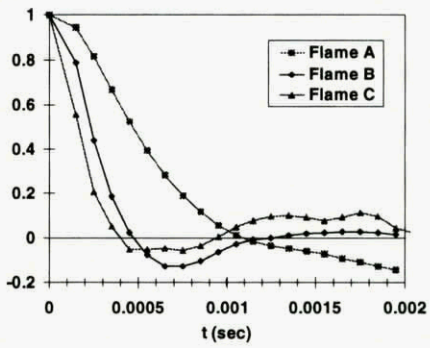


Fig. 4 - Analysis of the flame characteristics as a function of the reynolds number, for $x/l_r = 0.5$: Eulerian time correlations: flame A at r/d = 0.63; flame B at r/d = 0.61; flame C at r/d = 0.64.

Although the radial distributions of time-averaged temperature for the three conditions studied here are qualitatively similar, the analysis above suggests that the temporal structure of the flames is different and the related experimental evidence is provided by the probability-density functions of temperature of Figure 5. While Flame A is characterised by near bimodal temperature distributions across the reacting shear layer with significant probability for intermediate products, the distributions obtained for Flame C exhibit typically the near-Gaussian form characteristic of the distributed

reaction combustion regime. It is clear that the absolute values of the probability distributions are influenced by the shot noise characteristics of the photomultiplier used for the Rayleigh scattering measurements, but the qualitative trends shown in Figure 5 are not affected by experimental accuracy.

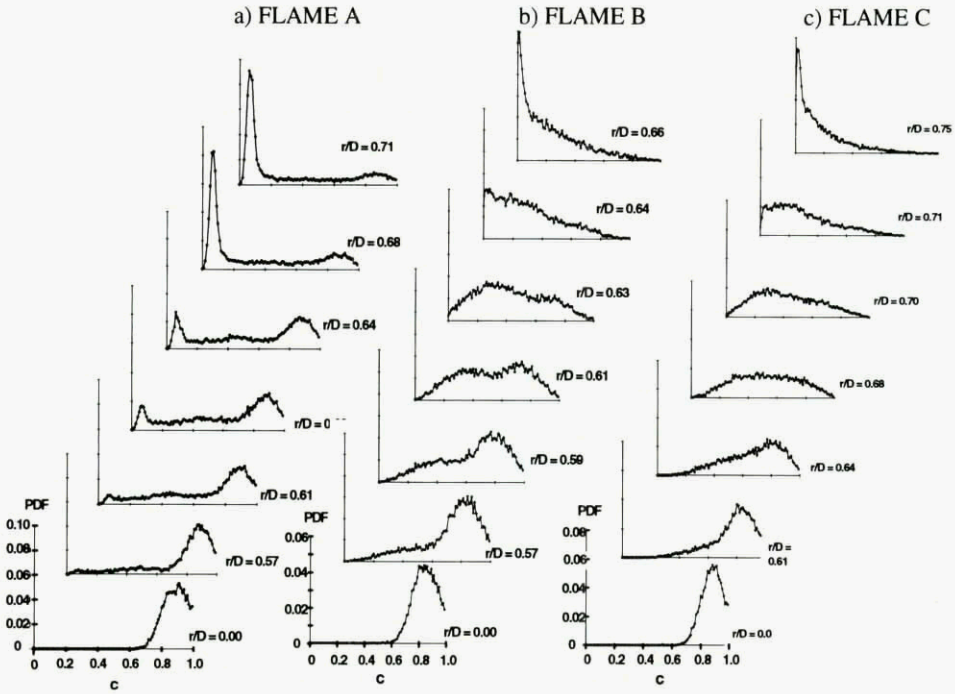


Fig. 5 - Radial distribution of the probability density function of temperature fluctuations, across the reacting shear layer.

The integral length scale of turbulence is, to a certain extent, a measure of the longest connection, or correlation distance, between the velocities at two points of the flow field. It is reasonable to expect, as pointed out by Hinze (1975), that the degree of correlation will decrease as the distance between the two measuring points, $\zeta$ , is increased and that, beyond some finite distance, L, this correlation will be practically zero. Thus, the integral length scale of turbulence, l, is defined by:

$$l = \int_0^{\infty} g(\zeta)\, d\zeta = \int_0^{L} g(\zeta)\, d\zeta$$

The measurements of the lateral velocity correlation coefficient were performed in several radial positions located at two characteristic axial locations of the flame B, namely at the rear stagnation point, and at the location of maximum width of the recirculation zone. Some results obtained for $g(\zeta)$ at different points for each location are represented in figure 6.

The shape of $g(\zeta)$ is qualitatively similar for all the conditions studied. but it can be clearly concluded that there are considerable differences in the values of the integral length scale of turbulence. The lateral velocity correlation coefficient rapidly decreases to zero in the points located at the reacting shear layer, as represented in Fig. 6, while within the recirculation zone the correlation do not reach zero within the measuring distance.

The results can be used to obtain of the length scales and the turbulence intensity characteristic of each location measured, and in particular, the reacting shear layer is characterised by length scales of about 3 mm, which is compatible with the result obtained by using the Eulerian time correlations..

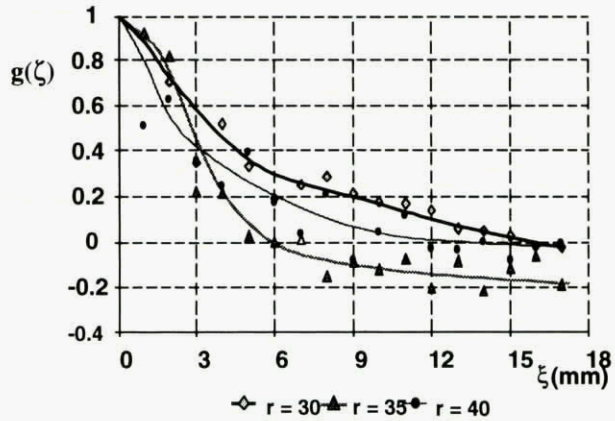


Fig. 6 - Lateral velocity correlation coefficient for the axial location of, X/D=1.2

### 3.2 – Premixed Combustion Regimes Characterisation

The burning conditions associated with Flame A are characteristic of a regime where the flame fronts become thick and bigger than the Kolmogorov length scale. Following Poinsot et al (1991) the construction of the turbulent combustion diagram is straightforward, as in figure 7.

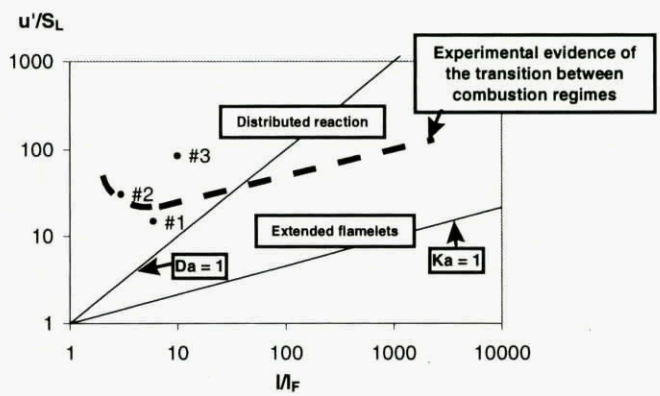


Fig. 7 - Diagram for turbulent premixed combustion (points as defined in the text).

The position in the reacting shear layer of flame A where a bimodal temperature distribution was identified (i.e., x/D = 1.0, r/D = 0.64; #1 in figure 7) is characterised by turbulent scales which act on the flame front in two different ways. First, eddies whose sizes are between the Kolmogorov scale and a "cut-off" scale will be inefficient and will not affect the flame front. Second, vortices larger than the "cut-off" scale will be able to affect the flame front, to wrinkle it or to form pockets but be unable to induce local quenching. Point #1 corresponds therefore to the extended flamelet regime of Poinsot et al (1991).

The other locations identified in figure 7 (namely, #2 for flame B at x/D = 0.71 and r/D = 0.61; and #3 for flame C at x/D = 1.27 and r/D = 0.68) are associated with scales that are capable of locally quenching the flame front. These scales are larger and faster than the Kolmogorov scale and correspond to the distributed reaction regime of turbulent combustion. It should be noted that the near-Gaussian distributions of Figure 5 associated with flame locations #2 and #3 exhibit values between ambient (c = 0) and adiabatic (c = 1) temperatures and, therefore, are not expected to be influenced by lack of temporal resolutions of the Rayleigh system.

Figure 8 shows measured values of turbulent axial heat fluxes, which are restricted to the thin zone along the shear layer where the radial gradients of mean temperature are larger. These quantities represent the exchange rate of

reactants responsible for the phenomena of flame stabilisation and previous results have shown that the turbulent heat transfer is essentially directed along the isotherms, rather than normal to them, as would be expected from gradient-transport models of he kind used in non-reacting flows. It should be noted that the radial fluxes are always positive, as expected in a recirculating flame. The flame is then established by the heat transfer between the hot products and the cold reactants with the sign of the radial heat flux in qualitative agreement with gradient-transport models. Similar behaviour has been observed in other turbulent premixed flames (Heitor et al., 1987) and has also been predicted analytically (Bray et al., 1985), and is expected to be due to the interaction between the gradients of mean pressure typical of the present flow and the large density fluctuations that occur in the flames.

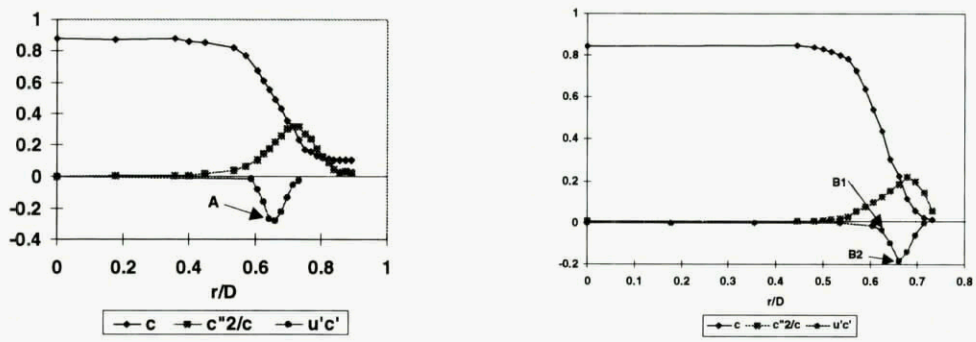


a) b)

Fig. 8 - Radial profile of temperature and turbulent heat flux characteristics:
a) For flame A at x/D = 1.0. b) For flame B, at x/D = 0.71.

The analysis above explains the process of "counter-gradient" heat transport in terms of the preferential deceleration of the products of combustion, relatively to the cold reactants (see Almeida et al, 1995, for further details). This can be easily observed through the joint probability distribution of velocity and temperature fluctuations and here the analysis follows the methodology of Cheng and Ng (1985) and Hardalupas et al. (1996), making use of weighted probability distributions. The corresponding plots should be analysed based on the relative importance of the entries in the four quadrants of figure 9, with quadrants 1 and 3 dominating the case of gradient diffusion. The entries in quadrants 2 and 4 arise when velocity fluctuations, which are respectively smaller and larger than the local mean, are associated with values of temperature fluctuations which are greater and smaller, respectively, than the mean value.

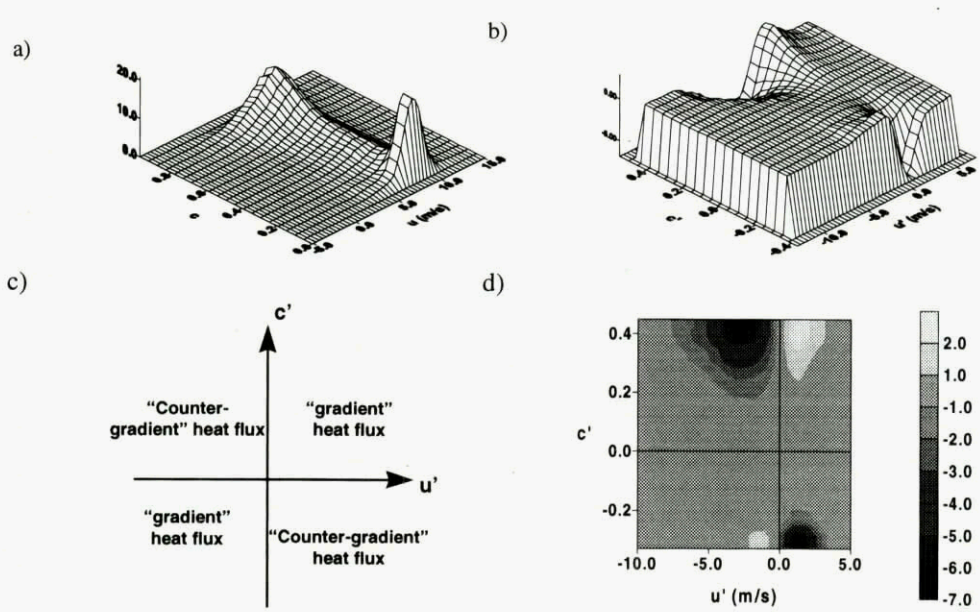


Fig. 9 - Analysis of joint pdf of velocity and temperature fluctuations for flame A at x/D = 1.0 and r/D = 0.64 ( Physical significance of the nature of the turbulent heat fluxes, as derived from the joint velocity temperature correlations)

A typical example is shown in figure 9, which clearly show that the "counter-gradient" quadrants are bigger and, consequently, the absolute value of the heat flux is dominated by the source terms which drive counter diffusion. A similar observation has been made by Hardalupas et al. (1996) for non-premixed flames and confirms that it is unreasonable to expect that calculations based on effective viscosity hypothesis are accurate to represent recirculating flames. The present results bring new experimental evidence of the magnitude of turbulence/combustion interactions in strongly sheared premixed flames and permits insight into the scale of the fluctuations of temperature and velocity, which gives rise to counter-gradient diffusion of heat.

## 4 . THE INFLUENCE OF SWIRL IN TURBULENT HEAT TRANSFER

The experiments were conducted in the same burner, were swirl was imparted to the premixed reactants by a set of curved blades, located upstream of the contraction and resulting in a rotating flow at the exit duct characterised by a swirl number, S, of:

$$S = \frac{\int_0^\infty r^2 \tilde{U} \tilde{W} \, dr}{R_0 \int_0^\infty r \left( \tilde{U}^2 - \frac{1}{2} \tilde{W}^2 \right) dr} = 0.33$$

The most salient features of the mean flow characteristics of the two flames studied can be inferred from the mean velocity vectors represented in figure 10. The single recirculation zone of the unswirled flame is to be contrasted to that of the swirling flame, which is shorter, wider and annular in shape because it includes an inner annular vortex with positive mean axial velocities along the centreline.

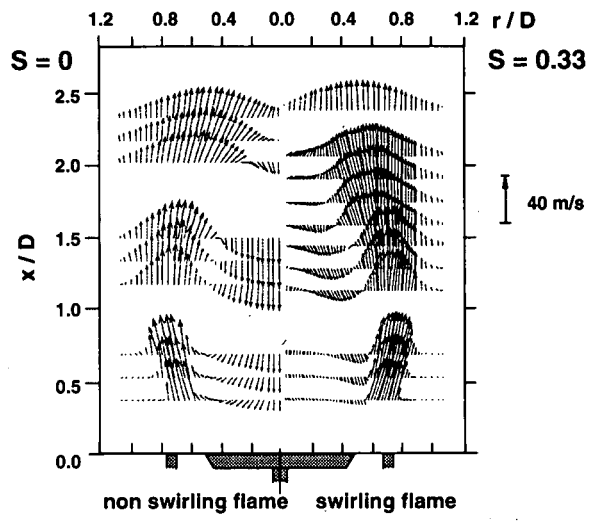


Fig 10 - Mean velocity vectors along a vertical plane of symmetry.

The inner recirculation zone is associated with positive mean axial velocities along the centreline up to the first stagnation point and rotates in the opposite sense to the outer recirculation zone. This nature of the swirling flame is characterised by a comparatively large inclination of the mean velocity vector at the burner exit which, together with the aspects mentioned before, represents the direct consequence of the centrifugal forces associated with the swirl motion.

The results of figure 11 show that the turbulent heat transfer r ate for the two flames considered is restricted to the reacting shear layers, with absolute values of u"c" considerably higher than those of v"c". As a consequence, a large component of the vectors of turbulent heat transfer is directed along the isotherms rather than normal to these, as would be expected from gradient-transport models of the kind used in non-reacting flows.

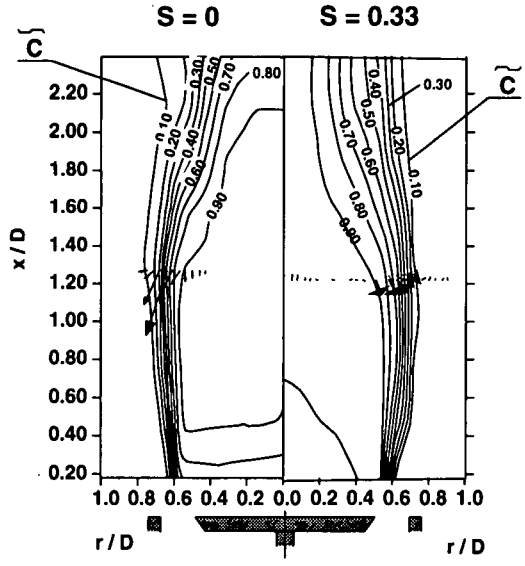


Fig. 11 – Isocontours of mean progress reaction variable, together with the turbulent heat flux vectors.

These quantities represent the exchange rate of reactants responsible for the phenomenon of flame stabilisation and the new feature provided by these results is that swirl decrease their magnitude due to the attenuation of the mean temperature gradients across the reacting shear layer.

The results for the non-swirling flame have been explained before in terms of the interaction between gradients of mean pressure and density fluctuations, which are important in the process of turbulent transport typical of reacting flows. The present results provide new evidence that this interaction is affected by the degree of swirl imposed on the flows. In general, the results confirm that predictions of these kind of flames must be based on second moment, rather than on effective viscosity, turbulence model closures so as to capture the effects of the mean pressure gradients on heat fluxes.

## 5 . CONCLUSIONS

Simultaneous measurements of time-resolved velocity and temperature have been obtained by laser-Doppler velocimetry and laser-Raylegh scattering in the near wake of premixed recirculating flames of propane and air. The experiments encompass the determination of the turbulent length scales for different flow conditions associated with different combustion regimes and Reynolds numbers.

The results bring new insight into the fluctuations that occur in these flames, which are expressed in terms of the shape of the weighted joint probability distributions of axial velocity and temperature fluctuations. These observations are related to the streamline curvature and are shown to occur even for a flame structure characterised by near-Gaussian probability distributions of the temperature fluctuations. In addition, the characterisation of the local length scales and turbulence intensities provide experimental evidence of the extension of the flamelet regime beyond the Klimov-Wiliams criterion.

## 6 . ACKNOWLEDGEMENTS

Financial support has been provided by the BRITE/EURAM programme of the DGXII of the Commission of the European Communities, under the contracts CT/95-0106.

## 7. REFERENCES


Almeida, P., Ferrão. P. and Heitor, M.V. 1995. The effect of swirl on the interaction between pressure gradients and density fluctuations in baffle-stabilised flames. Proc. of 10th Symposium on Turbulent Shear Flows. Vol. 2, pp. 16-7 to 16-12.

Bray, K.N.C., Libby, P. and Moss, J.H. 1985. Unified Modelling Approach for Premixed Turbulent Combustion – Part I: General Formulation. Combustion and Flame, 61: 87-102.

Borghi, R. 1985. On the Structure and Morphology of Turbulent Premixed Flames. Recent Advances in the Aerospace Science, Ed. Corrado Casci, Plenum Publishing Corporation, 117-137.

Caldas, F. D. Duarte, Ferrão, P., Heitor, M.V. and Pope, C, 1997. On the use of laser Rayleigh scattering to study the aerothermochemistry of recirculating premixed flames. In: Developments in Laser Techniques and Fluid Mechnics. Eds. Adrian et al., Springer Verlag.

Cheng., R.K. and Ng, T.T. 1985. Conditional Reynolds stress in a strongly heated turbulent boundary layer with premixed combustion, Phys. Fluids, 28, pp. 473-488.

Duarte, D., Ferrão, P. and Heitor, M.V. 1996. Flame structure charactrisation based on Rayleigh thermomtry and two-point laser Doppler measurements. In: Developments in Laser Techniques and Application to Fluid Mechnics. Eds. Adrian et al., Springer Verlag, 185-200.

Fernandes, E.C., Ferrão, Heitor, M.V. and Moreira, A.L.N. 1994. Velocity temperature correlation in recirculating flames with and without swirl, 9, pp. 241-249.

Ferrão, P. and Heitor, M.V. 1995. Turbulent mixing and non-gradient diffusion in baffl-stabilised flames. In: Turbulent Shear Flows - 9, Eds. Durst et al., Springer Verlag, pp. 427-437.

Hardalupas, Y., Tagawa, M. and Taylor, A.M.K.P., 1996. Characteristics of counter-gradient heat transfer in a non-premixed swirling flame. In: Developments in Laser Techniques an Applications to Fluid mechanics, ed Durst et al., Springer Verlag, pp. 159-184.

Heitor, M.V., Taylor, A.M.K.P. and Whitelaw, J.H., 1987. The interaction of turbulence and pressure gradients in baffle-stabilised premixed flames. J. Mechanics, 181, pp. 387-413.

Libby, P. and Bray, K.N.C. 1981. Counter-Gradient Diffusion in Premixed Turbulent Flames. AIAAJ, 19:205-213

Poinsot, T., Candel. and Trouvi, A. (1996). Applications of direct numerical simulation to premixd turbulent combustion. Prog. Energy Combust. Sci., 21, pp. 531-576.

Poinsot, T., Veynante, D. and Candel, S. (1991). Quenching process and premixed turbulent combustion diagrams. J. Fluid Mech., 228, pp. 561-606.

Takagi, T., Okamoto, T. Taji, M. and Nakasuji, Y., 1985. Retardation of mixing and counter-gradient diffusions ina swirling flame. Proc. 20th Symposium (Intl.) on Cobustion, pp. 251-258. The Combustion Institute, Pittsburgh.

Takagi, T., Okamoto, T., 1987. Direct measurement of the turbulent transport of momentum and heat in the swirling flame. In: Laser Diagnostic and Modelling of Combustion, Eds. Linuma, K. et al., pp. 273-280, Springer Vrlag, Berlin.

Paper 1
Author P. Ferrao et al.

Q: Hassa

Has the author measured the ratio between turbulent length scale and Rayleigh measuring volume? Is he concerned about gradients of the flow in the direction of the beam?

A: The turbulent length scales measured are of the order of 3mm, and the spatial resolution of the LRS system is of 50 microns. Also the temporal resolution of the system is quantified as 50 microseconds, a value which is to be compared with the measured time scales of about 1000 microseconds.

In the reaction shear layer, the gradients of velocity are not aligned with the direction of the beam. Therefore, a spatial resolution of 1mm in this direction does not constitute a concern for the measurements presented.

# The Simultaneous Measurements of Velocity, Pressure, Temperature and Heat Release in an Oscillating Flame

E.C. Fernandes and M.V. Heitor

Instituto Superior Técnico
Mechanical Engineering Department
Av. Rovisco Pais, 1096 Lisboa Codex
Portugal

## ABSTRACT

Optical and probe techniques are used for the analysis of the coupling mechanisms between pressure, velocity and heat release fluctuations typical of pulsed flames, through the combination of laser velocimetry, digitally-compensated thermocouples, chemiluminiscent emissions of free radicals in the flames, and the pressure oscillations is the upstream flows. The results quantify the periodic nature of the mixing process and characterize the momentum and heat flux fluctuations along a cycle of oscillation.

## INTRODUCTION

Combustion oscillations may occur in a variety of reacting systems, and their evidence is well documented in laboratory arrangements typical of afterburners (Heitor et al, 1984), gas turbine combustion chambers (Keller, 1995), pulse combustors (Keller et al, 1987) and dump combustors (Samaniego et al, 1993), as well as in the pratical situations typical of utility boilers (Eisinger, 1991). They are typically characterized by large amplitude pressure oscillations coupled with a fluctuating component of the heat release, according to the Rayleigh criterium (see Fernandes and Heitor, 1996), with the coupling mechanisms including changes in turbulent mixing rate, flames area variation, periodic air/gas supply, hydrodynamic instabilities and vortex shedding (Fernandes and Heitor, 1996). Since a serious structural damage may occur due to the presence of large amplitude pressure oscillations, together with the enhanced heat transfer to the walls (Perry and Culick, 1974), attempts have been made to passively control the instabilities (e.g. Schadow and Gutmark, 1992), although more recently the advantage of more powerfull microprocessors in speed processing were used to cancel actively the oscillations (see McManus et al, 1993).

Another important aspect linked with the ocurrence of combustions oscillations, to which attention has recently been given, is the attractive features recognised in the search of fuel savings, increased productivity and reduced emissions (Zinn, 1996, Charon et al, 1993) and an increase of the flame stabilization range (Gutmark et al, 1990). In order to understand the phenomena, for both control and energy savings, several experimental techniques have been used to characterize the oscillations, with emphasis given to sound pressure level together with global light emission from the flame (see for example Lang and Vortmeyer, 1987) and planar imaging (see for example Schadow and Gutmark, 1992). Also, laser Doppler velocimetry has been used (Keller et al, 1987; Lovett and Turns, 1993; Fernandes and Heitor, 1996) in order to obtain time resolved information on the characteristics of the oscillating flowfields. In spite of the efforts patented in the published works, there is a need of reliable data in order

*Paper presented at an AGARD PEP Symposium on "Advanced Non-Intrusive Instrumentation for Propulsion Engines", held in Brussels, Belgium, 20-24 October 1997, and published in CP-598.*

to understand the coupling mechanisms between pressure, velocity and heat release fluctuations, in order to take a full advantage of the influence resulting from the enhanced interaction between fluid mechanics and chemistry in oscillating flames.

To help achieving these objectives, the present work is focused on the study of a pulsed turbulent premixed flame, stabilized in the wake of a bluff-body, which is located at the end of a long pipe and in the vicinity of an acoustic antinode velocity. The next paragraphs analyse the experimental setup and the data acquisition system and present sample results obtained in the flame front for typical flow conditions.

## 2. EXPERIMENTAL APPARATUS AND PROCEDURES

### 2.1. Flow Configuration

The apparatus consists of a cylindrical duct of stainless-steel with a variable length, an a diameter of 186mm, which was placed on the top of a cubic plenum of $3m^3$, figure 1. The tube was designed to work with two acoustically-opened ends with a length varying from .25mm to 3m in steps of .25mm, allowing the fundamental resonance frequency to range between 50Hz and 1kHz. The burner holder can be moved continuously inside the duct, in order to search for the optimum driving location for heat addition (e.g. Fernandes and Heitor, 1996), and several flame stabilisers can be assembled on the top of it. However, for most of the results described here, the pipe length was kept constant and equal to 0.52m and the flame holder was positioned 10mm downstream of the pipe exit. The resulting flame is open to the atmosphere, but offers the advantage of easy access to the techniques described below.

The primary air was injected with a velocity of 3.4 m/s (Re = 20000) through the plenum, where it was seeded with powdered aluminum oxide (nominal diameter below 1.0$\mu$m before agglomeration) making use of a purpose-built cyclone generator. The burner consists of a conical bluff-body with a base diameter of Ø = 103 mm and heigth=250 mm. The pre-mixture is injected through a slot of .5 mm around the border of the base, as shown in figure 2, with an equivalence ratio ø =6 and a velocity of 15m/s.

### 2.2. Experimental techniques

Figure 1 shows schematically the various experimental techniques used throughout this work. The radiated sound intensity from the flame was measured with a free-field condenser microphone (B&K 4130) and with a pre-amplifier (B&K 2130) with a flat response over a frequency band of 20Hz to 10kHz. The pressure fluctuations along the duct were measured with a semi-infinite probe with a flat response up to 1kHz.

The light emitted from the flame was used as a signature of the rate of change of heat release (Keller and Saito, 1987) in terms of the chemiluminiscence emission due to the radiative decay of electronically excited radicals existing in the reaction zone, such as $<OH^*>$, $<CH^*>$ and $<C_2^*>$ (Gaydon and Wolfhard, 1979). The light from the flame was monitored from the $<C2^*>$ emissions, by collecting light along a cilindrical line-of-sight of 2mm in diameter, with a 20mm lens diameter with a focal distance of 50mm. The radiation emission was then guided through a fiber optic cable to the entrance slit of photomultiplier (EMI-9658 A), interfaced with an interference filter for 514.5nm with a bandwith of 4nm. Uncertainties in the ensembled time resolved measurements of light emission are estimated to be less than 2% (Yanta and Smith, 1978) due to a relatively high number of points used for calculating mean

quantities, in the order of 3000/phase. Due to the integrated nature of the results along a line-of-sight, a mathematical procedure was implemented based on the Abel's transformation (Tourin, 1968) to obtain

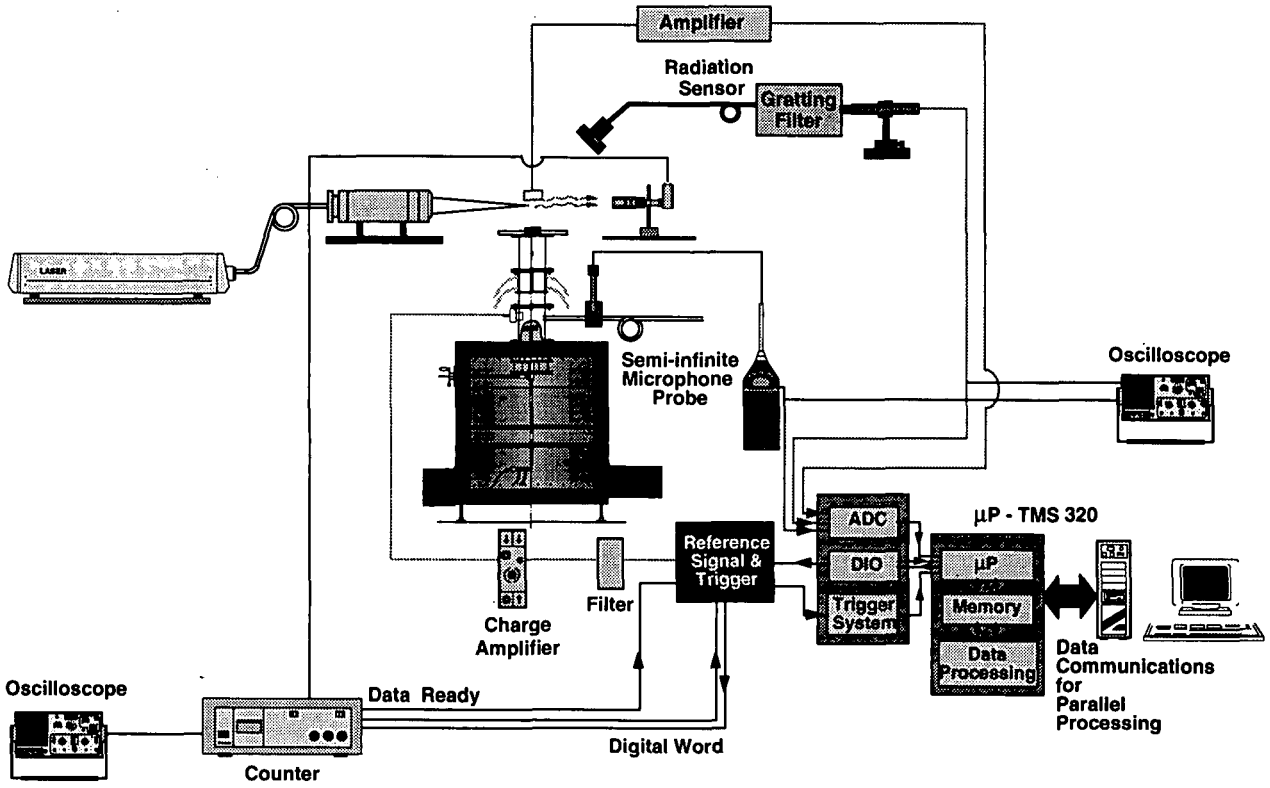


*Fig. 1. Schematic drawing of experimental apparatus with identification of the instrumentation used.*

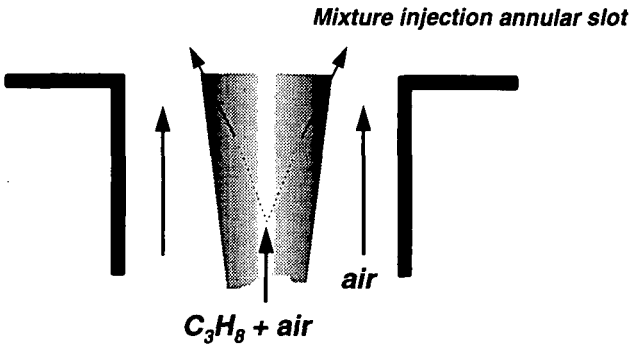


*Fig. 2. Schematic diagram of flame holder.*

the radial profile of radical emission coefficients (e.g. Beyler and Gouldin 1981). The error associated with the Abel's transformation depends on the type of derivative and integral methods implemented, but are less than 5%, according to calculations performed by Correia et al (1997).

Time-resolved velocity information was obtained with a laser-Doppler velocimeter which comprised an Argon-Ion laser operated at a wavelength of 514.5 nm and a power of around 1W. A fiber optic (DANTEC) was used to guide the beam to an optical unit arranged with a two beam system with sensitivity to the flow direction provided by light-frequency shifting from a Bragg cell at 40MHz, a 310

mm focal length transmission lens, and forward-scattered light collected by a 310 mm focal length lens at a magnification of 1.0. The half-angle between the beams was 5.53° and the calculated dimensions of the measuring volume at the $e^{-2}$ intensity locations were 2.3 and 0.219 mm. The output of the photomultiplier was mixed with a signal derived from the driving frequency of the Bragg cell and the resulting signal processed by a commercial frequency counter (DANTEC 55296) interfaced with a 16-bit DSP board. Measurements were obtained with the laser beams in the horizontal and vertical planes and by traversing the control volume along the horizontal and vertical directions to allow the determination of the axial, U, and radial, V, time-resolved velocities, respectively.

Although various weighting methods have been proposed to correct for velocity bias effects (e.g. Durst et al, 1981), no corrections were applied to the measurements reported here. The systematic errors that could have arisen were minimised by using high data acquisition rates in relation to the fundamental velocity fluctuation rate, as suggested for example by Erdman and Tropea (1981). This could be easily achieved because the rate of naturally-occurring particles was sufficiently high for the flow conditions considered here. Spectral analysis of LDV signals was carried out by resamplig the time series after a linear interpolation with minimum interval time given by the mean data rate.

Temperature measurements were obtained making use of digitally-compensated fine-wires thermocouples, with 38um in diameter, made of Pt/Pt-13%Rh. The related errors are quantified elsewere (see for example Ferrão and Heitor, 1997) and shown not to be higher than 60K for the time averaged values at the maximum temperature obtained in open flame, and up to 15% for the variance of the temperature fluctuations.

The paragraphs above described the different experimental techniques used throughout this work. We now describe briefly the procedures used to acquire the various signals simultaneously. The Doppler frequency and both scalars, namely pressure and temperature, where acquired simultaneously and post-processed making use of a microprocessor, Texas Instruments-TMSC320C40. The scalars where digitized with a sample-and-hold analog converter at a rate of 40kHz/channel and stored in a circular memory buffer. The acquisition starts only when the pressure signal is going from positive-to-negative, which is given by a pressure reference detector. The buffer access, to collect data simultaneously with the occurrence of a burst, was made through an active pointer, sensitive to velocity data ready signals. The complete system can go up to 12.5kHz of data ready signals, the delay of the board to the data ready signal is less than 100ns and the window resolution between velocity and scalars is less than 1/40kHz. The thermocouple output signal was digitally compensated (e.g Ferrão and Heitor 1992, Durão et al ,1992) from they thermal inertia, following the procedure outlined by Heitor et al (1985). The largest random error incurred in the values of temperature-velocity correlations, as higher as 15%, are due to the spatial separation of the measurements locations of the temperature and velocity because of the thermocouple junction must lie outside the mesuring control volume of the laser anemometer.

The complete measuring system was mounted in a three-dimensional traversing unit, allowing an accuracy of the measuring control volume within $\pm 0.25$mm.

## 2.3 Data analysis

Time resolved measurements of velocity, temperature, pressure and reaction rate data obtained under periodic oscillations were statistically analysed following the decomposition proposed by Hussain and Reynolds (1970), for a generic variable $\gamma$:

$$\gamma(t) = \bar{\gamma} + \tilde{\gamma}(t) + \gamma'(t)$$

where $\gamma(t)$ is the instantaneous value, $\bar{\gamma}$ is the long time average mean, $\tilde{\gamma}(t)$ is the statistical contribution of the organized wave, and $\gamma'(t)$ is the instantaneous value of turbulent fluctuations. An ensemble average over a large number of cycles yields (Hussain and Reynolds ,1970 and Tierderman et al 1988):

$$<\gamma>(t) = \bar{\gamma} + \tilde{\gamma}(t)$$

$$<\sqrt{\gamma'^2}>(t_i) \equiv <\gamma_{rms}> = \sqrt{\frac{(\gamma'(t_i) - <\gamma>(t_i))^2}{n-1}}$$

The ensemble average, or phase average, is then the average at any point in space, of the values of $\gamma(t)$ that are realized at a particular phase interval in the cycle of the periodic oscillations. The phase interval was chosen to be 18°, to minimize the influences of the phase averaging window size on the determination of turbulence quantities in unsteady turbulent flows, as discussed by Zhang et al (1997).

## 3. RESULTS AND DISCUSSION

Figure 3 shows a photographic image of "pulsed" and "steady" flames, which were obtained by a small change of less than 0.5% in the equivalence ratio around $\varnothing = 6$. The evolution from steady to unsteady regime is accompanied by a sharp increase in the sound pressure levels, from around 80 dB (steady flame), to values in excess of 110 dB. For the unsteady condition, the spectrum of the pressure fluctuations in any location of the pipe wall is associated with the excitation of a predominant frequency at 275 Hz, which is associated with a longitudinal standing half-wave. This cyclic process is, according to the Rayleigh criterium, sustained by the temporal and spatial phase relationship that exists between flame energy release and pressure oscillations. The question which does arises when turbulent flames are the main source of energy is due to the presence of a velocity turbulent flowfield, which will be considered below.

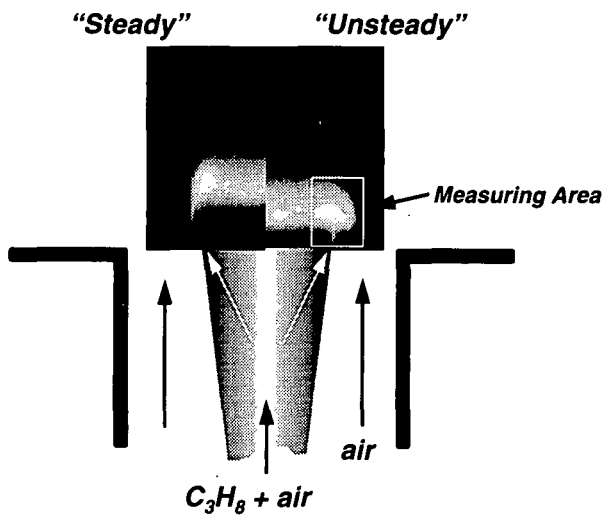


*Figure 3 - Photographic image of a "steady" and pulsed flames, together with the identification of the the measuring area and the schematic of the flame holder*

The analysis consider "rough" combustion conditions for $Ø_i$ = 6, $U_{jet}$ =15m/s and $U_{plenum}$ =3.4m/s, corresponding to an overall equivalence ratio at the pipe exit of $Ø_T$ =0.1. All data obtained under oscillating conditions were acquired using the instantaneous pressure signal as a temporal reference. The instantaneous pressure fluctuations corresponds to signals measured at middle of the pipe, where the amplitude of the pressure fluctuations is maximum.

Figure 4 shows signatures of chemical reaction, obtained after Abel's transformations, for the pulsed flame, as a time sequence for one period of oscillation, together with a schematic draw of the burner with their relative mean velocities. The results show that the large scale structure typical of resonance conditions, which develops along the reacting shear layer sourrounding the flow field, exhibits a periodic evolution in time. Generically, the reaction zone can be divided in two main regions, namely the inner flame, for r/R<1.1, which is aligned with the mixture injection slot and the outer flame, for r/R>1.15,which appears to be periodically ignited.

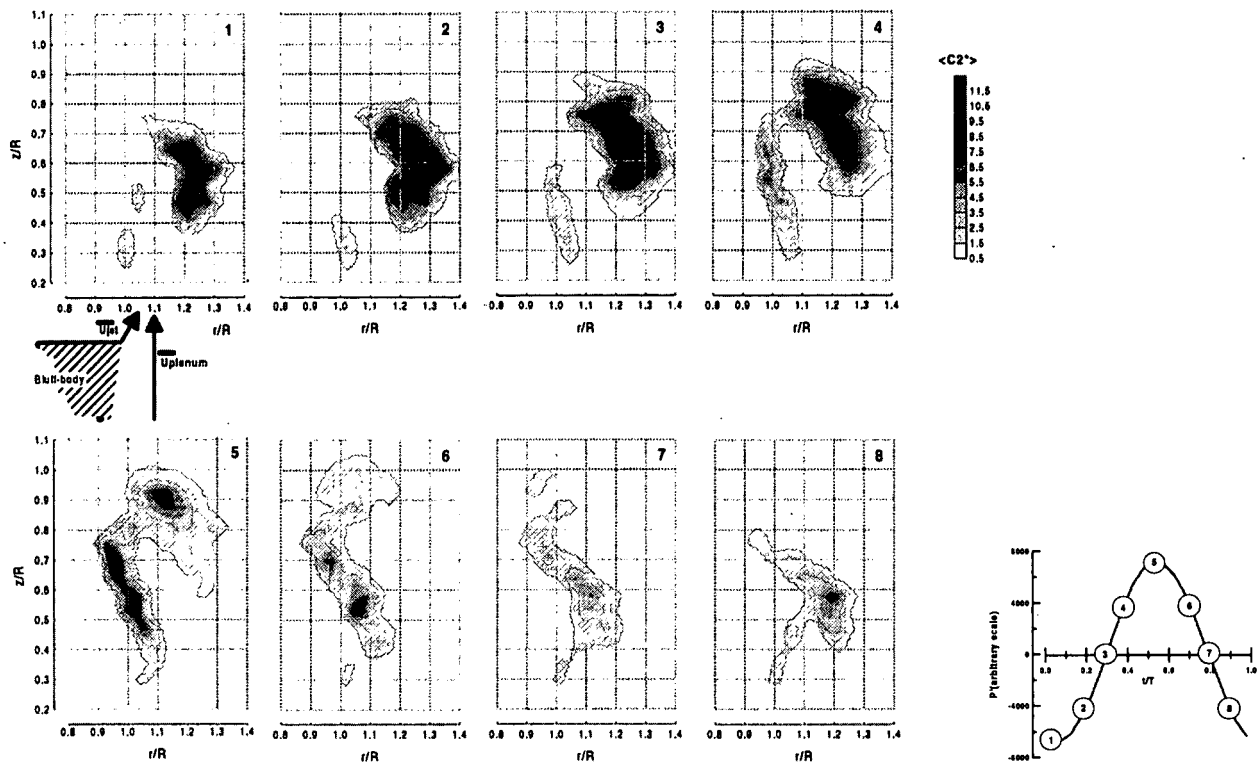


*Figure 4 - Time-resolved spatial distribution of phase average* $<C_2^*>$

The analysis shows that the inner flame structure is similar to a bluff-body stabilized flame (see for example Ferrão and Heitor, 1997) and works as a flame ignitor of the outher flame, (see image #6 of figure 4). After ignition, the outer flame moves radially outwards, up to r/R=1.3, as the signature of <C2*> emission increase in strength. Subsequently, the reaction zone moves vertically upwards towards the stagnation point, with an estimated velocity of 10 m/s. To improve understanding of this

process, the influence of such periodic reacting structure in the velocity and temperature field is analysed below along a radial profile at z/R=0.6.

Figure 5a and 5b shows mean values of axial, U, and radial ,V, velocity components together with their respective fluctuations, under resonance conditions. The radial distribution of axial component U, with a strong negative value at the centreline and a positive high value across the reacting shear layer, together with the radial velocity profile presented, are typical of recirculation zones downstream of bluff-bodies (e.g. Fernandes et al, 1994). The correspondent profiles of the r.m.s. of the velocity fluctuations, of both axial and radial component, are also similar to the works reported before for reacting shears layer, with peak values at regions where the radial gradients of mean values are high, with absolute values of the turbulent intensities as high as 60%.

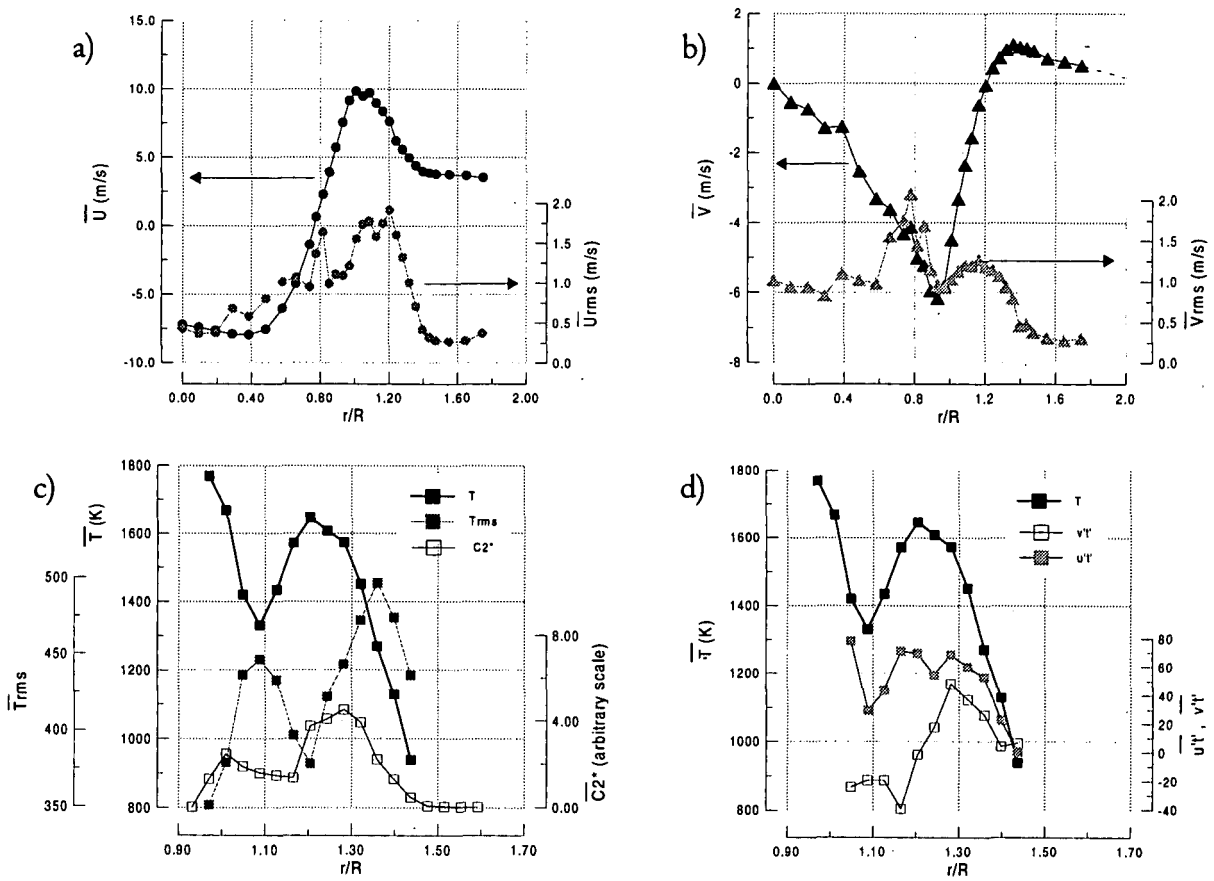


*Figure 5 - Time averaged analysis of flow properties at z/R=0.58 for the pulsed flame*
*a) Axial velocity component*
*b) Radial velocity component*
*c )Temperature*
*d)Velocity-temperature correlations: u't' and v't'*

The radial profiles of mean and fluctuating temperature, and the time averaged emission of <C2*> radicals, figure 5c, confirm the existence of two regions bounded at r/R=1.1, with maximum temperature values of the order of 1700K and diffrent reacting strengths. While the inner flame zone is subjected to a very strong temperature radial gradient and local temperatures in excess of 1700K, the outer zone is in the vicinity of a region with a local maximum temperature of T=1700K, and minimum

Trms. Both flame regions are dominated by the transfer of turbulent heat fluxes along the axial direction.

The extent to which the periodic oscillations affect the temperature and velocity flow field characteristics, and condition their temporal evolution, is discussed based on the instantaneous radial profiles presented in figures 6 and 7 for time instants of t/T=0, 0.25,0.5 and 0.75. The results show that the axial velocity profiles are affected by periodic oscillations for r/R>0.9, where changes are quantified to be in excess of 50%, close to the velocity peak. The associated radial velocity profile, presented in figure 6b, also reveals the same type of sensitivity between r/R=0.77 and r/R=1.74, and here the absolute variations are quantified to reach 2m/s when mean radial velocity is near zero. Also, the radial profile of the velocity turbulent fluctuations, for both axial and radial components, see figure 6c and 6d, are strongly influenced by the presence of periodic oscillations with variations of the order of 100%.

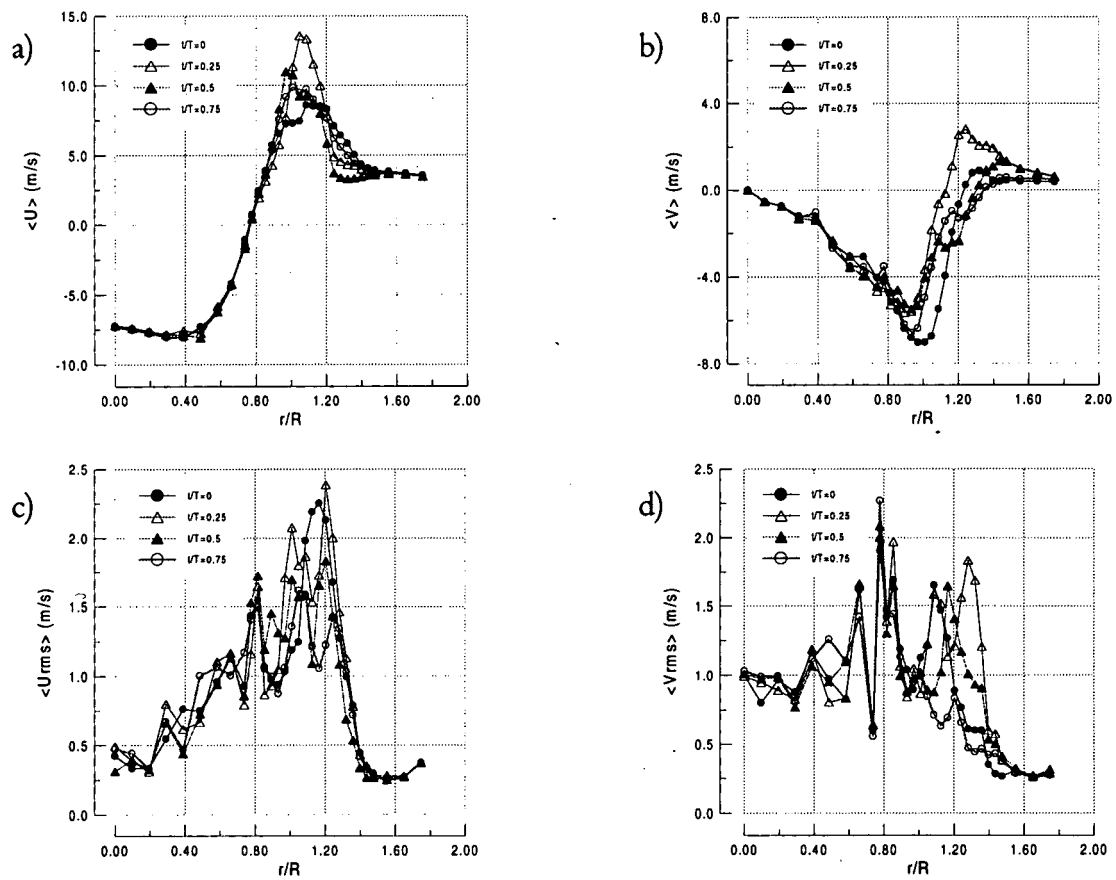


*Figure 6 - Instantaneous radial profiles of velocity flow properties at z/R=0.58 for t/T=0, 0.25,0.5,0.75*

*a)Phase average axial velocity component <U>*

*b) Phase average radial velocity component <V>*

*c) Phase average r.m.s. of axial velocity <Urms>*

*d) Phase average r.m.s. of radial velocity <Vrms>*

In this case the most affected region is again for r/R > 1, for which the radial profile shape are not kept constant. In fact instantaneously suppression large fluctuations may occur, as observed in figure 6d when comparing radial profiles obtained at t/T = 0 and t/T = 0.75. Also, the analysis shows that the influence of periodic oscillations seems to be limited to the reacting shear layer, for r/R > 1.

Figure 7 presents the temporal evolution of <C2*>, <T> <Trms> and velocity-temperature correlations, for the region 0.9 < r/R < 1.5, and clearly shows that reaction "starts" at the inner part of the flame, close to r/R = 0.9 and at t/T = 0.5, and evolves to the location r/R = 1.3 where the radical emission of <C2*> reaches maximum values for t/T = 0.25. On the other hand, the instantaneous ensemble average temperature profiles, figure 7b, show a rather compex nature, in that they suggest two typical high temperature regions, for r/R < 1.04 and at r/R = 1.2. Both maxima temperature are of about 1800K while the lowest temperature measured is of the order of 800K. The rms of temperature fluctuations, figure 7c, shows values in the range of 200K to 500K, in a way which is consistent with the findings of figure 7b in the sense that the maximum temperature fluctuations, at each time instant, occurs close to the regions where the instantaneous mean temperature exhibit a higher radial gradient. In addition, if <C2*> map are superimposed on the mean temperatue map, it is found that the instantaneous distribution of heat release from the flame is located in zones of large radial gradient of mean temperature, which coincides with the regions where temperature fluctuations are large. The vectors of turbulent heat flux, figure 7c, are high in these regions and normal to the instantaneous flame front, although they exhibit a direction along the isotherms in the vicinity of the flame stabilize, as well as further downstream. This vectors represent the exchange rate of reactants responsible for the phenomenon of flame stabilization and the presents results quantify for the first time there temporal evolution along a cycle of flame oscillations. Previous results in the literarture for steady state recirculating flames (e.g. Fernandes et al, 1994, Hardalupas et al, 1996, Duarte et al, 1997) have shown the occurrence of zones of non- and counter-gradient diffusion of heat which has been explained in terms of interaction between gradients of mean pressure and density fluctuations. The present results provide new evidence of this interaction in oscillating flames, which is associated with periodic fluctuations in flame curvature. In general, the results quantify the periodic ignition of large scale reaction zones, which drive the combustion induced oscillations reported in this paper.

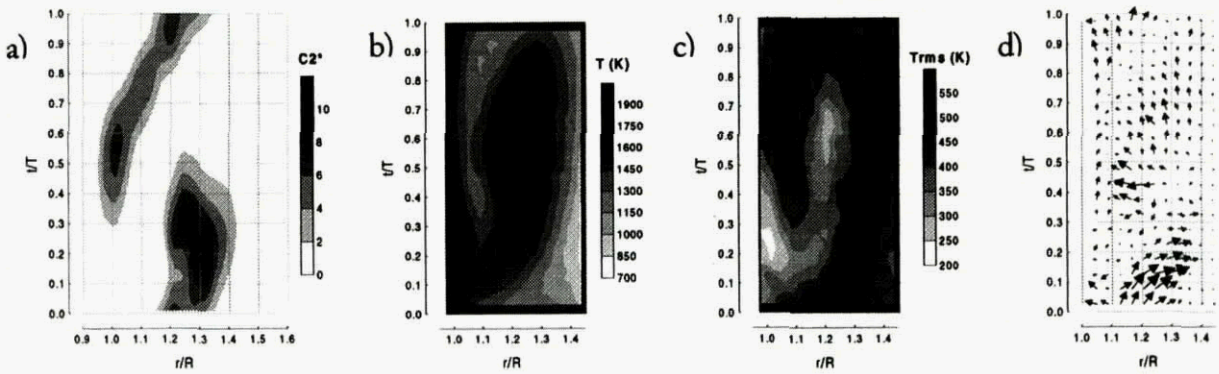


*Figure 7 - Temporal evolution of temperature characteristics and velocity-temperature correlations at z/R = 0.58*

*a) Phase average <C₂*>*

*b) Phase average temperature <T>*

*c) Phase average r.m.s. of temperature fluctuations <Trms>*

*d) Phase average <u't'>, <v't'> correlations*

## CONCLUSIONS

The experimental analysis of a naturally-pulsed premixed turbulent flame is reported making use of optical and probe diagnostics and including the time-resolved correlations of velocity, temperature, pressure and light emission signals. The results were obtained in the flame stabilized in a wake of bulff-body located on a velocity acoustic antinode, and show that the instanteous flame structure, based on the analysis of electronically-excited decay of C2 radicals, is composed by two, inner and outer, main regions. The inner flame, behaves as a typical bluff-body stabilized flame, although the influence of a strong unsteady flowfield results in appreciable spatial and temporal deformations. The inner flame acts as a periodic ignitor source of the second reactive structure present, which is considered here as an outer flame. This outer flame front emerges radially at an axial location of about 0.6R, followed by a vertical movement towards the rear stagnation point. This process is accompanied by large fluctuations in the axial and radial velocity components of the flow, with the two flame regions separated by the zone of maximum axial velocity. The time-resolved analysis show that both ensembled average flame fronts occupy sucessively regions where temperature exibhit high radial gradients, and large temperature fluctuations. In general the results quantify the time resolved process of turbulent mixing along a full pressure cycle in a pulsed flame and suggest that the cycle-resolved nature of the momentum flux may be represented, at least qualitatively, by gradient hypotesis. On the other hand, the nature of the cycle-resolved (i.e. phase averaging) turbulent heat flux shows zones of either gradient and non-gradient characteristics, which apperars to be influenced by the temporal evolution of the streamline curvature along a cycle of flame oscillations.

## REFERENCES


Beyler, C.L. and Gouldin, F.C. (1981) "Flame Structure in a Swirl Stabilized Combustor Inferred by Radiant Emission Measurements", 8th Symp. (Intl) on Combustion, The Combustion Institute, pp.1011-1019

Charon, O. and Jouvad, D. (1993) "Pulsated $O_2$/fuel flame as a new technique for low $NO_x$ emission", Combust. Sci. and Tech., 93, pp.211-222

Correia, D.P., Caldeira-Pires, A., Ferrão, P. And Heitor M.V. (1997) " A Temperature Tomographic Sensor for Combustion Analysis", 17th ICIASF,Pacific Grove, CA USA, September 28-October 2, 1997

Duarte, D., Ferrão,P and Heitor, M.V. (1997) " Turbulent statistics and scalr transport in highly-sheared premixed flames", Proc. 11th Turbulent Shear Flows Symposium, Grenoble, 8-10 September

Durão, D.F.G., Fernandes, E.C., Heitor, M.V., Moreira, A.L.N. and Simões, J.P (1992) LDA Measurements of Velocity and Turbulent Transport Processes in an 150kW Baffle-Stabilized Swirling Flame", 6th Intl. Symp. On Appl. Of Laser Techniques to Fluid Mechanics, July, 20th-23rd, Lisbon Portugal

Durst, F., Melling, A. and Whitelaw, J.H. (1981). "Principles and Practice of laser-Doppler Anemometry", Academic Press.

Eisinger, F.L. (1991) " Combustion air flow induced furnace vibration in an oil-fired utility boiler- a cse study" IMechE 1991, C416/095.

Erdman, J.C. and Tropea, C.D. (1981). "Turbulence-induced Statistical in Laser Anemometers". Proc. 7th Biennal Symp. on Turbulence, Rolla, Missouri.

Fernandes, E.C., Ferrão,P., Heitor,M.V. and Moreira A.L.M (1994) "Velocity temperature corelations in recirculaing flames with and without swril",Experimental Thermal and Fluid Science, 9, pp.241-249

Fernandes, E.C. and Heitor, M.V. (1996) "Unsteady flames and the Rayleigh criteria", in Unsteady Combustion, eds. Culick, F., Heitor, M.V. and Withelaw, J.H., Nato ASI Series, Series E: Applied Sciences- Vol. 306 ., Kluwer Academic Publishers, pp. 1-16

Ferrão, P. And Heitor, M.V. (1992) " Simultaneous Measurements of Velocity and Scalar Characteristics for the Analysis of Turbulent Heat Transfer in Recirculating Flames, 6th Intl. Symp. On Appl. Of Laser Techniques to Fluid Mechanics, July, 20th-23rd, Lisbon Portugal

Ferrão, P. And Heitor, M.V. (1997) "Probe and Optical Diagnostics for Scalr Measurements in Premixed Flames", Experiments in Fluids, to appear

Gaydon, A.G. and Wolfhard, H.G. (1979) Flames- their structure radiation and temperature, Ed. Chapman and Hall, Fourth Edition, London

Gutmark, E., Parr, T.P., Parr-Hanson, D.M. and Schadow, K.C. (1990) "Stabilization of a premixed flame by shear flow excitation", Combust. Sci. and Tech., 73 , pp. 521-535

Hardalupas, Y., Tagawa, M. and Taylor, A.M.K.P (1996) " Cahracteristics of counter-gradient heat transfer in a non premixed swirling flame". In: Developments in Laser Techniques and Applications to Fluid Mechanics, ed. Durst et al, Springer-Verlag, pp. 159-184

Heitor, M.V., Taylor, A.M.K.P. and Whitelaw, J.H. (1984) "Influence of confinement on combustion instabilities of premixed flames stabilised on axisymmetric baffles", Combust. and Flame, 57, pp. 109-121

Hussain, A.K.M.F. and Reynolds, W.C. (1970) "The Mechanics of an Organized Wave in Trubulent Shear Flow", J.Fluid Mech., vol.41, part2, pp.241-258

Keller, J.J. (1995) "Thermoacoustic oscillations in combustion chambers of gas turbines", AIAA Journal, 33, No.12, December 1995.

Keller, J.O. and Saito, .K. (1987) "Measurements of the combusting flow in a pulse combustor", Combust.Sci. and Tech., 53, pp. 137-163

Lang, W. and Vortmeyer, D. (1987) " Cross-correlatio of sound pressure and heat release rate for oscillating flames with several frequencies excited", Combust. Sci. and Tech. 54, pp. 399-406

Lovett, J. A. and Turns, S. (1993) "The structure of pulsed turbulent nonpremixed jet flames", Combust. Sci. Tech, 94, pp. 193-217

McManus, K.R., Poinsot, T. and Candel, S.M. (1993) "A review of active control of combustion instabilities", Prog. Energy Combust. Sci., 19, pp.1-29

Perry, E.H. and Culick, F.E.C. (1974) "Measurements of wall heat transfer in the presence of large-amplitude combustion-driven oscillations", Combust. Sci and Tech, 9, pp. 49-53.

Schadow, K.C. and Gutmark, E. (1992) "Combustion instability related to vortex shedding in dump combustors and their passive control", Prog. Energy Combust. Sci., 18, pp.117-132

Tierderman, W.G., Privette, R.M. and Philipds, W.M. (1988), "Cycle-To-Cycle Variation Effects On Turbulent Shear Stress Measurements In Pulsatile Flows" Experiments in Fluids, 6, pp.265-272

Tourin, R.H. (1966) Spectroscopic Gas Temperature Measurement Elsevier Publishing Company

Yanta, W.J. and Smith, R.A. (1978) "Measurements of Turbulent Transport Properties with a Laser Doppler Velocimter", 11th Aerospace Science Meeting, AIAA paper 73-169, Washington, USA

Zhang, Z. Eisele, K. And Hirt, F. (1997) "The Influence of Phase-Averaging Window Size on the Determination of Turbulence Quantities in Unsteady Turbulent Flows", Experiments in Fluids, 22, pp.265-267.

Zinn, B.T. (1996) "Pulse combustion applications: Past, Present and Futue", in Unsteady Combustion, eds. Culick, F., Heitor, M.V. and Withelaw, J.H., Nato ASI Series, Series E: Applied Sciences- Vol. 306 ., Kluwer Academic Publishers, pp.113-137

# Laser Two-Focus Flow Field Investigation within a High-Speed High-Pressure Centrifugal Compressor

**I.Trébinjac and I.Claudin**
Laboratoire de Mécanique des Fluides et d'Acoustique
UMR CNRS 5509 / ECL / UCB Lyon I
Ecole Centrale de Lyon, BP 163, 69131 Ecully Cedex, France

## 1. SUMMARY

The results of measurements carried out in a transonic centrifugal compressor with splitter vanes are presented and discussed. The laser two-focus anemometry technique is described, including the seeding control which is a crucial issue in a high temperature level environment. Whereas a potentiel flow structure exists up to the high meridional curvature region, the throughflow pattern is largely distorted in the radial part of the impeller. Noticeable differences in flow pattern between both channels are found, particularly through the low momentum fluid zone locations. A qualitative study of the vortical mechanisms ascribes them to the tip clearance effects.

## 2. INTRODUCTION

Advances in high-pressure centrifugal compressor design and analysis require a better understanding of the flow field, especially within the blade passages. Knowledge of the various interactions of secondary flows and the tip leakage flows are particularly important to ensure that numerical methods lead to realistic predictions of the flow structure.

In experimental studies whose objectives are improved understanding of flow physics, measurements can be classified through the scale of the experimental facilities. The investigations conducted by Hathaway et al. (1993) and Chriss et al. (1994) at the NASA-Lewis Research Center in a low-speed, large-scale facility are typical of those aimed at providing details of the flow. The results precisely document the development of the low-momentum fluid into the mainstream of the impeller passages. Moreover, the large size of the impeller enables measurements of all three velocity components with a spatial resolution allowing the assessment of the accuracy of computational fluid dynamic flow field predictions. The investigations conducted in high-speed facilities allow a study of strong interactions of secondary flows generated in particular by the Coriolis force. But the considerable difficulty in obtaining flow data in such complex narrow flow channels, characterized by long, twisted 3D passages with high curvature and a low aspect ratio, explains the scarcity of published results. Although the three-dimensional nature of subsonic centrifugal compressor flow-field has been studied (Eckardt, 1976; Senoo, 1979; Elder, 1987; Krain, 1988), there are fewer investigations concerning the inter-blade flow-field of supersonic centrifugal compressor rotors.

A research program seeking to obtain laser two-focus anemometry measurements within a transonic high-pressure unshrouded centrifugal impeller has been undertaken. The first phase of this program deals with the mapping of the inter-blade flow-field. A description is made of the flow pattern experimentally obtained and a phenomenological study of vortical mechanisms is proposed.

The second phase of this program will be to use the experimental data to calibrate numerical simulations. A comparative analysis of the calculated results will allow the assessment of the accuracy of the various models used in CFD codes.

## 3. FACILITY AND INSTRUMENTATION

### 3.1 The investigated compressor

The test compressor is a single-stage centrifugal compressor designed and built by Turbomeca and is composed of a backswept splittered unshrouded impeller coupled with a vaned diffuser. Some facility parameters are given in Table 1.

| | |
|---|---|
| overall pressure ratio | 9 |
| specific speed | 0.52 |
| specific diameter | 4.1 |
| flow coefficient | 0.26 |
| head coefficient | 0.77 |

Table 1 : Facility parameters

### 3.2 Instrumentation

A laser two-focus anemometer designed in the LMFA laboratory according the work of Schodl (1977) is used. Details of the system are described by Vouillarmet (1986) and Trébinjac and Vouillarmet (1988). This system operates with a laser light source (SP 4W argon-ion laser) which is coupled to the optical system via a polarization maintaining single-mode optical fiber.(Fig.1) The optics assembly has the following main characteristics :

- distance between the two spots, $s = 0.5$ mm
- incident beam angle, $\nu_i = \pm 5°$
- reflected light angle, $\nu_r = \pm 10°$

The whole optical system is mounted on a traverse table that fixes the axial, radial and circumferential positions of the measurement point. It is connected to photomultipliers via two multimode optical fibers. The processing of the electrical signals is performed by a dual-counter interfaced to a DEC computer and made

*Paper presented at an AGARD PEP Symposium on "Advanced Non-Intrusive Instrumentation for Propulsion Engines", held in Brussels, Belgium, 20-24 October 1997, and published in CP-598.*

up of two parts : a rapid counter whose resolution is 10 nanoseconds (denoted primary part) and a one microsecond resolution counter (denoted secondary part). The signals delivered by the receiving assembly (preamplifiers and filters) are sent to the primary part of this dual-counter.

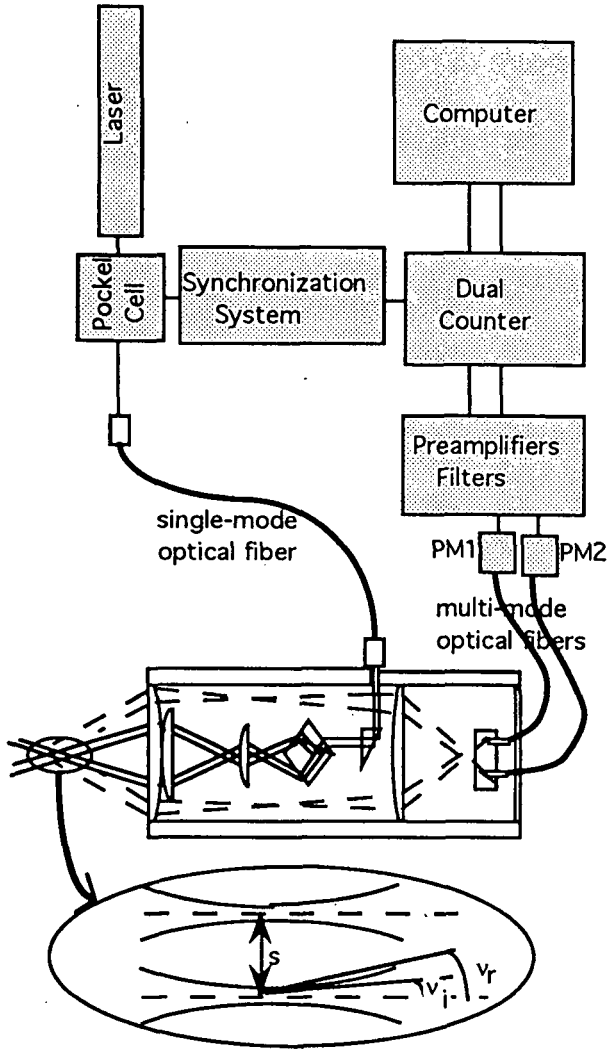


Fig.1 : Schematic arrangement of the L2F system

The synchronizer system, used for measurements within rotating passages, has two functions. First, the laser beam is strobed using a Pockel cell driven by an electric signal from a synchronized wave-shaper. This is to keep the light reflections from the rotating blades from saturating the photodetectors. The square wave signal, triggered by the pulses from an inductive transducer, has adjustable delay and duration. Secondly, the azimuthal position of every datum is determined using the secondary part of the dual-counter. This counting-system is reset by the wave-shaped signal (for each blade pass) and latched by the start signal from the photodetector.

The timing and transit time words are transferred to the computer and processed using data analysis software.

The software procedure manages the classification of the data in terms of their circumferential position in the rotating frame and offers considerable versatility. The blade pitch (between two resets of the counting system) is divided into a variable number of intervals whose widths can be chosen independently from each other. This allows the adjustment of the spatial resolution to the nature of the flow while taking into account the non-measurable zones (due to shadow and light reflection effects). Further details of such a blade pitch partition are described by Trébinjac et al. (1995). Furthermore, the number of validated data to be acquired is chosen independently for each azimuthal interval, allowing the maintaining of adequate accuracy even in weakly seeded zones.

A discrete azimuthal position value corresponding to the middle of each interval is assigned to the whole data collected in this interval.

### 3.3 Data reduction procedure

At each azimuthal position, the mean absolute angle, the mean absolute velocity, the angular and modulus standard deviations are calculated. The biasing correction suggested by Mac Laughlin and Tiederman is applied.

The measured velocity component is tangent to the shroud meridional direction at each measurement station. In order to visualize the throughflow field, the values of the statistic parameters are corrected by taking into account the angle $\xi$ between the meridional streamline and the perpendicular to the measurement station.

However, the meridional streamline is experimentally unknown. The value of $\xi$ is estimated from an axisymetric geometric meridional stream direction. This leads to :

$$\tan\alpha = \cos\xi \times \tan\alpha_{mes}$$

$$V^2 = V_{mes}^2\left(1+\cos^2\alpha_{mes}\times\tan^2\xi\right)$$

Moreover, the velocity is corrected to standard day conditions. Then, the mean relative parameters (W, $\beta$) and standard deviations ($\sigma_\beta$, $\sigma_W$) are calculated. The local relative Mach number is determined from the knowledge of the upstream flow field by assuming the conservation of the kinetic moment up to the leading edge of the rotor and the conservation of the relative total enthalpy from the leading edge up to the local point.

### 3.4 Seeding technique

The basic criteria for the choice of seed material are generally the ability of a particle of diameter d to track flow fluctuations, proportional to $d^{-2}$, and the amount of light scattered from it, proportional to $d^4$. But if measurements are performed in a high pressure compressor, another criterion becomes quasi-dominating : that is the local static temperature whose rise typically decreases the amount of light scattered from hot particles.

Solid seed particles do not degrade to around 2000°C and allow for LA measurements in configurations such as combustion chambers, but their use in the present case was proscribed because of a possible infiltration through the bearing. The

polystyrene latex spheres (PSL), that are now in current use, were ill-adapted because near 125°C they melt and adhere to the surfaces. Oils remain whose responses to the rise in temperature change according to the considered type as shown in Fig. 2. The acquisition frequency for paraffin, bearing oil and rhodorsil, whose burning points are respectively around 175, 200 and 300°C, is plotted versus static temperature under experimental conditions (laser power, photomultipliers supplying, detection threshold) analogous to those encountered during the current investigation. It must be noted here that, even if the detectability of the rhodorsil oil is one of the best, its viscosity ($500mm^2/s$) is ten times higher than that of the paraffin. This makes it rather difficult to atomize.

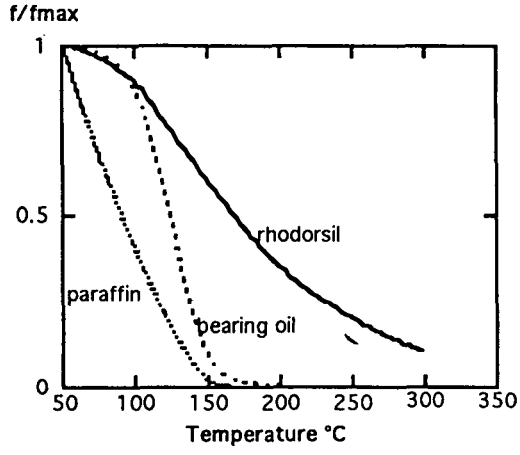


Fig.2 : Acquisition frequency with paraffin, bearing oil and rhodorsil seedings

With regard to the generation of seed, the current mass flowrate prevents any global seeding. Thus, the seed injection within the compressor must be achieved through a smoke probe located far enough upstream of the measurement point to avoid the probe wake interference. At the injection location, the static pressure was lower than the atmospheric pressure and thus, the pressure level has to be adjusted within the generator. If not, a seed jet was created whose kinetic energy was high enough to modify the aerodynamics at the measured point.

To sum up, the flow was seeded with oil particles injected through a chamfered smoke probe located 2m upstream of the impeller. Different types of oil were chosen according to the measurement locations (i.e. according to the local temperature). However, despite these changes, the mean data rate from the inlet to the exit typically varied from 1kHz down to 100Hz. The real size of the particles was not known; only its range can be estimated (0.5 - 1.5 microns).

## 4. MEASUREMENTS

### 4.1 Optical access and measurement locations

Separate laser flat windows provide optical access to the impeller in two main regions : the axial zone (inducer) and the radial zone. Because of mechanical constraints, no window can take place in the high meridional curvature region. For the measurements near the shroud which are the most sensitive to the perturbations due to the discontinuity between the flat glass and the curved shroud, a specific setting is used. The flat glass is set back to preserve the air-tightness and replaced by a perforated metal piece in continuity with the shoud.

A meridional sketch (Fig.3) of the centrifugal compressor shows the spanwise and streamwise locations where laser anemometer data have been acquired. Each measurement station is perpendicular to the shroud.

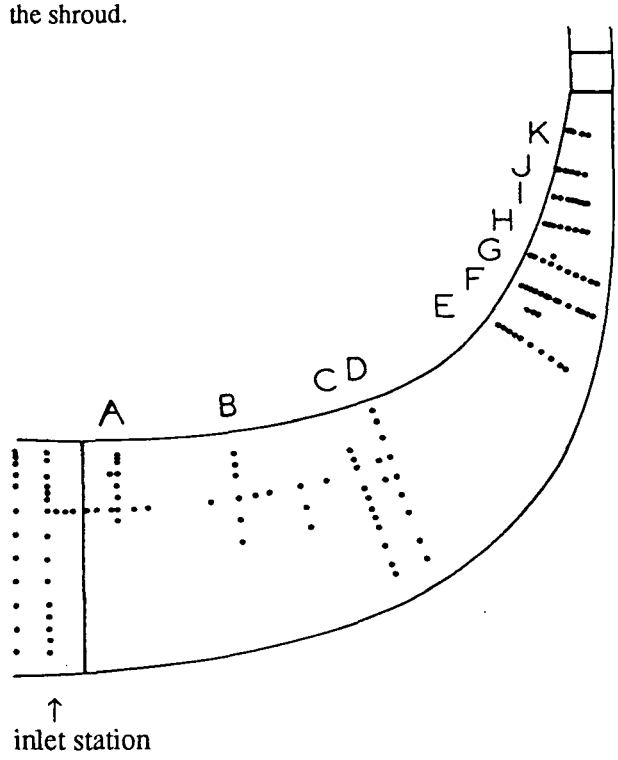


Fig.3 : Meridional sketch of the compressor

The nondimensional shroud meridional distances ($m/m_S$) of the stations which are presented below are listed in Table 2, where $m/m_S = 0$ is located at the leading edge of the impeller and $m/m_S = 1$ at the trailing edge.

| *station* | $m/m_S$ |
|---|---|
| inlet | - 0.05 |
| B | 0.215 |
| C | 0.361 |
| D | 0.408 |
| E | 0.637 |
| G | 0.750 |
| H | 0.806 |

Table 2 : nondimensional shroud meridional distances of the measurement stations.

### 4.2 Measurement uncertainties

An estimate of the uncertainties in the presented results has been made. It includes the uncertainties

inherent in the measurement technique (statistical process, resolution of the electronic counter...) and the errors connected with the experimental configuration (axial thrust, thermal dilatation...), without all error sources being taken into account (among others, those due to the seed material drag...). Throughout most of the impeller passage, the absolute velocity uncertainty levels are estimated to be +- 1.5% and the uncertainty of the relative flow angles is less than +- 1.7 deg. Finally, the uncertainty of the axial and radial locations of any measurement point is estimated to be +- 0.2 mm.

## 5. RESULTS

### 5.1 Presentation of the results

Most of the results shown hereafter are presented through iso-values maps plotted from the hub to the shroud and from the suction side of the main blade to the pressure side of the adjacent main blade. From station C, the maps show two distinct zones because of the presence of the splitters. The left part of each figure concerns the flow from the suction side of the main blade to the pressure side of the splitter (passage A) and the right part concerns the flow from the suction side of the splitter to the pressure side of the adjacent main blade (passage B).

Zones of lack of data are visible in each map. Near the blade surfaces, these zero-data zones arise from the shadow effects due to the blade twist and from the light reflections from the blade surfaces which lead to regions in which no data acquisition is possible either (Trebinjac et al.,1995). Near the shroud, if using the specific setting presented above, data should be reachable everywhere. But in fact, the glass window, even when it was set back, became very dirty probably because of a leakage of bearing oil. This also explains why few data are available in the inducer below 60 percent span.

### 5.2 The entrance region

At the inlet station ($m/m_S$ = - 0.05) and below around 65 percent span, the flow is subsonic and the pitchwise Mach number as well as the absolute angle distributions are quasi-uniform. Above, the flow is supersonic and both distributions reveal oscillations in the circumferential direction resulting from the crossing of the characteristics emanating from the rotor leading edge. A study of this supersonic entrance region is proposed through the calculation of the "unique incidence condition", assuming a two dimensional cascade flow (Levine, 1957). The unique incidence calculation, which is valid for started supersonic cascade with sharp blades, is extended to include the effects of detached shock waves in case of blunt leading edge (Bölcs, 1983). The shock detachment leads to a shift in the location of the limiting characteristic (the last captured Mach line), which results in an increase in inlet flow angle. The total pressure losses due to the detached bow shock are taken into account through the density calculation in the continuity equation along the limiting characteristic. The inlet flow angle, $\beta_{cal}$, calculated in this way is compared to the experimental angle, $\beta_{exp}$, for a section at 92.5 percent span. The procedure requires the knowledge of the inlet Mach number, which is the one along the neutral characteristic. Assuming that the neutral characteristic corresponds to a zero absolute flow angle (no pre-rotation), this leads to M = 1.13 (Fig.4). The prediction of the detachment distance d leads thus to a nondimensional value $d/m_S$ = - 0.03, which is consistent with the experiment because the flow was supersonic in all the measurement azimuthal intervals at the inlet station ($m/m_S$ = - 0.05). The calculation of the inlet flow angle leads then to $\beta_{exp} - \beta_{cal}$ = 0.3°. The agreement between the calculation procedure and the experiment is very good all the more the difference value is within the measurements errors. The assumption of a simple wave inlet bidimensional flow field is therefore validated.

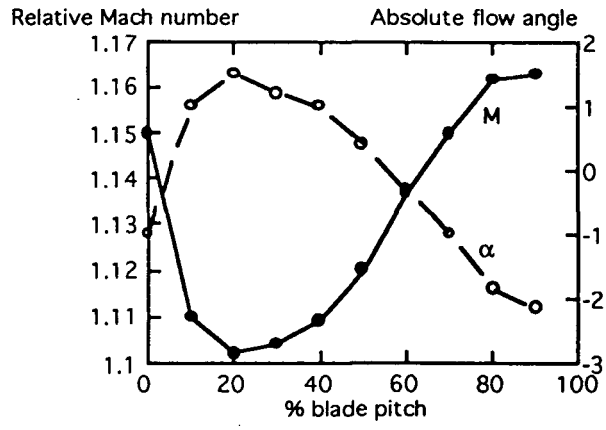


Fig.4 : Pitchwise distributions of relative Mach number and absolute flow angle at 92.5 % span and m/ms = - 0.05

Finally, it is interesting to note that the measurements performed without synchronisation in the inlet station lead to the same inlet values as above. In other words, this means that the mean values weighted by the mass flow are those being along the neutral characteristic.

### 5.3 The axial flow field

The contour map of the relative Mach number from $m/m_S$ = - 0.093 to $m/m_S$ = 0.321, at 70 percent blade height, is presented in Fig.5, where the origin of the abscissa corresponds to the blade suction side. A description of the shock pattern is made from the sonic line location. It is quasi-linear from 85% of the blade pitch at $m/m_S$ = 0 to 15% at $m/m_S$ = 0.167. A pocket of high Mach number values is observable in the half pitch near the suction side resulting from the divergent characteristics emanating from the convex suction surface. From these results, as from other results not shown here, the experimental shock pattern is plotted in the (m, θ) plane at 70 percent span (Fig.6). It can be noted here that a first calibration of numerical results should consist of making the calculated and experimental sonic lines meet exactly.

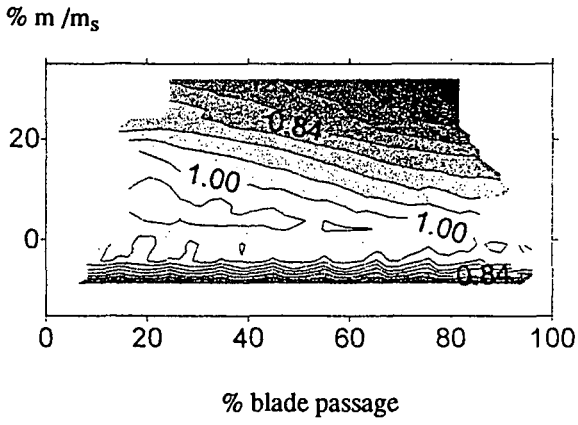


Fig. 5 : Contour map of the relative Mach number from $m/m_S = -0.093$ to $m/m_S = 0.321$ at 70 percent blade height

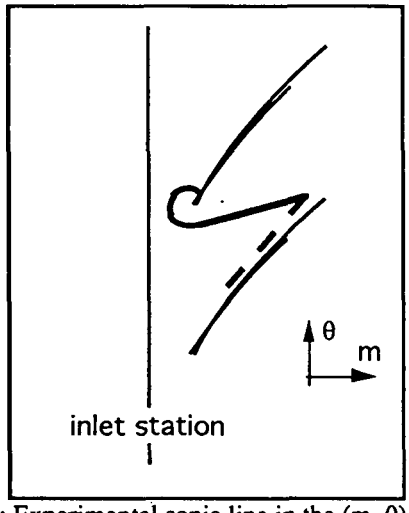


Fig.6 : Experimental sonic line in the (m, θ) plane at 70 % span

The contour maps of the experimental meridional velocity normalized by the inlet rotor tip speed (Vm/Ut) at stations B, C and D are presented in Fig.7. A negative gradient is observable from the suction side to the pressure side and from shroud to hub. That is in accordance with an inviscid nature of the flow, as expected. At station D, although the flow still seems to be dominated by inviscid properties, a decrease in meridional velocity appears near the shroud. The velocity fluctuations reach 15% in that zone, while they do not exceed 8% up this station.

### 5.4 The radial flow field

Fig.8, 9 and 10 show the experimental normalized meridional velocity contours at station E together with the velocity and angular fluctuations. Low meridional velocity zones are visible around midway between the blade passages in passage A and somewhat near the suction side in passage B. These low momentum fluid regions are associated with very high velocity and angular fluctuations that reach 20% and 12° respectively. Such a flow structure remains when moving downstream in the impeller as shown in Fig.11 and 12 at stations G and H respectively.

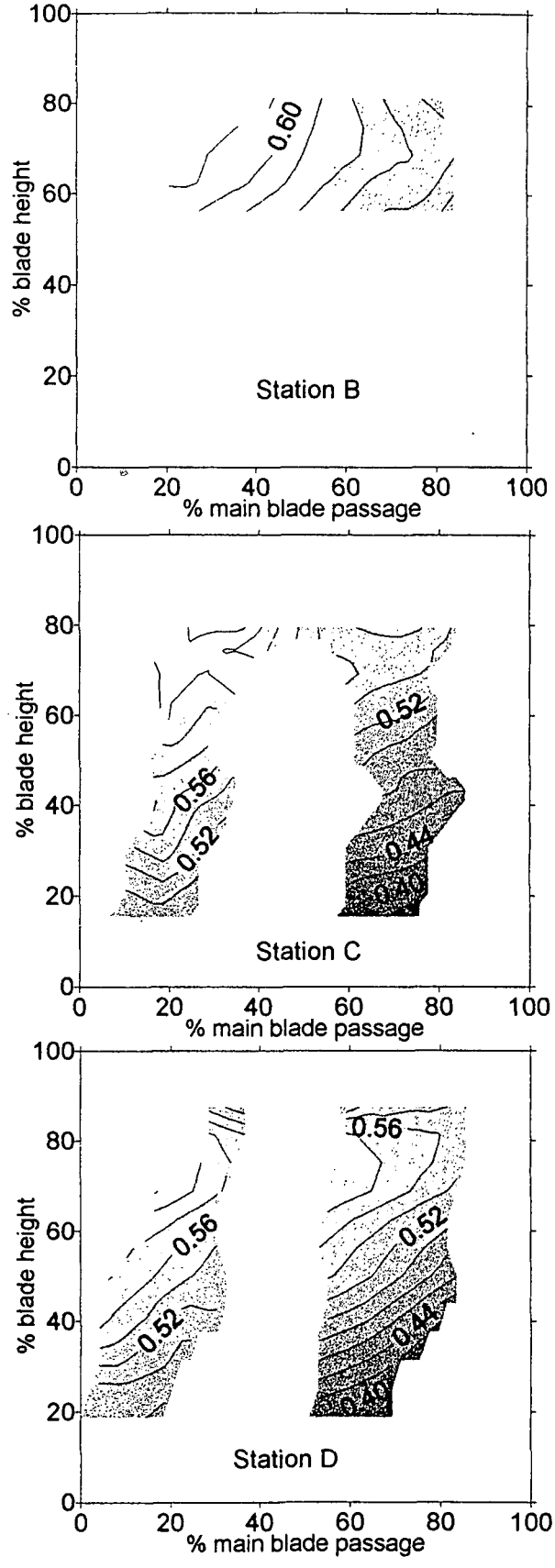


Fig. 7 : Lines of constant normalized meridional velocity ($V_m$ / $U_t$) at stations B, C and D

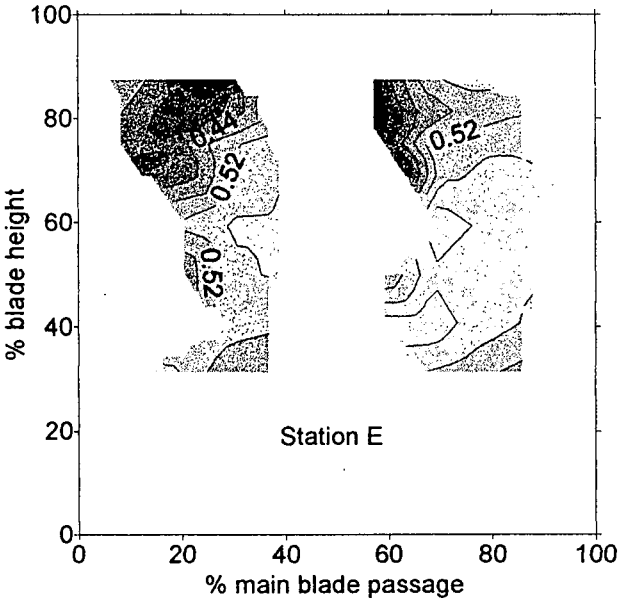


**Fig.8 : Vm / Ut at Station E**

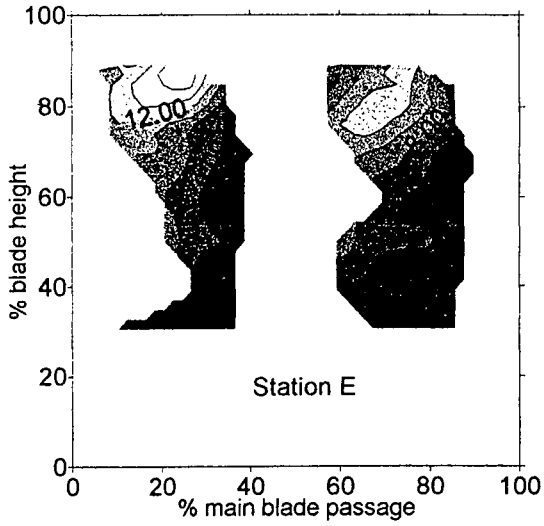


**Fig.9 : velocity fluctuations at Station E**

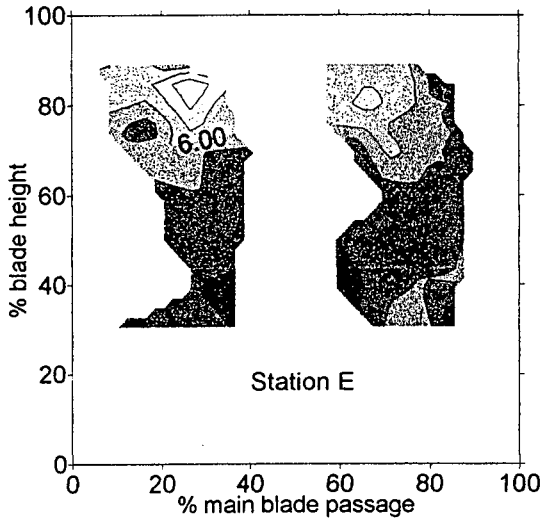


**Fig.10 : angular fluctuations at Station E**

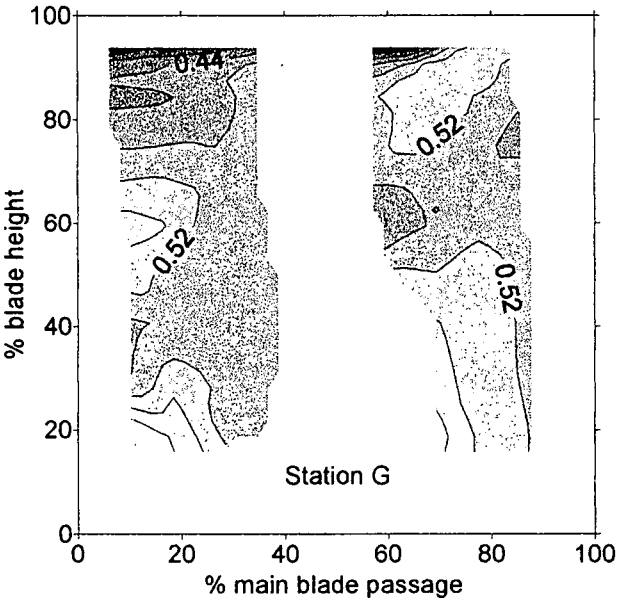


**Fig.11 : Vm / Ut at Station G**

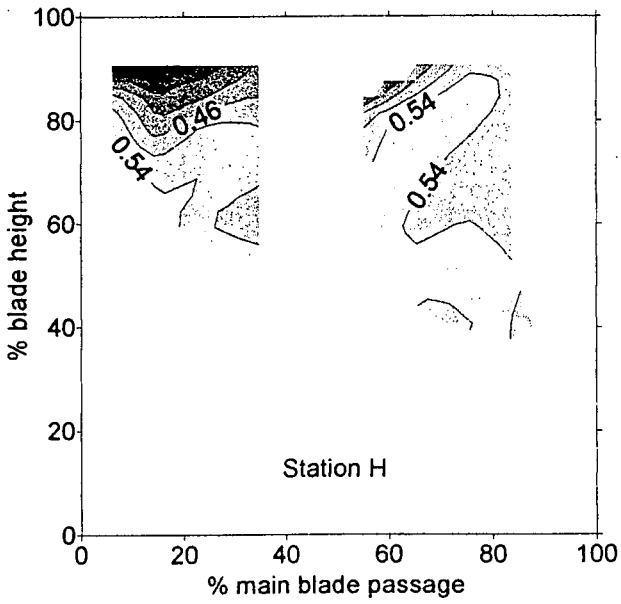


**Fig.12 : Vm / Ut at Station H**

From the high meridional curvature region, the throughflow pattern is largely distorted. The cause is thought to be in the vortex flows, as discussed below.

## 6. PHENOMENOLOGICAL STUDY OF VORTICAL MECANISMS

The meridional curvature of the impeller induces secondary flows due to the blade surface boundary layers, leading to a motion of the fluid from hub to shroud along the blade surfaces (denoted as PVM in Fig.13). When moving downstream in the impeller, the Coriolis passage vortex (PVC) gains in importance because the hub and shroud binormals have significant axial components, driving low energy fluid from the pressure to the suction side along the hub and the shroud. Finally, the blade-to-blade curvature generates secondary flows due to the hub and shroud boundary layers. The sign of this vortex (denoted as PVB) depends on the sign of the streamline curvature $K_{sn}$. In the case of backswept ending blades such as the present impeller, the passage vortices from blade-to-blade curvature and from Coriolis forces are contra-rotary.

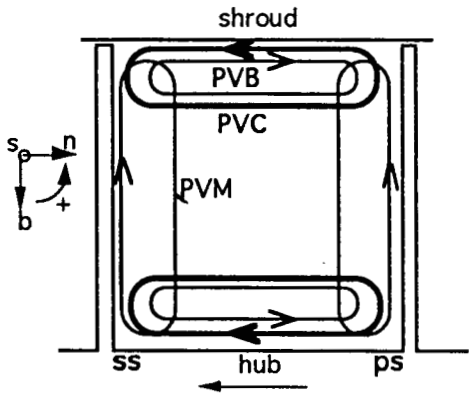


Fig.13 : Combination of passage vortices

Their relative strength (PVB vs PVC) can be quantified through the inverse of the Rossby number $\frac{1}{Ros} = \frac{K_{sn} W_s}{\omega_b}$. An evaluation of this ratio at stations E, G and H leads to 0.3, 0.12 and 0.08 respectively, i.e. the vortex due to the blade-to-blade curvature is too weak to conterbalance the vortex due to Coriolis forces. Therefore, from station E, the resulting motion indisputably drives low energy fluid from the pressure towards the suction surface. Thus, the interaction between the vortices from meridional curvature (PVM) and from Coriolis forces (PVC) leads to an accumulation of low velocity towards the suction surface / shroud corner, currently called the "wake" region. Such a low velocity zone seems to be through experiments in passage B. In order to understand the flow structure in passage A, the tip clearance effects have to be added. Indeed, for unshrouded impellers, the tip clearance flow acts in a direction opposite to the vortex due to Coriolis forces, PVC. If the tip clearance effects are strong enough, they can drive the low momentum fluid region somewhere towards the shroud / pressure side corner.

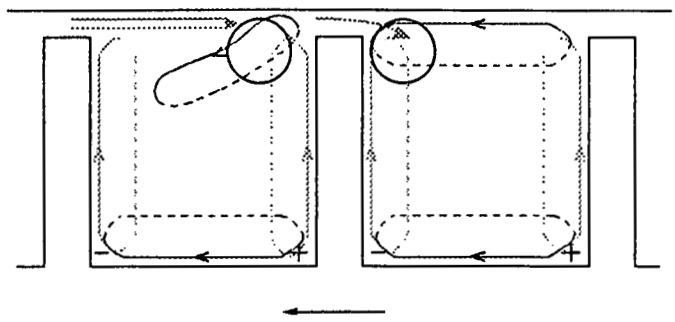

Fig.14 : Secondary flow structure depending on the intensity of the tip clearance effects

It is obvious that the leakage mass flow is much greater through the principal blade tip than through the splitter blade tip, but it tends towards the same level at the trailing edge. The resulting secondary flows structure depending on the intensity of the tip clearance effects can then be sketched as in Fig.14 : the low momentum fluid zone is located in the suction side / shroud corner in passage B whereas it is located somewhere in the midchannel in passage A, as suggested by the experimental results.

To pursue the quantification of the relative strength of the different vortices contributing to the formation and the transport of the wake, detailed data of boundary layers are required. Due to the considerable difficulty of obtaining these data experimentally within such an impeller, a solution is to rely on detailed numerical simulations solving the three dimensional viscous flow if the computed results are reliable enough. The expected reliability is obtained by calibrating the numerical simulations with the obtained experimental results. That is the second phase of this research program.

## 7. CONCLUDING REMARKS

L2F measurements have been performed within a high-speed high-pressure centrifugal splittered impeller. Although the unfavourable experimental conditions (small passage size, strong meridional curvature, complex aerodynamics, very high temperature) dramatically restrict the inter-blade zones that are really investigated, the results proved the ability of our laser anemometry system to provide measurements within such a complex configuration. Further developments of the measurement technique are in progress, notably including the seeding control. Indeed, the use of solid material should allow the performance of measurements up to the rotor exit and the diffuser.

The presented results are in very good agreement with analytical results in the entrance region. They reveal a potential flow structure up to the high meridional curvature region, and then a largely distorted throughflow pattern. A qualitative description of the contributions of the various secondary vortices is proposed. It tends to show the strong influence of the tip clearance effects on the low momentum fluid zone location. That is confirmed by the experimental results, as evidenced by the clear differences in the flow pattern between both passages A and B. Finally, the present

results make up a data bank in order to validate numerical simulations that are the only way to obtain a detailed understanding of such a complex flow.

ACKNOWLEDGEMENTS

We would like to thank TURBOMECA which placed the investigated compressor at our disposal and the Direction des Recherches, Etudes et Techniques (DRET) which supported this work.

REFERENCES

Bölcs, A., 1983, "Turbomachines Thermiques - Ecoulement Transsonique dans les Turbomachines", *Course of the Ecole Polytechnique Fédérale de Lausanne.*

Chriss, R.M., Hathaway, M.D., and Wood, J.R., 1994, "Experimental and Computational Results from the NASA Lewis Low-Speed Centrifugal Impeller at Design and Part Flow Conditions", ASME Paper 94-GT-213.

Eckardt, D., 1976, "Detailed Flow Investigations within a High-Speed Centrifugal Compressor Impeller", ASME *Journal of Fluid Engineering*, Vol. 98, pp. 390-402.

Elder, R.L., and Forster, C.P., 1987, "Measurements in Centrifugal Compressors", in Flow in Centrifugal Compressors, Von Karman Institute for Fluid Dynamics L.S. 87-01.

Hathaway, M.D., Chriss, R.M., Wood, J.R., and Strazisar, A.J., 1993, "Experimental and Computational Investigation of the NASA Low-Speed Centrifugal Compressor Flow Field", ASME *Journal of Turbomachinery*, Vol. 115, pp. 527-542.

Krain, H., 1988, "Swirling Impeller Flow", ASME *Journal of Turbomachinery*, Vol. 110, pp. 122-128.

Levine, P., 1957, "Two-Dimensional Inflow Conditions for a Supersonic Compressor with Curved Blades"*Journal of Applied Mechanics*, Vol 24.

Schodl, R., 1977, "Laser-Two-Focus Velocimetry (L2F) for Use in Aeroengines", AGARD L.S. 90.

Senoo, Y., Hayami, H., Kinoshita, Y., and Yamasaki, H., 1979, "Experimental Study on Flow in a Supersonic Centrifugal Impeller", ASME *Journal of Engineering for Power*, Vol. 101, pp. 32-41.

Strazisar, A.J., 1993, "Laser Anemometry Applications in Turbomachinery", *Proceedings, 2nd International Symposium on Experimental and Computational Aerothermodynamics of Internal Flows*, Prague, pp. 77-99.

Trébinjac, I., and Vouillarmet, A., 1988, "A Laser Anemometry Technique for Measurements in a Single-Stage Supersonic Compressor", *Proceedings, 9th Symposium on Measuring Techniques for Transonic and Supersonic Flow in Cascades and Turbomachines*, Oxford, pp.10.1-10.27.

Trébinjac, I., Vouillarmet, A., and Claudin, I., 1995, "Refinements of a L2F Anemometry Technique for Inter-Blade Flow Field Investigations", *Proceedings, 16th International Congress on Instrumentation in Aerospace Simulation Facilities*, Ohio, pp. 54.1-54.6.

Vouillarmet, A., 1986, "Measurements inside the Blade Row of a Transonic Compressor with a Time-of-Flight Velocimeter", *Proceedings, 8th Symposium on Measuring Techniques for Transonic and Supersonic Flow in Cascades and Turbomachines*, Genoa, pp.9.1-9.26.

Paper 3
Author: I. Trebinjac

Q: J. Edmonds

Have you considered how to wash the L2F windows?

A: Une serie de petits orifices a ete amenagee tout autour du verre de visee, afin d'injecter du solvent qui, convecte par l'ecoulement, assure le nettoyage de la vitre. Malheureusement, vues les hautes temperatures, rencontrees dans la presente investigation, le solvent (toluene) s'evapore presque des la sortie des orifices et le nettoyage s'est donc revele inoperant.

# 3-D LDA MEASUREMENTS IN AN ANNULAR CASCADE FOR STUDYING TIP CLEARANCE EFFECTS

A. Doukelis, K. Mathioudakis, M. Founti*, and K. Papailiou

National Technical University of Athens
Lab. of Thermal Turbomachines
*Thermal Eng. Section, Lab. of Steam Generators and Thermal Plants
P.O. Box 64069
GR 15710 Athens
Greece

## ABSTRACT

Literature survey indicates the lack of detailed 3-D flowfield data for high-speed flows inside turbomachines, especially in the region of the tip clearance gap, and points out the difficulties in conducting this kind of measurements. Such information is nevertheless essential in order to validate CFD codes, which give the possibility of understanding the flow and finally producing better designs of efficient turbomachinery components. This paper aims at presenting a 3-D LDA measurement technique, as applied for the measurement of the flowfield in an annular cascade used to study tip clearance effects. First the measurement system layout, signal processing and data acquisition and processing is presented in detail, together with an evaluation of the measuring accuracy and the measuring capabilities of the system in simple flows. Next the annular cascade configuration is described, together with a detailed account of all the aspects of execution of the measurements and the provisions taken in this study. Finally sample measurements results, demonstrating the kind of information provided, are presented.

## 1. INTRODUCTION

The possibility of measuring the three-dimensional flowfield in the vicinity of the blade tip clearance is of great importance in the field of turbomachinery. In this region a tip clearance jet is created due to the pressure difference between the pressure and suction side of the blade. The flowfield is dominated by the effect of the consequent roll-up of the jet close to the suction side to form the tip clearance vortex and its interaction with the flow in the blade passage. The understanding of these phenomena is essential, since a large portion of the losses generated inside the passage is due to the presence of the tip clearance gap. Since 1954 when Rains [1] conducted the first extensive study of the phenomena associated with the tip clearance gap in an axial water pump and attempted to model the flow, many researchers have conducted experimental and theoretical studies of the tip clearance flow. Yet, the available experimental data, both for compressors and turbines, is mostly confined to low-speed flows, where the flow can be regarded as incompressible. This data, although providing a good tool for the understanding of the nature of the tip clearance flow and the development and validation of Computational Fluid Dynamics (CFD) codes cannot provide a general tool for the case of industrial turbomachines, where near-to-Mach conditions can be encountered. The compressibility factor modifies the mass flux through the tip clearance gap, and this mechanism has to be taken into account for the development of CFD codes capable of accurately predicting the flowfield properties at the tip clearance region of the blades. Therefore, tip clearance measurements for high-speed compressors and rotors are important for the design and construction of more advanced turbomachine components.

Traditionally hot-wires, pitot-tubes, pressure tappings and flow visualization techniques have been applied in the study of the flowfield inside turbomachines. For example, Howard et al [2] conducted measurements with cobra and wedge pitot-probes inside a four-stage low-speed axial compressor for two different tip-clearance gap values for the rotor and one for the stator of each stage. Storer and Cumpsty [3] investigated the velocity through the clearance and the pressure distributions around the clearance using blade and wall pressure tappings and a miniature flattened Pitot probe. Lakshminarayana et al [4] used stationary and rotating hot wires in the tip region of a rotor in a single stage compressor. Several investigations have also been conducted at the inlet and exit region of isolated compressor and turbine rotors and stators or multistage engines.

Intrusive measuring techniques, such as the above described, have a major disadvantage: since the tip clearance gap is generally small, the effect of the insertion of protruding bodies with diameters of the same order of magnitude as that of the gap can be quite substantial. This problem can be overcome with the use of non-intrusive measuring techniques,

*Paper presented at an AGARD PEP Symposium on "Advanced Non-Intrusive Instrumentation for Propulsion Engines", held in Brussels, Belgium, 20-24 October 1997, and published in CP-598.*

such as Laser Doppler anemometry. The use of two and three-component LDA systems is increasing in the field of turbomachinery applications, since they provide additional interesting aspects, such as the small size of the optical probes and of the control volume, resulting in good spatial and temporal resolution. Three-component (3-D) LDA systems can be thus applied to perform measurements in high-speed flows, including tip-clearance effects.

Many researchers have conducted measurements in turbomachinery configurations using LDA. Chesnakas and Dancey [5] studied the flow field in a low-speed axial flow compressor using a three-color, three-component LDA, backscatter collecting optics, counter signal processors, frequency shift from 0 to 10 MHz and a 6.4 mm thick uncoated plexiglass window. A six-jet aerosol seeder was used to seed the flow with two micron mean diameter sugar particles. The seed was introduced locally into the flow upstream of the compressor bellmouth. No measurements were conducted close to the hub or tip, and there is no mention to the problem of window contamination. The three beam pairs were produced by a single laser source and focused into one common measuring volume. The system (laser source and optics) was mounted on a single optical table attached to a mechanical traversing mechanism, making the whole assembly quite bulky. Murugan et al [6] studied the flowfield in the exit region of a radial inflow turbine at low speeds using a 3-D LDA quite similar to the one mentioned above, two micron mean diameter propylene glycol particles as seeding and a 1.3 mm thick Lexan window. The flow was seeded with a six-jet TSI atomizer connected to the bottom of the settling chamber. The study included tip clearance flow investigation. Lakshminarayana and Murthy [7] conducted one-component LDA measurements of the axial and tangential velocity components in order to investigate the annulus wall boundary layer development in a low speed compressor rotor using an atomised spray of mineral oil as seeding, injected into the flow upstream of the rotor. The nearest radial station where measurements were conducted was 5 mm from the wall. They used a single channel dual-beam laser anemometer with on-axis backscatter light collection, mounted on a three-axis traverse table and a counter type signal processor. No window contamination has been reported. Strazisar [8] employed a single channel fringe anemometer and a 3 mm thick glass window to conduct measurements of flow periodicity and shock structure in a transonic fan rotor with a design tip relative Mach No. of 1.38. Liquid seed particles of 1-1.4 mm mean diameter were injected into the flow through a 6 mm diameter tube located upstream of the rotor. Kenneth Suder [9] used a two-color fringe type laser anemometer system in order to conduct detailed measurements of the tangential and axial velocity component of the flow upstream, within, and downstream a transonic axial compressor rotor with an inlet relative tip Mach number of 1.48. The researcher used 0.8 mean diameter polystyrene particles as seeding and an one-inch thick alumina silica window, contoured to conform to the rotor flowpath. The nearest radial station where measurements were conducted was 4 mm from the wall. Hobson and Dober [10] conducted three-component measurements upstream and downstream a linear cascade of controlled-diffusion stator blades inside a low speed cascade tunnel, using a three-color three-component fibre-optics LDA, backscatter collecting optics and counter signal processors. The two fibre-optic probes were mounted on an automated three axis traverse table. The flow was seeded with 0.9 mm mean diameter olive oil particles injected with an oil-mist generator upstream of the inlet guide vanes. The measurements nearest to the endwall were conducted 6.4 mm from the wall.

The above short review demonstrates the potentials of LDA techniques in turbomachinery configurations, as well as the lack of detailed flowfield measurements at high speed turbomachinery flows. It can be observed that for the high-speed flows studied, either the measurements inside the blade passage did not give an extensive coverage of the 3-D flowfield, or they were simply confined at the inlet and outlet of a blade row. This can be attributed to the fact that the specific problems encountered in conducting 3-D measurements inside a turbomachine with LDA are not negligible. For example, the flare conditions created when a solid surface is approached by the laser beams make near-wall measurements extremely difficult, because of the deterioration of the quality of the signal. Other problems include the adequate seeding of the entire flowfield under consideration and the fouling of the window due to contamination caused by the seeding. In order to produce detailed 3-D measurements inside high speed turbomachinery configurations, these problems have to be solved. The current study is an attempt to contribute in this field, by presenting a detailed account of a 3-D LDA measurement approach applied for the measurement of the flowfield in an annular cascade with the use of a specially designed three-component LDA.

The 3-D Laser Doppler anemometer and the signal processors that were used in the current study were specially selected in order to provide the ability of conducting three-component high speed measurements inside confined flows. The anemometer consists of two independent systems, a single component and a two component system, employing two independent laser sources, fibre optics and two small diameter back-scattered light optical probes providing high spatial resolution. This feature is unique, since other 3-D Laser-Doppler anemometers employ only one laser source producing the three beam-pairs. The two systems can be operated independently, providing large flexibility. In addition, the system is very compact in size and can be easily transported as a whole. The light-weight and small size of the two fibre-linked optical probes enables ease of traversing and of alignment. Three FFT signal processors have been selected for the signal processing, in order to provide a large bandwidth, enabling high speed measurements, and a high sensitivity for low SNR conditions, a situation encountered when approaching solid surfaces.

This work will present the adopted 3-D LDA measurement approach, as applied for the measurement of the flowfield in a high-speed annular cascade used to study tip clearance effects. First a detailed description of the 3-D LDA, data acquisition and processing will be presented, followed by an evaluation of the measuring capabilities of the system in simple flows. Next an account on several aspects of the measurement approach in the annular cascade facility will be described. Finally, sample measurement results, demonstrating the kind of information provided, will be presented.

## 2. THE THREE COMPONENT LDA SYSTEM

The layout of the 3-D Laser-Doppler anemometer is shown schematically in Fig.1. It consists of two independent systems: an one component (1-D) and a two-component (2-D) system, both employing fibre optics and small diameter optical probes for the transmission and collection of the scattered light from the three measuring volumes. The 2-D probe transmits two orthogonal beam-pairs, and measures two orthogonal velocity components. The 1-D probe transmits a third pair of laser beams, it can be positioned at any angle with respect to the 2-D probe and measures a component inclined with respect to the plane of the components measured by the 2-D probe, from which the third velocity component is derived. The two optical probes are housed on a small-base probe carriage allowing fine 3-D linear and rotational adjustment of the probe relative positions. The three measuring volumes are focused on the same point by adjusting the back reflections of the six beams, after reflection on a small highly polished sphere. The 3-D LDA system has been constructed by INVENT GmbH, Germany [11] and it has been selected for turbomachinery applications because of its robustness, easy handling and ease of traversing. The probe system has a small physical size and offers a wide range of focusing lens focal lengths and small dimensions of the resulting measuring control volume (mcv) that allows measurements in the vicinity of walls. The smallest size of the volumes that can be achieved using the minimum focal length of the focusing lens is 0.17 mm in length and 22 $\mu$m in diameter. The relative size of the three volumes is approximately the same for a pair of focusing lens with the same, or almost the same, focal length, enabling the proper alignment of the three volumes. The three-component LDA system is presented in detail in the following paragraphs.

### 2.1 The two component system

It consists of the following:

1. A 5W Argon-Ion laser (COHERENT GmbH, INNOVA 90-5) with control module and power supply is used as the light source for the 2-D optical system.

2. An Optical Transmission Unit (O.T.U.) [11], mounted on a rigid base plate. In the O.T.U. the incoming laser beam, containing multiple wavelengths, is split in two pairs of shifted and unshifted beams (blue beams of 488 nm wavelength and green beams of 514.5 nm wavelength), which are focused on four fibres, ending at the 2-D probe. Also, the separated light signals from the receiving fibre of the probe head are fed to two photomultiplier tubes, located in the O.T.U. The entire optical system is rigidly mounted on a sandwich type bread-board, and is equipped with a metal cover to avoid dirtying.

3. An LDA Supply Unit comprising one variable Bragg-cell driver, providing maximum frequency shift of 40 MHz, and a double downmixer allowing net shift frequencies between 100 KHz and 10 MHz, at each channel.

4. Two photomultiplier Power Supplies (the two photomultipliers are incorporated in the O.T.U.).

5. A 36 mm diameter, two component fibre-optic backscatter probe with six interchangeable front lenses (f=80, 120, 140, 160, 200, 250 mm). In order to create the two orthogonal beam sets the 2-D probe uses the 488 nm (blue) and 514.5 nm (green) beams from the laser, with an average output power per unfocused beam of about 40 mW and 80 mW respectively.

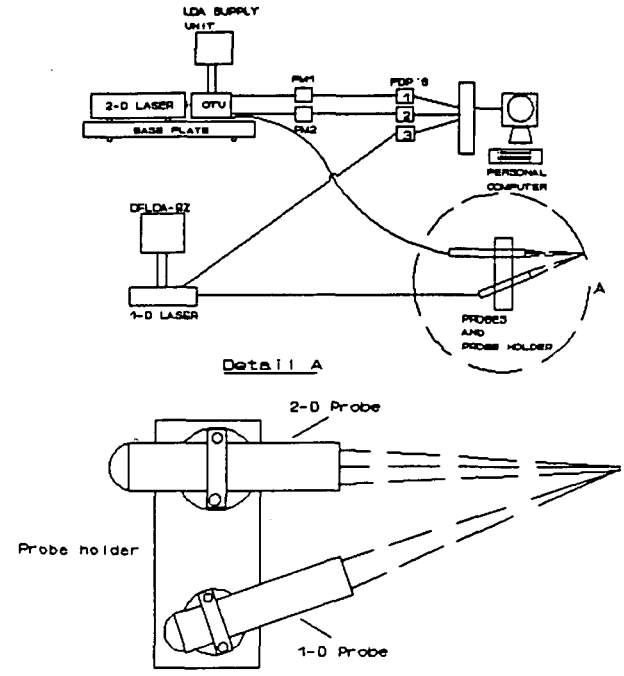


**Figure 1**: Layout of the 3-D LDA

### 2.2 The one component system

The Diode laser Fibre-optic Laser Doppler Anemometer (DFLDA) [12] comprises a Base Optical Unit (B.O.U.), a power control unit and a fibre-optic back-scatter probe, as follows:

1. The B.O.U. includes a 100 mW single-stripe, monomode, laser diode, an optical isolator, choice of double or single Bragg cells, fibre-optic couplers and an Avalanche Photo-Diode (APD). The laser diode emits light at 860 nm which is not visible, it is temperature regulated and the beam is corrected for astigmatism and for achieving a circular beam profile.

2. The power control unit includes all the electronic parts necessary to run the DFLDA system, namely the main power supply, the APD power supply, the Bragg-cell driver and the laser diode power supply. The unit includes a signal downmixer for operation with a single Bragg-cell, providing net frequency shifts between 100 kHz and 10 MHz. The frequency shift of the Bragg cell is 60 MHz, which is appropriate for measurements in high speed flows.

3. The fibre-optic backscatter probe is 30 mm in diameter and can be operated with five interchangeable front focusing lenses (f=60, 120, 150, 200, 250 mm), providing dimensions of the measuring volume similar to that of the 2-D probe. The average output power per unfocused beam is about 12 mW.

## 2.3 Signal processing and data acquisition

The processing of the Doppler signals delivered from the three beam-pairs is performed with three Frequency Domain Processors (Macrodyne Inc., U.S.A., Model 3107) [13], performing an FFT on each channel.

The FDP 3107 can measure frequencies up to 120 MHz with variable sampling rates of 300, 150, 75, and 37.5 MHz with a minimum sensitivity of 5mV full-scale. A selectable frequency domain validation technique, plus a percentage validation are utilized in each processing range. Maximum data throughput of Doppler frequency is sustained at a rate of approximately 3300 records/sec, for a digitization length of 32 words (Record Length - RCL). In order to increase the accuracy of frequency estimation a specific frequency estimator technique of high accuracy is utilized, providing an error of the order of $\pm 0.1\%$ of Nyquist frequency with full-scale noiseless sinusoidal input.

The three signals, corresponding to the three velocity components are fed to the three FDP's. The two signals, originating from the 2-D optical system, are either fed directly to two FDP's or via the double downmixer. Each signal can be appropriately filtered via a high and a low band-pass filter. The signal fed to the FDP is continuously digitized with a high-speed analog-to-digital converter whose output passes through a high-speed shift register. This register, user-selectable from 32 to 4096 words, is monitored to determine when the energy content exceeds a selected threshold indicating the presence of a signal burst. When a burst has been captured, the contents of the shift register are transferred to an in-line digital signal processor chip for transforming to the frequency domain using FFT techniques. The experimenter can select from one of two means of frequency domain validation to be used for each of the ranges: secondary peak to primary peak ratio and the ratio of Doppler signal energy to total energy. Peak Signal validation determines the ratio of the primary peak height with the next highest peak and compares the result with a user selected value (Peak Ratio Technique). If the determined value is less than the selected value, the spectrum is considered to be of a validated signal and the frequency of the primary peak is determined using an Energy Profile Estimator technique. A second user-selectable validation technique (Energy Ratio) calculates the energy contained within the primary peak and compares it with the energy in the Total Energy Spectrum of the selected Processing Range. If the ratio exceeds the selected value, the measurement is considered valid and the frequency of the primary peak is determined and produced as a digital output sent to a computer via a GPIB interface and a data acquisition board.

A personal computer is used for the processing of the data (frequencies) acquired from the 3 FDP's, via an IEEE data acquisition board. The acquisition board has a software programmable built-in coincidence detector giving the ability to acquire two or three-component measurements inside a predefined coincidence window, enabling thus the acquisition of time correlated events. This fact is crucial when it is desired to calculate shear stresses, since for a large number of events any set of random velocity components will give a value of shear stress equal to zero. In addition, the calculation of the mean velocity and rms of the non-orthogonal velocity component using uncorrelated events leads to an increased error, depending on the angle between the 1-D and 2-D probes, as was highlighted by Orloff and Snyder [14]. The coincidence window used depends on the expected time-scale of interest of the flow under consideration.

Data processing is performed using the custom-made Laser Velocimetry Software by ZECH-Electronics Co. and INVENT GmbH [15]. The software is capable of performing the simultaneous analysis of one, two, or three component velocity measurements. Mean and rms velocities and shear stresses are calculated for each measuring location, based on the collected data of measured frequencies. Data can also be acquired in raw form, accumulated and processed in a later time.

## 2.4 Evaluation of flowfield properties

The 2-D probe measures directly two orthogonal velocity components whereas the 1-D probe measures a component inclined with respect to the plane of the components measured by the 2-D probe, from which the third velocity component is derived. Since the positioning of the probe carriage may be such that the 2-D probe does not measure the desirable orthogonal components (e.g. axial and peripheral) it may be also necessary to transform these two velocity components. In this case, assume that the chosen coordinate system is $X_1X_2X_3$ and that the corresponding velocity components, which have to be calculated, are $U_1$, $U_2$, $U_3$ (Figure 2). In Figure 2 axis $X_3$ coincides with the axis of the 2-D probe, a case which is common for measurements inside turbomachines. The measured velocity components in the probe-fixed system of coordinates are $S_1$, $S_2$, $S_3$. Using the three orientation angles $\alpha_1$, $\alpha_2$, $\alpha_3$ and the angle between the two probes $\phi$ ("pie" angle) the measured velocities (S1, $S_2$, $S_3$) can be transformed to the velocities $U_1$, $U_2$ and $U_3$ using the following equations:

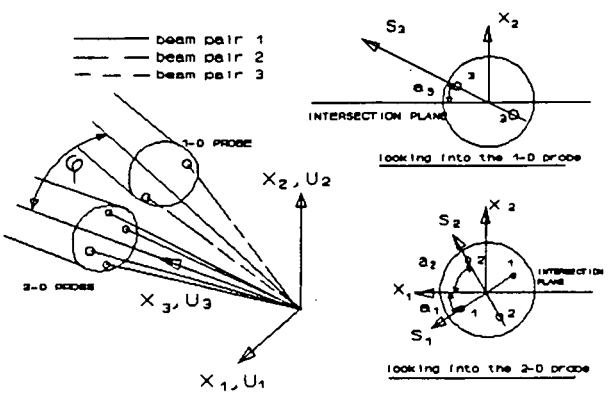


Figure 2: System of coordinates

$$U_1 = \frac{S_1 \cdot \sin\alpha_2 - S_2 \cdot \sin\alpha_1}{\sin\alpha_2 \cdot \cos\alpha_1 - \sin\alpha_1 \cdot \cos\alpha_2} \tag{1}$$

$$U_2 = \frac{S_2 \cdot \cos\alpha_1 - S_1 \cdot \cos\alpha_2}{\sin\alpha_2 \cdot \cos\alpha_1 - \sin\alpha_1 \cdot \cos\alpha_2} \tag{2}$$

$$U_3 = \frac{S_3 - U_1 \cdot \cos\phi}{\sin\phi} \tag{3}$$

Since equations (1)-(3) are in linear form the calculation of the mean velocities is correct even if the measurements of the components $S_1$, $S_2$, $S_3$ are not correlated in time. This is not the case for the calculation of the turbulent stresses, since the corresponding equations are not linear any more. Therefore in the current study, the placement of the probe system is done in such a way that it measures directly two velocity components (e.g $U_1$, $U_2$). The corresponding normal stresses are also measured directly and a transformation is needed only for the third component.

As mentioned previously, the measurement of shear stresses imposes the acquisition of the velocity components using a coincidence window. If the desired coincidence window is small, as is the case in high-speed flows, long measuring times would be necessary to conduct coincident measurements. In addition the small size of the volumes used in the current study is a fact that makes coincident measurements lengthier in time, since the increased spatial resolution is counterbalanced by a decreased temporal resolution and, even a small misalignment of the three volumes would make the situation even worse.

## 2.5 Evaluation of the measuring capabilities of the 3-D LDA

A very important aspect of any measuring system is the accuracy of the measured quantities. The statistical error of the measured quantities by LDA depends on the sample size used for the derivation of these quantities. The sample size used in the current study was 3000. Using the equations provided by Yanta [16] yields an error of $\pm 2.5\%$ for the normal and shear stresses and $\pm 1\%$ for the mean velocities for a value of 30% turbulence intensity, a value which was rarely exceeded in the current study. If the measurements are not correlated in time (use of coincidence window) then, according to Orloff and Snyder [14], the statistical error of the indirectly measured component, which is derived by the non-orthogonal velocity component, is multiplied by a factor depending on the angle created by the two probes. For the current study this angle ("pie angle ") was approximately 30 deg. This yields an error of $\pm 2.6\%$ for the indirectly measured velocity component, for the case of uncorrelated measurements, whereas the statistical error for the directly measured components remains unaffected ($\pm 1\%$). Another important source of error comes from the alignment of the probe carriage with respect to a given facility. The inaccuracy of angle measurement, which is of the order of $\pm 0.3$ deg. both for the angles created between the probe carriage and the facility and the angle between the two probes, yields a systematic error to the measurement of the three velocity components. This systematic error is of the order of $\pm 0.3$ deg. for the measurement of the flow angles (yaw and pitch angle).

In order to assess the measuring capabilities of the system a series of 3-D measurements have been performed in a small free-fet with a 20 mm nozzle exit diameter, (A. Doukelis et al [17]). The working fluid was air. The maximum centre-line axial mean velocity was about 85 m/sec with a low turbulence intensity (about 1% at the nozzle exit), corresponding to a Reynolds number of $1.63 \cdot 10^5$. The flow was seeded with 0.3 $\mu$m average diameter $TiO_2$ particles, which were injected in the flow from an RGB-1000 particle disperser [18].

Extensive measurements were conducted in the jet configuration [17]. Some representative results are presented here. Figure 3 shows the measured axial, radial and circumferential turbulence intensity profiles, at X/D = 15.5. The

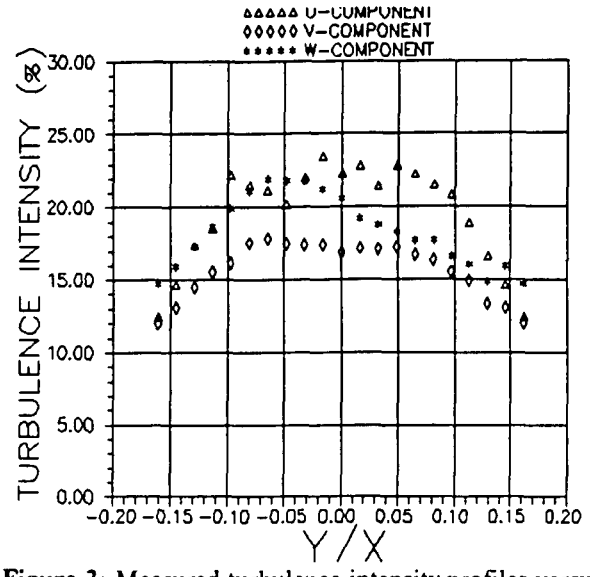


**Figure 3**: Measured turbulence intensity profiles versus Y/X

axial turbulence intensities are consistently larger than the measured values for the other two components. The above behaviour is expected on physical grounds (Tennekes and Lumley [19]) and has been observed in the earlier studies of Wygnanski and Fiedler [20] and Hussein et al. [21].

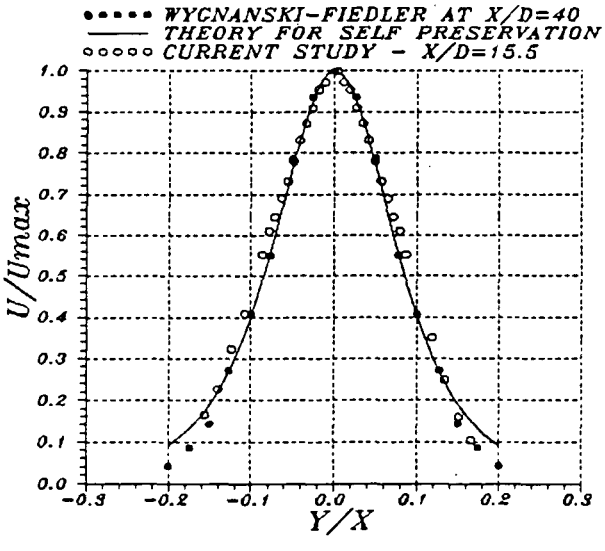


**Figure 4**: Comparison of axial mean velocity profiles

Figure 4 presents a comparison of the measured axial non-dimensionalized mean velocity profiles at X/D=20 with free-jet theory and measurements conducted by Wygnanski-Fiedler [20] at X/D=40. The agreement in the region of the jet centerline is very good, whereas in the outer region larger discrepancies are observed, due to the fact that the measurements were conducted at a position where self-preservation is not yet attained (X/D>70 according to Wygnanski-Fiedler [20]). Measurements were also conducted inside and at the exit of a circular tube of 20 mm internal diameter and wall thickness of 2 mm. These measurements were conducted with a 3-channel coincidence interval of 100 $\mu$s, in order to measure the shear stress distributions. Figure 5 presents the measured shear stress profiles at the exit of the tube, which show the expected trend: the $\overline{uw}$ and $\overline{vw}$ stresses are approximately zero whereas the $\overline{uv}$ shear stress

component is non-zero with a distribution as expected for an axisymmetric jet.

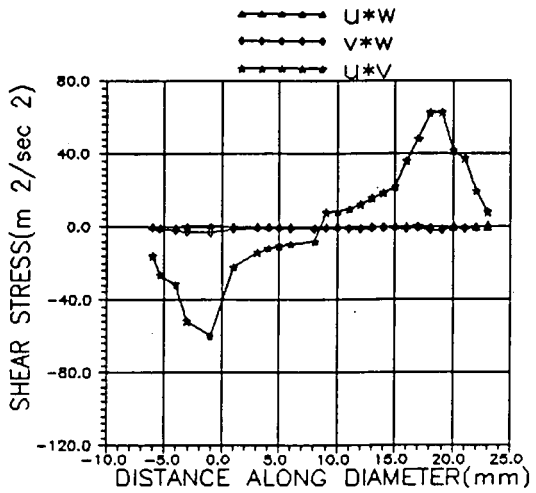


**Figure 5**: Shear stress profiles versus Y at X/D=3

## 3. ANNULAR CASCADE CONFIGURATION - EXECUTION OF MEASUREMENTS

A description of the annular cascade facility, together with an account of several aspects of the measurement approach followed in the current study is presented next.

### 3.1 Annular cascade facility

The layout of the annular cascade facility is shown in figure 6, whereas figure 7 presents a detailed drawing of the test section. The design and construction of this facility has been reported in detail by Mathioudakis et al [22]. The airstream enters the facility via a smoothly contracting bellmouth into a scroll. The scroll delivers the air flow with a swirl into a bent duct which gives to the annular space. The test section, on which the test cascade is mounted follows. The test cascade has 19 straight blades, with a chord of 100 mm, 0.8 aspect ratio and maximum thickness to chord ratio 4.58%. The geometrical inlet and outlet angles are 60.1 deg. and 44.6 deg. respectively, whereas the stagger angle of the blades at midspan is 51.4 deg. There are two sets of blades, with a tip clearance of 2% and 4% chord respectively. The hub wall at the test section region can be rotated by a controlled speed electric motor. The nominal rotational speed of the hub during the measurements was 6540 rpm, whereas the maximum local Mach number in the annular space was of the order of 0.62. After the exit of the test cascade the flow is entering a second cascade, whose purpose is to recover the swirl and bring the flow to the axial direction. A set of connecting ducts brings the flow to the inlet of the axial compressor, which is used to drive the facility.

### 3.2 Optical access

Measurements with the 3-D LDA system have been performed in several axial planes covering the whole blade passage from leading edge to trailing edge. Optical access to the blade passage has been ensured by two transparent curved glass windows of 1 mm thickness, specially manufactured in order to conform to the outer flowpath contour. The placement of these windows with respect to the blade passage is shown in figure 8, together with a drawing of the top view of one of the windows. The dimensioning of the windows has been chosen in order to allow the maximum possible coverage axially, in function of the structural restrictions imposed by the need to have a sufficiently rigid fixing of the adjacent blades.

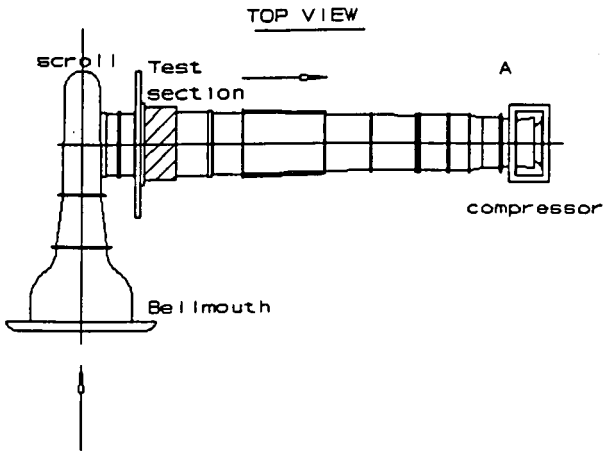


**Figure 6**: Layout of the annular cascade facility

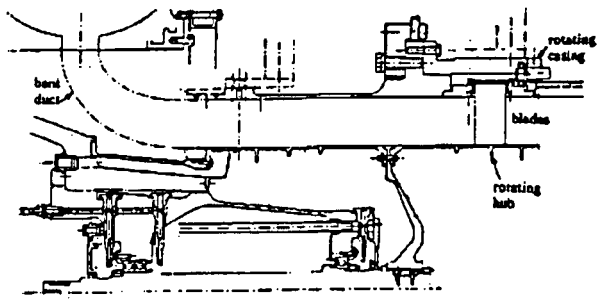


**Figure 7**: Layout of the annular cascade facility

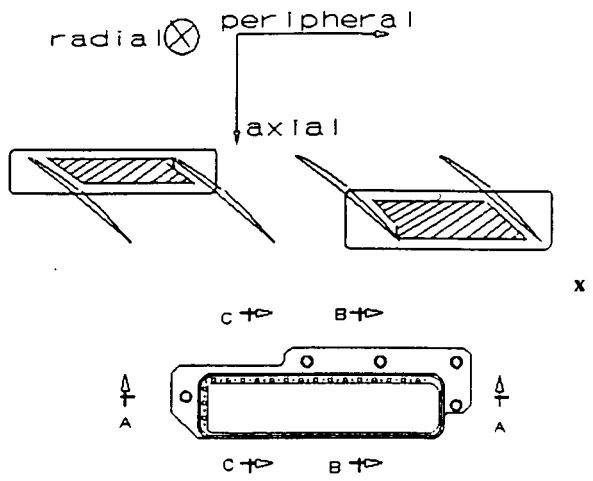


**Figure 8**: Layout of the two windows for coverage of the blade passage

A problem encountered when beams pass through transparent curved windows is the refraction of the laser

beams at the interface boundaries. Beam refraction affects:

a) the position of intersection of each beam-pair (i.e of each measuring volume - M.V.),
b) the shape of each of the M.V's and, consequently, the fringe spacing,
c) the orientation of each M.V. and hence of the corresponding velocity component.
d) the relative position in space of the three M.V's. In the general case the three M.V's may not cross any more after successive refractions. This fact may have serious implication to the correct evaluation of the rms velocity of the components not measured directly and of shear stress values, as was previously discussed.

It was therefore necessary to estimate the influence of refraction on the curved windows used for this study. The effects of beam refraction in a 3-D LDA for turbomachinery geometries has been studied in detail by Doukelis et al [23]. It was deduced that for the current case, where window thickness is quite small, refraction effects are generally kept minimal. The change in fringe spacing is less than 0.3%, whereas the directional change of a measured component is less than 0.1 deg. Therefore, the required corrections are of a small order of magnitude.

### 3.3 Flowfield seeding

An important factor of LDA measurements is the adequate seeding of the flow under investigation with light-scattering particles. The experimenter has to choose between global or localized injection of seeding in the test facility and, in the second case, determine the optimum position of seeding injection in order to achieve a number of particles leading to acceptable data rates at the measuring location. Since seeding of the whole flowfield requires a very expensive seeder and enormous amounts of seeding most experimenters chose local injection of the seeding. This was also our choice for the current study. A TSI Model 9306 Six-Jet Atomizer [24] was chosen as the seeding generator, because it met with all the requirements set with regard to the size range of particles/droplets and the flow rates. It offers a broad range of control over both the particle number concentration and over the total particle output. The mean diameter of the particles produced by the atomizer is approximately 0.6 $\mu$m, whereas the size distribution is quite narrow. Using the equations for the frequency response of a particle moving through a fluid, it was proved that particles of this size can follow closely the fluid motion even at high speeds.

Especially in the backscatter mode, where the intensity of the light reaching the receiving optics is one order of magnitude lower than in the forward-scatter mode, the quality of the seeding becomes a crucial factor for the measurements. After having tested several seeding mediums a 1:9 solution of paraffine oil and benzine was finally chosen, since it led to the optimum data rates observed and it gave a very good signal quality (high SNR).

According to Raj and Lakshminarayana [25] in flows of high degree of swirl, such as the one in consideration, the decay rate of the tangential velocity defect is much faster than the other components, giving rise to appreciable curvature in the wake centerline. Therefore, if a tube is inserted in the flowfield for the injection of seeding, the position of injection has to lie at a distance far enough from the measuring location so that the wake induced by the probe has decayed substantially and it produces a negligible disturbance on the flowfield properties.

Measurements with a 5-hole probe at the cascade indicated that, even for the more remote position of seeding injection upstream of the measuring location, which is almost 50 cm from the measuring locations, the insertion of a seeding probe inside the annulus causes serious disturbances of the initial flowfield properties. Therefore, the only solution was the injection of the seeding at the inlet of the facility (bellmouth) using the one-inch hose of the 6-jet atomizer. The appropriate injection position of the seeding from the bellmouth was determined by assuming that the seeding particles follow very closely the streamlines of the flow and that each position on a diameter of the bellmouth can be correlated to a position of the circumference of the annulus at the measuring location (360°). A seeding injection position was first estimated and then the optimum position was determined experimentally, by moving the hose in small steps and by recording the obtained seeding rate. The position that was finally experimentally selected lay very close to the one calculated, at midspan. Small changes of injection positions were found necessary, in order to get maximum data rates for the measurements near the hub or the tip at the test section. This fact was expected, since the flow angle varies across the annulus height. A single position cannot give the best results from the point of view of seeding density at the measuring location.

### 3.4 Window fouling

Window fouling is another problem that has to be addressed when using a fluid as seeding medium. Window contamination has been less severe when the seeding was injected from the inlet of the facility. Although, the mixture of paraffine oil and gasoline resulted in a milder window contamination than other fluids tested, the problem still existed. The contaminating fluid seems to come from the upstream direction, where it has been deposited on the tip wall. It appears in the form of oil streaks, starting from the upstream edge through the window. Within less than 5 minutes of operation of the facility at nominal conditions with the seeding activated, the streaks appear on the window causing fast deterioration of the signal quality (low SNR). In order to eliminate the problems caused by fouling of the windows special provisions were taken at the design of the windows. The windows were designed so that oil flowing on the upstream outer wall is prevented from reaching the window, by a thin slot which is kept in a slightly smaller

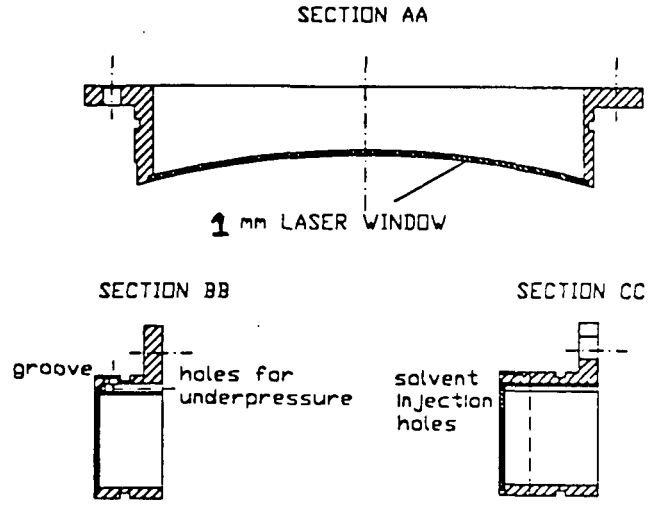


Figure 9: Configuration for the elimination of window fouling

pressure than the flow. This is ensured by connection to a point near the hub, where the smaller static pressure of the swirling flow occurs. On the other hand, a series of holes at the upstream edge of the window is used to inject a solvent which cleans the window when it has been contaminated. The fluid that was used for cleaning the window was methanol. The injection is done on-line during the execution of the experiments, with a remotely controlled electropneumatic arrangement. Figure 9 is a drawing of one of the two windows used for the LDA measurements, where the arrangements for the elimination of window fouling are shown. A fairly gratifying observation that was made during the current study should be pointed out: as the flow speed increases, the problem of window contamination becomes less intense. Oil formation on the window is more severe at lower rotational speeds. At higher rotational speeds the high velocity of the flow partially washes away the paraffine oil from the window.

### 3.5 Traversing mechanism of laser probes assembly

The two LDA-probe assembly is mounted on a remotely controlled carriage which enables radial traversing of the cascade. This, in its turn, is mounted on a manually operated two-axis mechanical traversing mechanism, which enables to move the assembly to a given axial position, whereas the circumferential position is set so as the axis of the 2-D probe coincides with the radial direction. The displacement accuracy of the traversing mechanism is $\pm 0.05$ mm for all three axes. With this arrangement the 2-D probe measures directly the axial and circumferential component of the flow, whereas the radial component is indirectly measured. Different circumferential positions with respect to the blades can be set by rotating the cascade, while the probes are at a fixed axial and circumferential position. The accuracy in the angular positioning of the cascade is $\pm 0.1$ deg. for a full rotation. At each axial location of interest the system is locked, and only the radial traversing is enabled. Thus, by rotating the cascade at different circumferential positions and conducting radial traverses, a measuring plane can be covered completely. The orientation of the Laser probes assembly on a plane perpendicular to the annulus axis is shown in figure 10. Orientation (a) is used for measurements near the pressure surface and (b) near the suction surface of the blades, since the topography of the laser probes does not enable full coverage of the plane with one orientation. The coverage of the passage in the blade-to-blade plane at the hub using the

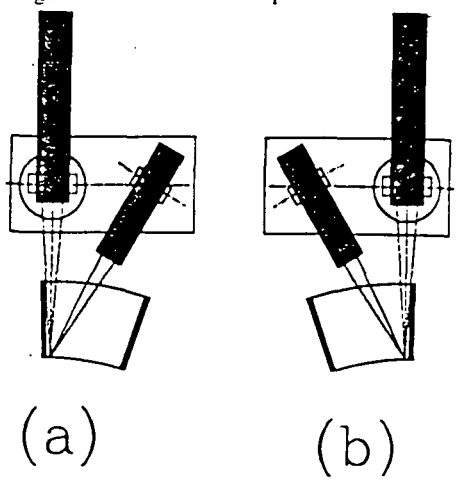


Figure 10: Orientations of the probe assembly for coverage of the passage

two orientations is shown by the hatched areas in Figure 10. There exists an overlapping measuring region close to the midpitch even at the hub, a fact which enables crosschecking of the proper alignment of the system with respect to the facility. It should be noted that, when positioning the control volume near the hub, the incident beams come too close to the window edges, restricting the possibility to measure very near the hub wall. This can be overcome by tilting the probes assembly by a few degrees.

## 4. CASCADE FLOW MEASUREMENT RESULTS

Detailed velocity measurements at different axial locations were conducted during this study for two different values of the tip clearance gap. A sample of these measurements, conducted at 33.5% chord from the leading edge of the blades and for a tip clearance gap value of 4 mm (4% chord), will be presented here. It proved extremely difficult to measure at locations closer than 3 mm to the hub, since the SNR deteriorated rapidly as the hub was approached, leading to a very bad signal quality and unacceptably low data rates. The same applies for the region close the window (above 90% span). The proximity of the beams to the window produces very high noise which makes near-window measurements difficult. For all the laser measurements conducted inside the passage a sample size of 3000 was used. The statistical errors associated with this sample size were presented in detail previously, as well as the systematic angular and positioning errors.

Figure 11 shows the magnitude distributions of the measured velocity components, whereas Figure 12 shows the measured local turbulence intensities of the axial and peripheral velocity components of the flow. No correction for velocity gradient effects has been applied to the measured velocity components presented in these figures. The gradients observed are mainly from the pressure to the suction side of the blades, while in the vicinity of the hub a viscous layer with strong radial gradients is developing, with a region of very low velocities in the centre of the passage. These areas also appear in the turbulence distributions of the axial and peripheral velocity components as areas of high turbulence, a fact that can be attributed to the energy dissipation inside the viscous layer. The radial velocity distribution indicates the influence of the tip leakage flow which is already quite strong at this axial location. High values of radial flow are observed inside the core of the leakage flow, a fact which is consistent with measurements conducted by other researchers and can be attributed to the presence of the tip leakage vortex.

Figure 13 presents the vector plot of the measured velocity inside the passage, whereas figure 14 presents the vector plot of the velocity defect, that is the difference between the measured velocity and the calculated circumferentially averaged velocity inside the passage. The initiation of the tip clearance leakage is best displayed here.

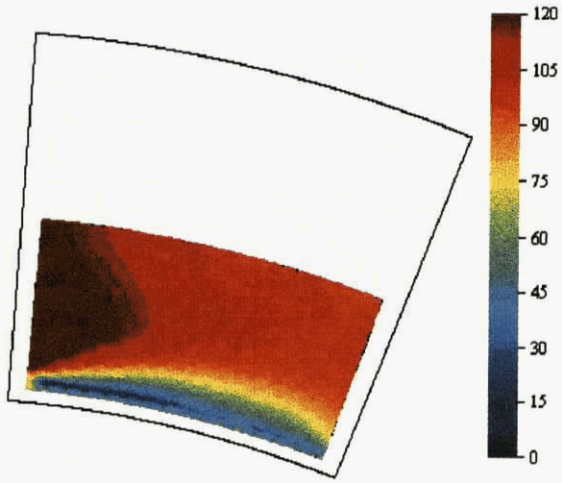


**(a)**: Measured axial velocity at 33.5% chord

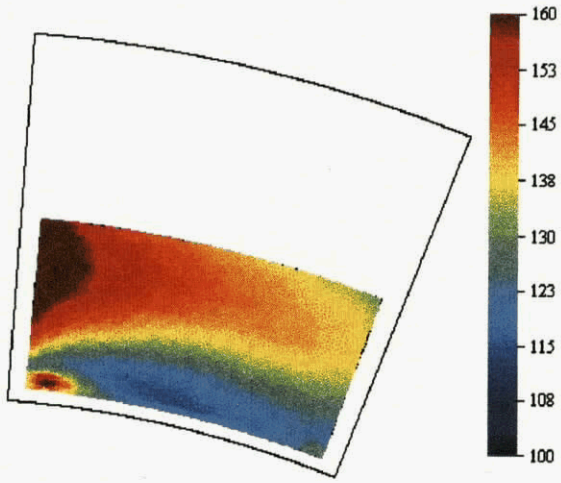


**(b)**: Measured peripheral velocity at 33.5% chord

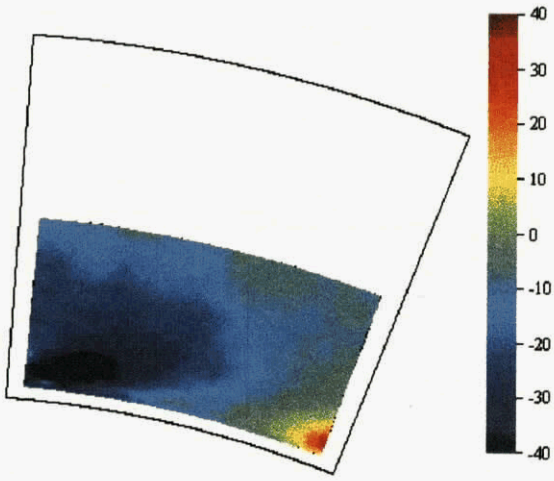


**(c)**: Measured radial velocity at 33.5% chord

**Figure 11**: Measured velocity components distributions at 33.5% chord

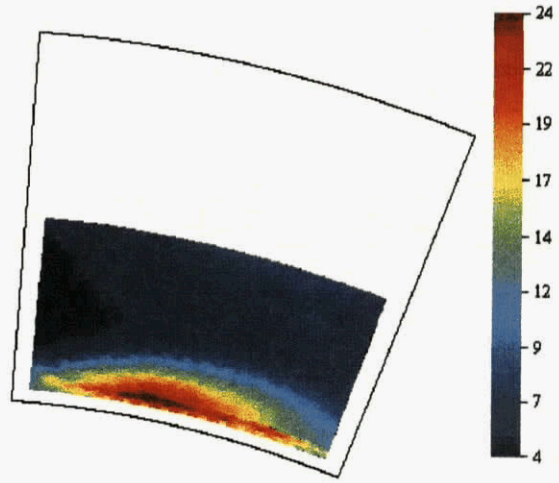


**(a)**: Measured axial turbulence intensity at 33.5% chord

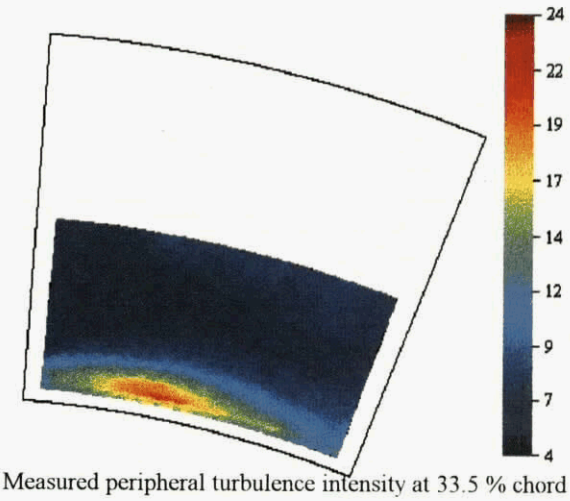


**(b)**:Measured peripheral turbulence intensity at 33.5 % chord

**Figure 12**: Measured turbulence intensity distributions at 33.5% chord

**Figure 13**: Vector plot of velocity at 33.5% chord

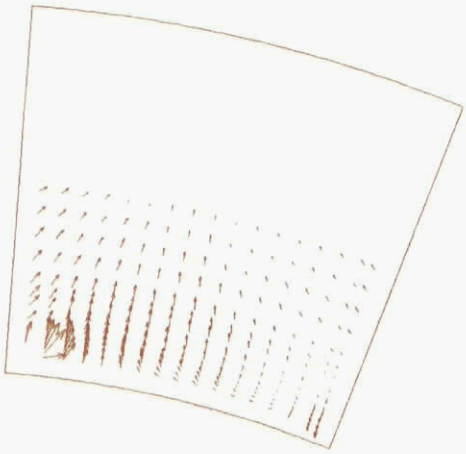

**Figure 14:** Vector plot of velocity defect

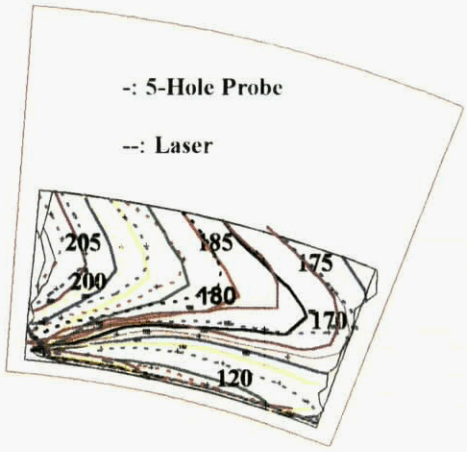


**Figure 15:** Comparison of measured mean velocity at 33.5% chord by laser and long-stem probe

Measurements at different axial locations inside the passage were also conducted with a specially designed long-stem 5-hole probe, in order to obtain pressure distributions, since LDA measurements do not provide this kind of information. In addition, these measurements have offered the ability to compare the flowfield quantities obtained by laser measurements inside the passage with those obtained by pneumatic measurements, which is a well-known and accepted measuring technique in turbomachinery applications.

Figures 15-17 present a comparison between laser and 5-hole probe measurements of the measured total velocity, yaw angle and pitch of the flow inside the passage at 33.5% chord. The comparison of the measured flow angles is good, whereas for the total velocity there is a difference of the order of 3%. Since this difference seems to be systematic it is highly probable that it is due to slightly different atmospheric conditions.

According to the calibration report of the probe [26] the expected errors of the measured quantities are: ±0.5 deg. for the yaw angle, ±1.3 deg. for the pitch angle, and ±1% for the total velocity. Yet there are several additional factors reducing the measuring accuracy of the probe. The great length of the stem introduced inside the flow is probably creating a disturbance of the flowfield properties. On the other hand, the position of the sensing head is sensitive to small placement errors. Aerodynamic force may result in slight bending of the head, leading to a measuring position different from the one anticipated from the positioning data. This may be the reason for which the velocity contours, Figure 15, have exactly the same form but are slightly shifted with respect to each other. Therefore the results obtained by laser measurements can be regarded as more trustworthy and any discrepancies observed between laser and five-hole probe measurements are probably due to the errors mentioned above.

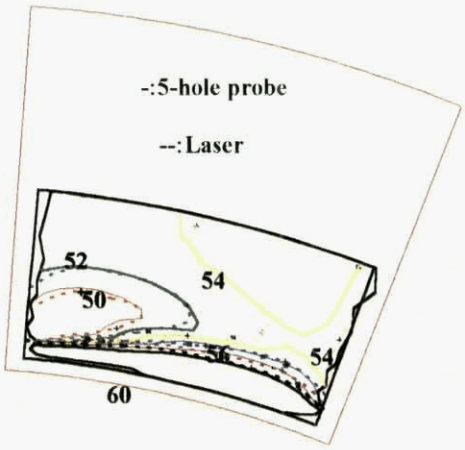


**Figure 16:** Comparison of measured yaw angle at 33.5% chord by laser and long-stem probe

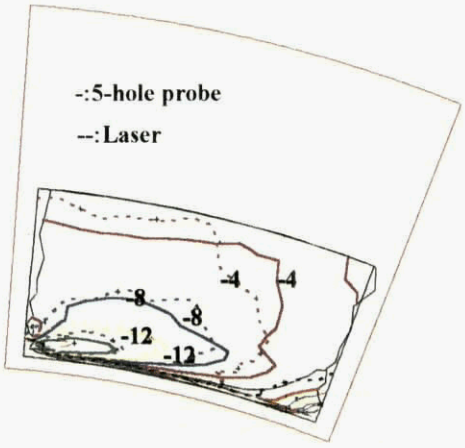


**Figure 17:** Comparison of measured pitch angle at 33.5% chord by laser and long-stem probe

## 3. CONCLUSIONS

The 3-D LDA measurement technique has been described, as applied for the measurement of the flowfield in a high-speed annular cascade used to study tip clearance effects. The system layout, data acquisition and signal processing have been presented in detail. A full description of the annular cascade facility and all the aspects of execution of the measurements have been given, together with representative measurements, demonstrating the ability of LDA to measure accurately the three mean velocity components and the corresponding turbulence intensities inside the passage and in the tip-clearance of the annular cascade facility. Overall, the mean velocities measured with LDA agreed within expected accuracy limits with pneumatic measurements conducted in the same facility.

## REFERENCES


**1.** Rains D. A., *Tip Clearance Flow in Axial Flow Compressors and Pumps*, California Institute of Technology, Hydrodynamics and Mechanical Engineering Laboratories Rep. No. 5, 1954.

**2.** Howard M. A., Ivey P. C., Barton J. P. and Young K. F., Endwall Effects at Two Tip Clearances in a Multistage Axial Flow Compressor with Controlled Diffusion Blading, *ASME paper 93-GT-299*, 1993

**3.** Storer J. A., Cumpsty N. A., Tip Leakage Flow in Axial Compressors, *ASME paper 90-GT-127*, 1990.

**4.** Lakshminarayana B., Pouagare M. and Davino R., Three Dimensional Flow Field in the Tip Region of a Compressor Rotor Passage.
Part 1: Mean velocity profiles and annulus wall boundary layer
Part 2: Turbulence properties
*Transactions of ASME, Vol. 104*, p.760-781, October 1982

**5.** C. J. Chesnakas and C. L. Dancey, Total Velocity Vector Measurements in an Axial-Flow Compressor Using a 3-Component Laser Doppler Anemometer, *AIAA/ASME/SAE/-ASEE 24th Joint Propulsion Conf., AIAA 88-2811*, Boston, Mass., July 11-13, 1988

**6.** D. M. Murugan, W. Tabakoff and A. Hamed, Flow Field Investigation in the Exit Region of a Radial Inflow Turbine Using LDV, *Intern. Gas Turbine and Aeroengine Congress and Exposition, paper No. 94-GT-101*, The Hague, Netherlands, June 13-16, 1994

**7.** B. Lakshminarayana and K. N. S. Murthy, Laser Doppler Velocimeter Measurement of Annulus Wall Boundary Layer Development in a Compressor Rotor, *Gas Turbine Conference and Exhibition, paper No. 87-GT-251*, Anaheim, Ca., May 31-June 4, 1987.

**8.** A. J. Strazisar, Investigation of Flow Phenomena in a Transonic Fan Rotor Using Laser Anemometry, NASA-Lewis Research Center, *J. of Engineering for Gas Turbines and Power*, vol.107, pp.427-435, 1985.

**9.** Kenneth L. Suder, Blockage Development in a Transonic, Axial Compressor Rotor, *ASME paper 96-GT-394*, 1996

**10.** G. V. Hobson and D. M. Dober, Three-Dimensional Fibre-Optics LDV Measurements in the Endwall Region of a Linear Cascade of Controlled-Diffusion Stator Blades, *ASME paper 94-GT-352*, 1994

**11.** INVENT GmbH, Fibre Optic two component laser-Doppler anemometer, *Technical Reference Manual*, INVENT GmbH, D-91058 Erlangen-Tennelohe, Germany, 1993.

**12.** DFLDA - Laser Diode Fibre Optic Laser Doppler Anemometer, *Technical Reference Manual*, INVENT GmbH, Germany, Oct. 1992.

**13.** MACRODYNE Inc., Laser Doppler Velocimetry (LDV) electronics. Multi-dimensional frequency domain processor, Model 3107, *Users Manual*, Rev. 9/15/92.

**14.** Kenneth L. Orloff and Philip K. Snyder, Laser Doppler Anemometer Measurements Using Nonorthogonal Velocity Components: Error Estimates, *Applied Optics*, Vol 21, No. 2, p. 339-344, 15 January 1982

**15.** ZECH Electronics, 1400A Laser Velocimeter Interface *Owner's Handbook*, Document Number 90-1400A

**16.** W. J. Yanta Turbulence Measurements with a Laser Doppler Velocimeter, *NOLTR 73-94*, White Oak, Silver Spring, Maryland, 1973.

**17.** A. Doukelis, M. Founti, K. Mathioudakis and K. Papailiou, A Three-Component Laser Doppler Anemometer for Measurements in a Turbomachinery Annulus, *EUROTHERM 46*, Pisa, Italy, 3-4 July 1995.

**18.** Bedienungsanleitung Feststoffispergierer RGB 1000, Palas Partikel und Lasermebtechnik.

**19.** H. Tennekes H. and J. L. Lumley, *A first course in Turbulence*, MIT Press, Cambridge, MA, p. 74-75, 1972.

**20.** I. Wygnanski and H. Fiedler, Some measurements in the self-preserving jet, *J. Fluid Mech.*, Vol. 38, part 3, p.577, 1969.

**21.** H.J. Hussein, W.K. George and S.P. Capp, Comparison between hot-wire and burst mode LDA velocity measurements in a fully developed turbulent jet, *AIAA 26th Aerospace Sciences Meeting, AIAA-80-0424*, Reno, NV, Jan. 11-14, 1988.

**22.** K. Mathioudakis, K. Papailiou, N. Neris, C. Bonhommet, G. Albrand, U. Wenger: An annular Cascade Facility for Studying Tip Clearance Effects in High Speed Flows, *XIII ISOABE* , Sept. 8-12, 1997, Chattanooga, Tennessee, USA.

**23.** A. Doukelis, M. Founti, K. Mathioudakis and K. Papailiou, Evaluation of Beam Refraction effects in a 3-D Laser Doppler Anemometry System for Turbomachinery Applications, *Measurements Science and Technology 7*, pp. 922-931, 1996.

**24.** Model 9306 Six-Jet Atomizer, *Instruction Manual*, TSI.

**25.** R. Raj and B. Lakshminarayana, Three Dimensional Characteristics of Turbulent Wakes Behind Rotors of Axial Flow Turbomachinery, *ASME paper 75-GT-1*, 1975

**26.** Five Hole Pressure Probe 960-15 No. 1 (S. No. 941/1), *Calibration report*, Dipl.-Ing. Alf Schneider, Univ.-Prof. Dr.-Ing. W. Koschel, Institut für Strahlantriebe und Turboarbeitsmaschinen, Rheinisch-Westfälische Technische Hochschule Aachen, June 1996.

## ACKNOWLEDGMENTS

The work has been performed within the frame of the AERO-CT2-0039, PN2031 contract and the financial assistance of the C.E.U. is gratefully acknowledged.

Paper 4
Author : K. Mathioudakis et al.

Q: Can you please comment on problems you could identify in connection with the appearance of back ground flare?

A: Background flare restricts the ability to measure close to the hub wall. In our case the hub wall was coated by anti-reflective paint and the minimum distance we could measure was 3mm from the hub wall, when the 2-D probe was introduced radially into the passage. It was found that closer to the wall points could be approached, by including the probe axis with respect to the vertical to the end-wall.

Q : Benson

Have you tried different seed materials ?

A: During the initial testing phase on the free jet, we used solid particles with very good results. All measurements on the annular cascade facility have, however, been performed using oil seeding, because of the risk of damage to the bearings if solid powder was used.

# Investigation of the spray dynamics of aeroengine fuel injectors under atmospheric and simulated pressure conditions

T. Behrendt, C. Hassa
DLR, Institut für Antriebstechnik
Postfach 90 60 58
D-51170 Köln
Germany

## SUMMARY

The two phase flow in the nearfield of an airblast atomizer in a cylindrical confinement was investigated with a three component (3D) dual mode PDA. An algorithm for the calculation of the mass flux in a strongly swirling spray was derived. The algorithm makes use of all three velocity components. The improved performance relative to a 2D-algorithm is shown for an atmospheric spray. The error of the integrated mass flux is about +/-15% at a distance of more than 10mm behind the nozzle exit.

The investigations were made in an attempt to get first information on the two phase flow under real pressure condition where the dense spray starts to modify the flow pattern and hence the fuel distribution. Similarity rules were derived for scaling the combustor idle condition with respect to the particle number concentration in the spray. The measurements were made under atmospheric and simulated pressure condition. The measured spray properties agreed well with the expected results calculated from the similarity rules. Several effects of the spray on the gasphase were identified under simulated pressure. A reduced turbulence of the gasphase, a decreased dispersion of the spray and a degradation of the effective swirl number were identified as dense spray effects. These phenomena are likely to occur under real pressure as well. Other effects identified were results of the particle inertia.

For the correct interpretation of the results it was necessary to estimate the degree to which the particle behaviour is influenced by its inertia under simulated and real pressure. Together with this evaluation the simulation of real engine condition with respect to the particle number concentration was successful within certain limits.

## 1. INTRODUCTION

One possibility of improving the performance of aircraft engines is to increase the pressure-ratio. This normally entails a higher temperature rise in the combustion chamber [1]. The rise of the pressure ratio enlarges the range of the operation conditions in terms of the overall combustor fuel air ratio. The primary zones of common combustors can operate only in a specific range of fuel-air-ratios. At high load soot production and NOx-emissions due to the high temperature increase. At low power settings the equivalence ratio reaches the lean stability limit. To overcome these limits the recent development leads to staged combustors [2] with an overall lean fuel-air-ratio in the main zone. But if the fuel distribution produced by the main burners is not homogeneous enough, local stoichiometric or rich zones will be generated, which are big enough to start excessive NOx and eventually soot production [3]. For the development of fuel nozzles satisfying the needs of staged combustion, it is therefore necessary to get reliable information about the fuel placement and homogeneity within the combustor primary zone.

Investigations under real engine conditions involve high costs and diagnostic risks. The need for the reduction of the development cost leads to simplified test procedures wherever possible [4]. In the case of the cold fuel spray, expensive tests under high pressure can be avoided to a certain degree. The possibilities and limitations of testing under atmospheric pressure are discussed in the following paragraphs with respect to the aim of the characterisation of the two phase flow in the burner nearfield. The success of the approach is then highlighted with results from a specific airblast atomizer nozzle. But before that, the discussion starts with the description of the specific experimental rig and the set-up and modification of the principal diagnostic technique, the dual mode Phase Doppler Anemometer (PDA).

## 2. EXPERIMENT

### 2.1 Airblast atomizer with combustor primary zone

The airblast atomizer with the combustor primary zone is shown in figure 1.

*Paper presented at an AGARD PEP Symposium on "Advanced Non-Intrusive Instrumentation for Propulsion Engines", held in Brussels, Belgium, 20-24 October 1997, and published in CP-598.*

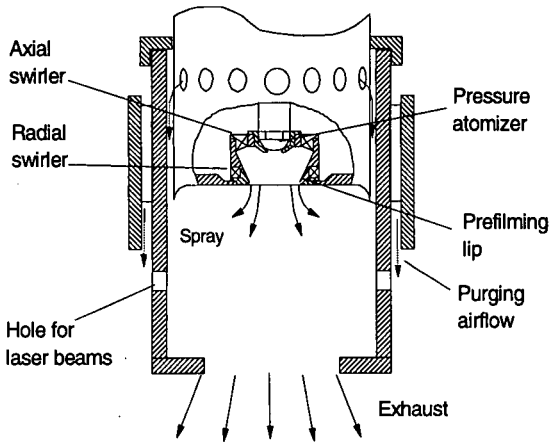


Figure 1: Airblast atomizer in combustor primary zone (not to scale)

The prefilming atomizer is equipped with an inner axial swirler and an outer radial swirler and is located in a plenum chamber. A pressure swirl atomizer is used to deposit the fuel on the prefilming lip. The plenum is placed in a tubular confinement to achieve the necessary flowfield similarity to the atomizer nearfield of a combustor primary zone. The nozzle exit diameter is 26 mm and the liner diameter is 94 mm, producing a typical ratio of nozzle exit to combustor dome velocity. Additional air emerges through holes in the plenum upstream of the nozzle and is directed along the inner wall to simulate the airflow of the heatshield. The amount of this airflow is about 40% of the atomizer airflow. The laser beams of the PDA and the scattered light are directed through small holes in the confinement to avoid loss of signal to noise ratio caused by kerosene spread on the windows. On the outer side of the confinement purging airstreams are located at these holes to block the motion of any large droplets flying through the holes. Test measurements with an atomizer with a spray cone angle of more than 120° revealed the effectiveness of the purging air together with the simulated heatshield airflow in the liner. The measured flowfield was not significantly influenced by the holes. The detailed description of the test facility is given in [5].

## 2.2 Diagnostics

A three component dual mode Phase Doppler Anemometer (PDA) is used for the investigations. The PDA has proved to be capable of measuring the two phase flow at atmospheric conditions with good accuracy [6]. The specific instrument used was a dual PDA built by DANTEC [7]. The dual mode concept is an extension of the conventional (standard) PDA with the capability of rejecting incorrect size measurements caused by effects, which are probable to occur if the particle diameter is not small against the diameter of the measuring volume [8]. The measured massflux distribution, as the primary measured quantity to judge the fuel placement of the nozzle, is very sensitive to erroneous size measurements of large particles because of the third power dependency of the diameter. On the other hand a small measuring volume is necessary to avoid the presence of more than one particle in the measuring volume at a time, a condition, which spoils the measurement.

The dual mode concept is realised by the implementation of a second pair of detectors (planar PDA) to measure the phase difference of the scattered light from a second pair of beams. Since these detectors lie in a different scattering plane, the phase difference shows a different response to the above mentioned effects. With an adequate validation algorithm incorrect size measurements can be recognised and rejected.

For measuring kerosene droplets with this method Mie-calculations of the scattered light had to be made to find the best possible optical set-up for transmitting and receiving optics. The only PDA delivers valid measurements, if one scattering mode is dominating. The scattered light of particles smaller than 30 µm was calculated with the Mie-theory [9]. On particles larger than 30 µm the laws of geometrical optics were applied. For the calculation the scattering angle, the wavelength of the beams and the beam expansion of the receiving optics were varied. The results were evaluated with respect to the linearity of the phase diameter relation of the standard PDA and the oscillation of the phase diameter relation of the planar PDA. Table 1 contains the parameters of the configuration with the best results.

| scattering mode | 1st order refraction |
|---|---|
| scattering angle | 40° |
| beam separation | 24 mm |
| wavelength standard PDA | 488 nm |
| wavelength planar PDA | 514.5 nm |
| beam expansion receiving optics | 1.98 |

Table 1: Set-up of the dual mode PDA

Unfortunately the receiver cannot be positioned at an scattering angle of 69° to make use of the Brewster condition for suppression of reflected light. Furthermore the diameter phase relation for Brewster's angle is quite insensitive against changes of the refractive index. The refractive index of kerosene decreases due to the heat-up of the droplets in a combusting spray [10]. Moreover the resulting length of the measuring volume would be smaller. However at scattering angles above 50° the ratio between the phase factors of the planar and the standard PDA gets too large. The phase difference of the planar PDA is used to resolve the $2\pi$-ambiguity of the standard PDA to enlarge the measuring range, see figure 2.

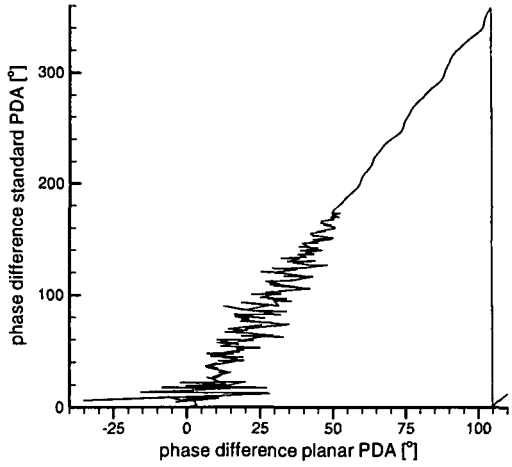


Figure 2: Relation between the calculated phase differences of the standard and the planar PDA for the selected configuration

If the ratio between the phase factors becomes too large, the $2\pi$-ambiguity cannot be resolved because of the oscillations of the planar phase diameter relation at small particles, see figure 3. As the phase differences are measured with a certain error caused by the finite accuracy of the signal processor, the relation in figure 3 represents the „best case". This deviation may cause the misinterpretation of a particle with a standard phase difference of 13° as a particle with a standard phase difference of 373°, causing an error in the particle diameter of about 60µm.

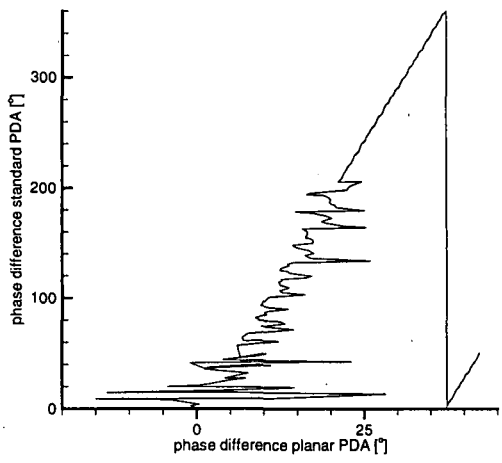


Figure 3: Relation between the calculated phase differences of the standard and the planar PDA for a scattering angle of 68.8°

The PDA was powered by an Argon Ion laser running at approximately 1.5W. The light was sent to the transmitting probes by optical monomode fibres. The focal length of the transmitting and receiving optics was 310 mm. The properties of the resulting measuring volume are listed in table 2. The length of the measuring volume is limited by the projection of a slit aperture in the receiving probe, giving a length of 195µm.

| | u | v | w |
|---|---|---|---|
| fringe spacing [µm] | 6.31 | 6.65 | 3.89 |
| Gaussian beam diameter [µm] | 72 | 76 | 140 |

Table 2: Properties of measuring volume

The resulting arrangement of the probes is shown in figure 4.

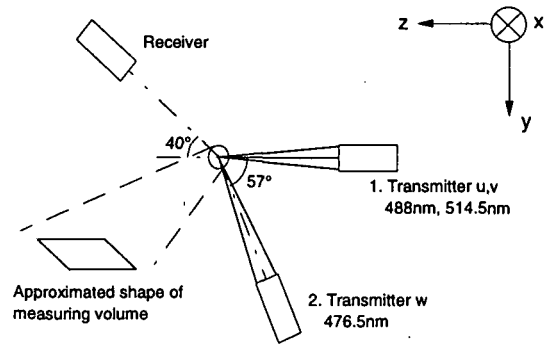


Figure 4: Optical set-up of the PDA

### 2.3 Calculation of mass flux

The mass flux $f_x$ into a specific direction $x$ can be calculated from the measured PDA-data by a summation of the mass flow referenced to the effective detection $A_{det}$ area over all particles.

$$f_x = \frac{\rho\pi}{6\Delta t}\sum_i \frac{d_i^3 * \mathrm{sign}(u_i)}{A_{\mathrm{det},i}} \qquad (1)$$

The light intensity in the measuring volume has a Gaussian distribution. Therefore the size of the detection volume is different for each particle diameter. The size of the effective detection area is a function of the projected slit width, the particle diameter and the particle trajectory. The relation between particle diameter and measuring volume diameter has to be calculated from the measured data. The measuring volume diameter is calculated from the spatial burst lengths under the assumption of axial-symmetric intensity distribution in the measuring volume. The software of the PDA contains an algorithm to compute the massflux distribution [7], which is based on the approach presented in [11]. The performance of the software was cross-checked with a patternator and other PDA instruments in [12]. The measurements were made 100 mm downstream of a pressure swirl atomizer and an airblast atomizer. The agreement of the measured data between the patternator and the calculated data from the PDA was good, especially for the pressure swirl atomizer. Nevertheless the used algorithm has two disadvantages:

- Only two velocity components are used for the calculations. The strong three-dimensional cha-

racter of the swirling flowfield in the combustor primary zone has a significant influence on the calculation.

- It is difficult to calculate the massflux in a certain direction accurately if the axes of the measuring volume are not aligned to the desired direction.

This lead to the development of a different algorithm for the mass flux measurement in strongly swirling flows with a 3-D PDA, which makes use of all three velocity components to calculate the diameter of the detection volume. It is based on the approach proposed in [13]. The shape of the measuring volume is approximated to a cylinder as shown in figure 4. The droplet trajectory in the vertical X-Y plane through the measuring volume has an angle $\alpha$=arctan($v/u$), see figure 5. It passes the volume with a distance $t$ to the optical axis of the 1st transmitter.

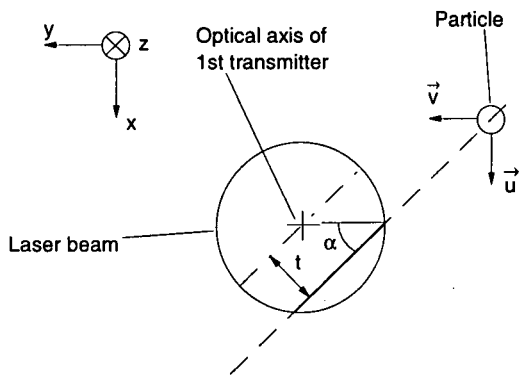


Figure 5: Particle trajectory through measuring volume

In figure 6 the measuring volume is shown in the plane defined by the optical axis of the 1st transmitter and a random particle trajectory. The angle $\beta$=arctan($w/vel$) with $vel = \sqrt{u^2 + v^2}$ describes the particle trajectory through the parallelogram. The measuring volume is cut into parallelograms by these particle trajectories, see figure 6. The angle $\gamma$ of the parallelogram depends on the angle $\alpha$. For a two-dimensional flow in the y-z-plane with u=0 the angle $\gamma$ equals the scattering angle, see figure 4. For the three-dimensional flow the angle $\gamma$ is the projection of the scattering angle of the y-z-plane into the z-$\alpha$-plane. The height $b$ of the parallelogram is a function of the location $t$ in the detection volume where the slice is cut.

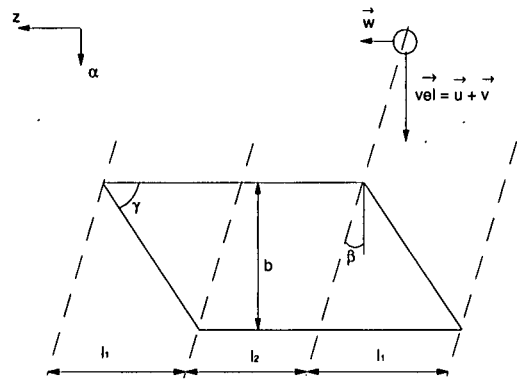


Figure 6: Measuring volume in the plane of particle trajectory and optical axis of 1st transmitter

For particles flying through the parallelogram in the section $l_2$, the true burst length is measured. In the sections $l_1$ the burst length is limited by the slit in the receiving optics. Here on the average only one half of the true burst length will be measured. The smallest measured burst length is defined by the minimum residence time of the particle in the measuring volume. This minimum residence time is needed by the electronics to detect the particle. The smallest burst length has to be taken into account in defining $l_1$, if it is not negligibly small against the diameter of the measuring volume. The values of $b$, $l_1$ and $l_2$ depend on the location $t$ in the measuring volume. An equation can be derived for the relation between the mean measured burst length and the height $b$ of the parallelogram. Integrating over all parallelograms by means of integrating over $t$ from 0 to $d_{mea}/2$ will lead to an expression of the diameter $d_{mea}$ of the measuring volume as a function of the mean measured burst length. These calculations have to be applied on every size class.

Poor statistics may cause calculations of wrong diameters $d_{mea}$. To suppress these errors, the calculated diameters $d_{mea}$ are fitted to the particle diameters $d_p$ with the following formula using a least squares approach:

$$d_{mea}^2 = A * \ln d_p + B \qquad (2)$$

It is based on the assumption that the scattered light intensity is proportional to the square of the particle diameter [7],[14].

For the calculation of the massflux or concentration a reference area or effective detection area must be defined normal to the desired direction of the flux. The size of this reference area depends on the angle between the particle trajectory and the direction of the flux to be calculated as well as on the size of the detection volume. Figure 7 shows how the reference area normal to the x-axis is approximated for a two dimensional particle trajectory.

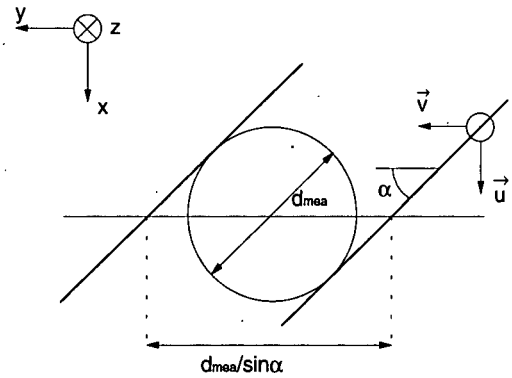


Figure 7: Approximation of effective detection area for two dimensional particle trajectory

This approximation becomes invalid, if the size of the elliptical area cut through the measuring volume by the projected slit is too large to be neglected, see figure 4 and 8. This gets important if the off-axis angle of the PDA is small (20°...40°) and if the angle $\alpha$ of the particle trajectory is small. The calculation of the reference area becomes even more difficult, if the particle has a three dimensional trajectory. To overcome this problem the surfaces of the measuring volume and the particle trajectory are treated as vectors, see figure 8.

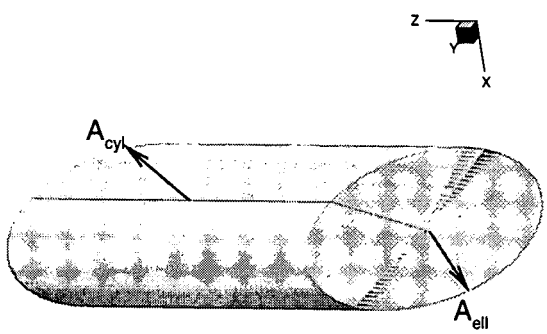


Figure 8: Surfaces of measuring volume

The length $l$ of the measuring volume is corrected with the particle diameter similar to a proposal in [14]. The size of the effective detection area is calculated in two steps: First the cross sectional area $A'$ of the detection volume normal to the unit vector of the particle trajectory $\vec{e}$ is calculated:

$$\left|\vec{A'}\right| = \vec{e}\cdot\vec{A}_{cyl} + \vec{e}\cdot\vec{A}_{ell} \qquad (3)$$

Next the effective detection area $A_{det}$ can be calculated with the unit vectors of the particle trajectory and the desired flux direction $\vec{e}_{flux}$.

$$\vec{A}_{Det} = \frac{\vec{A'}}{\vec{e}\cdot\vec{e}_{flux}} \qquad (4)$$

This approach has the advantage that the effective detection area is calculated correctly for any particle trajectory and for any desired flux direction.

In dense sprays, especially near the atomizer, the probability of the presence of two or more particles in the measuring volume normally leading to the rejection of the particles can cause large errors in the flux measurement. In [15] the relation between this probability and the number density [16] and mean residence time of the particles based on Poisson statistics is presented. A correction of the mass flux is applied according to the calculated rejection probability.

Measurements were made to evaluate the performance of this new algorithm. The spray of the atomizer was investigated without a confinement for the validation. In that case it is possible to balance the PDA-measured mass flow with the real mass flow, because no kerosene is spread on the wall of the confinement. The mass flow is calculated by integrating the measured mass flux over the radius in each measuring plane. The kerosene flow was 1.2g/s giving an AFR of 20. The pressure drop across the atomizer was 2.3%. Figure 9 shows a plot of the mass flux in axial direction and table 3 contains the error between the measured and the real value.

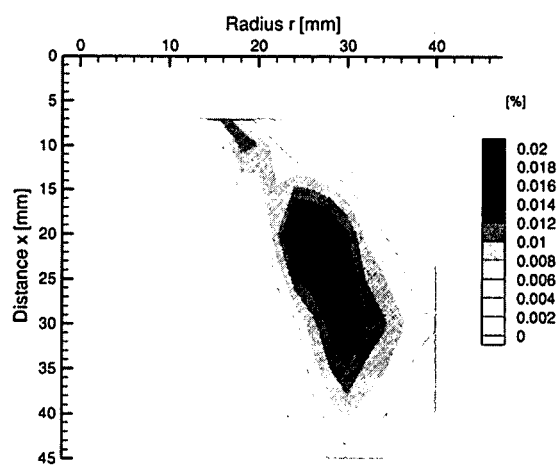


Figure 9: Measured mass flux

| Measuring plane | Error |
|---|---|
| 5 mm | -37% |
| 7.5 mm | -20% |
| 10 mm | -17% |
| 15 mm | -7.7% |
| 20 mm | -3.3% |
| 30 mm | +14.5% |
| 50 mm | -9.4% |

Table 3: Errors between measured mass flow and real mass flow

The error of +/-15% at minimum distance of 10mm behind the nozzle exit must be seen as a good value, even for a non-swirling flow, see [12]. Nevertheless it must be underlined, that this is only an integrated error. The larger deviations in the planes closer than 10mm to the nozzle are caused mainly by non-spherical particles which are rejected by the PDA. The acceleration causes large particles to become elliptical. The Bond-number, eq. (5), is a measure for non-sphericity of a droplet due to the acceleration $a$.

$$Bo = \frac{d^2 * a * \rho_P}{\sigma} \qquad (5)$$

In [17] value of 0.4 for the Bond-number is given as a threshold for non-sphericity. The Bond-numbers of the larger droplets were much higher than 0.4 in this spray region.

The influence of the third velocity component on the accuracy of the mass flux calculation is shown in figure 10. Comparative calculations between the presented 3D-algorithm and the algorithm of the PDA-supplier DANTEC were conducted with the same data set. The measurements were made 15mm behind the nozzle exit. The integrated error of the 3D-algorithm in this plane is listed in table 3. The PDA was set up in a way that the third velocity component, which is not used by the DANTEC-algorithm, is the component with the lowest magnitude, thus giving the minimum error for the 2D-DANTEC-algorithm. In this case it was the radial velocity of the swirling spray.

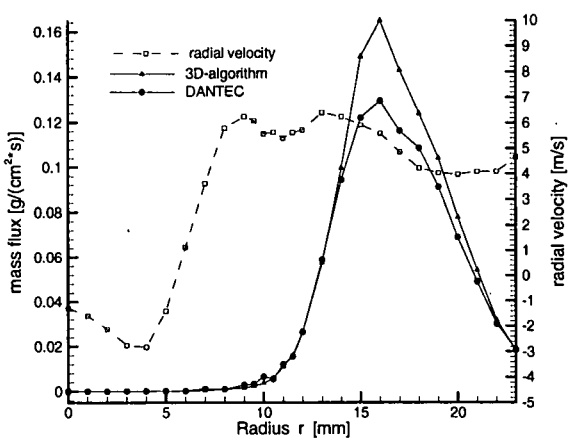


Figure 10: Comparison between results of 3D-algorithm and DANTEC-algorithm

The third velocity component is about 5 to 10 times smaller than the amount of the other two velocities. Even though the third velocity has a significant influence on the calculation of the mass flux. The mass flux computed by the DANTEC-algorithm is up to 25% too low.

### 2.4 Simulation of pressure conditions

The simulation of the pressure conditions is an attempt to get an idea of the behaviour of the dense two phase flow under real engine conditions. Such simulations are to reproduce a specific aspect of the spray, e.g. the atomization or the resulting spray density while neglecting other aspects, like fuel placement or dispersion. The assumptions made in the derivation of the similarity laws naturally limit the validity of the simulation. If e.g. the atomization is scaled with respect to the similarity rules of a specific atomization mechanism, the simulation will break down, if a different atomization mechanism is dominating, when changing to the pressure condition. In consequence the simulation cannot replace the investigations under real pressure conditions. But it can offer quick information about the probable consequences of modifications in the atomizer design. One can get information on the behaviour of the dense spray from parameter variations in an early stage of the development of the fuel nozzle. Furthermore it has the advantage, that investigations can be made under atmospheric conditions, where the costs are low. Moreover, optical access might be difficult or even impossible in a realistic combustor, then making this approach the only way to investigate the two phase flow in the atomizer nearfield.

In the literature different approaches exist on scaling the real engine conditions or investigating the interaction between a dense spray and the gas-phase, which shall be briefly reported here.

Wang et al. [18] used a three times the size model of a practical fuel nozzle. As the mass flow increases with the square of the scaling factor and the loading of the atomization lip increases with the first power of the scale, the local spray density near the lip is increased by the scaling factor 3. The air fuel ratio was 15.4 and the pressure drop was set to 7.5%. The observed interaction between gas-phase and spray was small. This is probably caused by the high air fuel ratio and by the comparatively small particle concentrations of water sprays. As the surface tension of water is three times larger than that of kerosene water sprays have larger and fewer particles.

The investigations of McVey et al. [19] were made to provide information of the flowfield behind the injector under real engine conditions. The air pressure drop was selected to achieve the same velocity as in the engine operating condition. The injectant flow was scaled to preserve the momentum ratio between air and injectant. Water was used for the experiments. The measured data were used for the evaluation of computational results. The drop sizes were measured, but the authors did not comment on the validity of the simulation with respect to atomization quality. On the other hand the particle drag was mentioned as a major effect in the two-phase flow. If prompt atomization as described by Lefebvre [20] is the dominating atomization process, the scaling of the air velocity would reproduce the atomization provided the original fuel is used.

In a recent investigation [21] it was attempted to simulate the pre-evaporation of the spray at idle condition. Air assist atomization was used to compensate the

poor atomization under atmospheric pressure. The air assist pressure had to be determined experimentally by comparing the droplet diameters with a reference spray under real engine condition. The scaling of the air flow was accomplished by preserving the air-fuel-ratio for the evaporated fuel and the fuel mass contained in small particles at the specific air temperature of the simulation. The fuel flow results from the constancy of the air fuel ratio. This leads to a thin spray, where consequently no dense spray effects can be observed. The use of water as the injectant must bias the evaporation rate, due to the lower boiling point in comparison to kerosene.

The scaling of the engine conditions presented in this contribution is aimed to reproduce the interaction between the dense spray and the gas phase. To achieve the high spray density the pressure drop across the atomizer is increased, the air fuel ratio (AFR) is reduced and the original JET-A1 fuel is used.

The considerations behind this scaling are described in the following section. Experiments reported in [22] revealed that the dominating atomization regime for this type of atomizer is the wavy sheet break-up. A correlation from [20] for the Sauter mean diameter (SMD) in dependence of air and liquid properties is used. Its most significant quantity is the dynamic pressure of the atomizing air.

$$SMD \propto \frac{1+\frac{1}{AFR}}{\sqrt{\rho_A * u_A^2}} \qquad (6)$$

$$u_A = \sqrt{\frac{2\Delta p_A}{\rho_A}} \qquad (7)$$

As kerosene is injected in the simulation the liquid properties can be omitted. The resulting number concentration *conc* can be estimated from the following equation.

$$conc \propto \left(\frac{1}{SMD}\right)^3 * \frac{1}{AFR} * \frac{1}{u_A} \qquad (8)$$

With these equations the scaled operation conditions of the atomizer can be calculated. Only one characteristic of the spray - mean diameter or number concentration - can be correctly simulated at one time. The engine conditions corresponding to the simulation are listed in table 4. In this example the fuel nozzle is operated in the real combustor at the following operating point:

- $\Delta p/p = 3\%$
- AFR = 25

| O P in simulation | SMD | Concentration |
|---|---|---|
| $\Delta p/p = 10\%$<br>AFR = 6 | P = 3.3bar | P = 6bar<br>T = 560K |

Table 4: Real engine conditions corresponding to simulation

According to the correlation, the air temperature has no influence on the Sauter mean diameter. This example shows how a number concentration similar to the concentration at real idle condition can be produced. The mean diameter of the droplets is larger, but here a compromise must be made. The deviation in the mean diameter is not too big because of the square root dependency of the pressure on the atomization quality, see eq. (6).

The Stokes-number *Stk* is an important criterion for the description of particle dispersion [17]. If the Stokes-number is small ($Stk \ll 1$) the particles will follow the flowfield very quickly. If the Stokes-number is large ($Stk \gg 1$) the particle trajectory will be dominated by its inertia and its initial conditions. The Stokes-number is defined:

$$Stk = \frac{\tau_{rel}}{T_S} \qquad (9)$$

The particle relaxation time $\tau_{rel}$ is the time in which the relative velocity between the particle and the gas-phase is decreased to 37% of its initial value.

$$\tau_{rel} = \frac{4}{3}\frac{\rho_P}{\rho_A}\frac{d^2}{c_D * \mathrm{Re}_P * \gamma_A} \qquad (10)$$

The particle drag coefficient $c_D$ is taken from [23].

$$c_D = \frac{24}{\mathrm{Re}_P}\left(1+0.15*\mathrm{Re}_P^{0.687}\right) \qquad (11)$$

$$\mathrm{Re}_P = \frac{|U_A - U_P| * d}{\gamma_A} \qquad (12)$$

The term $T_S$ is a characteristic time for the mean flowfield. Here the reciprocal value of the spatial change of the gas velocity is used:

$$T_S = \frac{\Delta l}{\Delta U} \qquad (13)$$

The velocity of the measured particles with a diameter smaller than 1µm is treated as the gas velocity. Hence the characteristic time $T_S$ can be calculated from the PDA-data.

Since the ratio of the liquid and gas density enters the particle relaxation time of eq. (13), inertia effects will be bigger in the simulation than in the reality. For the understanding of the particle dispersion under simulated pressure condition it is therefore necessary to evaluate the similarity of the Stokes-numbers between the simulated and the real engine condition, to have a chance to separate the effects of the spray density from those of the particle inertia.

## 3. RESULTS

All experiments were made under atmospheric pressure and ambient temperature. The atomizer was operated in the confinement at two different conditions, which are listed in table 5:

- fuel lean, atmospheric
- simulated pressure

| | simulated pressure | atmospheric |
|---|---|---|
| pressure drop Δp/p | 9% | 2.3% |
| AFR | 6.5 | 25 |
| fuel flow | 7.5g/s | 1.0g/s |

Table 5: Operating conditions

The Sauter mean diameter (SMD) for both test cases is shown in figure 11 and 12 respectively. The strong radial separation of the droplets caused by the particle inertia under simulated pressure can be seen clearly. The integral mass flux weighted SMD of the whole spray is 40.77μm for the atmospheric condition and 21.75μm for simulated pressure. The ratio of both diameters agrees very well with eq. (6), especially with respect to the error range for simulated pressure described in the following paragraphs. An explanation of the comparatively high SMD near the centreline of the spray under simulated pressure is given in the next paragraphs.

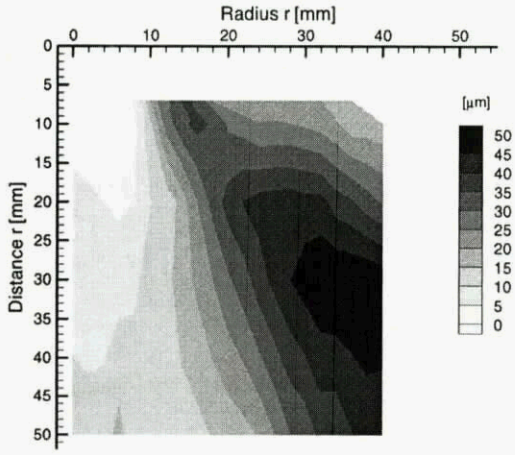


Figure 11: Sauter mean diameter for atmospheric condition

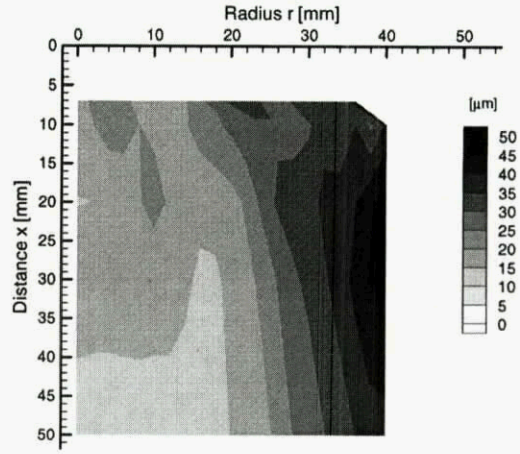


Figure 12: Sauter mean diameter for simulated pressure condition

The measured mass flux in axial direction for the atmospheric and the simulated pressure condition is shown in figure 13 and 14 respectively.

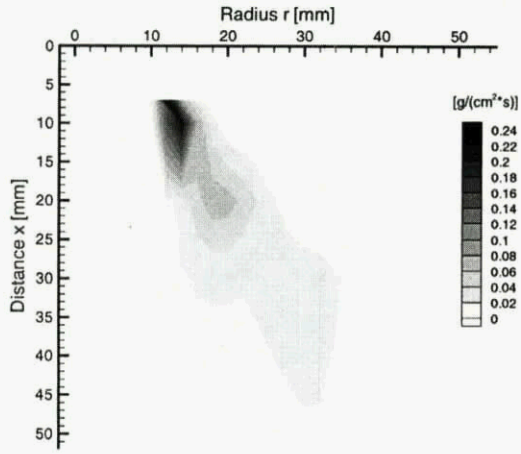


Figure 13: Axial mass flux, atmospheric condition

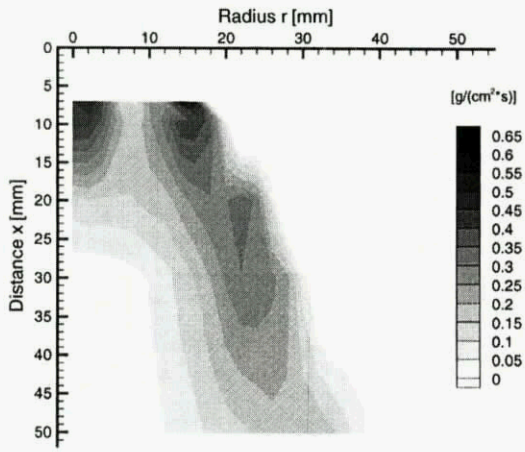


Figure 14: Axial mass flux, simulated pressure condition

The difference in the amount of the mass flux between both operating conditions is well reproduced by the PDA-data. The integrated errors of the kerosene mass flow for simulated pressure condition are listed in table 6:

| Measuring plane | Error |
|---|---|
| 7mm | -54% |
| 10mm | -45% |
| 20mm | -29% |
| 30mm | -25% |
| 50mm | -17% |

Table 6: Integrated errors between measured and real mass flow under simulated pressure

In this dense spray the errors are higher than under atmospheric conditions but still have moderate values. This is even more noticeable considering that the spray density is similar to the spray at actual idle condition in the combustor. So this dual PDA has proven its capability of making measurements under pressure conditions with reasonable accuracy. Although the particle number concentration is about one order of magnitude higher than for the atmospheric case the value of the errors only doubled. The error values of the mass flux can be seen as the upper limit, as this is one of the spray properties which is most error sensitive and most difficult to measure. In the measuring planes close to the nozzle the outer recirculation was not taken into account in the mass flow balance. The same calculation algorithm as for the atmospheric condition was used with no further modifications. The error sources are non-spherical particles near the nozzle exit and the extremely high spray density in this region. The spray density has two effects:

- The particle concentration in the measuring volume is too high to be corrected by the correction algorithm based on the Poisson statistic. Additionally the arrival time statistic may possibly not follow the Poisson statistic.
- The high spray density „in front of" the measuring volume leads to a distortion of the beam intersection causing a lower signal-to-noise ratio.

In the atmospheric case (figure 13) the dispersion of the particles can be identified by the broadening of the mass flux distribution with increasing distance to the nozzle exit (7mm<=x<=30mm). Under simulated pressure conditions (figure 14) the kerosene near the nozzle exit (x=7mm, r=14mm) is driven slightly further outwards. Further downstream the angle of the spray cone has decreased. In figure 15 and 16 the axial and radial velocities of the particles with d<=1μm are shown. The particles with d<=1μm are assumed to follow the gas flow without any slip.

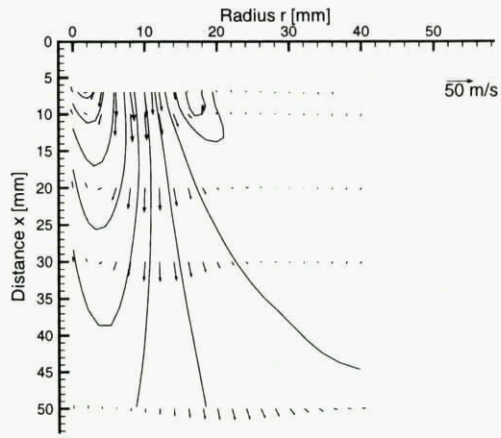


Figure 15: Axial and radial gas velocities, atmospheric condition

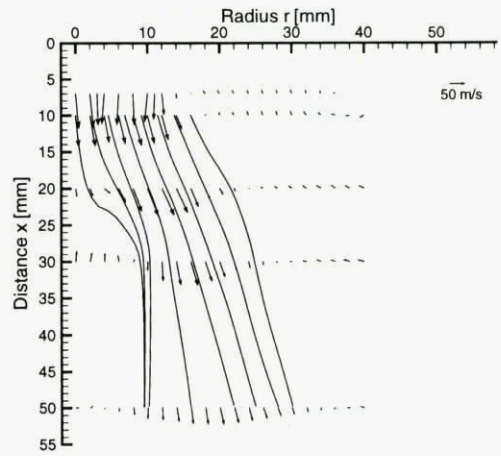


Figure 16: Axial and radial gas velocities under simulated pressure

The iso-lines of the axial massflux follow approximately the streamlines in both cases. So the different spreading of the spray is not caused by different relative motion of the particles; the spreading of the whole two-phase-flow has changed. The reason for this change will be given later

The second peak of the mass flux in figure 14 in the centre of the spray cone (r=0mm, 7mm<=x<=15mm) can be explained by processes inside the fuel nozzle. The given explanation also holds for the higher SMD described above. The axial momentum of the air is large enough to redirect a fraction of the spray from the pressure swirl atomizer. These droplets are not placed on the prefilming lip but fly directly through the nozzle exit into the combustion chamber near the axis of symmetry. This phenomenon is likely to occur under real pressure conditions as well, because there the momentum of the atomizing air is even larger due to the higher air density.

Another possible explanation of the second peak and the reason for the changed spray cone angle can be found in the figures 17 and 18. The axial and tangential gas velocities of both operating conditions at the axial position x=20mm are plotted. For ease of comparison the velocities are normalized with the ratio of the characteristic velocities corresponding to the pressure drops.

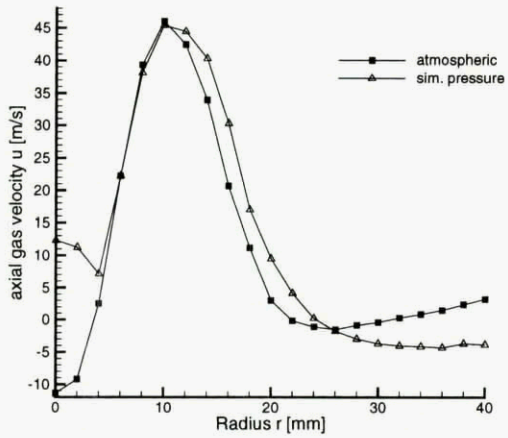


Figure 17: Normalized axial gas velocities at x=20mm

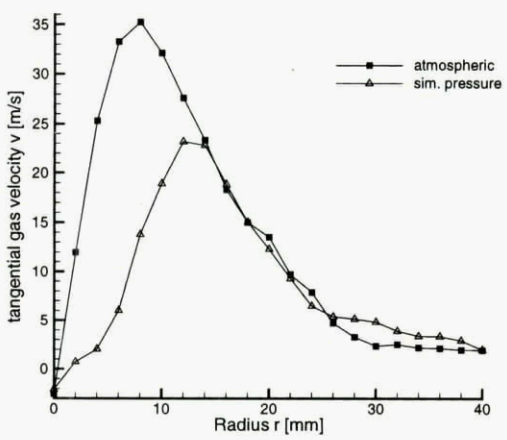


Figure 18: Normalized tangential gas velocities at x=20mm

The axial gas velocities of both test cases are very similar except of the centre region of the spray. In contrast the tangential gas velocities differ strongly. The peak of the tangential velocity is much smaller and is shifted outwards for the highly loaded two phase flow. The different behaviour of the tangential velocity results in a degradation of the swirl. It seems as if preferably the tangential momentum is exchanged between the gas phase and the particles. Here an effect of the dense spray can clearly be identified. This phenomenon has been reported in [24] as well, but still there has been found no explanation for this. Together with the droplets emerging the fuel nozzle at the centre line the reduced swirl leads to a weakening of the inner recirculation, see figure 15, 16.

Profiles of the axial mass fluxes at the location x=30mm are shown for both operating conditions in figure 19. The mass fluxes are normalized with the ratio of the integrated measured mass flows in this plane.

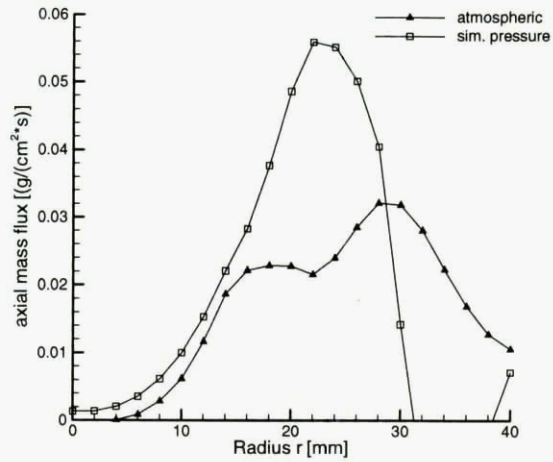


Figure 19: Normalized axial mass flux at x=30mm

The main difference can be found in the width of the distribution. The full width at half-maximum for atmospheric condition is 23mm and 13.5 mm for the dense spray. Unfortunately this phenomenon could not be found closer to the nozzle exit. Here the dispersion of the spray characterised by the broadening of the mass flux distribution is interfered by the mass flux of the particles leaving the nozzle near the centre line, see figure 14.

The low dispersion described above results in an enrichment of the local fuel concentration under simulated pressure condition. The volumetric fuel concentration for both test cases is shown in figures 20 and 21. Again the volume concentration is normalized by the integrated measured mass flow in each measuring plane. The larger fuel concentration in the simulated pressure condition is evident.

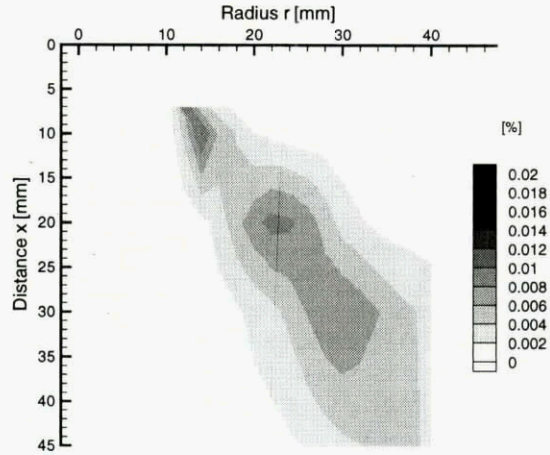


Figure 20: Normalized volumetric fuel concentration, atmospheric condition

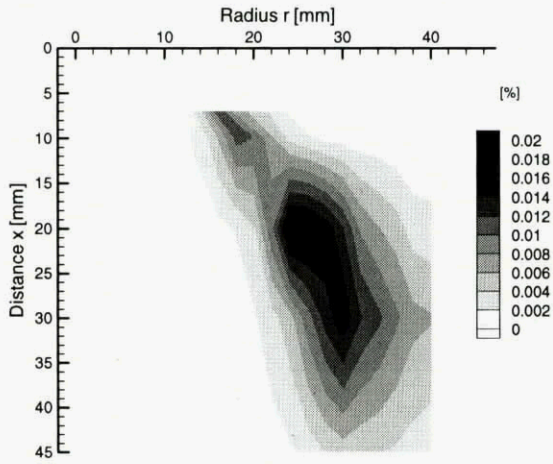


Figure 21: Normalized volumetric fuel concentration, simulated pressure condition

This reduced dispersion of the dense spray can be explained by the turbulence of the gas phase. The phenomenon can be classified as a dense spray effect. The high particle concentration damps the turbulence of the continuous phase leading to a suppression of the particle dispersion. The reduced turbulence of the gasphase under simulated pressure condition at x=20mm can be seen in figure 22. The turbulence grade *Tu* is defined by the ratio of the local radial turbulence energy to the axial kinetic energy, see eq. (14):

$$Tu = \frac{(rms\ radial\ vel.(r))^2}{2 * \frac{\Delta p}{p} * R * T} \qquad (14)$$

This quantity describes the turbulent dispersion perpendicular to the main flow direction.

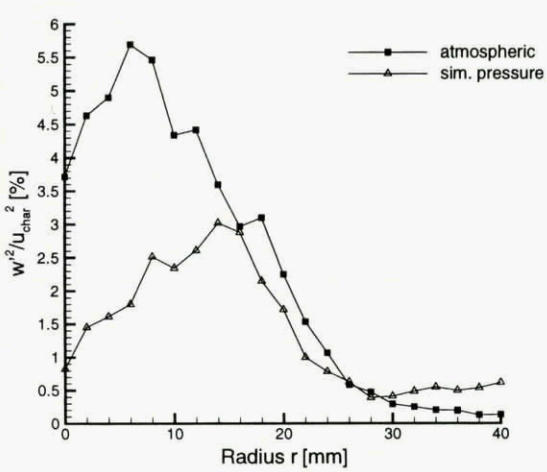


Figure 22: Turbulence grade of radial velocity of the gasphase at x=20mm

The reduced turbulence in the dense spray has been reported by other authors as well [18], [19], [24]. It is likely to appear under real pressure condition too. The increased fuel concentration probably leads to higher flame temperatures and higher soot production in the combusting case. From this point of view the simulation of pressure conditions can give first information of the spray properties under real engine condition in an early stage of the development of fuel nozzles.

For the interpretation of the measurements made under simulated pressure condition it is necessary to evaluate the similarity of the stokes-number between simulated and real engine condition. A measure for the similarity is the global ratio of the stokes-number for both cases. This ratio can be estimated from the equations given in the previous section. Assuming similarity of the single-phase gas flow for both conditions the characteristic time $T_s$ only depends on the velocity corresponding to the pressure drop. The Reynolds-numbers of the single-phase gas flow for simulated and real idle condition are 222800 and 288700 respectively. The different atomizing quality under real idle condition has to be taken into account. The estimated global ratio between the Stokes-numbers is:

$$Stk_{sim} / Stk_{real} = 4.4 \qquad (15)$$

As the Stokes-numbers of the particles under simulated pressure condition are about 4 times larger than under real engine condition, the behaviour of the particles is more dominated by their inertia and initial conditions. This means, that the phenomena observed under simulated pressure, which are caused by „Stokes-effects", are exaggerated to a certain degree. These phenomena represent the upper limit of what can be expected under real pressure.

## 4. CONCLUSIONS

A new algorithm, which makes use of all three velocity components, for the calculation of the mass flux was derived. A comparison with a 2D-algorithm revealed the improved performance. The error of the integrated mass flux is about +/-15% in measuring planes more than 10mm behind the nozzle exit. Even in a spray with a density similar to real engine idle conditions the used PDA was capable to measure the mass flux with moderate errors.

The simulation of real engine conditions is possible within certain limitations. One can get first information on the behaviour of the spray under pressure. Similarity rules were derived with respect to the particle number concentration. By increasing the pressure drop, reducing the air-fuel-ratio and by using original JET-A1 kerosene a number concentration similar to real idle condition was achieved. For the understanding of the results it is essential to distinguish between effects caused by the particle inertia („Stokes-effects") and effects caused by the spray density. The dense spray effects, which are likely to occur under real engine condition too, are reproduced by the simulation. An local enrichment of the spray due to the reduced dispersion can be identified, which may influence the NOx-emissions and soot production under real engine condition. The modifications caused by Stokes-

effects are exaggerated in the simulation. Furthermore one has to keep in mind, that in the real engine the spray combusts. The modifications induced by the combustion are not covered by this simulation.

Another application of this simulation is the code validation for numerical models. The results of the simulation can be used in the development of a numerical model for the calculation of dense sprays. After validation with this „cold" dense spray, the model can be implemented in a program for the simulation of the reacting flowfield in a combustion chamber.

Currently efforts are made at the DLR to combine PDA and kerosene LIF to overcome the limitations of the PDA in the atomizer nearfield.

## 5. ACKNOWLEDGEMENTS

The financial support from the German „Bundesamt für Wehrtechnik und Beschaffung", Auftragsnummer E/L41A/V0077/P5131 is gratefully acknowledged.

## 6. REFERENCES

[1] Lefebvre, A. H., „Gas Turbine Combustion", New York, Hemisphere Publishing Corp., 1983

[2] Bahr, D. W., „Technology for the Design of High Temperature Rise Combustors", Journal of Propulsion, Vol. 3, No. 2, March-April 1987, pp. 179-186

[3] Lefebvre, A. H., „The Role of Fuel Preparation in Low-Emission Combustion", Journal of. Eng. for Gas Turbines and Power, October 1995, Vol. 117, pp. 617-654

[4] Kennedy, J. B., „Gas Turbine Combustion", von Karman Institute for Fluid Dynamics, Lecture Series 1990-02

[5] Behrendt, T., Hassa, C., „Ein Prüfstand zur Untersuchung von Zerstäuberdüsen für Gasturbinen", Spray 96, Bremen 1996, Germany

[6] Hassa, C., Deick, A., Eickhoff, H., „Investigation of the Two-Phase Flow in a Research Combustor under Reacting and Non-Reacting Conditions", AGARD Conference Proceedings 536, 1993, Paper 41

[7] Dual PDA manual, DANTEC/invent measurement technology, 1996

[8] Tropea, C., Xu, T.-H., Onofri, F., Gréhan, G., Haugen, P., Stieglmeier, M., „Dual Mode Phase Doppler Anemometer", 4th Int. Congr. Optical Particle Sizing, 1995, Conference Proceedings, pp. 287-298

[9] „Streu", Software to calculate scattered light, DANTEC/Invent Measurement Technology GmbH

[10] Fitzky, G., Bohn, D., „Messung der komplexen Brechungsindizes von Heizöl EL und Kerosin in Abhängigkeit von Druck und Temperatur", Bericht Turboflam II Forschungsvorhaben „Messung der Zweiphasenströmung in einer Ölvormischstrecke", RWTH Aachen, Germany, 1995

[11] Saffman, M., „Automatic calibration of LDA measurement volume size", Applied optics, Vol. 26, No. 13, 1987, pp. 2592-2597

[12] Dullenkopf, K., Willmann, M., Wittig, S., Schöne, F., Stieglmeier, M., Tropea, C., Mundo, C., „Comparative mass flux measurements in spray using patternator and Phase Doppler technique", Proc. 8th inter. symposium on Appl. of Laser Anemometry to Fluid Mech., Lisbon 1996

[13] Brandt, M., „Liquid and Gaseous Fuel Measurements in a Premix Duct", ILASS 95, Nürnberg 1995, Germany

[14] Schöne, F., Bauckhage, K., Wriedt, T., „Size of the Detection Area of a Phase-Doppler Anemometer for Reflecting and Refracting Particles", Part. Part. Syst. Charact., 11 (1994), pp. 327-338

[15] Edwards, C. F., Marx, K. D., „Analysis of the Ideal Phase-Doppler System: Limitations imposed by the Single-Particle Constraint", Atomization and Sprays, vol. 2, 1992, pp. 319-366

[16] Hardalupas, Y., Taylor, A. M. K. P., „On the measurement of particle concentration near a stagnation point", Experiments in Fluids, 8, 1989, pp. 113-118

[17] Hassa, C., „Experimentelle Untersuchung der turbulenten Partikeldispersion in Drallströmungen", Dissertation, Ruhr-Universität Bochum, Germany, 1994

[18] Wang, H. Y., Sowa, W., McDonell, V. G., Samuelsen, G. S., „Spray Gas-Phase Interaction Downstream of a Co-Axial Counter-Swirling Dome Swirl Cup", ICLASS-91, Paper 76

[19] McVey, J. B., Kennedy, J. B., Russell, S., „Application of Advanced Diagnostics to Airblast Injector Flows", ASME 88-GT-12

[20] Lefebvre, A. H., „Atomization and Sprays", New York, Hemisphere Publishing Corp., 1989

[21] Han, Y. M., Yoon, M. S., Seol, W. S., Lee, D. S., Yagodkin, V. I., Jeung, I. S., „An Experimental Study on Modelling of Fuel Atomization for Simulating the Idle Regime of a Gas Turbine Combustor by Atmospheric Testing", ASME 97-GT-152

[22] Joost, F., „Low Emission Combustor Technology", Brite/Euram AERO 1019, Report 1991

[23] Schiller, L., Naumann, A., „Über die grundlegende Berechnungen bei der Schwerkraftaufbereitung", Zeitschrift des VDI, 77, 1933

[24] Brandt, M., Hassa, C., Eickhoff, H., „An Experimental Study of Spray - Gasphase Interaction for a Co-Swirling Airblast Atomizer", ILASS-Europe, October 1992, pp. 115-122

Paper 5
Authors: T. Behrendt, A. Hassa

Q: Weigand

Referring to Table 3 in your paper :what causes the increase of error in mass-flux measurements when the distance of the measurement place is increased beyond 30mm? Can the kind of thresholding you have given as the reason also explain the positive deviation of + 14.5%?

A: The increase in error beyond 30mm is caused by the criterion of at which radial location the measurements were stopped. Due to the large area of the ring corresponding to the large radial position even a low massflux has a slight influence on the integrated massflow.
The calculation algorithm is based on a few assumptions. If these assumptions are not fulfilled completely, the calculations can have a positive deviation as well.

# Laser Two Focus Anemometry (L2F-3D) for Three-Dimensional Flow Analysis in an Axial Compressor

**A. Vouillarmet & S. Charpenel**
Laboratoire de Mécanique des Fluides et d'Acoustique
UMR CNRS 5509/ECL/UCB Lyon I
Ecole Centrale de Lyon
BP 163 - 69131 - Ecully Cedex - France

## 1. SUMMARY

In order to improve the accuracy of numerical simulations applied to the new generation of high-loaded, high-speed turbomachines, a thorough understanding of the 3D phenomena is needed. For that purpose, the use of 3D experimental techniques, like 3D-L2F anemometry initiated by Schodl, is now absolutely necessary. This paper deals with a statistical method for processing the data. The point is that, during the acquisition procedure, marginal and conditionnal probability density fonctions (p.d.f.) are obtained, but they are already integrated quantities. Hence, it becomes impossible to derive analytical relations between the p.d.f. and the 3D first and second order momenta. However, an issue can be found using an isotropic tubulence hypothesis. This method has been, first of all, tested in an axisymmetrical free jet. Futhermore, an experimental investigation of the three-dimensional flow field within the tip area of a high-loaded, low-speed axial compressor was performed.

## 2. INTRODUCTION

Due to the increasing demand for improved performances and efficiency of the rotating machines, there is a growing need for methods to study and analyse the detailed flow behaviour. In this context, experimental systems allowing accurate measurement of the three-dimensional flow field in the rotating environment are needed.

The 2D-L2F technique, improved for fifteen years at Ecole Centrale de Lyon, was first developed and extended by Schodl [1] for three-dimensional measurements in turbomachinery. Schodl along with his co-authors are the only ones, at the present time, who have carried out measurements with the 3D-L2F device. First of all, they have made a critical test around a sphere located in the potential core of an axisymmetrical jet to check the system performances [2], and they have presented some results at the exit of a propfan test rig [3]. In all these works, three components of the mean velocity vector and only two standard deviations have been presented but the way they were calculated has not been described.

In this paper, a statistical calculation method for one and second order momenta with the 3D-L2F anemometer is presented. The results of a critical test carried out in an axisymmetrical free jet are used to understand the method limitations, and to validate the statistical analysis. In order to show that this three-dimensional anemometer, associated with the previous data processing technique, is efficient for turbomachinery applications, the flow field within a high-loaded, low-speed compressor is investigated in the tip area which allows to intercept the leakage vortex.

## 3. THREE-DIMENSIONAL LASER TWO FOCUS SYSTEM

### 3. 1. Measurement principle

The 3D-system is basically composed of two 2D-L2F devices which are symmetrically located, with a slant $\gamma$ of 7.5 deg, on both sides of the rotation axis of the whole system. Each 2D-L2F system allows the measurement of the velocity vector projections - modulus $u_i$ and direction $\alpha_i$ - in its own focal plane. Let us recall that, in fact, this measurement is only possible if the velocity vector lies within the plane of the two laser beams axes. In the case of figure 1, where the velocity vector is located in the symmetry plane of the 3D-system, one could see that it is neither in the first nor in the second single 2D device beams plane. Therefore, the velocity vector cannot be measured with any of the devices at that orientation. This situation ever exists, except if the velocity vector has no 3D component, i.e. if it lies in a plane perpendicular to the system axis (named reference plane). On the other hand, a small turning of the whole system of $\Phi_1$ will bring the velocity vector in the beams plane of the first system and a counter rotation of $\Phi_2$ in the beam plane of the second one. If we call $\alpha$ the velocity vector angle defined in the reference plane, two different angles $\alpha_1$ and $\alpha_2$ could be obtained in orientating, one after another, the two systems. This means that they could never be measured simultaneously. Because of the 3D-system symmetry, $\Phi_2 = -\Phi_1$ and we get the same modulus u ($= u_1 = u_2$) with the two 2D-devices. Thus, we have the following relations :

$$\alpha_1 = \alpha + \Phi_1 \quad (1)$$

$$\alpha_2 = \alpha + \Phi_2 = \alpha - \Phi_1 \quad (2)$$

Or : $$\alpha = (\alpha_1 + \alpha_2)/2 \quad (3)$$

$$\Phi_1 = -\Phi_2 = \Phi = (\alpha_1 - \alpha_2)/2 \quad (4)$$

From these measured values (u, $\alpha_1$, $\alpha_2$), it is possible to derive, from the geometrical situation, the three spherical components (V, $\alpha$, $\beta$) of the total velocity :

*Paper presented at an AGARD PEP Symposium on "Advanced Non-Intrusive Instrumentation for Propulsion Engines", held in Brussels, Belgium, 20-24 October 1997, and published in CP-598.*

$$\alpha = (\alpha_1 + \alpha_2)/2 \tag{5}$$

$$\beta = \arctan\left(\frac{\sin\Phi}{\tan\gamma}\right) \tag{6}$$

$$V = \frac{u}{\cos\Phi\cos\beta} = u\left[1 + \frac{\tan^2\Phi}{\sin^2\gamma}\right]^{1/2} \tag{7}$$

It should be noted that if $\beta$ is equal to zero, then both of the devices detect the same angle $\alpha_1 = \alpha_2$.

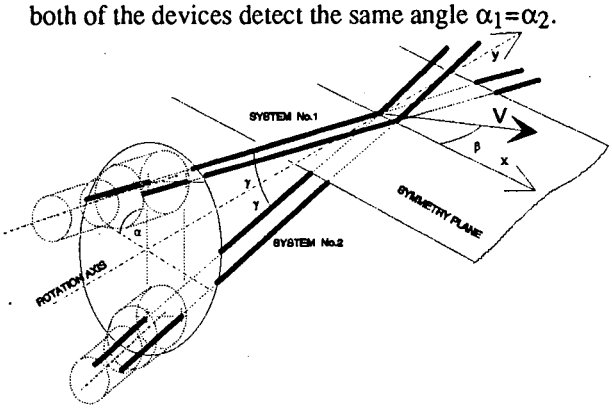


**Figure 1** : 3D-L2F device

### 3. 2. Uncertainties on the estimation of the third component

The laser anemometers (LDA or L2F) allowing the direct measurement of the three orthogonal velocity components in a Cartesian set are rarely encountered. The three orthogonal-component LDA measuring system used by Chesnakas and Simpson [4] to analyse the flow field behind a prolate spheroid, could be considered as an exception. Other LDA systems commonly used are non-orthogonal ones, which means that the optical axis of the third device is not perpendicular to the other two ones. Orloff and Snyder [5] have shown that systematic errors occur in the converting process to restore the cartesian components of the velocity vector, especially on the on-axis component, due to the fact that the third measured velocity component is coupled with the two other ones. Consequently, it would be advisable that the coupling angle should not stay below 30 deg. On the other hand, one must take into account the optical access restraints encountered in turbomachinery. The sight windows are rather narrow to ensure wall continuity and to minimize glass distorsions. Therefore, a compromise must be found, which leads, for most of the actual devices, to a 15 deg angle. The same kind of geometrical limitations occurs with the 3D-L2F anemometry technique.

Uncertainties on the measurement of $\alpha_1$ and $\alpha_2$ ($\Delta\alpha_1$ and $\Delta\alpha_2$) induce uncertainties on the determination of $\alpha$ and $\beta$. This could be estimated by a first order Taylor development of formulae 5 and 6 :

$$\Delta\alpha = (\Delta\alpha_1 + \Delta\alpha_2)/2 \tag{8}$$

$$\Delta\beta = \frac{\tan\gamma\cos\Phi}{\tan^2\gamma + \sin^2\Phi}(\Delta\alpha_1 + \Delta\alpha_2)/2 \tag{9}$$

It can be shown that the higher $\gamma$ is, the smaller the $\beta$ uncertainties are, but they also depend on $\beta$ values themselves. For our case, where a value of 15 deg was chosen for the angle $2\gamma$, assuming $\Delta\alpha_1 = \Delta\alpha_2$, the magnitude of $\Delta\alpha$ equal the one of $\Delta\alpha_1$ whereas the one of $\Delta\beta$ is 5.7 to 7.6 times $\Delta\alpha_1$ (for $\beta$ varying from 30 to 0 deg). This shows that small uncertainties on the $\alpha_1$ and $\alpha_2$ mean values induce very large errors on the $\beta$ one. Similar values have been found by Stauter [6] for a LDA device with a coupling angle of 16 deg.

## 4. STATISTICAL ANALYSIS

### 4. 1. Two-dimensional-L2F data processing

The 3D-L2F technique is based on the 2D-L2F procedure, so that it is interesting to call up briefly the two-dimensional data processing used in turbomachinery applications. Because the investigated compressors require high power rotating facilities driving, which leads to high cost experimentation, the acquisition procedure, used more often than not, requires two steps.

Firstly, a marginal angular probability density function (p.d.f.) $P_\alpha(\alpha)$ is reached. This p.d.f. allows the calculation of the mean value velocity vector direction :

$$\overline{\alpha} = \int \alpha P_\alpha(\alpha)\, d\alpha \tag{10}$$

With the associate standard deviation :

$$\sigma_\alpha^2 = \int (\alpha - \overline{\alpha})^2 P_\alpha(\alpha)\, d\alpha \tag{11}$$

Secondly, in orientating the probe volume parallel to the mean velocity direction $\overline{\alpha}$, a conditional p.d.f. of the velocity modulus $P(u)|_{\overline{\alpha}}$ could be obtained. Strictly, the total p.d.f. is given by :

$$P_{\alpha,u}(\alpha, u) = P_\alpha(\alpha) P(u)|_\alpha \tag{12}$$

However, if $\alpha$ and u are held to be statistically independent variables :

$$P_{\alpha,u}(\alpha, u) = P_\alpha(\alpha) P(u)|_{\overline{\alpha}} \tag{13}$$

Then, any statistical quantities could be determined and especially :

$$\begin{aligned} \overline{u} &= \iint u P_{\alpha,u}(\alpha, u)\, d\alpha\, du \\ &= \iint u P_\alpha(\alpha) P(u)|_{\overline{\alpha}}\, d\alpha\, du \\ &= \int P_\alpha(\alpha)\, d\alpha \cdot \int u P(u)|_{\overline{\alpha}}\, du \\ &= \int u P(u)|_{\overline{\alpha}}\, du \end{aligned} \tag{14}$$

and :

$$\sigma_u^2 = \int (u - \overline{u})^2 P(u)|_{\overline{\alpha}}\, du \tag{15}$$

The validity of the hypothesis of statistically independent variables will be discuss below in the case of an isotropic turbulence.

### 4. 2. Specific statistical problems dealing with the 3D technique

Previously, we have shown that the values of u, $\alpha_1$ and $\alpha_2$ can not be obtained simultaneously, so, do not correspond to a same particle. In fact, (u, $\alpha_1$) and (u, $\alpha_2$) are determined independently by the two 2D-L2F devices, one after another, so that we have no access to the three-dimensional p.d.f. $P_{u,\alpha_1,\alpha_2}(u,\alpha_1,\alpha_2)$. In this context, the only issue to calculate the mean and fluctuating values of the velocity vector components (V, $\alpha$, $\beta$) is to derive relations from the first and second order momenta of u, $\alpha_1$ and $\alpha_2$. However, an exact calculation is not allowed because the integration process leading to the determination of the standard deviations generates information losses. For example, an $\alpha$ variation can be detected as a same direction variation of $\alpha_1$ and $\alpha_2$, where a $\beta$ variation makes $\alpha_1$ and $\alpha_2$ varying in opposite ways. This information on direction variations is lost during the integration process and the knowledge of $\sigma_{\alpha 1}$ and $\sigma_{\alpha 2}$ values is not enough to determine $\sigma_\alpha$ and $\sigma_\beta$ : it has become impossible to know which part of the variations of $\sigma_{\alpha 1}$ and $\sigma_{\alpha 2}$ corresponds to a $\sigma_\alpha$ or a $\sigma_\beta$ variation. More distinctly the following formula can be derived from relations (5) and (6) :

$$\begin{aligned}\alpha_1 &= \alpha + \arcsin(\tan\beta \tan\gamma)\\ \alpha_2 &= \alpha - \arcsin(\tan\beta \tan\gamma)\end{aligned} \qquad (16)$$

Assuming that the value of tan $\gamma$ is small and tan$\beta$ = $\beta$ (with an error of 4 % for $\beta$ values lower than 20 deg), these formulae can be simplified :

$$[\alpha_1, \alpha_2] \approx [\alpha + \beta\tan\gamma, \alpha - \beta\tan\gamma] \qquad (17)$$

Considering $\alpha$ and $\beta$ variables independence, averaging procedures lead to :

$$[\overline{\alpha}_1, \overline{\alpha}_2] \approx [\overline{\alpha} + \overline{\beta}\tan\gamma, \overline{\alpha} - \overline{\beta}\tan\gamma] \qquad (18)$$

and :

$$\sigma_{\alpha_1} \approx \sigma_{\alpha_2} \approx \sqrt{\sigma_\alpha^2 + \tan^2\gamma . \sigma_\beta^2} \qquad (19)$$

It shows that only two independent quantities $\sigma_{\alpha 1}$ and $\sigma_u$ are available to derive the three standard deviations $\sigma_V$, $\sigma_\alpha$ and $\sigma_\beta$. This is due to the fact that, even if $\alpha$ and $\beta$ are independent variables, $\alpha_1$ and $\alpha_2$ are strongly correlated quantities, so that correlation coefficient (R) is :

$$R = \frac{\overline{(\alpha_1 - \overline{\alpha}_1)(\alpha_2 - \overline{\alpha}_2)}}{\sigma_{\alpha_1}\,\sigma_{\alpha_2}} = \frac{\sigma_\alpha^2 - \tan^2\gamma \cdot \sigma_\beta^2}{\sigma_\alpha^2 + \tan^2\gamma \cdot \sigma_\beta^2} \qquad (20)$$

Because of the small value of $\gamma$ (7.5 deg $\approx$ 0.13 rad), R remains close to 1. Otherwise, $\sigma_{\alpha 1}$ and $\sigma_{\alpha 2}$ are more sensible to the $\alpha$ fluctuations than to the $\beta$ ones. For example, for equal values of $\sigma_\alpha$ and $\sigma_\beta$, the second term of the square root of the equation (19) represents only 1.7 % of the first one, and if $\sigma_\beta$ is three times larger than $\sigma_\alpha$, it is still lower than 15 %.

### 4. 3. Isotropic turbulence hypothesis

Thus, to calculate the mean and fluctuating values of the velocity vector components (V, $\alpha$, $\beta$) from the first and second order momenta of u, $\alpha_1$ and $\alpha_2$, we are obliged, on the one hand, to assume the independence of the variables V, $\alpha$ and $\beta$, and, on the other hand, to find an additional relation between these second order momenta. With this object, it is interesting to put ourselves in the context of an isotropic turbulence model, which is a useful model, not so far from real flow fields conditions except in boundary layer and other shear flows.

A three-dimensional stationary homogeneous and isotropic turbulent flow field is described by the fluctuating Cartesian components $u_x$, $u_y$, $u_z$ which are considered as independent random variables following Gaussian distributions. The statistical field is defined by the p. d. f. :

$$\begin{aligned}P_{u_x,u_y,u_z}(u_x,u_y,u_z) &= P_{u_x}(u_x)\cdot P_{u_y}(u_y)\cdot P_{u_z}(u_z)\\ &= \frac{1}{\sigma\sqrt{2\pi}} e^{-\frac{u_x^2}{2\sigma^2}} \cdot \frac{1}{\sigma\sqrt{2\pi}} e^{-\frac{u_y^2}{2\sigma^2}} \cdot \frac{1}{\sigma\sqrt{2\pi}} e^{-\frac{u_z^2}{2\sigma^2}}\end{aligned} \qquad (21)$$

It can be shown that this p. d. f. expressed with the spherical components ($\xi$, $\theta$, $\varphi$) of the turbulent flow field becomes :

$$\begin{aligned}P_{\xi,\theta,\varphi}(\xi,\theta,\varphi) &= P_\xi(\xi)\cdot P_\theta(\theta)\cdot P_\varphi(\varphi)\\ &= \frac{2\xi^2}{\sigma^3\sqrt{2\pi}} e^{-\frac{\xi^2}{2\sigma^2}} \cdot \frac{\cos\theta}{2} \cdot \frac{1}{2\pi} = \frac{\xi^2\cos\theta}{\sigma^3(2\pi)^{3/2}} e^{-\frac{\xi^2}{2\sigma^2}}\end{aligned} \qquad (22)$$

Now, let us convect this turbulent flow field by a uniform mean velocity. The resultant flow field (see figure 2) is :

$$\begin{aligned}\vec{V} = \vec{\overline{V}} + \vec{\xi} &= (\overline{V} + \xi\cos\theta\cos\varphi)\,\vec{e}_V\\ &+ \xi\cos\theta\sin\varphi\,\vec{e}_\theta + \xi\sin\theta\,\vec{e}_\varphi\end{aligned} \qquad (23)$$

Then, the spherical components of this velocity vector are obtained, assuming a small fluctuation hypothesis and developing the previous formula at the first order :

$$\begin{aligned}V/\overline{V} &= 1 + \frac{\xi}{\overline{V}}\cos\theta\cos\varphi\\ \alpha - \overline{\alpha} &= \frac{\xi}{\overline{V}\cos\overline{\beta}}\cos\theta\sin\varphi\\ \beta - \overline{\beta} &= \frac{\xi}{\overline{V}}\sin\theta\end{aligned} \qquad (24)$$

By means of these relations, it is possible to show that V, $\alpha$, $\beta$ are non correlated random variables following the Gaussian law :

$$P_{V,\alpha,\beta}(V,\alpha,\beta) = \frac{\overline{V}^2\cos\overline{\beta}}{\sigma^3(2\pi)^{3/2}} e^{-\frac{(V-\overline{V})^2}{2\sigma^2}} \cdot e^{-\frac{\overline{V}^2\cos^2\overline{\beta}(\alpha-\overline{\alpha})^2}{2\sigma^2}} e^{-\frac{\overline{V}^2(\beta-\overline{\beta})^2}{2\sigma^2}} \qquad (25)$$

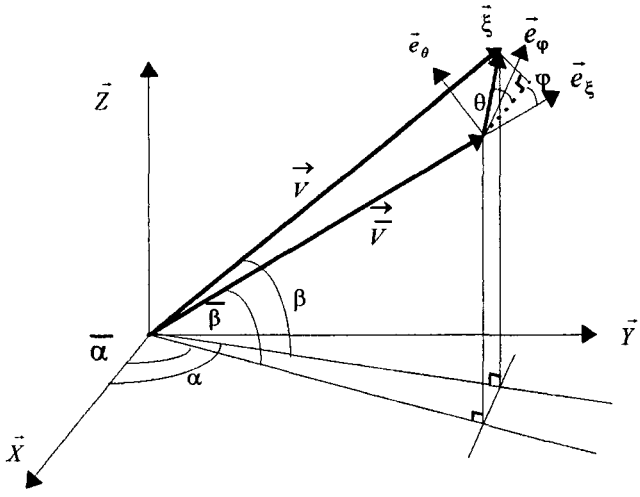


**Figure 2** : spherical coordinates

So that the marginal p. d. f. can be calculated :

$$P_V(V)=\frac{1}{\sigma_V\sqrt{2\pi}}e^{-\frac{(V-\overline{V})^2}{2\sigma_V^2}} \tag{26}$$

$$P_\alpha(\alpha)=\frac{1}{\sigma_\alpha\sqrt{2\pi}}e^{-\frac{(\alpha-\overline{\alpha})^2}{2\sigma_\alpha^2}} \tag{27}$$

$$P_\beta(\beta)=\frac{1}{\sigma_\beta\sqrt{2\pi}}e^{-\frac{(\beta-\overline{\beta})^2}{2\sigma_\beta^2}} \tag{28}$$

with :

$$\sigma_V=\overline{V}\cdot\sigma_\beta=\overline{V}\cos\overline{\beta}\cdot\sigma_\alpha=\sigma \tag{29}$$

In the same way and using the same hypothesis, it can be shown that, for a two-dimensional flow field, the polar components (u, α) of the velocity vector are also Gaussian random variables with $\sigma_\alpha$ equal to $\sigma_u/\overline{u}$. Experimentally, we verify that, in most cases, the velocity modulus and direction distributions actually look like Gaussian distributions and that $\sigma_\alpha \approx \sigma_u/\overline{u}$. This corroborates the validity of the previous hypothesis.
In the following, we will assume the independence of the variables V, α and β, and we will use the isotropic turbulence model to find the additional relation required between the second order momenta.

### 4. 4. Mean value calculations

As previously seen, V, α and β are non linear functions of $\alpha_1$, $\alpha_2$ and u (formula (4) to (7)). Unfortunately, we have no experimentally access to the 3D p.d.f. $P_{u,\alpha_1,\alpha_2}(u,\alpha_1,\alpha_2)$. Thus, it is not possible to calculate the mean values as follows :

$$\overline{f(\alpha_1,\alpha_2,u)}=\iiint f(\alpha_1,\alpha_2,u)\cdot P_{\alpha_1,\alpha_2,u}(\alpha_1,\alpha_2,u).d\alpha_1.d\alpha_2.du \tag{30}$$

A solution is to perform a Taylor development around the mean values of u, $\alpha_1$ and $\alpha_2$, restricted to the second order :

$$\begin{aligned}
f(\alpha_1,\alpha_2,u)=&\,f(\overline{\alpha_1},\overline{\alpha_2},\overline{u})+\left.\frac{\partial f}{\partial\alpha_1}\right|_{\overline{\alpha_1},\overline{\alpha_2},\overline{u}}.(\alpha_1-\overline{\alpha_1})\\
&+\left.\frac{\partial f}{\partial\alpha_2}\right|_{\overline{\alpha_1},\overline{\alpha_2},\overline{u}}.(\alpha_2-\overline{\alpha_2})+\left.\frac{\partial f}{\partial u}\right|_{\overline{\alpha_1},\overline{\alpha_2},\overline{u}}.(u-\overline{u})\\
&+\left.\frac{\partial^2 f}{\partial\alpha_1^2}\right|_{\overline{\alpha_1},\overline{\alpha_2},\overline{u}}.\frac{(\alpha_1-\overline{\alpha_1})^2}{2}\\
&+\left.\frac{\partial^2 f}{\partial\alpha_2^2}\right|_{\overline{\alpha_1},\overline{\alpha_2},\overline{u}}.\frac{(\alpha_2-\overline{\alpha_2})^2}{2}\\
&+\left.\frac{\partial^2 f}{\partial u^2}\right|_{\overline{\alpha_1},\overline{\alpha_2},\overline{u}}.\frac{(u-\overline{u})^2}{2}\\
&+\left.\frac{\partial^2 f}{\partial\alpha_1.\partial u}\right|_{\overline{\alpha_1},\overline{\alpha_2},\overline{u}}.(\alpha_1-\overline{\alpha_1}).(u-\overline{u})\\
&+\left.\frac{\partial^2 f}{\partial\alpha_2.\partial u}\right|_{\overline{\alpha_1},\overline{\alpha_2},\overline{u}}.(\alpha_2-\overline{\alpha_2}).(u-\overline{u})\\
&+\left.\frac{\partial^2 f}{\partial\alpha_1.\partial\alpha_2}\right|_{\overline{\alpha_1},\overline{\alpha_2},\overline{u}}.(\alpha_1-\overline{\alpha_1}).(\alpha_2-\overline{\alpha_2})+\varepsilon(3)
\end{aligned}$$

Averaging this relation and assuming that u is independent of $\alpha_1$ and $\alpha_2$, it leads to :

$$\begin{aligned}
\overline{f(\alpha_1,\alpha_2,u)}=&\,f(\overline{\alpha_1},\overline{\alpha_2},\overline{u})\\
&+\left.\frac{\partial^2 f}{\partial\alpha_1^2}\right|_{\overline{\alpha_1},\overline{\alpha_2},\overline{u}}.\frac{\sigma_{\alpha_1}^2}{2}\\
&+\left.\frac{\partial^2 f}{\partial\alpha_2^2}\right|_{\overline{\alpha_1},\overline{\alpha_2},\overline{u}}.\frac{\sigma_{\alpha_2}^2}{2}\\
&+\left.\frac{\partial^2 f}{\partial u^2}\right|_{\overline{\alpha_1},\overline{\alpha_2},\overline{u}}.\frac{\sigma_u^2}{2}\\
&+\left.\frac{\partial^2 f}{\partial\alpha_1.\partial\alpha_2}\right|_{\overline{\alpha_1},\overline{\alpha_2},\overline{u}}.R\,\sigma_{\alpha_1}\sigma_{\alpha_2}+\varepsilon(3)
\end{aligned} \tag{31}$$

*a. Calculation of the mean angle* $\overline{\alpha}$

The previous formulation applied to the angle α, given by eq. (5), induces directly :

$$\overline{\alpha}=\frac{\overline{\alpha}_1+\overline{\alpha}_2}{2} \tag{32}$$

*b. Estimation of the mean angle* $\overline{\beta}$

The formulation (31) applied to the angle β, given by eq. (6), leads to the β mean expression :

$$\overline{\beta} = \beta(\overline{\alpha_1}, \overline{\alpha_2}) + \left.\frac{\partial^2 \beta}{\partial \alpha_1^2}\right|_{\overline{\alpha_1}, \overline{\alpha_2}} \cdot \frac{\sigma_{\alpha_1}^2 + \sigma_{\alpha_2}^2 - 2R\,\sigma_{\alpha_1}\sigma_{\alpha_2}}{2} \quad (33)$$

Equations (19) et (20), assuming that $\tan\beta \sim \beta$, give :

$$\sigma_{\alpha_1}^2 + \sigma_{\alpha_2}^2 - 2R\,\sigma_{\alpha_1}\sigma_{\alpha_2} = 4\tan^2\gamma \cdot \sigma_\beta^2 \quad (34)$$

Then :

$$\overline{\beta} = \arctan\left(\frac{\sin\overline{\Phi}}{\tan\gamma}\right) - \frac{\sin\overline{\Phi}}{\tan\gamma}\left(1 + \cos^2\overline{\Phi} + \tan^2\gamma\right) \cdot \frac{\sigma_\beta^2}{2} \quad (35)$$

The second term of this relation is very small even for very penalising configurations. For example, if the $\beta$ value is equal to 30 deg and $\sigma\beta$ to 10 deg, its value is 1 deg. Thus, a zero order Taylor development should be considered satisfactory.

*c. Estimation of the mean velocity* $\overline{V}$

Using equation (7) and developing the same calculation as the $\beta$ one, we get :

$$\overline{V} = \overline{u}\left[1 + \frac{\tan^2\overline{\Phi}}{\sin^2\gamma}\right]^{1/2}[1+\varepsilon]$$

$$\text{,with: } \varepsilon = \frac{\sigma_\beta^2}{2\cos^2\gamma} \cdot \left[1 + 2\sin^2\overline{\Phi}\left(1 + \frac{\tan^2\overline{\Phi}}{\sin^2\gamma}\right)\right] \cdot \left[\frac{\sin^2\gamma + \sin^2\overline{\Phi}\cdot\cos^2\gamma}{\sin^2\gamma\cdot\cos^2\overline{\Phi} + \sin^2\overline{\Phi}}\right]^2 \quad (36)$$

Here we could also limit the Taylor development to order zero, the second term of the relation being about 0.015 for the previous conditions.

### 4. 5. Standard deviations estimations

*a. Angular fluctuations estimation*

In order to calculate the value of the standard deviation $\sigma\alpha$, from the equation (19), we have to estimate the value of $\sigma\beta$. For that, we will use the equation (29) resulting from the isotropic turbulence hypothesis. However, as above-mentioned, the approximated term $\tan^2\gamma\,\sigma\beta^2$ is much smaller than the main one $\sigma\alpha^2$. Then, we put ourselves in the framework of a weak hypothesis. So that :

$$\sigma_{\alpha_1} = \sigma_{\alpha_2} = \sqrt{\sigma_\alpha^2 + \tan^2\gamma\cdot\sigma_\beta^2} = \sqrt{\sigma_\alpha^2 + \tan^2\gamma\cdot\cos^2\overline{\beta}\cdot\sigma_\alpha^2} \quad (37)$$

Hence, we get :

$$\sigma_\alpha = \frac{\sigma_{\alpha_1} + \sigma_{\alpha_2}}{2\sqrt{1 + \tan^2\gamma\cdot\cos^2\overline{\beta}}} \quad (38)$$

*b. Velocity fluctuations estimation*

Applying equation (31) to $\left(V - \overline{V}\right)^2$, we get :

$$\sigma_V^2 = \left[1 + \frac{\tan^2\overline{\Phi}}{\sin^2\gamma}\right] \cdot \left[\sigma_u^2 + \frac{\overline{u}^2\tan^2\overline{\Phi}}{\sin^2\gamma\cdot\cos^2\gamma}\left[\frac{\sin^2\gamma + \sin^2\overline{\Phi}\cdot\cos^2\gamma}{\sin^2\gamma\cdot\cos^2\overline{\Phi} + \sin^2\overline{\Phi}}\right]^2\sigma_\beta^2\right] \quad (39)$$

## 5. CHECK OF THE MEASUREMENT TECHNIQUE IN A FREE JET

A preliminary test of the statistical method efficiency has been carried out in an axisymmetrical free jet. This experimental set-up has been chosen due to many measuring problems present in this configuration : in the potential core boundary area due to the eddy pattern, the high gradients and the seeding difficulties, and in the developed flow region due to high turbulence levels (up to 50 %). Furthermore, various results are available in the literature (Wygnanski and Fiedler [7]).

### 5. 1. Experimental facility and instrumentation

We use a 20 mm diameter ($\phi$) wind tunnel which allows a vertical development of the free jet. Because of stability problems, the velocity at the nozzle exit should stay between 40 and 65 m/s. Its value is given by a static pressure probe within an uncertainty band of 0.5 %.

The 3D-L2F anemometer consists of an Argon-laser operating in multi-colour mode, coupled with an optical head manufactured by Polytec. The four different distances existing between the start and the stop of the two 2D-devices permit the adjustment of the beam separation with the turbulence level in the flow field (Schodl [8]). Electronic and acquisition systems are identical to the 2D-ones previously developed in the L.M.F.A. at E.C.L [9]. All acquiring and processing procedures have been fitted to the 3D technique.

Laser measurements have been compared to those obtained with conventional probes : a Pitot probe for the mean values and a crossed hot wire probe for the fluctuating ones.

### 5.2. Some results

Measurements have been carried out in three sections downstream the nozzle exit, perpendicular to the jet axis as shown in figure 3.

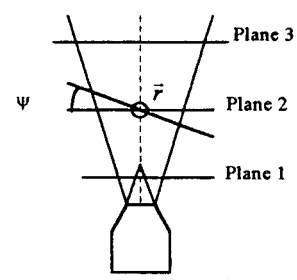


**Figure 3** : Measurement planes

The first plane is located in the potential core, whereas the second and the third ones are in the fully developed flow area. The free jet characteristics are presented in the following table :

| | Plane 1 | Plane 2 | Plane 3 |
|---|---|---|---|
| Distance from the nozzle (nb of $\phi$) | 2 | 10 | 20 |
| Jet diameter (mm) | 24 | 36 | 80 |
| $u_{rms}/U_m$ (%)* | 1.75 | 15 | 20 |
| $U_m$ (m/s)* | 40 | 50 | 25 |

* Jet axis mean velocities and turbulence level.

Furthermore, for each measurement plane, four radial traverses ($\vec{r}$ direction) were tested. The angle $\psi$, between the plane perpendicular to the jet axis and the optical axis of the 3D-device, was set to different values (0 ; 7.5 ; 15 and 30 deg) for each traverse, in order to simulate 3D flow effects.

For comparing 3D-L2F measurements and Pitot tube or hot-wire ones, all the results are projected in a cartesian set of coordinates associated with the jet longitudinal and radial directions for each measurement plane. We name $\overline{U}$ the longitudinal mean velocity, $\overline{V}$ and $\overline{W}$ the radial and the azimuthal ones. $u_{rms}$, $v_{rms}$, $w_{rms}$ are the associated second order momenta.

On figures 4a and 4b one could see that the restored mean longitudinal velocity ($\overline{U}$) profiles are well determined, whatever the angle $\psi$. Concerning the mean radial velocity ($\overline{V}$), the obtained pattern (figures 5 a and 5 b) are very similar to those derived by Wygnanski and Fiedler [7] from the continuity equation. The influence of the angle $\psi$ on the measurement accuracy seems quite negligible, except in the regions where the turbulent intensity is rather large (greater than 20 % in plane 3).

An attempt to deduce the longitudinal and radial fluctuations ($u_{rms}$ and $v_{rms}$) from $\sigma_\alpha$ and $\sigma_V$ has been performed in order to compare with the obtained hot wire anemometer values. We observe a rather good agreement in plane 1 (figures 6 a and 6 b) except near the boundaries of the jet, where intermittency occurs. For plane 3 (figures 7 a and 7 b), the results are also satisfactory, though a larger dispersion can be observed, related to the high turbulence level exceeding 20 % in this developed flow area.

Due to the fact that there is no azimuthal component of mean velocity in the jet, it is very easy to check the accuracy of the measured mean values of the 3D mean angle $\beta$ : they must be exactly equal to the values of $\psi$. On figure 8, one observes measured uncertainties on $\beta$ mean values, for different angles $\psi$, in the potential core of the jet where the turbulent level has a constant value of 1.75 %. Those uncertainties stay below 2.2 deg for $\overline{\alpha}_1$ and $\overline{\alpha}_2$ uncertainties about 0.5 deg, which shows a smaller factor between $\Delta\overline{\alpha}_1$ (or $\Delta\overline{\alpha}_2$) and $\Delta\overline{\beta}$ than in the theoretical example of the paragraph 3.2. The observed results corroborate the fact that the higher the angle ß, the smaller the uncertainties on the mean value of ß. On figure 9, for a $\psi$ angle of 30 deg, a drastic increase of the $\overline{\beta}$ uncertainties together with the turbulence level can be observed. However, they remain below 4 deg, for fluctuations below 20 % of the mean velocity.

Measurements in axisymmetrical free jet lead to conclude that in three-dimensional flow fields, with turbulence level up to 20 %, the accuracy reached for mean and fluctuating velocities, calculated with the statistical formulation developed in paragraph 4, seem to be quite good.

But, this study do not really take care of the measurement problems encountered in turbomachinery. Consequently, we propose, in the following part, to analyse measurements carried out in an high-loaded low-speed compressor in order to calibrate the developed statistical analysis in a real configuration.

## 6. MEASUREMENT IN A HIGH-LOADED LOW-SPEED COMPRESSOR ROTOR

The strong influence of secondary flows on turbomachines performances is well known, so that the understanding of the local flow behaviour remains essential to improve 3D-viscous numerical codes used for design procedure. In particular, the tip clearance effect is detrimental for efficiency and stability in axial flow compressors and could generate up to 23 % of total losses for Trébinjac [10] in a supersonic axial compressor and up to 40 % for Bindon [11] in a turbine cascade. However, the purpose of this section is not to develop a detailed analysis of the three-dimensional flow field in a high-loaded compressor, but to show that 3D-L2F anemometry is an efficient technique to study and analyse complex flow configurations in rotating environment. In this context, we have decided to carry out measurements in the tip region at 50 % chord, where we expected the presence of a leakage vortex.

### 6. 1. Experimental set-up

The investigated axial compressor is powered by a 17 kW electric motor at 1500 rpm. It consists of a 12 blade rotor with a 316 mm tip diameter and a 196 mm hub one. The blade profiles are NACA 65 series with 9% chord thickness distributed on a circular mean line. The chord varies from 166.7 mm at the hub to 151.5 mm at the tip. The tip clearance represents 1.1 % of the blade height, which means 1.3 mm. The nominal flow rate is 6.2 kg/s. However, the compressor is operated at a lower flow rate of 5.5 kg/s, which corresponds to a higher blade loading supposed to generate wider secondary flows and interactions between them (Nurzia, Puddu [12]). The flow in the blade row is measured at 50 % chord for various positions versus the blade height - 84 %, 86 %, 90 %, 91.7 %, 93.3 %, 95 %, 97.6 % and 98 % - in order to intercept the leakage vortex. The blade pitch was split in 10 variable width intervals using the procedure developed for two-dimensional measurements (Trebinjac & Vouillarmet [13]). At each interval, about 500 data were collected. The radial velocity (Vr) is considered positive from the tip to the hub and the azimuthal one in the rotating direction. Vz is the axial component of the velocity. The inlet Mach number and the Reynolds number are respectively 0.08 and 5 $10^5$.

Optical access is obtained through a plane window. A seeding probe is located about two chords lengths upstream from the leading edge, which is far enough to avoid any probe wake effect in the measurement zone.

### 6. 2. Background theory for the study of tip leakage flow in an axial compressor

Through the clearance existing between the tip of the blade and the shroud, a flow can take place because of the pressure gradient between the pressure side and the suction side. Two different kinds of flow field configurations may occur. The first one is common in compressor with sharp blades : the clearance flow separates from the blade tip and does not reattach over the main part of the chord generating a distinct jet of low loss fluid at the exit of the gap (Storer & al. [14]). The second one is more typical of the turbine blades, but could also be encountered in compressor (with thick blades). For those kinds of blades, the clearance flow reattaches, generating much more losses due to the mixing phenomena in the reattachment area inside the gap. Kang and Hirsch [] have given a complete description of the multiple tip vortex structure occuring for this configuration in a compressor cascade. Denton [15] has proposed a criterion : this second configuration happens only if the ratio between the blade thickness (e) and the clearance ($\tau$) stays above 4. Perrin [16] has analysed the two different configurations, and has also shown that a leakage vortex constituted of fluid particles coming from the viscous zones is associated to the clearance flow. Storer & al. [14] have put the stress on the fact that, for axial compressors, this leakage vortex is emitted around the minimum static pressure location on the suction side, which should be located before 50 % chord in our blade row. From its emission position to the trailing edge, the leakage vortex is transported from the suction side to the pressure side. However, most of the studies in which those phenomena are presented have been carried out in blade cascade so that the blade skewing and the real influence of the relative motion of the shroud with regard to the blade were not taken into account. This relative motion is supposed, first, to make the leakage vortex to be generated nearer to the leading edge. Second, it induces its trajectory to sweep from the suction side to the pressure side of the following blade. Lastly, it increases the flow rate throughout the gap so that the vortex becomes stronger.

### 6. 3. Results

All the results are presented on figures 10 to 13, versus the blade height and the azimuthal direction. The flow field is described from the suction side (0 % of the pitch) to the pressure side (90 % of the pitch), and from 84 % to 98 % of blade height (100 % corresponds to the blade tip) which is the limit until measurements become impossible close to the window. Because measurement times are longer in the shroud boundary layer, especially for 98 % of blade height, the window becomes dirty during the acquisition process. This caused the angular histograms to become rather flat in strong turbulence areas, so that it is prejudicial for the estimation of the $\alpha_1$ and $\alpha_2$ mean values (uncertainties up to 7 deg). This effect induced inaceptable ß uncertainties of about 53 deg. Consequently, in the following, the radial velocity will only be presented up to 96.7 % (figure 13).

From 84 % to 90 % of blade height, the axial velocity demonstrates an azimuthal gradient from the suction side to the pressure side (see figure 10). In the vicinity of the shroud from 92 % to 98 % of blade height, a low flow rate area appears, centered at 33 % of the pitch from the suction side and stretched from 15 % to 60 % of the pitch. It corresponds to a zone of maximum azimuthal velocity (see figure 11). Thus, in this area, the flow direction changes as much as 30 deg from the direction of the mean flow. Futhermore, we observe on figure 12 that a high level of turbulent kinetic energy is also present in this area which could be identified as the core of the tip leakage vortex. Indeed, this high turbulence level is characteristic of viscous zones, like suction side, pressure side and shroud boundary layers, from which the tip vortex fluid particles are coming. The 3D-anemometer allowed us to associate this zone with radial velocities, located close to the shroud, and which values reach 20 % of the blade velocity at the tip (see figure 13). That figure exhibits, near the shroud and from the suction side to 50 % of the pitch, a first kind of radial flow directed toward the shroud. This should correspond to fluid particles coming from the suction side boundary layer which are dragged by the jet at the exit of the gap. At about 95 % and down to 93 % of blade heigh, the direction of the radial flow changes, so that it is directed toward the hub. Those radial velocities confirm the presence of the tip leakage vortex at that location. Its center is located at about 33 % of the pitch from the suction side, and its radius is much larger in the azimuthal direction (from 15 % to 55 % of the pitch), than in the radial one (it lies above 93 % of blade height i.e. 6 times the clearance below the tip of the blade). This last observation disagrees with the common circular model for the tip leakage vortex.

On the pressure side, measurements are not close enough to the blade surface to corroborate the presence of small negative radial velocities, demonstrating the fluid motion toward the blade tip at the gap inlet. In the rest of the flow, no radial velocity can be observed so that any interaction between the tip leakage vortex and the passage vortex could not be detected by the 3D-L2F device in this section.

## 7. CONCLUSION

This study has focused on the data processing for 3D-L2F anemometry. It has shown that this measuring technique produces a lot of information losses due to the non-simultaneous measurement of the three velocity components. However, a statistical calculation method to restore the mean and the fluctuating flow fields has been developed assuming a velocity components independence model. Moreover, the measurement of $\sigma_\beta$ remains impossible, so that an additional relation should be found for $\sigma_\beta$ in order to estimate $\sigma_V$ and $\sigma_\alpha$. This statistical method has been tested in an axisymmetrical free jet. The obtained results agree with the fact that uncertainties for the 3D-angle ß could increase drastically for small value of ß (below 10 deg), and for high turbulence level (toward 20 %). It shows that the accuracy of the results, especially for the

on--axis velocity component, should be carefully established before to be taken into account.
In the compressor, radial velocities are detected by the 3D-L2F anemometer, which indicates a leakage vortex. Moreover, an intense shearing associated with a high turbulent kinetic energy level at the tip area was demonstrated.
We can conclude by saying that the three dimensional acquisition procedure used for this study has shown its ability for measuring the three dimensional flow field within a high-loaded compressor rotor, even in large local gradients area and close to the end walls.

**REFERENCES**


[1] R. Schodl, "Laser Two Focus Velocimetry", AGARD CP 399, Paper 7, 1986.

[2] R. Schodl & W. Forster, "Design and Experimental Verification of the 3D Velocimeters Based on the L2F Technique", 5th Int. Symp. on Appl. of Laser Anemometry to Fluid Mechanics, Lisbonne, Portugal, 1990.

[3] Maass, Forster & Thiele, "Unsteady Flow Experiments in the Exit of a Ducted Propfan Rotor", 30th AIAA/ASME/SAE/ASEE Joint Propulsion Conference, Indianapolis, Indiana, 1994.

[4] C. J. Chesnakas & P. L. Simpson, "Full 3D Measurements of the Cross Flow Separation Region of 6:1 Prolate Spheroid", Experiment in Fluids, vol. 17, pp 68-74, 1994.

[5] P. K. Snyder & K. L. Orloff, "Reduction of the Flow Measurement Uncertainties in Laser Velocimeter with Non-Orthogonal Channels", AIAA Journal, Vol. 22, Nb 8, August 1994.

[6] R. C. Stauter, "Measurement of the Three Dimensional Tip Region Flow Field in an Axial Compressor", ASME-JT, vol. 115, pp 468-477, July 1993.

[7] I.Wygnanski & H.Fiedler, "Some Measurements in the Self-Preserving Jet", J.F.M., vol 38, pp 577- 612, 1969.

[8] R. Schodl & W. Forster, "A New Multi-Colour Laser Two Focus Velocimeter for Three-dimensional Flow Analysis", ICIASF Record, pp 142-151, 1989.

[9] I.Trebinjac & A.Vouillarmet, "A Laser Anemometry Technique for Measurements in a Single Stage Supersonic Compressor", Proceedings of the 9th Symposium on "Measuring Techniques for Transonic and Supersonic Flows in Cascades and Turbomachines", pp.10.1-10.27, Oxford, March 1988.

[10] I.Trebinjac, A.Vouillarmet, G. Perrin, "A Contribution to the Understanding of the Flow Field in a Supersonic Compressor", 2 ISIAF, International Symposium on Experimental and Computational Aerothermodynamics in Internal Flows,.Prague, 1993.

[11] J.P. Bindon "The measurement and Formation of Tip Clearance Loss" ASME paper 88-GT-203, Amsterdam, 1988.

[12] F. Nurzia, P. Puddu, "Experimental Investigation of Secondary Flows in Low Hub-Tip Ratio Fan", ASME paper, 94-GT-377, The Hague, 1994.

[13] I.Trebinjac & A.Vouillarmet, "Laser Two-Focus Anemometry Investigation of the Flow Field within a Supersonic Axial Compressor Rotor", ASME paper 90-GT-298, Brussels 1990.

[14] J. A. Storer, N. A.Cumpsty, "Tip Leakage Flow in Axial Compressors", ASME J. of Turbomachinery, vol. 113, pp 252 - 259, April 1991.

[15] J.D. Denton, "Loss Mechanisms in Turbomachines", ASME paper,93-GT-435, Cincinnati, 1993.

[16] G. Perrin, "Experimentation Numérique Tridimensionnelle en Vue de la Modélisation et du Calcul des Ecoulements Secondaires dans les Turbomachines" Thèse Ecole Centrale de Lyon, 1994.

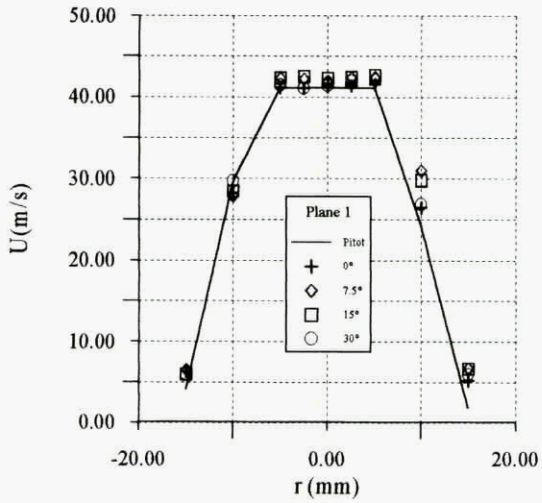


**Figure 4 a** : Longitudinal velocity for plane 1

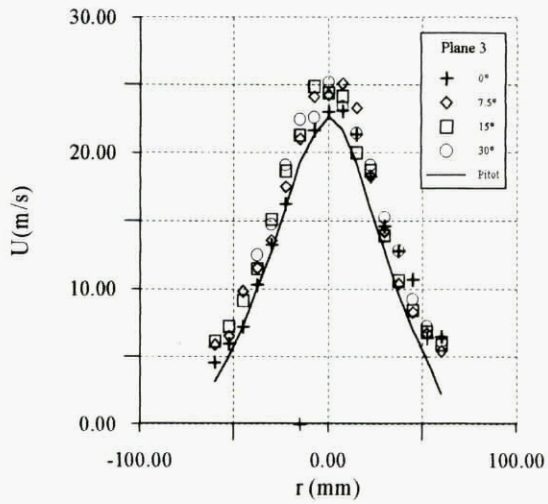


**Figure 4 b** : Longitudinal velocity for plane 3

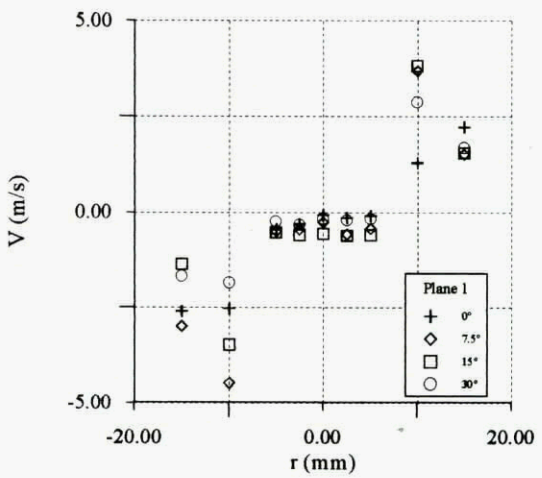


**Figure 5 a** : Radial velocity for plane 1

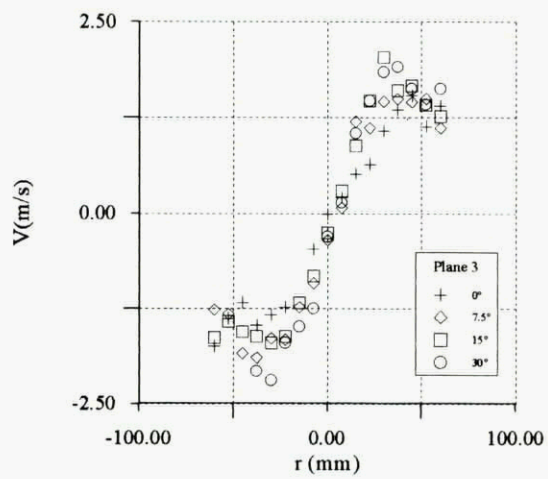


**Figure 5 b** : Radial velocity for plane 3

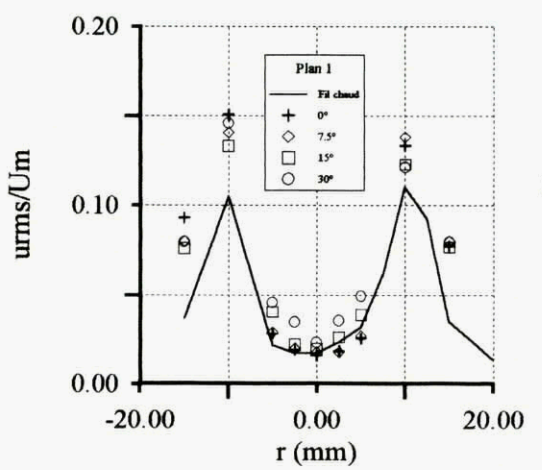


**Figure 6 a** : Longitudinal fluctuation for plane 1

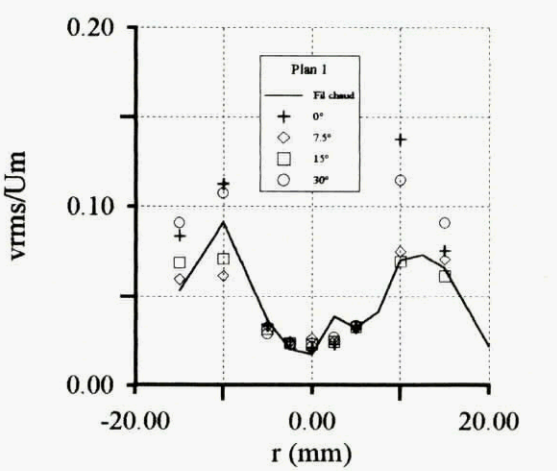


**Figure 6 b** : Radial velocity for plane 1

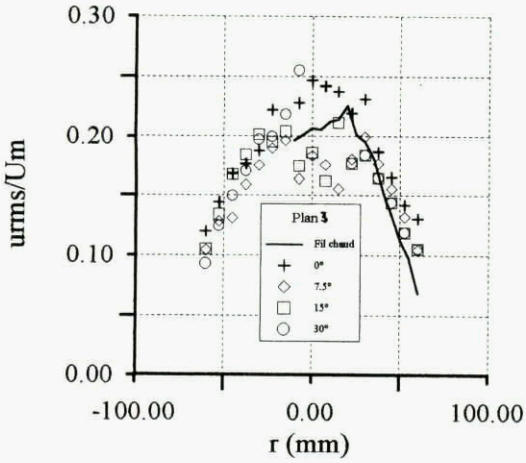


**Figure 7 a** : Longitudinal fluctuation for plane 3

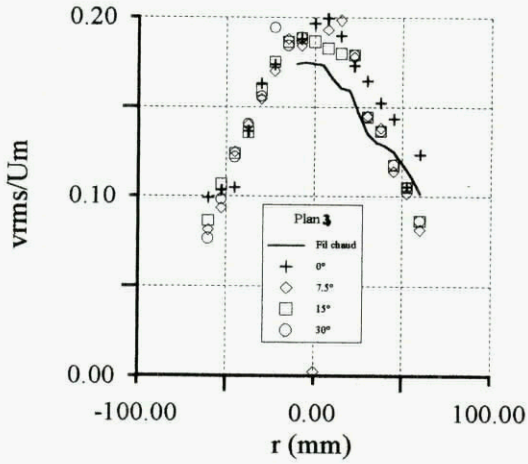


**Figure 7 b** : Radial velocity for plane 3

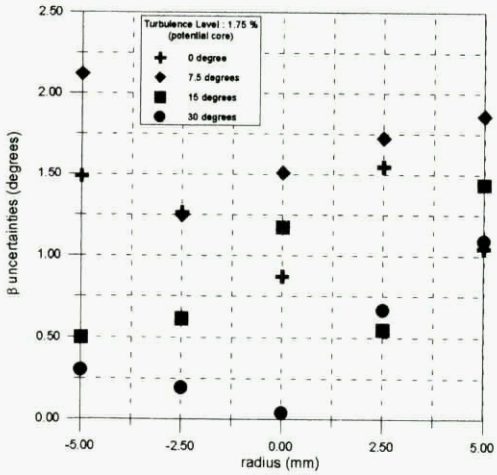


**Figure 8** : β uncertainties versus β

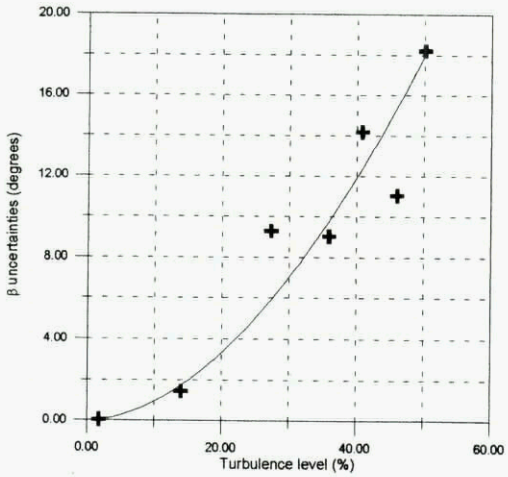


**Figure 9** : β uncertainties versus the turbulence level

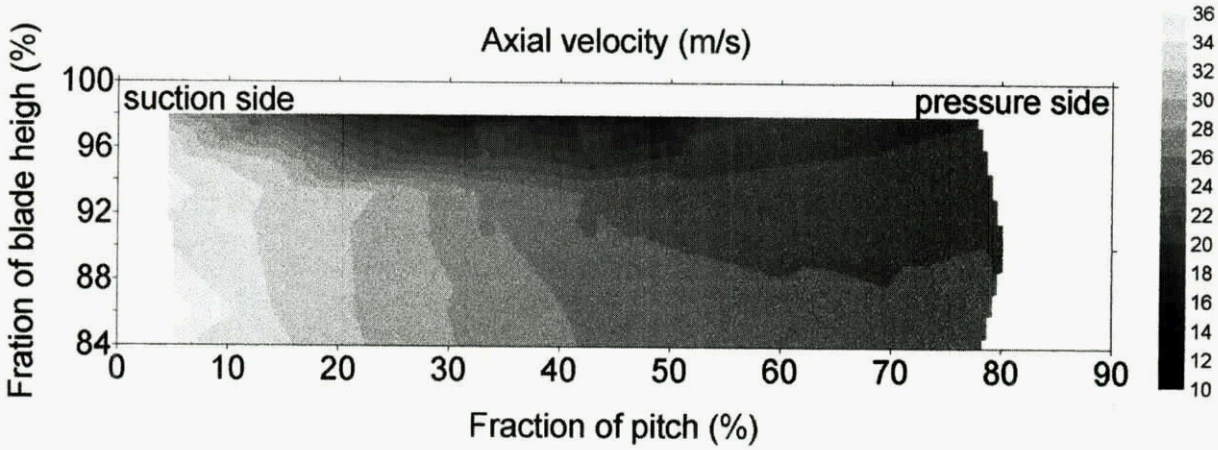


**Figure 10** : Axial velocity at the tip for 50 % chord

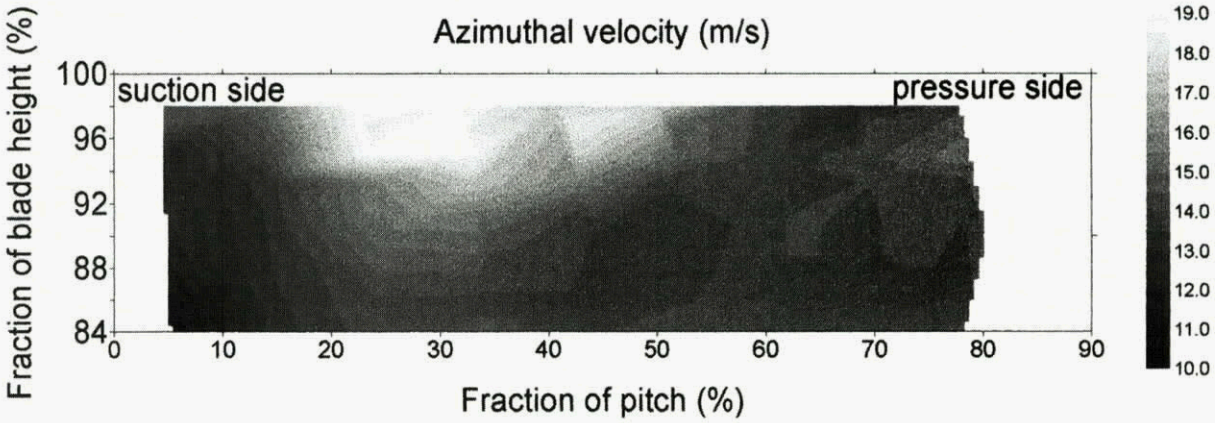


**Figure 11** : Azimuthal velocity at the tip for 50 % chord

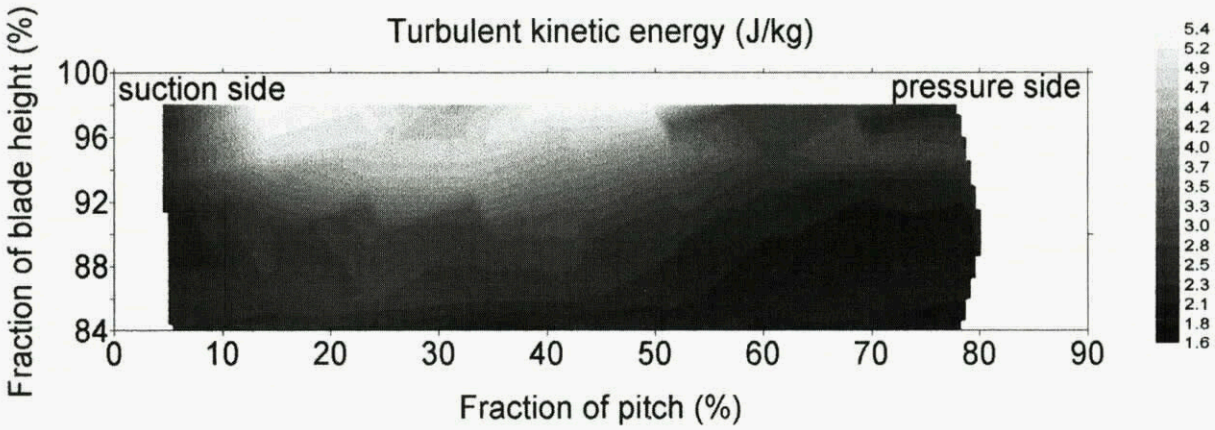


**Figure 12** : Turbulent kinetic energy at the tip for 50 % chord

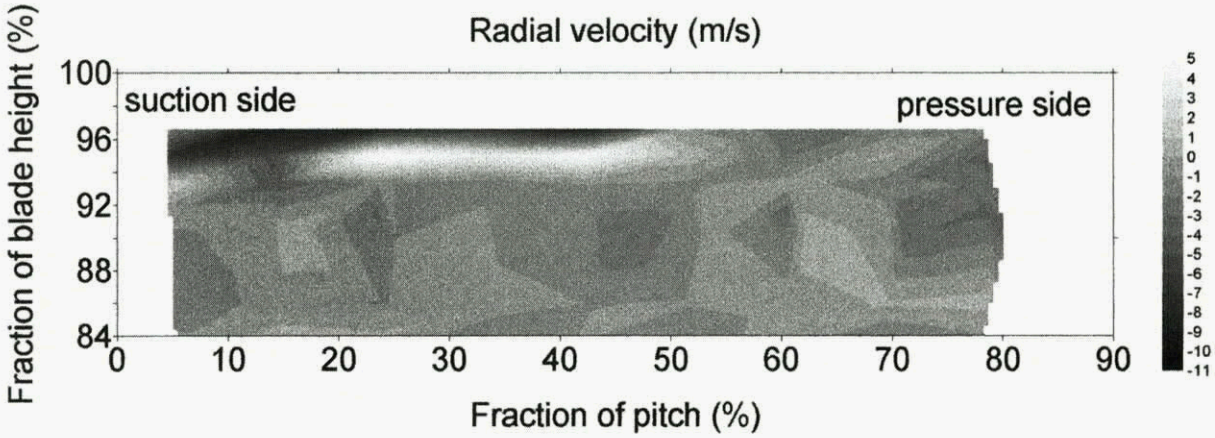


**Figure 13** : Radial velocity at the tip for 50 % chord

# Non-Intrusive Measurement Technique For Propulsion Engines

**M.F. Mulligan and J.D. MacLeod**
National Research Council of Canada - ICPET
Institute for Aerospace Research
Combustion Research Group, Bldg. M-9
Ottawa, Ontario, K1A 0R6, Canada

## 1. SUMMARY
With financial contributions from the Canadian Department of National Defence, the Structures, Materials and Propulsion Laboratory of the National Research Council of Canada (NRC) established a program for evaluating the effects of component deterioration on gas turbine engine performance. The effort was aimed at investigating the performance changes resulting from typical in-service faults. An important aspect of the engine test program was the use of non-intrusive sensors to supplement conventional instrumentation.

Combined gas and metal thermal patterns in the infrared radiation spectra, recorded using infrared thermography, were used to evaluate gas path patterns to identify possible fault conditions. Exhaust plane thermal patterns can be classified as "healthy" for no-fault conditions, and "distressed" where known faults are in existence. Several defective engine components, including fuel nozzles, combustor cans, turbine nozzles, and thermocouple probes were used to evaluate the effectiveness of this technique on an engine test bed.

This paper covers the project objectives, the experimental installation, and the results of the tests. Descriptions of the infrared thermography system, the data reduction and analysis methodology are also included.

## 2. INTRODUCTION
Traditional engine performance monitoring techniques have relied on the measurement of specific gas path parameters (MacLeod, et al., 1992). These measurements, typically temperature and pressure, are gathered from within a gas turbine using conventional methods such as thermocouples and pitot rakes. In some cases, these probes require cooling shrouds to provide protection from the harsh environments within a gas turbine. These relatively large probes can disrupt the flow field in the vicinity of the probe and thus interfere with the true measurement. This interference cannot be readily accounted for and is carried as some unknown bias in the data.

Most gas turbine engines use single point thermocouple probes for making temperature measurements that are used to control the engine. In some locations within the engine as many as 18 thermocouples are used to measure an average temperature. As a result of non-uniform temperature distributions, some thermocouples may be subjected to hot or cold regions, resulting in a measurement bias. In addition, changes in the temperature patterns resulting from component deterioration upstream could easily go undetected by the engine operator. These changes in temperature patterns can have serious effects on the rate of damage accumulation of the turbine components, resulting in higher overhaul costs due to increased parts replacement.

An infrared thermography system, which is capable of making thousands of measurements simultaneously and unobtrusively, can be utilized to completely map the thermal patterns in the exhaust plane. If the thermal pattern present in the exhaust plane is analogous to a fingerprint, i.e. unique to each engine, then a change in the "healthy" pattern would indicate to the observer that a change in the condition of the hot section of that engine had occurred. The ability to detect this change unobtrusively at an early stage in its development is the goal of this infrared diagnostic tool.

## 3. BACKGROUND
Infrared thermography has been in existence for more than 25 years (Gartenburg and Roberts, 1992). It is only in the last several years that research into the use of infrared technology for gas turbine applications has been carried out. Up to this point in time, the gas turbine applications have focussed on external casing temperature measurements (Burns, 1994, and Mahulikar, 1992) and plume observability detection (Balageas, 1992, and Breugelmans, 1993, 1994). Previous experience in the development of an infrared diagnostic system has been described by MacLeod et al., 1994 and by Mulligan et al., 1996.

Analysis of both metal and gas thermal spectra are considered important. Metal and gas thermal spectra can be separated by using infrared filters to obtain the individual components. However, for this investigation only images representing combined spectra were evaluated.

## 4. EXPERIMENTAL INSTALLATION
To assess the capabilities of an infrared imaging system to measure thermal patterns in the exhaust of a gas turbine engine a unique test setup with specialized instrumentation was required. The following description of the engine and instrumentation illustrates the installation for this project.

### 4.1 Engine Description
The test vehicle for this project was an Allison T56-A14LFE single spool turboprop engine from a CP-140 Aurora patrol aircraft. This engine was an excellent candidate for this study because it has no variable geometry or transient bleed valve operation that might affect the repeatability of the operation of the engine. The T56 engine has a fourteen-stage compressor, a six can-annular combustor and a four-stage turbine. A schematic diagram of the NRC test configuration is shown in Figure 1.

### 4.2 Infrared Instrumentation
The infrared imaging system selected for this project was the Hughes Model 7300 Thermal Video System consisting of an imager, an image processor, a power supply and a monitor. The imager converts infrared radiation into electronic signals which are interpreted by the image processor and displayed on the monitor.

*Paper presented at an AGARD PEP Symposium on "Advanced Non-Intrusive Instrumentation for Propulsion Engines", held in Brussels, Belgium, 20-24 October 1997, and published in CP-598.*

For the experiment, the imager was fitted with a telescopic lens and located approximately 6 metres downstream of the exhaust duct of the engine behind the exhaust augmentor tube (Figure 1). The camera, focussed at the exit plane of the turbine, was protected from the hot exhaust gases by a silicon window located in the elbow section of the augmentor tube. The silicon window has a uniform absorption loss of approximately 1% in the 2-5 micron infrared band.

Images created by the Thermal Video System were recorded by a SVHS video recorder and played back at a later time for analysis. An IBM compatible computer provided the platform for developing software required for analysing thermal images. Frame grabber boards within the computer were used for digitizing live or taped video images. The complete component configuration is shown in Figure 2.

### 4.3 Image Analysis Software

Software packages were written for acquiring, linearizing, smoothing, adjusting image brightness, producing statistical information and analysing infrared images. Images were digitized and then linearized before applying image smoothing and brightness adjustment techniques. Image smoothing was done to enhance the quality of the recorded images, while a brightness adjustment routine was used to correct for differences in the overall intensity of an image. The digital data were then processed through a routine designed to detect differences between images.

The analysis was done by comparing images and detecting changes in the thermal pattern of an image relative to a reference. It was found that visual comparisons could not be done, as minute differences in thermal patterns were extremely difficult to detect by eye. As a result, software was developed to perform the comparisons on a pixel by pixel basis. Those pixels of the test image that exceeded the specified tolerance of two standard deviations were flagged to indicate a change in the thermal pattern.

### 4.4 Operational Considerations

Generally, an infrared camera is used to obtain a temperature profile of an object. As the camera can only measure infrared radiation, an emissivity value is required to obtain temperatures. To obtain or estimate an emissivity value may be simple or, in some cases, very difficult as emissivity is a function of the surface condition of an object which may change dramatically under certain conditions. The angle of incidence also affects the measured value of emissivity and therefore curved surfaces are potentially problematic.

For this investigation, the thermal energy pattern was of primary importance with secondary interest in the measurement of temperature.

## 5. DESCRIPTION OF FAULTS

This section will describe the faults that were investigated during the test program. The engine components selected for the tests were fuel nozzles, combustor cans, turbine inlet thermocouples and turbine inlet guide vanes.

### 5.1 Fuel Nozzles

Fuel nozzles (Figure 3) have been identified as high maintenance components that can promote damage to other engine hardware. Fuel nozzle faults are most often caused by the formation of deposits on the end of the nozzle resulting in a "fouling" or "coking" condition. The deposits affect the fuel spray pattern and on the T56, result either in a "streaking" or "fanning" condition within the combustor of the engine. Nozzles that are categorized as "streaking" contain heavy concentrations of fuel within their spray pattern, whereas, "fanning" types exhibit a more uniform pattern but exceed the manufacturer's spray angle specification of 110°. These improper spray patterns can cause rapid deterioration of the combustor, turbine thermocouples and turbine inlet guide vanes. As malfunctioning fuel nozzles can have a significant impact on hot section life, tests were carried out to investigate this fault.

Baseline tests were performed using a low time (<200 hrs) set of overhauled fuel nozzles. The engine was operated at three power settings covering turbine inlet temperatures of 735, 875 and 1010 degrees Celsius. Several test runs were performed for each engine configuration under varying ambient conditions. For the faulted tests "fanning" or "streaking" nozzles were installed in the combustor at specific locations. Images and performance data were recorded for each configuration and at each power setting.

### 5.2 Combustor Cans

An increase in the combustor temperature can cause significant damage to the combustor liner (Figure 4). These higher temperatures can not only cause a burn-through condition, but can also cause significant deformation in the combustor can. This deformation can redirect the flow which may then cause severe damage to the turbine inlet guide vanes and alter engine performance.

For reference purposes, the location of each combustor is described by its circumferential position as viewed from the rear of the engine. The combustor located at the top of the engine is referred to as combustor can 1. All other combustors, which are positioned every 60°, are referenced clockwise to combustor can 1 (i.e. combustor can 2 is located 60° clockwise from combustor can 1).

For this experiment, two combustion liners, deformed near the outlet (indicated by dashed line in Figure 4), were installed in the engine at the 0° and 120° location (there are a total of six liners). The engine was operated at corrected turbine inlet temperatures of 735, 875 and 1010° Celsius. Thermal profiles were obtained at each power setting.

### 5.3 Turbine Inlet Guide Vanes

The turbine inlet guide vanes (Figure 5) direct the hot gases from the combustor into the first stage of the turbine. These hot gases promote wear to the vanes and in some cases cause the vanes to crack and even disintegrate. Damaged vanes disrupt the flow entering the turbine producing large spatial temperature variations. These temperature variations result in performance changes in the turbine downstream of the damaged vane. For the tests, a new set of vanes was installed into the engine. Before the installation, the vanes were grouped in sets so that the total vane flow area downstream of the combustor was balanced with their neighbouring sets. Following the installation, tests were performed to obtain thermal profiles downstream of the turbine. To investigate the effect of a damaged vane component, a set of

faulty turbine inlet vanes was installed in the engine at the 120° location. Tests were repeated to obtain thermal profiles of the turbine exhaust.

### 5.4 Turbine Inlet Thermocouples

The T56 engine is equipped with 18 thermocouple probes (Figure 6) for measuring the temperature of the gas at the outlet of the combustor. Each probe contains two thermocouples, one which is parallelled with each of the other 17 probes and used to control the engine, and a second which is parallelled to provide an indication of the turbine inlet temperature on a cockpit indicator.

Immersion of the thermocouples into the hostile environment downstream of the combustor results in a high failure rate of thermocouple probes. Failed thermocouple probes upset the control of the engine which can cause the engine to operate off-design and promote hot end component damage. In addition, faulty thermocouples can produce erroneous temperature indications on the cockpit indicator.

To simulate a shorted thermocouple within the engine control system harness, the probes located in the combustors at 0° and 120° were connected to ground through a set of manual switches. The switches were also employed to simulate an open thermocouple condition.

## 6. TEST RESULTS

The test results are based upon comparisons done with serviceable and faulty components. The components include fanning and streaking fuel nozzles, collapsed combustor can liners, damaged turbine inlet guide vanes, and open and shorted thermocouple probes. Correlations between the thermal images and the turbine inlet temperature thermocouples are also discussed.

For the analysis, a '1' in the bargraph figures represents a successful detection while a '-1' represents a failure to detect the fault. In all bargraphs, the IR results are represented by the red bars, whereas the results obtained with the TIT probes are indicated by green bars.

Some of the figures (e.g. Figure 7) contain temperature scales in the form of bargraphs which are used to indicate an approximate temperature change. The blue portion of the bargraph is used to indicate cooler areas, whereas, the red portion indicates hotter areas. The white portion of the bargraph, labelled as normal, indicates areas of no change. Those areas within an image where changes have been identified are circled in green.

### 6.1 Fanning Fuel Nozzle Fault

Baseline engine tests were done with serviceable fuel nozzles obtained from the engine overhaul contractor. A serviceable fuel nozzle, with an included spray angle of 106°, was installed into combustor can 3 located at 120°. The engine was operated at a turbine inlet temperature of 735, 875 and 1010° Celsius at a corrected turbine speed of 13820 RPM. Images downstream of the turbine were recorded at each power level. The fuel nozzle with an included spray angle of 106° was replaced with another serviceable nozzle that exhibited a spray angle of 109° and the tests repeated. Further tests were done using an unserviceable fuel nozzle (fanning) with a spray angle of 119°. Upon completion, the images were then passed through analysis software to determine image differences. It was found that the 109° and the 119° nozzles produced a cold spot (blue area) appearing in the image (Figure 7) downstream of the combustor containing the fault. As shown in Figure 8, the infrared method was successful in detecting a cold spot in 3 out of 6 test conditions, whereas the TIT probes failed to detect any change for all test conditions.

### 6.2 Streaking Fuel Nozzle Fault

To further investigate the nozzle fault tests, additional tests were completed with nozzles that exhibited a "streaking" flow pattern condition. A "streaking" nozzle with a similar flow rate as the serviceable nozzle was installed into combustor can 3 located at 120°. The engine was operated at a corrected speed of 13820 RPM and at corrected turbine inlet temperatures of 752, 894 and 1024 degrees Celsius. The streaking nozzle was found to produce a hot spot in the thermal image (Figure 9).

As shown in Figure 10, the infrared method was successful in detecting hot spots in 11 out of 12 streaking nozzle test cases, while the TIT probes failed to detect any change in all cases. Those cases, in Figure 10, where a successful detection is indicated for the TIT probes are results for nozzles with higher fuel flow rates. These higher flow rate nozzles, which appear to be faulty, are serviceable units which fall within the upper end of the fuel flow specification for the nozzle. The higher flows are approximately 2.7% above the median of 446 $lb_m$/hr. Furthermore, Figure 10 shows that the infrared system failed to detect a change in only one case.

### 6.3 Combustor Fault

A complete set of serviceable fuel nozzles and combustor cans was installed in the engine and a set of baseline tests was completed. Following the baseline tests, combustor can 1, located at 0°, and can 4, located at 180°, were removed and replaced with two faulty units. It was found that combustor can 1 produced a cold spot with a hook shaped tail extending towards the tailcone downstream of the turbine (Figure 11). Unfortunately, the flow from combustor can 4 was cut off from the view of the camera. The infrared system was successful (Figure 12) in detecting a change in three out of the six test cases, whereas, the TIT probes failed to detect any change.

### 6.4 Turbine Inlet Guide Vane Fault

A new set of turbine inlet guide vanes (IGV) was installed in the engine and a set of baseline runs was completed. Following the tests, a set of six faulty nozzle vanes was installed downstream of combustor can 3 located at 120°. The results (Figure 13) show that neither the infrared system nor the TIT probes were capable of detecting the IGV fault in all test cases. This suggests that the change in the thermal pattern was within the sensitivity of both the IR and thermocouple measurement systems.

### 6.5 Turbine Inlet Thermocouple Fault

Turbine inlet thermocouple faults were simulated by shorting (grounding) or disconnecting (opening) the probes from the engine control thermocouple harness itself. However, the simulation produced an overall cooler or hotter image caused by an increase or decrease in fuel flow promoted by a change in the signal to the fuel control. As the current analysis software compensates for an overall change in image intensity, this fault was undetectable.

## 7. CONCLUSIONS

1) A method to diagnose the condition of hot section components, at a relatively early stage of deterioration, has been developed. The method has been used to successfully detect faulty fuel nozzles in 14 out of 18 cases and combustor faults in three out of six cases. Turbine and turbine inlet thermocouple faults were not detectable with the current equipment and methods.

2) Faulty fuel nozzles contribute to the deterioration of hot section components. Replacement of fuel nozzles with similar flow rates may reduce the variation in the thermal pattern in the hot section, thus extending the life of hot section components.

3) Fuel nozzles which exhibited a streaking fuel flow pattern were found to produce hot spots in a thermal image while those producing a fanning flow pattern were found to produce cold spots.

4) Collapsed combustor cans produced cold spots in a thermal image with a distinctive hook towards the centre of the image.

5) The IR system allowed the mapping of the entire thermal pattern at the exit of the turbine, while thermocouples provided single point measurements that may misrepresent the actual conditions.

## 8.0 REFERENCES

Balageas, D., et al. "Quantitative Infrared Thermography CARAT 92". Proceedings of the Eurotherm Seminar No. 27, July 7-9, 1992 in Chatenay-Malabry, France.

Breugelmans, F.A.E., editor. "Measurement Techniques". von Karman Institute for Fluid Dynamics, Lecture Series 1993-05, April 19-23, 1993.

Breugelmans, F.A.E., editor. "Non-Intrusive Measurement Techniques". von Karman Institute for Fluid Dynamics, Lecture Series 1993-09, February 7-11, 1994.

Burns, M. "Temperature Measurement Using Infrared Imaging Systems During Turbine Engine Altitude Testing", NASA TM 105871, NASA Lewis Research Center, February 1994.

Gartenburg, E. and Roberts, S. "Twenty-Five Years of Aerodynamic Research with Infrared Imaging", Journal of Aircraft, Vol. 29, No. 2, March-April, 1992.

MacLeod, J.D., et al. "Implanted Component Faults and Their Effects on Gas Turbine Engine Performance", ASME Journal of Engineering for Gas Turbines and Power, Vol. 114, April 1992.

MacLeod, J.D., et al. "Infrared Thermal Imaging as a Diagnostic Tool for Gas Turbine Engine Faults",ASME 94-GT-344, 1994.

Mahulikar, S. P. "Prediction of Engine Casing Temperature of Fighter Aircraft for Infrared Signature Studies", SAE 920961, 1992 SAE Aerospace Atlantic, Dayton, OH, April 7-10, 1992.

Mulligan, M.F., et al, "Investigation of the Measurement Capabilities of an Infrared Thermal Imaging System", LTR-ST-2033, National Research Council of Canada, 1996.

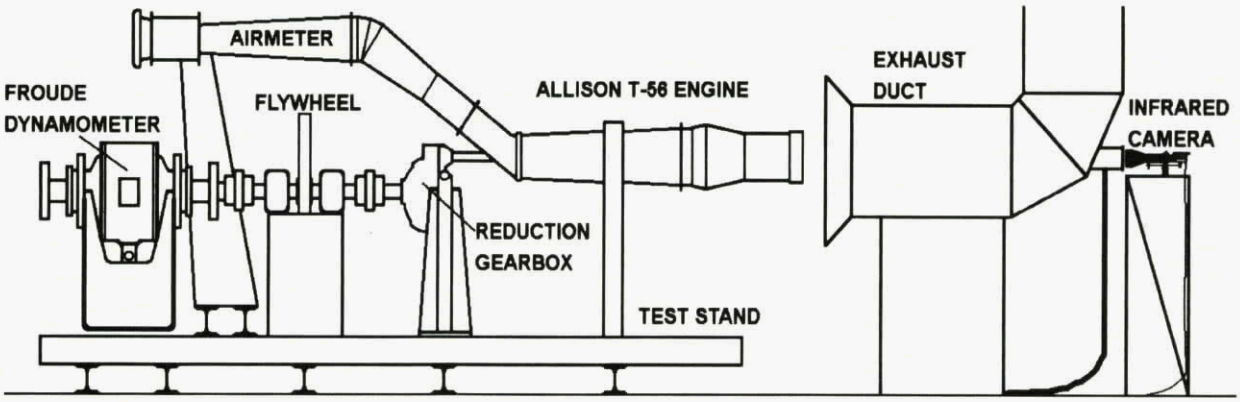


**Figure 1**. Engine/Imager Installation

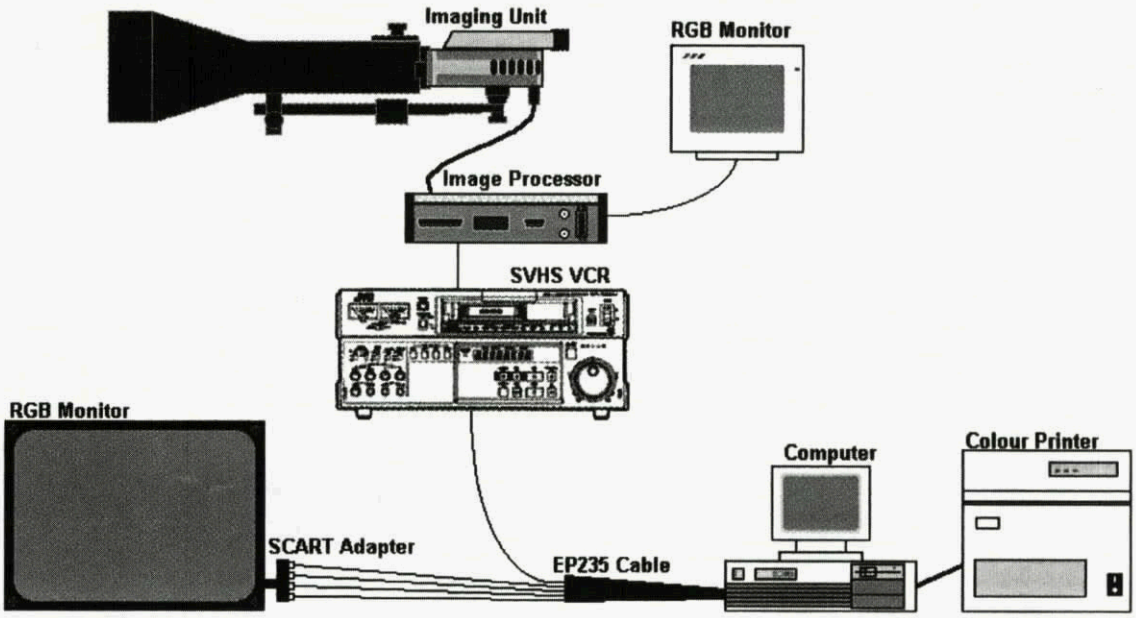

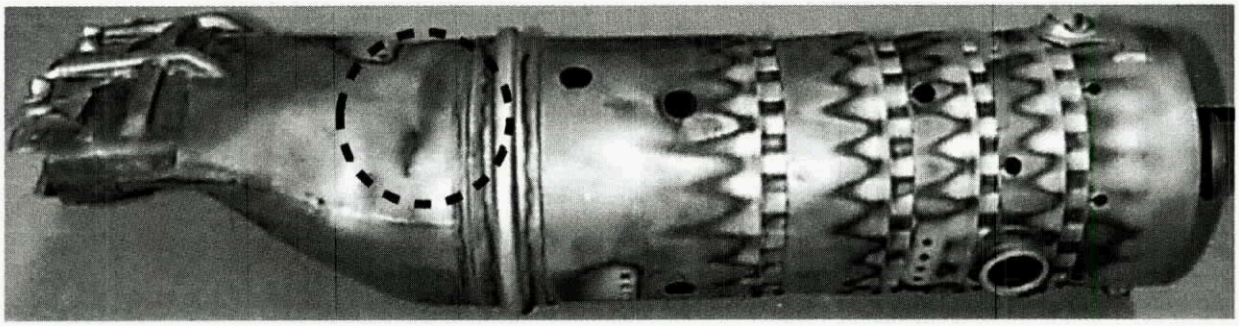

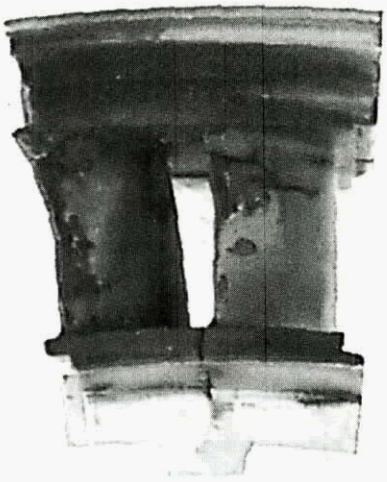

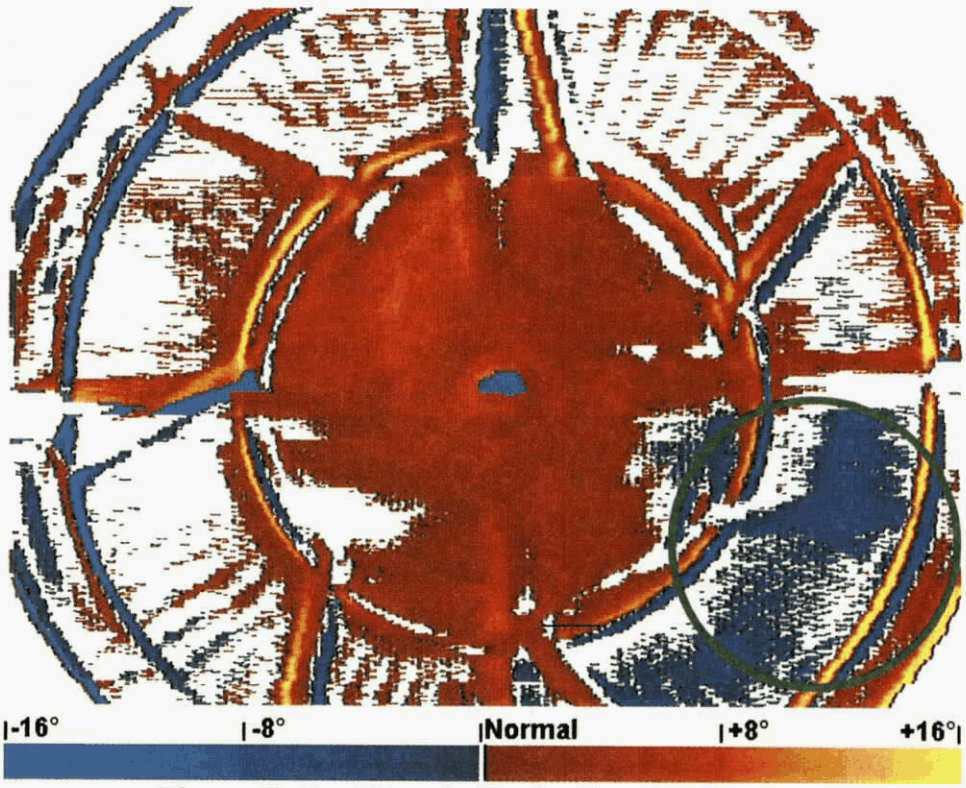


**Figure 7**. Fuel Nozzle Fault - Fanning Pattern

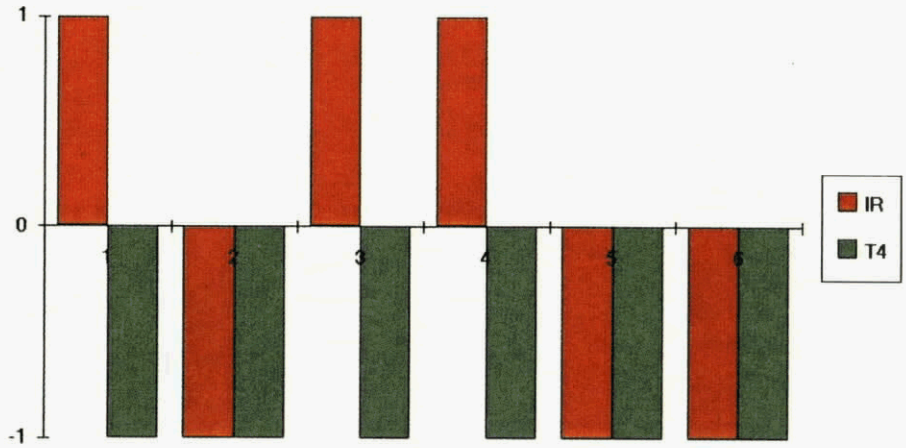


**Figure 8**. Fuel Nozzle Fault - Fanning Pattern

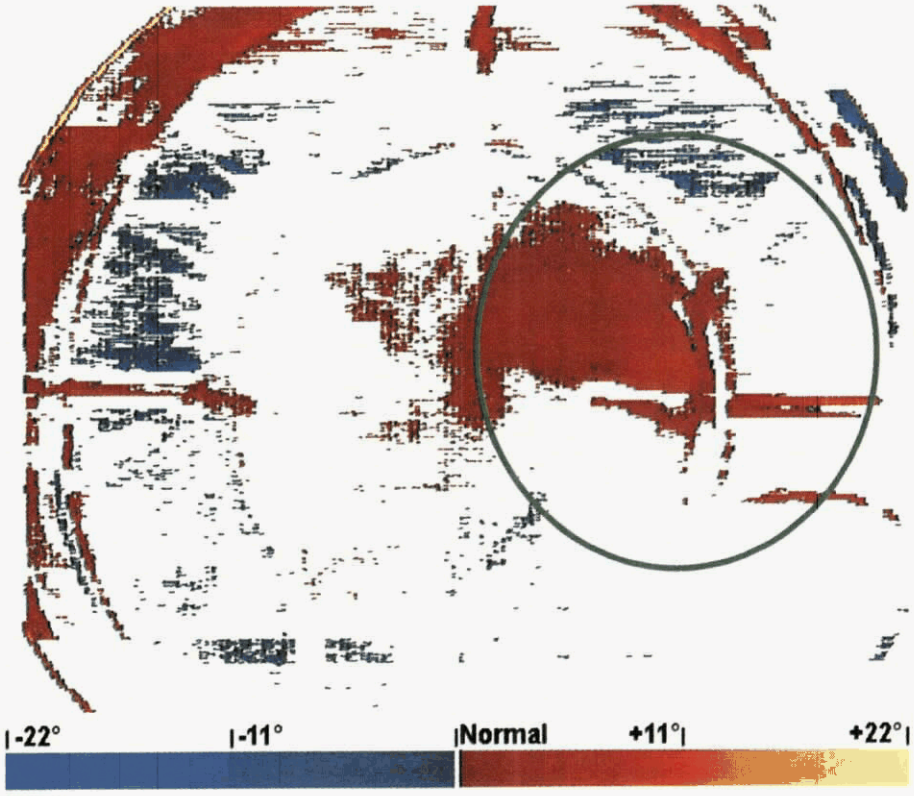


**Figure 9**. Fuel Nozzle Fault - Streaking pattern

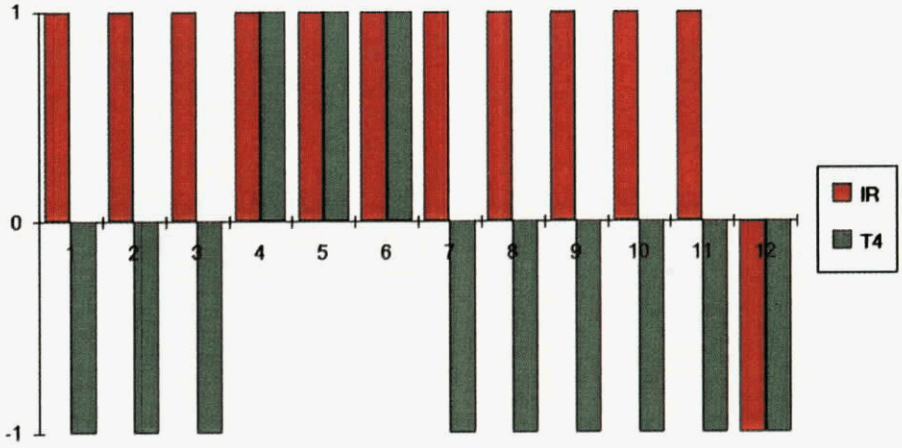


**Figure 10**. Fuel Nozzle Fault - Streaking Pattern

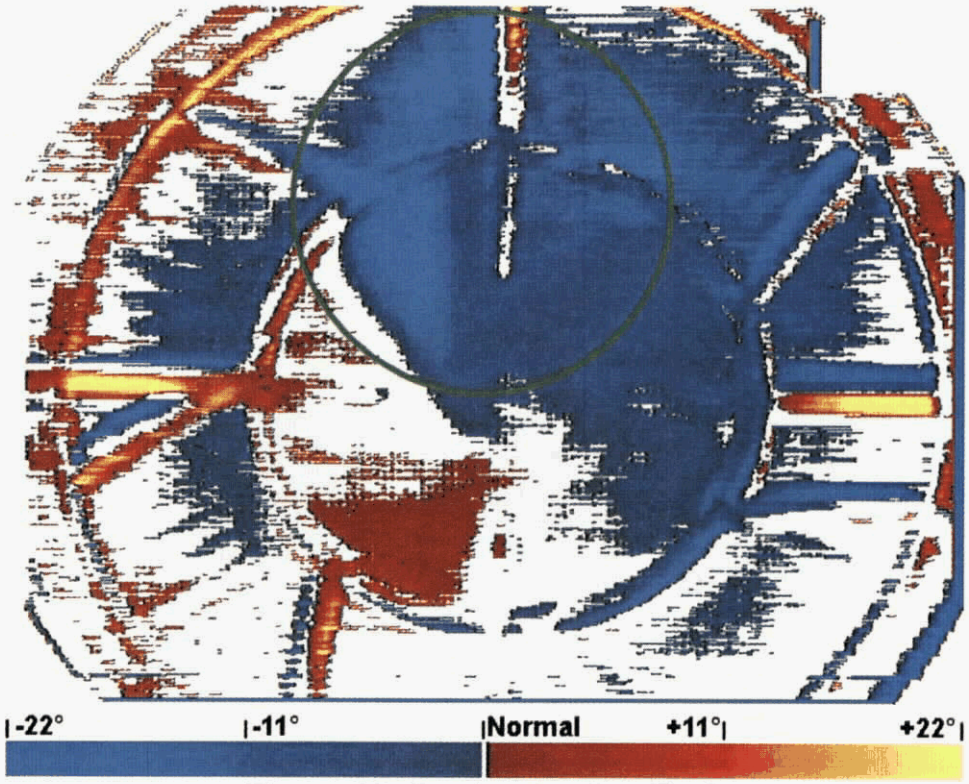


**Figure 11**. Combustion Can Fault

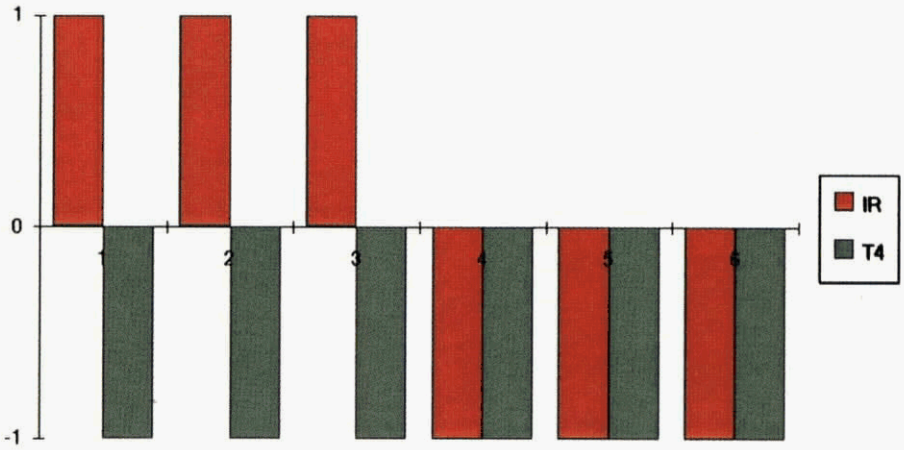


**Figure 12**. Combustion Can Fault

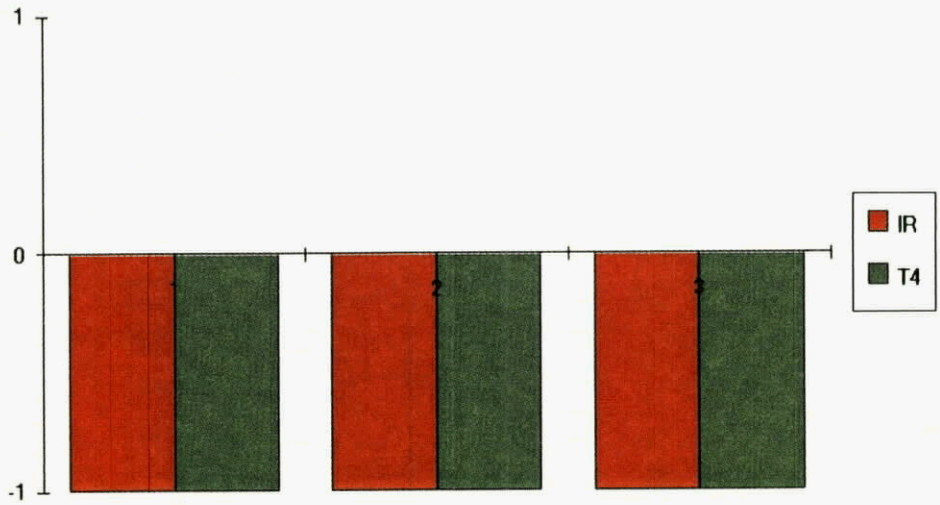


**Figure 13**. Turbine Inlet Guide Vane Fault

Paper 7
Author: M.F. Mulligan et al

Q: K. Benson

Are you going to deploy the system in the field?

A: Yes, currently there is one system installed at an engine overhaul centre gathering data

Q: A. Weigand

1) Did you encounter any problems with infrared emission of the exhaust plume?

2) In fig. 10, you also have detected the streak pattern with traditional equipment. Did that help in clarifying the reason for not observing the failure with IR in all cases?

A:
1) Emissions from the exhaust plume did not present any problems with respect to the results.

2) The success of detection of each system was treated individually. Moreover, it is anticipated that other techniques (traditional) could be used to complement the IR method.

Q: P. Kotsiopoulos

I observed that you have presented graphs referring to isolated healthy or distressed cases i.e. only nozzles or cans etc. Can you distinguish or quantify in the case of a combined fault i.e. a distressed pattern which resulted from the combined effect of a faulty nozzle and a faulty guide vane?

A: At this point only isolated faults have been studied. Future tests may be done to establish if combined faults can be detected.

Q: Lazalier

For combustors operating near stoichiometric conditions a "streaking" nozzle may drive the local fuel: air ratio above the stoichiometric value. In this case the "streaker" might produce a cooling effect. Two questions then arise:

1) how does one know if the "cold" spot resulted from a streaking nozzle operating above stoichiometric conditions compared to "fanning" nozzle below stoichiometric conditions?

2) how are absorption/radiation characteristics of the flow affected by the presence of unburned but perhaps cracked fuel?

A:
1) Currently there is no data to support an answer to this question.

2) In addition, there is no data available to support an answer to this question.

However, in a general sense, we are not really interested in what is causing the fault. What is important is the capability of the system in detecting the fault.

# Application of FTIR spectroscopy to measurement of gas turbine engine exhaust emissions

**M. Hilton, A.H. Lettington**
J.J. Thomson Physical Laboratory
University of Reading, Dept. of Physics
Whiteknights, P.O. Box 220
Reading RG6 6AF
United Kingdom

## 1. SUMMARY

Fourier Transform Infrared (FTIR) spectroscopy has been used to study the exhaust emissions from a static Rolls Royce Avon gas turbine engine. The thermal infrared emission from the hot exhaust gases was monitored non-intrusively from a distance of 5 meters using a high spectral resolution FTIR spectrometer fitted with a 16 cm aperture telescope.

The gas temperatures were determined by comparing the intensity of the measured saturated $CO_2$ emission band with the radiance of a black body radiation source at known temperatures. CO and $CO_2$ gas concentrations were determined by comparison with modelled spectra taking into account instrument effects.

The results were compared with earlier extractive gas analysis and non-intrusive measurements made on the same engine prior to its recent refurbishment. Improvements in the equipment used for non-intrusive measurements and in the analytical procedures have improved the sensitivity and the confidence with which such quantitative measurements may be made.

## 2. INTRODUCTION

There is considerable interest in non-intrusive techniques for monitoring propulsion engines. Advances in optical technology now permit the use of what used to be considered as laboratory based techniques in the hostile environment of gas turbine engine test beds and rigs. There are several advantages in using non-intrusive techniques for measuring exhaust emission from gas turbine engines.

The conventional extractive sampling gas analysis techniques in current use require expensive probe systems which must be traversed from point to point. Residual chemistry can occur in transporting the sample to the gas analysis equipment. Optical non intrusive techniques, which could provide real time multicomponent gas analysis, with the possibility of in flight continuous monitoring of pollutant levels, are attractive. FTIR spectroscopy is one of the techniques being studied for exhaust gas monitoring.

FTIR spectroscopic techniques have been used in a variety of configurations to study gases. Many atmospheric species have I.R. activity and can be monitored simultaneously and with high sensitivity. Extractive gas samples can be analyzed in an FTIR spectrometer using a long path cell(1). The cell contains mirrors to generate multiple reflections and increase the path length over which absorption can occur. This active technique probes the target gas with a beam of modulated I.R. radiation and then measures the spectral absorption. This technique can be adapted to non-intrusive investigations where the gas turbine exhaust plume is probed by an infrared beam which passes through it many times by reflection from opposing White cell mirrors on either side of the plume. Such a system is currently under investigation under the EU funded BRITE EURAM research project AEROJET to which our group at the University of Reading is contributing.

There are many applications where FTIR spectroscopic techniques have been useful in studying gases remotely rather than by obtaining samples. Industrial sites and landfill tips can be continuously monitored for gaseous pollutants using active long path systems (2-5). Active double ended techniques require a source of modulated radiation to probe the target gas on the far side of which is an I.R. detector or retroreflector to return the beam to the detector in the spectrometer.

Passive single ended techniques involve the measurement of I.R. emission and are generally less sensitive than active (probe beam) systems by 1 or 2 orders of magnitude. However, there are some remote monitoring applications where positioning a double ended system would be impractical, e.g. effluent plumes from tall smoke stacks and refinery flares. Passive I.R. radiation measurements have been used to retrieve the concentrations of CO, $N_2O$, NO, $SO_2$ and HCl in addition to $CO_2$ and $H_2O$ vapour from the smoke stack effluent of thermal power plants and municipal incinerators(6-8). The threshold detection limit of each species improves with increasing stack gas temperature.

Passive remote emissions monitoring systems have been used to study jet engine exhaust plumes in Holland and Germany (9,10). Heland (11) has measured $H_2O$, $CO_2$, CO, NO levels in the exhaust plumes of JT8 and CFM56-3 gas turbine engines. The exhaust gas temperatures varied with running conditions from 150 °C to 400 °C, the $H_2O$ and $CO_2$ content from 1% to 6%, CO from 10 to 1000 ppm and NO from 50 to 150 ppm. Hilton et.al (12) have made multiple line of sight measurements of gas temperatures and concentrations in the exhaust from a Rolls Royce Spey engine at DRA Pyestock (12).

This paper describes our recent non-intrusive single ended passive measurements of gas temperature and concentration in the exhaust plume of a Rolls Royce Avon industrial gas turbine engine. Our first experiments with this technique were made using the same Avon engine some years ago and have been reported elsewhere (13,14).

*Paper presented at an AGARD PEP Symposium on "Advanced Non-Intrusive Instrumentation for Propulsion Engines", held in Brussels, Belgium, 20-24 October 1997, and published in CP-598.*

## 3. FOURIER TRANSFORM INFRARED SPECTROSCOPY

From quantum theory, gases which are infrared active absorb or emit radiation as their molecules undergo spontaneous or induced transitions between different energy levels. Photons are emitted or absorbed at characteristic wavelengths determined by the structure of the molecules. A molecular species may be identified from the observed intensity at these wavelengths. The relative population of the energy levels is determined by the temperature dependent Boltzmann distribution. The intensity of the absorption or emission is therefore determined by both the gas temperature and the number of molecules present. The net radiance detected by an FTIR spectrometer system depends on the relative temperatures of all the molecules in the field of view (FOV). The spectrometer observes emission lines when the gas temperature is higher than that of the background or absorption lines when this temperature differential is reversed.

The instrument response function, its FOV and interferent species all affect the observed radiance of the target gas. In particular, the $CO_2$ and water vapour content of the atmosphere along the path absorbs extensive regions of the emission spectrum. The temperature of the plume gases can be determined from the radiance of the saturated part of the $CO_2$ band which approaches the radiance of a black body at certain wavelengths. When this thermodynamic gas temperature is known, the gas concentration can be obtained by matching the observed emission spectrum with modelled spectra (15,16). Where the spatial extent of the plume is well defined, as in the case of the Avon exhaust gases studied, the relative path lengths in air and the plume can be determined and average molecular concentrations in the plume calculated.

The Unicam FTIR spectrometer is based on a Michelson interferometer. In passive remote monitoring mode, I.R. radiation from a external source (in this case the thermal emission from the Avon engine exhaust gases) is collected by a 16 cm aperture reflective telescope. The reduced size image ~20 mm diameter enters the spectrometer via a salt window and the interferometer through a KBr window. The parallel beam of input radiation is split by a KBr beamsplitter into two beams one of which is reflected back to the beamsplitter by a static retroreflector and the other by a moving retroreflector. The moving retroreflector introduces an optical path difference between the two beams recombining at the beamsplitter. As the optical path difference between the beams changes with the movement of one retroreflector the intensity of the output beam is modulated by constructive and destructive interference.

The intensity of modulated output is recorded by a liquid nitrogen cooled InSb (Indium Antimonide) detector which has a higher sensitivity in the $CO_2$ and CO bands than the MCT (Mercury Cadmium Telluride) detector used previously. A Fast Fourier Transform chip inside the spectrometer converts the variation in intensity with optical path difference to produce a spectrum of the variation in intensity with spectral frequency. Data is collected over a time period of ~ 30 secs, in which time 20 or so scans of the moving mirror have occurred. Increasing the number of scans improves the signal to noise ratio (SNR) at the expense of time taken. The information is downloaded from the spectrometer via a serial data port to a laptop computer.

## 4. ANALYTICAL METHODS

While the wavelength of infrared spectral lines is specifically determined by the molecular structure of each species, the relative intensity of the spectral lines changes with the temperature of the molecules. The concentrations of hot $CO_2$ in gas turbine exhaust is usually sufficiently high for the gas to become optically thick in some spectral regions. In these circumstances, the transmission of the gas drops to zero and the radiance approaches that of a black body radiator. To determine the thermodynamic gas temperature, the radiance in these optically thick spectral regions (saturated bands) is compared with that of a black body calibration source at a number of temperatures. A calibration curve can be plotted so that the temperature of the gas can subsequently be calculated from the saturated band radiance.

Molecular concentrations are determined from the observed emission spectra by comparison with modelled spectral lines, taking into account instrumental features which can degrade the spectral features. The HITRAN (17) database contains line by line information about 32 naturally occurring atmospheric species. From this database, the temperature sensitive absolute line intensities can be calculated for individual spectral lines. The effect of atmospheric absorption by $CO_2$ or $H_2O$ present in the path to the exhaust plume can be included in the model. Once the FTIR spectrometer has been calibrated for radiance measurements, the number of molecules of each species can be obtained by comparing the observed line intensity with the modelled absolute line intensity.

Previously, emission spectra were taken with the spectrometer sighting on consecutive positions from the centreline to the outer edge of the exhaust plume, transverse to the gas flow. At each of these positions the radiance detected by the spectrometer is the sum of all the contributions from each volume element along the path. The distribution of exhaust gas species and temperature in the plume along the particular line of sight for these tests was found to be homogeneous. Species concentrations averaged over the whole length of the plume are therefore appropriate in this case.

## 5. EXPERIMENTAL SETUP

The Avon engine studied at Rolls Royce IPG has been adapted to be used principally to supply compressed air for rig testing. This engine has been used for a number of experimental projects and its performance is not representative of other engines of the same type being used commercially.

At the first trials some years ago, a conventional multihole extractive gas sampling rake was fitted immediately downstream of the final turbine stage. A single heated gas sampling tube transferred the combustion products to gas analysis equipment mounted in a mobile laboratory outside the test bed. The results from these extractive measurements were used to compare with the early non-intrusive measurements of gas concentrations. In the intervening time, the engine has been refurbished and should now run more efficiently although updated extractive gas analysis results are not available.

After the last turbine stage an approximately 2 m long 60 cm diameter jet pipe nozzle extends towards the larger diameter opening of the exhaust detuner which vents outside the test bed. There was a gap of ~ 1 meter free space between the jet

pipe nozzle and the detuner entrance across which infrared emission measurements could be made transverse to the exhaust gas flow.

The FTIR spectrometer contains optical components which must be critically aligned and free from vibration so it was not desirable to position the FTIR spectrometer too close to the Avon engine. A large amount of external air is entrained with the combustion gases into the detuner and considerable acoustic noise is generated when the engine runs at high speed.

The spectrometer was sited on a tripod some 5 meters horizontally away from the engine observing the plume through an open door way close to the jet pipe. The optical line of sight to the spectrometer was such that the plume was observed along the centreline and approximately transverse to the gas flow, slightly angled downstream.

During the same engine runs, exhaust gas spectra were also obtained remotely with a K-300 FTIR spectrometer by Jörg Heland of Fraunhofer Institut für Atmosphärische Umweltforschung (FhG-IFU), Germany. In the near future a comparison will be made between the two sets of engine data from two different types of FTIR spectrometer.

## 6. TEST RESULTS

In previous tests, problems were experienced when the engine was running because the noise levels and acoustic vibration in the region of the spectrometer were very high resulting in resonances within the instrument optical components. Additional vibration isolation and increased distance away from the engine meant that this was no longer a problem. The provision of a telescope with its large collection aperture and a sensitive InSb detector meant that the SNR in these spectra was an order of magnitude or more greater in these engine tests than they had been before. The sensitivity to the gases and the confidence with which quantitative measurements can be made is much increased. Figure 1 shows a typical emission spectrum.

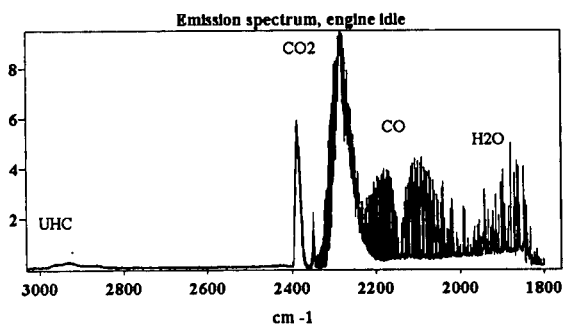


**Figure 1**

The vertical scale is a measure of the radiance in arbitrary instrument units. The horizontal scale is reciprocal wavelengths or $cm^{-1}$. The spectral lines centred on 2147 $cm^{-1}$ are characteristic of CO and those around 2350 $cm^{-1}$ of $CO_2$. The complex pattern of lines around 1800 $cm^{-1}$ is due to water vapour. These molecules are light and have sharp well spaced out spectral features. Unburnt hydrocarbons (UHC), since they are much heavier molecules, have very closely spaced spectral lines which are not resolved and can be seen as a broad low hump around 2900 $cm^{-1}$. UHCs were only observed at low engine speeds i.e. where the engine was running inefficiently. When the engine was running efficiently, CO levels dropped significantly.

Figure 2 shows an enlargement of Figure 1 highlighting the $CO_2$ and CO bands. The central portion of the $CO_2$ band exhibits the absorption by the cold atmospheric $CO_2$ in the ~ 5 m optical path to the exhaust plume. Surrounding this absorption region are the emission lines due to hot $CO_2$. The radiance of the saturated hot $CO_2$ band at around 2280 $cm^{-1}$ was used to calculate the thermodynamic gas temperatures. Once the temperature was known then other unsaturated spectral bands were chosen to calculate the average concentrations of the species in the exhaust plume.

The CO band from 2044 to 2140 $cm^{-1}$ was chosen to be fitted to modelled spectra created from the HITRAN96 database. In earlier work, the first calculated results had given CO

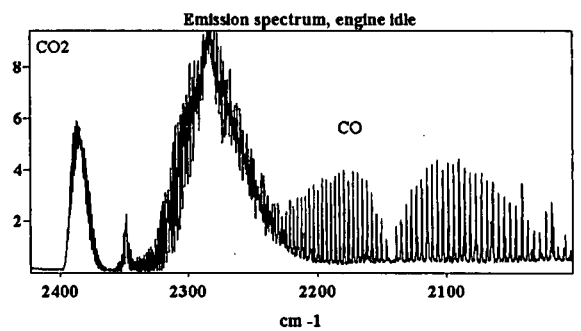


**Figure 2**

concentrations which were considerably lower than the extractive gas analysis results would have suggested. Gas analysis measurements were taken from the sampling rake just downstream of the last turbine stage. The rake, which combines samples from different regions of the flow was ~ 2 m upstream of the FTIR spectroscopy target region so results are not necessarily directly comparable. However, a new analysis procedure has been developed which takes into account the apparent reduction in peak height associated with instrumental line shape effects. This has produced quantitative measurements of concentrations which compared much better with what might be anticipated on the basis of past gas analysis results for the engine prior to refurbishment.

Table 1 shows the results obtained from these experiments. The calculated gas temperatures agreed well on a previous occasion with thermocouple measurements (to ~ ± 2%), so these values have been used as the gas temperatures for the gas concentration determination. Somewhat surprisingly, the temperatures at idle are higher than at 100% engine speed. This is because the air flow is low at lower speeds so the gas retains its high temperature. Although the engine runs hotter at higher speeds, greater air flow then reduces the gas temperature at the measurement point where entrained air mixes with the core air flow before entering the detuner.

**Table 1**

| Engine speed / % | Calculated Temp / K | CO2 / % N-I | CO / ppm N-I | CO2 / % extractive | CO/ppm extractive |
|---|---|---|---|---|---|
| idle | 718 | 2.14 | 986 | | |
| idle | 719 | 1.45 | 959 | | |
| 50 | 633 | 1.09 | 919 | 1.79 | 1141 |
| 50 | 636 | 1.10 | 910 | | |
| 75 | 530 | 1.27 | 693 | 1.52* | 619* |
| 75 | 531 | 1.27 | 725 | | |
| 100 | 655 | 1.17 | 37 | 2.90 | 65 |
| 100 | 656 | 1.27 | 36 | | |
| 100 f.o. | 518 | 3.08 | 31 | 3.47 | 73 |
| 100 f.o. | 521 | 3.00 | 31 | | |

* interpolated results from 70% and 80% data.
f.o. denotes flap opened to spill compressed air

The table shows some extractive gas analysis measurements for the same engine prior to refurbishment and from sampling points closer to the turbine exit than the observation area for the non-intrusive measurements. The results show that in general, the non-intrusive measurements gave slightly lower values for the gas concentrations than the extractive measurements. However, the engine emission levels may have altered as a result of its refurbishment and also the entrained air may have diluted the exhaust gases in the region where the non-intrusive measurement was made.

However, the main reason why the CO concentrations previously reported were considerably lower than the extractive gas analysis results is because the apparent intensity of the CO spectral lines is particularly sensitive to the instrument line shape (ILS) function of the spectrometer.

The intrinsic spectral features of CO are very sharp, more so than the $CO_2$ lines, with a line width at half max height of less than 0.1 $cm^{-1}$. The spectral resolution of the spectrometer is limited by its maximum optical path difference which for this instrument generates a maximum spectral resolution of 0.025 $cm^{-1}$.

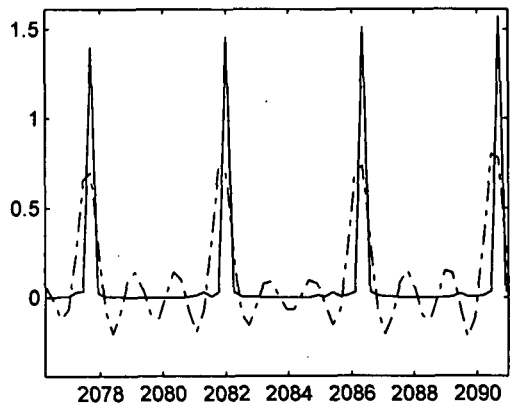


**Figure 3 Sharp CO lines degraded by the ILS**

The ILS function tends to flatten the spectral lines so that peak intensity values measured from the spectrum can be less (sometimes half the size) than those modelled without taking ILS into account. A correction for this is now incorporated into the analytical algorithm so that the ILS function is applied to modelled spectra reducing the peak heights of the modelled spectra and broadening the lines to match those observed in the experimental spectra, see Figure 3.

## 7. CONCLUSIONS

FTIR spectroscopy has been shown to provide useful information by non-intrusively monitoring the exhaust gas flow. In this instance the molecular species CO and $CO_2$ have been studied since their distinctive strong spectral lines can be easily identified and intensities measured.

Thermodynamic gas temperatures have been calculated from saturated $CO_2$ band radiance. Previous good comparisons between thermocouple measurements and non-intrusive temperature measurements have demonstrated the validity of the technique.

The radiance calibration and instrument response factors of the FTIR spectrometer which previously limited the accuracy of the average concentration measurements through the plume have been significantly ameliorated. The greater radiation throughput by using the telescope and the higher sensitivity of the InSb detector have contributed to this improvement in performance.

While it is relatively easy to obtain infrared spectra of exhaust plumes, the analytical procedures are complex and quantitative measurements of gas temperatures and concentrations can currently only be made off line.

However, improvements in the analytical procedures continue to be made, the results become easier and quicker to obtain with greater quantitative accuracy. There is great potential for this technique with its advantages of non-interference in the exhaust gas stream, the elimination of expensive sampling probes and the simplicity of obtaining spectral data.

8. ACKNOWLEDGEMENTS
The authors are grateful for the helpful assistance of Rolls Royce Industrial Power Group staff in performing the engine test running and gas analysis. Ian Thomas and Nick Davies in the Physics Department of Reading University helped set up the equipment and make measurements together with Jörg Heland of Fraunhofer Institut für Atmosphärische Umweltforschung (FhG-IFU), Germany.

This work has been carried out with the support of Rolls Royce, DERA and the EU Brite-EuRam Programme research contract no. BRPR-CT96-0142, AEROJET.

9. REFERENCES

1.Herget,W.F.,Lowry,S.R.'Auto exhaust gas analysis by FTIR spectroscopy' in proc. conference on Measurement of Atmospheric Gases, 1991, SPIE Vol 1433 p 275-289

2.Herget,W.F.'Analysis of gaseous air pollutants using a mobile FTIR system' 1982 *Am Lab* **14**(12) p 72-78

3.Partridge,R'Long-path monitoring of atmospheric pollution' 1990/91 *Meas. & Contrl.* **23** p 293-298

4.Reid,S.A.,HughesJ.I.L.,Roberts,P.T., Archibald,I.,Gregory,K.' Development of open path systems for emission rate measurements' 1993 *Proc. Air Waste Manage. Assoc.* **SP-89** p 305-321

5.Russwurm,G.M.,Kagann,R.H.,Simpson,O.A.,McClenny,W. A.,Herget,W.F.'Long-path FTIR measurements of volatile organic compounds in an industrial setting' 1991 *J. Air Waste Manage. Assoc.* **41**1062-1066

6.Wormhoudt,J,Conant,J.A.,Herget,W.F.' High resolution infrared emission from gaseous sources' 1985 *Infrared methods for gaseous measurements* Wormhoudt J Ed., (New York:Marcel Dekker)

7.Prengle,H.W.Morgan,C.A.,Fang,CS,Huang,LK.,Campani,P. Wu,W.W.' Infrared remote sensing and determination of pollutants in gas plumes' 1973 *Environ. Sci and Technol.* **7** (5) 417-423

8.Carlson,R.G.,Hayden,A.F.,Telfair,W.B. 'Remote observations of effluents from small building smokestacks using FTIR spectroscopy' 1988 *Appl. Opt.* **27** (23) 4952-4959

9.Schleijpen,H.M.A.,Crajé,M.W.J.,Eisses,S.M.'Highresolution spectroscopy in the field' proc conference Infrared Technology XIX 1993, SPIE vol 2020, p 225-233

10.Lindermeir,E.'Evaluation of infrared emission spectra of aircraft exhaust with the FitFas software'1994 *Ann. Geophysicae* **12** p 417-421

11.Heland,J.,Haus,R.,Schäfer,K.'Remote sensing and analysis of trace gases from hot aircraft engine plumes using FTIR-emission-spectroscopy' 1994 The Science of the TotalEnvironment, **158** 85-91

12. Hilton,M.,lettington,A.H.,Wilson,C.W.,'Gas turbine exhaust emissions monitoring using non-intrusive infrared spectroscopy' 1997 proc. International Gas Turbine Institute congress, Orlando,Florida, accepted for publication in Transactions of the ASME

13.Hilton,M.,Lettington,A.H.,Mills,I.M.,Cox,A.J.,Handy,R.M 'Non intrusive monitoring of gas turbine exhaust emissions using I.R.spectroscopy' 1995, proc. Royal Aeronautical Society conference on Environmental Aspects of Air Transport

14.Hilton,M.,Lettington,A.H.,'Industrial gas turbine engine exhaust emission monitoring using non-intrusive FTIR spectroscopy', 1996, proc. Applied Optics divisional conference of the Institute of Physics, Reading, p337-342

15.Haus,R.,Schäfer,K.,Mosebach,H.,Heland,J. 1993 'FTIS in environmental research: mobile remote sensing of air pollution' 1993 proc.conference SPIE vol **2089** p 319-319

16.Schäfer,K.,Haus,R.,Heland,J.'Measurement of gaseous compounds from emissions sources and in ambient air by Fourier transform infrared spectroscopy:method and results of FTIS-MAPS' 1993 *Proc. Air Waste Manage. Assoc.* **SP-89** p 455-465

17.Rothman,L.S.,Gamache,R.R.,Tipping,R.H.,Rinsland,C.P.,S mith,M.A.H.,BennerD.C.,Devi,V.M.,Flaud,J-M.,Camy-Peyret, C.,Perrin,A.,Goldman,A.,Massie,S.TBrown,L.R.,Toth,R.A., 'The HITRAN database: Editions of 1991 and 1992' 1992 *J. Quant. Spectrosc. Radiat. Transfer* **48**:5-6 p 469-507

Paper 8
Author: M. Hilton

Q: J.D. Rogers

Is it possible to rotate the IR system about the engine axis and with traversing, obtain data that could be used in a tomographic reconstruction of the whole cross-sectional area?

A: I believe it is entirely feasible to do as Dr. Rogers suggests. In a way, we have already done it - see my references 12 13 and 14. By obtaining spectra along the different lines of sight with a 1-D optical traverse mechanism, together with an assumption of axial plume symmetry, we have performed an Abel inversion and attempted with some success to reconstruct spatial distributions. We currently have a student working on developing a 2-D scanning system to perform the tomographic reconstruction of the whole cross sectional area.

Q: K. Benson

Have you tried to use your system in a combustor exit characteristics?

A: We have not yet tried to use the FTIR spectrometer to make non-intrusive measurements in a combustor rig. However, we have studied exhaust gas and flame emissions from a kerosene burner rig where it was possible to have an open path close to the rig exit. It would be very interesting to look at combustor exit characteristics using special windows if necessary.

Q: E.G. Pink

Have you used the technique to obtain results immediately downstream of a combustor?

A: We have not yet tried to use the FTIR spectrometer to make non-intrusive measurements in a combustor rig. However, we have studied exhaust gas and flame emissions from a kerosene burner rig where it was possible to have an open path close to the rig exit. It would be very interesting to look at combustor exit characteristics using special windows if necessary. (Same answer as above)

Q: H. Eisenlohr

Can you elaborate on the influence of the path length on your signals, i.e. how "deep" does your system penetrate the plume?

A: Absorption, emission and transmission of IR radiation is dependent on path length. Engine exhausts we have studied have plume diameters typically 60cm.

The depth of penetration of the non-intrusive FTIR spectroscopy system is dependant on the intensity of the emitted or absorbed radiation.

The penetration depth for unsaturated spectral bands will be greater (typically the entire plume diameter) than for saturated bands such as $CO_2$ where the penetration depth may only extend to the core.

# DIAL Measurements on a Gas Turbine Exhaust

**K D Brundish, C W Wilson**
DRA Propulsion Department
170 Building, Pyestock
Farnborough, Hants GU14 0LS
United Kingdom

**J T M Moncrieff, A G Wootton**
SPECTRASYNE
3, The Ringway Centre, Edison Road
Basingstoke, Hants RG21 6YH
United Kingdom

## 1. Summary

This paper summarises work undertaken by Defence Evaluation and Research Agency (DERA) and SPECTRASYNE, and examines the technique of DIAL as a measurement of gas turbine engine emissions. The work was jointly funded by the UK MOD and UK DTI.

The DIAL technique is based on LIDAR, which is a laser based range finding system, similar to RADAR. With the use of a tuneable laser it can be adapted for spectroscopic measurements of mass flux.

This technique was used to measure $NO_x$ and unburnt hydrocarbon mass fluxes from the vertical engine detuner, for two engines at three running conditions. The $NO_x$ measurements were converted to vppm values at the engine exit plane to allow comparison with intrusive probe measurements.

The DIAL measurements of $NO_x$ at idle and max. continuous were within 25% of the probe measurements. The DIAL measurements are performed at a plane downstream of the detuner exit, and rely on the wind to move the plume through this plane. Low windspeeds which are usually associated with variable wind directions, can result in increased uncertainty. However, minimum reheat values were considerably different, and cannot be explained by these uncertainties. This anomaly is as yet unresolved, although a possible solution may be from continued reactions in the detuner.

The unburnt hydrocarbon (UHC) measurements from both DIAL and the probe exhibited the same trends, although a direct comparison was not possible due to the unknown composition of the hydrocarbons exiting the engine. This made it impossible to calculate concentration from the mass flux measurements.

Further work on gas turbine engines should be performed under less arduous conditions for DIAL measurements than the reported tests. Measurements in open areas directly behind the engine with a horizontal plume, offers the best conditions.

## 2. Introduction

Nitrogen Oxide ($NO_x$) emissions are a leading driver in the development of aircraft gas turbine engines. Legislation is expected to be introduced which will lower the allowable output of $NO_x$ from civil aircraft. $NO_x$ emissions are also becoming of greater importance to military aircraft engines due to nitrogen dioxide ($NO_2$), the visible (brown) component of $NO_x$. Stealth properties of some aircraft are sufficient that the threat of detection at visible wavelengths is becoming greater than by other detection systems. Previous work performed at DERA has shown that as smoke levels are reduced, the brown $NO_2$ emitted from aircraft will become more dominant in plume visibility.

$NO_x$ can be formed by three mechanisms: Fuel bound nitrogen, prompt $NO_x$, and thermal $NO_x$. Fuel bound nitrogen is low in aviation fuel and this mechanism does not contribute significantly to the $NO_x$ emissions of aircraft engines. Prompt $NO_x$ contributes little to the overall $NO_x$ emissions at the pressure ratios in gas turbine engine cycles. Thermal $NO_x$ is by far the greatest contributor to $NO_x$ formation at high power engine conditions (Bonturi et al). $NO_x$ levels calculated using this mechanism (Miller and Bowman) are proportional to combustor flame temperature and residence time.

Engine trends towards higher thrust to weight ratios has lead to higher compressor ratios and more arduous operating air/fuel ratios (AFRs). These trends cause higher flame temperatures at the maximum power conditions, giving rise to high $NO_x$ emission levels. The majority of $NO_x$ at the exit of a gas turbine

*Paper presented at an AGARD PEP Symposium on "Advanced Non-Intrusive Instrumentation for Propulsion Engines", held in Brussels, Belgium, 20-24 October 1997, and published in CP-598.*

combustor is in the form of nitric oxide (NO), a colourless gas. However, under certain conditions, the NO converts into $NO_2$ further down the engine jet pipe (Foster and Wilson) and in the plume. This leads to visible plume emissions which degrades the aircraft's stealth properties.

Measurements of NO and $NO_2$ concentrations in the plume are not easily achievable using traditional intrusive techniques, but are important for furthered understanding of the conversion mechanisms occurring, and any subsequent $NO_x$ production that might exist in the plume. NO to $NO_2$ conversion chemistry is poorly understood, and validation of chemical kinetics models is required to allow accurate prediction of plume visibility. In order to achieve these measurements it is necessary to use non intrusive techniques. DIAL offers the possibility to measure emissions at a range of hundreds of metres and greater with some species (Boden et al).

This report examines the technique of DIAL (Differential Absorption LIDAR) as a non intrusive measurement of the emissions from a gas turbine engine. The measurements were performed with a view to establishing the applicability of the technique, with a future objective of engine plume measurements for validation of plume chemistry models.

## 3. DIAL Technique

Light/laser based technology systems for the remote monitoring of gaseous species in the atmosphere have been under development for the past two decades. The flagship of these developments is a Differential Absorption LIDAR or DIAL. DIAL is a development of LIDAR, a light based range finding system similar to RADAR. If a laser is used as the LIDAR light source, the collimated, coherent light emitted can be used to define the range of specific objects. A tuneable laser source can give LIDAR an additional spectroscopic capability as the source laser can alternately be tuned onto then off an absorption feature in the known 'spectral fingerprint' of a specific gas.

For a given target species, the laser signal is tuned to the specific wavelength. The laser is traversed across the target plume, and absorption occurs (Figure 1). A reference beam of similar wavelength and frequency to the tuned beam is also fired through the target plume. This beam should undergo similar attenuation and scattering through the plume, but will not be absorbed by the target species. The back scattered laser intensity is measured using a detector. With the comparison between the return signal intensities of the two beams, the number of molecules of the target species passing through the measurement plane can be determined (Killinger and Menyuk).

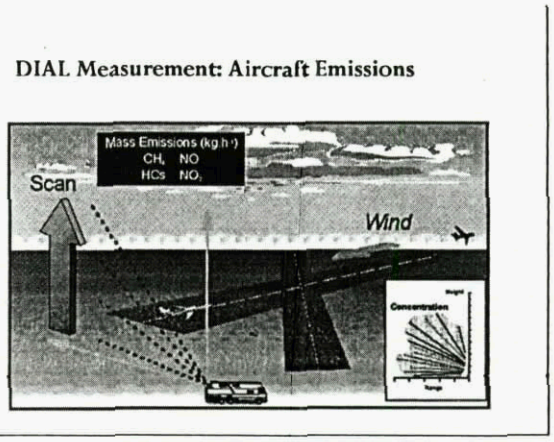


Figure 1 - DIAL Measurement Technique

DIAL measurements have a wide variety of applications. In the US the technique has mainly been used for ozone and water measurements for atmospheric monitoring. NASA developed an airborne DIAL system for water measurements (Browell et al (1986), Higdon and Browell (1991)) and a system for aerosol measurements (Browell and Shipley (1985). Other organisations have performed similar work, such as the Environmental Protection Agency (Mcelroy (1992)).

Throughout the 1980s and early 90s, at various critical development stages, validation and correlation work was carried out in the UK on DIAL concentrating mainly on the oil industry. The work ranged from making measurements through gas cells which had been filled with gravimetric standard gas mixtures to correlation exercises between DIAL concentration measurements and stack gas analyses collected using conventional gas analysers and gas chromatography equipment. Concentration correlation's at ambient/environmental levels against accredited thermal absorption tube data were also undertaken. In all cases the DIAL measured concentrations were within 8-15% of the standard of the data generated by the more conventional technologies.

However, since 1988, DIAL concentration data has been used with wind speed and direction to produce mass emission fluxes (kg/h) and some further validation work on the production of mass emission fluxes was undertaken. A number of mass emission correlation exercises between the SPECTRASYNE DIAL and other measurement techniques have been carried out during recent years. The other methods include calibrated releases of methane from a point source and marine tanker vent measurements. In all of these exercises the maximum divergence from the DIAL measurements recorded was 15%.

One of the most recent of the correlation exercises was carried out in 1993 with personnel from the European oil industries association, CONCAWE (Decaluwe).

The correlation exercise was carried out during one complete loading schedule of a river barge loading motor spirit, as this represented a discrete emission source.

The CONCAWE team calculated the mass hydrocarbon emission levels throughout the loading from the tank vent measurements and a knowledge of the loading rate and thus vapour displacement rate. The Spectrasyne DIAL measurements which were made some distance downwind of the barge. The sequential measurement data derived from the two methods were integrated over the loading period to provide total mass emission figures for each measurement technique. The resultant correlation was within 12%.

## 4. DIAL Equipment

The Spectrasyne DIAL is a mobile unit (Figure 2) based on two high energy (1.4J), 10Hz pulsed Nd:YAG pumped dye lasers (Figure 3). Tuneable ultraviolet and visible radiation is generated in one of the laser sets by selective use of frequency doubling and tripling crystals. The second laser set, which has an injection seeded Nd:YAG, is used to generate tuneable infrared radiation by means of the unique infrared source assembly.

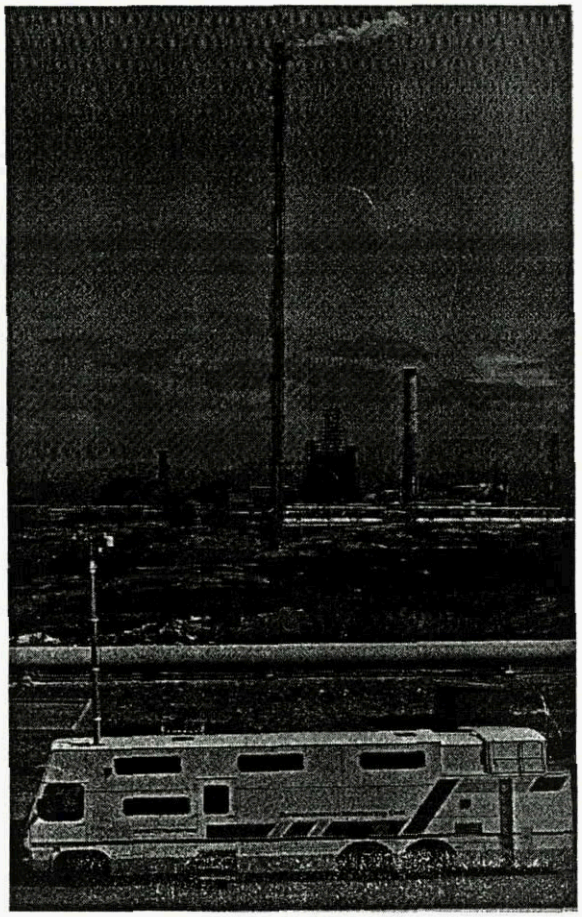

Figure 2 - Spectrasyne Mobile DIAL Measurement Unit

DIAL is single ended and its output beam is directed by means of a mirror steering system which rotates in two planes. The back-scattered light, which returns along the same path, is collected in a cassegrain-type receiving telescope and delivered to the appropriate detector through a multi-dichroic, beam splitting, collimating and focusing system.

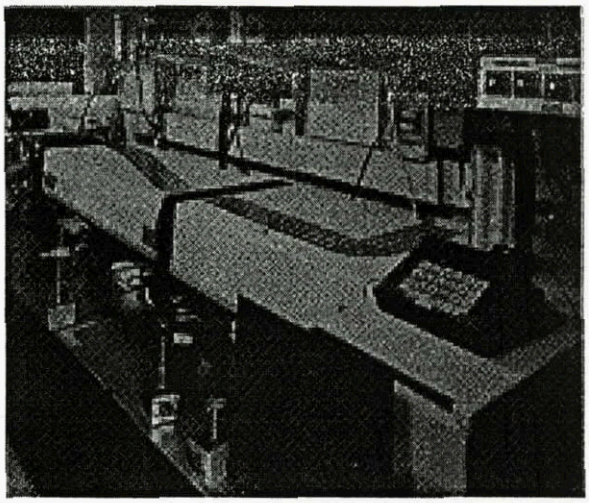

Figure 3 - DIAL Laser System

In order to collect, store, handle and process the DIAL signals a sophisticated, high speed data communication network has been developed in parallel with a unique software package. Computers are also used to perform a number of ancillary control functions and to store essential spectroscopic and ancillary databases.

The vehicle is also equipped with an extendible meteorological mast and a number of portable telemetric stations which are used along the DIAL scan lines to measure wind speed and direction, temperature and humidity. These data are displayed in real time and digitally logged for subsequent use with DIAL concentration data to produce mass emission fluxes. A sophisticated 3D Computational Fluid Dynamics (CFD) model can also be connected to the processing system; this is used to provide interpolation between measured wind speed data points for flux calculation and to assist in the definition of suitable measurement positions where the wind fields are complex. Telephoto and wide angle TV cameras are used on the steering system to facilitate beam pointing. The wide angle image is recorded on a time-lapse video recorder to be used if necessary to identify problems visually during subsequent data analysis.

## 5. DIAL Measurements

Measurements of gas turbine engine emissions have traditionally been performed at the exit plane of the engine using intrusive probe techniques. Non intrusive measurements are becoming of greater importance due to the effect of the presence of intrusive probes, and due to the difficulty of probe access. LASER type

measurements have been performed in a number of applications to gas turbine engines, and are now more often used in engine measurements.

DIAL measurements offer a good degree of accuracy over a substantial distance, the measurement range varying from a few hundred yards to several kilometres depending on the species measured and the atmospheric conditions. Due to this, it was possible to take measurements at the exit of a detuner from a gas turbine engine test cell. The detuner exit is some 20m downstream of the engine exit plane, however the plume was constrained within the detuner and was not representative of a free plume. The objective of the test programme was to establish the applicability of DIAL as a technique for plume emissions measurements. With this established, future measurements on free engine plumes may be used to validate plume modelling.

Two engines were operated at three conditions for the measurements; idle, maximum continuous and minimum reheat. Maximum reheat condition requires that cooling water is sprayed into the detuner and this increases the opacity of the plume, making the DIAL measurement at close range more difficult.

For DIAL measurements, ideally an unrestricted line of site, downwind, through the target plume is required. The Test bed at DERA Pyestock presented a particularly difficult challenge for plume measurements because, firstly, the detuner was completely surrounded by trees and buildings and, secondly, there was limited access in the area. The tall overhanging trees only provided a gap of a few metres, thus it was not possible to change the scan line in response to wind direction or engine condition.

On this occasion wind direction remained sufficiently stable not to present a problem but the large difference in the plume characteristics (gas concentration and particulate material) between idle and minimum reheat meant that the scan line was not optimal for either. Ideally measurements at idle would be done close to the detuner exit and the scan line moved progressively further away as the plume opacity increased at higher load conditions.

The mass flux of $NO_x$ and hydrocarbons at the detuner exit, were measured at the three operating conditions. A series of DIAL scans were performed at each of the three operating conditions, to minimise error. The data for each condition were then averaged.

Measurements were also taken using a gas analysis probe situated at the engine exit plane (Figure 4). The probe was designed to withstand the high loads at the engine exit. As well as the physical integrity design, the gas analysis probe was designed to conform with current EPA (Environmental Protection Agency) standards for probe designs for emissions measurements.

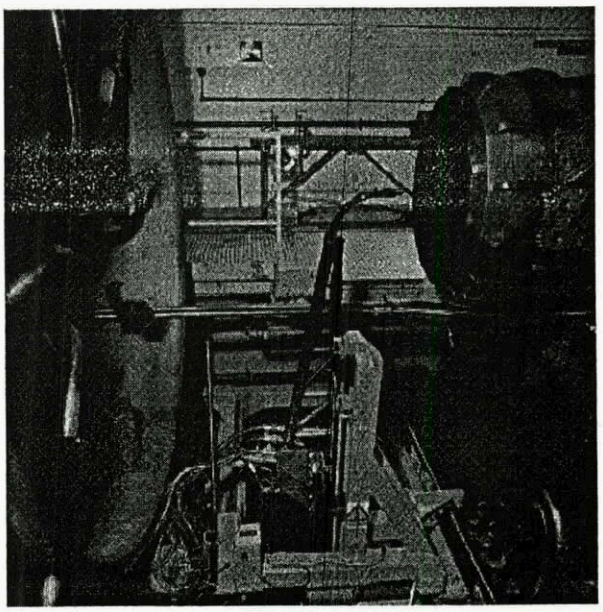

Figure 4 - DERA intrusive probe

The probe measurements were localised point by point measurements, and as such are subject to localised temperature fluctuations. This changes the density and measurement conditions from point to point. To obtain an overall average for the engine exit, density averaging must be performed. This is done by weighting the results to temperature (Tilston):

$$[NOx] = \frac{\sum [NOxi] * To / Ti}{\sum To / Ti}$$

where
[NOx] is average concentration of NOx
[NOxi] is local concentration of NOx
Ti is localised temperature

To is average temperature $To = \frac{n}{\sum 1/Ti}$

## 6. Results

In order to compare the data from the two methods, the detuner exit plane $NO_x$ mass fluxes were back-calculated to the engine exit plane, and converted into concentration (vppm) as follows:

1. $NO_2$ + NO mass flux converted into volumetric flow using the density of $NO_2$ and NO.

2. The volumetric flow at engine exit was calculated using the density of air (reasonable as the composition is mainly air at this plane).
3. The vppm concentration was calculated by dividing the $NO_x$ volumetric flow by the total engine exit volumetric flow.

The degree of uncertainty in the translation from the detuner plane to the engine exit plane decreased the accuracy of the results but trend comparisons were expected to be reliable.

Figure 5 illustrates the averaged non dimensionalised (against idle values) data at the engine exit planes from the probe, and the back-calculated DIAL measurements.

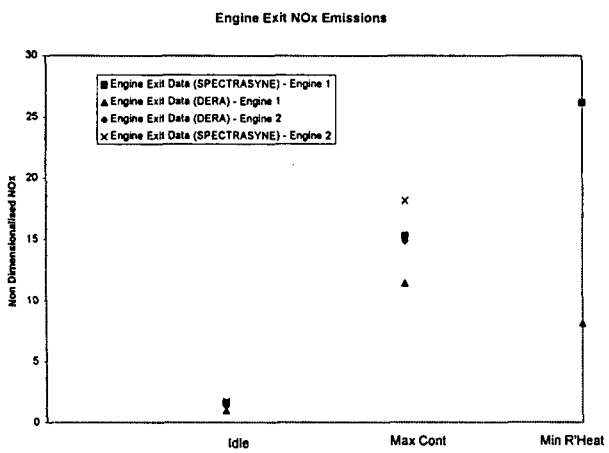


Figure 5 - $NO_x$ Emissions data

Surprisingly, the DIAL measurements were higher than the intrusive probe measurements. Errors normally associated with DIAL, such as loss of detectability at the diffuse edges of the plume , and beam attenuation, normally result in low readings. Beam scattering errors are considered small due to the close proximity of wavelengths for the measurement and reference beam, although complete capture can never be resolved.

The differences between the readings of the measurements methods were also higher than expected. Differences at idle were small, and max. continuous readings were within 25%. However, min reheat measurements showed a much larger disagreement.

In the case for the idle and max. continuous measurements the divergence between the two techniques were acceptable. Generally low wind speed can result in directional instabilities can cause over recording due to localised recirculation zones around the measurement plane. This is minimised with the use of accurate wind speed measurements at differing heights, complemented with CFD calculations to interpolate between the measurement heights.

It is likely that the difference between the readings at idle and max. continuous is a combination of the following sources of uncertainty:

1. Traditional chemiluminescence used with the probe measurements have inherent inaccuracies.
2. $NO_x$ production in the detuner.
3. Reactions in the probe.
4. Efflux velocity affecting DIAL.
5. Low wind speeds resulting in eddies and recirculation thus measuring parts more than once.
6. Conversion from DIAL measurement plane to Probe measurement plane.

A continuous steady rise in $NO_x$ measured with the DIAL system was seen with increasing engine load. However, a decrease in $NO_x$ concentrations was measured with the traverse probe from max. cont. to min. reheat conditions, resulting in a divergence between the two techniques.

Most of the uncertainties on the above list could not be responsible for such a large error, although they would contribution as with the idle and max. continuous cases. However, $NO_x$ formation in the detuner, and the possibility of probe reactions could account for the anomaly.

Investigation into the possibility of probe reactions was performed using argon dilution to 'stifle' any reactions (Foster and Wilson - unpublished). The results proved that $NO_x$ conversion did occur, however the total $NO_x$ concentration remained constant thus ruling out $NO_x$ production in the probe.

The possibility of $NO_x$ production from combustion beyond the exit plane was considered, but chemical modelling of kerosene is difficult due to the absence of a proven kerosene combustion scheme. Prompt $NO_x$ production, however, was possible but was considered as not sufficient for the measured increase. The average temperature was around 900K, below that necessary for thermal $NO_x$ production, however localised regions may be in excess of the temperature required. The inconsistency in trends is as yet unresolved.

NO and $NO_x$ were measured separately, to examine conversion. Table 1 shows the conversion values at the detuner exit plane. The values show that in all cases, the conversion to $NO_2$ was well above 80%. Thus, at plume distances of less than 80m from the engine exit, the plume visibility due to $NO_x$ had nearly reached maximum.

| Condition | $NO_2$/ $NO_x$ DIAL | $NO_2$/ $NO_x$ Traverse Probe |
|---|---|---|
| Idle | 0.87 | 0.3 |
| Max. Cont. | 0.86 | 0.11 |
| Min. Reheat. | 0.84 | 0.4 |

Table 1 - $NO_2$/ $NO_x$ conversion ratios

Measurements of unburnt hydrocarbons were also taken using both measurement techniques. The measurements using DIAL showed some methane content at the plume plane (see Table 2), however Fourrier Transform Infra Red (FTIR) spectroscopy measurements were also performed at the exit plane but methane was not detected. The presence of methane at the DIAL measurement plane is possibly due to the fuel continuing cracking (ie reacting) on its passage through the detuner. Thus the heavier hydrocarbons were cracked down to methane and other light species.

| Condition | Methane at Detuner Exit (kg/hr) |
|---|---|
| Idle | 0.1 |
| Max. Cont. | 7.9 |
| Min. Reheat | 37.5 |

Table 2 - Methane Mass Fluxes at Detuner Exit Plane

Only trends can be compared for hydrocarbon measurements due to the complexity of the chemical and physical properties of the fuel. The exact composition of the hydrocarbons exiting the engine, is unknown. This makes it impossible to calculate the density of the hydrocarbons, and thus conversion from mass flux to concentration is not possible. The trends between the DIAL and probe measurements were in good agreement (see Table 3).

| Condition | UHC DIAL (kg/hr) | UHC Engine Exit (vppm) |
|---|---|---|
| Idle | Not Measured | 91.32 |
| Max. Cont. | 31.1 | 4.9 |
| Min. Reheat. | 581.2 | 12191 |

Table 3 - Unburnt Hydrocarbon Measurements

High unburnt hydrocarbon values were present at idle and min reheat, with virtually none at max. continuous.

## 7. Conclusions

$NO_x$ concentrations were measured using the DIAL technique and compared to probe measurements at the engine exit plane.

Measurements of $NO_x$ using DIAL were within 25% of intrusive probe measurements for the power conditions of idle and max. continuous, showing that useful DIAL measurements can be performed on gas turbine exhausts.

One possible source of uncertainty with DIAL measurements with non ideal test location and meteorological conditions, stems from wind measurement and plume shift during the scans.

Tests under more favourable conditions would result in more accurate measurements for plume emissions at idle and max. continuous conditions.

The difference in readings at min reheat are as yet unresolved. Probe reactions have been ruled out but $NO_x$ production in the detuner may offer an answer.

Under the three engine operating conditions addressed, NO to N02 conversions of greater than 80% were observed at the DIAL measurement plane. Most of the conversion was believed to have occurred in the detuner although there were some indications of differences in ambient conversion depending mainly on wind speed and thus residence time to the scan plane.

Conversion of mass fluxes to vppm for UHC cannot be performed due to the unknown density of the complex UHC structure.

DIAL measurements UHC in the downwind plume at the three engine operating conditions showed high mass emissions at min reheat and virtually none at max. continuous, which agreed with intrusive probe measurements at the engine exit plane.

This work has shown that DIAL is suitable for gas turbine engine emissions measurements.

## 8. Recommendations

Further work examining hydrocarbon speciation using other non intrusive techniques is required to allow more detailed comparison between DIAL and intrusive measurement systems.

Further investigation of the disagreement in the trends of $NO_x$ from max. continuous to min reheat is required.

Measurements under less difficult conditions for DIAL would allow better investigation into the applicability of the technique for measurement of gas turbine exit emissions. Ideally, these would be performed in open areas with the plume exiting horizontally to the horizon.

## 9. References


Boden, J C, Tjessem, K, Wootton, A G, and Moncrieff, J T M (1996). evaluated Flare emissions Measured by Remote Sensing. *Petroleum Review, November 1996.*

Bonturi ,S, Pourkashanian, M, Williams, A, Oskam, G, and Wilson, C (1996). $NO_x$ Formation in Counter-Flow Opposed-Jet Diffusion $CH_4$/Air Flames. *Combustion Science and Technology; Vol. 1221, pp 217-233.*

Browell, E V, et al (1986). Development of a High Altitude Airborne System: The LIDAR Atmospheric Sensing Experiment (LASE). *13th International Laser Radar Conference, pp4.*

Browell, E V, and Shipley, S T (1985). Ultraviolet DIAL Measurements of O3 Profiles in Regions of Spatially inhomogeneous Aerosols. *Applied Optics, Volume 24, pp 2827-2830, Sept. 1985.*

Foster, T J and Wilson, C W (1997). Detailed Chemical Modelling Predictions of Emissions from a Reheated Gas Turbine Engine with Application to Future Supersonic Aircraft. *ASME Turbo Expo, Orlando, Florida, June 1997.*

Higdon, N S, and Browell, E V (1991). Airborne Water Vapour DIAL Systems and Measurements of Water and Aerosol Profiles. *4th Airborne Geoscience Workshop, NASA, Washington, pp167-168.*

Mcelroy, J L (1992). UV-DIAL Application to Clean Air Act Implementation. *International instrumentation Symposium, 38th, Las Vegas, pp215-225. April 1992*

Miller, J A, and Bowman C T (1989). Mechanism and Modelling of Nitrogen Chemistry in Combustion. *Process in Energy and Combustion Science 15, pp287-338. 1989*

Foster, T J and Wilson, C W (1998). To be presented at Combustion Symposium, Bolder Colorado.

Decaluwe, J (1995). Case Study: Using DIAL to Validate VOC Emissions Calculations - CONCAWES Experience. *CONCAWE Report No. 95/52.*

Killinger, D, K and Menyuk, N (1987). Laser Remote Sensing of the Atmosphere. *Science, Volume 235 1987.*

Tilston, J R (1991). Personal communication.

Whiteman, M (1997). Personal communication.

Paper 9
Author: Brundish

Q: Weigand

Why did you not use LIDAR for exhaust measurements in the near field of the plume?

A: The measurements were performed downstream in the plume so that the plume chemistry could be studied. Measurements of DIAL were compared to engine exit measurements to analyse NO/NO2 conversion for plume visibility. DIAL was used (not LIDAR) due to the increased accuracy with the use of a reference beam. Hot plume measurements are prone to a large number of interferences which require a reference beam to make sensible measurements.

Q: Prof Greenhalgh

Why did you not make probe measurements after the detuner as well as at the (engine) exit?

A: The exit of the detuner is some 20m from the ground making probe measurements of the plume after this difficult. In addition to this, the engine exit and detuner entry are not continuous, and entrained air dilates the plume. The entrainment is difficult to calculate and thus the mass flow at the detuner exit is unknown. Mass flow is required to compare the DIAL and probe measurements, so measurements at the detuner exit would be difficult to compare to either the DIAL or the engine exit measurements.

# UV ABSORPTION MEASUREMENTS OF NITRIC OXIDE COMPARED TO PROBE SAMPLING DATA FOR MEASUREMENTS IN A TURBINE ENGINE EXHAUST AT SIMULATED ALTITUDE CONDITIONS*

R.P. Howard
Sverdrup Technology Inc., AEDC Group
Building 690, Second Street
Arnold Engineering Development Center
Arnold AFB, TN 37389-4300
United States

## ABSTRACT

Nitric oxide measurements were conducted in the exhaust of a turbofan engine at simulated altitude conditions in a ground-level test cell using both optical nonintrusive and conventional gas sampling techniques. NO-UV absorption measurements, using both resonance and continuum lamps, were made through several chords of the exhaust flow near the nozzle exit plane as a part of a larger effort to characterize aircraft exhaust constituents over a wide range of steady-state engine operating conditions. This paper describes the NO-UV absorption measurements and compares radial profiles of NO concentrations and emission indices with measurements obtained using conventional gas sampling and tunable diode laser infrared absorption.

## INTRODUCTION

The NASA Atmospheric Effects of Aviation Program requires characterization of aircraft emissions including trace constituents to adequately assess and predict the impact of current and future fleets on atmospheric chemistry. The first of a series of NASA measurement programs[1] in ground-based engine test cells was performed at the Arnold Engineering Development Center (AEDC) at simulated altitude conditions ranging from sea-level-static to 15.3 km. The test article engine design and operation parameters were representative of a commercial-type bypass engine with an annual combustor, operating with aviation fuel. The engine was operated over a range of combustor temperatures and pressures at each of several simulated altitudes shown in Fig. 1, to provide NASA with parametric data for insight into exhaust emission variations as a function of combustor parameters and altitude at standard-day conditions. Measurement systems applied directly to the exhaust flow field are illustrated in Fig. 2. Techniques utilized for measurements of nitric oxide (NO) concentrations were conventional extractive sampling using a multipoint cruciform probe rake assembly, spectral UV resonance and continuum absorption applied over multiple lines of sight, and spectral infrared single line-of-sight absorption utilizing a tunable diode laser. This paper details the NO-UV absorption techniques, directly compares the results to probe-sampled data, and compares the resulting NO emission indices including the tunable diode laser results to show agreement within the respective error limits of each measurement technique.

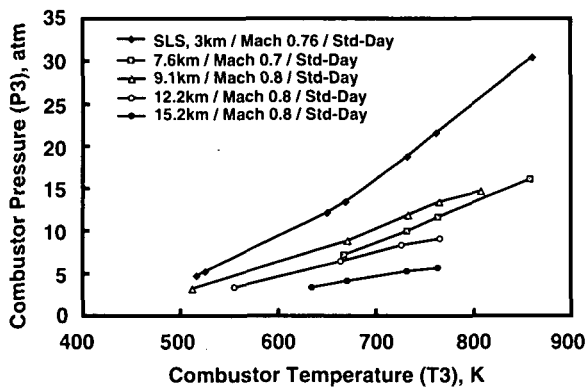


Fig. 1. Combustor pressure versus temperature for all test conditions.

Spectral interrogation of nitric oxide (NO) resonance electronic (A←X) transitions using ultraviolet (UV) absorption allows determination of NO density and, under appropriate conditions, thermodynamic state. NO-UV absorption techniques were developed in the 1970's[2] for measurements of low NO concentrations in gas turbine combustors and engines. These techniques were later modified and enhanced in response to new requirements for nonintrusive quantitative measurements in high-enthalpy test facility flows,[3,4] exhausts of liquid rockets (unpublished), and automobile exhausts.[5] The hardware was made robust and more reliable using spectrometer focal plane array detectors, fiber optics, and pulse-start power supplies for the resonance lamps. The line-by-line radiative transfer model, previously limited to the NO gamma (0,0) band, was extended to include the (0,1) band and thus allowed simultaneous determination of NO number density and ground electronic state-vibrational population distribution (reported as ground-state vibrational temperature) in many of the aforementioned applications. Renewed interest in the effects of turbine-powered aircraft on atmospheric chemistry has again prompted exhaust characterization studies and new requirements for quantitative measurements of NO concentrations in turbine engine exhaust.

## PROBE AND SAMPLING SYSTEMS

Exhaust samples were extracted using a multipoint cruciform rake assembly located near the engine nozzle exit plane with the versatility of single point and multiple probe average sampling. The rake illustrated schematically in Fig. 2 consists of two bars mounted perpendicularly (horizontally and vertically) with each completely spanning the exhaust flow field and beyond. Individual probe sampling allowed spatial mapping of the exhaust core, bypass, and intermediate mixed flow regimes as well as the region surrounding the exhaust which was found to contain low amounts of recirculated exhaust constituents. The horizontal bar also contained alternating Mach number/flow angularity (MFA) and stagnation temperature

* The research reported herein was performed by the Arnold Engineering Development Center (AEDC), Air Force Materiel Command. Work and analysis for this research were performed by personnel of Sverdrup Technology, Inc., AEDC Group, technical services contractor for AEDC. Further reproduction is authorized to satisfy needs of the U. S. Government.

*Paper presented at an AGARD PEP Symposium on "Advanced Non-Intrusive Instrumentation for Propulsion Engines", held in Brussels, Belgium, 20-24 October 1997, and published in CP-598.*

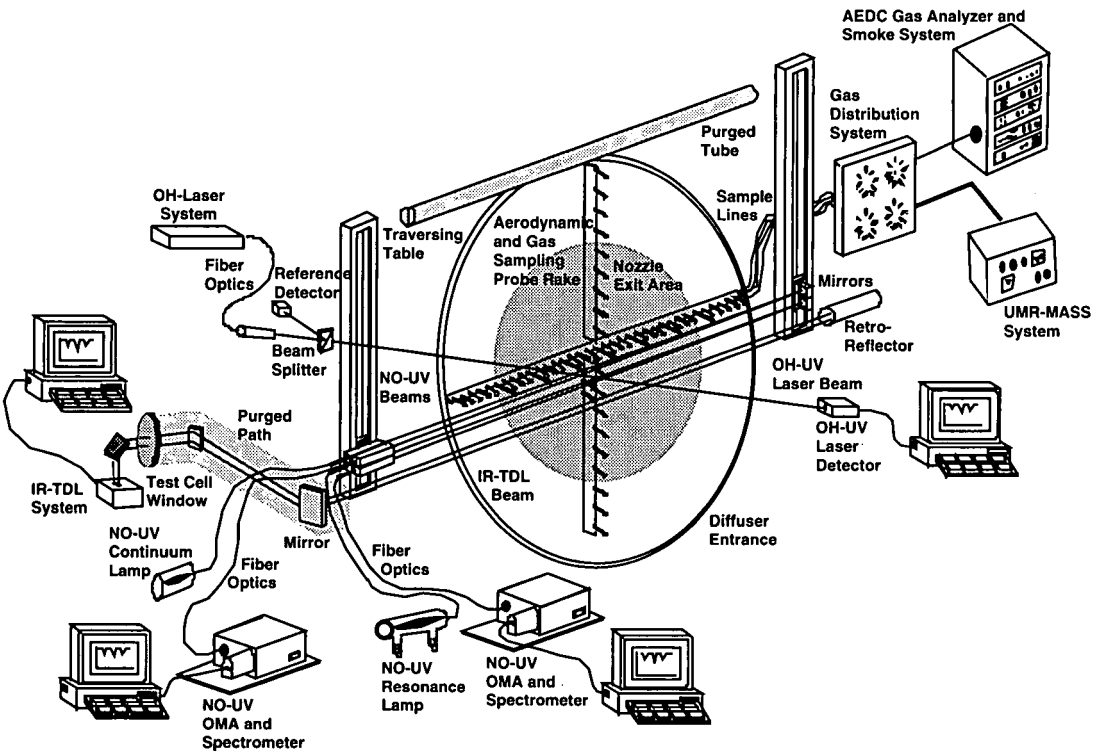


Fig. 2. Illustration of the turbine engine exhaust emissions measurement systems.

probes for determination of static temperature, static pressure, and gas velocity distributions required for analysis of optical data to yield species concentrations and mass fluxes. Construction and design details of each probe type are given in Ref. 1.

Gas samples collected by the rake positioned 12 cm downstream of the nozzle exit plane were passed through heated lines to a heated sample distribution system that allowed any combination of probe samples to be directed to the gas analyzer systems. As necessary during the test period, a stainless steel metal bellows pump was valved in line between the sample distribution system and gas analyzers to raise the sample pressure slightly above atmospheric pressure, a requirement for gas analyzer operation.

A suite of analyzers were used to measure concentrations of gaseous constituents which are reported in parts per million by volume (ppmv). A chemiluminescence analyzer was used to measure concentrations of NO after the sample was passed through a gas sample dryer. The emission index (EI) for NO, defined as mass of constituent per 1,000 pounds of fuel, was calculated according to Ref. 6 and reported as the $NO_2$ equivalent.

## UV ABSORPTION INSTRUMENTATION

The resonance and continuum absorption system components were similar except for radiation sources. The system and technique similarities make it convenient to describe system components, data acquisition, and data analysis for both systems simultaneously while pointing out differences only as necessary. Primary components per measurement system, resonance or continuum, included a lamp, a lamp shutter with an electronic controller, two fiber-optic cables, collimating and focusing optics, a grating spectrometer, an optical multichannel analyzer (OMA®) detector system with a computerized controller, and a personal computer for data acquisition and storage. The systems shared stepper motor-driven slide tables for traversing the optical beams across the exhaust flow field.

The resonance lamp, a source of NO resonant radiation, was a dc excited capillary discharge tube operated at 12 ma using a 5,000-V power supply with a 220-kΩ ballast resistance. A gaseous mixture of argon:nitrogen:oxygen, at a 12:3:1 ratio by volume, was flowed through the lamp tube while maintaining a static pressure of 10 torr. The capillary discharge tube was water cooled to tap water temperatures. Resonance lamp intensity characterization is discussed in the following section. The continuum system lamp was a constant voltage, 100 w, water-cooled deuterium lamp.

Each detector system consisted of a 0.32-m Czerny Turner spectrometer with a variable-width entrance slit, a 2,400 groove/mm grating (used in first order) and an EG&G Princeton Applied Research Model 1421-B silicon diode array detector. Each detector was UV enhanced and intensified over the full 1,024 pixel elements. A detector and detector controller (Model 1461) are referred to as the OMA. The spectral range for the resonance absorption system was 214 to 245 nm with a 0.029-nm-per-detector-element spectral dispersion and 0.16-nm spectral resolution (full-width-half-maximum). Measured normalized instrument response functions representative of single array elements for both the resonance absorption and continuum absorption systems are presented in Fig. 3. Differences are due primarily to spectral resolution differences for the two systems.

The configuration and reported spectral region for the UV continuum absorption measurement deserves explanation. This measurement system had been configured and installed with intentions of measuring OH resonance absorption near 300 nm. During an engine checkout run, this system failed to detect OH absorption. A spectrally scanned UV laser system, successfully installed for measurements of OH, freed this system to be reconfigured for measurements of NO using a spectral continuum

lamp. The optical fibers, excellent for measurements at 300 nm, had a steep attenuation gradient in the region of NO absorption near 226 nm. Lamp radiation saturated the detector in the region of the (0,1) absorption band for detector integration times allowing a sufficient signal-to-noise ratio at the (0,0) band absorption region. Therefore, the less important (0,1) spectral region was moved off the detector to avoid detector damage. Also, the fiber attenuation was too great for meaningful measurements at wavelengths below the (0,0) band. Measurements were performed effectively from 222 to 228 nm with a 0.029-nm-per-detector-element spectral dispersion and 0.21-nm spectral resolution (full-width-half-maximum). As mentioned earlier, measured normalized instrument response functions representative of single array elements are presented in Fig. 3.

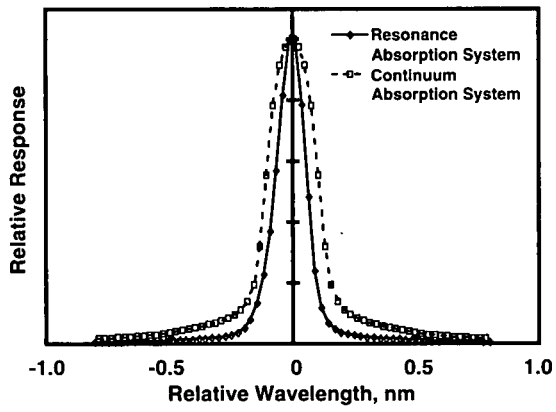


Fig. 3. Instrument response functions relative to the array element center wavelength.

## RADIATIVE TRANSFER MODEL AND RELATED PARAMETERS

A computer model based on the theoretical line-by-line radiative transfer for the NO gamma (0,0) band was used to determine the NO number density from spectral absorption measurements. The theoretical physics of NO molecular absorption, details of the model, and extension of the model from earlier work can be found in the references.[2,3,7,8] A brief overview is presented here to describe and document model parameters used for analysis of the present data. Basically, the fractional lamp radiation within the wavelength interval $\Delta\lambda$ transmitted through a medium of length, L, is given by the equation of radiative transfer,

$$\tau_{\Delta\lambda} = \frac{\sum_j \int_{\Delta\lambda} \left( I_C + I_{\lambda_i^o}(\lambda) \right) e^{-\sum_i \int_L k_{\lambda i}(\lambda) dL} g(\lambda) d\lambda}{\sum_j \int_{\Delta\lambda} \left( I_C + I_{\lambda_i^o}(\lambda) \right) g(\lambda) d\lambda} \qquad (1)$$

where

$g(\lambda)$ =spectral instrument response function,

$k_{\lambda i}(\lambda)$ =molecular absorption transition (line),

$I_{\lambda_i^o}(\lambda)$ =relative intensity of a resonance lamp transition,

$I_C$ =Lamp radiation factor, modeled as continuum radiation.

The interval $\Delta\lambda$ is limited by the spectral extent of $g(\lambda)$, the spectral response for an individual element of the linear array detector given in Fig. 3 for the current measurements. Absorption in the test media is modeled by molecular absorption transitions, $k_{\lambda i}(\lambda)$, which are described by Voigt line profiles that allow for pressure or collision broadening. The summation over i includes all transitions of the NO gamma (0,0) or (0,1) band contributing to absorption within $\Delta\lambda$. The absorption coefficient is a function of the static temperature, static pressure, directed velocity line center shifts (Doppler shifts), line center pressure shift parameter, broadening parameter (discussed later), and NO number density along the measurement path, L. For a single homogeneous path, the flow-field parameters are input to the model, and the NO number density is varied until the calculated [Eq. (1)] and corresponding measured transmittances agree. Calculations were compared to maximum absorption at the second bandhead, 226.23 nm or 236.3 nm, respectively, for the (0,0) and (0,1) bands using the resonance absorption technique and 226.18 nm for the (0,0) band using the continuum absorption technique. As discussed earlier, the (0,1) band was not measured with the continuum absorption system.

Absorption media line center shifts with respect to the fixed lamp radiation line positions are important to the NO densities derived from the model. Two shift mechanisms are modeled. However, Doppler shifts were negligible for these measurements due to small exhaust flow velocity components in the direction of the source beam. Collision-induced shifts were modeled according to the collisional shift parameter, $\delta = -0.18*(295/T)^{0.56}$, as quantified in Ref. 9. Here "P" is static pressure in atmospheres and "T" is static temperature in Kelvin.

The resonance lamp radiates several lines within, or contributing to, the spectral interval $\Delta\lambda$ of Eq. (1). Line intensities, $I_{\lambda_i^o}(\lambda)$, are modeled by Doppler profiles broadened to 950 K. The relative lamp line intensities were measured and characterized according the upper state population distribution shown in Fig. 4. Results for the (0,0) and (0,1) bands were similar as expected, since the upper states are common to both bands. The lamp emits low-level radiation ($I_C$) in addition to gamma band radiation. This radiation was not directly quantifiable from lamp characterization measurements, but was modeled as constant continuum radiation, $I_C$, over the spectral range $\Delta\lambda$, [Eq. (1)], with excellent results.

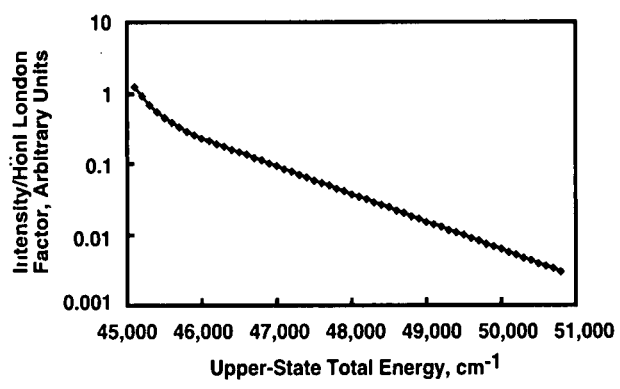


Fig. 4. Reasonance lamp line intensity distribution.

The lamp radiation for the continuum absorption technique was modeled as a simple spectral constant, achieved in Eq. (1) by setting, $I_{\lambda_i^o}(\lambda)$, to zero and $I_C$ to some arbitrary constant value.

For the resonance technique, the molecular broadening parameter, $a' = C*P/T^n$, and $I_C$ have been treated as instrument-dependent calibration factors[3] selected to minimize differences

in calculated and measured transmittances at controlled laboratory conditions. Here, "C" is referred to as the broadening constant and "n" the temperature dependency exponent. The broadening parameter, $a' = 31800*P/T^{1.5}$, was reported in 1981[7] but did not include a low-level lamp radiation factor, $I_C$. When this technique was reinstated in the late 1980's using the intensified array detector and a modified electronic lamp power supply, the radiative transfer model required a factor $I_C = 22$ (relative to the arbitrary scale used in Fig. 4) to accurately match laboratory-measured transmittances down to 0.2. Without $I_C$, the model predicted transmittances accurately down to about 0.8 but underpredicted at lower transmittances with increasing deviation. Since $I_C$ had little effect on transmittance calculations above 0.8, a′ was determined from a wide range of laboratory conditions (P, T, and NO number density) approximately independent of $I_C$. The results for a′ were consistent with the 1981 reported value. Also, a two parameter nonlinear least-squares fit to all the laboratory data with the temperature exponent, n, fixed at 1.5 gave $I_C \approx 22$ and, again, a′ consistent with the 1981 values. The study concluded that radiative transfer model calculations and laboratory data were in excellent agreement over the full range of laboratory conditions for $I_C = 22$ and $a' = 31800*P/T^{1.5}$. In recent years, the broadening parameters for individual lines have been measured directly[9] and reported as $a' = 6927*P/T^{1.25}$. It is both important and gratifying that this agrees extremely well with $a' = 31800*P/T^{1.5}$. Using the Ref. 9 value in the model, $I_C = 22$ was still the best fit value. Relative to the Fig. 4 lamp characterization values, $I_C$ and a′ were approximately equivalent for both the (0,0) and (0,1) bands.

The instrument-dependent code calibration parameter, a′, was determined independently for the continuum absorption system using continuum lamp transmittance measurements over a similar range of laboratory measurements. For the continuum absorption system, the broadening constant C = 23,250 provided the best overall fit to laboratory data with the temperature-dependency exponent, n, fixed at 1.5.

A radial inversion scheme, referred to as an onion peel technique, coupled to the line-by-line radiative transfer model, was used to determine radial profiles of NO number density from a series of line-of-sight (LOS) measurements at several radial locations during a steady-state test condition, as illustrated in Fig. 5. The flow field was modeled as concentric "homogeneous" zones, one for each LOS measurement. The NO density in the outer zone was determined using the outermost LOS measurement. Stepping inwardly, a new zone NO density was determined for each successive measurement. The static temperature and static pressure along the optical path were inferred from probe measurements as discussed in Ref. 1. Probe measurements at similar radial positions on opposite sides of the plume centerline were averaged and radial symmetry was assumed. Measurements of ambient test cell static temperature were assigned to positions beyond the lip of the diffuser and ambient pressure assigned to radial positions just beyond the nozzle exit radius, Re = 30 cm. Radial distance was normalized to the nozzle exit radius so that the extent of the engine exhaust was R/Re = 1.0 or a little beyond, depending upon exhaust expansion for each test condition. The probe measurement grid was sparse; thus, interpolation was required to determine the path average static temperature, static pressure, and axial flow velocities for each homogeneous zone along each LOS measurement path. Averages were area weighted over the width of the optical beam within respective zones. Figure 6 shows representative plots of zone-averaged temperature, pressure, and the axial component of velocity for an LOS through the center of the exhaust. Values inferred from probe measurements used to determine the zone averages are superimposed on the plot. These data were

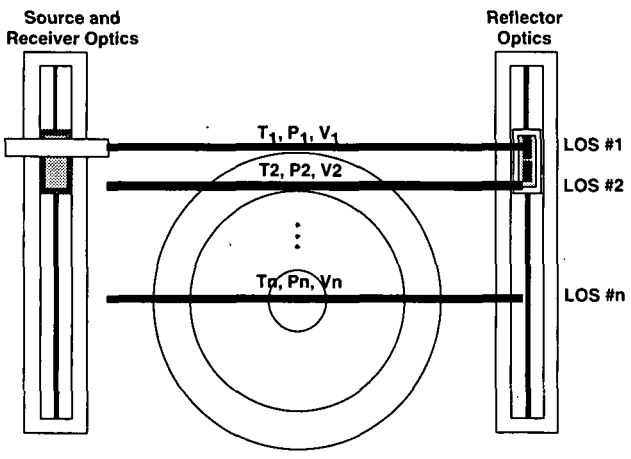


Fig. 5. Measurements through homogeneous zones.

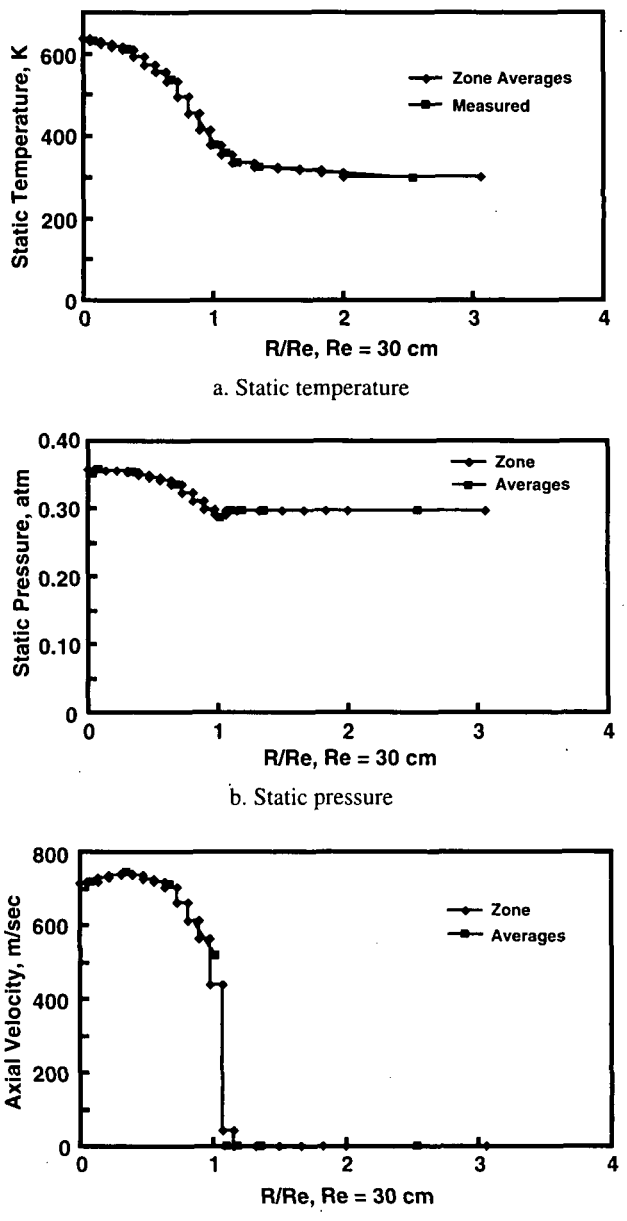


a. Static temperature

b. Static pressure

c. Velocity

Fig. 6. Measured and zone-averaged optical path characterization profiles.

acquired for the steady-state engine test condition described by the combustor inlet temperature 733 K at 9.15 km altitude. The zone path segments are obvious in the plot with approximately 2.54-cm (1.0-in.) lengths from the center to just outside the exhaust flow field and about 5.08 cm segment lengths in the test cell gas recirculation region. Zones beyond the nozzle exit radius represent measurements through the test cell air which contained small quantities of recirculated exhaust gases.

## TEST CELL INSTALLATION AND MEASUREMENTS

The placement of the NO-UV instrumentation and optical beam paths relative to other measurement and facility components in the test cell are illustrated in Fig. 2. The lamp radiation was transmitted through a 400-μm-diam, 9-m-long, fused silica fiber to a collimating lens mounted onto a traversing table near the engine exhaust. The radiation was imaged through the exhaust to an aluminum-surfaced mirror mounted on a second traversing table and reflected back through the exhaust to a second lens-fiber combination also mounted on the first traversing table. The beam diameter was approximately 2 cm. The transmitted and reflected beams were within the first 12 cm downstream of the nozzle exit plane. The resonance lamp beam was 6.35 cm above that of the continuum lamp. The reflected radiation was transmitted to the entrance slit of the spectral detector system. All optical lenses and fibers were made of UV-grade fused silica.

In addition to measurements through the exhaust, LOS measurements were made at several positions outside the exhaust flow field to quantify and account for the presence of NO in the test cell due to recirculated exhaust gases. Low levels of NO over rather long paths can have a significant effect on the optical measurements. A tube purged with dry nitrogen mounted at the top of the diffuser allowed measurements of reference spectra for each set of measurements across the exhaust flow field. For data analysis, cylindrical symmetry was assumed for recirculated gas components surrounding the exhaust flow field.

The slide tables traversed the collimated beam across the flow field in a plane parallel to the nozzle exit plane, as illustrated in Figs. 2 and 5. Each set of traversed data for the resonance absorption system consisted of measurements through the purged path at the top of the diffuser (with and without the shutter closed) and measurements at fixed radial positions from R = 70 to 36 cm in 5.08-cm increments and from R = 36 to 0 cm in 2.54-cm increments. The nozzle exit radius was 30 cm. The set of continuum absorption measurement positions were offset about 6.35 cm below the resonance absorption measurements, except for measurements through the purged tube. A traversing system output voltage (high during movement and low while stationary) was monitored by each OMA system for posttest determination of spectra acquired while the tables were in motion.

During earlier engine checkout runs, measurements made while the lamp was shuttered were found to be indistinguishable from background signal levels. Therefore, acquisition time was significantly reduced by not shuttering the lamp except at the centerline position. These centerline data were used to verify that exhaust radiation levels were negligible for each engine condition. It is also significant that measurements were not affected by test cell lighting. Background levels, measured with the lamp shuttered, were almost entirely integrated detector noise as discussed in OMA operation manuals.

## DATA REDUCTION

Spectral lamp transmission measurements, $I_T(\lambda_i)$, at a particular LOS (radial) position were reduced to spectral transmittance according to the equation

$$\tau_i = \frac{I_T(\lambda_i) - I_e(\lambda_i)}{I_0(\lambda_i) - I_b(\lambda_i)} \approx \frac{I_T(\lambda_i) - I_b(\lambda_i)}{I_0(\lambda_i) - I_b(\lambda_i)} \qquad (2)$$

where $\lambda_i$ denotes the spectral center of the $i^{th}$ element of the detector array. $I_0(\lambda_i)$ and $I_b(\lambda_i)$, respectively, are measurements of lamp reference and background at the purged path location. As mentioned earlier, measurement of lamp-shuttered signal levels at the exhaust, $I_e(\lambda_i)$, were indistinguishable from background, so $I_e(\lambda_i)$ can be approximated by $I_b(\lambda_i)$. Lamp and transmittance spectra (background subtracted) are presented in Figs. 7 and 8 for the resonance and continuum absorption systems, respectively. Prominent NO gamma band regions are labeled in the figures. Absorption features at the (0,0) band are readily evident, but further corrections were necessary to remove position-dependent lamp signal variations and attenuation effects of the exhaust and gas recirculation. These effects are exhibited as overall attenuation at spectral regions away from the (0,0) band absorption feature. A curve fit through spectral regions just above and below the (0,0) band feature served as the base line to quantify (0,0) absorption as illustrated by the "corrected" curve in Figs. 7b and 8b. Thus, the transmittance at the second bandhead of the NO gamma (0,0) band can be read directly from the "corrected" curves.

Previously, spectral bandhead transmittances were determined using pretest lamp reference spectra acquired at each radial position and then corrected for test media attenuation

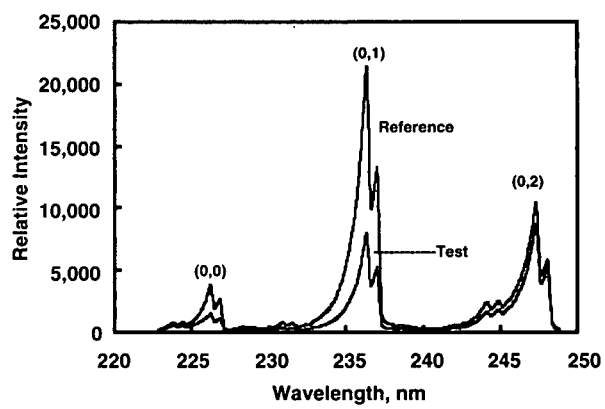


a. Lamp spectra

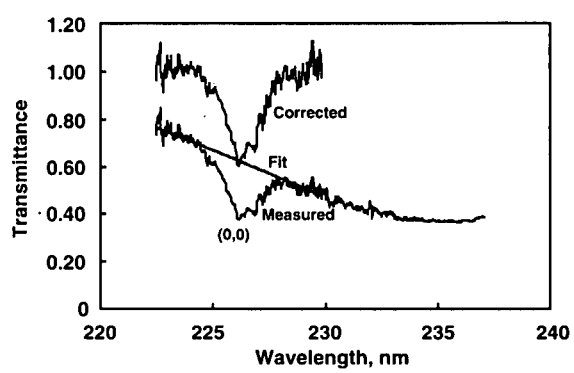


b. Spectral transmittance

Fig. 7. Resonance absorption system spectral data.

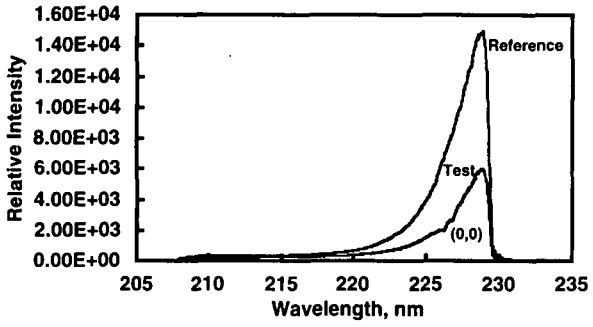


a. Lamp spectra

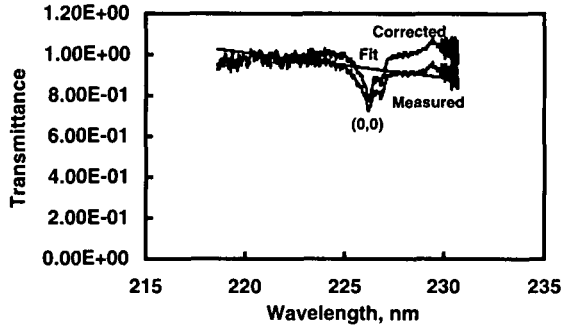


b. Spectral transmittance

Fig. 8. Continuum absorption system spectral data.

effects. Data were reduced both ways and gave equivalent results; i.e., differences in second bandhead transmittances from the two processes were far less than the statistical uncertainties. The purged path allowed an independent measure of lamp reference per data set and all the advantages that go with measuring lamp reference spectra within seconds of acquiring transmission measurements. Statistical uncertainty is discussed later.

Resonance absorption system radial profiles of (0,0) second bandhead transmittance, acquired at the five steady-state engine power settings at 9.1-km altitude, are shown in Fig. 9a. These

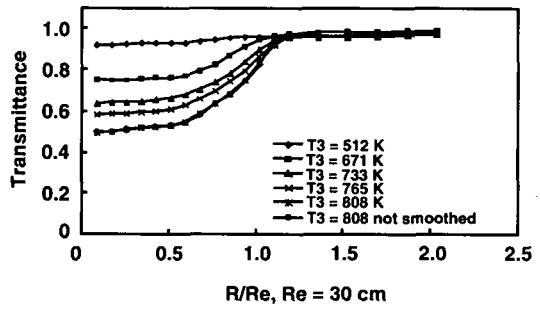


a. Resonance absorption system

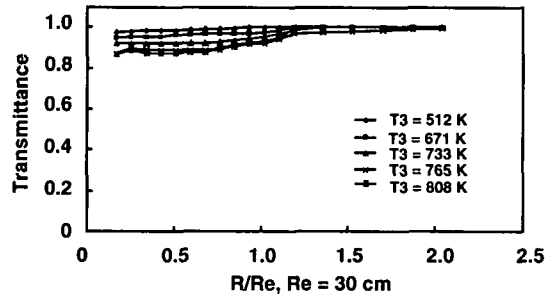


b. Continuum absorption system

Fig. 9. Radial profiles of (0,0) transmittance at 9.1-km altitude.

profiles were smoothed using a linear 3-point smoothing algorithm before insertion into the radial inversion scheme. Representative effects of the smoothing algorithm are illustrated by the smoothed and unsmoothed transmittance profiles in the figure for T3 = 808 K. Although random-like variations were reduced, changes in transmittance values were generally much smaller than statistical measurement uncertainty. Several sets of transmittance profiles acquired at the same steady-state engine condition were extremely repeatable, with smaller variations than statistical measurement uncertainty. The multiple transmittance profiles acquired during a steady-state test condition were averaged before application of the radial inversion scheme.

Continuum absorption system radial profiles of second bandhead (0,0) transmittance, also acquired at the five engine power settings at 9.1-km altitude, are presented in Fig. 9b. Comparing these profiles with resonance absorption profiles of Fig. 9a, it is obvious that the continuum absorption system was less sensitive to equivalent NO densities at the same test conditions. Additionally, continuum absorption was not observed for several low-power engine settings which produced relatively low NO densities. Preliminary results on selected data sets indicate higher uncertainties than results obtained from the resonance absorption data.

The higher-quality and more complete resonance absorption data were analyzed and are reported herein.

## ANALYSIS AND RESULTS

The radiative transfer model, [Eq. (1)], incorporated into the onion peel radial inversion scheme was applied to radial transmittance profiles for each steady-state engine test condition. Static temperature and pressure profiles required for the radiative transfer model were inferred from probe and facility measurements and averaged along "homogenous" zones for each LOS optical path. The analysis provides radial NO number density (molecules per volume) profiles. For a more direct comparison to probe sampling measurement profiles, radial NO-UV number density ($cm^{-3}$) profiles were converted to volumetric fractions (ppmv) using the ideal gas law. Profile comparisons are presented in Figs. 10 - 12 for the same combustor temperature setting, T3 ≈ 733 K, at three different altitudes, 3.1, 9.1, and 12.2 km, respectively. The NO-UV densities tend to be similar in shape to the sampling measurements, but lower by 10 percent for 9.1 and 12.2 km, and about 18 percent for SLS. The stronger deviation might be expected at higher engine power settings for the SLS condition because of the combined effects of greater quantities of NO recirculation in the test cell and pos-

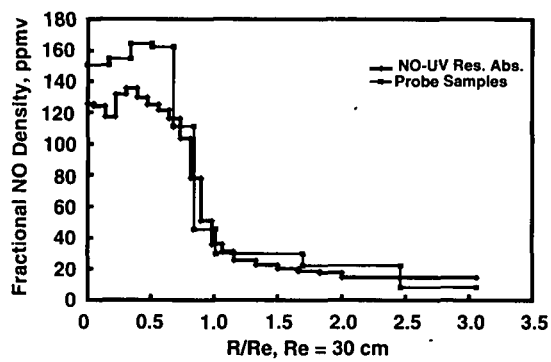


Fig. 10. Resonance absorption and probe sampling radial profiles of NO density for T3 = 733 K and sea-level-static (3-km) altitude.

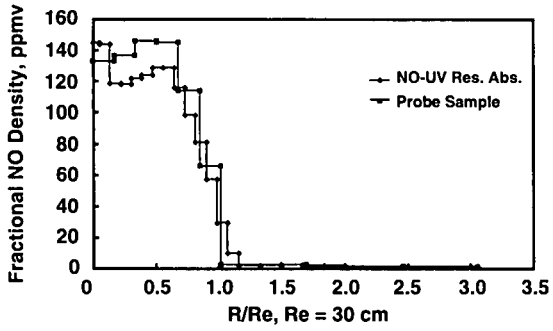


Fig. 11. Resonance absorption and probe sampling radial profiles of NO density for T3 = 733 K and 9.1-km altitude.

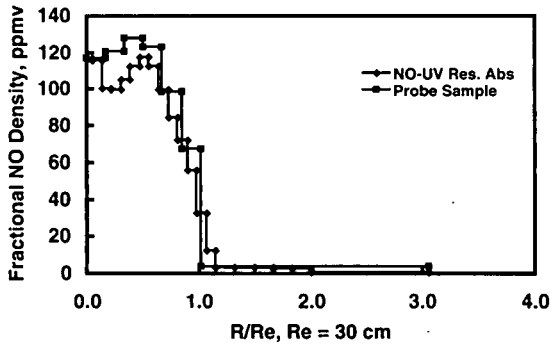


Fig. 12. Resonance absorption and probe sampling radial profiles of NO density for T3 = 733 K and 12.2-km altitude.

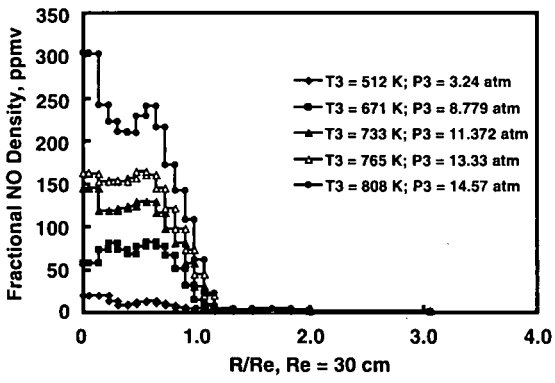


Fig. 13. Resonance absorption radial profiles of NO density for all combustor temperatures at altitude = 9.14 km.

sible non-radial symmetries (especially top to centerline) in the recirculation region. Figure 13 shows NO density profiles for each engine power setting at the 9.14-km altitude.

Direct comparisons of density profiles were limited to the few test conditions for which spatial probe sampling profiles were measured. For comparisons over the full set of test conditions, emission indices were calculated from NO-UV resonance absorption density profiles, aerodynamic flow-field properties derived from the rake data, and fuel flow rates measured by the test facility. An NO emission index EI(NO) using the molecular weight of $NO_2$ was determined for each engine condition according to

$$EI(NO) = \frac{1000 * M_{NO_2}}{N_A * (\text{fuel flowrate})} \left( \sum_j (n_{NO})_j \right) V_{x_j} A_j \quad (3)$$

where $N_A$ is Avagadro's number, and $M_{NO_2}$ is the gram molecular weight of $NO_2$. The quantities $n_{NOj}$ and $Vx_j$ are zone averaged NO number density and exhaust velocity, respectively, and $A_j$ is the cross-sectional zone area at the measurement axial station. These EI(NO) values are presented in Figs. 14 - 18, and are compared to probe sampling and infrared tunable-diode laser technique results. Measurements from all three measurement systems agree within respective uncertainty bands.

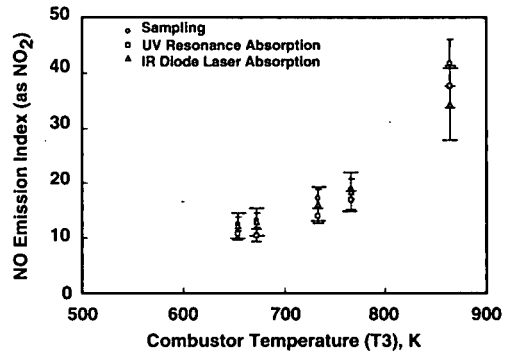


Fig. 14. Comparisons of EI(NO) at simulated sea-level-static condition.

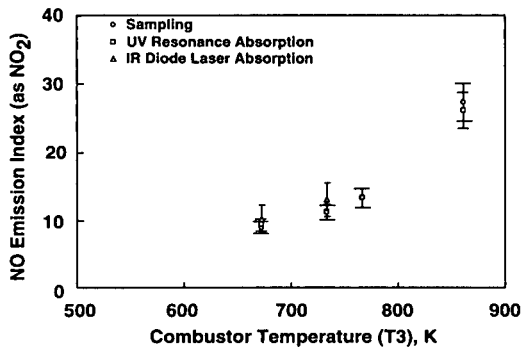


Fig. 15. Comparisons of EI(NO) at 7.6-km altitude.

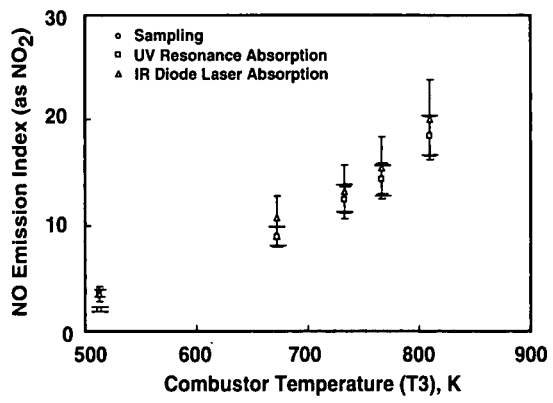


Fig. 16. Comparisons of EI(NO) at 9.1-km altitude.

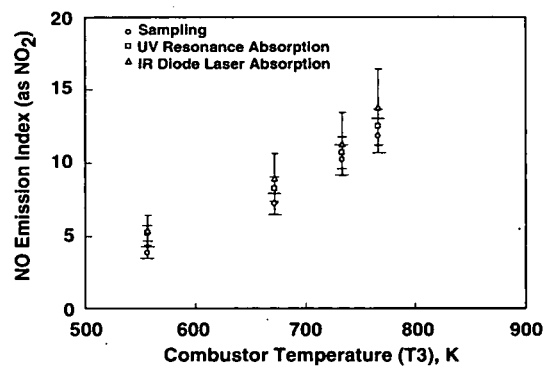


Fig. 17. Comparisons of EI(NO) at 12.2-km altitude.

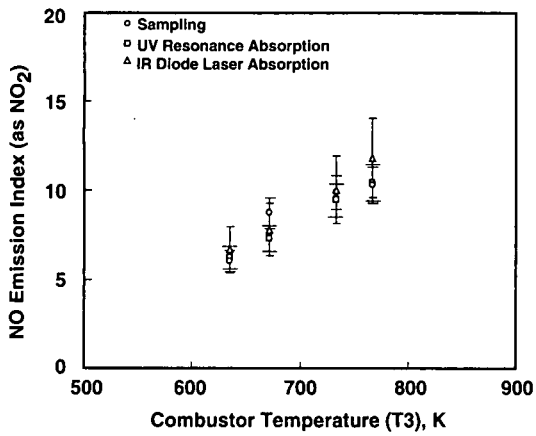


Fig. 18. Comparisons of EI(NO) at 15.2-km altitude.

UV EI(NO) measurements were in good agreement with probe sampling data, matching well within respective uncertainty bands. A contribution of uncertainty not addressed in these comparisons relates to aerodynamic flow-field properties determined from the rake probe data. As mentioned, total temperature and Mach flow-angularity probes were sparsely spaced, providing a coarse definition of property profile gradients. The slow-varying nature of these properties across the exhaust flow field provides confidence in values reported, except near the edge of the plume, where changes are more abrupt and the gradient steepens, especially in velocity. The uncertainty in the position at which the velocity drops abruptly to the ambient static condition outside the plume may be a major contributor to differences in EI reported by sampling and optical techniques.

An engineering statistical analysis process described in Ref. 10 was applied to steady-state test conditions for which several sets of measurements were obtained to establish confidence bands for the NO-UV resonance absorption results. Lamp reference and position-wise lamp transmission spectra were treated as independent measurements with random statistical uncertainty. The variance-covariance matrix developed for a set of profile transmittances accounted for codependency on lamp reference spectra, curve-fit correction factors, and the linear smoothing algorithm. Measurement uncertainty and a matrix of partial derivatives of NO number density with respect to transmittance for each zone of each LOS measurement path produced one-sigma variances for NO number densities at each radial location per set of data. Independently, statistical analyses were performed on these multiple data sets acquired at steady-state engine conditions, treating each set of spatial transmittances as independent measurements with random uncertainty. The resulting uncertainty in NO number density was similar. This tends to validate assumptions used for the lengthy and tedious engineering statistical analysis process[10] required for single data sets obtained for many of the steady-state engine conditions.

The position-wise NO number density uncertainties within the exhaust flow for several test conditions investigated ranged from ± 6 to 18 percent, with the higher uncertainties relating to data at higher combustor temperatures for the simulated sea-level-static condition. Statistical uncertainty on position-wise NO densities determined for the recirculation flow region were on the order of ± 15 to 25 percent. Statistical uncertainty for NO emission indices ranged from ± 7 to 13 percent assuming accurate velocities from the rake data.

For completeness, resonance absorption was also observed at the (0,1) band for a limited number of the higher combustor temperature conditions. NO densities determined from the (0,1) data are consistent with (0,0) results, but with larger uncertainties attributable to a greater sensitivity on static temperature.

## SUMMARY AND CONCLUSIONS

NO-UV resonance absorption measurements were performed at all test conditions consisting of several engine power settings at simulated altitudes ranging from sea-level-static to 15.2-km static. At an axial position within 12 cm of the nozzle exit plane, spectral transmission measurements at multiple radial stations across the exhaust plume flow field and surrounding region containing low-level recirculated exhaust gases were radially inverted to provide radial profiles of NO number density. Radial NO number density profiles in units of cubic centimeters were converted to radial profiles of NO concentrations in units of parts per million by volume and, subsequently, to NO emission indices. Radial profiles of static temperature, static pressure, and exhaust flow velocity inferred from probe rake data were utilized for analyses of the optical data.

The NO-UV measurement system proved to be reliable and robust. Measurements were extremely repeatable during steady-state test conditions, also indicating temporal stability of engine steady-state operation and test facility parameters. NO-UV radial concentration profiles agreed well (within uncertainty limits) with probe sampling measurements, both within the exhaust flow field and the surrounding gas recirculation regions. The NO-UV concentrations tended to have lower peak levels within the exhaust plume region. Greater deviations were expected in comparisons of NO emission indices due to the lack of spatial detail defining the velocity gradient near the edge of the plume. However, NO emission indices determined from NO-UV profile concentrations deviated only a few percent from the probe sampling results.

The NO-UV resonance absorption provided redundancy in NO concentration measurements with a technique independent of the extractive sampling system. Agreement among the two techniques gives confidence that the extracted sample reaching the analyzer was indeed representative of the exhaust gases, as well as validating the optical technique over this range of measurement conditions.

Agreement with the single line-of-sight tunable diode laser technique results are gratifying, but analyses of those data relied upon normalized spatial distribution profiles of NO from either the probe sampling or NO resonance absorption profiles. Traversing the TDL beam or directly comparing the TDL NO measurement with a similar TDL $CO_2$ along the same line of sight, as discussed in Ref. 1, would greatly enhance the utilization of that technique and provide a more meaningful comparison.

## REFERENCES

1. Howard, R. P., et al., "Experimental Characterization of Gas Turbine Emissions at Simulated flight Altitude Conditions," AEDC-TR-96-3 (AD-314312), September 1996.

2. Few, J. D., McGregor, W. K., and Glassman, H. N., "Resonance Absorption Measurements of NO Concentration in Combustor Exhausts," AIAA Progress in Astronautics and Aeronautics-Experimental Diagnostics in Gas Phase Combustion Systems, B.T. Zinn, ed., AIAA Press, Princeton, NJ, 1977.

3. Howard, R. P., Dietz, K. L., McGregor, W. K., and Limbaugh, C. C., "Nonintrusive Nitric Oxide Density Measurements in the Effluent of Core-Heated Airstreams," AIAA 21st Fluid Dynamics, Plasma Dynamics and Lasers Conference, AIAA-90-1478, June 18-20, 1990, Seattle, WA.

4. Roberts, W. L., et. al., "Measurement and Prediction of Nitric Oxide Concentration in the HYPULSE Expansion Tube Facility," 18th AIAA Aerospace Ground Testing Conference, June 20-23, 1994, Colorado Springs, CO.

5. Howard, R. P. and Phillips, W. J., "UV Absorption Technique for Monitoring Mobile Source NO Emissions," 86th Annual Meeting & Exhibition, June 14-18, 1993, Denver, CO.

6. "Procedure for the Calculation of Gaseous Emission from Aircraft Turbine Engines," SAE ARP1533, April 30, 1982.

7. Few, J. D. and Lowry, III, H. S., "Reevaluation of Nitric Oxide Concentration in Exhaust of Jet Engines and Combustors," AEDC-TR-80-65 (AD-A103118), August 1981.

8. Davis, M. G, McGregor, W. K., and Few, J. D., "Utilizing the Resonance Line Absorption Technique to Determine the Collisional Broadening Parameters of a Diatomic Molecule: NO γ-Bands as an Example," *Journal of Quantative Spectroscopy and Radiative Transfer*, Vol. 16, No. 12, December 1976, pp. 1109-1118.

9. Chang, A. Y., DiRosa, M. D., and Hanson, R. K., "Temperature Dependance of Collision Broadening and Shift in the NO A←X (0,0) Band in the Presence of Argon and Nitrogen," *Journal of Quantitative Spectroscopy and Radiative Transfer*, Vol. 47, No. 5, pp. 375-390, 1992.

10. Limbaugh, C. C., "An Uncertainty Propagations Analysis for an Infrared Band Model Technique for Combustion Gas Diagnostics,"AEDC-TR-76-155 (AD-A038063), April 1977.

Paper 10
Author: Howard

Q:

Your discussion referred to combustor inlet temperatures. It would be advantageous to report combustion exit temperatures for exhaust emission correlations and the modelling of emissions from combustor exit to engine exit.

A: Data reported were acquired on a military engine. Combustor temperatures are not measured explicitly. Combustor exit temperatures must be determined from the engine cycle deck. Release would require Air Force approval, which would first require a formal request.

Q:

You mentioned that the NO resonance lamp measurements are more sensitive to NO concentrations than the NO continuum lamp. Please explain further.

A: NO-UV resonance absorption refers to a measurement technique deducing NO concentrations from the absorption of resonance lamp radiation emitted from NO molecules and thus corresponding to absorption line frequencies within the flow field.

NO-UV continuum absorption refers to a measurement technique deducing NO concentrations from the absorption of spectral-continuum radiation emitted from a deuterium lamp. Since radiation from this lamp is not absorbed at frequencies between NO absorption lines, the integrated detector signal ($\approx$ 1.5 A° resolution) contains much lamp radiation that cannot be absorbed by the flow field. Very high resolution (<0.05 A°) detection would approach the sensitivity of the resonance technique, but would greatly complicate the measurement, in that it would measure rotational structure rather than the vibrational structure.

# LASER-2-FOCUS MEASUREMENTS ON A TURBINE CASCADE WITH LEADING EDGE FILM COOLING

**S. Ardey[1], L. Fottner[1], M. Beversdorff[2], H. Weyer[2]**

[1]Institut für Strahlantriebe, Universität der Bundeswehr
Werner Heisenberg Weg 39, D-85577 Neubiberg, Germany
[2]DLR Institut für Antriebstechnik
Postfach 90 60 58, D-51140 Köln, Germany

## ABSTRACT

In order to increase the understanding of the aerodynamic processes dominating the flow field of turbine bladings with leading edge film cooling, isothermal investigations were carried out on a large scale high pressure turbine cascade. Close to the stagnation point the turbine cascade has one row of film cooling holes on the suction side and another one on the pressure side. Blowing ratio, turbulence intensity, Mach number and Reynolds number are set to values typically found in modern gas turbines. Since a very sensitive flow pattern with high velocity gradients and reverse flow areas was to be expected near the blowing holes the Laser-2-Focus technique was selected for investigations in this area.

Two independent systems were used: A standard two dimensional Laser-2-Focus system permanently installed in the wind tunnel and a temporarily set up three dimensional Laser-2-Focus system of the DLR-Institut für Antriebstechnik, Köln.

The results of the two systems are in good agreement. They indicate vortices in the exit plane of the film cooling holes developing into a flow pattern with upwinds directly behind the holes and downwinds further downstream. In the wake of the pressure side holes a large recirculation zone can be observed located below the coolant jet.

## NOMENCLATURE

| | | |
|---|---|---|
| A | [mm$^2$] | area |
| D | [mm] | hole diameter |
| G | [m/s] | magnitude of the velocity vector |
| L | [mm] | chord length |
| $l_H$ | [mm] | hole length |
| M | [-] | blowing ratio (= $(\rho G)_c/(\rho G)_1$) |
| Ma | [-] | Mach number |
| P | [mm] | pitch of the holes |
| p | [hPa] | static pressure |
| Re | [-] | Reynolds number (Re = (G L)/ν) |
| s | [mm] | coordinate along the blade surface |
| T | [K] | temperature |
| Tu | [%] | turbulence intensity |
| U | [m/s] | velocity parallel to the surface (x) |
| V | [m/s] | velocity normal to the surface (y) |
| W | [m/s] | velocity in lateral direction (z) |
| x | [mm] | coordinate parallel to the blade surface |
| y | [mm] | coordinate normal to the blade surface |
| z | [mm] | coordinate in lateral direction |
| β | [°] | flow angle in circumferential direction |
| γ | [°] | injection angle in streamwise direction |
| Δ | [ ] | difference |
| κ | [-] | ratio of specific heats |
| ν | [m$^2$/s] | kinematic viscosity |
| ρ | [kg/m$^3$] | density |

### Subscripts

| | |
|---|---|
| c | cooling (secondary) air |
| H | referenced to the cascade inlet conditions |
| is | isentropic |
| K | tank conditions |
| Pl | plenum chamber conditions |
| PS | pressure side |
| SS | suction side |
| t | total (stagnation) |
| 1 | upstream of the cascade |
| 2 | downstream of the cascade |

### Abbreviations

| | |
|---|---|
| HGK | High Speed Cascade Wind Tunnel (Hochgeschwindigkeits-Gitterwindkanal) |
| L2F | Laser-2-Focus |
| 2D | two dimensional |
| 3D | three dimensional |

## 1. INTRODUCTION

The negative environmental effects caused by the exhaust gas of turbine engines can be diminished by reducing the specific fuel consumption. This requires to increase the cycle efficiency by better component-efficiencies, higher pressure ratios and raised turbine inlet temperatures. Currently turbine blades of high temperature material with internal cooling systems can stand up to about 1500 K. Beyond this limit additional film cooling by the ejection of air from inside the blade is necessary. Thermal and aerodynamic efficiency of film cooling must be balanced in order to optimize the over-all effectiveness. Special care has to be taken for the design of leading edge film cooling because the temperature reaches the stagnation level and the flow field shows high bending and velocity gradients.

In order to better understand the aerodynamic effects occurring in the mixing zone of the coolant and the main stream flow different test set-ups are used ranging from simple geometries as flat plates and cylinders to complete test rigs. There is always a trade-of to be made in between having a good spatial resolution and meeting realistic engine conditions.

All test set-ups share one problem: Introducing any kind of probe into the crucial mixing area with its high gradients will

*Paper presented at an AGARD PEP Symposium on "Advanced Non-Intrusive Instrumentation for Propulsion Engines", held in Brussels, Belgium, 20-24 October 1997, and published in CP-598.*

change the flow pattern. Depending on the probe size, its influence on the measured results can be severe. Therefore only non-intrusive measurement techniques may be used to determine the flow field in the immediate vicinity of the coolant ejection.

Observing the flow pattern of a leading edge film cooling configuration is even more difficult because coolant and main stream flow have about opposite directions. By mixing they create a turbulent flow field that is highly three dimensional and yields circumferential flow angles which may cover a full 360°-span.

The above mentioned aims and problems can be met effectively by using the Laser-2-Focus (L2F) technique for measurements in the jet exit area of a leading edge film cooling configuration. Because a three dimensional flow pattern is expected the L2F system should preferably have 3D capability. Nevertheless even two dimensional flow field data can help to understand the mixing process of coolant and main stream flow.

The experimental investigations on a large scale turbine cascade with leading edge film cooling presented in this paper focus on the data measured with a 2D-L2F system and a 3D-L2F system in the near hole region. Additional data on this cascade obtained by different measurement techniques can be found in a paper by Ardey and Fottner (1997).

## 2. EXPERIMENTAL SET-UP

### Turbine Cascade

The experimental investigations were carried out on a large scale high pressure turbine cascade named AGTB. The cascade consists of three blades with a maximized chord length in order to reach a high spatial resolution while still maintaining periodicity. Solely the center blade was used for the measurements. The aerodynamic and geometric data of the cascade are listed in Tab. 1.

GEOMETRY

| | | | |
|---|---|---|---|
| Chord Length: | 250 mm | Blade Height: | 300 mm |
| Pitch/Chord Ratio: | 0.714 | Stagger Angle: | 73° |

AERODYNAMICS

| Inlet: | | | Exit: | | |
|---|---|---|---|---|---|
| $Ma_1$ | = | 0.37 | $Ma_{2is}$ | = | 0.95 |
| $Re_1$ | = | 370000 | $Re_{2is}$ | = | 695000 |
| $\beta_1$ | = | 133° | $\beta_2$ | = | 28.3° |

Table 1: Design data of the turbine cascade AGTB

In order to simulate film cooling the blades are manufactured to have a plenum chamber inside which can be connected to a secondary air supply. One row of film cooling holes is located on the suction side and one on the pressure side near the stagnation point. The holes are aligned along the whole blade height. They are fed by the plenum and inject the secondary air into the main stream flow of the cascade. This blowing configuration named B1 is shown in Fig. 1 and its data are given in Tab. 2.

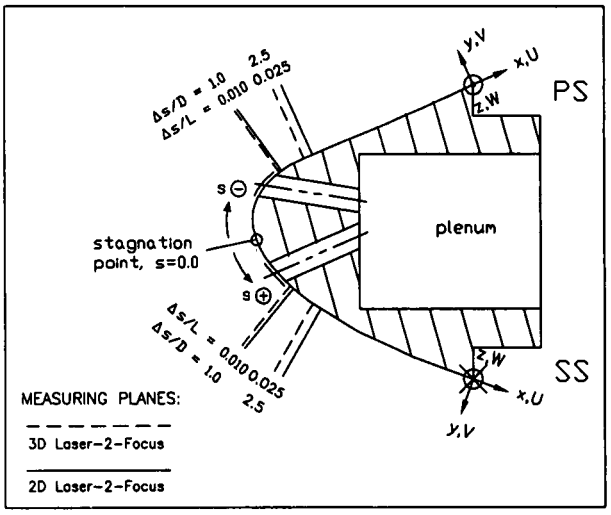


Figure 1: Leading edge of the turbine blade AGTB-B1

| | | | | | |
|---|---|---|---|---|---|
| $s/L_{SS}$ | = | 0.02 | $s/L_{PS}$ | = | - 0.03 |
| $\gamma_{SS}$ | = | 110° | $\gamma_{PS}$ | = | 120° |
| D/L | = | 0.012 | P/D | = | 5 |
| $D/l_H$ | = | 0.24 | $A_{c,(SS+PS)}/A_1$ | = | 0.00722 |

Table 2: Design data of the blowing configuration B1

### High Speed Cascade Wind Tunnel

The experiments were carried out in the High Speed Cascade Wind Tunnel of the Universität der Bundeswehr, München (Fig. 2).

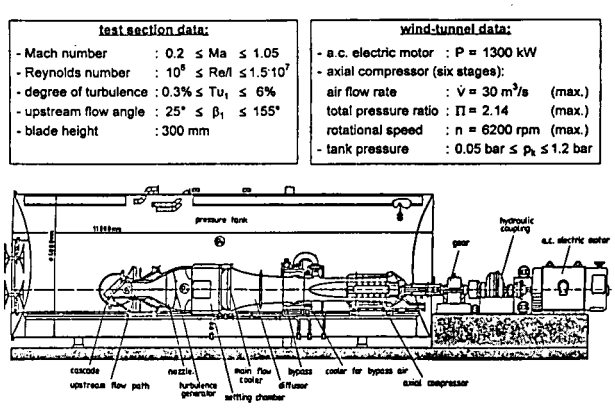


Figure 2: High Speed Cascade Wind Tunnel

This facility operates continuously in a large pressurized tank. The total temperature is kept constant and was set to 303 K for the AGTB-B1. Setting the compressor speed and the pressure level inside the tank allows for the independent variation of Mach number and Reynolds number. The

turbulence intensity in the test section can be varied using different turbulence generators in front of the nozzle. In this case it was set to 5 %.

The secondary air is supplied by a separate screw compressor which compresses air from the tank and is working in a closed circuit on the same pressure level as the test facility. A cooler adjusts the temperature of the secondary air in order to maintain isothermal conditions.

Figure 3 shows the test section of the wind tunnel with the AGTB-B1 turbine cascade. Adjustable guide vanes were mounted at the upper and lower wind tunnel walls in order to achieve a constant inlet pressure distribution. An orifice was set up in the duct of the secondary air for the determination of the mass flow rate. Quartz glass windows of 20 mm thickness were installed in the front part of the side walls in order to obtain optical access to the leading edge of the center blade.

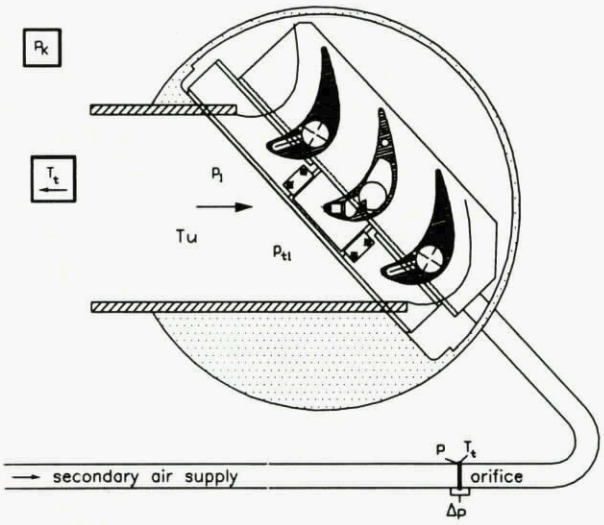


Figure 3: Test section of the wind tunnel with turbine cascade AGTB-B1

The following data was used in order to monitor the flow conditions of the cascade main stream flow (Sturm and Fottner, 1985): the total temperature in the settling chamber, the static pressure in the tank (downstream conditions), the static pressure and the total pressure of the main stream flow upstream of the cascade (Fig. 3).

For the setting of the secondary air mass flow rate, temperature, static pressure, and pressure drop at the orifice were measured. By observing the temperature and total pressures inside the plena of the blades a homogeneous secondary air supply was ensured (Fig. 3).

## 2D Laser-2-Focus System

A standard two dimensional Laser-2-Focus system permanently installed in the High Speed Cascade Wind Tunnel was used for the detailed flow field investigations in the immediate vicinity of the film cooling holes. It operates with a water cooled Argon Ion Laser generating an output power of 1 Watt in the single line operational mode. Two parallel laser beams are focused to a size of 8 μm in a distance of 168 μm forming a light barrier. Very small aerosol particles supplied by a pressurized spray generator pass through the focal volume and scatter the laser light. The scattered light is received by two photo detectors, amplified and sent to the signal processor (Fig. 4).

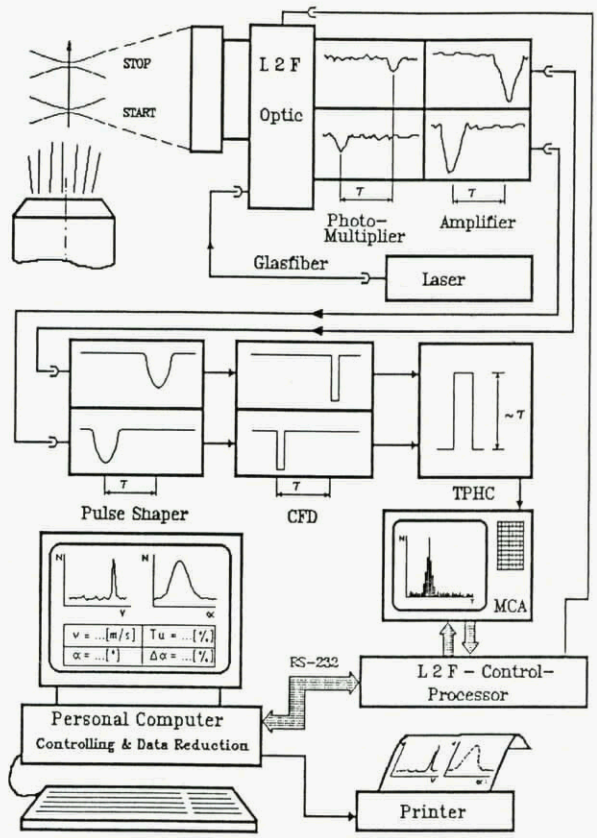


Figure 4: Signal processing for the 2D-L2F system

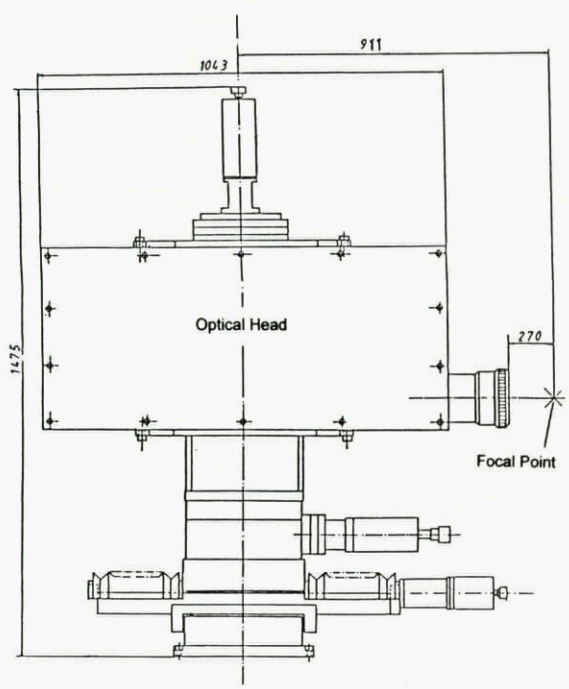


Figure 5: Traversing unit and optical head of the 2D-L2F system

The time in between the two signals is equivalent to the time-of-flight of the particles. Their velocity can be calculated from the known distance of the focal points. Because start and stop impulse can be triggered by two different particles the L2F-data has to be treated statistically. The flight direction of the particles is determined by turning the two focal points to different angular positions to find an over-all maximum of the statistical events (Schodl, 1989).

In the High Speed Cascade Wind Tunnel the optical head of the 2D-L2F system has to operate in depressurized conditions. Therefore this L2F system was among the first to use fiber optics for the transfer of the light from the laser located outside the pressure tank to the optical head inside (Beeck, 1992). The optical head is positioned by means of a highly precise traversing unit with 4 axes (3 translatory, 1 rotatory; Fig. 5).

## 3D Laser-2-Focus System

In addition to the 2D-L2F measurements the flow field investigations in the immediate vicinity of the film cooling holes were also performed by means of a three dimensional Laser-2-Focus system supplied and operated by the DLR-Institut für Antriebstechnik, Köln (Schodl and Förster, 1991). In one optical head this system combines two 2D-L2F systems which are inclined at about 7.5° to the rotating axis (Fig. 6). A detailed description of the 3D-L2F principle is given by Schodl (1989).

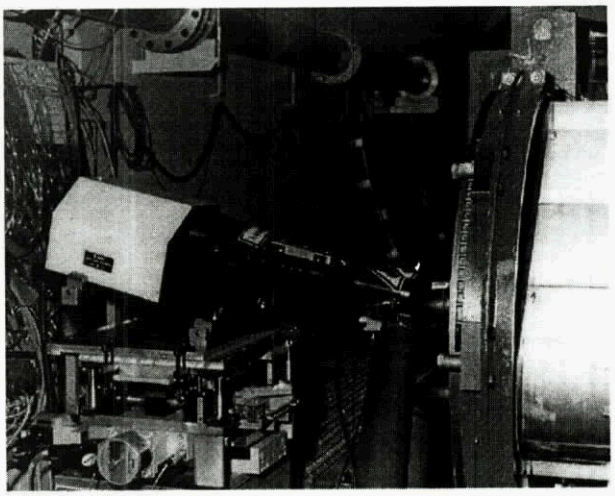

Figure 6: Set-up of the 3D-L2F system in the High Speed Cascade Wind Tunnel

The installation of the 3D L2F system in the High Speed Cascade Wind Tunnel required some modifications and adaptations. The three axes traversing unit for the 3D-L2F which was also supplied by the DLR-Institut für Antriebstechnik, Köln was mounted onto the rails that support the permanently installed 2D-L2F system when it is moved to its measuring position. The cables that were connected to the optical head and the traversing unit had to be inserted into the pressure tank by vacuum tight fixings.

The two angled 2D-L2F systems in the optical head of the 3D-L2F system form a cone around the rotational axis when theoptical head turns. To avoid shutting off one system while measuring close to the blade surface the receiving cone has to be placed tangentially to the surface. Therefore the system axis has to be inclined normal to the blade surface. On the strongly curved leading edge geometry each measuring plane thus demands the optical head to be adjusted to individual horizontal and vertical angles. This was achieved by a specially designed tilting mechanism (Fig. 7).

In the regular 3D-L2F arrangement the rotational axis of the optical head is oriented perpendicular to the window which provides optical access so that only one calibration is necessary to determine the sensitivity regarding the flow angle in the direction of the system axis. But if the receiving cone of the 3D-L2F system has to be positioned tangentially to the blade surface the rotational axis is inclined to the window. This implies that the laser light beams of the two systems are refracted differently depending on the angular position of the optical head. Fig. 7b displays the position in which the maximum difference is reached because one beam penetrates the window almost perpendicularly experiencing nearly no refraction while the other beam having the maximum angle towards the window is refracted to a full extent. The sensitivity of the 3D-L2F system towards the flow angle with respect to the optical axis depends on the inclination angle and on the thickness of the window. Consequently a calibration has to be performed at each inclination angle of the system for all flow angles i.e. rotational orientations of the optical head. This time consuming task is still in progress so that the 3D-L2F measurements are not yet evaluated to their full extent. Accordingly the detailed results presented in this paper concentrate on the 2D-L2F data.

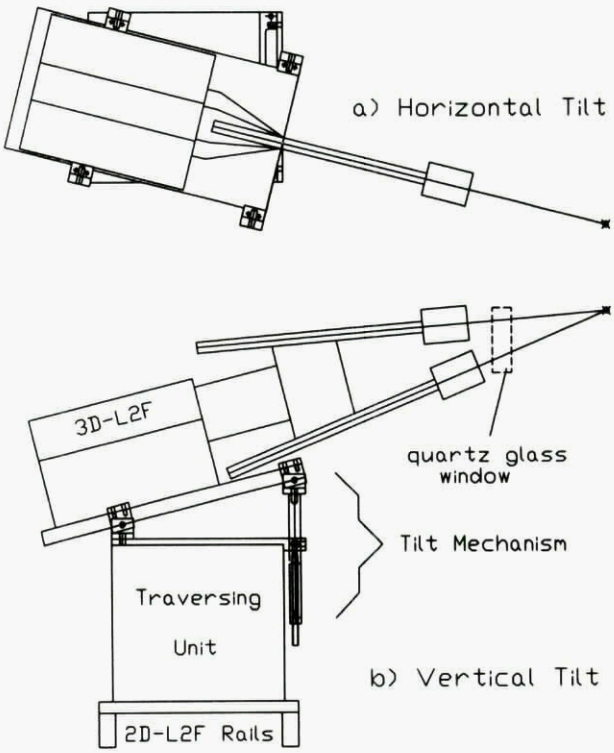


Figure 7: Optical head of the 3D-L2F, traversing unit and tilting mechanism as installed in the HGK

## 3. TEST PROGRAM

Since the cascade flow is transonic the flow conditions depend strongly on the mass flow rate of the cooling injection. Uniform conditions at the leading edge can only be guaranteed for varying blowing ratios by adjusting the upstream conditions to the design values $Ma_1 = 0.37$ and $Re_1 = 370000$. Because the Laser-2-Focus measurements are rather time consuming the detailed flow field investigations in the vicinity of the cooling holes were only performed for a blowing ratio of M = 1.1.

The radial depth of penetration of the 3D-L2F system was restricted to 32 mm by the aperture of the quartz glass windows in the side walls of the cascade because the laser beams form a 15° cone around the optical axis itself that must be kept clear. Therefore the 3D-L2F measurements were carried out downstream of the film cooling holes located at a distance of 22.5 mm towards the side wall. In this area the side wall boundary layer can still influence the flow pattern so that it seemed necessary to measure along a whole hole pitch even though the flow field for the blowing configuration was assumed to be symmetrical to the centerline of the hole (Ardey and Fottner, 1997). The measuring planes located 1 and 2.5 hole diameters downstream of the suction and pressure side holes (Tab. 3) were oriented normal to the blade surface (Fig. 1). The location of the measuring points in one plane is depicted as a mesh in Fig. 8.

| Δs/D | 1 | 2.5 |
|---|---|---|
| SS | 1 hole pitch<br>80 points | 1 hole pitch<br>80 points |
| PS | 1 hole pitch<br>90 points | 1 hole pitch<br>90 points |

Table 3: Test program of the 3D-L2F system

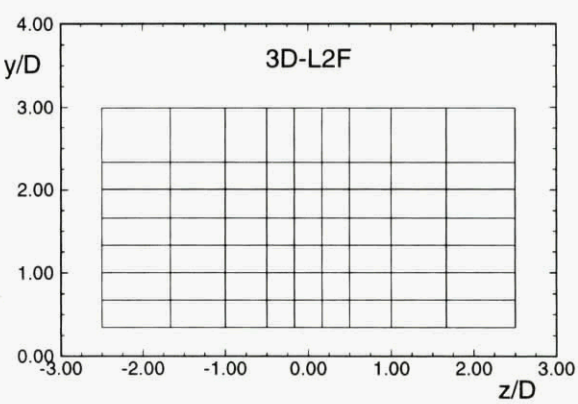


Figure 8: Mesh for a measuring plane of the 3D-L2F system

The measurements with the 2D-L2F system downstream of the holes were performed at slightly different locations than the 3D-L2F measurements (Fig. 1, Tab. 4) because in the course of the experiments it turned out that this allowed a higher degree of comparability to the other tests that were performed on the same cascade with different measuring techniques. The 2D-L2F measurements were carried out in the mid span section of the cascade so that a symmetry of the flow field to the centerline of the holes could safely be assumed. This allowed to investigate only half a hole pitch while mirroring the other one which increased the density of the mesh immensely (Fig. 9).

| Δs/L | ~ 0 % (hole) | 1 % | 2.5 % |
|---|---|---|---|
| SS | 45 points | ½ hole pitch<br>130 points | ½ hole pitch<br>143 points |
| PS | 45 points | ½ hole pitch<br>169 points | ½ hole pitch<br>169 points |

Table 4: Test program of the 2D-L2F system

In addition to the measuring planes located at Δs/L = 1 % and Δs/L = 2.5 % downstream of the cooling holes 2D-L2F surface parallel measurements were also carried out in the coolant exit plane 0.25 mm above the holes. Relying on the centerline (z/D = 0.0) symmetry 36 measuring points would have been sufficient to investigate the flow in the hole exit plane (Fig. 10). But to ascertain the exact location of the hole by the steep gradients of the velocity occurring at its borders measurements were also carried out at 9 additional locations situated in the second half of the hole so that only 27 measuring points had to be mirrored to fill the mesh.

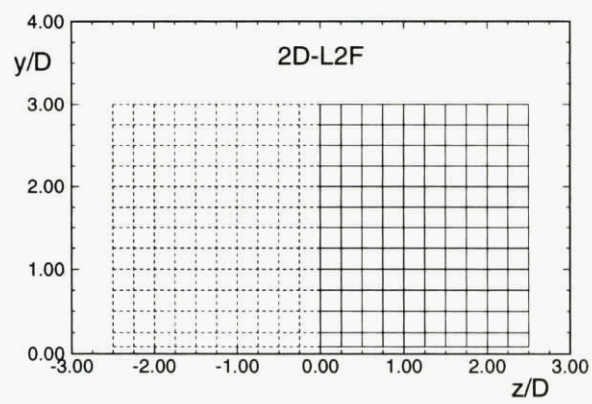


Figure 9: Mesh for a measuring plane of the 2D-L2F system

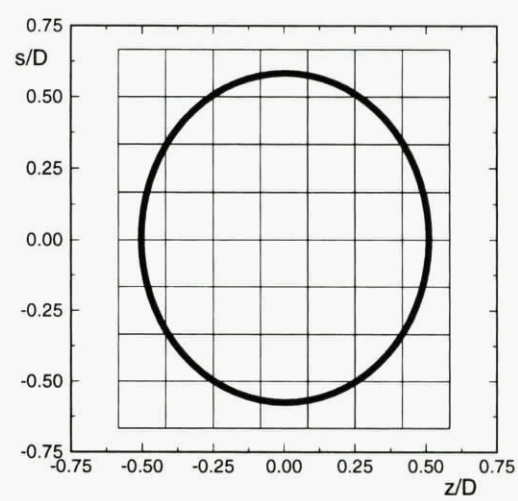


Figure 10: Mesh of the measuring plane above the film cooling holes (2D-L2F)

## 4. EXPERIMENTAL RESULTS

Due to the restricted optical access the 3D-L2F measurements had to be carried out close to the cascade side wall. The side wall boundary layer that could influence the film cooling flow was measured 30 mm in front of the cascade inlet plane by means of the 3D-L2F. Fig. 11 displays the amount of velocity near the side wall and its interpolation by the 1/7-power-law for a turbulent boundary layer. In this figure the coordinate z was set to 0.0 mm at the lateral location of the holes that served for the 3D-L2F measurements so that the side wall is located at z = -22.5 mm. As can be seen the side wall boundary layer thickness is about 18 mm affecting only one half of the hole pitch that was used for measuring purposes.

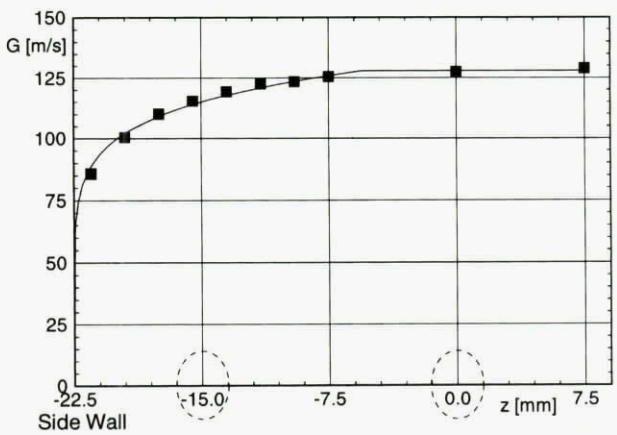


Figure 11: Side Wall Boundary Layer 30 mm in front of the cascade inlet plane

The results of the 3D-L2F measurements and the 2D-L2F measurements agree quite well. The spatial extent and the amount of the tangential velocity (U) correspond nicely (Fig. 12). The influence of the side wall boundary layer on the 3D-L2F measurements can be observed in the reduced tangential velocity component U at negative z values. Overall the vertical velocities (V) of the two systems match well. No 3D-L2F measuring points were placed in the area of $2.25 < y/D < 3.0$ so that the positive V-velocities on top of the jet could not be as clearly resolved as in the 2D-L2F measurements. Some flow structures are also not as highly defined in the 3D-L2F measurements as in the 2D-L2F measurements because the number of data sets is almost four times higher for the 2D-L2F enhancing the resolution drastically. The distribution of the lateral velocity component (W) measured with the 3D-L2F features a symmetry with opposite signs to the hole centerline that is found when looking at counter rotating vortices like for example the kidney vortices typically associated with a coolant jet.

### Flow Field Downstream of the Film Cooling Holes on the Pressure Side

The flow field downstream of the pressure side holes is displayed in Fig. 13 in the form of the tangential (U) and normal (V) velocity components and the turbulence intensity referenced to the inlet flow velocity of the cascade ($Tu_H$). At $\Delta s/L = 0.01$ a large reverse flow area with tangential velocities of - 80 m/s and normal velocities of about 20 m/s can be observed in the wake of the hole at $z/D = \pm 0.5$ and up to $y/D = 1$. This zone being about the size of the film cooling hole itself belongs to the big recirculation vortex system underneath the film cooling air. At $\Delta s/L = 0.01$ the center of the jet is being outlined by the maximum of the normal velocities ($y/D = 1.5$) because the coolant is still moving away from the surface of the blade. The cascade main flow has to pass around this disturbed area creating slightly increased tangential velocities on top of the jet above $y/D = 2.0$ and very high flow speeds up to 180 m/s next to the reverse flow area.

Velocity gradients amount to shear forces and generate turbulence. At $\Delta s/L = 0.01$ three major zones of increased turbulence intensity can be observed. The highest values of more than 30 % are found at $z/D = 0.5$ and $y/D < 1$ where the main stream flow (U = 180 m/s) and reverse flow (U = - 80 m/s) converge. Up to 20 % turbulence intensity are generated at $y/D = 2.0$ where the coolant jet (V = 40 m/s) and the main stream flow (V = 0 m/s) merge. The third high turbulence zone is found in the shear area between the reverse flow area and the film cooling air at $y/D = 1$ and $-0.5 < z/D < 0.5$. Inside the reverse flow area itself there is an astonishingly low turbulence level of about 10 % which indicates that the recirculation vortices are not only a strong but also steady flow phenomenon.

Further downstream at $\Delta s/L = 0.025$ the extent of the negative tangential velocities is reduced below $y/D = 0.25$. On top of the reverse flow area and below the center of the coolant jet at $y/D = 2.0$ the flow turns towards the blade surface to fill the deficit of kinetic energy. The upper part of the coolant still has a tendency to move upwards creating turbulence in its shear zone with the main stream flow. The reverse flow area is again indicated by a low turbulence zone in its center surrounded by a belt of high turbulence created through shear forces.

### Flow Field Downstream of the Film Cooling Holes on the Suction Side

The flow field downstream of the suction side holes is displayed in Fig. 14 in the form of the tangential (U) and normal (V) velocity components and the turbulence intensity referenced to the inlet flow velocity of the cascade ($Tu_H$). Contrary to the pressure side cooling air ejection there are no negative tangential velocities at $\Delta s/L = 0.01$. As is known from oil-and-dye flow visualizations the recirculation vortices downstream of the suction side film cooling holes are much smaller than those on the pressure side. The coolant is located in the area of reduced kinetic energy close to the surface at $z/D = \pm 0.5$, $y/D < 0.75$. It is surrounded by main stream flow that has accelerated to pass the jet. The main stream flow on top of the coolant which is moving away from the blade surface is pushed upwards while the main stream flow aside from the jet turns towards the blade surface enhancing the development of the kidney vortex. Further downstream at $\Delta s/L = 0.025$ the extent of the suction side coolant jet has increased. The velocity differences between the film cooling air and the main stream flow are reduced resulting in lowered turbulence intensities.

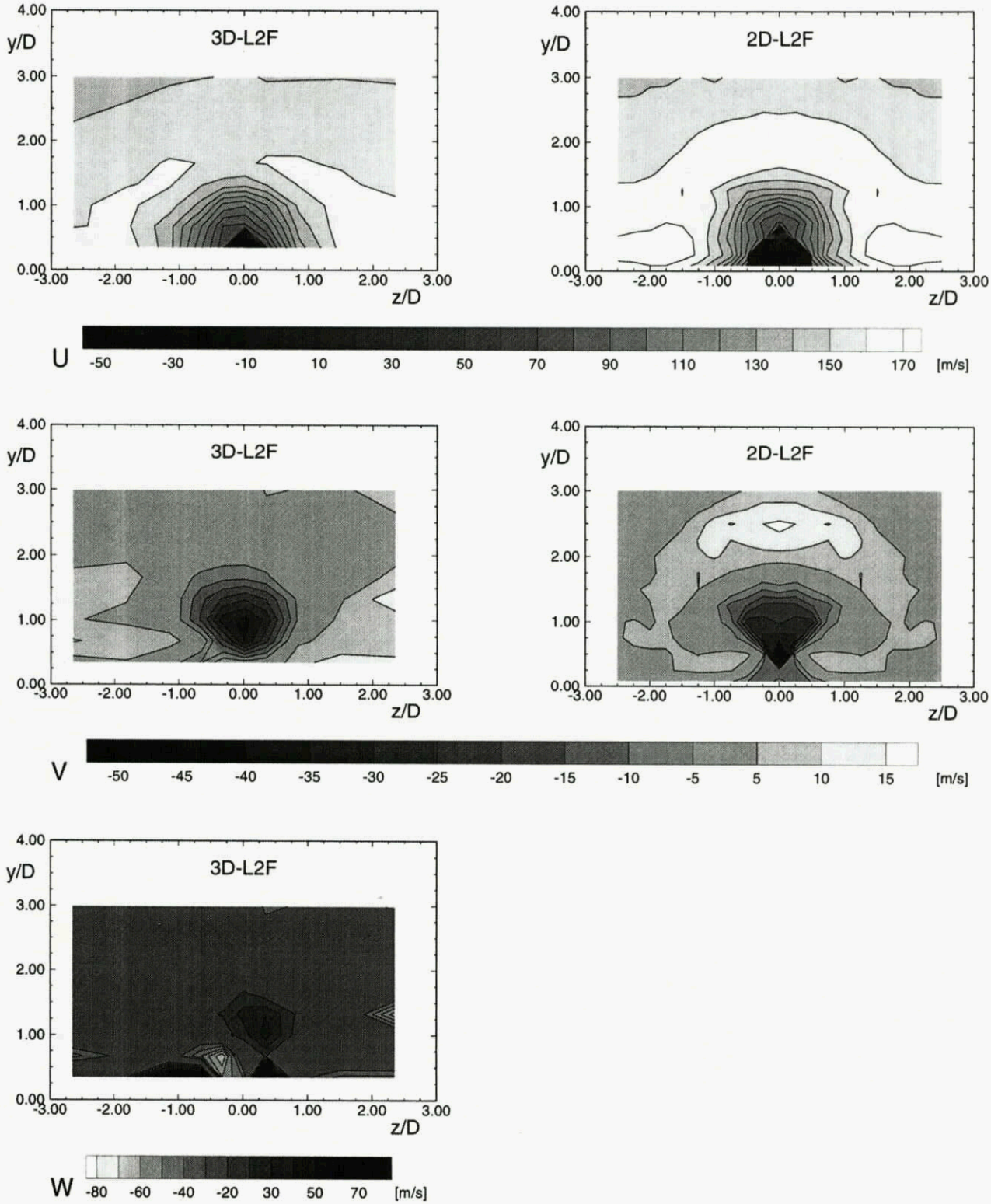


Figure 12: Comparison of velocities for 3D-L2F and 2D-L2F measurements on the pressure side, $\Delta s/D = 2.5$ (3D-L2F) and $\Delta s/L = 2.5$ % (2D-L2F)

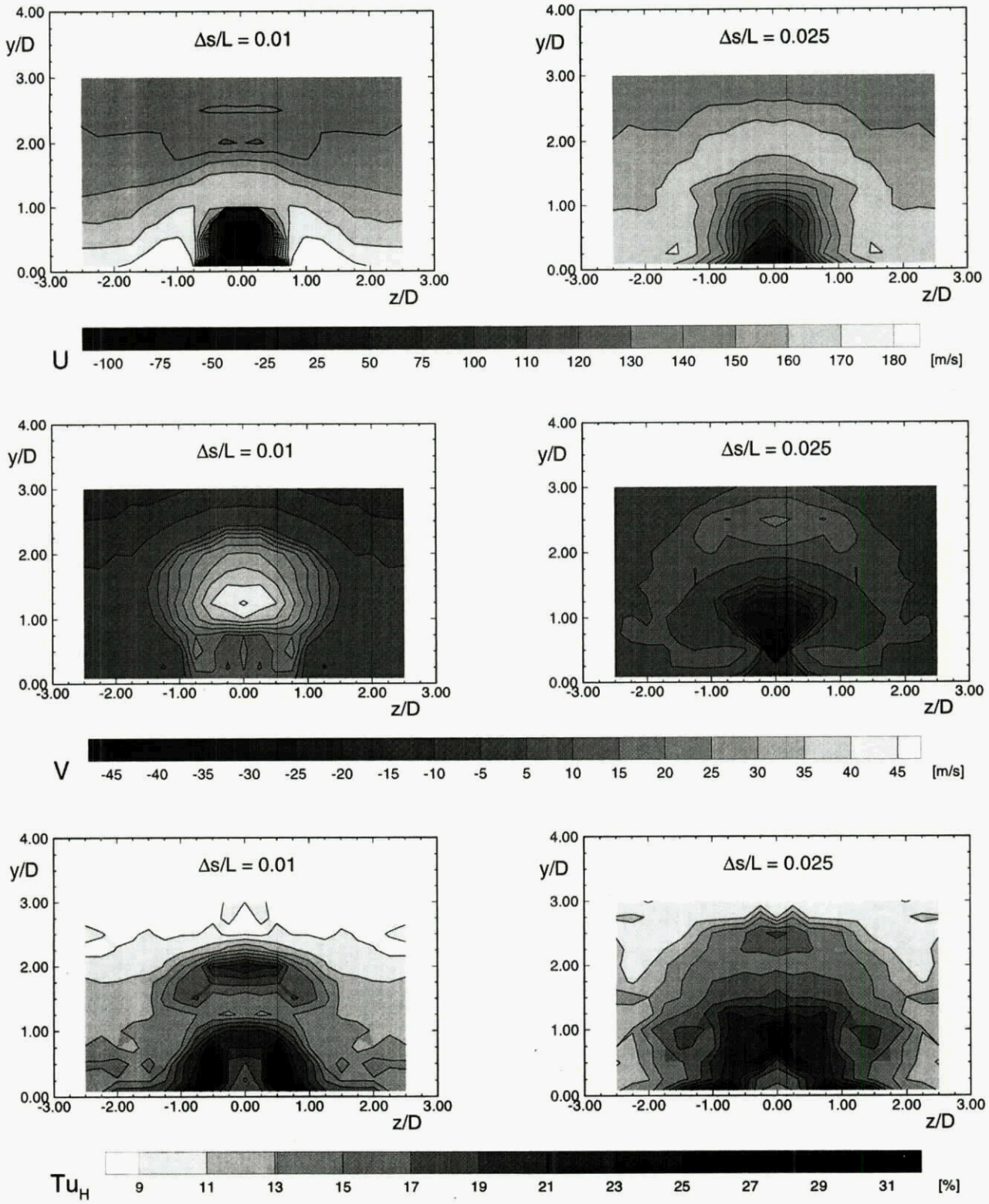


Figure 13: Flow field downstream of the pressure side holes; tangential velocity U, normal velocity V and turbulence intensity referenced to the inlet flow velocity of the cascade $Tu_H$

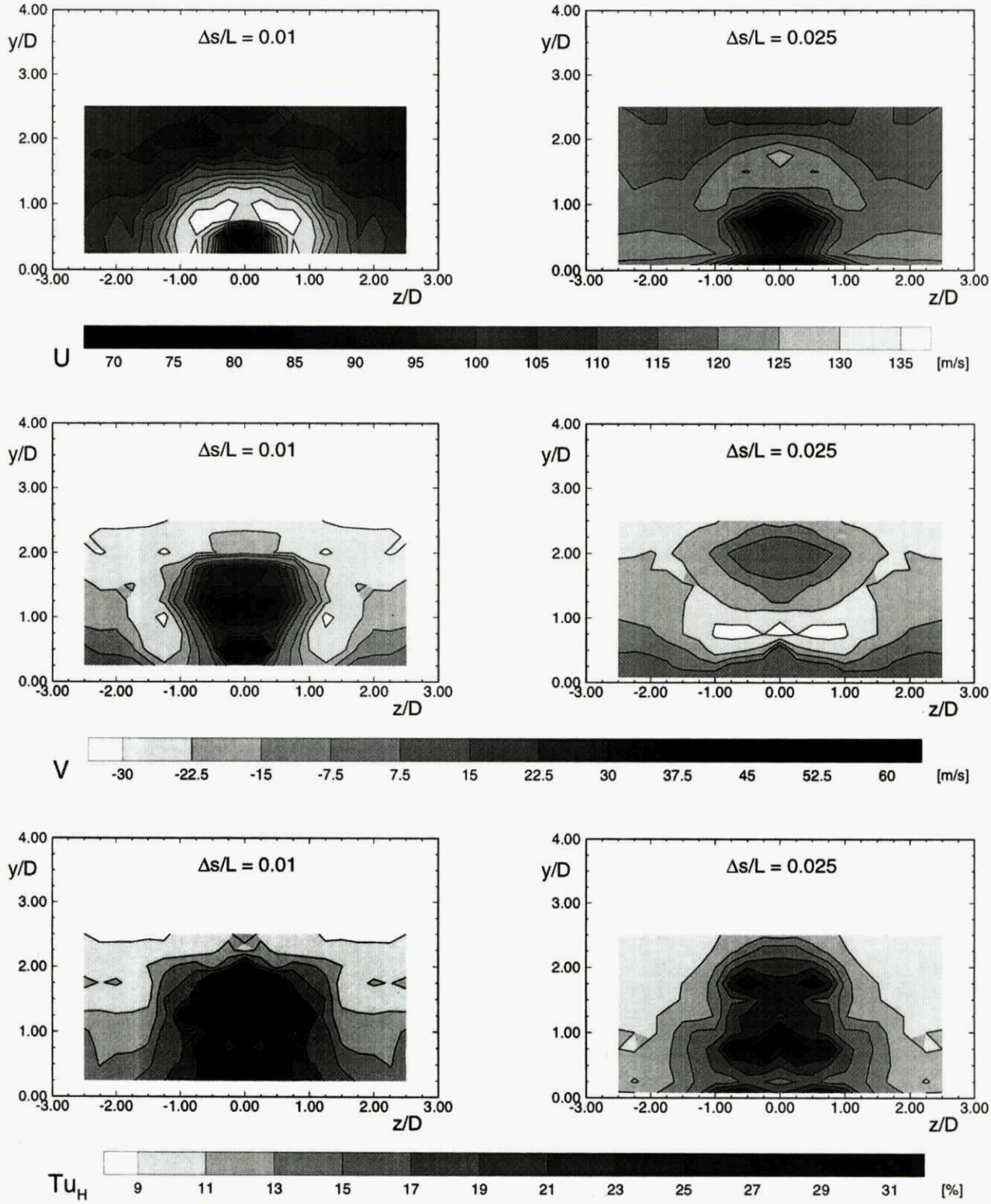


Figure 14: Flow field downstream of the suction side holes; tangential velocity U, normal velocity V and turbulence intensity referenced to the inlet flow velocity of the cascade $Tu_H$

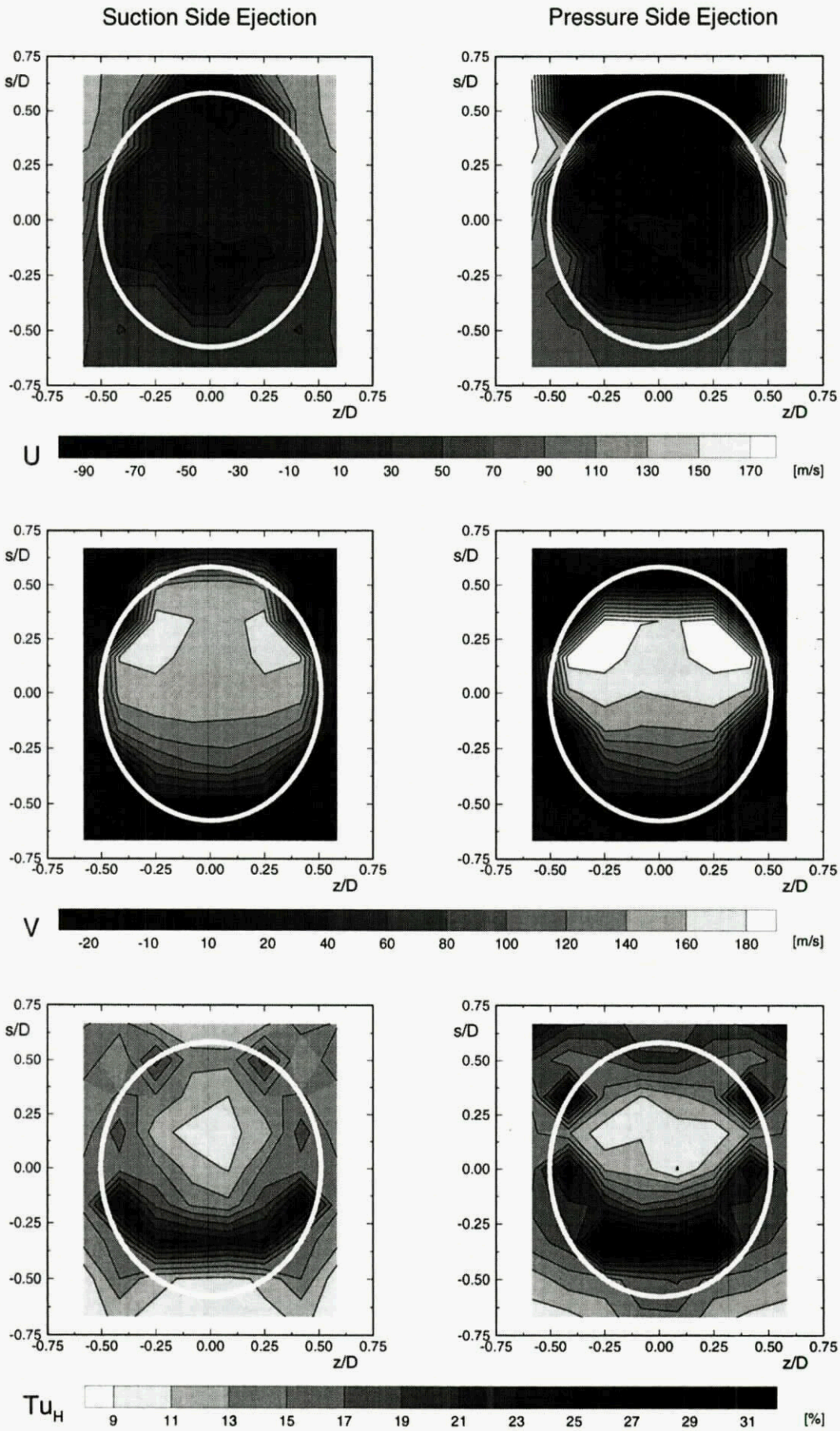


Figure 15: Flow field measurements 0.25 mm above the film cooling holes; tangential velocity U, normal velocity V and turbulence intensity referenced to the inlet flow velocity of the cascade $Tu_H$

## Flow Field in the Surface Parallel Exit Plane of the Film Cooling Holes

The flow field measurements 0.25 mm above the film cooling holes are displayed in Fig. 15 in the form of the tangential (U) and normal (V) velocity components and the turbulence intensity referenced to the inlet flow velocity of the cascade ($Tu_H$). Increased turbulence intensities clearly indicate the extension of the holes. The irregularity is caused by the orthogonal measuring grid which can not grasp the ring structure of the hole sufficiently. The upstream part of the holes ($s/D < 0$) is governed by turbulence levels up to 30 % which indicate the stagnation zone of the main stream flow that is created by the film cooling ejection. The main body of the coolant jet characterized by low turbulence intensities is situated in the downstream part of the holes. There the normal velocity V reaches its highest values forming two maxima that are probably related to the centers of the kidney vortices. The extent of the reverse flow area downstream of the holes is indicated by the tangential velocity U. The width of the pressure side recirculation amounts to a full hole diameter ($z/D = \pm 0.5$) while the suction side recirculation reaches only from $z/D = -0.125$ to $z/D = 0.125$. Inside the hole the pressure side jet is pushed further downstream than the suction side jet because the velocity of the main stream flow in front of the hole is about 45 m/s higher.

## 5. CONCLUSIONS

On a large scale turbine cascade the flow field in the immediate vicinity of film cooling holes was investigated using Laser-2-Focus Techniques. The most significant results can be summarized as follows:

- The flow phenomena in the immediate vicinity of the film cooling holes can only be observed with non intrusive measuring techniques to avoid influencing the flow field by a probe.
- With the Laser-2-Focus Technique it was possible to position a small measuring volume very close to the blade surface so that even reverse flow areas could be resolved.
- The results of the 2D-L2F system and 3D-L2F system showed a good agreement.
- Due to the geometric boundary conditions the rotational axis of the 3D-L2F system was inclined towards the window which provided optical access. This requires a more complex calibration than for the standard configuration.
- The main stream flow is accelerated when passing next to the coolant.
- The pressure side coolant jet is detached from the blade surface while the suction side coolant jet remains close to the wall.
- The extent of the recirculation zone in the wake of the hole is much bigger for the pressure side coolant ejection than for the suction side.
- The main body of the coolant jet exits in the downstream half of the film cooling hole.
- The maxima of the normal velocity in the hole exit plane indicate the formation of the kidney vortices.

Missing the lateral velocity component W some questions concerning the flow field close to the film cooling holes are still unanswered. Especially observing the generation of the kidney vortices requires lateral velocity information. In some cases the interpretation of the 2D-L2F data was only possible because the flow field around the film cooled leading edge of the AGTB-B1 cascade had also been investigated by means of other measuring techniques like 3D hot wire anemometry and oil-and-dye flow visualizations.

## 6. ACKNOWLEDGEMENTS

The reported investigations were performed in the scope of a project of the German research cooperation on high temperature gas turbines (AG Turbo) and was funded by the German Ministry of Education, Science, Research, and Technology (BMBF), the Motoren- und Turbinen Union München, and the Siemens AG. The support and the permission for publication is gratefully acknowledged.

## 7. REFERENCES

Ardey, S., Fottner, L., 1997, "Flow Field Measurements on a Large Scale Turbine Cascade with Leading Edge Film Cooling by Two Rows of Holes", ASME 97-GT-524

Beeck, A., 1992, "Strömungsfelduntersuchungen zum aerodynamischen Verhalten eines hochbelasteten Turbinengitters mit Kühlluftausblasung an der Vorderkante", Dissertation, Universität der Bundeswehr München (Germany)

Schodl, R., 1989, "Laser Two Focus Techniques", VKI-Lecture Series 1989-05 "Measurement Techniques in Aerodynamics"

Schodl, R., Förster, W., 1991, "Measurements in Gasturbine Components", DLR-Nachrichten Vol. 63

Sturm, W., and Fottner, L., 1985, "The High Speed Cascade Wind Tunnel of the German Armed Forces University Munich", 8th Symposium on Measuring Techniques for Transonic and Supersonic Flows in Cascades and Turbomachines

# Application of 3D- Laser Two Focus Velocimetry in Turbomachine Investigations

**M. Beversdorff**
DLR Köln
Institut für Antriebstechnik
D- 51170 Köln

**L. Matziol**
MTU München GmbH
Postfach 500640, D- 80976 München

**C. Blaha**
Technische Hochschule Darmstadt
Fachgebiet Gasturbinen und Flugantriebe
Petersenstr. 30, D- 64287 Darmstadt

## ABSTRACT

The further development of turbomachines is driven by the improved understanding of the three dimensional, secondary flow processes. Therefore experimental data are needed to analyse the 3D- flow in this machines and to provide data for computer code validation. In this context a 3D- L2F velocimeter was developed which enables 3D-flow vector measurements under the difficult conditions of turbomachines were the optical access is restricted.
The new design of the 3D- L2F velocimeter includes also a special multicolour set-up with selectable beam separation that helps to reduce measurement time especially in turbulent flow regions, where conventional L2F systems are working rather time consuming.
A special seeding probe which can be placed very close to the turbomachine inlet without generating flow distortions provides an increase of the particle concentration in the seeded streamline that passes the L2F probe volume, thus contributing also to a further measuring time reduction.
Flow investigations in a transonic compressor are described and selected results of the secondary flow field obtained are presented.

## LIST OF SYMBOLS

| | |
|---|---|
| s | beam separation in the probe volume |
| d | beam diameter in the probe volume |
| $\varphi$ | rotation angle around the system axis |
| $\alpha$ | flow angle with respect to reference plane |
| $\beta$ | angle between system axis and flow vector |
| $\gamma$ | half intersection angle of system 1 and system 2 |
| $\theta$ | relative angle between system 1 and system 2 |
| $\vec{u}$ | velocity vector |
| MV | measurement volume |
| PS | pressure side of blade |
| SS | suction side of blade |

## 1. INTRODUCTION

In the field of non-intrusive experimental fluid flow analysis L2F- velocimetry has achieved importance particularly in the experimental investigation of turbomachinery flows.
The detailed laser velocimetry data have contributed to an improved understanding of turbomachinery aerodynamics and the validation of numerical flow solvers.
However, this data provided only 2D- flow information. The further development of 3D- computer codes demands 3D- experimental data.
The typical way to conduct 3-dimensional flow measurements is an arrangement of two 2D- anemometers looking at the same measurement location from different directions. The 3-dimensional velocity vector follows from the geometrical transformation of the 2-dimensional results. To obtain a reasonable measurement accuracy for all velocity components it is necessary to align the two systems at a coupling angle of more than 30°. However, in turbomachinery applications the optical access to the measurement locations is often limited by the window size, so that this kind of arrangement can not be used and new ideas and concepts are needed.
At DLR different 3D- L2F designs have been developed and examined in turbomachinery experiments. All systems were operated under the conditions of limited optical access, corresponding to a f- number of 3 which is

*Paper presented at an AGARD PEP Symposium on "Advanced Non-Intrusive Instrumentation for Propulsion Engines", held in Brussels, Belgium, 20-24 October 1997, and published in CP-598.*

also typical for 2D- velocimeters, Ref.[1]. In comparison one design showed the best properties for stability, handling and reliability. This 3D- L2F system was selected for the measurements and will be described in the following.

## 2. 3D - L2F VELOCIMETER

### 2.1 L2F principle

The principle of the L2F, figure 1, is a time of flight measurement of small particles contained in the flow crossing two highly focused parallel laser beams. With the known separation s the flow velocity perpendicular to the optical axis can be determined. By turning the beam plane it is possible to detect the flow direction. The statistical sample of time of flight data will give mean values for flow velocity, flow angle and the turbulence intensities. This is described in detail in Ref. [1].

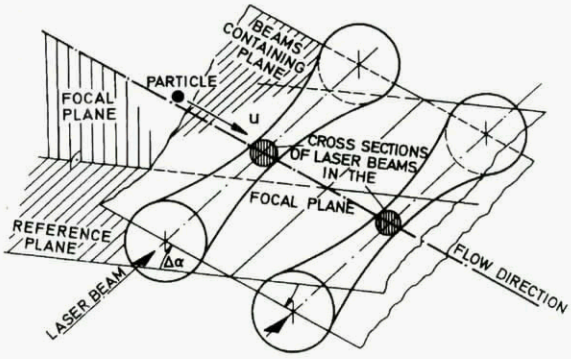


Figure 1: Principle of the laser-two-focus velocimeter

### 2.2 3D- L2F based on inclined beams

The 3D-system consists out of two 2D-L2F systems, further so-called system 1 and system 2, rotatable around a common axis (figure 2).

The beams start 1, stop 1 and start 2, stop 2 intersect at the points A and B, respectively. These points and the system axis determine a reference plane which bisects the coupling angle $2\gamma$ of system 1 and system 2. The two beam pairs and therefore the reference plane rotates around the system axis (angle $\varphi$).Turning of system 1 and system 2 adjusts the reference plane to an angle $\varphi_m$ that an arbitrarily chosen flow vector $\vec{u}$ lies just within this plane. The planes of the system 1 and system 2 beam pairs intersect in the line X. Turning of system 1 and system 2 adjusts the reference plane to an angle $\varphi_m$ that an arbitrarily chosen flow vector $\vec{u}$ lies just within this plane. The planes of the system 1 and system 2 beam pairs intersect in the line x. For the case shown in Fig. 1 $\vec{u}$ is neither in the system 1 nor in the system 2 measuring plane. Therefore, $\vec{u}$ cannot be measured at that orientation $\varphi_m$ of the reference plane even if we assume an infinite extension of the measurement volume. However, a slight clockwise turning to $\varphi_1$ will bring $\vec{u}$ into the plane of the system 1 beams and successful measurements occur within the system 1, but none within the system 2. A counter-clockwise rotation to $\varphi_2$ aligns the flow vector with the system 2 measuring plane and now this system recognises successful particle transits and the system 1 does not, Ref. [ 1]

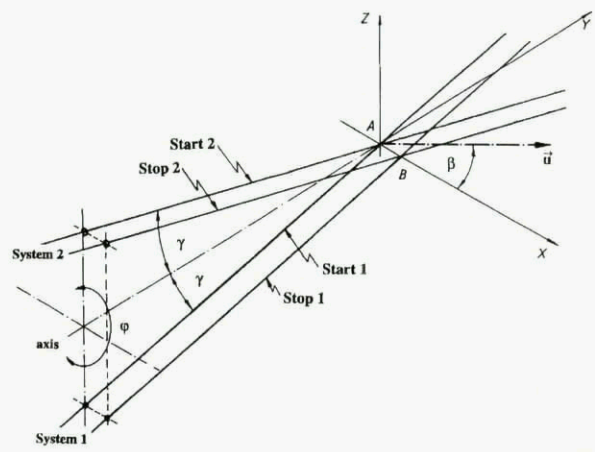


Figure 2: Principle of the 3D- L2F with inclined beams

The following equation describes the relationship between the measured flow angle difference $\varphi_1 - \varphi_2$ and the flow angle $\beta$ which is a measure of the on-axis velocity component of $\vec{u}$ :

$$\beta = \arctan \frac{\sin\left(\frac{\varphi_1 - \varphi_2}{2}\right)}{\tan \gamma}$$

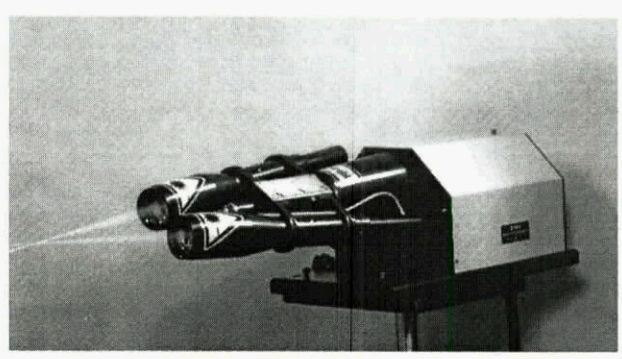

Figure 3: 3D- L2F Optical Head

The present 3D- velocimeter shown in figure 3 has a coupling angle $\gamma$ of 7.5°. For this case the theoretical sensitivity curve is shown in figure 4 . The detecting range for the angle $\beta$ is about -45° to +45°. The working distance is about 250 mm. The total transmitting and receiving aperture corresponds to a f- number of 3.

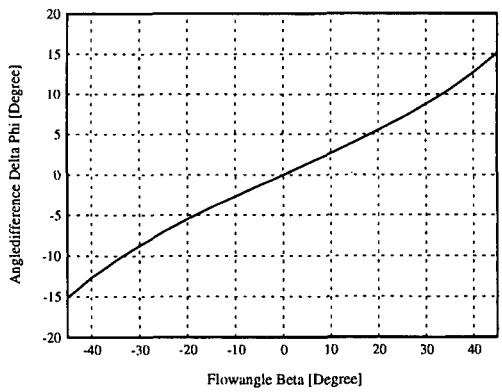


Figure 4: Sensitivity curve of the 3D- L2F

Generally, it is not necessary to calibrate the measurement system, but therefore the coupling angle $\gamma$ has to be known precisely and the adjustment of system 1 and system 2 beam planes relative to each other has to be perfect. In practice it is more convenient to calibrate the system in a free jet nozzle which can be adjusted to certain flow angles $\beta$ in a range, e.g. from -20° to +20°. For any angle $\beta$ the corresponding angles $\varphi_1$ and $\varphi_2$ of both L2F-systems are measured. From this data the coupling angle $\gamma$ and the angle offset $\theta$ (caused by an inaccuracy of both beam planes) can be determined by a linear regression.
The measured flow angle $\beta_{meas.}$ follows with:

$$\beta_{meas.} = \arctan \frac{\sin\left(\frac{\varphi_1 - \varphi_2 + \theta}{2}\right)}{\tan\gamma}$$

This calibration procedure is especially necessary if both, a window is placed in the beam path - this is usual in turbomachinerie applications- and the optical axis is not aligned perpendicular to the window surface.
In the case of multicolour L2F systems as they were chosen for the 3D- L2F set-up (see part 2.3) the diffraction of the glass window causes a rotation of the beam planes which changes the offset angle $\theta$ in dependence of both, the line of sight with regard to the window normal and the flow angle $\varphi$. In this situation a calibration arrangement within the free jet, that simulates the experiment (the same window, the same flow angle range and the same line of sight angle), is necessary to determine the factors $\theta$ and $\gamma$.

## 2.3 Multicolour L2F- System

One remarkable property of the L2F technique is the excellent signal-to-noise ratio. This plays an important role when examining the flow in narrow blade channels and in boundary layers. However, high turbulence intensities characterise the boundary layer flows. Under such conditions the L2F-measuring process becomes rather time consuming, because the higher turbulence levels reduce the probability of a successful dual beam transit. This probability depends also from the probe volume dimensions, exactly from the ratio of beam diameter to beam separation. It can be shown, see Ref. [2], that the measuring time can be minimised without losing measurement accuracy if the probe volume dimensions are matched to the flow turbulence intensities. Small values of the beam diameter-to-separation ratio are required in flows of low turbulence intensities and high values can be tolerated for higher turbulence intensities.

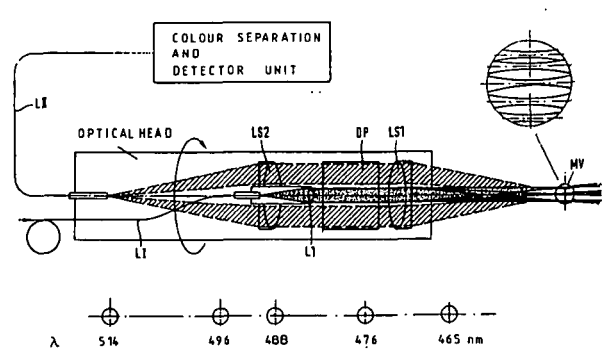


Figure 5: Principle of the multicolour 2D-L2F velocimeter

Since a system with variable beam separation is difficult to design and to keep in alignment a multicolour L2F system has been developed, Ref. [2]. This system figures several parallel beams of different colours, generated by an Argon- Laser, into the measurement volume MV (see figure 5). By selecting a pair of colours in the detection unit for the start and the stop detectors the corresponding beam separation is established for the measurement. In this way the beam separation can be matched stepwise to the flow turbulence and a measurement time reduction of a factor 5 can be achieved.
This multicolour set-up was used for the 3D- L2Fdesign.

## 3. SEEDING PROBE DESIGN

L2F-measurements in turbomachines are often time consuming and therefore expensive, because a sufficient number of measurement events for accurately statistical analysis is necessary.
Artificial flow seeding to achieve high particle rates in the probe volume is needed for measurement time reduction.
Normally a seeding probe, for example a tube, is placed upstream to inject particles into the streamline which will pass through the probe volume. In order to minimise flow distortions at the measurement location, due to the wake generated by the probe, it is practical to place the probe upstream in the settling chamber.
However, if the settling chamber is placed very far upstream, the seeded streamline expands in the turbulent tube flow considerably and the particle concentration becomes rather low at the measurement location.
In order to increase the particle concentration the seeding probe has to be placed very close to the measurement location, but flow distortions must be considered.
To analyse the amount of flow distortion induced by seeding probes, different designs have been investigated in a tube flow for a relevant Mach Number range at MTU.
Three examples of investigated probe shapes are shown in figure 6. Probe 1 with a circular cross-section, Probe 2 with a flattened, rectangular design and probe 3 with an elliptical cross-section.
The elliptical probe turned out with the best results from this optimising process and showed negligible flow distortions up to Mach numbers of 0.6 and could be positioned 0.5 m upstream the measurement location. If the Mach number was lower than 0.2 the elliptical probe could be placed only 0.15 m upstream the measurement location. This probe was used for the compressor tests.

## 4. TEST COMPRESSOR

Since the development of the 3D-L2F velocimeter several investigations in turbomachines have been carried out. However, the results are usually confidential and not accessible for the public. The single stage transonic compressor rig at the Darmstadt University of Technology does not have this restrictions. The rig is representative of the first stages of contemporary high pressure compressors. The rig was designed at MTU Munich GmbH as part of a gas turbine research program launched by the German Ministry of Education and Research (BMBF).

| | |
|---|---|
| Pressure ratio | 1.50 |
| mass flow rate | 16.0 kg/s |
| rotor tip speed | 398 m/s |
| meridional Mach-number (inlet/outlet) | 0.57/0.48 |
| inlet flow / outlet flow | axial/axial |
| stage loading | 0.407 |
| flow coefficient | 0.600 |
| shaft speed | 20.000 rpm |
| shaft power | 634 kW |
| tip diameter | 0.38 m |
| blade numbers (rotor / stator) | 16/29 |
| rotor solidity (hub / mid / tip) | 1.9/1.5/1.2 |
| stator solidity (hub / mid / tip) | 2/1.6/1.3 |
| hub to tip ratio rotor | 0.51 |
| aspect ratio rotor | 1.06 |

Table 1: Test Compressor Design Parameters

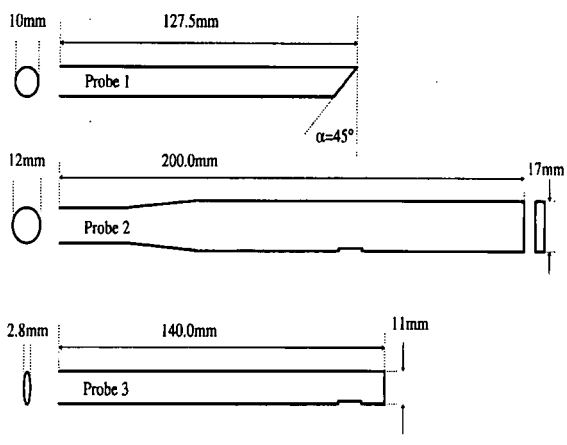


Figure 6: Different Seeding Probes

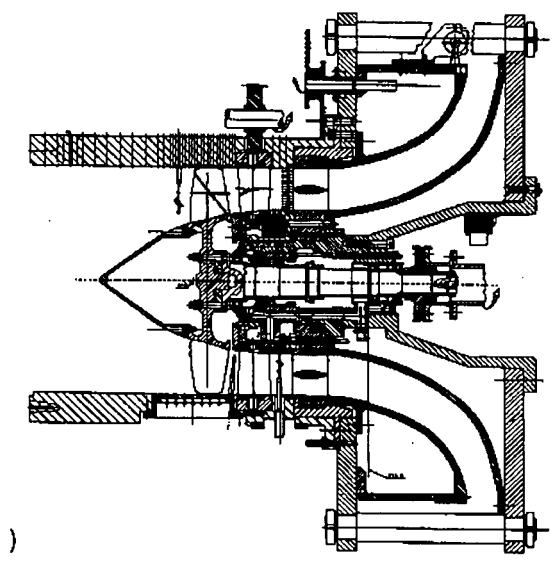

Figure 7: Cross section of the rig

The task is to investigate transonic compressor flows and to provide an experimental data base to software developers for code validation.
In addition to the modern aerodynamic attributes the rig is a demonstrator for new technologies regarding design and materials, figure 7. The rotor is a bladed disk assembly, a technology not yet firmly established in civil engines. The outlet guide vanes consist of composite material.
The compressor design parameters are shown in table 1.

## 5. RESULTS OF MEASUREMENTS

Readings were taken at 12 positions in chordwise and at 5 positions in spanwise direction corresponding to figure 8. At each position in circumference direction the blade pitch was resolved into 16 windows. A total of approximately 170 windows had successful measurements at each blade-to-blade plane, because the blade itself and the blade shadow have to be taken into account. The spanwise positions refer to 20%, 40%, 60%, 80% and 95% relative span from hub.

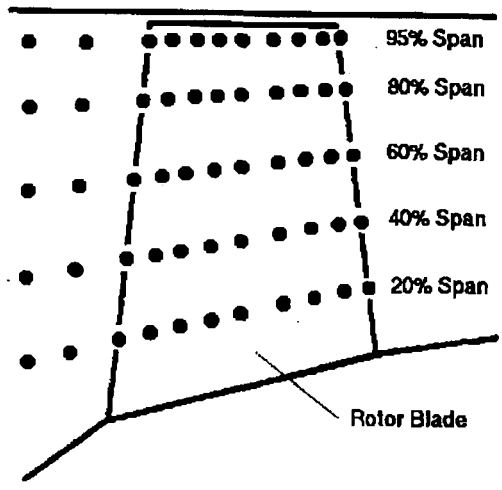


Figure 8: Measurement positions in spanwise and chordwise direction

The rectangular plane window in the compressor casing enabled the optical access to the rotor blades.
The flow was seeded with dispersed paraffin oil using the optimised seeding probe.
The flowfield of the rotor was examined in detail at different rotor speeds and varying operating points like near stall, peak efficiency and near choke conditions. For example some results at 100 % speed and peak efficiency are presented.
In Figure 9 velocity vectors in the meridional plane at mid pitch are shown. Close to the casing at 24% chord the flow is displaced towards the hub and at 65% chord the flow moves radial outward again. This region of blockage was identified by numerical analysis using a 3D-Navier-Stokes solver, as an area of reversed flow due to tip vortex shock interaction ,Ref. [3].

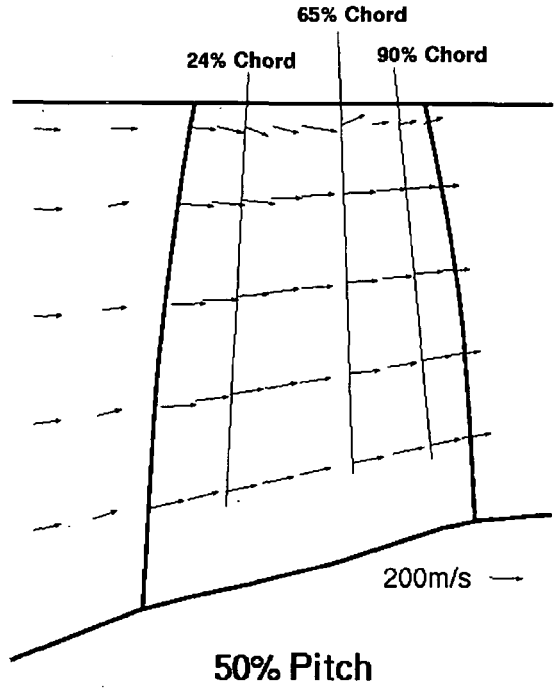


Figure 9: S2-Plane

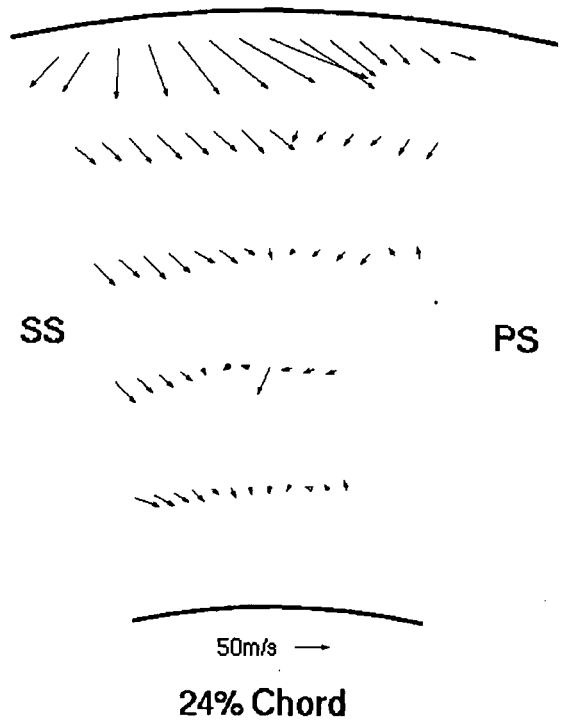


Figure 10: 24% Chord

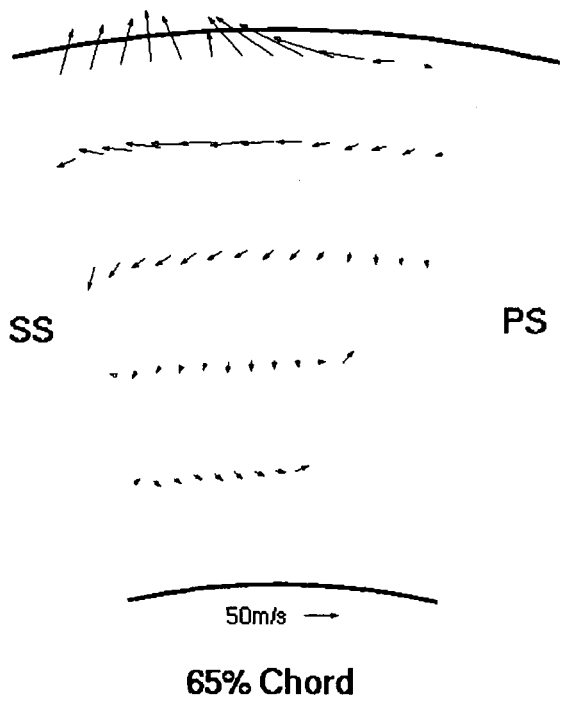


Figure 11: 65% Chord

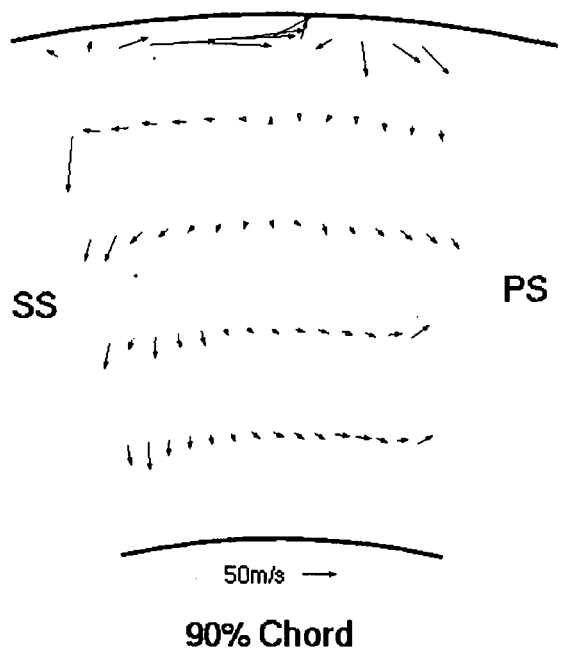


Figure 12: 90% Chord

Figures 10-12 show the secondary flow vectors at 24%, 65% and 90% chord. The secondary flow direction in the meridional plane was found as the deviations of the measured flow direction to "quasi-streamlines" at the specified spanwise position, formed by lines of constant relative span. In the blade-to-blade plane the secondary flow direction is considered as the deviation to the direction of the blade section mean line at the specified meridional position. The figures show the displacement of the flow close to the casing at 24% chord and the "reattachment" at 65% chord. At 90% chord a fully developed secondary flow field is displayed. More detailed discussions of the results will be given in a next publication.

## 6. CONCLUSION

The multicolour 3D- L2F velocimeter has demonstrated successfully its capability to measure in turbulent 3-dimensional flows under the conditions of restricted optical access in turbomachines.
A seeding probe with an elliptical shape was found to be suitable for an application close to a compressor stage for increasing particle rates with negligible flow distortion.
Secondary flow effects have been measured in transonic compressors as well as in turbines and will give detailed data bases for the validation of 3D- flow solvers.

## 7. ACKNOWLEDGEMENTS

The support for experimental investigations of the compressor rig through the German Ministry of Education and Research (BMBF) under the AG Turbo research program (contracts BEO/310326801D and BEO/310326801X) and the E3E research program (contracts 20T9402) is gratefully acknowledged.

## 8. REFERENCES

[1] Schodl,R.,1989, "LASER TWO FOCUS TECHNIQUES", VKI- Lecture Series 1989-05 "Measurement Techniques in Aerodynamics", Rhode-St. Genese

[2] Schodl, R., Förster, W., 1988, "A Multi-Colour Fiberoptic Laser-Two-Focus Velocimeter for 3-Dimensional Flow Analysis", Fourth Int. Symp. On Appl. of Laser Anemometry to Fluid Mechanics, Lisbon

[3] Fritsch, G., Hoeger, M., Blaha, C. , Bauer, D.:, July 1997, "Viscous 3D Compressor Simulations on Parallel Architectures - Design Tool Development and Application to a Transonic Compressor Stage", AIAA Paper 97-2876, Joint Propulsion Conference, Seattle

Paper 13
Author: Beversdorff

Q: F. Leboeuf

Do you use a curved or a flat window?

A: Flat windows of different width have been used: a large one to measure in the hub region and a smaller one to measure the tip flow.

Q: K. Navarra

How close to the tip can you obtain data with the DLR system? (Data only shown up to 95% span)

A: The 3D-L2F system can obtain data up to 0.5 mm from the surface, but this depends on the surface itself. The 0.5 mm is relevant for a black surface.

# Characterization of Gas Turbine Combustion Chambers with Single Pulse CARS Thermometry

**R. Lückerath, V. Bergmann, and W. Stricker**
Institut für Physikalische Chemie der Verbrennung
Deutsches Zentrum für Luft- und Raumfahrt e.V. (DLR)
Pfaffenwaldring 38-40
D-70569 Stuttgart
Germany

## 1. SUMMARY

Temperature results of three measuring campaigns with the mobile CARS system of the DLR Stuttgart are presented. The experiments were performed on different combustion chambers: a thrust nozzle test facility, a RQL combustor, and a ramjet combustor. Single pulse CARS $N_2$ thermometry was used to characterize the homogeneity of the flame at the exit plane of the combustion chamber, to address the quality of mixing of fuel-rich burnt gas of the primary zone with secondary air, to find an improved design for the $H_2$ injection into a high speed air flow, and to measure the temperature and pressure variations in the shock controlled free jet flame. In the last case both the temperature and the pressure could be determined from the CARS spectrum.

## 2. INTRODUCTION

In general, for the characterization of the combustion process the temperature including the absolute mean value, the most probable temperature, and the fluctuations plays an important role. Temperature measurements in technical combustion devices are often performed using thermocouple probes, which suffer from a low temporal and spatial resolution, possible damage due to high temperatures and the turbulent flow field, and possible perturbation of the flame. The procedure to convert the measured voltage into temperature and to correct for effects like radiative heat loss contains many sources of error /1/. In contrast, laser-based methods like Coherent Anti-Stokes Raman Scattering (CARS) work non-intrusively and time-resolving as single pulse techniques. CARS $N_2$ thermometry offers the possibility for temperature measurements with high accuracy and good spatial resolution /2-4/. The temperature information is derived from the spectral shape of the $N_2$ Q-branch spectrum, which displays the population of the rotational and vibrational states of the $N_2$ molecules which is correlated with the absolute temperature. As the CARS signal is coherently generated and emitted in a laserlike beam, this method is especially applicable for practical flames with limited optical access. With the commonly used broadband CARS technique it is possible to detect an entire CARS spectrum with a single laser pulse lasting about 10 ns leading to instantaneous temperature values. These instantaneous temperature values measured at the same location in the flame with the lasers' repetition rate of 10 Hz are represented in histograms from which the temperature fluctuation at this position can be read.

In this paper the results of the temperature measurements using the mobile CARS system of the DLR Stuttgart are presented from experiments in three different practical model combustors:

(i) A combustion chamber of a thrust nozzle test facility operated with $H_2$/air at atmospheric pressure, but without nozzle (DLR Köln):
The temperature distributions measured in the exit plane of the combustion chamber were used to get informations about the fuel/air mixing and the entrance conditions (temperatures) for the thrust nozzle.

(ii) A combustion chamber of a RQL (rich burn - quick quench - lean burn) combustor operated with kerosene/air at atmospheric pressure (DLR Köln):
Important informations on the quality of mixing of primary zone hot gases and secondary air were obtained from the distribution and the absolute value of the temperature within the mixing zone.

(iii) A ramjet combustor operated with $H_2$/air at 3 bar (University of Stuttgart):
The efficiency of the combustion could be correlated with the design of the chamber (variation of $H_2$ injection into the high speed air flow) by comparing temperature histograms measured for different burner configurations. Additionally, the temperature *and* pressure variations in the free jet flame were measured.

## 3. EXPERIMENTAL

### 3.1 Mobile CARS System

The mobile CARS system was designed for single pulse $N_2$ Q-branch thermometry in an industrial environment /5,6/. The equipment consists of compact, transportable units which are dust protected and partly temperature stabilized. The laser as well as the receiver optics container must be set up in immediate vicinity of the combustor. Therefore, they are thermally insulated and vibrationally damped.

A Nd:YAG laser with a frequency doubler (pump laser beam) and a broadband dye laser (Stokes laser beam) are used to excite the CARS spectra in the USED CARS phase matching configuration /7/. In this configuration the Stokes laser beam is coaxial with and inside the annular pump laser beam which results from the unstable resonator geometry of the Nd:YAG laser. The two laser beams overlap only in the focal region, and the overlapping length depending on the focal length of the optics determines the spatial resolution in beam direction. The USED CARS arrangement is best suited for turbulent flames with fluctuating density gradients, because the Stokes laser beam is surrounded by the pump laser beam and therefore both beams overlap in any case near the focus. For the experiments presented in this paper the laser beams were focused with a lens with a focal length of 300 mm or 500 mm. In the receiver container, the CARS signal was separated from the two exciting laser beams by dichroic mirrors, fed into a 20-m-long quartz fiber of 600 µm core diameter and then passed on to a spectrograph. The dispersed CARS signal was detected with a gated, image intensified diode array camera.

*Paper presented at an AGARD PEP Symposium on "Advanced Non-Intrusive Instrumentation for Propulsion Engines", held in Brussels, Belgium, 20-24 October 1997, and published in CP-598.*

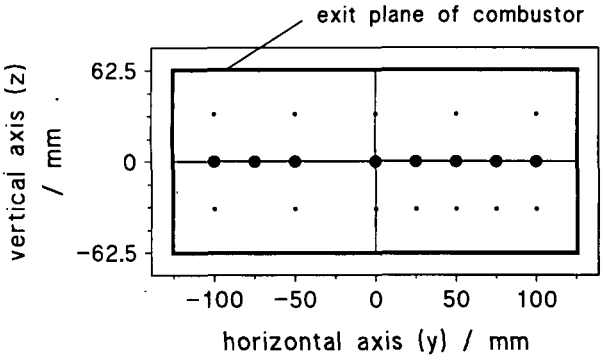


**Fig. 1:** Measuring positions in the thrust nozzle test facility at a distance of x = 50 mm from the exit plane.

### 3.2 Thrust Nozzle Test Facility

The $H_2$/air combustion chamber of the thrust nozzle test facility was operated at atmospheric pressure, but without nozzle. The use of 10 g/s $H_2$ and 400 g/s air resulted in an oxygen/fuel ratio of $\lambda$ = 1.16. The exit plane had a cross section of 250 x 125 mm$^2$. The measuring positions were located outside the combustion chamber in a plane with a distance of x = 50 mm from the exit plane. In this paper the results from the measuring positions marked with the large dots in Fig. 1 are shown.

### 3.3 RQL Combustor

The rectangular RQL combustor (MTU design) had three fuel injection nozzles arranged linearly on the backplate with a distance of 83 mm in between. The combustor was fueled with approx. 4 g/s kerosene and 203 g/s air (43 g/s primary air and 160 g/s secondary air, preheated to $T_{air}$ = 650 K) leading to oxygen/ fuel ratios of $\lambda_{total}$ = 3.39, $\lambda_{prim.}$ = 0.73, and $\lambda_{sec.}$ = 2.68. The combustor was operated at atmospheric pressure. The measuring positions were inside the combustor in four different planes. The presented results belong to the two

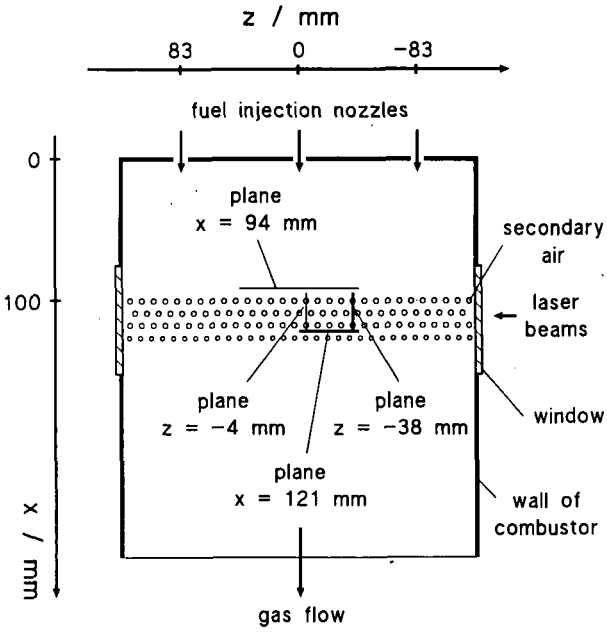


**Fig. 2:** Schematic representation of the RQL combustor (top view) with the three fuel injection nozzles, the four rows of inlet holes for the secondary air, the windows for optical access, and the positions of the four planes where CARS measurements were performed.

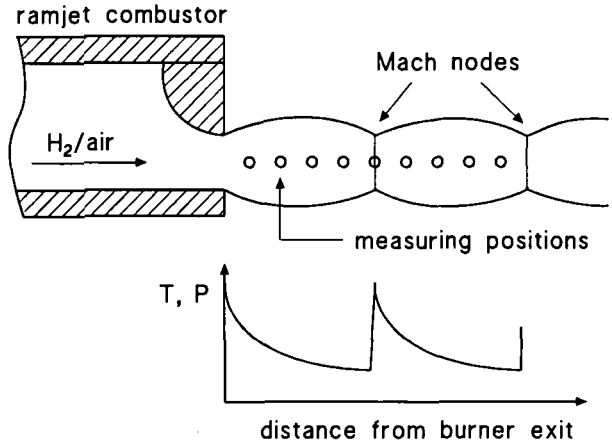


**Fig. 3:** Schematic plot of the ramjet combustion chamber. The circles on the centerline outside the combustion chamber indicate the positions of CARS measurements.

planes drawn with the thick lines in Fig. 2. The upper and lower walls of the combustor were located at y = ±40 mm.

### 3.4 Ramjet Combustor

The ramjet combustor of the *Institut für Thermodynamik der Luft- und Raumfahrt (ITLR)* of the University of Stuttgart was a downscaled segment of a ramjet engine. The combustor was fueled with 3.7 g/s $H_2$ and 129 g/s air resulting in near stoichiometric combustion. The pressure inside the combustion chamber was approx. 3 bar. The combustion chamber had a length of 300 mm and a rectangular contoured exit of 32 x 14 mm$^2$. Because the emerging gas had sonic velocity at the chamber exit the gas flow showed a structure of Mach nodes as schematically shown in Fig. 3. The measuring positions outside the combustion chamber are indicated by open circles.

## 4. DATA EVALUATION

All CARS spectra were recorded as single pulse spectra, because averaging of CARS spectra in turbulent flow fields leads to erroneous temperatures due to the non-linear CARS process. For the accurate temperature determination several corrections of each single pulse spectrum have to be made: subtraction of the averaged value of the flame luminosity, corrections for the nonlinearity of the diode array detector, and normalization to the spectral intensity distribution of the dye laser /6/. The temperature was deduced from each single pulse $N_2$ CARS spectrum by means of fitting theoretical spectra to the experimental data. To accelerate the data analysis a library of theoretical spectra was precalculated for the expected temperature range within 50 K steps. The resulting temperature was then determined by interpolation. The start temperature of the library based least squares fitting routine was given by a quick fit method (e.g. using the ratio of the integrated intensity of the fundamental and first excited vibrational band). The reliability of the data evaluation procedure has been tested in an electrically heated furnace. A more detailed description of the data evaluation is given in Ref. 6.

Due to the contoured exit of the ramjet combustion chamber, a shock-controlled flow field behind the burner exit is expected with varying temperature and pressure as shown schematically in Fig. 3. As the shape of the $N_2$ Q-branch CARS spectrum depends on both the temperature and pressure /8/ it is principally possible to deduce both values from the same spectrum. However, simultaneously fitting of the temperature and the pressure leads to unreliable results. Therefore, different parts of the spectrum are used to deduce the temperature

or the pressure. The region of Raman shifts below 2280 $cm^{-1}$ is mainly sensitive to the pressure due to the different dependence of the resonant and non-resonant susceptibilities on pressure. Minimizing the deviation between the experimental spectrum and the calculated one in this spectral range yields a fairly good estimate of the pressure. This average pressure value is then used as a fixed input parameter to deduce the temperature from the single pulse CARS spectra in the usual way, that means fitting the temperature sensitive part of the spectra to theoretical ones /8/. The accuracy of the pressure is approx. ±12% resulting in an additional uncertainty of the temperature of about ±2%.

Usually, at each position 1200 single pulse CARS spectra were measured from which the temperature distribution at this position was deduced. In case of the ramjet experiment for some series only 600 single pulse spectra were recorded due to the limited time of operation of the combustor. The accuracy of the temperature measurements is typically in the range of ±3 - 5% for single pulse CARS spectra. At all measuring positions of the three investigated combustors the signal-to-noise ratio of the recorded spectra was comparable to that of the test measurements in a high temperature furnace except at the positions y = -50 mm to -100 mm for the thrust nozzle test facility. Here the accuracy is in the range of ±5 - 7% due to a reduced signal-to-noise ratio. This can be explained by the influence of the strong gradients of the refractive index on the laser beams due to the longer traveling distance inside the flame up to the measuring volume compared to the other locations. This beam steering effect causes a decrease in quality of the overlap of the two laser beams in the focal region leading to a significant decrease in signal intensity. Due to the uncertainty of the determination of the pressure, in the ramjet experiment the temperature accuracy is approx. ±5 - 7%.

## 5. RESULTS AND DISCUSSIONS

In Table 1 the operation conditions of the three different combustors, some optical parameters, and the achieved accuracy of temperature and pressure have been summarized. The spatial resolution in beam direction is defined as the length in which 95% of the CARS signal is generated. The diameter of the measuring volume is a few tenths of a millimeter.

**Table 1:** Operation conditions and some experimental informations of the three different combustors.

| | thrust nozzle test facility | RQL | ramjet |
|---|---|---|---|
| fuel | 10 g/s $H_2$ | 4 g/s kerosine | 3.7 g/s $H_2$ |
| air | 400 g/s<br>$T_{air}$ = 300 K | 203 g /s<br>$T_{air}$ = 650 K | 129 g/s<br>$T_{air}$ = 300 K |
| oxygen/fuel ratio | $\lambda = 1.16$ | $\lambda_{total} = 3.39$<br>$\lambda_{prim.} = 0.73$<br>$\lambda_{sec.} = 2.68$ | $\lambda \approx 1$ |
| pressure in combustor | 1 bar | 1 bar | ≈ 3 bar |
| focal length | 500 mm | 500 mm | 300 mm |
| spatial resolution | ≤ 5 mm | 2.3 mm | 3.2 mm |
| temperature accuracy (single pulse) | ±3 - 5%<br>(±5 - 7%) | ±3 - 5% | ±5 - 7% |
| pressure accuracy | - | - | approx. ±12% |

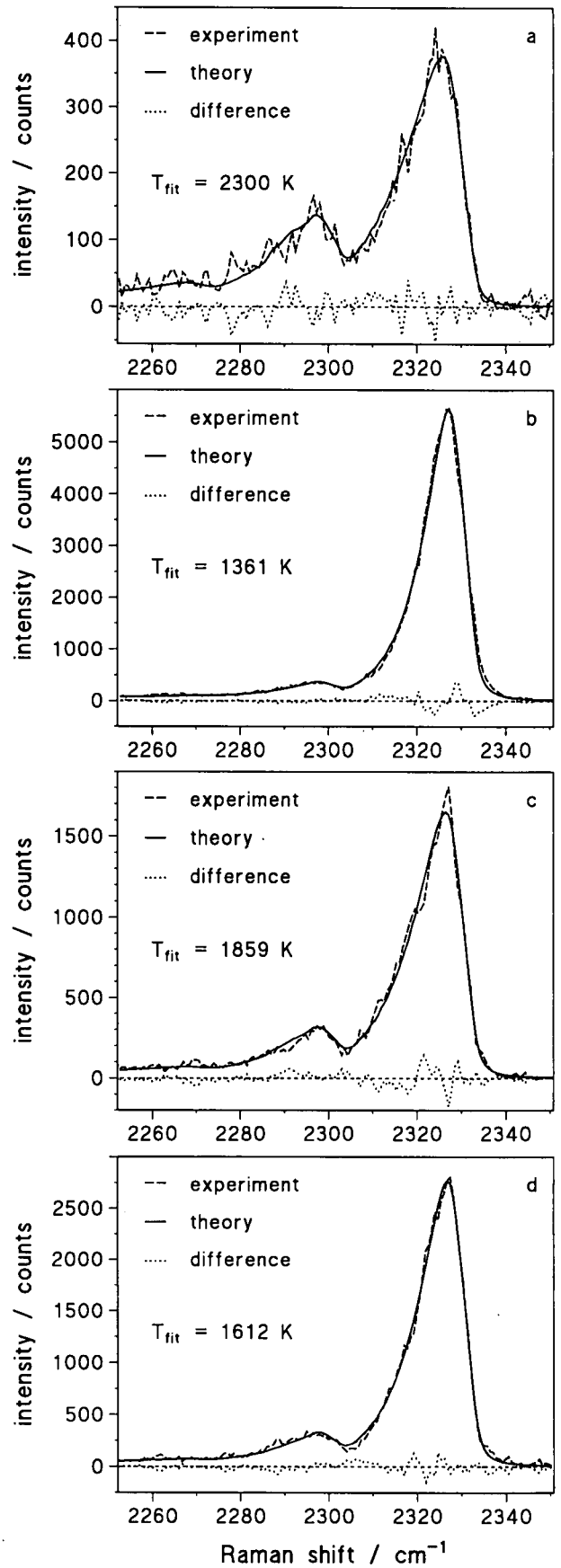


**Fig. 4:** Successively recorded single pulse CARS spectra measured in the thrust nozzle test facility at the position y = 100 mm and z = 0 mm.

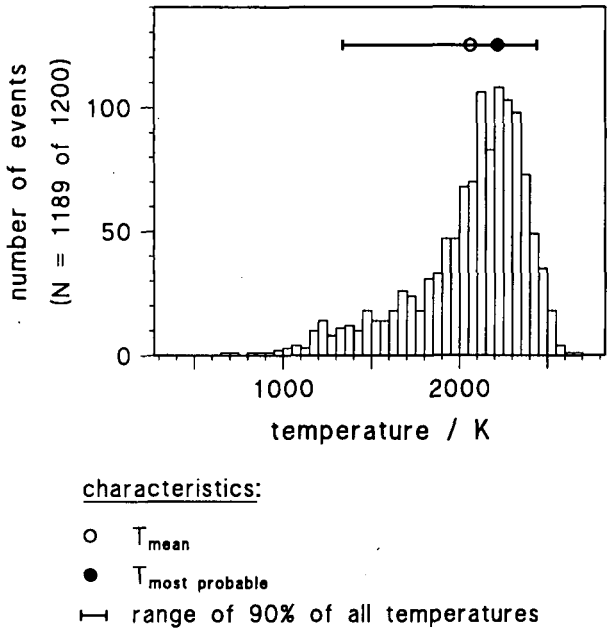


**Fig. 5:** Temperature histogram of the thrust nozzle test facility at the position y = 100 mm and z = 0 mm.

### 5.1 Thrust Nozzle Test Facility

In Fig. 4, four typical, successively recorded $N_2$ CARS spectra (dashed line) are shown, together with the best fit (solid line), the resulting difference curves between fit and experiment (dotted line), and the deduced temperatures. The spectra were recorded with the 10 Hz repetition rate of the excitation lasers. That means that the time between the instantaneous temperature values is 100 ms. The large fluctuations in temperature from pulse to pulse indicate the highly turbulent mixing of fuel and air at this location. The corresponding temperature histogram is shown in Fig. 5 with the following three characteristics: (i) the mean temperature $T_{mean}$ (open circle), (ii) the most probable temperature $T_{mp}$ (filled circle), and (iii) the range in which 90% of all temperature values occurred (indicated by the bar). For such asymmetric temperature distributions the standard deviation $\sigma$ is not a sufficient characterization of the temperature fluctuation. For this case, the most probable temperature with the 90% interval of all temperatures is defined.

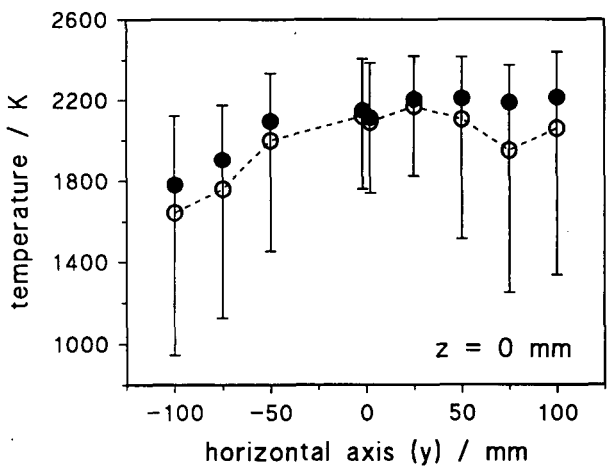


**Fig. 6:** Temperature profile of the thrust nozzle test facility near the exit plane of the combustion chamber (symbols as in Fig. 5).

As an example, the temperature profile at z = 0 mm (horizontal central axis) is presented in Fig. 6. As in Fig. 5, the open circles represent the mean temperatures and the filled circles the most probable temperatures. The data points of the mean temperature are connected by a line. The bars at the individual data points indicate the range which comprises 90% of all temperature values. The length of these bars is a measure of the temperature fluctuations at this position and mirrors the width and symmetry of the temperature distributions (compare Fig. 5).

The results reveal an asymmetry of the temperature profile with respect to the vertical central axis (similar results were found for z = ±32.5 mm): on the average, for y < 0 mm the temperatures are lower than for y > 0 mm (up to 400 K, see Fig. 6). These differences are real although the accuracy is slightly reduced for y < 0 mm. The same asymmetry was also observed in the visible flame structure recorded with a video camera from the top. Under the condition of operation for this run, for positions y < 0 mm a shorter flame length than for y > 0 mm was observed. Apart from a decrease of the temperature at one side of the exit plane, the large fluctuations of the temperatures down to 1000 K indicate an incomplete fuel/air mixing.

In Fig. 7, all evaluated single pulse temperatures were plotted versus time at the position y = 100 mm (as in Fig. 5) and y = -100 mm at z = 0 mm. The time interval of 120 s corresponds to 1200 single pulse measurments. The dashed lines indicate the range which comprises 90% of all measured temperatures at this position. There is no systematic dependence of the temperature values on time, which means that the observed asymmetric temperature distribution is not caused by the start up procedure of the combustor.

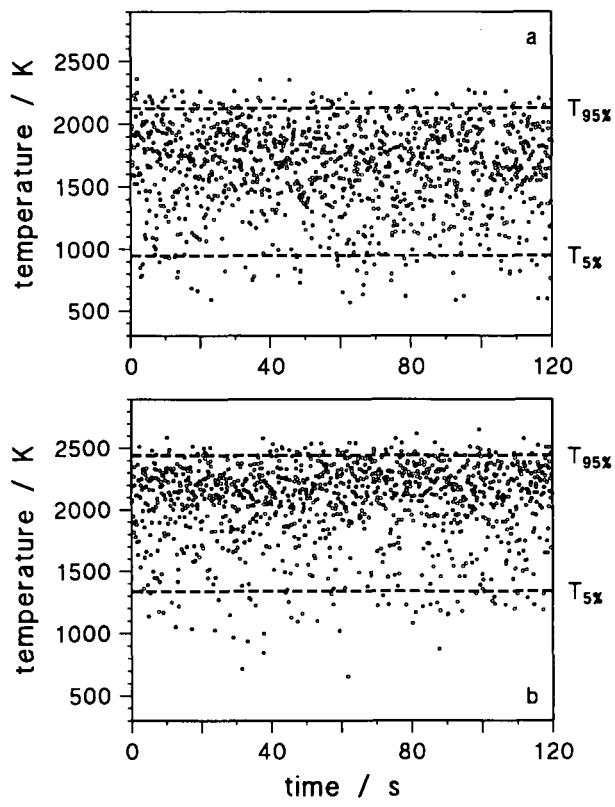


**Fig. 7:** Temporal evolution of the measured temperatures at the position y = -100 mm (a) and y = 100 mm (b) at z = 0 mm.

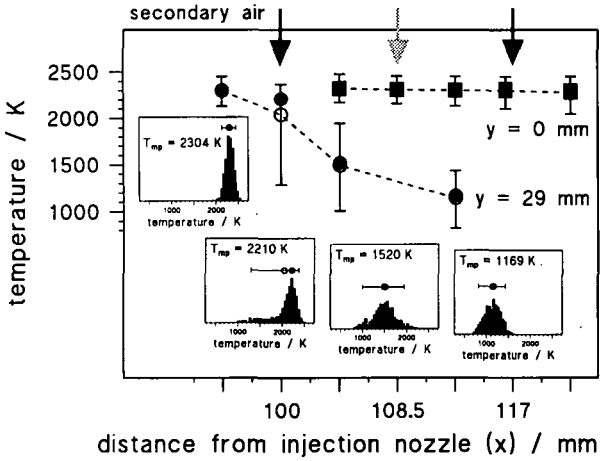


**Fig. 8:** Temperature profiles in the RQL combustor in the plane z = -38 mm (symbols as in Fig. 5). The histograms correspond to the data points of the profile at y = 29 mm.

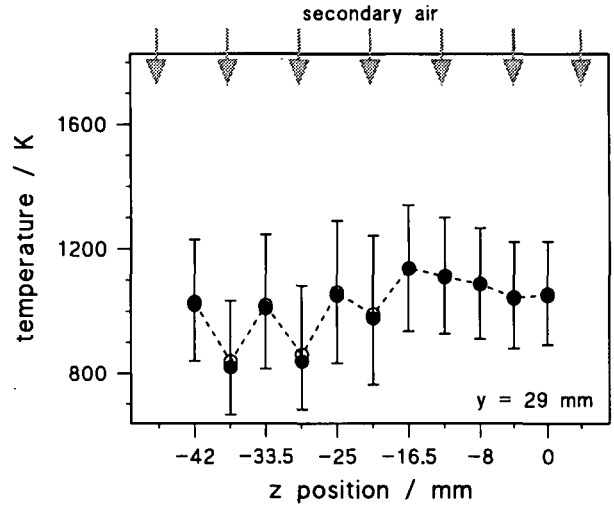


**Fig. 9:** Temperature profile in the RQL combustor in the plane x = 121 mm (symbols as in Fig. 5).

### 5.2 RQL Combustor

The temperature has been measured in several planes as indicated in Fig. 2. As an example, temperature profiles in the planes z = -38 mm (horizontal profile in direction of the gas flow) and x = 121 mm (horizontal profile perpendicular to the gas flow) are plotted in Fig. 8 and 9, respectively. The used symbols have the same meaning as stated before.

In Fig. 8 two temperature profiles in the direction of the gas flow (compare Fig. 2) are presented. For the profile at the height y = 29 mm (11 mm below the upper wall) the insert near each data point shows the corresponding histogram. The position of the inlet holes for the secondary air are indicated by arrows in the upper part of the picture. The inlet holes arranged in the measuring plane are represented by dark arrows and the holes located behind it by light arrows. The first data point at a distance of x = 95.7 mm from the injecting nozzles is at the end of the fuel-rich primary zone. The temperature histogram at this position shows a high temperature of $T_{mp}$ = 2304 K and a narrow distribution. The beginning of the mixing zone is characterized by asymmetric distributions with $T_{mp}$ above 2000 K, but also with some lower temperatures down to 1000 K. Further downstream the temperatures become lower and the distribution narrower. At the center of the combustor at y = 0 mm the temperature profile shows narrow temperature distributions for all measuring positions. The most probable temperatures are in the range of 2300 K. These high temperatures in the mixing zone indicate, that the streams of secondary air injected from the upper and lower wall do not reach the center of the combustor.

Due to the spatial resolution of $L_{95\%}$ = 2.3 mm the mixing behaviour of the secondary air could be characterized. This is demonstrated in Fig. 9, where the temperature profile measured in the plane at x = 121 mm (perpendicular to the gas flow) and at the height y = 29 mm is plotted. The profile shows a significant change of the fluctuations of the mean temperature as a function of the z position. Whereas in some part of the profile a temperature fluctuation of approx. 200 K is observed, which is correlated to the measuring position below an inlet hole of the secondary air or between, for z > -20 mm the temperature profile flattens. This may be caused by the interacting flow field of two neighbouring fuel injection nozzles.

### 5.3 Ramjet Combustor

The temperature histograms in Fig. 10 (measured 5.5 mm behind the chamber exit) represent different burner configurations and indicate the dependence of the efficiency of the $H_2$/air mixing on the design of the chamber. The histograms in Fig. 10a/b were recorded using a first version of the $H_2$ injection geometry. By increasing the turbulence of the air the probability of lower temperature values is reduced indicating an improvement of $H_2$/air mixing. Additional changes of the injection geometry lead to improved mixing conditions. In this case, as shown in Fig. 10c/d the temperature histograms show no significant variations of the temperature distribution on turbulence strength, though also this configuration does not give a satisfying mixing of fuel and air, which is visible from the asymmetric distribution towards lower temperatures.

With the optimized mixing configuration the temperature profile was measured along the flame axis from 5.5 mm to 45.5 mm apart from the combustion chamber exit. This profile is shown in Fig. 11 together with the average pressure which was also determined from the CARS spectra. Both curves show the expected structure (see Fig. 3). The peak values of

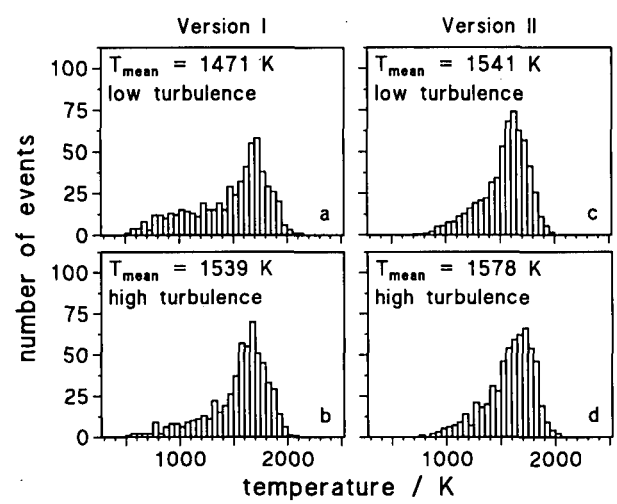


**Fig. 10:** Temperature histograms for two different configurations of the ramjet combustion chamber, both with low and high turbulence of the air.

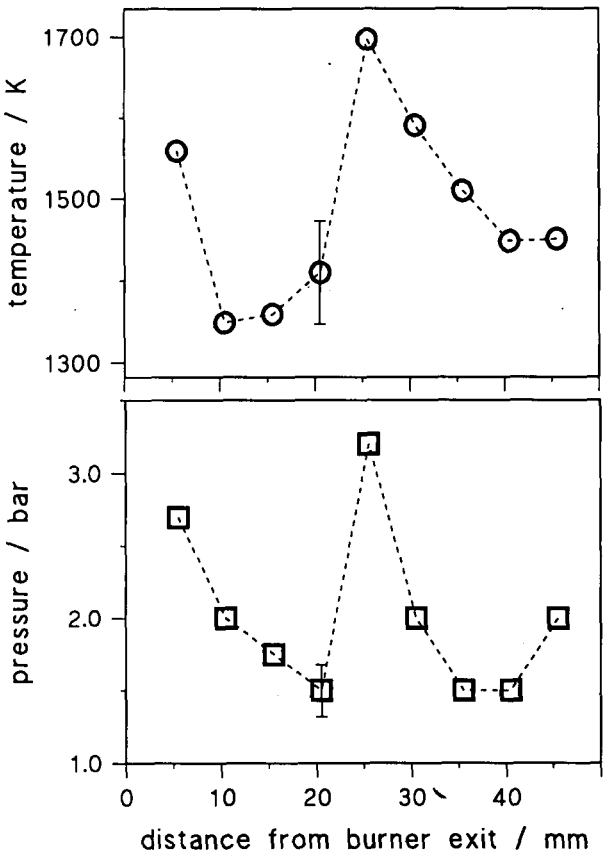


**Fig. 11:** Axial profiles of the mean temperature and the average pressure in the outer flame of the ramjet combustor.

the mean temperature and the average pressure coincide with the first Mach node at a distance of approx. 25 mm.

## 6. CONCLUSIONS

The application of CARS for temperature measurements in practical model combustors was demonstrated. With the mobile CARS system single pulse CARS $N_2$ thermometry was performed in three different combustion devices with a spatial resolution in beam direction of 2.3 mm to 5 mm. The accuracy of the single pulse temperatures was in the range of ±3 - 7%. The mean temperature, the most probable temperature and the temperature fluctuations were used to characterize the performance of the combustors, in particular the quality of fuel/air mixing. The symmetry of the temperature histograms gives valuable informations about the homogeneity of the combustion process, the temperature fluctuations about the state of the fuel/air mixing, and the temperature level about the efficiency of the combustion. In contrast to thermocouple measurements the temperatures could be measured with high spatial and temporal resolution, high accuracy, and without disturbing the gas flow.

In the first experiments on the combustion chamber of the thrust nozzle test facility an asymmetry in the temperature profiles across the exit plane was observed. The temperature difference was up to 400 K comparing the right and the left edge of the combustor. Moreover, an incomplete fuel/air mixing was indicated by the large width of the temperature distributions. This evident misfunction of the combustor could be eliminated by adjusting the fuel injection system.

The temperature distributions measured in the RQL combustor demonstrated, that the penetration depth of the secondary air was not sufficient. At a distance of 11 mm from the injection holes of the secondary air a good mixing of the rich burned gas of the primary zone with the secondary air was found. But in the center of the combustor (40 mm apart from the injection holes) the high temperatures of the primary zone were observed also at the end of the mixing zone. This leads to undesired high NO emissions.

In the case of the ramjet combustor, the measured temperature distributions allowed the distinction of the better design for the injection of the $H_2$ into the high speed air flow. The improved design was characterized by the temperature distribution that contained less low temperature values. In addition, the temperature distribution was not influenced if the turbulence of the air was increased. In the free jet flame temperature and pressure were measured along the flame axis. Both, the temperature and the pressure were evaluated from the same $N_2$ CARS spectrum. The measured profiles of temperatures and pressure show the expected structure. The position of the first Mach node outside the combustor was identified.

## 7. LITERATURE

/1/ M. V. Heitor and A. L. N. Moreira, Prog. Energy Combust. Sci. **19**, 259 (1993).

/2/ W. Stricker and W. Meier, Trends Appl. Spectrosc. **1**, 231 (1993).

/3/ A. C. Eckbreth, in: *Laser Diagnostics for Combustion, Temperature and Species*, Energy and Engineering Science Series, A. K. Gupta and D. G. Lilley, eds., (Abacus Press, Turnbridge Wells, Kent. and Cambridge, Mass. 1988), Vol. 7.

/4/ D. A. Greenhalgh, in: *Advances in Non-Linear Spectroscopy*, R. J. H. Clark and R. E. Hester, eds. (Wiley, New York 1988), p. 193.

/5/ R. Lückerath, W. Kreutner, W. Meier, and W. Stricker, in *Coherent Raman Spectroscopy: Applications and New Developments*, E. M. Castellucci, R. Righini, and F. Foggi, eds. (World Scientific, Singapore, 1993), p. 159.

/6/ R. Lückerath, M. Woyde, W. Meier, W. Stricker, U. Schnell, H.-C. Magel, J. Görres, H. Spliethoff, and H. Maier, Appl. Opt. **34**, 3302 (1995).

/7/ L. C. Davies, K. A. Marko, and L. Rimai, Appl. Opt. **20**, 1685 (1981).

/8/ W. Stricker, M. Woyde, R. Lückerath, and V. Bergmann, Ber. Bunsenges. Phys. Chem. **97** 1608 (1993).

Paper 14
Author: Luckerath

Q: Voigt

Do you take into account absorption effects when you analyse LIF images ?

A: Of course, we checked the absorption in our experimental configuration. Due to the excitation of OH on a line with relatively small line strength (Q1(7)), absorption is negligible.

Q: Black

In your RQL measurements, did you use polarisation discrimination to eliminate non-resonant CARS background? The presence of vaporised kerosine would give a large value of non-resonant CARS background.

A: No, it was not necessary in our case. The measuring positions were located at the end of the primary zone and in the mixing zone. At these positions a concentration of unburned hydrocarbons which might lead to a marked increase of the non-resonant background were not expected and not observed in these experiments.

# CARS Diagnostics on Model Gas Turbine Combustor Rigs.

John D. Black and Stephen S. Wiseall
Rolls-Royce Applied Science Laboratory,
P.O. Box 31,
Derby, DE24 8BJ,
U. K.

tel. 44-(0)1332-246142 fax. 44-(0)1332-247129
e-mail rrasl.optics@dial.pipex.com

**Summary**

Rolls-Royce Applied Science Laboratory has been active in CARS thermometry in aero gas turbine related combustion rigs for over ten years. This paper describes the mobile CARS system currently used for temperature measurements on research rigs, the current limitations of the technique, and future plans for improvements and implementation.

## Introduction

For a full review of the CARS process see for example Eckbreth, 1988. CARS is a laser light scattering technique in which two lasers, whose frequencies differ by the frequency of a Raman active molecular transition, interact in their region of overlap to generate a laser-like signal at a higher frequency. If one of the generating lasers is broadband in frequency, the signal will be broadband and can be dispersed on to a multichannel detector. The spectrum of the CARS signal is related to the Raman spectrum of the molecules being probed, and the form of this Raman spectrum depends on the distribution of molecules in energy levels, i.e. static temperature. Temperature is normally obtained by fitting the spectral shape. Since CARS thermometry depends on the shape of a spectrum and not on a measurement of signal intensity, it is particularly suited to hostile environments such as liquid kerosene fuelled combustion rigs where refractive index gradients, soot particles, and fuel droplets may cause large variations in signal strength.

Following initial demonstrations in atmospheric pressure gas turbine can combustors (Eckbreth, 1980 and Greenhalgh et al, 1983), CARS (Coherent Anti-Stokes Raman Spectroscopy) became reasonably well established as a non-intrusive thermometry technique in practical engineering devices, especially research internal combustion engines (for examples see Eckbreth, 1988 or Goss, 1993). Although CARS has been applied on the exhaust of a reheated aero-engine (Eckbreth et al., 1984), its use within gas turbine combustion rigs has been relatively limited. Measurements have been obtained in can type combustors and sector rigs fuelled with liquid kerosene running at conditions close to ground idle at SNECMA (by ONERA) (Magre et al, 1991), ONERA - LAERTE (Magre et al., 1996(a) , and Rolls-Royce (Black et al., 1996).

The main reason for CARS thermometry has been a desire to obtain data for the validation of CFD codes which model combustion in rigs. Rolls-Royce has an in-house developed CFD code (PACE) which has been in use for the last 20 years and is now being superseded by a more modern version (BOFFIN) developed in conjunction with Imperial College, London. The commercial CFD packages FLUENT and PHOENICS are used for some specialised applications. Generally, PACE produces good agreement with experimental data in non-combusting flows, for example isothermal mixing rigs (Spooner, 1991) and labyrinth seals (Brownell et al., 1989). However, the results of CFD simulations of combustion systems are much more difficult to validate. Usually the only data available are temperature and emissions data obtained by a limited number of probes at rig exit. In addition, because the modelling of realistic combustor configurations is non-trivial, CFD simulations tend to be carried out on full engine combustors at high power conditions where combustor stress and emissions problems are most likely to occur, but where it is most difficult to obtain internal data for CFD validation. The only data at high power conditions available to Rolls-Royce has been obtained using a gas sampling probe inserted from the exhaust end of a sector rig by DERA, Pyestock (Bullard et al., 1991).

CARS has not been used on gas turbine combustion rigs operating at high power conditions (pressures around 40 bar) because of difficulties in optical access and problems with high densities of soot particles and refractive index gradients. CARS spectra were obtained at 7 bar in small (0.5 Mw thermal power) can combustor provided by SNECMA where optical access was via primary air holes, but the data rate was low (Black, 1991). However, good spectral data were obtained at many locations in a three sector double annular combustion rig running at simulated ground idle conditions (3.2 bar) (Black et al., 1996). It is under these type of conditions that CARS thermometry can provide useful temporally resolved and averaged data for CFD validation.. The first comparisons of PACE predicted temperatures with CARS data was made in a single sector atmospheric pressure rig in 1995 (Black et al., 1996).

*Paper presented at an AGARD PEP Symposium on "Advanced Non-Intrusive Instrumentation for Propulsion Engines", held in Brussels, Belgium, 20-24 October 1997, and published in CP-598.*

**Experimental Considerations**

Nearly all practical CARS systems employ a frequency doubled Q-switched Nd/YAG laser as pump. The laser in the Rolls-Royce mobile CARS system produces 400 mJ per pulse of frequency doubled light at wavelength 532 nm (green) in 10 ns long pulses at a repetition rate of 10 pulses per second. When the system is configured to record nitrogen vibrational spectra for thermometry, part of the green light is used to pump a broadband dye laser producing up to 10 mJ in the range 605 - 610 nm (orange). The remaining green beam is split into two parallel beams which are aligned parallel with the dye laser beam. The three beams are focused with a common lens so that they overlap and generate a CARS signal in the region around their common focus. This three beam arrangement, known as folded BOXCARS (Eckbreth, 1978), gives well defined spatial resolution (see below). The direction of the signal beam is defined by the physics of the CARS process. The only practical folded BOXCARS configurations involve near forward scattering with the centres of the three pump beams, which are typically around 10 mm in diameter, separated by 10 - 25 mm. The signal beam, at a wavelength around 473 nm (blue-green) emerges from the overlap region at a small angle to the generating beams. Thus it can be spatially separated from them. It is normally recollimated with a lens identical to the focusing lens and steered to a grating spectrograph which disperses the signal on to a multichannel detector.

**Figure 1: Rolls-Royce Mobile CARS System**

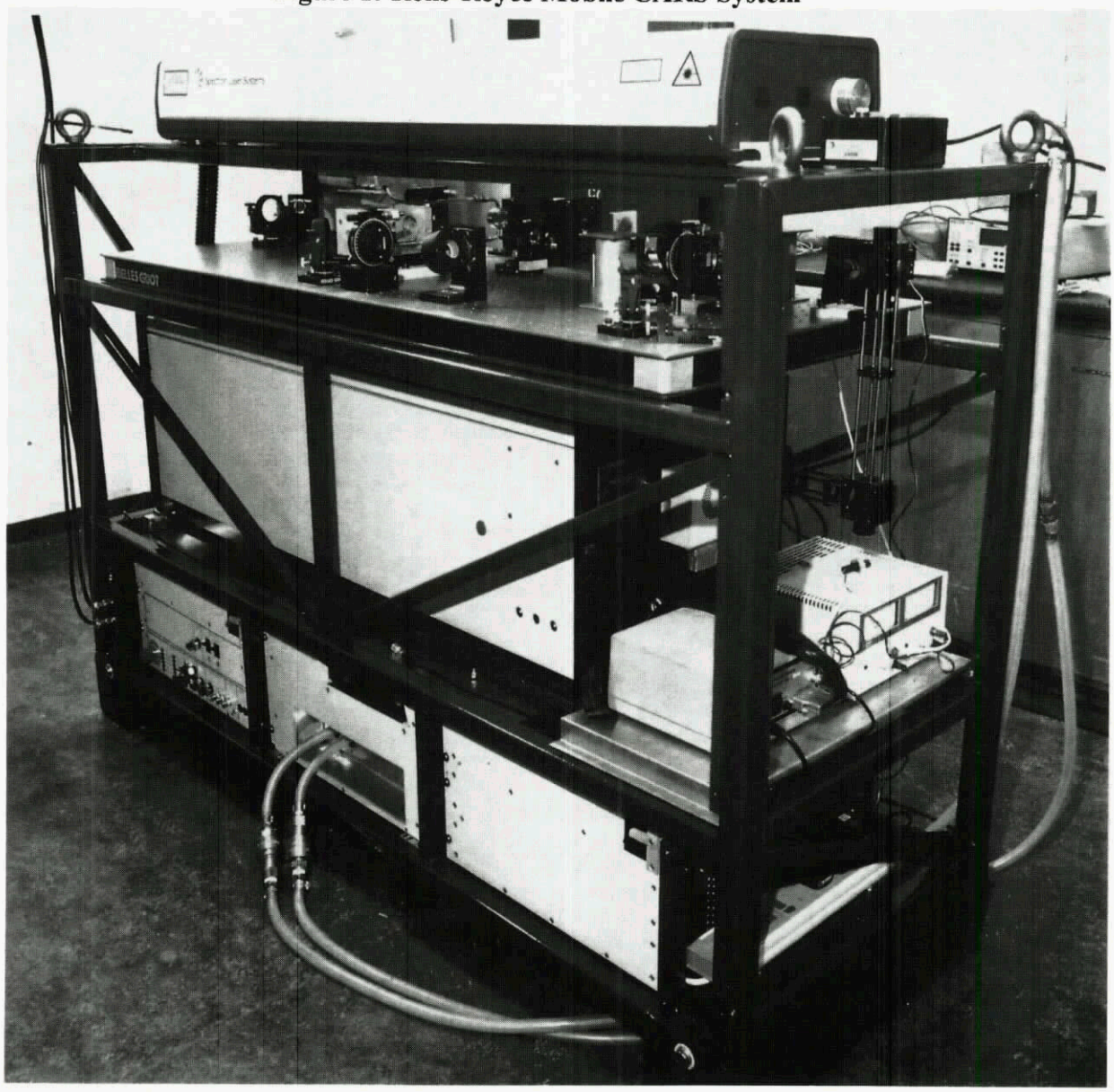

Figure 1 shows the Rolls-Royce mobile CARS system with the covers removed. The Nd/YAG laser is on the top level, the dye laser and beam handling optics on the next level, the spectrograph (Spex 1.26 m focal length spectrometer) with the detector (Wright Instruments thinned chip back illuminated CCD) on the level below, and the laser power supplies on the bottom level. The whole unit weighs 700 Kg with dimensions L = 1.85 m, W = 0.68 m, H = 1.44 m. The system has been designed to be compact (for transportability), to be robust enough to sit in a test cell alongside a running combustion rig (The heavy steel frame helps to damp rig induced vibration.), and for remote operation from a control room. The system, which was built in 1993, has been used on various combustion rigs in two test cells in-house at Rolls-Royce in Derby and on a sea level engine test bed at DERA, Pyestock.

Installation of the mobile system can normally be carried out by one person in around 1 hour. However, to date, beam steering optics to allow probing of a number of points, and hence temperature mapping within a rig, have been built up from standard components to suit the particular rig. This part of setting up a CARS test can take much longer, especially if traversing in three axes is required. Although every combustion rig is different, most are contained in pressure vessels which are pipes between 0.5 and 1.0 m in diameter. A three-axis traversing system which can be readily adjusted to accommodate any rig of this type is shown in Figure 2. This system allows the CARS measurement volume to be placed anywhere within a 200 mm sided cube within a 'pipe' type combustion rig. The aim is to reduce total installation time of the CARS equipment for a combustion rig test to less than one man-day.

**Figure 2: Three-Axis Traverse System on a Combustion Rig.**

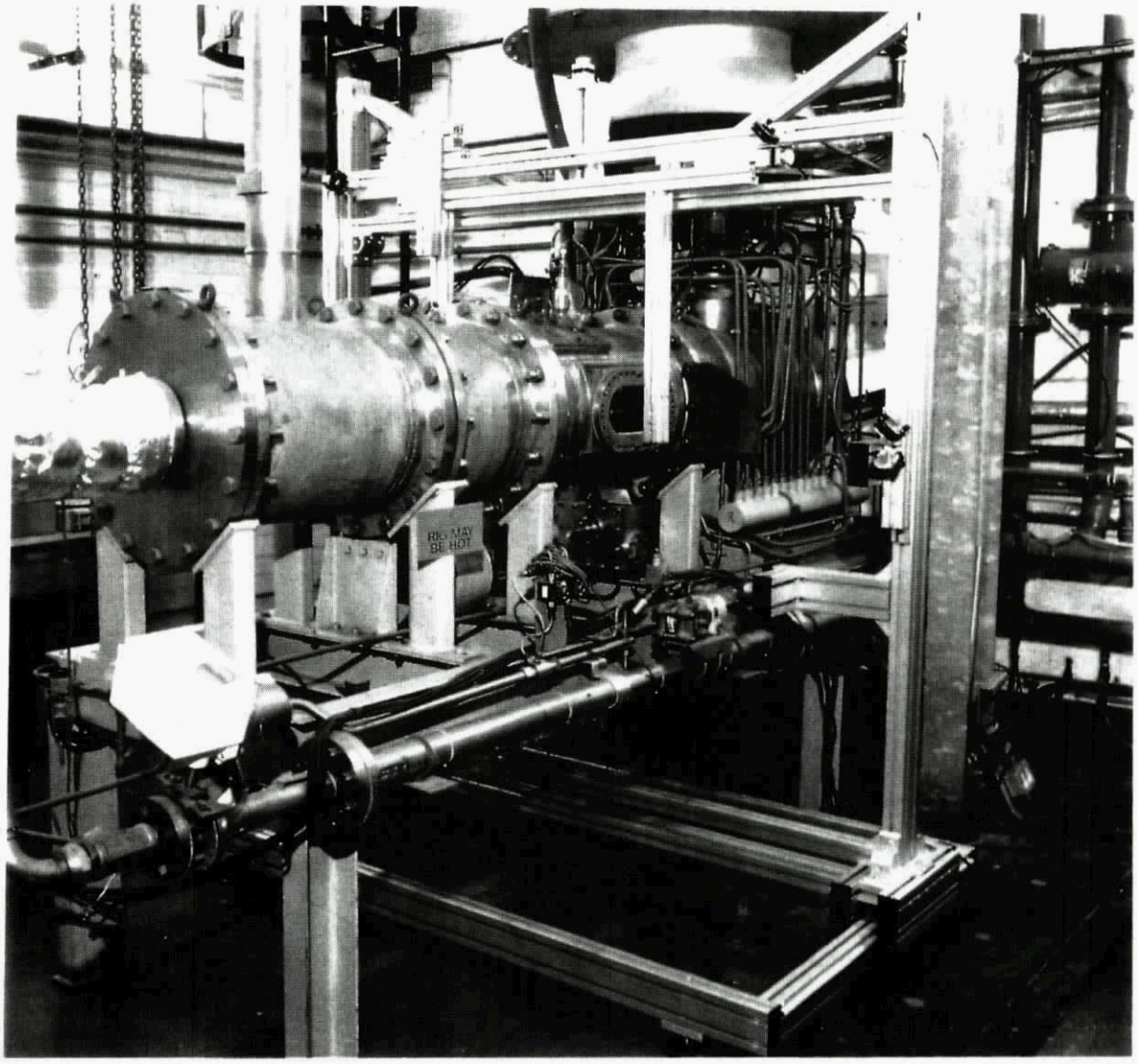

The dispersed CARS spectra are recorded on a thinned chip, back illuminated CCD (384 x 576 device manufactured by EEV) in a Wright Instruments camera with Peltier cooling. The camera package measuring 100 x 100 x 85 mm bolts conveniently on the spectrometer. The 'hot' side of the Peltier cooler is air cooled and the unit is evacuated so that there are no external water or dry gas connections to the camera, making it very convenient to use in a mobile CARS system. The unit is connected by a 1 m ribbon cable to an electronics box contained within the CARS rig which is connected to the PC which controls the camera and acquires data by a single co-ax cable. Cable lengths up to 25 m have been used. Most CARS systems employ intensified detectors where the spectrum is amplified in a commercial image intensifier coupled to a CCD or diode array. Historically, many problems in CARS thermometry have been associated with the intensifier, e.g. restricted dynamic range due to photocathode saturation and persistence of strong spectra from one laser pulse to the next (see for example Snelling et al., 1989), although current intensifiers suffer less from these problems than older versions. The thinned chip CCD is extremely sensitive (quantum efficiency ~80% at 473 nm) and no intensifier is required. The one disadvantage of the unintensified CCD is that it can not be electronically gated synchronously with the laser pulse to discriminate against continuous background light. The exposure time is controlled by a mechanical shutter. However, gating has not been necessary on any of the combustion rigs examined by CARS at Rolls-Royce.

The data acquisition rate is limited by the laser repetition rate (10 Hz). A dispersed hot nitrogen spectrum covers around 200 CCD pixels in the dispersion direction with a height of around 20 pixels. The central 320 of the 384 pixels in the smaller dimension of the thinned chip show maximum sensitivity, with reduced sensitivity near the edges. Spectral resolution depends on the focusing at the spectrometer entrance slit and is typically around 0.8 $cm^{-1}$. The 20 pixel height is due to the astigmatism of the spectrometer, which is actually an advantage because it helps to reduce saturation on individual pixels near the peak of strong spectra, thus increasing the dynamic range of the detector. The 20 pixel high image of the spectrum is binned into a single line 320 pixels wide and read out into the memory of the controlling computer. This is accomplished in well under the 100 ms interval between laser pulses. Practical experience has shown that files of 500 sequential single pulse spectra are sufficiently large to determine temperature PDFs in most combustion rigs. At the end of the 50 s acquisition there is an overhead while the computer organises the data in memory and writes it to hard disk. This storage time, together with an automated file naming procedure which ensures that data cannot be accidentally overwritten, takes around 10 s per file on the 486/33 PC currently used with the system. After each file of 500 spectra two backgrounds are recorded with the dye and pump blocked in turn. These backgrounds show if there is any stray laser light reaching the detector, or if there are any laser induced processes other than CARS, e.g. dielectric breakdown or fluorescence, taking place. Normally this is not the case and there is little pulse to pulse variation in the backgrounds. A smaller number of backgrounds, normally 100 single pulses with each laser blocked , is recorded. The current minimum total acquisition time per point including backgrounds is 100 s. The 10 s file organisation could be shortened by using a faster computer, and there is potential to reduce the total time to ~75 s.

The signal detected at any detector pixel from a single laser pulse is :-

$$\mathbf{S = KAIpIp^{/}I_S + background} \qquad \mathbf{(1)}$$

where **K** is a proportionality constant which depends on the CARS susceptibility of the medium under investigation at the wavelength corresponding to pixel and the number density of active molecules, **Ip** and **Ip** are the intensities of the two pump laser beams in the crossing region, $\mathbf{I_S}$ is the Stokes (dye laser) intensity, and **A** is a factor which accounts for phase mismatch between the various input beams.

In the current system the two pump beams are derived from a multi-longitudinal mode Nd/YAG laser and no attempt is made to match their path lengths. The dye laser is a completely separate oscillator. Therefore, there is no correlation between the phases of the beams. **A** varies randomly from pulse to pulse and ratioing the CARS signal against the signal from a reference cell containing a non-resonant gas gives no improvement in signal to noise. In the near future the Nd/YAG laser will be converted to single mode operation by injection seeding. ONERA have a CARS system based on a single mode Nd/YAG laser where they employ a reference leg which gives an improvement in signal to noise (Pealat et al, 1985) and the possibility of referencing will be investigated.

**Spectral Processing**

Spectra are currently processed off-line using the library fitting routine QUICK developed by AEA Technology, Harwell. In QUICK, spectra are compared with a library of precalculated spectra produced by another Harwell developed program, CARP2. The best fit temperature is interpolated between the library temperatures to minimise the sum of squares of residuals.

Before spectra can be presented to QUICK, any non-CARS background must be subtracted and the spectra must be corrected for the effect of the frequency profile of the broadband dye laser. This is done using in-house pre-processing code. Various options are available for dealing with spectra with different levels of interference from different sources, but all involve subtraction of background followed by division by a non-resonant "spectrum" to compensate for the dye laser profile. This division also compensates for sensitivity variations across the CCD detector. The preprocessed data at each spectral point ($\mathbf{S_{pre}}$) which is entered in the QUICK program are generated as follows :-

$$S_{pre} = (S_{raw}-S_{bck})/(S_{nr}-S_{nrbck}) \quad (2)$$

$S_{raw}$ raw signal count
$S_{bck}$ averaged background signal count
$S_{nr}$ nonresonant signal count
$S_{nrbck}$ background signal count corresponding to the nonresonant spectrum

The background consists of laser dependent components, e.g. laser induced fluorescence from $C_2$ and scattered light, and independent components, e.g. flame luminescence and $C_2$ emission. Because backgrounds cannot be recorded on the same pulse as single pulse spectra, an average background generated by averaging a file of single-pulse backgrounds is subtracted from individual single pulse spectra during preprocessing. However, the single pulse background data from each spatial location is always stored. The degree of interference and its source can be confirmed by inspection of the stored single-pulse backgrounds recorded with each laser blocked.

Nonresonant "spectra" are usually generated in propane which has a high nonresonant CARS susceptibility and no vibrations in the frequency range of the nitrogen vibrational spectrum. Normally nonresonant spectra are recorded as 100 pulse (10 s) integrations on the detector. The time averaged nonresonant spectrum mirrors the average frequency profile of the broadband dye laser subject to the same sensitivity variations across the detector as the test spectra. The single-pulse spectra of broadband dye lasers show a frequency structure which varies from pulse to pulse (Greenhalgh and Whittley, 1985) which limits the ultimate accuracy of single-pulse CARS measurements producing temperature PDFs with widths of typically 80 K from single-pulse data from an isothermal furnace. Mean temperatures of 500 single-pulse spectra have been recorded within 1% of pyrometer temperatures over the range 1100 - 2600 K in an isothermal heated filament device. In combustion rigs observed temperature PDFs are always much wider than the inherent width determined by the dye laser.

**Figure 3: Comparison of CARS Measured and PACE Predicted Temperature PDFs at Three Locations in a Single Sector Atmospheric Pressure Rig**

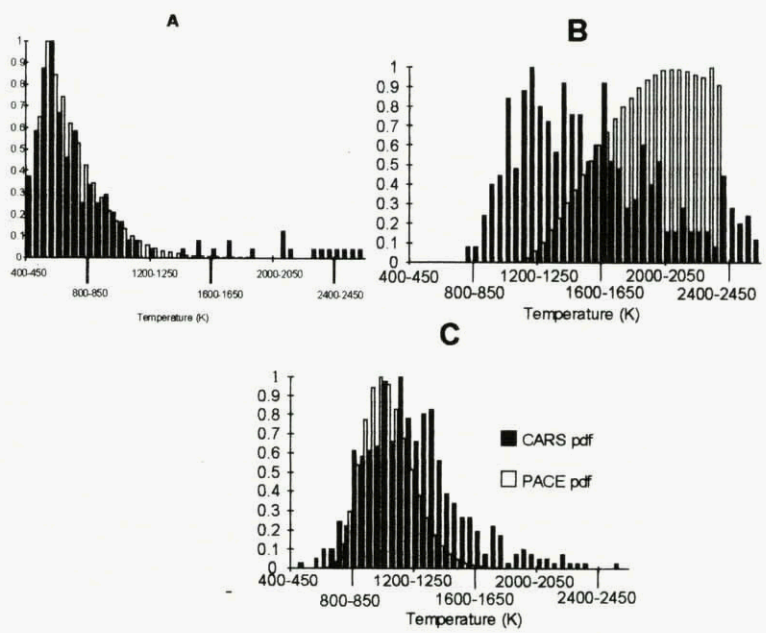

At present data acquisition and preprocessing is performed on a 486/33 PC and preprocessed spectra are transferred to a Pentium 133 PC which runs QUICK and CARP. Typical test procedure is to acquire one day's data on hard disk, preprocess and back up to tape at the end of the day. The preprocessing normally takes around 10 minutes. A maximum of 80 spatial locations in a combustion rig has been examined in one day. 500 spectra were recorded at each location together with associated backgrounds. Tape back up of raw and preprocessed data takes around 15 minutes. The tape is also used to transfer preprocessed data to the PC which runs the Harwell programs. Temperature fitting time using QUICK is variable depending on how far the best fit temperature is from the starting temperature which is input to the program. Typically 500 spectra are processed in about 5 min. Processing is usually carried out in batch runs overnight.

The QUICK program fits temperature by minimising the sum of squares of residuals. This may not be the best procedure to employ when dealing with noisy spectra such as those obtained from combustion rigs. For example, when the program is presented with a very weak spectrum, there is a tendency for any least squares fitting algorithm to return a temperature close to the starting value because the algorithm is unable to find a well defined minimum.

To avoid this situation spectra are always fitted with a starting temperature of 2800 K, well above the adiabatic flame temperature for kerosene burning in air of 2340 K. Spectra returning fitted temperatures >2400 K are rejected in the calculation of PDFs and mean temperatures. The QUICK program has the option to set the maximum number of iterations and returns the value of sum of squares of residuals. These factors can be used as acceptance criteria which can be set arbitrarily.

Spectra can be selected on signal to noise grounds before fitting, but there is then a risk that data will be wrongly conditioned. High temperature spectra are most likely to be rejected since the intensity of the spectral peak is approximately inversely proportional to temperature cubed. The Rolls-Royce approach is to attempt to fit any spectrum which shows a maximum in the correct position, no matter how weak or noisy it appears. This undoubtedly leads to some errors because the fitting routine mistakes weak spectra with noisy baselines for high temperature spectra.

Figure 3 shows temperature PDFs obtained from CARS data at three locations in the central plane of a single sector, atmospheric pressure, liquid kerosene fuelled combustion rig together with PACE predictions of the same PDFs. Figure 3(a) is a PDF from a location in an unmixed air jet where there is remarkably good agreement between the measurements and the prediction. 3(c) is from a location slightly downstream of an air jet. The measured PDF is centred at higher temperature, but has almost the same shape and width as the prediction. The agreement between prediction and experiment at these location gives some confidence in both the experimental and predictive methods. 3(b) is from a point on the rig centreline. Here, there is clearly disagreement between the prediction and the measurements. There is no allowance for radiation from soot in the PACE model; hence it is expected that it will overpredict mean temperature. The CARS PDF, which is extremely broad with temperatures ranging from just above inlet air to adiabatic flame temperature, does not appear to be biased to high temperature which would be the case if a large number of weak and noisy spectra were erroneously fitted as high temperatures. The impossibly high temperatures have been left in the PDFs to show their relative number.

**Spatial Resolution**

A common problem in CARS is biasing to low temperature when there are regions of unmixed hot and cold gas in the measurement volume. Since the spectrum of cold nitrogen is much stronger than that of hot, 'mixed' spectra are fitted to temperatures which are lower than the true volume average over the beam overlap volume. There have been several studies of this effect in laboratory flames (Bradley et al., 1992, Boquillon et al , 1988). Estimates of the length of the beam overlap region were made in the lab by translating a 0.7 mm diameter propane jet through the measurement volume and measuring the ratio of the nonresonant propane signal to the cold nitrogen signal. In the normal configuration used for combustion rigs with 300 mm focal length focusing and recollimating lenses the overlap length was measured as 3.2 mm. By expanding the beams before the focusing lens it was possible to reduce this to 0.8 mm while maintaining the 300 mm throw from the focusing lens. The peak temperature measured in a small Bunsen flame with the 3.2 mm beam overlap length was 1589 K. Reducing it to 0.8 mm increased the peak measured temperature to 1908 K. In the single sector rig where the PDFs of Figure 3 were obtained 127 mm focal length lenses were used so that the beam overlap length was ~1 mm. The highest mean temperatures measured in this rig were >1800 K, suggesting that biasing because the measurement volume length was too large was not a severe problem.

In larger combustion rigs 300 mm focal length lenses are normally used. In the triple sector, double annular rig shown in Figure 4 mean temperatures >1800 K were measured with a 3.2 mm measurement volume length, again suggesting that the spatial resolution was sufficient. The only comparison of CARS with another technique within a combustion rig was carried out in this triple sector rig. A sapphire rod probe was used to obtain intrusive temperature measurements in two axial planes where CARS measurements were also taken. In this probe the tip of a 1 mm diameter rod is coated with iridium to form a small blackbody cavity.

**Figure 4: Triple Sector Double Annular Combustion Rig**

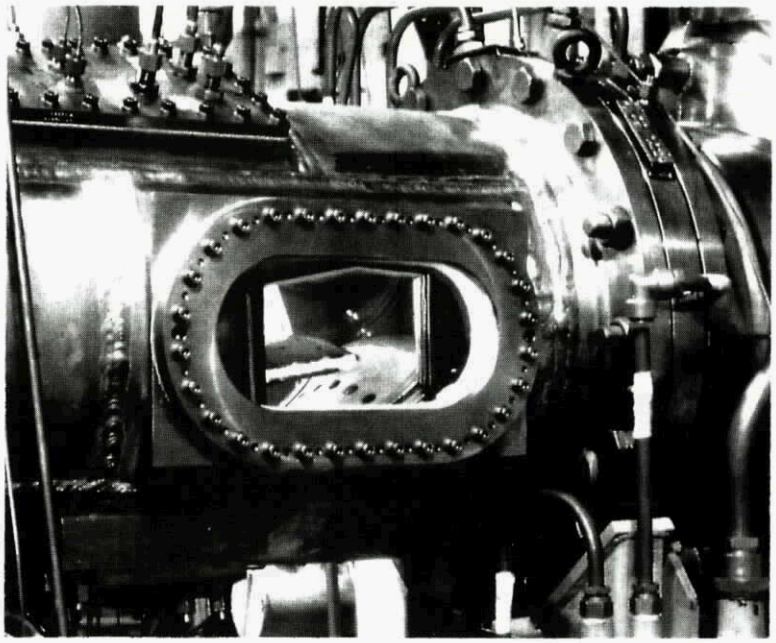

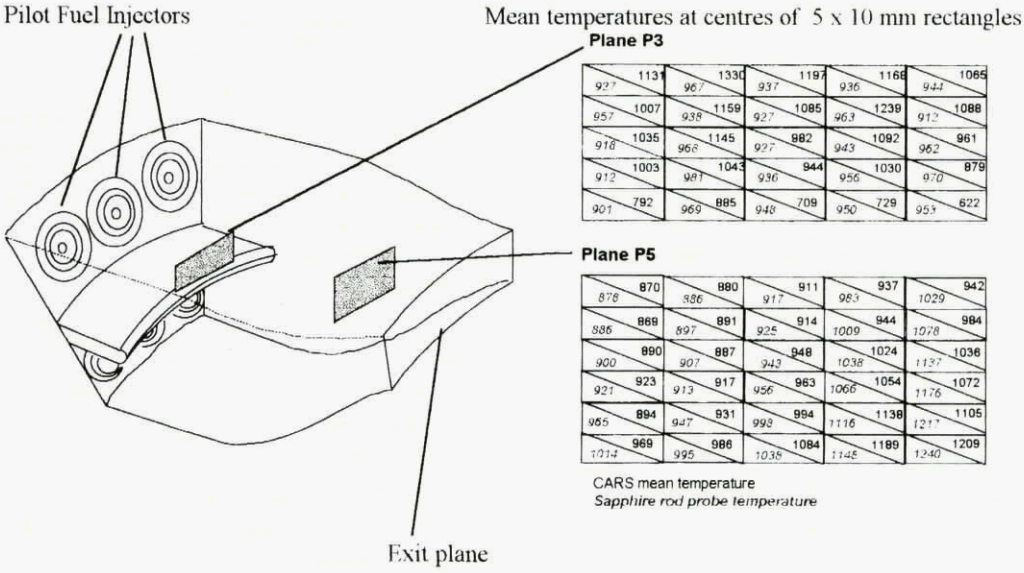

Radiation from the cavity along the sapphire rod is coupled into an optical fibre link to a conventional single colour pyrometer. A comparison of CARS mean temperatures from 500 single pulse measurements with probe temperatures is shown in Figure 4. Measurement points were in the stream of the central outboard (pilot) fuel injector separated by 10 mm horizontally and 5 mm vertically. The rig was running at simulated ground idle conditions (1.1 $Kgs^{-1}$ airflow, AFR 90, 3.18 bar pressure, 30:70 fuel split between pilot and main injectors). In the downstream plane, well into the dilution zone, there is good agreement between CARS and probe measurements <2.5% difference in most locations and <10% everywhere. In the upstream plane, close to the end of the splitter, the CARS data show structure associated with unmixed air jets and the splitter boundary layer (apparent in the lowest line of measurement points). The probe data shows little variation across the plane, ranging from 901 to 970 K while CARS mean temperatures range from 622 to 1330 K.

**Current Status of CARS Thermometry**

CARS thermometry is the only non-intrusive technique which has provided temperature information from within liquid kerosene fuelled combustion rigs, and this information has been used for CFD validation and to indicate the direction which CFD modelling must take. For example, droplet evaporation models must be included when modelling combustion in atmospheric pressure rigs (Black et al, 1996).

The accuracy of the CARS data from practical combustors is difficult to verify, or even estimate, since there is often no other measurement for comparison, and, even when there is, the other technique may not provide information which is directly comparable. However, the sapphire rod measurements in the triple sector rig and some comparisons of CARS and thermocouple measurements at the exit plane of a combustor by ONERA (Magre et al., 1991) and in a simple tubular propane fuelled combustor at Wright-Patterson AFB (Carter and Nejad, 1994) give some confidence in CARS measurements in gas turbine related combustors.

Another question is the significance of time averaged temperature measurement in highly turbulent burning rigs where temperature PDFs may be extremely broad (e.g. Figure 3(b)) or bi-modal. CARS data in such rigs has always to be collected as single pulse data since a time integrated CARS spectrum does not represent an average spectrum. Though traditionally CFD has been used to predict time averaged temperature, it can be used to predict temperature PDFs which can be validated using CARS.

CARS spatial resolution in practical combustion rigs is always likely to be a few millimetres, limited by the physical size of the rig and the need to cross beams at a small angle to obtain sufficient signal. Minimum turbulence length scales (Kolmogorov) are predicted to be ~0.1 mm, but it is not clear how much effect very small scale turbulence has on the temperature field. The effect of spatial averaging over a few mm is certainly not as dramatic as in small laboratory flames.

In recent years, since cooled slow-scan CCD detectors have become available, most research in combustion diagnostics has concentrated on techniques with the potential for two dimensional imaging, e.g. laser induced fluorescence, laser induced incandescence, Rayleigh/spontaneous Raman, and degenerate four wave mixing. At present CARS has only been used in combustion rigs to measure one point at a time, although some work on simultaneous CARS measurement along a line in flames has been reported recently (Jonuscheit et al., 1997). However, there is no 2-D thermometry technique which is applicable over the whole range of temperature of interest in combustion and which can be applied in kerosene fuelled rigs.

Acquiring sufficient CARS data for CFD validation or to determine, say, the extent of penetration of an air jet in a combustor takes a considerable amount of time. For example constructing a grid of 170 points with 500 spectra stored at each point in the single sector atmospheric pressure rig was achieved over 5 days running. Although, by the end of the test 80 points were examined in a day. When compared to set up times, test rig running times are comparatively short, and the rigs examined to date have not cost much to run. Hence, most of the current effort in Rolls-Royce is aimed at reducing set up and installation times and improving system reliability. The data acquisition rate is limited by the laser rep. rate of 10 Hz.

A principal perceived disadvantage to CARS thermometry has been the time taken to extract temperatures from spectra. At the time of the first demonstrations on combustion rigs around 1980 producing a temperature PDF took many months, and this still influences perceptions of the technique today. ONERA have been able to process spectra on-line since 1990 using conventional least squares fitting to a library of precalculated spectra (Magre et al., 1996(b)). With the current Rolls-Royce processing capability a factor of 5 increase in processing speed would be required for on-line display of temperature PDFs during testing. On-line processing means that temperature PDFs can be displayed during test runs, for example while optics are being moved to examine the next point in a traverse. Real time processing where temperatures are extracted in the interval between one spectrum and the next being acquired is possible if backgrounds are not required at each location examined, but there is then the problem of how to present data to the operator at this rate. All raw spectral data is stored.

A neural network approach to temperature extraction has been examined at Rolls-Royce. In this method a library of precalculated spectra is used to pre-train a neural network which then assigns temperatures to test spectra on the basis of how closely they resemble the examples used in training. The neural network method has the potential to be extremely fast (real time) using existing computer hardware.

At first 250 spectral points were used as input neurons for a three layer back propagation network with 15 neurons in a middle layer and temperature as the single output neuron (Black and Kerr, 1993). Although much faster, this network was found to be less sensitive and less robust in dealing with noisy spectra than conventional fitting and required long training times. The current system, using clustered training data (Van der Steen and Black, 1997), is more robust and has been demonstrated on some of the data from the triple sector rig. It has yet to be used during a rig test.

Although nearly all CARS thermometry to date has used the nitrogen vibrational spectrum, but there may be other approaches which may be more accurate or better able to cope with noise and interference in particular situations. Examples are rotational CARS which has been extensively studied by Lund University, Sweden (Bengtsson, 1994) and applied to internal combustion engines, and dual pump CARS giving simultaneous $N_2$ and $CO_2$ vibrational spectra. The ratio of the integrated $N_2$ and $CO_2$ spectra depends exponentially on temperature, varying most rapidly at low temperature, although, of course, it also depends on the relative concentrations (Wies, 1993).

**Conclusion**

Nitrogen vibrational CARS thermometry has been used to provide data for CFD validation from research combustion rigs running under realistic conditions where no other experimental data is available. Although the CARS process is conceptually difficult and the equipment will always be relatively expensive and complex, the present aim in Rolls-Royce is to make the already rugged system sufficiently versatile and easy to install that it can be used more routinely on research rigs, and possibly on engine development programmes. At the same time it is intended to incorporate those advances in CARS technology which lead to improved accuracy and reliability and transfer of temperature data to customers.

**Acknowledgements**

Work described in this paper was partially funded by the U.K. Department of Trade and Industry through DERA, Pyestock and partially by the E. U., BRITE/EURAM contract number AERO-CT92-0036. The authors wish to thank R. P. Barnes for performing the sapphire probe measurements and assistance in rig running and H. T. Brocklehurst for performing CFD calculations.

**References**

Bengtsson P.-E., L. Martinsson, M. Alden, S. Kroll, and J. Bonamy (1994), "Dual Broadband Rotational CARS Measurements in an IC Engine" 25th Combustion Symposium (International).

Black J. D. (1992), "CARS Gas Temperature Measurements in SNECMA Tubular Combustor. BRITE/EURAM Low Emissions Combustor Programmme" Rolls-Royce report number RR(OH)1220.

Black J.D. and Kerr N. C. (1993), "Application of Neural Networks in the Analysis of Coherent Anti-Stokes Raman Spectra" in *Coherent Raman Spectroscopy*, eds. E. M. Castellucci, R. Righini, and P. Foggi, World Scientific (Singapore).

Black J. D., H. T. Brocklehurst, and C. H. Priddin (1996), "Non-Intrusive Thermometry in Liquid Fuelled Combustor Sector rigs Using Coherent Anti-Stokes Raman (CARS) and Comparison with CFD Temperature Predictions," ASME-IGTI Paper No. 96-GT-185.

Boquillon J. P., M. Pealat, P. Bouchardy, G. Collin, and P. Magre (1988), "Spatial Averaging and Multiplex CARS Temperature Measurement Error" Opt. Letters **13** 722 - 724.

Bradley D. J., M. Lawes, M. J. Scott, C. G. W. Sheppard, D. A. Greenhalgh, and F. M. Porter (1992), "The Measurement of Temperature PDFs in Turbulent Flames by the CARS Technique" 24th Combustion Symposium (International), Sydney, Australia.

Brownell J. B., J. A. Millward, and R. J. Parker (1989) "Non-intrusive Investigations into Life-Size Labyrinth Seal Flow Fields," J. Eng. Gas Turbines and Power **111**, 335.

Bullard J. B., C. D. Hurley, and N. C. Eccles (1991), "An Advanced Combustion Research Facility for Validating Computational Fluid Dynamic Codes" 3rd European Propulsion Forum, ONERA, Paris.

Carter C. D. and A. Nejad (1994), Wright Laboratories, Wright-Patterson AFB, Dayton OH, USA, personal communication.

Eckbreth A. C. (1978),"BOXCARS: Crossed Beam Phase Matched CARS Generation in Gases" Appl. Phys. Lett. **32**, 421 - 423.

Eckbreth A. C. (1980),"CARS Thermometry in Practical Combustors" Combust. Flame **39**, 133 - 147.

Eckbreth A. C., G. M. Dobbs, J. H. Stufflebeam, and P. A. Tellex (1984),"CARS Temperature and Species Measurements in Augmented Jet Engine Exhausts" Appl. Opt. **23**, 1328 - 1339.

Eckbreth A. C. (1988), *Laser Diagnostics for Combustion Temperature and Species*, Vol. 7 of *Energy and Engineering Series*, eds. Gupta A. K. and Lilley D. G., Abacus (Tunbridge Wells).

Goss L. P. (1993) "CARS Instrumentation for Combustion Applications" in *Instrumentation for Flows with Combustion*, ed. A. M. K. P. Taylor, Academic Press (London)

Greenhalgh D. A., F. M. Porter, and W. A. England (1983), "The Application of Coherent Anti-Stokes Raman Scattering to Turbulent Combustion Thermometry" Combust. Flame **49**, 171 - 181.

Greenhalgh D. A. and S. T. Whittley (1985), "Mode Noise in Broadband CARS Spectroscopy" Appl. Opt. **24** 907 - 913.

Jonuscheit J., A. Thurmann, M. Schenk, T. Seeger, and A. Leipertz (1997), "Accuracy and Precision of Single-Pulse One-Dimensional Vibrational Coherent Anti-Stokes Raman Scattering Temperature Measurements" Appl. Opt. **36** 3253 - 3260.

Magre P. G. Collin, D. Ansart, C. Baudouin, and Y. Bouchie (1991), "Mesures de Temperature par DRASC et Validation d'un Code de Calcul sur Foyer de Turboreacteur" 3eme Forum Europeen sur la Propulsion Aeronautique EPF91, ONERA Paris.

Magre P., G. Collin, and P. Moreau (1996(a)), "CARS Temperature Measuremets in a 3-Sector Combustor Chamber" ONERA Report Number RT 11/3608 EY.

Magre P., P. Moreau, and M. Poirot (1996(b)), "CARS Temperature Measurements on a RQL Combustor" ONERA Report Number RT 8/3608 EY.

Pealat M., P. Bouchardy, M. Lefebvre, and J.-P. Taran (1985), "Precision of Multiplex CARS Temperature Measurements" Appl. Opt. **24** 1012 - 1022.

Parameswaran T. and D. R. Snelling (1996), "Effect of spatial averaging on CARS derived tempratures" Combust. Flame **106** 511 - 514.

Snelling D. R. , G. J. Smallwood, and T. Parameswaran (1989), "Effect of Detector Nonlinearity and Image Persistence on CARS Derived Temperatures" Appl Opt. **28**, 3233 - 3241.

Spooner M. P. (1991), "Mixing Study Using LIF on Phase 5 Perspex Sector", Rolls-Royce report number CRR89693.

Van der Steen H. J. L. and J. D. Black (1997), "Temperature Analysis of Coherent Anti-Stokes Raman spectra Using a Neural Network Approach", Neural Computing and Applications, **5**, 248 - 257.

Wies B., F. Scheuermann, Y. Waschke, S. Heshe, and D. Bruggemann (1993), "Theory and Applications of Dual Pump CARS for Simultaneous Measurements of Temperature and Concentrations" " in *Coherent Raman Spectroscopy*, eds. E. M. Castellucci, R. Righini, and P. Foggi, World Scientific (Singapore).

Paper 15
Author: J.D. Black

Q: H. Weyer

Which corrections did you apply to compare data of CARS and SAPPHIRE probes, which provide total temperatures from a physical point of view and which is an "arbitrary" average?

A: Gas velocities in the rig are 30 m/s. Hence the difference between total and static temperature is <1K. More measurements with a better designed probe, with improved spatial resolution would be required to investigate the issue of averaging.

Q: D.A. Greenhalgh

When comparing CARS and solid probe (e.g. sapphire probes) temperatures it is important to note that CARS will be volume weighted but the probe will be FAVRE or density weighted. This can lead to differences of 200K. For highly turbulent systems as shown previously normally the solid probe temperature will be lower.

A: In our case the discrepancy between mean CARS and probe temperatures in the upstream plane varied from T CARS-TPROBE = 363 to - 331 K in a definate pattern. In the downsteam plane the average Tcars-Tprobe is - 22.83 K, contrary to the expectation from the FAVRE vs volume averaging argument. The reason for this is not understood. More measurements with a better designed probe area are required to clarify this issue.

# Recent Developments in the Application of Laser Doppler Anemometry to Compressor Rigs

Jonathan D. Edmonds, David Harvey and Stephen. S.Wiseall
Rolls-Royce Applied Science Laboratory,

ROLLS-ROYCE plc
PO Box 31
Derby DE24 8BJ
U.K.

tel. (44)-(0)1332-247508, fax. (44)-(0)1332-247129
e-mail rrasl.optics@dial.pipex.com

## Summary

A 3D Laser Doppler Anemometry (LDA) system capable of measuring comprehensive in rotor flowfields on high-speed compressor rigs has been developed by the Rolls-Royce Applied Science Laboratory. This paper describes the system and presents data from a recent compressor rig test.

## Introduction

LDA is non-intrusive and can traverse at will (subject only to the limitations of blade shadowing) through both stationary and rotating blade rows. It has the ability to map turbulent three-dimensional flows at a range of conditions and to provide quantitative flow fields for comparison with computational predictions.

As improvements are made in axial turbomachinery compressor efficiency, performance tends to converge to an asymptote. With this progress an ever-improving knowledge of the detailed flowfield is essential both to determine the optimum performance and to improve 3-D prediction methods. The implementation of improvements such as aerofoil end bends and casing treatment will rely heavily on accurate diagnostic instrumentation.

Rolls-Royce has applied anemometry to high speed axial flow turbomachinery since its earliest development (ref. 1-3). Previous work on fan rigs has in the past mainly focused on the use of 2D Laser Twin Focus (L2F) systems, while a 2D LDA system optimised for use on High Pressure (HP) compressors was developed. More recently the need has arisen to acquire 3D measurements on fans and a system has been developed to meet this requirement whilst still maintaining the capability to measure on HP rigs.

The aim of the development program was to build and improve on the performance of the previous systems and to include the lessons learn from them. These include, lower weight, fewer bespoke components, improved cross-collection, flexibility of application, flexible time-gating and modular object oriented software for easier maintenance.

The pressure of test schedules on test facilities capable of running high-speed turbomachines means that any measurement systems must be able to be quickly transported and installed with the absolute minimum of time allowed for optical alignment and system set-up.

Due to the high running costs of transonic flow rigs a high priority is given to data acquisition rate. As data collection typically involves operating non-stop for up to 10 hours of running, the system minimises user input to reduce the opportunity for human error. Additionally, to minimise the time consuming process of stopping and restarting rigs to allow access to the LDA system, the system is operated remotely at up to 50 m range.

This paper presents descriptions of the system hardware and software together with some experimental data to illustrate the instrument capabilities.

## System Description

At Rolls-Royce a computer controlled 3-D Laser Doppler Anemometry system has been developed to meet these requirements. The system features a narrow angle 3-D optical head, mounted on a high precision 5 axis remote controlled traverse (figure 1). The optical probes feature a modular design to maximise versatility and scope for optimisation

*Paper presented at an AGARD PEP Symposium on "Advanced Non-Intrusive Instrumentation for Propulsion Engines", held in Brussels, Belgium, 20-24 October 1997, and published in CP-598.*

without major rework. The control software was developed in house and designed to allow maximum flexibility in its operation.

Some of the key features of the system include: -

- fully integrated graphical user interface (GUI) controlled data acquisition
- the ability to input a CFD grid for measurement positions
- ability to change optical head orientation remotely
- real time display and logging of rotor resolved time tagged velocities in engineering units

**Figure 1 LDA System Mounted on 5 axis Traverse**

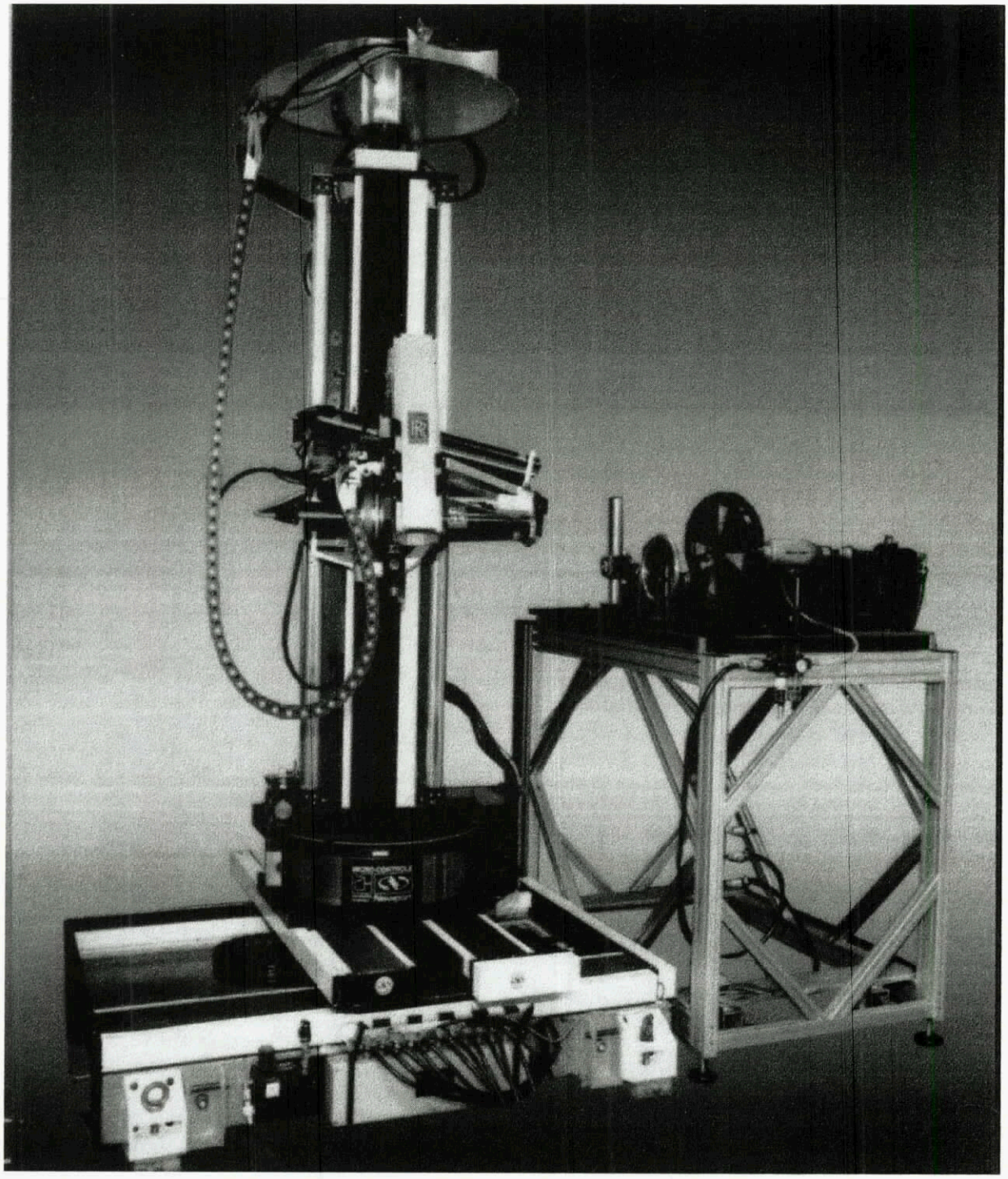

The architecture used in developing the system software follows an object-orientated philosophy. This approach allows low level software objects that communicate with hardware to be developed and debugged independently. Commercial GUI builders were then used for rapid prototyping and development of the GUI. The architecture allows the underlying hardware to be isolated from the GUI so that multiple hardware can be supported by the same GUI. For example the same traverse GUI can control either a large 5 axis traverse or a simple 3 axis system.

## Optical Head

The 3D optical head was designed to be robust, fibre delivered and based on commercial technology as far as was possible. It had to have features to allow: -

- in rotor passage measurements
- quick on-rig alignment
- operation in a hostile temperature and sound field environment with oil mist
- easy re-configuration of fringe spacing, optical throw, and included angle

Figure 2 shows the optical head, it is a modular system based on two Dantec fibre launched heads. Channel separation is achieved using wavelength division multiplexing of three Argon ion wavelengths (476.5, 488, 514.5 nm).

The two heads are mounted on an optical rail allowing any included angle ($2\theta$) between the two

**Figure 2 Optical Head**

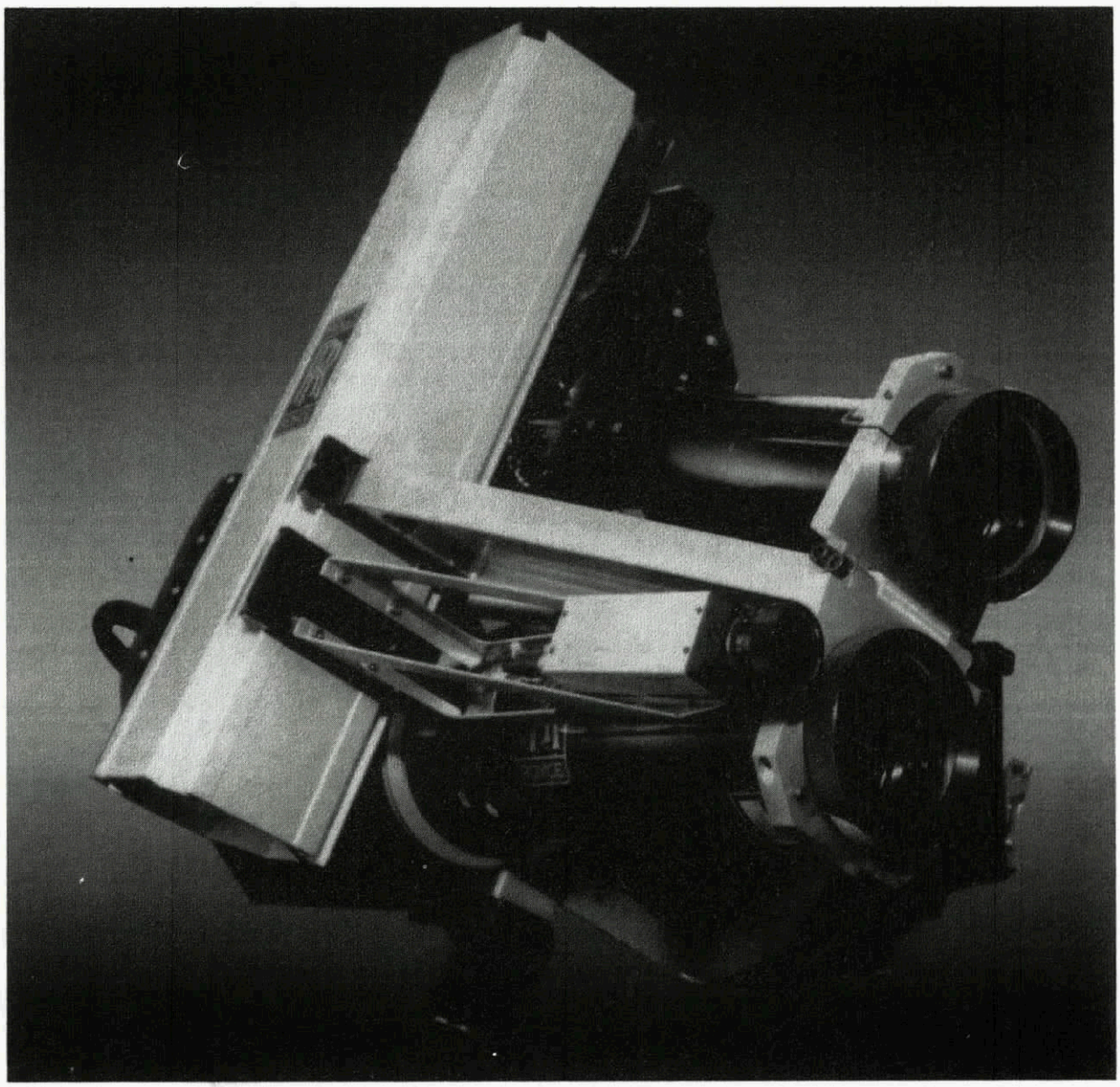

optical axes from 15 to 45 degrees. Off-axis collection is used to improve flare rejection and reduce the on-axis measurement volume length.

The system uses a 40 MHz Bragg shift to allow measurement of reversing flows.

To reduce the predicted flare problem when measuring close to blade roots and ease the problem of Photo Multiplier Tube (PMT) saturation due to reflections from the passing blades, two flare rejection schemes have been implemented.

A circular polarisation flare rejection scheme operates on the principle that the reflected flare light experiences an additional $\pi$ phase shift compared to the primarily refracted Doppler light, i.e. the signal light arises mainly from a refraction phenomenon, whereas the flare originates by reflection. The technique uses a combined linear polariser and quarter wave-plate arrangement to produce circular polarised projection beams. In the back (or near-back) propagation direction through the wave-plate, the flare is converted to the orthogonal linear polarised state and subsequently blocked by the polariser.

In total two polariser cubes and two quarter-wave-plates are used and mounted in modules compatible with the Dantec Fibreflow system. The specifications of the quarter-wave-plate are as follows: -

- Optically contacted quartz
- Effective zeroth order retardation plate (thus having negligible temperature sensitivity);
- Designed to have less than 5% phase retardation error at all three wavelengths used (476.5nm, 488nm and 514.5nm)

Lab based experiments show that this flare rejection scheme gives approximately a factor of four improvement to the Doppler signal to flare ratio.

The second flare reduction scheme allows the laser beam to be switched off when the measuring volume is incident onto a reflective surface. The system uses a Bragg cell that allows the laser beams to be switched with a rise and fall time of under 100 ns. A computer controlled delay generator can be triggered from a once per blade signal, the operator can then interactively adjust the offset and duration of the laser blanking to optimise near blade data collection. Inserting the Bragg cell does reduce laser launch efficiency so the system is designed to allow rapid insertion or removal without transmitter realignment.

In transonic rigs the flare rejection performance of the polarisation scheme in cross collection has proved adequate to allow measurement near blade surfaces without the overhead associated with operation of laser blanking.

It is important that the optical head remains aligned with up to ±15 degrees of traverse pitch and yaw applied. The optical misalignment is held to less than ten percent of the measurement volume diameter, by careful opto-mechanical design and the use of triangulation.

The optical system is designed to allow the alignment of the crossing points of the three pairs of projection beams to within ten percent of the measuring volume diameter, without exposing any of the optical components to the rig environment. Exterior collection fibre translation in one probe allows the two heads to be quickly aligned onto a common point, using laser back projection down the collection fibre.

The successful application of LDA to transonic flow requires high laser power. Several lasers have been tested during the development of the instrument. For good signal to noise performance it is important the laser maintains good $TM_{00}$ gausian output beams from all three wavelengths at high powers

## Traverse

Ideally, an LDA traverse system should be capable of positioning the measurement volume at any required location with any optical axis orientation. However if rotation stages are added to a traverse it becomes increasingly difficult to convert traverse positions into compressor relative axial, radial and circumferential co-ordinates. The system software has been designed to allow a CFD grid to be imported and all measurement positions to be specified as CFD grid points, this then allows easy comparison of the data with CFD results.

The traverse is required to incline the head due primarily to optical access constraints introduced by the high twist of a modern fan blade. This means that large areas of the in rotor blade passage are shadowed for any single optical axis orientation. To obtain a complete survey of in-rotor flow data from the suction surface to the pressure surface requires measurements to be collected at two separate inclinations, everywhere but at the tip of the blade. As outer annulus curvature prevents flat windows extending as far upstream as would be desired, the yaw stage must be used to extend measurement

beyond the window extent. The best angular orientation of the second LDA optical probe to avoid tip shadowing is determined primarily by the blade tip stagger angle. To allow the widest range of turbomachinery applications a manual roll stage has been incorporated that positions the second optical head at any orientation around the primary optical axis.

Full ergonomic exploitation of the 5 degrees of freedom remote traverse requires the software to insulate the user from co-ordinate systems. The system uses datuming features on the compressor to allow automatic co-ordinate conversion. This enables the user to read a CFD grid into the software and to specify the measurement grid in compressor relative co-ordinates. To determine the traverse motor positions the software then calculates the linear position in the traverse frame of reference, calculates the deltas caused by the interposed glass, the casing movement and the current traverse angles. This enables the engineer to plan measurement traverses with minimal difficulty.

This full control of measurement volume position and orientation allows the traverse pitch and yaw angles to be altered at will, if for example part of the window is contaminated the yaw angle can be altered and the software will calculate the linear traverse offsets to maintain the measurement position.

The co-ordinate conversion to compensate for any misalignment of the traverse and compressor axes is calculated using 3 datum positions on the compressor casing whose position is known in the compressor reference frame, and can be measured in the traverse frame of reference. The software also automates the tracking of the datum features, and the blade tip position, as the rig reaches its equilibrium temperature after a change of rig condition.

To achieve the desired accuracy on position it is important that the traverse in calibrated on all of its axes, to correct angle changes of up to ±15 degrees to within ±100μm requires angular accuracy of better than ±0.001 degrees. It is also important that the traverse is mounted on a stable base to prevent mechanical distortion as the optics are traversed, a 1000 kg granite block provides stability for the system.

## Signal Processing

The signal processing uses Dantec Burst Spectrum Analysers (BSAs) driven by the in-house software. The BSA processors use a hardware Fast Fourier Transform (FFT) to measure and to validate the LDA signal at up to one hundred thousand bursts per second. The software allows real time display of time resolved velocity information in the compressor frame of reference, as the measurement progresses. This allows the operator to concentrate on the fluid parameter being measured rather than the LDA signal. The ability to see, in real time the blade relative shock position, and to visualise the variation against blade number has proved to be a valuable diagnostic feature.

The software is capable of continually transferring, analysing, displaying and logging all of the bursts in real time without any loss of data at up to 6kHz per channel validated burst rate.

In the narrow angle 3D configuration the on-axis component of velocity is measured by the vector difference of two near parallel components, the optical transformation matrix F can be said to be ill conditioned. As the included angle ($2\theta$) is reduced below 90 degrees, the resolution of the on-axis velocity becomes inferior to the transverse components. The effect of any errors in measuring F on the accuracy of the on-axis velocity component are magnified. In the configuration used for fan tests the magnitude of this error multiplier is estimated to be ten times.

Simultaneously measuring all three components of velocity does have many advantages. The data can be measured with the optics at any orientation to the flow, so removing a significant constraint on optical access. Signal frequencies can be converted to 3D velocities along the axes of interest in the compressor frame of reference without any assumptions about the magnitude of the radial component.

The benefit of 3D remains even with the inferior resolution and precision of the on-axis component due to the narrow angle allowed for by access constraints. The contribution to the error in the circumferential axial plane velocities from the on-axis measurement error is small provided the on-axis velocities are small compared to the transverse components.

In order to minimise the velocity errors due to this ill conditioned optical transformation matrix F much attention is given to its accurate measurement. Using the precision traverse the calibration can be most accurately measured in laboratory conditions, this allows the conversion from 3 signal frequencies to velocity in the optical head frame of reference and then to the compressor reference frame. Two

methods are used to measure and verify the measurement of F.

The first method computes F by measuring the signal frequencies $f_i$ generated at three positions off the surface of a disk of spun at a precise rotational speed. In order that the inverse is not ill conditioned one of the velocity measurements must have a significant velocity component along the optical axis. This on-axis velocity can be achieved by using the yaw stage of the traverse to align the optical head away from the disk surface normal. The velocity vectors $\upsilon_i$ for the three positions is the cross product of the disk rotation vector and the three position vectors.

Alternatively, F can be calculated by measuring the direction vectors of the 6 laser beams. A light detector behind a 20μm pinhole locates each beam centre, scanning the laser head with the traverse allows the calculation of each beam direction vector in the traverse frame of reference. The sensitive vector of each beam pair is the unit vector orthogonal to the bisector of the beams in the plane of the beams. (Ref. 8)

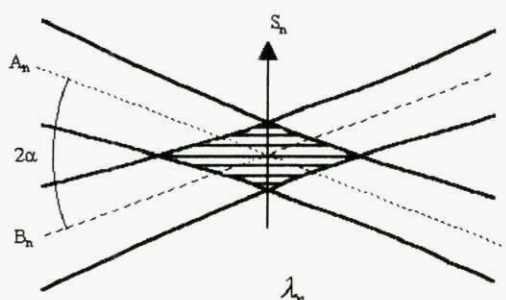


$$\mu_n = \frac{\lambda_n}{2.\sin(\alpha)}$$

**Fig. 3** Sensitive vector direction $S_n$

As this measurement of fringe spacing $\mu_n$ is only valid at the gausian beam waists, a beam profiler must be used to ensure that all six laser beams waists overlap at the centre of the measurement volume (fig. 3).

F is then the inverse of the vector combination of the sensitive vectors $S_i$ of the 3 Doppler beam pairs, multiplied by the reciprocal of their fringe spacing.

$$F = \begin{pmatrix} S_{11}/\mu_1 & S_{12}/\mu_1 & S_{13}/\mu_1 \\ S_{21}/\mu_2 & S_{22}/\mu_2 & S_{23}/\mu_2 \\ S_{31}/\mu_3 & S_{32}/\mu_3 & S_{33}/\mu_3 \end{pmatrix}^{-1}$$

The advantage of the first technique is that it gives a complete system calibration, and it can easily be used in situ to give confidence that any alignment of the optics has not altered the calibration. The second method can calibrate the system to within 0.3 % accuracy on velocity and 0.2 degrees on angle for the transverse measurements. A combination of the two methods for calculating F is used before, during and after an experiment to give confidence in the stability of the calibration.

## Application on Compressor Rigs

LDA measurements have been taken on a variety of high speed axial compressor rigs. The tests include a multistage high pressure compressor rig. This rig utilised window cassettes mounted in rotating rings to enable multiple stator pitch circumferential traverses, the traverse had to be capable of pitching the optical head from -15 to + 15 degrees without loss of positional accuracy.

Data are presented from a transonic fan test. This test demonstrates the advantages of a five degree of freedom traversing arrangement. Blade shadowing would have limited a simple traversing system to measuring a very constrained flowfield, in order to achieve best visibility on a single axial traverse up to ten different yaw and pitch combinations were used.

The flow field was measured upstream of the rotor, in the intra-blade region and downstream after the outlet guide vane. Combinations of axial, radial and circumferential traverses were taken to characterise the flow field as completely as possible given the constraints of measurement time. A once per rev signal was used to time tag the data with a resolution of more than 14000 time bins per rev. This time tag is recorded along with the LDA signal frequencies from the 3 channels for every burst. This allows the data to be reanalysed to whatever time resolution gives the appropriate statistical properties. Data were recorded at more than 2000 positions at several running conditions.

Optical access was provided using four 6mm thick flat glass windows mounted in metal cassettes. Two interchangeable windows covering the axial extent of the rotor were used, one of small circumferential extent for near tip work and one large window for greater immersion. Windows were also provided downstream of the stator and upstream of the rotor.

Mineral oil was atomised to produce 0.4 μm seeding particles to seed the flow. A far upstream remote controlled seeding input rake was used that enabled

any sector on a three by three grid to be selected. The data rate could then be optimised by sector selection. Earlier studies (ref. 1-7) have demonstrated the effective flow following properties of sub micron seed in the transonic regime, the use of 0.4μm seed gives a reduced particle inertia with acceptable visibility for this optical configuration.

Various seeding solutions have been tested including Polystyrene latex solutions in an atomiser, atomised mineral oil has proved to produce good results without contaminating the rig environment.

Data rates area maintained for prolonged periods of running using a system of remote controlled window washing. Solvent is flowed over the window to remove seeding deposits and air borne dirt. Various schemes for introducing the solvent have been tried, the use of holes rather than slots has proved more successful. The over rotor window has proved difficult to wash successfully, the variation in static pressure due to the work done by the fan, necessitating an internal weir system to equalise the flow of solvent across the window.

## Data reduction

At each spatial location, typically 30000 bursts were acquired for all three colours. All flow statistics are computed after the measured frequencies have been transformed into burst velocities in the compressor frame of reference. The rotor resolved flow velocity and turbulent intensity could then be ensemble averaged to any temporal resolution. As the blade to blade geometrical variation on this fan has been shown to be low, all of the blade passage data can be averaged to present the average blade passage data.

The data presentation focuses on average blade passage contour maps of rotor relative Mach number. The data are normalised by the inlet mach number. The data is presented with minimal "enhancement". In order to present the whole flow field data taken with the optical axis angled towards the suction surface is merged with data taken with a pressure surface inclination. The data are then contour plotted with any missing data interpolated from adjacent points to prevent spurious excess contours in the

**Figure 4 Axial traverse data from Fan Test**

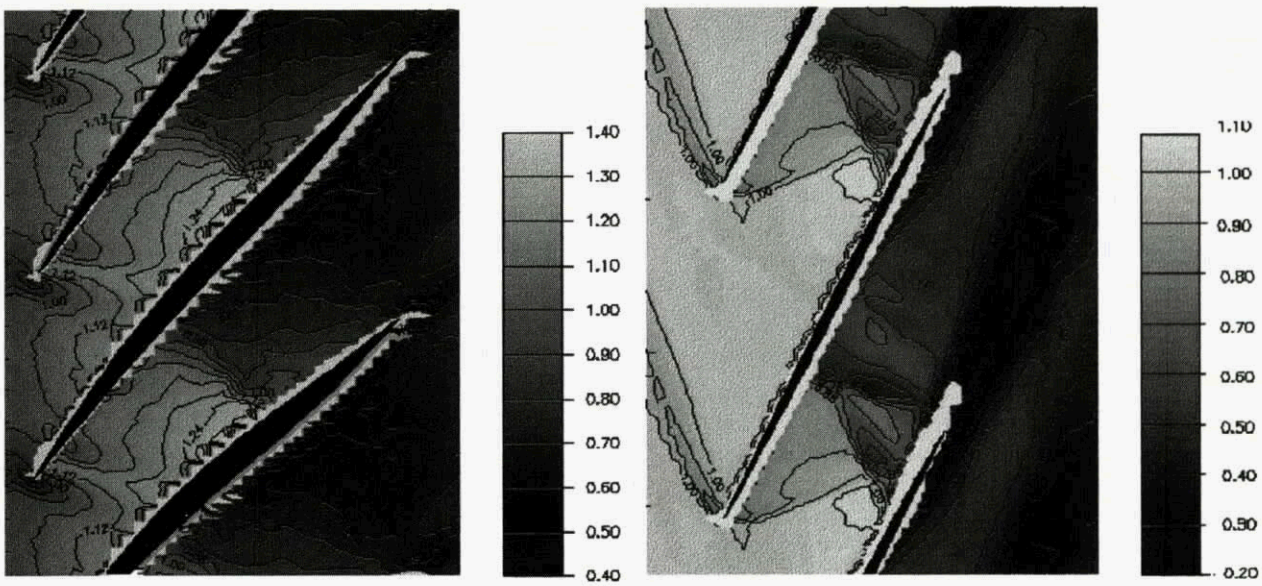


Measured relative Mach number at 35% span normalised by inlet Mach number, 100% speed

Measured relative Mach number at 90% span normalised by inlet Mach number, 100% speed

plot, the contours are then masked where data are absent and the blade profile overlaid. To aid visualisation the average passage data are repeated to form multiple blade passages.

Figure 4a shows data from 35% blade span at 100% speed, this data demonstrates the ability of the system to acquire a near complete blade passage at deep immersions.

Figure 4b shows a typical plot of a 38 spatial point axial streamline traverse. The data are presented with a 64 time bins per blade passage temporal resolution. The data were measured at 100% speed at 90% blade span. The data demonstrates the fine resolution on shock geometry that the LDA using sub micron seed particles can achieve.

## Conclusion

A computer controlled LDA system has been developed by Rolls-Royce, the system has been applied successfully to high speed compressor rigs in a development rig environment. The present aim in Rolls-Royce is to incorporate the already rugged and versatile system into an automated data acquisition system with automatic data transfer to customers.

## Acknowledgements

Work described in this paper was partially funded by the UK Department of Trade and Industry, MOD and DERA Pyestock.

## References

Moore CJ, Jones DG, Haxell CF, Braynston-Cross PJ, Parker RJ, 1981 "Optical methods of flow diagnostics in turbomachinery" proceedings of International Conference on Instrumentation in Aerospace Simulation Facilities, ICIASF81, pp244-255

Jones DG, Parker RJ, Wiseall SS, 1989, "Flow measurements in turbomachinery using laser anemometry and holography", 3rd international conference on Laser anemometry advances and applications Swansea IL 2.1-2.20

Ahmed NA, Hamid S, Elder RL, Forster CP, Tatam RP, Jones JDC, 1992, "Fiber optic laser anemometry for turbomachinery applications", Optics and lasers in engineering, vol.16, no.2-3, pp.193-205

Calvert WJ, Stapleton AW, 1994, "Detailed flow measurements and predictions for a 3-stage transonic fan", Journal of turbomachinery-Transactions of the ASME, Vol.116, No.2, pp.298-305

Suder KL, Chima RY, Strazisar AJ, Roberts WB, 1995, "The effect of adding roughness and thickness to a transonic axial compressor rotor" Journal of turbomachinery-Transactions of the ASME, Vol.117, No.4, pp.491-505

Suder KL, Celestina ML, 1996, "Experimental and computational investigation of the tip Clearance flow in a transonic axial compressor rotor". Journal of turbomachinery-transactions of the ASME,Vol.118, no.2, pp.218-229

Foley AC, Ivey PC, 1996, "Measurement of tip-clearance flow in a multistage, axial-flow compressor", Journal of turbomachinery-transactions of the ASME vol.118, no.2, pp.211-217

Boutier A, 1990, "Laser Velocimetry", VKI lecture series on "Measurement techniques for hypersonic flows" Rhôde-Saint-Gènese

Paper 16
Author: Edmonds

Q: Schodl

Is your automation software universal, e.g independent of compressor test rig and blade geometry, and independent of the positioning of the optical head?

A: To make the software for co-ordinate conversion universal there are data files containing both rig specific geometry and traverse/optical head geometry. The combination of these data files allow a fully universal system for rigs.

Q: Schodl

When you align the inclination angle of both optical heads to the blade geometry and when you change from rotor to stator position, how do you realign the receiving optics to the probe volume ?

A: It is our experience that with a 15 ° included angle optical head we must align with the glass normal to the bisector of the two heads. If this is done that head can be angled to the window by up to 15° with less than 10% of the 90 micrometres measurement diameter misalignment.

# PSP - Intensity and lifetime Measurements for steady and nonsteady flow

R.H. Engler, Chr. Klein
DLR Göttingen, Abteilung Windkanael
Bunsenstr. 10, D-37073 Göttingen
Germany

## Abstract

DLR started at 1995 with there own PSP activities. A phase of extensive exploration of hard- and software components followed and internal measurements using the intensity and lifetime method which includes spectra, calibration curves, etc. were performed. A repeatability study was made on the DASA HYTEX model, comparing the Inteco OPMS measurements from 1992/94 with the now existing DLR PSP system. Therefore, different lamps and laser illumination systems were tested. This included several cameras (intensified CCD and non-intensified CCD) for comparison of different paint samples in an external calibration chamber. After these pre-tests in the calibration chamber, measurements were performed in the Transonic Wind Tunnel Göttingen (TWG).

## Introduction

At the beginning of 1996, DLR started again with investigations of different cameras, light sources, data acquisition systems, image processing tools, signal controlling, paints, spectroscopy, etc. After construction of a calibration chamber with a pressure and temperature control device, and an additional facility for fast pressure variation, several paints were investigated. It was decided mainly to use the L4 and F2 one component Optrod paint from TsAGI (Russia) in the exploration phase.

To install the complete PSP system for all necessary components at the wind tunnel, a system was developed with short implementation times. This system has been optimized for the different wind tunnels but mainly for the Transonic Wind Tunnel Göttingen (TWG).

The same DASA HYTEX model from 1994 was taken again for comparisons between DLR PSP and OPMS results. Therefore the intensity method in the same wind tunnel (TWG) and under identical test cases was used. It was expected that this repeatability check gave an impression about the PSP accuracy under real wind tunnel conditions, including handling and management and software and data for different paints. Prior to real wind tunnel measurements various paints were investigated in view of pressure sensitivity, temperature influence, photo-degradation, illumination differences, etc. Also cameras and illumination sources were checked for the real situation (0.5m to 1.0m distance from light source and camera positions) to the model surface of the TWG.

Parallel lifetime measurements were performed to investigate this technique and the possibility to use it in the wind tunnel instead of the intensity method.

Results of several wind tunnel tests as well as lifetime investigations now can be presented including basic tests using the external calibration chamber.

## DLR-PSP hardware and software components

After testing different cameras of different distributors Princton CCD and ICCD cameras were used for the measurements. Two different types of water-cooled 16 bit CCD back-illuminated cameras with an 512 x 512 or 1024 x 1024 CCD chip were used. The ICCD is a frame transfer fiber-coupled 16 bit system with 512 x 512 pixels and a gate time minimum of 50 ns.

After testing these cameras, a type with a vacuum chamber in the sensors front was selected. There was an option for using a multi component paint system. With the aid of a connector, a spectrometer can be installed on the cameras head. Different camera objectives are necessary for an optimal solution of model sizes for wind tunnel tests.

Numerous light sources were tested for the UV excitation range from 320 - 350 nm and the visible range. The main problem is the stability of the light source (intensity), and the output energy for the UV wavelength.

After a series of tests, it was found that pulsed light sources should be chosen to have the possibility to realize time-resolved and non-time-resolved PSP measurements. By using a cw-light source an external shutter is necessary to reduce the process of photo degradation. For the tests, two different illumination sources were used:

*Paper presented at an AGARD PEP Symposium on "Advanced Non-Intrusive Instrumentation for Propulsion Engines", held in Brussels, Belgium, 20-24 October 1997, and published in CP-598.*

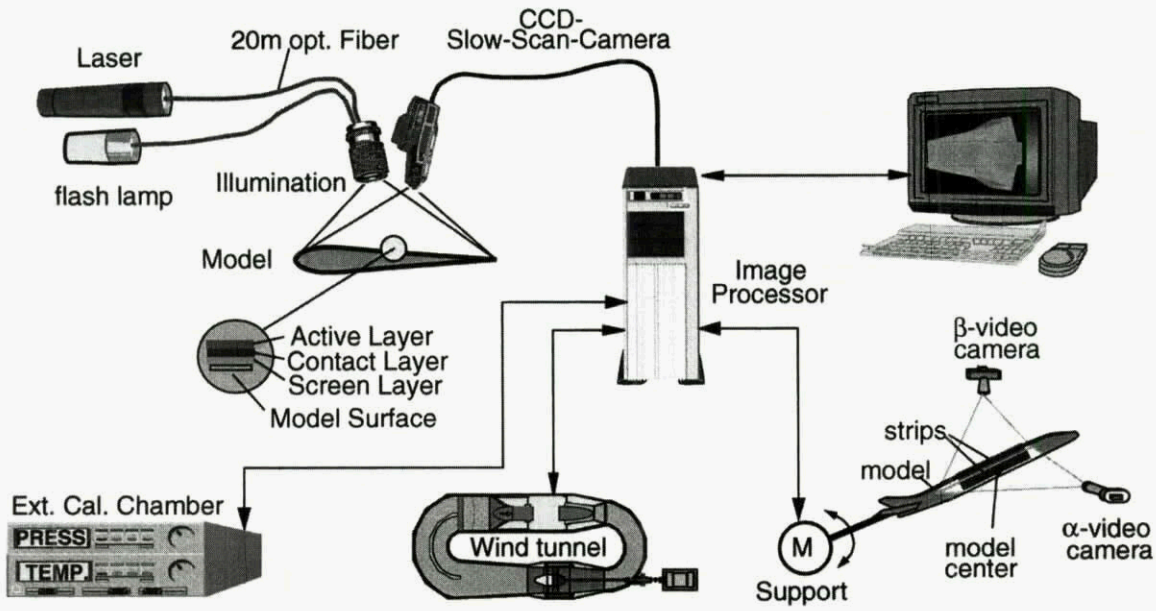


Fig. 1: PSP system composition including data acquisition and control system

Xenon flash lamp:

| | |
|---|---|
| Model : | JML-DLR |
| ext. trigger: | max. 40 Hz |
| single pulse time: | 20 ms |
| energy (all lines): | 4.8 mJ after a 1m long optical fiber each |

This lamp is built by DLR and an industrial partner. The box of the lamp is designed with four light output ports for connection of four optical fibers. The transmission rate of the fiber is better than 60% at 300 - 600 nm wavelength. The length of each fiber is 15 m, and the angle of output divergence without any lenses is 75°. The filters in front of the optical fiber inputs can be exchanged. For the Optrod L4 paint a DUG11 filter was used. These fiber optics can be connected to a laser, to laser diodes and e. g. to Mercury and Xenon lamps. For the paints with 450 nm excitation wave length an Argon-Ion-laser was used for several tests.
The laser can also be connected to another set of four 20 m long multi mode optical fibers. The lamp or laser can be triggered by the controller of the camera.

Laser:

| | |
|---|---|
| Model : | VSL nitrogen laser |
| ext. trigger: | max. 50 Hz |
| single pulse time: | 4 ns |
| energy/pulse: | 250 mJ |

For different other measurements an ordinary Argon-Ion laser with 6 W output energy and coupled mono mode optical fibers were used. Here a prism can select special wavelengths for visible paint excitations. Tests for different paints with different light sources were performed - here in the visible excitation and emission range. Using different light sources a recognizable phase shift is detectable in the emission spectra. Therefore, knowledge about the light source is important for later filter setting. The PSP data acquisition system is fully integrated in the wind tunnel control and data acquisition system DeAs.
DeAs is a managing system for the control of Mach number, pressures and temperatures, etc., data acquisition and monitoring. It has been developed for wind tunnels and can be operated from workstations in the control room, or any other location.
The PSP system is presently fully integrated in the DeAs system, with the advantage that all data from PSI (p), T, Ma, etc. can be written in the header of PSP images. Also an important advantage is the implementation of the optical angle of attack control system OWI. This system determines and controls the exact angle of attack, independent of wind-on or wind-off conditions. The necessary support angle is set and starts an automatic optimization with an accuracy of 1/100 degree. After reaching this value the PSP measurement starts including laser/lamp trigger and shutters automatically. For the real wind tunnel measurements a typical camera exposure time is 1 -2s. For example, at constant Mach number, 10 different angles of attack can be measured in 10 minutes, including all the imaging and acquisition of other necessary parameters.
For periodic and unsteady flow field investigations, e.g. os-

cillating wings, propellers, rotor blades, short time intensity measurements were performed. Here measurements on the model shown in Fig.12 were realized, with a single flash illumination of 25 µs in the TWG.
A pre-acquisition of data will be performed by the PC, followed by an evaluation on a SUN workstation. By this technique, a quasi real time computation is possible, and therefore the interesting aerodynamic effects can be detected and investigated in detail in a short time.

### Comparison of DLR-PSP and Inteco-OPMS

First measurements using the DLR-PSP components were performed at the end of October 1996 under real wind tunnel conditions. Different cameras, illumination systems, including lasers and lamps, were tested.

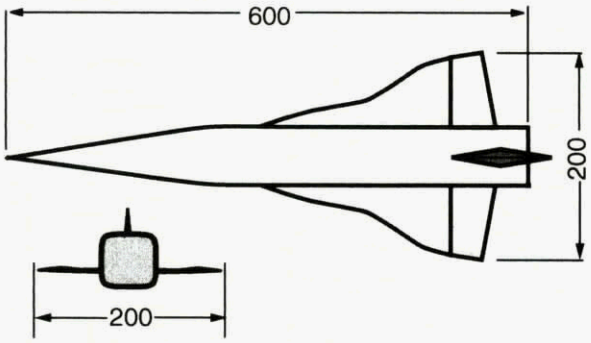


Fig. 3: DASA HYTEX model

For later comparisons the DASA HYTEX model, given in Fig. 3 was chosen for an assessment of results obtained by the Inteco OPMS video system, and the DLR slow scan camera system. Typical test cases were Mach numbers between Ma = 0.5 and 1.1 at various angles of attack between a= -2° and +15°. The pressure distribution on the upper side of the model with the curve of absolute pressure Pabs along the cursor line is given in Fig. 4. The influence of the existing well-known vortices is excellent visible. A qualitative comparison is shown in Fig.5. The smooth curve obtained by Inteco OPMS 1994 in white and the detailed peak curve obtained by the DLR system 1996 in grey are nearly identical. The fuselage vortices influence is well visible and some details of the wing vortices. The DLR curves give more details of the aerodynamic phenomena. It should be remarked that no special alignment program or smooth filters was used in the results presented here.
Reference paint spots for a later intensity correction of the one component paint, and a number of markers for model alignment corrections and resection are visible in Fig.4.
The distance between the camera and illumination position was 0.5 m as already mentioned. The optical fiber output was used without any lenses. That means the divergence angle is near 75°. For a fast decision the pseudo color version Fig.4 was used to optimize the illumination.

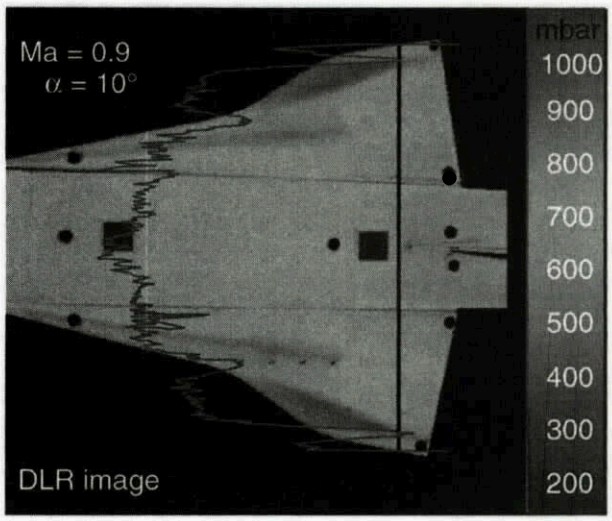


Fig. 4: Pressure distribution at the DASA HYTEX model with the curve of absolute pressure $p_{abs}$ along the cursor line

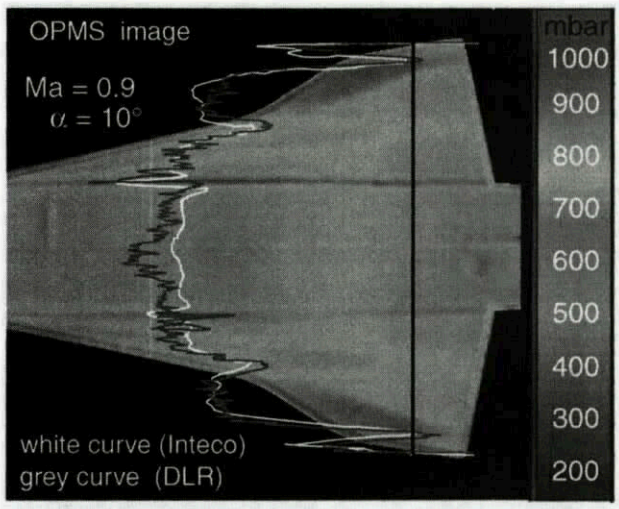


Fig. 5: Comparison of pressure distribution between Inteco and DLR measurements at the DASA-HYTEX model with the curve of absolute pressure $p_{abs}$ along the cursor line

Luminescence reference paint markers are useful for intensity correction. For a first view, the intensity image was obtained to control the aerodynamic effect in a free run mode of the CCD camera. At the earlier measurements in April 1994 using the OPMS system and the DASA HYTEX model the three vortex touches in the rear part of the models wing are clearly detectable by the DLR-PSP system again. To re-find these touches was the main criterion for the first test for identical cases - angle of attack and Mach number. As mentioned before two different illumination sources

were used for comparison of the final pressure results. Fig.6 shows the image after dividing the wind-off and wind-on image with laser illumination.

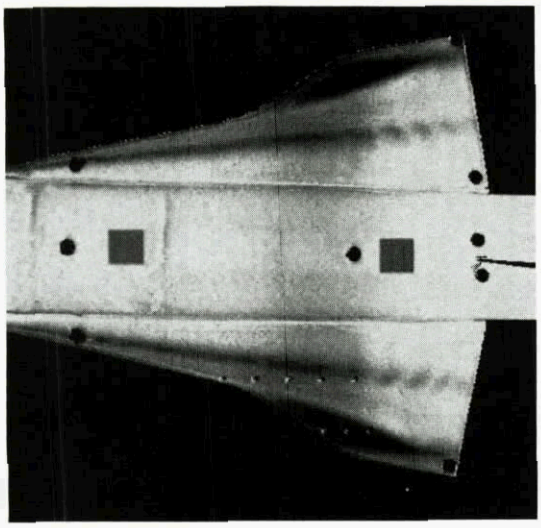

Fig. 6: Final pressure distribution image (divided images) using the laser illumination

In comparison to Fig. 6 an impression of the lamp illumination is given in Fig. 7. The three touches of the trailing edge vortex are in fact clearly visible independent of the light source. The short exposure time of 1s gives sharp contours of the model and pressure taps in comparison to Fig.5 of the Inteco video image.

To discuss the following PSP and PSI results it should be remembered that the test section with perforated walls of the Transonic Wind Tunnel Göttingen can be

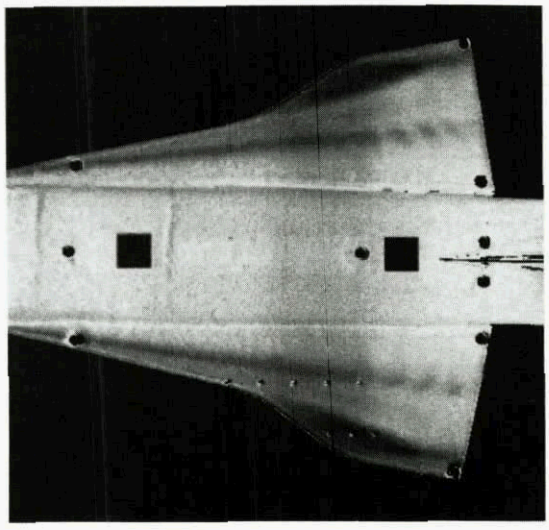

Fig. 7: Final pressure distribution image (divided images) using the lamp illumination

pressurized and, therefore, the performance of calibrations of the pressure sensitive paint in the wind tunnel itself is possible. Tests were carried out with a constant location of the camera including large angle of attack changes of the investigated model. Comparisons between the pixel by pixel calibration in the wind tunnel and the external calibration chamber were made.

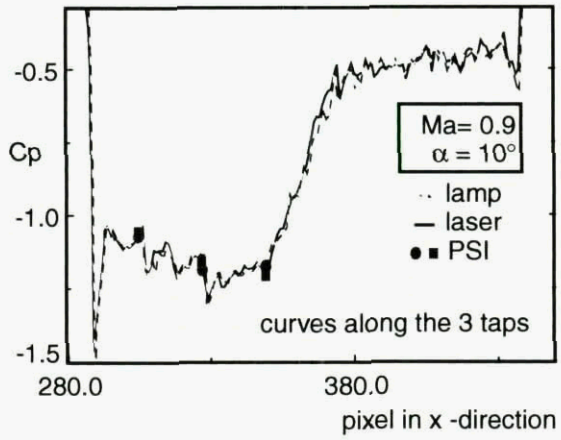


Fig. 8: Cp distribution on the HYTEX model using a lamp and laser for illumination in comparison with PSI values

Furthermore the diagrams of Fig.8 and Fig.9 show the influence between the two illumination methods in comparison to the conventional PSI pressure measurements. There is an excellent agreement between the two different methods: laser and lamp illumination. The results have been corrected with respect of light intensity distribution.

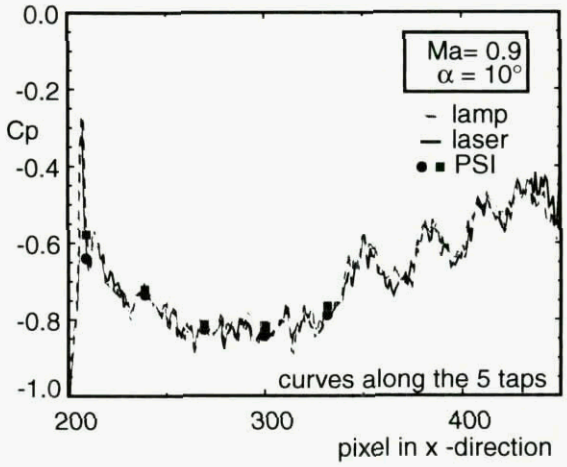


Fig. 9: Cp distribution on the HYTEX model using a lamp and laser for illumination in comparison with PSI values

For this part an own software package was developed for a fast correction calculation.

A repeatability check of the PSI values with and without

paint as squares and circles is presented in addition. Especially the three dips in the curve for the Mach number Ma=0.9 and a = 10° are clearly visible, also the fine structures. For presentation and exploitation no smoothing filter techniques were used. Independent of the illumination system the same characteristics at same positions can be detected.

### Oscillating wing measurements

For aerodynamic flutter tests measurements on a 2-d wing, a NLR 7301 profile, with 1.0m span and 0.3m chord were performed in the TWG. To produce aerodynamic effects the oscillation frequency was varied between 5 and 42 Hz with a $\Delta\alpha = \pm 0.6°$ for different constant angles of attack. For accuracy tests two different methods of pressure measurements for field investigations were used:

- accumulation
- single flash.

For the accumulation technique the above described Xenon flash lamp was triggered by the phase angle of the model oscillation driving system. After a number of tests, 20 triggered single flashes for accumulation gave a good signal to noise ratio and an excellent dynamic range of the CCD-camera and therefore this parameters were used for the following

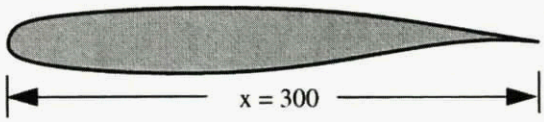


Fig. 10: Profile of the NLR 7301 model

measurements.The NLR 7301 profile design for the investigated Mach numbers and angles of attack shows no separations or bubble generation for the investigated flow parameters.

The output of two optical liquid fibers, connected to the flash lamp produced a homogeneous illumination for the observation area of 0.5x0.5m of the wing surface. In Fig. 10 the contour of the NLR 7301 profile is presented. Fig. 11 shows the PSP result for Ma=0.7 at $\alpha = 3°$ and an oscillation frequency of $\Delta\alpha = \pm 0.6°$ for unsteady measurement with 20 Hz wing oscillation frequency and light accumulation over 20 flashes with 25µs duration time of each flash. The noise of the 16bit slow scan camera gives for this values 600 counts and 50 000 counts for the signal. The identical configuration and flow parameters were used for a single flash measurement. The result is depicted in Fig. 12, but the signal is around 3000 counts at the same 600 counts noise.

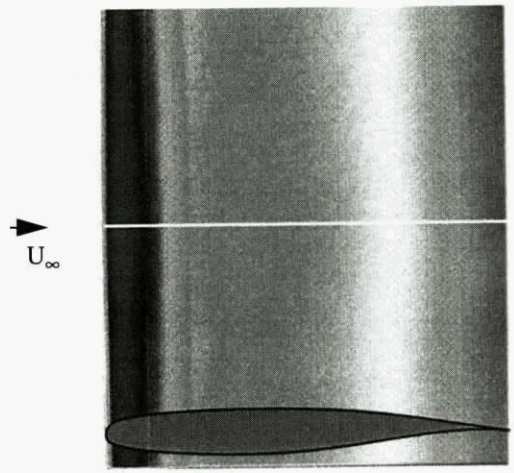


Fig. 11: PSP result for the oscillating wing for Ma=0.7, $\alpha = 3.0°$ and $\Delta\alpha = \pm 0.6°$. $\alpha_{eff} = 2.4°$, accumulation over 20 flashes with 25µs pulse duration

This is well to understand because the intensity of a single flash is lower then the accumulation of 20 flashes. Fig. 12 shows the same wing section as before and identical flow parameters but obtained only by a single flash with 25µs pulse duration time.

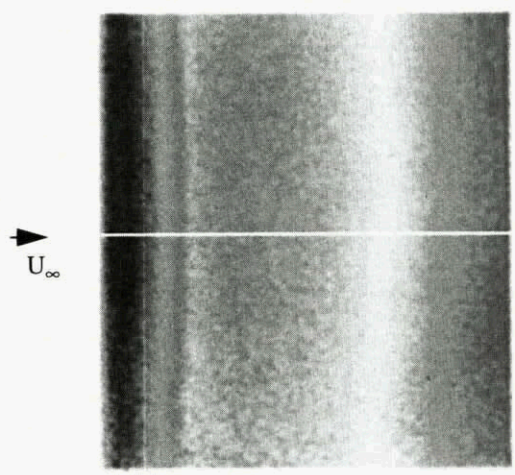


Fig. 12: PSP result for the oscillating wing for Ma=0.7, $\alpha = 3.0°$ and $\Delta\alpha = \pm 0.6°$. $\alpha_{eff} = 2.4°$ 1 flash with 25µs pulse duration

The plotted Cp values from the midsection (white cursor line), shown in Fig. 13 gives a good impression about the accuracy of this both techniques. There is no eminent distortion detectable between the single flash and accumulation technique.

For comparison with the standard pressure tap technique a test under steady conditions without oscillation was obtained for Ma= 0.82, $\alpha = 0.24°$. Here the first 3d-effects are visible in the PSP image.

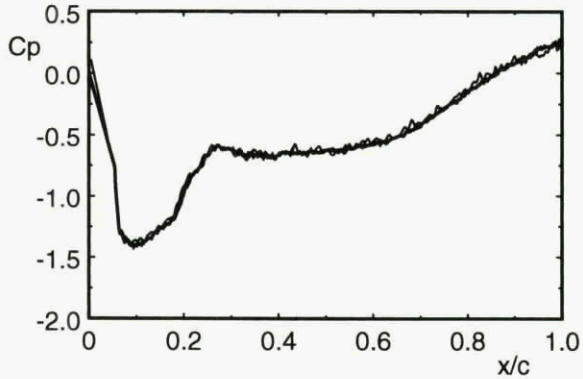


Fig. 13: PSP obtained Cp-distribution for Ma =0.7, $\alpha = 3.0°$ and $\Delta\alpha = \pm 0.6°$. $\alpha_{eff} = 2.4°$

— 20 flash accumulation with 25µs pulse duration

— 1 flash with 25µs pulse duration

These investigations were performed to detect and control stability effects. From the PSP images the full pressure- or Cp information in the region of ±0.25m of the midsection can be obtained but a lack of information using the pressure taps only placed in the midspan is given. As visible the flow is not symmetric because of any leakages at the wing ends.

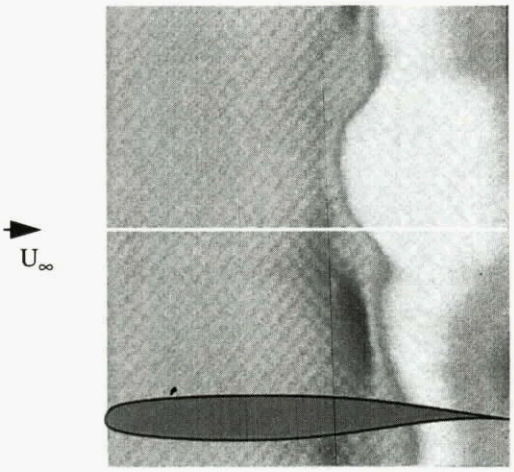


Fig. 13: PSP result for Ma=0.82, $\alpha = 0.24°$ and accumulation over 20 flashes with 25µs pulse duration

The continuous line in Fig. 14 presents the PSP measured curve along the midsection and the black circles the pressure tap values. There is a good agreement between this both simultaneously performed measurements. The pressure distribution in this case is locally constant indeed but not symmetric as visible by the complete PSP image.

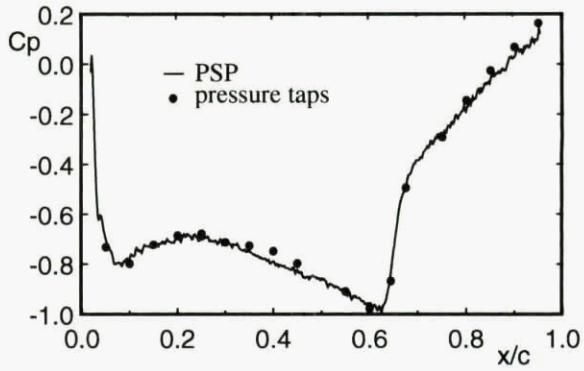


Fig. 14: Cp-distribution for Ma =0.82, $\alpha = 0.24°$ and 20 flash accumulation with 25µs pulse duration

## Paint

Different paints were investigated with the two basic excitation wave lengths in the range of 340 nm and 450 nm. The paints are differently sensitive to temperature and pressure at different excitation wave lengths.

DLR started to contact paint distributors including Russian and American companies for spraying paints and paint folios. Various paints were investigated with CCD and PMT and also by a spectrometer connected to the slow scan camera.

These investigations were made to gain our own information about temperature influence. There are different statements about the temperature sensitivity at room temperature in the emitted fluorescence bandwidth. As recognizable in Fig.15 a shift in the emitted light using different light sources is detectable for the same kind of paint.

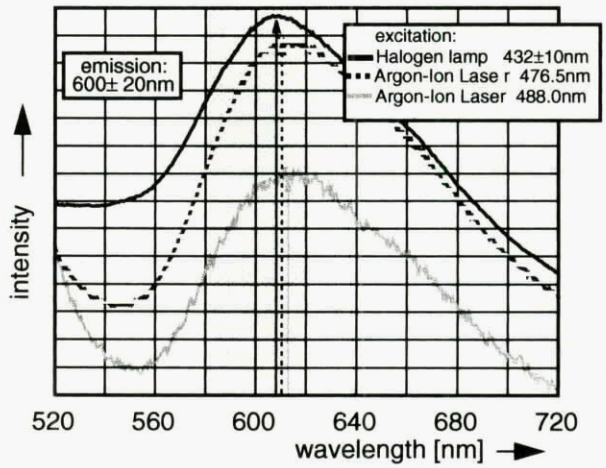


Fig. 15: Phase shift of emission spectra using different light sources

## Alignment and Resection

As well known, an alignment between wind-on and wind-off images is necessary for accurate PSP results. To reduce the main influence of sting distortion, the self correcting angle of attack system OWI was installed. In fact, the model moves with an parallel shift closer to the CCD camera - mounted in the upper wall panel. This parallel image shift due to model displacement, has to be minimized by an image alignment procedure before dividing the two wind-on and wind-off images. In this case the shift was not automatically corrected. Fig.16 gives an impression of the result without the alignment procedure.

For the alignment procedure a two dimensional transformation was performed, using power series. This transformation is expressed as:

$$x = E_1(x', y')$$

$$y = E_2(x', y')$$

where E is a correction function and the unprimed coordinates (x,y) are used for the wind-off image and the primed coordinates (x',y') for the wind-on image.

$$E_1(x',y') = a_0 + a_1 x' + a_2 y' + a_{11} x'^2 + a_{12} x' y' + a_{22} y'^2 + \ldots$$

$$E_2(x',y') = \underbrace{b_0}_{\text{const.}} + \underbrace{b_1 x' + b_2 y'}_{\text{linear}} + \underbrace{b_{11} x'^2 + b_{12} x' y' + b_{22} y'^2}_{\text{biquadratic}} + \ldots$$

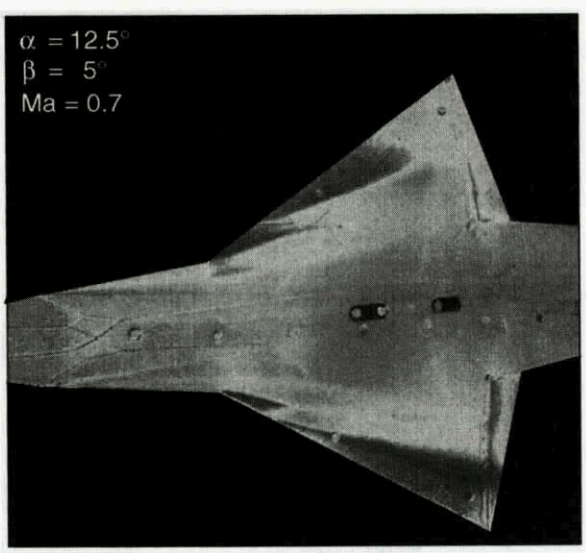


Fig. 16: Model surface without alignment procedure (flow parameter: $\alpha = 12.5°$, $\beta = 5°$, Ma= 0.7)

By the assumption that a few points (x,y) and (x',y') can be related together exactly, and that for the other points the transformation characteristics is identical, the following equation can be written as in the equation before. The coefficients $a_1$, $b_1$ can be calculated with known pairs of points (x,y) and (x',y'). We get an linear equation system with ($a_0$,$a_1$,$a_2$, .....) and ($b_0$,$b_1$,$b_2$, .....) as unknown quantities.For the biquadratic formulation the location of a minimum of six points on the model surface (wind-on and wind-off image) must be known. Therefore markers, e.g. circles, must be placed on the model surface for the recognition of the related points in both images. At last a two dimensional bicubic spline interpolation was used to obtain the intensity values at the non-distorted pixel location.

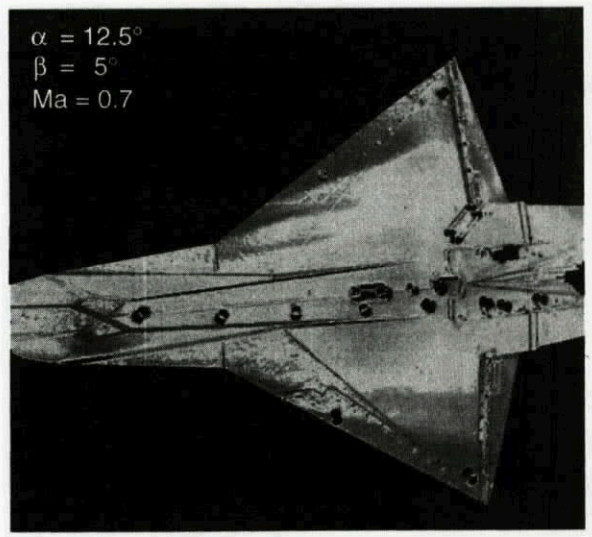


Fig. 17: Model surface using alignment procedure (flow parameter: $\alpha = 12.5°$, $\beta = 5°$, Ma= 0.7)

Using the same wind-on and wind-off images as before, the significant changing can be seen in Fig.17.

The typical error without angle of attack correction is in the range of 8-10 pixels. Using the OWI system -shown in Fig.18, the shift can be reduced to nearly 2-3 pixels. Therefore accurately obtained PSP images, optimized by the OWI system, is the best start condition for the final alignment and resection program. Our results showed a precsion of 0.5 pixel in shift. The numbers, form, structure and position of the markers is important for a later optimization of an exact detection and alignment. An alignment and marker recognition software was developed by DLR to minimize the image shift. In addition an automatically analysis system for markers and the real geometry of the model is under development. Finally a resection program is necessary for a real pixel transformation.

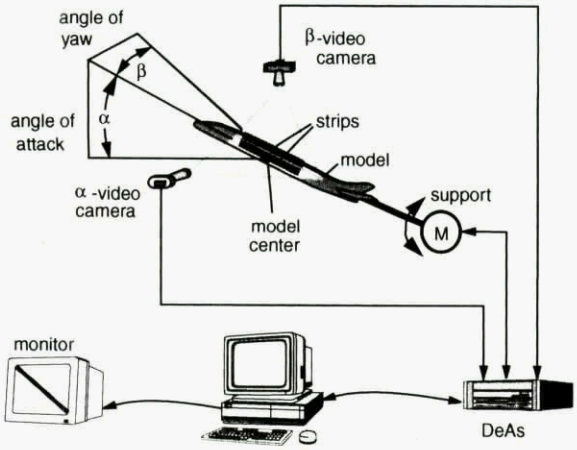


Fig. 18: Schematic sketch of the video-controlled support system OWI

## Lifetime Measurements

Parallel to the intensity measurements lifetime tests were performed. Fig. 19 shows the test setup for the first system. Tests were carried out by using a photomultiplier combined with a 800 MHz scope, a photon counter and a boxcar integrator. The main problem are intensity variations of the light source - in this case of the 10 Hz pulsed excimer dye laser. For minimization of this laser instability the intensity was controlled by a photo diode. These preliminary investigations were done to determine the value of $t_0$ for vacuum conditions.

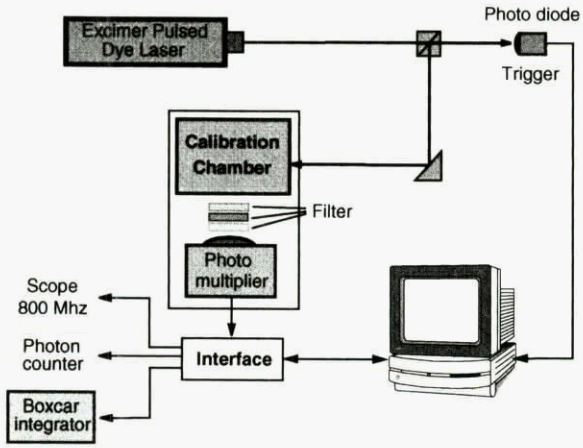


Fig. 19: Lifetime - system composition

The intensity variation is depicted in Fig. 20. A test with different paints shows a reasonable possibility to use this technique for wind tunnel measurements.

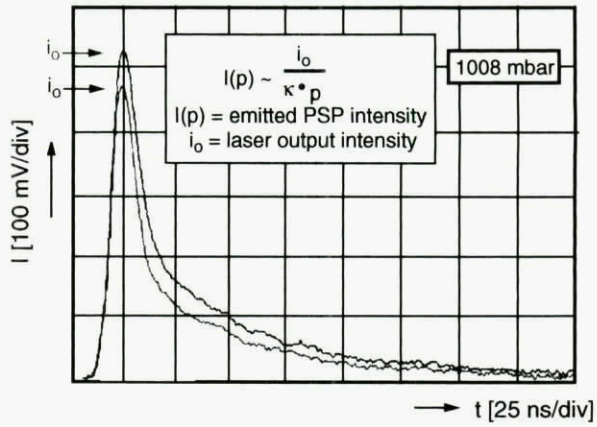


Fig. 20: Influence of light stability

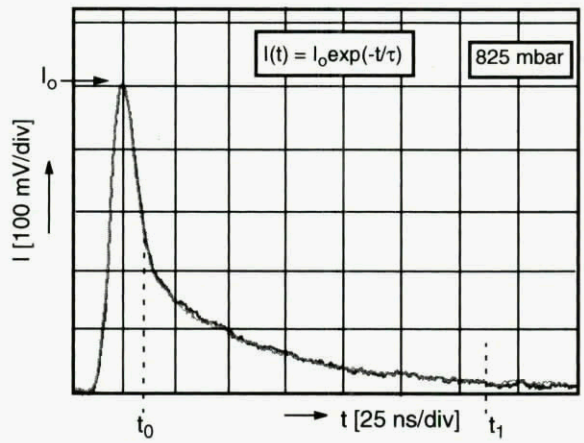


Fig. 21: Result of the stabilized laser light

After intensity stabilizing of the laser a curve as depicted in Fig. 21 can be obtained. To perform accurate measurements, different methods were checked:

- two flash method
- direct method
- indirect method
- intensified camera

The quenching coefficient k can be taken from the calibration and detection of the Stern-Volmer-equation. The advantage of the lifetime method is the fact that no reference image needs to be taken, and typical lifetimes in our case are shorter than 200ns. Therefore, unsteady measurements are possible but temperature influences must be controlled accurately. The test setup for point wise PSP lifetime measurements is given in Fig. 22.

After several tests with a number of light sources one result is given in Figure 23. The curve in the diagram shows the characteristics of the Optrod L4 paint.For a calibration in the external calibration chamber the typical exposure time of the CCD camera was in the range of 1 - 2 s for the DLR lamp (flash) and laser illumination.Using the intensified CCD camera under the same conditions, the grey curve with the exposure time (gate time) of 150 ns can be taken.

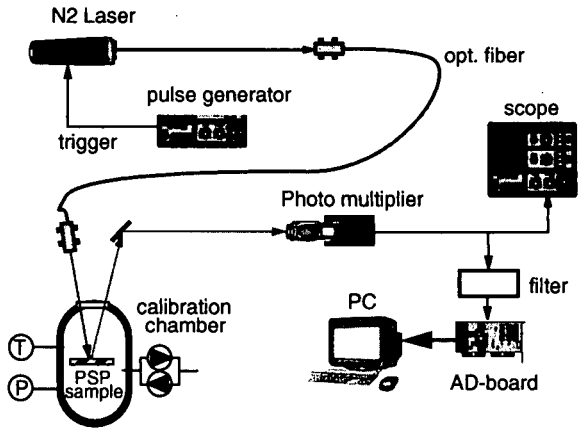


Fig. 22: Test setup for direct point wise PSP-Lifetime measurements

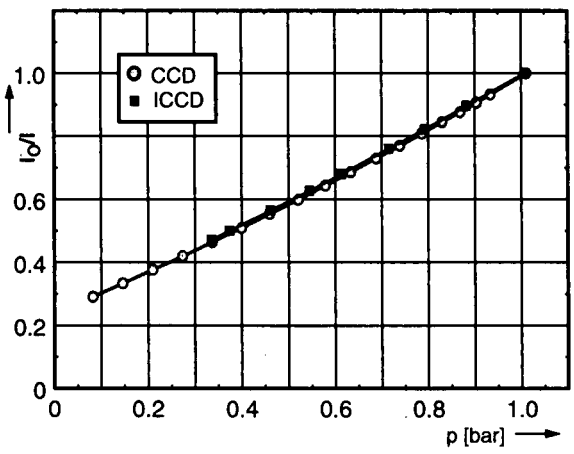


Fig. 23: Result of the calibration with an CCD and ICCD camera

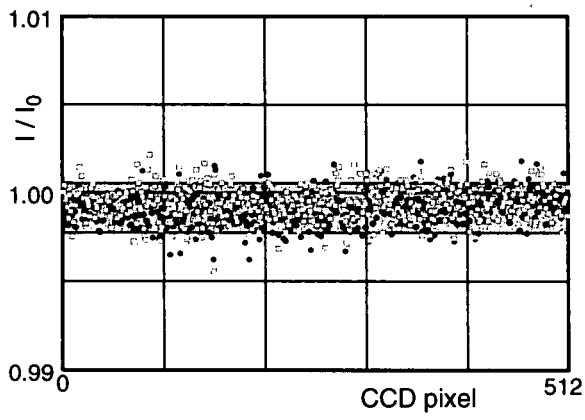


Fig. 24: PSP intensity measurements using the CCD slow scan camera

An area of 80x55 pixels from the total 512x512 pixels was selected. The intensity average of this area was the basis for the calculations. Here each pixel gives an intensity, and the indirect lifetime in the interval $t_0$ - $t_1$ of Fig.21 can be obtained. However, to understand the mechanism of accuracy an analysis of the noise of the CCD and ICCD camera is necessary. The result of an global flat field correction of two pixel lines is given in Fig. 24.
Here the typical error is < 0.01% for the 16 bit slow scan camera.
In comparison, the intensified CCD slow scan camera gives a typical error of 5% for an identical global flat field correction of two pixel lines as depicted in Fig.25. Please notice the different $I/I_0$ scale.

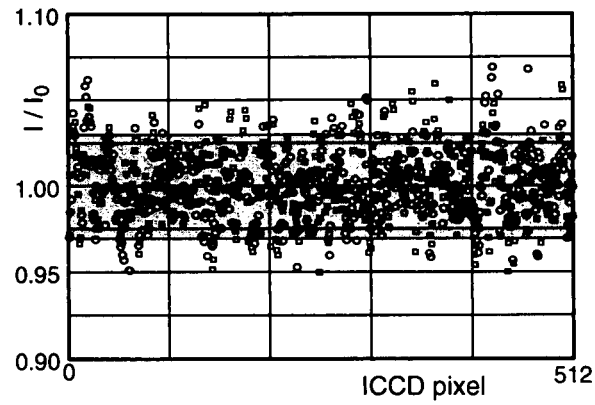


Fig. 25: PSP intensity measurements using the intensified CCD slow scan camera

For accurate lifetime measurements by an ICCD camera the following steps are necessary:

- time and temperature stable amplifier
- flat field correction
- knowledge of camera induced noise and paint
- lens correction
- stable light source

The new generation of ICCD cameras have approximately the same characteristic as shown in Fig. 25. Therefore it can be stated that the lifetime method can be used to cover whole areas of PSP measurements (512x512 pixels) according to the intensity method.

## Conclusion

It was proven that the designed PSP system can be used for steady and unsteady flow measurements as well. After the exploration phase, real wind tunnel measurements using different models were performed. The results presented here for the intensity method in the transonic speed range shows a acceptable accuracy.
DLR repeatability tests to the earlier OPMS system from the Inteco company from Italy using the DASA HYTEX model give much better results than before. The known vor-

tex structures on this model are clearly visible and the pressure distributions in comparison with the measurements from 1994 show a good „restart" with the DLR PSP system. A lot of industrial measurements have already been performed and evaluated. These measurements under real wind tunnel conditions gave experiences of great value. In combination with laboratory tests a PSP measuring system using the intensity method is now available at DLR.
Additional equipment for tests using the lifetime method is under development, first measurements have already been performed.

Steps of development for the DLR PSP system:

- Definition of a CCD and ICCD slow scan camera
- Development of an illumination system (sources and fiber optics)
- Development of a calibration chamber and a calibration procedure
- Investigation of different paints (spectra, temperature dependence, photo-degradation, humidity, sensitivity, etc.)
- Assessment with the early OPMS measurements
- Lifetime measurement investigation.

**References**

[1] J.F. Donovan, M.J.Morris, A.Pal, M.E.Benne, R.C. Crites, „Data Analysis Techniques for Pressure- and Temperature-Sensitive Paint", 31st Aerospace Sciences Meeting & Exhibit, Reno, NV, AIAA Paper 93-0176, Jan. 1993

[2] V.Borovoy, A.Bykov, V.Mosharov, A.Orlov, V.Radchenko, S.Fonov, „Pressure Sensitive Paint Application in Shock Wind Tunnel", 16th ICIASF Congress, Dayton, Ohio, July 1995

[3] A.Bykov, S.Fonov, A.Kishalov, A.Orlov, S.Ostroukhov, V.Radchenko, „Application of Luminescent Pressure Technology to Propellers", Preprint No. 99, TsAGI, Moscow 1995

[4] R.H.Engler, K.Hartmann, B.Schulze, „Aerodynamic Assessment of an Optical Pressure Measurement System (OPMS) by Comparison with Conventional Pressure Measurements in High Speed Wind Tunnel", 14th ICIASF Congress, Rockville, MD, October 1991

[5] R.H.Engler, „Further Developments of Pressure Sensitive Paint for Non Flat Models in Steady Transonic Flow and Unsteady Conditions", 16th ICIASF Congress, Dayton, Ohio, July 1995

[6] J.H.Bell, B.G.McLachlan, „Image Registration for Luminescent Paint Sensors", 31st Aerospace Sciences Meeting & Exhibit, Reno, NV, AIAA Paper 93-0178, Jan. 1993

[7] Y.Le Sant, M.C.Merienne, "An Image Resection Method Applied to Mapping Techniques", 16th ICIASF Congress, Dayton, Ohio, July 1995

[8] M.E.Sellers, J.A.Brill, „Demonstration Test of Pressure Sensitive Paint in the AEDC 16-ft Transonic Wind Tunnel Using the TST Model", 18th AIAA Aerospace Ground Testing Conference, Colorado Springs, CO, AIAA Paper 94-2231, June 1994

# Optical Measurements of Surface Pressure and Temperature in Turbomachinery

**Kelly Navarra**
**Larry Goss**
**Jeffery Jordan**
ISS Inc., 3845 Woodhust Court
Beavercreek, Ohio 45430-1658, USA

**Doug Rabe**
**Jim Gord**
**David Car**
Aero-Propulsion and Power Directorate
WL/POTE, Bldg 18D
Wright-Patterson AFB, Cleveland OH 45433, USA

## 1.0 SUMMARY

A new pressure-measurement technique which employs the tools of molcular spectroscopy has recently received considerable attention in the aerospace community. Measurements are made via oxygen-sensitive molecules attached to the surface of interest as a coating, or paint. The pressure-sensitive-paint (PSP) technique is now commonly used in stationary wind-tunnel tests; this paper presents extension of the technique to advanced turbomachinery applications. New pressure- and temperature-sensitive paints (TSPs) have been developed for application to a state-of-the-art transonic compressor where pressures up to 2 atm and surface temperatures to 140°C are expected for the first-stage rotor. PSP and TSP data images have been acquired from the suction surface of the first-stage rotor at 85% of the correct design speed for the compressor peak-efficiency condition. The shock structure is clearly visible in the pressure image, and visual comparison to the corresponding computer prediction shows quantitative pressures similar to the PSP data. The measurement error is estimated to range from 0.36 kPa in low-pressure regions to 4 kPa in high-pressure regions. The errors were significantly increased by a failure mode of the camera which will be described.

## 2.0 INTRODUCTION

The turbomachinery community is continually striving to improve the performance of gas turbine engines. The engine performance depends upon the compressor pressure ratio and efficiency where the stage pressure ratio is a function of the work, inlet total temperature, and stage efficiency. The turning of the flow which creates work is induced by the pressure profile over the suction and pressure surfaces of the blade. Because the pressure is rising through the rotor passage the amount of turning is limited by blade-surface and end-wall boundary layer behavior. Boundary layers in an adverse pressure gradient tend to separate, which can cause a loss of efficiency and prevent any further increase in the pressure ratio. Currently, the stage pressure ratio and stage efficiency is determined experimentally by measuring the inlet and exit total pressure and temperature of the stage. Because of the complex flow interactions which occur in a rotor, it would be most beneficial to also know the pressure profile of the blade surface.

Early surface pressure measurements of a subsonic rotor were made by Sexton, O'Brien, and Moses in 1973 where blade-mounted pressure transducers and a multi-channel radio telemetry system were used[1]. Still today, blade-mounted pressure transducers are the only means to measure surface pressure on rotors. Unfortunately, such transducers cover a limited region (< 5%) of the blade surface, result in some compromise to the structural integrity of the blade and to the flow integrity, and have limited reliability in full-scale transonic turbomachinery environments. For these reasons, improved blade-surface pressure-measurement techniques are needed to aid the understanding of flow behavior in turbomachinery components.

A relatively new technique that employs the tools of molecular spectroscopy to measure pressures by optical means is the subject of this paper. Measurements are made via photoluminescent oxygen-sensitive molecules attached to the surface of interest as a coating, or paint; hence, the technology is referred to as pressure-sensitive paint (PSP). The objective of this research effort was to develop a PSP suitable for the harsh turbomachinery environment and to demonstrate the measurement technique for turbomachinery applications.

*Paper presented at an AGARD PEP Symposium on "Advanced Non-Intrusive Instrumentation for Propulsion Engines", held in Brussels, Belgium, 20-24 October 1997, and published in CP-598.*

## 3.0 MEASURMENT CONCEPT

Table 3.1 summarizes the typical pressure-measurement concept. In this scheme, a photoluminescent species (A) absorbs light of appropriate energy (hυ) and is promoted to an excited electronic state (A*). The excited-state molecules then return to the ground electronic state either by some radiative-decay process involving the emission of a photon (fluorescence or phosphorescence) or by a non-radiative pathway such as dynamic quenching. Dynamic quenching is the non-radiative phenomenon in which the excess energy is transferred to the motion of the quencher, which in this case is oxygen. Because of the effective competition between the luminescence and oxygen quenching, the luminescence can be used to quantify the local oxygen concentration. Oxygen quenching is usually modeled by some variation of the Stern-Volmer relation. In its simplest form, the relation is given by

$$I = \frac{I_0}{1 + K_0 P_{O_2}} = \frac{I_0}{1 + k_q \tau_0 P_{O_2}} \qquad (1)$$

where I is the luminescence, $I_o$ the luminescence in the absence of oxygen, $P_{O2}$ the partial pressure of oxygen, and $K_o$ the Stern-Volmer constant. The Stern-Volmer constant is a product of the bimolecular quenching rate, $k_q$, and the lifetime of the molecule at a vacuum, $\tau_o$. Unfortunately, the pressure-sensitive probe molecules have other mechanisms by which they can return to the ground state which are manifested in a sensitivity to temperature[2-4]. As a result, development has begun on compatible temperature-sensitive paints[5-7]. As with pressure-sensitive coatings, the luminescence of temperature-sensitive coatings can be related to the surface temperature and can be measured with essentially the same instrumentation. For capitalizing on this compatibility, efforts are underway to combine both temperature and pressure probe molecules in the same layer of paint.

**Table 3.1** Pressure-measurement concept based upon $O_2$ quenching of photoluminescent probe molecules.

**Photoluminescence and Quenching Process:**

| | |
|---|---|
| $A + h\nu \rightarrow A^*$ | **Absorbtion** |
| $A^* \rightarrow A + h\nu'$ | **Luminescence** |
| $A^* + O_2 \rightarrow A + O_2^*$ | **Quenching** |

**Temporal Behavior of Photoluminescence:**

$d[A^*]/dt = -k_s[A^*]$

$k_s = k_1 + kq[O_2]$

$[A^*]_t/[A^*]_0 = \exp(-k_s t)$

To acquire surface pressure measurements in a wind tunnel test intensity fields are commonly measured because of the simplicity of the data acquisition procedure. To apply a Stern-Volmer model, the luminescence intensity at a reference pressure level, Iref, must be divided by the luminescence intensity at some test condition, I, over the area of interest. For this method, the ratio of luminescence intensities is calibrated to indicate the surface pressure. The intensities are generally sampled over the surface of interest by a detector array such as a charge-coupled device (CCD) camera. With today's CCD cameras having a million or more pixels, PSP can provide continuous surface pressure measurement at an unequaled spatial resolution. The output of the CCD array can be visually represented as a two-dimensional image, with the luminescence corresponding to a gray scale.

## 4.0 PAINT DEVELOPMENT

The basic pressure-sensitive paint is diagrammed in Fig. 4.1. A binder material which is oxygen-permeable (typically silicone-based) is used to suspend luminescent probe molecules whose emission is effectively quenched by a collision with molecular oxygen. The probe molecules can either be fluorescent (short lifetime <~300 ns) or phosphorescent (long lifetime >100 μs). The luminosity or lifetime of the excited paint is related to the oxygen concentration by the Stern-Volmer relations previously presented.

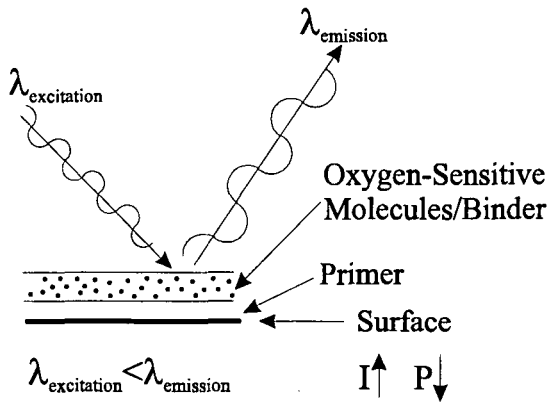


**Figure 4.1** Basic PSP structure.

Given an oxygen-sensitive molecule, there are three primary factors involved in fabricating a suitable PSP. First, the binding medium used to attach the probe to a surface must be oxygen permeable in order to permit oxygen quenching. Second, the binding medium must be compatible with the probe molecule. For example, if the polymer is highly polar and the probe molecule is non-polar, the resulting paint could be completely insensitive to pressure. Finally, the binding medium must provide a stable environment for the probe. Often, significant variations in paint performance over time results from continued reorganization of the polymer system. Thus, it is beneficial to

use a polymer which cures quickly near room temperature. The first two factors can effectively be satisfied through the appropriate selection of probes and polymers. The final factor is the most difficult to achieve, the primary obstacle being a result of temperature effects.

The sensitivity of pressure paints to temperature involves both the vibrational activity of the probe molecule itself and the binding medium. However, the temperature-sensitivity effects are currently dominated by the binder. The Stern-Volmer constant of the pressure paint can be expressed as a function of temperature and binder viscosity by

$$K_o = 8RT / 3000\eta \tag{2}$$

where R is the gas constant, and η is the viscosity of the binder. Another effect of temperature on paint performance involves the solubility of oxygen in the paint binder. The solubility of oxygen in a silicone binder is given by Henry's Law

$$[O_2(T)] = [O_2]_0 \exp(-\Delta H / RT) \tag{3}$$

where ΔH is the enthalpy of solution (-3.0 kcal/mole for silicone). Therefore, the paint performance is inconsistent throughout the paint layer where temperature variations exist. As a result, care must be taken in designing the correct binder, both for homogeneous performance and compatibility with the probe molecule.

### *4.1 Paint Performance*

After screening numerous molecular probes/binder combinations, one prototype paint was selected for demonstartion in a state-of-the-art transonic rotor. The selected paint utilized a derivative form of pyrene (1-pyreneacetic acid) in a white RTV (GE 734). While ordinary pyrene in RTV typically yeilds satisfactory surface pressure measurements[8], the pyrene could not withstand the elevated temperatures of a transonic compressor[9]. For the rotor under study the suction surface blade temperatures and pressure were expected to approach 140 °C and 2 atm, respectively[9]. By using a derivative form of pyrene, which has a higher boiling point compared to pyrene, a paint which survived the extreme temperature was developed. The temperature surviability was, however, obtained at the expense of some pressure sensitivity. As presented in Figure 4.2, the Stern-Volmer calibration of the 1-pyreneacetic acid (PA) paint at room temperature shows a decrease in pressure sensitivity of ~ 15% as compared to pyrene. Pyrene, on the other hand, vaporizes at ~80 °C[9]. The calibration of the PA paint over pressure and temperature is presented in Fig. 4.3. Figure 4.4 presents the calibration of five independently painted samples representing the sample to sample repeatability.

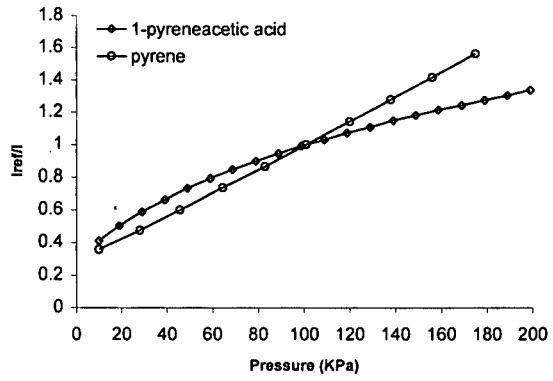


**Figure 4.1** Calibration comparison of pyrene and 1-pyreneacetic acid (room temperature).

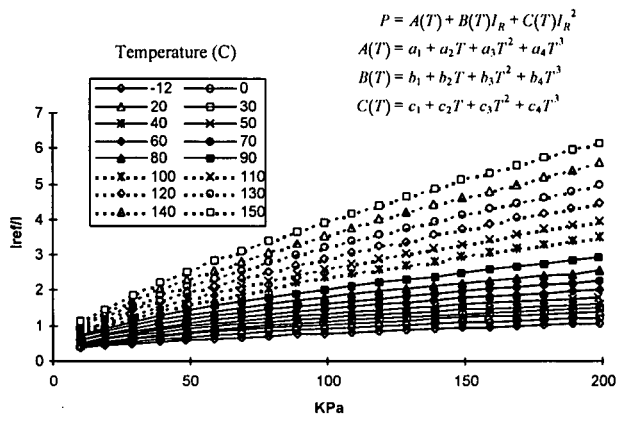


**Figure 4.3** Performance of PSP developed for turbomachinery.

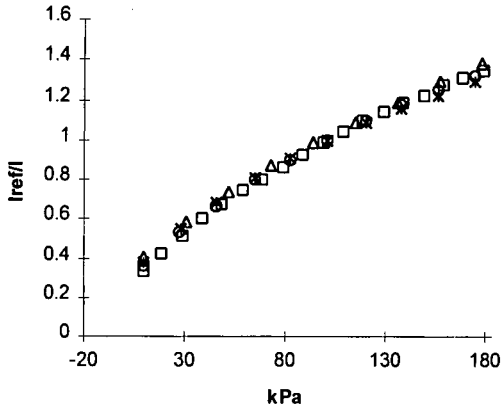


**Figure 4.4** Calibration variation of four independent PSP samples at room temperature. (final data will be of 5 data sets)

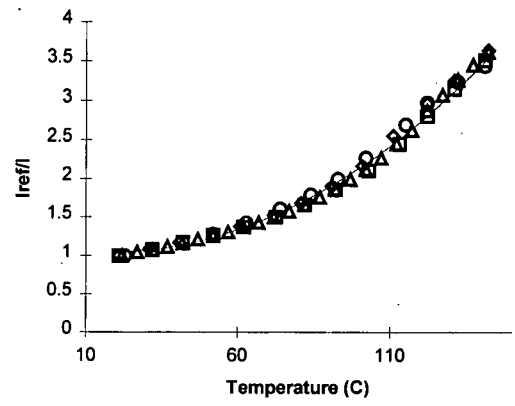


**Figure 4.5** Performance of TSP developed for turbomachinery.

As can be seen in Figure 4.3, despite efforts to minimize temperature sensitivity the PSP remains quite sensitive to temperature. In order to correct for the temperature-sensitivity of the PSP, a temperature-sensitive paint was also developed. Thus, in a rotor test, two blades would be painted and surface pressure and temperature measurements could be obtained sequentially. The design of a temperature sensitive paint is similar to that of a PSP with the exception that the selected binding medium was impermeable to oxygen. For the TSP a fluorescent laser dye (1,3-bis(1 pyrene)propane) was suspendend in a marine caulk (Bostick). The Stern-Volmer Calibration for the TSP is presented in Fig. 4.5.

### *4.2 Paint Photodegradation*

All luminescence-based paints display a common characteristic referred to as photodegradation, whereby the paint-intensity signal deteriorates as a function of time with continued exposure of the paint to visible light. Figures 4.6 and 4.7 show the photodegradation results of the PSP and TSP as a function of input energy. (These plots will later be combined into one) The paint photodegradation is expressed in terms of percent of the initial intensity. In general, the PSP displayed a higher rate of degradation than the TSP and absorbed a larger amount of input energy before the rate started to decline. At 30 mJ of total energy delivered to the paint the PSP degraded ~ 6.6% while the TSP degraded ~ 1.3%. The rate of photodegradation circumvents the advantage of using increased illumination power to improve signal levels. Hence, the effect of photodegradation must be considered when designing a PSP experiment.

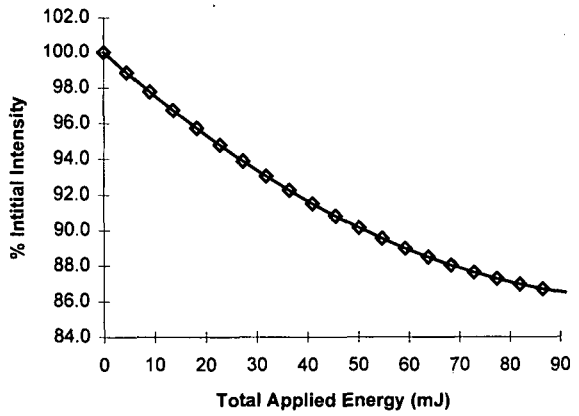


**Figure 4.6** PSP rate of photodegradation as a function of total energy delivered to the paint.

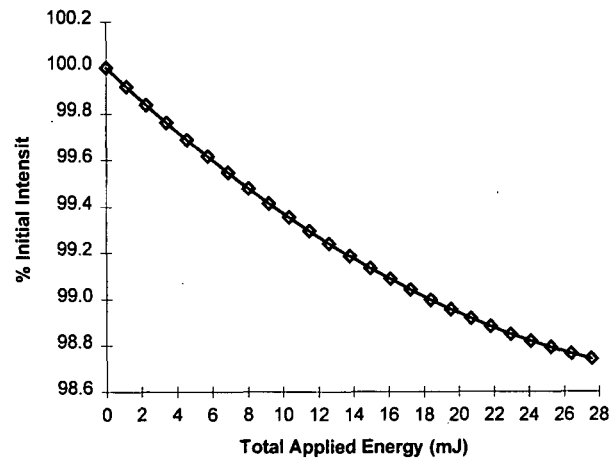


**Figure 4.7** TSP rate of photodegradation as a function of total energy delivered to the paint.

### *4.3 Paint Pressure Sensitivity*

A PSP image of a jet impinging on a flat plate will be presented. Figure 4.8 will present an image of the pressure gradient created by the jet and Figure 4.9 will show a cross section comparing PSP data with transducer data. Examples of these figures are attached. Final figures will include error bars etc.

## 5.0 TEST ARTICLE DESCRIPTION

For application demonstration, the selected pressure-sensitive paints were applied to a state-of-the-art transonic compressor. The compressor test was conducted from September 1996 to January 1997 at the Turbine Engine Research Center (TERC) located at Wright-Patterson Air Force Base. The primary objective of this test was to obtain quantitative pressure measurements from the suction surface of the first stage rotor. The following paragraphs describe the test article description, test set up, and data acquisition procedure. The two-stage test compressor is presented schematically in Figure 5.1. The general airfoil geometry for this rotor is described in Table 5.1. At the aerodynamic design point, the relative Mach number was supersonic over 75% of the blade span. Table 5.2 presents the demonstrated baseline performance of this rotor at the design condition where the rotor speed is 13,288 rpm.

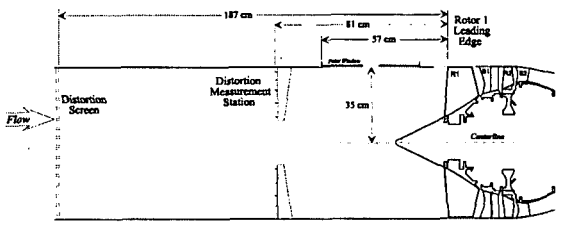


**Figure 5.1. Profile Schematic of Test Compressor.**

**Table 5.1. Airfoil Geometry Parameters for Rotor 1.**

| Parameter | Value |
|---|---|
| Number of Blades | 16 |
| Average Aspect Ratio | 1.22 |
| Rotor Tip Radius, cm | 35.24 |
| Inlet Radius Ratio | 0.33 |
| Average Radius Ratio | 0.47 |
| Tip Solidity | 1.5 |
| Max. Thickness/Chord | 0.028 |

**Table 5.2 Rotor 1 Performance at 98.6% Speed, Design Pressure Ratio and Flow.**

| Parameter | Value |
|---|---|
| Total Adiabatic Efficiency, % | 88.9 |
| Total Pressure Ratio | 2.5 |
| Total Temperature Ratio | 1.3 |
| Corrected Tip Speed, m/s | 480.7 |
| Corrected Mass Flow, kg/s | 71.8 |
| Average Tip Clearance, mm | 0.96 |
| Tip Clearance to Actual Chord, % | 0.46 |

In this study, PSP and TSP data at peak efficiency (PE) operating point at 85% corrected speed were obtained. Peak efficiency at 85% speed was the overall peak efficiency of the compressor[10]. Therefore, the first stage rotor was at least moderately loaded for the peak efficiency condition used in this demonstration.

### *5.1 Test Setup*

The rotor test setup is shown in Fig. 5.2. A 305 x 25 mm window was placed ~260 mm upstream of the rotor leading edge. A 16-bit Princeton Instruments intensified charge-coupled device (ICCD) camera (576 x 384-pixel Thompson chip), fitted with a 50-mm f/1.2 lens, was located ~0.5 m upstream of the rotor. The camera viewed the blades across the flow path and was angled ~5 deg below the centerline to avoid viewing the bullet nose. A 2-mJ nitrogen pulsed laser beam (337 nm, 1-ns pulse) was launched into a fiber which was mounted adjacent to the camera. The laser was used in the pulse-on-demand mode—the laser only fired when the command was given to the ICCD to acquire an image. The beam (measured at 0.4 μJ at the exit of the fiber) was expanded to illuminate the visible suction surface of the first-stage rotor. With the presented viewing angle, the adjacent blade prevented viewing beyond 52% chord at the tip, and the image size restricted viewing inboard of 62% span.

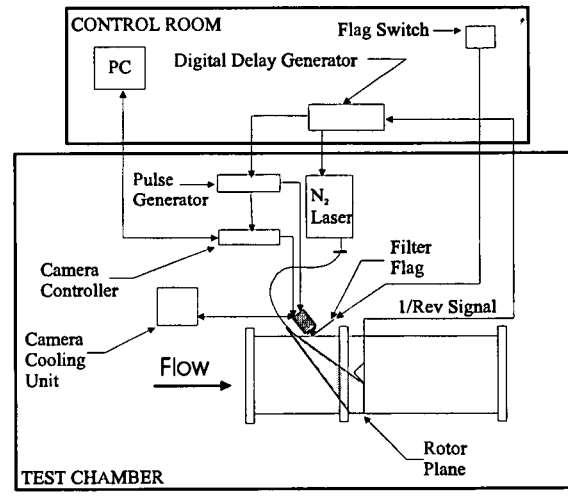


**Figure 5.2 PSP Test Set Up.**

The Princeton Instruments detection system included the ICCD, an ST-138 camera controller for image acquisition and readout via the personal computer, and an FG-100 pulse generator for triggering the camera. The camera system and laser were mounted on an optical table inside the test chamber. A Neslab cooling unit was used to maintain the ICCD chip at -20° C to minimize readout noise. The camera and nitrogen laser were remotely controlled from an adjacent room. As mentioned previously, TSP requires a blue filter on the detector while PSP does not. A filter arm (flag) was configured with a switch to allow remote positioning of the blue filter. When switched on, the current in the flag created a magnetic field which attracted the flag towards another magnet mounted on the optical table. Thus, the switch could be used to move the filter in and out of the camera path.

The following procedure was used to image the blade and acquire data images. Once the operator sends the command to initiate image acquisition, the CCD camera was charged, and the once-per-revolution pulse (1/rev) from the test article was used to initiate the timing sequence. The 1/rev signal was delayed by the amount, $\Delta t_{delay}$, required to rotate the desired painted blade into the image plane. A Stanford Research DG535 delay generator, triggered by the 1/rev, was used to send out two pulses--the first to trigger the pulse generator, which in turn triggered the camera, and the second to trigger the laser. The second pulse trailed the first by 13 μs to take into account the time required for the camera electronics to respond to the trigger. This allowed synchronization of the arrival of the laser light at the blade surface and the activation of the camera intensifier for collecting the resulting fluorescence emission. The period of operation of the intensifier (gate time) was

determined by the laser pulse width and subsequent fluorescence emission of the paint. For this test a 1-ns laser pulse was used, and the maximum fluorescence lifetime was determined from calibration to be 323.5 ns (at vacuum and room temperature). The gate time was selected to be 10 μs to take into account laser jitter on the order of 1 μs. Therefore, the timing required to image the blade (< 2 μs) was achieved by the combination of the short laser pulse and the short-lived fluorescence of the paint--not by the gate of the intensifier. The camera "shutter," or charge time, was preset to a minimum of one rotor revolution. After the shutter closed, the acquisition of another image could not be initiated until the CCD downloaded the data to the computer. The readout time of the 221,184-pixel CCD chip was 234 ms. This limits this particular camera to steady state measurements since another image can not be acquired until the readout is complete.

### *5.2 Data Acquisition Procedure*

Four types of images were required in PSP and TSP measurements: a wind-off reference image, a wind-on test image, a black image, and a white image. The black images were taken with the lens cap on to define the thermal noise of the CCD array. The white image was taken of a uniformly illuminated surface of arbitrary intensity. This image provided a flat-field correction for the "honeycomb" pattern on each image which results from the "minifier"--the tapered fiber-optic coupling between the photocathode and the CCD chip. Both the black and white images were only camera-dependent and could be taken either before or after the test. Thus, during a scheduled testing period, only the wind-off and wind-on images were acquired.

Wind-off images were acquired both before and after each test; pre- and post-test wind-off images could be compared to determine whether oil might be present in the compressor and to check for paint photodegradation. For acquiring the wind-off images, the rotor rotated 150 rpm where the pressure gradient was well below the current resolving capability of the paints. This approach provided valid reference images while allowing the timing circuitry to be used for accurate positioning of the blade images. For acquiring the wind-off images, the camera shutter was set to 400 ms. Sequential images were acquired using various timing delays until the desired painted blade appeared in the image. Care was taken to determine the delays required to place the TSP and PSP blades in the same location. The locations were determined by the image pixel coordinates of the blade leading edge. The delay and coordinates of each blade were recorded. Fifty wind-off images were acquired for each paint for steady-state averaging.

Once the wind-off images were acquired, the compressor was throttled to a desired test speed and condition. For the wind-on images, the camera shutter was reduced to 50 ms. To provide a constant background noise from image to image, the shutter value remained constant for all of the wind-on images, regardless of the rotational speed. From the coordinates previously recorded during the acquisition of the wind-off images, the delays required to superimpose the TSP and PSP blades were determined, and the corresponding wind-on images were acquired. Fifty wind-on images were acquired from each blade at each test condition for averaging.

## 6.0 IMAGE PROCESSING

The post-processing was carried out mainly using PAINTCP, a program developed for NASA Ames by Sterling Software, Inc[11]. This package is used in PSP image analysis for wind-tunnel aircraft model tests. For the purposes of this experiment, many of the functions within the code were not required; however, the program was used for its ability to register the alignment marks in each image and transform the wind-off image to align it with the wind-on image. A separate computer program was used to perform basic functions such as image averaging, subtraction, and division.

Each image captured by the ICCD camera can be described as a product of camera sensitivity, S(x,y), illumination power, P(x,y), and the paint emission, E(x,y), plus thermal background noise, B(x,y), as follows:

$$I(x,y) = S(x,y)P(x,y)E(x,y) + B(x,y) \qquad (4)$$

where each parameter varies spatially. As a result of equation 4, two corrections were required for the wind-off and wind-on images prior to division and conversion to quantitative temperature or pressure data: 1) a background correction to take into account the thermal noise on the ICCD chip, and 2) a flat-field correction to take into account the spatial variations in camera sensitivity and illumination (attenuation). The thermal noise was removed by subtracting the background image, which only contained B(x,y), from the wind-off and wind-on images. Removal of the camera attenuation was more difficult. A flat-field correction was used to remove the attenuation caused by the minifier--which results in a honeycomb pattern on the data image. This pattern--a mechanical effect of the camera--was fixed in all images; therefore, manipulation of the wind-on image to align it with the wind-off image would skew this pattern relative to the wind-on image, adding unnecessary pattern noise to the final image, as illustrated in Fig. 6.1.

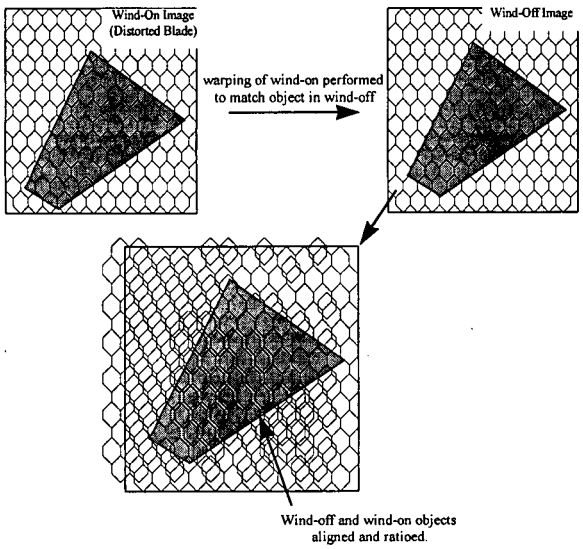


**Figure 6.1** Honeycomb-pattern noise caused by ICCD minifier.

To remove the honeycomb pattern caused by the ICCD minifier prior to using PAINTCP, both the background-corrected wind-off and wind-on images were divided by a white image--which was also background corrected. The process is depicted by equation 5:

$$
\begin{aligned}
I_{x_{corrected}} &= \frac{I_x - I_{black}}{I_{white} - I_{black}} \\
&= \frac{\{S(x,y)P(x,y)E(x,y) + B(x,y)\} - \{B(x,y)\}}{\{S(x,y)P(x,y)E_o(x,y) + B(x,y)\} - \{B(x,y)\}} \\
&= \frac{E(x,y)}{E_o(x,y)} \qquad (5)
\end{aligned}
$$

where x represents either the wind-off or wind-on condition and the white image records the sensitivity, illumination power, and a reference emission, $E_o(x,y)$. All of the images (white, wind-off, and wind-on) were corrected for thermal noise, B(x,y), by subtracting the background image, $I_{black}$. Dividing the wind-off and wind-on images by a white image should effectively remove S(x,y) and P(x,y), leaving only the ratio of the paint emission, E(x,y), and the reference emission used to create the white image, $E_o(x,y)$. Therefore, the final images should be free of the thermal noise caused by the CCD and the honeycomb pattern caused by the fiber-optic coupler of the camera. The reference emission, $E_o(x,y)$, cancels later in post processing when the corrected wind-off image is divided by the corrected wind-on image.

Once the wind-off and wind-on images were corrected, the PAINTCP program was used to locate the alignment marks on the corrected images and the program was used to "warp" the corrected wind-on image to match the pattern of alignment marks in the corrected wind-off image. The wind-off image was then divided by the properly aligned wind-on image, and the final-image ratio is written to an IEEE floating binary file. This procedure was performed twice for each test condition--once for the TSP data and once for the PSP data. In order to temperature-correct the PSP data, the TSP image was also aligned with the PSP image. Therefore, all of the pressure and temperature images were aligned to the same wind-off PSP image.

The output from the PAINTCP program was read into a software package which allowed simple matrix and image manipulation. The equation determined from the paint calibration for the TSP was applied to the temperature matrix to convert the intensity ratio to surface temperatures (in ° C). These results were output to a new matrix. Because the temperature image was aligned with the pressure image using PAINTCP, the temperature image could be used to calibrate the pressure image directly. The surface-temperature information and the intensity-ratio data from the PSP image were input into the calibration equation for the PSP, and the resulting surface-pressure information was output to a second matrix. The final temperature image and temperature-corrected pressure image were scaled and plotted with false-color.

## 7.0 TRANSONIC ROTOR RESULTS

Figure 7.1 depicts the area of the blade where temperature and pressure data were acquired. The lines are used to outline the physical image region of the blade because the photograph of the blade was taken at a different point-of-view than the data acquired from the paints. The approximate dimensions of the viewable area of the blade where data were acquired are from 0-52% chord at the tip and from 62-100% span at the leading edge. Approximately 61,500 pixels were focused on the blade for P/TSP measurements. Accounting for pixel blur, the actual spatial resolution obtained was 1.2 mm in the direction of rotation and 0.4 mm radially. Therefore, the PSP offers a measurement point ~ 27% of the size of a 1.5-mm diameter transducer. While the spatial resolution was maintained in the radial direction, only 1/3 of the

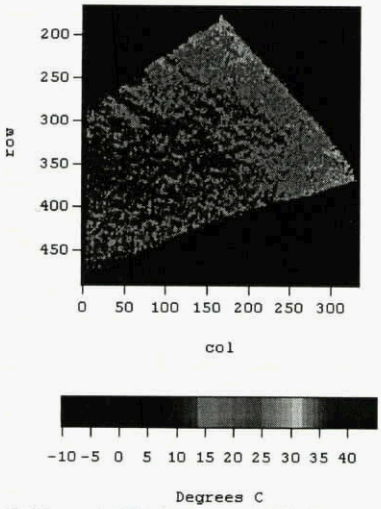


**Figure 7.2** Calibrated TSP image at 85% Nc, peak-efficiency operating condition.

The average of fifteen TSP and 15 PSP images obtained at the 85% Nc, peak-efficiency condition were processed as described previously. Figures 7.2 presents the final TSP results. The surface temperatures at the leading edge ranged from 25° C at ~62% span to 50° C at the tip. At ~52% chord the temperatures ranged from 0° C at ~ 62% span to 50° C at the tip. Figure 7.3 shows the final PSP data corrected for temperature using the TSP data. The two chordwise streaks are the result of some oil present in the test article. The oil contamination was visible in the wind-off TSP image. Because the oil was present in only one image it was not ratioed out. Furthermore, since the oil affected the TSP image, the streaks were propagated into the PSP data when the data was corrected for temperature. Figure 7.3 also shows the CFD prediction for 85% Nc for qualitative comparison. The CFD code used was developed by NASA Lewis[12]. The shock location in the PSP agrees with the prediction.

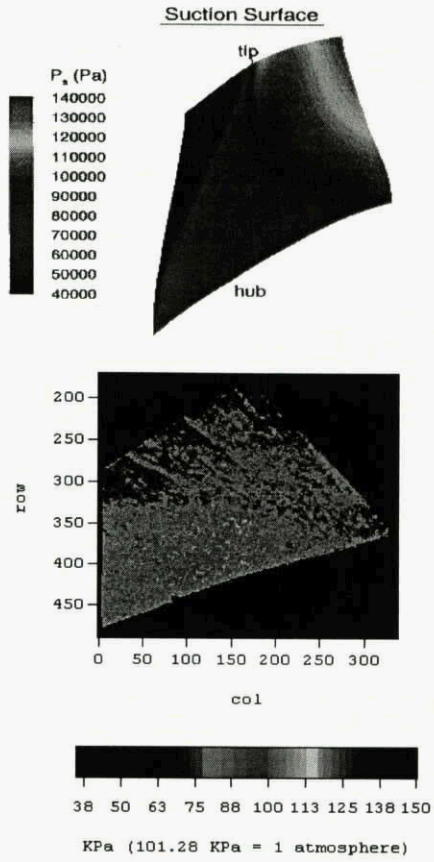


**Figure 7.3** CFD prediction and temperature-corrected PSP image, 85% Nc, peak-efficiency operating condition.

## 9.0 DISCUSSION

-prototype paints successfully endured environment and adequately demonstrated the technology potential.

-paints need to be improved. "Off-the-shelf" RTVs are not the binder of choice. It is very difficult to engineer crosslinked polymers (RTV's) to get desired binder performance (e.g. temperature stability, oxygen permeability). Paint development will continue using sol-gels and synthesized polymers.

## ACKNOWLEDGEMENTS

The authors would like to thank all the employees of the Turbine Engine Research Center (TERC), Wright Laboratory, for their support during the compressor test. We would like to thank Dr. Chunill Hah of NASA Lewis Research Center for providing the CFD code used for qualitative comparison to the

PSP data and Dr. James Bell of NASA Ames Research Center for providing the PAINTCP code used for image processing.

## REFERENCES

(1) Sexton, M. R., O'Brien, W. F., and Moses, H. L., "An On-Rotor Investigation of Rotating Stall in an Axial Compressor," Defense Technical Information Center (DTIC) Technical Report, Cameron Station, Alexandria, VA, pp. 33.1-10, 1973.

(2) Kavandi, J., Callis, J., Gouternam, M. , Khalil, G., Wright, D., Green, E., Burns, D. , and McLachlan, B., "Luminescent Barometry in Wind Tunnels," *Rev. Sci. Instrum.*, Vol. 61, No. 11, pp. 3340-3347, 1990.

(3) Sabroske, K. R., Rabe, D. C., and Williams, C., "Pressure-Sensitive Paint Investigation for Application in Turbomachinery," ASME Paper No. 95-GT-92, ASME International Gas Turbine and Aeroengine Congress and Exposition, Houston, Texas, 1995.

(4) Lepicovsky, J., Bencic, T. C., and Bruckner, R. J., "Application of Pressure-Sensitive Paint to Confined Flow at Mach Number 2.5", AIAA- Paper No. 97-3214, AIAA/ASME/SAE/ASEE Joint Propulsion Conference and Exhibit, Seattle, WA, 1997.

(5) Hamner, M., B. Campbell, T. Liu, and J. Sullivan, "A Scanning Laser System for Temperature and Pressure-Sensitive Paint," AIAA- Paper No. 94-0728, AIAA 32nd Aerospace Sciences Meeting and Exhibit, Reno, NV, 1994.

(6) Morris, M. J., and Donovan, J. F., "Application of Pressure- and Temperature-Sensitive Paints to High-Speed Flows", AIAA- Paper No. 94-2231, AIAA 32nd Aerospace Sciences Meeting and Exhibit, Reno, NV, 1994.

(7) Liu, T., Johnston, R., Torgerson, S., Fleeter, S., and Sullivan, J., "Rotor Blade Pressure Measurement in a High Speed Axial Compressor using Pressure and Temperature Sensitive Paints," AIAA Paper No. 97-0162, AIAA 35th Aerospace Sciences Meeting and Exhibit, Reno, NV, 1997.

(8) Gruber, M. R., Nejad, A. S., and Goss, L. P., "Surface Pressure Measurements in Supersonic Transverse Injection Flowfields," AIAA Paper No. 97-3254, 33rd AIAA/ASME/SAE/ASEE Joint Propulsion Conference and Exhibit, Seattle, WA, 1997.

(9) Navarra, K. R., "Development of the Pressure-Sensitive-Paint Technique for Turbomachinery Applications", Master's Thesis, Virginia Polytechnic Institute and State University, Blacksburg, VA, May, 1997.

(10) Russler, P., Rabe, D., Cybyk, B., and Hah, C., "Tip Flow Fields in a Low Aspect Ratio Transonic Compressor," ASME Paper No. 95-GT-089, ASME International Gas Turbine and Aeroengine Congress and Exposition, Houston, Texas, 1995.

(11) *PaintCp V2.2 User's Guide*, Sterling Software Technical Note TN-93-8006-000-48, 1994.

(12) Copenhaver, W. W., Hah, C., and Puterbaugh, S. L., "Three-Dimensional Flow Phenomena in a Transonic, High-Through-Flow, Axial-Flow Compressor Stage," *J. Turbomachinery*, Vol. 115, No. 2, pp. 240-248, 1993.

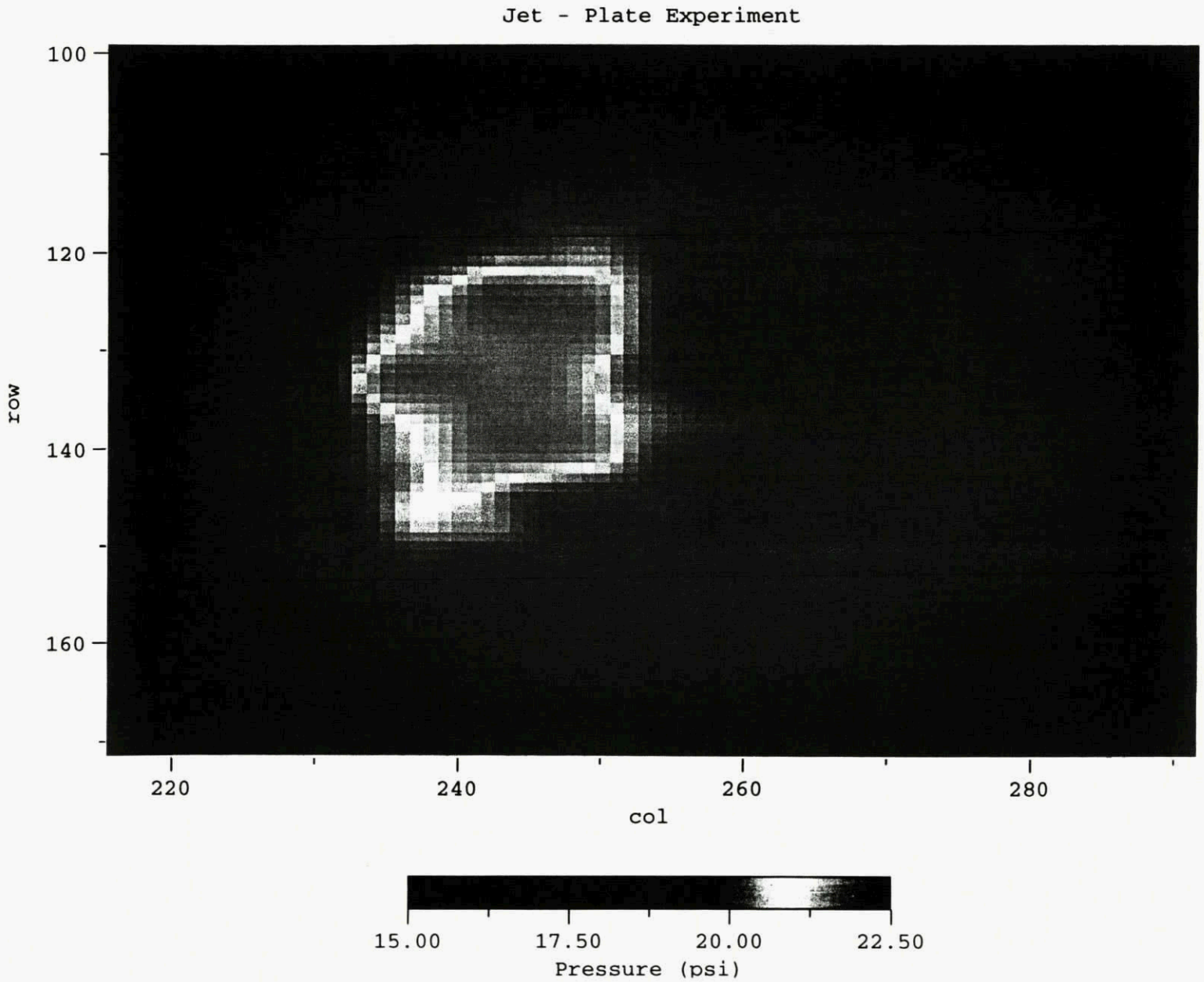
Jet - Plate Experiment
100
120
140
160
row
220
240
260
280
col
15.00
17.50
20.00
22.50
Pressure (psi)

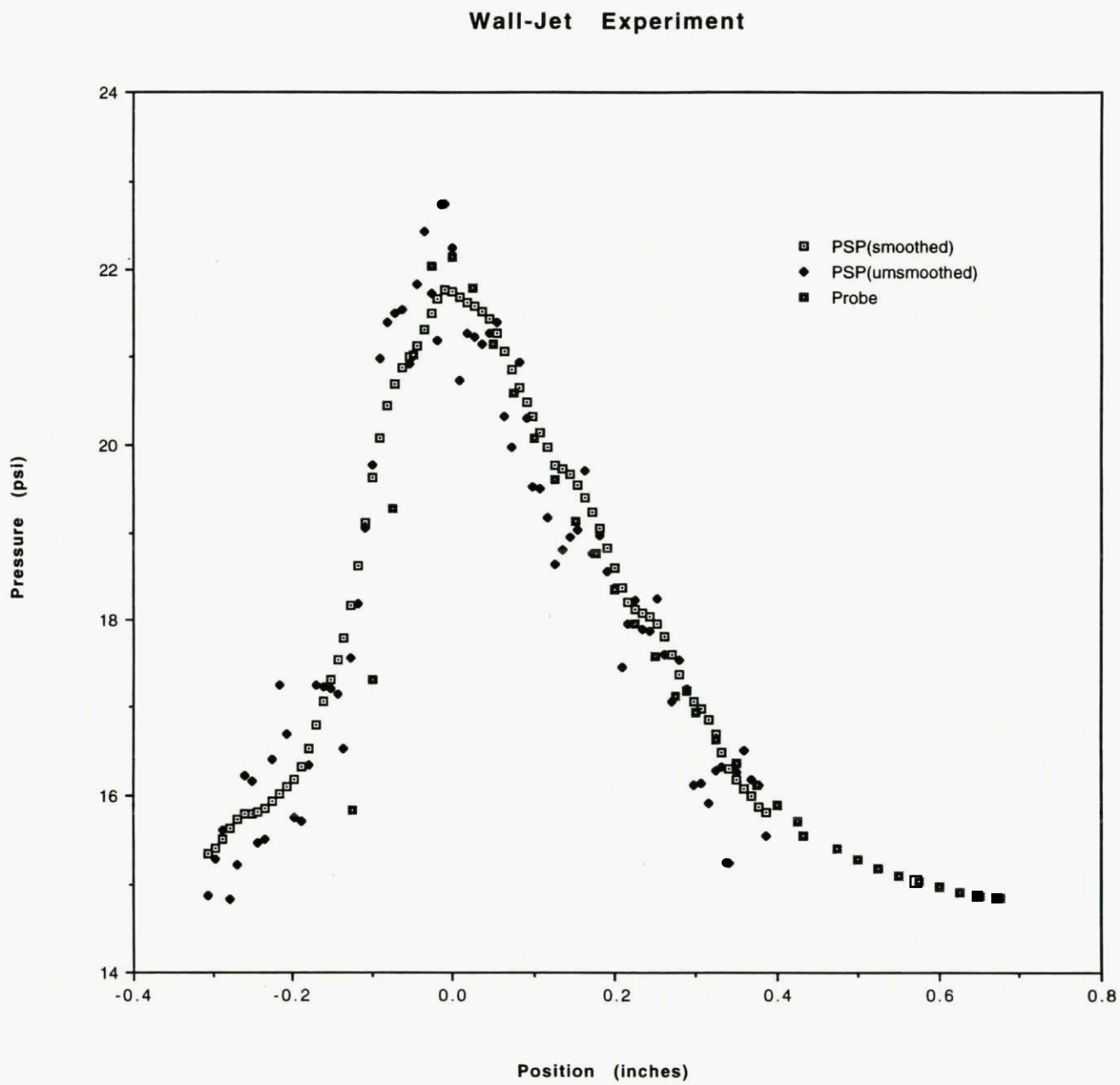
Wall-Jet Experiment
PSP(smoothed)
PSP(umsmoothed)
Probe
Pressure (psi)
Position (inches)
24
22
20
18
16
14
-0.4
-0.2
0.0
0.2
0.4
0.6
0.8

Paper 18
Author: Navarra

Q: Voigt

Since the honeycomb is a consistent pattern in the images that have been taken with an intensified CCD-camera, it should be possible to suppress the effect in the frequency domain; where the pattern will appear as a peak at a certain spatial frequency. Did you try this ?

A: No, this was not attempted but, it is believed that this would not be sufficient to correct the data because of the noise.

Q: Versluis

Referring to the poor quality of the images (in your paper attributed to the ICCD camera). Are you sure these effects are not caused by pulse-to-pulse fluctuations of the pulsed $N_2$ - laser ?

A: No, the pulse-to-pulse fluctuation of the laser is ~1% and therefore was not a concern. Again, the major noise source was from the intensified CCD camera.

Q:

Did you observe or have to correct for any self-illumination effects in your work within the confined spaces in turbomachinery ?

A: No, the painted blades were not adjacent, they were sufficiently spaced such that self-illumination was not an issue.

# Rotor Blade Pressure Measurement in a Rotating Machinery Using Pressure and Temperature Sensitive Paints

Torgerson, S., Liu, T. and Sullivan, J.
School of Aeronautics and Astronautics
Purdue University, 3 Purdue Airport
West Lafayette, IN 47906-3371, USA

## Summary

Pressure and temperature sensitive paints have been utilized for the measurement of blade surface pressure and temperature distributions in a high speed axial compressor and an Allied Signal F109 gas turbine engine. Alternate blades were painted with temperature sensitive paints and then pressure sensitive paint. This combination allows temperature distributions to be accounted for when determining the blade suction surface pressure distribution. Measurements were taken and pressure maps on the suction surface of a blade were obtained over a range of rotational speeds. Pressure maps of the suction surface show strong shock waves at the higher speeds.

## Introduction

Pressure and temperature sensitive paints (PSP and TSP) offer a unique and inexpensive means of determining surface pressure and temperature distributions. Continuous surface pressure and temperature distributions, impossible to obtain using conventional measurement techniques, are critical for understanding complex flow mechanism and allow direct comparisons with results from computational fluid dynamic calculations (CFD). Not only is the cost of installing these conventional probes an issue, but the aerodynamics and structural dynamics of the model can be seriously altered by modifications to accommodate the transducers and static pressure taps. PSP measurements on rotating machinery were conducted by Burns and Sullivan [1] with a laser-PMT based system. They obtained pressure distributions on a small wooden propeller and a TRW Hartzell propeller. Their PSP-derived pressure distributions across the blades show reasonable trends. Bykov et al[18] have shown extensive pressure measurements on propellers using a proprietary Russian pressure paint. Bencic [19]at NASA Lewis has recently completed a series of test using PSP for fan blade pressure measurements on a model high-by-pass ratio fan. Navarra and colleges [20]at Wright Patterson Air Force Laboratory are also developing PSP/TSP systems for large scale turbomachinery

In this study, the PSP and TSP techniques are further used to measure pressure and temperature distributions on rotor blades in a high speed axial compressor and in an Allied Signal F109 gas turbine engine.

**PSP and TSP Theory and Measurement Techniques**

The physical processes involved in behavior of PSP and TSP have been thoroughly presented in literature [3-11], but will be covered briefly in this section for completeness.

The paint layer is composed of luminescent molecules and a polymer binder material. The resulting 'paint' can be applied to a surface using a brush or sprayer. As the paint dries, the solvent evaporates and leaves behind a polymer matrix with luminescent molecules embedded in it. Light of the proper wavelength to excite the luminescent molecules in the paint is directed at the model and luminescent light of a longer wavelength is emitted by the molecules. Using the proper filters, the excitation light and luminescent emission light can be separated and the intensity of the luminescent light can be determined using a photodetector. Through the photo-physical processes known as thermal- and oxygen-quenching, the luminescent intensity of the paint emission is related to temperature or pressure. Hence, from the detected luminescent intensity, temperature and pressure can be determined.

**Pressure Sensitive Paint**

PSP operation is based on the principle that certain fluorescent molecules are quenched by the presence of oxygen. In the molecules of interest, oxygen interacts with the excited molecules and the excess energy is transferred to the oxygen in a collisional process, with no photons being emitted. This process, known as oxygen quenching, is the basis for the pressure sensitive paint method. According to Henry's law, oxygen concentration is proportional to the partial pressure of oxygen, which is proportional to static pressure. The result is that if there is a locally high pressure area, the fluorescent molecules will be quenched by oxygen.

The oxygen quenching process and can be modeled with the Stern-Volmer relation:

$$\frac{I_{ref}}{I} = A(T) + B(T)\frac{p}{p_{ref}}$$

where A and B are the coefficients to be determined experimentally, I is the measured luminescent intensity, $I_{ref}$ is a reference luminescent intensity, p is the pressure, and $p_{ref}$ is a reference pressure. In general, the coefficients A and B are temperature-dependent. The PSP used in this

*Paper presented at an AGARD PEP Symposium on "Advanced Non-Intrusive Instrumentation for Propulsion Engines", held in Brussels, Belgium, 20-24 October 1997, and published in CP-598.*

study is Ru($ph_2$-phen) + silica gel particles in GE RTV 118. Figure 1 shows the Stern-Volmer plots for this paint across a range of temperatures useful in rotating machinery. The temperature-dependent Stern-Volmer coefficients are :

$$A(T) = a_0(1 + a_1(T - T_{ref}))$$

and

$$B(T) = b_0(1 + b_1(T - T_{ref}))$$

where

$a_0 = 0.13$, $a_1 = 2.82$,
$b_0 = 0.87$, $b_1 = 4.32$,
T is in Celsius, and 20 °C < T < 60 °C.

The temperature dependence of A is due to the thermal quenching as in TSP. The temperature dependence of B is due to the temperature dependence of diffusivity of the polymer binder.( Torgerson [14] , Schanze et al.[21]) Therefore, for accurate pressure measurements, surface temperature must be determined. In this study, TSP is used for temperature measurement.

**Temperature Sensitive Paint**

In TSP radiationless transitions in the molecule release energy through vibrational and rotational motions of the molecule. In certain molecules, these non-radiative transitions are dependent upon temperature

For a TSP, it is assumed that the paint layer is not oxygen-permeable so that $[O_2] = 0$. Hence, the quantum yield is simply given by

$$\Phi = \frac{I}{I_a} = \frac{k_L}{k_L + k_D} = k_L \tau_0$$

The deactivation term $k_D$ may be decomposed into a temperature-independent part $k_0$ and a temperature-dependent part $k_1$ that is related to thermally activated intersystem crossing (i.e. $k_D = k_0 + k_1$). The rate $k_1$ can be assumed to have an Arrhenius form

$$k_1 = C \exp(-E/RT)$$

where C is a constant, E is the Arrhenius activation energy, R is the universal gas constant and T is the thermodynamic temperature (in Kelvin).

The temperature dependence of luminescent intensity can be approximated by the simple Arrhenius relation over a certain temperature range

$$\ln\left(\frac{I(T)}{I_{ref}(T_{ref})}\right) = \frac{E}{R_g}\left(\frac{1}{T} - \frac{1}{T_{ref}}\right)$$

where I is the measured luminescent intensity, $I_{ref}$ is a reference luminescent intensity, T is the temperature in Kelvin, $T_{ref}$ is a reference temperature in Kelvin, E is the Arrhenius activation energy, and $R_g$ is the universal gas constant. The constant $E/R_g$ can be determined experimentally.

The TSP used is Ru(bpy) in Shellac. Figure 2 shows the Arrhenius plot of calibration data obtained over several days. The constant $E/R_g$ is 1,070 for Ru(bpy)-Shellac paint. The PSP and TSP were coated on alternating blades by spraying or dipping the blades in the paint, resulting in a thickness of approximately 20 microns.

In intensity-based PSP and TSP measurements, a reference signal (image for a CCD camera system) is taken prior to the experiment starting. This signal (image) of the luminescence is known as a "wind off" or reference signal (image) and is ratioed with the signal (image) taken under test conditions. This ratio method acts to remove nonuniformities in illumination and luminescent intensity variations due to uneven paint thickness.

Estimates of the error in the pressure and temperature measurements are:

$$T = T \pm 1^0 C$$

$$p = p \pm .5 psi$$

Details of the error estimates are given in Refs. 10,13 and 14. In wind tunnel testing using PSP, several pressure taps are used to perform an in situ calibration to significantly reduce the pressure error. The pressure error in the present case is primarily due to the lack of a known pressure on the compressor blade with which to correct the PSP results.

## Axial Compressor Facility

The Purdue Research Axial Fan Facility features a 30.48 cm (12 in.) diameter, 2/3 hub-tip ratio compressor rotor which is integral with the shaft. The drive system consists of a 400 horsepower AC motor driving a magnetic clutch with a variable speed output that drives a gearbox, as shown in Figure 3. Eighteen inlet guide vanes are twisted to produce a free vortex whirl into a 19 blade axial flow rotor. Both the inlet guide vanes and the rotor blades are designed with NACA 65 series airfoil sections on circular arc meanlines. The aluminum rotor blades have 2 in. chord and 2 in. span from the hub to tip. Located downstream of the rotor are eight aerodynamic struts that support the rotor bearing housing. Axial spacing between the trailing edge of the rotor and the leading edge of one of the struts nondimensionalized by the rotor chord $C_R$ is $L/C_R = 3.47$. For these experiments, axial IGV-to-rotor spacing to chord ratio is set at $Z/C_R = 0.6$ ($10^o$ IGV stagger angle). Note that the selection of rotor speeds is dictated by the vibrational level of the machine. The velocity measurements have been made using hot-film sensors between the IGV and rotors. A detailed discussion about hot-film measurements in the compressor is given by Johnston and Fleeter [2].

**Laser Scanning System**

Instead of a CCD camera system commonly used for TSP and PSP measurements in wind tunnels, a laser scanning system was adopted for measurements in the compressor where optical access is very limited. Descriptions of the laser scanning system was given by Burns [1] and Hamner et al. [12]. Recently, a two-dimensional laser

scanning system has been developed for TSPs and PSPs [13, 14]. The laser scanning system used is shown in Figure 4. An air-cooled Argon laser with filtered output of 488 nm was used as an illumination source for both the PSP and TSP. It was mounted upstream of the inlet such that the beam passed between the upstream inlet guide vanes and arrived at the rotor blades. Using a computer-controlled scanning mirror, the 1 mm diameter laser spot was scanned across radial locations over each blade. As the rotor blades rotate, the laser illuminated the painted blades across the chord at each radial location. There was a minimum of 100 data points in the chordwise direction, depending on rotational speed. Luminescence was detected with a Hamamatsu PMT after the excitation light was filtered from the signal with a long-pass optical filter. Data were collected by a PC with a 12 bit A/D converter operating at a maximum of 500 KSamples/s. Pressure and temperature distributions were calculated from the calibration relations.

## Results - Axial Flow Compressor

Typical raw intensity signals from the PSP and TSP on suction surface are shown in Figure 5 for several rotational speeds (1,000, 13,500 and 17,000 rpm). As the rotational speed increases, the luminescent intensity of the TSP decreases, indicating increase of surface temperature. The PSP depends on both pressure and temperature. The change in the distribution of the PSP intensity as the speed increases can been observed in Figure 5. The change in shape is mainly due to pressure variations on surface. In particular, an intensity drop at 17,000 rpm occurs within a position range from the 90$^{th}$ to 100$^{th}$ data point (0.6 to 0.67 chord), which corresponds to a large pressure jump produced by a shock.

In order to calculate temperature and pressure, the signal at the lowest speed of 1,000 rpm was used as the "wind off" intensity and the signals at the larger speeds as the "wind on" intensity. Figure 6 shows radial surface temperature distributions at mid-chord at different rotational speeds The mean temperature on the blade surface was found to increase with rotational speed. This is attributed to friction heating on the rotating blade. The highest blade surface temperature is about 43$^{o}$C at 17,800 rpm.. Surface temperatures are higher at larger radial distances since the relative velocity is greater near the tip. Figure 7 shows measured temperatures at 50% span on Mylar and aluminum surfaces at several relative Mach numbers (several rotational speeds) along with stagnation temperatures. Obviously, the insulating properties of the surface affects surface temperatures.

Surface pressure distributions were obtained using the Stern-Volmer relations with the temperature-dependent coefficients by taking the temperature effects into account. Figure 10 shows a surface pressure map at a rotational speed of 17,800 rpm. This two-dimensional maps clearly indicate the formation of a shock that produces a rapid pressure rise across it. The black patch at the right edge results from blade overlap near the root. A composite view of both the temperature blade and the pressure blade is given in Figure 12.

A cascade analysis was performed at the 0.75 span of the rotor blade using Rotor Viscous Code Quasi-3D from R. Chima at NASA Lewis Research Center [15, 16]. This is a Navier Stokes code that was used with a Baldwin-Lomax turbulence model. A body-fitted C grid (301×61) was generated by a companion code [17]. Figure 14 shows comparison between CFD results and PSP data at 75% span for different rotational speeds. The Pressures are normalized with the upstream stagnation, wich is atmospheric pressure for the experiment. The PSP-derived pressure distributions exhibit the same trend as those given by the CFD code. Quantitatively, the measured pressure data are lower than the CFD results.

## Allied Signal F109 Engine

The laser scanning system demonstrated in a high speed axial compressor gave excellent results. In this section, the technique is adapted for use on a modern gas turbine engine. This test serves to illustrate the capabilities of pressure sensitive paints using the laser scanning system in a more complex test environment.

The F109 is a two-spool, contrarotating concentric shaft, non-augmented, fixed geometry turbofan engine with a bypass ratio of 5. It was designed to produce 1330 lbs. of thrust. The fan section is 18 inches in diameter and contains 30 compressor blades. The F109 was designed for use as the propulsion unit for a jet trainer aircraft, but was never put into production. The Department of Aviation Technology at Purdue acquired several of the engines from the Air Force and Allied Signal for instructional use. The engine used in these tests is mounted in an indoor test cell in the Aviation Technology building at the Purdue Airport. The engine had 30 hours of operation at the start of these tests. A schematic of the F109 is shown in Figure 14.

Previous PSP experiments in the F109 [1] used a hollow probe mounted in the bellmouth with a mirror attached at the end with a 45° angle to pass the laser into the fan section and also collect the fluorescence. Using this method, only one radial location may be tested at any moment due to the fixed angle of the mirror. Since the objective is to measure full two-dimensional pressure distributions, the laser and optics were mounted upstream of the bellmouth This is an arrangement similar to Figure 4. In doing this, there are several factors that must be considered. Due to the large mass flow into the engine, the laser and optics must be placed far enough upstream to not interfere with the engine intake air. Also the flow velocities must be small around the optics so that movement due to turbulence in not a problem. Placing the optical setup far from the blades reduces the F number of the basic system, so that a large collection lens must be added to focus an acceptable amount of fluorescence on the PMT. Also, due to the laser beam's divergence, a long focal length lens system must be used to focus the laser onto the paint.

**Paint Adhesion**

One of the challenging aspects of applying the PSP to the rotor blades is to make sure that the paint adheres at the highest rotational speeds. Ideally, the paint should be very thin, since the centrifugal force increases with thickness but the trade-off is that the fluorescence intensity decreases

The initial paints chosen for this test were bathophen ruthenium chloride in G.E. RTV 118 for the pressure paint and Ru(bpy) in shellac for the temperature paint, as in the axial compressor tests.

When scanning across several different paints, as in this test, it is important that the intensity levels of the paints be very similar. This allows the full range of the A/D to be utilized, maximizing sensitivity and accuracy. This process is done by making one paint and then adjusting the mixture and thickness of the other to result in similar fluorescence intensity levels as seen by the PMT with the appropriate long pass filter. This can be time consuming, but is very important for good results.

Initially, four blades were painted, alternating between PSP and TSP. The tests were conducted at 3600, 6000, 8000, 10000, 12000, 13000 and 14000 rpm, with the idle position, 3600 rpm, used as the reference condition. The pressure and temperature paints performed well at the lower rotational speeds. However, as the speed reached 10,000 rpm, some of the paint began to come off. By 14,000 rpm, all of the pressure paint as well as some of the temperature paint had been pulled off due to the large centrifugal forces. The shellac-based temperature paint, while not coming completely off of the blade became . very uneven due to shearing of the polymer.

After researching the adhesion of various substances on the titanium blades, it was found that the RTV-based PSP produced a very strong and durable paint layer when applied directly to the blades. The main drawback to directly applying the paint directly to the blade is that the fluorescent intensity is reduced without the normal white undercoat. This did not present a large problem due to the effectiveness of the large collection lens in front of the PMT. A new binder for the temperature paint was used to solve the shearing problems. This consisted of DuPont Chroma Clear 7500s clear urethane paint. This paint withstood the high forces better than the shellac-based temperature paint. In subsequent tests both new paints adhered well at all speeds.

**Data Acquisition**

A program written in Labview was used to move the laser beam and acquire the fluorescence from the paints. The program allows rapid setup of scanning and A/D parameters with the ability to monitor the effects of these changes immediately.

Since there was no once per revolution trigger signal available to start the data acquisition, one of the blades was painted with a temperature paint that had an excessive amount of Ru(bpy), resulting in an intensity that was several times higher than the other blades. The A/D board could trigger off of this blade as the number of counts went full scale.

## Results - F109 Engine

In order to reduce the pressure data, the temperatures must first be calculated. The temperature distribution at 90% span is shown in Figure 15. As expected, the temperature rises considerably at the higher rotational speeds, with a maximum temperature increase of 30°C. The ambient temperature during the tests was 11°C. Previous temperature results [1] on the F109 gave a temperature increase of about 27°C.[6]

Using the measured temperature distributions and the Stern Volmer equation, the pressure distributions can be calculated. Figure 16 shows the results 14,000 rpm. The compressor blade outline and the damper blade are outlined in the figure for reference. A shock waves is clearly visible at this high speed.

Pressure distributions are plotted in Figure 17 at 70% of the span. Shock waves are located between 15% and 30% chord. As expected, the shock waves move aft as the speed is increased

## Conclusions

Pressure and temperature sensitive paints have been used for the measurement of blade surface pressure and temperature distributions in a high speed axial compressor environment and an Allied Signal F109 Engine. Measurements of the suction surface pressure were made from the hub to tip at several rotational speeds. The surface pressure maps clearly indicate the presence of a shock wave at higher rotational speeds and are in moderate agreement with CFD results..

## Acknowledgments

This work is supported by The Boeing Company, NASA Lewis, NASA Ames and AFOSR.

## References


[1] Burns, S. and Sullivan, J., "The Use of Pressure Sensitive Paints on Rotating Machinery," Proc. 16th Int. Cong. Instrumentation in Aerospace Simulation Facilities (ICIASF), Institute of Electrical and Electronics Engineers, Wright-Patterson Air Force Base, Dayton, OH, USA, 1995, pp. 32.1-32.14.

[2] Johnston, R. T. and Fleeter, S., "High-Speed Rotor Wake, Vortical and Potential Forcing Functions," AIAA Paper 95-2482, 1995.

[3] McLachlan, B. G., Kavandi, J. L., Callis, J. B., Gouterman, M., Green, E. and Khalil, G., "Surface Pressure Field Mapping Using Luminescent Coatings," Experiments in Fluids 14, 1993, pp. 33-41.

[4] McLachlan, B. G. and Bell, J. H., "Pressure-Sensitive Paint in Aerodynamic Testing," Experimental Thermal and Fluid Science, 10, 1995, pp. 470-485.

[5] Morris, M. J., Benne, M. E., Crites, R. C. and Donovan, J. F., "Aerodynamics Measurements Based on Photoluminescence," AIAA Paper 93-0175, 1993.

[6] Morris, M. J., Donovan, J. F., Kegelman, J. T., Schwab, S. D., Levy, R. L. and Crites, R. C., "Aerodynamic Applications of Pressure Sensitive Paint," AIAA Journal, Vol. 31, No. 3, March, 1993, pp. 419-425.

[7] Troyanovsky, I., Sadovskii, N., Kuzmin, M., Mosharov, V., Orlov, A., Radchenko, V. and Phonov, S., "Set of Luminescence Pressure Sensors for Aerospace Research," Sensors and Actuators B, 11, 1993, pp. 201-206.

[8] Liu, T., Campbell, T., Sullivan, J., Lafferty, J. and Yanta, W., "Heat Transfer Measurement on a Waverider at Mach 10 Using Fluorescent Paint," J. of Thermophysics and Heat Transfer, Vol. 9, No. 4, 1995, pp. 605-611.

[9] Liu, T., Campbell, B. and Sullivan, J., "Fluorescent Paint for Measurement of Heat Transfer in Shock-Turbulent Boundary Layer Interaction," Experimental Thermal and Fluid Science 10, 1995, pp. 101-112.

[10] Liu, T., Campbell, B. T., Burns, S. P. and Sullivan, J. P., "Temperature- and Pressure-Sensitive Luminescent Paints in Aerodynamics", Applied Mechanics Reviews Vol. 50, No. 4, April 1997, pp227-246.

[11] Campbell, B., Liu, T. and Sullivan, J., "Temperature Sensitive Fluorescent Paint System," AIAA Paper 94-2483, 1994.

[12] Hamner, M., Campbell, B., Liu, T. and Sullivan, J., "A Scanning Laser System for Temperature and Pressure Sensitive Paint," AIAA Paper 94-0728, 1994.

[13] Torgerson, S. D., Liu, T. and Sullivan, J. P., "Use of Pressure Sensitive Paints in Low Speed Flows," AIAA Paper 96-2184, 1996.

[14] Torgerson, S. D., "A Laser Scanning System for Use With Pressure and Temperature Sensitive Paints," M. S. Thesis, School of Aeronautics and Astronautics, Purdue University, West Lafayette, IN , 1997.

[15] Chima, R.V., "Explicit Multigrid Algorithm for Quasi-Three-Dimensional Viscous Flows in Turbomachinery", Journal of Propulsion and Power, Vol. 3, No. 5, 1987, pp. 397-405

[16] Chima, R.V. , Turkel, E. ,Schaffer, S., "Comparison of Three Explicit Multigrid Methods for the Euler and Navier-Stokes Equations", NASA TM-88878, 1987.

[17] Sorenson, R.L., "A Computer Program to Generate Two-Dimensional Grids about Airfoils and Other Shapes by the Use of Poisson's Equation" NASA TM-81198, 1980.

[18] Bykov, A., Fonov, S., Kishalov,A., Mosharov,V., Orlov, A., Ostroukhov, S., Radchenko, V. "Application of Luminescent Pressure Sensor Technology to Propellers", Preprint 99. Central Aero-Hydrodynamic Institute, Moscow 1995.

[19] Bencic, T., "Rotating Pressure Measurements on a Scale Model High-by-Pass Ratio Fan using PSP at NASA LeRC", Fifth Pressure Paint Workshop, Tullahoma ,TN. 1997.

[20]Navarra, K., "Development of the Pressure Sensitive Paint Technique for Advanced Turbomachinery Applications", Fifth Pressure Paint Workshop, Tullahoma ,TN. 1997.

[21]Schanze KS, Carroll BF, Korotkevitch S, et al.,(1997) Temperature dependence of pressure sensitive paints, AIAA J 35: (2) 306-310

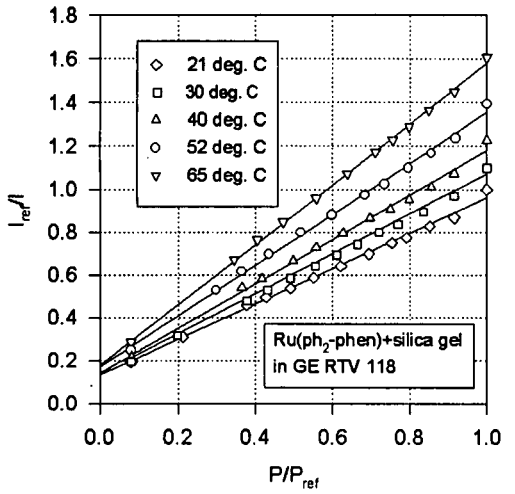


Figure 1. Stern-Volmer plots for Ru(ph$_2$-phen) + silica gel particles in GE RTV 118

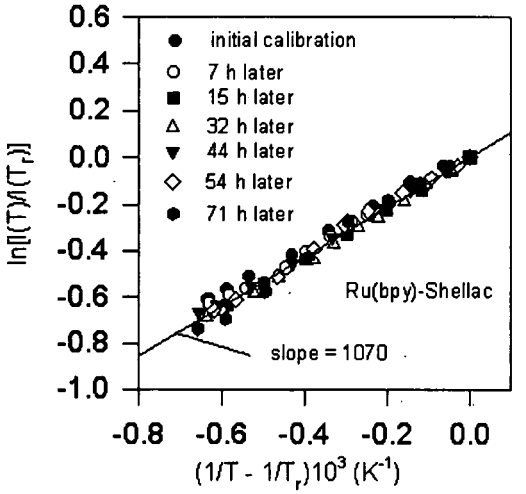


Figure 2. Arrhenius plot for Ru(bpy) in Shellac

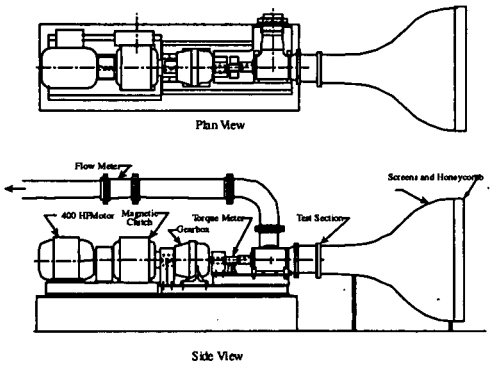


Figure 3. Purdue Research Axial Fan Facility

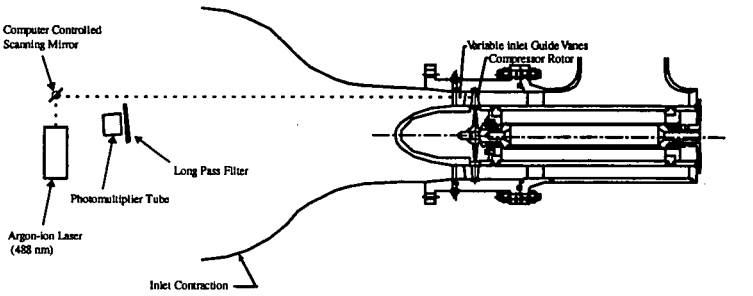


Figure 4. Pressure and temperature sensitive paint optical access

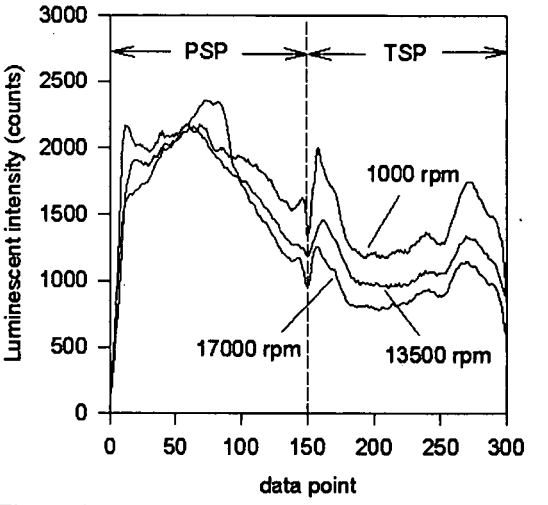


Figure 5. Raw PMT signals from PSP and TSP at three rotational speeds: 1,000, 13,500, and 17,000 rpm

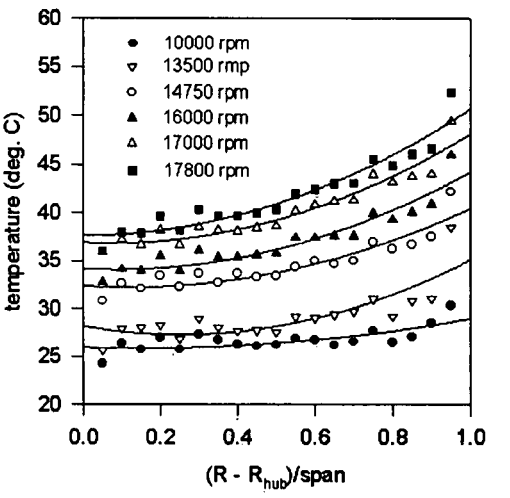


Figure 6. Spanwise surface temperature distributions at mid-chord at different rotational speeds

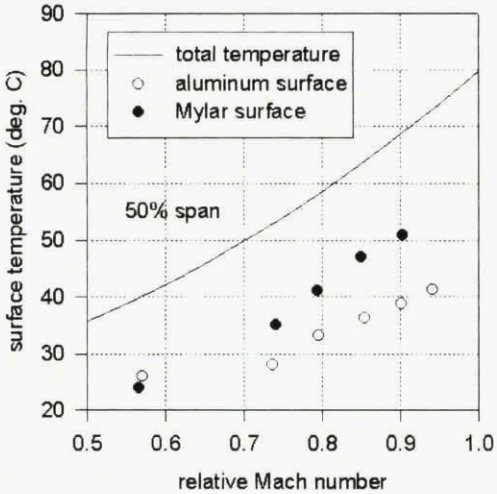


Figure 10. Surafce temperatures at different relative Mach number on Mylar and aluminum surfaces

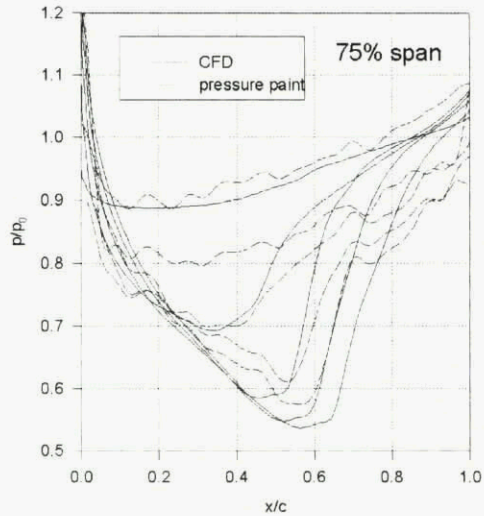


Figure 13. Comparison of PSP data and CFD results.

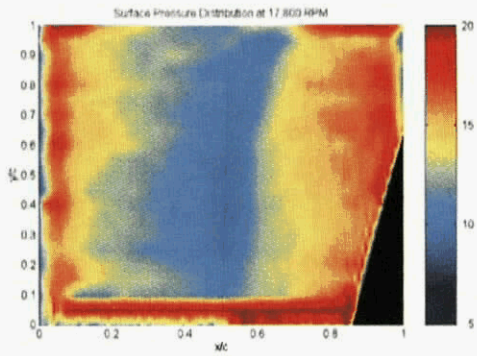

Figure11. Compressor blade suction surface pressure map at 17,800 rpm (scale in psia).

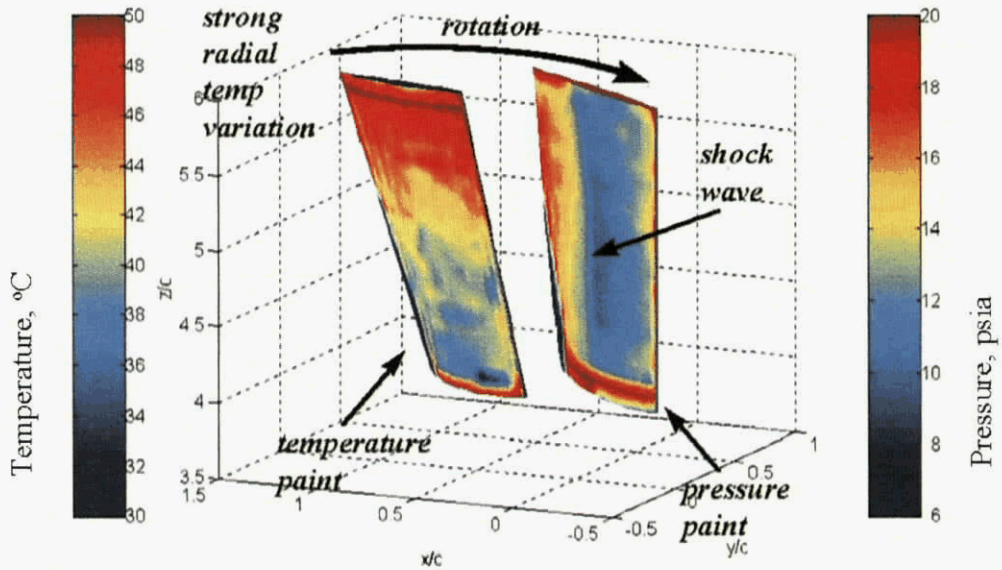


Figure 12. Composite View of Temperature Blade and Pressure Blade

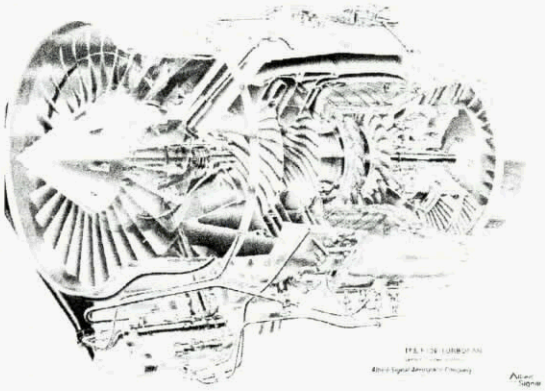

Figure 14. Allied F109 turbofan engine.

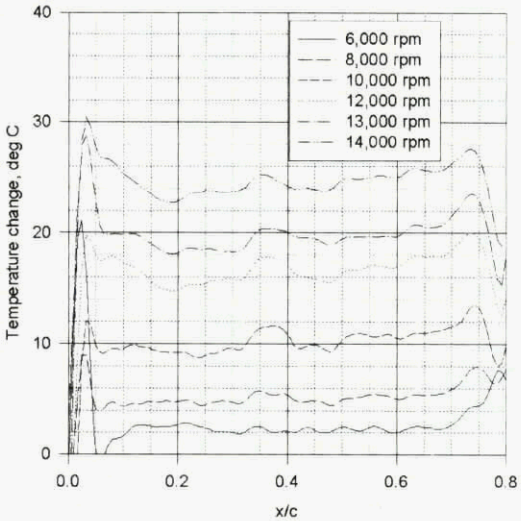


Figure 15. Chordwise temperature distribution at 90% span

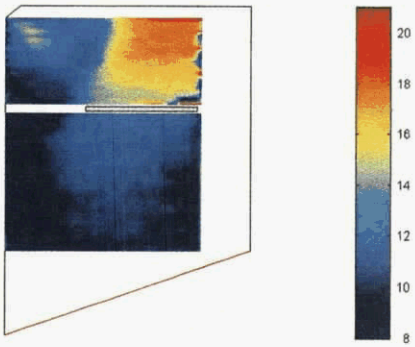


Figure 16. Fan blade pressure distribution at 14,000rpm (scale in psia).

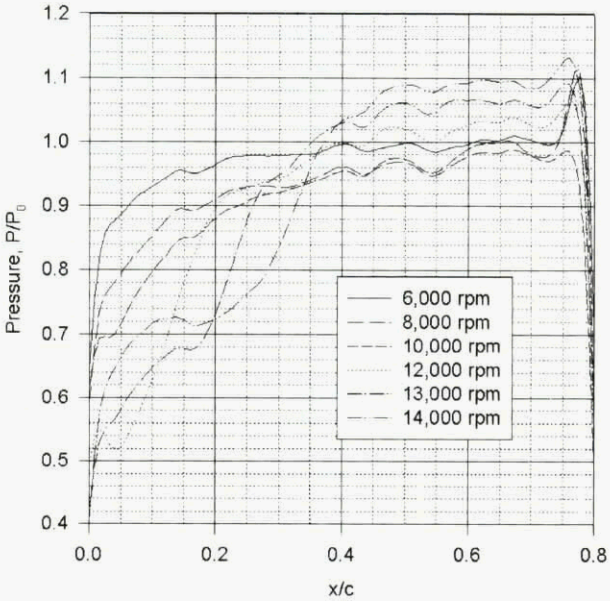


Figure 17. Pressure distribution at 70% span

Paper 19
Author: Sullivan

Q: Greenhalgh

Is there any chemi-sorption effect which could result in a hysteresis for the absoption/desorption processes for $D_2$ in PSP ?

A: For a uniform polymer near standard temperature, the permeability of the polymer to oxygen dominates the time response of the PSP. If solid or porous silica particles are added to the polymer then absorption may be an issue, especially at low temperatures.

Q:

Is there a limitation across the blade chord where you can no longer measure the surface pressure due to the large angle between the surface normal and the angle of incidence of the illumination laser beam and detector location ?

A: We have calibrated PSP and TSP up to an angle of 90 degrees from the normal. So for the measurements presented, we obtain data to within 1mm of the leading edge of the blade before losing the signal.

Q: Weyer

Is the unusual radial position of the shock-wave within the transonic rotor related to shock boundary layer interaction ? The shock strength is much higher at tip than at hub. Thus, the pressure rise affects the boundary layer more intensely near the tip, forming most likely λ-shoots ?

A: The shock boundary layer interaction may propagate radially affecting the shock position. Also the thickness of the blades varies with radius, so the local Mach number depends not only on rotational Mach number but blade properties.

# USE OF LIQUID CRYSTAL TECHNIQUES TO MEASURE FILM COOLING HEAT TRANSFER AND EFFECTIVENESS

**S.M. Guo, C.C. Lai, J.H. Jeong, T.V. Jones and M.L.G. Oldfield**
University of Oxford, Dept. of Engineering Science
Parks Road, Oxford 0X1 3PJ, UK

**G.D. Lock**
Department of Mechanical Engineering, University of Bath, England

**A.J. Rawlinson**
Rolls-Royce plc, Derby, England

## *ABSTRACT*

The transient liquid crystal technique has been used to measure the heat transfer coefficient and cooling effectiveness over heavily film cooled nozzle guide vanes (NGVs). The measurements were performed in the complex environment of a transonic annular cascade which simulates the flow in the gas turbine jet engine. Engine-representative Mach and Reynolds numbers were created and the aerodynamic and thermodynamic characteristics of the coolant flow (momentum flux and density ratio between the coolant and mainstream) have been modelled by using heavy foreign gases ($SF_6$ /Ar mixture).

The Red-Green-Blue (RGB) components have been separated from the colour response of wide-band encapsulated liquid crystals which react to changes of the NGV surface temperature during the transient experiment. Optical access to the test NGV was problematic and the thermochromic response of the crystals was sensitive to both the lighting and the wide range of viewing angles subtended at the camera. An *in situ* calibration is used to translate the RGB histories to measurements of the surface temperature history, and hence local heat transfer coefficient and adiabatic wall temperatures were obtained. The colour data has been gathered using a miniature CCD camera and recorded directly to computer memory without the use of video tape recorder.

The transient liquid crystal technique is shown to be capable of accurately gathering data over any portion of the NGV surface visible to the camera used. As the data is collected in an environment which models the engine, the data is of benefit for both CFD code validation and directly to the engine designer.

---

* Present address: Advanced Research Group, Korea Atomic Energy Research Institute

P.O. Box 105, Yusong, Taejon 350-600, KOREA

*Paper presented at an AGARD PEP Symposium on "Advanced Non-Intrusive Instrumentation for Propulsion Engines", held in Brussels, Belgium, 20-24 October 1997, and published in CP-598.*

## NOTATION

| | |
|---|---|
| $c$ | Specific heat at constant pressure |
| $h$ | Heat transfer coefficient |
| $k$ | Thermal conductivity |
| $q$ | Heat transfer rate |
| $t$ | Time |
| $T$ | Temperature |

## GREEK SYMBOLS

| | |
|---|---|
| $\rho$ | Density |
| $\eta$, $\zeta$ | Film cooling effectiveness |
| $\beta$ | Dimensionless time |
| $\gamma$ | Ratio of specific heats |

## SUBSCRIPTS

| | |
|---|---|
| $aw$ | Adiabatic wall |
| $c$ | Coolant |
| $m$ | Gas, mainstream |
| $r$ | Recovery |
| $s$ | Surface |

## *1 INTRODUCTION*

The power output and level of efficiency of gas turbine engines improves with increased turbine entry temperatures. In the modern aeroengine, such temperatures can exceed the metallurgical limit of blade materials. To achieve acceptable durability, both temperature levels and temperature gradients can be controlled in the engine components exposed to the hot gas stream by using coolant which has been diverted, at cost, from the engine compressor. An efficient cooling system uses a minimum amount of coolant and the optimisation of such a system is one of the primary goals of the engine designer.

There is a vast quantity of experimental and computational work on the topic of gas turbine film cooling, dating back to the 1940s (Kercher 1996; Goldstein 1971; Hartnett 1985). The main quantities of interest in film cooling experiments are the convective heat transfer coefficient ($h$) and the film effectiveness ($\eta$). The former is the constant of proportionality between the local heat flux ($q$) and the difference between the surface temperature ($T_s$) and convection driving temperature of the gas ($T_{aw}$, or *adiabatic wall temperature*) at that point:

$$q = h(T_s - T_{aw}) \qquad (1)$$

The adiabatic wall temperature is chosen since it is desirable to define, and measure, a heat transfer coefficient which is independent of the temperature boundary conditions and a function of the aerodynamic character of the flowfield alone. This is not strictly possible as there are well known and predictable differences between an isothermal wall situation and a constant heat flux boundary condition (Eckert et al. 1957, Butler and Baughn 1996). However, for small streamwise gradients in temperature and constant fluid properties a

wall temperature variation has only a minor influence on local convective heat transfer. For two-temperature convection cases (i.e. without a separate coolant flow) $T_{aw}$ is the local gas recovery temperature. In film cooling, with two flows present, $T_{aw}$ is intermediate between the coolant ($T_{oc}$) and mainstream ($T_{om}$) total temperatures, and depends upon the geometry and degree of mixing between these gases upstream of the point of interest on the surface. To eliminate the temperature dependence a conventional dimensionless adiabatic film effectiveness is defined for constant property compressible flow on an adiabatic surface:

$$\varsigma = \frac{T_{aw} - T_r}{T_{oc} - T_r} \qquad (2)$$

where $T_r$ is the local mainstream gas recovery temperature. An alternative definition of cooling effectiveness, based on superposition (Jones 1991) and similar to the isoenergetic definition of Eckert (Goldstein 1971), is used here:

$$\eta = \frac{T_{aw} - T_r}{T_{oc} - T_{om}} \qquad (3)$$

where $T_{aw}$ corresponds to the temperature of an isothermal wall which is adiabatic at the local point of interest. In practice there is only a small difference in the results using either definition.

The cooling effectiveness and heat transfer coefficients are a function of the following: cooling geometry (the angles of inclination and orientation, the relative spacing of the coolant holes, the hole shape); the state of the oncoming boundary layer; the freestream turbulence intensity; the surface curvature; and the ratios of the coolant-to-mainstream density, mass and momentum fluxes, and specific heats. Most film cooling studies are conducted using a flat-plate geometry. There are very few film cooling studies where measurements are made in an engine-representative environment.

This paper will demonstrate the application of the transient liquid crystal technique to measure heat transfer coefficient and film cooling effectiveness in a transient, short-duration tunnel which creates engine-representative conditions in a transonic annular cascade. The test section of the cascade is a scaled nozzle guide vane typical of that used in a modern aeroengine. Optical access to the test section is difficult and complex surface curvature makes the use of liquid crystal techniques difficult. The data demonstrate the capability of accurately gathering data over any portion of the NGV surface visible to the camera. As the data are collected in an environment which models the engine, the data are of benefit for both CFD code validation and directly to the engine designer.

## 2 TRANSIENT EXPERIMENTAL TECHNIQUE

Several different measurement techniques have been employed to obtain film cooling data. The heat-mass transfer analogy is used in the Swollen Polymer (Hay et al. 1984) and Naphthalene Sublimation (e.g., Cho and Goldstein 1995; Richter et al. 1996) techniques to determine heat transfer coefficient and effectiveness. Effectiveness alone may also be found using gas concentration techniques of which the Ammonia and Diazo (Friedrichs et al. 1995; Haslinger and Hennecke 1996) technique is an example.

The transient method determines the heat transfer coefficient and effectiveness by measuring the transient response of surface temperature to a change in fluid temperature. By assuming that uniform, semi-infinite flat plate boundary conditions apply, it is possible to express the instantaneous heat flux as an analytical function of this transient surface temperature (Schultz and Jones 1973; Jones et al. 1993). Effects of surface curvature can also be taken into account (Buttsworth and Jones 1997). Thin film gauges or thermochromic liquid crystals (TLC) can be employed to measure the surface temperature history. The TLC method has a great advantage over thin film gauges as it provides such temperature histories on the entire wetted surface visible to the camera, rather than an average over the gauge width at fixed locations.

The application of thermochromic liquid crystals to heat transfer experiments is described in detail by Ireland et al. (1993). TLC can be bought commercially in micro-encapsulated form and in the work reported here are spray-painted onto a acrylic (perspex) test piece. The crystals display colour from blue to green to red as the surface temperature cools from a temperature above the high threshold level (or in reverse if the surface is heated from below the lower threshold temperature.) Above this upper threshold and below the lower threshold level, the TLC is clear. They are air-sprayed onto the test piece which has previously been spray-painted black to create a contrasting background for the TLC colour changes. The thermal response of TLC has been measured to be of the order of 3 ms (Ireland and Jones 1987).

Both narrow-band and wide-band TLC are available. Narrow-band crystals typically make the transition from red through green to blue over a change of about 1 C, and a single colour within that range can be used to determine the surface temperature to an accuracy of about 0.1 C. The use of such a crystal accurately identifies when the surface temperature reaches a particular value if the surface colour play has been monitored using a CCD camera, video recorder and image-processing system. The use of more than one narrow-band TLC on the surface identifies multiple moving isotherms as the test surface heats or cools. If the thermal transient is produced by a step-change in fluid temperature, measurements of the time taken for the surface to reach temperatures identified by two narrow-band crystals from a known initial temperature can lead to measurements of both $h$ and $Taw$. Here the classical solution of the one-dimensional conduction equation with a semi-infinite boundary condition is solved (Schultz and Jones 1973):

$$\beta = \frac{h\sqrt{t}}{\sqrt{\rho ck}}, \qquad \frac{T_s - T_{init}}{T_{aw} - T_{init}} = 1 - e^{\beta^2} erfc(\beta) \qquad (4)$$

where $\sqrt{\rho ck}$ is the thermal product of substrate density, specific heat and thermal conductivity and $t$ is the time.

The two unknowns ($h$ and $T_{aw}$) can be obtained from the simultaneous solution of a pair of equations of the form above. If the coolant mainstream and recovery temperatures are known, equation (3) then yields the effectiveness. The conditions necessary for the valid application of this equation are as follows: lateral conduction is negligible; the gas temperature change can be represented by a step function; and the substrate is semi-infinite, i.e., the TLC colour response is short compared with the time taken for the transient thermal response to penetrate through the thickness of the acrylic model.

If the RGB response of the narrow-band TLC is used, rather than information at a single colour, then the solution of the transient heat equation is over-determined and regression analysis can be used to improve the accuracy of the data. The accuracy can be further improved if wide-band TLC is employed as the temperature history can be gathered over a greater range.

## *3 EXPERIMENTAL APPARATUS*
### 3.1 FILM COOLING TEST FACILITY

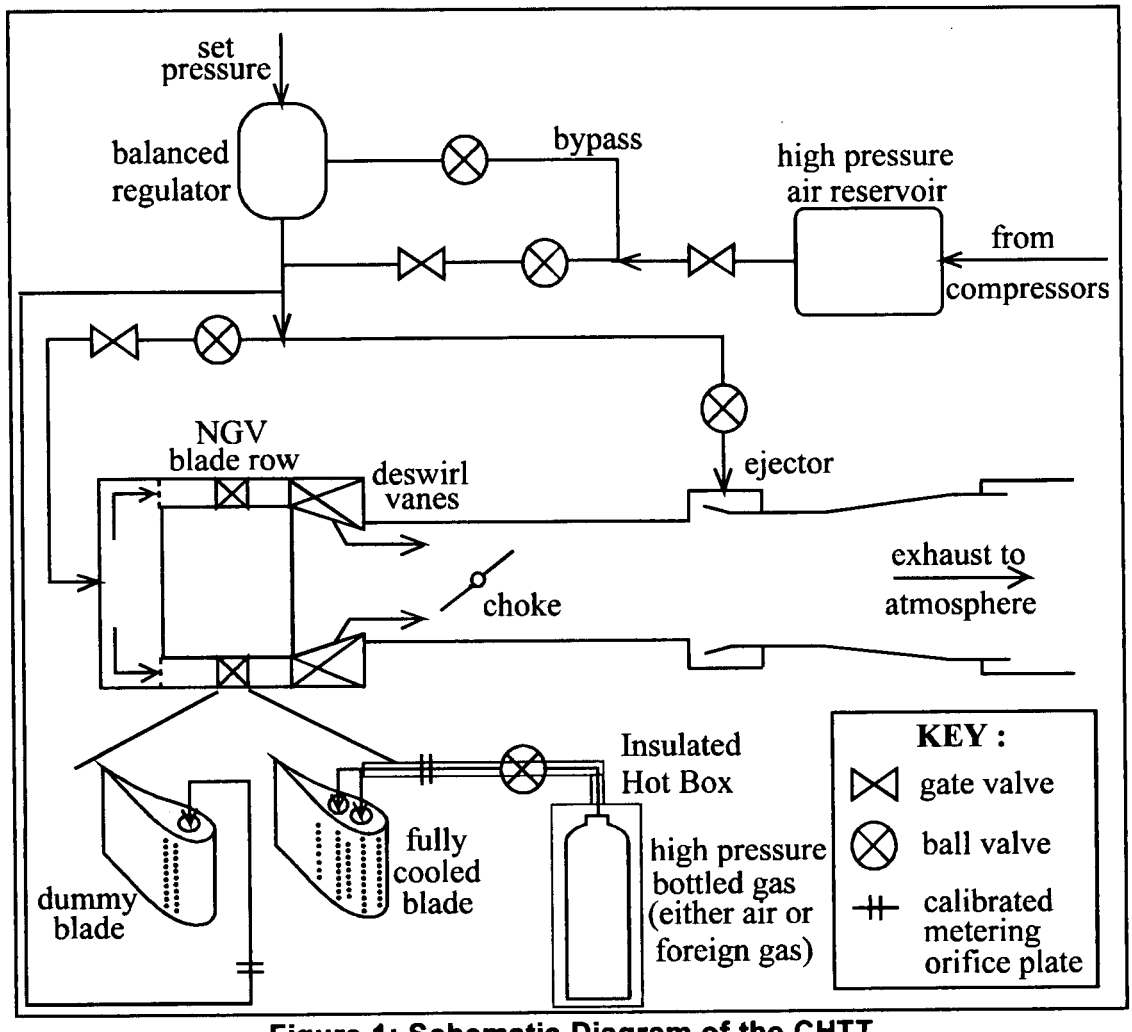


**Figure 1: Schematic Diagram of the CHTT**

The measurements were conducted in the Oxford University Cold Heat Transfer Tunnel (CHTT). The test section of the tunnel is an annular cascade of 36 NGVs at 1.4 times larger than engine scale, and described in detail elsewhere (Martinez-Botas et al. 1993). The NGV instrumented with the liquid crystals and its four immediate neighbours can be either preheated or precooled before the test begins. The tunnel is part of a blowdown facility with the main reservoir at room temperature. The test duration is typically 3-5 seconds. The tunnel allows an independent variation of Reynolds and Mach numbers, or equivalently the upstream and downstream pressures of the cascade can be independently

and continuously varied. All of the results presented here are at an engine design condition (Reynolds number and Mach number at exit of $2 \times 10^6$ and 0.96, respectively) and with a freestream turbulence intensity and length scale of 13% and 21 mm at NGV inlet. Figure 1 is a schematic view of the facility. One of the main features is a balanced upstream regulator which maintains a constant pressure within the tunnel while the main reservoir pressure falls.

### 3.2 NGV COOLING GEOMETRY

The NGV under investigation is from the first stage turbine (downstream of the combustor) of a modern Rolls-Royce aeroengine. The cooling configuration consists of fourteen rows with a total of approximately 350 cooling holes. The holes are fed from one of two internal cavities, as illustrated in figure 2. These cavities are independently supplied with coolant so as to maintain the engine coolant-to-mainstream total pressure ratios. This pressure ratio is fixed and determined by the loss in pressure between the compressor exit and vane compared with that lost for the flow which passes through the combustor. The forward cavity supplies twelve of the fourteen rows, a total of almost 300 cooling holes, positioned around the leading edge, the early regions of the pressure surface and suction surface. The rear cavity feeds two rows, a total of approximately 50 cooling holes, nearest the trailing edge on the pressure surface.

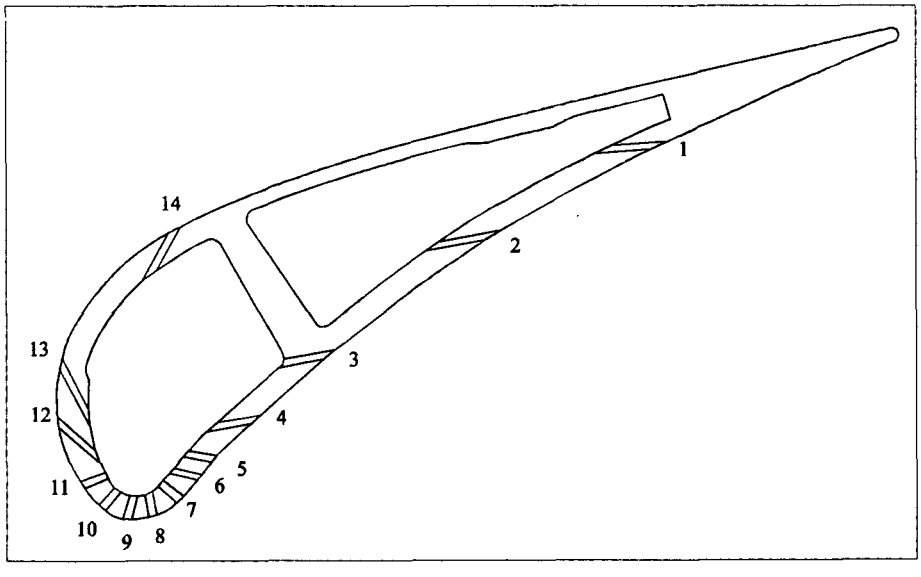


**Figure 2 : Cross-Section of a CHTT NGV having the Full Film Cooling Geometry, Illustrating Row Positions**

The NGV was manufactured on a five-axis NC milling machine from engineering drawings supplied by Rolls-Royce. Two film cooling geometries are to be tested. The first is with all holes cylindrically shaped. The second was with rows 1-4 and 11-14 fanned. Only the former geometry has been used for the research presented here.

### 3.3 COOLANT MODELLING

The experiments were designed to model the engine situation where the coolant is at a lower temperature, and hence more dense, than the mainstream flow. It has been demonstrated (Teekaram et al. 1989) that this density ratio can be simulated using a heavy,

foreign gas. A mixture of $SF_6$ (30.2% by weight) and Ar (69.8% by weight) is used here which has the same ratio of specific heats ($\gamma = 1.4$) but is 1.77 times more dense than air. By matching the total pressure ratio of coolant to mainstream, the velocity ratio and density ratio can be made to correspond to engine conditions. Thus mass flux ratio and momentum flux ratio are also identical. Table 1 compares operating conditions between the CHTT and engine.

**Table 1 Engine/Tunnel Comparison**

| Parameter | Engine | Tunnel |
|---|---|---|
| Inlet Total Pressure | 32 bars | 2 bars |
| Coolant/Main Stream Pressure Ratio | 1.02 | 1.02 |
| Coolant/ Main Stream Density Ratio | 1.77 | 1.77 |
| Turbine Inlet Temperature | 1750-1800 K | 290 K |
| *Exit Reynolds Number | $2.02\times10^6$ | $2.02\times10^6$ |
| Exit Mach Number | 0.96 | 0.96 |
| Mass Flow Rate | 120 kg/s | 38 kg/s |

- Based on axial chord and downstream flow conditions

Coolant is supplied to the 36 NGVs through calibrated metering orifices as illustrated in figure 1. Thirty-three of the vanes have a simplified coolant geometry, while three test vanes have the full coolant geometry discussed below. Both air and foreign gas are available as coolant from high pressure reservoirs. The gas in these reservoirs can be preheated to satisfy thermal boundary conditions in the heat transfer experiments. Because the external heat transfer is the subject of the study, the coolant temperature was set equal to the initial temperature of the NGV to minimise internal heat transfer within the film cooling holes. The coolant total temperature varied by less than 2° C over the course of the experiment. The influence of such variation in the measurement of external heat transfer can be taken into account (Drost et al. 1997) but with such small variation the influence was ignored.

## 3.4 HEAT TRANSFER CASSETTE

Three NGVs with the full coolant configuration, and two guard vanes with the simplified coolant geometry, have been machined from perspex and form a cassette which can be removed from the test section. The NGVs are preheated before the experiment by isolating four passages of the annulus with a shutter mechanism. The shutters, upstream and downstream, are removed during the experiment once steady flow conditions have been achieved. The tunnel requires about 1.5 seconds for an initial start-up transient to end and steady freestream temperatures and pressures to exist through the transonic cascade. The shutters are used to create the boundary conditions for a step-change in gas temperature.

Figure 3 is a photograph of the heat transfer cassette. Two independently driven shutters are used to isolate the five NGVs in the annulus. The upstream shutter seals against the leading edge of the two outside vanes and along the inlet contraction to the NGVs on the inner casing. The downstream shutter seals by registering along the inner casing behind the vanes and touching the trailing edges of the two outer vanes, creating a sealed volume. There is a difference between the outer and inner casing radii and a spring-loaded step has been designed so that the shutter plates are able to preserve the curvature of the outer casing when retrieved and seal against the inner casing when deployed. The springs are of sufficient stiffness to ensure the steps restore the inner casing curvature before the shutters arrive at the outer casing.

The shutters are driven by two pistons. The heat transfer cassette is placed in the side of the CHTT test section (see figure 4) so that the motion of the shutters is horizontal. In order to absorb the momentum of the shutters efficiently and without mechanical damage, heavy-load oil dampers are coupled with the double-ended pistons. The shutter plates move on two heavy-duty bearing-rail assemblies capable of withstanding the large forces the shutters experience during normal operation. The large forces exist when they open during experiment where the pressure difference across them is about 1.5 bar. The position of the moving shutters are recorded using four miniature proximity switches. These yield measurements of the times when the shutters leave the inner casing and arrive at the outer casing. Thus travel times of the shutters are obtained and time markers are available to assess any disturbances of the flow caused by their motion. To create the step-change in gas temperature, the piston and shutter assembly was designed with the intention of opening as quickly as possible. During actual operation, with flow through the cascade, a travelling time of less than 100 ms was achieved.

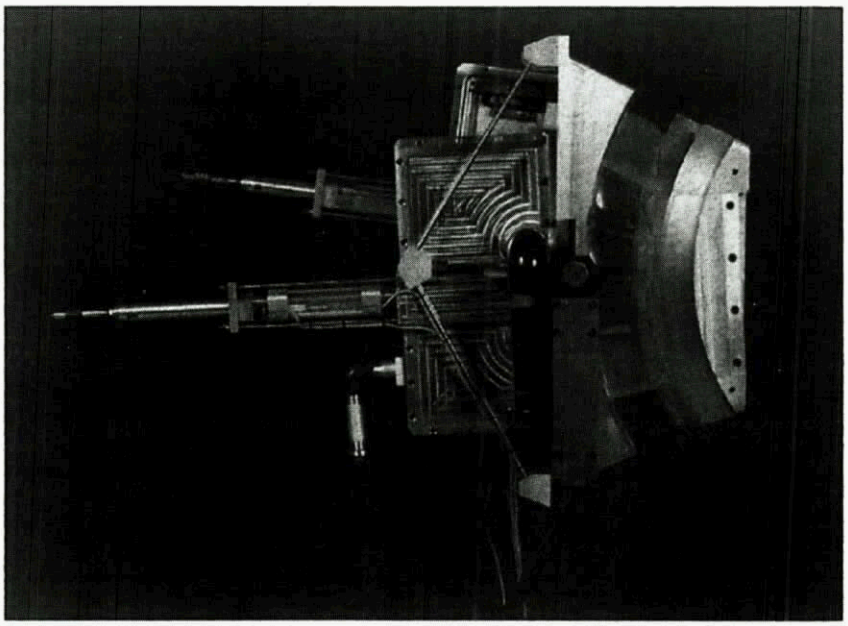

**Figure 3: The heat transfer cassette**

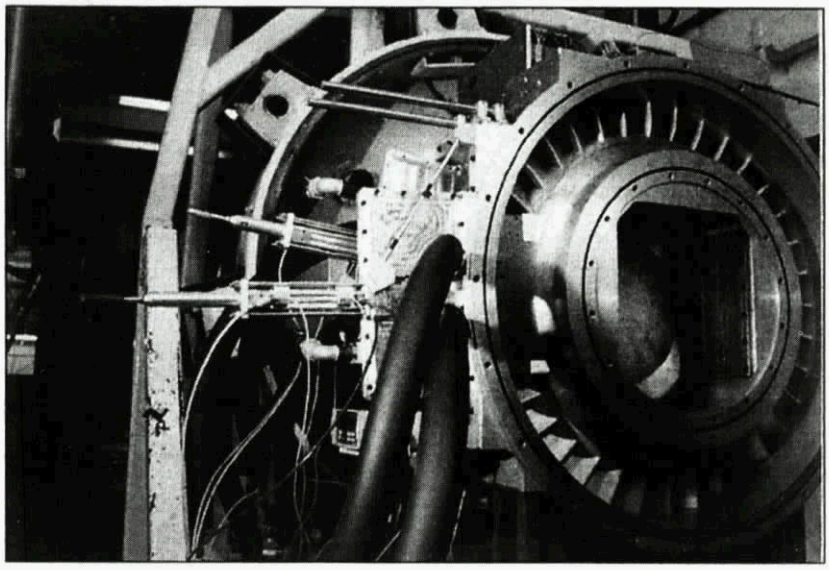

**Figure 4: Photograph showing the shutters deployed in the CHTT**

As mentioned above, the enclosure is preheated. This is achieved by using a system of pipework which re-circulates hot air. There are four air inlets to the cassette through which the air passes into twelve internal passages within the shutter plates. By introducing the hot air into the enclosure in this manner the shutter plates themselves are preheated, eliminating the possibility of disturbing the temperature uniformity of the NGV surfaces by the proximity of a cold surface.

The coolant is introduced into the cassette from a separate feed system which has itself been preheated. The coolant flow begins as the tunnel operation starts and passes through the NGV coolant holes with the shutters in place. The coolant operates at a constant total temperature equal to the initial temperature of the NGV, which eliminates any internal heat transfer and also helps maintain the surface uniformity prior to the shutters opening.

# 4 EXPERIMENTAL PROCEDURE

## 4.1 LIQUID CRYSTALS AND IMAGE PROCESSING

As discussed above, the test NGV is preheated to a known initial temperature (at all depths) and the colour response viewed by cameras. Two wide-band crystals have been employed, active over a 40 C range. The RGB histories are translated into temperature histories via *in situ* calibration which is discussed in the next section.

To observe the colour changes during the experiment, three miniature CCD cameras are placed inside the tunnel. Two are located upstream to view the pressure surface and leading edge, and a third is located downstream and observes the suction surface via a mirror mounted on a sting designed to minimise aerodynamic disturbances. The head diameter of the cameras is 17.4 mm and each body is 60 mm long. The upstream cameras are staggered considerably to avoid shedding a wake into the passage under study. The lighting for the enclosure comes from both inside and outside of the cascade, the latter through the transparent perspex outer endwall. This lighting is supplied by a series of 50

W miniature Halogen lamps. Only data from one of the upstream cameras was used in the results presented in this paper.

The RGB images are stored digitally, rather than the conventional method of recording the images onto video tapes which results in a loss of image quality. A frame-grabber card is used together with a PC holding 192 MBytes of RAM. This system is capable of recording images at 25 frames per second for 5 seconds. The RGB histories at any pixel location within view can then be extracted.

A typical image of the pressure surface and shower-head region, recorded with the system during an experiment, is shown in figure 5. The outer and inner casings have been identified. The trailing edge of the NGV is not visible in this view. The cooling footprints downstream of many of the film cooling holes are clearly visible. The view from the camera monitoring the leading edge gives more detail in the shower-head region. Close-up lenses are available to gain more detail when required.

The RGB history at a single pixel, converted to hue (Gonzalez and Woods, 1993), is shown in figure 6. Here the RGB has been scaled between 0 and 1 and the shutter operating times are marked. In this example only the first 20 C band crystal has been activated. As the camera view and lighting angles are identical to those during calibration, these RGB values can be converted to temperature. Any of the three colours can be used for this conversion and that which is located at its most sensitive colour-temperature response is usually chosen. It should be noted that the colour response can not be monitored during the first (approximately) 0.25 seconds as the shutters are opening and the camera iris takes a short time to react to the resultant change in lighting. Consequently part of the surface temperature history is not obtained.

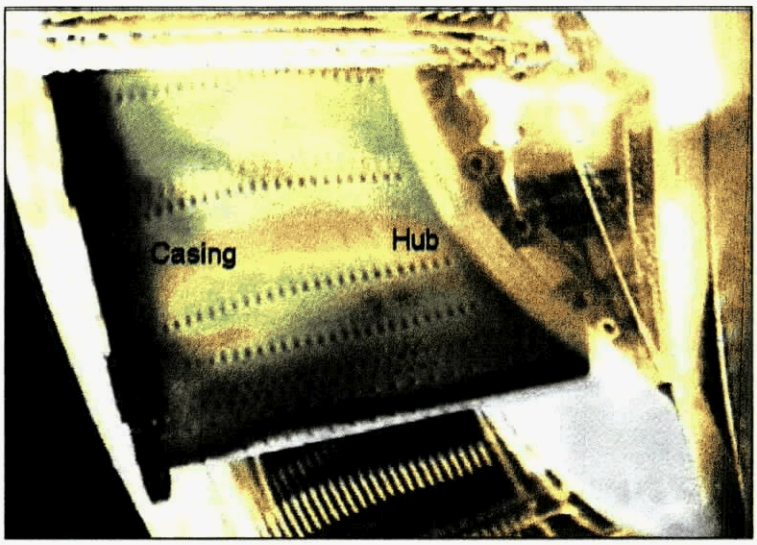


**Figure 5: Liquid crystal colour image during the test**

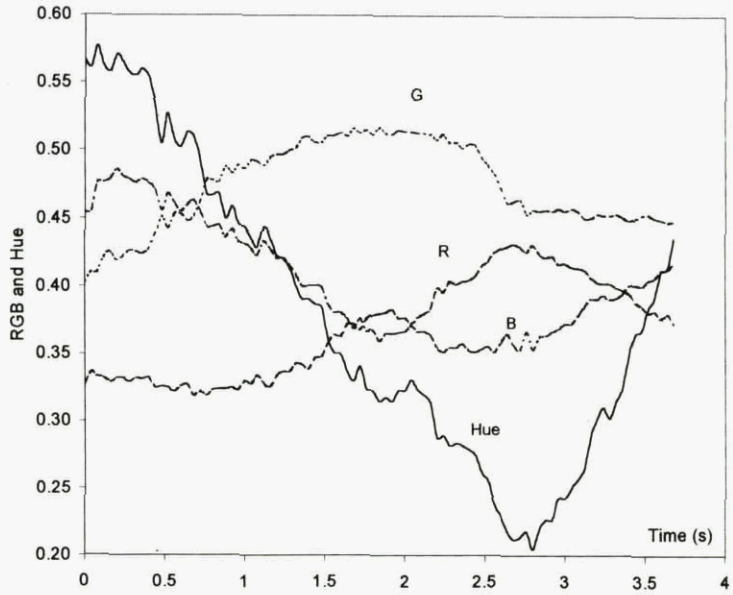


**Figure 6: RGB and Hue versus time at a pixel**

## 4.2 IN SITU TLC CALIBRATION

The thermal response of the RGB signals from wide-band crystals are sensitive to both the lighting and camera viewing angles, which makes calibration difficult. The calibration of narrow-band crystals is much more straightforward as the active thermal range is very small. Different parts of the NGV subtend a range of angles at the camera. An accurate calibration was only possible if it was conducted *in situ* and under identical lighting conditions to that which will occur during experiment.

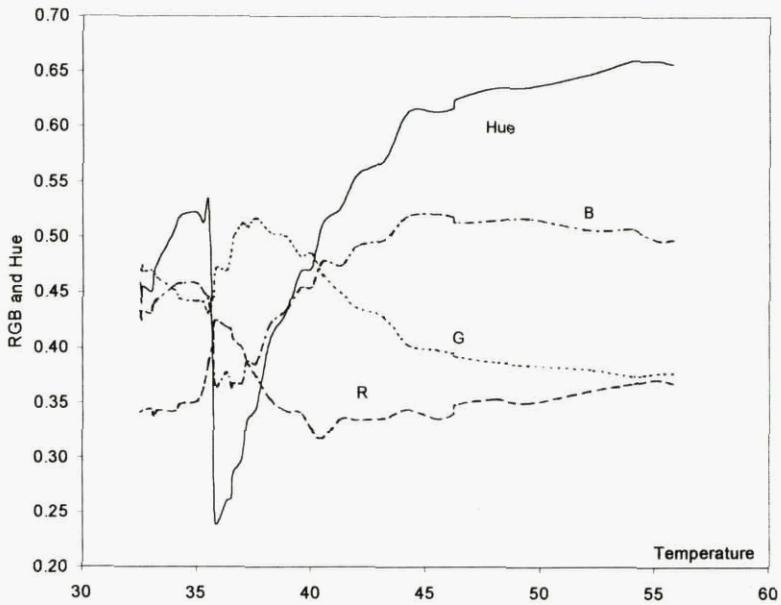


**Figure 7: Surface temperature versus Hue for a single pixel**

Such a calibration was performed by heating the NGV within the heat transfer cassette enclosure to a uniform temperature, monitored by thermocouples around the surface. With the shutters open, images were recorded and the RGB matched carefully to these temperatures. As the TLC response is sensitive to viewing angle, each pixel (or area of pixels) requires its own individual calibration for the camera used. A calibration is performed before each experiment to eliminate any degradation of RGB response as the crystals age. A typical calibration of $T_s$ versus hue (for the location corresponding to the data for figure 6 is shown in figure 7.

## 4.3 TEMPERATURE HISTORIES

Surface temperature history measurements around the central NGV within the cassette, coolant temperatures within the forward and rear cavities of the NGV and the total temperature of the mainstream are shown in figure 8. These have been recorded using thermocouples. The following times are marked: when the tunnel begins operation, when the coolant is introduced, and when the shutters begin and end their travel. The temperature on the NGV surface, up to the point where the shutters are opened, is seen to remain constant at its initial value near 55 C and is not influenced by the hot 'coolant' or cold mainstream air passing through the 32 passages outside the cassette. The total temperature of the mainstream has two initial peaks associated with compression heating of the gas upstream of the test section. The shutters are opened once this mainstream temperature has stabilised, and over the 3 seconds course of the experiment this total temperature decreases by less than 1 C. The NGV surface temperature is observed to fall rapidly once the shutters have opened.

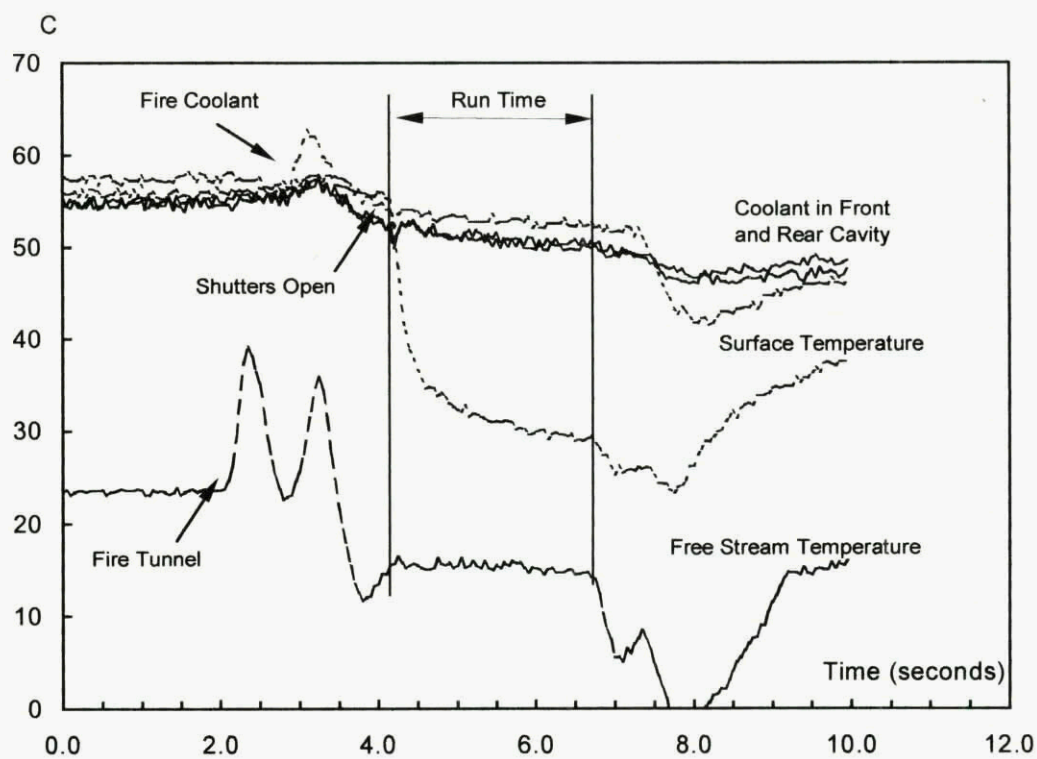


**Figure 8: Coolant cavity and NGV surface temperature**

A typical temperature history obtained using the TLC is shown in figure 9. The initial temperature is accurately known but the first short segment of the data is missing as the iris of the camera requires a short time to adjust to the changes in lighting when the shutters open. A curve fit through the data of the form of equation (4), obtained by regression, is also shown. The heat transfer coefficient around the NGV was calculated from the fitted curve. The curve fits appropriate to a step-change response matched the data well.

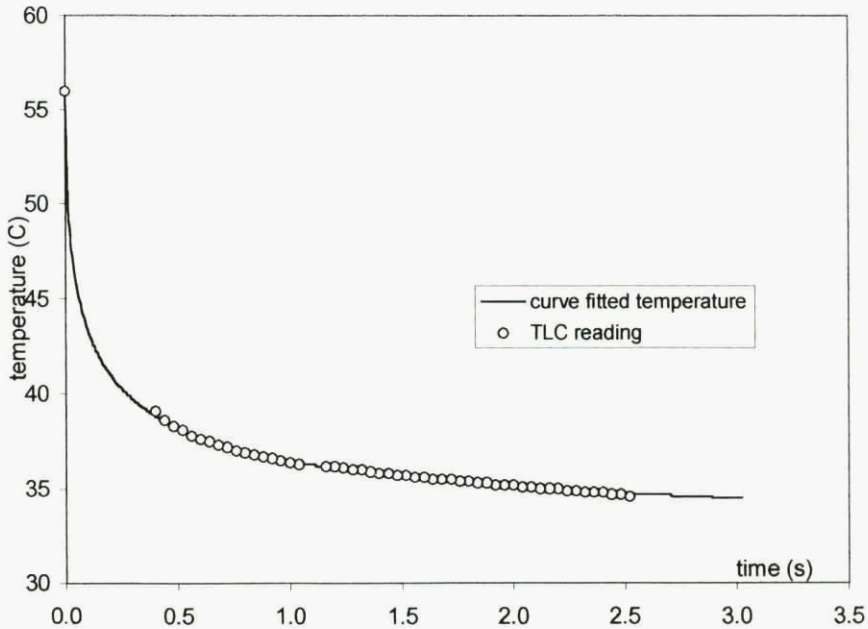


**Figure 9: Temperature history from TLC and the fitted temperature curve**

## *5 EXPERIMENTAL RESULTS AND DISCUSSION*

Figure 10 illustrates the isentropic Mach number distribution measured around the midspan on the pressure and suction aerofoil surfaces with film cooling in operation. Similar data is available at 10 and 90% span. The local mainstream recovery temperature $T_r$ is calculated from an interpolation of these Mach numbers, the upstream total temperature and a recovery factor based on the Prandtl number to the third power.

The cooling effectiveness is plotted against fraction of surface distance along the midspan streamline in figure 11. These measurements have been averaged over areas which cover the width of three film cooling holes and thus give a spanwise average effectiveness. The maximum resolution for the image processing system and from the camera position used in the experiment was over 50,000 points. The data in figure 11 has been averaged over a region of 120 square pixels. The vertical lines in the figure (and in those figure following) are the positions of the film cooling holes. The effectiveness is seen to reach local peaks downstream of each film cooling row, though not necessarily immediately downstream, indicating that films may be lifting off the surface. Liquid crystal data is only presented on the pressure surface between rows 2 and 7 (see figure 2). In future, data will be available from the leading edge and downstream camera views and the entire surface will be covered.

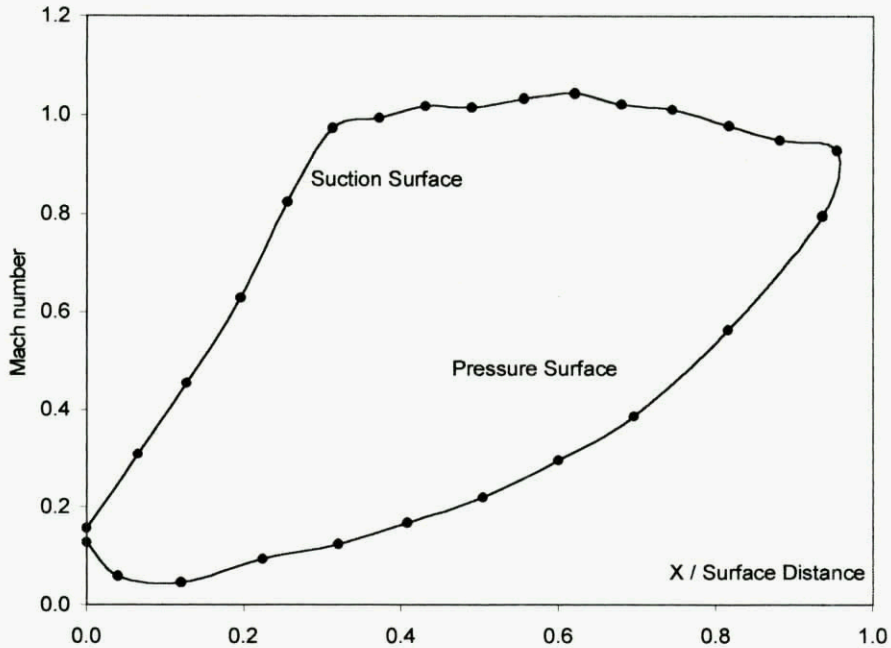


**Figure 10: Isentropic Mach number around midspan**

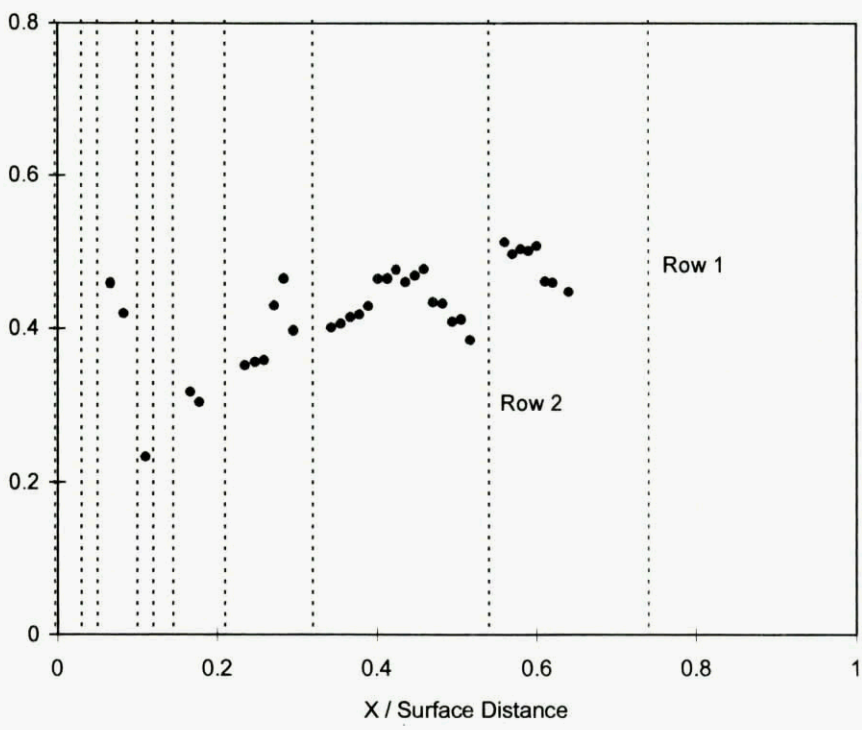


**Figure 11: Pressure surface cooling effectiveness**

The heat transfer coefficient around midspan is shown in figure 12. Here the heat transfer coefficients for the solid blade (i.e., no film cooling) are plotted for comparison (Martinez-Botas et al. 1995). The ejection of coolant into the turbulent boundary layer generally

increases the heat transfer coefficient with some significant local increases in regions downstream of the cooling rows, as would be expected. The heat transfer coefficient is seen to obtain maximum between the film cooling rows at positions which coincide with those of maximum effectiveness. Again this indicates that some of the films may be lifting off the surface and impinging downstream of the rows. Away from the influence of the film cooling, the heat transfer coefficients fall to those levels obtained without film cooling.

To illustrate the detail available from the TLC data, figure 13 show the heat transfer coefficients and film cooling effectiveness span-wise across five holes, rather than the average across this area. The detailed area (50 pixels in width) is marked in the figure. Figures 13 show clearly the peaks along streamlines aligned with the centre-line of the holes and the regions of low effectiveness and heat transfer coefficient between them. It is notable that the variations in peak height are similar in the plot. These spanwise variations in effectiveness are important to the engine designer since they provide information about the magnitude of local metal temperature gradients on the NGV, ultimately leading to calculations of thermal stresses. Further analysis will provide detailed data everywhere on the wetted surface in view of the camera.

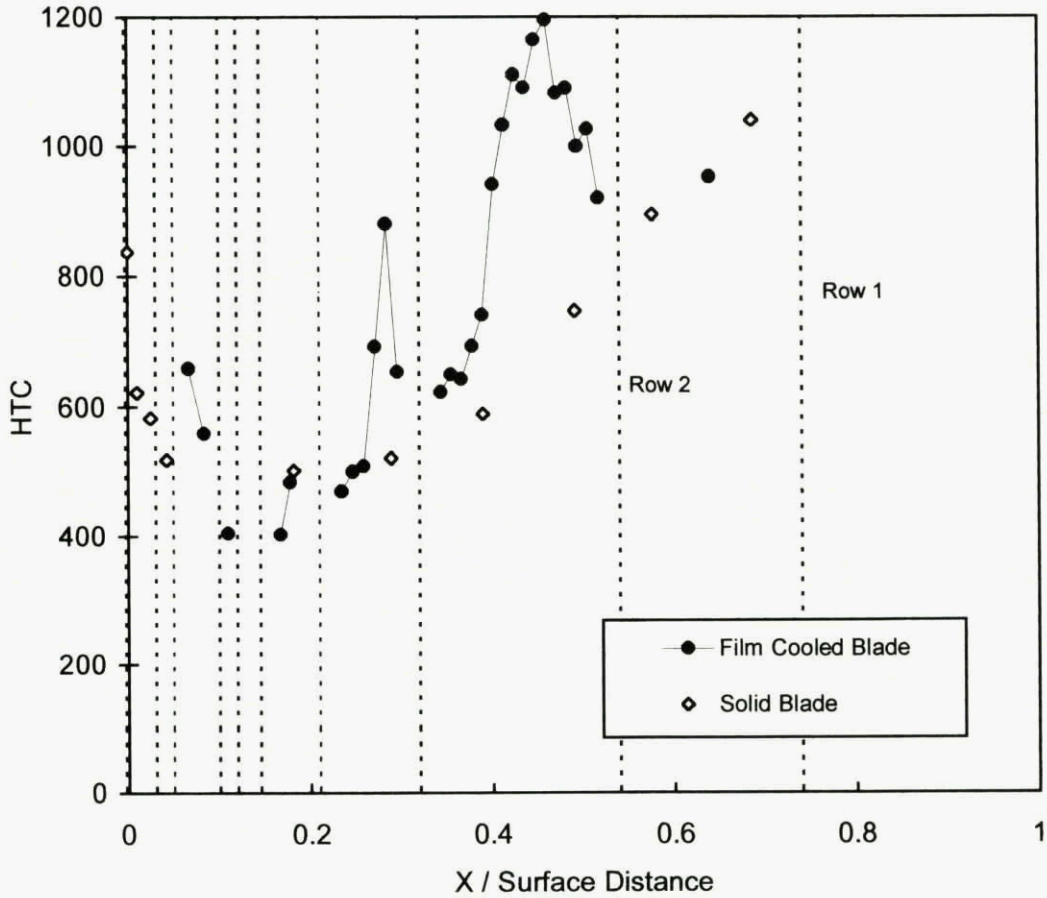


**Figure 12: Heat Transfer Coefficient ($W/m^2K$) along midspan on Pressure Surface**

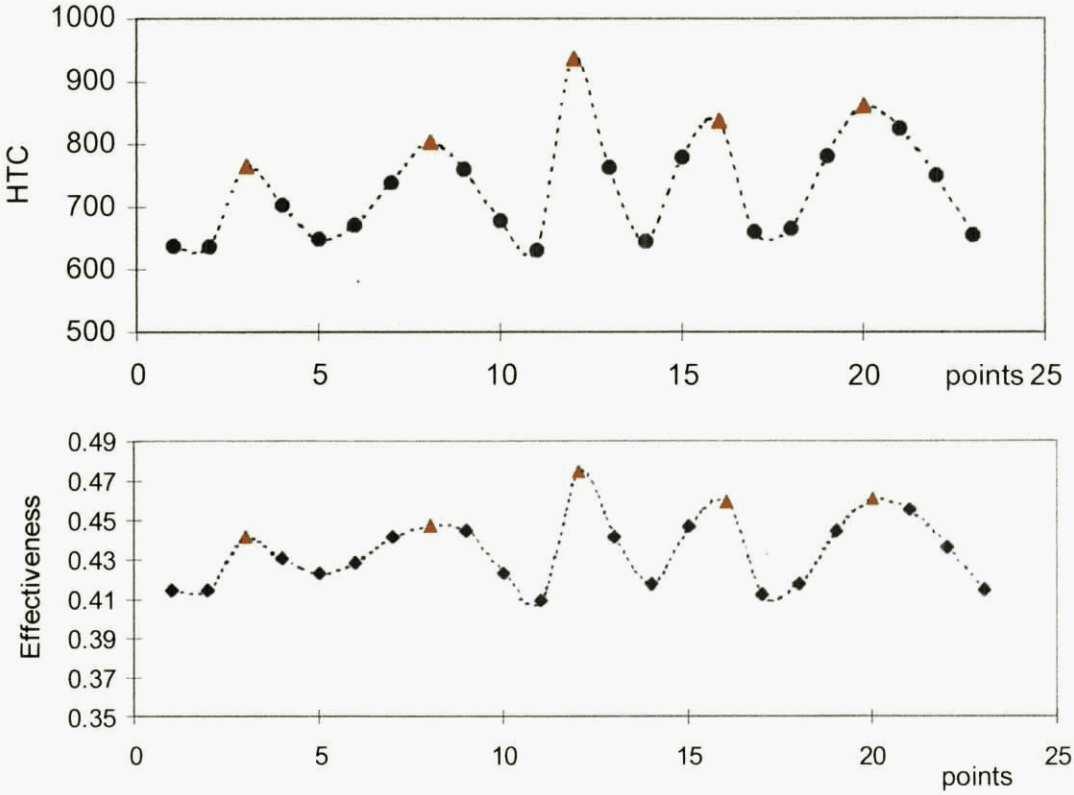


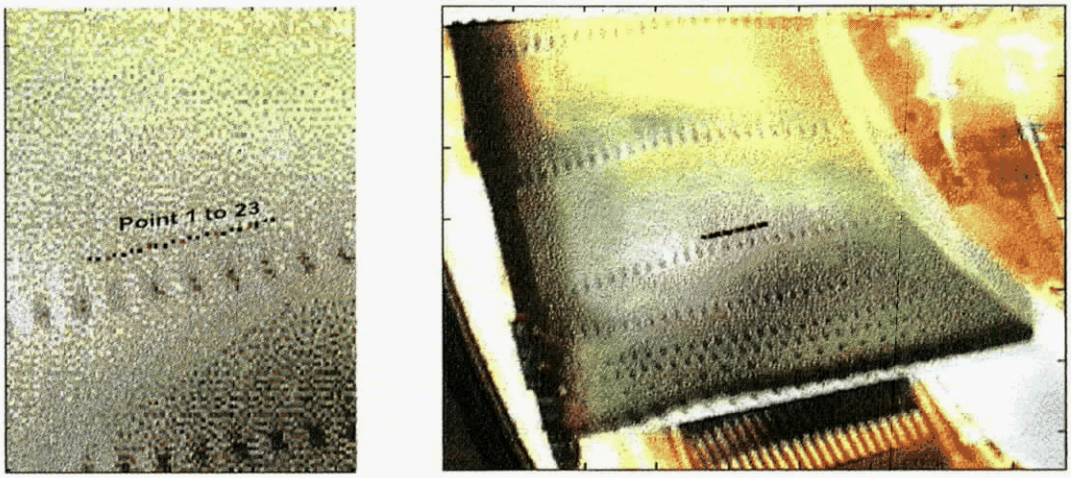


**Figure 13: Heat transfer coefficient (HTC) and effectiveness along a spanwise line**

## 6 CONCLUSIONS

The transient liquid crystal technique has been used to measure the heat transfer coefficient and cooling effectiveness over the midspan of a heavily film cooled nozzle guide vane. The measurements were performed in a transonic annular cascade at engine-representative Mach and Reynolds numbers. The RGB components of the temperature response of two wide-band crystals have been recorded directly onto computer without the use of video tape, and matched to a surface temperature from an *in situ* calibration at each pixel location on the NGV. A regression method, based on curve fits appropriate for a step-change boundary condition, has been used to obtain the data from the measured surface temperature histories. The data compares well with measurements made without film cooling present. Data is presented along the midspan of the pressure surface and some examples of the detailed data off the NGV midspan are presented, demonstrating the powerful advantage of this measurement technique over thin film gauges.

## 7 ACKNOWLEDGEMENTS

This work was funded by Rolls Royce plc, the Defence Research Agency, MoD and DTI. The authors are grateful for the assistance of D.A. Rowbury, D.R.H. Gillespie and P.T. Ireland.

## 8 REFERENCES

Butler, R.J. and Baugh, J.W., 1996, *The Effect of the Thermal Boundary Condition on Transient Method Heat Transfer Measurements on a Flat Plate With a Laminar Boundary Layer,* Journal of Heat Transfer, (118), 831-837.

Buttsworth, D.R. and Jones, T.V., 1997, *Radial Conduction Effects in Transient Heat Transfer Experiments,* The Aeronautical Journal, (101), 1005, pp 209-212.

Cho, H.H. and Goldstein, R.J., 1995, *Heat (Mass) Transfer and Film Cooling Effectiveness with Injection through Discrete Holes: Part II - On the Exposed Surface*, ASME Journal of Turbomachinery, **(117)**, pp 451-460

Drost, U., Bolcs, A. and Hoffs, A., 1997, *Utilization of the transient liquid crystal for film cooling effectiveness and heat transfer investigations on a flat plate and a turbine airfoil*, ASME 97-GT-26

Eckert, E.R.G., Hartnett, J.P. and Birkebak, R., 1957, *Simplified Equations for Calculating Local and Total Heat Flux to Nonisothermal Surfaces*, Journal of Aeronautical Sciences, **(24)**, No.7, pp 549-550.

Friedrichs, S., Hodson, H.P. and Dawes, W.N., 1995, *Distribution of Film-Cooling Effectiveness on a Turbine Endwall Measured Using the Ammonia and Diazo Technique*, ASME Paper 95-GT-1

Goldstein, R.J., 1971, *Film Cooling*, Advances in Heat Transfer, **(7)**, pp 321-379.

Hartnett, J.P., 1985, *Mass Transfer Cooling*, Chapter 1 of *Handbook of Heat Transfer Applications*, McGraw Hill.

Gonzalez, R.C. and Woods, R.E., *Digital Image Processing*, Addison-Wesley 1993.

Haslinger, W. and Hennecke, D.K., 1996, *The Ammonia and Diazo Technique with $CO_2$ - Calibration for Highly Resolving and Accurate Measurement of Adiabatic Film Cooling Effectiveness with Application to a Row of Holes*, ASME Paper 96-GT-438.

Hay, N., Lampard, D. and Saluja, C.L., 1984, *Effects of Cooling Films on the Heat Transfer Coefficient on a Flat Plate with Zero Mainstream Pressure Gradient*, ASME paper 84-GT-40

Ireland, P.T. and Jones, T.V., 1987, The Response Time of a Surface Thermometer Employing Encapsulated Thermochromic Liquid Crystals, Journal of Physics E, Vol 20, pp 1195-1199

Ireland, P.T., Wang, Z.W. and Jones T.V., 1993, *Liquid Crystal Heat Transfer Measurements,* von Karman Institute for Fluid Dynamics 1992-1993 Lecture Series.

Jones, T.V., 1991, *Definition of Heat Transfer Coefficient in the Turbine Situation*, Symposium in Turbomachinery: Latest Developments in a Changing Scene, IMechE Paper C423/046.

Jones, T.V., Oldfield, M.L.G., Ainsworth, R.W. and Arts, T., 1993, *Transient-Cascade Testing*, Chapter 5 of Advanced Methods for Cascade Testing, AGARD AG-328.

Kercher, D.M., 1996, *Film Cooling Bibliography 1946-1996*, GE Aircraft publication.

Martinez-Botas, R.F., Main, A.J., Lock, G.D. and Jones, T.V., 1993, *A Cold Heat Transfer Tunnel for Gas Turbine Research in an Annular Cascade*, ASME Paper 93-GT-248.

Martinez-Botas, R.F., Lock, G.D. and Jones, T.V., 1995, *Heat Transfer Measurements in an Annular Cascade of Transonic Gas Turbine Blades Using the Transient Liquid Crystal Technique,* Journal of Turbomachinery (117), 3, pp 425-431.

Richter, J., Jung K. and Hennecke, 1996, *An Investigation of Heat Transfer by Leading Edge Film Cooling Applying the Naphalene Sublimation Technique*, ASME Paper 96-GT-463.

Schultz, D.L., and Jones, T.V., 1973, *Heat Transfer Measurements in Short-Duration Hypersonic Facilities*, AGARD AG-165.

Teekaram, H.J.A., Forth, C.J.P. and Jones, T.V., 1989, *The Use of Foreign Gas to Simulate the Effects of Density in Film Cooling*, Journal of Turbomachinery, **(111)**, pp. 57-62.

Paper 20
Author: Guo et al

Q: Leboeuf

The RGB calibration curve seems to give two values of temperature for one value of RGB. How do you distinguish between the two temperatures ?

A: Two wide-band liquid crystals were used in the experiment. The first was active between 55 to 35C, and the second between 40 to 20C. In the experiments the test NGVs were preheated to a temperature at the top of the higher band. The gas temperature was always ambient and hence the NGV surface always cooled during the short duration of the experiment. This cooling was recorded at 25frames/second and hence the cooling could be followed and it was clear which liquid crystal band was active at any time.

Q: Weigand

How accurate is your temperature measurement using liquid crystals ?

A: The double wide-band liquid crystals were calibrated in situ in the heat transfer cassette under identical lighting and camera viewing angles to those used during the experiment. The recorded hue at each pixel location was matched to the nearly uniform surface temperature (in steady state) which was obtained from 10 surface mounted thermocouples around the NGV. The calibration was conducted immediately before and after the test. Such a calibration reduces uncertainty associated with variations in the recorded hue with viewing the lighting angles. Thus the error in temperature arises from the uncertainty in the calibration of hue versus temperature and also the accuracy with which the hue was determined in the test. The former was approximately +0.1 C and the later +0.4C giving an estimated error of +0.5 C.

# Surface Temperature Measurement In Turbines

*C Bird, J E Mutton, R Shepherd, M D W Smith and H M L Watson*

*Rolls-Royce Commercial Aero Engines Ltd, P O Box 31, Derby, DE24 8BJ, UK*

## 1 SUMMARY

This paper reports on some of the turbine surface temperature measurement techniques and instrumentation currently in use and under development in Rolls-Royce. Firstly, thermal paints are reviewed highlighting the development of new computer aided analysis and interpretation techniques. Thin film thermocouples are described with their applicability to gas turbine engine components, especially those with thin skins. Finally, the novel technique of photoluminescence thermometry using so-called "thermographic phosphors" is described. Examples of measurements on static engine components and developments for measurements on rotating turbine blades are given.

## 2 INTRODUCTION

Future gas turbine engines will have higher component and gas temperatures in order to increase their thermal efficiencies. In order to achieve this, new designs and materials including ceramics and thermal barrier coated components will be increasingly employed.

Accurate temperature measurement of these components is needed in order to validate the computer models used for their design and to determine the expected life of these components during operation. Accurate models are a prerequisite for cost effective engine development programmes helping to ensure that new designs conform to the ever more stringent safety and environmental regulations.

Currently, temperatures of components in gas turbine engines are measured in a variety of ways. Thermal paints give a "one shot" temperature map of most of the required engine components at one operating condition. However, at present the interpretation of the results can take a long time. Conventional, surface mounted thermocouples are approaching their limit of serviceability at the higher operating temperatures, especially on high speed rotating components, and bonding to the new materials can prove problematic. Additionally, the signal lead-outs on rotating components can be unreliable and expensive to install. Radiation pyrometry can be used in gas turbine engines, but accuracy can be severely compromised, for instance by the lack of knowledge of the component emissivity and reflected radiation, especially from the combustor.

Novel instrumentation and analysis techniques are being developed in order to provide accurate and cost effective component temperatures. These techniques include:

- the automation of the analysis of thermal paints;
- the replacement of conventional surface mounted thermocouples with thin-film devices offering the potential for lower aerodynamic drag and high bonding reliability; and
- thermographic phosphors which have the potential to provide "non-contact", accurate temperature measurement on the new materials in close proximity to the combustor without errors resulting from reflected radiation.

## 3 THERMAL PAINTS

### 3.1 Background

Engine development at Rolls-Royce has, since the late 1950's, involved extensive use of thermal paints to establish temperature profiles of combustion and turbine components.

Early techniques involved the use of proprietary paints obtained from Thermindex in Great Britain, Faber Castel in Germany and the Temple Corporation in America. However, most of the paints used only gave a single temperature indication. Therefore, combinations of paints had to be used to obtain temperature profiles e.g. five different temperature paints on five turbine blades of the same standard to yield a composite result with five temperatures.

Meaningful information could therefore be obtained from rotating components but a large sample was required to generate the results. Problems with paint adhesion to the pressure surfaces of blades were also experienced. However, this approach could not be used on static components such as combustor hardware or nozzle guide vanes where a multi-change thermal paint was required to provide full profile information.

*Paper presented at an AGARD PEP Symposium on "Advanced Non-Intrusive Instrumentation for Propulsion Engines", held in Brussels, Belgium, 20-24 October 1997, and published in CP-598.*

In the mid 1960's, Rolls-Royce commenced the development of a range of multi-change paints to meet the growing needs of the RB211 development programme. All of the early HP nozzle guide vane and HP turbine blade cooling programmes relied heavily on the information gleaned from the first two multi-change high temperature thermal paints, TP5 and TP6. These early tests were often marred by the loss of paint due to erosion on the leading edges and pressure surfaces of vanes and blades; the blades being especially affected.

Over the years, development has continuously taken place to improve the range, quality and strength of the paints. On a 3 minute thermal paint engine test, a 100% paint coverage can now be confidently expected.

### 3.2 Current Use

Rolls-Royce uses several types of paint and the current standard range is shown in Table 3. The paints are normally calibrated for 3, 5, 10, 30 and 60 minutes using painted coupons at 10°C increments. A calibration is illustrated for paint TP8 in Table 1. Some examples of the use of the different thermal paints are given in Table 2.

| | | Calibration Time (Mins) | | | | | | |
|---|---|---|---|---|---|---|---|---|
| Code | Colour | 1 | 2 | 3 | 5 | 10 | 30 | 60 |
| N | Light Mauve | 440 | 440 | 430 | 430 | 420 | 410 | 400 |
| T | Fawn | 550 | 540 | 530 | 530 | 520 | 500 | 480 |
| P | Blue | 640 | 620 | 610 | 610 | 600 | 570 | 560 |
| G | White | 790 | 780 | 770 | 760 | 750 | 740 | 720 |
| M | Midnight Blue | 880 | 870 | 860 | 850 | 840 | 820 | 810 |
| Y | Matt Black | 940 | 920 | 910 | 900 | 880 | 860 | 840 |
| R | Black Glaze | 950 | 930 | 930 | 920 | 910 | 890 | 870 |

**Table 1 - Calibration of Paint TP8**

(All calibration data are in °C. Temperatures quoted for 1 and 2 minutes duration are based on a computer curve fit from actual recorded values).

| PAINT TYPE | USE | LIMITATIONS |
|---|---|---|
| TP5<br>TP 6<br>TP 11 | Nozzle Guide Vanes, Turbine Blades, Combustor (Internal), Discharge Nozzles, Burners, Variable Area Nozzles. | None on a short dedicated test. |
| TP12 | Combustor (Internal), Discharge Nozzles, Burners, Vanes and Blades and limited running conditions. | Prone to flaking |
| TP8 | Turbine Blades, Casings, Support Structures, Jet Pipes, Thrust Reverser Units | Extended running leads to bleaching. |
| TP9<br>TP10 | Combustor (External), Discharge Nozzles, Discs, Blade Shanks, Gas Leakage Detection | Subject to detrimental effects from gas contamination, can cause metallurgical interactions (Ti specifically) |
| Single-Change | Casings, Supports, Discs, Tail Bearing Housing, Bolts, Accessories, Low Temperature Areas, Thrust Reverser Units | Time consuming to interpret, less accurate in providing an overall pictorial result. |

**Table 2 - Examples of Use of Temperature Indicating Paints**

| Paint Type | Range (3 mins) | No of Change Points |
|---|---|---|
| TP5 | 510-1110°C | 7 |
| TP6 | 550-1180°C | 7 |
| TP8 | 430-930°C | 7 |
| TP9* | 470-1170°C | 9 |
| TP10* | 280-1050°C | 10 |
| TP11 | 480-1020°C | 8 |
| TP12 | 530-1090°C | 7 |
| Single Change | 130-580°C | 1 |

* Not suitable for combustion gas environments.

**Table 3 - Current Range of Temperature Indicating Paints**

The main attraction of using thermal paints is the ability to obtain a global temperature profile of the component under test. Achieving this level of detail using more conventional techniques would be extremely difficult.

The main limitation is associated with the effect of running times on the calibration accuracy and overall quality of the paints. To achieve good results a dedicated test must be carried out and the time at maximum condition be limited to 3 or 5 minutes.

Because of the high costs associated with an engine disassembly required for a dedicated thermal paint test, development of boroscope interpretation of thermal paints is currently being carried out. However, the quality of information obtained from a dedicated thermal paint test is such that it has always been a firm policy to continue with this dedicated testing in the authors' Company.

Increased engine temperatures and the use of non-metallic components have necessitated the development of paints with higher temperature ranges. The current development paints have a temperature capability of around 1380°C and high temperature paint development work continues.

### 3.3 Digital And Automated Analysis Of Thermal Paints

#### 3.3.1 Background

The widespread use of thermal paints in Rolls-Royce with large sections of the engine painted in dedicated engine runs leads to large transient workloads. Thermal paints provide data from large surface areas of the engine. This means that the analysis and interpretation process is very labour intensive with consequent long turn around times. In addition, the manually interpreted data is not in a form which is easy to transfer to the 3D temperature/structure analysis packages currently used. A system that automates part or all of the process would drastically reduce interpretation time and speed manipulation of the temperature data ready for input into thermal models.

Paints appear coloured[1,2] by selectively scattering different wavelengths of the light incident on the surface. This is illustrated in Figure 1.

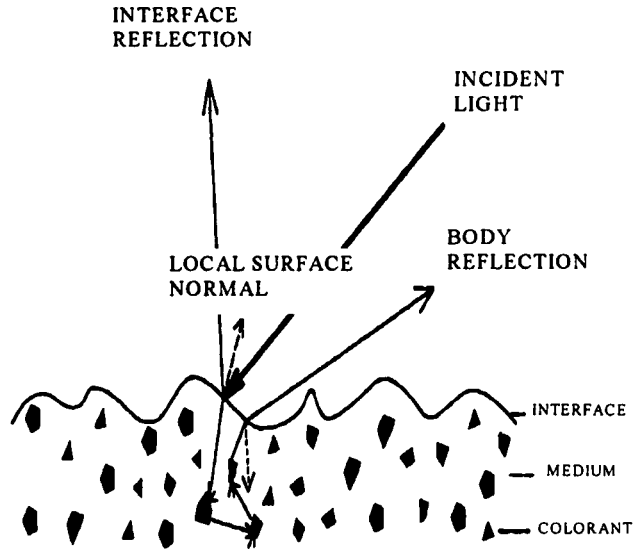


**Figure 1 - Light reflection of pigmented dielectric materials**

In this model the pigment containing particles are embedded in the surrounding medium. These particles are the bodies responsible for the characteristic colour of the paint. The surrounding medium is considered colourless and only contributes to the appearance of the surface by dielectric reflection. This reflection is governed by the refractive indices of the air and the dielectric medium. In general, these refractive indices are not strongly dependant on the wavelength of the light, so the surface reflection will have the same colour as the incident light, generally white. The colorant particles do not contribute to this as they are evenly distributed in the media and not present on the surface in significant quantities. This surface reflection is unwanted as it contains no information on the paint colour. Indeed, for some incident angles when a paint glaze occurs, this reflection can become dominant for surface illumination and viewing angles that conform to the reflection laws.

At present, analysis techniques rely on the manual interpretation of paint colour. This will be strongly influenced by the characteristics of the human eye and visual interpretation of the image by the brain. In general this is strongly biased towards edge detection and difference detection. This is because the human eye is capable of detecting subtle colour changes when the colours are in close proximity, but very bad at absolute colour perception. Thus thermal paints have "change points" where the colour/luminance value changes rapidly. This yields an isotherm which at present is marked out manually.

The present work on automating the thermal paint analysis process relies on either:

I. Reading in isotherms from components that have been marked out manually.

II. The direct interpretation of thermal paint colours into temperatures.

Method I. still requires the manual identification of each isotherm line with a temperature. Method II. is more challenging, but has greater rewards. The current approaches to this problem of direct interpretation differ from the way the human/manual interpretation method operates. These have relied on interpreting the absolute colour values of the surface and, for a specific camera, red (R), green (G) and blue (B) values are generated. To maintain consistency between images, control and compensation of the illumination are now required.

It is interesting to note that thermal paints have developed to have sharp colour-value change points, which may not be necessary for automatic digital interpretation of thermal paints. The digital interpretation technique does not rely on sharp colour-value change points and so paints could be developed to exploit this.

### 3.3.2 Illumination

Both analysis methods require control or compensation of illumination and some examples are shown in Figure 2. Some methods rely on light boxes, in which the 3D component is located, to provide a uniform illumination ( Figure 2 (a)). Another approach involves viewing the surface at a normal angle with the light source illuminating this area at 45° (Figure 2 (b)). For cylindrical type components, for example turbine blades and combustors, the cross section is relatively constant. The imaging can be performed using a line scan camera. However, complex 3D shapes would require data to be recorded normal to every point on the components' surfaces. A further approach is to provide consistent known illumination which is not necessarily uniform. This should reduce shadows to a level where compensation can be applied (Figure 2 (c)).

### 3.3.3 Direct Thermal Paint Colour Interpretation

The 'digital' interpretation of thermal paints must contend with the above difficulties, but the image consistency is much more critical. Calibration cards with reference white and dark patches are required to normalise acquired images to a known standard and to correct for colour casts.

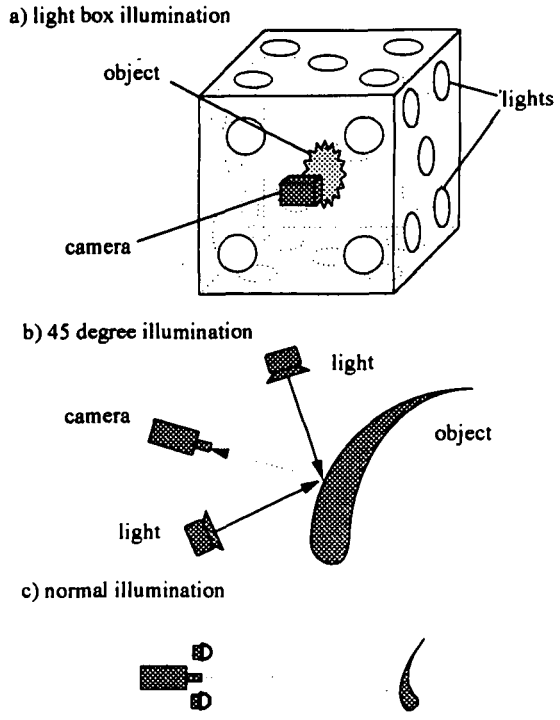


Schemes a) and c) are susceptible to surface reflections or 'highlight' type reflections.

**Figure 2 - Illumination Schemes**

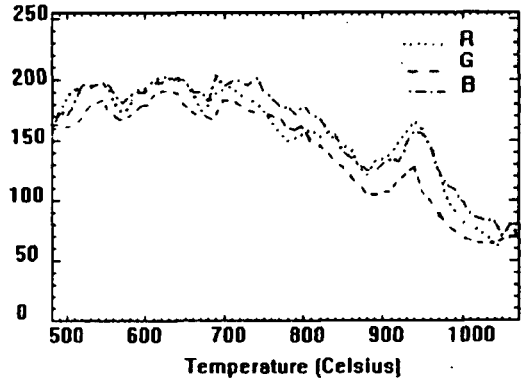


**Figure 3 - TP12 RGB Colour Values with temperature**

The colour curves of a thermal paint are shown in Figure 3. It can be seen that these curves are complex and multivalued which can lead to ambiguities. This poses difficulties in assigning temperatures to sections of those curves as more data must be obtained for each condition to provide a sufficiently accurate digital calibration of the paint. Note that thermal paints are affected by pressure and gas composition, especially combustion gases.

The Rolls-Royce Thermal Paint Laboratory is pursuing a programme to develop this technology and has already developed a Thermal Paint Analysis System which uses a 2D approximation and neglects illumination corrections. The capabilities of the system are:

- Normalisation and initial processing of images.
- Colour data acquisition against temperature for:
  - room temperature (atmospheric) calibration coupons
  - engine run components with known temperature distributions
- The manipulation of this data to give colour versus temperature calibration files for each condition.
- The interpretation of normalised images with this calibration file to give a temperature array/image.

An example of a painted turbine blade heated in the laboratory is shown in Figure 4.

**Figure 4 - Digital Interpreted Engine Component.**

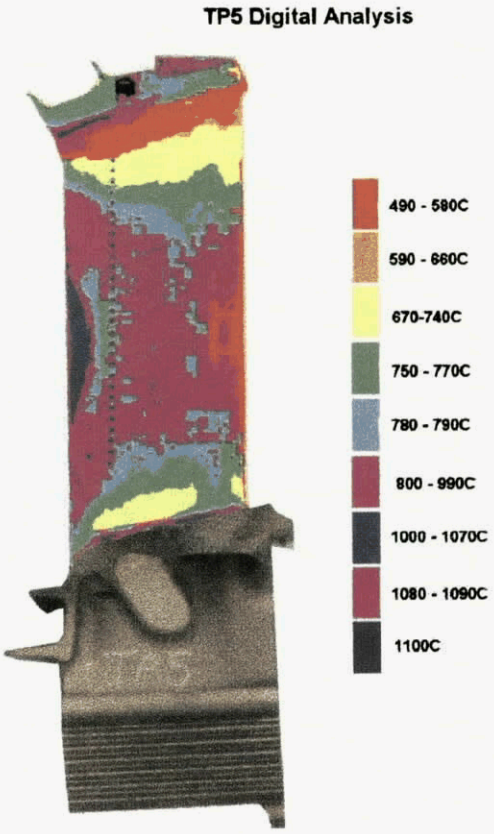


### 3.3.4 Future Work

Future Work will extend this technique to produce a genuine 3D system that establishes a mapping between the 2D colour image and the 3D CADDS image. This mapping will allow for different views of the component and incorporate correction for the illumination.

The relationship between paint colours and pressure/atmosphere conditions will be investigated.

To take advantage of the differences in analysis of this system over the manual method a "digital thermal paint" is also being developed, using the lessons learnt from the 2D work.

## 4 COMPONENT SURFACE TEMPERATURE MEASUREMENT USING THIN FILM SENSORS

### 4.1 Background

During engine testing it has been common practice to measure the component temperature using surface mounted thermocouples to validate advanced combustion and turbine cooling designs and thermal barrier coatings.

On air washed surfaces the conventional method would involve machining a groove in the component to bury a small diameter NiCr/NiAl (Type-K) mineral insulated thermocouple cable. The cable would be $\phi$0,3 mm and the slot 0,45 mm deep and wide. The slot would be filled with a Ni based vacuum furnace braze if possible or with a NiAl alloy flame spray. The excess would then be ground off to produce a smooth surface finish to cause minimum disturbance to the air flow.

However, the grooves cause problems with the stressing of the component and alter the heat transfer through the component. This limits the number and locations where sensors could be installed. The temperature measurement may be inaccurate since the measuring point is below the component surface and surrounded by a large thermal mass. Several research blade designs have also had thin section walls where the application of these thermocouples would be impossible.

### 4.2 Thin Film Development

An alternative technique is to use a physical vapour deposited thin film sensor. Previous work conducted for Rolls-Royce has demonstrated thin film platinum

resistance grids up to 800°C. Also, a limited amount of work on Pt-Rh/Pt thermocouples to 1200°C has been performed. This was on a thin skinned component where the use of conventional wire thermocouples was not possible. Figure 5 shows a thin film sensor array deposited on a thin skinned nozzle guide vane.

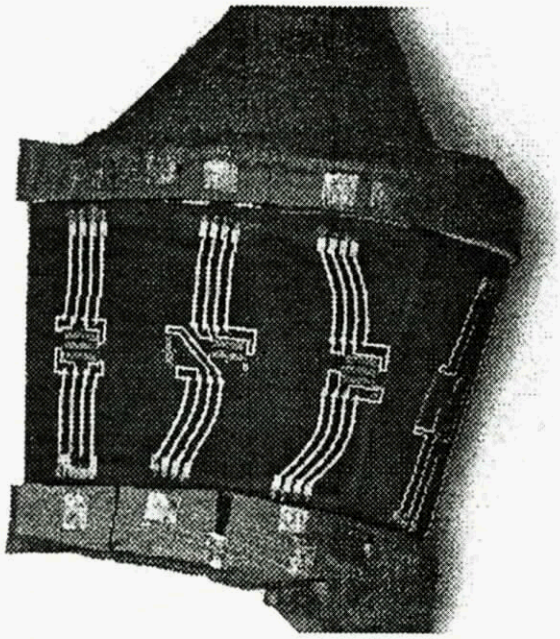

**Figure 5: Pt resistance temperature sensor array on thin skinned nozzle guide vane**

A further step was taken in a Brite Euram funded European Collaborative research programme[3]. This demonstrated thin film thermocouples of Platinum Rhodium/Platinum and Platinel types on Ni based super alloys to 1000°C using a NiCoCrAlY plus thermally grown oxide insulation system.

The intended technique would prepare the component surface by polishing prior to depositing an electrical insulating thin film layer over the whole component. The components would then be prepared for the formation of the sensor patterns using a "lift off" patterning technique or a physical mask depending on the size and definition of the pattern required. For the "lift off" technique, a photoresist material would be applied to the component and then exposed to ultraviolet light through a contacting mask. On development of the photoresist the required pattern would be defined on the surface of the component. The first leg of the sensor would be deposited onto the component. When the photoresist is removed the excess material is lifted off leaving the required pattern on the component. The second leg would then be applied using the same method.

The insulator and sensor material coatings would be applied using a vacuum deposition magnetron sputtering technique from 'targets' of the required materials. The ability to achieve good electrical insulation at the measuring temperatures is one of the most challenging areas of this technology.

Connection to the films have been made by a number of methods, including parallel gap welding of lead-out wires.

Problems experienced have included the differences in EMF between films and standard tables, due to differences between bulk and film properties, and adhesion of the sensor materials to the component. Annealing of the deposited thermocouples in a neutral gas allowed the achievement of sensitivities as high as 97% of the bulk values. The difference between film and bulk properties may necessitate a 3, or perhaps a 4, lead output so that compensation can be made for the junction temperature.

In addition thermal ageing of the thermocouple due to inhomogenities result in changes in EMF versus temperature curves. This may include a change in composition by selective oxidisation or environmental contamination. This was found to be a problem with the Platinel thermocouples in particular. Thus it is necessary to protect the sensors in contact with the air from oxidation at high temperatures.

Rolls-Royce has established an in-house facility to produce thin film sensors and has recently started its own development of thin film thermocouples of Platinum-Rhodium/Platinum for turbine applications. Future developments may include the development of sensors for components with thermal barrier coatings where the conventional method of buried mineral insulated cables produces a poor yield of satisfactory sensors.

## 5 REMOTE THERMOMETRY USING THERMOGRAPHIC PHOSPHORS

### 5.1 Background

Photoluminescence thermometry using so-called "thermographic phosphors" is an emerging optical non-contact surface temperature measurement technique which promises to overcome many of the traditional problems of radiation pyrometry. The technique uses the optical properties of thermographic phosphors which consist of high temperature crystalline materials doped with rare earth metals. The resulting high temperature photoluminescent materials absorb light at one wavelength, usually ultraviolet (UV) and emit light at a longer wavelength, usually

visible. If the phosphor material is illuminated using a pulsed UV light source at a suitable wavelength, the phosphor will emit a pulse of light which decays exponentially in time. Many phosphors exhibit a rapid variation (generally a decrease) of decay lifetime with temperature. Such materials may be suitable for accurate temperature determination of a phosphor coated surface by calibration of the luminescence decay lifetime with temperature.

Fibre optic and optical non-contact methods have demonstrated numerous advantages of over existing instrumentation. Amongst these, immunity from electromagnetic interference, electrical isolation, non intrusiveness of the measurement, freedom from lead-outs and increased capability have lead to a rapid increase in the use of optical and laser based techniques. Luminescence decay time thermometry offers several potential advantages over existing surface temperature measurement techniques commonly applied to gas turbine engines.

Bonded on and embedded thermocouples can achieve a good accuracy of around ±1% at temperatures in excess of 1000°C and can measure temperatures in areas inaccessible to line of sight instruments. However, leadouts can be difficult and unreliable, especially on rotating components where slip rings or radio telemetry are required. Bonding to ceramic and composite surfaces can be problematic and many thermocouples may be required to provide the required coverage of measurements.

Radiation pyrometry offers a much simpler installation, requiring only line of sight access. It can have a fast speed of response (less than 1μs) and a reasonable temperature resolution (of the order of a degree Celsius) and can produce measurements for all blades in a turbine stage from the single instrument. However, knowledge of the surface emissivity is required and variations in this can produce significant errors, particularly with ceramic surfaces where emissivity can be low and variable. Radiation from hot particulates in the gas stream produces very low signal to noise ratios and can cause problems in signal processing. Reflected radiation from nearby objects (such as the combustion chamber) and attenuation of radiation due to contamination of optics and atmospheric absorption can produce large errors which are difficult to quantify. The resulting measurement may therefore offer a high resolution but often a large uncertainty (possibly up to ± 30°C). The technique is only suitable for measurement of high temperatures, having a lower limit of around 600°C when using a silicon detector.

## 5.2 The Luminescence Technique

The luminescence thermometry technique does not require measurement of absolute intensities as with radiation pyrometry. As such it should prove immune to signal attenuation and spurious reflections as long as the shape of the decay curve can be resolved. The resulting technique therefore promises a relatively simple installation similar to radiation pyrometry but with a high unbiassed accuracy similar to thermocouples.

A number of systems based on luminescence decay lifetime variation have been reported over the past several years. Several systems which utilise a sample of phosphor encapsulated onto the end of an optical fibre have been reported by Grattan et al [4-6]. These have exhibited good sensitivity and repeatability up to 800°C, and systems are commercially available. Work on remote non-contact thermometry has been carried out by several groups[7-11] at Oak Ridge and Los Alamos National Laboratories, EG&G Energy Measurements, Allison Engine Company and the Ontario Hydro Research division. Most notably, measurements were performed at high temperatures on a Pratt & Whitney first stage nozzle guide vane in an operating gas turbine[7,8], and on a coupon in an atmospheric burner rig[10]. Measurements have been performed at ambient temperatures on a turbine disk in a spin pit and an electrical power generator rotor[11] and signals were observed from coated turbine blades during non-fuelled windmilling of a gas turbine[12].

The phosphor intensity generally becomes weaker at higher temperatures as well as having a faster decay time. For a particular system the maximum temperature capability is therefore reached when the luminescence signal becomes too small compared with the collected blackbody radiation and other spurious signal sources. Decays have been measured in the laboratory[9] up to 1600°C and to around 1100°C in gas turbine environments[10,13] and the technique is equally suitable for cryogenic temperatures.

## 5.3 Luminescence Development

A system is being developed at Rolls-Royce with the aim of accurately measuring turbine blade surface temperatures. The system uses a Nd:YAG laser operating at 266nm (UV). It is coupled into a fibre-optic which transmits the excitation pulse to a probe similar in construction to that used in radiation pyrometry. The laser pulse is projected onto the turbine blade which is coated with the phosphor material. The visible luminescence signal emitted by the phosphor is collected by the probe and transmitted

by a fibre-optic to detection and data acquisition and analysis equipment.

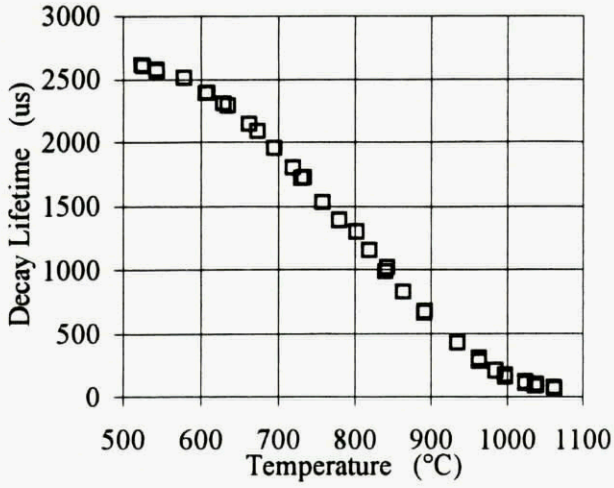


**Figure 6: Decay lifetime variation with temperature of YAG:Tb phosphor.**

Figure 6 shows the decay lifetime variation with temperature measured from YAG:Tb phosphor up to 1050°C using this instrument. Figure 7 shows residuals from a fit to this data. Note that the laser stimulation in this case was 355 nm. The instrument has been demonstrated on a thermal barrier coated nozzle guide vane shown in Figure 8 in an operating engine. The phosphor was applied using a chemical bonding technique and survived for long periods (a few hundred hours) on the guide vane.

Application of the technique to a rotating turbine blade measurement requires the consideration of several additional factors. The optical probe must have an extended field of view to allow observation of a wide range of decay lifetimes in order to provide the instrument with sufficient temperature range. The phosphor must be sufficiently bright and the decay lifetime must also be shorter than the transit time of the blade through the field of view. Work is continuing to address these issues and apply the technique to a turbine blade in an operating gas turbine.

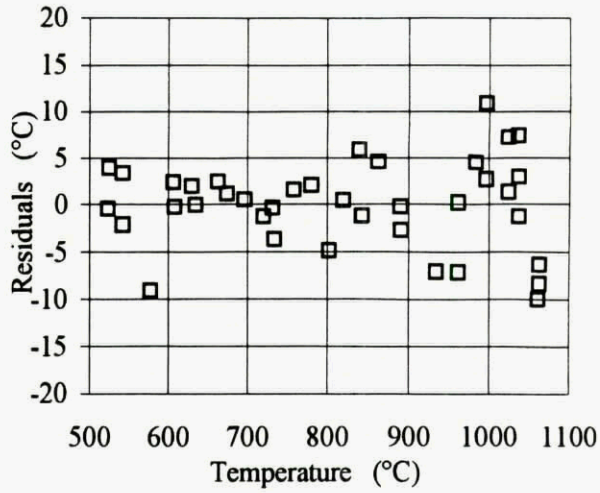


**Figure 7: Residuals from polynomial fit to YAG:Tb decay lifetime.**

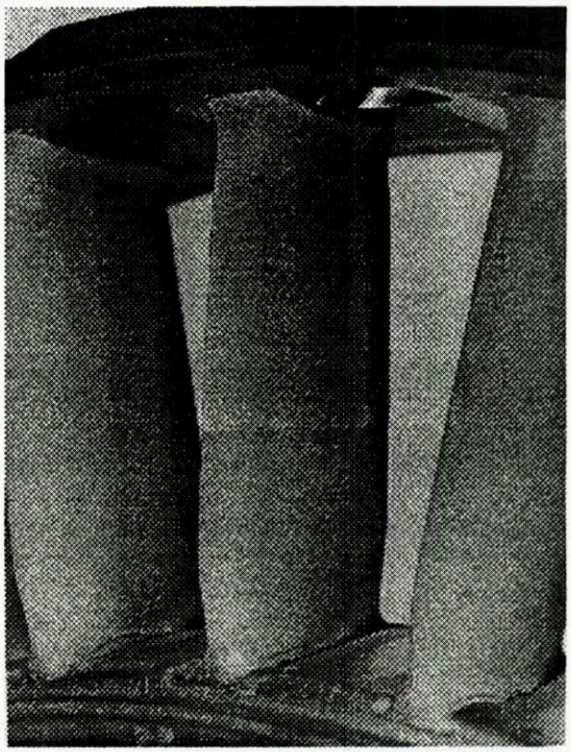

**Figure 8: Phosphor coated nozzle guide vane used in engine testing.**

## 6 ACKNOWLEDGEMENTS

This work has been carried out, in part, with the support of the Ministry of Defence which is gratefully acknowledged. The authors would also like to thank Rolls-Royce plc for permission to publish this paper. The views expressed are those of the authors and not necessarily of Rolls-Royce plc.

## 7 REFERENCES

1) Klinker, Gudrun J, 1993, AK Peters Ltd, ISBN1-S6881-013-X PP9-34. A physical approach to Color Image Understanding,

2) Wyszecki G W and Stiles W S, Color Science, 2nd ed 1975,

3) Dunker R (1992),"Advances in Techniques for Engine Applications" Wiley ISBN 0471 953636

4) Zhang, Z, Grattan K. & Palmer A (1992), "Fibre optic high temperature sonsor based on fluorescence lifetime of Alexanderite.", Rev Sci Instruments, vol 63 p3869-73.

5) Grattan K, Palmer A & Wilson C, (1987), "A miniaturised microcomputer based neodymium decay mtime temperature sensor.", J Phys., vol E20 p1201-5.

6) Grattan K T V, Zhang Z Y (1995), "Fiber Optic Fluorescence Thermometry", ISBN 0 412 62470 2, Chapman & Hall, London

7) Noel BW, Borella H M, Lewis W, Turley W D, Beshears D L, Capps G J, Cates M R, Muhs J D and Tobin KW (1990), "Evaluating thermographic phosphors in an operating turbine engine.", presented at the Gas Turbine and Aeroengine Congress and Exposition, June 11-14, 1990, Brussels, paper number ASME 90-GT-266

8) Tobin K W, Cates M R, Beshears D L, Muhs J D, Capps G J, Smith D B, Turley W D, Lewis W, Noel B W, Borella H M, O'Brian W F, Roby R J, Anderson T T, (1990), "Engine testing of thermographic phosphors, Parts 1 & 2", Oak Ridge National Laboratory report ORNL/ATD-31

9) Allison S W, Beshears D L., Cates M R, Noel B W, Turley W D, (1995), "Phosphor thermometry of gas turbine surfaces", presented at the Gas Turbine and Aeroengine Congress and Exposition, June 5-8, 1995, Houston, Texas, paper number ASME 95-GT-385

10) Alaruri S, M^CFarlandD, Brewington A, Thomas M, Sallee N, (1995), "Development of a fiber-optic probe for thermographic phosphor measurements in turbine engines.", Optics and Lasers in Engineering 22 (1995) 17-31

11) BrownS K, Mannik L., (1991), "Field testing of a fiber-optic rotor temperature monitor for power generators.", SPIE vol. 1584 p.15-22

12) Tobin K W, Beshears D L, Turley W D, Lewis W, Noel B W, (1991), "Fiber-sensor design for turbine engines.", SPIE vol. 1584 p.23-31

13) Bird C, (1995), "Luminescence Thermometry - Phosphor Calibration and Decay Analysis Method", Rolls-Royce internal report EIM00358, unpublished proprietary data.

Paper 21
Author: Bird, et.al.

Q: Pink

For thermally-painted combustors, how long would they typically be run in order to access colour changes ?

A: Usually for a combustor tested in an engine, the standard run time of 3 minutes at condition would be used. Time calibration of the points, however, allows running for up to 20 minutes at condition for use in combustor rigs where it is necessary to run for longer to allow other measurements (e.g. emissions analysis) to be made.

# Effective Spectral Emissivity Measurements of Superalloys and YSZ Thermal Barrier Coating at High Temperatures Using a 1.6 μm Single Wavelength Pyrometer

**Sami Alaruri, Lisa Bianchini, and Andrew Brewington**
Allison Engine Company, Rolls-Royce Aerospace Group,
Box 420, M/S W03A, Indianapolis, IN 46206-0420, U.S.A.

## 1. SUMMARY
A method employing an integrating sphere and a single wavelength (1.6 μm) pyrometer for measuring the spectral effective emissivities of superalloys in the temperature range (~650-1050°C) is described. The spectral effective emissivities for five superalloys, namely, MARM-247, MARM-509, CMSX-4, Inconel-718, N-155, and two René-N6 samples coated with YSZ thermal barrier coating were measured. Correcting the pyrometer measurements for the variations in the object emissivity would reduce the uncertainty in the temperature measurements to <±1%.

## 2. INTRODUCTION
Single wavelength pyrometers are used extensively as a diagnostic and health monitoring noncontact temperature measurement tool in the development and research of advanced high-temperature military and commercial gas turbine engines [1]. In addition, these intensity-based IR sensors are widely used for gathering noncontact temperature measurements in petrochemical, material processing, and laser-machining industries [1]. In contrast with the widely used temperature sensors, namely thermocouples, pyrometers have several advantages over thermocouples. First, the absence of wires makes pyrometers attractive for noncontact surface temperature measurements of rotating parts (i.e., blades). Second, the temperature measurements gathered using pyrometers are immune to the electromagnetic interference generated from the surrounding environment. Third, temperature measurements can be collected nonintrusively and without perturbing any of the system parameters (i.e., gas flow patterns).

In spite of these advantages single wavelength radiation thermometry instruments (i.e. single wavelength pyrometers) suffer from three major problems:

1. Inferring the object temperature from the spectral radiance measurements without knowing the emissivity of the object at different temperatures.

2. Correcting temperature measurements for the extraneous reflection and emission components (i.e., background radiance) that can be produced by flames, walls, or particles in the field of view.

3. Correcting for the attenuation of the optical signal due to the variable transmissivity of the optical path.

To circumvent some of these problems multiwavelength [1,2] and reflectance [1] pyrometers were developed. Despite the several advances in the development of these instruments in recent years, measurements gathered using these instruments lack accuracy, especially when used in flame environments for viewing low emissivity (i.e., high reflectivity) components such as ceramics [1]. In view of these difficulties, the development of algorithms for correcting the measurements gathered using pyrometers for the emissivity variations and the contribution due to the reflected radiation components was deemed necessary.

In the work herein, a practical method for determining experimentally the effective spectral emissivity of engine components at high temperature using a single wavelength pyrometer is described. Emissivity measurements pertaining to Ni, Co, Ni-Fe, and Ni-Co-Fe based superalloys and yttria-stabilized zirconia (YSZ) thermal barrier coating (TBC) are discussed. In addition, an error analysis for the collected measurements is presented.

## 3. EXPERIMENTAL
The spectral effective emissivity for selected superalloys, namely MARM 247 [3], MARM 509 [3], CMSX-4 [4], Inconel 718 [3], N155 [3], and YSZ TBC deposited on René-N6 superalloy (coated with a thin layer of platinum aluminide [PtAl] bond-coat) was examined in air over the temperature range ~650 to 1050°C. The TBC layer was applied to the PtAl bond-coat using an electron beam physical vapor deposition (EB-PVD) technique. As illustrated in Figure 1, a disc (~2 cm in diameter) made from the alloy under investigation was instrumented with two type K thermocouples (nickel-chromium versus nickel-aluminum alloy). The sensing ends of the two thermocouples were spot welded into the center of the disc. In the case of the YSZ TBC disc the sensing ends of the two thermocouples were adhered to the center of the sample using ceramic cement (Ceramabond 569, Aremco Products, Inc.). For commercial type K thermocouples a calibration tolerance of ±0.4% is specified over the temperature range 0-1250°C by ASTM standards. Furthermore, a block of metal was spot welded to the back of the disc to ensure the generation of a quasi-isothermal surface area. The surface area of each superalloy disc was roughened before instrumenting the disc with thermocouples using a fine sand blaster. To prevent the infrared radiation generated from the surrounding environment from interfering with the collected signals, the disc was mounted at one of the open-ends of a 30 cm long alumina tube (~4.6 mm wall thickness). The other open end of the alumina tube was coupled to the entrance port of an integrating sphere (Newport-P/N 819-IS-2). The integrating sphere inner surface is coated with a Spectralon, which has a 0.991 reflectance (ρ) at 1.6 μm (8 deg hemispherical) [5].

It is worth noting that the integrating sphere was introduced to the measurement setup to ensure the nonlambertian radiant flux emitted from the surface area of the disc [6] is transformed into a circular lambertian source at the exit port. During all experiments the monolithic thermoplastic integrating sphere was air cooled by blowing air at the surface area facing the furnace to maintain the thermal stability of the sphere. By placing the disc and the isothermal block inside a three-zone furnace (Lindberg, model 55347), the photons emitted from the surface area of the coupon at different temperature settings were measured. The temperature of

*Paper presented at an AGARD PEP Symposium on "Advanced Non-Intrusive Instrumentation for Propulsion Engines", held in Brussels, Belgium, 20-24 October 1997, and published in CP-598.*

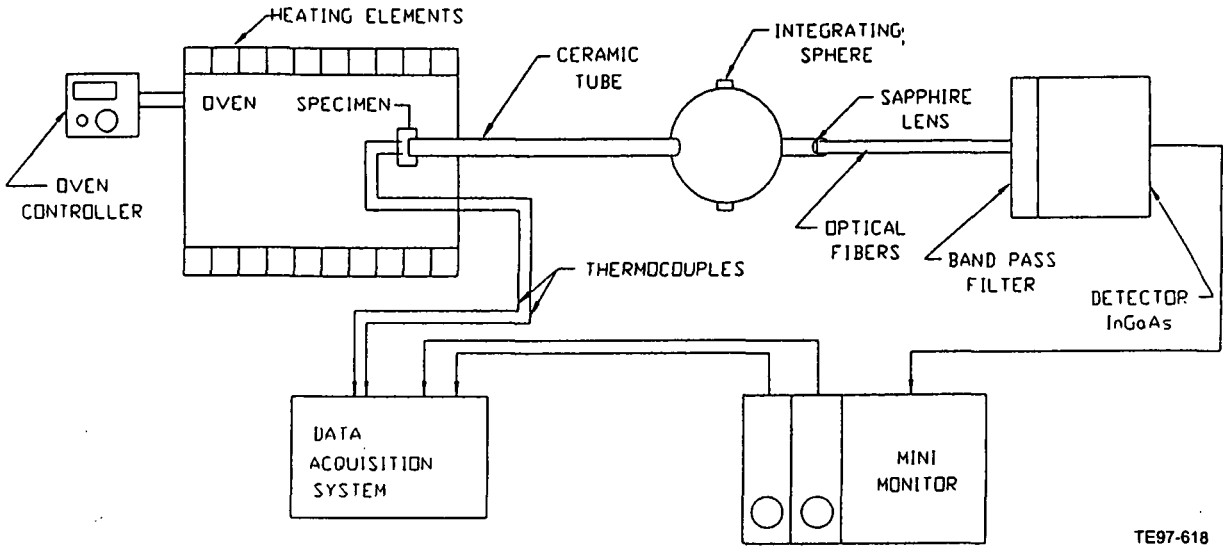


Figure 1. Schematic Diagram of the Experimental Setup Used for Measuring the Effective Spectral Emissivity of the Superalloys and the YSZ Samples Using a Single Wavelength (1.6 μm) Pyrometer.

the three-zone furnace was controlled via a programmable temperature controller (Eurotherm model 818). Further, the analog output of the pyrometer amplifier-filter module and the readings of the two thermocouples were monitored using a data acquisition system (HP 75000 B) equipped with 16-channel thermocouple and high-voltage relay multiplexer cards (HP E1345-66201). During each data collection cycle the data acquisition system was programmed to calculate the average of ten readings for each channel. Additionally, the standard error was calculated for each measurement.

A commercial pyrometer system (Land Turbine Sensors, Inc., Type 699.057) consisting of three major components, collection optics, detector, and data acquisition electronics, was used to measure the throughput of the integrating sphere. All measurements were gathered with the pyrometer emissivity setting set at 1.0. Before any measurements were collected, the pyrometer system was calibrated with respect to a blackbody cavity (Mikron-model 330). The blackbody cavity was heated with molybdenum disilicide elements and the temperature of the cavity was monitored using a platinum B-type thermocouple. The accuracy of the blackbody was rated at ±0.25% of the ±1 digit for temperature readings above 600°C, whereas the emissivity of the cavity was rated at 0.990±0.005. Figure 2 depicts the calibration curve of the instrument used in this work.

As shown in Figure 1, the radiant flux emitted from the heated disc was collected and coupled into a bundle of 200 μm core-diameter waveguides by means of a short focal length sapphire lens ($f$=12.5 cm). Radiation emerging from the distal end of the waveguides was coupled into a InGaAs detector. By placing a band-pass filter in front of the detector, the output of which was fed into an amplifier-filter module for signal processing, the spectral response of the detector was restricted to a 75 nm spectral band centered at 1.6 μm.

## 4. RESULTS AND DISCUSSION

Using least-squares linear regression analysis, a functional relationship expressing the temperature of the blackbody cavity as a function of the pyrometer spectral radiance temperature was calculated. The calculated functional form illustrated in Figure 2 is given by

$$T_{BB}=(1.012\pm0.005)T_{\lambda}-17.400\pm2.462 \qquad (1)$$

where $T_{BB}$ is the temperature indicated by the blackbody cavity and $T_{\lambda}$ is the spectral radiance temperature indicated by the pyrometer. The calculated coefficient of determination ($r^2$), the standard deviation of the slope, and the standard deviation of the intercept were 0.999, ±0.005, and ±2.462, respectively.

Next, the calibrated pyrometer was used to measure the spectral effective emissivities for each alloy over the temperature range ~ 650-1050°C. The relationship expressing the effective spectral emissivity in terms of the pyrometer spectral radiance temperature and the temperature of the alloy as indicated by the thermocouples (Equation 5) is deduced from the arguments that follow.

The spectral radiance (sterance), $L(\lambda,T)$, of a blackbody radiator (i.e., emissivity = 1) at temperature T is described by Planck's equation

$$L(\lambda,T)=(2hc^2)\lambda^{-5}/[e^{(hc/\lambda kT)}-1] \qquad (2)$$

where h is Planck's constant, c is the speed of light in vacuum, $\lambda$ is the wavelength in meters, k is Boltzmann's constant, and T is the absolute temperature of the blackbody in degrees Kelvin.

In the case of a greybody (i.e. emissivity <1) the output signal of the pyrometer system, $\phi(\lambda,T)$, may be expressed, as a first order approximation, as [7]

$$\Phi(\lambda,T)=\Psi\varepsilon(\lambda,T)L_{greybody}(\lambda,T) \qquad (3)$$

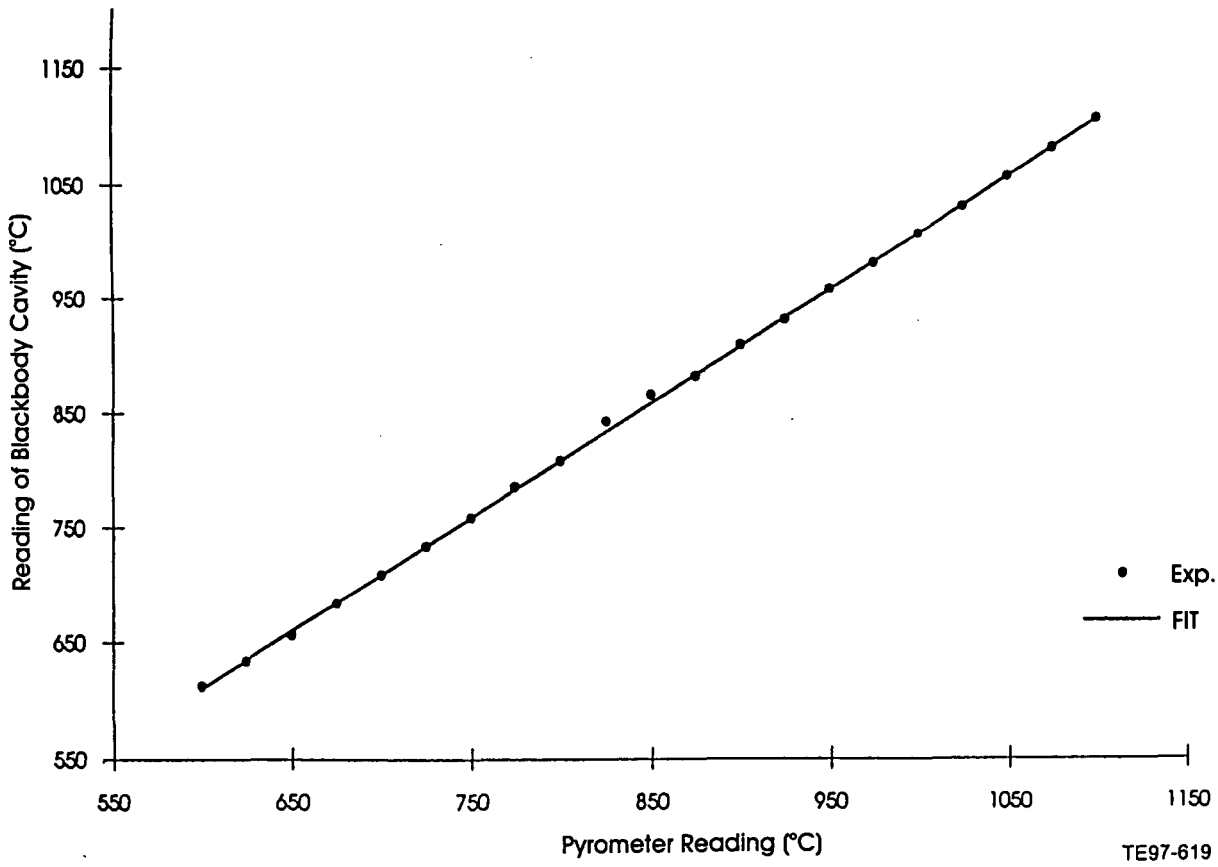


Figure 2. Calibration Curve for the Pyrometer Used in this Work. The Solid Line Represents the Straight Line Calculated Using the Calibration Measurements.

where $\Psi$ is the instrument constant and $\varepsilon(\lambda,T)$ is the effective spectral emissivity of the greybody at a given temperature and spectral band width. Further, the emissivity depends on surface quality and geometry of the object. The instrument constant, $\Psi$, which appears in Equation 3 is generally evaluated in terms of the path transmittance ($\tau_p$), the detector detectivity ($D^*$), the detector effective area ($A_s$), the spectral band width of the system ($\Delta\lambda$), and the solid angle subtended by the detector ($\Omega_s$).

Likewise, the output signal measured for a blackbody by a pyrometer may be represented as

$$\Phi(\lambda,T)=\Psi L(\lambda,T) \quad (4)$$

From Equations 2, 3, and 4 the effective spectral emissivity of the greybody can be written as

$$\varepsilon(\lambda,T)=e^{[(1/T-1/T_\lambda)C_2/\lambda)]} \quad (5)$$

where the value of $C_2$ is 14,388 μm K, the value of $\lambda$ is 1.6 μ m, T is the temperature of the greybody as indicated by the thermocouples, and $T_\lambda$ is the spectral radiance temperature indicated by the pyrometer. Consequently, the temperature of the greybody can written as

$$T=(\lambda/C_2 \text{ Ln } \varepsilon(\lambda,T)+1/T_\lambda)^{-1} \quad (6)$$

It is worth noting that the derivation of Equation 5 implies the replacement of Planck's law (Equation 2) by Wien's approximation, which is valid for short wavelengths and low temperatures (i.e., $C_2 >> \lambda T$). Wien's approximation introduces an error of the order of 0.1% and does not affect the correctness of the results significantly.

By employing Equation 5 and utilizing the temperature measurements, the effective spectral emissivities for the alloys noted previously were determined experimentally. The results are presented in Figures 3, 4, 5, 6, and 7. The solid line in each graph depicts the calculated empirical fit using the relationships listed in Table I. The calculated coefficients of determination for these empirical fits ranged between 0.90 and 0.85. Table I also tabulates the elemental percentage weight composition, the calculated average effective spectral emissivity, and the standard error of the emissivity measurement for each alloy. Since the standard deviation of the emissivity measurements did not exceed ±5%, it can be assumed as a first order approximation that the emissivity for each alloy was constant over the temperature range ~650-1050°C.

By comparing the measured average effective spectral emissivities for CMSX-4 ($\varepsilon$=0.806±0.003), MARM-247 ($\varepsilon$=0.817±0.002), and Inconel-718 ($\varepsilon$=0.853±.009) as a function of the percentage weight concentration of Ni, it can be seen that the value of the spectral effective emissivity increased with the decrease in the alloy's Ni concentration. As shown in Table I, the percentage concentration of Ni for CMSX-4, MARM-247, and Inconel-718 is 61.7%, 59.0%, and 52.5%, respectively.

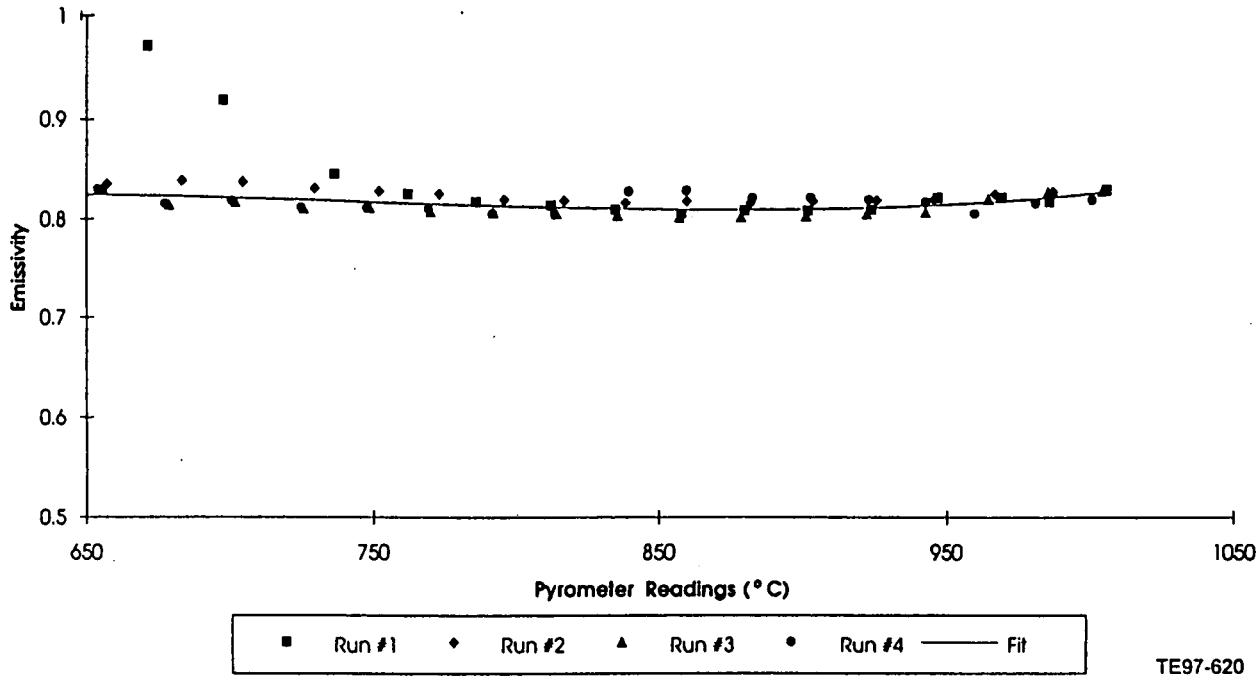


Figure 3. Scatter Diagram Showing the Measured Effective Spectral Emissivity for MARM-247 Over the Temperature Range ~650-1050°C.

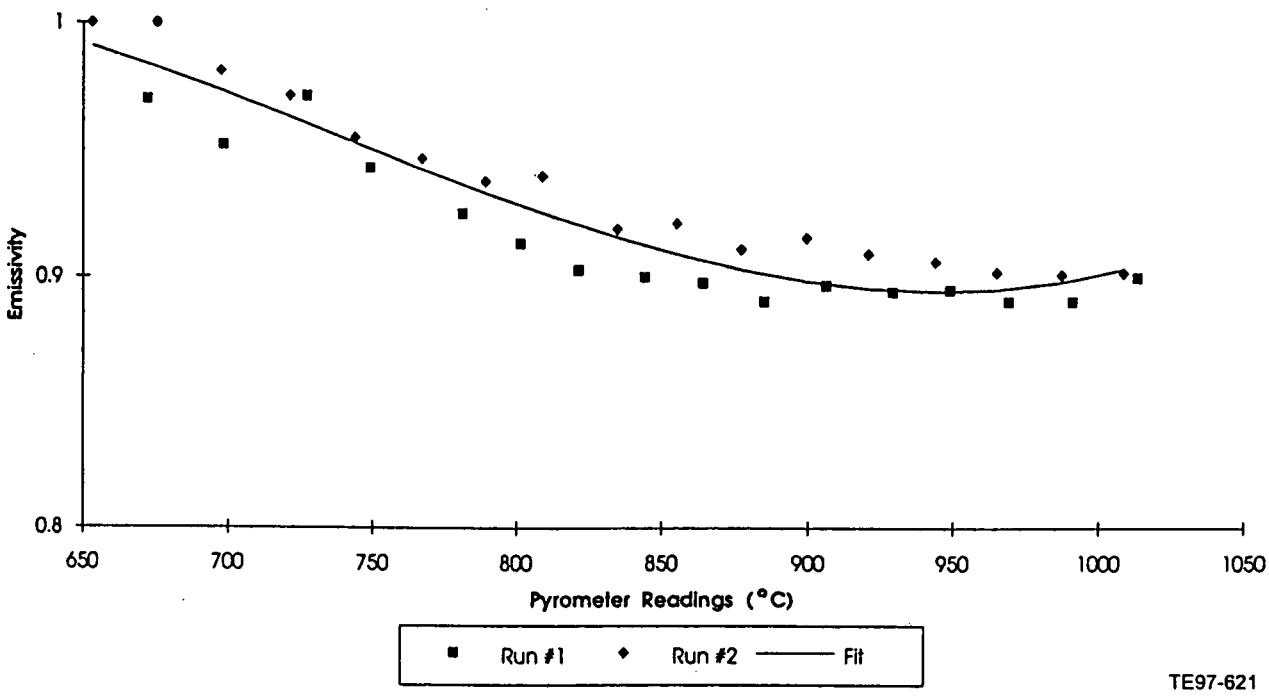


Figure 4. Scatter Diagram Showing the Measured Effective Spectral Emissivity for MARM-509 Over the Temperature Range ~650-1050°C.

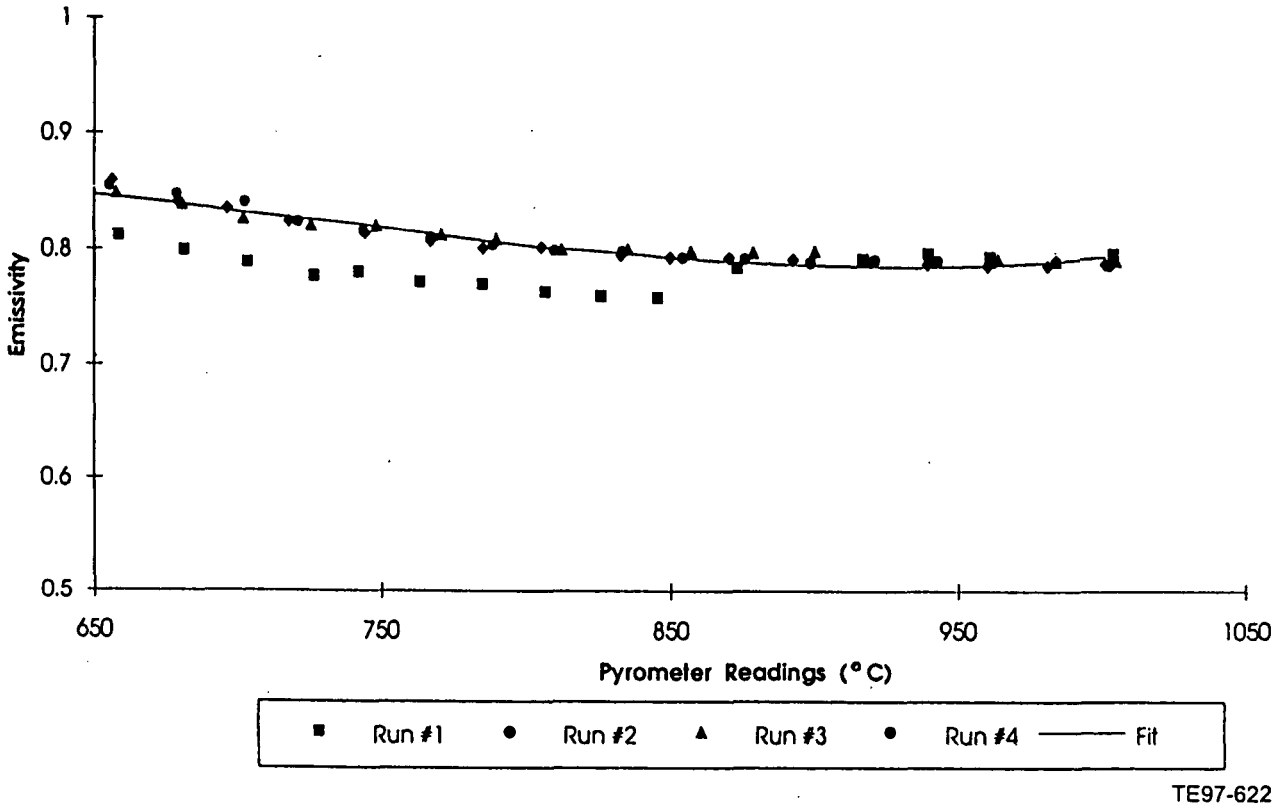


Figure 5. Scatter Diagram Showing the Measured Effective Spectral Emissivity for CMSX-4 Over the Temperature Range ~650-1050°C.

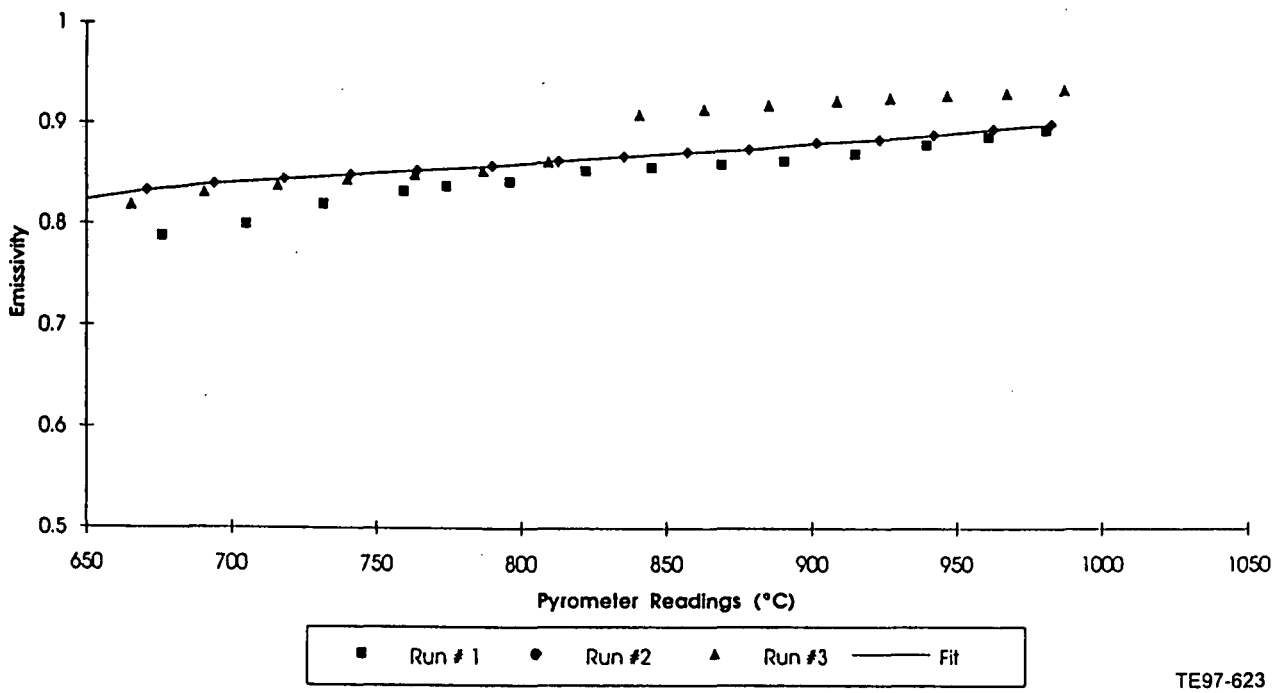


Figure 6. Scatter Diagram Showing the Measured Effective Spectral Emissivity for Inconel-718 Over the Temperature Range ~650-1050°C.

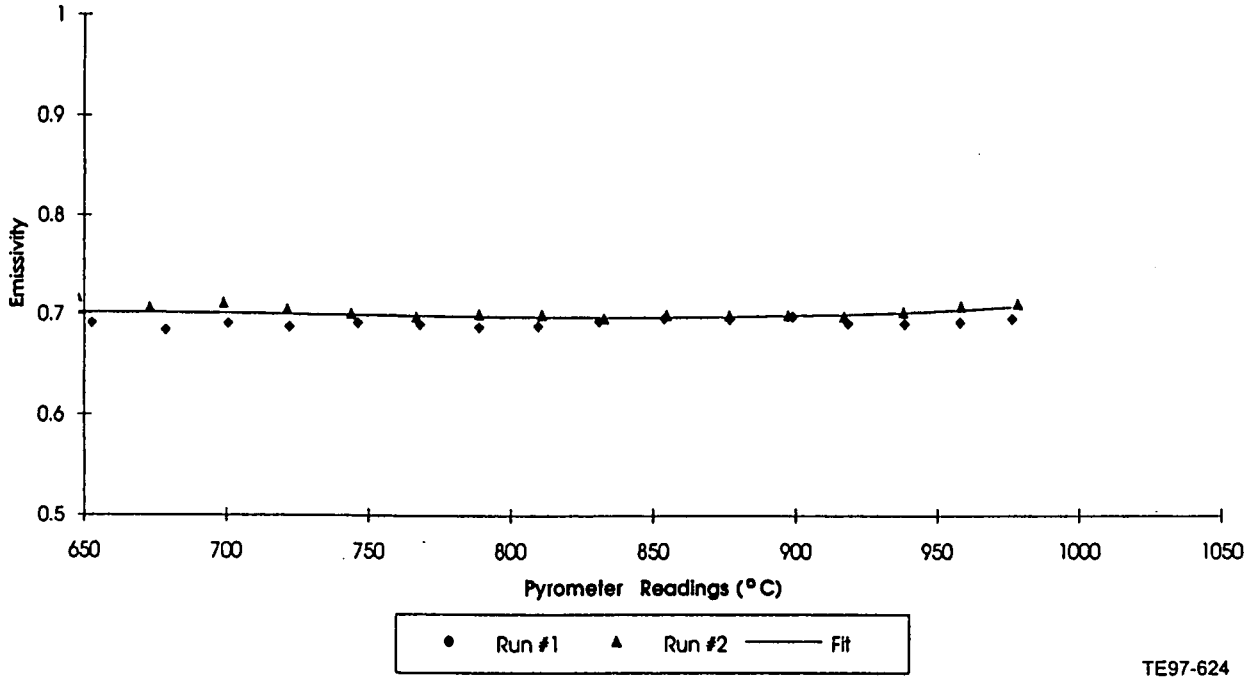


Figure 7. Scatter Diagram Showing the Measured Effective Spectral Emissivity for N-155 Over the Temperature Range ~650-1050°C.

Table I.
Regression Fits, the Percentage Elemental Composition, Average Effective Spectral Emissivity and Emissivity Standard Errors Calculated for Each Superalloy.

| Alloy – % composition | Empirical fit | Average emissivity |
|---|---|---|
| MARM-247 (Ni-based alloy) 59.0 Ni-10.0 Co-<0.5 Fe | $\varepsilon=3.5\times10^{-3}T_\lambda-4.7\times10^{-6}T_\lambda^2+2.1\times10^{-9}T_\lambda^3$ | 0.817 ± 0.002 |
| MARM-509 (Co-based alloy) 10.0 Ni-54.5 Co | $\varepsilon=4.8\times10^{-3}T_\lambda-7.1\times10^{-6}T_\lambda^2+3.21\times10^{-9}T_\lambda^3$ | 0.926 ± 0.006 |
| CMSX-4 (Ni-based alloy) 61.7 Ni-9.0Co | $\varepsilon=3.9\times10^{-3}T_\lambda-5.7\times10^{-6}T_\lambda^2+2.6\times10^{-9}T_\lambda^3$ | 0.806 ± 0.003 |
| Inconel-718 (Ni-Fe based alloy) 52.5 Ni-18.5 Fe | $\varepsilon=2.5\times10^{-3}T_\lambda-2.5\times10^{-6}T_\lambda^2+9.7\times10^{-9}T_\lambda^3$ | 0.853 ± 0.005 |
| N-155 (Ni-Co-Fe based alloy) 20 Ni-20 Co-30 Fe | $\varepsilon=39.9/T_\lambda+2.5\times10^{-3}T_\lambda-3.2\times10^{-6}T_\lambda^2+1.4\times10^{-9}T_\lambda^3$ | 0.697 ± 0.002 |

To test whether the three mean emissivities (i.e., $\varepsilon_{CMSX-4}$, $\varepsilon_{MARM-247}$, $\varepsilon_{Inconel-718}$) are significantly different or not, two hypotheses were tested by subjecting the emissivity means to a $t$-distribution test (i.e., $H_0$ [null hypothesis]: $\varepsilon_1=\varepsilon_2$ for critical region $t_{calculated} < t_{critical}$ -accept hypothesis $H_0$ and reject $H_1$; $H_1$: $\varepsilon_1\neq\varepsilon_2$ for critical region $t_{calculated} > t_{critical}$ -reject hypothesis $H_0$ and accept $H_1$)[8]. As such, $t_{calculated}$ was greater than $t_{critical}$ for the three possible emissivity mean combinations, that is $\varepsilon_{CMSX-4}$ versus $\varepsilon_{MARM-247}$; $\varepsilon_{CMSX-4}$ versus $\varepsilon_{Inconel-718}$; and $\varepsilon_{MARM-247}$ versus $\varepsilon_{Inconel-718}$. Thus, the null hypothesis was rejected and the alternative hypothesis was accepted for the three possible emissivity combinations. This result, at 85% confidence level, implies that the emissivity values are indeed significantly different. Based upon this result, one may conclude a 14.9% decrease in the Ni concentration would result in a 5.5% increase in the value of the measured spectral effective emissivity. It is worth noting that throughout this work the hypothesis tests were carried out under the assumption the emissivity measurements were random samples drawn from a normal distribution.

Likewise, the emissivity measurements were examined as a function of the Co weight percentage concentration in three alloys, namely MARM-509 (54.5% Co), MARM-247 (10.0% Co), and CMSX-4 (9.0% Co). Clearly, a decrease in the percentage weight concentration of Co resulted in a decrease in the measured spectral effective emissivity of the alloy. In a similar manner, the three mean emissivities were tested by assuming a null hypothesis ($H_0$: $\varepsilon_1=\varepsilon_2$) and an alternative hypothesis ($H_1$: $\varepsilon_1\neq\varepsilon_2$). The results of the statistical inference indicated that $\varepsilon_{MARM\text{-}509}$ versus $\varepsilon_{MARM\text{-}247}$ and $\varepsilon_{MARM\text{-}509}$ versus $\varepsilon_{CMSX\text{-}4}$ were significantly different and the null hypothesis was rejected for each combination. In the case of $\varepsilon_{MARM\text{-}509}$ versus $\varepsilon_{CMSX\text{-}4}$ the null hypothesis was accepted at a 99.5% confidence level. Consequently, $\varepsilon_{MARM\text{-}247}$ and $\varepsilon_{CMSX\text{-}4}$ are not significantly different in value. As shown in Table I, it can be seen that a decrease of approximately 81.6% in the Co percentage concentration yields a decrease of 11.8% in the value of the spectral effective emissivity of the sample [9].

The effective spectral emissivities for two YSZ TBC coated samples were measured as a function of temperature using the apparatus shown in Figure 1. The obtained results are depicted in Figure 8. Each set of data (i.e., run) was collected over an 8-hour time period. As shown in Figure 8 and listed in Table II, an average increase of approximately 45.3% in the measured effective spectral emissivity values was observed after the first heat cycle. After run no. 1 (i.e., 8-hour heat cycle) the effective spectral emissivity values for both samples ranged between 0.70 and 0.78. Such an increase in the measured emissivity values between the first run (i.e., run no. 1 for S1 and S2) and the later runs was attributed to the migration of aluminum and aluminum oxide from the PtAl bond-coat into the TBC layer. The migration of aluminum from the bond-coat into the surface area of the TBC structure was detected using a scanning electron microscope (JXA-35, JEOL). As illustrated in Figure 9, the elemental surface structure measured for a fresh YSZ sample does not indicate the presence of aluminum in the surface area. Whereas the presence of aluminum in the surface area of a sample heat cycled for 32 hours (S2 [run no.4]) is evident (Figure 10). It was reported that the migration of aluminum and aluminum oxide from the bond-coat into the TBC leads to the spallation of TBC, thereby leading to temperature rise of the airfoil and premature failure of engine components [10].

To test whether the three mean emissivities (i.e., $\varepsilon_{1,2}$, $\varepsilon_{2,3}$, and $\varepsilon_{2,4}$, where $\varepsilon_{i,j}$ i = sample number [i = 1,2] and j = run number [1,2 ...4]) are significantly different, two hypotheses were tested by subjecting the emissivity means to a *t*-distribution test

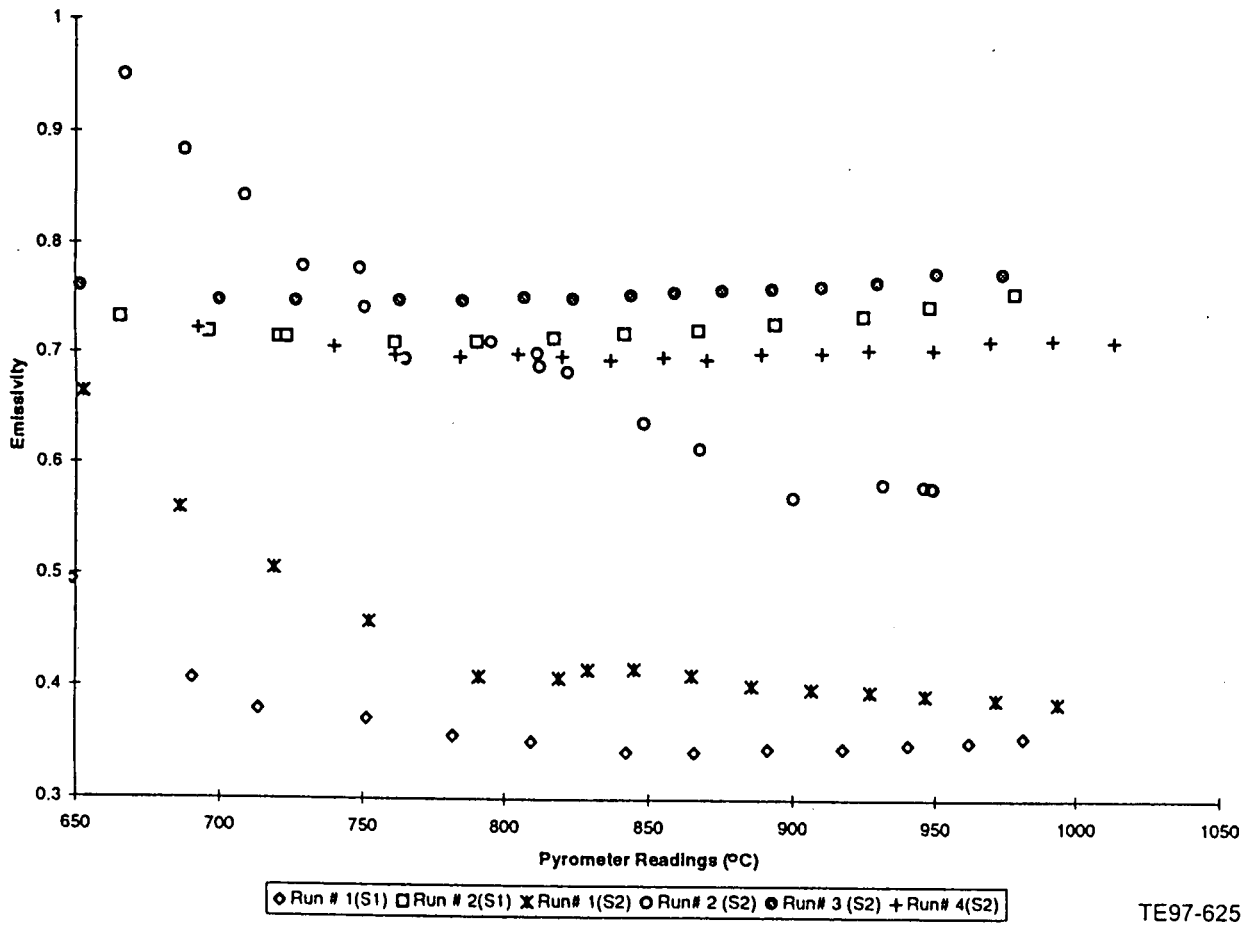


Figure 8. Scatter Diagram Showing the Measured Effective Spectral Emissivity for the Two (S1&S2) Heated YSZ Samples.

Table II.
Calculated Average Effective Spectral Emissivities and Their Standard Errors for the Two YSZ Samples After Each Heat Cycle.

| Sample no. | Run no. | Duration of heat cycle –hours | Average emissivity |
|---|---|---|---|
| S1 | 1 | 8 | 0.3582 ± 0.0189 |
| S1 | 2 | 24 | 0.7248 ± 0.0136 |
| S2 | 1 | 8 | 0.4399 ± 0.0766 |
| S2 | 3 | 24 | 0.7576 ± 0.0089 |
| S2 | 4 | 32 | 0.7038 ± 0.0075 |

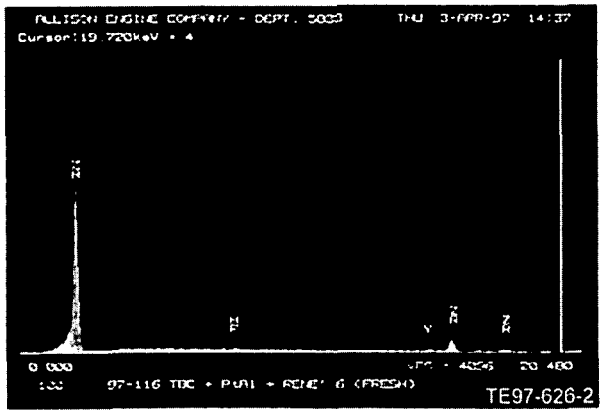


Figure 9. Relative K-Ratio Scanning Electron Microscope Output Showing the elemental Composition of a YSZ Sample Before Exposing the Sample to Heat (Zr = Zirconium; Hf = Hafnium; Y= Yttrium).

(i.e., $H_0$ [null hypothesis]: $\varepsilon_{i,j} = \varepsilon_{i,j}$ for critical region $t_{calculated} < t_{critical}$, accept hypothesis and reject $H_1$; $H_1$: $\varepsilon_{i,j} \neq \varepsilon_{i,j}$ for critical $t_{calculated} > t_{critical}$ region, reject hypothesis $H_0$ and accept $H_1$). As such, $t_{calculated}$ was greater than $t_{critical}$ for the three possible emissivity mean combinations, that is $\varepsilon_{1,2}$ versus $\varepsilon_{2,3}$, $\varepsilon_{1,2}$ versus $\varepsilon_{2,4}$, and $\varepsilon_{2,3}$ versus $\varepsilon_{2,4}$. Thus, the null hypothesis was rejected and the alternative hypothesis was accepted for the three possible emissivity combinations. This result, at 99.5% confidence level, implies the emissivity values are indeed significantly different and the surface area of the TBC layer did not reach stability after several heat cycles. For practical purposes an average emissivity value of 0.7287 ± 0.0128 (average for $\varepsilon_{1,2}$, $\varepsilon_{2,3}$, and $\varepsilon_{2,4}$) can be used as the effective spectral emissivity for the YSZ layer at 1.6 μm. Based upon these findings one may conclude the optical characteristics for TBC change drastically due to the migration of aluminum from the bond-coat into the TBC layer. After a short heat cycle the emissivity values for the TBC layer

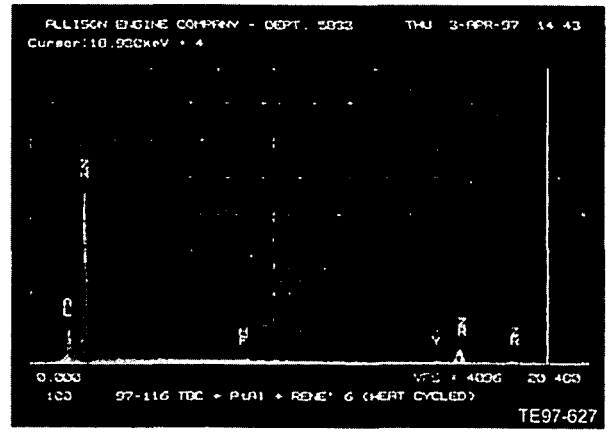


Figure 10. Relative K-Ratio Scanning Electron Microscope Output Showing the Elemental Composition of a Heat Cycled YSZ Coupon (Al = Aluminum; Zr = Zirconium; Hf = Hafnium; Y= Yttrium).

become comparable in value to that measured for superalloys over the same temperature range. Consequently, the transmittance of the YSZ layer, which is very high at long wavelengths (Figure 11), will be reduced drastically. Such a result suggests that using long wavelength pyrometry measurements for monitoring the surface temperature of TBC coated engine parts does not offer a clear advantage over short wavelength TBC pyrometry measurements. In an actual turbine engine environment the columnar structure of the TBC layer would allow particulate matter from the engine flow path to be deposited between the YSZ columns. As a result the optical properties of the TBC layer will be transformed into properties similar to that obtained from metallic surfaces. It is also worth noting that due to the high thermal expansion coefficients of these particulate matters relative to the YSZ columns, they can contribute in a significant manner to the spallation of the TBC layer.

Lastly, we examined the percentage relative errors that resulted from setting the pyrometer emissivity control at 1 (i.e., assuming $\varepsilon = 1$). The relative errors were calculated by normalizing the difference between the pyrometer and the thermocouple readings by the temperature measurements obtained using type K thermocouples. As illustrated in Figure 12, such an assumption as the data for N-155 alloy suggests can lead to ±6.3% error (~±63°C at 1000°C) in the temperature measurements. The magnitude of such errors can be reduced to <±1% when the correct emissivity of the superalloy is selected. As shown in Figure 13, the percentage relative errors for the first two heat cycles of the two YSZ samples varied between 10% and 16% over the 650 to ~1000°C temperature range. The values of the percentage relative error dropped to an average value of 4.98±0.08% (average for run no. 2 [S1], run no. 3 [S2], and run no. 4 [S2]) after the first heat cycle. This result implies that a reduction in the magnitude of the percentage relative error can be achieved by heat cycling the TBC coated turbine engine components before gathering temperature measurements in an engine. However, the impact of the heat cycle on the lifetime of the engine part and the integrity of the TBC layer is not clear at this stage.

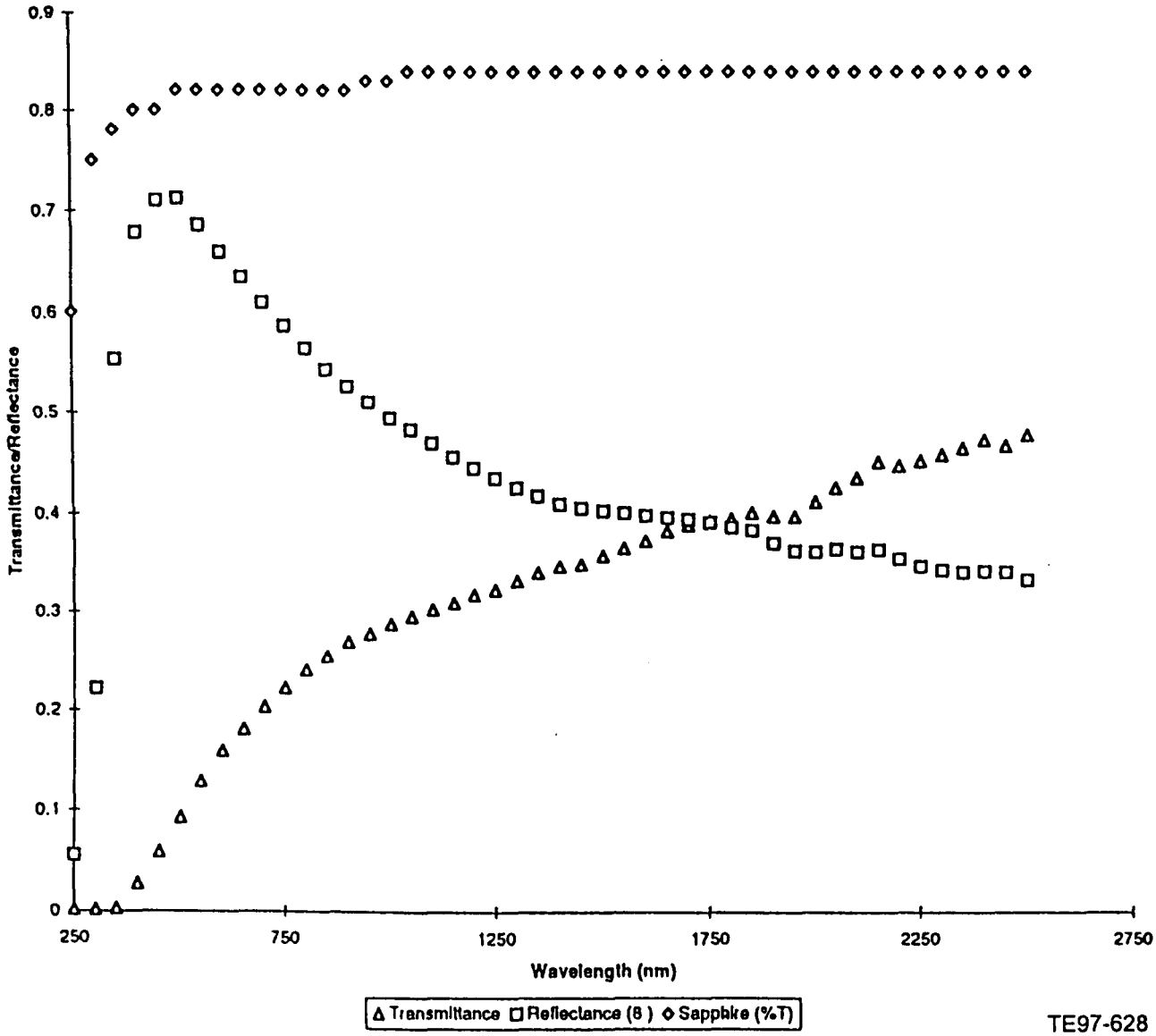


Figure 11. Transmittance and Reflectance Measurements for the YSZ Layer (~ 0.330 mm Thick) Deposited on a Sapphire Disc Using a EB-PVD Method. Also, the transmittance Measurements for a 1mm Thick Sapphire Disc Over the Spectral Region 250-2750 nm Are Shown.

## 5. CONCLUSIONS

Analysis of the emissivity measurements indicated that at 1.6 μm a decrease in the Ni concentration (61% - 52% weight composition of the alloy) would result in an increase in the value of the measured emissivity. Whereas a decrease in the Co concentration (54.5% -9.0% of the weight composition of the alloy) would result in a decrease in the emissivity of the alloy. Further, the average effective spectral emissivity of YSZ thermal barrier coating increased from 0.3991 ± 0.0289 to 0.7287 ± 0.0128 after a short heat cycle. A significant reduction in the contribution of the emissivity error component and consequently the reflection component can be achieved by heat cycling YSZ TBC coated engine parts prior to taking any temperature measurements using pyrometers.

## 6. ACKNOLEDGEMENTS

The authors wish to express their thanks to Mr. Pete Linko and his colleagues at General Electric Aircraft Engines for supplying the TBC coated samples.

## 7. REFERENCES

1. NASA Lewis Research Center, Remote Temperature Sensing Workshop, 1994.
2. Hiernaut, J., Beukers, R., Heinz, W., Selslag, R., Hoch, M., and Ohse, R., "Submillisecond Six-Wavelength Pyrometer for High-Temperature Measurements in the Range 2000 to 5000 K," *10 ETPC Proceedings*, Vol. 18, 1986, p. 617-625.
3. J. R. Davis, *ASM Materials Engineering Dictionary*, 1992.

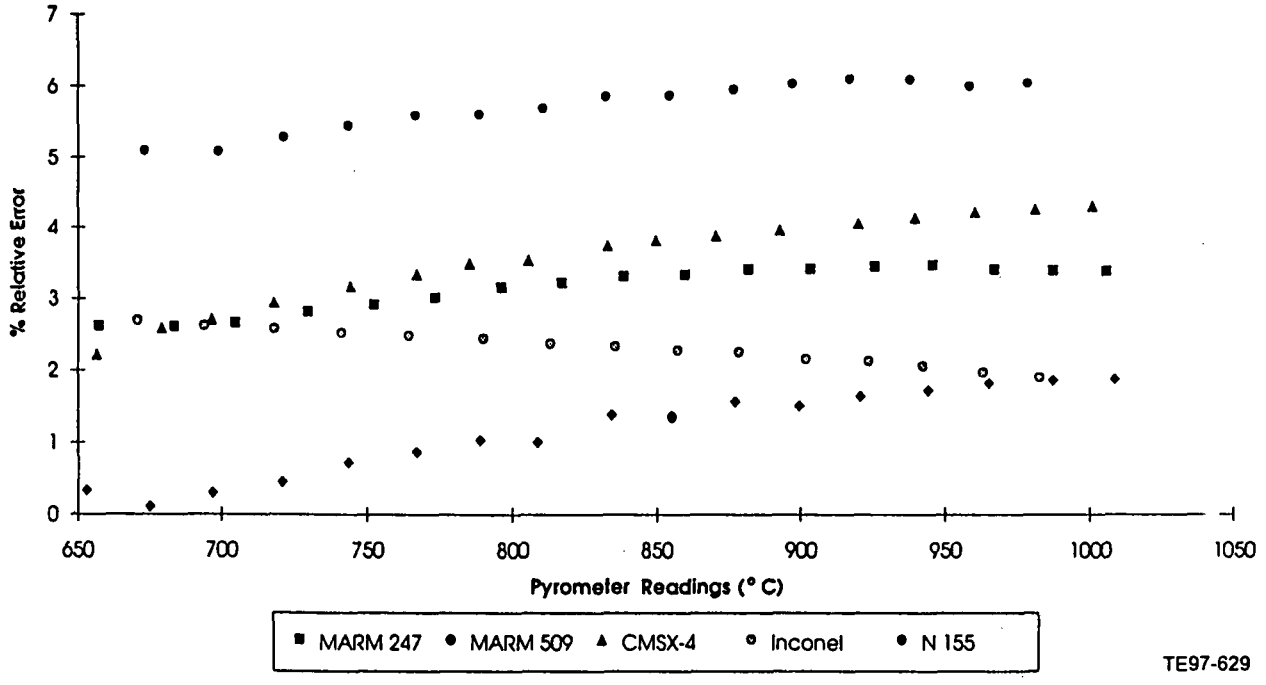


Figure 12. Relative Errors (% Relative Error = {[Pyrometer Reading-Thermocouple Reading]/Thermocouple Reading}*100) Calculated for Each Superalloy with the Pyrometer Emissivity Set at Unity.

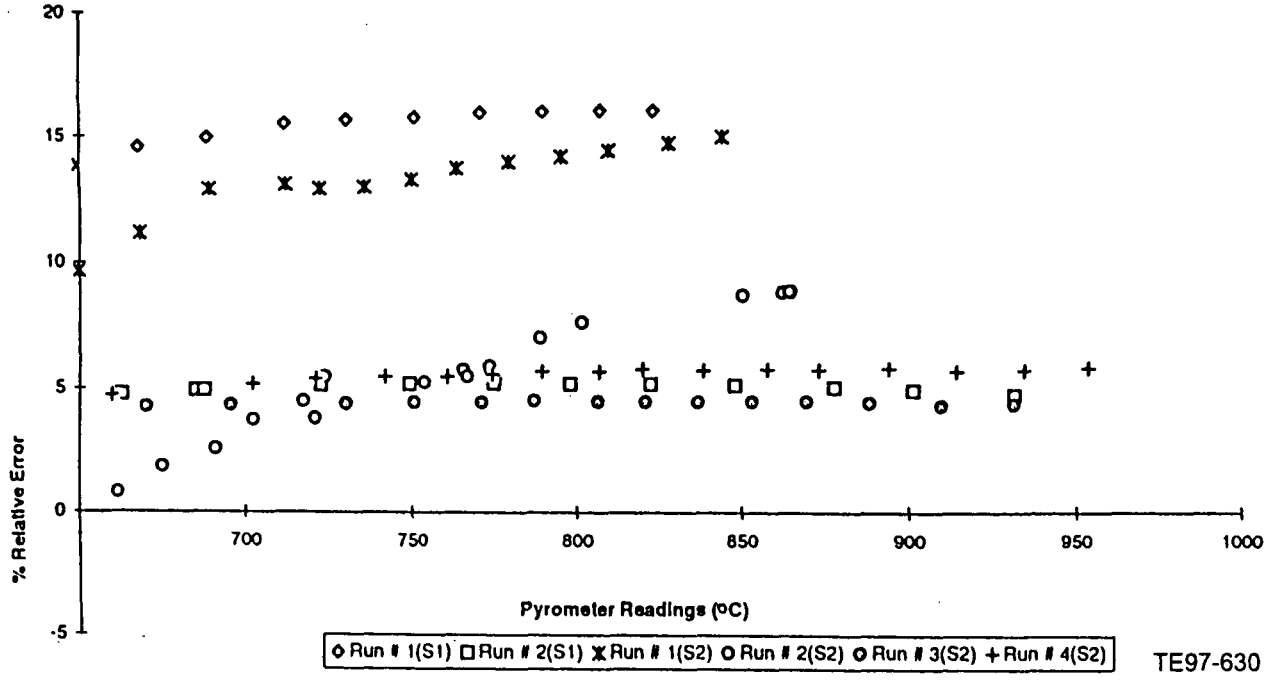


Figure 13. Relative Errors % Relative Error = {[Pyrometer Reading-Thermocouple Reading]/Thermocouple Reading}*100) Calculated for the Two YSZ Samples with the Pyrometer Emissivity Set at Unity.

4. Fullagar, K., Broomfield, R., Hulands, M., Harris, K., Erickson, G., and Sikkenga, S., "Aeroengine Test Experience with CMSX-4 Alloy Single Crystal Turbine Blades," *39th ASME/IGTI International Gas Turbine and Aeroengine Congress and Exposition*, The Hague, Netherlands, June 13-16, 1994.
5. Newport Corporation, Newport catalog, Irvine, California, 1992, p. k-28-30.
6. DeWitt, D. and Gene Nutter, D., "*Theory and Practice of Radiation Thermometry*, " John Wiley, USA, 1988, p. 91-187.
7. Wyatt, C., *Radiometric System Design*, Macmillan Publishing Company, New York, 1987.
8. Guenther, W., *Concepts of Statistical Inference*, 2nd Edition, McGraw-Hill Kogakusha, Ltd, Tokyo, Japan, 1973.
9. Alaruri, S., Bianchini, L., Brewington, A., Jilg, T. and Belcher, B., "Integrating Sphere Method for Determining the Effective Spectral Emissivity of Superalloys at High Temperature Using a Single Wavelength Pyrometer," *Opt. Eng.* 35, 9, 2736, (1996).
10. J. Daleo and D. Boone, "Failure Mechanisms of Coating Systems Applied to Advanced Turbine Engine Components," *The 42nd ASME Gas Turbine and Aeroengine Congress*, 97-GT-486, Orlando, Florida (June 2-5, 1997).

Paper 22
Author: Alaruri

Q: Evers

Have you made tests in order to check the influence of the view angle on the spectral emissivity? What will the influences be?

A: Unfortunately, I have not measured the spectral emissivity as a function of view angle. There should be a dependence between the view angle and the emissivity.

# Development and application of laser induced incandescence (LII) as a diagnostic for soot particulate measurements

**D. R. Snelling, G. J. Smallwood, I. G. Campbell, J. E. Medlock and Ö. L. Gülder**
National Research Council of Canada
Building M-9, Montreal Road
Ottawa, ON, Canada K1A 0R6

## 1. SUMMARY

LII is a promising diagnostic for *in-situ* measurements of particulates. The LII signal is shown to be proportional to soot volume fraction. Due to the large dynamic range of the LII technique, we have been able to measure time-averaged soot concentrations in the part per billion range with a spatial resolution of ~0.5 mm in each dimension. The decay of the LII signal in the post evaporative region is shown to be a sensitive measure of primary particle size. A numerical model has been developed which accurately predicts post evaporative LII signal decay rates. The prediction of the excitation curve is unsatisfactory, with more work needed to correctly model the particle behaviour during the soot evaporation phase. Also, the model predicts that the prompt LII signal will vary as the 3.33 power of particle diameter. However, this predicted departure from strict proportionality between LII signal and soot volume fraction was not experimentally observed.

## 2. INTRODUCTION

Soot volume fraction measurements are important for studies of soot formation, radiation processes, and for monitoring post-flame particulates. Light extinction is a commonly used diagnostic technique for measuring soot volume fraction. However, it suffers from the drawback of measuring a line-of-sight average, and while tomographic reconstruction can be used to calculate soot profiles in radially symmetric flames, this is not possible in turbulent flames. Elastic scattering of light has been widely investigated for soot measurements but the fact that the signal is proportional to the square of the particle diameter means that the technique is more useful for particle sizing than volume fraction measurements. More importantly, for agglomerated soot particles (which are definitely not spherical), it has become increasingly clear in the last few years that the approach of applying Mie theory by assuming spherical soot particles results in large errors[1-4].

Laser induced incandescence (LII) has emerged as a promising technique for measuring spatially and temporally resolved soot volume fraction in flames[5-14]. In LII the soot is heated by a short duration laser pulse to produce incandescence. With sufficiently high laser energies, numerical models of the heat transfer indicate that the soot particles reach temperatures of 4000-4500 K.[5,6,10,12,13] The resultant radiation, which is blue shifted relative to soot radiation at normal flame temperatures and is of short duration, can readily be detected. LII typically has a temporal resolution of 10 ns and can be used to perform both point measurements and 2-D planar visualization.

In this paper we describe our development of the LII technique for point measurement in flames. Since LII provides only relative soot volume fraction measurements, an absolute calibration is necessary. This was performed in a simple laminar diffusion flame, where the radial soot volume fraction profiles were measured by Abel inversion of line-of-sight attenuation measurements. We have implemented a numerical model of the LII processes to aid in the interpretation of experimental results. Model predictions and their comparison to experiment are presented. Finally, the application of LII to a confined $C_3H_8$/air turbulent diffusion flame is investigated.

## 3. EXPERIMENTAL

### 3.1 Laser Induced Incandescence

The schematic of the LII setup is shown in Fig. 1. A Continuum Surelite1 Nd:YAG laser with Gaussian optics operating at its fundamental wavelength of 1064 nm was used as the pulsed light source. The beam quality was improved by inserting an aperture in the laser cavity. This modification reduced the maximum energy to 40 mJ. Further attenuation of the beam, by using a half wave plate to rotate the plane of polarisation in combination with a vertical polariser, was used to control the energy delivered to the flame. The aperture resulted in a laser beam whose near-field intensity distribution was Gaussian.

The beam was then focussed through a beam expander and a cylindrical lens to form a sheet with Gaussian fit parameters ($1/e^2$ full width) of 3.62 mm (height) and 0.44 mm (width). The beam intensity profiles were near perfect fits to a Gaussian distribution as measured with a Coherent BeamView system. The LII signal from the

*Paper presented at an AGARD PEP Symposium on "Advanced Non-Intrusive Instrumentation for Propulsion Engines", held in Brussels, Belgium, 20-24 October 1997, and published in CP-598.*

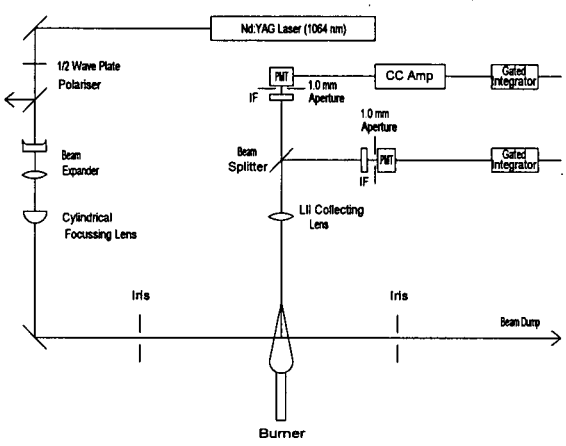


**Figure 1.** Top-view schematic of LII apparatus

centre of the laser sheet was imaged at 2:1 magnification with a 54 mm diameter lens of 190 mm focal length onto apertures of 1.06 mm diameter in front of the photomultipliers (PM's). Thus the sample volume in the flame was a cylinder of diameter 0.53 mm whose length was the width of the laser sheet (0.44 mm).

The LII signal was split equally between two PM's each equipped with an interference filter centred at 455.5 nm with a bandwidth of 11.0 nm. One of the PM's was connected directly to a gated integrator whose gate width was set at 25 ns to measure the peak of the LII signal (subsequently referred to as the prompt signal). The other PM was connected to a charge-coupled amplifier which measured the total charge collected during the LII pulse and thus measured the time integrated LII signal.

### 3.2 Calibration

#### 3.2.1 Flame

The laminar diffusion flame used in these experiments was similar to that used by Gülder[15] except that the fuel tube was 13.9 mm in diameter. The $C_2H_4$ flow rate was 3.27 $cm^3/s$ and the surrounding air flow rate 170 SLPM. The visible flame height was 67 mm.

#### 3.2.2 Line-of-Sight Attenuation

Both 532 and 1064 nm laser attenuation experiments were performed, with a 3 times beam expander followed by a 1 m focal length lens used to reduce the beam diameter through the flame. At 1064 nm the focal beam diameter in the flame, $\omega_0$, was 0.24 mm (Gaussian $1/e^2$ diameter); and the confocal parameter (total distance between the points at which the beam diameter had increased to $\sqrt{2}\cdot\omega_0$) is 160 mm. This ensured that there was little variation in beam size across the maximum flame diameter, which was 6 mm at the heights investigated.

A beam splitter directed part of the pre-flame laser beam onto a silicon photodiode detector (detector A) and the transmitted laser beam was measured with a second detector (B). Signals from both detectors were detected with gated integrators whose outputs were ratioed to give A/B on a shot-by-shot basis. In this way we were able to correct for small changes in laser pulse energy, and the flame transmission could be measured to an accuracy of ~0.25%. The transmission measurements were made every 0.1 mm across the flame, at heights of 30, 35, and 40 mm.

## 4. RESULTS AND ANALYSIS

### 4.1 Attenuation Results

In the Rayleigh limit the soot volume fraction, $f_V$, is given by

$$f_V = \frac{\ln(T)\lambda}{6\pi L E(m)} \qquad (1)$$

where T is the flame transmission, $\lambda$ the wavelength and $L$ the flame width. The complex refractive index is denoted by $m=n+ik$, and $E(m) = -\mathrm{Im}\{(m^2-1)/(m^2+2)\}$, thus

$$E(m) = \frac{6nk}{(n^2-k^2+2)^2+4n^2k^2} \qquad (2)$$

Using the dispersion relationship from Dalzell and Sarofim[16] to calculate the refractive index we obtain: $m$=1.59+0.58$i$ and $E(m)$=0.264 at 532 nm; and $m$=1.63 + 0.7$i$ and $E(m)$=0.303 at 1064 nm.

The Abel inversion of the transmission measurements was performed using the 3 point Abel algorithm of Dasch[17] with a data spacing at the recommended 0.2 mm. The resultant curves are shown in Fig.2, where it can be seen that there is generally very good agreement between the

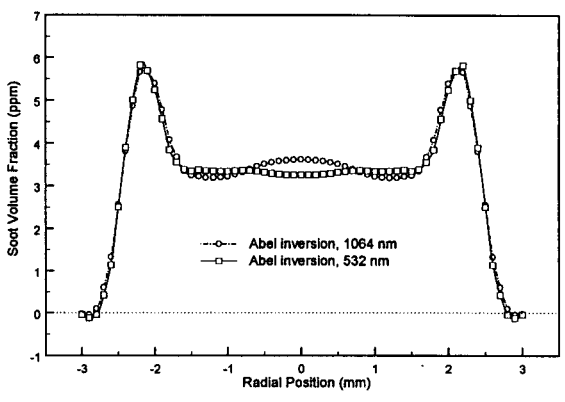


**Figure 2.** Comparison of radial profiles from Abel inversion of line-of-sight attenuation data acquired at 532 nm and 1064 nm. Data was acquired at a height of 40 mm in an ethylene/air flame.

532 nm and 1064 nm data. This agreement is not necessarily expected since the undesirable effect of scattering is enhanced with decreasing wavelength, increasing the laser attenuation beyond what would be expected from absorption, and can thus lead to an overestimate of the soot concentration.[2,18,19] For visible wavelengths, errors of 30-100% in soot concentration are expected depending on the size and morphology of the soot agglomerates. The uncertainty in the refractive index and its wavelength dependence can mask such effects.

### 4.2 LII Calibration

LII measurements were performed at the same locations in the laminar diffusion flame. As the energy of the 1064 nm laser is increased (above the LII detection threshold) there is an initial sharp increase in LII signal. With a peak laser fluence (at the centre of the sheet) of 0.32 J/cm$^2$ a further increase in energy produces very little increase in LII signal as shown in Fig. 3. The LII detection is typically operated in this plateau region.[5,8,13,20,21] We have used a peak laser fluence of 0.48 J/cm$^2$ for our LII measurements, which are shown in Fig. 4 with the 532 nm Abel inverted data for comparison.

In Fig. 4 the LII data has been scaled to the Abel data so that the integrated soot volume fraction over the total flame width is the same for all the curves. In general it can be seen that there is good agreement between the soot profiles from LII and Abel inverted transmission measurements, with the prompt LII data following the Abel inverted data more closely. Thus in the soot concentration range 0.5-5.0 ppm the prompt LII and the extinction measurements are linearly related. This result is in agreement with other studies that have found a linear relationship over this concentration range.[8,21,22] Vander Wal, using gravimetric sampling for calibration, has

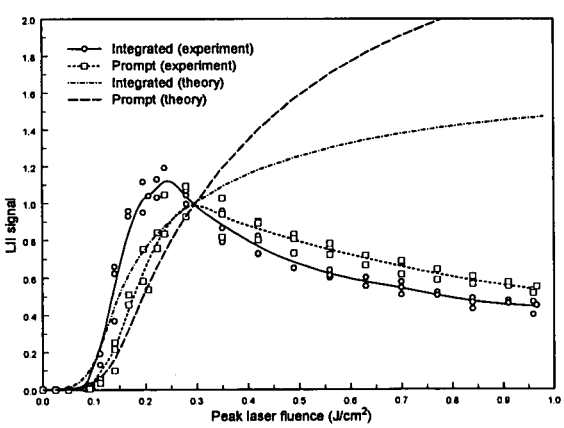


**Figure 3.** Excitation curves indicating relative LII signal as a function of the peak laser fluence for both prompt and integrated signal detection. Measured and predicted values are shown for the region of maximum soot concentration ($r$ = 2.1 mm) at a height of 40 mm in an ethylene/air flame.

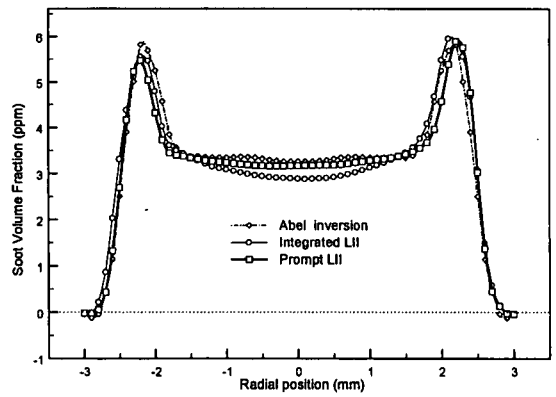


**Figure 4.** Comparison of soot volume fraction determined by LII to radial profiles from Abel inversion of line-of-sight attenuation data at 40 mm above the burner

observed good linearity in the 0.035-1.5 ppm soot concentration range.[23]

## 5. NUMERICAL MODEL

### 5.1 Heat Transfer To and From Soot Particles

The numerical modelling of the transient heating and subsequent radiation and cooling of soot particles exposed to short duration (10 nsec) laser pulses is briefly described below. The approach is similar to that used by several authors.[6,10,12,13,24,25] Our approach most closely follows that of Hofeldt[10] and only the differences between the two models will be emphasized.

The previous LII numerical modeling has assumed the particles to be equivalent spheres and calculated the absorption from Mie theory.[5,6,10,13] In recent years it has become clear that Mie theory based on equivalent spheres introduces large errors in calculating the scattering and absorption of real soot particles[1-4] (and references contained therein), and that soot absorption is well described by Rayleigh theory, provided that the primary particle diameter is within the Rayleigh limit (significantly smaller than the light wavelength).

The equations describing the soot heat transfer presented here are for a more realistic soot morphology in that we assume the soot particles to be agglomerates of $N_P$ just touching primary particles of diameter $d_P$.[1] This approach has also been recently adopted by Mewes et al.[12]

The heat transfer energy balance equation is:

$$C_a q - \frac{2K_a(T-T_0)\pi N_P d_P^2}{(D_{ES}+G\lambda_{MFP})} + \frac{H_v}{M_V}\frac{dM}{dt} + q_{rad} - \frac{1}{6}\pi N_P d_P^3 \rho_S c_s \frac{dT}{dt} = 0 \qquad (3)$$

The first term, $C_a q$, is the absorbed laser energy, where, in the Rayleigh limit, the absorption cross section $C_a$ is given by:

$$C_a = \frac{\pi^2 N_P d_P^3 E(m)}{\lambda} \qquad (4)$$

This will certainly be true in our experiments since we are clearly in the Rayleigh limit, having used 1064 nm laser excitation.

The second term involves heat transfer to the surrounding medium for a particle in the transition regime between continuum and free molecule (Knudsen) heat transfer. Since the mean free path in the gas is typically much larger than the soot particle diameter, the particle is largely in the free molecule limit, and thus the heat transfer coefficient is independent of particle size. $G$ is a geometry dependent heat transfer factor[26], equal to $8f/(\alpha(\gamma+1))$ where $f$ is the Eucken factor (5/2 for monatomic species), $\alpha$ is the accommodation coefficient, and $\gamma=c_p/c_v$ (= 1.40 for air). A value of $\alpha$~0.9 has generally been adopted in previous work.[6,10,13]

The third term is heat loss due to evaporation of the soot and is given by:

$$\frac{dM}{dt} = \frac{\rho_s}{2}\pi D^2 \frac{dD}{dt} = -\pi N_P d_P^2 \frac{\dfrac{P_S(T) N_{AV}}{RT}}{\dfrac{1}{\beta}\left(\dfrac{2\pi M_V(T)}{RT_S}\right)^{1/2} + \dfrac{D_{ES}}{2D_{AB}}} \qquad (5)$$

Again the flux of carbon vapour is dominated by the free molecule regime (the first term in the denominator of Eq. 5) and is independent of particle size. The soot vapour pressure has generally been calculated using fixed values of the heat of vaporisation $H_v$ and soot vapour molecular weight $M_V$. We have used the temperature dependent values of these quantities $P_S(T)$, $M_V(T)$ calculated using the empirical relationships of Leider et al.[27] in solving the equations.

The fourth term, representing radiative loss for a single primary particle, can be approximated as:

$$q_{rad_p} = 4\pi^2 N_P d_P^3 \sigma_{SB} T^4 \left(\frac{E(m)}{\lambda}\right)_{600} \qquad (6)$$

where the expression in parentheses is evaluated at some average wavelength, 600 nm in this case. This approximation, including the selection of evaluation wavelength, is not limiting since soot particle heat loss due to radiation is insignificant compared to the other heat loss terms.

The particle equivalent sphere diameter dependence ($D_{ES}$) in the denominator of Eqs. 3 and 5 is the equivalent sphere diameter given by $D^3_{ES}=N_P d^3_P$ and it reflects the dependence of heat transfer and the flux of evaporating soot on this soot size in the continuum limit. Since the soot particle diameter is very much less than the gas mean free path these continuum terms are not important and for soot evaporation have been neglected in much of the earlier modelling.[6,13] In our approach, these equations constitute a coupled set of differential equations for $D$ and $T$ that have been solved numerically using a Runge-Kutta integration routine. From this solution we can calculate the time history of the LII signal using the relationship:

$$I(\lambda) = \frac{2\pi c^2 h}{\lambda^5}\left[e^{-\frac{hc}{k\lambda T}} - 1\right]^{-1} \pi N_P d_P^2 K_{ap}(\lambda)\, d\lambda \qquad (7)$$

$$\text{where } K_{ap} = \frac{4\pi d_p E(m)}{\lambda}$$

The LII signal $I$ is a function of $T$, $d_P$, $N_P$, time ($t$), and laser fluence ($F$). To calculate values of $I$ to compare with experiment we must integrate $I$ over the range of laser fluence values encountered in the laser sheet. Since our probe volume only occupies a region of the sheet 0.53 mm diameter the distribution of laser fluence is essentially constant in the plane of the sheet. However, there is a Gaussian distribution of fluence across the thickness of the sheet (i.e. along the LII viewing axis). This can be described by

$$F(x) = F_0 \exp\left(-\frac{x^2}{w_x^2}\right) \qquad (8)$$

where the sheet half width $w_x$=0.22 mm, and $F_0$ is the peak fluence at the centre of the sheet. $I(F,t)$ can then be integrated across these fluence values to give a signal $I_G(t)$ that can be compared to our experiments. The prompt and integrated LII signal for a given laser fluence can be obtained by the appropriate time integration of $I_G(t)$.

## 5.2 Comparison Of Model To Experiments

### 5.2.1 LII Excitation

To compare our experimental results to the predictions of the numerical model we need information on both the primary particle diameter and the agglomerate size in our burner. Megaridis and Dobbins[28] have used thermophoretic sampling of an $C_2H_4$/air flame, coupled with electron microscopy, to measure the soot primary particle size in the regions of maximum soot concentration. Their burner is very similar to ours but because of small differences in flow rate and burner diameter our flame height (67.5 mm) lower than theirs (88 mm). We have scaled their measurements accordingly to

our flame heights to obtain the values shown in Table 1.

We have used the method of solution outline above to calculate the expected dependence of the prompt and integrated LII signal as a function of laser energy. The theoretical curves are shown in Fig. 3 where the predicted LII signals are shown as a function of peak laser fluence. Since the LII signal is in arbitrary units, the experimental and theoretical curves have been scaled to a value of 1 at a peak fluence of 0.3 J/cm$^2$.

Although the model satisfactorily predicts the onset of the sharp rise in LII signal, it does not predict the observed fall-off at higher fluence values. The shapes of the experimental excitation curves reported in the literature vary widely. With the exception of Ni et al.[21], in no other study has the excitation fluence been directly measured and reported. Ni et al.[21] used an aperture close to the flame to ensure constant fluence. They observed an LII signal (measured with an 18 ns gate) that peaked at 0.35 J/cm$^2$ and decreased a factor of 2 with a further twofold increase in fluence. Vander Wal et al.[8] observed a similar qualitative behaviour with an imaging system that largely limited the effective fluence variation to that of a presumably Gaussian distribution along the LII collection axis. Other workers[20,22,29] have generally observed a monotonically increasing LII signal with an abrupt decrease in slope at higher fluences.

Our experiences in setting up our experiment was that it was quite difficult to obtain a simple Gaussian distribution of intensities in the LII excitation region. Laser beams whose intensity profiles were markedly non-Gaussian in the near field produced focal images with an intense central spot surrounded by more diffuse, weaker wings. This was particularly true if screens or hard apertures were used to control the laser beam intensity profile. With this type of excitation one would expect an excitation curve that does not saturate since, with increasing laser energy, the weaker radiation in the wings will continue to produce large increases in LII signal after the intense centre core saturates. This points to the necessity of carefully measuring the laser fluence in the region of LII excitation if one is to compare LII saturation behaviour.

**Table 1. Primary particle size ($d_p$), number of primary particles per agglomerate ($N_p$), and the equivalent sphere diameter ($D_{ES}$).[28]**

| Height (mm) | $d_P$ (nm) | $N_P$ (nm) | $D_{ES}$ (nm) |
|---|---|---|---|
| 20 | 13 | 8 | 26 |
| 30 | 29.5 | 35 | 96.5 |
| 35 | 32 | 45 | 113.8 |
| 40 | 32.5 | 60 | 127.2 |

The failure of the LII model to successfully predict the saturation at high fluences is quite dramatic and remains to be explained. It should be remembered that the equations describing the evaporation of soot are only correct in the limit of low vaporization rates[10] which may not be true at the largest excitation fluences used in this and other experiments.

### 5.2.2 LII Decay

It is interesting to compare the experimental LII time decays with model predictions. The experimental decays measured at various radial positions at a 40 mm height in our burner are shown in Fig. 5. The decay curves are, to a good approximation, logarithmic in the time range 300 to 1000 ns. The time constant of these decays decreases dramatically as we go from the region of maximum soot to the centre of the burner. The results of the numeric modelling show that the decay of LII signal in this time range is almost totally dominated by heat transfer to the surrounding gas. Evaporation of soot has ceased to be important with the large drop in particle temperature and radiation is unimportant in this time range. Thus the faster decays are expected since elastic scattering experiments have shown a large decrease in soot particle diameter between the flame centreline and the region of maximum soot.

Using the data in Table 1 we have calculated theoretical decay curves for the region of maximum soot and for the Gaussian excitation used in our experiments. The theoretical curves are shown in Fig. 5 for values of the accommodation coefficient of 0.26 and 0.9. The 0.9 accommodation coefficient curve incorrectly predicts a very fast decay whilst the 0.26 accommodation coefficient curve is in quite good agreement with experiment. The value of 0.9 has been widely used in the literature[6,10,13,14]

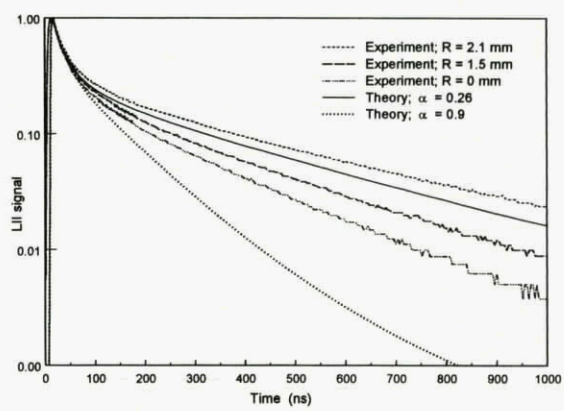


**Figure 5.** LII signal decay curves indicating variation in time constant in post evaporation (>300 ns) region. Measured and predicted values are shown for a height of 40 mm in an ethylene/air flame.

but recent measurements of the accommodation coefficient of nitrogen on solid graphite in the temperature range 300-1000 K give the value of 0.26[30]. Interestingly, a similar calculation assuming an equivalent sphere diameter for the particle and an accommodation coefficient of 0.9 also give good agreement with experiment. This results from a cancellation of errors in that the equivalent sphere model under predicts the heat transfer rate by almost a factor of 4 compared to the agglomerate model, but this is compensated for by the almost 4 times increase in accommodation coefficient.

Will et al.[14] have used LII imaging and ratioed images of LII signals taken at different times to obtain 2-D maps of particle size. The particle size estimation was based on a comparison of the measured decay rate with that calculated from numerical modelling of the soot cooling assuming the particles to be single spheres. It is apparent from our modeling that the size determined from these decays is much closer to that of the primary particle size rather than some average agglomerate size. This conclusion is also supported by the recent analysis of Mewes et al.[12]

We can use our decay data to estimate the primary particle size at the burner centreline. At a height of 40 mm, the ratio of the time constant at $r$=0 mm (230 ns) to that in the region of maximum soot at $r$=2.1 mm (375 ns) is 0.61. Since the decay is dominated by heat transfer to the medium, where the heat loss scales as primary particle area,

$$\frac{d_{P_2}^2}{d_{P_1}^2} = \frac{\tau_2}{\tau_1} \qquad (9)$$

where $\tau$ is the LII signal decay time constant. This result implies a primary particle size of 25.5 nm ($0.61^{1/2}$ x 32.5 nm) at burner centre.

## 6. APPLICATION

To demonstrate the feasibility of eventually applying LII in a gas turbine combustor, preliminary experiments were made in a confined bluff-body stabilized turbulent diffusion flame. This burner was fuelled by propane burning in air at an overall equivalence ratio of 0.65. The flame was stabilized by a weak recirculation zone attached to the bluff-body, and reached a mean peak temperature of 1980 K (Pt/Pt-Rh thermocouple type S) along the centreline of the 100 mm diameter, 400 mm long chamber. The steel walls of the burner were blanketed by insulation to minimize heat transfer losses. A clever window design allowed LII measurements to be made in a grid pattern over an axial range of 57 to 370 mm, at approximately 25 mm steps, and radially at each axial station in 5 mm increments. A weak nitrogen purge minimized soot buildup on the windows.

The incident beam (1064 nm) was unattenuated while the scattered light signal detected at 440 nm suffered attenuation up to 40% in heavy sooting regions. At each grid location 5000 samples of prompt and integrated signals were collected. The mean of the soot volume fractions recorded at each location is reported, providing a time-averaged result in this turbulent flame. Soot was observed to first form at the outer tip of the recirculation zone, approximately 100 mm from the nozzle. Downstream of the 100 mm point the soot levels increased with axial distance along the centreline and the width of the sooting zone also increased with axial distance, as shown in Fig 6. The highest level of soot, averaging 4 ppb, was located on the centreline at the furthest axial location. From gas chromatography measurements, it is known that the bulk of the fuel and lighter hydrocarbon remained within the "recirculation" zone. However, some fuel penetrated the recirculation zone, to form soot in the slow moving high temperature zone.

Over the measuring region a maximum of only 4% of the 5000 samples produced a measurable LII signal. The probability of a single shot recording a signal significant enough to determine soot volume fraction is indicated in Fig. 7. Unlike the soot volume fraction measurements,

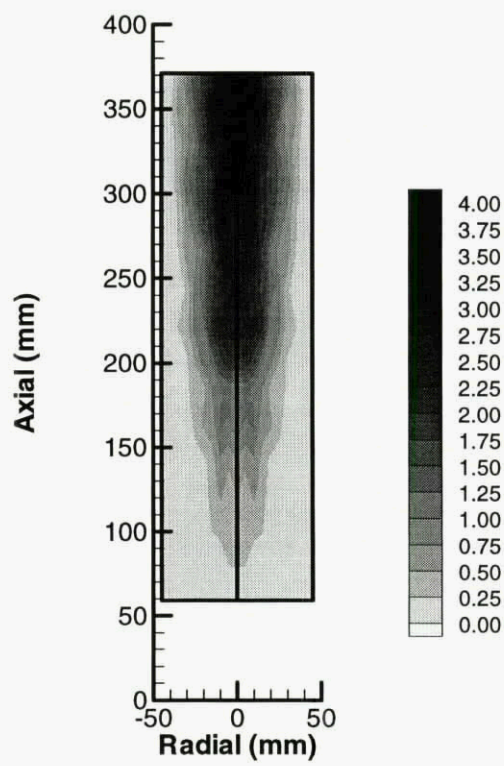


**Figure 6.** Distribution of time-averaged soot volume fraction (parts per billion) acquired by LII in a confined turbulent diffusion flame. Data at each grid location is the mean of 5000 single-shot measurements.

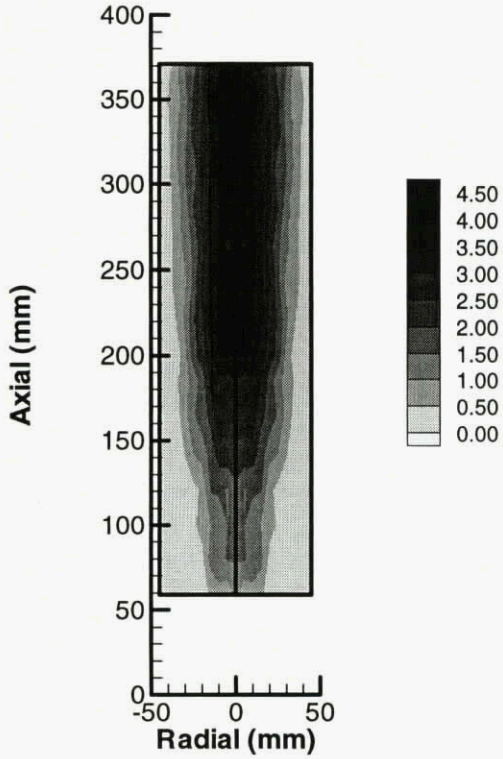


**Figure 7.** Probability (in percent) that measurable quantities of soot are present in the probe volume on a single-shot basis. Data acquired in a propane/air diffusion flame by LII.

this probability did not increase beyond 200 mm from the nozzle, although the width of the zone was observed to expand.

## 7. CONCLUSIONS

Significant progress has been made in the characterization of the LII process, and in development of LII for single-shot time-and-space resolved quantitative measurement of particulate concentration in practical applications, such as turbulent combustion.

1. The LII signal has been shown to be proportional to soot volume fraction over the range 0.5 - 5 ppm.

2. Due to the large dynamic range of the LII technique we have been able to estimate soot concentrations in the 10 part per billion range while maintaining a spatial resolution of ~0.5 mm cubed. A further factor of ten increase in sensitivity could be obtained by relaxing the dimensions of the probe volume to a 1.0 mm cube.

3. The rate of decay of the LII signal in the post evaporative region (>300 ns after excitation) is shown to be a sensitive measure of particle size. For soot, the size measured appears to be the primary particle size rather that some average agglomerate size. While the numerical model was able to successfully predict post evaporative LII signal decay rates.

4. More work needs to be done before the currently available LII models can correctly predict the soot particle behaviour during soot evaporation.

5. The application of LII to measure soot volume fraction in a turbulent diffusion flame has been successfully demonstrated.

## 8. FUTURE WORK

It remains to be demonstrated that the LII signal is strictly proportional to soot volume fraction over several orders of magnitude change in soot concentration. Both our results and the original modelling of Melton[6] predict that the prompt LII signal will vary as the 3.33 power of particle diameter (for LII detection at 450 nm). This predicted departure from strict proportionality between LII signal and soot volume fraction has not been experimentally observed in this work or by others.

**Acknowledgements:**

This work was supported in part by PERD Committee 1.5 of the Canadian Government, by the National Research Council's internal research funds, and by the Department of National Defence. We thank: Dan Gareau for his technical support in configuring the LII apparatus and the laminar burner, and in performing the experiments; Doug Logan for his technical support with the turbulent burner; and Dan Fetter for assistance in modelling and data analysis.

**Nomenclature:**

| | |
|---|---|
| $c$ | - speed of light |
| $C_a$ | - soot particle absorption cross section |
| $c_p$ | - specific heat at constant pressure |
| $c_s$ | - specific heat of carbon |
| $c_v$ | - specific heat at constant volume |
| $D_{AB}$ | - interdiffusion coefficient for soot vapour into surrounding gas |
| $D_{ES}$ | - diameter of soot equivalent sphere |
| $d_P$ | - diameter of soot primary particles |
| $f$ | - Eucken factor |
| $G$ | - geometry dependent heat transfer factor |
| $H_v$ | - heat of vaporisation |
| $K_a$ | - thermal conductivity of ambient air |
| $K_{ap}$ | - absorption efficiency (for primary particles) |
| $K_n$ | - Knudsen number ($K_n=\lambda_{MFP}/D_{ES}$) |

$M$ - mass of carbon
$M_V$ - molecular weight of carbon vapour
$M_A$ - molecular weight of air
$N_{av}$ - Avogadro's number
$N_P$ - number of primary particles in agglomerate
$P_S(T)$ - pressure of soot vapour
$q$ - laser fluence
$T$ - soot surface and vapour temperature
$T_0$ - gas temperature
$\alpha$ - accommodation coefficient
$\gamma$ - $c_p/c_v$
$\lambda$ - wavelength
$\lambda_{MFP}$ - mean free path
$\rho_s$ - density of soot
$\sigma_{SB}$ - Stefan-Boltzmann constant
$\tau$ - LII decay signal time constant
T - light transmission through flame

**References**


1. R. A. Dobbins and C. M. Megaridis, "Morphology of flame-generated soot as determined by thermophoretic sampling," Langmuir **3**, 254-259 (1987).
2. R. A. Dobbins and C. M. Megaridis, "Absorption and scattering of light by polydisperse aggregates," Applied Optics **30**, 4747-4754 (1991).
3. U. O. Koylu and G. M. Faeth, "Optical properties of overfire soot in buoyant turbulent diffusion flames at long residence times," Journal of Heat Transfer **116**, 152-159 (1994).
4. U. O. Koylu and G. M. Faeth, "Optical properties of soot in buoyant laminar diffusion flames," Journal of Heat Transfer **116**, 971-979 (1994).
5. C. J. Dasch, "New soot diagnostics in flames based on laser vaporization of soot," 20th Symposium (International) on Combustion, , 1231-1237 (1984).
6. L. A. Melton, "Soot diagnostics based on laser heating," Applied Optics **23**, 2201-8 (1984).
7. J. E. Dec, A. O. zur Loye, and D. L. Siebers, "Soot distribution in a D.I. diesel engine using 2-D laser-induced incandescence imaging," SAE Transactions **100**, 277-288 (1991).
8. R. L. Vander Wal and K. J. Weiland, "Laser-induced incandescence: Development and characterization towards a measurement of soot-volume fraction," Applied Physics B **59**, 445-452 (1994).
9. R. Puri, T. F. Richardson, R. J. Santoro, and R. A. Dobbins, "Aerosol dynamic processes of soot aggregates in a laminar ethene diffusion flame," Combustion and Flame **92**, 320-333 (1993).
10. D. L. Hofeldt, "Real-time soot concentration measurement technique for engine exhaust streams," SAE Paper No. 930079 (1993).
11. P. E. Bengtsson and M. Alden, "Soot-visualization strategies using laser techniques: Laser-induced fluorescence in C2 from laser-vaporized soot and laser-induced soot incandescence," Applied Physics B **60**, 51-59 (1995).
12. B. S. Mewes and J. M. Seitzman, "Soot volume fraction and particle size measurements with laser-induced incandescence," Applied Optics **36**, 709-717 (1997).
13. N. P. Tait and D. A. Greenhalgh, "PLIF imaging of fuel fraction in practical devices and LII imaging of soot," Berichte der Bunsengesellschaft fuer Physikalische Chemie **97**, 1619-1625 (1993).
14. S. Will, S. Schraml, and A. Leipertz, "Two-dimensional soot-particle sizing by time-resolved laser-induced incandescence," Optics Letters **20**, 2342-2344 (1995).
15. Ö. L. Gülder, "Influence of hydrocarbon fuel structural constitution and flame temperature on soot formation in laminar diffusion flames," Combustion and Flame **78**, 179-194 (1989).
16. W. H. Dalzell and A. F. Sarofim, "Optical constants of soot and their application to heat flux calculations," Journal of Heat Transfer **91**, 100-104 (1969).
17. C. J. Dasch, "One-dimensional tomography: a comparison of Abel, onion-peeling, and filtered backprojection methods.," Applied Optics **31**, 1146-1152 (1992).
18. R. A. Dobbins, R. J. Santoro, and H. G. Semerjian, "Analysis of light scattering from soot using optical cross sections for aggregates," 23rd Symposium (International) on Combustion , 1525-1532 (1990).
19. G. M. Faeth and U. O. Koylu, "Soot morphology and optical properties in nonpremixed turbulent flame environments," Combustion Science and Technology **108**, 207-229 (1995).
20. C. R. Shaddix and K. C. Smyth, "Laser induced incandescence measurements of soot production in flickering methane, propane, and ethylene diffusion flames," Combustion and Flame **107**, 418-452 (1994).
21. T. P. Ni, J.A.; Gupta, S.; Santoro, R.J., "Two-dimensional imaging of soot volume fraction by the use of laser-induced incandescence," Applied Optics **34**, 7083-7091 (1995).
22. B. Quay, T. W. Lee, T. Ni, and R. J. Santoro, "Spatially resolved measurements of soot volume fraction using laser-induced incandescence," Combustion and Flame **97**, 384-392 (1994).
23. R. L. Vander Wal, Z. Zhou, and M. Y. Choi, "Laser-induced incandescence calibration via gravimetric sampling," Combustion and Flame **105**, 462-470 (1996).
24. A. C. Eckbreth, T. J. Anderson, and G. M. Dobbs, "Conditional sampling for fuel and soot in CARS thermometry," 21st Symposium (International) on Combustion , 1747-1754 (1986).
25. C. J. Dasch, "Continuous-wave probe laser investigation of laser vaporization of small soot particles in a flame," Applied Optics **23**, 2209-2215 (1984).

26. B. J. McCoy and C. Y. Cha, "Transport phenomena in the rarefied gas transition regime," Chemical Engineering Science **29**, 381-388 (1974).
27. H. R. Leider, O. H. Krikorian, and D. A. Young, "Thermodynamic properties of carbon up to the critical point," Carbon **11**, 555-563 (1973).
28. C. M. Megaridis and R. A. Dobbins, "Comparison of soot growth and oxidation in smoking and non-smoking ethylene diffusion flames," Combustion Science and Technology **66**, 1-16 (1989).
29. J. Appel, M. Jungfleisch, M. Marquardt, R. Suntz, and H. Bockhorn, "Assessment of soot volume fractions from laser-induced-incandescence by comparison with extinction measurements in laminar premixed flat flames," 26th Symposium (International) on Combustion , 2387-2395 (1996).
30. O. Leroy, J. Perrin, J. Jolly, and M. Pealat, "Thermal accommodation of a gas on a surface and heat transfer in CVD and PECVD experiments.," Journal of Physics D **30**, 499-509 (1997).

# Application de la Fluorescence de l'Iode Induite par Laser aux Mesures de Pression, Température et Vitesse.

**Lefebvre X., Leporcq B.**

Office National d'Etudes et de Recherches Aérospatiales,

Institut de Mécanique des Fluides de Lille,

5, Boulevard Painlevé, F- 59045, Lille - Cedex, France.

## 1. SOMMAIRE

La fluorescence induite de l'iode par laser notée F.I.I.L., est une méthode optique non intrusive qui permet non seulement de visualiser un écoulement, mais aussi d'accéder aux grandeurs locales et instantanées telles que la pression, la température et la vitesse. Après validation dans une cellule statique où les paramètres P et T sont facilement mesurables, des mesures des trois paramètres ont été réalisées sur un jet supersonique et dans une boucle aéraulique en utilisant un laser multimode gaussien et un laser à colorant monomode accordable.

## 2. INTRODUCTION

Le développement de la fluorescence de l'iode par laser a débuté dans le cadre de la qualification des zones de mélange des lasers chimiques [1, 2, 3]. Le champ d'application de cette technique s'étend de la simple visualisation par tomoscopie, permettant par exemple d'étudier le mélange de jets [4 à 6] aux véritables moyens d'investigation métrologiques [7, 8]. La fluorescence de l'iode induite par laser permet en effet d'effectuer des mesures locales et non intrusives de concentration [9], de vitesse [10, 11], de température [12, 13] et de pression [14 à 17]. Ensemencé de façon homogène avec des molécules d'iode dont la concentration est de quelques parties par million, l'écoulement est éclairé par un rayonnement laser absorbé par l'iode, le rayonnement fluorescent émis dépend des grandeurs caractéristiques locales de l'écoulement. L'ensemencement par un traceur gazeux permet un suivi parfait de l'écoulement, même dans les zones de forts gradients de pression. Le volume de mesure peut être réduit à $10^{-3}$ $mm^3$. Le découplage entre les réflexions parasites du rayonnement excitateur et la fluorescence est réalisé facilement au moyen d'un filtre en verre coloré. Des mesures sont possibles jusqu'à une distance d'environ 100 µm d'une paroi.

## 3. PRINCIPE DE LA METHODE

D'une manière générale, le phénomène de fluorescence correspond à la désactivation d'un état excité d'un atome, ou d'une molécule, par émission lumineuse spontanée. L'état excité peut être atteint par absorption d'un rayonnement laser dont la longueur d'onde est accordée sur l'une des raies d'absorption de l'espèce fluorescente. Dans le cas de l'iode la fluorescence se produit dans une bande de fréquence comprise entre 520 nm et 1000 nm, le maximum de fluorescence se situant dans la partie jaune du spectre électromagnétique.

La réaction de pompage de l'iode correspondant à l'absorption des photons, s'écrit pour un rayonnement à la longueur d'onde $\lambda$ :

$$I_2X_{(v''=0\,;\,J''=j'')} + h\nu \xrightarrow[\lambda]{} I_2B_{(v'=i\,;\,J'=j')}$$

où v' représente le niveau vibrationnel et J' le niveau rotationnel de l'état excité $I_2B$, $I_2X$ le niveau fondamental, v" un de ses niveaux vibrationnels et J" un de ses niveaux rotationnels (figure 1).

L'émission lumineuse due à la fluorescence correspond à la réaction :

$$I_2B_{(v'=i\,;\,J'=j')} \xrightarrow[\Gamma_0]{} I_2X_{(v''=k\,;\,J''=j'')} + h\nu_{(v'=i\,;\,J'=j',\,v''=k\,;\,J''=j'')}$$

avec $\Gamma_0$, probabilité d'émission spontanée.

La désactivation sur un niveau vibrationnel v' de l'état X s'effectue suivant une probabilité donnée par le facteur de Franck-Condon.

L'émission fluorescente est limitée par la désactivation non radiative due aux collisions avec d'autres molécules :

$$I_2B_{(v'=i\,;\,J'=j')} + M \xrightarrow[Kq]{} I_2X_{(v''=k\,;\,J''=j'')} + M$$

où M est une molécule de l'écoulement et Kq la constante de désactivation dépendant de la température [14]. La compétition entre l'émission fluorescente des molécules d'iode et leur désactivation collisionnelle, permet de rendre compte de l'évolution de la pression statique dans un écoulement. La détermination de la température s'appuye sur l'évolution de la fraction de Boltzmann en fonction de la température.

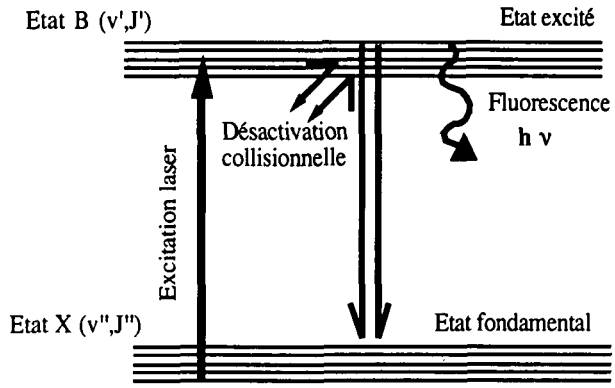


Figure 1 : Mécanismes d'absorption et d'émission

La résolution des équations gouvernant la cinétique de l'absorption du rayonnement laser par un niveau d'absorption de l'iode, ainsi que la désactivation de l'état

*Paper presented at an AGARD PEP Symposium on "Advanced Non-Intrusive Instrumentation for Propulsion Engines", held in Brussels, Belgium, 20-24 October 1997, and published in CP-598.*

excité conduit à la détermination de la concentration en iode dans l'état excité [18 à 22]. Le signal de fluorescence est directement proportionnel à la concentration en iode excitée $[I_2B]$ qui dépend de la pression et de la température.

Le rayonnement laser absorbé dépend de la nature de celui-ci, en particulier de sa fréquence, mais aussi de son caractère monomode.

L'iode est un traceur moléculaire intéressant, sa pression de vapeur saturante est de l'ordre de quelques Pascals à la température ambiante [23], ce qui permet un ensemencement de l'écoulement principal suffisant pour assurer la présence de quelques parties par million. Le spectre d'absorption de l'iode dans la partie visible du spectre électromagnétique est riche de plusieurs milliers de raies dont chacune a été parfaitement caractérisée par Luc et Gerstenkorn [24, 25]. Chaque raie présente une sensibilité à la pression et à la température plus ou moins significative.

### 3.1 Cas d'un rayonnement laser multimode

Le moyen le plus simple de réaliser des mesures par fluorescence de l'iode induite par laser est d'utiliser le rayonnement vert à $\lambda$=514,5 nm multimode à large bande spectrale du laser à argon ionisé puisque l'émission coïncide fortuitement avec la double raie d'absorption P13-R15 (43-0). La largeur de raie d'un laser à argon ionisé multimode gaussien s'étend sur une bande d'environ 10 GHz (0,33 $cm^{-1}$), elle couvre un domaine spectral d'environ 0,165 $cm^{-1}$ de part et d'autre du centre de la raie laser [26]. La raie d'émission laser à $\lambda$=514,5 nm est décalée de 2 GHz du centre de la double raie d'absorption P13-R15 (43-0) du spectre d'absorption de l'iode. Il peut donc y avoir transfert résonnant d'énergie.

Le rayonnement laser excitateur à large bande spectrale à caractère multimode est susceptible d'être absorbé par des raies adjacentes à la raie P13-R15 situées dans le domaine spectral défini par la largeur de la raie laser. Le signal total de fluorescence est égal à la somme des contributions pondérées par leur facteur de force de raie, apportées par chaque raie compte tenu de sa position spectrale $\Delta\nu_i$. Le facteur de la force de raie est égal au produit de l'intensité et du facteur de Franck-Condon. Chaque raie étant indicée i, le signal de fluorescence total s'exprime par la relation :

$$S_f = C_{opt} V_c B_{12} \frac{A_{21}}{A_{21}+Q} X_{I2} \frac{P}{kT} \sum_i f_{1i}(T,J'') FFC_i P_{eff}(P, T, \Delta\upsilon_i)$$

avec :

$A_{21}$, coefficient d'émission spontanée

$B_{12}$, coefficient Einstein d'absorption

Copt, constante liée à la chaîne optique

$FFC_i$, facteur de Franck-Condon caractérisant la raie i

$f_{1i}(T,J'')$, fraction de Boltzmann de la raie d'absorption i à la température T

k, constante de Boltzmann

P, pression

$P_{eff}$, densité spectrale du rayonnement incident

Q, taux de désactivation collisionnelle

$S_f$, signal de fluorescence

T, température

Vc, volume de collection

$X_{I2}$ , fraction molaire d'iode.

$\Delta\nu_i$, décalage spectral

Le signal de fluorescence théorique est calculé à l'aide des 35 raies d'absorption contenues dans une bande spectrale de 2 $cm^{-1}$ correspondant à la zone spectrale soumise à l'élargissement collisionnel dont la manifestation est significative pour des pressions élevées. Cet élargissement collisionnel diminue également l'intensité de fluorescence. Il a été montré que le signal de fluorescence induit par un rayonnement laser multimode gaussien est très dépendant de la température avec la fraction de Boltzmann $f_1(T)$ et de la pression à travers le terme de désactivation collisionnelle Q.

### 3.2 Cas d'un rayonnement laser monomode

Lorsque le signal de fluorescence est le résultat de l'absorption par l'iode d'un rayonnement issu d'un laser monomode de largeur de raie faible (500kHz) exactement accordé à une raie d'absorption de l'iode, l'expression de celui-ci est considérablement simplifié puisqu'inversement proportionnel à la pression :

$$S_f = C_{opt} V_c B_{12} A_{21} P_{laser} f_1(T,J'') X_{I_2} \frac{1}{P}$$

avec : $P_{laser}$, puissance laser.

L'analyse de l'expression du signal de fluorescence montre une double dépendance aux paramètres de pression et température. L'exploitation de cette propriété conduit à la possibilité de mesure simultanée de ces deux grandeurs de l'écoulement par découplage paramétré.

## 4. APPLICATION AUX MESURES DE PRESSION

Le signal de fluorescence est le résultat de la compétition entre la fluorescence et la désactivation collisionnelle. L'exploitation de ce signal permet donc d'effectuer des mesures locales de pression.

### 4.1 Mesure de la pression avec un rayonnement laser multimode

Pour déterminer la pression à partir du signal de fluorescence mesuré expérimentalement, une connaissance de la température locale est nécessaire. Celle-ci peut être déterminée soit par une mesure expérimentale supplémentaire, soit en effectuant une hypothèse sur l'évolution de la température [27], soit par fluorescence induite par laser en s'appuyant sur la méthide décrite au chapitre 5.

Dans le cas particulier d'un écoulement supposé isentropique, le signal de fluorescence pourra s'exprimer sous la forme d'une fonction de la pression uniquement :

$$S_f = K.f(P, T) = K.f(P, Cte\ P^{\left(\frac{\gamma-1}{\gamma}\right)})$$

Une approximation polynomiale de l'expression du signal de fluorescence a été déterminée en fonction de la pression et pour une température $T=(cte\ P^{(\gamma-1)/\gamma})$, sur un domaine de pression encadrant celui de l'écoulement. Cette approximation a été effectuée à l'aide d'un polynôme de Tchebychev :

$$S_f = K'\ g(P)$$

La constante de proportionnalité K' est déterminée à l'aide d'une mesure à un point de référence où la pression est supposée connue :

$$S_{f\,ref} = K'\ g(P_{ref}, T_{ref})$$

L'équation $S_f = K'\ g(P)$ est ensuite résolue par une méthode itérative utilisant des dichotomies.

### 4.2 Mesure de la pression avec un rayonnement laser monomode

Pour effectuer des mesures de pression dans des écoulements où il n'existe pas de relation connue à priori entre la pression et la température, il est nécessaire de parvenir à découpler l'influence de ces grandeurs. Pour minimiser la dépendance en température du terme $f_l(T,J")$ dans l'expression du signal de fluorescence afin d'en extraire uniquement la pression, il est nécessaire d'étudier l'évolution de la fraction de Boltzmann $f_l(T,J")$ en fonction de la température et du nombre rotationnel fondamental J". La fraction de la population des molécules d'iode du niveau (v, J), est décrite par le produit de la fraction vibrationnelle $f_v$ des molécules dans l'état vibrationnel v et de la fraction rotationnelle $f_r$ dans l'état rotationnel J" [20] :

$$f_l(T, J") = FGH(J").(2J"+1)\left(\frac{\theta_r}{T}\right)e^{-J"(J"+1)\left(\frac{\theta_r}{T}\right)}.e^{-v\left(\frac{\theta_v}{T}\right)}.\left(1-e^{-\left(\frac{\theta_v}{T}\right)}\right)$$

avec :

J", niveau quantique rotationnel de la raie d'absorption

v, niveau quantique vibrationnel de la raie d'absorption

FGH(J"), constante caractérisant la structure hyperfine de la raie d'absorption

$\theta_r$ , température rotationnelle de la molécule d'iode

$\theta_v$ , température vibrationnelle de la molécule d'iode.

La possibilité de rendre minimale la dépendance en température de la fraction de Boltzmann repose sur le choix d'un état rotationnel dont la population est peu sensible à une variation de température dans le domaine de température de l'expérimentation (figure 2). Ceci est possible en analysant la dérivée partielle de la fraction rotationnelle en fonction de la température. Le niveau rotationnel optimal noté $J_{opt}$ est :

$$J"_{opt} = 0{,}83\sqrt{\frac{T}{B_v(cm^{-1})}}$$

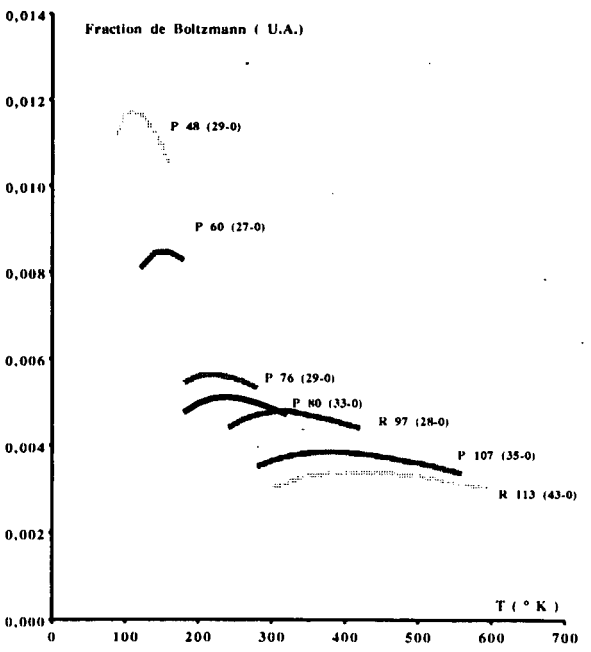


Figure 2 : Evolution de la fraction de Boltzmann en fonction de la température pour différentes raies d'absorption

Le choix du niveau rotationnel optimal est très important pour plusieurs raisons [28, 29] :

- pour minimiser l'effet de la température sur la fraction de Boltzmann ;
- pour avoir une population dans l'état absorbant la plus forte possible et un facteur de Franck Condon [25] le plus élevé possible, le signal de fluorescence étant directement proportionnel à ces grandeurs ;
- pour sélectionner une raie d'absorption la plus isolée possible des raies d'absorption voisines pour minimiser leurs contributions sur le comportement global du signal de fluorescence mesuré. En figure 2 les différentes raies d'absorption présentent un plateau dans l'évolution de la fraction de Boltzmann pour un domaine de température donné. L'utilisation d'un laser à colorant accordable s'impose.

La mesure de la pression est ensuite déduite du signal de fluorescence obtenu par excitation d'une raie d'absorption de l'iode présentant le niveau rotationnel J" optimal dans la gamme de température donné.

Ainsi le signal de fluorescence est exprimé comme un terme inversement proportionnel à la pression pour la raie d'absorption principale, et des termes supplémentaires décrivant la contribution des raies d'absorption voisines à cette raie principale :

$$S_F = \sum_{1}^{Nb\ raies} S_{F_i} = K\, f_l(T)\,\frac{1}{P} + \sum_{1}^{Nb\ raies\ Adjacentes} S_{F_j}$$

La contribution des raies d'absorption voisines est connue. Le signal de fluorescence expérimental est ensuite comparé à la valeur du signal de fluorescence calculé [30 à 33]. Deux techniques sont alors utilisées, d'une part celle utilisant une mesure de référence suivie d'une résolution itérative, d'autre part celle s'appuyant sur l'évolution complète du signal de fluorescence par corrélation avec un signal théorique à pression et température connues issu d'une bibliothèque. Cette seconde technique présente l'avantage de déterminer également la température; cette technique est détaillée au paragraphe 5.2..

## 5. APPLICATION AUX MESURES DE TEMPÉRATURE

Il a été montré que la fraction de Boltzmann joue un rôle déterminant dans la mesure de la température par fluorescence induite de l'iode par laser.

### 5.1 Mesure de la température avec un rayonnement laser multimode

Pour des pressions supérieures à 20000 Pa, à la température ambiante le taux de désactivation collisionnelle Q étant très supérieur au taux d'émission spontanée $A_{21}$, le terme $A_{21}/(A_{21}+Q)$ caractérisant l'efficacité de la fluorescence se réduit à $A_{21}/Q$ [34]. L'expression du taux de désactivation collisionnelle dépend de la température et de la pression et d'une constante caractérisant le mélange air-iode présent dans l'écoulement [35]:

$$Q = C_{q\,(air\text{-}iode)}\,\frac{P}{\sqrt{T}}$$

A partir des approximations justifiées telle que la faible influence en température du terme $P_{eff}$ dans le cas de la double raie P13-R15 et des expressions du taux de désactivation

collisionnelle et de la fraction de Boltzmann, l'expression du signal de fluorescence normalisé par la puissance laser mesurée localement se résume à une expression à une seule variable, la température :

$$S_f = \frac{C'}{T^{\frac{3}{2}}} e^{-\left(J(J+1)\frac{\theta_r}{T}\right)} (1-e^{-\left(\frac{\theta_v}{T}\right)})$$

avec $\Theta_v$, la température caractéristique vibrationnelle ($\Theta_v$=308,62K) et $\Theta_r$, la température caractéristique rotationnelle ($\Theta_r$=0,0538K). C', est une constante incluant les constantes physicochimiques de la molécule, la fraction d'ensemencement, le volume de collection du signal, la chaîne optique ainsi que les termes de degré 0 apparaissant dans l'expression de la fraction de Boltzmann en ne considérant que les raies d'absorption du niveau fondamental v"= 0. La mesure de la température à partir du signal de fluorescence expérimental est possible de façon similaire aux mesures de pression, la constante C' est évaluée à partir d'un point de l'écoulement où la pression et la température sont connues.

A partir de cette expression du signal de fluorescence il est donc possible de déterminer l'évolution de la température dans l'écoulement puis d'utiliser ces valeurs pour déterminer l'évolution de la pression. La pression est alors obtenue par résolution itérative d'une équation relativement complexe puisqu'il est nécessaire d'évaluer la fraction de Boltzmann de chacune des trente cinq raies d'absorption. Les évolutions de la pression et de la température dans un écoulement peuvent être connues à partir d'une mesure unique du signal de fluorescence.

### 5.2 Mesure de la température avec un rayonnement laser monomode et couplage aux mesures de pression

La mesure de la température locale d'un écoulement par fluorescence induite de l'iode par laser nécessite l'emploi d'un laser à colorant monomode accordable [36]. La température est obtenue à partir du rapport des signaux de fluorescence de deux lignes d'absorption moléculaire excitées au cours d'un même balayage en longueur d'onde. Pour déterminer la température, il est nécessaire de faire le rapport des maxima de deux signaux de fluorescence résultant de l'excitation de deux niveaux rotationnels issus d'un même niveau vibrationnel v" :

$$T = B / \ln((S_{F2}/S_{F1})/A)$$

Où A et B sont des constantes définies par :

$$A = (FGH(J_2).Cte_2 / FGH(J_1).Cte_1)\frac{(2J_2+1)}{(2J_1+1)}$$

$$B = [J_1(J_1+1) - J_2(J_2+1)]\,\theta_r$$

Dans le cas de mesures simultanées de pression et de température, une raie d'émission laser accordable est utilisée pour exciter sélectivement et successivement deux transitions de l'iode, la première correspondant à un niveau rotationnel $J''_{opt}$, la seconde présentant une évolution de la fraction de Boltzmann sensible dans le domaine de température de l'écoulement. Dans le cas choisi, le laser à colorant balaye un domaine de fréquence de 30 GHz dans la région spectrale de l'iode contenant les deux transitions R97(28-0) et P60(27-0) proche de 543 nm. Ces deux raies d'absorption présentent respectivement une bonne sensibilité à la température et à la pression, pour un domaine de température donné.

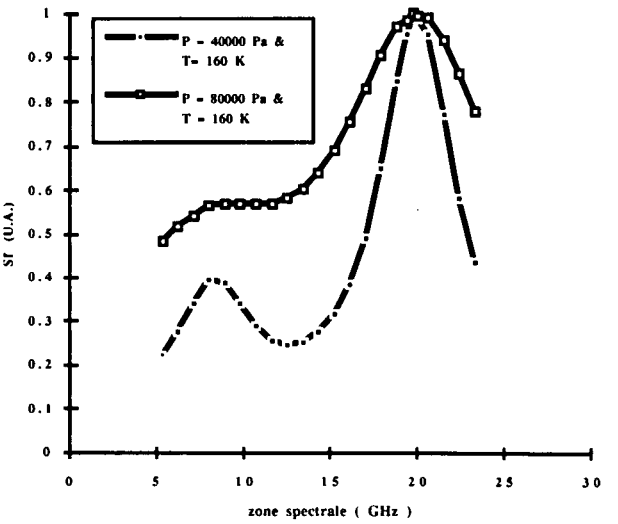


Figure 3 : Evolution du signal de fluorescence à température constante

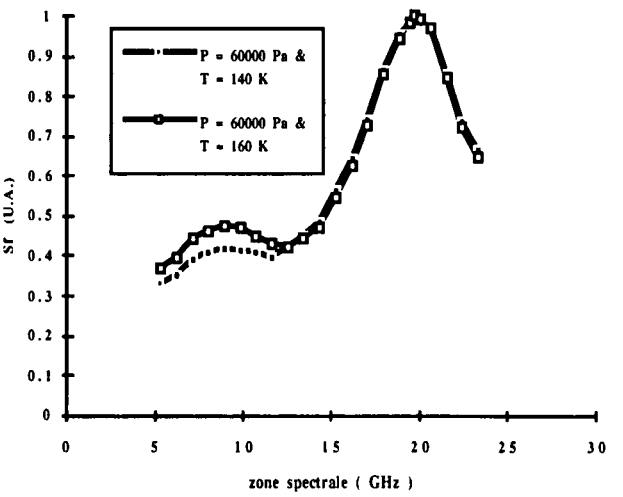


Figure 4 : Evolution du signal de fluorescence à pression constante

Les figures 3 et 4 montrent l'évolution du signal de fluorescence théorique dans la bande d'absorption contenant les raies d'absorption R97 et P60 à pression constante pour différentes températures et inversement. Une bibliothèque de spectres de référence a été construite pour ces deux raies, pour des pressions comprises entre 10 000 Pa et 200 000 Pa par pas de 2 500 Pa et pour des températures comprises entre 100 K et 400 K par pas de 5 K prenant en compte les raies d'absorption voisines dans une gamme spectrale de 60 GHz corespondant à l'élargissement collisionnel autour de ces deux raies principales.

Le signal de fluorescence expérimental obtenu par excitation successive de ces deux raies d'absorption est ensuite comparé à la bibliothèque de spectres théoriques. La corrélation des signaux théoriques et expérimentaux fournit directement les mesures de pression et de température dans le volume de mesure, sans recours à une mesure de référence en un point de l'écoulement où les paramètres P et T sont connus.

## 6. APPLICATION AUX MESURES DE VITESSE

Il a été montré que la technique de mesure de pression et de température par FIL pouvait être aisément couplée à des mesures de vitesse par vélocimétrie laser interférentielle ou bi-point [37, 38], le rayonnement laser étant identique.

Le décalage spectral Doppler d'une raie d'un traceur fluorescent en mouvement dans l'écoulement est proportionnel à la composante de la vitesse dans la direction excitatrice du rayonnement laser monomode accordée sur cette raie d'absorption [12]. Le décalage Doppler est :

$$\Delta \nu_D = \frac{u}{\lambda}$$

avec :

$\Delta \nu_D$ décalage Doppler en fréquence,

u module de la composante de la vitesse suivant la direction de propagation de la radiation,

c vitesse de la lumière,

$\nu_0$ fréquence de la radiation laser.

Deux méthodes de mesure de vitesse par F.I.L. ont été estimées.

La première méthode utilisant le balayage en fréquence est la plus précise, mais son emploi doit être réservé à des écoulements stationnaires dont la vitesse est limitée inférieurement à 20 m/s. Cette technique donne simultanément une mesure de la pression et une mesure d'une composante de la vitesse.

La méthode utilisant une fréquence laser fixe présente une résolution temporelle bien supérieure à la méthode utilisant le balayage en fréquence. Cette deuxième technique permet d'effectuer des mesures de vitesses instationnaires inférieures à 1000 m/s pour des écoulements dont la pression est inférieure à 50000 Pa. Son emploi peut être envisagé pour l'étude d'écoulements instationnaires.

### 6.1 Mesure du décalage Doppler par balayage de la raie laser

Le faisceau laser est divisé au moyen d'une lame séparatrice, puis dirigé par un jeu de miroirs vers le volume de mesure pour former un couple de deux faisceaux coaxiaux à propagation opposée. La fréquence du laser accordable est calée au voisinage de la position spectrale d'une raie d'absorption connue, puis un balayage en fréquence est effectué sur un domaine spectral correspondant à la largeur de raie.

Le signal de fluorescence relatif à chacun des deux faisceaux est obtenu de manière indépendante par l'alternance du passage du rayonnement vers le volume de mesure [39]. Deux spectres correspondant à chacun des sens de propagation du rayonnement laser sont obtenus et sont décalés en fréquence du double du décalage Doppler. Ce décalage temporel de l'excitation laser est réalisé au moyen d'un obturateur mécanique placé juste après le dispositif de séparation en deux faisceaux. On en déduit la composante cherchée de la vitesse, voire la pression et la température par exploitation complète du signal de fluorescence.

Lorsque l'écoulement est bidimensionnel, il est nécessaire de déterminer successivement les deux composantes du vecteur vitesse $u_1$ et $u_2$. Trois faisceaux laser à directions linéairement indépendantes sont alors utilisés afin de décomposer le vecteur vitesse sur la base formée par les faisceaux F1 et F2 et au troisième F3, dont la direction est à 45° de F1 et F2 [40].

Cette méthode de détermination directe du décalage Doppler présente l'avantage d'offrir une bonne précision et de ne pas être limitée supérieurement en vitesse. La précision sur la mesure du décalage Doppler étant de 25 MHz, soit la limite du pas en fréquence de la raie laser, conduit à une incertitude sur la mesure de vitesse de l'ordre de 13 m/s. La résolution temporelle de cette technique est limitée par le temps de balayage en longueur d'onde de la raie laser, qui peut être réduit au minimum à 0,1 s pour une déplacement de raie sur 10 GHz dans le cadre d'une programmation interne du système AUTOSCAN [41, 42]. Une programmation externe du fonctionnement de ce laser a été développée permettant de réduire l'acquisition.

### 6.2 Mesure à fréquence laser fixe

Cette méthode offre la possibilité de réduire le temps d'acquisition, donc de réaliser des mesures instationnaires, puisque le temps de balayage n'intervient pas directement dans la détermination du décalage Doppler [43, 44]. La technique de mesure de vitesse repose sur les propriétés du spectre d'absorption de la molécule d'iode dont le profil est décrit par l'intégrale de Voigt $g_{I2}(\nu)$. Ce profil, dit de Voigt, est une fonction de la pression et de la température. Il présente une partie linéaire située au maximum de pente qui est très sensible aux décalages fréquentiels. La raie laser doit alors être positionnée dans cette zone spectrale perceptible en figures 3 et 4 afin de déterminer le décalage Doppler. La fréquence laser est accordée au maximum de pente du profil d'absorption dans la partie linéaire. Afin de lever l'incertitude sur la valeur de la longueur d'onde, l'utilisation d'un couple de faisceaux coaxiaux alternés à propagation opposée de même source, indicés a et b, est également faite. Chaque faisceau est absorbé à des fréquences décalées par effet Doppler d'une valeur respective de $\pm \Delta\nu$, le signe dépendant de la composante de la vitesse se trouvant dans la direction de propagation laser. Les valeurs de la fonction de Voigt aux fréquences décalées par effet Doppler des faisceaux a et b sont référencées respectivement par $g_{I2\,a}$ et $g_{I2\,b}$. Il est possible d'exprimer $g_{I2\,a}$, $g_{I2\,b}$ et $\Delta\nu$ en fonction de la pente locale du profil d'absorption $\left(\frac{\partial g_{I2}}{\partial \nu}\right)_{\nu_0}$ :

$$\operatorname{tg} \alpha = \frac{g_{I2a} - g_{I2b}}{2\,\Delta\nu} = \left(\frac{\partial g_{I2}}{\partial \nu}\right)_{\nu_0}$$

On en déduit pour la composante de la vitesse :

$$u = \frac{c}{\nu_0}\Delta\nu = \frac{c}{\nu_0}\,\frac{g_{I2\,a} - g_{I2\,b}}{2\left(\frac{\partial g_{I2}}{\partial \nu}\right)_{\nu_0}}$$

Expérimentalement le paramètre mesurable est le signal de fluorescence Sf qu'on exprime en fonction du profil d'absorption par la relation :

$$Sf = K\,I\,gI2$$

avec :

Sf, signal de fluorescence mesuré

K, constante caractérisant la chaîne optique

$g_{I2}$, fonction de Voigt, déterminée à la fréquence d'excitation

laser
I, intensité laser.
Pour les faisceaux a et b, l'expression du signal de fluorescence se résume à :

$$Sfa = K\ Ia\ gI2\ a$$
$$Sfb = K\ Ib\ gI2\ b$$

L'intensité laser I est différente pour chacun des deux faisceaux : elle peut varier selon le trajet optique et n'est pas répartie uniformément dans la section droite du faisceau. La constante K est identique puisqu'elle caractérise la chaîne optique. L'expression de la composante de la vitesse devient alors :

$$u = \frac{c}{\nu_0} \frac{\frac{S_{fa}}{Ia} - \frac{S_{fb}}{Ib}}{\frac{S_{fa}}{Ia} + \frac{S_{fb}}{Ib}} \left( \frac{g_{12}}{\left( \frac{\partial g_{12}}{\partial \nu} \right)} \right)_{\nu_0}$$

L'adaptation de cette technique à un écoulement bidimensionnel s'effectue de façon similaire à celle énoncée pour la méthode à balayage fréquentiel. La généralisation de la méthode décrite précédemment à la détermination du vecteur vitesse s'effectue par l'utilisation d'une excitation laser à trois faisceaux afin de décomposer le vecteur-vitesse. La seule détermination de l'intensité optique de chaque faisceau permet à partir du signal de fluorescence d'exprimer les composantes du vecteur-vitesse.
La pente normalisée du profil d'absorption ne dépend que de la pression et de la température locale. Si l'écoulement est incompressible et adiabatique, il est possible de déterminer la pente normalisée en utilisant un point où la vitesse est connue. Pour un écoulement compressible la pente normalisée du profil d'absorption varie d'un point de mesure à un autre ; une détermination expérimentale est nécessaire et elle peut être réalisée à partir d'une mesure avec un quatrième faisceau à fréquence connue, légèrement décalé par rapport aux trois autres faisceaux [45].
La fréquence du quatrième faisceau $\nu_s$ doit appartenir au domaine spectral correspondant à la partie linéaire du profil d'absorption. Un modulateur acousto-optique permettant d'obtenir un décalage $\Delta\nu_s$ de 200 Mhz a été utilisé.

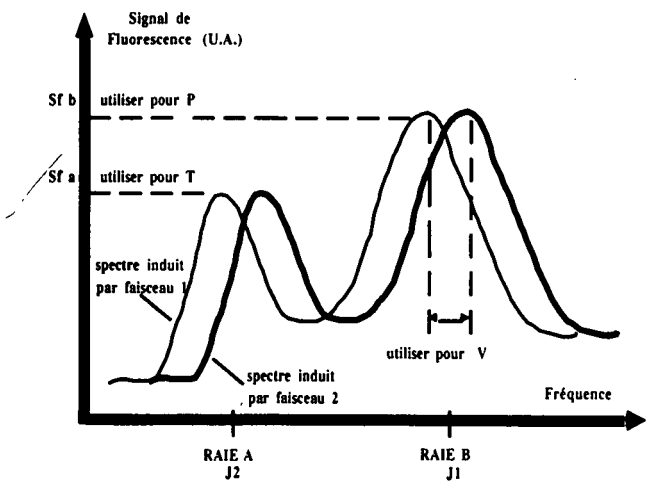


Figure 5 : Exploitation du signal de fluorescence

## 7. MESURE SIMULTANÉE DES PARAMÈTRES PRESSION, TEMPÉRATURE ET VITESSE

La mesure simultanée des paramètres pression, température et vitesse par F.I.L. est possible par une méthode de balayage en fréquence dans un domaine d'émission du laser monomode accordable couvrant au moins deux raies d'absorption de l'iode choisies en fonction des critères précédemment établis [46, 47, 48] telles que les deux raies d'absorption R97 et P60. La figure 5 présente le principe de détermination des paramètres.

## 8. DISPOSITIF EXPÉRIMENTAL

Le dispositif expérimental (figure 6) comprend trois parties principales : la source laser, l'ensemencement de l'écoulement en iode moléculaire, et le dispositif de collection et de traitement du signal de fluorescence.

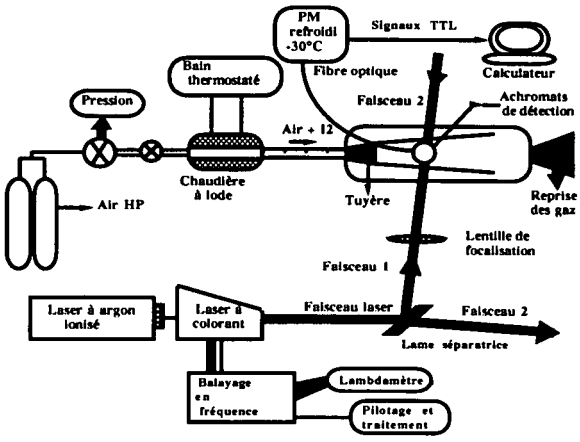


Figure 6 : Dispositif expérimental

L'émission laser est obtenue soit par un laser multimode gaussien à argon ionisé Coherent Innova 100, soit par un laser à colorant Coherent 899-29 en anneau pompé par ce même laser à argon ionisé. Ce laser à colorant accordable est équipé d'un ensemble de mesure de la fréquence d'émission et d'un système de calage et de pilotage en fréquence dit Autoscan. En utilisant comme milieu actif le colorant Pyrométhène 556, le laser peut être accordé à une longueur d'onde comprise entre 520 nm et 560 nm correspondant à une zone spectale du visible où l'on recense de nombreuses raies d'absorption. La puissance du laser est supérieure à 1W pour une puissance de pompage du laser à argon ionisé de 6W. Le laser à colorant 899-29 émet une fréquence monomode stabilisée de largeur de raie inférieure à 500kHz grâce à un système asservi qui comprend des étalons intracavité et une cavité de référence. La lame galvanométrique de Brewster permet un balayage sur une bande de fréquence de 30 GHz. Le système est équipé d'un lambdamètre haute résolution permettant un recalage en fréquence de précision inférieur à 200 MHz. En sortie du laser, le faisceau est ensuite guidé par un système périscopique, puis séparé en deux faisceaux colinéaires et de directions opposées vers le volume de mesure.

L'écoulement est ensemencé par passage sur un tube thermostaté contenant un manchon d'iode. Une faible fraction molaire d'iode (< 100 ppm) ensemence l'écoulement d'air sec.
Le système de détection est constitué par une lentille achromatique permettant de faire focaliser le signal de

fluorescence sur un tube photomultiplicateur à comptage de photons AsGa refroidi à -30°C par effet Peltier. La lumière laser diffusée par les particules et par les parois est bloquée par un filtre optique passe-haut à 570 nm. Le nombre de photons reçu par le photomultiplicateur est enregistré. Le volume de détection a comme dimensions en considérant la focale de l'achromat et le diamètre du faisceau laser, 100µm de long et 150µm de diamètre. Celui-ci est positionné à l'endroit souhaité par des tables de déplacement pilotées correspondant généralement à un maillage prédéfini de l'écoulement étudié. Le signal de fluorescence est enregistré pendant un temps constant. Le signal du photomultiplicateur est normalisé par la mesure instantanée de la puissance laser. Les deux méthodes de mesures des paramètres pression et température par fluorescence induite de l'iode avec un rayonnement laser multimode gaussien à 514,5nm et monomode accordé à des raies spécifiques de l'iode ont été testées dans des conditions statiques puis dans des conditions d'écoulement sur un jet supersonique issu d'une tuyère sous détendue de petites dimensions.

Une étude expérimentale a été menée afin de vérifier la validité des principes théoriques énoncés et de tester la possibilité d'obtenir des informations sur le champ de pression et de vitesse d'un écoulement ensemencé en iode moléculaire.

## 9. APPLICATION AU CAS D'UN JET SOUS DÉTENDU

### 9.1 Description aérodynamique de la tuyère et du jet

L'écoulement choisi est un jet issu d'une tuyère supersonique sous-détendue. Ce jet qui présente d'importantes variations spatiales des propriétés du fluide, notamment de la pression locale et de la vitesse, est bien connu des aérodynamiciens. Des modèles de calcul existent, permettant la détermination de ces propriétés. Dans le cas présent, un calcul par résolution des équations d'Euler a été mis en œuvre.
Pour cela, une tuyère de révolution présentant un diamètre au col de 4 mm environ est apparue comme un bon compromis entre le débit d'air et la pression génératrice disponible, conditionnant l'intensité des gradients de pression et de vitesse dans le jet et les difficultés mécaniques liées à l'usinage de la tuyère. Dans ce type d'écoulement, des mesures intrusives sont impossibles.
Les paramètres de calcul suivants ont été retenus :

- pression génératrice : $5{,}5.10^5$ Pa
- température génératrice : 293 K
- pression à la sortie : $1{,}5.10^5$ Pa
- nombre de Mach de sortie : 1,5
- éjection des gaz à la pression atmosphérique.

Le calcul du profil de la tuyère est effectué dans un premier temps en fluide non visqueux, à l'aide de la méthode des caractéristiques, puis un couplage avec un modèle de couche limite a été mis en œuvre, permettant ainsi de corriger la géométrie de la tuyère de l'épaisseur de déplacement. Le profil est peu divergent, puisque les diamètres calculés au col et dans le plan de sortie sont respectivement :

- diamètre au col : 4,56 mm
- diamètre dans le plan de sortie : 5 mm.

La géométrie de la tuyère est réalisée avec une précision de 2 µm et le profil est rectifié jusqu'à obtention du minimum de défaut. Le matériau choisi, devant résister au mieux à l'oxydation par l'iode est un acier spécial de type 316 TI. Un calcul des caractéristiques aérodynamiques du jet a été réalisé sur une distance de huit fois le diamètre au col, afin d'obtenir une représentation de la quasi périodicité des évolutions de pression et de vitesse. Le calcul est effectué en fluide non visqueux par une méthode pseudo-instationnaire de résolution des équations d'Euler. Le jet présente une structure alternée de détentes et de recompressions moyennement intenses en raison du taux de détente modéré de la tuyère. Le domaine de pression s'étend de $2.10^4$ Pa à $1{,}7.10^5$ Pa. Les températures locales varient dans la gamme 120K à 220K. Les vitesses calculées sont comprises entre 400 et 600 $m.s^{-1}$.

### 9.2 Mesure de pression sur l'axe du jet supersonique par fluorescence induite de l'iode par un rayonnement multimode et monomode

Les figures 7 et 8 présentent l'évolution de la pression déterminée expérimentalement par la méthode multimode à large bande spectrale (figure 7) et la méthode monomode (figure 8), sur l'axe du jet supersonique, comparée aux valeurs issues du calcul d'Euler. Les deux méthodes expérimentales révèlent les oscillations de pression prévues par le calcul. Pour chacune des deux méthodes, l'évolution théorique du signal de fluorescence montre que sa dynamique est plus faible que la dynamique en pression. Le phénomène est d'autant plus marqué en multimode, ce qui signifie que de petites variations de pression seront difficilement détectables par cette technique. Dans le cas d'une excitation laser multimode, la pression est déterminée à partir du signal de fluorescence soit au moyen d'une hypothèse d'évolution de la température selon une loi d'écoulement isentropique $P_{(T\ isentropique)}$, soit à partir d'une détermination de température exploitant également le signal de fluorescence $P_{(T\ FIIL)}$.

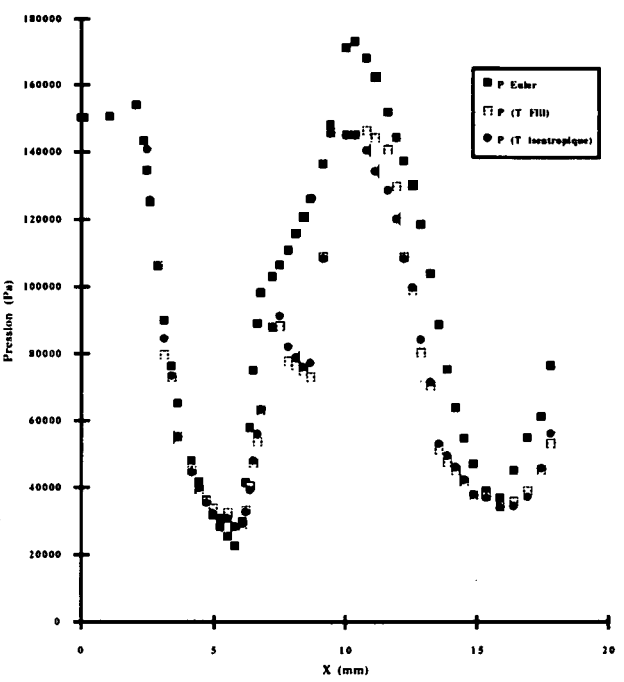


Figure 7 : Evolution de la pression sur l'axe du jet

L'évolution de $P_{(T\ FIIL)}$ est plus précise que l'évolution de $P_{(T\ isentropique)}$. Pour les mesures réalisées à partir du rayonnement laser monomode (figure 8), les valeurs de

pression déterminées par la corrélation de spectres théoriques correspondent aux points notés $P_{(Biblio)}$ ne nécessitent aucun point de référence dans l'écoulement contrairement aux points de la courbe $P_{(ref\ monomode)}$. L'écart observé est dû en partie aux imperfections de ces méthodes et pour une autre partie à l'hypothèse de fluide non visqueux faite dans le code Euler. Pour les deux premières structures de type détente recompression, les minima et maxima de pression obtenus expérimentalement coïncident avec ceux déterminés par le calcul Euler. L'incertitude en positionnement du faisceau laser est évaluée à 0,1mm. Pour les deux méthodes, l'amplitude de l'oscillation présente une décroissance régulière de type décrément logarithmique, bien que la pression Euler évolue sous forme d'oscillations quasipériodiques et pratiquement de même amplitude.

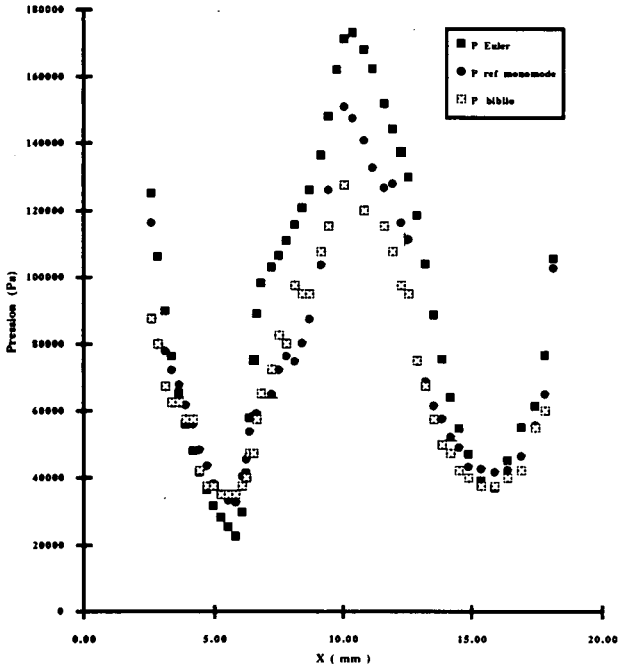


Figure 8 : Evolution de la pression sur l'axe du jet

Expérimentalement il est remarqué que l'atténuation est plus importante pour les maxima que pour les minima. Cette atténuation des gradients de pression non prédite par le calcul Euler, peut provenir du fait que les effets visqueux non pris en compte par le modèle le sont expérimentalement. De plus il est rappelé que la couche limite se développant dans le divergent de la tuyère a pour effet de provoquer une répartition du premier faisceau de détente sur l'épaisseur de la couche limite. Il en résulte un étalement de la zone du premier minimum de pression et une diminution de l'intensité de la détente. L'écart entre théorie et expérience est aussi imputable à la dimension trop importante du volume de mesure (150 $\mu m)^3$ par rapport à l'évolution locale de la pression, surtout dans la zone où le gradient de pression s'inverse.

### 9.3 Mesure de température sur l'axe du jet supersonique par fluorescence induite de l'iode par un rayonnement multimode et monomode

Les températures déterminées expérimentalement par fluorescence induite par laser dans le cas du rayonnement laser multimode sont en bon accord avec les valeurs théoriques du code Euler (figure 9). L'écoulement compte-tenu des valeurs de pression et de température peut être considéré comme pratiquement isentropique.

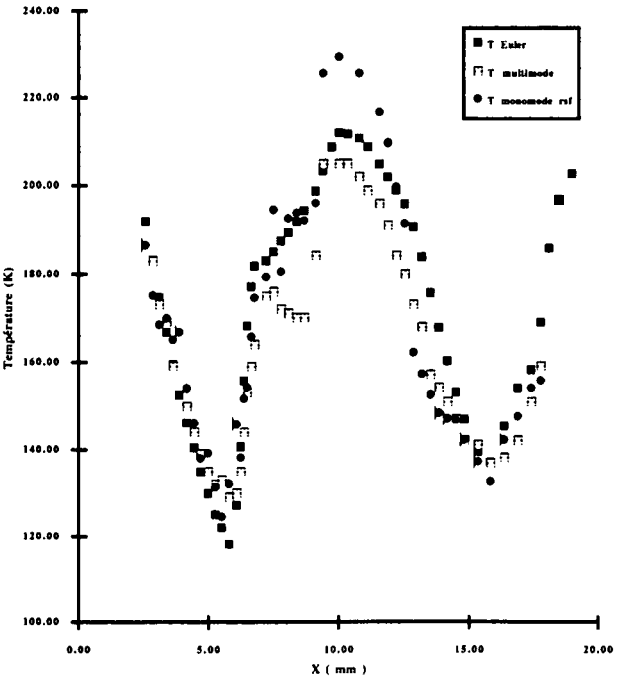


Figure 9 : Evolution de la température sur l'axe du jet

Les valeurs des mesures de température obtenues dans le cas d'un rayonnement laser monomode sont présentées sur cette même figure pour une zone de l'écoulement. Les valeurs des températures théoriques du code Euler sont comparées aux valeurs expérimentales obtenues à partir du rapport des signaux de fluorescence enregistrés lors du balayage en fréquence de la raie laser sur deux raies d'absorption voisines. Les écarts les plus importants observés correspondent aux maxima de pression engendrant un élargissement collisionnel conséquent.

### 9.4 Mesure de vitesse sur l'axe du jet supersonique par fluorescence induite de l'iode par un rayonnement monomode

Les mesures de vitesses obtenues à partir d'un balayage en fréquence de la raie laser présentées en figure 10 sont comparées à la fois aux mesures de vitesses obtenues sur ce jet par vélocimétrie laser Doppler (LDV) et par vélocimétrie laser bipoint (L2F) ainsi qu'aux valeurs théoriques du code Euler. Là, encore les effets visqueux et la taille du volume de mesure comparée aux dimensions du jet peuvent expliquer les différences. Les valeurs des vitesses obtenues par FIL sont intermédiaires entre les valeurs expérimentales L2F et LDV laissant supposer un suivi de l'écoulement plus facile par les molécules que par des particules.

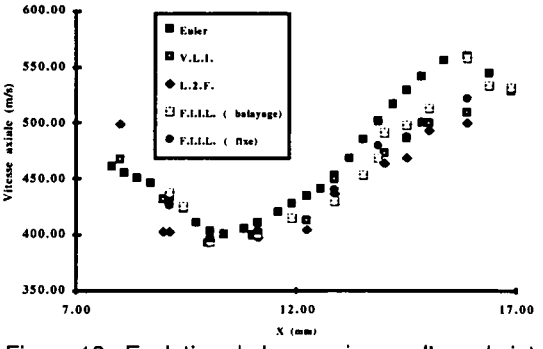


Figure 10 : Evolution de la pression sur l'axe du jet

### 9.5 Mesures simultanées de pression, de température et de vitesse sur l'axe du jet supersonique par fluorescence induite de l'iode par balayage en fréquence d'un rayonnement monomode

La mesure des trois principaux paramètres d'un écoulement a été réalisée à partir d'un spectre de fluorescence obtenu aux cours du balayage en fréquence des deux faisceaux colinéaires se propageant en sens contraire. La direction des faisceaux fait un angle de 30 degrés avec l'axe du jet. Le signal de fluorescence est simultanément normalisé par l'intensité laser. Une mesure de bruit correspondant au signal de fluorescence normalisé par l'intensité laser dans le cas d'un écoulement non ensemencé en iode est réalisée. Le bruit est retranché du signal de fluorescence normalisé par l'intensité laser. La pression est obtenue par corrélation avec la bibliothéque de spectres théoriques, la température par exploitation du rapport des signaux de fluorescence des deux raies d'absorption.

## 10. CONCLUSION ET PERSPECTIVES

L'utilisation de la fluorescence de l'iode induite par laser comme outil en métrologie optique des écoulements a été démontrée. Après avoir fait l'objet d'une modélisation et d'une validation dans des conditions statiques, la technique a été testée dans des conditions d'écoulements externes et internes. Outre son excellente résolution spatio-temporelle et le parfait suivi de l'écoulement réalisé au moyen d'un ensemencement moléculaire homogène, la technique présente l'avantage d'obtenir deux ou trois informations essentielles sur l'écoulement étudié à savoir la pression, la température et la vitesse à partir d'une unique mesure expérimentale du signal de fluorescence [50].

Deux types d'excitation laser permettent la mesure couplée de la pression et de la température. **Le laser à argon ionisé multimode** présente l'avantage d'émettre intensément à la longueur d'onde de 514,5 nm coïncidant fortuitement avec la longueur d'onde de la double raie d'absorption de l'iode notée P13-R15 (43-0). Ce type de rayonnement permet de rendre compte de l'évolution de pression à partir de la préconnaissance de l'évolution de température soit par une loi d'évolution, soit par une détermination expérimentale de la température réalisée par F.I.L.. L'utilisation de ce type d'excitation impose une mesure de référence où la pression et la température sont connues; ce qui permet de s'affranchir de la connaissance de différentes constantes liées à la physico-chimie du phénomène et au type d'excitation laser.

L'autre type de source laser utilisable est un **laser monomode accordable à colorant** permettant de choisir une raie d'absorption de l'iode dont la dépendance en température est négligeable; ce qui permet d'obtenir une expression du signal de fluorescence simplifiée puisque celui-ci est inversement proportionnelle à la pression. La mesure de température est possible à partir du rapport des signaux de fluorescence induit par deux raies voisines du spectre d'absorption de la molécule d'iode. La détermination de cette zone spectrale permet des mesures de température sur une large gamme. L'autre avantage du choix de cette excitation laser réside dans le fait qu'il n'est plus nécessaire d'effectuer une mesure de référence puisqu'une corrélation entre le spectre de fluorescence expérimental et ceux inclus dans une bibliothèque de spectres théoriques issus de la modélisation est effectuée permettant une détermination directe de la pression. Enfin l'intensité laser émise par le laser à colorant, quoique inférieure à celle émise par le laser à argon ionisé, offre désormais un bon rendement avec l'emploi de colorants tels que les Pyrrométhènes et Rhodamines.

Cette méthode peut également être étendue à la mesure de vitesse par comparaison du décalage fréquentiel Doppler entre le spectre de fluorescence et celui obtenu à partie d'une cellule statique à iode utilisée comme standard de fréquence.

Le champ d'application de cette méthode intéresse les écoulements gazeux dont la pression évolue entre 0.2 et 5 bars avec une précision de 5 % et dont la température demeure inférieure à 600 K avec une précision inférieure à 3 %.

Des mesures dans le champ d'un plan laser des mêmes grandeurs caractéristiques peuvent être réalisées assez facilement, mais elles nécessitent des moyens adaptés de visualisation par caméra intensifiée.

L'inconvénient majeur de cette technique réside dans le fait que l'iode présente un caractère corrosif sous forme d'acide en milieu humide nécessitant l'emploi de matériaux appropriés tels que le téflon, le PVC, l'acier 316TI ou plus simplement d'utiliser de l'air sec.

## REMERCIEMENTS

Les auteurs remercient Jean-Paul Bourez et Christophe Verbeke pour leur assistance technique.

## BIBLIOGRAPHIE

[1] R.L. McKenzie. "Progress in laser spectroscopic techniques for aerodynamic measurements : an overview", AIAA Journal, Vol. 31, No.3, March 1993.

[2] N.L. Rapagnani, S.J. Davis. "Flow visualisation in supersonic flows", Laser Probes for Combustion Chemistry, ACS Symposium Series, No134, March 1980.

[3] N.L. Rapagnani, S.J. Davis. "Laser-induced fluorescence: a diagnostic for fluid Mechanics", Lasers and Applications, pages 127-131, May1985.

[4] B. Leporcq, F. Lemoine, R. Arbus, J.C. Demarais. "Etude du mélange entre un jet supersonique et des jets subsoniques par fluorescence induite par laser", Quatrième Colloque de Visualisation et de Traitement d'Images en Mécanique des Fluides, Lille, 29 mai au 1er juin 1990.

[5] R.J. Hartfield, J.D. Abbitt, J.C. McDaniel. "Injectant mole fraction imaging in compressible mixing flows using planar laser-induced iodine fluorescence", Optics Letters, Vol. 14, No. 16, August 15, 1989.

[6] P. Guiraud, J. Bertrand, J.Costes. "Visualisation par fluorescence induite par laser. Application au mélange en jets confinés", Entropie, No. 150, 1989.

[7] J.C. McDaniel, R.K. Hanson. "Quantitaive planar visualization in gaseous flowfields using laser-induced fluorescence", Flow Visualization III, Proceeding of the Third International Symposium on Flow Visualization, Ann Arbor, Michigan, USA, p. 113-117, september 1983.

[8] R. J. Hartfield, S. D. Hollo, J.C. Mc Daniel. "Planar Measurement Technique for compressible flows using laser-induced iodine fluorescence", AIAA Journal, Vol. 31, No. 3, March 1993.

[9] J. C. McDaniel. "Quantitative measurement of density and velocity in compressible flows using laser-induced iodine fluorescence", AIAA 21st Aerospace Sciences Meeting, January 10-13, 1983/Reno, Nevada

[10] D. Keefer. "Laser fluorescence velocimeter", Applied optics, Vol. 26, No. 1, January 1987.

[11] D.G. Fletcher, J.C. McDaniel. "Temperature measurement in a compressible flow field using laser-induced fluorescence", Optics Letters, Vol.12, No.1, January 1987.
[12] K. P. Gross, R. McKenzie. "Measurements of fluctuating temperatures in a supersonic turbulent flow using laser-induced fluorescence",AIAA Journal, Vol. 23, No.12, 1984.
[13] J.M. Donohue, K.G. Victor, J.C. McDaniel. "Computer-controlled multi-parameter mapping of 3D compressible flowfields using planar laser-induced iodine fluorescence", AIAA 30st Aerospace Sciences Meeting & Exhibit, Reno, Canada, January 1993.
[14] J.C. McDaniel. "Nonintrusive Pressure Measurements with laser-induced fluorescence", AIAA 18th Thermophysics Conference, Montreal, Canada, June 1983.
[15] F. Lemoine, M. Descieux, B. Leporcq. "Application de la fluorescence induite par laser à la mesure de la pression", 5ème Colloque National de Visualisation et de Traitement d'Images en Mécanique des Fluides, Poitiers, 21 - 5 Juin 1992.
[16] F. Lemoine, B. Leporcq. "Applications de la fluorescence induite de l'iode par laser à la mesure de pression", La Recherche Aérospatiale, n°1, pp. 51-59, 1993.
[17] B. Leporcq. "Static pressure measurements for near isentropic flows using laser induced iodine fluorescence", Measurement techniques (Lecture Series 1993-05), Von Karman Institute for Fluid Dynamics, Rhode Saint Genèse, Belgique, April 19 - 23 1993.
[18] J. B. Koffend, R.Bacis, R. W. Field. "Continuous wave optically pumped iodine laser", Journal of Molecular spectroscopy 77, 202-212, 1979.
[19] B. Hiller, R.K. Hanson. "Properties of iodine molecule relevant to laser induced fluorescence experiments in gas flows", Experiments in fluids 10, 1-11, 1990.
[20] Herzberg R. "Spectra of diatomic molecules", Second Edition, D Van Nostrand Compagny, Inc-1951.
21] J.I. Steinfeld, R.N. Zare, L. Jones, M. Lesk, W. Klemperer. "Spectroscopic Constants and vibrational Assignment for the B3P0u+ state of iodine", The Journal of Chemical Physics, vol.42, No. 1, January 1964.
[22] F.Martin, R. Bacis, S. Churassy, J. Vergès. "Laser induced fluorescence Fourier transform spectrometry of tje XO+g state of I2 : Extensive Analysis of the BO+u-->XO+g, Fluorescence Spectrum of I2", Journal of Molecular spectroscopy 116, 71-100, 1986.
[23] P. Pascal., Nouveau traité de chimie minérale, "Propriétés physiques de l'iode", p 456 à 465, Edition Masson et cie.
[24] S.Gerstenkorn, P. Luc. "Assignments of several groups of iodine (I2) lines in the B-X system", Journal of Molecular spectroscopy 77, 310-321, 1979.
[25] S. Gerstenkorn, P.Luc. "Atlas du spectre de la molécule d'iode de 14800 à 20000 cm-1", Editions du CNRS.
[26] F. Chabannes. "Les lasers", Editions de l'ENSTA, 1981.
[27] F. Lemoine, B. Leporcq. "Static pressure measurements for near isentropic flows using laser induced iodine fluorescence", 114th ASME Winter Annual Meeting, New Orleans, Louisiana, Nov. 28 - Dec. 3. 1993.
[28] J. Tellinghuisen. "Intensity factors for the I2 B<->X band system", J. Quant. Spectrosc. Radiat. Transfer., Vol.19. pp 149-161, 1977.
[29] J.D. Simmons and J.T Hougen. "Atlas of the I2 spectrum from 19000 to 18000 cm-1", Journal of Reseach of the National Bureau of Standards-A. Physics and Chemistry, vol. 81A, No. 1, January-February 1977.
[30] B. Leporcq. "Mesure de pression locale par fluorescence induite par laser" Journée thématique : Aérodynamique instationnaire turbulente ; aspects numériques et expérimentaux, DRET 30 Juin 1994.
[31] F. Lemoine, B. Leporcq. "Optical pressure measurement in compressible flows using laser-induced iodine fluorescence", 2nd European Fluid Mechanics Conference. September 20-24, 1994, Warsaw, Poland.
[32] F. Lemoine, B. Leporcq. "Investigation on an optical pressure measurement using laser induced fluorescence", Z.F.W. 19 (1995) 109-118.
[33] F. Lemoine, B. Leporcq. "An efficient optical pressure measurement in compressible flows by laser induced iodine fluorescence", Experiments in Fluids 19 (1995) 150-158.
[34] A.C. Eckbreth. "Spatially precise laser diagnostics for combustion", ICIASF'81 Record, pp 71-89, 1981.
[35] J.I. Steinfeld. "Rate for inelastic collision processes and the diatomic halogen molecules", J. Phys. Chem., Ref. Data, Vol. 13, No. 2, 1984.
[36] D. G. Fletcher, J. C. Mc Daniel. "Laser induced iodine fluorescence techniques for quantitative measurement in a non reacting supersonic combustor", AIAA Journal, Vol. 27, N°5, May 1989.
[37] G. Janssens, J. Labbé, F. Lemoine, B. Leporcq. 11th Symposium on Mesuring Techniques for Transonic and Supersonic Flow in Cascades and Turbomachines
Münich, 14 et 15 septembre 1992.
[38] G. Janssens , J. Labbé, B. Tanguy, F. Lemoine, B. Leporcq. "Mesures de vitesses supersoniques", 3ème Congrès Francophone de Vélocimétrie Laser, Toulouse, 21 - 24 Septembre 1992.
[39] J. C. McDaniel, B. Hiller, R.K. Hanson. "Simultaneous multiple-point velocity measurements using laser-induced iodine fluorescence" Optics letters, Vol. 8, No. 1, January 1983.
[40] B. Hiller, R. K. Hanson. "Simultaneous planar measurements of velocity and pressure fields in gas flows using laser-induced fluorescence" Applied optics , Vol. 27, No. 1, January 1988.
[41] F. Lemoine, B. Leporcq. "Mesures de pression et de vitesse par fluorescence induite par laser", 10 ème Congrès Français de Mécanique , Lille - Villeneuve d'Ascq, 6 - 10 Septembre 1993.
[42] X. Lefebvre, B. Leporcq, J-P. Bourez. "Simultaneous measurements of pressure and velocity in a supersonic flow using laser induced iodine fluorescence", EUROMECH Colloquim 335, Rome, 5 au 7 Juin 1995.
[43] B. Hiller, L. M. Cohen, R. K. Hanson. "Simultaneous measurements of velocity and pressure fields in subsonic and supersonic through imge-intensified detection of laser-induced fluorescence" AIAA 24th Aerospace Sciences Meeting, Reno/Nevada, January 6-9, 1986.
[44] B. Hiller, J. C. McDaniel, E. C. Rea, Jr, R. K. Hanson. "Laser-induced fluorescence technique for velocity-field measurements in subsonic gas flows", Optics letters, Vol. 8, No. 9, September 1983.
[45] B. Hiller, R. K. Hanson. "Two-frequency laser-induced fluorescence technique for rapid velocity-field measurements in gas flows", Optics letters, Vol. 10, No. 5, May 1985.
[46] X. Lefebvre, F. Lemoine, B. Leporcq, J -P. Bourez. "Mesures de pression et de vitesse par fluorescence induite par laser", 6ème Colloque National de Visualisation et de Traitement d'Images en Mécanique des Fluides, Saint Etienne, 30 Mai - 2 Juin 1995.
[47] F. Lemoine, X. Lefebvre, B. Leporcq. "Pressure and

velocity measurements in a compressible flows using iodine fluorescence induced by a single mode laser", 4th Symposium on Experimental and Numerical Flow Visualization of the American Society of Mechanical Engineers, 13 - 18 August 1995.
[48] X. Lefebvre, B. Leporcq. "Simultaneous measurements of pressure, temperature and velocity using laser-induced iodine fluorescence", 1996 ASME Fluids Engineering Division, Summer Meeting. San Diego July 7 - 11, 1996.
[49] F. Lemoine. "Application de la fluorescence induite de l'iode par laser à la mesure de pression. Extension aux principes de la mesure de vitesse", Thèse de Doctorat de l'Université de Paris VI Soutenue le 9 - 12 - 1993.
[50] X. Lefebvre. "Application de la fluorescence induite de l'iode par laser à la mesure simultanée de pression, température et vitesse.Extension aux mesures de pression dans une turbomachine ", Thèse de Doctorat de l'Université de Paris VI en cours de rédaction.

Paper 24
Author: Leporcq

Q: Schodl

How does your technique perform when used at pressure levels exceeding 1bar ?

A: For pressure levels below 510 Pa measurements are possible. See the table.

Q: Versluis

With this iodine technique, do you have any problems with fluorescence trapping ?

A: Nous sommes tres eloignes des conditions de saturation du milieu.

Q: Roehle

How do you achieve a homogenous and constant seeding of iodine ?

*A:* Par passage de l'écoulement dans une chaudière à iode thermostatée, nous obtenons un ensemencement homogene et constant.

# Development of Planar Laser Induced Fluorescence for Fuel: Application to Gas Turbine Combustion

**D. A. Greenhalgh, D. J. Bryce, R. D. Lockett, and S. C. Harding.**
**School of Mechanical Engineering, Cranfield University,**
**Bedford, MK43 0AL. U.K.**

## ABSTRACT

Planar Laser Induced Fluorescence (PLIF) offers advantages over mechanical patternators, gas sampling and other laser diagnostics in providing high resolution instantaneous two-dimensional images of liquid and vapour fuel concentration in operating gas turbine combustors. The technique has been developed at Cranfield and successfully applied to three different situations. Firstly the power of the method for fundamental mixing studies is illustrated with respect to a simple jet mixing experiment. Secondly the practical application of the method to an atmospheric pressure LPP combustor and a high-pressure double annular combustor are presented. Radial and axial imaging of both the liquid and vapour phases has been performed with fuel markers that are capable of distinguishing between different boiling-point fractions. Such data allows investigation of the fuel-air mixing in the combustor, as well as the behaviour of the spray cone angle and patternation with varying fuel rate.

## INTRODUCTION

In gas turbine combustion, new regulations demand greatly reduced levels of emissions of pollutants such as soot, oxides of nitrogen ($NO_x$), unburnt hydrocarbons (UHC) and carbon monoxide (CO). Such emissions result from inadequate mixing of the fuel and air; a combination of the atomiser performance and the aerodynamics of the combustor.

Two features of interest are the overall fuel placement and the spray dropsize distribution. A description of mechanical methods for measuring these features is given in Lefebvre (1989). Laser diagnostics generally offer advantages over physical measurement devices in that they measure a property directly without perturbing the system. In addition, the instruments can be remote from the system, allowing measurements to be made in harsh environments. Dropsize distributions can be routinely acquired using pointwise Phase Doppler Anemometry [Bachalo, 1980; Wigley, 1994]. As far as fuel placement is concerned, a mechanical patternator could not be used in a combusting system, since the fuel would be consumed; an optical diagnostic is necessary.

Three-dimensional scalar measurement techniques [Long, 1993; Maas and Gruen, 1995] are still some way from being applicable to operating gas turbine combustors. However, there are several two-dimensional fuel mapping techniques that can be applied to various planes within such a system. Typically, the measurement region is illuminated with a thin laser sheet, with orthogonally scattered light being captured onto a two-dimensional device. Photographic film can be used, offering simplicity and very high spatial resolution [Zheng et. al., 1996], but the response to incident light is non-linear, the quality of images cannot be determined interactively and image processing involves extensive manual effort. The use of a CCD camera, with its linear response, prompt display and digital processing techniques, overcomes these problems. Datasets of hundreds of instantaneous images can be captured, stored and processed electronically in a matter of minutes.

The strongest scattering process is the elastic scatter of the laser light from the system - Mie scatter from structures larger than about 1 μm (liquid phase) and Rayleigh scatter from small particles (vapour phase). The signal strength

*Paper presented at an AGARD PEP Symposium on "Advanced Non-Intrusive Instrumentation for Propulsion Engines", held in Brussels, Belgium, 20-24 October 1997, and published in CP-598.*

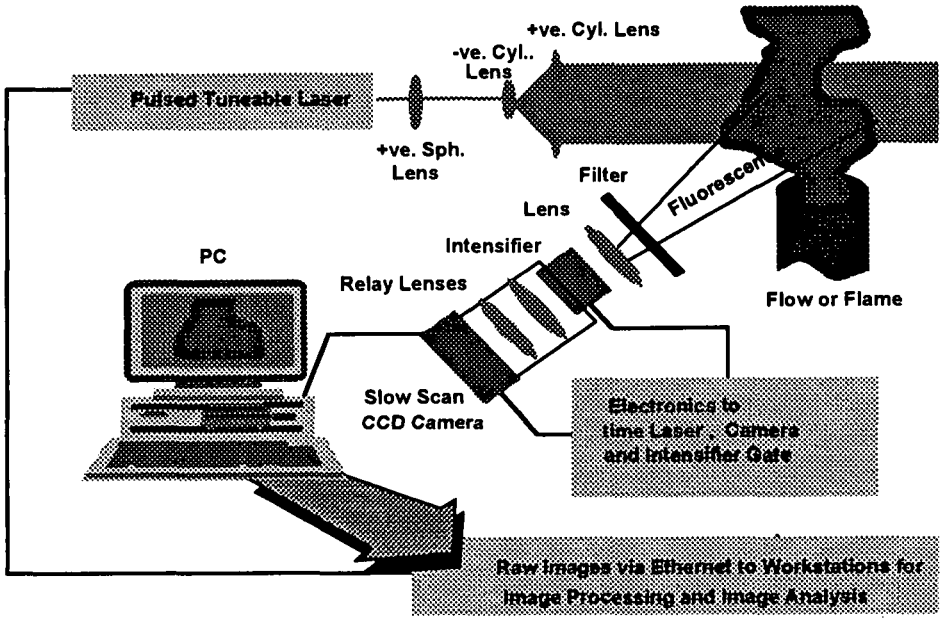


**Figure 1** Schematic of general set-up for Planar LIF imaging experiment.

from elastic scattering varies in different size regimes. For droplets larger than about 5 μm, the dropsize dependence is $d^2$ [Bohren and Huffman, 1983], indicating that Mie scatter imaging over-emphasises smaller droplets.

Laser Induced Fluorescence (LIF) [Eckbreth, 1988; Seitzman and Hanson, 1993; Greenhalgh, 1994] can be used to image fuel placement in both the liquid [Serpengüzel et. al., 1992] and vapour phases [Tait and Greenhalgh, 1992]. In an optically thin vapour phase, the non-saturated fluorescence signal will be proportional to the density of the excited species. In the liquid phase, in the limit of no laser absorption, the fluorescence signal is expected to be proportional to the local liquid volume fraction.

For most applications of PLIF a key factor is the choice of fluorescent seed to mark the fuel is critical. For light fuels such as gasoline ketone type compounds have been widely shown to be suitable and to give very good PLIF data [Arnold 1990, Berckmüller, 1994, 1996 & 1997, Neij 1994]. Their main advantages are that they are insensitive to oxygen quenching and have simple temperature dependence.

The studies reported here applied PLIF to three different gas turbine combustors. One concerns a cold gas-gas mixing study whilst the second two experiments were performed under combusting conditions. The first at nominally atmospheric inlet pressure, the second at an intermediate inlet pressure of 3 bar. The ability to apply a measurement technique as closely as possible to the normal operating conditions is clearly advantageous in minimising the uncertainty of the effect of scaling between test flow conditions and those encountered in full gas turbine cycle.

## EXPERIMENTAL SET-UP

The general set-up for a planar LIF imaging experiment is shown in Figure 1. The beam from the laser was formed into a thin collimated sheet using one spherical converging lens and a combination of one diverging and one converging cylindrical lens. In these experiments, a Lambda Physik EMG-150 MSC excimer laser was used in narrow band tunable mode at 308 nm, producing up to 165 mJ of energy per 20 ns duration pulse. Since this emission is ultra-violet, fused silica sheet-forming lenses were used. For the enclosed combustors, the laser sheet was introduced to the measurement region and the signal was collected through windows.

An intensified CCD camera positioned orthogonally to the laser sheet imaged the

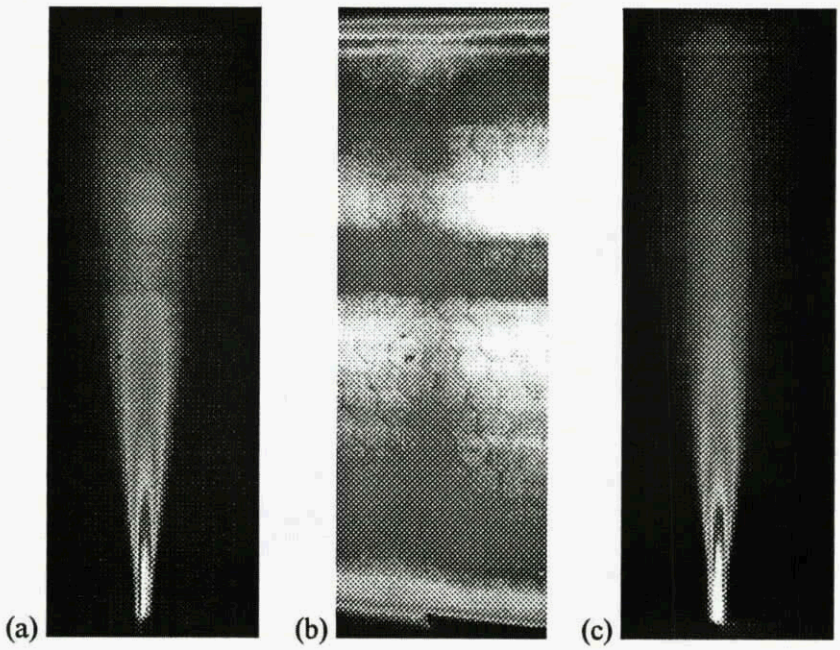


**Figure 2** (a) Raw PLIF image, (b) PLIF normalisation image (c) final mean PLIF image.

fluorescence signal. Such cameras have a linear response to the fluorescence signal and allow data sets of hundreds of single shot images to be rapidly acquired and stored. The cameras used in the two studies described had chip sizes of 600 x 400 and 578 x 384 pixels respectively and had 15 bit grey-scale resolution. Elastic (Mie) scattering was discriminated out through the use of a long-pass filter in front of the CCD camera.

The PLIF images obtained were corrected for background scatter, variations in the laser sheet intensity profile and variations of the intensifier gain function [Seitzman and Hanson, 1993]. The laser sheet profile was obtained by flooding the combustor with homogeneous acetone vapour. For the jet experiments a large thin enclosure was filled with acetone vapour and used to record the laser sheet profile of the measured region.

## PLIF MEASUREMENTS ON AN ACETONE SEEDED JET

A simple theory for the mixing in a simple jet into a stagnant fluid has been long established [Hinze, 1959]. Theory predicts a Gaussian radial distribution and for gasses experimental evidence from Rayleigh scattering supports this [Dowling and Dimotakis, 1990]. Recently PLIF of acetone seeded gases has been demonstrated to be a sensitive method for detailed studies of mixing [Tait and Greenhalgh 1992, 1993, Lozano 1992]. The following experiment was designed to explore the application of PLIF to a fundamental study of gas-gas mixing [Bryce 1996].

The experiment consisted of a 1.5 mm jet of ambient temperature, approximately 2% acetone in nitrogen issuing into stagnant ambient air. Measurements were made for three jet Reynolds numbers (Re = 5,000, 16,000 and 40,000). Each measurement consisted of between 250 and 300 single pulse images. Figure 2 illustrates the approach to imaging and clearly demonstrates the essential requirement of normalisation of the measured image by an image including correction factors for the laser sheet profile and image transfer function (Figure 2b).

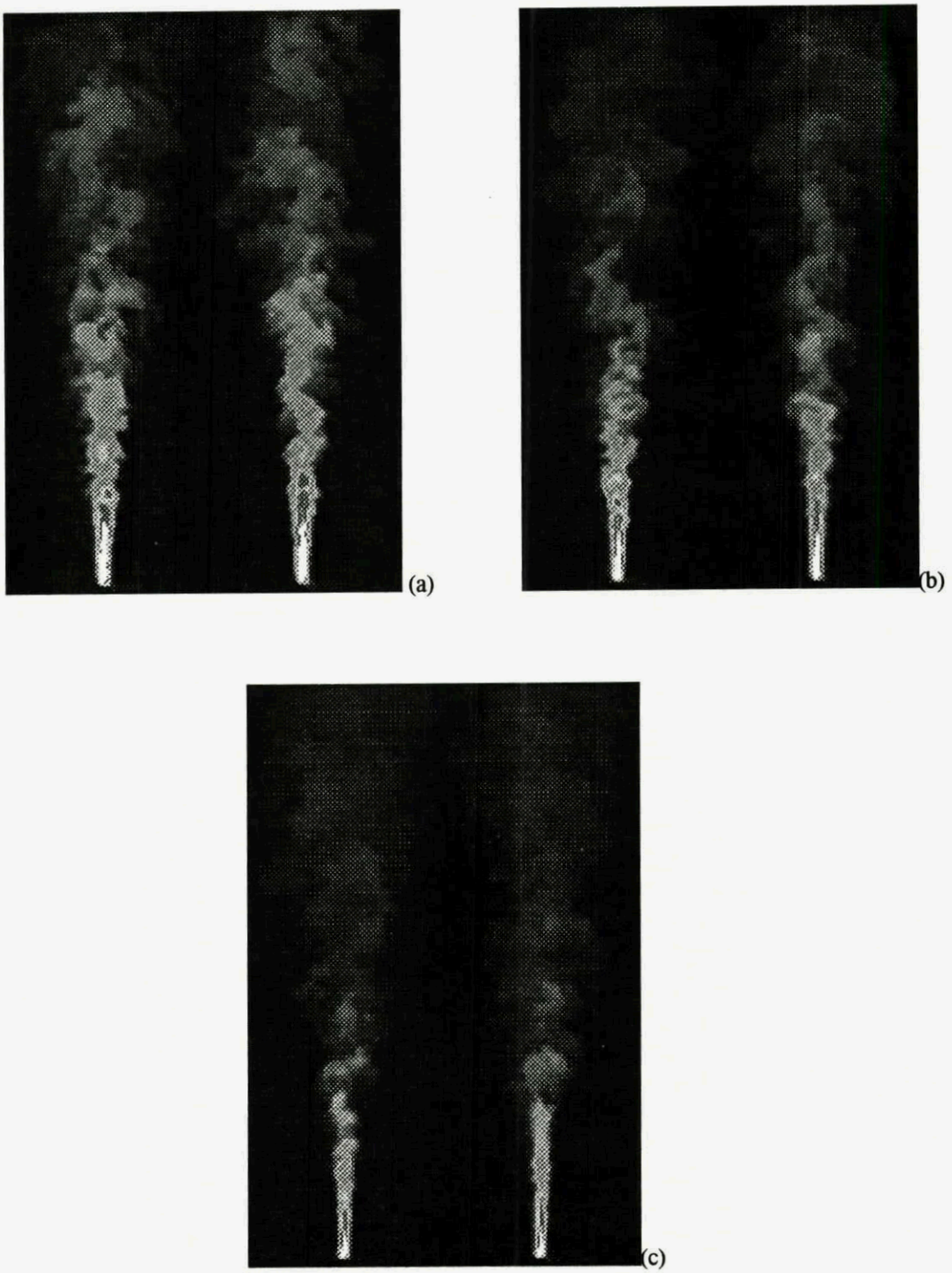


**Figure 3** Single pulse images: (a) Re=5000, (b) Re=16000, (c) Re=40000.

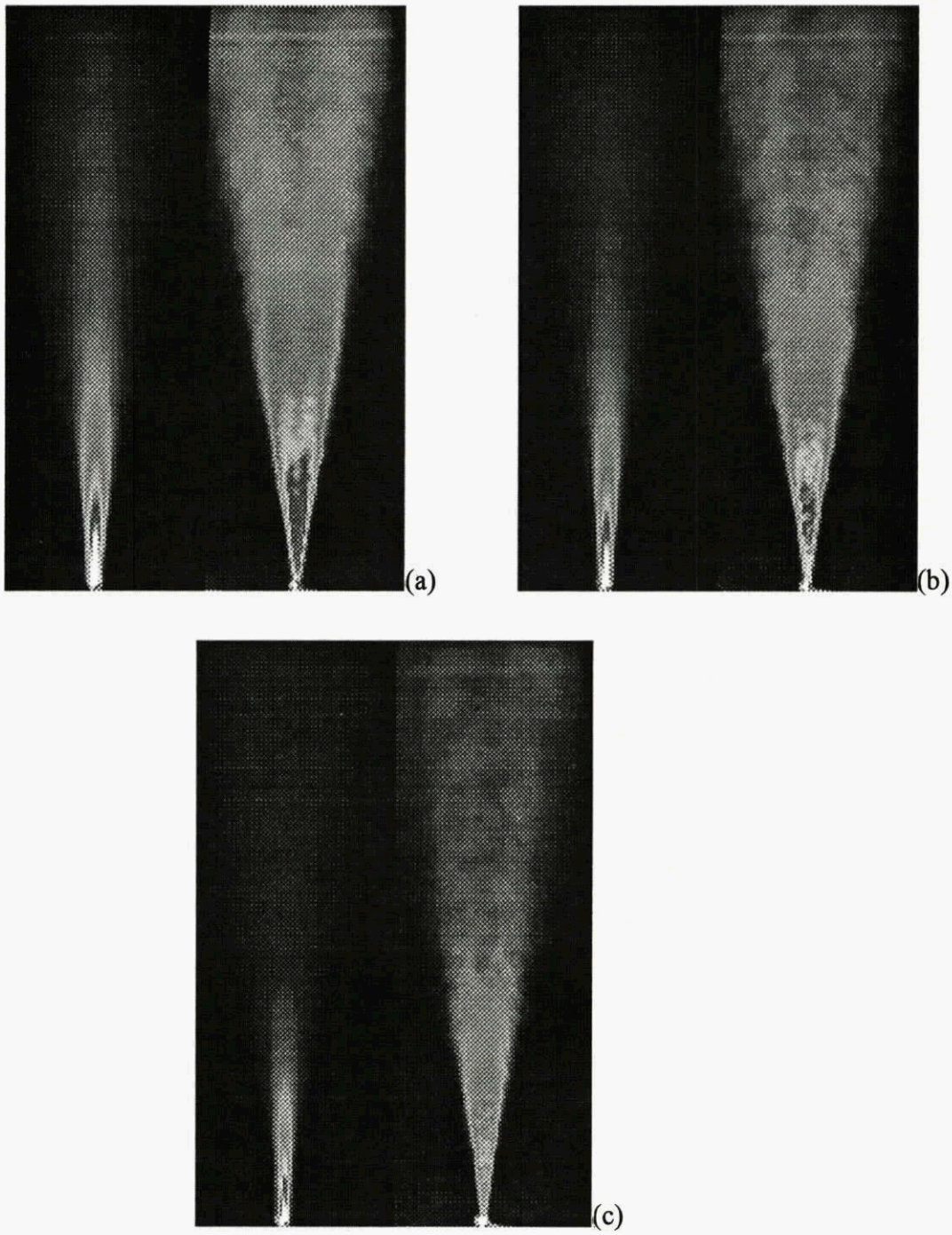

scale for mean images (fuel concentration)

scale for standard deviation images (fuel concentration)

**Figure 4** Corrected mean (left of each pair) and standard deviation (right of each pair) images. (a) Re=5000, (b) Re=16000, (c) Re=40000.

To establish the precision of the data the uncertainty was calculated for an ensemble single shot data set of calibration images. The uncertainty was found to be of order 5% which is higher than the 3% observed for studies of i.c. engines [Berckmüller, 1997] where the small imaging area assures an order of magnitude higher laser fluence. This error does not contribute significantly when using the normalisation image to correction to the flow images because a mean image is used. The maximum error of the mean normalisation image was 1.2%. The laser power was found to be stable, with the fluctuation of order 3% during measurement with a powermeter and therefore the final single pulse images are accurate to of order 5%.

Figure 3 illustrates some single pulse images for the three Reynolds numbers and provides an idea of mixture fluctuations. This data may then be processed to reveal the essential statistics of the mixing fluids, figure 4.

Following Dowling (1990) self-similarity in the mixing predicts that radial concentration profiles should be identical in form when normalised and scaled by a cylindrical co-ordinate system. The mean fluid concentration of the jet fluid is then:

$$\overline{C}(x,r) = \kappa \frac{C_0 d^*}{x - x_0} g\left(\frac{r}{x - x_0}\right) \equiv \kappa \frac{C_0}{\chi} g(\eta)$$

Eqn. .1

Where $C_0$ is the concentration at the jet pipe exit, $x_0$ is a virtual origin, $x$ the distance down stream, $r$ is radial distance and d* is the momentum diameter of the jet given by:

$$d^* = \frac{2\dot{m}_0}{\pi \rho_\infty J_0}$$

Eqn. 2.

where $\dot{m}_0$ is the nozzle mass flux, $J_0$ the nozzle thrust and $\rho_\infty$ the ambient density. For density matched fluids this reduces to the geometric nozzle diameter $d$ with an assumed top hat exit velocity profile; this assumption was made in the following analysis. Equation 1 defines the similarity co-ordinates $\chi$ and $\eta$and predicts matched smooth profiles $g(\eta)$ normalised by a constant $\kappa$ Note that and x0 are experimental parameters. Figure 5 compares this model with the experimental data and gas sampling data analysed by a mass spectrometer. The gas sampling data shows general agreement however the data close to the jet exit is likely to be distorted by probe blockage effects. Equation 1 shows that along the jet centreline (r=0) the concentration is predicted to be inversely proportional to the axial distance. The plots were fitted and values of the virtual origin $x_0$ and the constant $\kappa$ were determined for each case.

The values extracted from the curves were $\kappa$ = 4.66, $x_0$ =-4.66d for Re=5000. This is compared with the results $\kappa$ = 5.11, $x_0$ =-3.7d of Dowling and Dimotakis (1990) (D&D). Results at Re = 16000 were $\kappa$ = 3.64, $x_0$ =-3.64d, compared to $\kappa$ = 4.73, $x_0$ =+0.5d (D&D). At Re = 40000, $\kappa$ = 2.49, $x_0$ =-2.49d, scarcity of measurements did not allow D&D to quote accurate values at this condition.

The signal along the centreline departs from the $1/x$ dependence near the nozzle exit. This departure is at least partially due to the spatial resolution achieved in these experiments. The images correspond to approximately 0.3 mm per pixel which, including intensifier cross-talk gives a resolution of about 1mm. The plots of figure 5 are for a single strip of pixels along the centreline and hence spatial resolution is inadequate close to the 1.5 mm jet. Residual flare from the nozzle also compromises the signal at this point. Fine scale, small sheet imaging would be required to determine if there is a genuine departure from theory. The difference in experimental parameters compared to Dowling (1990) at Re=5000 are approximately 9%, this corresponds to the uncertainty in the parameters of the fit to centreline concentration. The fit was most sensitive to the choice of the virtual origin. The mean concentration profiles would come even more in line with those of Dowling (1990) when assigning the same values of $\kappa$ and $x_0$. Dowling (1990) discussed the difference in $\kappa$ and $x_0$ between Reynolds number conditions and suggested that the similarity variables are *specific* to the level of turbulence. This is confirmed in this study by the approximate inverse proportionality between $\kappa$ and Re

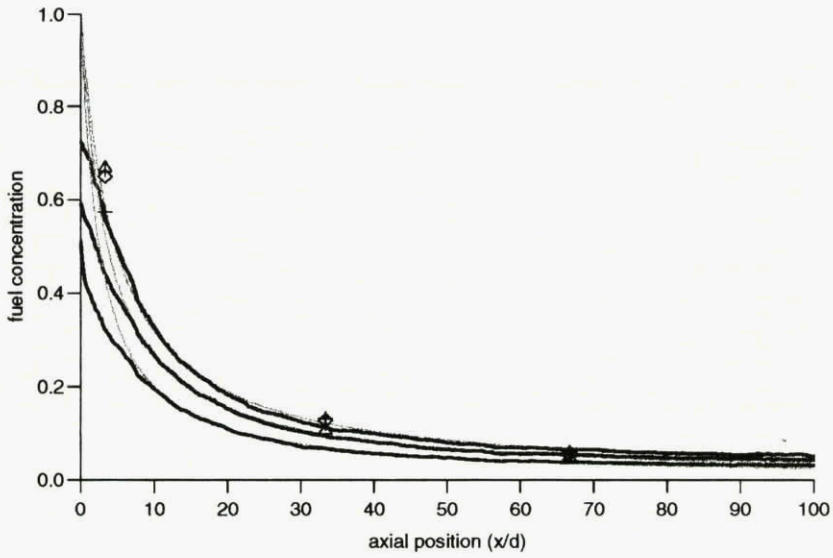


**Figure 5** Signal and theory along the jet centreline, Re=5000 (top), Re=16000 (middle) and Re=40000 (lowest). Gas sampling: diamonds Re=5000, crosses Re=16000, triangles Re=40000.

Figure 6 compares the scaled radial profiles for mean concentrations. Apart from small discrepancies at *x/d*=80, which is at the end of the jet and close to the edge of the laser sheet where image normalisation errors are largest, all the profiles demonstrate a Gaussian self-similarity.

In this study we find that the fluctuation profiles do not collapse to self-similarity as claimed by Dowling (1990). However the fluctuations of Dowling required optimal filtering of each time series and this could have resulted in an overestimation of the fluctuation. Note that the fluctuation profiles flatten at higher Re. which is also seen in the fluctuation images, figure 4. The mean concentration profiles depart from similarity near the top of the jet and these differences increases with Re.

The axial momentum in this region is low, and large vortices roll over towards the centreline probably resulting in the breakdown of the simple theory. This feature is seen in the mean images, where the distribution rounds off at the op of the jet. The effect may be more pronounced at higher Re., possibly due to an increased crossflow associated with the higher turbulence.

PDFs were determined for various regions within the images. The PDF was normalised such that the integral was unity and the concentration was scaled by the mean concentration at that point. The PDFs are shown in figure 8. The PDFs are symmetric at large *x/d* and become increasingly skewed at lower *x/d*. The PDFs are self-similar the local instantaneous concentration is normalised by the mean. The squat PDFs at x/d=20 is partly due to the finite size of the interrogation region, giving an average over a convoluted flowfield. The similarity between PDFs scaled in this manner, over all Re, strongly suggests that the scaled concentration is a *general* similarity variable.

Although theses PDFs compare very well to those of Dowling (1990) there is one important difference. At *r/d*=8 the PDFs of Dowling intercepted the y-axis at values as high as 0.5 and this intercept is used to estimate an intermittency. There is some uncertainty in Dowling's work due to a poor SNR associated with the low signal levels of the Rayleigh Scattering technique. By comparison the intrinsic noise level with PLIF is much lower, however we believe that the PLIF spatial resolution is compromised by detector *cross-talk background.*

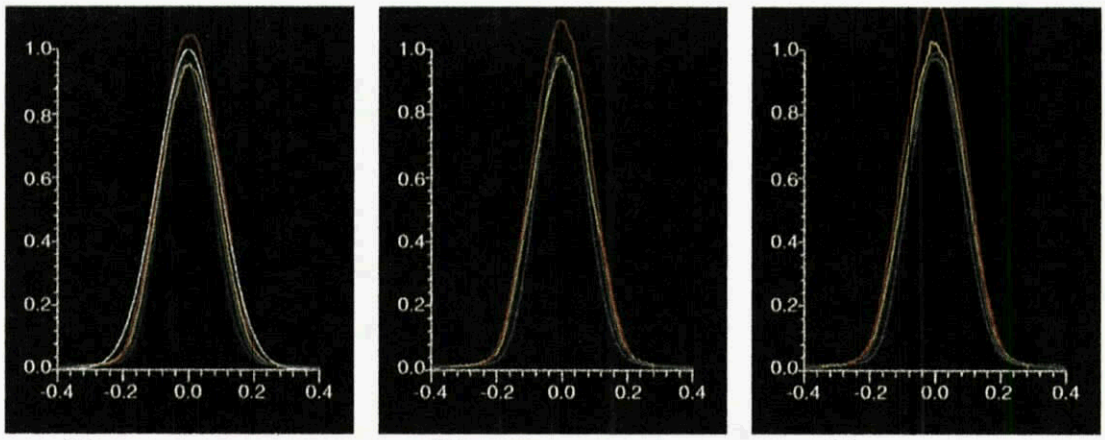


(a) (b) (c)

**Figure 6** Scaled mean concentration ($\chi\overline{C}(\chi,\eta)/\kappa$) versus scaled radial co-ordinate ($\eta = r/(x-x_0)$) for (a) Re=4000, (b) Re=16000 and (c) Re=40000. Colour Key: blue *x/d*=20, green *x/d*=40, yellow *x/d*=60, red *x/d*=80. The additional (white) curve in (a) is that of Dowling (1990).

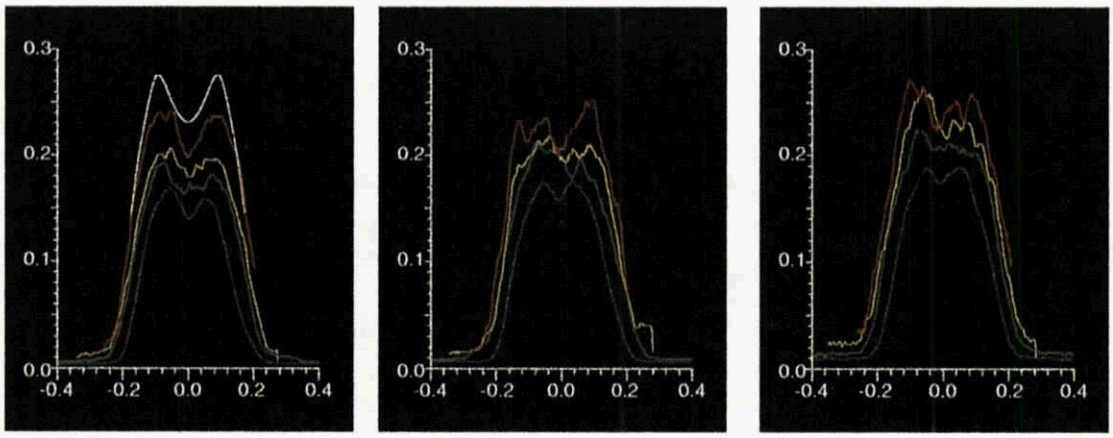


(a) (b) (c)

**Figure 7** Fluctuation profiles for (a) Re=4000, (b) Re=16000 and (c) Re=40000. Axes have been scaled by same parameters as for concentration profiles. Colour Key: blue *x/d*=20, green *x/d*=40, yellow *x/d*=60, red *x/d*=80. The (white) curve in (a) is that of Dowling (1990).

At large distances from the an illuminated pixel the signal falls away in a Lorenzian fashion and therefore contributions to the background can arise from spatially well separated image segments. In Appendix 1 we show that this background could be easily of the order of 0.01-0.1 times the average pixel intensity. This cross-talk background will primarily only affect PDF data for low concentrations, effectively resulting in a near zero probability of finding a zero signal. The effect on the mean and variance of concentration is likely to be very small. This is a detector specific issue and is particularly problematic for intensifiers with point spread functions, with Lorenzian like wing character. Unintensified CCDs give a significantly improved performance in this respect. In principle the effect could be corrected for by processing images to determine the cross-talk background using eqn. A1. Estimating the effect of cross talk background on the PDFs shown in figure 8 suggests that at Re=5,000 (top right) the intermittency is probably 0.2, at Re=16,000 (middle right) it will be close to 0.4 and at Re = 40,000 (bottom right), it lies between 0.3 and 0.6. This accords with Dowling (1990). The problem will also be exacerbated by the finite spatial resolution of the PLIF technique (~1.5mm) particularly for the Re = 40,000 case where the mixing scales

will be at there smallest. Hence the true intermittency probably lies towards the upper end of the estimate given above.

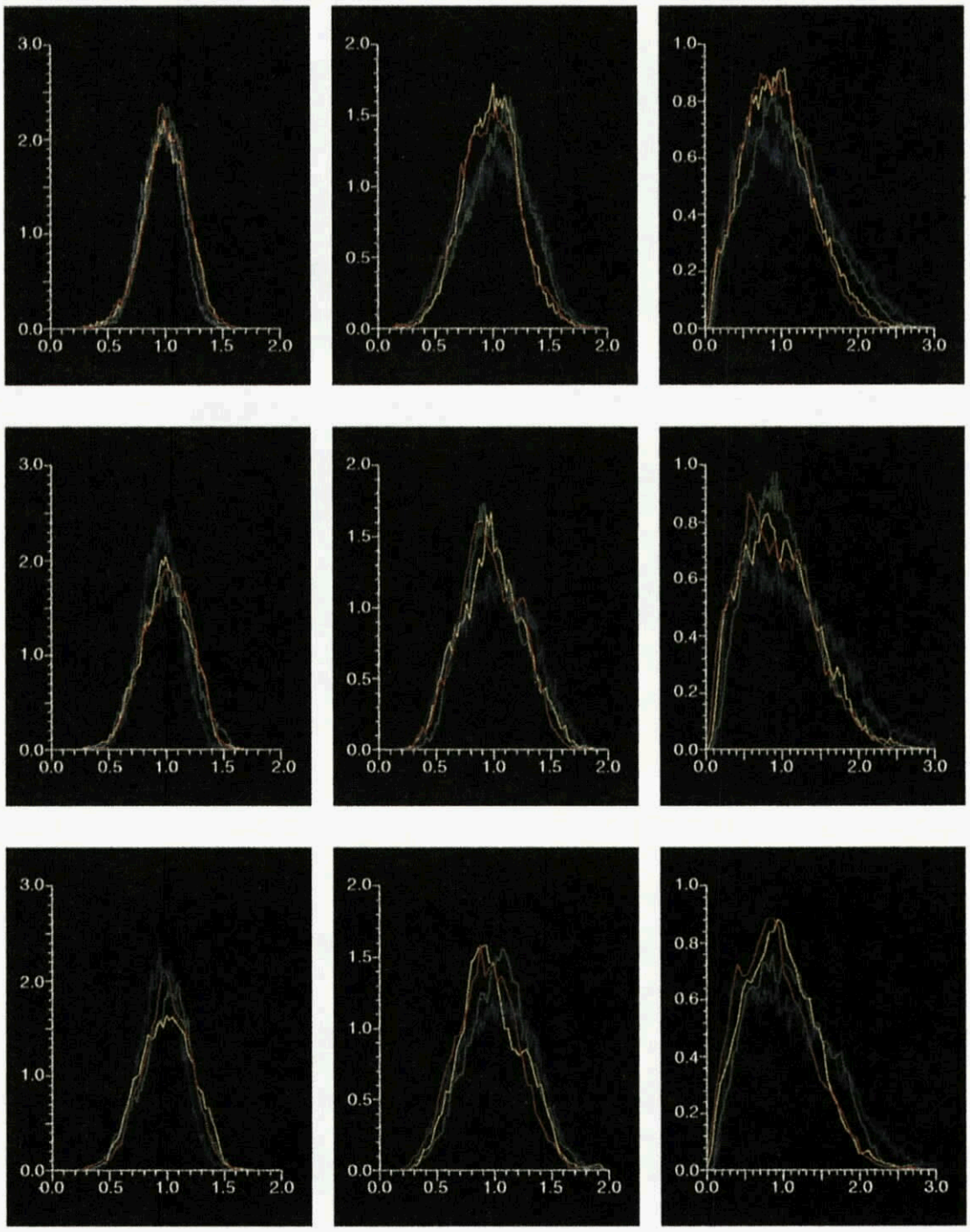


**Figure 8** Probability density versus scaled concentration for Re=5000 (top row), Re=16000 (middle row) and Re=40000 (bottom row). For each row, LHS graph is along centreline ($\eta$=0), middle graph is 3° off centreline ($\eta$=0.06) and RHS graph is 7°off centreline ($\eta$=0.12). Colour Key: blue $x/d$=20, green $x/d$=40, yellow $x/d$=60, red $x/d$=80.

## LIQUID STATE IMAGING IN A CONVENTIONAL COMBUSTOR

Planar fluorescence imaging of liquid fuel was performed on the combusting spray from an airblast atomiser in a conventional double annular combustor, running at an intermediate inlet pressure of 3 bar. Fused silica windows allowed optical access for both axial and radial imaging. In these experiments the PLIF was used to obtain only qualitative data on the structure of the fuel patternation from the injector.

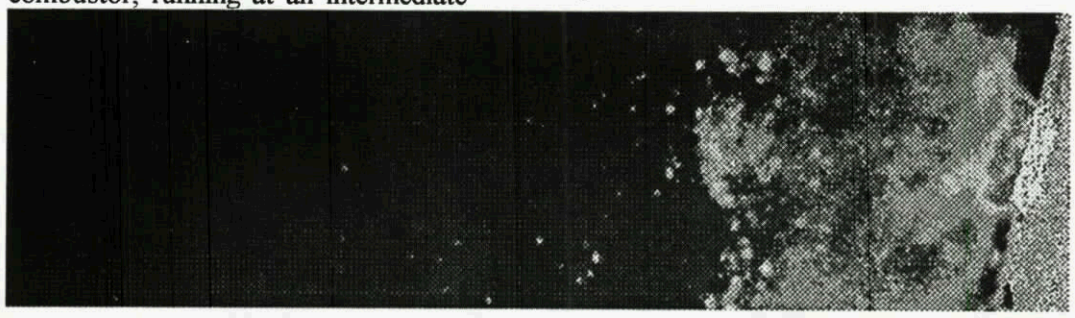

**Figure 9a** Instantaneous LIF image of PPO seeded mineral spirits (liquid phase only)

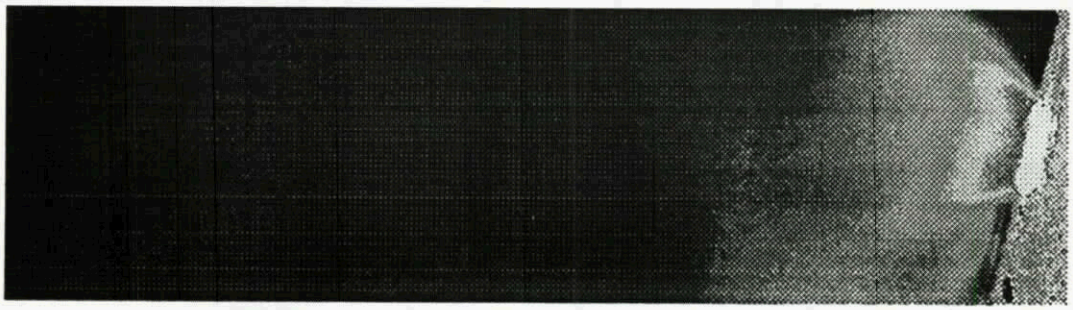

**Figure 9b** Mean of 200 LIF images of PPO seeded mineral spirits - liquid phase only

Kerosine (the standard fuel for gas turbine combustors) will fluoresce naturally, but the fluorescence efficiency varies between batches with the content of aromatics [Harding, 1996]. For consistent fluorescence yield, odourless mineral spirits (kerosine without any fluorescing compounds) was used, with a controlled concentration of a fluorescent aromatic. For liquid fuel imaging, the dopant was 2,5-Diphenyloxazol (PPO). This is an excimer dye which occurs naturally in kerosine. It is excited strongly at 308 nm, fluorescing in a broad spectrum up to 450 nm. PPO doped mineral spirits does not fluoresce in the vapour phase, due either to oxygen quenching or molecular dissociation of the PPO [Harding, 1996]. In these experiments it should be noted that the temperature along the premixer duct does not change significantly and further that the fuel an air are already partially mixed at inlet. Oxygen quenching undoubtedly will compromise the results, however Harding (1996) has shown that the estimated radially integrated fuel flux by PLIF along the duct is essentially constant. If quenching was significant this above result is unlikely because the quenching should be more prevalent for the fully mixed case where the oxygen concentration per mole of fuel is, on average, higher.

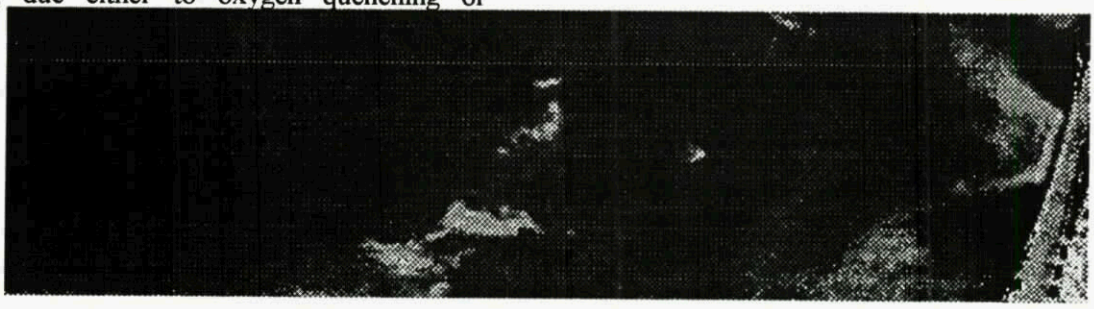

**Figure 10** Instantaneous LIF image of naphthalene seeded mineral spirits - liquid and vapour phases.

Figure 9a shows an example instantaneous axial LIF image of the liquid fuel spray. In the limit of low absorption of the laser light, the fluorescence signal is proportional to the liquid volume fraction. Such axial images show the cone angle, and the distribution, including penetration, of the spray before evaporation. These parameters can be compared with the design assumptions. A data set of 200 such images was acquired, from which statistical information about the spray, such as the mean distribution (Figure 9b); fluctuations etc. could be derived.

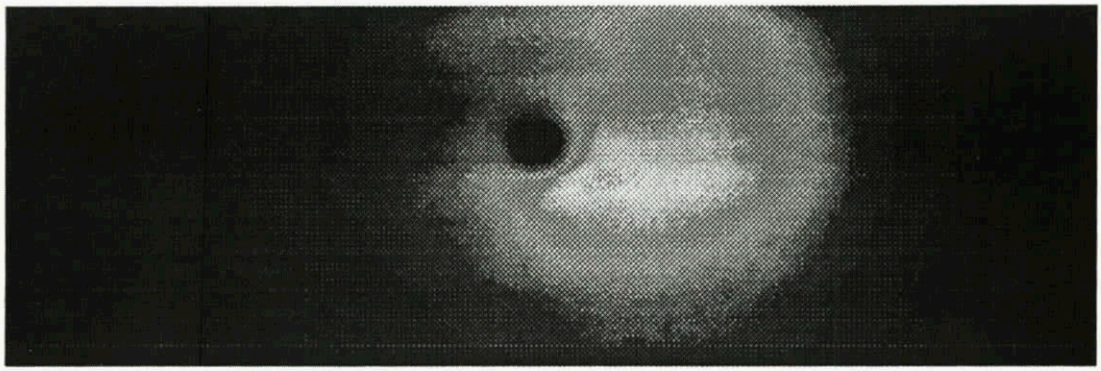

**Figure 11a** Radial LIF image of low fuel flow rate.

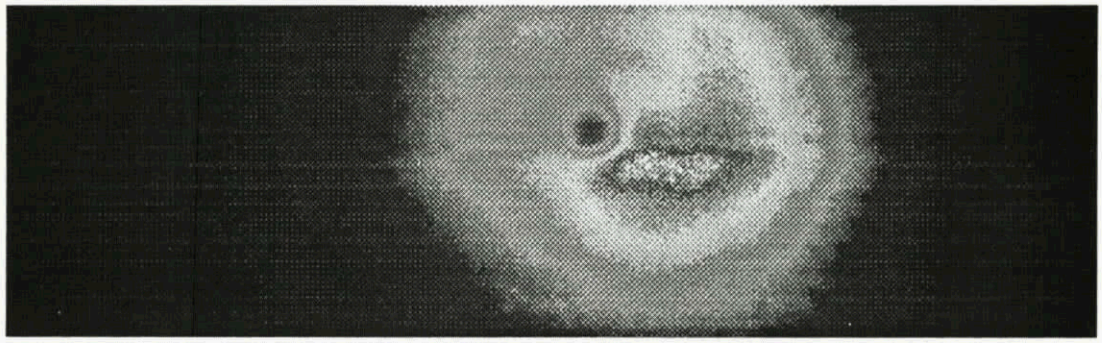

**Figure 11b** Radial LIF image of high fuel flow rate.

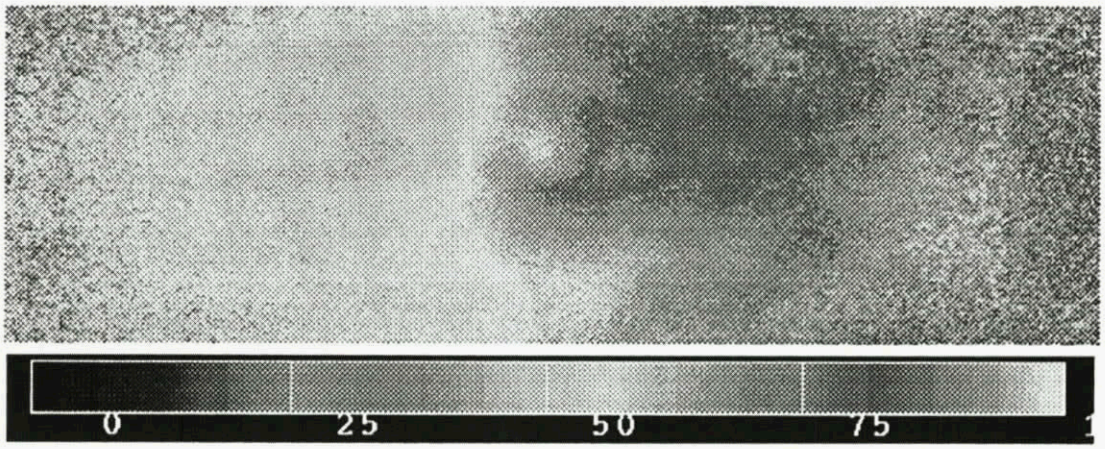


**Figure 11c** Ratio of Figures 4a and 4b (scale is in percent).

Figure 10 shows an instantaneous PLIF image with naphthalene seeded mineral spirits as the fuel, which fluoresces in both the liquid and vapour phases. Comparing Figure 10 with Figure 9a, there is a common signal region corresponding to liquid fuel. In addition, Figure 10 shows fluorescence regions not present in Figure 10b. These correspond to fuel vapour and can be seen downstream of the liquid spray and also at the bottom of the image, where vapour accumulated by a metal wall. In principle, vapour fluorescence images in this

combustor could be obtained by dual imaging Mie scatter and fluorescence from mineral spirits doped with naphthalene. The Mie image would be dominated by the liquid phase and could be used to mask the fluorescence image, leaving a vapour fluorescence image.

When the laser sheet was introduced parallel to the atomiser face, with the camera imaging from downstream, radial liquid fuel LIF images were obtained, shown in Figure 11, where the measurement plane was 10 mm downstream of the injector. After correction for laser light absorption, these images show the patternation of the spray from the injector. Figure 11a is a mean of 200 images taken with a relatively low fuel flow rate. It shows a large asymmetry, with more fuel on the right of the image. Since the laser sheet was introduced from the left of the image, this is clearly not a spurious feature due to laser absorption. Figure 11b is a mean of 200 images taken at a higher fuel flow rate and shows a reduced asymmetry in the fuel patternation. This is confirmed by Figure 11c, which shows the ratio of Figures 11a and 11b. On the right hand side, the ratio of fluorescence signal is close to the ratio of fuel flow rates, i.e. 77 %. On the left side, the ratio is lower, indicating that there is less fuel on that side in Figure 11a than in Figure 11b. This can be explained by the fuel galleries in the atomiser filling more efficiently at higher fuel flow rates. Such radial images are a great aid to designers and developers and can help to explain asymmetries in emissions and temperature profiles at the exit of the combustor under different operating conditions.

## LIQUID AND VAPOUR PHASE IMAGING IN AN LPP RIG

Lean, premixed, prevaporisd (LPP) combustion is a recent development for producing very low emissions levels. Optical access to the rig allowed both axial and radial imaging of fuel-air mixing in the premixing duct of the combustor. This rig was of realistic scale and ran under typical operating conditions, except that the inlet was at nominally atmospheric pressure [Harding, 1996], see figure 12.

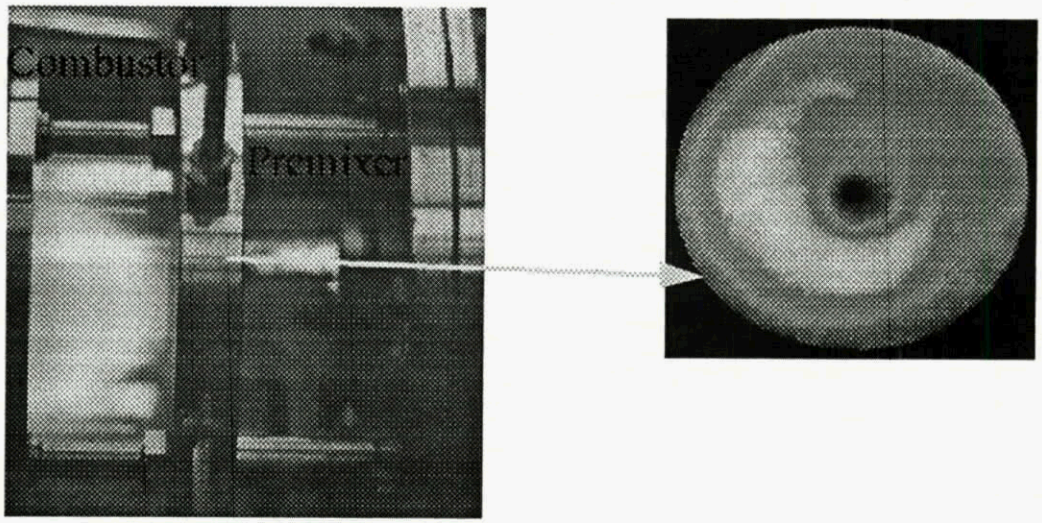


**Figure 12** Photograph of an operating optical LPP combustor and a LIF image of the fuel distribution as marked by naphthalene at the premixer exit.

As in the previous study PPO was used as a dopant to mark the liquid phase. Figure 13 illustrates three images which show the strongly intermittent nature of droplet packets in the evaporating flow.

For vapour phase measurements the rig was fuelled with doped mineral spirits. 4 % by mass of naphthalene (boiling point 491 K) was used to image mixing of lower boiling point fractions; while 0.4 % by mass of fluoranthene (boiling point 653 K) was used to image higher boiling point fractions. Both of these compounds occur in kerosine.

Figure 14 shows three images of naphthalene fluorescence, each of which is a mean of 200 instantaneous radial LIF images at planes 30,

55 and 80 mm from the injector tip. At the start of the duct, there is fluorescing material throughout most of the cross-section. The vapour mixes as it progresses downstream, shown by the increased homogeneity of Figures 14b and 14c.

**Figue 13** Three instantaneous images of droplet fluorescence using PPO seeded kerosene. The vertical axis is on the centre line of the duct with the inlet beneath the bottom of each image.

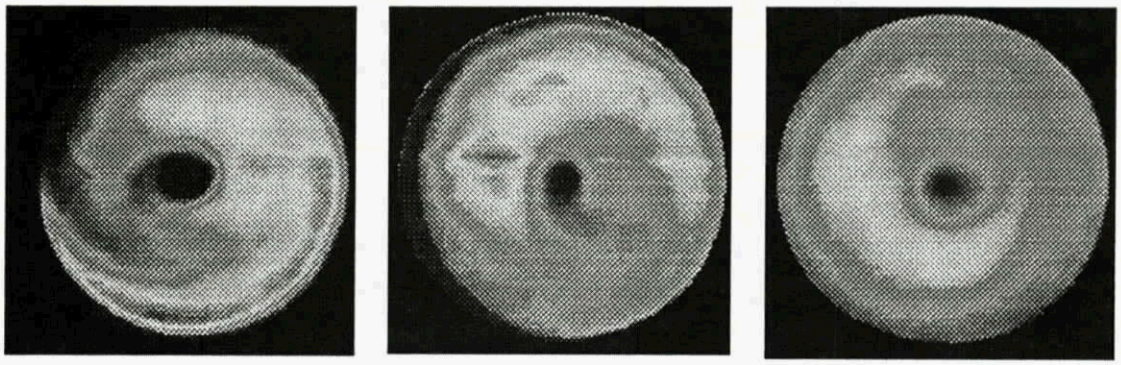

**a)** 30 mm downstream **b)** 55 mm downstream **c)** 80 mm downstream

**Figure 14** Radial naphthalene fluorescence along the premixing duct.

Figure 15 shows equivalent LIF images of fluoranthene fluorescence. In Figure 15a, the vapour exists in an annulus at the outer edge of the duct, and whilst there is mixing along the length of the duct, the higher boiling point fractions of kerosine are still not well mixed by the duct exit and the combustion zone (Figure 15c).

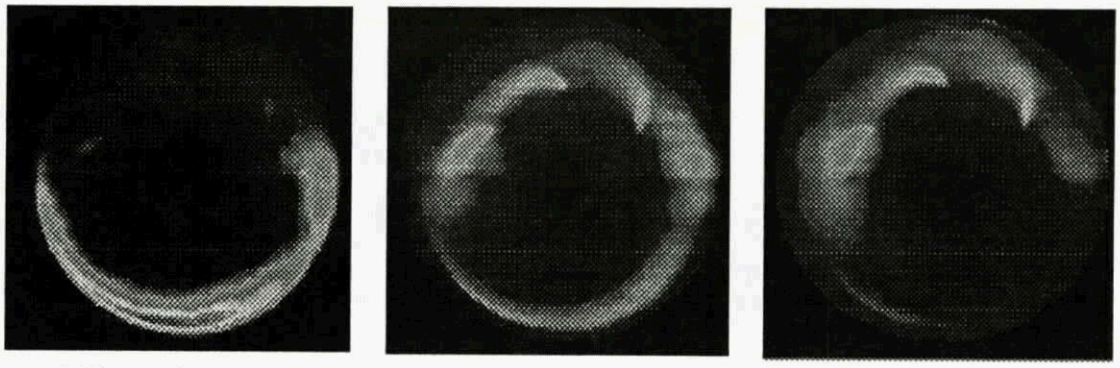

**a)** 30 mm downstream **b)** 55 mm downstream **c)** 80 mm downstream

**Figure 15** Radial fluoranthene fluorescence along the premixing duct.

Such images illustrate to the designer the occurrence of variations in AFR, which lead to different burning rates. Also, additives used in a fuel will tend to follow the fraction of similar boiling point and thus may not be present throughout the combustion zone.

## CONCLUSION

Planar Laser Induced Fluorescence has been used to study both fundamental gas-gas mixing and to obtain images of fuel in both the liquid and vapour phase from operating gas turbine combustors. Measurements at both atmospheric and intermediate inlet pressures have been shown to be possible.

Detailed measurements of gas-gas mixing from a jet support self-similarity and illustrate the low noise capability of the technique. Analysis of PDF data however, taking into account cross-talk background clearly shows that intensified CCD cameras are limited in there capability to study intermittency in mixing.

For quantitative imaging in a gas turbine combustor, a fuel of doped mineral spirits was used and the images were corrected for systematic experimental errors.

Axial PLIF imaging of the liquid phase shows the overall spray geometry, including the cone angle. Radial imaging at various downstream plane shows the liquid phase patternation and the vapour phase fuel-air mixing. The use of different dopants allowed the progress of different fuel fractions to be tracked.

These experiments collectively demonstrate the ability of the method for, in particular, semi-quantitative patternation of fuel sprays in operating combustors. We believe this method has the potential for routine "in situ" fuel patternation.

## ACKNOWLEDGEMENTS

The authors would like to gratefully acknowledge the support of Rolls-Royce plc. Parts of the work were sponsored by CEC project AER2-CT92-0036: "Low-NOX II" and by EPSRC grant number GR/H78238.

## REFERENCES

Arnold A., Becker H., Suntz R., Monkhouse R., Wolfrum J., Maly R. and Pfister W. (1990) Opt. Lett. **64** 831.

Bachalo, W. D. (1980) *Appl. Opt.* **19**, 3, 363-370.

Berckmüller M., Tait N.P., Lockett R.D., Greenhalgh D.A., Ishii K., Urata Y., Umiyama H., Yoshida K. (1994) *In-Cylinder Crank-Angle-Resolved Imaging of Fuel Concentration in a Firing SI Engine Using Planar Laser-Induced Fluorescence*, Twenty-Fifth Symposium (International) on Combustion, The Combustion Institute, pp. 155-156.

Berckmüller M., Tait N.P., Greenhalgh D.A. (1996) *The Time History of the Mixture Formation Process in a Lean Burn Stratified-Charge Engine*, Transactions of the SAE International Fuels & Lubricants Meeting & Exposition, San Antonio, Texas, SAE Technical Paper Series 961929.

Berckmüller M., Tait N.P., Greenhalgh D.A. (1997) *The Influence of Local Fuel Concentration on Cyclic Variability of a Lean Burn Engine*, Transactions of the SAE International Congress & Exposition, Detroit, SAE Technical Paper Series 970826.

Bohren, C. F. and Huffman, D. R. (1983) *Absorption and Scattering of Light by Small Particles.* Wiley.

Bryce, D.J. (1996) ) *PhD Thesis*, Cranfield University.

Dahm WJA and Dimotakis P.E. (1990) *Mixing at Large Schmidt Number in the Self-Similar Far Field of Turbulent Jets* Journal of Fluid Mechanics Vol 217 pp 299-330.

Dahm W.J.A. Southerland K.B. and Buch K.A. (1991) *Direct, High Resolution, Four-Dimensional Measurements of Fine Scale Structure of Sc>>1 Molecular Mixing in Turbulent Flows*. Physics of Fluids A Vol 3 No. 5 pp 1115-1127 May 1991.

Dowling D.R. (1990) and Dimotakis P.E. *Similarity of the Concentration Field of Gas-*

*Phase Turbulent Jets* Journal of Fluid Mechanics Vol. 218 pp 109-141.

Eckbreth, A. C. (1988) *Laser Diagnostics for Combustion Temperature and Species.* Abacus Press.

Greenhalgh, D.A. (1994) Chapter in *Optical Diagnostics for Flow Processes* (ed L. Lading, G. Wigley, P. Buchhave) Plenum Press.

Greenhalgh D.A. (1988) *"Quantitative CARS Spectroscopy"* within "Advances in Non-Linear Spectroscopy" Edited by RJH Clarke and RE Hester, John Wiley and Sons Ltd.

Harding, S. C. (1996) *PhD Thesis*, Cranfield University.

Hinze J.O. (1959) *Turbulence: An Introduction to its Mechanism and Theory* McGraw-Hill, New York.

Lefebvre, A. H. (1989) *Atomisation and Sprays*. Taylor and Francis.

Long, M. B. (1993) Chapter in *Instrumentation for Flows with Combustion* (ed A. M. K. P. Taylor) Academic Press.

Lozano A. (1992) Yip B. and Hanson R.K. *Acetone: a Tracer for Concentration Measurements in Gaseous Flows by Planar Laser-Induced Fluorescence* Experiments in Fluids Vol 13 pp 369-376

Maas, H.-G. and Gruen, A. (1995) Opt. Eng. **34**, 7, 1970-1976.

Neij H., Johansson B. and Alden M. (1994) *Development and Demonstration of 2D-LIF for studies of Mixture Prepartaion in SI Engines,* Comb. and Flame **99**, 449-457.

Seitzman, J. M. and Hanson, R. K. (1993) Chapter in *Instrumentation for Flows with Combustion* (ed A. M. K. P. Taylor) Academic Press.

Serpengüzel, A., Swindal, J. C., Chang, R. K. and Acker, W. P. (1992) *Appl. Opt.*, **31**, 18, 3543-3551.

Tait, N. P. and Greenhalgh, D. A. (1992) *Twenty-Fourth Symposium (Int.) on Combustion.* The Combustion Institute. 1621-1628.

Tait N. P. and Greenhalgh D. A. (1993) *PLIF Imaging of Fuel Fraction in Practical Devices and LII Imaging of Soot.* Ber. Bun.-Ges. Phys. Chem., **97**, 1619-1625.

Wigley, G. (1994) Chapter in *Optical Diagnostics for Flow Processes* (ed L. Lading, G. Wigley, P. Buchhave) Plenum Press.

Zheng, Q. P., Jasuja, A. K. and Lefebvre, A. H. (1996) *Twenty-Sixth Symposium (Int.) on Combustion.* The Combustion Institute.

## APPENDIX 1 - SPATIAL RESOLUTION AND CROSS-TALK BACKGROUND

This appendix considers the different amounts of cross-talk background that can be produced for differing point spread functions or blooming.

The thickness of the laser sheet and the resolution of detector equipment primarily determine the spatial resolution within a measurement volume. The CCD chips used in the study consisted of 600x400 pixels, each of size approximately 25μm. The intensifier consists of bundles of about the same size. For an unitensified CCD pixel size would be the fundamental limit on spatial resolution for an aberration free optical system. An estimate for an upper limit, due to aberration and misalignment would be approximately double the fundamental limit. In these experiments a lens coupled Gen. II Princeton Instruments Intensifier was used, this degrades the spatial resolution (i.e. increases the point spread function width) due to increased cross talk (also termed blooming). The blooming is due to the effect of the phosphor and photomultiplication process. Images containing a series of signals from very small carbon particles were used to gauge the spread function. A typical point spread is illustrated in figure 0.1. The second graph of the figure (b) also plots Gaussian and Lorenzian traces.

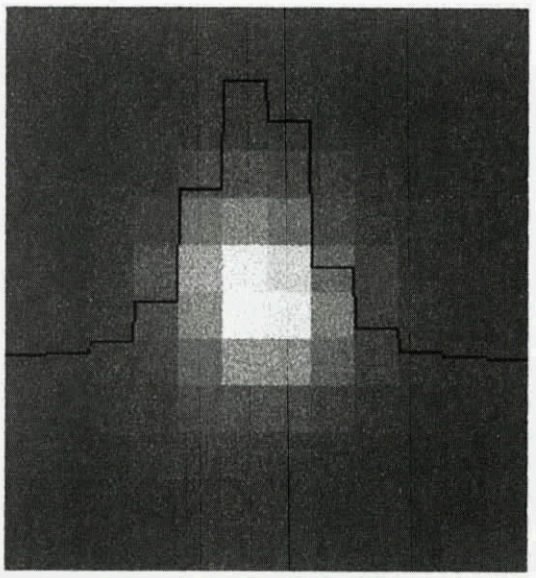

(a)

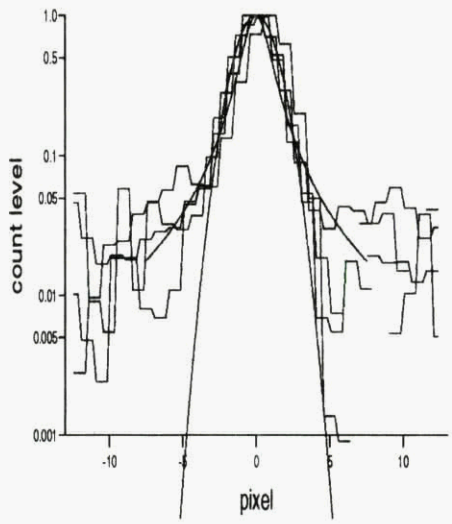


(b)

**Figure A1** (a) 2D spread and 1D plot of a typical spread function. (b) graph showing a series of point spread and fits by Gaussian and Lorenzian functions on a logarithmic scale.

The contribution to the cross-talk background, $I_b$, at a given pixel, for a point spread function $g(\Delta)$ is given by:

$$I_b = \left[ I_{av} \int_0^{2\pi}\int \Delta \times g(\Delta) \times I(\Delta,\theta) d\Delta d\theta \right] - I(0,\theta)$$

Eqn. A1

where $\Delta,\theta$ are the polar co-ordinates of each pixel and $I(\Delta,\theta)$ is the intensity at each pixel. To estimate the likely background it is useful to assume all surrounding pixels have even illumination intensity $I_{av}$. Further if we also assume that the background rather than the signal arise blooming from pixels which are at least 5 times further away than the characteristic of the point spread function, eqn. A1 can be simplified to:

$$I_b \approx I_{av}\int_0^{2\pi}\int_{\Delta\min}^{\Delta\max}\Delta \times g(\Delta)d\Delta d\theta$$

Eqn. A2

For the case of a Gaussian point spread function the normalised function is

$$g_G(\Delta,\theta)=\left(\frac{1}{\Gamma\sqrt{\pi}}\right)^2\exp\left(-\frac{\Delta^2}{\Gamma^2}\right)$$

Eqn. A3

where $\Gamma$ is the 1/e halfwidth. Eqn. A3 can be readily inserted into eqn. 2 and integrated to give:

$$I_b=\left[\exp\left(-\frac{\Delta^2}{\Gamma^2}\right)\right]_{\Delta\min}^{\Delta\max}$$

Eqn. A4

For $\Delta_{max} = \infty$ and choosing $\Delta_{min}$ to be $5\Gamma$ where $\Gamma$ is typically 2 pixels gives a value of $I_b = 1.4\times10^{-11}I_{av}$. The effect of a Gaussian blooming would therefore be undetectable given an error of at least ±2 counts from the CCD.

For a Lorenzian point spread function of the general form,

$$g_L(\Delta,\theta)=K(\Delta_{\max})\left(\frac{1}{\Gamma^2+\Delta^2}\right)$$

Eqn. A5

which has no definite integral because it does not converge for large $\Delta$. The 2D Lorenzian function can be evaluated if $\Delta$ is truncated at $\Delta_{max}$ such that $K$ is a normalisation constant *specific* to the truncation limit. Thus $K$ can be evaluated from:

$$1/K(\Delta_{\max})=\pi\left[\ln\left(\Gamma^2+\Delta^2\right)\right]_0^{\Delta\max}$$

Eqn. A6

and an estimate of $I_b$ can be obtained using:

$$I_b=I_{av}K(\Delta_{\max})\pi^2\left[\ln\left(\Gamma^2+\Delta^2\right)\right]_{\Delta\min}^{\Delta\max}$$

Eqn. A7

As for the Gaussian case if $\Gamma$ is of order 2 pixels and then the fraction of $I_{av}$ contributing to the background can be determined. In figure A2 eqn. A7 has been plotted for $I_{av}$ =1 for a range of truncation limits $\Delta_{min}$. For values of $\Delta_{min} > 5\Gamma$ or 10 pixels substantial background signals of order 0.1 $I_{av}$ are predicted.

Clearly a 2D Lorenzian point spread function is not physically realistic, however a truncated form provides a suitable model function and is entirely consistent with point spread functions found and widely used in the analysis of data from Gen. II intensifiers coupled to diode arrays (Greenhalgh, 1988). Also the data of figure A1b strongly supports the notion of a Lorenzian like point spread function for intensified CCD systems. The key issue is the truncation limit, which cannot be determined with appropriate accuracy from the data in figure A1b. Lorenzian like point spread functions can generate a significant background signal from both near and possible spatially distant other image features. To estimate this background more precisely, for a given image, the image should be de-convoluted using eqn. A1 with an appropriate function $g$ and by integrating for $\Delta$ greater than say $5\Gamma$.

Contributions to the background of this type are likely to be an important factor for any detector with large wings and a non-intensified system would be preferable. This additional background we refer to as *cross-talk background*.

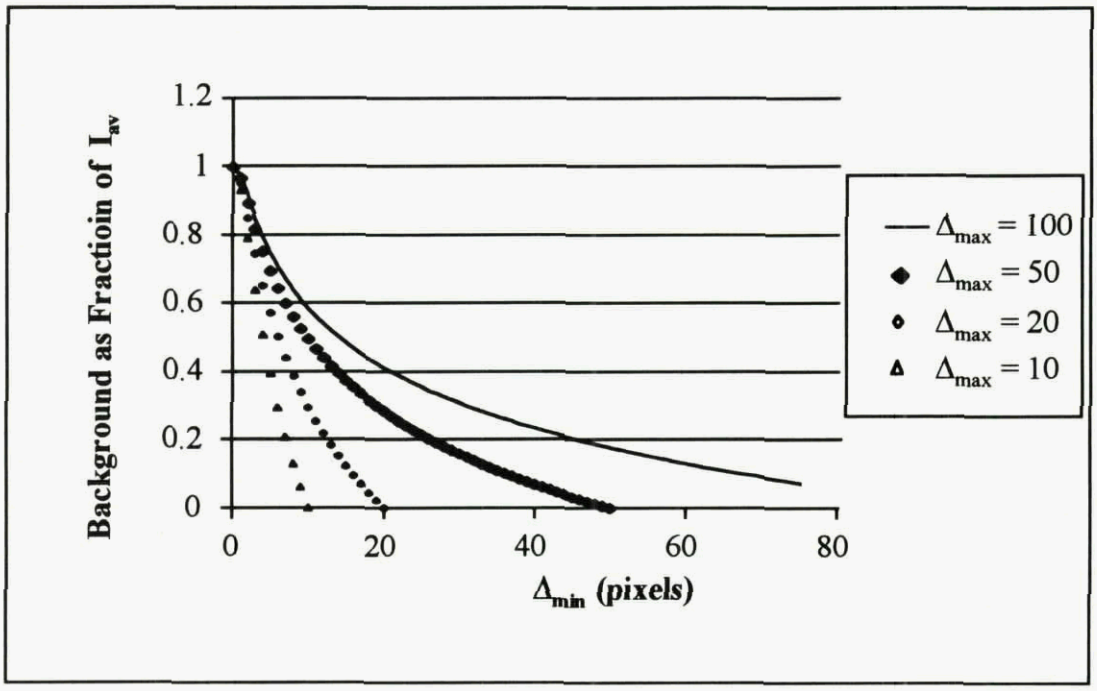


**Figure A2** Fraction of $I_{av}$ contributing to cross-talk background as a function of $\Delta_{min}$ in pixels for *different truncation radii for the Lorenz,* $\Delta_{min}$ *for an assumed* $\Gamma = 2$, *see eqn. Below.*

Paper 25
Author: Greenhalgh

Q: Behrendt

Could you comment on the possibilities of using your technique under elevated pressures? Do you have any problems with the penetration depth attenuation of the light sheet in dense sprays?

A: There are no major limitations for applying the technique at high pressure. The main problem so far is the cost of providing optical access to combustors operating at over 5 bar pressure. We have used these methods successfully at high pressure in petrol and diesel engines with pressures of up to 100 bar. For ketone seeding the limit will be about 800 K - for naphthalene and similar the limit will be a higher temperature. However, at high pressure the naphthalene fluorescence will be reduced by quenching - this appears to be linear therefore the increased fuel concentration to maintain air fuel ratio compensate. There is an outstanding need for quenching data for naphthalene for temperatures up to 900k and pressures up to 40 bar.

We have found that commercial kerosene, supplied to a high specification, has considerable variation in fluorescence behaviour from batch to batch. Given the sensitivity of fuel placement to boiling point shown in this paper, it is better to use mineral spirit with an optimum concentration of a fluorescent seed. This type of system will have very low attenuation at the excitation wavelength of 308nm. Emission is around 430nm where the system is transparent and therefore there is no radiation capture.

# High-Temperature Surface Measurements of Turbine Engine Components Using Thermographic Phosphors

**Sami Alaruri and Andy Brewington**
Allison Engine Company, Rolls Royce Aerospace Group,
P.O. Box 420, M/S W3A, Indianapolis, IN 46206, U.S.A.

## 1. SUMMARY
A laser-based system for single point high-temperature measurements of turbine engine component surfaces coated with thermographic phosphors is described. Decay lifetime calibration measurements obtained for $Y_2O_3$:Eu over the temperature range ~530-1000°C are presented. Further, the results obtained from a coupon placed in the outlet gas flow of an atmospheric-combustor are described.

## 2. INTRODUCTION
New designs of advanced turbine engines strive to increase the thermal efficiency of engine components, and thus performance, by introducing sophisticated airfoil cooling schemes, new composite materials, and new design methods. As a result, a new generation of advanced engines with shorter combustion chambers, higher inlet temperatures and pressures, lower specific fuel consumption, and reduced weight is emerging. The high-temperature environments of these advanced engines are creating new challenges for the two widely used temperature measuring sensors, namely thermocouples and pyrometers [1-3].

Currently, infrared pyrometers, which are used for engine diagnostics, control, and general health monitoring purposes, are incorporated into several commercial and military engine tests for collecting surface temperature measurements [1-3]. Despite several advances in the recent years in the areas of radiation detector technology and data acquisition systems, single wavelength intensity-based radiation thermometry instruments suffer from three major problems:

1. Inferring the object surface temperature from the spectral radiance measurements without knowing the emissivity of the object at different temperatures.
2. Correcting temperature measurements for the extraneous reflection and emission components (i.e., background radiance) that can be produced by flames, walls, and particles in the field of view (in advanced engines the magnitude of the reflection component can constitute up to 70% of the measured signal [2].
3. Correcting for the attenuation of the optical signal due to the variable transmissivity of the optical path.

The emissivity-temperature dependence can be a significant source of error in the case of single wavelength pyrometers ±60°C at 1000°C [4,5]. Algorithms for correcting pyrometer temperature readings for different uncertainty components have been treated in several publications [1-5]. Due to the complexity of these multicomponent radiation problems, data reduction algorithms were developed around several assumptions and empirical approximations. Consequently, the confidence level in the precision and accuracy of the temperature measurements gathered using these instruments is low, especially when used for gathering surface temperature measurements from blades coated with thermal barrier coatings under extreme extraneous radiation conditions.

In this paper, we describe a prototype laser-based system for remotely measuring the surface temperature of parts coated with thermographic phosphor ($Y_2O_3$:Eu-europium-activated yttrium oxide) over the temperature range ~530-1000°C. Unlike infrared pyrometry, temperature measurements collected utilizing the decay lifetimes of thermographic phosphors are independent of the target emissivity, the spectral characteristics of the coated object, and the reflected radiation component. Furthermore, the absence of lead wires, as is the case in thermocouples, makes this technique immune to electromagnetic radiation interference and very attractive for measuring the surface temperature of rotating engine parts (i.e., blades). Referenced to the output of K-type thermocouples, the accuracy of this technique was estimated to be approximately ±2%. Similar work reported thus far by groups at Oak Ridge National Laboratory, Los Alamos National Laboratory, and EG&G [6-9] has demonstrated the feasibility of this noncontact temperature-sensing technique for turbine engine, furnace, ambient-spin rig, and centrifuge applications where high temperature and harsh environments are encountered.

This paper also presents $Y_2O_3$:Eu fluorescence decay lifetime versus temperature data and the measurements obtained from a proof-of-principle test conducted on a stationary target coated with $Y_2O_3$:Eu that was placed in the outlet gas flow of an atmospheric pressure combustor. This new high-temperature measurement technique can provide engine designers with accurate and reliable temperature measurements and can aid them in evaluating the performance of new engine components and designs.

## 3. EXPERIMENTAL
The laser induced fluorescence (LIF) stationary target measurement system consists of four major components: laser system, fiber-optic probe, signal collection, and data acquisition system. The LIF system is schematically depicted in Figure 1.

As shown in Figure 1, the laser beam (266 nm/4-6 ns pulse width at FWHM) generated from an Nd: YAG laser (Quanta Ray GCR-4-30, Spectra Physics) was upled into a 2000 μm core diameter fused silica-on-fused silica optical fiber (Fiberguide Industries, Superguide G) using a short focal length fused silica lens. During each data collection cycle the fluctuations in the laser beam energy were monitored using a pyroelectic joulemeter (Molectron-Model J50). The spot size of the launched laser beam was adjusted to overfill the numerical aperture of the delivery optical fiber (i.e., overfill the core diameter of the launch fiber). Generally, the input surface damage of the used high $OH^-$ step-index fiber was measured around 3.5 J/cm$^2$ [10]. Nine 1000 μm core diameter optical fibers were used to collect the

*Paper presented at an AGARD PEP Symposium on "Advanced Non-Intrusive Instrumentation for Propulsion Engines", held in Brussels, Belgium, 20-24 October 1997, and published in CP-598.*

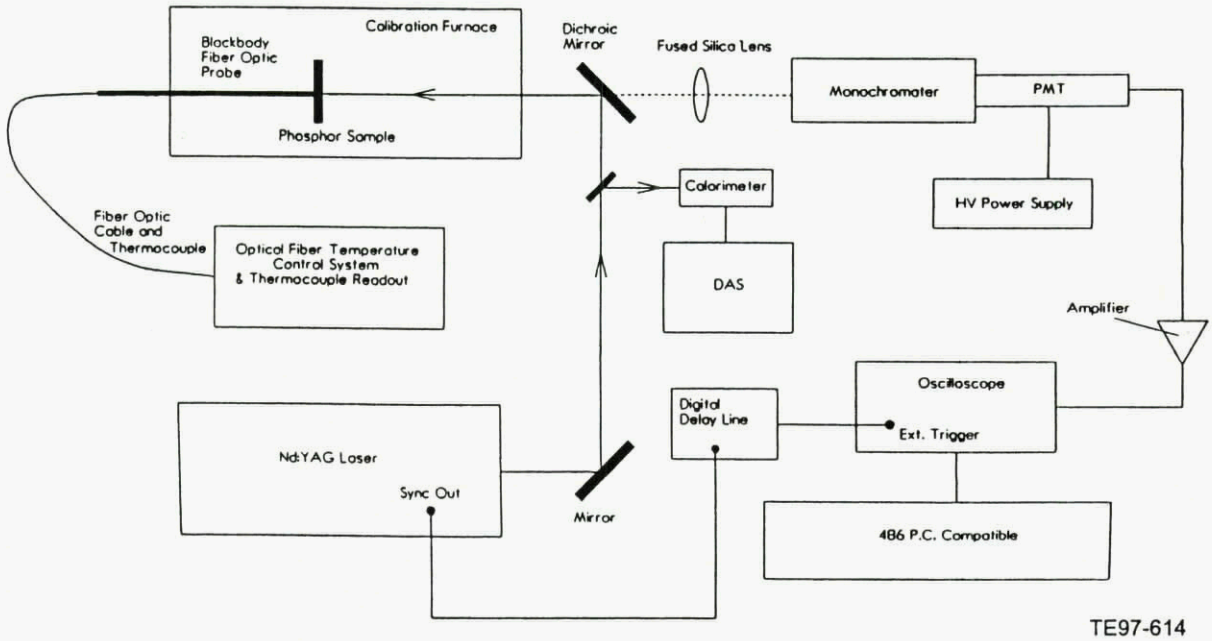


**Figure 1. Schematic Diagram of the LIF Experimental System Used for Measuring Fluorescence Decay Lifetimes as a Function of Temperature (DAS is a Data Acquisition System; PMT is a Photomultiplier Tube).**

fluorescence signal emanating from the phosphor coated air-cooled target. The maximum area inside the housing of the optical probe was utilized by arranging the collection fibers circumferentially around the launch fiber. An air-cooled probe was developed and fabricated [10] to protect the collection and delivery fibers against the engine harsh thermal and dynamic environment. Other optical probes designed for turbine engine thermographic phosphor measurements have been reported in References 11 and 12. In comparison with these optical probes, Allison's fiber optic probe reduces the interference between the collected fluorescence pulses and the background pulses generated by the energetic 266 nm laser beam by isolating the launch optical path from the collection optical path. Since generating microbends along the rigid 2000 μm core-diameter launch fiber or wrapping the fiber around a mandrel to achieve equilibrium mode distribution (EMD) was not feasible, the spot size and the spatial profile of the excitation beam were governed by the initial launch conditions into the numerical aperture of the optical fiber [13,14]. Usually a surface area approximately 1 mm in diameter was covered by the excitation laser beam.

The $Y_2O_3$:Eu-611 nm emission wavelength was selected by coupling the collection fibers into the entrance slit of a Czerny-Turner configured programmable monochromator (f/3.9, 0.275 meter-Acton Research Corporation-Spectra Pro 0.275). The gathered 611 nm optical radiation was converted into an electrical signal by the means of a 12-stage fast risetime (~2 ns) photomultiplier tube (Philips-XP2233B) the output of which was amplified and fed into a 350 MHz oscilloscope (LeCroy-Model 9450). During each measurement cycle, 300 fluorescence pulses were accumulated and averaged by the oscilloscope. The resultant averaged pulse was then transmitted to a PC for additional processing via IEEE-488 communication interface.

Because of the negligible contribution of the fiber's dispersive-pulse broadening mechanisms on the constant of the decay lifetimes (1000 to 1 μseconds), employing a deconvolution technique to correct for the impulse response of the collection optical fibers was deemed unnecessary at 611 nm [14].

## 4. RESULTS AND DISCUSSION

Utilizing the previously reported LIF calibration system [15], fluorescence decay lifetimes over the temperature range ~530-1000°C were collected for $Y_2O_3$:Eu (4.52% Eu). The fluorescence decay lifetimes were calculated by taking the natural logarithm of the resulting averaged fluorescence pulse, $f(t)$, which can be expressed assuming a first-order sample approximation as

$$F(t)=F_0 \exp(-t/\iota) \qquad (1)$$

where $\iota$ is the average fluorescence decay lifetime and $F_0$ is the signal amplitude. The best fit for the linear portion of the data (i.e., slope = $-1/\iota$) was computed using linear least-squares regression analysis. Figure 2 depicts three sets of fluorescence decay lifetime measurements obtained for the 611.0±0.2 nm-$Y_2O_3$:Eu emission line. Clearly, the onset quenching temperature for $Y_2O_3$:Eu is approximately 510.0±0.6°C. No variation in the fluorescence decay lifetime was recorded beyond 1000°C. At 1000°C the measured average decay lifetime for the 611 nm emission line was 0.480±0.005 μs. The thermal quenching of rare-earth doped thermographic phosphors at the onset quenching temperature can be ascribed to a charge-transfer phenomenon that is best described by Struck and Fonger [16,17]. Utilizing Mathematica® [18], empirical regression fits were calculated for the temperature response of $Y_2O_3$:Eu as a function of

decay lifetimes. The obtained functional forms are listed in Table I.

The solid line that appears in Figure 2 represents the empirical fit calculated using the regression relationships given in Table I. The standard deviation for each temperature measurement is given by [19]

$$\sigma_z=((\partial f/\partial x)^2 S_x^2+(\partial f/\partial y)^2 S_y^2)^{1/2} \quad (2)$$

where x, y, and z = f(x, y) are independent variables and $S_x$, $S_y$, and $S_z$ are the standard deviations for these variables. In deriving Equation 2 the errors in x and y were assumed to be independent and uncorrelated (i.e. $S_{xy} = 0$). Further, for n measurements the standard error can be written as

$$S_z=\sigma_z/\sqrt{n} \quad (3)$$

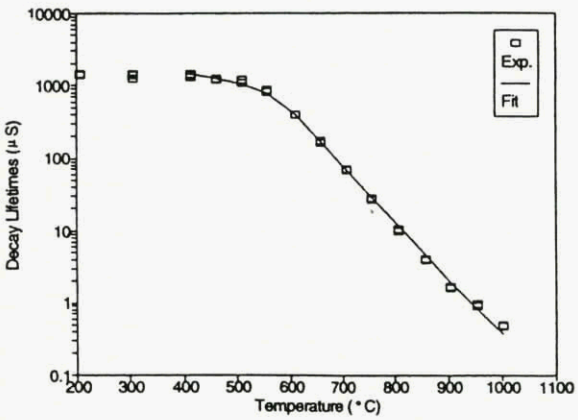


TE97-615

**Figure 2. Decay Lifetimes Versus Temperature Collected for the $Y_2O_3$:Eu-611.0±0.2 nm Emission Line Using 266 nm Excitation**

**Table I**
**Regression Fits Calculated for 611 nm $Y_2O_3$:Eu Over the Temperature Range 530-1000°C**

| Decay lifetimes μs | Fit | Values of constants and $r^{2a}$ |
|---|---|---|
| $1392 \geq \iota > 396{\cdot}9$ | $T = [c_1 + c_2\iota^3]^{-1}$<br>$410 > T > 610°C$ | $c_1 = 0{\cdot}002$<br>$c_2 = 2{\cdot}776 \times 10^{-3}$<br>$r_2 = 0{\cdot}949$ |
| $396 \cdot 9 \geq \iota > 4{\cdot}03$ | $T = c_1 + c_2 \ln(\iota)$<br>$610 > T > 850°C$ | $c_1 = 932{\cdot}293$<br>$c_2 = -53{\cdot}136$<br>$r_2 = 0{\cdot}999$ |
| $4 \cdot 03 \geq \iota \geq 0{\cdot}48$ | $T = \exp(c_1 + c_2\iota)$<br>$850 \geq T \geq 1000°C$ | $c_1 = 7{\cdot}033$<br>$c_2 = -0{\cdot}177$<br>$r_2 = 0{\cdot}998$ |

[a] $r^2$ is the coefficient of determination

The standard errors calculated for the three temperature regions are shown in Table II. Based upon the derived standard errors an average standard error of ±2% was calculated for the three empirical fits.

Other phosphors such as YAG:Tb (terbium activated yttrium aluminum gallium oxide) may be used for obtaining high surface temperature measurements from engine parts. Because YAG:Tb fluorescence lies in the green region of the electromagnetic spectrum (544 nm), it is a particularly useful phosphor when used in engine locations where a large background signal component would be detected. However, the quantum yield of YAG:Tb-544 nm emission line is smaller than the $Y_2O_3$:Eu-611 nm by roughly a factor of two, which makes $Y_2O_3$:Eu the favored phosphor for turbine engine applications [15].

### 4.1 Field Test of LIF System

Two experiments were conducted using the LIF system, to read the surface temperature of a superalloy single-crystal coupon coated with $Y_2O_3$:Eu. During these experiments, the thermographic phosphor-coated coupon was mounted in an open burner rig (Figure 3). The objectives of the field test were to examine the magnitude and the decay lifetimes of the fluorescence and background signals in a combustion environment, and

**Table II**
**The Calculated Standard Deviations for Each Temperature Range**

| Temperature range °C | Standard deviation |
|---|---|
| $410 > T > 610$ | $\sigma_T = [\{-3\, C_2\, \iota^2/(C_1 + C_2\iota^3)^2\}^2 S_\iota^2]^{1/2}$ |
| $610 \geq T > 850$ | $\sigma_T = [(C_2/\iota)^2 S_\iota^2]^{1/2}$ |
| $850 \geq T \geq 1000$ | $\sigma_T = [\{C_2 \exp(C_1+C_2\iota)\}^2 S_\iota^2]^{1/2}$ |

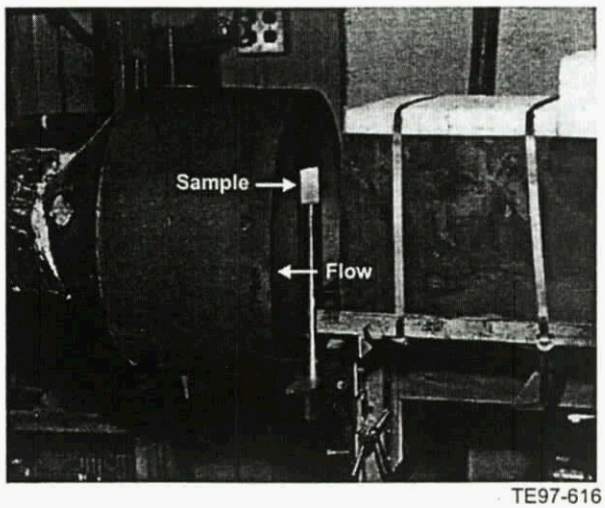


TE97-616

**Figure 3. Coupon Coated With $Y_2O_3$:Eu Mounted in the Open Burner Rig. As This Photograph Illustrates, the Coupon was Rotated with Respect to the Flow Direction to Allow Optical Access to the Front Surface**

to estimate the survivability of a phosphor-chemical binder in an engine-like environment. In this test the coupon was subjected to gas flow velocities ranging between 407 and 245 m/s and pressures of ~ 14-7 psi. Typical pressures and gas velocities in a turbine engine range between Mach 0.8-0.9 and ~300 psi, respectively.

The $Y_2O_3$:Eu was applied to the surface of the coupon using a proprietary chemical binder. An air brush was utilized in applying the mixture of phosphor and chemical binder to the coupon front surface. The average thickness of the deposited films was 25±5 μm. The temperature of the phosphor-coated coupon was monitored using K-type thermocouples embedded into the back of the coupon.

Using an identical coupon made of the same material thickness and instrumented with small diameter K-type thermocouples at both surfaces (6 thermocouples embedded into the backside and 6 thermocouples embedded into the front side), the temperature gradient between the two surfaces at different temperature settings was established for the open burner rig test. The collected temperature readings for the front and back surfaces were used to compute an empirical relationship correlating the back surface to the front surface temperature measurements at different temperature settings. A data acquisition system (HP 75000B) equipped with a thermocouple relay multiplexer card was used to read the thermocouple outputs.

Figure 4 depicts the decay lifetime versus the corrected front surface temperature measurements obtained for a single-crystal coupon coated with $Y_2O_3$:Eu, during the open burner rig test. The figure represents the measurements obtained for the same sample after two consecutive periods, 7.5 and 14.7 hours, of thermal exposure in the burner-rig. An excellent reproducibility between the calibration data and the two sets of measurements (i.e. 7.5 and 14.7 hours) was obtained. In this test, the chemical binder coating started to degrade after approximately 15 hours of continuous thermal exposure in the burner-rig. Approximately 50 to 60% of the coating was lost after 15 hours.

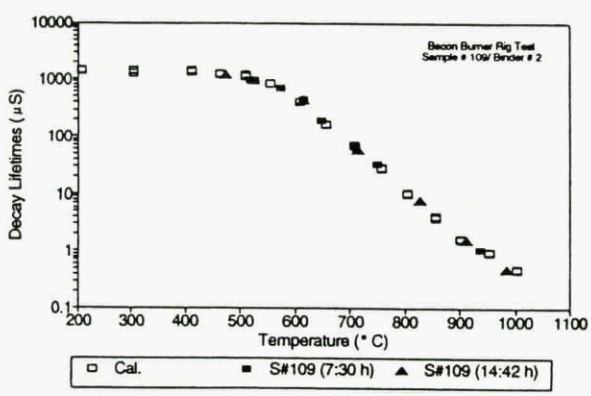


TE97-617

**Figure 4. Plot of the Decay Lifetime-Temperature Measurements Obtained From a coupon Coated with $Y_2O_3$:Eu After Two Consecutive Periods, 7.5 and 14.7 h, of Thermal Exposure in the Open Burner Rig**

## 5. CONCLUSIONS

Rare-earth doped thermographic phosphors can be used for monitoring the surface temperature of turbine engine parts. The overall accuracy of the temperature measurements using the described above technique was estimated to be ± 2%.

## 6. REFERENCES


1. Suarez, E., "Temperature Measurement of Thermal Barrier Coated Turbine Blades," Remote Temperature Sensing Workshop, NASA Lewis Research Center, 1994.

2. Suarez, E., and Przirembel, H., "Pyrometry for Turbine Blade Development," *J. Propulsion*, Vol. 6, No. 5, 1990, p. 584-589.

3. Atkinson, W., and Strange, R., "Turbine Pyrometry for Advanced Engines," AIAA-87-2011, AIAA/SAE/ ASME/ASEE 23rd Joint Propulsion Conference, 1987.

4. DeWitt, D., "Emissivity Compensation Techniques for Radiation Thermometry," Remote Temperature Sensing Workshop, NASA Lewis Research Center, 1994.

5. Alaruri, S., Bianchini, L., Brewington, A., Jilg, T., and Belcher, B., "An Integrating Sphere Method for Determining the Spectral Emissivity of Superalloys at High Temperature Using a Single Wavelength Pyrometer," *Opt. Eng.*, Vol. 35, No. 9, 1996, p. 2736-2742.

6. Goss, L., Smith, A., and Post, M., "Surface Thermometry by Laser-Induced Fluorescence," *Rev. Sci. Instrum.*, Vol. 60, No. 12, 1989, p. 3702-3706.

7. Noel, B., Borella, H., Lewis, W., Turley, W., Beshears, D., Capps, G., Cates, M., Muhs, J., and Tobin, K., "Evaluating Thermographic Phosphors in an Operating Turbine Engine," International Gas Turbine Conference, Brussels,-Belguim, 1990.

8. Tobin, K., Allison, S., Cates, M., Capps, G., and Beshears, D., "Remote High-Temperature Thermometry of Rotating Test Blades Using $YVO_4$:Eu and $Y_2O_3$:Eu Thermographic Phosphors", AIAA/ASME/SAS/ASEE 24th Joint Propulsion Conference, 1988.

9. Bugos, A., *Characterization of the Emission Properties of Thermographic Phosphors for the Use in HighTemperature Sensing Applications*, M.S. Thesis, University of Tennessee, Knoxville, 1989.

10. Alaruri, S., McFarland, D., Brewington, A., Thomas, M., and Sallee, N., "Development of a Fiber Optic Probe for Thermographic Phosphor Measurements in Turbine Engines," *Optics and Lasers in Engineering*, Vol. 20, 1995, p. 17-31.

11. Allison, S., Cates, M., Gillies, G., and Noel, B., "Fiber Optic Pulse Delivery System for Remote Temperature Sensing," *Opt. Eng.*, Vol. 26, No. 6, 1987, p. 538-546.

12. Tobin, K., Cates, M., Beshears, D., Muhs, J., Capps, G., Smith, D., Turely, W., Lewis, W., Noel, B., Borella, H., O'Brain, W., Roby, R. and Anderson, T., "Engine Testing of Thermographic Phosphors: Parts 1 & 2," Oak Ridge National Laboratory, ORNL/ATD-31, 1990.

13. Hentschel, C., *Fiber Optics Handbook*, 3rd Edition, Hewlett-Packard GmbH, Germany, p. 118-120, 1989.

14. Alaruri, S., Brewington, A., and Bijak, G., "Measurement of Modal Dispersion for a Step-Index Multimode Optical Fiber in the UV-Visible Region Using a Pulsed Laser," *Applied Spectroscopy*, Vol. 48, No. 2, 1994, p. 228-231.

15. Alaruri, S., Brewington, A., Thomas, M., and Miller, J., "High-Temperature Remote Thermometry Using Laser-Induced Fluorescence Decay Lifetime Measurements of $Y_2O_3$:Eu and YAG:Tb Thermographic Phosphors," *IEEE Transactions on Instrumentation and Measurements*, Vol. 42, No. 3, 1993, p. 735-739.

16. Struck, C., and Fonger, W., "Dissociation of $Eu^{+3}$ Charge-Transfer State in $Y_2O_3$:Eu and $La_2O_2S$ into $Eu^{+2}$ and a Free Hole," *Physical Review B*, Vol. 4, 1971, p. 22-34.

17. Struck, C., and Fonger, W., "$Eu^{+3}$ $^5D$ Resonance Quenching to the Charge-Transfer States in $Y_2O_2S$, $La_2O_2S$ and LaOCl," *J. Chem. Phys.*, Vol. 52, 1970, p. 6364-6372.

18. Wolfram, S., *Mathematica*, Version 2.2, Wolfram Research, Champaign, Illinois, 1994.

19. Andraos, J., "On the Propagation of Statistical Errors for a Function of Several Variables," *Journal of Chemical Education*, Vol. 73, No. 2, 1996, p. 150-154.

Paper 26
Author: Alaruri

Q: Benson

Have you explored the heat transfer characteristics of coating a large surface area with the Thermographic Phosphors ? Has there been any base material characteristics changes (cracking, embrittlement, etc) with the Phosphors coatings ?

A: No, I have not. No cracks or degradation were observed on the surfaces we coated with Thermographic Phosphors.

# OPTICAL INSTRUMENTATION FOR TEMPERATURE AND VELOCITY MEASUREMENTS IN RIG TURBINES

**I. Ceyhan, E.M. d'Hoop, G.R. Guenette, A.H. Epstein**
Gas Turbine Laboratory
Massachusetts Institute of Technology, 77 Massachusetts Avenue
31-266 Cambridge, MA 02139, USA

**P.J. Bryanston-Cross**
University of Warwick, Optical Engineering Dept.
Coventry, CV4 7AL, UK

## ABSTRACT

Non-intrusive optical measurement techniques have been examined in the context of developing robust instruments which can routinely yield data of engineering utility in high speed turbomachinery test rigs. The engineering requirements of such a measurement are presented. Of particular interest were approaches that provide both velocity and state-variable information in order to be able to completely characterize transonic flowfields. Consideration of all of the requirements lead to the selection of particle image velocimetry (PIV) for the approach to velocity measurement while laser induced fluorescence of oxygen ($O_2$ LIF) appeared to offer the most promise for gas temperature measurement. A PIV system was developed and demonstrated on a transonic turbine stage in the MIT blowdown turbine facility. A comprehensive data set has been taken at one flow condition. Extensive calibration established the absolute accuracy of the velocity measurements to be 3-5 %. The $O_2$ LIF proved less successful. Although accurate for low speed flows, vibrational freezing of $O_2$ prevented useful measurements in the transonic, 300-600 K operating range of interest here.

## INTRODUCTION

The advances in computational fluid mechanics achieved over 30 years of concerted effort have given us the capability of calculating the three-dimensional, unsteady flowfields in multi-row turbomachinery. These calculations yield hitherto unachievable levels of flow detail, facilitating improved turbomachinery designs, problem diagnosis, and reduced development time and cost. Our abilities to experimentally document such flowfields in rigs and engines have lagged far behind, however. Thus, we can now calculate turbine and compressor flows in great spatial and temporal detail but we can measure them at only a few locations and with limited temporal response.

The work described herein was aimed at improving the spatial coverage, the spatial detail and the overall accuracy of flow measurements within high speed compressors and turbines. Description of such an energetic, compressible flowfield requires spatially and temporally resolved knowledge of both the velocity and a state variable (temperature, pressure, or density) in order to completely characterize the flow. The primary application focus was the development of techniques which yield information of engineering utility in high speed compressor and turbine research and development rigs which operate in the 300-600 K static gas temperature range. The applicability of these techniques to engines was a secondary consideration. The approaches examined were limited to non-intrusive optical techniques capable of yielding spatially and temporally resolved data within rotor blade passages, information which is otherwise unavailable if the more common intrusive probes are used. The intent of this program was not to invent new optical schemes on a fundamental level, but to produce practical instruments that are robust in the large, high speed turbomachinery rig environment and are capable of routinely yielding useful data.

In the following sections we delineate the engineering requirements for these measurements, briefly review previous work in this area, and then describe work performed at MIT on the development of two complementary optical measurement instrumentation techniques, one of which proved successful, the other of which did not yield useful information.

## ENGINEERING REQUIREMENTS

For measurements to be of engineering utility, requirements for absolute accuracy precision, spatial resolution, and temporal resolution must be established so that the measurement process can be selected and the instrumentation engineered so as to meet these requirements. The measurement requirements vary with the intended use (for example - heat transfer, Mach number determination, efficiency) and the size and flow properties of the machine under test (inlet and outlet temperatures and pressures, velocity range, etc.). For example, gas temperature in a warm flow turbine rig may need to be measured to only 10 K accuracy for heat transfer measurements, but to 2 K for Mach number determination, and 0.2 K for efficiency estimation. Similarly, the spatial resolution and time response needed for the measurements increase as the machine size decreases for constant fractional resolution. None of the requirements for high speed turbomachinery are easy to achieve with current technology, but the difficulty increases as the turbomachine speed increases and its size goes down. Table 1 lists the requirements for sev-

*Paper presented at an AGARD PEP Symposium on "Advanced Non-Intrusive Instrumentation for Propulsion Engines", held in Brussels, Belgium, 20-24 October 1997, and published in CP-598.*

TABLE 1
ENGINEERING REQUIREMENTS FOR TYPICAL RIG COMPRESSORS AND COLD TURBINES

| Rig | Spatial Resolution | Temporal Resolution | Pressure Range (atm) | Temperature Range |
|---|---|---|---|---|
| 3-stage, small engine comp. | 200 μm | 0.74 μs | 0.8-3.8 | 274-455°K |
| Transonic fan stage, 0.5m dia | 900 μm | 3.4 μs | 0.8-1.4 | 274-320°K |
| Supersonic thruflow comp. | 660 μm | 1.9 μs | 0.7-1.7 | 265-345°K |
| Cold flow 0.5m HPT, blowdown | 900 μm | 2 μs | 1-6 | 300-500°K |

eral high speed rig compressors and turbines. Another concern is that the data rate must be compatible with the facility capabilities. For steady-state facilities, operating time and cost is the major concern here. For transient (<1 sec) facilities, the data rate is a dominant selection factor since detailed flow characterization may require several thousand data points per blade passage.

The turbomachinery rig environment adds some additional constraints compared to wind tunnel-type applications: limited optical access (favoring "back-scatter" type techniques and approaches with high optical efficiencies), strongly reflective geometries (favoring frequency shifting techniques), difficult to clean and keep clean windows (complicating the problem of establishing light intensities incident to the measurement volume), refractive gas paths (which tend to defocus and distort images), high ambient vibration levels, and often poorly-controlled ambient temperatures. Engineering an optical system for robustness under these constraints has often proven to be as difficult as the invention of the underlying optical approach.

## TECHNIQUE SELECTION

Since the intent of this program was to take useful engineering data in high speed turbomachinery rather than develop new, innovative optical methods, emphasis was placed on identifying existing techniques which could be adapted to the turbomachinery rig environment.

The one optical technique which has been well-proven to yield useful data in high speed turbomachinery is the measurement of velocity with laser anemometry. In most implementations, the flow is seeded with small (submicron diameter) particles and the instrument measures the particle velocity through any one of a variety of optical and electronic processing methods. Turbomachinery laser anemometry has been developed to a high degree of reliability by a number of groups, most notably Strazisar and his colleagues in the US [1] and Schodel in Germany [2]. The accuracy and spatial resolution of laser anemometry is quite satisfactory for most purposes (except for measurements near walls), but since systems measure only one point at a time, relatively long test times (many days) are required to map the flow in a single-stage machine. Thus, anemometry is a practical tool for steady-state rigs only, not for short duration facilities.

Another particle-based technique is particle image velocimetry (PIV), which can yield velocity data at a higher rate than laser anemometry since data is taken over an entire plane at one time. Although widely used in low speed flows [3], PIV had not been demonstrated in high speed turbomachinery at the start of this project. Bryanston-Cross and Epstein [4] first quantitatively demonstrated PIV in transonic flowfields. There are now also a variety of spectroscopic-based gas velocity imaging techniques under development, many making use of very narrow band filters to measure the Doppler shifts of excited molecular emission [5]. Since the spectroscopic techniques are much less developed than PIV and require a larger investment in equipment, PIV was selected as the approach to velocity measurement.

State variable measurement techniques suitable for use in high speed turbomachinery were and are much less developed than those for velocity measurement. In this study , only gas species spectroscopic techniques were examined. Table 2 lists the principal species considered, chosen for their familiarity to spectroscopists. Species not present in air (NO, CO, $CH_2O$, $CH_2COCOCH_2$) were rejected either because of toxicity problems (NO, CO, $CH_2O$) or the difficulty and expense of seeding the large airflow rates characteristic of many turbomachinery test rigs (of order 50-100 kg/sec). $N_2$ Ralyeigh scattering was rejected because there is no frequency shift between the incident light and the return signal, complicating the problem of scattered incident light rejection which is usually a serious constraint in turbomachinery geometries [16]. $N_2$ Raman was considered as a possibility for density measurement but it has relatively little sensitivity to temperature. Laser-induced fluorescence of oxygen ($O_2$ LIF) is sensitive to both temperature and density variation. Thus, the laser-induced fluorescence of oxygen ($O_2$ LIF), perhaps backed or normalized by $N_2$ Raman, was selected as the technique of choice, offering relatively high sensitivity, signal output, and reflection rejection [6].

The use of laser-induced fluorescence of $O_2$ for gas dynamic measurements had been described by several investigators. Massey and Lemon [7] used $O_2$ LIF to measure gas temperature and density, claiming a calculated accuracy of 1 K, a spatial resolution of 1 $mm^3$, and a temporal resolution of 1 microsecond. Laufer and McKenzie [8] measured temperature fluctuations in a hypersonic

TABLE 2
TECHNIQUES CONSIDERED [6]

| Molecule | Technique | State Variable Sensitivity | Preliminary Assessment |
|---|---|---|---|
| NO | LIF(1) | Temp. & Density | Possible |
| $O_2$ | LIF | Temp. & Density | Possible |
| CO | LIF | Temp. & Density | Low S/N |
| $CH_2O$ | LIF | Temp. & Density | Toxic |
| $CH_2COCOCH_2$ | LIF | Density | Possible |
| $N_2$ | Raman Scattering | Density | Possible |
| $N_2$ | Rayleigh Scattering | Density | Low S/N(2) |

(1) LIF = Laser Induced Fluorescence
(2) No frequency shift, cannot reject scattered light

wind tunnel. Cohen *et al.* [9] published several 2-D images taken across the slightly underexpanded supersonic freejet. More complete references on $O_2$ LIF can be found in [10].

Thus, the program at MIT selected PIV for velocity measurement and $O_2$ LIF for gas temperature measurement. The instruments were developed separately but were designed to be first used on the MIT Blowdown Turbine Facility [11], a 0.5 meter diameter, short duration (0.3 sec test time), transonic turbine rig with an inlet temperature of about 500 K. Both instruments were first tested on a heated supersonic freejet as a proof of principle demonstration. The following sections describe the PIV and LIF measurement principles, instrument realization, and test results.

## PARTICLE IMAGE VELOCIMETRY

Particle Image Velocimetry (PIV) in a turbine can best be explained with the aid of Figure 1. In this embodiment, light planes are projected through the turbine stage from periscopic probes upstream and downstream of the blade rows. With the camera shutter open, the light sheet is pulsed twice so that the particle positions at two instants in time are recorded. The in-plane velocity vectors can then be deduced from measurement of the particle displacement given knowledge of the pulse separation period.

There are several characteristics of the high speed turbomachine environment which are drivers for the design of the PIV optical instrument. The high speed of the flow requires short light pulse times (a few nanoseconds) to prevent blurring. It also sets the light pulse separation period (a few hundred nanoseconds for transonic flows). The seed particle diameter must be sufficiently small to follow abrupt flow velocity changes, such as through shockwaves, and must withstand the thermal environment. The high level of unsteadiness in the fluid (both periodic and aperiodic) requires multiple images to fully define the flowfield. Also, optical access is highly restricted due to airfoil geometry and the need to keep the flow undisturbed by the instrumentation.

All PIV systems consist of four major elements - flow seeding, an illumination subsystem, an image recording subsystem, and post-test data processing - whose interaction is an important design consideration. Optical access to the measurement volume is another limiting aspect of the engineering of the illumination and imaging subsystems. We will discuss these elements in turn.

The seed particles must be sufficiently small that viscous forces predominate over inertial effects so that the particles follow sharp velocity changes. Transonic velocities dictate particle sizes in the 0.3-0.5 micron diameter range. Smaller particles follow the flow better but the intensity of the scattered light scales approximately with the fourth power of the particle diameter. Thus, small

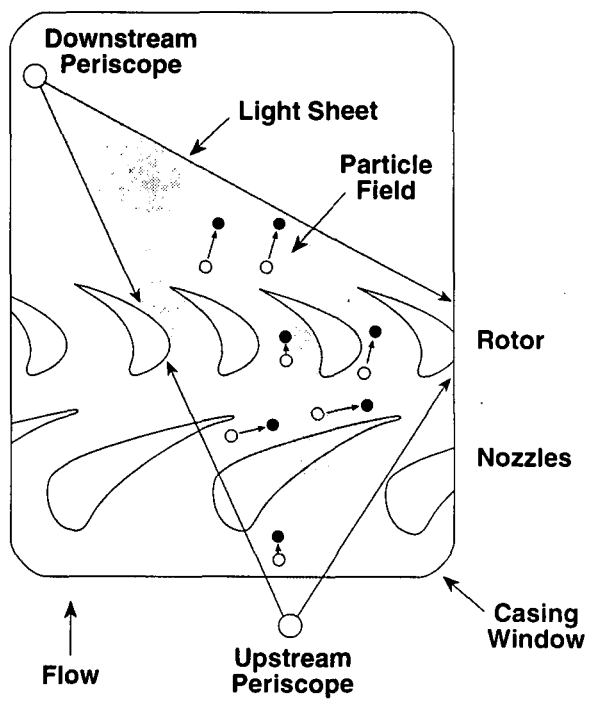


Figure 1: Conceptual view of particle image velocimetry (PIV) in a single-stage turbine.

particles can be costly in terms of light budget. The MIT Blowdown Turbine Facility operates at an inlet temperature of about 500 K to obtain complete physical similarity of both heat transfer and aerodynamics with full-scale engine turbines. This is too hot for the latex particles commonly used for PIV and laser anemometry. The ash from incense (Gonish #2) has proven stable at high temperature and has a diameter of about 0.35 microns [4]. However, testing showed the intensity of the scattered light from these particles to be marginal by a factor of 2-4. So, 0.5 micron diameter latex particles were used by reducing the rig turbine inlet temperature to about 370 K. Under these conditions, the aerodynamics of the turbine was matched but the heat transfer was not during the flow visualization testing. Prior to the start of a test, the particles were seeded into the supply tank from which the main turbine flow blows down. The particle density and size were checked before a test with a laser particle sizer. Particle concentration in the measurement volume in the turbine rotor was approximately 1 per cubic millimeter during the test time.

The illumination system tends to dominate the cost of high speed PIV systems. Large pulse energies (many tens of millijoules) are needed with small-sized particles. The high flow speed requires short pulse separations (a few hundred nanoseconds). The short run time of the facility favors high pulse pair repetition rates to maximize the data per test. The wavelength of the light source is a free variable. Ultraviolet would yield more efficient scattering (since the wavelength-to-particle-diameter ratio would be lower), but is more difficult to accommodate in terms of the practical considerations (optical material and sensor choices, and focusing ease) than are visible wavelengths. These considerations suggested that a frequency-doubled YAG laser operating at 532 nm would be the best choice at that time. The laser cost is a function of total energy and power. The unit selected (Spectra Physics PIV-200) consists essential of two separate laser heads mounted on a common base with their output beams combined, fed by a common power supply. This arrangement gives wide flexibility in the separation period of the 10 ns pulses. As operated, the laser produced 100 mj per pulse, 15 pulse pairs per second.

The laser output was split into two separate beams to feed the upstream and downstream periscopes. The planar beam-forming optics were mounted within the 6 mm diameter periscopes. The large transient facility shakes the building during operation, so accommodation of high vibration levels was a major concern. This was accomplished by mounting the laser on a vibration isolation table and adjusting the beam diameters to overfill the input apertures of the rig-mounted periscopes such that all rig motion remained within the beams. This approach proved superior to fiber optic coupling because the very high fluence levels damaged the fibers. A schematic of the layout is shown in Figure 2.

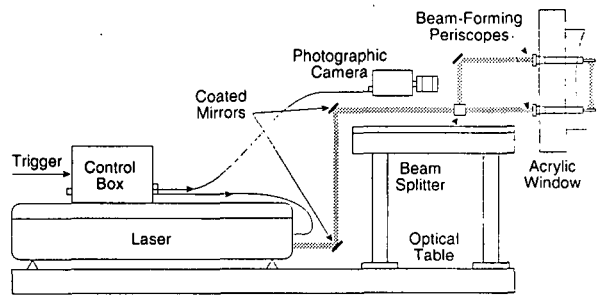


Figure 2: PIV setup on blowdown turbine facility.

Optical access to the blowdown turbine rig was enhanced in an unusual fashion. Due to the large turning angles characteristic of highly loaded turbine airfoils, the airfoils can obstruct much of the flow field, making it difficult to uniformly illuminate the rotor passage. This problem was eliminated by fabricating nozzle guide vanes from a clear plastic and illuminating the upstream part of the rotor passage through the vane, as indicated in Figure 1. (This is feasible in a short duration rig since the run time is short enough that the airfoils do not heat up appreciably even though the gas temperature, 500 K, is well above the melting point of the transparent material.). The radial position of the measurement plane can be changed by altering the immersion of the periscopes, as illustrated in Figure 3. The illuminated plane is viewed through a cylindrical glass window on the turbine outer endwall which maintains the flowpath contour. The exterior surface of this window has a contour different from the flowpath, chosen so as to minimize the overall image distortion introduced by the window. An outer planar acrylic window serves as the rig pressure seal (the pressure within the blowdown turbine varies from vacuum before the test to 4-7 atm during the test time). Conceivably, data could be taken on a radially-oriented plane by bringing the light sheet through the cylindrical casing window and then viewing through a periscope, but this has not been attempted to date.

The light scattered from the particles was collected with a 90 mm macro lens stopped down to f/11 to minimize dis-

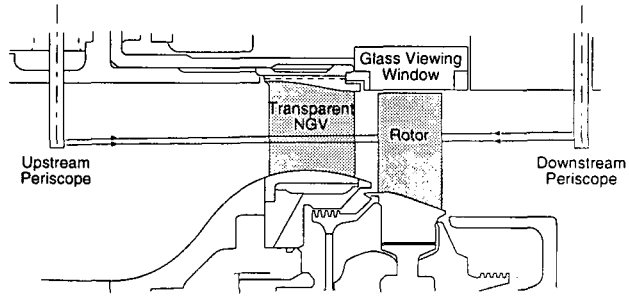


Figure 3: Upstream and downstream periscopes are used to form and position the incident light plane.

tortions. Note that, since the particle diameter is no larger than the wavelength of the laser light, images of the particles are not collected. Rather, a diffraction pattern results and this pattern is readily apparent with an imaging system of sufficient resolution and freedom from distortion. Image recording was done with a high speed 35 mm photographic sequence camera using Kodak TMAX 3200 film, push-processed. A previous study [4] had shown this film to yield the best resolution-speed tradeoff for PIV applications. The negatives were scanned into a computer after the test for processing and analysis. The laser was synchronized to the camera. The turbine angular position and velocity at each measurement time were recorded separately. A video system was considered for this application since such an approach offers considerable benefit in terms of run and data turnaround times. At that time, however, film offered better spatial resolution (and thus velocity accuracy) than commercially available video equipment at 15 frames per second. (Also, the photographic camera was available.) The magnification of the imaging system was established by photographing grids of known geometry positioned in the turbine along the laser light plane.

Once recorded, the images must be processed to yield the in-plane velocity vectors. There are many processing options available, as described extensively in the literature. The technique employed here was to fit a Gaussian profile to each gray scale particle image and then measure the distance between image pairs. This approach can yield high velocity accuracy when the seeding density is sufficiently low that particle pairs can be readily identified [12]. Correlation techniques have also been used effectively. Accuracy increases with increasing number of gray scales (permitting more accurate determination of the particle position) and increases with distance in pixels between particle pairs. Thus it may vary from particle to particle over the 100-500 particle pairs in a typical image. The net overall accuracy of these measurements was estimated at 3-5% of the absolute velocity.

Once images are reduced to absolute frame velocity vectors (the quantity directly measured), the blade relative velocity (the quantity generally desired) is calculated using the rotor speed measured at the image recording time. At this point, images may be grouped by their angular position relative to the turbine nozzle guide vanes (NGVs) and then added to yield the time-averaged velocity field at particular NGV positions. Also, all of the images can be added to produce the "average" turbine flow field.

An instantaneous image of the rotor relative velocity at midspan is illustrated in Figures 4 and 5 in terms of vectors. The tail of the vector is the measurement position, the length the velocity. Figure 5 shows a magnified view of the trailing edge region, illustrating the information density obtained. Note that little data is obtained close to the blade surfaces. This is due to obstruction from reflections from the blade surface and from shadowing by the blade tips.

A complete data set consisting of some 60 images has been obtained and processed at one turbine operating point at the rotor midspan. This data is now being analyzed and compared with analytical and numerical flow predictions.

## LASER-INDUCED FLUORESCENCE OF OXYGEN

Laser induced fluorescence of oxygen ($O_2$ LIF) was selected as the most promising technique identified for state variable measurement in high speed turbomachinery. In the following sections, we briefly describe the spectroscopic processes involved, describe the instrument built to exploit these techniques, and present experimental results. During this discussion, it is important to keep in mind that the final instrument/technique must be sufficiently accurate and stable to yield results of engineering interest. For the turbomachines of interest here, this translates to a temperature absolute accuracy (*i.e.* traceable to international standards) of about 10 K for heat transfer data, 2 K for Mach number determination (given the velocity field), and 0.2 K for stage efficiency measurement.

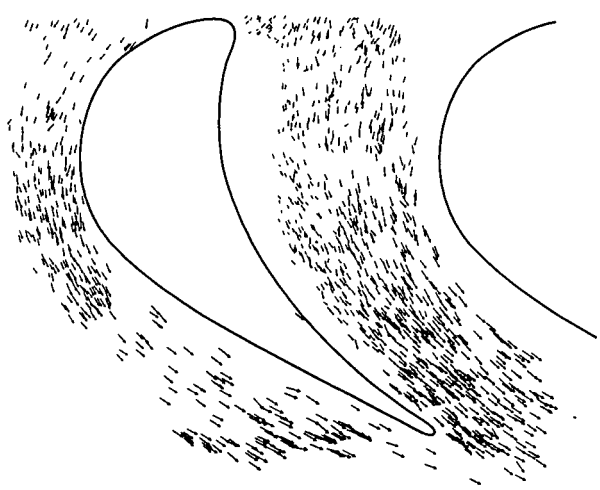

Figure 4: Instantaneous snapshot of rotor velocity deduced from a PIV image at midspan.

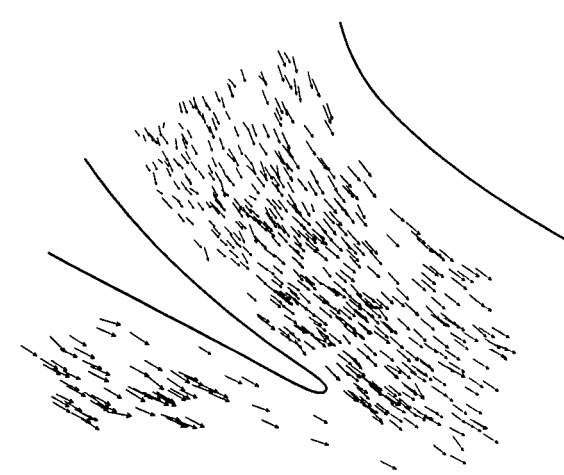

Figure 5: Blowup of rotor exit region from Figure 4.

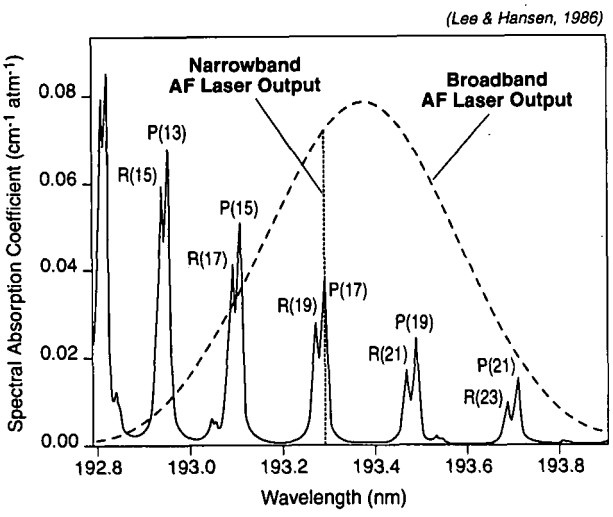


Figure 6: $O_2$ absorption spectrum at 300 K (after [14]).

In $O_2$ LIF, the gas is illuminated by a laser in the ultraviolet and fluoresces at longer ultraviolet wavelengths. The details of the internal photo-processes which result in this absorption and emission have been studied experimentally and theoretically in a detail which is beyond the scope of this paper (more details may be found in [10] and [13]). In general, the wavelength-dependent amplitude of the induced emission is a nonlinear function of gas temperature, density, and incident wavelength distribution and intensity. The emission involves both rotational and vibrational transitions, the type and number depending upon the temperature range and exciting frequencies.

An argon fluoride excimer laser (ArF) is a convenient light source for this work since its light output is at a wavelength (about 193 nm) which matches $O_2$ absorption and it can deliver high powers (hundreds of watts average power) and high pulse repetition rates (hundreds of hertz). The emission spectrum of an ArF laser is shown superimposed over the room temperature absorption spectrum of $O_2$ in Figure 6 [14]. It is possible to operate an ArF laser in two manners, narrow band and broad band. Narrow band operation results in emission line widths of about 0.005 nm, narrower than an $O_2$ absorption line, thus permitting excitation of particular transitions within the molecule. This narrow band process is more readily modeled than wide band processes and thus has been studied extensively. Wide band operation spreads the laser emission over about 1 nm, exciting many transitions. Narrow band operation reduces the net laser power output by about a factor of at least 2 compared to that of wide band. The laser chosen for these experiments, a Lamda-Physik EMG160MSC, which outputs 10-20 watts average power at 250 Hz broadband, was the only laser commercially available at the time which would also operate narrow band (by mode locking). The narrow band operating frequency did not prove stable over the long term, however. Thus, while bench top experiments could be performed in which the laser was tuned daily (with some difficulty), this level of robustness was judged insufficient for routine operation in a turbomachinery test cell type environment. Therefore, the instrument development was focused on broadband techniques.

In addition to a light source, a LIF instrument requires a detector subsystem. In this application, only a single point is measured at a time (rather than a line or 2-D image) so it is sufficient to use a spectrometer equipped with a linear CCD detector array, commonly known as an optical channel analyzer (OMA). The unit chosen (a 275 mm focal length spectrometer, ARC model SpectraPro 275, equipped with a Princeton Instruments IPDA-1024 cooled detector array and digitizer) yielded 16 bit amplitude resolution and a spectral resolution of 1 part in 1024 of the spectral range. For most of these experiments, a 1200 line/mm grating was used in the spectrometer, set to produce a spectral range of 200-270 nm, thus yielding a spectral resolution of 0.68 nm (FWHM). The detector and digitizer could be operated at the full 250 Hz repetition rate of the laser, permitting a complete spectrum to be taken on every laser pulse. A conceptual layout of the instrument is shown in Figure 7. Oxygen must be removed from the entire instrument light path exterior to the turbomachine window to avoid influencing the readings. This is done with an $N_2$ purge.

Excited with a broadband ArF laser, the $O_2$ LIF emission spectra of air measured in a flowing gas calibration cell at atmospheric pressure is shown at three different temperatures in Figure 8. All of these emission lines are a result of $O_2$ LIF processes with the exception of the lowest wavelength peak, which results from Raman scattering from $N_2$. Note that the $N_2$ Raman signal is relatively insensitive to temperature (it does scale with gas density however).

The measured $O_2$ LIF signal is a function of several other variables in addition to temperature: incident laser beam

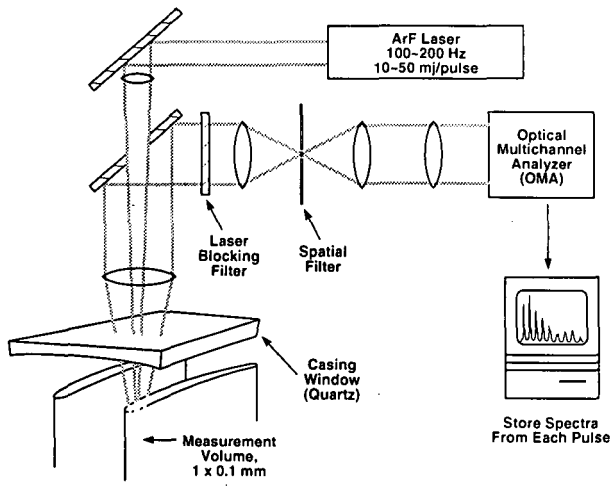


Figure 7: Conceptual layout of $O_2$ LIF temperature measurement instrument.

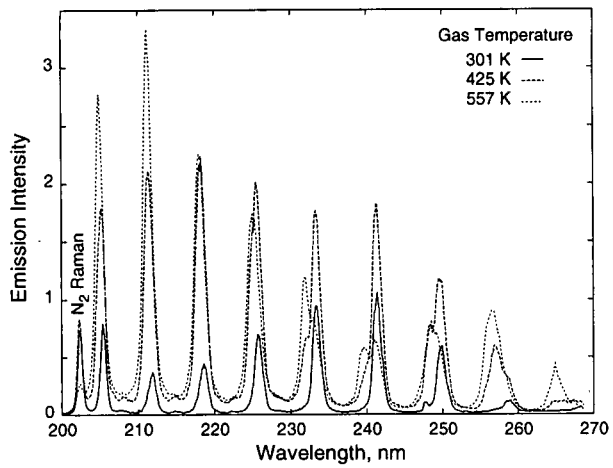


Figure 8: $O_2$ LIF at atmospheric pressure. (The $N_2$ Raman peak is truncated by the KBr filter used to reject reflected laser light.)

intensity, gas density, measurement geometry (volume and collection solid angle), and detector efficiency. The effect of these variables on the signal can be of the same order as that of temperature. Also, since these fluorescence signals are very weak compared to the incident laser intensity, noise from many sources plays an important role. The statistical noise in the emission and detection processes can be reduced by increasing the incident laser intensity (until limited by nonlinear effects and damage to the windows), maximizing the light collection geometry (constrained by the turbine geometry), and adding the output from multiple laser pulses (limited by rig stability and measurement time permitted). Other photo-processes can contribute unwanted signals. Hydrocarbons present in turbomachinery rigs (such as lubricants) and surface coatings fluoresce in the $O_2$ LIF region. At very high laser intensities, $O_2$ LIF is strongly influenced by nonlinear processes, notably emission from $O_2^+$, which underlies the $O_2$ spectrum, the presence of which significantly complicates data interpretation. The onset of the nonlinear processes sets a practical limit to the incident laser intensity, a limit which can be an order of magnitude below the maximum laser power. All of these effects must be considered in the instrument design and data reduction process.

The effects of gas density and laser intensity can be accounted for by normalizing the temperature-sensitive emission lines (such as those between 204 and 234 nm) to those spectral features which are relatively insensitive to temperature such as the $N_2$ Raman signal. The optimal selection of the signal and normalizing spectral features is a function of the temperature range of interest. These was established through careful measurements and extensive analysis [10]. Also, there is a tradeoff between statistical noise (which favors high laser intensities) and nonlinear effects (which favor low intensities) which results in an optimal value for the incident laser intensity. The net measurement uncertainty in gas temperature in a slowly flowing gas, accounting for all known sources of uncertainty, is illustrated in Figure 9, as a function of the number of laser pulses averaged over versus the intensity of each pulse. A more complete description of the apparatus and data reduction procedure may be found in [10].

After calibration on a variable pressure and temperature flowing (4 m/s) gas cell, the $O_2$ LIF instrument was moved to a heated supersonic axisymmetric freejet rig and the measurement point traversed down the jet centerline through the Mach disk formed at a jet pressure ratio 5.5. Rather than the 140 K temperature rise expected through the shock wave (as predicted by a CFD code), the instrument indicated a jump of less than 5 K. After experimental error was ruled out through re-calibration, cross-checking, etc., the spectroscopic theory of $O_2$ LIF was re-examined. The discrepancy was traced to the vibrational relaxation time of $O_2$, which is unusually long ($10^{-3}$ sec), while the rotational relaxation time is very fast ($10^{-9}$ sec). At temperatures below 300 K, the dominant photo-processes in broadband excited $O_2$ are rotational, while between 300-600 K vibrational transitions are responsible for most emission. Since transonic flow velocities are on the order of 300-500 m/s, the flow is vibrationally frozen for the millimeter resolution of interest here, frozen through the few centimeter long blade row, frozen through the entire compressor or turbine! This freezing is conceptually illustrated in Figure 10, which shows the static and vibrational gas temperatures across the centerline of the supersonic jet as a shock wave is crossed. The conclusion is that while techniques based on the vibrational processes in $O_2$ may be appropriate for low speed flows, they cannot work in high speed turbomachinery.

This problem with $O_2$ LIF was pointed out by Grinstead and Laufer in 1991 [15], but was not widely appreciated by the engineering community who have published papers interpreting $O_2$ LIF measurements in high speed flows

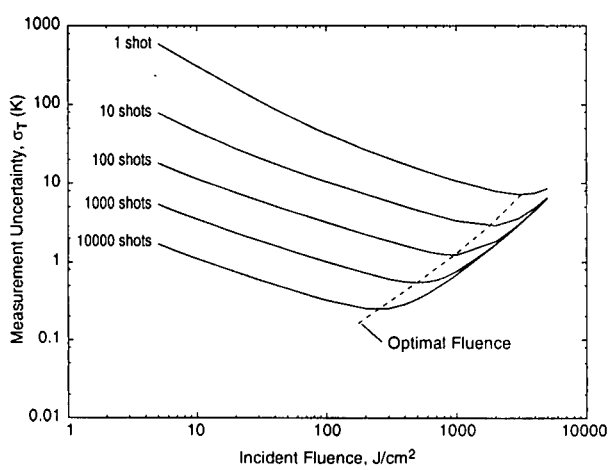


Figure 9: Measurement error and uncertainty at 428 K and 3.8 atm as a function of incident laser fluence and the number of laser pulses averaged over.

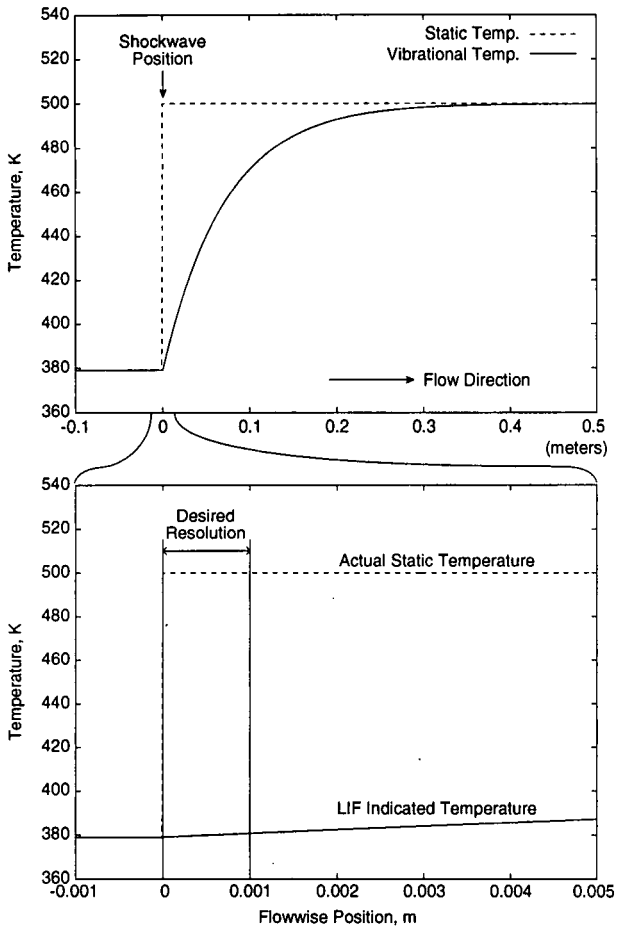


Figure 10: Illustration of the time lag in vibrational temperature (as would be measured by $O_2$ LIF) compared to static gas temperature in a supersonic freejet.

as temperature fields ([9] for example). Can this problem be avoided? Conceptually yes, by using narrow band laser excitation and tuning the excitation to a particular rotational transition. To implement this in a practical fashion would require a robust, very stable, narrow band ArF laser with a locking efficiency near 100% (to avoid broadband energy output which would excite vibrational transitions at the temperatures of interest). The authors know of no such laser available commercially or, indeed, of one demonstrated in the laboratory at this time.

## SUMMARY AND CONCLUSIONS

Non-intrusive optical measurement techniques have been examined in the context of developing robust instruments which can routinely yield data of engineering utility in high speed turbomachinery test rigs. Of particular interest were approaches that provide both velocity and state-variable information in order to be able to completely characterize transonic flowfields. Particle image velocimetry (PIV) was selected as the approach to velocity measurement while laser induced fluorescence of oxygen ($O_2$ LIF) appeared to offer the most promise for gas temperature measurement.

A PIV system was developed and demonstrated on a transonic turbine stage in the MIT blowdown turbine facility. A comprehensive data set has been taken at one flow condition. Extensive calibration established the absolute accuracy of the velocity measurements to be 3-5 %. This establishes PIV as a practical technique for high speed turbomachinery. The continuing rapid development of PIV by many investigators implies its value as a tool may increase with time. The $O_2$ LIF approach proved less successful. Although accurate for low speed flows, vibrational freezing of $O_2$ prevents useful measurements in the transonic, 300-600 K operating range of interest here.

## ACKNOWLEGEMENTS

The PIV research was supported by ABB, SNECMA, and the USAF Office of Scientific Research. The $O_2$ LIF work was supported by NASA Lewis Research Center, Dr. A. Strazisar technical monitor.

## REFERENCES

1. Strazisar, A.J., "Laser Fringe Anemometry," AGARD CP 399, Paper No. 6, AGARD Converence, *Advanced Instrumentation for Aero Engine Components*, Philadelphia, May 1986.

2. Schodl, R., "Laser Two Focus Anemometry," AGARD CP 399, Paper No. 7, AGARD Converence, *Advanced Instrumentation for Aero Engine Components*, Philadelphia, May 1986.

3. Adrian, R.J., "Particle-Imaging Techniques for Experimental Fluid Mechanics," *Annu. Rev. Fluid Mech.*, Vol. 23, 1991, pp. 261-304.

4. Bryanston-Cross, P.J., Epstein, A.H., "The Application of Sub-Micron Particle Visualization for PIV (Particle Image Velocimetry) at Transonic and Supersonic Speeds," *Prog. in Aerospace Sci.*, Vol. 27, 1990, pp. 237-265.

5. Miles, R., Lempert, W., "Flow Diagnostics in Unseeded Air," AIAA Paper AIAA-90-0624, presented at 28th Aerospace Sciences Meeting, Reno, NV, January 1990.

6. Annen, K., "State Variable Diagnostic Studies," Aerodyne Research Inc. Tech. Report ARI-RR-766, February 1990.

7. Massey, G., Lemon, C., "Feasibility of Measuring Temperature and Density Fluctuations in Air Using Laser-Induced $O_2$ Fluorescence," *IEEE Journal of Quantum Electronics QE20*, May 1984, pp. 454-457.

8. Laufer, G., McKenzie, R.L., "Temperature Measurements in Hypersonic Air Flows Using Laser-Induced $O_2$ Fluorescence," AIAA Paper AIAA-88-4679-CP, 1988.

9. Cohen, L.M., Lee, M.P., Paul, P.H., Hanson, R.K., "Two-Dimensional Imaging Measurements in Suupersonic Flows Using Laser-Induced Fluorescence of Oxygen," AIAA Paper AIAA-87-1527, 1987.

10. Ceyhan, I., "A Quantitative Study of the Feasibility of Oxygen Laser Induced Fluorescence for Engineering Gas Temperature Measurements," Ph.D. Thesis, MIT Department of Mechanical Engineering, February 1997.

11. Epstein, A.H., Guenette, G.R., Norton, R.J.G., "The MIT Blowdown Turbine Facility," ASME Paper 84-GT-116, 1984.

12. Udrea, D.D., Bryanston-Cross, P.J., Lee, W.K., Funes-Gallanzi, M., "Two Sub-Pixel Processing Algorithms for High Accuracy Particle Centre Estimation in Low Seeding Density Particle Image Velocimetry," *Optics and Laser Technology*, Vol. 28, No. 5, pp. 389-396, 1996.

13. Laufer, G., McKenzie, R.L., Huo, W.M., "Radiative Processes in Air Excited by an ArF Laser," *Optics Letters 13*, Vol. 2, February 1988, pp. 99-101.

14. Lee, M.P., Hanson, R.K., "Calculations of $O_2$ Absorption and Fluorescence at Elevated Temperatures for a Broadband Argon-Fluoride Laser Source at 193 nm," *Journal of Quantitative Spectroscopy and Radiative Transfer 36*, Vol. 5, 1986, pp. 425-440.

15. Grinstead, J.H., Laufer, G., "Requirements for Temperature Measurements in Nonequilibrium Flows Using Laser-Induced $O_2$ Fluorescence," in *International Congress on Instrumentation in Aerospace Simulation Facilities (CIASF),* 1991, pp. 262-269.

16. Fiedler, K., Sieber, O., Jakiel, C., "Quantitative Density Measurements by Rayleigh Scattering Behind a Plane Turbine Cascade," *AIAA Journal*, Vol. 35, No. 8, 1997, pp. 1303-1308.

Paper 27
Author: Epstein

Q: Black

Do the windows fluoresce after a high temperature run even when they have not been subjected to the laser? We (Rolls-Royce) have found windows on a combustion rig fluoresce when excited at 22.6mm after the rig has been run, even when they have not been subjected to the Laser. We do not know what temperature the windows reach during a run.

A : No, the windows do not fluoresce. The gas temperatures in our rigs never exceed 500°K. The short run times (less than 15 sec) result in the windows remaining at close to room temperature.

# APPLICATION OF LASER-INDUCED FLUORESCENCE (LIF) TO LIQUID-PROPELLANT ROCKET ENGINE TESTING*

C. W. Brasier, J. A. Drakes, and M. A. Simmons
Sverdrup Technology Inc. AEDC Group
Arnold Engineering Development Center
Building 690, Second Street
Arnold Air Force Base, TN 37389-9013, USA

## ABSTRACT

Combustion exhausts present a challenging problem for researchers due to the extremely harsh environment, and nonintrusive diagnostics are often sought to provide flow property information. Laser-induced fluorescence (LIF) is one technique in which a chosen flow molecule or marker is probed to yield gross flow properties, such as static temperature and flow velocities. The work presented herein describes the application of LIF to the combustion exhausts of several full-scale liquid-propellant rocket engines spanning a wide range of operational parameters. The method is based upon the use of cw ring-dye lasers which scan in frequency over either the Na $D_1$ or $D_2$ line at 5896 and 5890 Å. Na is used as a basis for this approach since it occurs as a trace element in both hydrogen and amine rocket fuels. The generic apparatus is described, including a discussion of the collection and interpretation of the LIF signal to yield radial and temporal profiles of radial flow velocity, static temperature, and fuel distribution. It was found that the LIF technique provides quality data in most cases. Certain stressing situations were also found in which data on the flow properties were not obtainable. Also, computational fluid dyanamics (CFD) modeling of the plumes was used to provide baseline estimates of the exhaust flow properties. The model reasonably predicted the gross behavior of the flow as determined by the LIF technique, although some items of fine spatial structure were not reproduced very well.

## INTRODUCTION

The ever-present need to monitor rocket engine health and performance has been a continual driver for the development of nonintrusive diagnostic tools. Much of the work is based upon the premise that information obtained from the exhaust flow at the nozzle exit plane can be directly related to combustion and operational characteristics of the engine itself. The introduction of laser-induced fluorescence (LIF) to the arena of full-scale rocket engine testing has greatly improved the knowledge of exit plane properties. For the past several years, Arnold Engineering Development Center has been modifying the standard LIF techniques to fit the specific requirements of rocket engine testing, at both sea-level stands and simulated high-altitude chambers. To date, three key performance parameters have been determined. These are spatial and temporal resolutions of gas static temperature, radial gas flow velocity, and relative fuel distribution in the exhaust plume flow field. These measurements can be analyzed to provide experimental evaluation of both rocket engine performance and injector mixing/vaporization and overall combustion efficiency.

The key feature of these measurements is that they exploit the inherent sodium impurity present in both amine and hydrogen fuels as a flow probe. The trace amounts of sodium, typically at the parts-per-billion level, are made to fluoresce using a continuous-wave, frequency-scanned dye laser when the excitation source is tuned to 589.0 nm, the absorption frequency of the sodium atom. The fluorescence detection system consists of a set of optically tuned filters and a remote control lensing system placed in front of gain-controlled CCD arrays. The images are recorded at standard video rates on digital tape (D2) recording devices. The images are then digitized using a large-scale video digitizer and placed in a format suitable for computer analysis. Since the sodium atoms serve as a "tag" for the fuel species, radial sodium fluorescence intensity measurements made in the vicinity of the nozzle exit plane can be directly correlated to the radial fuel distribution in the flow. This serves as an indicator of the internal injector mixing efficiency of the oxidizer and fuel streams. The radial velocity of the gaseous exhaust can be determined by the Doppler shift of the sodium absorption frequency. The gas static temperature is provided in a straightforward manner by the Doppler-broadened absorption profile. For altitude testing, the profile is predominantly Gaussian due to the low pressure while at atmospheric pressure, a Voigt spectral line profile is more appropriate. In either case, the temperature is obtained from numerical fitting of the spectral line profile to obtain the line width, and, hence, translational temperature.

The evolution of the LIF technique to full-scale rocket motors can be summarized by reviewing the four measurement programs of Table 1. The engines were the Stennis Space Center Diagnostic Test Facility (DTF) motor, the Space Shuttle Orbital Maneuvering System (OMS), the Space Shuttle Main Engine (SSME), and the Titan IV Second Stage (LR91) engine.[1] The propellants, test conditions, and other details are indicated in Table 1, in which the considerable variation of test parameters and configurations can be seen.

In the following, results from recent measurement efforts at AEDC and several NASA sites will be discussed. Comparisons of the measurement results with the physics-based computational simulations of the exhaust plume flow field properties will be presented. It will be demonstrated that the results obtained from the LIF measurements show good agreement with some of the model predictions, although certain flow features in the data were not predicted *a priori*.

## APPARATUS

The essence of the LIF diagnostic method, as developed at AEDC for full-scale rocket engines, is the reliance upon the Na inherently present in the fuels as a result of the fuel manufacturing process.[1,2] For example, the production of the amine

* The research reported herein was performed by the Arnold Engineering Development Center (AEDC), Air Force Materiel Command. Work and analysis for this research were performed by personnel of Sverdrup Technology, Inc., AEDC Group, technical services contractor for AEDC. Further reproduction is authorized to satisfy needs of the U. S. Government. **Approved for public release; distribution unlimited.**

*Paper presented at an AGARD PEP Symposium on "Advanced Non-Intrusive Instrumentation for Propulsion Engines", held in Brussels, Belgium, 20-24 October 1997, and published in CP-598.*

Table 1. Full-Scale Rocket Applicatons of LIF

| | NASA Stennis Space Center Diagnostic Test Facility (DTF) | NASA STS Space Shuttle Orbital Maneuvering System (OMS) | NASA STS Space Shuttle Main Engine (SSME) | Titan IV Second Stage (LR91) |
|---|---|---|---|---|
| Propellants | $GH_2$/LOX | MMH/$N_2O_4$ | $LH_2$/LOX | AZ50/$N_2O_4$ |
| Nominal O/F | 5.01 | 1.6 | 6.0 | 1.8 |
| Oxidizer Flow Rate, lbm/sec | 1.82 | 11.8 | 176.0 | 211 |
| Fuel Flow Rate, lbm/sec | 0.36 | 7.2 | 26.1 | 117 |
| Nominal Thrust, lb | 1,200 | 6,000 | 500,000 | 105,000 |
| Nominal Chamber Pressure, psia | 484 | 130 | 3,200 | 850 |
| Nozzle Exit Diameter, cm | 7.8 | 110 | 244 | 168 |
| Nozzle Cooling Method | Water | Radiation | $LH_2$ Circulation | Fuel-Film |
| Area Ratio | 6.1 | 55 | 77.5 | 49 |
| Test Location | NASA Stennis | NASA White Sands | NASA Marshall | AEDC |
| Test Simulated Altitude, km | 0 | 33 | 0 | 25 |
| Firing Duration, sec | 6 - 27 | 10 - 168 | 200 | 275 - 300 |

fuel for storable propellant rocket motors utilizes sodium hypochlorite.[2,3] During the combustion of the fuel, the atomic Na is chemically released, making it an ideal tracer to identify the spatial disposition of the fuel in the flow. Furthermore, the optical cross section of Na is very large, requiring only minute quantities of Na to generate measurable LIF signals.[4] Previous applications of the LIF technique demonstrated success with as little as 1 part-per-billion of Na.[5] The LIF measurement technique reported here uses a continuous-wave (cw) laser beam that is propagated across the exhaust flow and frequency tuned in a controlled fashion in a range about the frequency of the Na fluorescence line. The cw laser used in these test programs has a line width of 500 kHz. This implies that the cw laser acts as a very fine probe of the spectral structure of the Na fluorescence line which has a nominal width of 1 to 2 GHz, or $10^3$ times the laser width, in this type of application. As the laser tunes, portions of the flow fluoresce to a stronger or lesser extent, depending upon the Doppler-induced frequency shift of the fluorescence line with respect to the laser frequency. Thus, by using a standard video camera operating at a frame rate of 30 frames/sec, it is possible to capture the spatially resolved LIF signal with each video frame corresponding to an average of laser frequencies over the frame integration time interval. For example, if a 30-GHz laser scan requires a 5-sec time interval, the frequency interval averaged in a single video frame is roughly 0.2 GHz. From the video sequence, the spectral shape of the fluorescence line can be reconstructed for each spatial point in the flow. The shape and spectral shift of the spectral line will be used to determine the radial velocity and temperature of the flow.

The basic LIF system is shown schematically in Fig. 1, and the components are described in Table 2. The system consists of an Ar-Ion pump laser, a ring dye laser, a fiber-optic cable to transport the beam into the test cell, a fiber-optic cable head unit located within the test cell, and an absorption detector. The output beam of the pump laser was used to drive a Coherent 699-21 continuous-wave, frequency-scanning ring dye laser. The ring dye lasers have the capability of tuning over a 30-GHz frequency interval centered at either the $D_1$ resonance line of the Na atom at 5896 Å (corresponding to the transition between the $^2P_{1/2}$ state and the ground $^2S_{1/2}$ state) or the $D_2$ resonance line of the Na atom at 5890 Angstroms (corresponding to the transition between the $^2P_{3/2}$ state and the ground $^2S_{1/2}$ state). After exiting the dye laser, the laser beam was split by a 60/40 beam splitter into two portions. The weaker portion of the beam was split again, with one beam directed into a Na hollow cathode lamp located on the optics table with the laser, and the other beam directed into a Burleigh WA-2000 wavemeter. The wavemeter measured the gross frequency of the beam, and the Na hollow cathode lamp ensured that the laser frequency was finely tuned to the appropriate Na resonance frequency. The fluorescence generated in the lamp was monitored by a photomultiplier tube, and the output was recorded by a PC-based data acquisition system. Also recorded was the laser scan driving voltage.

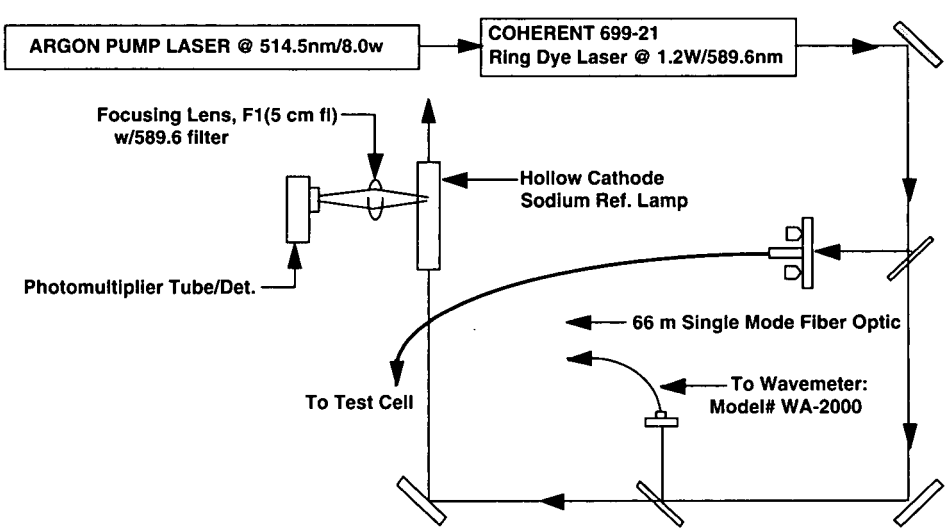


Fig. 1. Na LIF laser system schematic.

Table 2. LIF System Specifications

| | OMS |
|---|---|
| Pump Laser | Spectra Physics 171-09 or Coherent Innova 400-20 |
| Power | 8.0 W |
| Center Wavelength | 5145 Å |
| Dye Laser(s) | Coherent 699-21 scanning ring-dye |
| Dye | Rhodamine 6G |
| Linewidth | less than 500 kHz |
| Power | ~1300 mW (out of laser)<br>~80 mW (out of fiber in test cell) |
| Frequency Scan Range | 30 GHz |
| Scan Rate | 1 scan per 5 seconds |
| Fiber-Optic Cables | 33 or 66 m, 5-μm-diam, single mode |
| LIF Visualization Detectors | 1 to 3 gain controlled, CCD camera with 5- or 10-nm Na line filters |

The second portion of the ring dye laser beam was directed into a fiber-optic coupler that transferred the beam into a single-mode, 5-μm core, fused silica optical fiber. The terminus of the fiber was in a fiber-optic head unit also containing a beamsplitter and a reference power photodiode detector. The fiber-optic head unit was placed inside the test cell. On the opposite side of the test cell was located a photodiode absorption detector, aligned with the particular laser beam. The voltages from both the reference power and beam absorption photodiodes were also recorded by the PC data acquisition system. A fiber-optic cable was required to remove the laser system from the harsh environment associated with the test cell. The total output of the fibers used was on the order of 100 mW or approximately 25 percent of the incident power on the fiber input coupling lens. A single-mode fiber was implemented to achieve as near a collimated beam as possible, with the resulting output beam diameter being about 3 mm and a beam divergence of approximately 1 mrad. The use of a multimode fiber would result in a much greater beam divergence and, therefore, less collimation would be achieved. It is desired to achieve as near as possible a collimated beam diameter that will closely allow the vertical spatial resolution to match the horizontal spatial resolution. In addition to the reduced laser power available from the fiber, the output polarization changes associated with the fiber birefringence must be considered. The induced birefringence from stresses, movement, or vibration of the fiber greatly impacts the magnitude of laser light reflected off the reference power beamsplitter. This effect must be taken into account when selecting the mounting angle of the reference power beamsplitter, since the reflectivity of the "s" and "p" polarization states has a strong angular dependence.

For the programs presented in this paper, laser operations personnel are required to evacuate the test area approximately 45 minutes prior to motor firing. To ensure proper operation of the laser system during the evacuation period, laser system diagnostics are implemented to remotely monitor laser operations. The diagnostic parameters are not only recorded during evacuation and during motor firing, but also routed to the main control room area where the operations personnel are located during the evacuation period. To reduce the amount of cabling required to transfer these data to the control area, an inexpensive CCD camera is positioned with the laser system to view the metering devices. The resulting video signal is then routed to a video monitor located in the control room so laser personnel can monitor laser frequency, frequency stability, laser power entering and exiting the fiber, the alignment of the beam to the laser absorption detector, and proper operation of the CCD cameras used in the fluorescence detectors inside the test cell.

Once the imagery was collected on the D2 tape format, it was processed using a real-time digitizer at a resolution of 720 pixels horizontally by 496 pixels vertically. The portion of the image in which the laser signal was apparent was summed in the vertical direction, i.e., a spatial integration over the beam profile, at each horizontal pixel, yielding a LIF signal profile for each image. Note that since the laser scan frequency is correlated with the image, every LIF signal profile is associated with a laser frequency. A correction for the angular response of the system, as well as the variation in the laser power as measured by the reference photodiode, was made to each LIF signal profile. In general, background illumination is subtracted from the imagery using a polynomial fit to each video frame in the vicinity of the beam.

To interpret the LIF signal data, a model of the Na fluorescence profile was created, using standard methods. The model was constructed of two pieces, a first-principles model for the spectral shape of the Na fluorescence line, and a downhill simplex or Nelder-Mead algorithm[6] to optimize the free parameters of the spectral line model, i.e., line width, baseline, amplitude, and frequency shift. Although the capability to vary the relative strength of the transitions between the upper $^2P$ state and the hyperfine components of the lower $^2S$ state was originally invoked, the ratio of the hyperfine Na line components was eventually set to the nominal theoretical value of 0.375 for the higher energy $F_1$ line and 0.625 for the lower energy $F_2$ line.[7] The model used a 1.77-MHz separation between the hyperfine lines. At each of these transitions, a Voigt profile was generated using identical temperatures and broadening parameters. The resulting Na fluorescence line profile was the sum of the two Voigt profiles of the hyperfine components. The entire line profile was then compared to the data. Items not addressed in the Na fluorescence model were pressure shifting of the fluorescence line and radiative transfer of the emitted fluorescence through the plume.

Prior to the tests, the plume flow field was modeled using standard physics-based Joint-Army-Navy-NASA-Air Force (JANNAF) codes, specifically including the flow properties at the axial locations of the LIF measurements. The thrust chamber was modeled using a methodology similar to the Two-Dimensional Kinetic (TDK) computer program[8] for simulating the spatial flow-field properties and performance of axisymmetric thrust chambers. The solution includes the effects of rate-controlled chemical kinetics and approximates a viscous boundary-layer flow near the nozzle wall. Nozzle film cooling and nozzle wall ablation effects were not included in this simulation. The chemical equations and kinetic rates included in the simulation are for the primary combustion reactions involving carbon, hydrogen, oxygen, and nitrogen. Reactions involving trace species such as Na would not significantly influence the overall energy and chemistry and were not included. The thrust chamber solution domain commences in the combustion chamber assuming chemical equilibrium conditions, and subsequently performs a finite-rate chemical kinetics solution through the nozzle throat region and the diverging nozzle region. The solution terminates at the nozzle exit plane, providing static temperature, pressure, radial and axial velocity, and chemical composition, to be subsequently used as initial start-

ing conditions for the plume expansion model. The simulated nozzle exit plane conditions and the free-stream conditions at the simulated test altitude were provided to the Standard Plume Flowfield (SPF) computer program.[9] The near-field plume expansion was simulated from the nozzle exit plane to the test cell diffuser location. The objective of the external plume simulation was specifically to obtain the radial velocity and static temperature profiles at axial positions for comparison with the LIF-deduced profiles.

## RESULTS

### DTF

The first application of the Na-based LIF by AEDC to full-scale rocket exhausts was at the Stennis Space Center (SSC) on the Diagnostic Test Facility (DTF) thruster engine. The DTF, built for exhaust plume diagnostic sensor development and evaluation, is a 1,200-lbf rocket engine fueled by gaseous hydrogen ($GH_2$) and liquid oxygen (LOX). The laser system consisted of the same components and layout as described earlier. The laser beam was routed to the test stand from the laser trailer via a 33-m single mode fiber-optic cable delivering a collimated beam approximately 5 mm in diameter and a laser power of approximately 70 mw. System specifications are given in Table 2. System layout relative to the test stand is shown in Fig. 2.

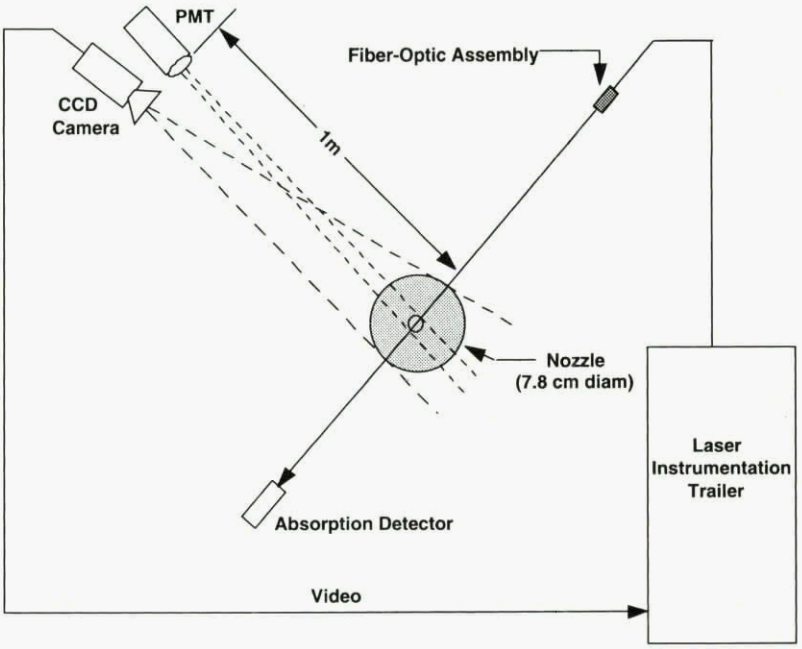


Fig. 2. DTF LIF installation.

Video output of the LIF camera and the signal from the absorption photodiode were routed to recorders in the laser trailer. A CCD camera pointed at screens of the primary system diagnostics was used to monitor the status of the controlling electronics. The video was routed to the trailer housing the operating personnel. From this video monitor, operating personnel could monitor proper operation of the equipment prior to engine ignition and during the motor firing. Both video and LIF data were acquired on 14 of 17 firings of the DTF motor. Burn durations ranged from 6 to 27 sec. The O/F ratio for the 14 firings on which LIF data were obtained ranged from 4.65 to 5.41. Sodium concentrations at the nozzle exit plane were estimated to be on the order of 1 ppb.

The data obtained on the DTF plume consist of qualitative flow visualization provided by the sodium-filtered camera. This data set provides information on the positions of the plume boundary and nozzle-induced shock. Figure 3 is a digitized image of a single video frame of the plume taken at the midpoint of the burn. During this test program, it was learned that: (1) Na concentrations of 1 ppb would provide sufficient signal levels for the geometry used on the DTF; (2) system operation using a single mode fiber-optic cable to transfer the beam to the test area is feasible; and (3) a full-field viewing CCD camera can provide point-to-point flow comparisons.

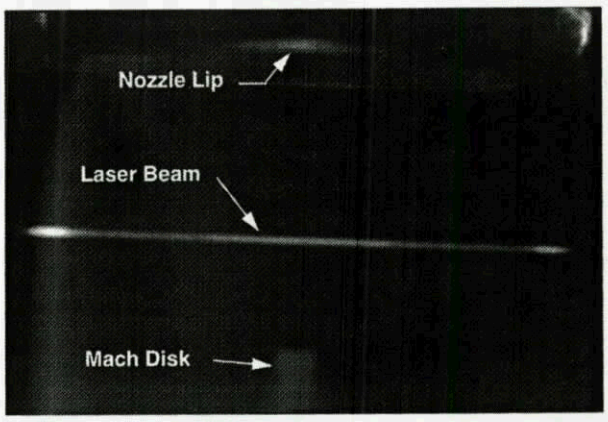


Fig. 3. Digitized DTF LIF image.

### OMS

A program was conducted at the NASA/Johnson White Sands Test Facility (WSTF) to measure radiative and flow-field properties at the exhaust of a Shuttle Orbital Maneuvering System (OMS) engine. This program was sponsored by the Strategic Defense Initiative Organization (SDIO) through the Phillips Laboratory at Edwards Air Force Base, CA. The OMS engine was tested in Test Cell 403 at the WSTF. This cell is a steam-pumped test facility capable of testing engines at simulated altitudes up to 40 km. The OMS engine is a pressure-fed, fixed-thrust, regeneratively cooled system with multiple start and gimbaling capability and uses nitrogen tetroxide ($N_2O_4$) and monomethylhydrazine (MMH) as propellants. The exhaust nozzle has a 14.8-cm-diam throat and a 109.5-cm-diam exit which provides an expansion ratio of 55:1. The divergent nozzle incorporates a bell contour with an 8.4-deg half-angle and is 146 cm long from throat to exit. The expansion cone is radiation cooled from an area ratio of 6:1 and is fabricated from columbium alloy FS-85. The specific parameters for this test are given in Table 1.

For the OMS test sequence, the cw dye laser tuned across the $D_1$ absorption line of the sodium atom at 5896 Å. The laser beam was directed across the plume centerline 4 in. downstream of the nozzle exit plane, as shown in Fig. 4. A single gain-controllable, unintensified Dage CCD-72 camera having an array size of 768 pixels horizontally and 493 pixels vertically with a 54-in.-diam field of view, was used as the detector. The camera lens was equipped with a 5-nm bandwidth line filter centered on the $D_1$ line of the sodium atom. The 30-Hz video output of the camera was recorded on VHS tape using a standard recorder.

Once the initial processing of the imagery was complete, the LIF signal profiles were compiled according to laser frequency scans. For the OMS, approximately 165 LIF signal profiles (5.5 sec times 30 Hz) were acquired during each laser scan. Figure 5 illustrates the set of 165 profiles as a color map in which the 165-pixel vertical dimension is the laser frequency, the 720-pixel horizontal dimension is the radial location across the plume, and the color indicates the value of the LIF signal profile. These data were acquired from 79.3 to 84.8 sec of OMS Test OFL2-6. During this laser scan, the laser tuned from −18 GHz (upper edge) to +12 GHz (lower edge), relative to the Na fluorescence line. The physical extent of the horizontal dimension is from −67.3 to 69.2 cm, relative to the OMS nozzle centerline. Several features of the fluorescence can be clearly observed from Fig. 5, including the vertical slope of the fluorescence due to the Doppler frequency shift. Note the subtle reverses in the velocity apparent in the image, which will be described in more detail below. Also, the large intensity of the Na fluorescence near the outer edge of the flow is apparent, as well as the narrowing of the frequency line width in the most intense region of fluorescence.

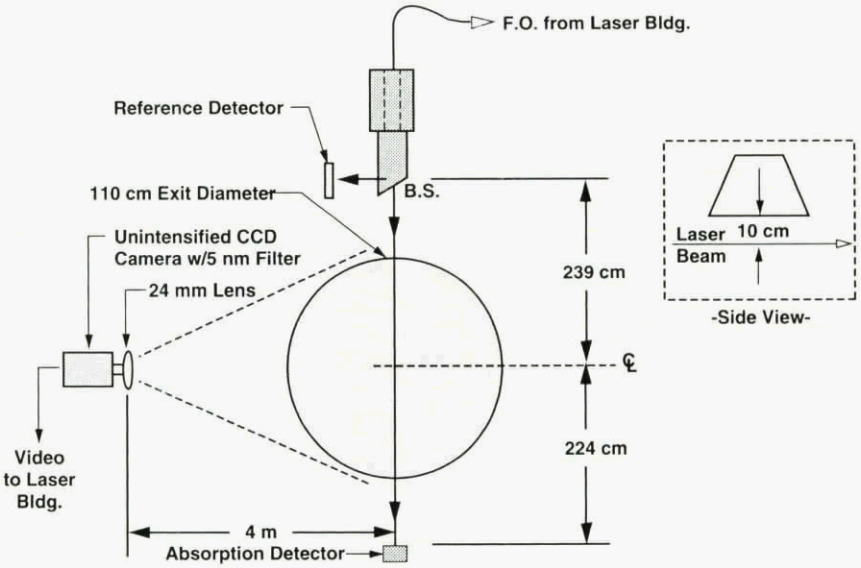


Fig. 4. DMS LIF installation, top view.

Fig. 5. Fluorescence signal acquired during one laser scan from OMS Test OFL2-6.

Figure 6 shows a typical raw LIF image from the OMS test during a time when the laser frequency was near the Na fluorescence line center frequency. The Na fluorescence model was applied to the data, such as that shown in Fig. 5. Figure 7 shows three spectral profiles taken from Fig. 5, at radial positions in the flow of 10.4, 46.5, and 55.9 cm relative to the nozzle centerline. Recall from Table 1 that the nozzle radius is 55 cm; hence, the plume has expanded compared to the nozzle at this axial station. First note that since all three profiles are acquired on the side of the nozzle where the exhaust flow is approaching the laser, the frequency shift is to progressively higher frequencies for positions farther from the nozzle centerline. This is reflected by the radial velocity determined for each spectral profile as denoted on the figure. Also, note the relative heights of the three spectral profiles where it is seen that the outer region of the flow has a much higher density of Na than does the inner portion. In addition, the structure of the fluorescence is clearly evident for the low-temperature region near the center, where it is possible to discern the two hyperfine components. As the temperature increases toward the outer region of the flow, this structure becomes washed out. Finally, note the excellent agreement of the fit to the data.

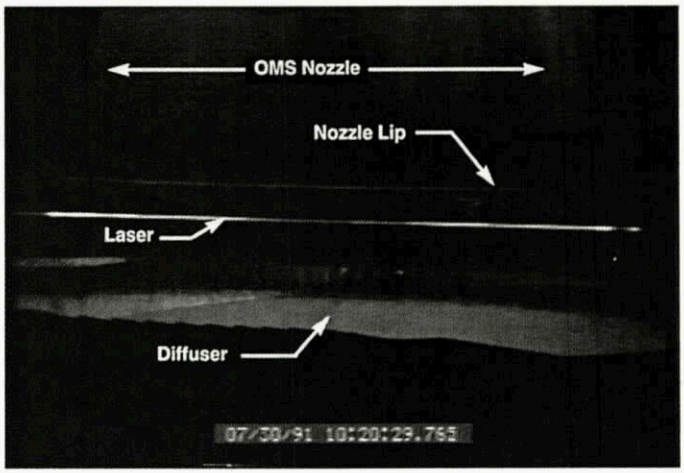


Fig. 6. Raw Image from OMS Firing OFL2-6.

Figure 8 displays the radial velocity observed at three times in the burn, roughly 4, 73, and 120 sec, as a function of radial distance across the plume. It is interesting to note the repeatability of the experimental results at the widely separated times. Also shown on this plot is the result of the SPF calculation. Overall, the agreement of the CFD model with the data is rather good for regions away from the center. Note, however, the feature in the data at ± 35 cm, which is not evident in the model results. In the region from −20 to 20 cm, there exists a signifi-

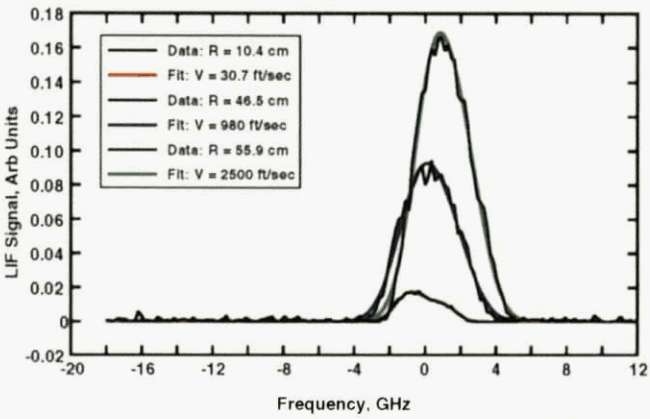


Fig. 7. Spectral profiles and fits taken at three radial positions of Fig. 5.

cant discrepancy between the model and the data. Posttest modeling of the start conditions was able to replicate the measurement results. These discrepancies are much larger than the uncertainty of the data, which is dominated by the systematic term due to the averaging of the laser frequency during individual video image acquisition. Since the camera averages the fluorescence signal for 33 msec while the laser is continuously scanning (at a rate of 30 GHz over 5.5 sec for OMS), the systematic radial velocity uncertainty is $\pm 2.5 \times 10^3$ cm/sec.

The results for the exhaust flow static temperature for this test are shown in Fig. 9, as well as the SPF modeling result. The systematic uncertainty due to the frequency averaging results in a minor uncertainty, nominally ± 50 K for most of the flow. The prediction is in qualitative agreement with the data in the core flow region. Near the flow axis, the prediction is only slightly lower than the data, but the agreement worsens significantly farther from the plume centerline. The plume core is seen to be extremely steady as a function of time, as indicated by the three temperature profiles taken at different times of the burn. There is a qualitative disagreement of the data with the model near the shear layer interface. The data show two peaks in the temperature near the outer flow edges, at roughly ± 52 and 58 cm. (Note the peak at –60 cm in Fig. 9 is an artifact.) The SPF model shows a smeared peak located between the two data peaks, perhaps indicating the limitation of the shear layer mixing model. Even more interesting is the temperature variation of the shear layer peaks as a function of time. Clearly, the inner core flow temperature is steady during the entire burn. However, the shear layer temperature peaks exhibit a curious variation in time in which the outer peak temperature rises during the burn while the inner peak decreases. One possibility for this is the convective heating of the external free stream during the burn, causing the outer peak temperature to rise. Simultaneous with the radiative heating is the cooling of the boundary-layer flow adjacent to the nozzle interior, which would serve to decrease the temperature of the inner peak. Further analysis is required to verify this hypothesis, but it is noteworthy that the LIF data can track small changes in the flow character during the firing.

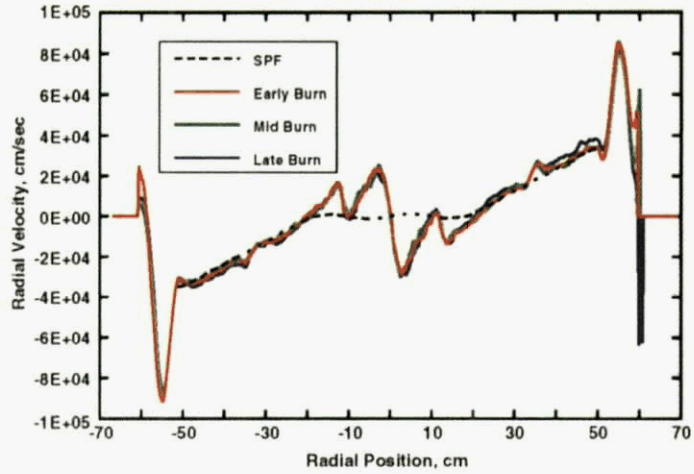


Fig. 8. Measured radial velocities of OMS Test.

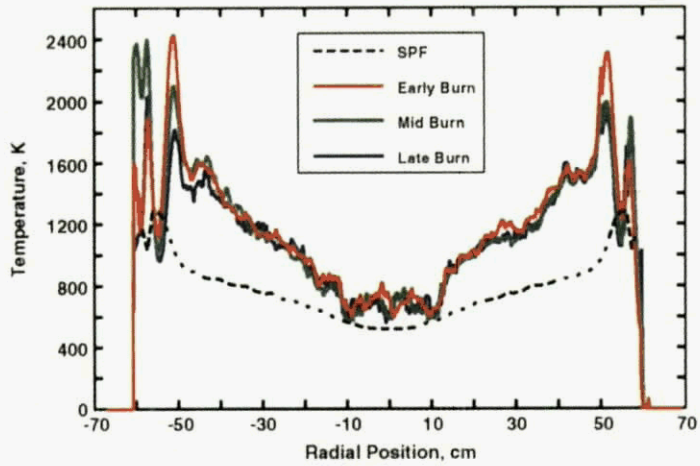


Fig. 9. Measured gas static temperatures of OMS Test.

## SSME

An LIF measurement was made on the Space Shuttle Main Engine (SSME) at the NASA Marshall Technology Test Bed (TTB) facility. The purpose of this study was to determine the feasibility of acquiring LIF data for determining flowfield parameters on the SSME. There was great concern as to whether or not the laser systems could maintain optical alignment and single frequency operation during the SSME firings, due to high vibration levels during motor firings. To ensure operation during a motor firing, two complete scanning ring-dye laser systems were set up in the instrument room of the test stand, and the laser beams were routed to the test area via fiber-optic cables. A system layout is shown in Fig. 10. Both laser systems were tuned to the sodium D1 line, 0.5896 microns.

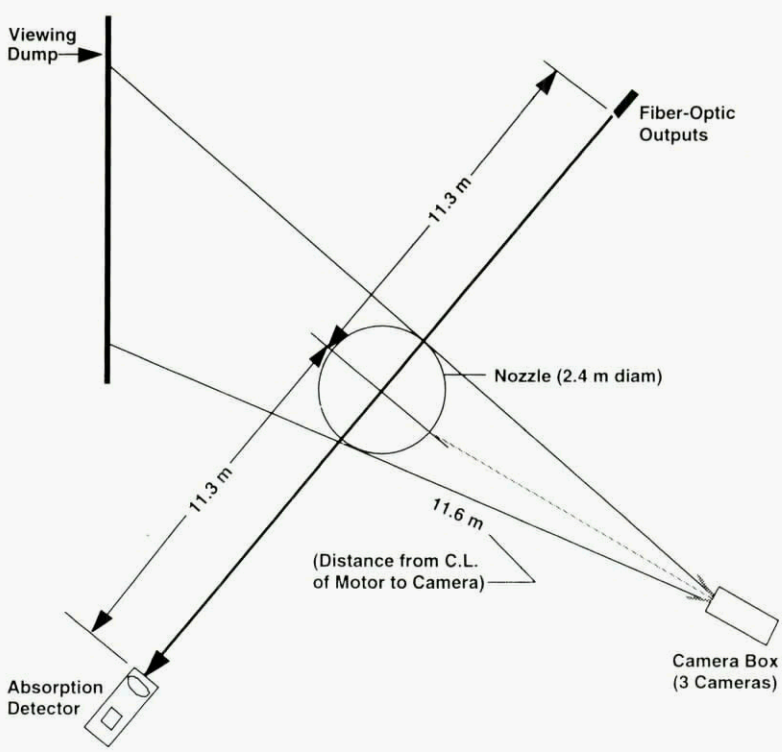


Fig. 10. SSME LIF installation.

The frequency-scanned dye laser outputs were coupled to 33-m optical fibers on the optical bench and routed to the engine deck. Each had a power output of approximately 80 mW. From one laser system, a 1.5-in.-diam collimated beam was generated from the fiber-optic output and directed across the motor centerline approximately 3.5 in. downstream of the nozzle exit plane, while from the second laser system a beam of approximately 2.0 in. in diameter was generated and directed approximately 13.5 in. downstream of the nozzle exit plane. Three cameras viewing perpendicularly to the laser beams were used to view the beams at motor centerline: a Xybion Model 250 intensified CCD camera, an RCA Model TC1030/H24 SIT camera, and a Dage Model CCD 72 CCD camera. All three cameras were equipped with 5-nm optical bandpass filters centered at the D1 sodium line. The Xybion field of view was approximately 122 cm and viewed the motor center line to the edge of the plume; the Dage and RCA cameras were set to provide full-field viewing, or approximately 252 cm. All three cameras were tilted toward the top of the motor to avoid having the Mach disk within the camera viewing area. The output of each camera was recorded on videotape for posttest analysis. Time reference was obtained by recording IRIG time on the videotape.

The laser beam terminated on a photodiode mounted on the opposite side of the test cell to monitor laser beam absorption versus laser frequency. This was to provide a measure of whether or not the plume was optically thin. Laser system specifications are noted in Table 2.

Three SSME firings were conducted during this test program: two 205-sec burns and one 46-sec burn. LIF of the sodium in the engine exhaust was not observed on any of the three firings. This is believed to be due to a combination of collection geometry, low sodium concentration, and insufficient laser beam power densities. It was learned in this technology development program that the laser systems would maintain optical alignment and single frequency operation throughout the full motor firing. This was verified via the system health monitor located in the control room. The laser was somewhat noisy, but the reference fluorescence indicated laser stability was sufficient to tune on and off the absorption line of sodium. All three cameras survived all motor firings, however, the video was saturated during the first motor firing due to sunlight reflection off the test stand structure and the water cooling vapor cloud. To eliminate light scatter off the vapor cloud and structure, a tarp was placed as a viewing dump for the video cameras for the second and third firings. This appeared to provide sufficient blockage of the sunlight and provided a good, dark background for the video cameras. Even with the reduced background on the video cameras, there was no visible fluorescence detected on the final two motor firings. There was sufficient vibration of the fiber-optic output assembly on all firings such that the beam alignment on the absorption detector was lost at motor ignition. Review of the video obtained by the Xybion camera indicates that the laser beam position was still near the nozzle centerline. This was determined by observing particulate scatter of the laser beam from the purge gas through the nozzle after shutdown.

**LR91**

A simulated-altitude nozzle certification test for a nozzle skirt extension to the LR91-AJ-11 rocket engine using a recently developed Low-Density (LD) quartz phenolic liner was conducted in the J-4 Development Test Cell at AEDC. The test program was conducted using both nozzle skirt extension liner materials, the original asbestos phenolic, and the LD quartz phenolic. Both nozzle liners rely on considerable fuel-film cooling (FFC) for protection. The LR91 is a large, amine-fueled rocket engine used as the second stage of the Titan IV launch vehicle which achieves a thrust level of nominally 105,000 lbf. The basic LR91 engine is constructed with a thrust chamber integrated with a regeneratively cooled nozzle that expands to an area ratio of 12. Inside the chamber, there are 7 axial internal baffles which are cooled by flowing $N_2O_4$ through them. From there, $N_2O_4$ sprays into the combustion chamber at the bottom of the baffles. At positions where the baffles are joined to the wall and in the center where the baffles join together, the baffles use fuel cooling rather than oxidizer. A nozzle skirt extension is used in conjunction with the basic chamber-nozzle combination to continue the flow expansion to an exit diameter of 168 cm and an area ratio of 49.2:1. The axial length of the nozzle and skirt extension from the throat to the exit plane is 183 cm. The nozzle and skirt extension liner is film cooled with approximately 16 percent of the total fuel flow being dedicated to film cooling. Note that 12 percent is used for cooling the chamber walls, while the remainder is used for cooling of the baffles. Data from LR91 Tests 3 and 4 tests will be presented for this work.

Since the LR91 test sequence was initially scheduled to have only one firing, it was decided to minimize the risk of data loss by duplicating the measurement. Thus, two complete and independent laser systems which performed redundant tasks were used. These laser systems were installed in an instrumentation building located just outside the test cell. Furthermore, it was desired to traverse the beams across the flow in a plane normal to the plume axis in an attempt to obtain a two-dimensional map of the exhaust flow properties. For Test 3, computer-controlled traversing tables physically translated the fiber-optic head units and the corresponding absorption detectors in a plane normal to the nozzle centerline axis, as shown in Fig. 11a. The motion began at the nozzle centerline, denoted as Station 1, and proceeded in discrete 10-cm steps outward. The relative orientation of the beams with the cameras was maintained at all times, and the beams were traversed to 8 radial stations out to the nozzle boundary (therefore, the last radial station was 70 cm from the nozzle centerline). Prior to engine shutdown, the beams returned to Station 1. For Test 4, the fiber-optic head units remained fixed, and mirrors were mounted to the traversing carts. The beams were traversed through 10 radial stations in 10-cm increments which extended past the nozzle boundary (to a radial station 90 cm from the nozzle centerline), and the beams did not return to Station 1 prior to shutdown. The traverse position was also recorded on the PC data acquisition system for all tests.

Fluorescence detection was done with three unintensified Dage CCD-72 array cameras operating at a standard video rate of 30 frames/sec. Each camera was spectrally filtered with a 10-nm bandpass filter centered about the Na fluorescence line. The large size of the LR91 necessitated the use of 10-nm bandpass filters rather than the 5-nm bandpass filters, due to the increased off-axis rejection of the narrower filters. Camera 1 was set with a 61-cm-diam field of view to provide plume boundary viewing while cameras 2 and 3 had a nominal field of view of 178 cm in diameter to provide full plume diameter viewing, as shown in Fig. 11b. Cameras 1 and 2 utilized computer-controlled zoom lenses to optimize the spatial resolution at each traverse position

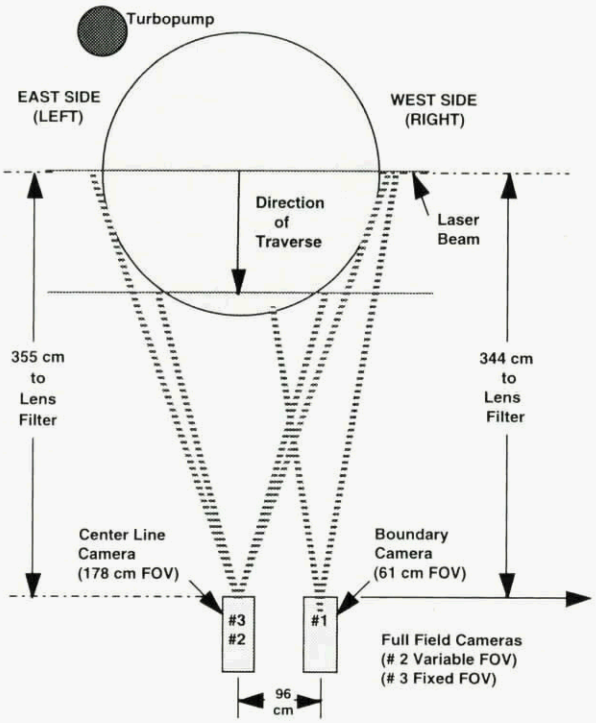


a. Top view

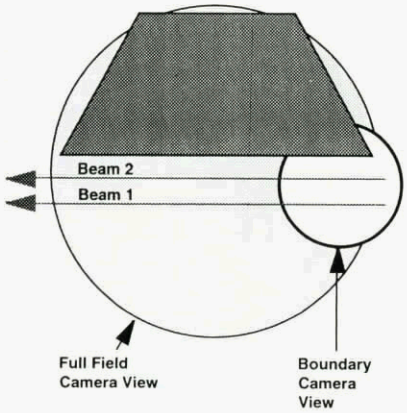


b. Side view

Fig. 11. LIF installation for LR91 testing.

of the laser beams. Measurements of transmission versus radial position were made on each camera/filter assembly for each lens setting in order to account for the angular dependence of the overall video response. The video signals from cameras 1 and 2 were sent to the main control room where they were recorded onto two independent Sony D-2 digital recorders. Additionally, the video signals from each camera were fed into the laser area where they were recorded onto three independent Panasonic VHS recorders as a backup. The beam from laser system #2 was located 7.62 cm axially downstream of the nozzle exit, while the beam from laser system #1 was located axially 15.24 cm downstream of the nozzle exit. In Test 3, the two beams propagated in opposite directions, while in Test 4, they both propagated from the same side.

For the LR91, considerable background illumination was present, due in part to test cell lighting for other diagnostic measurements. The 10-nm filters, as opposed to the 5-nm filters used for OMS, gave a higher level of plume visible radiance than the OMS, and numerous objects with highly reflective surfaces near the test article. Hence, significant portions of some of the LR91 LIF signal profiles were fatally corrupted by the background.

The LR91 test results are greatly influenced by the fact that the nozzle cooling mechanism is a reliance upon heavy amounts of fuel-film cooling (FFC). Since Na is a trace species of the fuel, the heavy FFC led to very significant Na densities in the boundary layer of the exhaust flow. In fact, a review of the data establishes that the plume structure can be categorized into three distinct annular regions. The outermost region was thin, ~ 1 cm, and contained a Na density that led to reasonable fluorescence measurements. Inward of the thin sheath was a ~10-cm region of very high Na density, as well as particulates, which was directly attributable to the nozzle FFC. The remaining core of the exhaust flow could again be characterized as having suitable Na densities for fluorescence measurements. While the outer sheath region and the inner core flow were anticipated prior to testing, the existence of a physically and optically thick layer composed of particulates and very high Na concentration was unexpected. In the FFC region the particulate component of the video signal presented a minor inconvenience for the LIF analysis by decreasing the effective dynamic range and producing a nonzero baseline in certain portions of the flow. However, the more important factor in the LIF analysis is the extreme optical depth of the FFC layer. In fact, it was found that at the Na line center frequency, the laser beam was totally absorbed. However, the laser beam did propagate through the FFC layer at frequencies off line center, and fluorescence was observed in both the particle layer and the inner core flow.

The video data acquired by Camera 1 from Test 3 at the 7.62-cm downstream position, i.e., laser 2, near the flow radial periphery displayed considerable Na fluorescence. As mentioned above, the data reduction process generates a spectral line at each point in the flow along the laser beam. The map given in Fig. 12 displays the Na fluorescence data of Camera 1 as was done in Fig. 5, with the frequency in the vertical dimension corresponding to −18 GHz and +12 GHz at the upper and lower edges, respectively, relative to the Na fluorescence line of the reference cell. The horizontal dimension is the field of view of Camera 1, corresponding to an absolute radial position in the flow from 58 to 98 cm relative to the nozzle centerline axis. The outermost plume fluorescence begins at ~ 94 cm. For radial positions between 90 and 88 cm in Fig. 12, the camera was saturated, and information on the peak intensity was lost. However, this represented no significant loss of information since the spectral fitting utilized the line wings. The centroid of the fluorescence displays a monotonic trend to more positive frequencies from 94 cm all the way to ~ 85 cm, at which point the velocity reaches a maximum. At positions interior 85 cm of Fig. 12, a given fluorescence line, i.e., a vertical or frequency profile, appears to have two peaks. This is simply due to the strong laser beam attenuation of the frequency-shifted line center by the optically dense outer portion of the flow. Yet there is considerable fluorescence in the wing of the Na line, indicating a

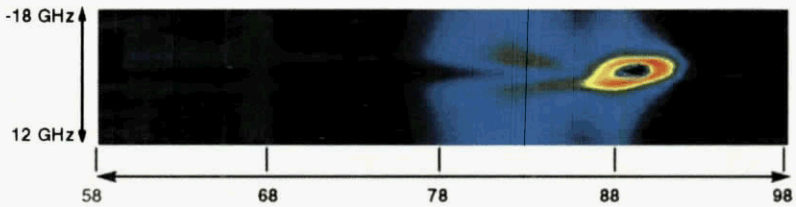


Fig. 12. Fluorescence signal acquired during one laser scan from LR91 Test 3.

high Na density. Inward of 78 cm, there is a precipitous drop in the Na density, indicating the boundary between the inner core flow and the particulate region discussed above. There is weak fluorescence in this region, although the S/N ratio is very small.

Vertical profiles of Fig. 12 were taken, analogous to those shown in Fig. 7. It was found that in the very narrow region outside the FFC layer, the Na fluorescence displayed the usual hyperfine structure. However, as one moves further into the FFC layer, the optical depth significantly attenuates the line profile, precluding a simple determination of the gas static temperature in the FFC region. Spectra acquired within 78 cm, in the low Na density core flow, suffered from a low signal-to-noise ratio. This is largely due to the fact that only the far wings of the lines were obtainable, since the kernel of the line was absorbed in the FFC region.

Although the temperature was indeterminable in this flow, the radial velocity is rather insensitive to homogeneous line profile distortions. Hence, the spectral lines, using either the complete profile or only the wings, were fit and a comparison was made to the SPF results. These are shown in Fig. 13 for Test 3. The agreement of the data with the prediction of the location and value of the radial velocity of the plume shear layer at the 7.62 cm axial position is quite satisfactory. It is interesting to note, though, that the data indicate a slightly wider shear layer than the predictions. The systematic uncertainty of the radial velocity was estimated to be $\pm 10^4$ cm/sec for a laser frequency scan period of slightly less than 5 sec.

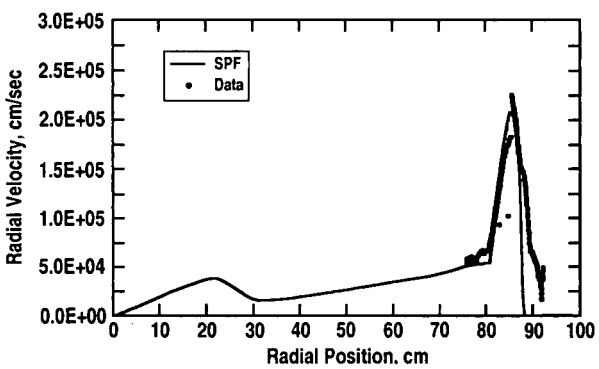


Fig. 13. Comparison of the measured radial velocity with the SPF predictions, Test 3.

The LIF data from Test 4 were manipulated in a similar manner to that of Test 3. However, in this case, Laser 1 (at the 15.24 cm axial position) was utilized. The character of Test 4 data is similar to that of Test 3, and only the final results are given here for brevity. A plot of the fit results for the radial velocity is given in Fig. 14. The results compare favorably with the SPF predictions at 15.24 cm downstream of the nozzle exit. Curiously, the data seem to indicate a thinner shear layer than that predicted by SPF. As before, the optical depth of the FFC region was excessive in Test 4, and no accurate temperature information can be derived from this data.

A fortunate turn of events during this test was the combined use of the laser attenuation and scattering data to ascertain the identity of the particles in the flow. After considerable analysis, it was discerned that the particles were unvaporized AZ50 droplets which survived the combustion process due to the significant amount of FFC used in this motor and nozzle assembly.

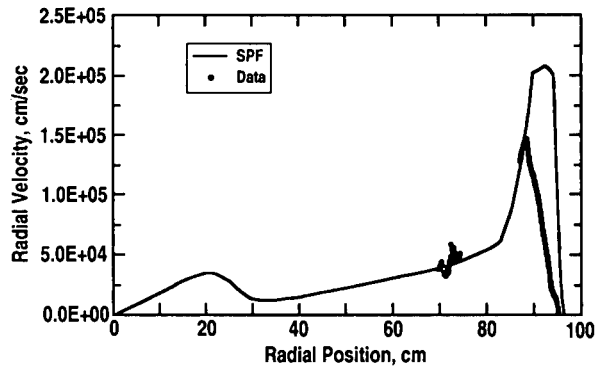


Fig. 14. Comparison of the measured radial velocity with the SPF predictions, Test 4.

## CONCLUSIONS

Overall, the Na LIF measurements performed on vastly different full-scale rocket engines at both sea-level and simulated altitude conditions were highly successful. The initial work on the DTF demonstrateed the potential that Na LIF probing of rocket flows has in providing crucial information on nozzle design, thermal integrity, and combustor mixing and performance.

The OMS program provided an excellent data set which yielded gas static temperature, radial velocity, and fuel distribution. Part of this success is due to a very low background light level, resulting in very clean data signals. The agreement of SPF modeling of the shear layer with the data was encouraging, but points out areas for code improvement. Furthermore, the SPF modeling of the centerline flow needs review for the case of the OMS engine. The data show a much more dynamic region, with the flow reversing radial direction twice near the core, and with significant magnitudes which were much greater than predicted. The temporal effect of the OMS flow-field boundary is interesting in that it may shed light on the heat-transfer characteristics of the nozzle itself, while it was seen that the static temperature of the inner core flow was extremely steady during the burn duration.

The SSME effort indicated the difficulty in attempting to probe an extremely large motor in daylight. Presumably, the fluorescence levels fell below the background levels and could not be distinguished. Hence, future diagnostics of the SSME should consider other schemes such as night testing or very narrow line filters with the associated narrow angular field of view.

The results of the LR91 work indicated the robustness of the radial velocity measurement, even in the face of an extremely optically thick environment. Future work with such very heavily fuel-film cooled motors should take into consideration the severe distortion of the fluorescence spectral line profile boundary layer when attempting temperature determination, even though the velocity determination is oblivious to this effect. An important LR91 result is the observance of the AZ50 droplets in the flow. While this result was not anticipated, the data are consistent with this identification for the particles. It would be useful to carry out a dedicated test sequence which defines the minimum FFC level to operate the LR91, or other FFC engine, in order to maximize payload capabilities.

A desired improvement for future measurements is the reduction of the background signal, in order to raise the LIF signal-to-noise ratio. In the LR91, the tradeoff to obtain the entire nozzle coverage at the expense of a narrow bandpass filter was too much in favor of the spatial coverage. In future efforts, a reduced field of view should be accepted, if need be, in favor of the narrow filters. For heavily fuel-film cooled rocket engines, the problem of optical depth remains, without a simple resolution. A possible alternative, which still exploits Na in the fuel, is to incorporate a pump-probe arrangement. Regardless, pretest efforts to quantify the amount of Na present in the fuel should be increased.

In addition, the next phase of development of this technique is further reduction of complexity and the associated costs in an attempt to make Na-based LIF a practical diagnostic tool for routine use. This currently involves automating the laser and camera control systems and reducing the data reduction procedure.

## REFERENCES

1. Brasier, C. W., Drakes, J. A., Anspach, K. M., Porter, R. G., Simmons, M. A., and Pruitt, D. W., "Laser-Induced Fluorescence Measurements of OMS and LR91 Amine Rocket Exhausts," AIAA Paper No. 97-2378, Atlanta, GA, June 1997.

2. Aerojet-General Corporate Report No. LRP198, "Storable Liquid Propellants, Nitrogen Tetroxide/Aerozine 50," June 1962.

3. Schmidt, E. W., *Hydrazine and Its Derivatives*, John Wiley & Sons, NY, 1984.

4. Fairbank, W. M., Hansch, T. W., and Schalow, A. L., *J. Opt. Soc. Am.*, Vol. 65, 1975.

5. Brasier, C. W. and Porter, R. G., "Development of a Laser-Induced Fluorescence System for Application to Rocket Plumes," AEDC-TR-92-6 (AD-A259760), January 1993.

6. Press, W. H., Flannery, B. P., Teukolsky, S. A., and Vetterling, W. T., *Numerical Recipes*, Cambridge University Press, 1986.

7. Cheng, S. S., "Resonant Doppler Velocimetry in Supersonic Nitrogen Flow," Ph.D. Dissertation, Princeton University,1982.

8. Nickerson, G. R., "Two-Dimensional Kinetics (TDK) Nozzle Performance Computer Program," NASA-36863, March 1989.

9. Wolf, D. E., Dash, S. M., and Pergament, H. S., "A Shock-Capturing Model for Two-Phase Chemically Reacting Flow in Rocket Nozzles," AIAA Paper No. 85-0306, Reno, NV, January 1985.

Paper 28
Author: Brasier

Q: Roehle

You determine the temperature by the width of a sodium line. The shape and the line width will be broadened not only by the temperature but also by the turbulent velocity fluctuation in the flow. How far does this effect your temperature measurements ?

A: The "turbulence" contribution is very small relative to broadening from the temperature.

Q: Versluis

When you determine your temperature from the line profile, don't you have problems with saturation broadening of the absorption line ?

A: Yes, when the line is saturated. We must ensure that the line is not saturated when making temperature measurement via the line profile.

Q: Lonwers

What's the reason for using LIF instead of PLIF ?

A: Insufficient laser power with the CW-dye laser technique.

# MEETING THE ADVANCED INSTRUMENTATION THE NEEDS OF THE INTEGRATED HIGH PERFORMANCE TURBINE ENGINE TECHNOLOGY AND HIGH CYCLE FATIGUE PROGRAMS

William A. Stange
Aero Propulsion & Power Directorate WL/POTC
1950 Fifth St Bldg 18
Wright-Patterson AFB OH 45433

## 1. SUMMARY

This paper presents an overview of current research efforts aimed at improving turbine engine structural instrumentation capabilities. Emphasis is placed on non-intrusive concepts which will be applicable to the advanced engines currently in use, or being designed for initial operational testing shortly after the turn of the century. Technologies to be described include; blade tip deflection sensors to determine dynamic stress, thermographic phosphors to measure metal temperature, pressure sensative paints and air etalons to measure dynamic pressure, and micro electro mechanical systems to assess a variety of parameters. Advantages of the various systems, potential problems and limitations, as well as, an assessment as to their applicability to either the Integrated High Performance Turbine Engine Technology or the High Cycle Fatigue initiative is discussed.

## 2. INTRODUCTION

Structural instrumentation is used to characterize the engine envirorunent and to identify any potential problem which may occur during an engine test. Knowledge of a potential problem allows the test engineer to take corrective action before damage to, or failure of the engine occurs. The turbine engine industry relies on structural instrumentation to verify structural design techniques and analytical prediction capabilities. These techniques are used to assess turbine engine component life and to predict strain and temperature at different operating conditions. The operating environment of today's turbine engine taxes every capability of current strain gages and thermocouples. Consequently, we cannot adequately and reliably instrument current technology gas turbine engines, and for future engines the problem will grow even worse.

Two efforts which are currently being pursued by the Air Force and other US Govenunent agencies to develop future engines are the Integrated High Performance Turbine Engine Technology (IHPTET) and High Cycle Fatigue (HCF) programs. Both of these efforts present the instrumentation engineer with an enormous challenge.

IHPTETs goal of doubling propulsion capability by the year 2003, without reducing engine life or reliability, will necessitate radical changes in virtually all

*Paper presented at an AGARD PEP Symposium on "Advanced Non-Intrusive Instrumentation for Propulsion Engines", held in Brussels, Belgium, 20-24 October 1997, and published in CP-598.*

aspects of turbine engine technology. Achieving this goal will require tomorrow's engines to: run at much higher temperatures while using little or no cooling air, operate at even higher tip speeds, utilize an array of new materials, and incorporate radical changes in design philosophy. Each of these requirements hinders our ability to make adequate strain and temperature measurements on the various structural components.

Similarly, achieving the goal of the HCF program, to double the damage tolerance capability of engine components, is dependent on having non-intrusive sensors which are very accurate in the test cell environment, as well as long-lived non-intrusive sensors for engine health monitoring systems. These sensors must be capable of accurately determining the dynamic response characteristics of engine components, as well as the dynamic flow field characteristics of the gas path in which they operate.

Attempting to address the needs of both of these programs has resulted in our investigating a number of innovative concepts which have demonstrated significant potential for providing us with the measurement capabilities needed for the advanced turbine engine technology coming on line in the next century. This paper will review prior and current research efforts which are intended to address the IHPTET program, as well as recently initiated efforts which more specifically address the HCF program.

## 3. BLADE TIP DEFLECTION SENSORS

This measurement system uses blade tip time of arrival measurements to determine the dynamic tip deflection characteristics of a stage on a running turbine engine. The Noncontacting Stress Measurement System (NSMS) as it is called, consists of a number of probes mounted to the case of an engine directly outside a stage of interest, (Fig 1) and computational and software systems to process the sensor output.

NSMS is a very attractive alternative to conventional dynamic strain gages. A major advantage of this technique is the fact that it is a non-contacting measurement system. As such, it requires no telemetry or slip rings to transmit the data, and has nothing affixed to the blade to disturb the flow field or other blade parameters.

The sensors will consist basically of two fiber optic bundles, a lens, and a photo detector. The input fiber optic bundle will carry light from a source and emit it through the lens and the case "window". The lens serves two functions, first, to focus the emitted light to the plane of blade tip passage, and then to focus that light which is diffusely scattered by the blade tip's passage into the output fiber bundle. The output fiber optic bundle then transmits the light pulse to the photo detector which emits an electrical pulse denoting the exact time of blade passage. This measured time of blade tip passage is then compared with the anticipated or expected time of blade tip passage to determine the time deviation. In addition to providing an accurate indication of the instant of blade tip passage, these sensors have to withstanding high levels of temperature, pressure, and case vibration.

The output from the sensors is then conditioned and digitized. A tip deflection raw data base is determined by the product of the time deviation and the circumferential velocity of the blade tip. The tip deflection raw data base is mathematically converted into deflection amplitude vs. frequency.

This conversion is analogous to a Fourier transform(and is in fact a direct Fourier transform if no integral order modes are participating in the vibration). The tip deflection amplitude vs. frequency data is converted into useful engineering data by means of a previously determined library of tip deflection vs. dynamic stress characteristics. The software which accomplishes this task basically does a "look up" of the dynamic stress distribution at each of the participating resonant frequencies. The library of tip deflection vs. dynamic stress distribution would typically be created using finite element analysis, although alternative inputs and/or corrections could be made from strain gage and/or laboratory test techniques such as Thermoelastic Stress Analysis. The integration of these stress patterns will yield the overall dynamic stress distribution of the blade.

Previous engine test programs have demonstrated the capability to measure non-integral order vibration of fan and compressor stages. The major shortcomings of previous systems were their limited tip deflection accuracy measurement capability, their inability to adequately measure integral order vibration, limitations in their multiple mode sensing capability, and the fact that they were incapable of converting tip deflection to dynamic stress. A number of sources have done developmental work on various blade tip deflection sensors, and have had some success in addressing these shortcomings(Ref 1,2,3).

Although the U. S. Air Force had sponsored a number of NSMS development activities in the early 80's, budgetary constraints and competing priorities were responsible for a lack of government sponsored work in this area for approximately ten years. The requirements of the High Cycle Fatigue (HCF) initiative refocused the need to further develop and expand the capabilities of this technology. As a result, a new program has been initiated which is working to develop what is being termed Generation 4 NSMS. This activity is being carried out by the Propulsion Instrumentation Working Group (PIWG), a consortium comprised of the major U. S. engine companies, as well as the U. S. Air Force and NASA-Lewis. The goal of this program is to develop an improved NSMS system with a 5X improvement in tip deflection measurement capability concurant with improvements in integral order and multiple mode sensing.

The overall goal for the noncontacting stress measurement system is a device which seems almost too good to be true, i.e., a system which measures stress for every airfoil on a stage over the entire surface of the airfoil with sensors which are easily removed from the exterior of the case in the event of sensor failure. This goal presents a number of challenges in several different technology areas, but the potential payoff, as well as the encouraging results encountered thus far make them well worth undertaking.

## 4. DYNAMIC PRESSURE SENSING

A number of concepts are under development which have the potential to significantly improve our ability to nonintrusively determine aerodynamic pressure fluctions in both rig tests and in the engine environment. The principle techniques currently being evaluated by the Aero Propulsion & Power Directorate(APPD) are Pressure Sensitive Paint(PSP) and Air Etalons.

PSP is a measurement technique which has been increasingly used in stationary wind tunnel applications over the past several

years. The principle differences between the PSPs used by the wind tunnel community and those needed by the turbine engine community are the requirements for higher temperature capability, and for higher dynamic response. Significant research efforts are underway at APPD to develop PSPs which meet these needs, and to validate the measurement capabilities of PSPs for turbomachinery applications. Details on the status and results of these research activities are summarized in Ref. 4, presented separately at this conference, and will not be repeated here.

The Air Etalon is a sensing concept based on Fabry-Perot interferometry. In its simplest form, a Fabry-Perot etalon consists of two mirrors separated by a certain distance. When light is incident upon an etalon, optical interference occurs so at certain optical resonance frequencies, corresponding to interference fringes, virtually all of the incident light is transmitted through the etalon and none is reflected, while at other frequencies most of the light is reflected. The position of the optical resonance frequencies depends on the optical path length between the two mirrors. This fact can thus be utilized to design a pressure sensor based on a Fabry-Perot etalon where the change in optical resonance is monitored as the optical path length changes due to pressure changes.

One manner in which an etalon sensor can be designed is to deposit a mirror directly on an engine blade, followed by a transparent solid spacer material, followed by partially reflecting mirror. However after going through the equations governing etalon behavior using realistic values for an engine sensor, it was determined that a solid etalon would be several times more sensitive to a 1 degree change in temperature than to a 1 atmosphere change in pressure. Thus as a pressure sensor, a solid etalon would be well suited to environments where the temperature change is very small compared to the pressure change, which is unfortunately not the case for a turbine engine.

In order to increase both the overall sensitivity and the pressure sensitivity relative to the temperature sensitivity, an air gap etalon can be employed. An air-gap etalon can be constructed on an engine part by chemical vapor deposition of the mirror surfaces combined with standard photolithography and etching to produce the air cavity. The result is a mirror layer separated from the base mirror layer by an air-gap supported by solid columns or posts(Fig. 2). The sensitivity to pressure for this air etalon is much higher than in the solid etalon case, and for most of the temperature and pressure ranges of interest, its sensitivity to pressure is much higher than its sensivity to temperature. Thus, with this sensor configuration it should be possible to measure pressure changes in the midst of temperature changes provided one could attain a separate temperature reading through some other optical technique such as conventional optical pyrometry or thermographic phosphors.

Contractual efforts are underway which will further develop both of these sensor's capabilities, as well as conduct a comparative evaluation of these sensing concepts under a variety of realistic engine operating conditions. These contractual efforts should be complete in late 1999.

## 5. THERMOGRAPHIC PHOSPHORS

Turbine engine metal temperatures are currently measured using either

thermocouples or optical pyrometry. Problems associated with these techniques limit both their accuracy and areas of applicability. Thermocouples are expensive, short-lived, require trenching when applied to blades or vanes, and necessitate telemetry or slip rings when applied to rotating hardware. Optical pyrometry, while highly desirable for its noninvasiveness, is ineffective in those regions of the engine where either a high level of reflected radiation is present, or where the metal temperature is below approximately 1300 degrees F. High levels of inaccuracy occur as the temperature approaches the lower bound of approximately 1300 degrees F and when moderate levels of reflected radiation are present. These limitations severely curtail the usefulness of these sensors in turbine applications, and virtually preclude their use in the fan or compresser.

Previous work done by the US Department of Energy (Ref 5) and by Allison Engine Co. has demonstrated that thermographic phosphors have the potential to alleviate many of the problems associated with current metal temperature measurement. Thermographic phosphors exhibit a fluorescence spectrum whose spectral line amplitudes and decay times vary uniquely with temperature (Fig 3). These phosphors are typically excited to fluoresce by means of short wavelength (ultra-violet) pulsed laser radiation. This laser induced fluorescence (LIF) is then passed through an optical bandpass filter to select the desired emission line, and to eliminate any extraneous background radiation. The filtered LIF is then fed into a waveform processing oscilloscope which determines the decay time of the fluorescent signal. This decay time yields a direct indication of the temperature of the phosphor. Prior Air Force sponsored programs have characterized a number of phosphors to temperatures approaching 3000 F and have developed bonding techniques applicable to advanced engine materials and environments.

## 6. MICRO ELECTRO MECHANICAL SYSTEMS

Microfabrication technology, and more specifically silicon micromachining, has been a key factor in the rapid progress of microsensors. Micromachining is currently used to fabricate a wide variety of mechanical microstructures. These microstructures, both with and without integrated electronics, have been used successfully to realize a wide range of microsensors.

Microsensor development started with physical sensors, partly because of existing market demand and partly because mechanical sensors can be easily scaled or transferred from conventional sensors. Furthermore, the fabrication technology developed for integrated circuits was easily adapted to fabricate the mechanical components for physical sensors. These microsensors are currently seeing widespread usage in numerous low temperature applications. Unfortunately, the principal sensing need in the turbine engine area is for high temperature sensors. Silicon based microsensors will not provide anything close to the temperatures required for turbine engine utilization. Activities have recently been initiated to investigate the capabilities and fabricability of microsensors based on silicon dioxide as opposed to silicon. These sensors are expected to have several hundred degrees greater temperature capability, but unfortunately require significant development prior to their introduction as turbine engine sensors.

## 7. CONCLUSIONS

An area of ever increasing concern and difficulty in the turbine engine community is the accurate determination of the strains and temperatures under which engine components must operate. As we strive for higher thrust/weight ratios, structural efficiency becomes even more important. To ensure components are not overdesigned, and therefore heavier than necessary, it is vital that systems and instrumentation are developed which predict and subsequently confirm exactly what temperatures and stresses are encountered. Furthermore, the HCF problems recently experienced by the Air Force clearly demonstrate the need to improve our measurement and analytical prediction capabilities. The state-of-the-art of structural instrumentation has many shortcomings in both the strain gage and thermocouple areas, but a number of alternative sensing concepts are in various stages of development and have the potential to provide solutions to many of these problems. Future turbine engine tests will demonstrate the capabilities of these new sensing concepts, as well as pointing out the areas requiring additional work.

The state-of-the-art of structural instrumentation does not adequately address the needs of today's turbine engine test programs. The IHPTET initiative with its higher temperatures and new materials requires a dramatic increase in instrumentation capability. The HCF initiative further intensifies the need to improve turbine engine instrumentation. Although a number of efforts are underway to address these needs, additional research programs are imperative to providing the advances which are required.

## 8. REFERENCES


1. Roth, H., "Vibration Measurements onTurbomachine Rotor Blades with Optical Probes", Measurement Methods in Rotating Components of Turbo-Machinery, pp 215-224, March 1980

2. Watkins, W.B., Robinson, W.W., and Chi, R.M., "Noncontact Engine Blade Vibration Measurements and Analysis", AIAA paper 85-1473, AIAA/SAE/ASME/ASEE 21st Joint Propulsion Conference, July 1985

3. Jones, H.T., "Development of a Noninterference Technique for Measuring Turbine Engine Rotor Blade Stresses", AIAA paper 85-1472, AIAA/SAF,/ASME/ASEE 21st Joint Propulsion Conference, July 1985

4. Navarra, K. R., et al, "Optical Measurements of Surface Pressure and Temperature in Turbomachinery", presented at the 90th AGARD PEP Symposium on Advanced Non-Intrusive Instrumentation for Propulsion Engines, October 1997.

5. Noel, B.W., et al, "Evaluating and Testing Thermographic Phosphors for Turbine Engine Temperature Measurements", AIAA paper 87-1761, AIAA/SA.E/ASME/ASEE 23rd Joint Propulsion Conference,June-July 1987.

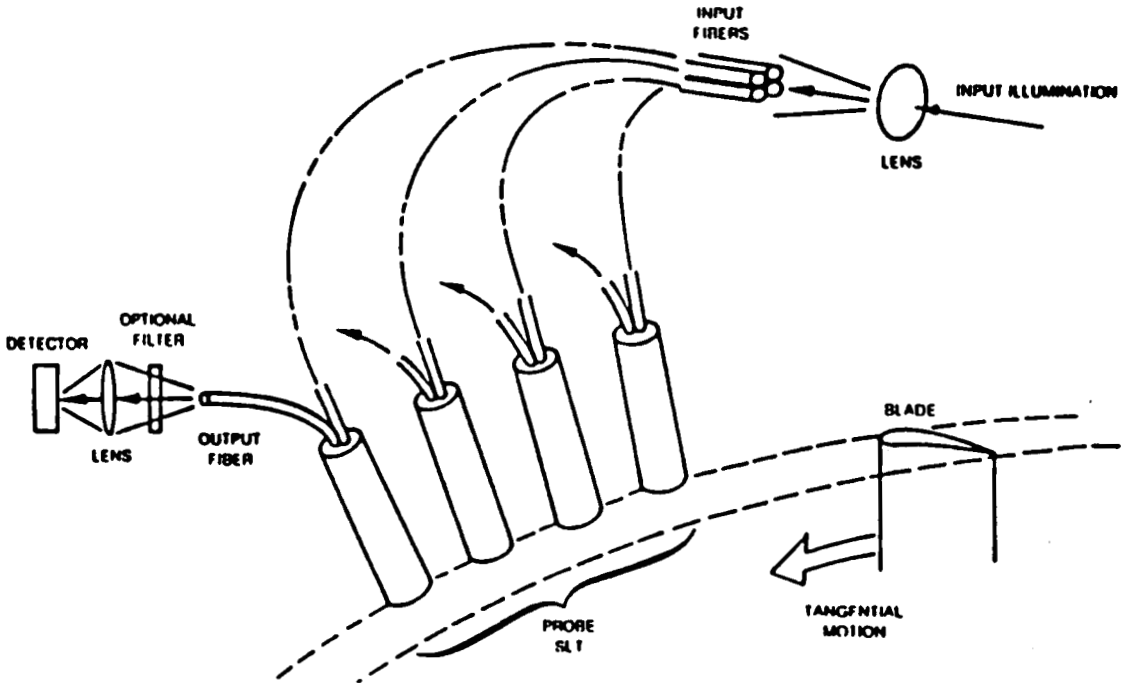


Figure 1 Non-Contracting Tip Deflection Measurement System

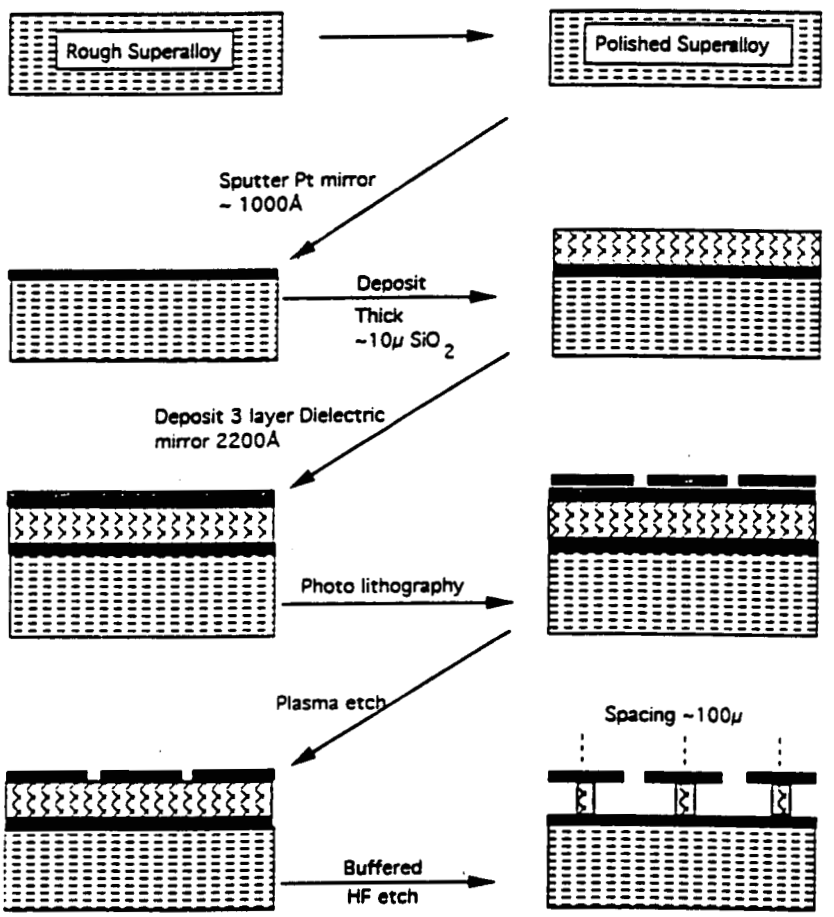


Figure 2 Air Gap Etalon Fabrication Methodology

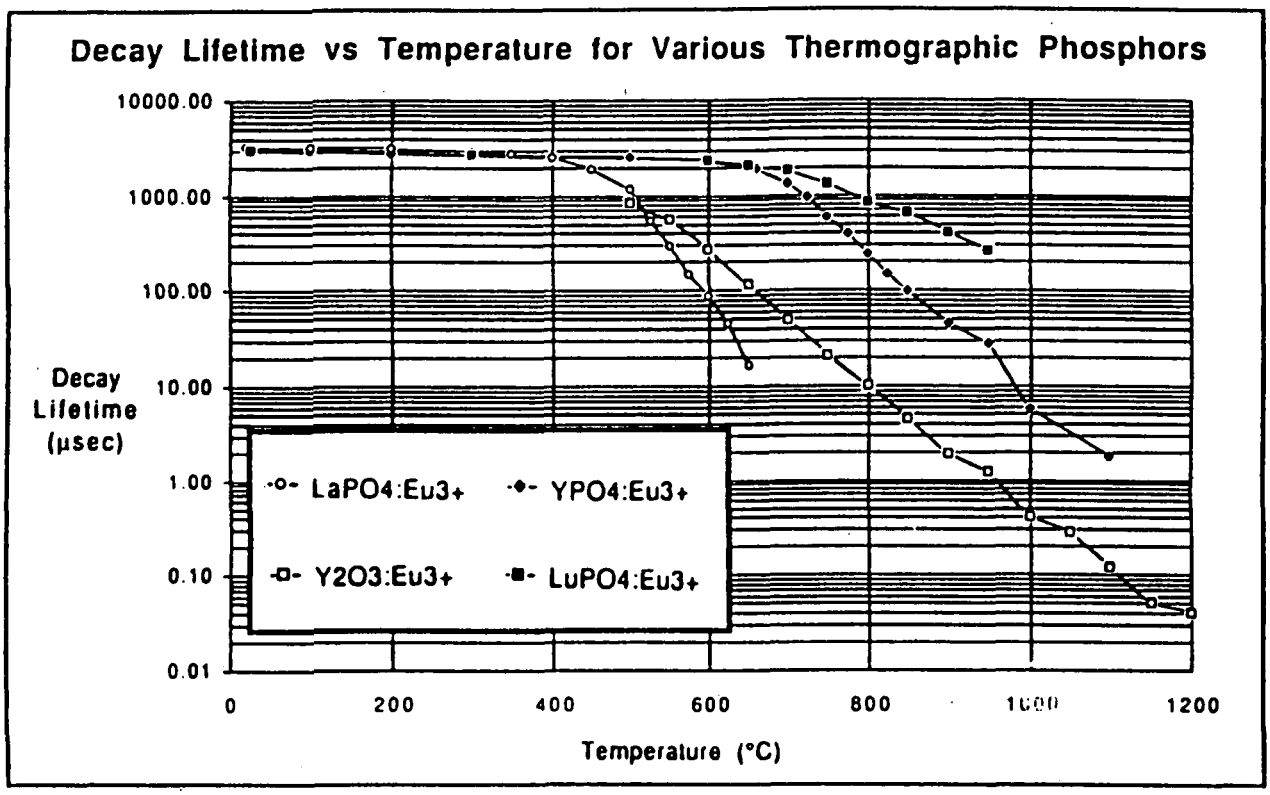


Figure 3 Fluorescent Decay Time vs. Temperature

Paper 30
Author: Stange

Q: Eyraud

What is the accuracy you achieve with actual NSMS systems and what are the improvement planned with generation NSMS?

A: Our current tip deflection measurement resolution is between .001" and .002" for non-integral order modes and in the range of .005" to .01" for integral order modes.

We expect generation 4 NSMS to provide a factor of 5 improvement to both of these resolutions

Q: Decker

How are the measurement techniques developed for the aeroelastic instability research of the late 70's and early 80's being integrated into this program?

A: We are aware of the measurement techniques developed in that time frame, especially the early development work on NSMS. Our NSMS program is being conducted by the propulsion instrumentation working group, a consortium of the major engine manufacturers as well as NASA and the Air Force. By having all of the major players involved we feel confident these earlier efforts will be integrated into our program.

# OPTICAL BLADE VIBRATION MEASUREMENT AT MTU

**M. Zielinski and G. Ziller**
Electronics & Measurement Technology Department
DASA MTU München, TEMS
Dachauer Str. 665, Postfach 500640
D-80976 München, Germany

## ABSTRACT

Compressor rotor blade vibration measurements are crucial to the proper assessment of critical operating conditions and the prediction of blade life. Generally, at MTU these measurements are performed using strain gauges or the frequency-modulated grid system.

In an attempt to provide an advanced alternative solution to the two standard techniques, MTU commenced work on an optical blade vibration measurement (OBM) system some years ago. For OBM, several optical trigger probes are installed in the compressor casing above the rotor, and the blade transit times between the probes are measured. An analysis of these transit times then provides information on blade vibrations.

This paper describes the details of MTU's experimental OBM system and the analysis methods used. The capability of the system is demonstrated by means of various measurement tasks: vibrations excited by resonances with amplitudes as low as 10 $\mu m_p$ can be measured. Blade vibrations caused by compressor surges were analysed successfully. Comparative measurements show good agreement between OBM and strain gauge results. As an option the untwist of blades with increasing rotational speed can be measured.

## 1. INTRODUCTION

The aerodynamically optimised blades of advanced axial compressors show an increasing tendency towards vibrations which are excited in many different ways. Residual unbalance of the rotors, non-concentric casings resulting in varying blade tip clearances around the rotor circumference as well as irregular pressure distributions within the airflow caused by the engine intake geometry produce exciting forces of low integral engine orders. Depending on the number of stator vanes the stators located upstream and downstream of the rotors cause pressure variations of higher integral engine orders in the flow. Vibrations asynchronous with respect to rotor speed are excited by flutter, rotating stall and compressor surging. Fracture of a blade owing to fatigue frequently results in the destruction of the entire engine, or at least leads to an engine shutdown.

Theoretical modal shape analysis taking the blade geometry, the rotational speed and the temperature into account provides data on those speed ranges where synchronous vibrations are likely to occur. Furthermore this analysis identifies limits for the vibration amplitudes which cannot be exceeded for longer periods of time without incurring the risk of a blade failure. The actual vibration amplitudes during engine operation, however, can - at best - be roughly estimated.

As a result, it is necessary that the vibration amplitudes of the blades are determined under realistic conditions during the development phases of a compressor. This allows any critical vibrations to be identified immediately so that secondary damage can be prevented. At the same time the measured data provide information on the expected service life of the blades.

## 2. STANDARD MEASURING METHODS

At MTU blade vibrations are normally measured using strain gauges with the signals being transmitted from the blades to the data recording system by means of telemetry or a slip ring. The elongations measured are evaluated using theoretical modal shape analysis. Although this method is well established and has proven its suitability in practice the effort it requires in terms of strain gauge instrumentation, routing of cables and telemetry or slip ring is considerable. Therefore, the use of strain gauges is restricted to a few blades per rotor stage.

For the second standard method, the frequency modulated grid system (FM grid), permanent magnets are fitted on the tips of some blades and a specially formed wire is installed in the compressor casing above the magnets. As it passes the wire the magnet produces an alternating voltage in the wire. Blade vibrations then result in a modulation of this basic a.c. voltage. For this method no signal transmitter between rotor and stator is needed, but the wire requires a special casing and the number of blades monitored at a time is limited to a maximum of 3 per rotor stage.

## 3. OPTICAL BLADE VIBRATION MEASUREMENT

As an alternative to the two standard measuring methods MTU has been using the optical blade vibration measurement (OBM) technique for some time now. The basic concepts of this technique have already been known for many years [1] [2] [3]. For OBM, several optical trigger probes are installed in the compressor casing above the rotor, and the blade transit times between the probes are measured.

*Paper presented at an AGARD PEP Symposium on "Advanced Non-Intrusive Instrumentation for Propulsion Engines", held in Brussels, Belgium, 20-24 October 1997, and published in CP-598.*

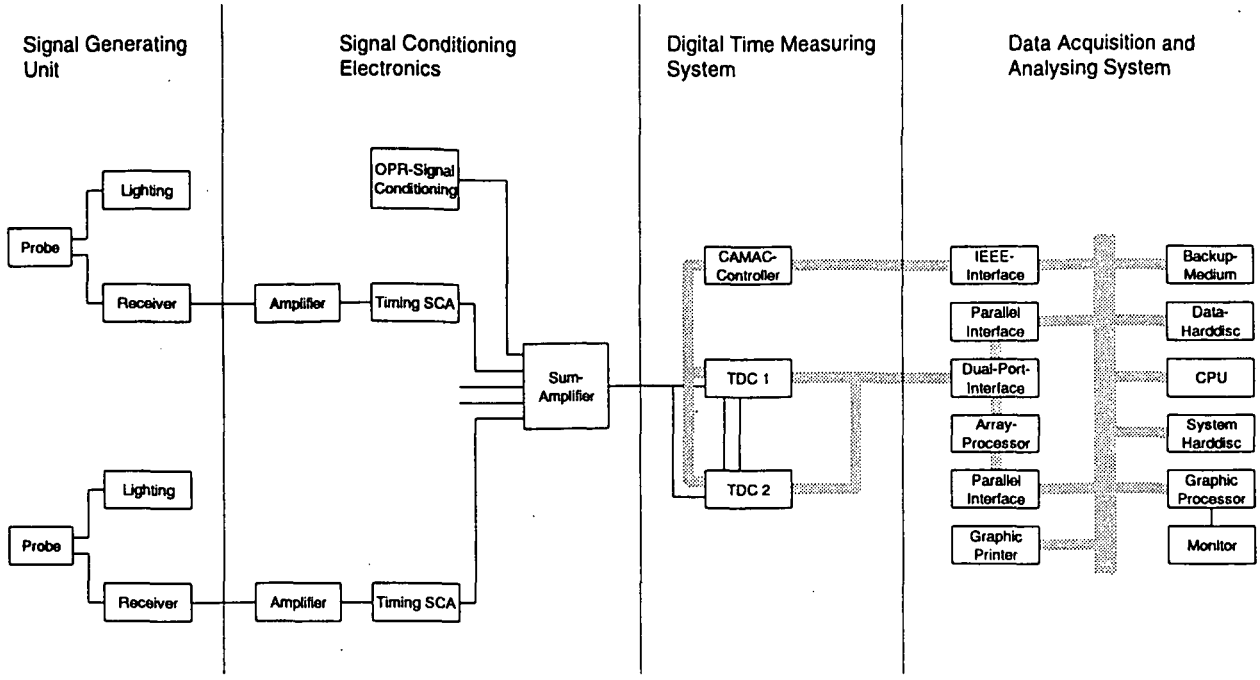


Fig. 1: Setup of the experimental OBM system

In the absence of blade vibrations, these transit times are a function of rotor speed, rotor radius and circumferential probe position. If there are blade vibrations the blade transit times deviate from those in the undisturbed condition, with the blades passing the probes earlier or later than normal, depending on their momentary deflection. An analysis of these transit time deviations will then identify the amplitudes and frequencies of the blade vibrations encountered.

The major advantages of the OBM system over the strain gauge and FM grid systems are:

- no instrumentation on the blades
- reduced instrumentation effort on the casing
- no transmission medium between the rotor and the stator
- concurrent measurements on all blades.

The OBM technique therefore appreciably reduces cost, economizes preparation and setup times and moreover enables vibration measurement of all blades.

The OBM technique has one drawback insofar that the blade vibration sample frequency is limited by the rotor speed and the number of probes installed. Generally, then, it has to be accepted that the output data can be ambiguous. However, by use of theoretical modal shape analysis, it is usually possible, to correct the data to an unique result.

## 4. EXPERIMENTAL OPTICAL BLADE VIBRATION MEASUREMENT SYSTEM

To gain experience with the optical method of blade vibration measurement, an OBM system was developed and setup at MTU, consisting of:

- optical probes with lighting device and electronic receiving circuitry
- electronic signal conditioning circuitry for an once-per-revolution signal
- timing system
- computer and software for test data acquisition, storage and analysis.

The system is shown schematically in **Fig. 1**. Optical probes are used to ensure a high triggering accuracy and thus a high amplitude resolution. The probes emit a light beam with clearly defined geometry and receive the light scattered back by the blades (see **Fig. 2**). For the lightbeam a laser is used whose light is guided to the probe by means of an optical fibre (1). From there the light is focussed onto the blade tip (3) through a

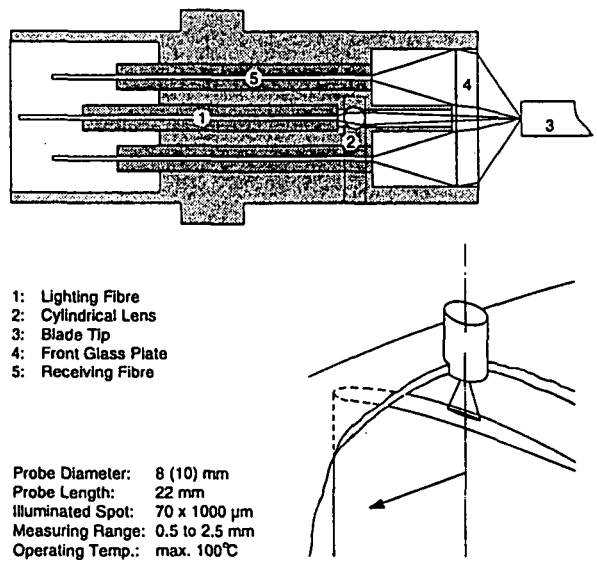


Fig. 2: Functioning of the optical probe

cylindrical lens (2). The size of the illuminated spot on the blade is about 70 x 1000 µm. It is aligned parallel with the edge of the blade tip by adjusting the probe accordingly. If the blade enters the light beam the intensity of the scattered light increases to the maximum value within 70 µm only. At the same time, the extension of the illuminated spot along the blade edge allows averaging over any scratches present on the blade tip surface.

The reflected light then hits the round front glass plate (4) of the probe which - except for the center - is roughened to form a scattering plate which feeds part of the reflected light into 4 receiving fibres (5). The advantage of this receiving concept, which does not require optical image formation using lenses, lies in the large effective solid angle which the probe covers above the illuminated spot on the blade tip. This results in stable signals which are reproducible from one rotor revolution to the next, even if the scattered light is subject to great directional variations owing to unevenness of and scratches on the blade tips.

The receiving fibres pass the reflected light on to the electronic receiving and signal conditioning circuits (see **Fig. 1**) where it is amplified. Standardized trigger pulses are then derived by means of leading-edge trigger which - because of the sharply rising flanks and the stability of the blade signals - mark, with high accuracy, the points in time when the blades enter the light beam of the probe.

The trigger pulses of all probe/blade combinations are routed via a summing amplifier into a common channel and then to the timing system. Bringing together all trigger pulses allowed the use of a timing system consisting of two LeCroy TDC 4204 time digital converters which alternately measure the time between the successive trigger pulses.

The transit time of a blade between two probes is determined from this data by summation of a certain number of successive values. The correct initial and final values are defined by a once-per-revolution signal which is, however, not included in the time measurement. The transducer for the once-per-revolution signal is positioned on the compressor shaft in such a manner that the pulse occurs between two blade signals $B_{i-1}$ and $B_i$ from one optical probe $P_k$. The pulse is then synchronized with the next blade signal $B_i$ by the electronic conditioning system and delayed by 1 µs. Thereafter, it likewise passes through the summing amplifier and the timing system. For each rotor revolution the data flow thus contains $N_B \times N_P + 1$ measurements ($N_B$: number of blades, $N_P$: number of probes). At the beginning of the additional 1 µs value blade $B_i$ arrived at the probe $P_k$ position.

The data elements are fed into the host computer (DEC µVaxII) via a parallel dual-port interface and stored on magnetic disk for a precise off-line evaluation. At the same time the interface transfers the data to an array processer (Analogic AP500) for on-line analysis the results, which are likewise fed into the host computer for subsequent screen display.

The advantages of this setup lie in the fact that a standard timing system can be used and that the once-per-revolution signal (which is not accurate in terms of time) is not included in the time measurement. The disadvantage is that the probes must be positioned such that the sequence of the signals from the various blade/probe combinations remains the same all the time, since signal exchanges in the data flow cannot be recognized and the timing system has a dead time of approx. 0.5 µs. This may cause problems in cases where a larger number of probes and blades and/or higher vibration amplitudes are involved.

## 5. ANALYSIS METHODS

In the development of the analysis methods for the experimental OBM system particular attention was paid to the measurement of vibrations excited by integral engine orders. These vibrations, which are coupled to speed and compressor casing in terms of frequency and phase, respectively, are measured using 2, 3 or 5 probes around the circumference. Their common axial position above the blades is selected such that the vibration modes to be investigated do not have nodes in these areas. This information is obtained from a prior modal shape analysis. Evaluated are the blade transit times between the probes, and more precisely, the changes in transit times as compared with the undisturbed values which are calculated from probe angular spacing, rotor radius and speed. The once-per-revolution signal is not time-critical. It serves to allocate the measured values to the blades or probes.

The different analysis methods used at MTU are described below. The formulae derived serve to explain the methods and are, therefore, partly shown in simplified form. Thus, it is presupposed that the motion of the blade tips caused by the vibration is much slower than the movement caused by rotation and that the vibrations are only slightly damped. Also, the window function which has to be used for Fourier analysis is not included here.

### 5.1 Measurements using 3 or 5 probes, synchronous vibrations

The following measuring method uses 3 probes spaced 120° circumferentially or 5 probes spaced 72° circumferentially. The momentary deflection $a_k$ of a blade vibrating synchronous with respect to rotor speed as it passes one of the probes $P_k$ is

$$a_k \cong a \cdot \sin(n\vartheta_k + \gamma) \qquad (1)$$

where $a$ is the vibration amplitude, $n$ is the exciting integral engine order, $\vartheta_k$ is the circumferential position of probe $P_k$ and $\gamma$ is the phase position of the vibration. This data serves to calculate the theoretical change $\delta t_{k-1,k}$ in transit time between two adjacent probes $P_{k-1}$ and $P_k$:

$$\delta t_{k-1,k} \cong \frac{a_{k-1} - a_k}{2\pi R f_R} \qquad (2)$$

where $R$ is the rotor radius and $f_R$ is the rotational speed. The values $\delta t_{k-1,k}$ are used to perform selec-

tive Fourier Transformations (FT) at the frequency points $f_R$ (1st EO-FT) and $2f_R$ (2nd EO-FT):

$$T_1 = \frac{1}{N}\sum_{k=1}^{N} \delta t_{k-1,k} \cdot e^{i2\pi k/N}$$
$$T_2 = \frac{1}{N}\sum_{k=1}^{N} \delta t_{k-1,k} \cdot e^{i4\pi k/N} \qquad (3)$$

where $N$ is the number of probes. These equations apply to one rotor revolution in each case. To improve the amplitude resolution it is recommended to determine the mean for a certain number of revolutions. Of course, the vibration amplitude should not change significantly during this period. Equation (3) then delivers for the absolute values of $T_1$ and $T_2$:

$$|T_1| = a \cdot |F_1| / (2\pi R f_R)$$
$$|T_2| = a \cdot |F_2| / (2\pi R f_R) \qquad (4)$$

The absolute values of $F_1$ and $F_2$ are summarised in **Tab. 1**.

| Tab. 1 | $N=3$ | $N=5$ | |
|---|---|---|---|
| $n$ | $\lvert F_1\rvert$ | $\lvert F_1\rvert$ | $\lvert F_2\rvert$ |
| 1 | 0.866 | 0.588 | 0 |
| 2 | 0.866 | 0 | 0.951 |
| 3 | 0 | 0 | 0.951 |
| 4 | 0.866 | 0.588 | 0 |
| 5 | 0.866 | 0 | 0 |
| 6 | 0 | 0.588 | 0 |
| 7 | 0.866 | 0 | 0.951 |
| 8 | 0.866 | 0 | 0.951 |
| 9 | 0 | 0.588 | 0 |
| 10 | 0.866 | 0 | 0 |

The calculation of $T_1$ and $T_2$ as per equation (3) using the measured values $\delta t_{k-1,k}$ and transformation of equation (4) (to obtain $a$) results in the following:

$$a = 2\pi R f_R \cdot |T_i| / |F_i| \qquad (5)$$

According to **Tab. 1** all synchronous vibrations of orders 1, 2, 4, 5, 7, 8 etc. can be measured with 3 probes, with the momentary vibration amplitude $a$ being calculated from equation (5). Vibrations of integral orders 3, 6, 9 etc. cannot be measured since in these cases the blades pass all probes in the same vibration condition and there is no change in transit time as compared with the undisturbed case. All (measurable) vibrations occur at the aliasing frequency $f_A = f_R$ (1st EO) since all engine orders from the 2nd EO up are insuffiently sampled (sample frequency $f_S = 3f_R$).

With a 5-probe system the orders 1, 4, 6, 9, etc. appear as 1st EO and orders 2, 3, 7, 8, etc. as 2nd EO, as can be seen from **Tab. 1**. Orders 5, 10, etc. cannot be measured. If a combination of the 3-probe system and the 5-probe system is used with one probe being assigned to both systems (i.e. a total of 7 probes) all orders can be measured except for 15, 30, etc.

### 5.2 Measurements using 2 probes, synchronous vibrations

Where installation of 3 or 5 equispaced probes is not possible due to the restricted space available, a 2-probe system may be used either alone or together with one of the other systems. The pertinent evaluation method has already been described by Roth [2] [3]: In the case of a blade subjected to synchronous vibrations excited by a certain integral engine order the speed-dependent vibration amplitude a can be approximately described by

$$a \cong \hat{a} \cdot \sin\varphi \qquad \tan\varphi \cong \frac{f_{Ro}\, d / \pi n}{f_{Ro}^2 - f_R^2} \qquad (6)$$

where $\hat{a}$ and $f_{Ro}$ are the vibration amplitude and the speed at the resonance point and $d$ is the damping constant. With the above definitions the change in transit time between the two probes $\delta t_{1,2}$ can be calculated as follows:

$$\delta t_{1,2} \cong \frac{a_1 - a_2}{2\pi R f_R}$$
$$\cong -\frac{\hat{a}}{\pi R f_R} \cdot \sin\varphi \cdot \cos(\tfrac{1}{2} n \vartheta_{1,2} + \psi - \varphi) \cdot \sin(\tfrac{1}{2} n \vartheta_{1,2}) \qquad (7)$$

where $\vartheta_{1,2}$ is the angular spacing between the two probes and $\psi$ is the phase of the exciting force. The momentary amplitude $a = \hat{a} \cdot \sin\varphi$ cannot be derived from this equation, since the phase $\psi$ is unknown. If, however, the resonance range is covered completely by varying the speed of rotation, $\varphi$ changes continuously from $0$ to $\pi$, and resonance curves $\delta t_{1,2}(f_R)$ are obtained where the distance between the minimum and maximum values does not depend on $\psi$:

$$\delta t_{1,2max} - \delta t_{1,2min} \cong \frac{\hat{a}}{\pi R f_R} \cdot \sin(\tfrac{1}{2} n \vartheta_{1,2}) \qquad (8)$$

This results in:

$$\hat{a} = \frac{a'_{max} - a'_{min}}{\sin(\tfrac{1}{2} n \vartheta_{1,2})} \quad \text{with} \quad a' = \pi R f_R \delta t_{1,2}(f_R) \qquad (9)$$

If $a'$ is plotted versus $f_R$ the peak amplitude $\hat{a}$ at the resonant point can be seen from the resulting curve (see **Fig. 7**). This method can be applied only if the entire resonance range is covered and if the amplitude distribution versus speed has been correctly described by equation (6). In many cases, however, the validity of this is limited, e.g. when there is strong interaction between the blades of one rotor stage.

### 5.3 Measurements using 3 or 5 probes, waterfall diagram

With the two analysis methods described so far allocation of the measured resonance lines to the blade vibration modes is essentially based on the location of the lines in the speed plot with the results of the theoretical modal shape analysis being used as an aid.

This is frequently ambiguous, since at certain speed points several vibration modes can be excited by different integral engine orders. Additional information can be obtained by applying the 3-probe or 5-probe system also to asynchronous vibrations. For this purpose, a set of measured values is used in a Fourier analysis for the entire frequency range up to half the sample frequency:

$$T(f) = \frac{1}{M}\sum_{k=1}^{M} \delta t_{k-1,k} \cdot e^{i2\pi fk/Nf_R}$$

$$|T(f)| = \frac{a \cdot \sin(\pi f / Nf_R)}{2\pi R f_R} \qquad (10)$$

with $0 \le f \le Nf_R / 2$, where $N$ is the number of probes (3 or 5) and $M$ is the number of measured values. Transformation of equation (10) to obtain $a(f)$ results in the following:

$$a(f) = \frac{2\pi R f_R \cdot |T(f)|}{\sin(\pi f / Nf_R)} \qquad (11)$$

The scale factor $\sin(\pi f / Nf_R)$ appears because blade deflections are not measured directly at defined points in time. Instead, running times are analysed which are influenced by the blade deflections at the start and stop probes.

Most of the vibration frequencies occur as aliasing frequencies in the spectra since the sample frequency is generally not the required 2x vibration frequency as would be required for an unambiguous vibration analysis. The aliasing frequency is calculated as follows:

$$f_A = \pm f_S + mNf_R \qquad (12)$$

with $0 \le f_A \le Nf_R / 2$, where $f_A$ is the aliasing frequency, $f_S$ is the vibration frequency and $m$ is an integer. If measurements are taken during slow accelerations and decelerations of the compressor the Fourier spectra can be calculated and plotted in the form of a waterfall diagram which shows the individual vibration modes of the blades in the form of characteristic zigzag lines (see **Fig. 5**). The vibration modes can now be unambiguously identified by comparison with the results of a theoretical modal shape analysis.

### 5.4 Scale factor

It has to be noted that the OBM system provides information on the vibration amplitudes in circumferential direction along the track of the probes. These amplitudes have to be converted into the actual vibration amplitudes in the direction of vibration. The corresponding scale factors result from the geometry of the measurement setup and the forms of movement of the vibration modes which are known from the theoretical modal shape analysis.

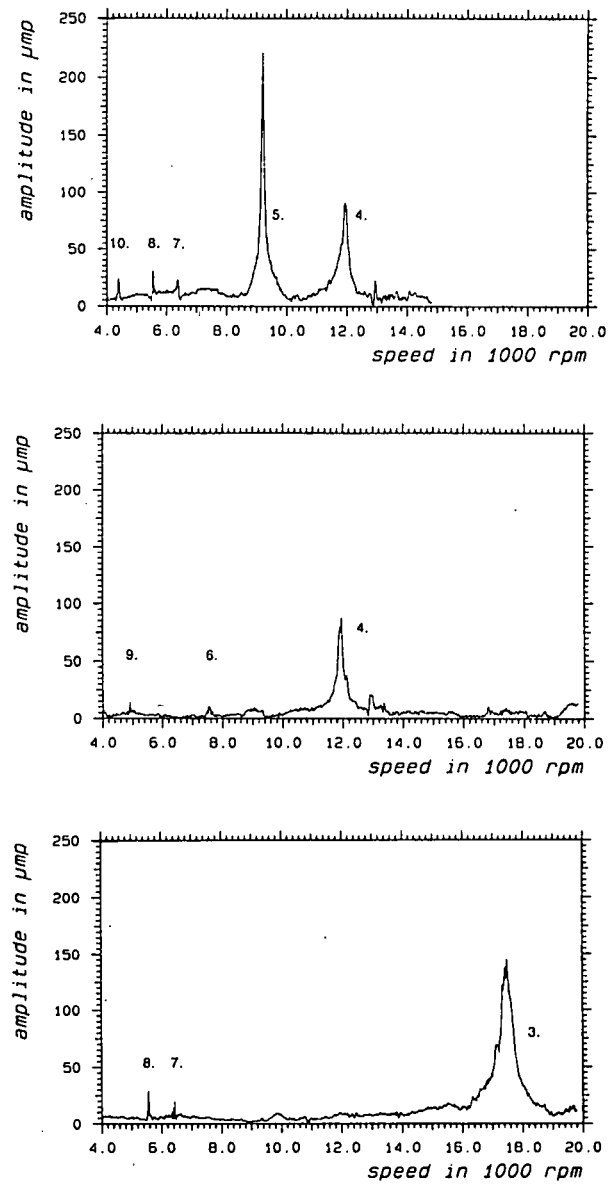


Fig. 3: Results of a 3-probe and a 5-probe measurement performed on a single-stage low-pressure compressor:
3-probe measurement: 1st EO-FT (top)
5-probe measurement: 1st EO-FT (center), 2nd EO-FT (bottom)

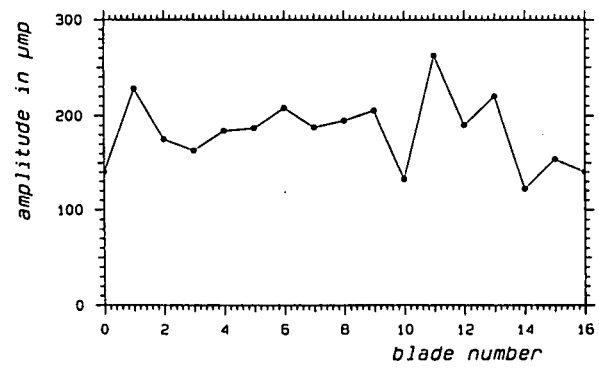


Fig. 4: Peak amplitudes of the individual blades (blade 0 corresponds to blade 16) in the 1F/5th EO resonance at 9200 rpm (see Fig. 3)

## 6. MEASUREMENT RESULTS

The experimental OBM system has been successfully used at MTU for low-pressure as well as high-pressure compressor rig and engine tests. In cases where the temperature exceeded 100°C the probes were mounted on water-cooled flanges. The main test objective was to verify that the vibration amplitudes were in the uncritical range and that the compressor could be safely operated without further vibration monitoring. Blisks (bladed disks) were subjected to tests involving high permanent vibrational loads to determine the endurance limit. In this case OBM served the purpose of monitoring all blades of the blisk on-line to be able detection of the first incipient crack in a blade immediately and consequently to shutdown the rig. Other tests were aimed at assessing the effects of various methods of blade vibration damping or of methods to avoid fretting at the blade roots. In these tests, too,

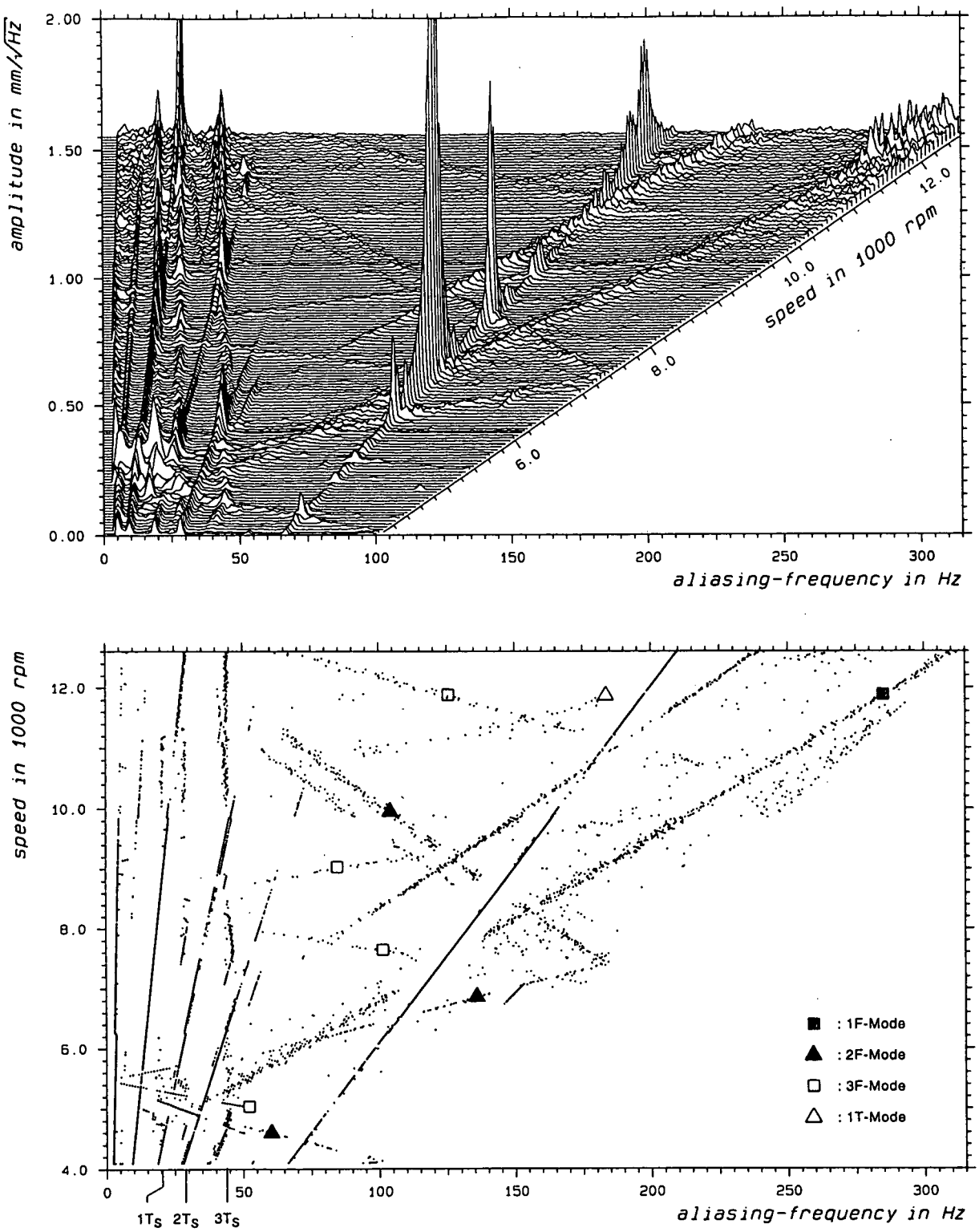


Fig. 5: 3-probe measurement on a single-stage low-pressure compressor (rig II): Waterfall diagram (top), peak plot (bottom). For explanations see text

the major advantage of OBM, i.e. concurrent measurement of all blades, was advantageous. With one probe fitted in the area of the leading edge and another probe in the area of the trailing edge of the blades it was possible to measure blade untwist at rising rotational speed or centrifugal force. The angle amount of untwisting must be taken into account in blade manufacture to ensure an optimum blade angle at the compressor design point.

The following contains a description of typical applications of the measurement system and the results obtained. **Fig. 3** shows the results of a 3-probe measurement (top) and a 5-probe measurement (center, bottom) on a single-stage low-pressure compressor (rig I). The amplitudes determined from the 1st and 2nd EO-FTs are plotted versus the speed. Vibrations of appreciable amplitudes were observed in the first flap mode only. As mentioned above the 3-probe system allows measurement of the exciting orders 4, 5, 7, 8 and 10 whereas the 5-probe system allows measurement of the exciting orders 4, 6 and 9 using the 1st EO-FT and orders 3, 7 and 8 using the 2nd EO-FT. As can be seen from the figures the resolution of the measurement system is very good; even resonance amplitudes as small as 10 $\mu m_p$ are visible. Another noticeable result is that the amplitudes are highest for the exciting integral engine orders 3 and 5. Presumably, it is the probes themselves that cause the strongest exciting forces. **Fig. 4** shows the peak amplitudes measured for the individual blades at the 9200-rpm resonance (1F/5th EO). The scatter of the individual blade amplitudes clearly shows that concurrent monitoring of all blades is of vital importance.

**Fig. 5** is the waterfall diagram plotted for the 3-probe measurement of another single-stage low-pressure compressor (rig II). It clearly shows the lines of the 1F, 2F, 3F and 1T vibration modes. More clearly visible still are these lines in the peak plot below where all local peaks of the waterfall diagram are represented as points. As described above, insufficent sampling of the vibrations results in aliasing effects causing the lines to take a zigzag course in the plot. The intersections of these lines with the speed line ($f_A = f_R$) indicate the peaks of the vibrations excited by integral engine orders. In the left-hand area of the figures torsional vibrations of the rotor drive shaft can be seen at 20 Hz, 28 Hz and 43 Hz which were excited by the rough running of the geared-down electrical drive motor of the compressor rig. In **Fig. 6** the synchronous vibrations, evaluated via a 1th EO-FT, are plotted versus the speed. The major resonances are listed in **Tab. 2**.

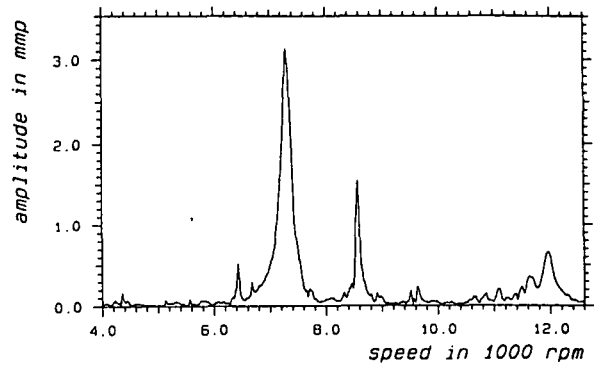


Fig. 6: Synchronous vibrations from the 1th EO-FT of the 3-probe measurement on rig II. Plotted are the OBM track amplitudes of an individual blade.

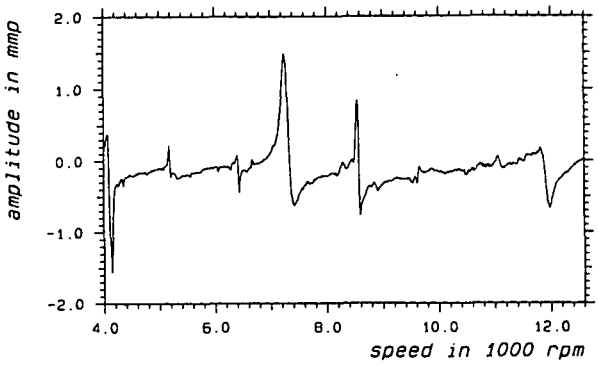


Fig. 7: Results of a 2-probe measurement ($\vartheta_{1,2}$ = 40°) on rig II. Plotted is the amplitude $a'(f_R)$ according to equation (9) for the blade shown in Fig. 6.

In order to allow a comparative 2-probe measurement to be carried out an additional fourth probe was installed at 40° from one of the three others. The results of this measurement are contained in **Fig. 7** where the amplitude $a'$, according to equation (9), is plotted. As compared with **Fig. 6** there are two additional resonances, i.e. 1F/3rd EO at 4100 rpm and 2F/6th EO at 5200 rpm, both of which could not be measured with the 3-probe system. For the other resonances the curve provides amplitudes which are also listed in **Tab. 2**.

In **Fig. 7** the amplitudes for the 1F and 2F resonances are approx. 5% higher than those in **Fig. 6**. Probably, the amplitude distributions versus speed in **Fig. 7** cannot exactly be described by equation (6). Another cause of variations is the superposition of resonance lines. Depending on the phase position of the vibra-

| Tab. 2 | | | 3-probe measurement | 2-probe measurement | | |
|---|---|---|---|---|---|---|
| mode | EO | speed (rpm) | amplitude ($mm_p$) | $a'_{max} - a'_{min}$ ($mm_p$) | $sin(n\vartheta_{1,2} / 2)$ | amplitude ($mm_p$) |
| 2F | 5 | 6420 | 0.51 | 0.52 | 0.985 | 0.53 |
| 1F | 2 | 7270 | 3.10 | 2.12 | 0.643 | 3.30 |
| 2F | 4 | 8580 | 1.54 | 1.60 | 0.985 | 1.63 |
| 1T | 5 | 11950 | 0.66 | 0.83 | 0.985 | 0.84 |

tions and the probe locations different cumulative amplitudes are obtained.

For the 1T resonance the variation is as high as 24%. This is mainly due to the fact that on this rig radial offset of the rotor axis occurs at higher speed resulting in a change of the effective probe spacing. This effect cannot be fully accounted for at present.

Vibrations could also be successfully measured for transient operating conditions such as compressor surges. **Fig. 8** shows the vibrating movement of a blade versus time as measured with 3 equally spaced (120°) probes during surging. Shown below is the curve of the strain gauge signal obtained for the same blade. As can be clearly seen there is good qualitative agreement between the two curves, although they do not coincide exactly since the actual amplitude distribution is not fully sampled by the OBM and the vibration modes (in this case mainly 1F and 2F) affect the curve with their different scale factors. Furthermore, the OBM signal is superimposed with the torsional vibrations of the rotor drive shaft which are not included in the strain gauge signal.

For the purpose of a quantitative comparison a Fourier analysis of the signals was performed. Then the average amplitude of the 1F mode was determined for the period from 1.77 to 2.27 s (see **Fig. 8**) and converted into the vibration amplitude at the blade tip leading edge using the appropriate scale factors. These factors were determined by means of a theoretical modal shape analysis which takes the centrifugal force into account and provides data on the stress distribution over the airfoil, the local relative vibration amplitude and the local direction of vibration. **Fig. 9** is a comparison of the OBM amplitudes of the individual blades and the strain gauge amplitudes of the blades fitted with strain gauges (blades 1, 7 and 14). The OBM values and the strain gauge values vary by approx. ± 15%.

During the last few years the results of optical blade vibration measurements and strain gauge measurements have been compared repeatedly. Very good agreement was obtained on a specially designed test rig using simple plate cantilevers as blades. For actual compressors the theoretical modal shape analysis, which provides the relationship between the OBM values at the blade tip and the strain gauge values at the airfoil, proved to be critical. In view of the complex three-dimensional blade geometries and the fact that centrifugal force and temperature must be taken into account, calculation of this relationship is a difficult task; particulary, since the root geometry and the clamping conditions of the root in the rotor disk also play an important role. Investigations using different computing programs and different resolutions for the root geometry the variations between the values calculated were as high as ± 30%. With an optimum design of the computing program the OBM values and the strain gauge values agreed within approx. ± 10%.

As a last example of OBM applications **Fig. 10** shows the results of an untwist measurement performed on the first stage of another low-pressure compressor (rig III). 3 probes spaced 120° around the circumference

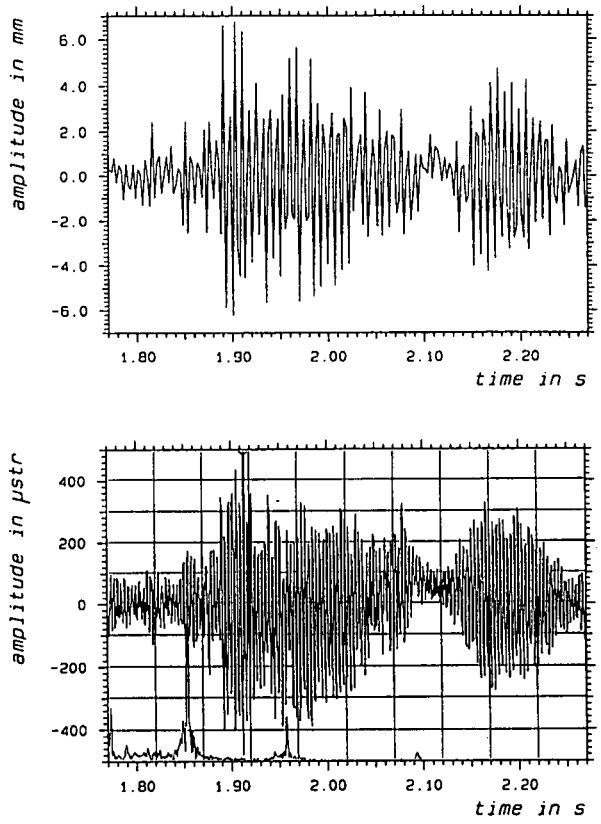


Fig. 8: Signal distribution during compressor surging: OBM signal (top), strain gauge signal (bottom).

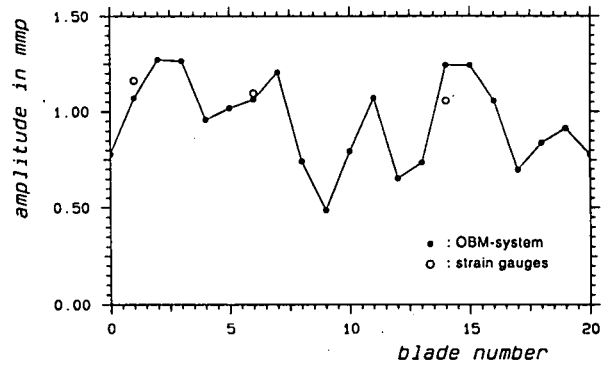


Fig. 9: Time-averaged vibration amplitudes of the individual blades (blade 0 corresponds to blade 20) in the 1F mode during compressor surging (see Fig. 8).

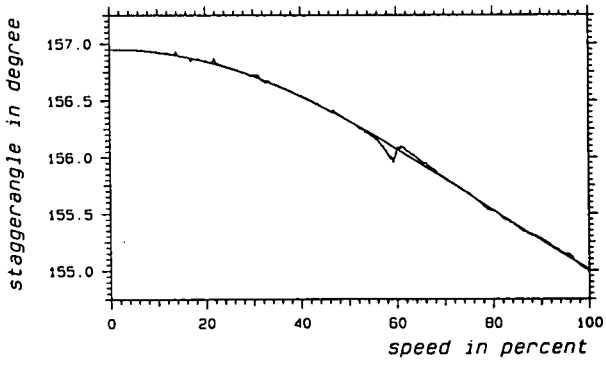


Fig. 10: Results of an untwist measurement performed on the first stage of a low-pressure compressor

were used to measure in the leading edge area of the blades and an axially offset fourth probe was used to measure in the trailing edge area. To improve the accuracy all blades and all 3 probe combinations used for the untwist measurement were evaluated and the mean value was calculated. Nevertheless, the curve is still slightly disturbed owing to blade vibrations (1F mode in various engine orders). To smoothen the curve a compensating curve was fitted to the measured values. The accuracy of the measured values is in the region of ± 0.16° with this value having to be considered as an offset for the entire curve. The accuracy of the curve which reflects the blade untwist is significantly higher, i.e. approx. ± 0.03°. In this case the difference between the measured value and the theoretical value was as low as 0.02°.

## 7. OUTLOOK

The optical blade vibration measurement system is successfully in use at MTU. Owing to the great potential this method obviously offers it was decided to continue development work on the experimental OBM system and to set up a so-called prototype OBM system.

One of the major objectives of the development work involves the probes whose operating temperature range is to be increased from presently approx. 100°C to over 250°C (uncooled). Furthermore, the reliability of the electronic signal conditioning circuitry is to be improved, and the circuitry should be of a more compact design and capable of automatic operation. The timing system will be a multi-channel system which is less restrictive in terms of probe positioning and which ensures reliable measurement of higher vibration amplitudes occurring, for example, during compressor surges. The use of advanced computer technologies will reduce analysis times and allow comprehensive analyses to be performed on-line.

The analysis algorithms used so far will be further improved. Even with high exciting engine orders, small amplitudes and superposition of resonance lines the system should permit reliable quantitative measurements of synchronous vibrations, at least off-line. Another objective consists in providing as much information as possible on-line, in particular on critical vibration conditions such as flutter and rotating stall.

## 8. REFERENCES

[1] I. Ye. Zablotskiy, Yu. A. Korostelev, and L. B. Sviblov
Contactless Measuring of Vibrations in the Rotor Blades of Turbines
Technical Translation FTD-HT-23-673-74, pp 1-19, 1974

[2] H. Roth
Schwingungsmessungen an Turbinenschaufeln mit optischen Methoden
Brown Boveri Mitt. 1-77, pp 64-67, 1977

[3] H. Roth
Vibration Measurements on Turbomachine Rotor Blades with Optical Probes
Measurement Methods in Rotating Components of Turbomachinery, pp 215- 224
New Orleans, Louisiana, March 10-13, 1980

Paper 31
Author: Zielinski

Q: Benson

What type of computer do you use for data acquisition ?

A: The computer of our experimental OBM system is 8 years old. It is a MicroVAX II with VMS as operating system. For data acquisition we use a special software and a high speed hard disc. Our new OBM system will use a PC based data acquisition system.

Q: Eyraud

To improve resolution toward small amplitudes what means will you use - new design of probe, increasing clock counting frequency, other ?

A: There is no necessity to develop a new probe design, because the signals yielded by the probes now are well suited for high accuracy triggering.

The resolution of the time measuring system will be reduced from now 156 ps to 3ns in the new system, sufficient for an amplitude resolution of about 1.5 microns.

To improve the resolution towards small amplitudes, especially in the case of superposed resonance lines, the suitability of least square fits of theoretical curves to the measured data will be investigated, using the data of all blades and taking into account the coupling of the blades.

# TURBOMACHINERY BLADE TIP MEASUREMENT TECHNIQUES

**S Heath, T Slater, L Mansfield, P Loftus**

*Rolls-Royce Civil Aero Engines Ltd, P O Box 31, Moor Lane, Derby DB24 3DJ, UK*

## 1.0 SUMMARY

The efficiency of axial flow compressors and turbines is critically dependent on the size of the tip to casing gaps (tip clearance) as is the surge margin of compressors. Optimisation of tip clearance control schemes requires measurements of tip clearances throughout the operating envelope of the engine.

The dynamic design of rotor blading to avoid damaging integral order and self excited resonance's is complex and still defies routine right-first time design. This necessitates monitoring of blade vibration during testing which is time consuming and costly with conventional strain-gauging techniques.

Both of the above requirements may be addressed by easily mounted tip probes, the design and operation of which are discussed in this paper. Until recently the market for such devices has provided insufficient incentive for instrumentation suppliers to invest in the development of such devices leaving engine manufacturers to develop their own solutions to these unique problems. The Rolls-Royce experience is described.

## 2 INTRODUCTION

Gas Turbine casing rotor paths provide the simplest and most obvious access for non-intrusive instrumentation to monitor the blading during development programmes. The most common of such applications are tip clearance probes and tip timing (Non-interference Stress Measurement)[3] Systems. The lack of suitable commercial systems has lead to gas turbine manufacturers developing instrumentation, often in isolation. This paper describes the recent Rolls-Royce developments of second generation systems for the measurement of both of these parameters.

## 3 TIP CLEARANCE

### 3.1 Background

The efficiency of axial flow compressors and turbines is critically dependent on the size of the tip to casing gaps (tip clearance) as is the surge margin of compressors. Optimisation of tip clearance control schemes requires measurement of tip clearances throughout the entire operating envelope of the engine on the test bed in order to validate the design models.

The system described here was designed to enable a comprehensive tip clearance survey to be performed during the development of the Trent family of engines. The survey required the simultaneous measurement of 30 intermediate pressure compressor tip clearances to enable the behaviour of the tip clearance/casing movement to be understood. It was required to accurately measure, via 7 metres of cable, clearances from 0.5 to 5 mm. No commercial system was available that would meet these performance specifications. It was decided therefore to design a new system based on previous, frequency modulated capacitive tip clearance systems[1, 2] but using an entirely new oscillator design approach for this type of measurement.

The total system was brought together by the successful co-ordination of several key activities.

The Probe/cable used was developed by a specialist instrumentation supplier in close collaboration with the end users. The calibration rig/probe jig was developed by a second specialist supplier, and the electronics were conceived and designed by the authors' department.

### 3.2 System Design

Previous systems have relied on the use of a triaxial cable between the probe tip and the oscillator which is to be frequency modulated by the variation in capacitance caused at the probe due to blade proximity. The probe simply forms a shunt capacitance which shunts the inductance in the oscillator circuit. In order to maximise sensitivity and range it is current practice to "drive out" the cable capacitance by a guard drive circuit which must operate at the frequency and phase of the oscillator itself. Long cables between probe and oscillator cannot be used with such a system because of the difficulty in driving the large guard capacitance at the system frequency (typically 5-10 MHz). This new system utilises the properties of transmission lines to avoid this problem totally. Not only does it allow a much longer cable than previously used but the cable is

*Paper presented at an AGARD PEP Symposium on "Advanced Non-Intrusive Instrumentation for Propulsion Engines", held in Brussels, Belgium, 20-24 October 1997, and published in CP-598.*

now coaxial rather than triaxial resulting in considerable cost savings.

A block diagram of the system (one channel) is shown in **Figure 1**. As can be seen the implementation at a high level is very similar to previous systems the major differences being:-

a) The use of a transmission line oscillator arrangement .

b) The use of a low noise FM IF strip as the demodulator.

c) The fact that all of the electronics is integrated together rather than the 'two box' construction of standard types.

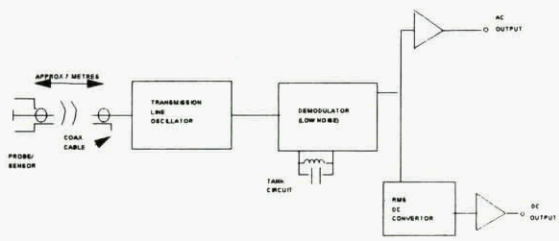


**Figure 1 Block Diagram**

3.2.1 Probe and Cable

A photograph of the probe is shown in **Figure 2**. This probe has been designed for the aforementioned application and is capable of operating at temperatures of up to 800°C. Other probes are available for use at up to 1100°C. The cable is constructed using a copper inner core with silicon dioxide (silica) dielectric for low capacitance and low RF loss. The cable outer is Inconel. The coaxial hard-line is 5 metres long in one continuous length and has a diameter of 1.5 mm. This enables ease of routing through the engine casing. The cable is extendible with a 2 M flexible extension of RG178B/U co-axial cable to enable easy connection to the electronic rack. This flexible cable operates at temperatures up to 200°C.

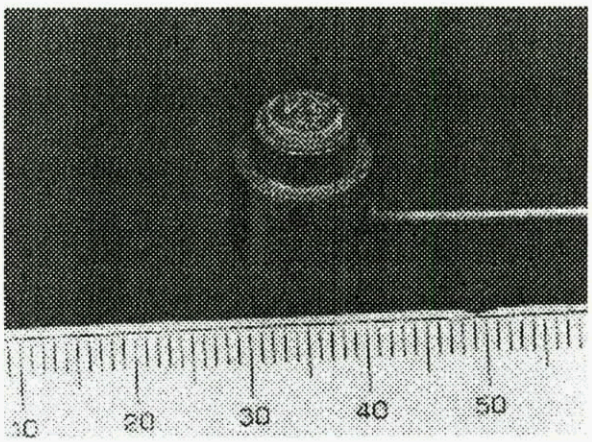


**Figure 2 Probe**

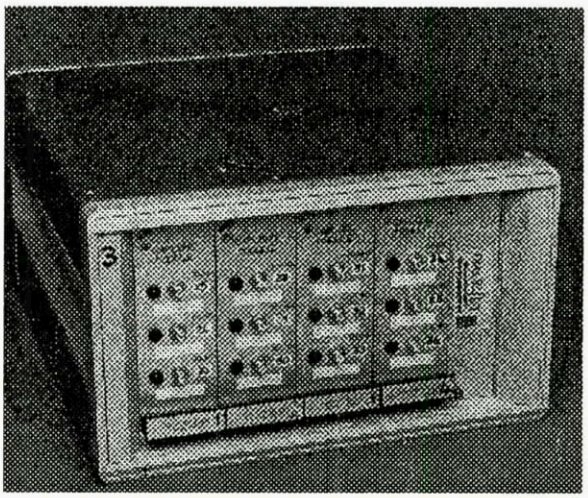

**Figure 3 12 Channel Prototype Rack**

3.2.2 The Electronic Rack

**Figure 3** is a photograph of a 12 channel prototype rack. This unit takes up to 12 probes and fully demodulates the signals to provide analogue outputs. Effectively the rack contains 12 times the electronics shown in **Figure 1**.

It is the oscillator circuit which allows the use of long lengths of coaxial cable between the probe and the electronics. The coaxial cable forms a ½ wavelength resonator which is the frequency determining element of the oscillator. One property of ½ wavelength transmission lines is that apart from absolute phase and losses whatever changes occur at one end (such as change of loading capacitance) are transformed to the other end of the line. This has the effect of making the long line immaterial almost as if the probe were connected directly to an oscillator. This eliminates any need for a guard and results in a system with exceptional sensitivity. This exceptional sensitivity

partly results from the use of a very low noise demodulator circuit..

### 3.3 Calibration

System calibration is performed in a way common to prior systems.

A model of the rotor over which the probe will be measuring is mounted on a spinning rig. The probe is mounted in a specially designed holder which can 'simulate' the probes immediate surroundings when mounted in the engine casing. A graph is produced by stepping the probe away from the rotating blade model in known increments and logging the system output voltage. This process is repeated for all probes and channels. For maximum accuracy probes are paired with channels, then calibrated and used thus.

### 3.4 Typical Performance

A typical calibration curve is shown in **Figure 4**.

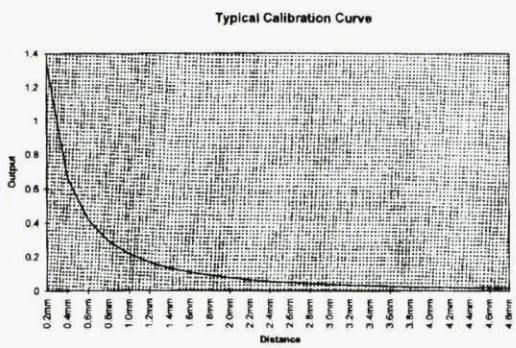


3.4.1 System Range

The system noise performance is such that measurements can be made at a probe to blade spacing of 5 mm (with a 1 mm blade thickness) using a mm diameter electrode.

3.4.2 System Resolution

The noise floor is such that system is capable of resolving 0.01 mm change at 1,5 mm range from a 1 mm thickness blade to 95% confidence. The resolution at 5 mm range is 0.05 mm with a 1 mm blade thickness.

### 3.5 Installation And Operation

The first use of this system was on the Intermediate Pressure Compressor of a Trent engine in December 96. The data obtained during the testing has been good. A sample of data is printed in **Figure 5**.

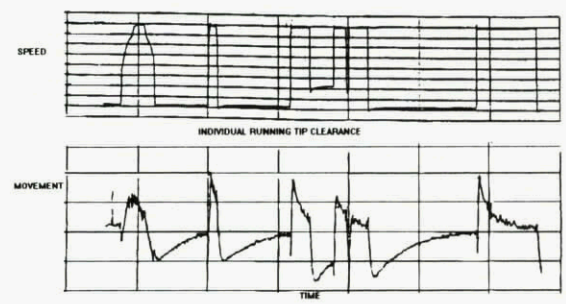


**Figure 5**

3.5.1 Probe and Electronics Installation

A specially machined housing has been designed for the probes used on this test. A screw clamp arrangement locks the probes into position in the compressor casing such that their datum faces are in a known position. The probes are mounted underflush in the abraidable liner to avoid damage during blade rubs. The amount of mounting under flush must be simulated during probe calibration on the spinning rig. The probe cable is regularly clipped, using stainless steel shims and spot welding, to the casing on its route out of the compressor area. Clipping regularly helps to reduce any vibration induced noise, although the system is relatively insensitive to this. The 7 metres cable length allows the electronic conditioning rack(s) (**Figure 3**) to be mounted well clear of the engine in a stable environment.

3.5.2 Recording Equipment

The method used here of recording the mean blade clearance is with a sampling data logger. Input into the logger is also the calibration data for each probe so that plots can be produced in engineering units. Signals are connected via standard test bed cables from the electronics in the test cell to the logger in the measurement facility.

## 4.0 BLADE TIP TIMING

### 4.1 Background

All turbomachinery blades experience vibration during operation. As undesirable structural motion affects fatigue life, performance and integrity, measurement systems are used both to identify the nature of the vibratory phenomena and to monitor the assembly response levels. Although many well established measurement and data processing techniques exist for non-rotating structures, no single system can reliably provide natural frequency, damping and mode shape data for rotating bladed-disks. Current experimental set-ups can be classified as contacting and non-contacting systems, the former involving a transducer that is mechanically attached to the rotating blade and the latter relying on a laser beam to capture the motion. This paper will focus on non-contacting measurement and data processing methods, the tip timing systems, so-called as the laser beam is usually directed towards some point on the blade's tip.

The types of transducers currently used in the authors' company, the measurement hardware and the installation methods are described. The data analysis methods and example results are also presented.

Blade tip timing measurement systems aim to determine the time at which a point on a rotating blade tip passes a stationary optical laser probe. In the absence of any structural vibration, the blade arrival time would be dependent only on the rotational speed. However, when the tip of the blade is vibrating, the blade arrival times will depend on the amplitude, frequency and phase of vibration, and hence the blade motion can, in principle, be characterised from knowledge of such data. A blade tip timing system performs three distinct tasks: (i) the acquisition of raw arrival time data from a number of stationary probes placed in the casing, (ii) the derivation of characteristic parameters, such as blade displacement, velocity and acceleration, from the measured data and (iii) the processing of the characteristic parameters in order to describe the vibration properties of the bladed-disk assembly.

A compromise must be reached between the number of transducers or probes fitted and hence the intrusiveness and the depth of information available. Currently Rolls-Royce uses a system based on three probes per rotor. This presents a minimal intrusion into the test vehicle, low cost of installation and a low impact on the vehicle build time. Consequently the depth of information is limited and the technique is used to complement strain gauge based measurements.

### 4.2 Measurement System

**Figure 6** shows a diagrammatic layout of a typical measurement system.

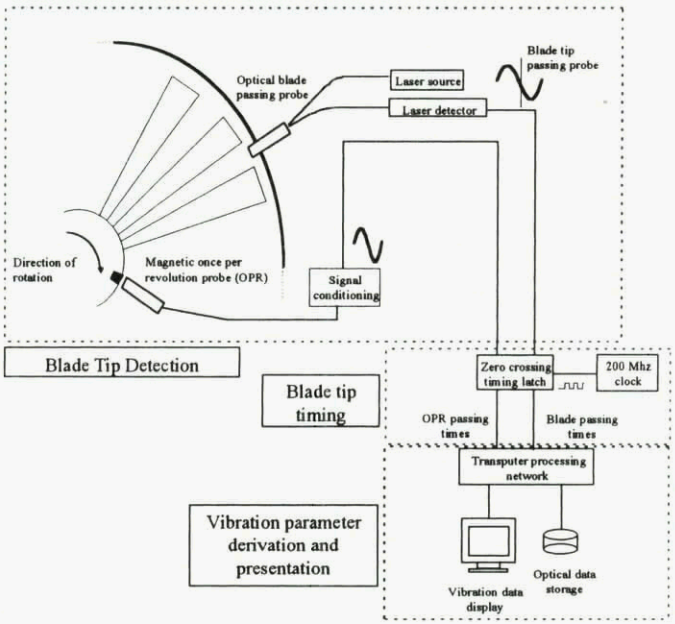


The system can be broken down into three elements;

1) Probe - Fibre Optic blade passing detection probe.

2) Probe Conditioning System (Analogue electronics).

3) Timing and Processing Unit (Digital electronics)

Each of these elements is now discussed below.

### 4.3 Transducer

The majority of blade vibration measurements with blade tip timing systems are made on compressors. A typical environment would be , rotor blade tip speed up to 400 m/s, blade tip width of 1 mm, temperatures up to 500°C and pressures of up to 600 psi. Additionally there is the likelihood of blade tip rubs producing debris. Despite this environment the requirement for high timing and positional accuracy has led to the widespread use of optical probes for these measurements in preference to more robust designs, such as capacitive and inductive which have been shown to be less accurate. An example low temperature probe is shown in **Figure 7**.

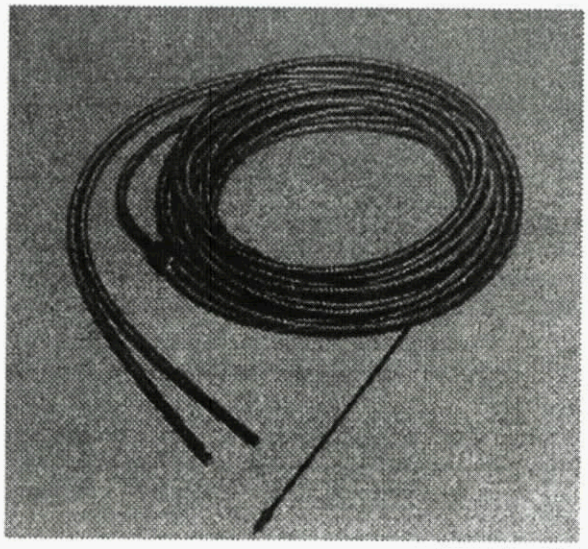

**Figure 7**

The probe consists of a bundle of approximately 200 100 μm core low loss glass fibres housed within an armoured metal jacket. The effective diameter at the tip is 1,20 mm. No lenses are used and this gives a spot size of about 2 mm at typical probe to blade clearances. Repeatability in detection point on the blade is dependent on the blade tip geometry but is typically 200 μm.

### 4.4 Probe Conditioning System

The light source used is a 100 mw infra-red semi-conductor laser. This is housed in the same module as the detector and conditioning electronics.

A detailed discussion of the circuit design cannot be given here but the basic features are;

1) Automatic control of the laser output power based on the probe pulse return level.

2) High gain range to compensate for degradation in the signal due to probe/blade tip contamination.

3) Active differentiator to give a zero crossing signal.

4) TTL pulse coincident with blade passing.

5) Built in test signal generation.

Interlocked enclosure to prevent egress of laser radiation.

### 4.5 Timing and Processing Unit

**Figure 8** shows the main system elements. Data is transferred from the timing and acquisition subsystem (DTU) using three transputer links, one dedicated to each probe. The timing latch uses ECL technology with a probe event timing resolution of 5 ns. The rewritable magneto-optical disk allows all the probe data to be stored concurrently with data processing at maximum blade tip passing frequencies. The PC server displays processed vibration data and issues network control and configuration commands. The current system can process three probes at blade passing rate of up to 60 kHz.

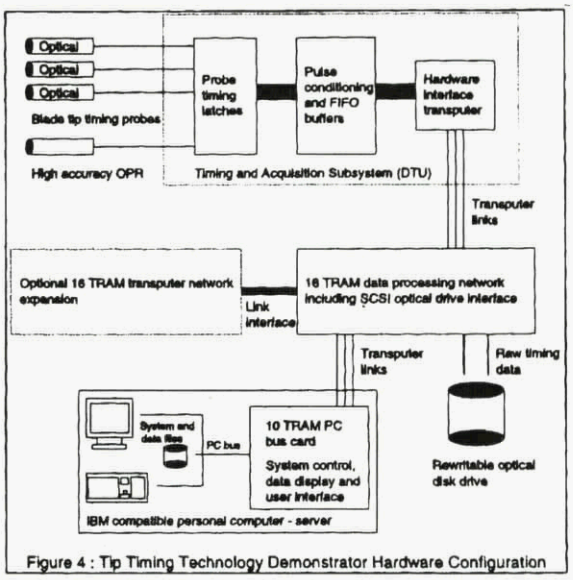


**Figure 8 Timing and Processing Unit**

The acquisition software is implemented entirely in parallel C. The system is highly tolerant to probe data errors, either through additional or missing probe signals. This is achieved by using data windows around the expected probe signal position relative to the once per revolution (OPR) probe signal. The validated data from the windowing processes can be considered error free by subsequent processes in the data pipeline.

### 4.6 Analysis Methods

#### 4.6.1 Classes of data

For the purposes of tip-timing data analysis, there are two distinct classes of response, namely synchronous and asynchronous. Synchronous (or integral order) resonance's are assembly modes that are excited at multiples of the rotational speed. Asynchronous resonance's are mainly due to aerodynamic instabilities such as rotating stall and flutter.

### 4.6.2 Asynchronous Response Tip-Timing Analysis Methods

#### 4.6.2.1 Analysis Approaches

Asynchronous response analysis methods aim at identifying the amplitude and frequency of non integral order assembly resonance's measured at the blade tips.

The known asynchronous response analysis techniques are summarised in **Figure 9**.

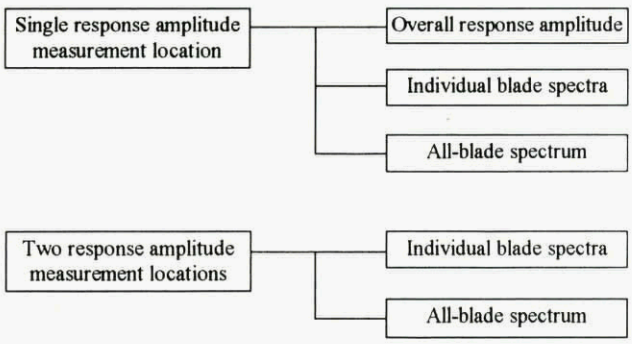


**Figure 9 : Known asynchronous response analysis methods**

4.6.2.2 Overall Response Amplitude

Hohenberg[4] indicated that the asynchronous response amplitude could be determined from the measurement of a single blade tip response parameter at a single location. The measured maximum-to-minimum amplitude over a finite period is assumed to be equal to the actual maximum-to-minimum amplitude of the assembly response. The method does not provide resonant frequency information and hence the determination of assembly stresses requires prior knowledge of this quantity.

The measurement of the overall response amplitude using a single probe is the simplest analysis method and it is widely used for safety monitoring of turbomachines. Although the actual overall amplitude has contributions from all assembly response modes, the maximum assembly stress calculated from overall amplitude measurements while traversing a single mode has been shown to be within 10% of the value obtained from strain gauge measurements.

4.6.2.3 Single Blade Analysis

A number of methods are available for identifying resonance frequencies from a Fourier analysis of the response parameters [5, 6, 7, 8]. All these tip-timing analysis methods have been shown to identify the resonance frequency and the maximum amplitude correctly as extensive checks have been made against strain gauge data. Broadly speaking, when the assembly vibration is dominated by a single resonance, the frequency of that resonance can be identified with good accuracy. The frequency content of tip-timing response measurements cannot be limited prior to "sampling" and the samples will inevitably contain signals and noise at frequencies above the sampling rate. The maximum frequency in the single blade spectrum is half the assembly rotation frequency such that most resonance's are present as aliases in the spectrum. Furthermore, the signal to noise ratio is low as noise is aliased into a limited frequency range from a wide frequency range. The true frequency can be derived from:

$$f_a = \left| k f_s - f_r \right| \quad (1)$$

where $f_a$ is the frequency in the single blade spectrum, $f_s$ is the sample frequency, $f_r$ is the resonance frequency and $k$ is an integer. The application of (1) requires the measurements to be made at approximately constant speed. So, only a restricted number of samples can be used in the Fourier analysis which results in a poor spectrum. For typical turbomachine vibration surveys, where speed changes continuously and contains random variations, single spectra are formed from 256 samples giving a typical frequency resolution of 0.7 Hz[6] Ensemble averaging of spectra is not possible as there are significant differences in acquisition conditions between the individual spectra. In practice, the low frequency resolution, poor signal-to-noise ratio and aliasing of all response frequency components into a limited band do not allow accurate estimates of the spectral peak frequencies. It is the authors' opinion that resonance frequencies cannot be identified reliably using the single blade spectra technique, unless the resonant frequencies have been measured by some other independent technique.

4.6.2.4 All-Blade Spectrum Analysis

All-blade spectrum analysis assumes that the bladed-disk assembly vibrates in nodal diameter modes, that is to say the contour of the stationary points coincide with a certain number of diameters of the disk as illustrated in the holographic interferrogram shown in **Figure 10**.

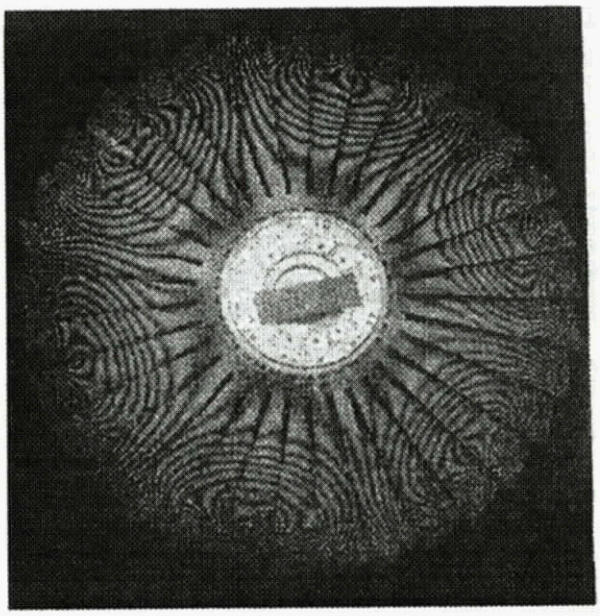

**Figure 10 : Double-pulsed hologram of blades assembled into a fan**

Because of circular symmetry, the nodal diameter modes will come in orthogonal pairs which will become travelling waves under the effect of rotation. Forward travelling waves correspond to the rotation of the nodal lines in the same direction as assembly rotation and backward ones from their rotation in the opposite direction to assembly rotation. A spatial Fourier analysis of the measured response amplitude of successive blades will give the travelling wave response in the stationary (or measurement) reference frame. This approach is referred to as all-blade or travelling wave analysis. The stationary reference frame frequency, $\omega_{stationary}$, is given by (2), which is consistent with the form given by Watkins et al. [6].

$$\omega_{stationary} = \omega_{rotating} + n\Omega \qquad (2)$$

The sample rate of the all-blade spectrum is equal to the number of blades times the assembly rotation rate. In general, resonant frequencies are not aliased in the all-blade spectrum, thus eliminating the problems of multiple frequency aliasing and of resolving the true resonant frequency associated with the individual blade spectra. The increased spectrum bandwidth also improves the signal-to-noise ratio, thus enabling spectral peaks to be identified more readily. A typical all-blade spectrum tip-timing analysis of data acquired from a compressor by the authors is shown in the form of a Z-plot in Fig. 11. A Z-plot is a modified Campbell diagram in which the print density indicates the strength of the vibration.

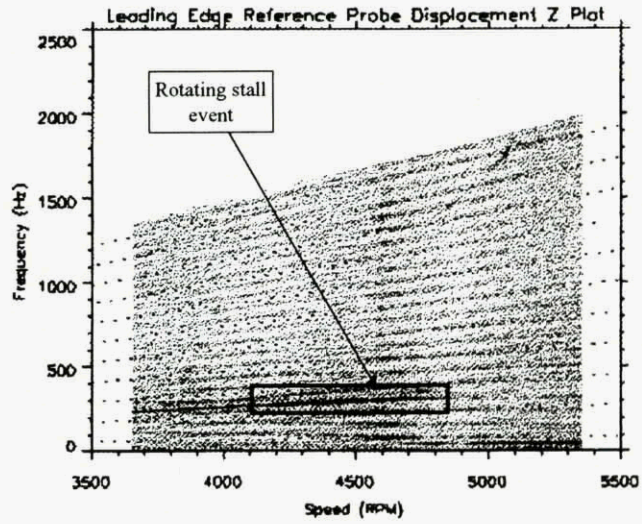


**Figure 11 : All-blade Z-plot for rotating stall event**

Although it is generally accepted that tip-timing techniques cannot provide accurate values of resonant frequencies, measurements at two locations can yield acceptable estimates of asynchronous resonant frequencies and amplitudes. Experience suggests that confident identification of resonance's still requires close predictions of their values. Typical Rolls-Royce development programmes use strain gauges where possible for initial vibration measurements on new designs and tip-timing methods during the subsequent extensive testing of these designs or their derivatives.

### 4.6.3 Synchronous Response Tip-Timing Analysis Methods

The current standard analysis methods typically take one or two response samples from each assembly rotation as a synchronous assembly resonance is traversed. Therefore, they can only give a single frequency component, i.e. the resonant frequency. As the resonance is traversed, the excitation and response characteristics change due to changes in the assembly rotation speed. Typically, this gives the engine-order of the resonance and a mean value of the associated frequency has to be calculated from the assembly rotation speed range over which resonance occurs.

One such method proposed by Zablotsky and Korostelev[9] has become a de-facto standard method for determining the amplitude of single synchronous resonance's, with recent applications being reported by Chi and Jones[3]. The analysis technique is based on measuring a single tip response parameter, such as displacement (or velocity, or acceleration), using a

single probe. The resonance is excited by varying the assembly rotation speed in such a way that the assembly is forced to traverse the resonance of interest. The form of the measured displacement versus rotational speed characteristic depends on the position of the measurement probe, typical plots at different measurement positions being shown in **Figure 12**. The actual resonance amplitude is the peak response amplitude at the measurement location on the blade. It is identical to the measured response amplitude at the datum location. The angular location of the probes refers to a fixed position expressed in terms of the wavelength of the response. Consider a forced response of order $n$ excited at a frequency below the resonance of interest. The origin for angular position on the assembly casing is chosen to be at a response node and, as angular displacement increases, the response amplitude increases for the first half cycle of the response. Therefore, an angular location of $\alpha$ on the resonance corresponds to an angular location of $\alpha/n$ on the casing.

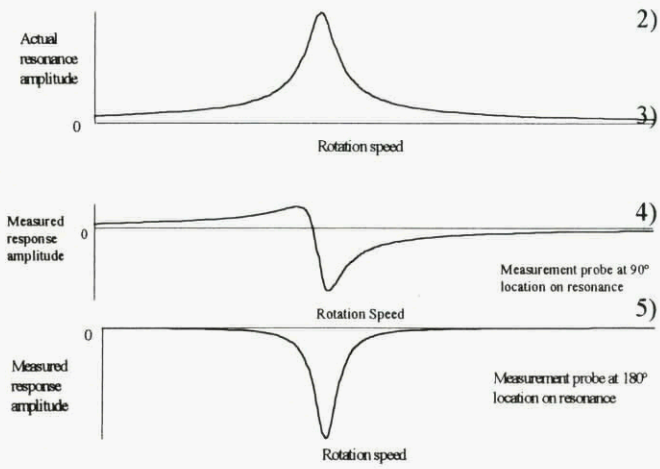


**Figure 12 : Comparison of actual and measured response amplitudes for different measurement positions**

**Figure 13** shows a typical displacement versus speed plot for such a situation. The measured displacement in this figure is relative to a non-vibrating datum which has a fixed offset of approximately 50 mm. The maximum resonance amplitude measured in this example is about 1.mm.

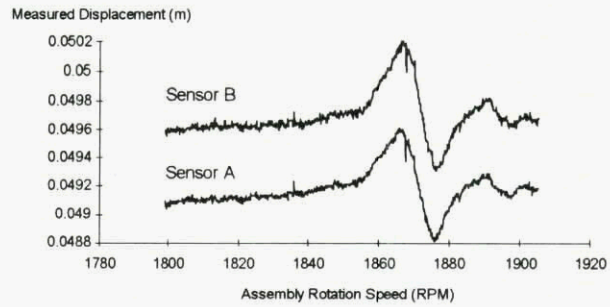


**Figure 13 : Measured displacement versus speed characteristic as a resonance of order 2 is traversed**

## 5 CONCLUDING REMARKS

1) A novel development of the capacitive tip clearance probe has been demonstrated and offers the ability to operate with 7 m of co-axial cabling significantly easing the installation of such probes on large engines.
2) The performance characteristics of these probes have proved to be superior to those of conventional probes of which the authors are aware.
3) The method is being introduced as standard practice for compressor testing in the authors' Company.
4) A review of tip-timing methods has been carried out and the performance of these methods has been discussed.
5) If the number of timing probes can be selected so that a straightforward Fourier analysis of the measured data can be conducted, there are no analysis difficulties in identifying the vibration characteristics. However, the use of a large number of probes, say more than 10, is impractical and alternative, albeit approximate, methods need to be developed. As the rotor diameter increases, the possibility of increasing the number of probes also increases but at significant additional cost. It is common aerospace practice to install a maximum of four probes per stage of blading.
6) Tip-timing has become an accepted vibration measurement technique in the turbomachinery industry. The number of strain gauge measurements has been reduced significantly, creating substantial savings on development and commissioning costs. However, tip-timing systems described in the open literature have rudimentary presentation and analysis capabilities and there are no equivalent commercial systems. Therefore, improvements to the user interface and further development of validated analysis methods will allow a more wide-spread use of the tip-timing method.

## 6 ACKNOWLEDGEMENTS

The authors would like to thank Rolls-Royce PLC for permission to publish this paper. The views expressed are those of the authors and not necessarily of Rolls-Royce plc.

## 7 REFERENCES

1) Chivers J W H, "A Technique for the measurement of Blade Tip Clearance in a Gas Turbine", PhD Thesis, Imperial College, London, 1989.

2) Chivers J W H, "A Technique for the measurement of Blade Tip Clearance in a Gas Turbine", 1989 AIAA89-2916 1989.

3) Chi R M and Jones HT, 1988, "Demonstration Testing of a Non-interference Technique for Measuring Turbine Engine Rotor Blade Stresses", AIAA/SAE/ASME/ASEE 24th Joint Propulsion Conference, Boston, MA, AIAA-88-3143

4) Hohenberg R, 1967, "Detection and Study of Compressor Blade Vibration", Experimental Mechanics, Vol. 7, No 2, pp 19-24

5) McCarty PE, Thompson JW and Ballard RS, 1980, "Development of a Noninterference Compressor Blade Stress Measurement System", Instrument Society of America, ISBN 87664-473-6, pp 745-757

6) Watkins W B, Robinson WW and Chi R M, 1985, "Noncontact Engine Blade Vibration Measurements and Analysis", AIAA/SAE/ASME/ASEE 21st Joint Propulsion Conference, Monterey, CA, AIAA-85-1473

7) Watkins W B and Chi R M, 1987, "A Noninterference Blade Vibration Measurement System for Gas Turbine Engines", AIAA/SAE/ASME/ASEE 23rd Joint Propulsion Conference, San Diego, CA, AIAA-87-1758

8) Kurkov A and Dicus J, 1978, "Synthesis of Blade Flutter vibratory Patterns Using Stationary Transducers", Gas Turbine Conference and Products Show, London, England, 78-GT-160

9) Zablotsky I Ye and Korostelev Yu A , 1970, "Measurement of Resonance Vibrations of Turbine Blades with the ELURA Device", Energomashinostroneniye, , Vol. 2, No 2, pp 36-39

Paper 32
Author P. Loftus

Q: Evers

What is the lower limit for the rotational speed of the FM capacitative blade tip clearance measurement system?

A: The low frequency cut off has been set to cover idle speeds on an RB211 fan. The stability of the oscillator would however allow much lower blade passing speeds to be studied during shut down and rotor baring to avoid rotor-bow. This may require an adjustment to the filter time constant.

Q: Benson

What type of light probe do you use, spot or line?

A: We use spot probes.

Q: Weyer

Can you please comment on the effect of blade tip shape on the reading of both the techniques ?

A: In the case of the tip clearance probe, the measured capacitance is a function of the blade tip thickness as well as the tip clearance. This dependence is calibrated out. However, if the blade tip thickness underneath the probe varies with axial movement of blades then significant errors will result, hence my comment that a full uncertainty analysis is complex and application specific.
In the case of blade tip timing (NSMS) it is the angle of the blade tip which is significant but we are not generally aiming for very small measurement uncertainties with these measurements and for the applications we have addressed the variation in tip angle with axial position has been modest and acceptable. Most of our experience is in compressors because most of our turbines are shrouded. I would expect to experience more problems with this issue in turbines where the curvature of the aerofoils is much greater.

Q: Stange

What is the resolution capability of your NSMS system?

A: Similar to that quoted by the questioner - around 1-2 thousandths of an inch for synchronous vibration, 3-5 for asynchronous (FFT noise floor).

# Vibrational Analysis of Engine Components Using Neural-Net Processing and Electronic Holography

Arthur J. Decker, E. Brian Fite, Oral Mehmed and Scott A. Thorp
National Aeronautics and Space Administration
Lewis Research Center, MS 77-1, 21000 Brookpark Rd
Cleveland, Ohio 44135
United States

## 1. SUMMARY

The use of computational-model trained artificial neural networks to acquire damage specific information from electronic holograms is discussed. A neural network is trained to transform two time-average holograms into a pattern related to the bending-induced-strain distribution of the vibrating component. The bending distribution is very sensitive to component damage unlike the characteristic fringe pattern or the displacement amplitude distribution. The neural network processor is fast for real-time visualization of damage. The two-hologram limit makes the processor more robust to speckle pattern decorrelation. Undamaged and cracked cantilever plates serve as effective objects for testing the combination of electronic holography and neural-net processing. The requirements are discussed for using finite-element-model trained neural networks for field inspections of engine components. The paper specifically discusses neural-network fringe pattern analysis in the presence of the laser speckle effect and the performances of two limiting cases of the neural-net architecture.

## 2. INTRODUCTION

As NASA's Turbomachinery Center of Excellence, Lewis Research Center (LeRC) is involved in the testing of various types of rotating machinery including compressors, turbines, fan blades and propellers. Blades are tested in an electronic holography laboratory to obtain frequency and mode shape information for use in wind tunnel and test cell research programs. Over time, this process has been found to be a reliable way of predicting frequencies and mode shapes of blades as well as other test articles. Laboratory electronic holography has become an integral part of the turbomachinery testing, design and fabrication process.

One way to reduce the cost of wind tunnel testing is to inspect components in situ rather than the laboratory. Non-interference inspection to detect crack damage in blades is needed after high vibration stress amplitudes and cycles occur during testing with rotating blades. High stress amplitudes and cycles have been encountered at resonance, flutter and stall conditions during mapping and operability testing of turbojet engine fan models at LeRC. A blade inspection is wise when the stresses exceed the safe stress limits that have been preset.

Removing the blades from a rotor for laboratory inspection for damage or changed vibration characteristics is expensive in terms of lost test time and facilities costs. Hence, whole-field, real-time, in-situ optical inspections using electronic holography are especially attractive. Electronic holography is non-intrusive and has the potential to reduce the number of expensive-to-install, intrusive strain gages needed for wind tunnel testing and for detection of damaged regions.

One defect of electronic holography is that the display of the displacement distribution of a vibrating component may require as many as twelve previously acquired frames.[1] A pipeline processor maintains the illusion of a real-time display, but the speckle patterns must remain correlated between members of sets of twelve frames. That requirement is hard to maintain outside a laboratory. Regardless, neither the characteristic fringe patterns of classical time-average holography nor the displacement distributions that can be calculated from electronic time-average holography are ideal for inspecting for damage. Instead, the bending induced strain distribution[2] has been shown to be a much better indicator of damage to composites as well as cracking in metals.[3] But the bending distribution must be calculated from a very accurately known displacement distribution.

Artificial neural networks are being tested as alternative processors for electronic holography at LeRC. The goal is to extract damage specific information from as few frames as possible so that electronic holography will be convenient to use for structural inspections in the 9X15 wind tunnel and spin rigs at LeRC. In fact, an electronic hologram can be recorded during a single, electronically shuttered field of a television frame using a continuous wave laser. Short-exposure, time-average holograms can be recorded electronically to achieve the goals suggested for flashlamp pumped dye lasers at another AGARD conference more than ten years earlier.[4] That paper proposed using time-average holography for measuring velocity field information in a flow rather than for measuring structural displacement and strain fields.

The neural network processor requires a computational-model generated training set. The model consists of a phenomenological model and a model of the optical measurement process. A finite element model is the phenomenological model used to compute the predicted vibration modes of a fan blade.[5] A crack model is incorporated for predicting damage. The electronic holography process must be modeled realistically to include a fluctuating laser speckle effect, variations in the sensitivity vector, variations in the CCD camera response and variations in vibration amplitude.[6] A training set consists of records, and a record contains input and output patterns. The input pattern is the characteristic fringe pattern generated by the electronic holography process. The output pattern is a distribution of a component of the bending induced strain.

The trained neural network is then tested for robustness by presenting it with model generated test patterns that vary these factors. Then the neural network is tested with patterns recorded from real structures. The final stage is to encode, compile and link the neural network with the electronic holography video.

The next section discusses the setups, computers and facilities where the work is being done.

## 3. FACILITIES AND EXPERIMENTAL EQUIPMENT

Graphics workstations containing various hardware and software video and graphics options[7] perform the electronic holography and the neural-net processing. The neural networks are generated and trained using a commercial software package.[8] The trained nets are then converted to C language code for linking with the electronic holography software. The performances of the workstation resident

*Paper presented at an AGARD PEP Symposium on "Advanced Non-Intrusive Instrumentation for Propulsion Engines", held in Brussels, Belgium, 20-24 October 1997, and published in CP-598.*

neural networks and electronic holography are discussed later.

Trained neural networks are tested with both model generated and experimental data. The experiments are performed in a holographic vibration analysis laboratory with a large vibration isolation table; argon-ion, helium-neon, diode and Nd:YAG lasers; and several means for mounting and vibrating turbomachinery blades and other components.
The laboratory is used routinely for electronic holographic surveys of turbomachinery components and has been used for holography in general since 1976. Lewis Research Center's Low Noise Fan Program and outside industries[9] have been frequent, recent customers.

Electronic holograms are transferred directly to the workstations using ordinary NTSC (American television standard) 30 frame-per-second, 60 field-per-second, CCD (charge coupled device) cameras. The workstations handle as easily PAL (the European television standard). The hardware employs DMA (direct memory access) to transfer the television frames to RAM (random access memory). The workstations are intended specifically to implement color graphics such as OpenGL[10] on color monitors. Hence pixels are packed in multiple byte format. The work reported in this paper used RGBA format consisting of red, green, blue and alpha bytes or RGB_332_P format where three colors are packed into a single byte. These formats are really very inefficient for electronic holography which depends on single-byte luminance values.

Processing the holograms in RAM prior to displaying the results can slow down the response considerably. However, we can process a few hundred to a few thousand large pixels (finite element resolutions) while maintaining the 30 frame-per-second display.

A more serious potential problem is frame-to-frame or field-to-field extraneous motions and speckle-pattern de-correlations, particularly outside the laboratory. The actual hologram exposure time can be controlled by the electronic shutters in the CCD cameras. For electronic time-average holography, the shutter needs to be open only for about one vibration cycle. The time between frames can be similarly short, if a locally available high-speed array of CCD cameras is used. Then, bursts of 50,000 or more frames per second become feasible.

LeRC's 9x15-foot wind tunnel is a target facility for applying neural-net processing and electronic holography. Some of the authors have recently been involved with tests of advanced fan models in this wind tunnel. Two of the fan models required blade inspections for crack damage after vibration stresses exceeded preset limits.

Accurate and complete models are critical for effective use of neural-net processing in electronic holography as discussed in the next section.

## 4. STRUCTURAL AND ELECTRONIC-HOLOGRAPHY MODELS FOR TRAINING ARTIFICIAL NEURAL NETWORKS

The models contain phenomenological and optical components and must generate representative sets of training records. The neural networks must also be trained, by example, to ignore irrelevant variations. For example, the neural networks might be trained to ignore irrelevant variations in mode shapes caused by blade mounting variations. The neural networks must be trained to perform accurately in the presence of the laser speckle effect. Modeling introduces a multidisciplinary expert requirement for using neural networks in electronic holography.

A finite element model is the phenomenological component for this discussion. Finite element models can be used to generate about the first six vibration modes of a blade with good engineering accuracy. A simple cantilever plate serves as the object for this discussion.

Three analytical flat plate models were developed and used as training sets for the neural network. The models simulated both damaged and undamaged plates. All three flat plate models are 7.62 cm (3") wide by 15.24 cm (6") long and have a thickness of 0.254 cm (0.1"). A finite element model was generated consisting of a 20x42 mesh of quadrilateral elements along the mid-thickness of the plate ( Figure 1 ). The plate models were idealized as cantilevered plates with the bottom edge constrained in all six degrees of freedom. The material is 6061-T6 Aluminum with a Young's Modulus of 66.19 GPa ($9.6 \times 10^6$ psi) , a Poisson's Ratio of .33, and a Mass Density of 2712.832 kg/m$^3$ ($2.536 \times 10^{-4}$ lbs sec$^2$/in$^4$).

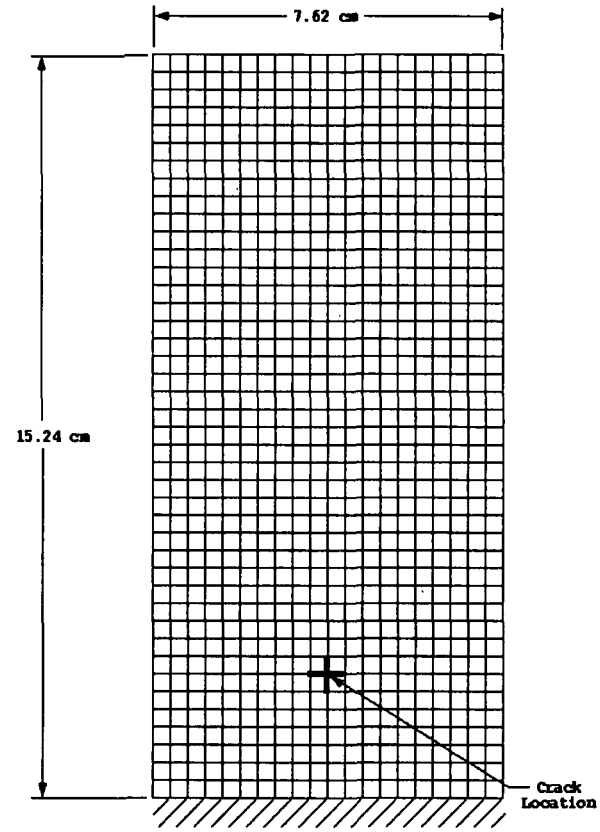


**Fig. 1-Finite Element Model.**

The first model is a flat plate with no damage included. The second and third models include a vertical and horizontal crack, respectively. Both cracks are located 3.81 cm (1.5") from the long edge and 2.54 cm (1") from the bottom edge. The crack was simulated by creating two coincident grids at this location. The connectivity for the adjacent elements surrounding this location was defined to generate an idealized horizontal crack for the second model ( Fig. 2 ) and a vertical crack for the third model ( Fig. 3 ).

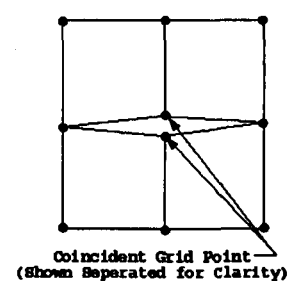


**Fig. 2-Horisontal Crack.**

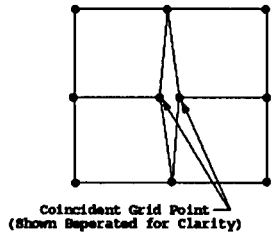


**Fig. 3-Vertical Crack.**

MSC/NASTRAN Solution 103 was used to solve for eight normal modes and frequencies. The eigenvectors were normalized with respect to the generalized mass. An output file of the eigenvalues, eigenvectors, and modal strains was then provided to train the neural network.

The optical model of electronic holography in the presence of the laser speckle effect has been discussed in another publication.[6] A training record contains input and output vectors to be received and generated, respectively, by a feed forward artificial neural network. The input vectors contain finite element resolution characteristic fringe patterns. Figure 4[6] shows characteristic fringe patterns, respectively, from an old silver-halide-emulsion time-average hologram of a vibrating blade, from two electronic holograms of a vibrating cantilever plate, from model-generated, finite-element-resolution holograms of a vibrating cantilever plate, and from two finite-element-resolution, electronic holograms of an actual vibrating cantilever plate. The mode shown is the first chord-wise mode of interest in tip cracking of blades. The model generated and measured characteristic fringe patterns appear very similar.

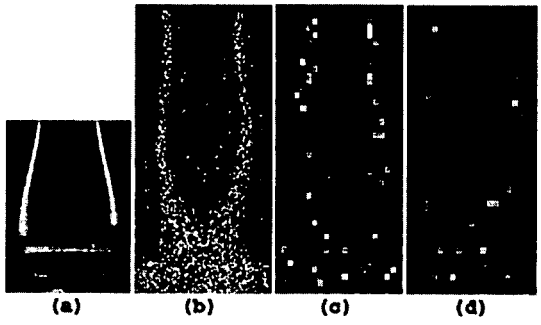


**Fig. 4-First Chord-Wise Mode: (a) Silver Halide Hologram, (b) Electronic Holograms, (c) Model Generated Holograms at Finite Element Resolution, (d) Electronic Holograms at Finite Element Resolution.**

Electronic holography has been discussed in various forms by many authors. Electronic time-average holography is explained very well, for example, by Stetson and Brohinsky.[4] The holographer records image plane holograms consisting of the interferences between smooth reference beams and speckled object beams from vibrating structures. The vibration amplitude distribution can be estimated from twelve holograms containing combinations of hologram-to-hologram phase shifting and phase modulation, if the speckle patterns remain correlated between holograms. The simplest application of electronic time-average holography is accomplished with two frames, where the reference-beam phase is shifted by $\pi$ between two frames and the frames are subtracted. These actions provide visualization of the characteristic fringe patterns as shown in fig. 4.

The two-frame (or two-field) method of electronic time-average holography supplies the input records for training neural networks. The input patterns are given mathematically by

$$\text{(Speckle Pattern) X } J_0(2\pi \mathbf{K} \bullet \delta)$$

where $\delta$ is the displacement vector in wavelengths provided by the finite element modeler and $\mathbf{K}$ is the sensitivity vector given as the difference between the input and reflected light-ray directions. Speckle patterns in general are modeled with a negative exponential intensity distribution and a uniform phase distribution. The workstations have pseudo random number generators with enormous periods to assure sample-to-sample independence of the speckle patterns. The input patterns are generated from the absolute value of the zero order Bessel function $J_0$ and are usually normalized between 0 and 1. A saturation effect is sometimes introduced by multiplying the patterns by an arbitrary factor followed by setting inputs greater than 1 at 1.

The model generated output vectors of the training records could contain the displacement amplitude distribution, but a quantity proportional to the bending induced strain is more useful for inspection. Bending induced strain, computed from fringe patterns reconstructed from double-exposure holograms, has been shown to be very sensitive to damage such as cracking.[3] Performing inspection for damage is the principal reason for using neural networks for processing electronic holograms. In fact, visual inspection of characteristic fringe patterns is not a very sensitive way to look for damage. Figure 5 shows characteristic fringe patterns computed from the structural model of a damaged cantilever plate. The damage induced variation in displacement changes by an order of magnitude from picture to picture. Not until the final picture does the characteristic pattern show a significant visual change. Artificial neural networks can be trained to recognize damage much earlier.

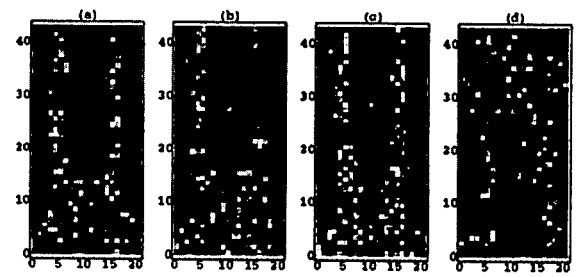


**Fig. 5-Characteristic Patterns for Crack Induced Displacement Changes of (a) 1X, (b) 10X, (c) 100X (d) 1000X the model value.**

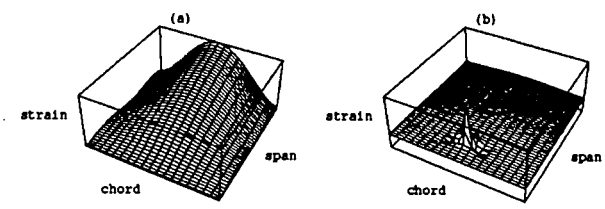


**Fig. 6-Strain Patterns for (a) Undamaged and (b) Cracked Cantilever Plates.**

Surface bending induced strain is computed from the second derivatives of the normal component of displacement.[2] Holography visualizes the quantity $\mathbf{K} \bullet \delta$, but $\mathbf{K}$ often varies slowly enough that the second derivatives of $\delta$ are adequate.

Figure 6 shows model generated, chord-wise bending induced strain patterns for the mode shown in fig. 4. The patterns are shown for undamaged and cracked samples.
The vertical crack model (Fig. 3) was used to generate the patterns.

The formats, training, testing and performances of the neural nets are discussed next.

## 5. NEURAL NETWORKS FOR DETECTING DAMAGED VIBRATING STRUCTURES

This work is based exclusively on feed forward neural networks with one hidden layer. These networks have been divided into two classes: sparse and dense. Sparse neural networks, where the number of hidden-layer nodes is less than 10 percent of the number of inputs, have been discussed for vibrational analysis in another publication.[6] Sparse neural networks train rapidly and can be linked to a workstation's video without degrading the real-time performance. The number of hidden-layer nodes, by contrast, in a dense neural network approaches the number of input nodes or nodes in the finite element model. The parallelized code (loop free) for these networks requires large resources for compilation and linking with the workstation video. The dense nets train slowly and degrade the real-time performance of the workstation video. But the dense nets are more immune to variations in vibration amplitude. The sparse nets yield false readings outside a narrow range of vibration amplitudes. Regardless, the neural networks must be trained to be immune to the laser speckle effect.

The remaining discussion in this section refers to a cantilever plate with the displacement given at 903 nodes. The chord by span arrangement of the nodes is 21 X 43 . Blade designs typically use between a few hundred and a few thousand finite elements. The speckle pattern problem can be placed in perspective by noting that there are $256^{903}$ possible input patterns given an 8-bit dynamic range for representing luminance. But there are only 903 linearly independent patterns. Response surface methods used in the study of sparse nets for vibrational analysis showed that very few hidden-layer nodes and about 10 percent of a set of linearly independent speckle patterns confer immunity to the speckle effect. Only 100 speckle patterns and 6 hidden-layer nodes were needed to train a speckle-effect-immune net to recognize the difference between damaged and undamaged cantilevers. The bending induced strain distributions for this test are shown in fig. 6. Samples of the performance of the neural-net video are discussed in the next section.

The conditions under which the sparse nets can be used to inspect for blade damage are restricted. The nets were able to learn to distinguish only two or three distinct characteristic patterns (different vibration amplitudes) in the amplitude range from 0.25 waves to 0.75 waves of maximum displacement. The sparse nets were actually unable to learn the minimum crack contained in the original models. In fact, successful training required that the effect of the crack be amplified. The modeled damaged and undamaged distributions were subtracted; the difference was multiplied by a factor; and the amplified difference was added to the undamaged amplitude distribution. Figure 5 shows the effect of this process on the calculated characteristic fringe pattern for factors ranging from 1 to 1000. The minimum factor for successful training was 7 . The sparse nets still responded with a false identification rate of 20 percent at an amplification factor of 10 (Fig. 5b) . The false identification rate was 0 percent for an amplification factor of 100 (Fig. 5c). A more difficult restriction on the use of sparse nets has been the need to control the vibration amplitude to avoid false readings. A network that was model trained at a maximum vibration amplitude of 0.5 waves responded accurately to a set of test examples only when the test amplitudes were controlled within ±0.05 wave of 0.5 waves. A point to be noted is that these inspections were used to detect cracks near the base of the cantilever approximation to a blade. A crack was simulated in a physical cantilever by grinding a groove near the position of the modeled crack. The first chord-wise mode (lyre mode) is most sensitive, in fact, for detecting tip cracks.

The response surface study used to optimize the sparse nets showed that the generalization (interpolation and extrapolation) capability of the neural networks improved slowly as the number of hidden-layer nodes was increased. This improvement was found to continue as the number of hidden-layer nodes exceeded 10 percent of the inputs. Subsequently, neural nets were tested on both model generated and measured characteristic patterns where the number of hidden-layer nodes equaled or exceeded 100 . The performances of the nets for training and crack identification depended on the crack amplification factor as in the case of the sparse nets. But the dense nets were able to separate damaged from undamaged samples over a larger range of amplitudes than the sparse nets. Non optimized compilation of the parallelized C language code for the neural nets was limited to nets containing about 100 hidden-layer nodes. The object file for a sparse net is less than a megabyte. The object code for a dense net containing 100 hidden-layer nodes is about 10 megabytes. The memory and swap space required for compilation are orders of magnitude larger. Research continues on the use and performance of dense nets as well as sparse nets.

The real-time performance of the neural networks in the video system is discussed next.

## 6. PERFORMANCE OF WORKSTATION RESIDENT NEURAL NETWORKS FOR DAMAGE INSPECTION

Real-time vibrational analysis and inspection using electronic holography and neural-net processing imply image update rates measured in frames per second. The following results were obtained with holograms and synchronization provided by an off-the-shelf monochrome CCD camera and processed and displayed by one of the workstations.[11]

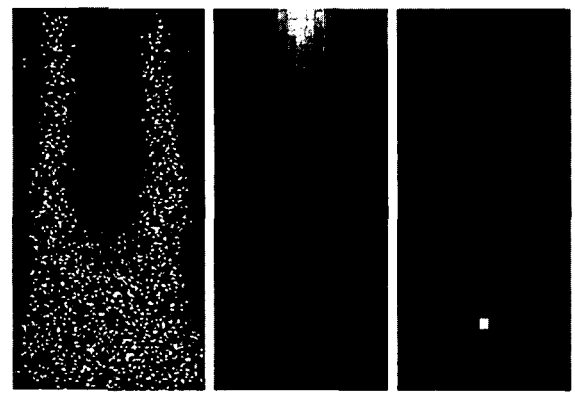

(a) (b) (c)

**Fig. 7-Video Displays of (a) Characteristic Pattern, (b) Neural-Net Output for Undamaged Cantilever, (c) Neural-Net Output for Cracked Cantilever.**

Figure 7 was created from inputs and outputs processed at about ½ frame per second. Pairs of holograms were captured of cantilevers vibrating in the lyre or first chord-wise mode. A vibrating mirror was synchronized with the CCD camera and was used to shift by $\pi$ the reference-beam phase between holograms. The 640 X 480 pixel holograms were cropped to the size of the cantilever image (about 153 X 303 pixels); subtracted; zoomed without filtering to the 21 X 43 pixel finite element resolution; converted to binary format; normalized; and processed by the neural network. The output of the neural network was converted to image format, stored, and displayed. Post capture processing was accomplished with the workstation's standard image processing commands and with a slightly modified version of the image subtraction command. This slow processor is very convenient for storing a statistically relevant sample of frames for measuring the false positive and false negative rates for crack detection as

well as measuring the performance of electronic holography in the presence of environmental disturbances. Figure 7a shows a characteristic pattern at about the 153 X 303 pixel resolution; fig. 7b shows a density pattern of the output of the neural network for an uncracked cantilever plate; and fig. 7c shows an output of the neural network for a cracked cantilever plate. The outputs of the neural network are displayed at the 21 X 43 pixel resolution.

The display format at the higher frame rates is the same as shown by fig. 7, but the neural-net and image processing routines must be linked with the workstation's video library. The measured frame rate is about 30 frames per second for the sparse nets containing 6 hidden layer nodes and 903 inputs. The measured frame rate decreases to about 10 frames per second when the number of hidden-layer nodes is increased to 100 . Synchronization of the camera, the workstation video, the neural-net processing and the workstation graphics can be challenging at the higher frame rates.

## 7. CONCLUDING REMARKS

Artificial neural networks have been used to process finite-element-resolution time-average fringe patterns at video rates. The full video rates are available to neural networks containing a few hidden-layer nodes. Neural networks with many hidden-layer nodes generalize better, but at slightly lower frame rates. The procedure was developed for electronic holography and vibration analysis, but can be generalized to other applications where there are good phenomenological and visualization models.

The structural application has proven to be very sensitive to small changes in the mode shapes. Perhaps, the major challenge in using the holographic laboratory has been realistic mounting of blades and other components for vibration analysis. The mounting and excitation techniques as well as damage produce subtle variations in the vibration mode shapes. Some of the artificial neural networks are very sensitive to these subtle variations. The work so far has shown that neural networks can be trained to generalize on the laser speckle effect and that dense nets can handle vibration amplitude variations. Whether neural networks can be trained to ignore irrelevant variations in mode shapes remains to be discovered.

To perform a holographic inspection without removing blades from the rotor requires the blades to be seated properly in their retention and vibrated. In model designs at NASA, the blades are normally loose in their retention when the rotor is stationary and are seated during rotation. Thus, a means has to be devised to conveniently seat installed blades to do in-situ damage inspection. This is another challenge that must be overcome to make this method of inspection practical.

As demonstrated in this paper, artificial neural networks can serve as high-speed interfaces between computational models and experiments or tests that generate optical patterns. Whether these interfaces will be efficient, practical and cost effective remains to be discovered.

## 8. REFERENCES


1. K. A. Stetson and W. R. Brohinsky, "Fringe-Shifting Technique for Numerical Analysis of Time-Average Holograms of Vibrating Objects", *J. Opt. Soc. Amer.* **A5**, pp. 1472-1476, 1988.

2. C. M. Vest, *Holographic Interferometry*, pp. 153-157, Wiley, New York, 1979.

3. A. J. Decker, "Holographic Interferometry with an Injection Seeded Nd:YAG Laser and Two Reference Beams", *Appl. Opt.* **29**, pp. 2696-2700, 1990.

4. A. J. Decker, "Beam-Modulation Methods in Quantitative and Flow-Visualization Holographic Interferometry", *Advanced Instrumentation for Aero Engine Components*, AGARD-CP-399, pp. 34-1 - 34-16, 1986.

5. H. G. Schaeffer, *MSC/NASTRAN Primer Static and Normal Modes Analysis*, PDA Engineering, Costa Mesa, CA, 1979.

6. A. J. Decker, E. Brian Fite, O. Mehmed and Scott A. Thorp, "Processing Speckle Patterns with Model Trained Neural Networks", *Optical Technology in Fluid, Thermal, and Combustion Flow III, Proc. SPIE.*, **vol. 3172**, to be published.

7. The workstations used to perform the reported research were all vended by Silicon Graphic, Inc., 2011 N. Shoreline Blvd., Mountain View, CA 94043-1389.

8. The neural networks used to perform the reported research were assembled, trained, tested and converted to C language code using *Neural Works Professional II Plus* vended by Neural Ware, Inc., 202 Park West Drive, Pittsburgh, PA 15275.

9. The availability of the holographic vibration analysis laboratory was most recently announced at the *LeRC Business and Industry Summit* held in Sept. 1996.

10. OpenGL Architecture Review Board, *OpenGL Reference Manual*, Addison-Wesley, Reading, MA, 1992.

11. The results were generated with a Silicon Graphics O2 workstation with the R5000 option.

Paper 33
Author: Decker

Q: Russo

How long does it take to train the neural nets typically?

A: The sparse nets require a minute or two. The dense nets containing, say 100 hidden layer neurals might require 20 minutes to an hour.

# MESURE NON-INTRUSIVE DE LA VITESSE DE REGRESSION D'UN MATERIAU ENERGETIQUE
## *NON-INTRUSIVE MEASUREMENT OF AN ENERGETIC MATERIAL REGRESSION RATE*

Franck CAUTY
Office National d'Études et de Recherches Aérospatiales
29, avenue de la Division Leclerc
B.P. 72 - F-92322 Châtillon Cedex - FRANCE

**RESUME - ABSTRACT**

La méthode non-intrusive de détermination de la vitesse de régression d'un matériau énergétique développée à l'ONERA est basée sur le temps de propagation d'une onde ultrasonore à travers le matériau testé. Cette méthode de mesure directe, locale et quasi-instantanée vise à déterminer la loi classique de vitesse de combustion des propergols solides dans un large domaine de pression et de température initiale.

La technique utilisée est d'une bonne précision pour des régimes de combustion variés, avec une mention spéciale pour la combustion érosive, et pour différents types de propergols. Des exemples marquants sont présentés dans le domaine de la combustion des propergols solides. Le champ d'application de la méthode ultrasonore s'étend à d'autres matériaux pour la propulsion hybride ou le suivi de la dégradation des protections thermiques internes.

La méthode ultrasonore ONERA ainsi que les appareils électroniques associés sont opérationnels autant comme outil de contrôle industriel pour la fabrication des propergols solides qu'outil de diagnostic utile pour les ingénieurs de recherche.

*The non-intrusive method of an energetic material regression rate determination developed by ONERA is based on the ultrasound wave propagation time through the tested material. This direct, local and quasi-instantaneous method is aimed at determining the classical burning rate law of solid propellants in large pressure and initial temperature ranges.*

*This technique demonstrates a good accuracy in various combustion regimes, with a special mention to erosive burning, and for different solid propellants. Significant examples are presented in solid propellant domain. The application field of the ultrasound method extendes to other materials for hybrid propulsion or thermal protective insulator degradation.*

*The ONERA ultrasonic method and its associated electronic devices are operating either as an industrial procedure tool for solid propellant manufacturing or as a helpful diagnostic tool for research engineers.*

## 1- INTRODUCTION

Les capteurs ultrasonores sont largement utilisés en contrôle non destructif dans l'industrie pour détecter et estimer les dimensions des défauts dans les matériaux. On peut élargir le champ d'application de cette technique à la mesure en continu de l'évolution de l'épaisseur d'un matériau en cours de régression. C'est cette méthode qui a été utilisée dès 1973 à l'ONERA [1] pour déterminer, sur propulseur d'étude au banc d'essais, la vitesse de combustion d'un propergol solide, donnée indispensable au dimensionnement d'un propulseur à propergol solide.

Une façon simple d'établir la relation liant la vitesse de combustion à la pression est et demeure la mesure de la durée de combustion d'échantillons de propergol dans une enceinte pressurisée. Cette méthode présente l'inconvénient d'être très longue, un point de mesure par essai, et de ne pas couvrir la totalité des applications car elle n'intègre pas l'effet de l'écoulement des gaz de combustion (régime érosif) ou des variations rapides des conditions locales (combustion instationnaire). Avec la technique de mesure par ultrasons, ces paramètres sont pris en compte. Il s'agit, de plus, d'une méthode directe, non perturbatrice.

## 2-MÉTHODE DE MESURE ULTRASONORE

### *2.1 Principe de la méthode*

Le principe de la méthode est semblable à celle de la technique Sonar: un capteur ultrasonore émet une onde mécanique qui se propage à travers les matériaux (figure 1). Elle se réfléchit sur la surface en régression du fait de la forte différence d'impédance acoustique entre les gaz et le matériau et revient exciter le transducteur.

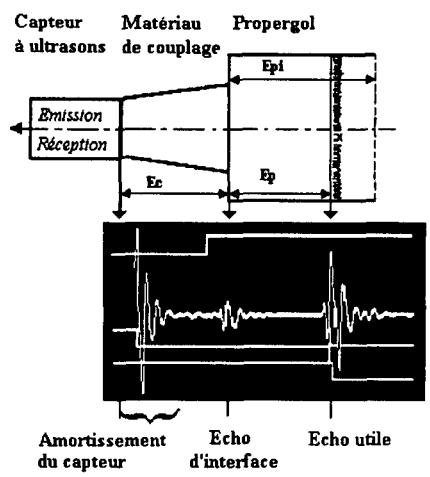


*figure 1 - Principe de la méthode de mesure*

Le capteur est très rarement en contact direct avec le matériau à tester. Un matériau « tampon » est interposé entre le capteur et celui-ci pour jouer le rôle de ligne à retard permettant un suivi jusqu'à épaisseur nulle de l'échantillon et pour isoler le capteur des conditions sévères de pression (jusqu'à plusieurs dizaines de MPa) et de température (jusqu'à plus de 3500 K) qui règnent dans les chambres de combustion. Cet élément est constitué soit d'une résine thermodurcissable adaptée acoustiquement, coulée dans une perforation usinée dans les viroles métalliques des montages d'étude ou il s'agit directement de la structure bobinée (Carbone ou Kevlar) de l'engin.

La mesure du temps de propagation aller-retour de l'onde mécanique est reliée à l'épaisseur des matériaux par l'intermédiaire des célérités des ondes mécaniques. Si la célérité des ondes (C) était constante, indépendante des conditions locales des milieux traversés, l'épaisseur de

*Paper presented at an AGARD PEP Symposium on "Advanced Non-Intrusive Instrumentation for Propulsion Engines", held in Brussels, Belgium, 20-24 October 1997, and published in CP-598.*

l'échantillon ($E_p$) serait directement proportionnelle au temps de parcours: $\tau = 2*E_p/C$. Or, la célérité des ondes varie avec la température (T) du milieu (valeur initiale et profil thermique) et avec le champ de contrainte lié à la pression (P) et à la géométrie.

$$\frac{C_{ref}}{C} = (1 + k_T(T - T_{ref}))(1 - k_P(P - P_{ref}))$$

L'analyse de la méthode permet d'établir des relations liant les paramètres influents sur la propagation et ainsi, l'épaisseur du matériau et sa vitesse de régression peuvent être déterminées à partir de la variation du temps de parcours. Le détail de l'analyse de la mesure adapté aux différents cas rencontrés peut être trouvé dans les documents publiés spécifiques dont sont extraits les exemples qui illustrent cet article.

De manière générale, l'effet de la température et de la pression seront plus forts sous des conditions instationnaires, c'est-à-dire, lors de variations de pression et de flux thermique incident. On trouve deux types de comportements qui peuvent être définis par rapport au niveau de vitesse de régression, la frontière se situant grossièrement autour de 1 mm/s. Au dessus de cette valeur, ce qui correspond à la plupart des propergols solides, le profil thermique n'a pas d'influence notable sur l'épaisseur brûlée et la vitesse de combustion mais l'effet induit par la pression doit être pris en compte pour corriger le niveau de vitesse obtenu à cause de la sensibilité de la mesure ultrasonore au gradient de pression dP/dt [2,3,4].

Pour des phénomènes de combustion ou de dégradation plus lents , si l'effet de la pression doit toujours être pris en compte, le paramètre principal devient la variation du profil thermique. La position de l'écho ultrasonore sera modifiée par la quantité de chaleur entrée dans le matériau. Quand la température augmente, la célérité des ondes décroît entraînant un accroissement du temps de propagation. Des exemples montreront que le flux de chaleur peut avoir autant d'effet (opposé) que la dégradation elle-même.

## *2.2 Matériel de mesure ultrasonore ONERA*

Cette classification selon le niveau de vitesse de régression nous a amené à développer deux types de chaînes de mesure.

Pour les vitesses supérieures à 1 mm/s, comme c'est le cas pour la plupart des applications avec propergol solide, l'Office a développé un appareil électronique spécial (figure 2). Ces principaux constituants sont une horloge interne de base de temps, un générateur d'impulsions, un amplificateur haute-fréquence, des circuits spécifiques tels des masques, un contrôleur de seuil de détection, une fonction échelon générée afin de suivre le déplacement de l'écho de surface et, enfin, un intégrateur analogique établissant un signal de sortie proportionnel à la variation du temps de parcours.

La fréquence de récurrence de l'émission ultrasonore est réglable de 1kHz à 20kHz, ceci dépendant du niveau de vitesse de combustion et de l'épaisseur de l'échantillon. Ce signal de sortie est numérisé puis traité sur station de travail Unix à l'aide des logiciels adaptés aux cas étudiés.

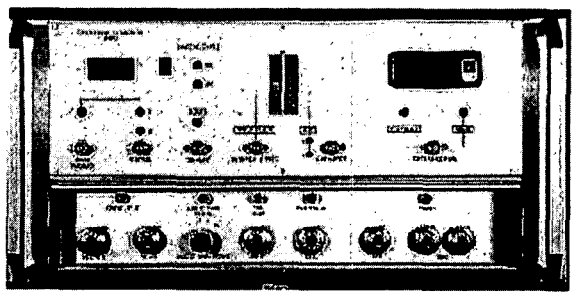

*figure 2 - Appareil de mesure ultrasonore ONERA*

Le comportement de matériaux tels les protections thermiques internes demande la mise en oeuvre de moyens de mesure plus amont. Le déplacement de l'écho de la surface du matériau n'est plus seulement dû à sa regression; il n'est plus question de pré-régler l'électronique de mesure. C'est le signal ultrasonore lui-même qui doit être numérisé pour un traitement ultérieur au lieu de l'être en temps réel.

L'équipement de mesure ultrasonore est composé de 10 systèmes ultrasonores émission/réception synchronisés par une horloge interne 1 kHz (figure 3). Le nombre de canaux nécessaires pour l'essai est choisi et la cadence de répétition des signaux multipléxés est adaptée pour leur transfert vers le système d'acquisition .

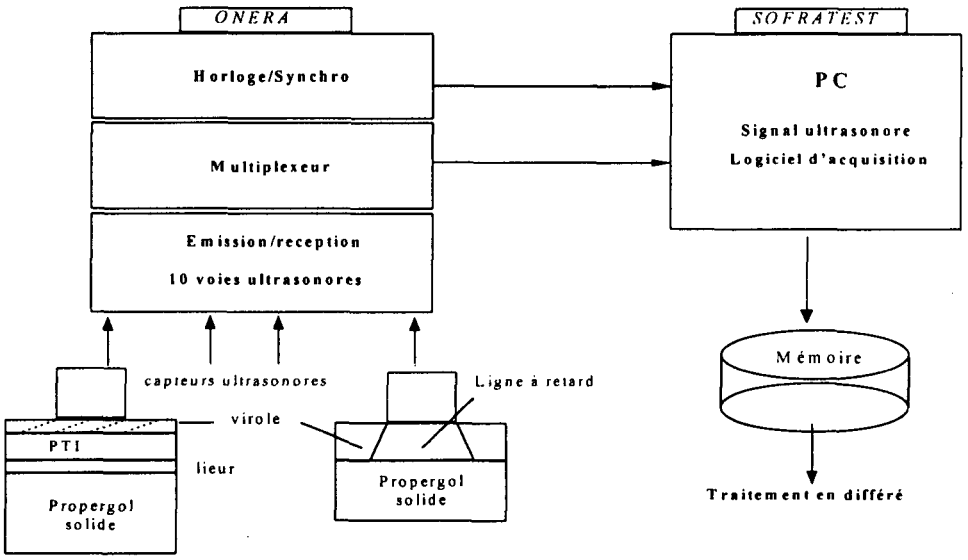


*figure 3 - Schéma de l'équipement de mesure multi-canaux ONERA*

La cadence de répétition doit rester limitée à 500 Hz à cause de la vitesse limitée de transfert en mémoire sur PC. Un logiciel ultrasonore spécialisé a été développé par la Société Sofratest: le signal ultrasonore multipléxé est repéré puis numérisé, à haute cadence (10,25 ou 50MHz), dans une fenêtre temporelle, après chaque émission.

La taille de la fenêtre et un retard initial destiné à éliminer l'onde amortie de l'émission ou des échos non désirables sont sélectionnés. Les échos sont stockés en mémoire pour un traitement après essai qui doit permettre de reconstituer une mesure proportionnelle au déplacement de l'écho. Dans certains cas difficiles, des techniques de traitement du signal par corrélation sont mises en oeuvre.

## 3 - COMBUSTION DES PROPERGOLS SOLIDES

### *3-1 Détermination des propriétés balistiques et contrôle*

La mesure par ultrasons est aujourd'hui très utilisée tant à l'ONERA qu'à la SNPE, le fabricant français de propergols solides, pour la caractérisation de la combustion normale des propergols solides en régime quasi-stationnaire [4,5].

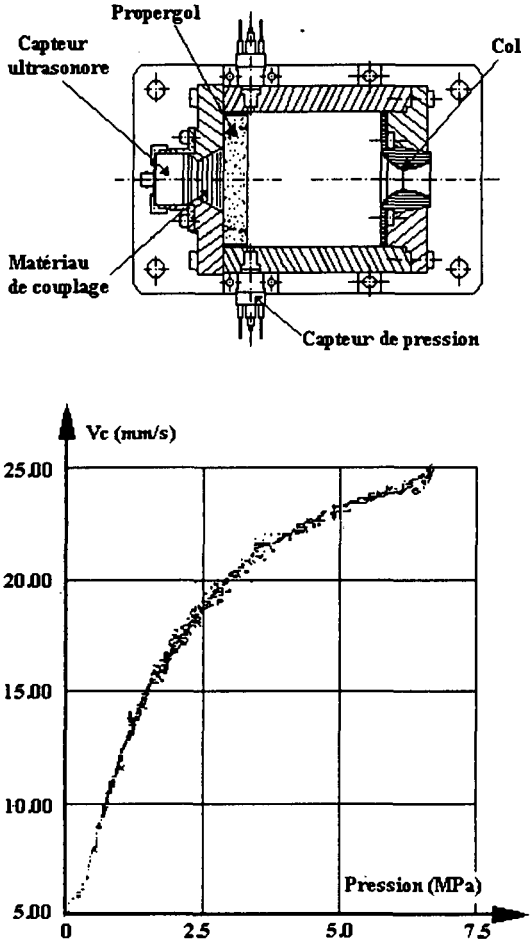


*Figure 4 - Détermination des lois de vitesse de combustion stationnaire*

Pour déterminer la loi de vitesse de combustion classique $V_b = a P^n$, il suffit d'un propulseur très simple (figure 4) équipé d'un chargement à combustion frontale et d'un col en matériau ablatable pour obtenir, en un nombre réduit d'essais, une loi de vitesse de combustion sur un large intervalle de pression. Un exemple de résultats obtenus avec sept essais montre que la dispersion de la mesure est d'environ ±0.3 mm/s pour le propergol rapide étudié. Bien maîtrisée, cette méthode s'avère plus précise et très concurrentielle vis à vis de celles généralement utilisées. Une différence de 0.2 mm/s entre deux propergols possédant une vitesse moyenne proche de 8 mm/s à 7 MPa a ainsi pu être mesurée [6].

Un propergol solide pouvant être soumis à des variations importantes de température, la sensibilité de la vitesse de combustion à la température initiale à pression constante, $\sigma_p$, a besoin d'être qualifiée. Un mode opératoire complet a été mis au point et testé sur les propergols homogènes, composites et à liant énergétique, en prenant en compte la tenue mécanique des matériaux de couplage, leur impédance acoustique, la qualité des collages ainsi que la réalisation d'un capteur ultrasonore spécial basses températures [4]. Une enceinte fermée de volume variable pressurisée par les gaz de combustion eux-mêmes permet, avec une géométrie d'échantillon adaptée, de balayer une large gamme de pression.

L'ensemble du montage est conditionné en température entre -50°C et +80°C. L'influence de la température initiale sur la vitesse de combustion d'un propergol composite chargé en Aluminium est représentée sur la figure 5. Le coefficient de sensibilité à la température initiale est déduit de ces trois courbes et comparé avec les valeurs obtenues d'après analyse classique: le niveau est identique mais la plage de détermination est beaucoup plus grande. Un changement de pente est observé pour le niveau de pression auquel l'exposant de pression de la loi de vitesse augmente soit vers 13-14 MPa.

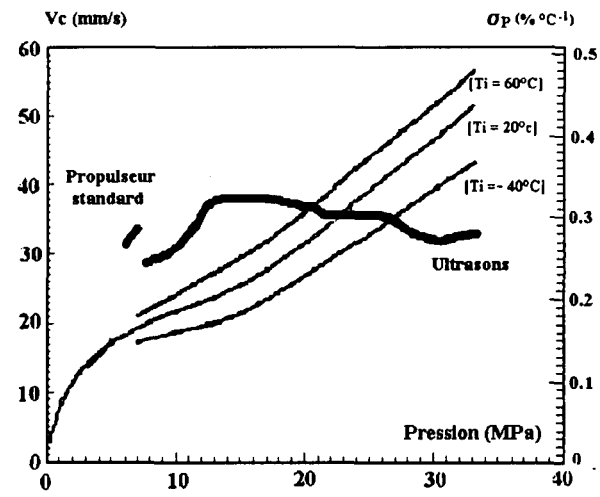


*figure 5 - Sensibilité de la vitesse de combustion à la température initiale (propergol composite avec Aluminium)*

La technique de mesure ultrasonore est utilisée comme outil de contrôle des propergols industriels mais aussi, en amont, en phase de développement de nouveaux propergols, par exemple pour les propergols aérobies à fort exposant de pression [7].

La qualité du produit vis à vis des spécifications est un souci permanent du fabricant de propergol: pouvoir contrôler ses caractéristiques en cours de malaxée va dans ce sens.

Déterminer la vitesse de combustion d'un propergol pâteux, non réticulé, a demandé la mise au point d'une procédure spécifique. La technique suivie pour la préparation de l'échantillon de pâte conditionne la qualité du résultat [8].

La figure 6 présente les résultats obtenus pour le propergol composite des boosters d'Ariane5: l'évolution de la vitesse de combustion du propergol non réticulé et du produit fini se superposent et suivent assez bien la loi " officielle"(o).

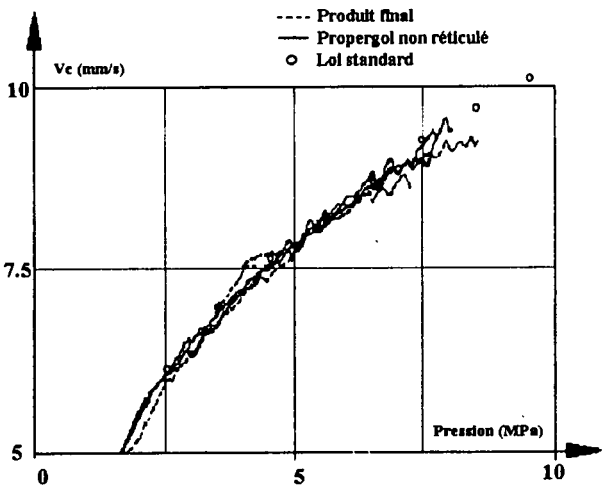


*figure 6 - Contrôle des propriétés balistiques du propergol non réticulé*

### *3.2 Combustion érosive*

L'influence sur la vitesse de combustion d'un propergol solide de l'écoulement des gaz de combustion au voisinage de sa surface (régime érosif) nécessite, outre la mesure du niveau de vitesse de combustion , la détermination du débit massique spécifique passant au droit du point de mesure. La technique ultrasonore rend accessibles ces deux paramètres puisque, à partir d'une géométrie initiale connue, il suffit de prendre en compte les épaisseurs brûlées de propergol pour obtenir les sections de passage des gaz et d'intégrer le débit de combustion lié à la vitesse de combustion mesurée en amont de la section considérée.

La caractérisation expérimentale de la combustion érosive des différents types de propergols solides est menée à l'ONERA depuis de nombreuses années [8,9]. Quatre montages équipés de points de mesure ultrasonore ont permis d'obtenir des données significatives.

Le premier est un propulseur sans tuyère axisymétrique à échelle réduite (750 mm de long, 20 mm de diamètre initial) utilisé dans le cadre des études d'accélérateur intégré pour missile à statoréacteur (figure 7) [11].

Cinq emplacements de mesure ultrasonore équipent ce montage. Lors du fonctionnement, un gradient longitudinal de pression est présent avec un niveau de pression qui décroît avec l'augmentation de la section de passage des gaz. La combustion érosive est d'autant plus marquée que l'on s'approche de l'extrémité aval (points 3,4 et 5). Les points 1 et 2 correspondent à un régime stationnaire non érosif : on y retrouve l'évolution de vitesse déterminée avec le propulseur décrit sur la figure 4.

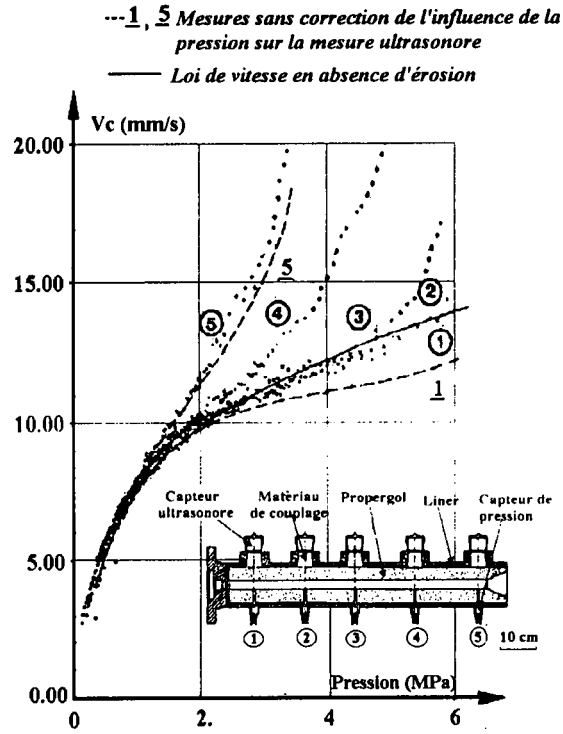


*figure 7 - Propulseur sans tuyère à échelle réduite*

Le second montage est un propulseur de laboratoire avec deux blocs parallélépipédiques de propergol (figure 8). Il a été utilisé pour étudier l'effet de la combustion érosive sur la réponse aux instabilités de pression d'un propergol de type composite (couplage vitesse) [12]. Cinq points de mesure sont répartis le long du propulseur. L'analyse des mesures met en évidence l'effet du débit massique unitaire sur le facteur érosif ($V_c/V_{c,n}$) avec une loi à seuil de déclenchement.

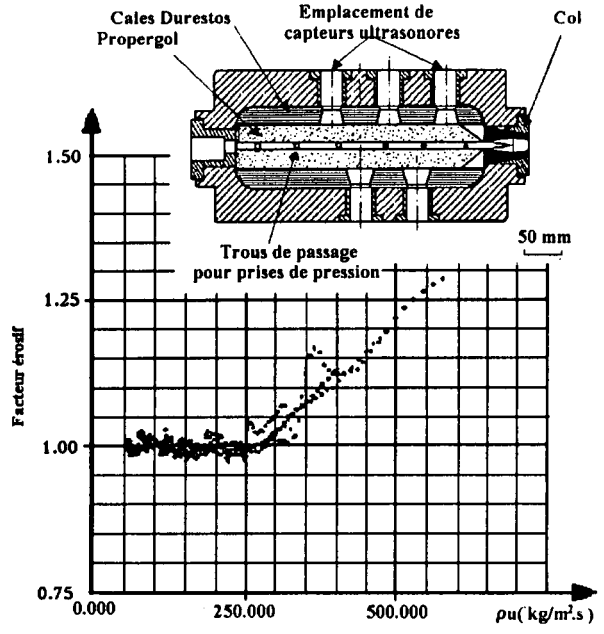


*figure 8 - Propulseur bidimensionnel d'étude de la combustion érosive*

Un troisième montage axisymétrique de section réduite (blocs diamètres 32/16 mm) a posé bien des difficultés technologiques pour la mise en place de la mesure ultrasonore avec des capteurs de petit diamètre (1/2").

La qualité du collage et de l'adaptation d'impédance du matériau de couplage devait être maximale du fait du niveau élevé de pression (propergol homogène) et du faible élément de la surface qui contribue à réfléchir l'onde mécanique (une ellipse fort allongée!).

Les mesures ont fait apparaître un phénomène d'érosion dite "négative" pour un propergol homogène contenant des additifs balistiques (figure 9). Cet effet est dû à l'entraînement par l'écoulement du résidu carboné présent en surface et qui est à l'origine de la survitesse initiale (zone de plateau).
Une fois enlevé ce résidu, le propergol suit une loi de vitesse de niveau plus faible correspondant à un propergol sans additifs.

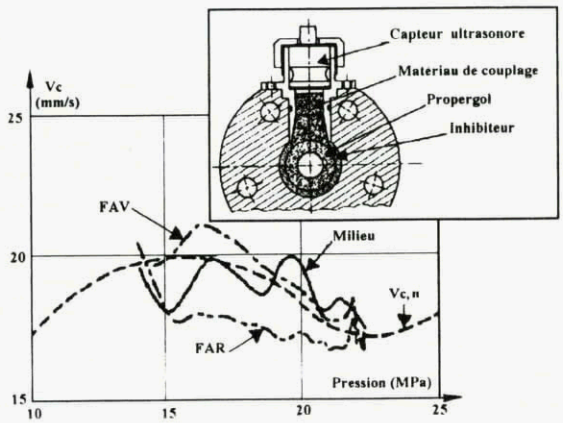


*figure 9 - Combustion érosive des propergols homogènes à additifs balistiques*

Enfin, le dernier montage est un ensemble échantillon-générateur séparé (figure 10). Le débit massique provient essentiellement du générateur , jusqu'à 0.5 kg/s environ, l'échantillon de propergol à tester est de taille réduite (5 mm d'épaisseur, 50 mm de long et 30 mm de large), il est placé dans un canal rectangulaire qui détermine le débit massique spécifique (environ 6000 kg/m$^2$-s max).

Ce montage a été consacré à une étude systématique des paramètres influents sur la combustion érosive [10]. Des changements de niveau de pression, de taille des particules de Perchlorate d'Ammonium ou des additifs ont permis de moduler la vitesse de combustion du propergol composite de base de 9.9 à 30 mm/s à 6-7 MPa.

Les résultats expérimentaux montrent l'influence de la vitesse normale de combustion sur le comportement érosif: plus rapide est le propergol, plus faible est la pente et le niveau de l'érosion et plus élevé est le seuil d'apparition du phénomène. La modélisation de la combustion érosive reproduit tout à fait le comportement expérimental déduit de la mesure ultrasonore.

L'apport de la méthode de mesure ultrasonore dans le domaine de la combustion érosive est évident puisque tous les paramètres pertinents deviennent accessibles et ceci en différentes positions. De plus, la mise en oeuvre de la méthode de mesure ne nécessitant que la réalisation d'un passage tronconique à travers la virole métallique d'un propulseur de laboratoire pour le matériau de couplage, elle est adaptable sur des montages déjà existants: ceci a été le cas pour le propulseur sans tuyère.

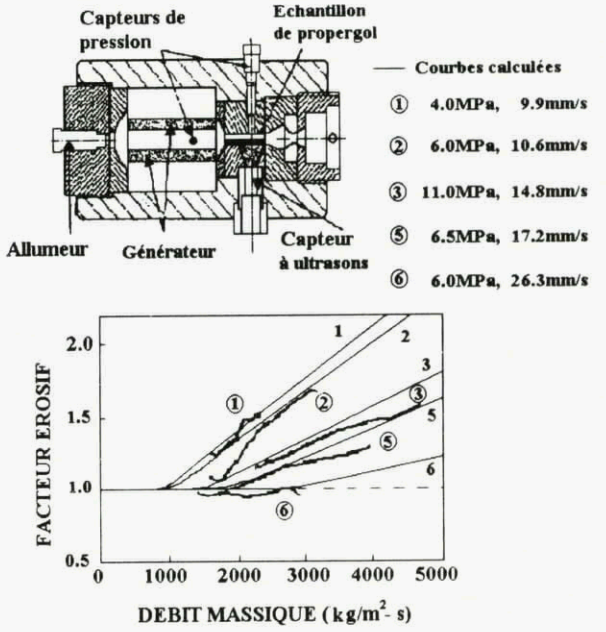


*figure 10 - Combustion érosive mesurée sur montage générateur-échantillon et comparée avec les résultats issus de la modélisation*

### *3.3 Combustion instationnaire*

Les instabilités de combustion se manifestent dans les systèmes énergétiques par un fonctionnement oscillatoire, souvent imprévu, gênant voire dangereux pour le système. Les propulseurs à propergol solide peuvent être instables. Selon la taille de l'engin, les fréquences des instabilités vont d'une dizaine de Hertz, pour les boosters P230 Ariane 5, à quelques dizaines de milliers de Hertz dans le cas des missiles tactiques [13]. Les instabilités se traduisent par des fluctuations de pression qui vont engendrer des variations de vitesse de combustion ($V_b$=a$P^n$). Selon le propergol concerné, le comportement sera différent : une amplification ou un amortissement du phénomène sera observé. On définit ainsi la réponse au couplage pression d'un propergol : il s'agit d'une grandeur complexe qui varie principalement avec la fréquence des oscillations et qui est définie par:

$$R_P = (V_b' / \overline{V_b}) / (P' / \overline{P})$$

$f'$ : composante instationnaire de la grandeur $f = \overline{f} + f'$ avec $f' << \overline{f}$

La méthode de mesure ultrasonore contribue à la détermination du comportement instationnaire des propergols sous deux aspects:

- données relatives au fonctionnement stationnaire pour établir la géométrie de la chambre à chaque instant (contribution à une modélisation du phénomène),
- détermination de la réponse au couplage pression (méthode directe).

L'application la plus simple de la mesure en régime instationnaire consiste dans l'étude de la frontière de stabilité d'un propergol composite dans des conditions particulières rencontrées en fin de combustion d'un propulseur sans tuyère. La pression n'est alors que de quelques bars, le volume de la chambre est maximum, le fonctionnement peut devenir oscillatoire, entraînant l'extinction du bloc suivi parfois de son réallumage.

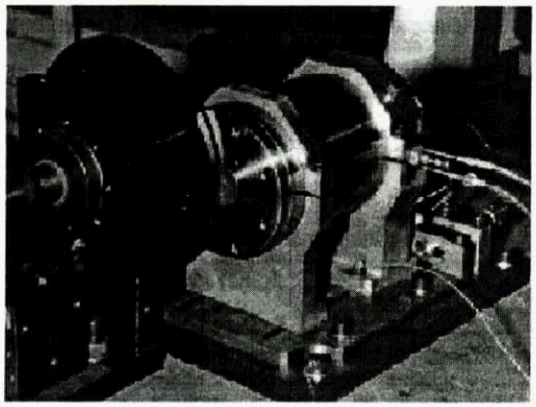

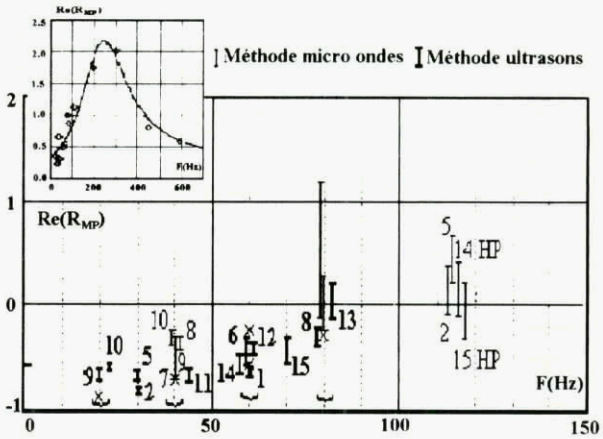


*Figure 11 -Mesure directe en combustion instationnaire: propulseur à éjection modulée et synthèse des résultats*

Ces instabilités dites en $L^*$ (Volume de la chambre/ Section du col) ont été étudiées avec le montage de la figure 4 avec un volume de chambre augmenté. Le déclenchement de la phase oscillatoire traduit le franchissement de la frontière de stabilité. Avec la mesure ultrasonore, on déduit l'épaisseur de propergol brûlé donc le volume de la chambre. A l'aide d'une loi de pyrolyse du matériau du col ablatable, on obtient la valeur de la section du col donc la longueur caractéristique $L^*$. La valeur de la pression étant bien sûr enregistrée, le diagramme de stabilité du propergol en basse fréquence et basse pression peut être tracé.

La détermination de la réponse d'un propergol a fait l'objet de nombreux travaux pour mettre au point des techniques expérimentales. Qu'il s'agisse de méthodes indirectes basées sur l'analyse des évolutions de pression [14] ou de méthodes de mesure directe [15], l'information donnée par la mesure ultrasonore est importante. Le temps de séjour des gaz dans la chambre doit être calculé: il l'est grâce au suivi de l'épaisseur brûlée de propergol. Dans le cas de la technique de mesure par magnétohydrodynamique, des sondes sont implantées dans la chambre. Un paramètre important de l'analyse est la distance entre le plan des électrodes et la surface de combustion : la mesure ultrasonore donne accès à cette donnée. Dans ces deux cas, la mesure ultrasonore aide à la détermination de la réponse mais n'entre en rien dans le modèle.

A l'ONERA, une théorie de la mesure ultrasonore en régime instationnaire a été établie et testée sur deux propergols composites. Le premier, non métallisé, a permis de valider la théorie de la mesure et d'en dresser les limites. Le second propergol est celui utilisé pour les boosters d'Ariane 5: la méthode ultrasonore a été appliquée en tant que moyen opérationnel et les résultats ont été comparés avec ceux obtenus par d'autres techniques [15,16].

Les propulseurs à propergol solide segmentés de grande taille comme les boosters P230 d'Ariane 5 ou ceux de la Navette Américaine sont sujets à des instabilités de combustion contrôlées par des phénomènes de déclenchement tourbillonnaire à des fréquences proches du premier mode longitudinal de l'engin (vers 20 Hz). La détermination expérimentale de la fonction réponse du propergol solide considéré dans le domaine des basses fréquences est requise pour s'assurer d'une bonne prévision de la stabilité de fonctionnement.

Un programme expérimental a été conduit en utilisant la méthode de mesure ultrasonore sur un propulseur à éjection modulée ONERA. La fréquence des oscillations de pression est obtenue au moyen d'une roue à profil sinusoïdal en rotation dans le plan de sortie de la tuyère limitée à sa partie convergente, venant modifier périodiquement la section du col (figure 11).

La théorie de la mesure est explicitée dans la référence [16]. Une réponse apparente est obtenue, les paramètres correctifs reprennent toutes les grandeurs ayant une influence sur la propagation des ondes: pression, profil thermique, lois de célérité et géométries. L'analyse du profil thermique instationnaire est basée sur un modèle de combustion des propergols composites. La qualité des résultats en terme de réponse est très bonne mais la difficulté réside dans l'évaluation précise des paramètres correctifs. La partie réelle de la réponse est liée à l'évolution du déphasage entre les composantes instationnaires de variation de temps de parcours et de pression. L'amplitude 0-crête de temps de parcours reste très faible : au plus 0.1 µs à très basse fréquence en début de tir. Quand ceci est traduit en épaisseur équivalente, les amplitudes sont de l'ordre de quelques multiples de 9.2 µm (=0.01 µs). C'est là que réside la limitation majeure de la méthode de mesure ultrasonore : il faut rester à des niveaux de fréquence inférieurs à 100 Hz pour garder un rapport signal/bruit suffisant. Cette remarque est valable pour toute mesure directe en phase condensée : la technique de mesure par micro-ondes est également limitée en fréquence (<200 Hz) [14].

Les valeurs de réponse obtenues ont été comparées à celles issues de la mesure micro-ondes (figure 11).

Une synthèse de l'évolution de la réponse au couplage pression du propergol composite Ariane 5 regroupe, jusqu'à 600 Hz, les valeurs moyennes en intégrant aux résultats de mesure directe quelques points obtenus par méthode indirecte (f>200 Hz). La courbe moyenne est ajustée selon l'expression théorique de la réponse (paramètres physico-chimiques A et B). Cette loi est ensuite intégrée dans les calculs de stabilité de fonctionnement [17].

La technique de mesure ultrasonore appliquée à la combustion des propergols solides est devenu au fil des années un moyen opérationnel utilisé d'une manière systématique : la mise au point de nouveaux produits et le contrôle de leurs propriétés balistiques en est facilité, l'accès à des mesures localisées qualifie des comportements du type érosif ou des effets particuliers liés aux gros chargements (effet "bosse").

L'élément de surface de combustion sur lequel se réfléchit l'onde acoustique a un diamètre de l'ordre de grandeur du tiers de celui du capteur émetteur-récepteur : la mesure est donc moyennée sur cette surface. Les phénomènes très locaux liés au mécanisme de combustion des composés du propergol ne seront pas décrits par la mesure, tout comme d'ailleurs le comportement global d'un chargement. Cependant la qualité des données obtenues à l'aide de ce moyen est excellente, une fois la technologie et l'analyse de la mesure maîtrisés par l'utilisateur.

## 4 - DÉGRADATION-ABLATION DE DIVERS MATÉRIAUX ÉNERGÉTIQUES

Depuis quelques années. le champ d'application de la méthode de mesure ultrasonore s'est étendu à l'étude de la dégradation des matériaux énergétiques divers tels le PBHT, le PE (polyéthylène) et le PMMA (Plexiglas) ou le PTFE (Téflon) et les protections thermiques internes.
Le niveau de vitesse de dégradation est très souvent faible, les flux thermiques sont rarement stationnaires : le suivi des échos ultrasonores et l'analyse de la mesure ne sont pas facilités.

### *4.1 Propulsion hybride*

La propulsion hybride associe un oxydant s'écoulant sur la surface d'un combustible solide et réagissant entre eux. L'oxydant peut être initialement liquide comme le Peroxyde d'azote pour lanceurs spatiaux ou tout simplement être apporté par l'air dans le cas des missiles statofusées .

Le contrôle de la dégradation des combustibles solides ablatables est essentiellement relié au flux thermique entrant dans le matériau, flux issu des réactions entre les gaz de dégradation et l'oxydant [18]. Les travaux les plus nombreux ont été consacrés à l'étude du PBHT tant en France [18,19] qu'aux Pays-Bas [20] et aux États-Unis [21,22]. La caractérisation du comportement du combustible solide y est effectuée à l'aide d'une technique de mesure ultrasonore.

L'un des montages expérimentaux ONERA est représenté sur la figure 12: la veine de mesure ou chambre d'ablation est raccordée à un banc réchauffeur pilotable en richesse et en température ($H_2/O_2$).

Le résultat des mesures ultrasonores met en avant les phénomènes thermiques qui modifient les conditions de propagation des ondes : la phase de mise en régime du réchauffeur se traduit par une variation apparente d'épaisseur liée au ralentissement des ondes ultrasonores avec la température (figure 13). Lors des phases de fonctionnement quasi-stationnaire, la vitesse d'ablation est cependant bien évaluée par la dérivée temporelle de la variation de temps de parcours sans prise en compte des effets thermiques. Les estimations de vitesse d'ablation sont d'assez bonne qualité malgré les effets de l'échauffement initial.

Les matériaux considérés dans la propulsion hybride se dégradent sans laisser un dépôt ou résidu sur la surface. Cependant, certains d'entre eux subissent un changement de phase avant dégradation complète : une couche liquide (PMMA) ou un gel (PTFE) recouvre la surface du matériau. Dans ce cas la mesure ultrasonore est modifiée: le changement d 'état du matériau entraîne une variation d'impédance acoustique suffisante pour qu'une partie de l'énergie ultrasonore soit réfléchie à la transition et l'on voit apparaître un écho supplémentaire.

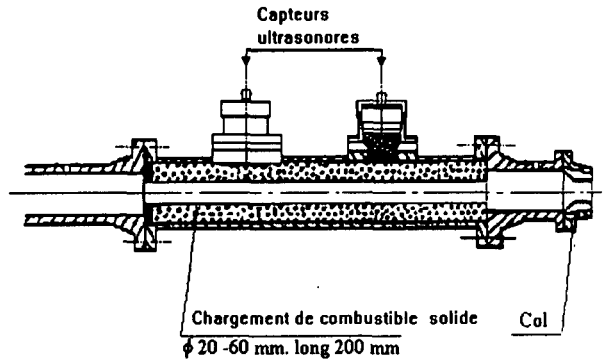


*Air provenant du réchauffeur (ρu < 3000kg/m²-s. P<5MPa)*

*figure 12 - Combustibles ablatables: montage expérimental*

Le suivi de ces modifications ne peut être effectué qu'avec le système d'acquisition numérique des échos ultrasonores avec un traitement en différé. C'est également le cas pour les matériaux qui présentent un résidu en surface, résidu dont le comportement va venir modifier les conditions d'échange thermique en surface et donc influencer les conditions de propagation des ondes.

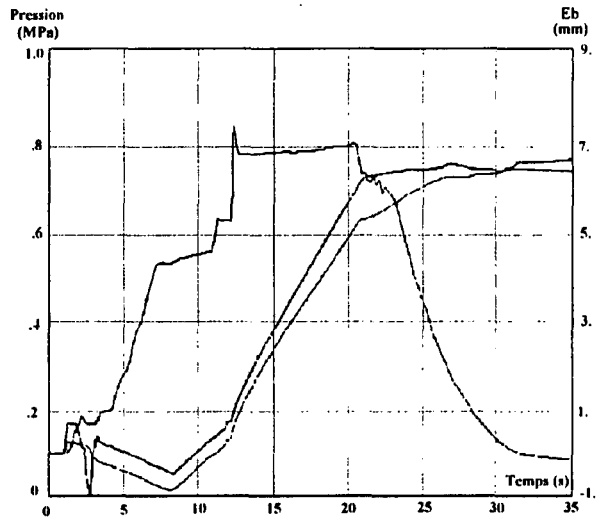


*figure 13 - Combustibles ablatables: mesure ultrasonore avec effets thermiques*

### *4.2 Protections thermiques internes*

Les matériaux de protection thermique interne (PTI) des propulseurs à propergol solide sont réalisés à partir d'une base EPDM chargée avec différents produits retardateurs (Silice, Kevlar...). La pyrolyse du matériau donne naissance à un résidu dont la tenue mécanique plus ou moins forte selon le produit va conditionner le comportement (figure 14).

Deux types de PTI ont été testées: la différence réside dans la nature de la charge isolante. Lorsque la PTI contient des fibres de Kevlar, le résidu a une très bonne tenue mécanique, il reste présent en surface faisant écran thermique. La température de surface du résidu atteint vite des températures élevées, la quantité de chaleur entrant dans le matériau devient telle que l'écho de la surface de pyrolyse diminue d'amplitude jusqu'à disparaître, empêchant toute mesure ultrasonore.

Pour la protection thermique interne contenant de la Silice, le contrôle du niveau de dégradation piloté par le flux thermique incident dépend de la présence ou non du résidu. Si les contraintes mécaniques issues de l'ecoulement parallèle à sa surface sont trop faibles pour l'éjecter, il y aura pyrolyse du matériau mais le processus de pyrolyse sera de faible vitesse et thermiquement instationnaire. La mesure ultrasonore permet un suivi de la surface avec, bien sûr, une interprétation délicate puisque les effets thermique sur la propagation sont de niveau comparable à la régression de surface.

A l'opposé, lorsque les contraintes de paroi éliminent le résidu au fur et à mesure de sa production, le régime sera alors ablatif et quasi-stationnaire. La mesure ultrasonore s'apparente alors à celle obtenue pour un propergol solide: les effets thermiques sont négligeables.

Entre ces deux régimes, on observe un enlèvement du résidu par strates de faible épaisseur, comme montré sur la figure 14.

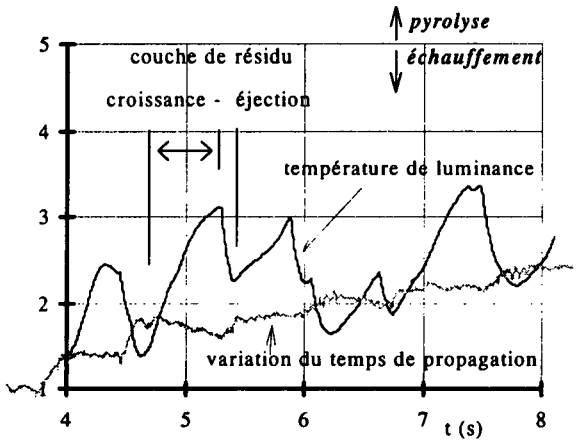


*figure 14 - Formation et éjection du résidu: cycle affectant la propagation ultrasonore*

L'alternance de phases de pyrolyse et d'effet thermique ne peut être interprétée qu'à l'aide de la modélisation du comportement thermo-ablatif du matériau rendant accessible le profil thermique dans le matériau en cours de dégradation.

Connaissant la variation de célérité des ondes dans le matériau et un critère de réflexion lié à une porosité limite, il est possible de calculer le temps de parcours à chaque instant selon des conditions d'échange thermique présupposées. Ce résultat est comparé avec la mesure effectuée et ainsi les effets de pyrolyse et d'échauffement sont dissociés.

Le couplage de la mesure ultrasonore avec un code thermo-ablatif: PTIMAD, version SEP/ONERA du code CMA (Charring Material Ablation ) d'Aerotherm est effectué. Les résultats sont très encourageants dans le cas où le résidu reste en place mais il n'est pas encore possible d'analyser les phases pulsées avec éjection périodique du résidu. Le comportement des matériaux sans résidu doit pouvoir être bien représenté par le code sous réserve d'une bonne connaissance des grandeurs thermiques et des caractéristiques de pyrolyse du produit, données d'entrée du code. L'intérêt du couplage mesure/calcul réside dans l'établissement de l'historique du flux à l'origine de l'échauffement puis de la dégradation : la mesure ultrasonore devient un fluxmètre.

## 5 - MESURE SUR ENGIN REEL [23]

Jusqu'à présent, les applications de la mesure ultrasonore concernaient des mesures effectuées sur propulseurs ou montages de laboratoire. Les travaux réalisés dans le cadre de l'étude du comportement des protections thermiques internes avec la SEP (Société Européenne de Propulsion) nous ont amenés à tester et de valider les possibilités d'adaptation de la technique de mesure sur propulseur réel (échelle 1). De telles mesures sont réalisées aux États-Unis mais l'analyse n'est peut-être pas aussi avancé [24].

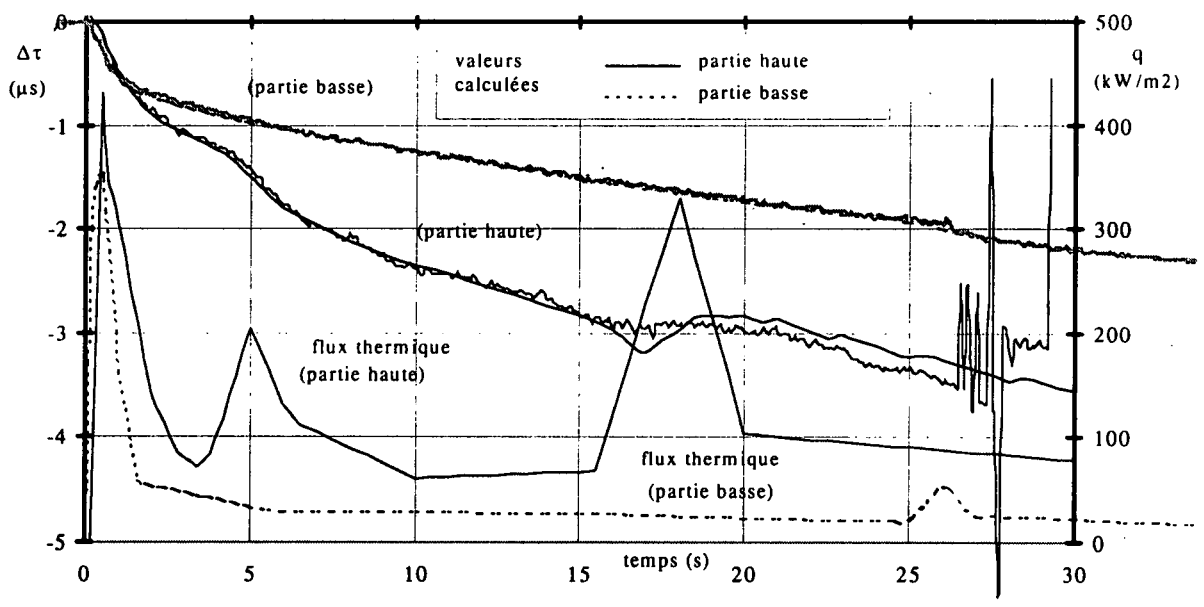


*figure 15 - Séquence de flux thermique établie à partir de la comparaison mesure/calcul sur propulseur réel à structure bobinée*

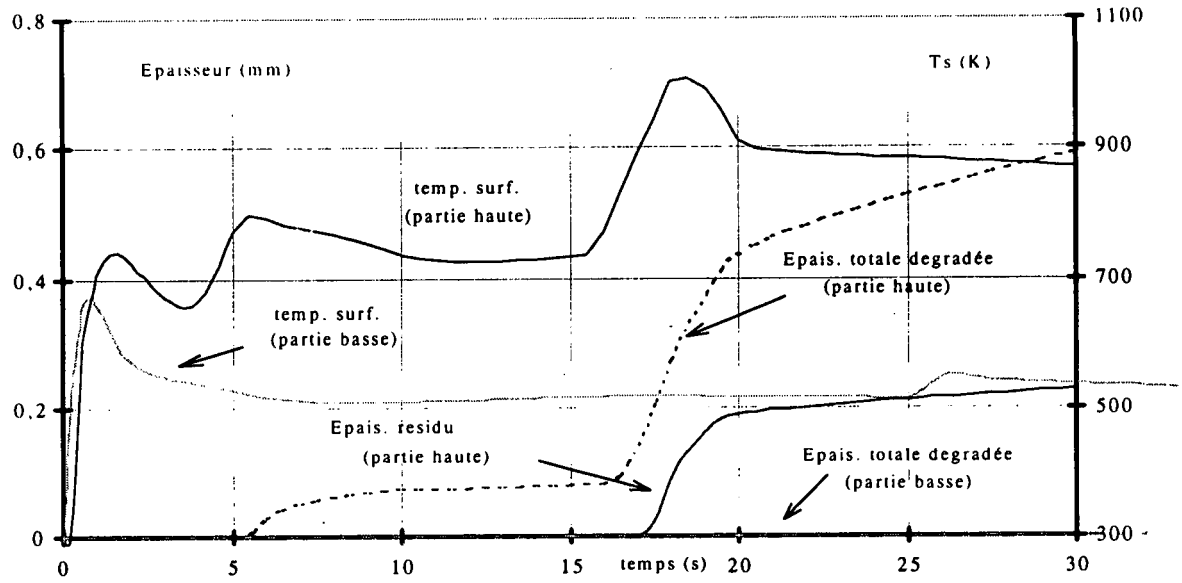


*figure 16 - Températures de surface et épaisseurs dégradées calculées*

La mise en place des capteurs ultrasonores est faite par collage direct sur les structures bobinées sans réalisation d'une traversée comblée par une résine acoustiquement adaptée.

L'application est limitée aux engins à structure non métallique: il aurait fallu prévoir un perçage de la virole (autorisation !) pour s'affranchir de la différence énorme d'impédance acoustique entre un métal ($\rho C = 45*10^6$ kg/m$^2$-s) et une PTI ($\rho C = 1.6*10^6$ kg/m$^2$-s) ou un propergol ($\rho C$ =2.5 à $3*10^6$ kg/m$^2$-s), différence qui bloque l'énergie acoustique dans la structure.

Les échos ultrasonores sont numérisés en cours d'essai, les images obtenues sont traitées après tir. La modélisation du comportement à chaque point de mesure est entreprise afin de déterminer l'évolution des échanges thermiques et leur ordre de grandeur. L'exemple présenté sur la figure 15 montre l'effet de la position de l'engin lors d'un tir au sol à l'horizontale.

Les évolutions des mesures ultrasonores en peau décollée au fond avant à même diamètre sont caractéristiques d'un effet thermique prépondérant: le temps de parcours s'accroît, mais l'effet n'est pas symétrique. L'échauffement thermique est plus prononcé en partie haute, un changement de pente est observé vers t =17 s : il est possible que la pyrolyse débute alors. La protection thermique interne subit une dégradation en partie haute, là où le poids du chargement de propergol solide va plutôt ouvrir l'intervalle. Seul un échauffement est noté en partie basse, la peau décollée étant plutôt fermée.

La comparaison mesure/calcul donne l'évolution du flux thermique incident qui est à l'origine de la variation de temps de parcours. Après une phase de flux élevé liée au remplissage de la cavité par les gaz de combustion du chargement, les flux sont de niveau assez faible surtout en partie basse (30 kW/m$^2$), le double est obtenu en partie haute avec deux pics de flux à t= 5 et 18 s. On notera qu'en première approximation, l'évolution du flux thermique est proportionnelle à la dérivée temporelle de la variation de temps de parcours. Les sorties du code thermo-ablatif décrivent l'élévation de température de surface et les épaisseurs de matériau dégradé et de résidu (figure 15).

En partie basse, l'échauffement a été insuffisant pour démarrer la pyrolyse, la température est restée sous le seuil de 700 K, départ des réactions. Ce résultat a été confirmé par les contrôles après tir : l'analyse de la mesure a été validé.

La mesure par ultrasons présente l'intérêt supplémentaire de permettre une évaluation des flux thermiques ; ceci demande un investissement au niveau de la connaissance du matériau. En multipliant les points de mesure, on peut établir une cartographie de la dégradation des protections thermiques internes. Les données lors de tir effectués au sol constituent une banque de données importante pour le dimensionnement des protections. On peut également envisager une mesure embarquée.

Quelques autres résultats de la mesure ultrasonore appliquée aux engins réels sont à noter pour le propergol solide: topage de passage du front de combustion par suivi du découvrement de la PTI, évaluation de la vitesse de combustion en fin de tir avec une limitation de l'épaisseur traversée à quelques centimètres (limite non technologique). [24]

## 5 - CONCLUSION

La présentation des diverses applications de la mesure ultrasonore est malheureusement trop rapide. Le lecteur trouvera des informations complémentaires dans les articles cités en référence.

La méthode de mesure ultrasonore est devenue un outil opérationnel mis en oeuvre de manière naturelle sur les montages expérimentaux de laboratoire au même titre qu'un capteur de pression. Contrairement à d'autres techniques telles les microondes, l'implantation du capteur ultrasonore ne demande pas de montage expérimental spécial. Il peut être intégré sur des montages déjà existants. La seule difficulté reste la mise au point du matériau de couplage, la ligne à retard - traversée de paroi, qui doit être chimiquement compatible et acoustiquement adapté avec le produit testé, de tenue mécanique suffisante (attention à l'effet de la température initiale!) et avoir de bonnes qualités de collage.

L'analyse de la propagation des ondes est bien maîtrisée dans le cas des propergols solides, un peu moins pour les matériaux à faible vitesse de régression.

La précision du résultat final, la vitesse de combustion, dépend des conditions expérimentales (dP/dt), des conditions d'acquisition (de 25 à 20000 mesures par seconde), des conditions de calcul de la dérivée (moyenne, lissage ...) et de l'opérateur. Estimer la précision est difficile: la mesure est locale mais non ponctuelle et l'expérience montre que la combustion elle-même n'est pas tout à fait stable pour des conditions fixes ($P,T_i$).

C'est à la fois un outil de recherche, l'étude de la combustion érosive en est l'exemple phare, et un outil de contrôle de fabrication avec une réduction des coûts pour une précision accrue. Les mesures sur engin réel à structure bobinée sont en plein essor avec un lot d'information intéressant le concepteur tant des protections thermiques que le fabriquant du chargement à propergol solide. Là aussi, une réduction des coûts est attendue grâce à l'emploi plus généralisé de la méthode de mesure ultrasonore.

Certes, l'investissement de départ peut être considéré comme important : le matériel de mesure reste assez cher mais c'est l'expérience que doit accumuler l'opérateur qui demeure la charge la plus lourde avant le retour sur investissement.

## REFERENCES


[1] P.Kuentzmann, J.C.Démarais, F.Cauty
"Mesure de la vitesse de combustion des propergols solides par ultrasons ", La Recherche Aérospatiale, n°1-1979 - pp 55-79

[2] F.Cauty
"Mesure par ultrasons de la vitesse de combustion des propergols solides", ONERA Rapport Technique n°5/3173 EY, 1983

[3] F.Cauty, J.C.Traineau
"Mesure par ultrasons de la vitesse de combustion d'un propergol solide: perfectionnement et applications à divers régimes de fonctionnement", 19st International Congress of ICT, Karlsruhe, 1988

[4] F.Cauty, J.C.Démarais, C.Éradès
"Determination of solid propellant burning rate sensitivity to the initial temperature by the ultrasonic method", *Non Intrusive Combustion Diagnostics*, edited by K.K.Kuo and T.P.Parr, Begell House, Inc., New York, 1994

[5] AGARD PEP Working Group 27,"Evaluation of methods for solid propellant burning rate measurement report: Chap.4.0 Non intrusive burning rate measurement technologies", to be published

[6] M.Pasquier
"Comparaison de différentes méthodes de détermination des courbes v(p) des propergols solides composites", Note 86.390/SNPE/DAT/BES, 1987

[7] B.Fourest, Ch.Masson
"Recherche et développement de propergols aérobies à fort exposant de pression", 21st International Congress of ICT, Karlsruhe, 1990

[8] F.Cauty, J.Cl.Démarais
"Ultrasonic measurement of the uncured solid propellant burning rate", 21st International Congress of ICT, Karlsruhe, 1990

[9] J.C.Godon, J.R.Duterque, G.Lengellé
"Solid propellant erosive burning", Journal of Propulsion and Power, Vol.8, n°4, July-August 1992, pp 741-747

[10] J.C.Godon, J.R.Duterque, G.Lengellé
"Erosive Burning in Solid Propellant Motors ", Journal of Propulsion and Power, Vol.9, n°6, Nov.-Dec. 1993, pp 806-811

[11] J.C.Traineau, P.Kuentzmann
"Ultrasonic measurements of solid propellant burning rates in nozzeleless rocket motors", Journal of Propulsion and Power, Vol. 2, n°3, 1986 , pp 215-222

[12] G.Avalon, J.Pascal, F.Cauty
"Experimental Investigation of a Type of Solid Propellant Velocity Coupling", AIAA Paper 87-1727, 1987, San Diego, CA

[13] P.Kuentzmann
"Études récentes à l'ONERA sur les instabilités de combustion dans les moteurs-fusées à propergol solide", dans "Solid Rocket Motor Technology", AGARD CP-259, Juillet 1979, Paper 22

[14] J.Cl.Traineau, M.Prévost, P.Tarrin
"Experimental Low and Medium Frequency Determination of Solid Propellants Pressure-Coupled Response Function", AIAA Paper 94-3043, 1994, Indianapolis, IN

[15] F.Cauty,P.Comas,F.Vuillot,M.Micci
"Magnetic Flow Meter Measurement of Solid Propellant Pressure-Coupled Responses Using an Acoustic Analysis", Journal of Propulsion, Vol.12, n°2, 1996, pp 436-438

[16] F.Cauty
"Measurement of solid propellant response function at low frequency by means of ultrasonic method". Colloque CNES/ONERA/CNRS "Écoulements Propulsifs dans les Systèmes de Transport Spatiaux". Bordeaux (France), 9/11-15/1995

[17] T.Basset, E.Daniel, F.Vuillot, J.Dupays, N.Lupoglazoff
"2-D Navier-Stockes Stability Computations for Solid Rocket Motors: Rotationnal, Combustion and Two-Phase-Flow Effects", AIAA Paper 97-3326, 1997, Seattle, WA

[18] G.Lengellé, B.Fourest, J.Cl.Godon, C.Guin
" Condensed Phase Behavior and Ablation Rate of Fuels for Hybrid Propulsion", AIAA Paper 93-2413

[19] B.Fourest
"Statofusée à combustible ablatable: essais réalisés dans le cadre d'une coopération TNO/SNPE/ONERA", ONERA Rapport Technique n°3/7501 EY, 1995

[20] R.Dijkstra, P.Korting, R.van den Berg
"Ultrasonic Regression Rate Measurement in Solid Fuel Ramjets", AIAA Paper 90-1963, Orlando, FL

[21] T.A.Boardman, L.G.Porter, F.W.Brasfield, T.M.Abel
"An ultrasonic fuel regression rate measurement technique for mixture ratio control of a hybrid motor", AIAA Paper 95-3081, San Diego, CA, 1995

[22] M.Chiaverini G.Harting, Y.C. Lu, K.K.Kuo, N.Serin, D.Johnson
"Fuel decomposition and boundary-layer combustion processes of hybrid rocket motors", AIAA Paper 95-2686, San Diego, CA, 1995

[23] F.Cauty, J.Cl.Démarais, C.Eradès, Cl.Caugant
"Internal insulation and solid propellant behavior measured by ultrasonic method on solid rocket motors", AIAA Paper 97-2994, Seattle, WA, 1997

[24] "Acoustic measurements during solid rocket motor testing" Arnold Engineering Development Center, Arnold Air Force Base, Tenn. 37389, Jan. 1995

Paper 34
Author: Cauty

Q: Moritis

Un de vos projets d'amélioration de la technique est la mesure d'épaisseurs plus grandes que vous ne pouvez mesurer actuellement. Peut-on arriver à ce but par le seul emploi d'ondes sonores à frequence plus basse ou il y a des ramifications dont l'effet doit être mitigé ?

*A:* En effet, une diminuation de la frequence d'excitations de la céramique du capteur ultrasonore rend possible la traversée d'epaisseur de materiaux plus élevée. Dans notre cas, le caractère visco-elastique manque des produits testés (propegols solides et materiaux energetiques à base de polymère ou de EPDN) entraine de tels niveaux d'attenuation que cette solution n'est pas en peu efficace, sauf à descendre très bas en frequence (qq. dynamis de kHz).

A ce moment là, d'autres problèmes prendraient naissance avec l'allongement du temps d'amortissement de la ceramique et les accroissements des périodes des alternances des échos. Une possibilité plus comfortable réside en une modification des conditions de sollicitations electriques du capteur.

*Q:* Hors de votre exposé il a été question de corrections par introduites le logiciel de traitement, afin d'aneantir les effets de le temperature et de la pression sur la vitesse de propagation de l'onde sonore. Par contre, si j'ai bien compris, vous n'employez pas de capteurs de température, ni de pression. Les donnes, d'ou proviennent-elles ?

*A:* La pression est mesurée hors de chaque essai: c'est un paramètre primordial dans nos études- les evolutions de pression n'ont pas été indiquées sur les planches pour ne pas alourdir la representation.

La celêrité des ondes dans les produits étudiés peut être exprimée par une loi de type ..

La sensibilité à la pression (kp) est entrenue par des essais sans combustion dans une enceinte pressurisée. De l'evolution du temps de parcours on peut remonter à la sensibilité recherchée. Pour la temperature, il faut considerer 2 cas: les propegnols solides et les materiaux energetiques.

Pour les propegnols solides, la sécurité pyrotechnique nous interdit que depasser 80-100°C. Les informateurs recueillies sont importants pour les essais en temperatures différentes de l'ambiante, mais sont insuffisantes pour tenir compte d'un profil therimique en combustion. Comme celui-ci est peu penetrant (inversement proportionnel à le vitesse de combustion), établie très vite et peu modifié par les variations de pression, on le néglige ou on le remplace par une approximation lineaire avec un coefficient kt estimé (correction 2ème ordre).

Pour les materiaux energetiques, il en va autrement, l'effet de la quantité de chaleur entrant dans le materiau est très important. Des mesurees statiques peuvent être menés jusqu'a 200°C environ. Au delà, la loi est extrapolée, et ajustée en fonction des analyses des essais qui s'accumulent.

# SOLID ROCKET PROPELLANT BEHAVIOR DURING STATIC FIRING TEST USING REAL TIME X RAY RADIOSCOPY

J. M. TAUZIA, P. LAMARQUE
SNPE PROPULSION
DIRECTION DES OPERATIONS SCIENTIFIQUES ET TECHNOLOGIQUES
BP 57 33160 ST. MEDARD EN JALLES
FRANCE

**ABSTRACT**

Unlike ordinary motors, solid propellants rockets operate only once and for a very short period of time.
So, a method able to investigate the behavior of the grain during static firing test is of high interest for the people in charge of the development program especially regarding the following phases :
- ignition
- burning surface Propagation
- defects behavior and motors failure modes.
The connection of high speed video camera with real time X Ray equipment allows valuable data acquisition during the firing and fulfil the need of direct investigation of the related phenomenon.
In this paper some examples are presented, analyzed and compared with computed simulation.

**RESUME**

Contrairement aux moteurs classiques les moteurs à propergol solide ne fonctionnent qu'une fois et souvent pendant en temps très court.
Aussi les méthodes permettant de " voir" l'évolution du bloc de propergol en tir sont elles d'un grand intérêt pour les personnes chargées du développement de ces moteurs ; particulièrement pour des phases transitoires telles que :
- l'allumage
- l'évolution de la surface de combustion
- l'évolution d'un défaut et les défaillances.
L'utilisation d'un système à rayons X couplé avec une caméra vidéo rapide permet d'acquérir des données intéressantes concernant les phases précitées.
Dans ce papier quelques exemples d'utilisation sont présentés et comparés aux prévisions balistiques calculées.

## 1 - INTRODUCTION

Dans le passé les développements de moteurs à propergol solide conduisaient à des qualifications s'appuyant sur une série de tirs pour acquérir une confiance suffisante dans leur bon fonctionnement.
Durant la dernière décennie, des contraintes nouvelles sont apparues. on peut citer entre autres:
- un besoin d'augmentation de performances associé à une réduction des masses inertes qui a conduit à l'emploi de matériaux plus légers et qui s'oriente maintenant vers une meilleure connaissance des marges de fonctionnement,
- des niveaux d'exigences en fiabilité et en sécurité globalement plus élevées,
- une tendance à la réduction des coûts de développement se traduisant par une baisse du nombre d'essais.
Pour ces raisons les activités de conceptions ont dû faire appel à de nouveaux outils d'analyses et de visualisation des modes de fonctionnement des moteurs à propergol solide afin d'améliorer ou de permettre :
- la compréhension des phénomènes qui régissent leur fonctionnement,
- la validation des modèles de simulation numérique,
- l'incidence d'un défaut de fabrication sur la fiabilité ou les performances.

Traditionnellement, les méthodes permettant, en phase de conception, la compréhension des modes de fonctionnement et la validation des modèles faisaient appel à la multiplication des essais qui permettait une certaine statistique et aux essais avec extinction du propergol en cours de fonctionnement à un instant choisi afin de figer une phase de fonctionnement particulière.
Ces méthodes présentent deux inconvénients importants : on ne peut d'une part figer qu'une

*Paper presented at an AGARD PEP Symposium on "Advanced Non-Intrusive Instrumentation for Propulsion Engines", held in Brussels, Belgium, 20-24 October 1997, and published in CP-598.*

phase de fonctionnement par essai et d'autre part leur multiplication est onéreuse.
La mise en oeuvre de techniques de contrôle non destructif constitue une alternative intéressante car l'essai n'est pas perturbé et peut se dérouler jusqu'à son terme.
Parmi les techniques permettant de « voir » à l'intérieur du moteur lors de son fonctionnement en tir au banc, on peut citer la radioscopie télévisée (TV) par rayons X et les ultrasons.
La suite de l'article développe l'utilisation de la radioscopie T.V. par rayons X et donne des exemples d'utilisations.

## 2 - PRINCIPE DE LA RADIOSCOPIE T.V.

Une image radiante Rayons X est formée sur un détecteur qui la convertit en image visible.
Lorsque le détecteur est couplé à une caméra vidéo temps réel on obtient une image contenant toutes les particularités et évolutions de l'objet examiné.
Ce principe très simple est illustré, ci-après, sur la figure 1.

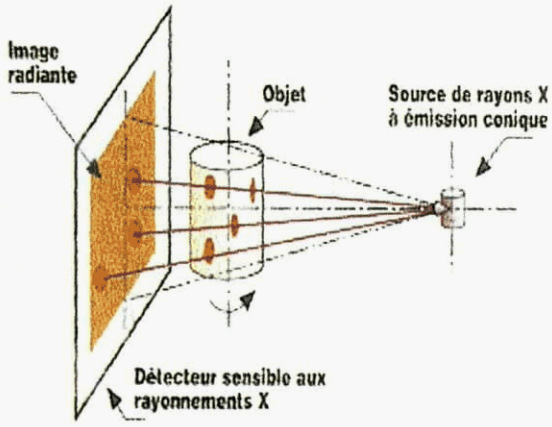


Figure 1

Un des principaux avantages de ce type d'examen réside dans sa totale indépendance par rapport à l'échantillon observé.
Selon la rapidité du phénomène à observer deux types de caméras sont utilisés :

- pour des phénomènes relativement lents comme des évolutions de surfaces de combustion (quelques millimètres par seconde) les caméras vidéo classiques à 25 images par seconde présentent le meilleur compromis entre sensibilité et résolution.
- pour des phénomènes plus rapides comme des phases d'allumage ou l'évolution éventuelle d'un défaut, il est nécessaire d'utiliser des caméras vidéo rapides ( jusqu'à 1000 images par seconde ) en général intensifiées afin d'obtenir la meilleure sensibilité possible pour les cadences de prise de vues élevées.

Selon la taille des objets à observer deux types de rayons X sont utilisés :

- pour des objets de taille inférieure à 300 mm un générateur à rayon X classique de quelques centaines de Kev est utilisé avec comme détecteur associé un amplificateur de brillance.
- pour des objets de taille supérieure un accélérateur linéaire de plusieurs Mev est nécessaire en association avec un détecteur spécifique.

Bien entendu de nombreuses contraintes de mise en oeuvre existent :
- protection du matériel à l'environnement d'un gros moteur en fonctionnement (bruit, vibration, chaleur...)
- protection vis-à-vis des rayonnements ionisants.

## 3 - VISUALISATION DE FRONTS DE COMBUSTION

Une des utilisations principales de ce type d'outil est la visualisation en temps réel de l'évolution d'un profil de combustion. Il permet de réaliser une comparaison directe avec l'évolution théorique.
Le premier exemple montre l'évolution du front de flamme d'un chargement axisymétrique.
Ces images sont réalisées avec un accélérateur linéaire délivrant des rayons X de 8 Mev, car le moteur fait 600 mm de diamètre ; la cadence d'acquisition est de 25 images / seconde.

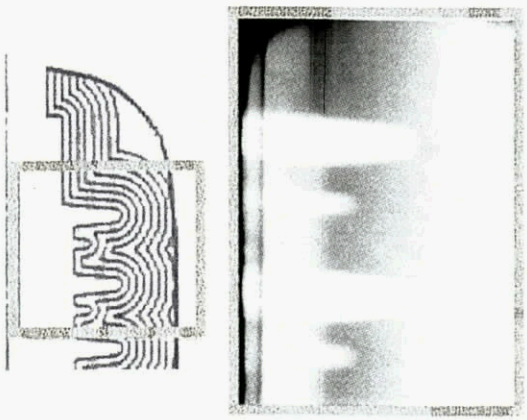

Figure 2 : Le rectangle gris montre la zone du chargement examiné et la partie gauche l'image RX obtenue avant l'allumage.

Les séquences suivantes montrent l'évolution en combustion du canal central avec en superposition en blanc l'évolution théorique.
La déformée à l'allumage du profil de combustion est très bien visualisée.
Compte tenu des erreurs dues à la projection géométrique et aux erreurs de parallaxe il est difficile d'avoir une mesure précise, mais l'ordre de grandeur est très bien retrouvé.
La précision de mesure est de l'ordre du pixel image, soit dans ce cas 1 millimètre.

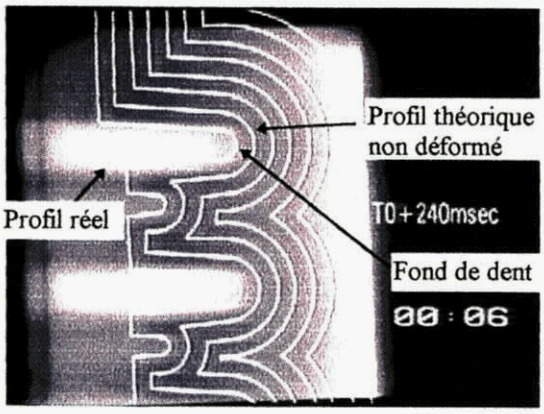


Figure 3 : A l'allumage ($T_0$ + 240 ms) l'image montre la déformation du profil, les dents sont décalées vers l'arrière et leur diamètre intérieur est augmenté.

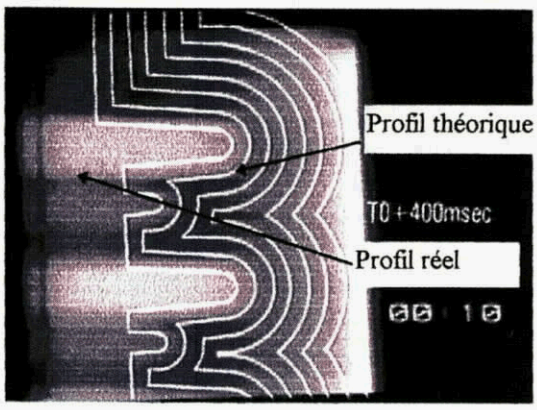


Figure 4 : $T_0$ + 400 ms. La combustion progresse mais le décalage du profil de combustion créé par la déformation à l'allumage par rapport au théorique n'est pas absorbé.

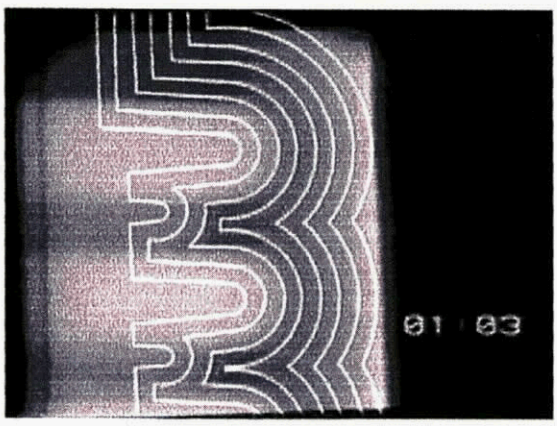


Figure 5 : $T_0$ + 1, 3 ms. Le profil de combustion est pratiquement sur le profil théorique.

La fin du tir permet également de visualiser les résiduels de combustion et de les comparer au calcul théorique toujours délicat de la queue de combustion.

## 4 - VISUALISATION D'ANOMALIES DE COMBUSTION

Afin de suivre le front de combustion, comme le moteur est en général fixe, l'ensemble d'imagerie poste RX et détecteur du type amplificateur de brillance, est monté sur un banc travelling qui est illustré sur la photographie ci-après.

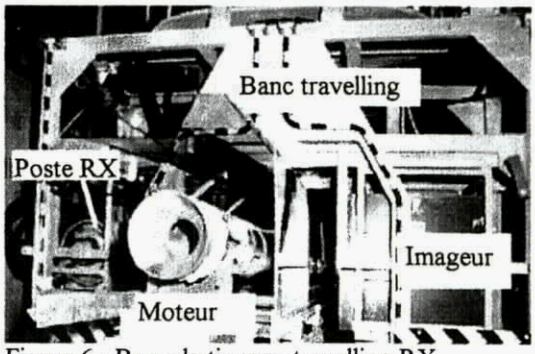


Figure 6 : Banc de tir avec travelling RX

Cet équipement permet de visualiser et de suivre de façon commode, en pilotant l'ensemble, l'évolution de surface d'un bloc à combustion frontale ou l'évolution d'un défaut présent dans le propergol lorsque qu'il est atteint par le front de combustion.
Ce banc permet de visualiser des moteurs d'un diamètre inférieur à 300 mm.

***L'évolution au tir d'un propergol poreux.***

Le calcul du devenir en tir d'un défaut est souvent difficile et nécessite de nombreuses hypothèses.
Par exemple l'observation directe de l'évolution en combustion d'une zone de propergol poreux apporte des informations difficilement calculables.

Les images suivantes montrent l'évolution calculée du front de flamme généré par un semi de bulles représentatif d'un défaut réel et provoquant une survitesse locale de 30 %.

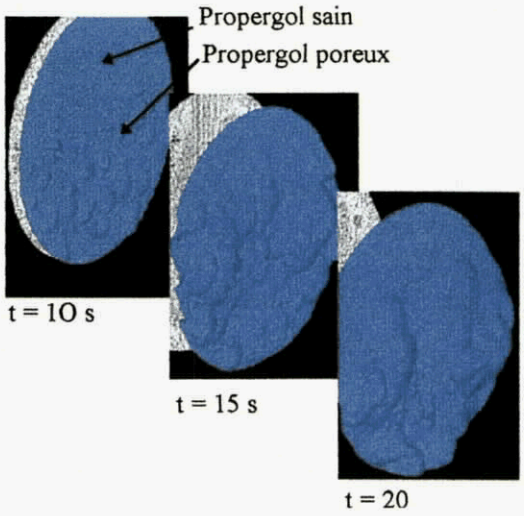


Figure 7 : Evolution théorique calculée avec le code SNPE 3D.EVOLINA.

Les images suivantes montrent l'évolution réelle de la simulation précédente elles sont prises à la cadence vidéo de 25 images/seconde.
La partie supérieure de l'échantillon est saine, la partie inférieure est poreuse mais les cavités sont trop petites, quelques millimètres pour les plus grosses, pour être visualisées par le système d'imagerie à travers la bombe de tir.

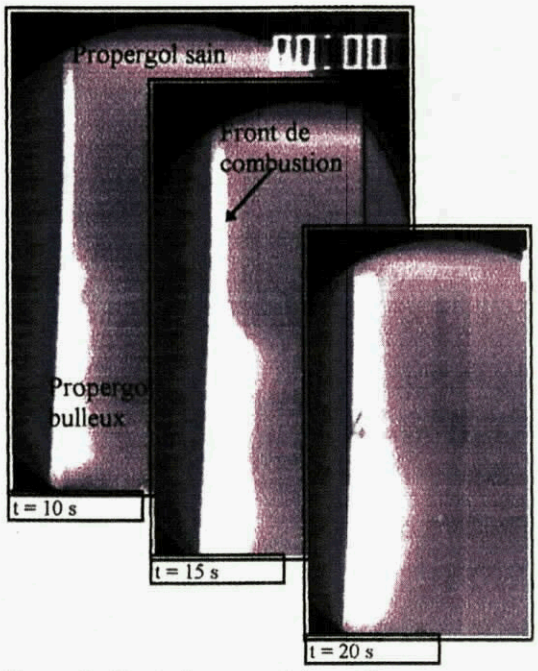


Figure 8 : Evolution porosités au tir.

L'analyse des images sur la durée totale du tir montre que la survitesse moyenne est bien de l'ordre de 30 % mais les images RX montrent que la survitesse locale peut aller jusqu'à 90%.

Certaines porosités peuvent aussi évoluer de façon plus rapide (effet de fissuration) comme le montre l' image ci après effectuée sur un autre échantillon.
Ce cas de figure est très difficile à modéliser.

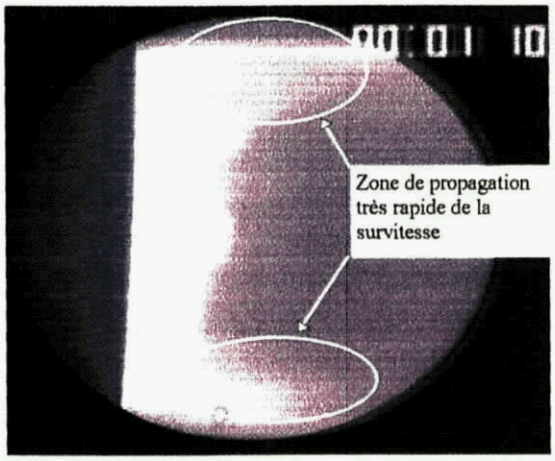


Figure 9 : Evolution de type fissuration.

Dans l'exemple précédent la survitesse vue sur les images est de l'ordre de 10 fois la vitesse nominale.

***Evolution de cavités au tir***

L'exemple suivant montre l'évolution de cavités à l'allumage et les conséquences sur la combustion.
Le moteur présente des cavités dans la zone avant La surface initiale présente 2 cônes ( Cf. figure 10 ) et la combustion est pilotée par fils ( trop fins pour être visibles sur l'image ).

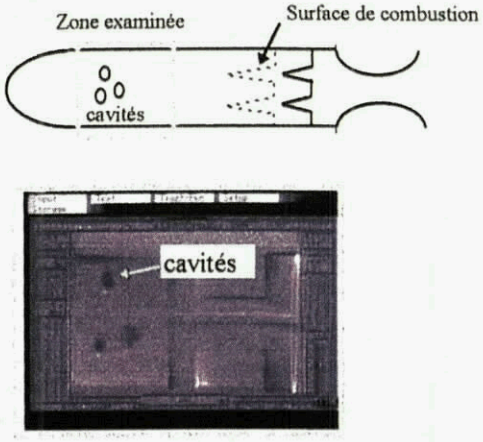


Figure 10 : Image RX avant allumage

Les images suivantes montrent la phase d'allumage et l'écrasement des cavités qui disparaissent.
La vitesse d'acquisition des images est de 250 images / seconde, ce qui explique la dégradation de leur qualité.

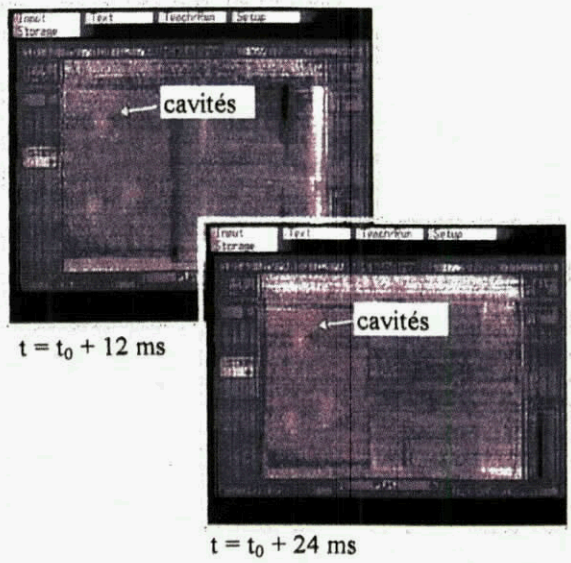


Figure 12 : Allumage

Pendant la phase d'allumage à la mise en pression les cavités sont écrasées et à $t_0$ + 40 ms elles sont complètement aplaties et disparaissent de l'image.

La séquence suivante montre l'arrivée du front de flamme dans la zone des cavités.
Les deux images sont séparées en temps par 4 ms.
Sur la première la combustion est normale.
Sur la seconde on note sur la gauche de la zone avec les cavités une prise en feu qui se développe en moins de 4 ms.
On peut penser que l'écrasement des cavités à généré autour d'elles des fissurations invisibles sur l'image car elles sont comprimées et qui ont propagé le front de flamme à son arrivé.

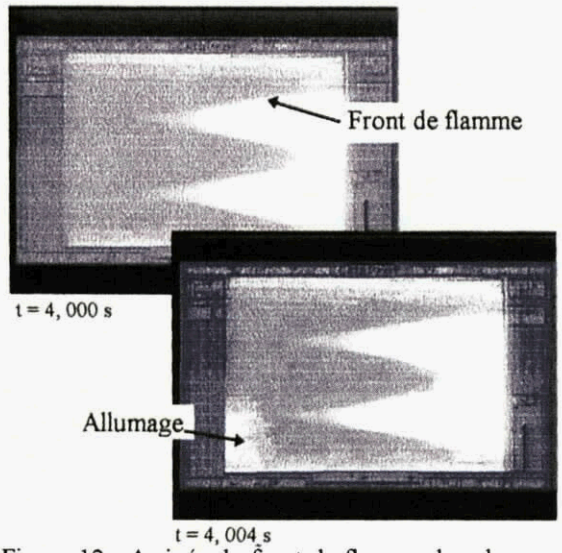


Figure 12 : Arrivée du front de flamme dans la zone des cavités.

***Compression d'une cavité***

Les images précédentes montrent que pour des phénomènes très rapides, bien que l'on puisse les mettre en évidence, il est malgré tout difficile d'avoir beaucoup d'informations au niveau d'un tir sur le devenir d'une cavité.
Pour pallier cette difficulté, l'exemple suivant montre l'évolution d'une cavité sous une contrainte de compression simulant la mise en pression.
Dans un premier temps, pour simplifier la mise en oeuvre de l'essai, la vitesse de mise en pression est inférieure à celle du tir, de l'ordre de plusieurs secondes.
La figure suivante montre le dispositif d'essai.

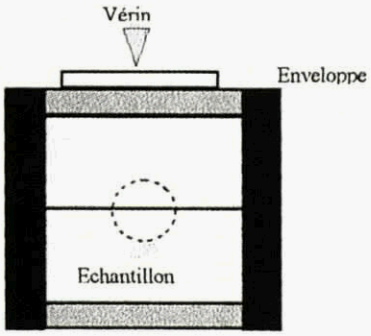


Figure 13 Dispositif d'essai.

Ce dispositif permet de faire varier le temps de sollicitation et la raideur de l'enveloppe.
Les images suivantes montrent l'évolution d'une cavité sphérique et la comparent à la déformée numérique.

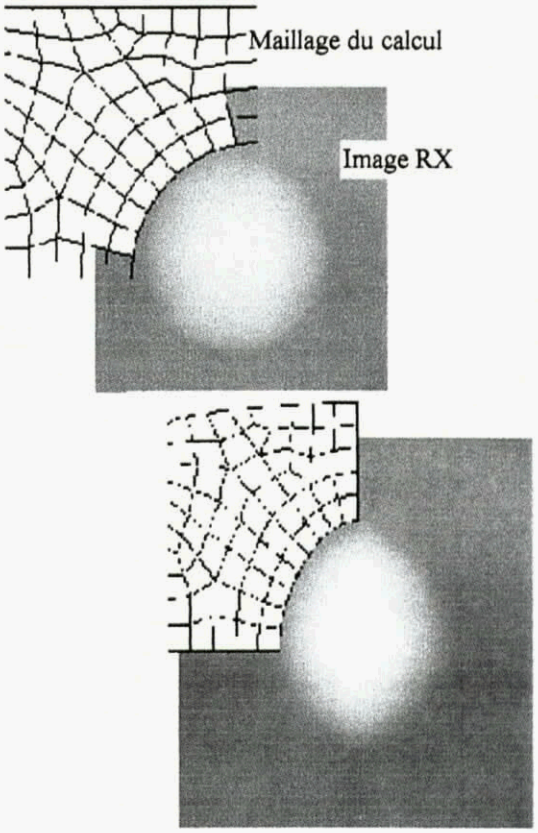


Figure 14 : Petites déformations

Pour des petites déformées on observe une bonne adéquation entre le calcul et l'expérience.

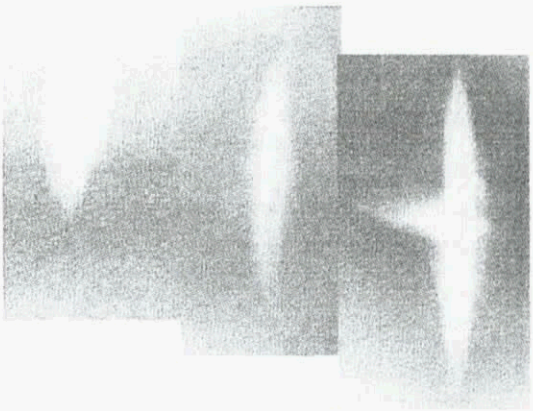

Figure 15 : Grandes déformées et fissuration de la cavité initiale.

Pour des déformations importantes le calcul ne rend plus compte de l'expérience avec la même précision.
Il est vrai que la compression d'une cavité sphérique est contraignante car elle présente de fort taux de déformation avec des contraintes élevées et les modèles utilisés présentent des instabilités numériques qui ne permettent pas d'aboutir aujourd'hui à la simulation de l'écrasement total de la cavité et à sa fissuration.
Ce type de visualisation permet par la comparaison directe avec l'expérience de tester de nouvelles lois de comportement du propergol afin de restituer au mieux les déformations réelles de la cavité.

## 5 - CONCLUSION

Les quelques exemples que nous avons montrés illustrent les différentes utilisations possibles de la radioscopie télévisée par rayons X comme moyen d'analyse non intrusif du fonctionnement des moteurs à propergol solide.

Par sa capacité à produire des images de bonne qualité dans des conditions très variées, cette technique s'avère très utile pour visualiser les évolutions de surfaces de combustion pendant toute la durée d'un tir et c'est un bon complément, voire une méthode de remplacement dans certains cas, aux essais avec extinction.
C'est un outil particulièrement intéressant pour apprécier comment l'évolution d'un défaut va jouer sur les performances ou la fiabilité d'un moteur.
Il permet également par une confrontation directe du comportement numérique du modèle avec celui observé en cours d'essais, l'amélioration des méthodes de dimensionnement et de calcul numérique.

## REMERCIEMENTS

Ces travaux ont été, en partie, financés par des contrats d'études DGA/DME/ST3S et CNES et les essais réalisés avec diverses collaborations, notamment le CAEPE et CELERG.

# Developments in High Energy X-Ray Radiography of Running Engines

**M. J. Allen and J. D. Rogers**
Rolls-Royce plc
Applied Science Laboratory
P.O. Box 31
Derby DE24 8BJ

## 1. SUMMARY

There has been substantial industrial development of radiographic techniques for quantitative measurement of component and/or material clearances or movement within static or operating test pieces or machinery. Important examples of applications are in the fields of aeronautics, armaments, space sciences and nuclear engineering (Pullen, 1971; Buchanan, 1973; Davies *et al*, 1980).

Following the demonstration and installation of a suitable high energy X-ray source for use with operating aero-engines, Rolls-Royce has been routinely carrying out high-energy X-ray radiography of engines on test beds since 1971 (Stewart, 1975; 1987).

The current Rolls-Royce X-ray imaging equipment includes a film plate changer system, used for analysis of steady-state or slow transient events, that enables sequences (up to 10 shots) of high-resolution film radiographs to be obtained at short (~ 2 s) exposure times. A real-time X-ray video imaging system producing up to 25 frames.$s^{-1}$ is used for faster transients or where cyclic behavior is being investigated by strobing with the pulsed X-ray source.

An Electronic Radiography imaging system, based on a cooled high-resolution CCD camera (Burt, 1991), has been developed to replace film radiography. This system enables long sequences (> 100 images) of high resolution images to be obtained at fast data acquisition and transfer rates (up to 8. $10^6$ pixel.$s^{-1}$).
Movements of regions of interest in sequences of images during an engine operating cycle are measured using cross-correlation tracking software (Davies, 1980).

The performance of a new Rolls-Royce imaging system for test bed use is discussed and the results of an X-ray test on an Adour engine are described.

## 2. INTRODUCTION

The two X-ray sources currently in use are electron linear accelerators (Raytech SX1500 and SX3000) of maximum energy 11 MeV that are transportable between suitably radiation-shielded test beds at Bristol, Hucknall (Fig. 1) and Pyestock.

Sequences of film or video images are obtained during different engine transients to determine the complete envelope of component movements in each cycle. Each image is analysed by photogrammetrists who take measurements either manually or with the use of automated template-tracking software.

The whole process is very labour intensive with the film analysis, in particular, requiring many weeks of work. It is only possible, therefore, to provide a limited analysis of experimental results within a short period after completion of the actual X-ray tests

## 3. ELECTRONIC RADIOGRAPHY

The replacement of film by electronic radiography systems incorporating cooled CCD cameras gives the advantages of:

- high dynamic range with low noise characteristics
- inherently stable system giving high measurement accuracy
- digital format of images for cheaper and simpler archiving
- ability to process and analyse images rapidly using customised computer software

An Astrocam 4100 cooled CCD camera was selected for the electronic radiography work to investigate the replacement of the current Rolls-Royce film system. The principal characteristics of the CCD used in this camera are given in Table 1.

| | |
|---|---|
| CCD Chip | Kodak KAF-1300L |
| Pixel Size | 16μm x 16μm |
| Number of Pixels | 1280 x 1024 |
| Signal Resolution | 12 bit (4096 grey levels) |
| Dark Current | 10 $e^-$.$pixel^{-1}$ .$s^{-1}$ at -40°C |
| Read-out Rate | 8.$10^6$ pixel.$s^{-1}$ (maximum) |

**Table 1 - ASTROCAM CCD CAMERA DATA**

An X-ray image is obtained using an X-ray scintillation screen (Moharil, 1994) mounted on the inner front face of a light-tight housing (Fig. 2). This screen, measuring 450mm x 360mm, is viewed with the CCD camera via two separate mirrors set up to position the camera out of the radiation beam. The camera is optically coupled to the screen using a range of lenses whose focal length is selected to match the requirement of pixel size and field of view for the particular test application.

## 4. CCD CHIP OPERATING PARAMETERS

For the Kodak KAF 1300-L selected for this work, the full well capacity is ~ 150,000 electrons. Built-in anti-blooming, that allows for considerable light overloads (x1000) without the production of charge spillage onto adjoining pixels, reduces the effective area occupied by the imaging pixels by ~ 30%. This also reduces the quantum efficiency of the CCD by the same proportion. Peltier cooling maintains the chip at a temperature of ~ -40°C for low dark current operation, resulting in a figure of 10 $e^-$ .$pixel^{-1}$.$s^{-1}$ . There is, in addition, noise associated with the read-out of each pixel. This is, typically, 8 $e^-$ .$pixel^{-1}$ at 1.$10^6$ pixel.$s^{-1}$ and 40 $e^-$ .$pixel^{-1}$ at 8.$10^6$ pixel.$s^{-1}$ read-out speeds.

The total signal: noise ratio for any pixel will, therefore, be determined by the individual contributions from the imaging

*Paper presented at an AGARD PEP Symposium on "Advanced Non-Intrusive Instrumentation for Propulsion Engines", held in Brussels, Belgium, 20-24 October 1997, and published in CP-598.*

process (Stark *et al*, 1992):-

- the electrons generated in the pixel as a result of absorption of the light photons produced by X-ray interactions in the converter screen
- electron noise in individual pixels (dark current)
- read-out noise in the transfer of charge to the output ADC

The noise contributions become significant if the full well capacity of the chip is not utilised, such as when the test object very strongly attenuates the X-ray beam and produces a low X-ray beam intensity at the screen or when short time exposures are necessary. In both these cases, electronic gain is required that reduces the well depth by a factor of up to x18. As the signal:noise ratio in a radiographic image (Van Biesen, 1989) has a direct influence on the achievable accuracy of the template tracking software, there will be a different associated measurement accuracy for every region of interest in each image.

The behavior of the dark current in individual pixels (reflected in the overall level of noise) is one of the factors to be considered in determining achievable accuracy. Radiation damage effects on the CCD chip resulting in an increase in dark current have therefore to be minimised (Hopkinson, 1994) and correction factors applied, where possible, to the image grey scale value of those pixels ("hot" pixels) that have significantly higher dark current (Mohammadzadeh *et al*, 1997; Prytherch, 1996).

## 4. TEMPLATE TRACKING SOFTWARE

Computer software is used to carry out automatic analysis of each region of interest in an image and to track the movement of a specific feature in that image from frame to frame .

This technique requires the definition of a template for each region of interest. The template incorporates pixels in the image that characterise the shape of that specific component and this is used to carry out a search for the best new position of the component . With this defined template, a cross-correlation technique is used to search for the best match for this template in all new images. The matching process generates a 3D correlation surface that should have one maximum indicating the best matching position in coordinates x, y that correspond to the pixels in the image. The position of the maximum is then determined to sub-pixel accuracy by using interpolation techniques over the surface.

A new software program has been written that aids in the definition of templates by first carrying out edge detection on the region of interest. The number of pixels across an edge is user-selectable and may be defined in terms of the gradient at that edge. Following the definition of all the templates, using the first image of the sequence, all the subsequent images in the sequence are analysed. This software is implemented on a Sun SPARC network.

Tests have been carried out using the template tracking software on radiographic images of a micrometer gauge taken with a 225keV X-ray set (Fig. 3) . For each selected micrometer clearance, sequences of images were obtained and measurement errors determined from the tracking software results (Table 2). Errors given are the standard deviation in the difference between two tracked points (the tips of the two jaws of the micrometer) for five repeat measurements at each micrometer spacing. The pixel size corresponds to 372 μm. No preliminary image processing was used prior to carrying out the template tracking. The changes (Δ) are the differences between two successive measured micrometer spacings and the results correspond to the type of data that would be extracted from sequences of X-ray images of an engine under test. These good quality images were of high contrast and low noise with signal:noise ratios at the two template positions of ~ 16 dB. This ratio is defined by the signal - background grey scale difference divided by the standard deviation of the background noise in grey levels. Maximum grey scale level (4096) corresponds to 12 bits.

| Micrometer spacing (μm) | Measured spacing (μm) | Change Δ (μm) |
|---|---|---|
| 1005 ± 5 | 1003 ± 4 | - |
| 2005 ± 5 | 2001 ± 3 | 1002 ± 5 |
| 2505 ± 5 | 2525 ± 18 | 524 ± 18 |
| 3005 ± 5 | 3046 ± 6 | 521 ± 19 |
| 3305 ± 5 | 3379 ± 8 | 333 ± 10 |
| 3605 ± 5 | 3686 ± 6 | 307 ± 10 |

**Table 2 - ACCURACY MEASUREMENTS**

## 5. HIGH-ENERGY X-RAY TESTS ON AN ADOUR ENGINE

During dynamic testing of an Adour engine on No. 104 Test Bed, Filton, Bristol in May 1995, electronic X-ray radiography was carried out using the RR Applied Science Laboratory cooled-CCD camera system. Approximately one hour of engine running time was used to investigate image quality and measurement accuracy over a number of engine operating cycles. A typical image from the sequences obtained is shown in Fig. 4. This covers the region of the compressor indicated in the general arrangement of Fig. 5.

Because of the off-set of the imaging system from the engine casing, the X-ray image obtained is magnified by a linear factor of x .31. The field of view, given by the size of the screen (450mm x 360mm), actually corresponds to an area of 347mm x 278mm on the engine and therefore, defines the pixel size as 271μm.

During these X-ray tests, images were recorded to disc every 17 seconds. This was the result of a 4 seconds exposure, 2 seconds read-out, 4 seconds of writing the image to disc and 7 seconds for clearing the camera for the next exposure. With the improvements to computer hardware and image acquisition software, tests today requiring exposures of 4 seconds would result in total cycle times of 6 seconds. Speed of acquisition now is limited by the exposure time necessary to obtain signal levels in each pixel to match the accuracy required from measurements. Under best conditions, good quality images may be obtained in 1-2 seconds using the present X-ray linac sources.

A sequence of 100 images was acquired during a 30 minute engine performance cycle test. In analysis of images, any number of templates of different regions of interest may be defined. In this example, four templates were defined in the first frame of the cycle. Templates 1 and 2 were points on a tungsten calibration bar fixed as a datum reference on the front of the X-ray imaging housing and Templates 3 and 4 were the

4th stage compressor casing and root platform (Fig. 5).

All four templates were tracked throughout the 100 images and either absolute values were plotted e.g. axial (x) values of Template 4 as a function of time (Fig. 6), giving gross engine movement, or difference values were obtained e.g. radial (y) variation in the compressor root-casing clearance , Template 3 - Template 4 (Fig. 7).

The results of the gross axial movement of the 4th stage compressor shown in Fig. 6 demonstrate the changes that result during rapid accelerations and decelerations and these match the changes in logged engine parameters during the same run.

The variation in compressor root-casing radial clearance (Fig. 7) indicates an increase of ~ 1 mm during slam decels from maximum to idle. The small degree of scatter in the results for the period of steady-state running from 500 to 1000 seconds, given the large number of data points obtained, gives confidence in the measurements and in the accuracy of the results.

## 6. MEASUREMENT ACCURACY CHECK

In order to obtain quantitative estimates of measurement repeatability in these Adour tests, Templates 1 and 2 were tracked in the sequence of 100 images. The axial (x) difference between these two fixed points should remain constant. The results, given in Fig. 8, indicate the spread of results about a mean value (4.12 mm), with the ± 1 standard deviation limits included. This shows that most of the results fall within a standard deviation of 0.05 pixels, corresponding to ~ 17μm . The larger scatter during the acels/decels could either be due to relative movement of external components causing changes in the radiographic images or to vibration in the housing resulting from increased air flows and/or noise levels . The results give a good demonstration of the sub-pixel accuracy obtainable with the template tracking technique.

## 7. CONCLUSIONS

Good quality X-ray images are obtainable using a cooled-CCD camera imaging system in an operating engine environment on a test bed. Analysis of a sequence of 100 images taken during a performance cycle of an Adour engine demonstrates the capability of the system for observing and measuring component movement to sub-pixel accuracy.

The CCD chip should be ciosely monitored during its operating life to determine the degree of deterioration in dark current of individual pixels with X-ray operation and the extent to which these changes affect the required measurement accuracy.

## 8. REFERENCES


Buchanan, R.A. (1973), "High Energy Radiography" , Lockheed Palo Alto Research Laboratory Report LMSC-D354728, October.

Burt, D..J. (1991), "CCD performance limitations : theory and practice", *Nuclear Instruments and Methods in Physics Research* **A A305**, 564-573.

Davies, D.L., Smith, P.H. and Liutermoza, J.F. (1980) "Discontinuous registration of industrial radiographs using profile analysis and piecewise correlation techniques" , *Optical Engineering* **19**, No. 3, May/June, 425-432.

Hopkinson, G.R. (1994), "Radiation effects on solid state imaging devices", *Radiat. Phys. Chem.* **43**, No. 1/2, 79-91.

Mohammadzadeh, A. , Hopkins-Bond, I., Holmes-Siedle, A., Watts, S.J. and Holland , A. (1996), "The effects of radiation damage on the imaging performance of charge-coupled devices", in C.O. Fischer, J.Stade and W. Bock (eds.) *Proceedings of the Fifth World Conference on Neutron Radiography*, Berlin, Germany, DGZfPE.V., June 1997.

Moharil, S.V. (1994), "A review of X-ray imaging phosphors", *Bull. Mater. Sci.* **17**, No. 1 February, 25-33.

Prytherch, H. (1996) , "Dark signal anomalies in the Kodak KAF 1300-L charge-coupled device" , *Optical Engineering* **35**, No. 6, June, 1796-1798.

Pullen, D.A. , (1971) "Radiography applied to determining dynamic conditions inside aero-engines", *British Journal of Non-Destructive Testing*, **13**, No. 2, March.

Stark, B., Nölting, B. Jahn, H. and Andert, K. (1992), "Method for determining the electron number in charge-coupled measurement devices" , *Optical Engineering* **31**, No. 4, April, 852-856.

Stewart, P.A.E. (1975), "Engine testing using advanced techniques" , *The Aeronautical Journal of the Royal Aeronautical Society*, August , 331-343.

Stewart, P.A.E. (1987) , "Imaging techniques for gas turbine development" , International Seminar on Laser and Opto-Electronic Technology in Industry" , SPIE **699** 94 - 110.

Van Biesen, J. (1989) , "Measurements of signal-to-noise ratio (SNR) of industrial X-ray film" , in J. Boogard and G.M. van Dijk, (eds.) *Proceedings of the 12th World Conference on Non-Destructive Testing*, Amsterdam, Netherlands, 23-28 April, **1**, 117-119.



## ACKNOWLEDGMENTS

This work has been carried out with the support of DERA Pyestock. The authors wish to thank Rolls-Royce plc for permitting presentation of this paper.

FIGURE 1: NO. 10 X-RAY TEST BED AT HUCKNALL

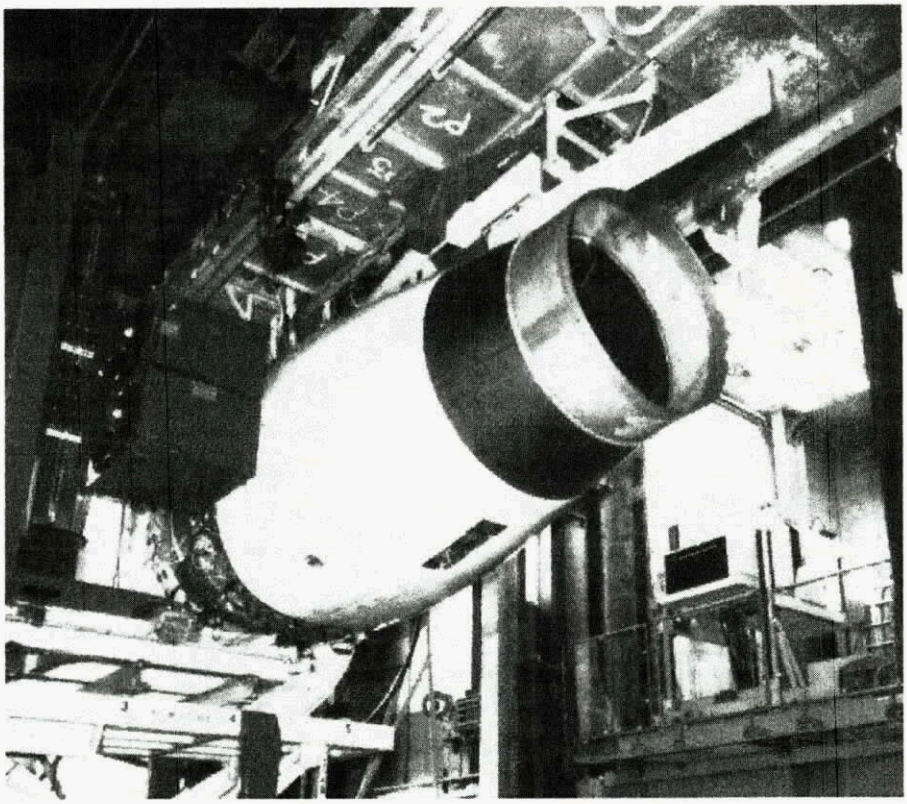

FIGURE 2: SCHEMATIC DIAGRAM OF CCD CAMERA HOUSING

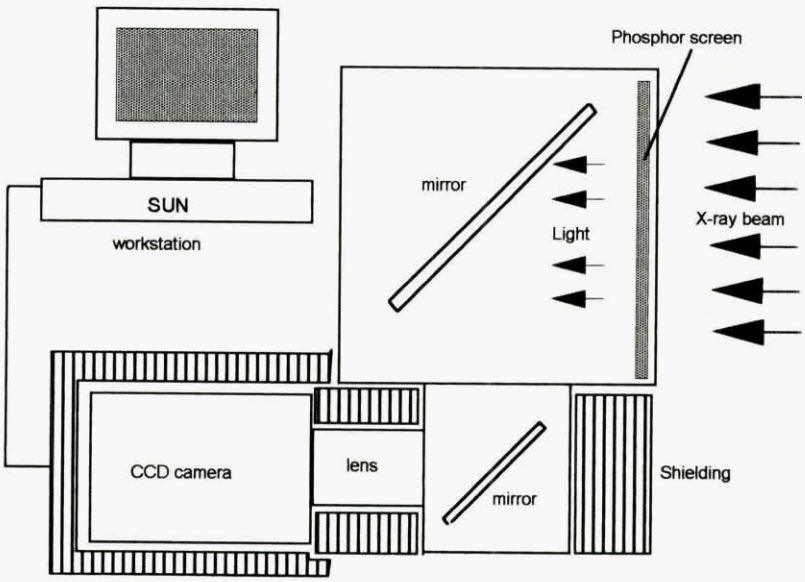

FIGURE 3: RADIOGRAPHIC IMAGE OF MICROMETER TEST GAUGE

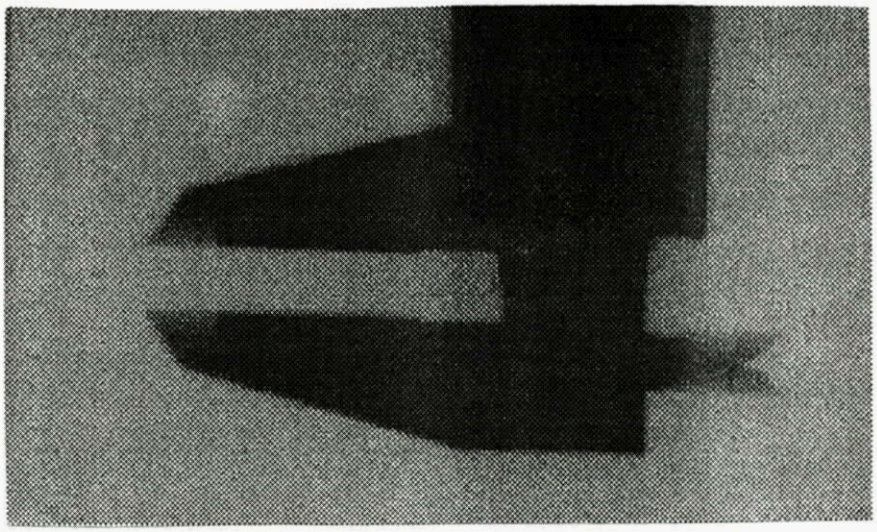

FIGURE 4: ELECTRONIC RADIOGRAPHY IMAGE OF THE COMPRESSOR SECTION OF AN ADOUR ENGINE ON TEST

FIGURE 5: GENERAL ARRANGEMENT OF THE ADOUR ENGINE COMPRESSOR

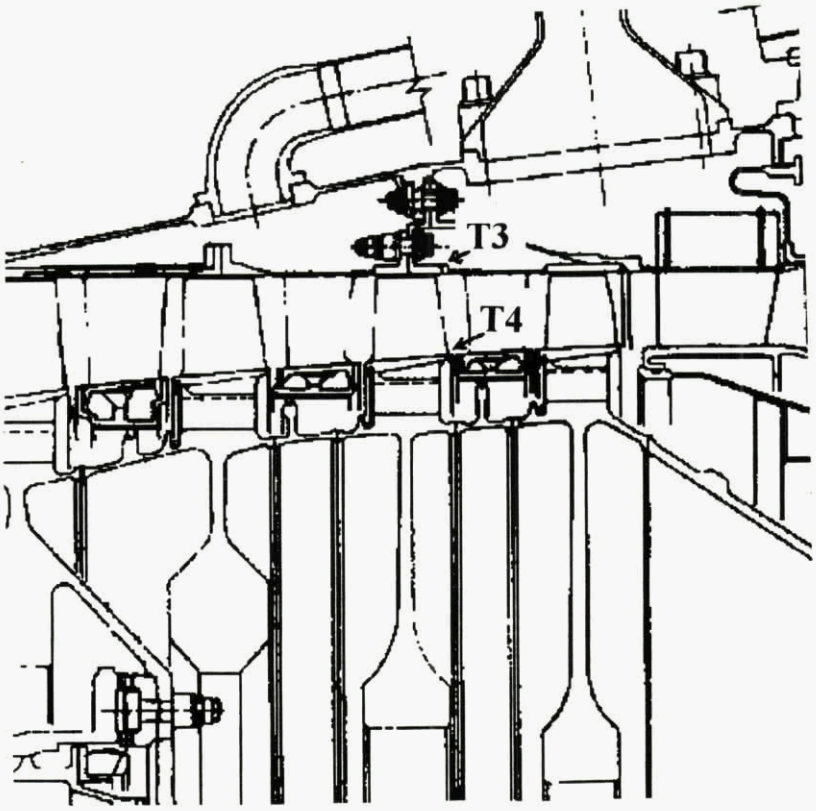


FIGURE 6: GROSS AXIAL MOVEMENT OF THE 4TH STAGE COMPRESSOR OF THE ADOUR ENGINE

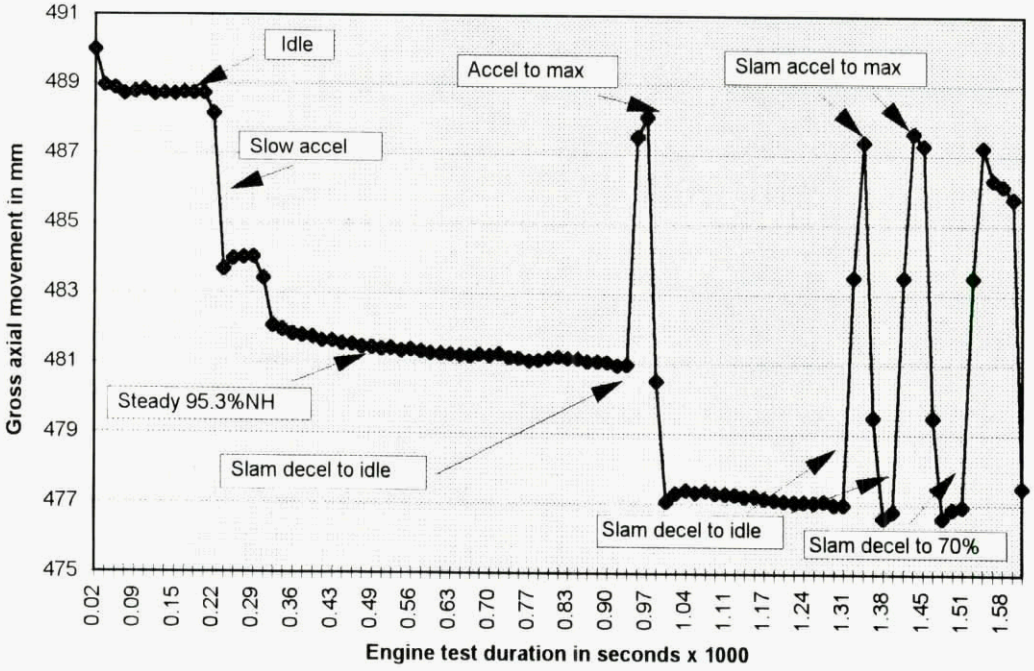

FIGURE 7: RELATIVE MOVEMENT OF 4TH STAGE COMPRESSOR ROOT PLATFORM WITH RESPECT TO CASING

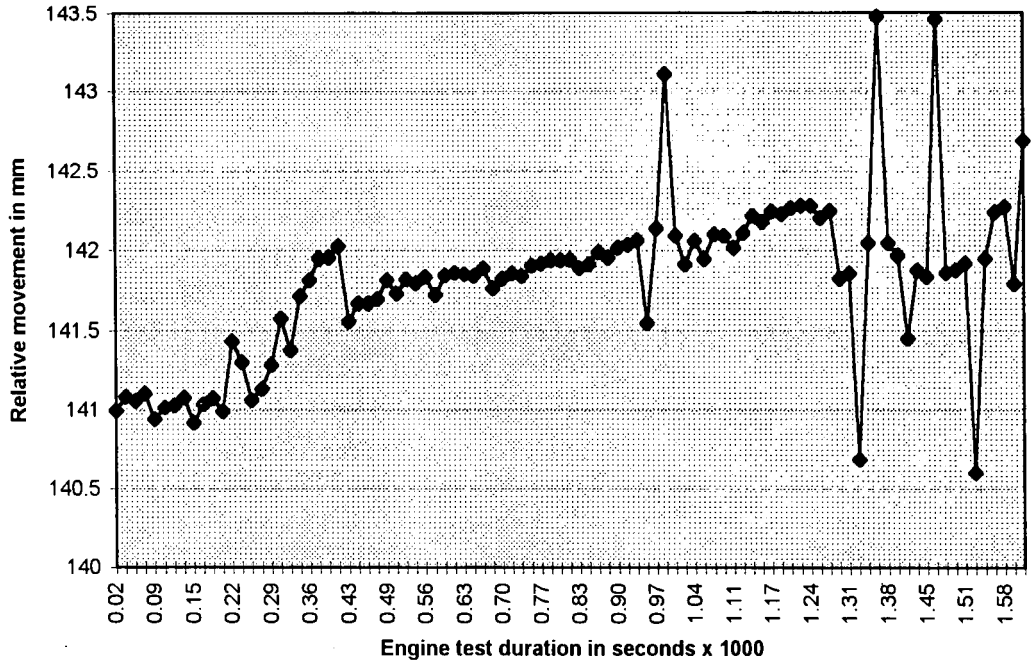


FIGURE 8: MEASURED POSITIONS OF TWO FIXED POINTS ON CALIBRATION BAR

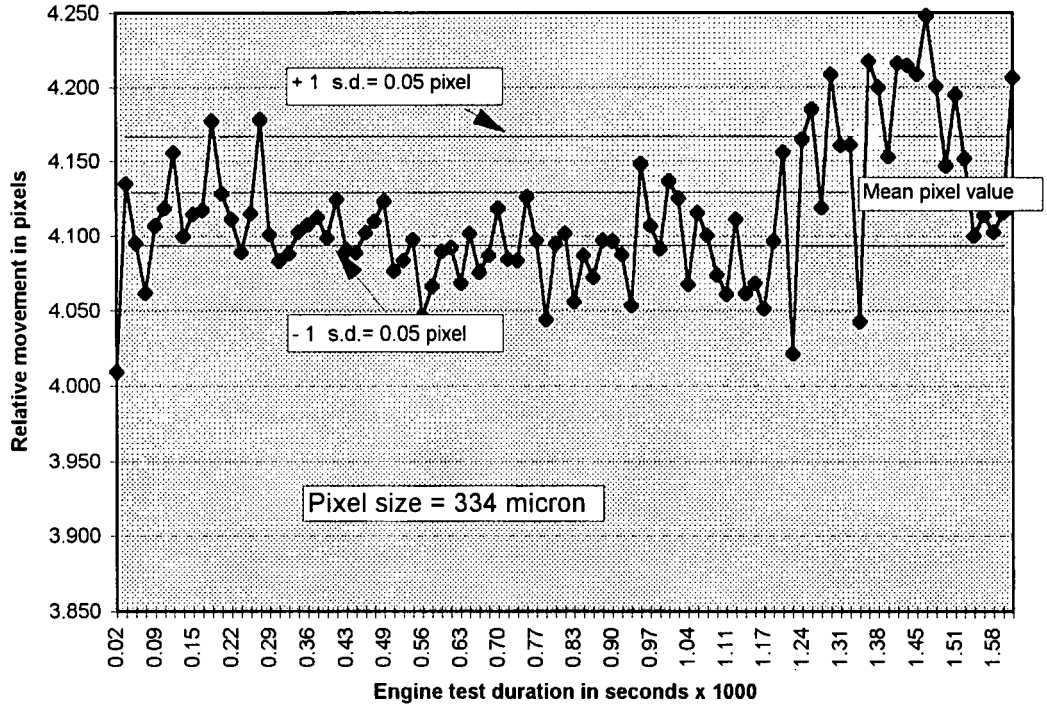

Paper 36
Author J.D. Rogers

Q: Lamarque

What is the life time of the CCD sensor exposed to the radiation?

A: We have incorporated a considerable amount of X-ray shielding into the housing of our new Electronic Radiography system. To date we have only had approximately 1 hour continuous operation into high energy X-rays (if up to 11 μv) although it has been used for more than 20 hours operation at low energies (up to 225 μv). This operation has resulted in little change to dark current performance and no noticeable change in measurement accuracy. Larger term operation will require monitoring and CCD chip replacement will be carried out when necessary.

Q: Russo

Could you comment on the reliability of electronic radiography versus current X-ray imaging equipment ?

A: We have used our electronic radiography system twice with operating engines on test beds. This experience leads us to believe that, with the necessary radiation and acoustic shielding of electronics, reliability of the equipment will be high, certainly higher than that of the current system which utilises a mechanical film cassette changing mechanism.

# Measurement of Unsteady Wake-Boundary Layer Interaction Using Hot Films

Zenebe Gete & R. L. Evans
The University of British Columbia
Department of Mechanical Engineering
2324 Main Mall
Vancouver, B.C. V6T 1Z4, CANADA

**Abstract**
Boundary layers developing on a surface subject to the intermittent passage of wakes, such as those on turbomachinery blading, are known to be highly unsteady. In this experimental study, a flat plate mounted in a wind tunnel downstream of a moving wake generator was used to model the wake-boundary layer interaction process in actual turbomachines. The boundary layer and the wall shear stress developing on the flat plate in this unsteady environment were measured using hot wire Anemometry and hot film sensors mounted on the plate surface. Measurements were taken at several locations downstream of the plate leading edge, and at several values of the reduced frequency. The results from the hot-film sensors showed that the unsteady boundary layer resulted in significantly higher losses in comparison to a steady boundary layer developing in the absence of passing wakes.

## 1. Introduction

Flows in compressors, turbines, reciprocating engines, propulsion engines, and on aircraft surfaces, ships, rockets, etc., are mostly turbulent. In particular, the flows in turbomachines are marked with the combined effects of turbulence and periodic fluctuations. In practical applications, periodic unsteadiness may be the source of vibration, noise, structural failures, reduced performance due to boundary layer growth and separation, and time dependent heat transfer processes. Turbulent boundary layers in turbomachines are both three-dimensional and unsteady. The flow becomes periodically unsteady due to the relative motion of the rotor and stator blades in a stage. Streamlined ( slender shaped ) bodies like airplane wings and turbomachinery blades are subject to significant friction forces. Estimation of these forces may be obtained experimentally through velocity and wall shear stress measurements in the boundary layers.

The ultimate goal of many experimental studies of fluid flow is to determine surface effects like skin friction, heat transfer and pressure distribution. In particular, knowledge of the drag created by fluid flowing over a solid surface is essential in the understanding and design of many practical applications, whether it is a turbomachine, an aircraft wing or flow through a pipe.

Skin friction and heat transfer gages have been traditionally used to disclose particular features of surface flows. Some devices used to measure the wall shear stress depend on the flow in the immediate vicinity of the sensor. These methods also relay on established correlations between the flow and the shear stress. The flush-mounted sensor is such an instrument [11].

The heat transfer rate $Q_w$ to the fluid is related to the wall shear stress $\tau_w$ by

$$Q_w \propto \tau_w^3.$$

Heat is supplied to the probe via a high gain feedback amplifier maintaining a constant temperature above the ambient fluid temperature. In the mean time, heat is continuously conducted from the film to the fluid. This method has been applied to determine the time average wall shear stress in turbulent boundary layer flows under the assumption that the thermal boundary layer generated by the probe is smaller than the viscous sublayer thickness of the hydrodynamic turbulent boundary layer. In its early stages, the technique was developed and used by Ludwieg [5,6], Liepmann & Skinner [4 ] and Bellhouse & Schulz [1 ].

## 2. Structure Of Turbulent Boundary Layers

The structure of the turbulent boundary layer plays an important role in the measurement of wall shear stress. The velocity profiles of turbulent boundary layers, at least in moderate pressure gradients, have inner layers for which the velocity scale is the friction velocity $u_\tau$ defined by $u_\tau = \sqrt{\tau_w/\rho}$ ,[9]. Assuming a constant shear stress in the vicinity of the wall, the part of the

*Paper presented at an AGARD PEP Symposium on "Advanced Non-Intrusive Instrumentation for Propulsion Engines", held in Brussels, Belgium, 20-24 October 1997, and published in CP-598.*

velocity profile adjacent to the wall can be represented by:

$$\frac{u}{u_\tau} = f\left(\frac{yu_\tau}{\nu}\right) = f(y^+), \qquad 2\text{-}1$$

where u is the velocity in the boundary layer, y is the distance from the wall, ν is the kinematics viscosity, $u_\tau$ is the friction velocity, $\tau_w$ is the wall shear stress and ρ is the density of the flow medium.

For the viscous sublayer the equation reduces to a linear equation as

$$\frac{u}{u_\tau} = \frac{yu_\tau}{\nu} = y^+. \qquad 2\text{-}2$$

In the logarithmic region, the equation for the velocity profile becomes:

$$\frac{u}{u_\tau} = A\log\left(\frac{yu_\tau}{\nu}\right) + B. \qquad 2\text{-}3$$

A and B are universal constants.

The viscous or linear region extends from the wall to $y^+ \approx 5$, the buffer zone extends from $y^+ \approx 5$ to $y^+ \approx 45$, the logarithmic region spans from $y^+ \approx 45$ to $y/\delta \approx 0.2$ while the wake region extends from $y/\delta \approx 0.2$ to the free stream where δ is the boundary layer thickness. The turbulent boundary layer is characterized by large scale eddies in the outer region. Characteristic length and time scales are proportional to δ and $\delta/U_o$ respectively. The eddies have long life times because of the low shear stress environment in which they reside.

The logarithmic region is marked with eddies having length scale proportional to $y^+$ and time scale proportional to $t^+ = \nu/u_\tau^2$. The logarithmic region tends to adjust to the flow conditions more rapidly. The viscous region is also characterized by length and time scales that depend on the wall units ($y^+$ and $t^*$) as shown by Haritonidis [2]. The distinguishing feature of this region is its ability to adjust rapidly to changes of the wall conditions. This unique behavior makes it a suitable portion of the boundary layer to infer some flow characteristics to the wall conditions. It may be used to determine the instantaneous wall-shear stress.

## 3. Measurement of Wall Shear Stress by a Heated Element

### 3.1 Experimental Setup

A 2-Dimensional model of a turbomachine stage was designed and integrated in a low-speed wind tunnel located in the aerodynamics laboratory in the Department of Mechanical Engineering at the University of British Columbia. The test section of the wind tunnel has a 400 mm X 250 mm cross-section, and the maximum free stream velocity is about 20 m/s. Prior to the inclusion of the unsteady wake generating mechanism the free stream turbulence intensity was 0.5%.

The unsteady wake generating rig was installed immediately upstream of the test section. The moving mechanism has airfoils attached to rotating synchronized gear belts thereby generating periodic wake disturbances in the oncoming air flow. The stator blade in a real machine was represented by a flat plate in the wind tunnel. The leading edge of the flat plate was located at 60 mm downstream from the 1/4th chord length of the airfoils ( the location at which they are attached to the gear belts). The flat plate was tripped at x=20 mm from the leading edge in order to generate a turbulent flow base before the periodic perturbations of the traveling wakes. The wind tunnel along with the unsteady rig and the flat plate on which the shear stress sensor is glued is illustrated in Figure 1.

The rate of local heat transfer from the solid surface (of the flat plate) to the moving fluid is related to the local skin friction. A wall shear stress measurement can be inferred from the heat transfer from a small element embedded in the surface of a body. The important aspects of hot elements in heat transfer operation are their sensitivity and frequency response. Since thin films have very short response time, they are suited for dynamic measurements.

In proximity to the wall, a viscous sublayer forms where the shear stress essentially remains constant, equal to the wall shear value. A thermal boundary layer develops within a laminar or turbulent boundary layer over the heated film embedded or glued on the wall. In order to neglect the effect of turbulent diffusion in the case of a turbulent boundary layer, it is assumed that the thermal boundary layer is completely submerged within the viscous sublayer.

To measure fluctuating shear stress a DISA 55P47 glue-on shear stress probe was selected. The sensor is 0.1 x 0.9 mm Nickel film deposited on a 0.05 mm thick polyimid foil carrying a 0.05 μm quartz coating as shown in Figure 2. The wall shear stress probe was calibrated against results obtained by using a Preston tube [7,8]. Wall shear stress measurements were taken at nine downstream stations on the surface of the flat plate.

**Table 1 Experimental Conditions for Wall Shear Stress Measurement.**

| X [m] | | S=0.1m | | | S=0.2m | | |
|---|---|---|---|---|---|---|---|
| | Re x$10^5$ | 20 Hz | 30 Hz | 40 Hz | 10 Hz | 15 Hz | 20 Hz |
| 0.07 | 0.144 | 0.47 | 0.7 | 0.93 | 0.23 | 0.35 | 0.47 |
| 0.1 | 0.205 | 0.67 | 1.0 | 1.33 | 0.33 | 0.5 | 0.67 |
| 0.15 | 0.308 | 1.0 | 1.5 | 1.99 | 0.5 | 0.75 | 1.0 |
| 0.2 | 0.411 | 1.33 | 2.0 | 2.67 | 0.67 | 1.0 | 1.33 |
| 0.3 | 0.616 | 2.0 | 3.0 | 4. | 0.99 | 1.5 | 2.0 |
| 0.4 | 0.822 | 2.67 | 4.0 | 5.33 | 1.33 | 2.0 | 2.67 |
| 0.5 | 1.03 | 3.33 | 5.0 | 6.66 | 1.66 | 2.5 | 3.33 |
| 0.6 | 1.23 | 4.0 | 6.0 | 7.99 | 1.99 | 3.0 | 4.0 |
| 0.7 | 1.44 | 4.67 | 7.0 | 9.33 | 2.33 | 3.5 | 4.67 |

### 3-2 Wall Shear Stress Under Traveling Periodic Disturbances

The boundary layer was perturbed by an external organized fluctuation of the traveling wave type. It was the response of the surface shear stress that was sought as a result of wake-boundary layer interactions. The cases investigated and the number of downstream stations at which wall shear stress measurements were taken are shown in Table 1. The reduced frequencies were determined from the free stream velocity, the downstream location, and the fluctuation frequency.

### 3-3 Unsteady Wall Shear Stress Results by Glue-on Probe Measurement

Typical time histories of the ensemble-averaged wall shear stress under a periodic traveling wave disturbance are given in Figure 3. The figures depict skin friction coefficients at some longitudinal stations at the indicated frequencies. The effect of the perturbations is stronger at the first few X-stations than at the far downstream stations. The effect of the disturbance produced step-like responses at the wall. This phenomenon is clear for the 30 and 40 Hz frequencies. Although the ensemble average results are not oscillatory in the fashion of the perturbations, there is an increase in the magnitude of the wall shear stress whenever there is a wake disturbance.

Figure 4 also gives sample time histories of the random fluctuation of skin friction at X = 0.1 m for the same frequencies. Figure 5 on the other hand shows time histories of the random fluctuations at successive locations along the flat plate. The random fluctuations of the wall shear stress are clearly influenced, through the interaction of the passage of the traveling wakes. These fluctuations

jump to higher levels of magnitude and remain higher than the random fluctuations without perturbation of the traveling wakes. This pattern of periodic wake - random fluctuation interaction remains significant along the flat plate as given in Figure 5 for the indicated frequencies. Higher frequencies resulted in increased wall shear stress random fluctuations which are indicative of the additional skin friction imposed on the wall.

Figure 6 depicts plots of time-averaged skin friction coefficients as a function of Reynolds number for the blade spacing S = 0.1 m. All wall shear stress values were normalized with the corresponding local free stream velocities. It is apparent that the wall shear stresses in the unsteady turbulent boundary layer flow cases ( with a few exceptions close to the leading edge where transitional effects are observed) were higher in magnitude than the corresponding steady flow values. The flow which was originally turbulent on the tripped flat plate underwent a transitional flow condition whenever it interacted with the oncoming wakes of the rotating airfoils. The velocity defect in each wake is responsible for being intermittently transitional in the near leading edge region of the flat plate.

The response of the wall shear stress was found to be highly frequency sensitive as is evident from the figures. Skin friction clearly increases with increasing frequency due to increasing nonlinear interaction of the traveling wave with the boundary layer. For instance, at x = 0.3 m ($Re_x$ = 0.6X$10^5$), the friction coefficient is greater by

approximately 10%, 20%, and 78% for 20 Hz, 30 Hz and 40 Hz disturbance frequencies respectively.

It is important to investigate the responses of the boundary layers very close to the wall, and the mechanisms by which they are driven. In general, it is known that shear stresses are dependent on the prevailing velocity gradients across the boundary layer and on the Reynolds stress terms resulting from the mixing and momentum exchanges throughout the layer. The presence of a periodically fluctuating disturbance, and its nonlinear interaction with the mean flow and random fluctuations, subjects the boundary layer to additional forces on top of the steady turbulent boundary layer case. Similar to the way in which random fluctuations lead to Reynolds stresses, periodic fluctuations also impart extra stresses to the boundary layer flow. The different forces can be identified experimentally as shown by Hussain and Reynolds [3] through the technique of triple decomposition. Such an analysis was also adopted by Telionis [10], by forming the governing differential equations similar to the treatment of steady turbulent boundary layer equations. For example, the mean momentum equation in the classical form is given as;

$$u\frac{\partial u}{\partial x}+v\frac{\partial u}{\partial y}=-\frac{1}{\rho}\frac{\partial p}{\partial x}+\nu\frac{\partial^2 u}{\partial y^2}-\frac{\partial}{\partial y}(\overline{u'v'})-\frac{\partial}{\partial y}(\overline{\tilde{u}\tilde{v}}) \quad 3\text{-}1$$

and the equation for the oscillating flow becomes;

$$\frac{\partial \tilde{u}}{\partial t}+\tilde{u}\frac{\partial u}{\partial x}+u\frac{\partial \tilde{u}}{\partial x}+\tilde{v}\frac{\partial u}{\partial y}+v\frac{\partial \tilde{u}}{\partial y}=-\frac{1}{\rho}\frac{\partial \tilde{p}}{\partial x}+\nu\frac{\partial^2 \tilde{u}}{\partial y^2}+$$

$$\frac{\partial}{\partial y}(\overline{\tilde{u}\tilde{v}}-\tilde{u}\tilde{v})-\frac{\partial}{\partial y}(<u'v'>-\overline{u'v'}) \quad 3\text{-}2$$

In these equations the Reynolds stress terms are obtained from the periodic and the random fluctuations. Therefore, an increase in the wall shear stress appears to be significant due to the coupling and nonlinear interactions of the organized fluctuation with the boundary layer.

Although it is difficult to quantify exactly what the contributions of the random and periodic fluctuations are separately, overall evaluation of the wall shear stress shows growth with the presence of organized fluctuations.

## 4. Evaluation of Wall Shear Stress From Velocity Curve Fits

One of the techniques available to approximate the wall shear stress in a boundary layer is making use of careful velocity measurements across the profile. Usually it is very difficult to produce accurate velocity measurements from hot wire probes in close proximity to the wall. The ensemble-averaged velocity data were fit with ninth order polynomials for all unsteady turbulent boundary layers at the respective stations. The best fit curves were then formulated for each velocity profile in terms of the transverse scale $y/\delta$. By evaluating the velocity derivative of each equation at the wall, the corresponding wall shear stresses were derived. Increased velocity gradients suggest higher stresses on the surface of the flat plate.

Results obtained through this technique as compared to the results of glue-on probe measurements for unsteady flows are illustrated in Figure 7. The figure depicts skin friction coefficient in terms of the reduced frequencies( $\varpi = x\omega/Ue$ ). Making use of the reduced frequency did not result in the collapse of the skin friction results. There are significant discrepancies between results obtained by glue-on probe and those obtained from the velocity curve fit data. The variation appears to be large for the lowest frequency shown. The gap, however, gets closer as the frequency was increased. All results from velocity curve fits overestimated the wall shear stress values irrespective of frequency and measurement station. Nevertheless, the increase of the skin friction when wakes interact with the boundary layer have been reproduced. Moreover, sensitivity of the skin friction to frequency is also in agreement with glue-on probe measurement results and the decay of skin friction in the downstream direction is also replicated.

A certain amount of discrepancy is expected from these two different methods. Along with the errors associated with each probe, the difficulty of measuring velocity accurately very close to the wall enhances the error when a hot wire probe is employed. In this case the uncertainties are on the order of 10% to 15%.

## 5. Conclusion

A fundamental study of unsteady wake-boundary layer interaction and the response of the ensuing wall shear stress on a flat plate have been conducted. Experimentally, traveling wave disturbances were generated upstream of the flat plate by a rotating mechanism carrying a cascade of airfoils. Unsteadiness in either a real machine or the physical model is marked with periodic regularity as a result of the relative motion of the rotor and the stator.

Skin friction results obtained from both glue-on shear stress probe measurements and those derived from velocity curve fit profiles to hot wire velocity measurements show

sensitivity of the wall resistance to the externally imposed traveling fluctuations. Skin friction coefficients increased with increasing disturbance frequency. Compared to steady turbulent boundary layer results, resistance in all the unsteady cases were higher.

For a free stream amplitude $\Delta u/Ue$ of order 0.1, frequency parameter $\varpi \approx 0.33 - 9.33$, and Reynolds number $Re_x = (0.144 \text{ to } 1.44)x10^5$, skin friction values on a tripped flat plate at x = 0.02 m from the elliptical leading edge increased by up to twice that of the undisturbed boundary layers. With the exception of near-leading edge stations, that show transitional behavior, skin friction decreased in the downstream direction but values remained higher than that of the steady case. Therefore, in approximating skin friction losses in a turbomachine stage there is a clear need to account for losses due to periodic unsteadiness. The experimental results show that the mean skin friction in periodically unsteady boundary layer flow due to external traveling oscillatory disturbances should not be estimated with steady flow skin friction results.

## REFERENCES

[1] Bellhouse, B.J. and Schulz, D.L., "Determination of Mean and Dynamic Skin Friction, Separation and Transition in Low Speed Flow with a Thin Film Heated Element," J. Fluid Mech. 1966, Vol. 24, Part 2, pp. 379-400.

[2] Haritonidis,T.H., "The Measurement of Wall Shear Stress," Advances in Fluid Mechanics Measurements, 1989, Vol. 45, pp. 231-261.

[3] Hussain, A.K.M.F. and Reynolds, W.C., The Mechanics of an Organized Wave in Turbulent Shear Flow," J. Fluid Mech. 1970, Vol. 41, pp. 241-258.

[4] Liepmann, H.W. and Skinner, G.T., "Measurements by Use of Heated Elements," NACA TN 3268, 1954.

[5] Ludweig, H., "Instrument for Measuring the Wall Shear Stress of turbulent boundary Layers," NACA TM 1284, 1950.

[6] Ludweig, H., and Tillmann, W., "Investigations of the Wall Shear Stress in Turbulent Boundary Layers," NACA TM 1285, 1950.

[7] Patel, V.C., "Calibration of the Preston Tube and Limitations on its Use in Pressure Gradients," J. Fluid Mech. 1965, Vol. 23, Part I, pp. 185-208.

[8] Preston, J.H., "The Determination of Turbulent Skin Friction by Means of Pitot Tubes," J. Roy. Aero. Soc. 1954, Vol. 58, pp. 109-121.

[9] Schlicting, H., "Boundary Layer Theory," McGraw-Hill Inc. 7th Ed. 1979.

[10] Telionis, D.P, "Unsteady Boundary Layers, Separated and Attached," J. Fluids Engineering, 1979, Vol. 101, pp. 29-43.

[11] Winters, G.J., "An Outline of the Techniques Available for the Measurement of Skin Friction in Turbulent Boundary Layers," Prog. Aerospace Sci. 1977, Vol. 18, pp. 1-57.

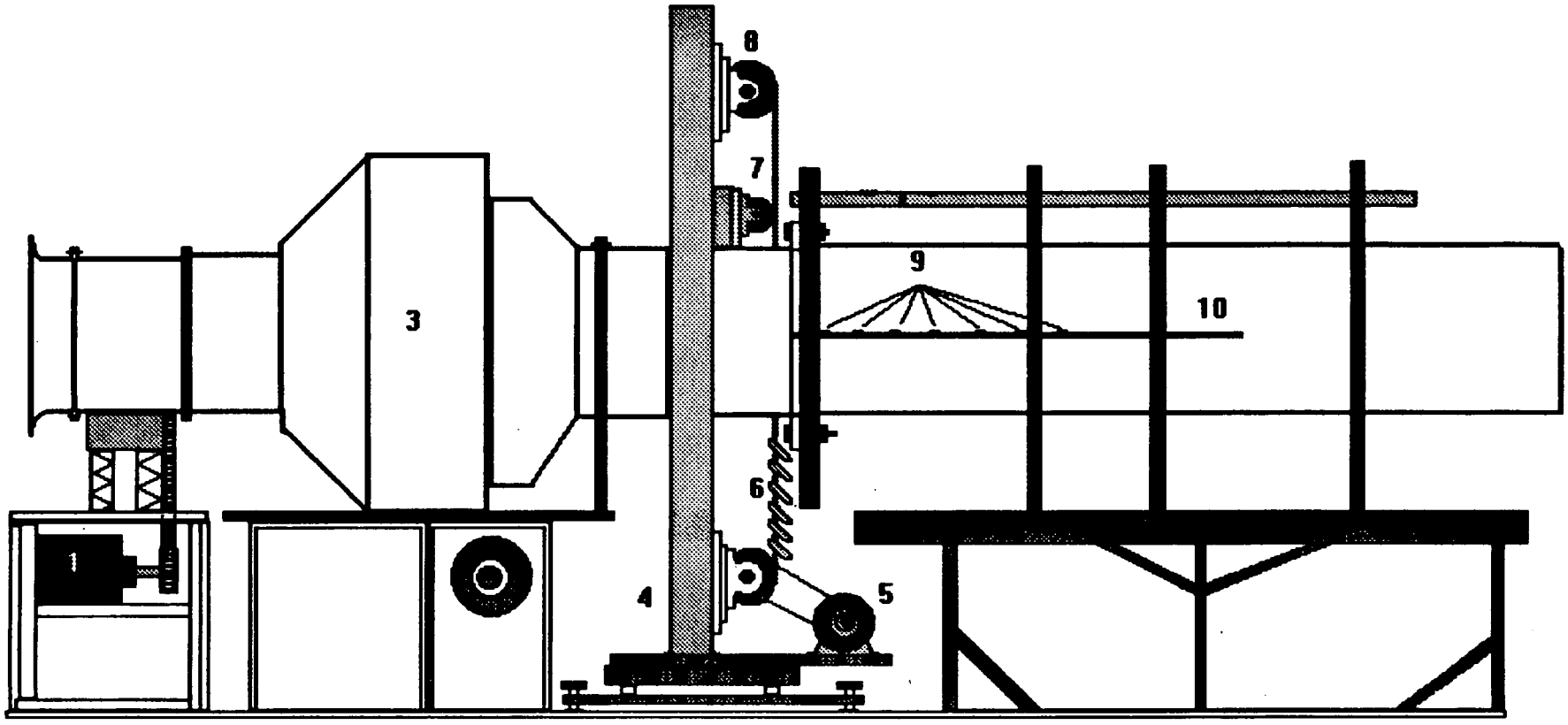


1. Wind tunnel motor
2. Fan
3. Settling chamber
4. Rig
5. Rotor drive motor
6. Airfoils
7. Gear belt
8. Gear pulley
9. Wall shear stress sensor
10. Flat plate

Figure 1. Wind Tunnel and Experimental Rig - Schematic

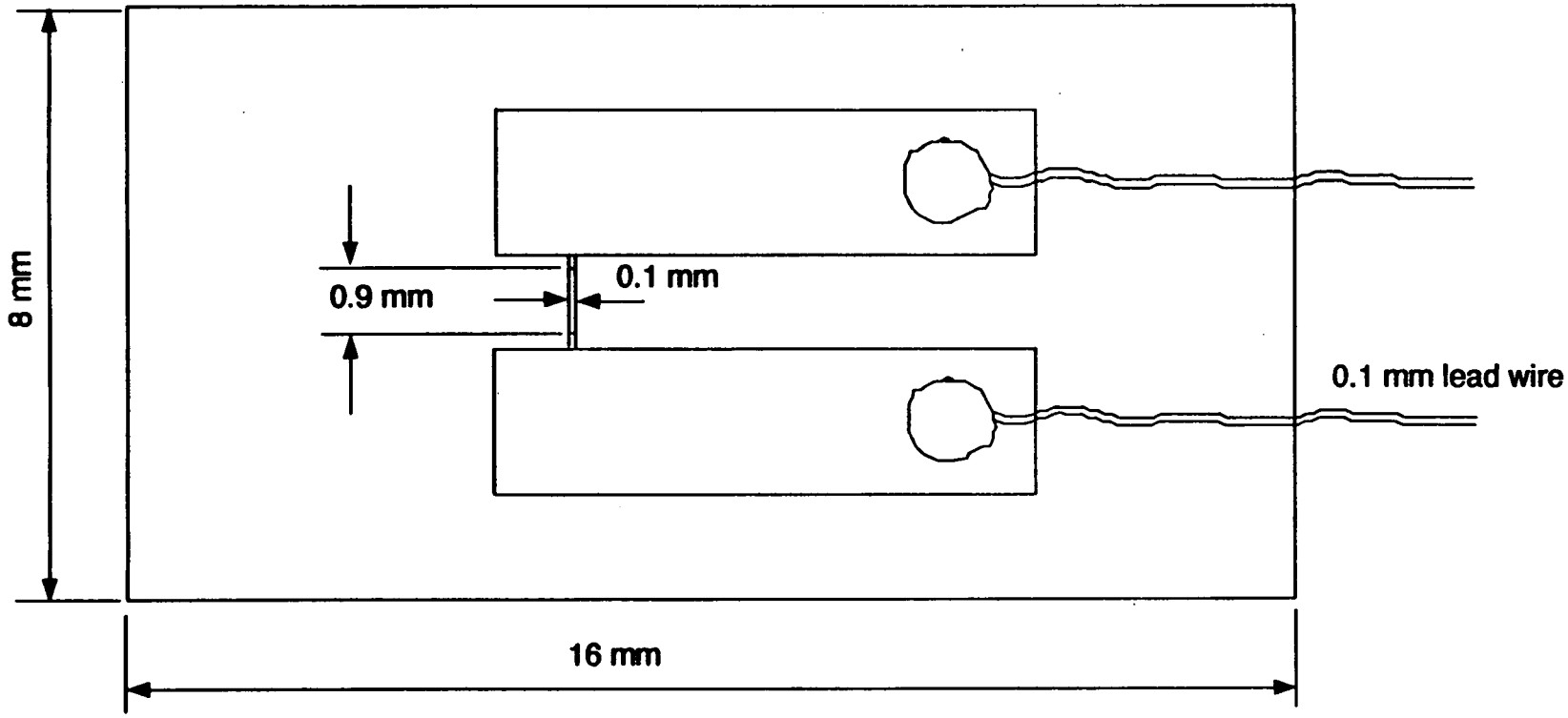


Scale 10 : 1

Figure 2. DISA 55P47 Glue-on Probe: Sensor 0.1 X 0.9 mm, Nickel Film Deposited on a 0.05 mm Thick Polymid Foil.

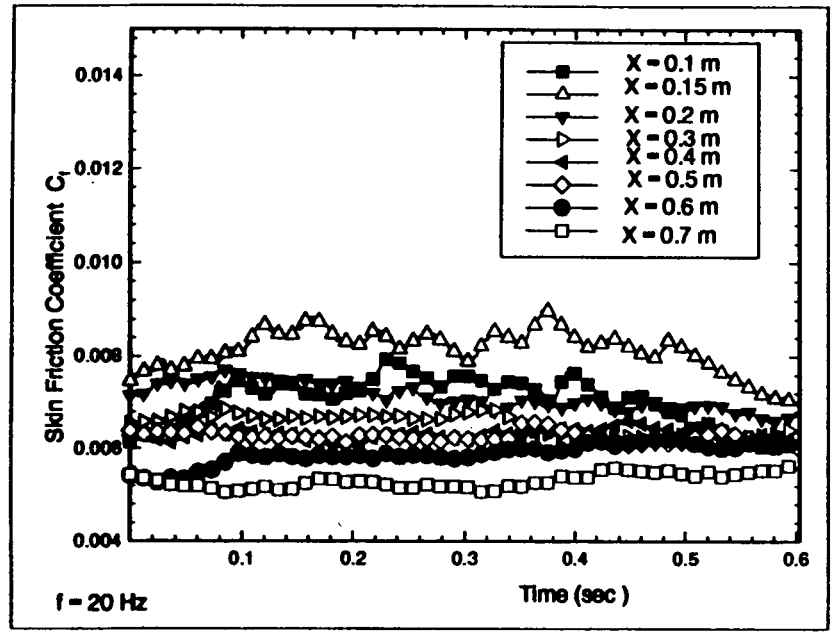


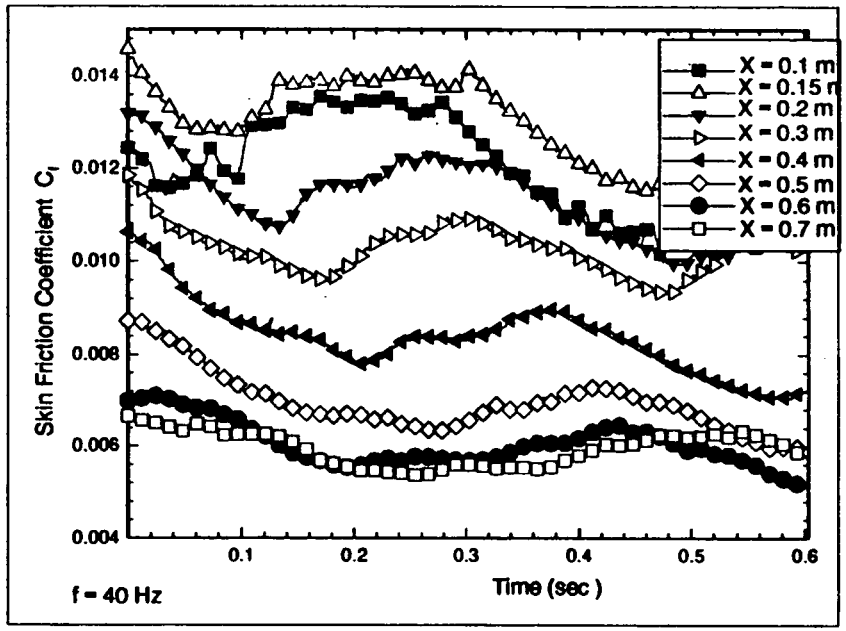


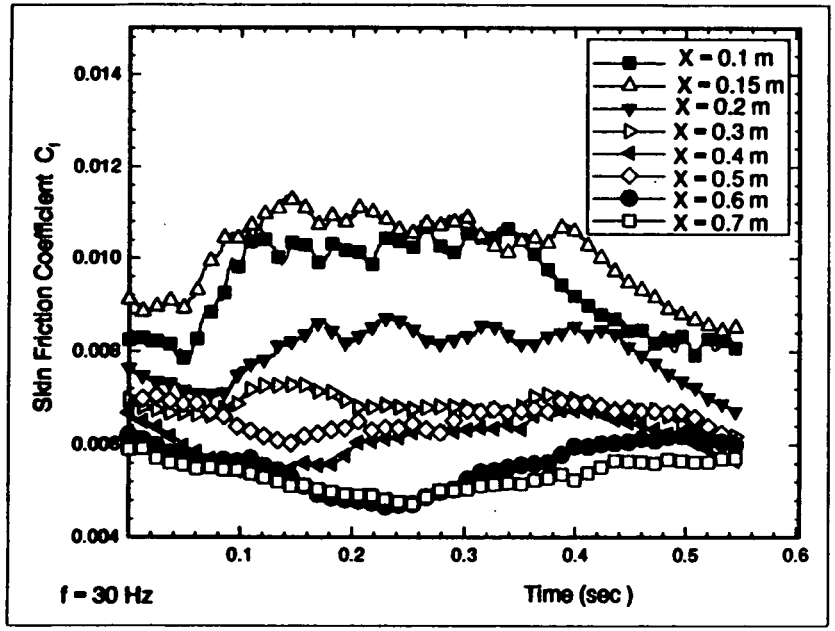


Figure 3. Time History of Wall Shear Stress Coefficient Along the Flat Plate at Constant Frequency

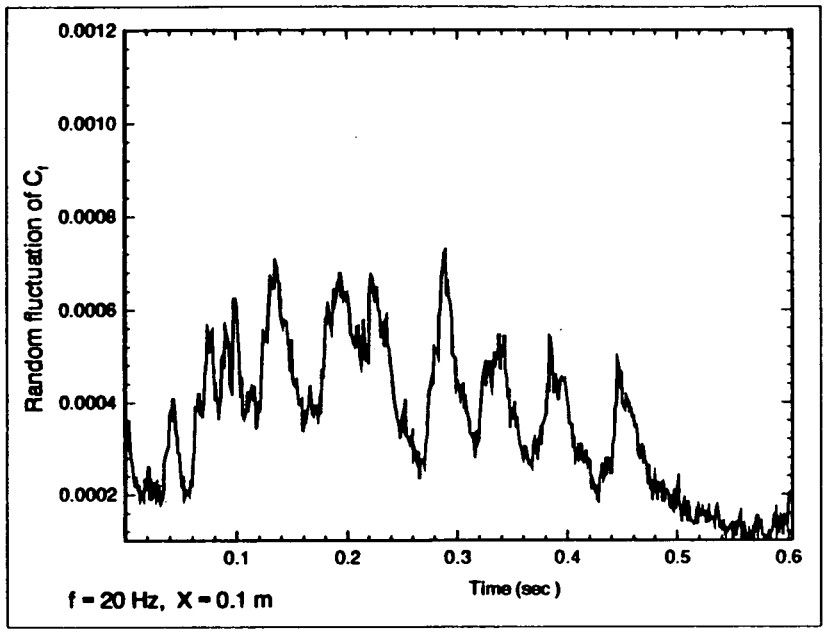


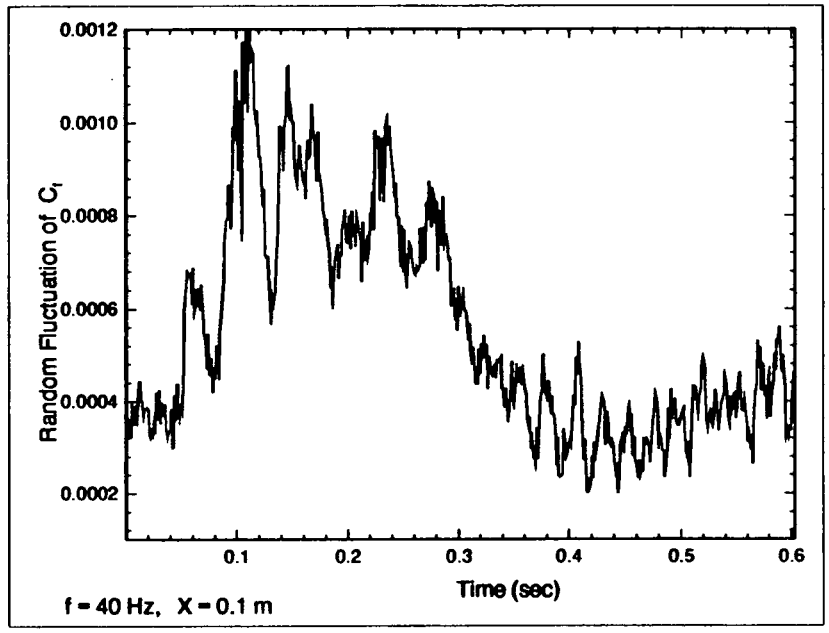


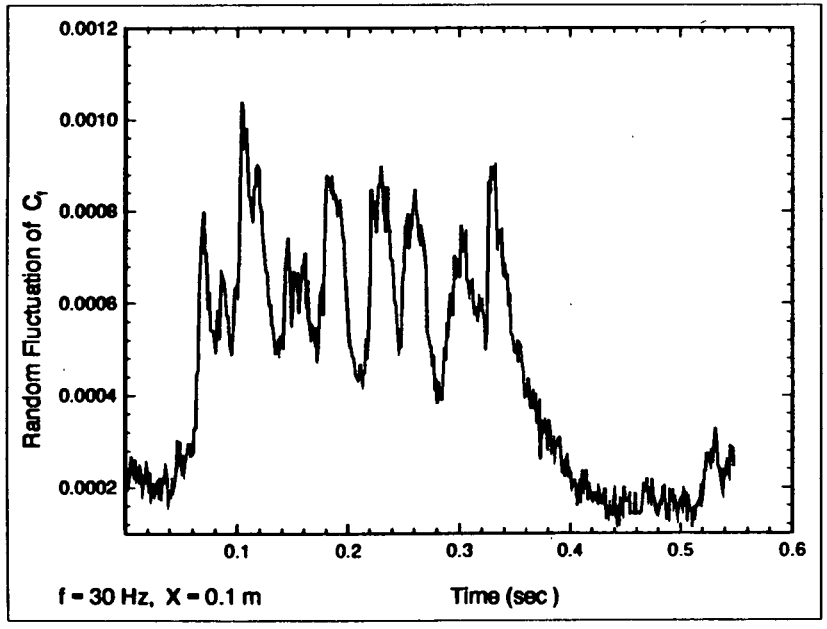


Figure 4 Time History of the Ensemble-averaged Random Fluctuation of Wall Shear Stress Coefficient Along the Flat Plate at Constant Frequency

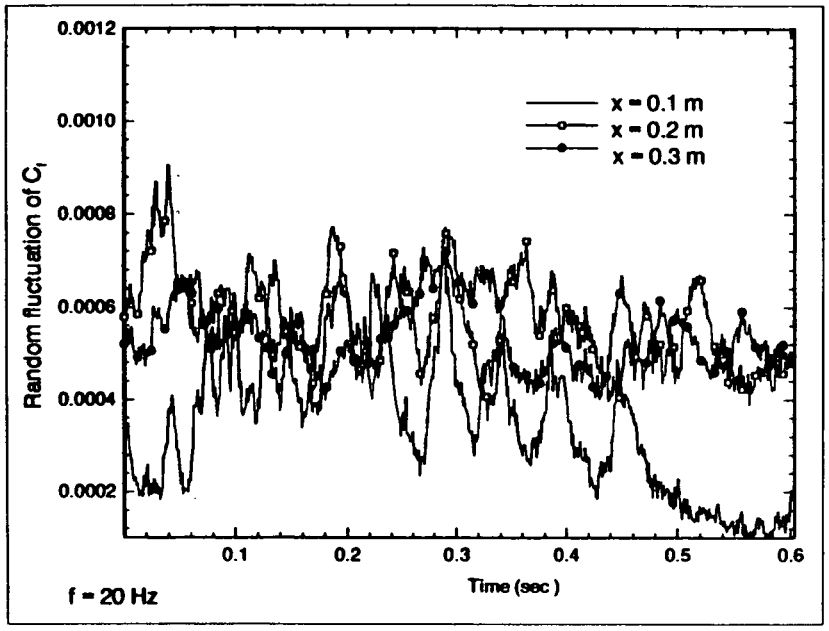


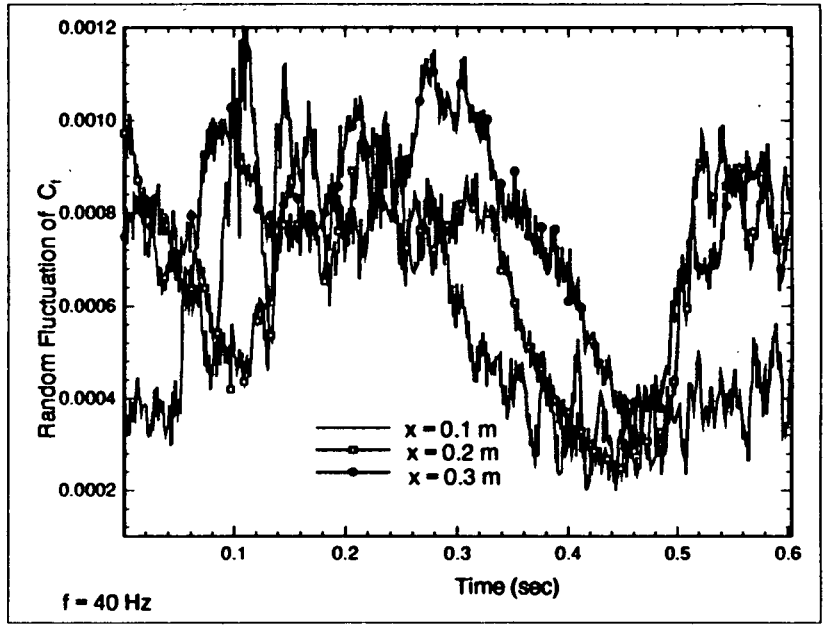


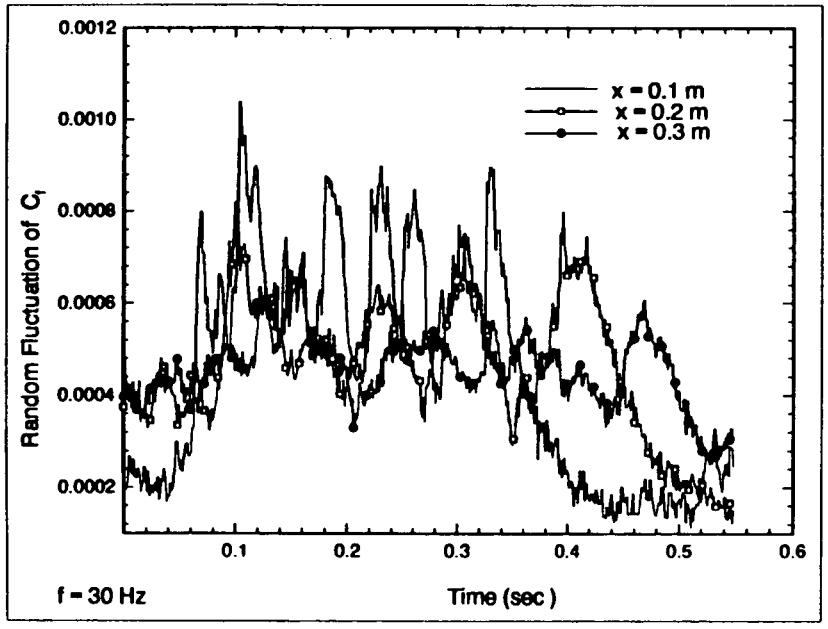


Figure 5 Time History of the Ensemble-averaged Random Fluctuation of Wall Shear Stress Coefficient Along the Flat Plate at Constant Frequency

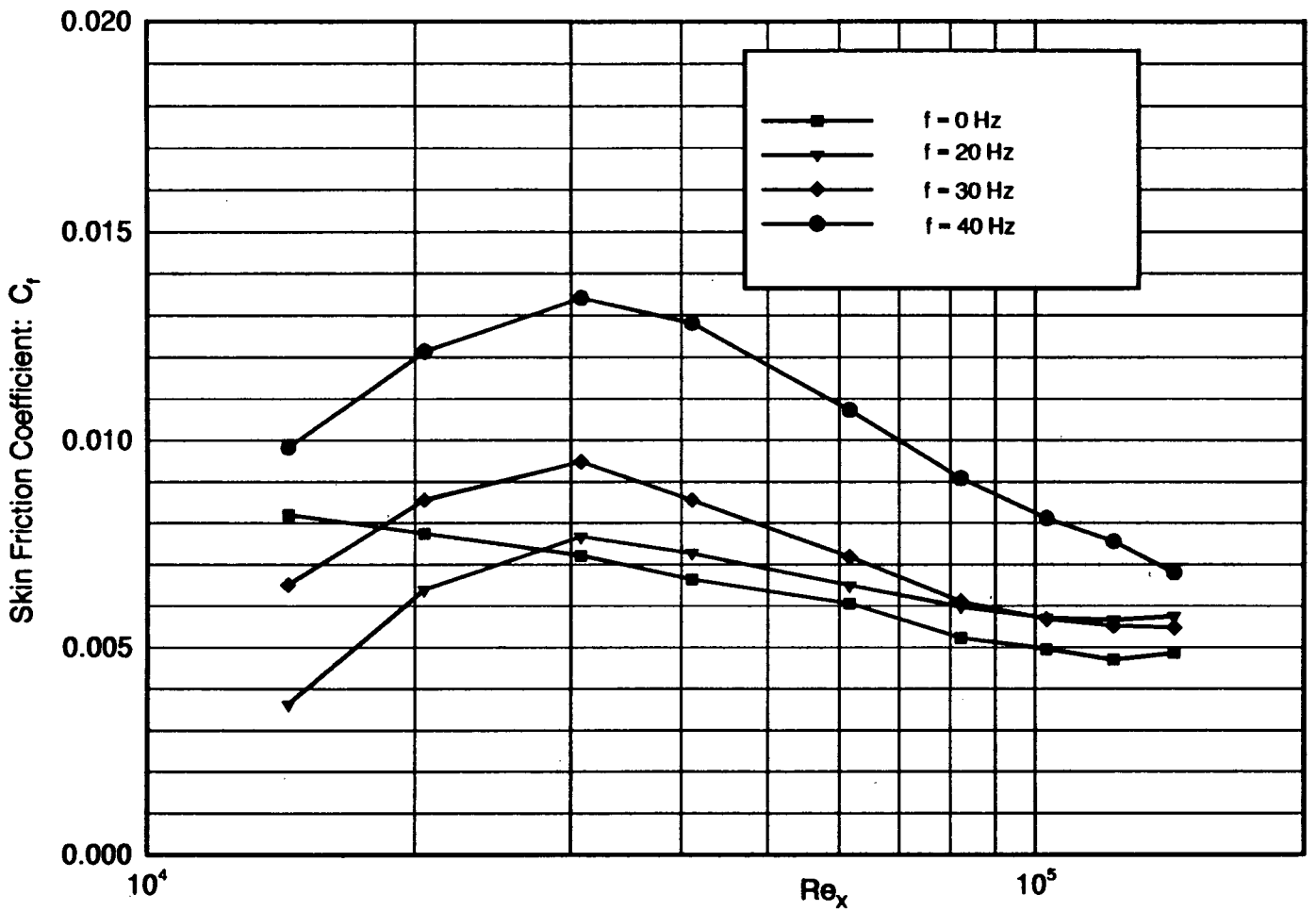


Figure 6 Comparison of Measured Skin Friction Coefficients With Varying Disturbance Frequency: S = 0.1 m
Wall Shear Stress Normalized With the Local Free Stream Velocity

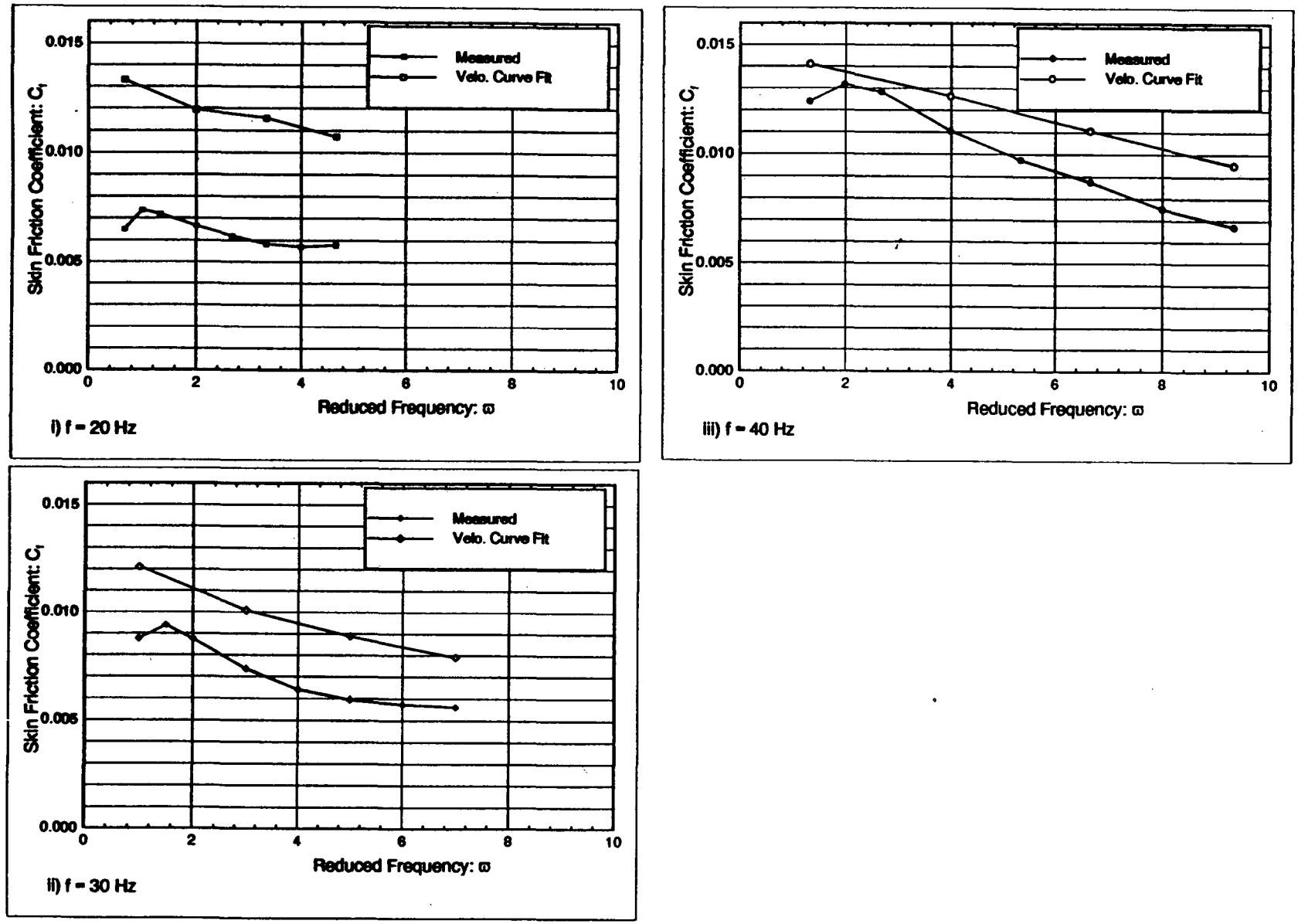


Figure 7. Comparison of Skin Friction Coefficients Obtained by Direct Measurement and Velocity Profile Curve Fits

Paper 37
Author: Evans

Q: Warnack

How do the frequencies investigated relate to the frequencies in real machines?

A: The actual frequencies are very low compared to a real machine, but the important point is that the reduced frequencies, $\omega x/U_\infty$, are of the same order as those in a real turbomachine.

# Measurements With Surface Mounted Hot-Film Sensors on Boundary Layer Transition in Wake Disturbed Flow

**Volkmar Haueisen**
Darmstadt University of Technology
Fachgebiet Gasturbinen und Flugantriebe
Present Affiliation:
**ABB** Turbo Systems Ltd
CH-5401, Baden, Switzerland

**Thomas Schröder**
MTU, München GmbH
Abt. TPA Postfach 500640
D-80976 München, Germany

**Dietmar K. Hennecke**
Darmstadt University of Technology
Fachgebiet Gasturbinen und Flugantriebe
Petersenstrasse 30
D-64287 Darmstadt, Germany

**Abstract:** Boundary layer transition with and without transitional separation bubbles on a circular cylinder in crossflow was investigated. Measurements were carried out in undisturbed, steadily disturbed, and periodically disturbed flow. Besides the surface static pressure distribution and besides the measurement of velocity profiles with a hot-wire probe the investigations were focussed on the signal distributions of surface mounted hot-films. The reaction of separation and transition to changes of the Reynolds number or the degree of disturbance can be observed. In comparison with the hot-wire traverses, which were carried out in parallel with the hot-film measurements, the experiments show that the surface-mounted hot-film-technique is suitable to obtain reliable information on transition and separation phenomena with both high spatial and temporal resolution. Measurements with surface-mounted hot-film sensors in a multistage aero-engine low-pressure turbine show that use of this technique is not only restricted to laboratory conditions but is as well suitable for complex geometry and engine conditions.

**Nomenclature:**

| | |
|---|---|
| $a$ | constant for calibration |
| $b$ | width of the wake |
| $C_p$ | pressure coefficient |
| $C_0$ | constant in King's law |
| $C_E$ | voltage coefficient |
| $d$ | diameter of the cylinder |
| $d_b$ | diameter of a bar |
| $E_0$ | constant in King's law |
| $E_0$ | base voltage of a hot-film sensor |
| $E$ | voltage |
| $e'$ | voltage fluctuation |
| $f$ | frequency |
| $H_{12}$ | shape parameter |
| $l_s$ | disturbed length |
| $l_u$ | undisturbed length |
| $M$ | number of samples per burst |
| $N$ | number of bursts |
| $Q$ | heat flux |
| $R$ | electrical resistance |
| $Re$ | Reynolds number |
| $Sr$ | Strouhal number |
| $Sr^*$ | weighted Strouhal number |
| $t$ | pitch |
| $t$ | time |
| $T$ | time for one period |
| $U_\infty$ | free-stream velocity |
| $u$ | circumferential velocity of the bars |
| $\delta$ | boundary layer thickness |
| $\mu$ | skewness |
| $\varphi$ | circumferential angle |
| $\tau$ | shear stress |

**1. Introduction:** Blade rows in turbomachines typically do not operate under steady, undisturbed conditions, as they are often achieved in wind-tunnels, but the flow is much more complex. Especially the periodic change of the velocity and of the turbulence level according to the passing wakes generated by rows upstream is characteristic for turbomachinery flow. These flow phenomena are of striking importance for separation and laminar-turbulent transition on the blade profiles and thus for the performance of turbomachines. These phenomena are not yet completely understood. Nevertheless this understanding is a basis for optimizing the design in order to satisfy today's requirements for economic performance. In this process experimental data are needed, not only to learn about the flow physics but also to validate computational methods. Surface-mounted hot-film-sensors provide a very appropriate technique for an experimental approach to these flow phenomena.

With surface-mounted hot-film-sensors, first of all, the heat transfer between a wall and a fluid can be measured. According to Reynolds' analogy the heat transfer is a measure of the shear stress at the wall. Thus, this technique is principally suitable for the analysis of separation and transition, because the streamwise shear stress distribution can be used as an indicator for these flow phenomena, which are of great technical interest. Since the early Eighties surface-mounted hot-film-sensors increasingly have been used for the analysis of separation and transition. But, taking into account the possibilities this technique offers with relatively little effort compared with other methods, its application is rather scarce. Oldfield et al. (1981) [10] have published interesting measurements on turbine profiles, which are compromised a little by the low quality of the sensors. More recent investigations, e.g. Hourmouziadis et al. (1986) [7] and Pucher and Göhl (1986) [15], show the applicability of hot-films in turbomachines. Pucher and Göhl gained informative results about transition along a separation bubble. Hodson and Addison (1990) [6] performed hot-wire and hot-film measurements in parallel and thus prove the capability of the hot-film technique to detect separation. Salomon and Walker (1995) [17] rendered multimode transition described by Mayle (1991) [9] visible using hot-films on a compressor blade in periodically disturbed flow. Walker, Hodson et al (1995) [20] presented detailed hot-film investigations on compressor and turbine blades. But many investigations lack clear interpretation of hot-film-signals.

The aim of the present paper is to identify typical signal distributions of hot-film sensors in the region of separation and transition for different states of the boundary layer. This is obtained by parallel measurements with hot-films and with the proven hot-wire technique as a reference. For these investigations a calibration of the hot-films is not necessary. The different boundary layer states are obtained by varying the

*Paper presented at an AGARD PEP Symposium on "Advanced Non-Intrusive Instrumentation for Propulsion Engines", held in Brussels, Belgium, 20-24 October 1997, and published in CP-598.*

Reynolds number and the degree of disturbance or, in other words, the turbulence intensity. Of special interest is the periodically disturbed flow, which is predominant in turbomachines, where the degree of disturbance changes periodically with the passing wakes. The investigations show, that the hot-film technique is very well suitable for revealing complex separation and transition phenomena even in unsteady, periodically disturbed flow.

**2. Experimental setup:** The investigations presented were performed on a circular cylinder placed in a low-speed wind-tunnel with its axis perpendicular to the flow direction. With the cylinder's diameter of 300 mm, the Reynolds numbers could be set from $3.0 \cdot 10^5$ up to $6.0 \cdot 10^5$. Downstream of the cylinder a splitter plate had been installed in order to avoid vortex shedding due to von Karman vortices induced by the cylinder. Upstream of the cylinder a "disturbance generator" was installed, consisting of two driven discs –covered to preclude interference with the flow– and bars between these discs crossing the flow channel. By driving the discs the bars move on a circular path perpendicular to the flow, when they cross the stagnation point streamline of the cylinder. The number of the bars and their diameter as well as the discs' turning frequency can be varied. Thus, periodic wakes are generated. By adjusting bars with low circumferential distance as a "package", wakes of variable width can be generated. Steady disturbance is obtained, when a bar is positioned directly on the stagnation point streamline increasing the turbulence intensity around the cylinder. The experimental facility was also used by Schröder (1985) [19] and Orth (1990)[11], (1991) [12], (1992) [13]. Figure 1 presents a sketch of the wind-tunnel.

Boundary layer profiles were measured with a single-wire probe. The probe was positioned in the lateral center of the cylinder and could be moved radially from the cylinder's surface up to 14 mm distance from the wall. The probe support was mounted together with a stepper motor inside the cylinder. The cylinder itself could be turned by a second stepper motor. Both positioning devices were computer controlled and every angular and radial position could be attained with high precision. They were calibrated before each experiment. For measuring the static wall-pressure pressure taps at the exact angular position of the hot-wire were used.

The hot-films themselves were produced by vapor deposition on a Kapton® foil with a thickness of 0.3 µm. The array consisted of fifteen sensors, but because of the angular positioning only one sensor was needed. The foil was glued on the lateral center of the cylinder on the opposite side of the hot-wire probe. To avoid a step around the outer edges of the piece of foil carrying the sensors, the cylinder's entire surface was covered with the Kapton® foil. In figure 2 a cross-section through the cylinder is depicted, and figure 3 shows the foil with the sensors.

It should be emphasized that it was not the aim to investigate cylinder-flow in paticular, but the cylinder was used, because different transition modes can be observed with this setup, see Orth (1991), and because a very high spatial resolution in flow direction can be obtained, even with the hot-films.

**3. Measurement technique, data aquisition, and evaluation:** The measurements with the hot-wire technique were performed by a commonly used method with an anemometer containing a symmetrical bridge with temperature compensation to eliminate errors caused by temperature fluctuations. Hot-film measurements require –in principle– the same hardware in spite of the sensors. But with standard anemometers temperature-compensated hot-film-measurement is not possible. Thus a standard bridge was used, making it necessary to ensure that the flow temperature did not change during the experiment. The bridge was adjusted to attain a sensor temperature 60 K higher than the flow temperature. Experience made by several other authors shows that this is the best trade-off between the quality of the signals and the life time of the sensors. A more detailed description of hot-film handling is given by Römer (1990) [16] and Haueisen (1996) [5].

The anemometer output voltage was digitized and stored on magnetic tape for later evaluation. 12-bit AD-converters were used and rates of 50 kHz and 25 kHz were selected. A low-pass filter was installed to prevent aliasing. In periodically disturbed flow a sampling rate of 25 kHz was chosen and 100 phase-locked bursts containing 4096 samples were recorded, according to Bendat and Piersol (1971) [2] a bottom for reliable results. In the experiments with steady flow a sampling rate of 50 kHz and a recording of 5 bursts consisting of 4096 samples each was preferred.

Evaluation of the hot-wire signals was performed in the usal way according to King's law given by

$$u = C_0 \cdot \left(E^2 - E_0^2\right)^m .$$

Calibration of $C_0$ and $m$ was done in situ once per day of experiments. Qualitative results of the hot-film measurements are sufficient for the present studies, thus, calibration was not necessary. However, the basic voltage $E_0$ on the sensor had to be measured, which means the voltage across the sensor without flow due to free convection and heat transfer from the heated sensor to the wall. The standard way of mapping hot-film results is by listing the term $(\overline{E} - E_0)/E_0$, which eliminates the influence of the individual sensor. In the present paper this term is transformed into an equation of a coefficient $C_E$ according to

$$C_{\overline{E}} = \frac{\overline{E} - \overline{E}_{\min}}{\overline{E}_{\max} - \overline{E}_{\min}}$$

in order to eliminate the quantitative influence of the Reynolds number too. Additionally, results of different flow conditions become better comparable. $\overline{E}_{\max}$ and $\overline{E}_{\min}$ are the extrema in the laminar region, where the $C_E$ -distribution is independent of the Reynolds number and the turbulence intensity.

Data evaluation was performed in the usal way by time-averaging and ensemble-averaging according to the following formula, where $\tilde{c}_i(t_i)$ stands for the ensemble-averaged value, $\sqrt{\widetilde{c_i'^2}(t_i)}$ for the fluctuations, and $\sqrt{\overline{c_r'^2}}$ and $\sqrt{\overline{c_p'^2}}$ for the random and periodic fluctuations.

$$\tilde{c}_i(t_i) = \frac{1}{N}\sum_{j=1}^{N} c_{ij}(t_i)$$

$$\sqrt{\widetilde{c_i'^2}(t_i)} = \sqrt{\frac{1}{N-1}\cdot\sum_{j=1}^{N}\left(c_{ij}(t_i) - \tilde{c}_i(t_i)\right)^2}$$

$$\overline{c} = \frac{1}{n}\sum_{i=1}^{n}\tilde{c}_i(t_i)$$

$$\sqrt{\overline{c_r'^2}} = \sqrt{\frac{1}{n}\sum_{i=1}^{n}\left(\widetilde{c_i'^2}(t_i)\right)}$$

$$\sqrt{\overline{c_p'^2}} = \sqrt{\frac{1}{n}\sum_{i=1}^{n}\left(\tilde{c}_i(t_i) - \overline{c}^2\right)}$$

Calibration of hot-films is often carried out according to

$$a \cdot \tau_w = \frac{\dot{Q}_w}{\Delta T} ,$$

where $\dot{Q}_w$ is the heat emitted by the sensor and $\Delta T$ the difference in temperature between the sensor and the flow, Bellhouse and Schultz (1966) [1]. $\dot{Q}_w$ can be expressed in terms of electrical power with the voltage on the sensor and its resistance

$$\dot{Q}_w = \frac{E^2}{R} - \frac{E_0^2}{R_0} .$$

The constant $a$ is determined by calibration. The formula is often used, but, unfortunately, its validity is restricted to significant simplifications, Haueisen (1996) [5]. For many investigations, it would not have been necessary to calibrate the sensors and to denote terms containing $\tau_w$ instead of just mapping output voltages, because only a qualitative information is needed and used. On the other hand, for quantitive conclusions much attention has to be paid to accuracy, because of the restricted validity of the formula. In recent times some authors have worked on the formulation of calibration laws for a reliable quantitative hot-film analysis, e.g. Davies and Duffy (1995) [3].

**4. Measurements in steady flow:** The investigations in undisturbed and disturbed steady flow yield the knowledge of the fundamental behaviour of the boundary layer at different Reynolds numbers and different turbulence levels. The present investigations show that different types of transition and separation can be uniquely identified by the signals of the surface-mounted hot-film sensors. The different states of the boundary layer in steady undisturbed and disturbed flow mark the limits, between which the boundary layer may alternate in periodically disturbed flow. In undisturbed flow with low Reynolds number ($3.0 \cdot 10^5$) a laminar separation without reattachment can be observed. This case is not covered by this paper, it is published in [5]. At a high Reynolds number ($6.0 \cdot 10^5$) the flow reattaches after a laminar separation. In steadily disturbed flow the boundary layer reattaches even at the low Reynolds number, and at the high Reynolds number laminar-turbulent transition can be observed without any separation occuring. These phenomena are described by several authors, see especially Orth (1990) [11], (1991) [12] or Ladwig (1992) [8]. The steady disturbance for the measurements presented is obtained by positioning a 2 mm diameter bar 650 mm in front of the stagnation point.

**4.1 Measurements in undisturbed flow:** Figure 4 shows the velocity profiles at several streamwise positions. The Reynolds number is $6.0 \cdot 10^5$. The stagnation point is at $\varphi = 0°$ of the circumferential angle. The velocity profiles visualize the behaviour of the boundary layer. Up to approx. 95° the boundary layer stays laminar, expressed by a relatively low increase of the speed in the vicinity of the wall, meaning low wall shear stress. In the region between $\varphi = 95°$ and 105°, there is almost no increase of the speed in the wall-normal direction. The velocity stays nearly zero, but it has to be taken into account that the measurements were performed with a single-wire probe, and reverse flow within a vortex or the so-called "inactive motion" cannot be distinguished from the propagating flow. Further downstream the profiles show a steep slope indicating a turbulent boundary layer with comparably high wall shear stress. Thus, the velocity profiles visualize a laminar separation in combination with turbulent reattachment, a so-called separation bubble. Downstream of 120° the profiles become less steep close to the wall and a turbulent separation develops.

In comparison with this more obvious approach to the flow and transition physics figure 5 presents the signal distribution of the hot-films. Additionally, the pressure distribution in terms of the well known pressure coefficient $C_p$ is shown. The pressure distribution itself reveals the separation bubble by forming a plateau. In the region of the bubble the separated flow is not able to follow the contour and thus the compression, but with the transition momentum is transported into the near-wall region and the flow reattaches forcing an increased compression in the rear of the bubble. But, how is this behaviour reflected by the hot-films?

First, let us concentrate on the $C_E$-distribution. What is evident is the increase of this coefficient from the stagnation point in the region of acceleration, which means an increase of the wall shear stress. When acceleration decreases upon reaching the point of maximal speed, $C_E$ and thus the wall shear stress will decrease too, becoming very low with a minimum of approx. zero at 105°. This point is identified as the center of the separation bubble and the beginning of transition by the velocity profiles. In accordance with the profiles the $C_E$-values rise downstream, indicating the developing turbulent boundary layer with its high wall shear stress. Downstream of 120°, shear stress decreases again and turbulent separation will occur. Interpreting hot-film-signals not only time-averaged mean values should be considered but also the distribution of the fluctuations, $\sqrt{\overline{e_i^2}} / E_0$, have to be taken into account. Evidently, in the laminar region there is no special behaviour of the values. The level is very low and, thus, shear stress does not change with time. But in the region of separation and transition the distribution of the fluctuation becomes characteristic. At approx. 95° there is a low local maximum, which means, that the wall shear stress changes in this region with time. Using the information from the velocity profiles and the pressure distribution, this maximum can be interpreted to be an oscillating separation point, and, indeed, separation is always three-dimensional and unsteady. At 105° the fluctuations are very low, so shear stress is very stable here. It is the center of the separation bubble, as mentioned above. Then, downstream, the fluctuations increase significantly, reaching a high maximum right in the middle of the slope of the $C_E$-distribution. This maximum has to be interpreted as the "point" of transition. It is the region, in terms of intermittency, where the intermittency factor is 0.5, which means a maximum change of turbulent and laminar or separated state, respectively, of the boundary layer. Further downstream the fluctuations decrease again rapidly, reaching a minimum right at the same angular position, where the $C_E$-values are a maximum. So, here the turbulent boundary layer is fully developed and stable. The wall shear stress is high and does not change with time.

The distribution of the shape factor $H_{12}$ –the ratio of the displacement thickness and the momentum-loss thickness– is also plotted in the diagram. It can be interpreted as a condensed form of the information given by the velocity profiles. A value for $H_{12}$ greater than 3.5 indicates separation, according to Pohlhausen [14]. Turbulent boundary layers are characterized by low $H_{12}$ values. Thus, a direct comparison between the hot-wire and the hot-film measurements is given.

When the Reynolds number decreases, the separation zone moves upstream, and reaching a Reynolds number level of approx. 3.0 the boundary layer remain separated and does not reattach at all.

Transition is initiated by instabilities along the boundary layer. These instabilities can be observed after a Fourier- transformation of the hot-film-signals in the form of a typical amplification in a frequency band around 3 kHz. This effect is discussed more in detail in [5], see also Orth [12] 1991.

**4.2 Measurements in steadily disturbed flow:** In the case of steadily disturbed flow the turbulence intensity is higher than in the undisturbed case and, thus, momentum is transported to the near-wall region more intensively. This enables the

boundary layer to follow a higher decelaration at a given Reynolds number. Figures 6 and 7 visualize, what happens in steadily disturbed flow. The velocity profiles in figure 6 show that even at the low Reynolds number, at which in undisturbed flow a laminar separation without reattachment can be observed, now laminar-turbulent transition via a separation bubble occurs. However, it seems to be a very similar boundary layer configuration as shown at the high Reynolds number in the undisturbed case. Regarding the velocity profiles in figure 7 for the high Reynolds number, no separation can be observed at all. In the whole circumferential segment shown there is a distinct increase of flow speed in the wall-normal direction. But, profiles in the region from $\varphi = 90°$ to 100° can be recognized, which are somehow deformed and not as typically laminar any more as they are upstream. Downstream of that region the profiles become turbulent. Thus, a direct laminar-turbulent transition takes place without any separation. Therefore the disturbance seems to have a similar influence on the transition mode as an increase of the Reynolds number, a phenomenon also observed by Ladwig (1992) [8] and Römer (1990) [16] on turbine cascades.

In comparison with the velocity profiles, figures 8 and 9 show the hot-film-signals together with the pressure distribution. Figure 8 for the low Reynolds number is very similar to figure 5, the undisturbed case at the high Reynolds number. Figure 9 for the high Reynolds number presents new characteristics.

Firstly, the pressure distribution is smooth and no plateau is visible and herewith no laminar separaration occurs. And, indeed, this conclusion is confirmed by the $C_E$ -distribution. Downstream of the laminar region a value of approx. zero is not reached and, thus, the wall shear stress does not vanish. So, no laminar separation occurs. But instead, little upstream of the position, where in the other cases a laminar separation occurs, a minimum –significantly greater than zero– is reached and further downstream the distribution rises sharply and, along with it, the wall shear stress. The boundary layer becomes turbulent and transition starts before the flow tends to separate. Regarding the fluctuations, we notice that there are no longer two maxima, but only one. This pronounced maximum is a superposition of fluctuations caused by the oscillating onset of transition and by intermittency itself. The peak is at the same streamwise position as the minimum of the time-averaged value. The boundary layer becomes more and more turbulent, wall shear stress increases and at approx. 108° transition is completed. The boundary layer is turbulent and stable, indicated by low fluctuations. The shape factor $H_{12}$ confirms this interpretation. Its maximum is at the same position as the peaks of the hot-film-signals and the value here is much lower than the one indicating separation.

For the direct transition no amplification of certain frequencies can be observed in the Fourier-transformed signals. Thus, transition is in this case not initiated by instabilities but by the higher turbulence intensity itself, see [5]

The investigations in steady flow visualize the dependence of both separation and laminar-turbulent transition on the Reynolds number and on the turbulence intensity. Both parameters are responsible for the transport of momentum in the boundary layer and both influence separation and transition with similar consequences. These results in these investigations repeat some of the results found by Orth (1990) [11], (1991) [12] using the same test facility. Ladwig (1992) [8] and Römer (1990) [16] describe the same behaviour of the boundary layer on turbine and compressor cascades at higher Mach numbers. Besides the aspects of the flow physics, the investigations in steady flow show the reliability of the hot-film measurements. The hot-film-signals uniquely visualize separation and laminar-turbulent transition by providing characteristic distributions for different boundary layer states. Many details of the flow in the wall-near region become visible and a high spatial resolution can be achieved with reasonable effort.

**5. Measurements in periodically disturbed flow:** Measurements in periodically disturbed flow were performed at the low and at the high Reynolds number ($3.0 \cdot 10^5$ and $6.0 \cdot 10^5$). The periodic disturbances were generated by the wake-generator, shown in figure 1, with bars perpendicularly crossing the stagnation-point streamline. The degree of disturbance now is no longer determined only by the bar diameter and their distance from the cylinder –at least representing a turbulence intensity–, but there are some more parameters like the flow speed $U_\infty$ and the frequency $f$ of the bars' wakes. A Strouhal number $Sr$ can be defined by

$$Sr = \frac{f \cdot d}{U_\infty},$$

where $d$ is the cylinder's diameter (300 mm). This Strouhal number can be interpreted as a length ratio –and thus as a kind of geometrical parameter–, as the ratio between the diameter $d$ and the length of the streamline influenced within one wake-period. See the sketch in figure 10.

$$\frac{U_\infty}{f} = l_u + l_s \quad \text{and} \quad f = \frac{u}{t}.$$

What should be additionally described is the portion of the disturbed part within one period. It is the ratio between the wake width $b$ and the pitch $t$. According to Schlichting (1965) [18] the width of a wake generated by a cylindrical bar with a diameter $d_b$ is given by $b = 0.62 \cdot (x \cdot d_b)^{0.5}$, where x [m] is the distance from the bar. The ratio $b/t$ for turbomachines is typically approx. 0.5. Weighting the Strouhal number $Sr$ with this ratio, we define the parameter $Sr^*$, the ratio between the cylinder diameter $d$ and the disturbed length within one period $l_s$

$$Sr^* = \frac{f \cdot d}{U_\infty} \cdot \frac{t}{b}.$$

As a typical length for $Sr$ and $Sr^*$ respectively the diameter $d$ was chosen. Instead of a geometrical length a typical length of the flow may be preferred, e.g. the momentum loss thickness.

The wake width $b$ can be varied by fitting some bars on the circumference of the wake-generator closely together as a package. So the wakes of the single bars are no longer distinguishable at the position of the cylinder, but a wide wake is generated with always the same turbulence structure belonging to the wake of a single bar. Only bars of 2 mm in diameter were used, just like in steady flow investigations.

Here, two types of periodic disturbances are discussed. The first configuration, indicated by "Disturbance I", contains 10 bars in a package. In the rest of the wake generator there are no bars. So, a very low value of $b/t$ is achieved and the wake frequency –in this configuration equal to the turning frequency of the wake-generator– is comparatively low. Because of the sampling time two wakes within one revolution are captured, since the package crosses the stagnation point streamline twice, once in the position "far" and once in the position "near". With this configuration the principal effects of periodic wakes on the boundary layer can be studied very well. The sampling time equals the time of one revolution. "Disturbance II", the second configuration investigated, consists of several packages with 3 bars each. In this case revolution time, sampling time, and triggering are chosen in such a way, that three wake-periods only from the position "far" were measured. This configuration is more turbomachinery-like. According to Dullenkopf (1992) [4] a value of $Sr > 2$ is typical of turbomachines (defined with the blade chord-lenth). The following table presents the relevant parameters for the two different configurations.

| Measurements in periodically disturbed flow | | | | |
|---|---|---|---|---|
| | Dis.I (pack.à 10 bars) | | Dis.II (packs.à 3 b.) | |
| Re | $6.0 \cdot 10^5$ | $6.0 \cdot 10^5$ | $3.0 \cdot 10^5$ | $6.0 \cdot 10^5$ |
| Position | near | far | far | far |
| $Sr$ | 0.053 | 0.053 | 1.220 | 0.573 |
| $Sr^*$ | 0.947 | 0.791 | 1.661 | 0.779 |
| $f$ [Hz] | 6 | 6 | 65 | 65 |
| $b/t$ | 0.056 | 0.067 | 0.734 | 0.734 |

**5.1 Measurements with Disturbance I:** In figure 11 time-averaged results for Disturbance I at the high Reynolds number (Re = $6.0 \cdot 10^5$) are presented. In this diagram the distribution of the periodic fluctuations is also plotted. At first sight, the picture seems to be very similar to the undisturbed case with the same Reynolds number, where a laminar separation bubble occurs followed by turbulent reattachment. Anyway, there are some details indicating substantial differences. First of all, the plateau of the pressure distribution is not as clear-cut as it is in the undisturbed case. Furthermore, the mimimum of the $C_E$ -distribution is greater than zero and a little upstream. The peak-value of the shape-parameter $H_{12}$ is lower and occurs a little upstream, too. Thus, these are indicators that a laminar separation might not take place. But the rise of the $C_E$ values and the decrease of the shape parameter downstream of approx. 105° are typical of turbulent transition. Additionally, the peak of the random fluctuations is at the same position as it is in the undisturbed case. On the other hand, the comparison with the steadily disturbed case at the same Reynolds number shows that there are also differences compared with the case of direct transition without separation. Regarding the periodic fluctuations of the hot-film-signals we see that the peak of this distribution is exactly in the region, where separation occurs in the undisturbed case. The periodic fluctuations indicate the periodically occuring changes in the boundary layer, periodically with the passing wakes. Thus, in the region of undisturbed separation the boundary layer is heavily influenced by the passing wakes, whereas in the laminar region and in the fully developed turbulent boundary layer the periodic wakes cause no effects at all.

Figure 12 visualizes the unsteady behaviour of the boundary layer. Here, the ensemble-averaged –or phase-locked– distributions of $C_E$ are shown within half a period. The wake from the position "far" impinges at $t/T = 0$. Before its impingement the hot-film-signals are typical of a laminar separation with turbulent reattachment in the case of undisturbed flow. In the instant the wake impinges the boundary layer switches to the disturbed state. Now, there is no separation any more, but the onset of transition moves upstream from the previous region of separation. Further on the boundary layer does not switch back suddenly to the separated state, but develops relatively slowly a new separation bubble. It takes a typical time, concerning the problem of stability, to reach the undisturbed state again. Later on we see the wake from position "near" impinging and causing the same effects. Now the distributions of the time-averaged values in figure 11 are becoming understandable. They do not represent a steadily existing physical state of the boundary layer, but they are the computational mean-values of the periodically alternating behaviour.

The alternation of the boundary layer between the undisturbed and the disturbed state can even be observed in the amplitude spectra of the hot-film-signals. In the undisturbed part of a period, amplifications caused by instabilities can be observed and they diappear during the time of disturbance, see [5].

Walker, Hodson et al. (1995) [20] performed hot-film measurements on the third stage of a compressor. They describe in detail the same behaviour of the boundary layer on a stator blade as was observed here on the cylinder in the wind-tunnel.

At the low Reynolds number the undisturbed boundary layer separates completely, as mentioned, without reattachment. In this case, not further discussed here, Disturbance I prompts the boundary layer to form a separation bubble for a moment, but complete separation occurs again within one period before the next wake impinges. Therefore, this disturbance configuration cannot prevent complete separation. For details see Haueisen (1996) [5].

**5.2 Measurements with Disturbance II:** In terms of periodical disturbances, Disturbance II is much stronger than Disturbance I, see table above. Figure 13 shows the time-averaged mean-values for the low Reynolds number. The distributions indicate a boundary layer forming a separation bubble just like in the steadily disturbed case at the low Reynolds number. Thus, the periodic disturbance seems to prevent complete separation for the major part of a period. The periodic fluctuations are comparatively low, indicating that the disturbed state is predominant and the single wake does not have such a heavy influence. But especially a little way downstream of 90°, the periodic fluctuations are significant. This is the region, where complete separation occurs in the undisturbed case at this Reynolds number, here prevented by the periodic wakes.

Looking at the ensemble-averaged $C_E$ distributions in figure 14, we see that a complete separation does not occur at all. Three complete periods are shown and the wakes impinge at $t/T = 0,1,2$. The impinging wakes cause a steep minimum, and in the time after, the region of separation increases and moves upstream a little, but the boundary layer does not reattach and does not turn into a turbulent state. The separation bubble is oscillating and pulsating. The boundary layer needs a typical time after a wake has passed to develope to the undisturbed state. During this time the next wake passes and therefore complete separation is prevented. Here the influence of the wake frequency can be observed. With a lower frequency reattachment would be delayed to the end of the period, and the boundary layer would separate completely until the impingment of the next wake.

This interpretation of the hot-film-signals is reflected in the results of hot-wire measurements. Figure 15 shows the phase-locked velocity profiles at the position of $\varphi = 105°$, located in the region of the separation bubble. It can be seen that within one period no complete separation occurs, but the extent of the separation bubble in wall-normal direction alternates with the frequency of the wakes. Thus, the separation bubble is not only pulsating in the streamwise direction, as indicated by the hot-film-signals, but in wall-normal direction, too. In order to give a compact overview of the velocity measurements, figure 16 presents the ensemble-averaged distribution of the shape-factor $H_{12}$. Over the whole period, the distributions indicate the turbulent reattachment by the typical sharp, concave shaped decrease of downstream of approx. 105°. But up to the end of each period an increase of the peak value can be observed, whereby typical turbulent values are attained further downstream. It is not necessary to mention that with the hot-film technique measuring by far less effort is needed for the analysis of these flow phenomena than with the hot-wire technique. An additional advantage offered by the hot-film technique is that it reveals much more details in the flow-region near the wall.

For the high Reynolds number figure 17 shows the results for Disturbance II. The picture is very similar to that of Disturbance I with the same Reynolds number, figure 11. Now the plateau of the pressure distribution is even smoother, the peak value of the shape factor $H_{12}$ is lower and the minimum of the

$C_E$ -values is a little higher and a little more upstream. Additionally, the increase of the periodic fluctuations begins further upstream. All these aspects indicate, that, looking at the time-averaged values, the behaviour of the boundary layer corresponds a little more to the steadily disturbed case than to the case with Disturbance I. And, in fact, the phase-locked $C_E$ distributions in figure 18 confirm this interpretation. The direct transition induced by the disturbating wakes prevents the boundary layer from separating for a while. After a wake has passed the boundary layer again forms a separation bubble, for which a typical time duration is needed. But this separation stays only a comparatively short fraction of a period, until the next wake passes.

The results of the velocity measurements are consistent with those of the hot-film measurements. Figure 19 presents the ensemble-averaged velocity profiles in the region of the separation bubble at $\varphi = 105°$. Again three periods are shown. The alternation between already attached turbulent profiles and the still separated "bubble-profiles" is obvious. In addition to the profiles at this one position, the shape factor is used again to give an overall picture of the hot-wire measurements over a wider angular range in figure 20. The attached turbulent state at the beginning of each period is seen from the deep "valleys" in the distribution. Especially in the isolines the different reaction-speeds of the boundary layer on the impinging and on the leaving wake become visible. The boundary layer adapts very quickly to the disturbed state, but it needs a significant longer time to return to the undisturbed state again.

A direct comparison between the different types of disturbances is given in figure 21. The hot-film signals, the shape factor, and the pressure distribution are presented simultaneously for the undisturbed, the steadily disturbed and the periodically disturbed case. All values are time-averaged. It is readily apparent that the periodically disturbed case may be understood as some average of the two steady cases within one period. Figure 21 also shows that the onset of transition moves upstream with an increasing degree of disturbance. With higher turbulence intensity the boundary layer becomes turbulent, before the region, where separation can occur, and the higher momentum in the near-wall region prevents the boundary layer from separating.

**6. Measurements with surface-mounted hot-film sensors in multistage aero-engine low-pressure turbines:** In the late 1980's in the course of the development of low-pressure turbines for civil aircraft turbofan engines MTU performed a variety of experimental investigations into unsteady flow phenomena in those turbines, see Binder et al. [21], Arndt [22], Schröder [23] and Schröder et al. [24]. Considering that these low-pressure turbines operate at low Reynolds numbers, one aim of these investigations was to gain more profound insights into the unsteady transition and separation mechanisms in the boundary layers on the stator vanes, which are subjected to periodically incoming rotor wakes. Today, in retrospect, it can be stated that the findings gained from these investigations have substantially contributed to a better understanding of these complex flow mechanisms and have given rise to new concepts of low-pressure turbine blading, which are now being developed for the turbines of the next decade.

MTU-design hot-film sensors surface mounted on the airfoils made these investigations possible. A typical example of the application of these sensors is shown in Figure 22. Nevertheless the results of the investigations also made it apparent that a comprehensive fundamental investigation of the boundary layer transition and separation processes under unsteady wake-induced flow conditions would be very helpful for refining the understanding and interpretation of the hot-film sensor signals obtained under these flow conditions. Therefore the investigation presented here was initiated at the Darmstadt University of Technology. Besides providing for a detailed analysis and interpretation of the boundary layer transition and separation processes in steady and unsteady wake disturbed flow - as presented here - the striking result of this investigation is that the findings of analyses and interpretations of surface hot-film measurements in low-pressure turbines as performed by MTU have been corroborated and explained further. This was achieved as in this investigation on a circular cylinder, it was possible to perform measurements of the ensemble-averaged unsteady boundary layer velocity profiles.

Today new blading concepts for low-pressure turbines which take the unsteady wake-induced boundary layer transition mechanisms into account are under development and will be introduced in the near future. These are for instance the so-called "clocking"-arrangement of stator (and possibly rotor) airfoils or the increase of airfoil lift, which affords a reduction of the number of airfoils in stators and rotors, see Schulte and Hodson [25]. The testing based on these new turbine blading concepts now again requires measurements with surface-mounted hot-film sensors in low-pressure turbine rigs. The fact that such investigations can now rely on the findings of this fundamental investigation on a circular cylinder thus proves to be of enormous benefit.

As obviously it is not possible to perform boundary layer velocity profile traverses in turbine rigs of generic dimensions, new analysis procedures have to be applied with regard to the hot-film sensor signals to obtain the desired information about boundary layer transition and separation. A very promising technique used to obtain valuable information on boundary layer transition and also on separation bubbles is the analysis of the skew of the hot-film sensor signal. The skew is the third-order moment of this signal which is computed according to the ensemble-averaged random unsteadiness as:

$$\mu_{i,3} = \frac{1}{\left(\tilde{c}_i(t_i)\right)^3} \cdot \frac{1}{N-1} \cdot \sum_{j=1}^{N} \left(c_{ij}(t_i) - \tilde{c}_i(t_i)\right)^3$$

Non-zero values of the third-order moment indicate asymmetry (i.e. skew) of the probability density distributions (histograms) of for instance the hot-film sensor signal, and therefore the skew is indicative of the state of the boundary layer transition. If a phase-lock averaging process is applied to an ensemble of unsteady signal data - as in the present case - of course a skew value is obtained for every instant in time.

In principle the skew shows whether peaks of the oscillations of a hot-film signal would predominantly rise above a mean value level (skew > 0) or drop below the mean value level (skew < 0). Hence the skew gives an indication of the value of intermittency of a boundary layer transition process as follows: At the start of transition (intermittency $\gamma = 0$) the skew is zero, between $\gamma = 0$ and $\gamma = 0.5$ the skew is positive, reaching a maximum at $\gamma = 0.25$. Between $\gamma = 0.5$ and $\gamma = 1.0$ the skew is negative, reaching a minimum at $\gamma = 0.75$. This concept of evaluating the skew of surface-mounted hot-film sensor signals for the analysis of boundary layer transition processes is explained in detail e.g. in Halstead et al. [20]. If separation bubbles appear prior to the start of transition in the boundary layer this is also shown in the distributions of the skew by negative values.

Figure 23 shows a typical time-space diagram of the skew from a measurement with surface-mounted hot-film sensors on a stator vane in a multistage low-pressure turbine rig. Clearly visible in the right hand part of the diagram, at normalized distances of 0.75 to 0.96, are the line of the start of transition (skew rising from zero to positive) which oscillates in its

streamwise direction under the influence of the incoming wakes, and downstream of it the line of the middle of the transitional range (zero skew) which displays the sharp drop from positive to negative values and which also varies under the influence of the wakes. The end of the transitional range in the case illustrated is not yet reached at the position of the last sensor on the airfoil. At some instances in time "islands" of negative skew are visible in some "bays" ahead of the line of start of transition. These islands show that an oscillating separation bubble exists on this profile which periodically is suppressed by the influence of the wakes of the preceding rotor on the transition process, in the same way as this was the case in the investigations on the circular cylinder.

Thus this diagram illustrates how instrumental the measuring technique with surface-mounted hot-film sensors and the findings from the investigations on this circular cylinder are in developing state-of-the-art low-pressure turbine blading concepts.

**Conclusion:** The boundary layer on a circular cylinder in crossflow was experimentally investigated. The measurements were carried out in undisturbed, steadily disturbed, and periodically disturbed flow at two different Reynolds numbers, $Re = 3.0 \cdot 10^5$ and $6.0 \cdot 10^5$. In periodically disturbed flow additionally the frequency of the passing wakes was varied. The measurements were performed in parallel with a single-wire probe and with a surface-mounted hot-film sensor. The aim of these investigations is not only to discuss the behaviour of the boundary layer under these different flow conditions, but also to show that the hot-film technique is a suitable method for analysing separation and transition efficiently.

As shown by the measurements in steady flow, the boundary layer is heavily influenced by the Reynolds number and by the turbulence intensity resulting from disturbance. Depending on the two parameters, different types of transition and separation can be observed, such as laminar separation without transition and reattachment, transition with a separation bubble, and direct transition without any separation.

For these various boundary layer states characteristic distributions of the hot-film signals can be identified. Separation and transition can be studied in even more detail by analysing the hot-film-signals than this can be done by analysing the hot-wire measurements, whereby the measuring effort can be kept to a reasonable level. Calibration of the hot-film sensors is not necessary for this type of flow analysis.

In periodically disturbed flow, a time-averaged behaviour of the boundary layer can be observed, which corresponds to some state in between the undisturbed and the steadily disturbed case. Ensemble-averaged evaluation reveals that the time-averaged behaviour does not correspond to a physically existing state, but is a result of a periodical alternation of the boundary layer between the undisturbed and the steadily disturbed state. Particularly the periodic fluctuations show, how the boundary layer is influenced by the periodic disturbances. Depending on the frequency of the disturbances, the time-averaged behaviour of the boundary layer tends to be more of the disturbed or of the undisturbed type. It can be observed that the boundary layer reacts to the impinging wake simultaneously, but it takes quite a long time after a wake has passed to return to the undisturbed state again. This development may be cut by the next wake passing, depending on the wakes frequency. This is also a matter of boundary layer stability.

Also in unsteady, periodically disturbed flow, boundary layer development can be studied very efficiently using the hot-film signals. Detailed investigations into separation and transition mechanisms with high spatial and temporal resolution are feasible, which require a reasonable effort. Additionally, the hot-film technique can be applied to a wide variety of geometries even without necessitating calibration.

**Acknowledgement:** The instrumentation of the cylinder with the hot-film-sensors and the financial support both provided by the MTU Motoren- und Turbinen-Union München GmbH in Munich (Germany) is gratefully acknowledged by the authors. Valuable help was provided by Dr.U.Orth, whose experience was essential in questions on hot-wire measurements and data aquisition.

**References:**


[1] B.J. Bellhouse and D.L. Shultz. Determination of Mean and Dynamic Skin Friction, Separation and Transition in Low-Speed Flow With a Thin Film Heated Element. Journal of Fluid Mechanics, 24: 379-400, 1966.

[2] J.S. Bendat and A.G. Piersol. Random Data: Analysis and Measurement Procedures. John Wiley & Sons, 1971.

[3] M.R.D. Davies and J.T. Duffy. A Semi-Empirical Theory for Surface Mounted Aerodynamic Wall Shear Stress Gauges. Int. Gas Turbine and Aeroengine Congress and Exposition ASME, 95-GT-193; 5-8 June, 1995

[4] K. Dullenkopf. Untersuchungen zum Einfluß periodisch instationärer Nachlaufströmungen auf den Wärmeübergang konvektiv gekühlter Gasturbinenschaufeln. Dissertation, TU Karlsruhe. 1992

[5] V. Haueisen. Untersuchungen des Grenzschichtumschlags am Kreiszylinder bei unterschiedlichen stationären und instationären Zuströmbedingungen. Dissertation, TH Darmstadt, 1996.

[6] H.P. Hodson and J.S. Addison. Unsteady Transition in an Axial Flow Turbine: Part I – Measurements on the Turbine Rotor. J. of Turbomachinery; Trans. of the ASME, 112: 206-214, 1990.

[7] J. Hourmouziadis, F. Buckl and P. Bergmann. The Development of the Profile Boundary Layer in a Turbine Environment. ASME-Paper 86-GT-244, 1986.

[8] M. Ladwig. Experimentelle Untersuchungen zum Einfluß von Eintritts-Strömungsinhomogenitäten auf die Entwicklung des Strömungsfeldes in Turbinenschaufelgittern. Dissertation, Universität der Bundeswehr, München, 1992

[9] R.E. Mayle. The Role of Laminar-Turbulent Transition in Gas Turbine Engines. J. of Turbomachinery; Trans. of the ASME, 113: 509-537, 1991

[10] M.L.G. Oldfield, R. Kiock, A.T. Holmes and C.G. Graham. Boundary Layer Studies on Highly Loaded Cascades Using Heated Thinfilms and a Traversing Probe. ASME-Journal of Engineering for Power, 103(1): 1981

[11] U. Orth. Boundary Layer Transition on a Cylinder With and Without Separation Bubbles. Experiments in Fluids 10, 23-32, Springer-Verlag1990

[12] U. Orth. Untersuchung des Umschlagverhaltens von Platten- und Zylindergrenzschichten bei ungestörter und stationär oder periodisch gestörter Zuströmung. Dissertation, TH Darmstadt, 1991

[13] U. Orth. Unsteady Boundary Layer Transition in Flow Periodically Disturbed by Wakes. Int. Gas Turbine and Aeroengine Congress and Exposition ASME, 92-GT-283; 1.-4. Juni, 1992.

[14] K. Pohlhausen. Zur näherungsweisen Integration der Differentialgleichung der laminaren Reibungsschicht. Zeitung für angewandte Mathematik und Mechanik, 1(3), 1921.

[15] P. Pucher and R. Göhl. Experimental Investigations of Boundary Layer Separation With Heated Thin-Film Sensors. ASME-Paper 86-GT-254, 1986.

[16] N. Römer. Theoretische und experimentelle Untersuchungen zum Umschlagverhalten der Profilgrenzschicht an Verdichter- und Turbinengittern. Dissertation, Universität der Bundeswehr, München, 1990.

[17] W.J. Salomon and G.J. Walker. Observation of Wake-Induced Transition on an Axial Compressor Blade. Int. Gas Turbine and Aeroengine Congress and Exposition ASME, 95-GT-381; 5-8 June, 1995.

[18] H. Schlichting. Grenzschicht-Theorie. G. Braun, 1965.

[19] T. Schröder. Entwicklung des instationären Nachlaufs hinter quer zur Strömungsrichtung bewegten Zylindern und dessen Einfluß auf das Umschlagverhalten von ebenen Grenzschichten stromabwärts angeordneter Versuchskörper. Dissertation, TH Darmstadt, 1985.

[20] G.J. Walker, H.P. Hodson, D.E. Halstead, D.C. Wisler, T.H. Okiishi and S. Hyoun-Woo. Boundary Layer Developement in Axial Compressors and Turbines Part I-IV. Int. Gas Turbine and Aeroengine Congress and Exposition ASME, 95-GT-193; 5-8 June, 1995.

[21] A. Binder, Th. Schröder and J. Hourmouziadis. Turbulence Measurements in a Multistage Low-Pressure Turbine. J. of Turbomachinery; Trans. of the ASME, 111: 153-161, 1989.

[22] N. Arndt. Blade Row Interaction in a Multistage Low-Pressure Turbine. J. of Turbomachinery, Trans. of the ASME, 115: 137-146, 1993.

[23] Th. Schröder. Investigations of Blade Row Interaction and Boundary Layer Transition Phenomena in a Multistage Aero Engine Low-Pressure Turbine by Measurements with Hot-Film Probes and Surface Mounted Hot-Film Gauges. Von Karman Institute for Fluid Dynamics, 1990-1991 Lecture Series Programme, 9. Boundary Layers in Turbomachines, 2-6 September 1991.

[24] Th. Schröder, R.D. Baier and K. Broichhausen. Laminar Flow and Unsteady Phenomena in Boundary Layers of Turbomachinery Bladings. Proceedings First European Forum on Laminar Flow Technology, pp. 201-211, Hamburg, 1992.

[25] V. Schulte and H.P. Hodson. Unsteady Wake-Induced Boundary Layer Transition in High Lift LP Turbines. ASME-Paper 96-GT-486, 1996.

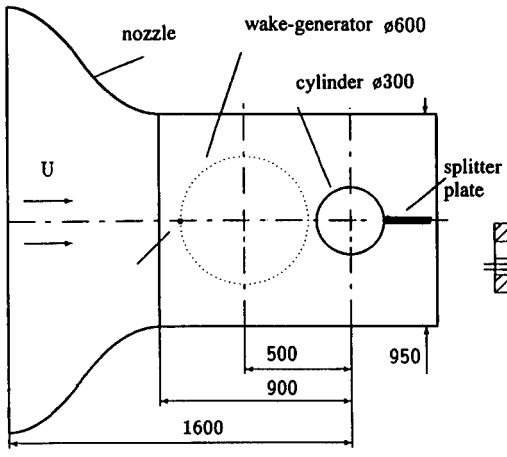


**Fig. 1:** Sketch of the wind tunnel with the cylinder and the wake-generator

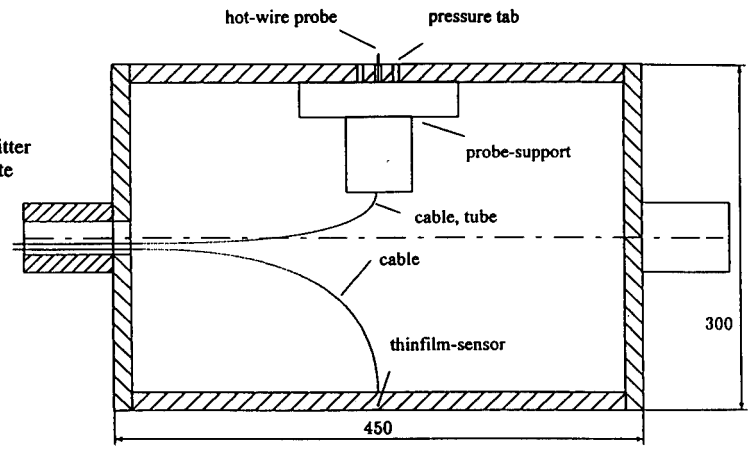


**Fig. 2:** Sketch of a cut through the cylinder

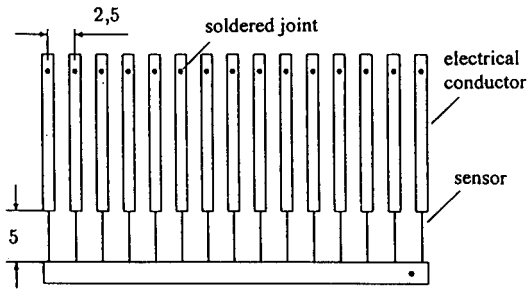


**Fig. 3:** Arrangement of the thinfilm-sensors on the Kapton® foil

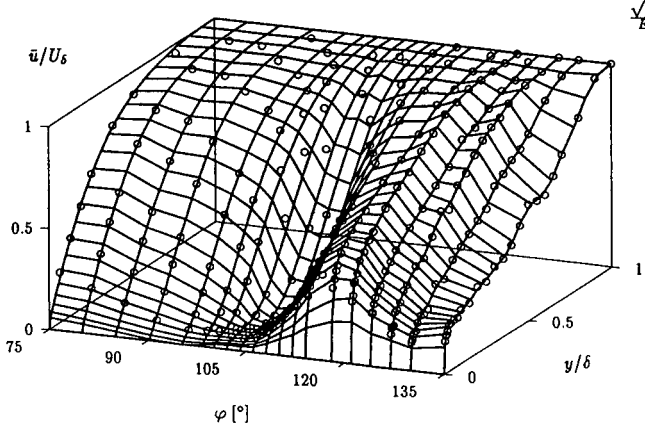


**Fig. 4:** Velocity profiles, $Re = 6.0 \cdot 10^5$, undisturbed flow

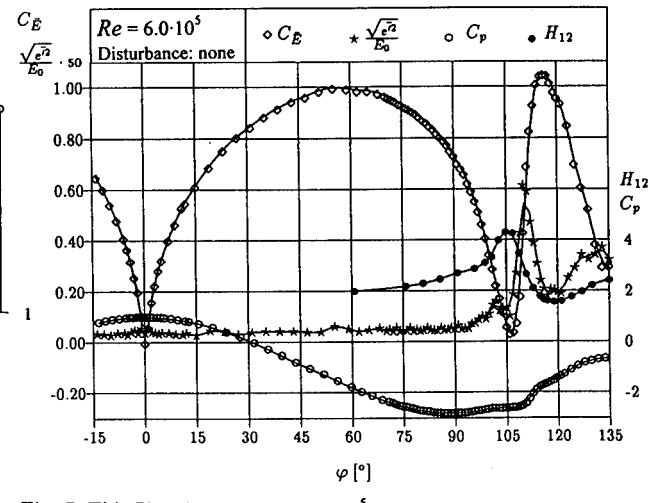


**Fig. 5:** Thinfilm signals, $Re = 6.0 \cdot 10^5$, undisturbed flow

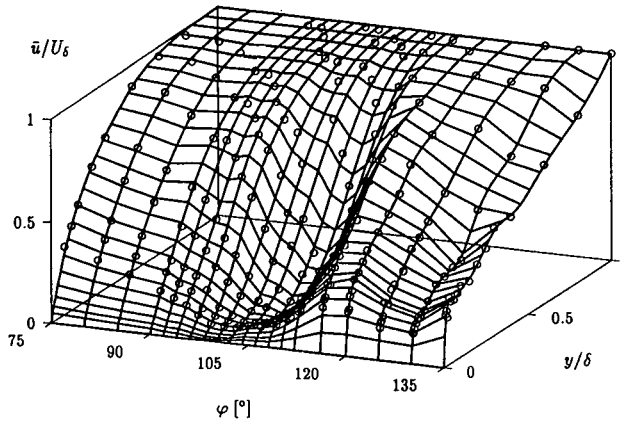


**Fig. 6:** Velocity profiles, $Re = 3.0 \cdot 10^5$, steadily disturbed flow

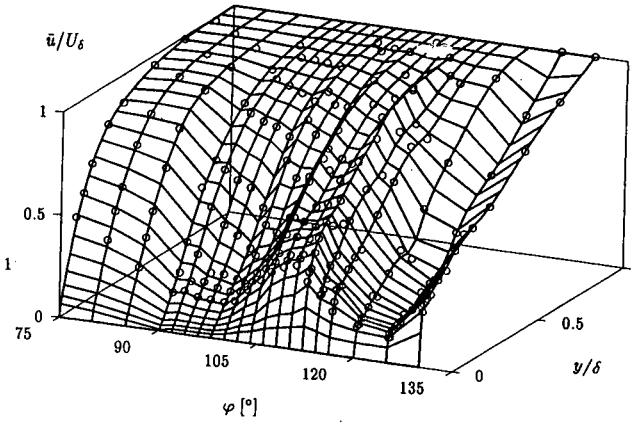


**Fig. 7:** Velocity profiles, $Re = 6.0 \cdot 10^5$, steadily disturbed flow

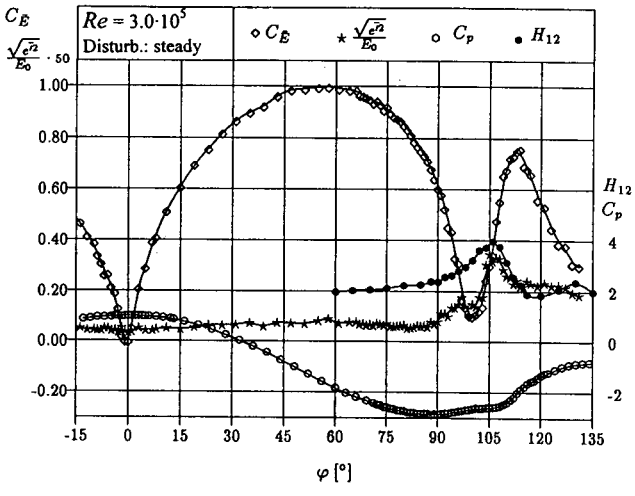


**Fig. 8:** Thinfilm signals, $Re = 3.0 \cdot 10^5$, steadily disturbed flow

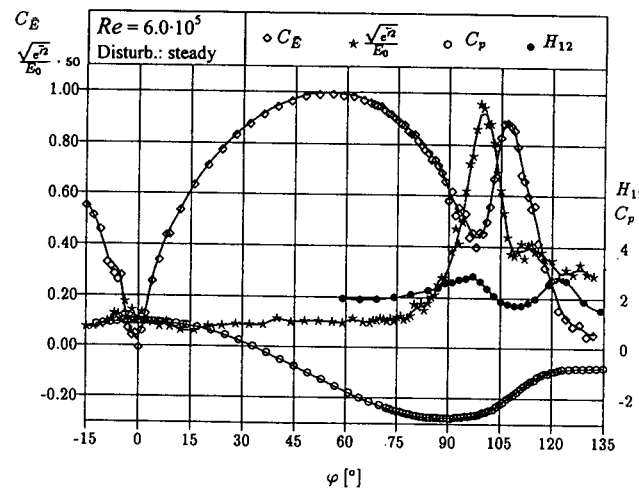


**Fig. 9:** Thinfilm signals, $Re = 6.0 \cdot 10^5$, steadily disturbed flow

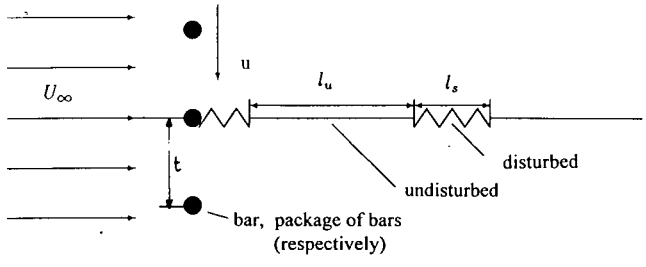


**Fig. 10:** Sketch of the effects of periodical disturbances on a streamline

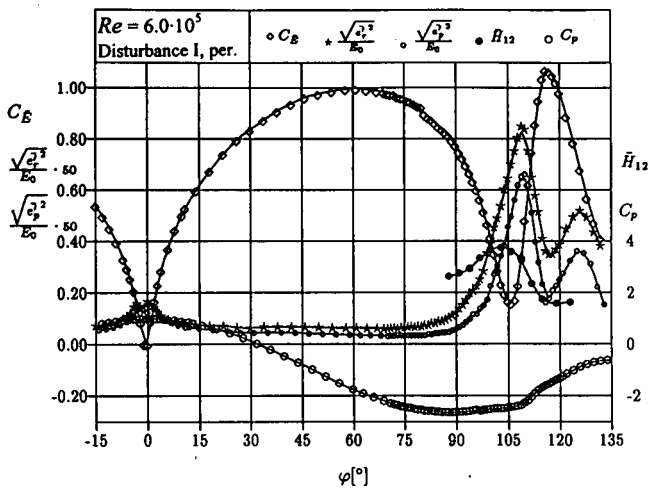


Fig. 11: Time-averaged thinfilm signals, $Re = 6.0 \cdot 10^5$, Disturbance I

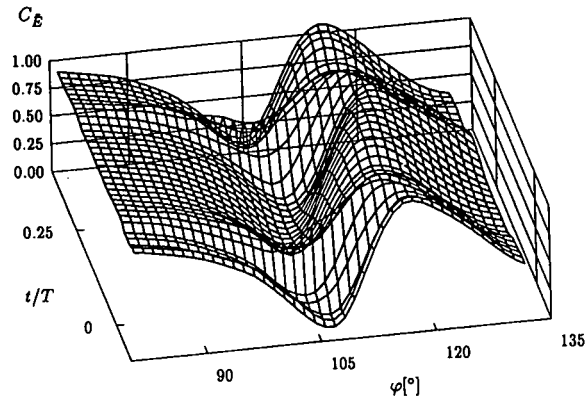


Fig. 12: Ensemble-averaged thinfilm signals, $Re = 6.0 \cdot 10^5$, Disturbance I

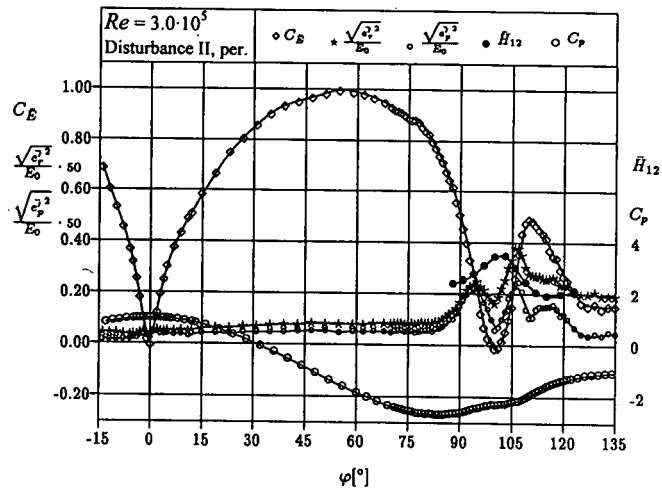


Fig. 13: Time-averaged thinfilm signals, $Re = 3.0 \cdot 10^5$, Disturbance II

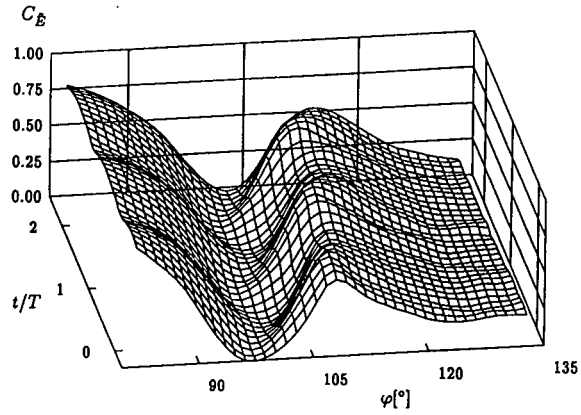


Fig. 14: Ensemble-averaged thinfilm signals, $Re = 3.0 \cdot 10^5$, Disturbance II

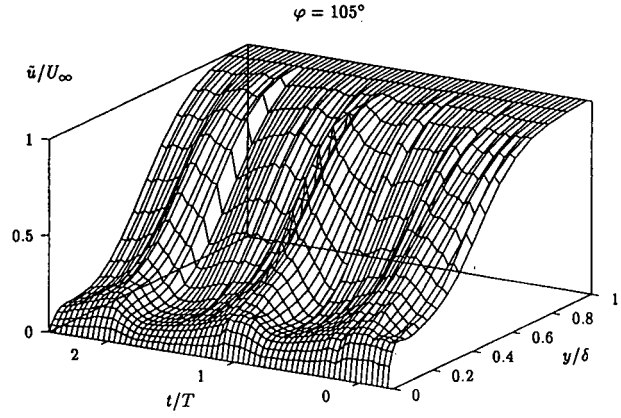


Fig. 15: Ensemble-averaged velocity profiles, $Re = 3.0 \cdot 10^5$, Disturbance II

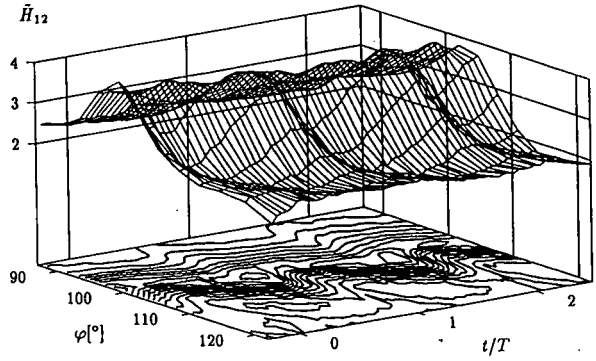


Fig. 16: Ensemble-averaged shape factor, $Re = 3.0 \cdot 10^5$, Disturbance II

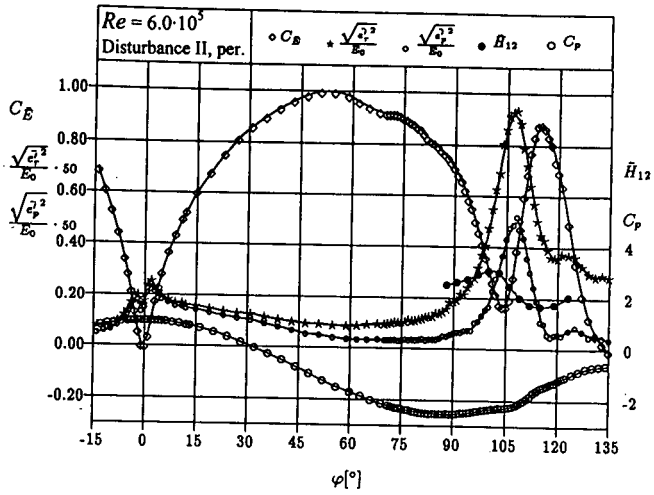


Fig. 17: Time-averaged thinfilm signals, $Re = 6.0 \cdot 10^5$, Disturbance II

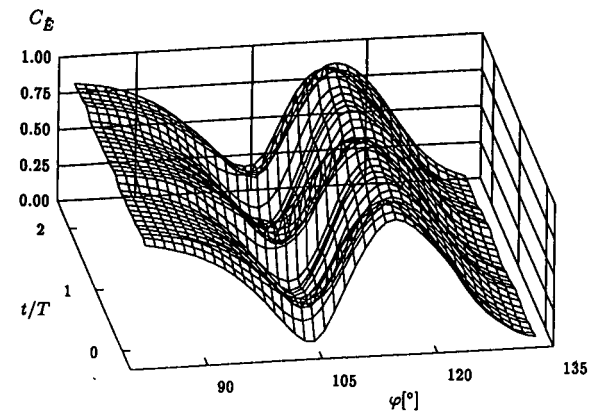


Fig. 18: Ensemble-averaged thinfilm signals, $Re = 6.0 \cdot 10^5$, Disturbance II

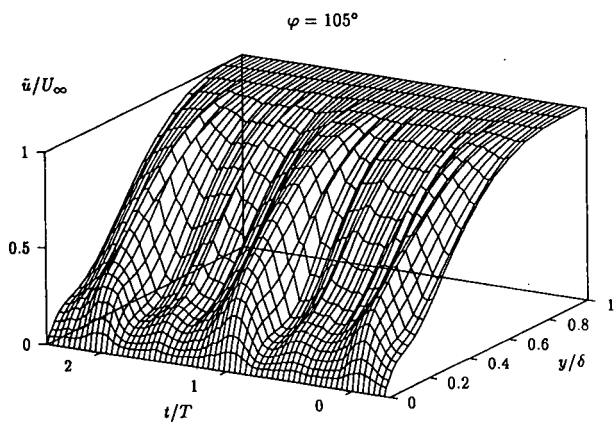


Fig. 19: Time-averaged thinfilm signals, $Re = 6.0 \cdot 10^5$, Disturbance II

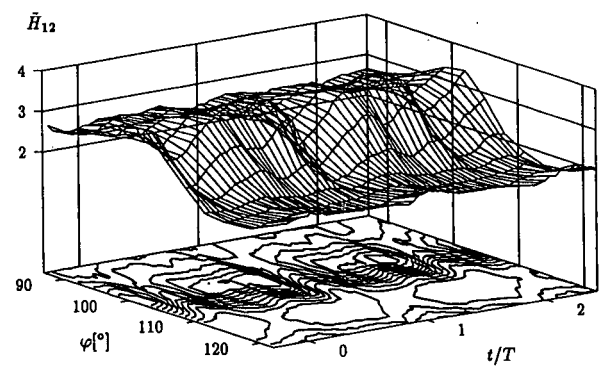


Fig. 20: Ensemble-averaged shape factor, $Re = 6.0 \cdot 10^5$, Disturbance II

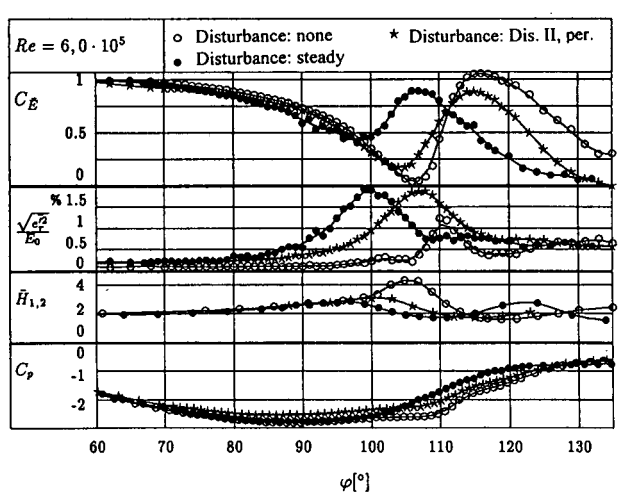


Fig. 21: Comparison between different types of disturbance, $Re = 6.0 \cdot 10^5$, Disturbance II

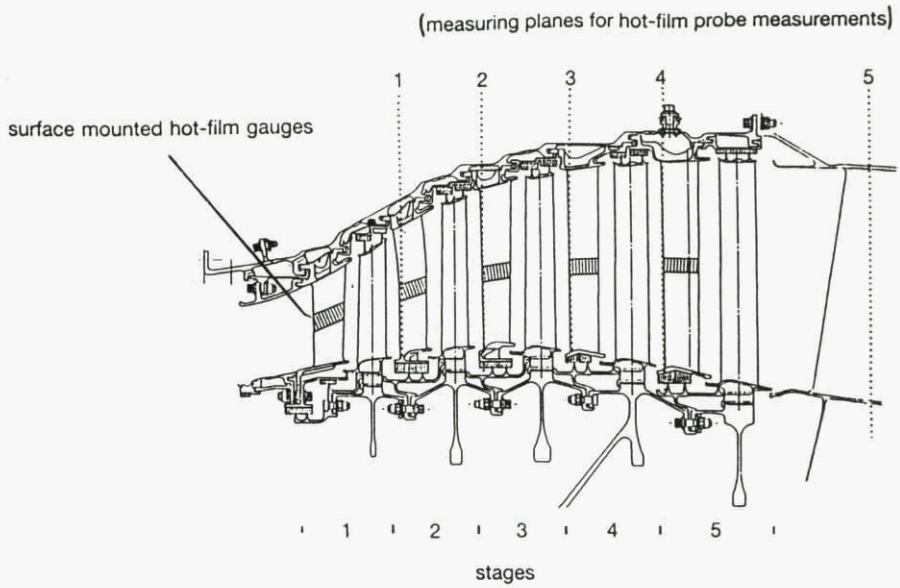


**Fig. 22:** Five-stage low-pressure turbine, sensor application

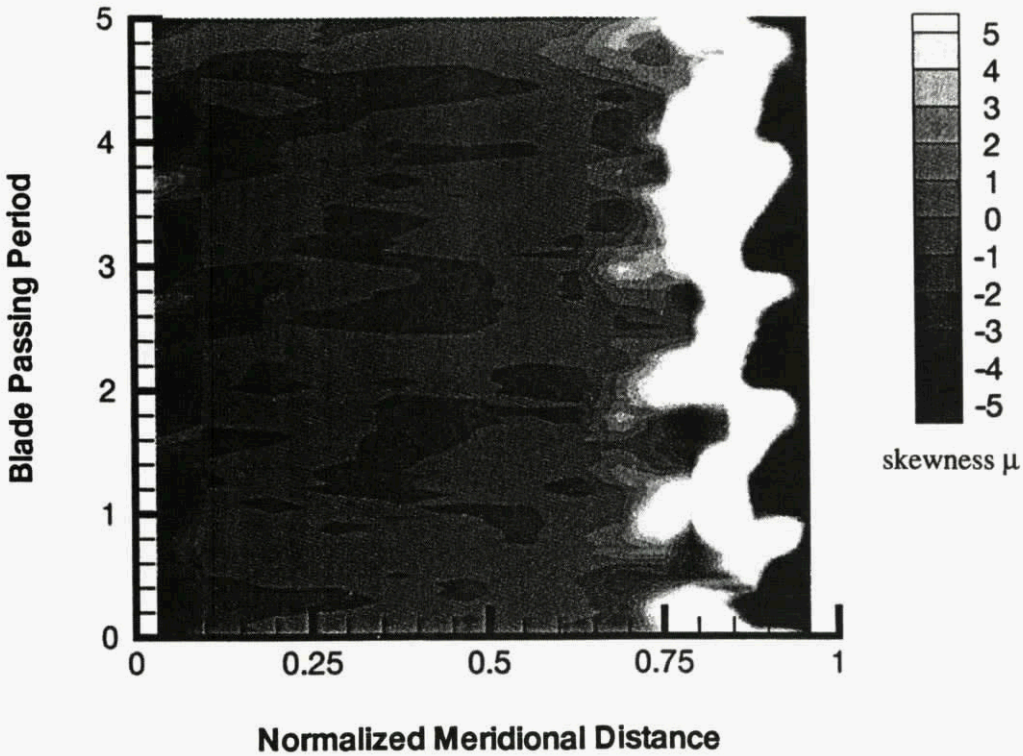


**Fig. 23:** Time-space distribution of skew on a stator vane in a multistage low-pressure turbine

Paper 38
Author V. Haveisen, et.al.

Q: Sieverding

In your paper you do not at all refer to the periodic flow unsteadiness induced by the von Karman vortices, but it is well-known that the separation point on the cylinder is extremely strongly influenced by the vortex shedding. Please comment !

A: To avoid the von Karman vortices induced by the cylinder, a flat plate was inserted downstream close to the cylinder. It was demonstrated that vortex shedding was suppressed by the addition of this plate.

Q: Pink

Q : The position of separation occurred in a region of low static pressure ratio due to geometric effects of the cylinder. On aerofoils, the position of transition occurs with relatively higher pressure ratios than that for the cylinder. What would be the effect of the sensitivity of pressure ratio in the presence of upstream disturbances?

A: The fundamental effects due to periodic wakes are not dependent on the geometry (e.g. flat plate, cylinder, airfoil). Of course, transition is dependent on the pressure and Mach number gradients and thus on the geometry. But in cases where transition and separation occur, the principal influence of periodic wakes is the same.

# Time Resolved Measurements of Turbine Blade Flow Phenomena

**T.E. Diller, W.F. Ng and J.A. Schetz**
Virginia Polytechnic Institute and State University
213 Holden Hall, Blacksburg, Virginia 24061-0203
USA

## 1. SUMMARY

The facility and instrumentation are described for studying the effects of time-dependent flow phenomena. The components of unsteadiness from upstream rotor blades and the combustor of a gas turbine engine are modeled individually as shocks, wakes and freestream turbulence. The decomposition of the unsteadiness allows fundamental physical modeling of the effects on the flow structure and blade heat transfer. The strength and spacing of the shocks, the intensity and length-scale of the turbulence, and the wake velocity defect and turbulence can all be independently controlled.

The blow-down facility provides 30 seconds of heated flow through a stationary blade cascade that matches the Reynolds number, Mach number and temperature ratio characteristics of advanced gas turbine engines. Detailed observations are provided by spark shadowgraphs ($10^{-8}$ sec.), laser interferometry ($10^{-7}$ sec.) to obtain the instantaneous global density field, and surface pressure and heat flux measurements. The heat flux measurements have a time response of less than 10 μsec with a continuous voltage output. Because the sensors are less than 2 μm thick, they are non-intrusive to the flow and temperature fields. As one example of the capabilities, computer visualization from shadowgraphs of shock propagation through a blade passage with simultaneous surface pressure and heat flux measurements will be shown.

## 2. INTRODUCTION

The optimization of the aerodynamic and thermal performance of turbomachinery blading requires a detailed knowledge of the internal flow field with respect to the factors that induce losses and promote heat transfer to the blade surface. These factors include boundary layer growth, boundary layer transition location, trailing edge shock characteristics and mixing losses downstream of the trailing edge.

The flowfields encountered in current turbomachines are not only viscous and compressible but also highly unsteady[1,2,3]. A better understanding of these unsteady phenomena is crucial for further improvements to advance the state of the art in axial turbomachines. It has been widely documented that these flows have a significant influence on the efficiency, reliability, aeroelastic stability, forced response and noise generation in modern axial-flow turbines.

Flow unsteadiness in turbine engines arises largely from the relative motion of the blade rows in the alternately stationary and rotating turbine stages.There are three major sources of flow unsteadiness in the interaction between turbine rotor and stator blade rows.

The first cause of flow unsteadiness is a purely subsonic effect termed[4] "potential flow interaction" where the complete inviscid flowfield around each blade is affected by the presence of the neighboring upstream and downstream blade rows.

The second cause of flow unsteadiness in rotating turbine stages is termed "wake passing". The wake passing effect is due to the repeated passage of a downstream blade row through the wakes shed from the trailing edges of the upstream stationary blade row. Of the three major sources of flow unsteadiness, potential flow interaction and wake effects have received considerable prior attention.

Third, for transonic turbines, significant unsteadiness occurs due to the nozzle guide vane (NGV) trailing edge shock structure impinging on the downstream rotor blades[5]. This source of flow unsteadiness, "shock-wave passing", has received much less attention due to the complexity of creating repeatable passing shock events at the required spacing to simulate a real engine environment. However, if progress is to be made in modern turbine blade design, reliable experimental results and computational methods will be required in this flow regime.

The transonic turbine cascade facility at Virginia Tech has been modified to allow the study of unsteady passing shock flow. Here, a shock tube is used to pass a two-dimensional shock along the cascade leading edge in order to simulate the shock impingement from a nozzle guide vane row onto the first high pressure rotor stage in a transonic turbine engine. To allow for time-resolved study of these phenomena, we altered our previous steady interferometric flow visualization system. This, combined with the use of high-frequency heat flux gages and surface pressure gages and spark shadowgraphs, permits detailed observations of these critical unsteady processes.

## 3. EXPERIMENTAL FACILITIES

### 3.1 Wind Tunnel

The experiments for this work were conducted in the Virginia Polytechnic Institute Transonic Cascade Wind Tunnel (Fig. 1), which has been documented

*Paper presented at an AGARD PEP Symposium on "Advanced Non-Intrusive Instrumentation for Propulsion Engines", held in Brussels, Belgium, 20-24 October 1997, and published in CP-598.*

previously[6]. Briefly, the facility is a blow-down wind tunnel which is capable of run times of approximately 30 seconds. The air supply for the tunnel is pressurized by a four stage reciprocating compressor and stored in outdoor tanks. The facility is capable of providing heated flow by way of a heating loop incorporated into the tunnel. The tunnel has a Mach number at the inlet to the test section of approximately 0.36 and a Mach number of 1.26 at the cascade exit. The Reynolds number based on blade chord and throat conditions is $5 \times 10^5$.

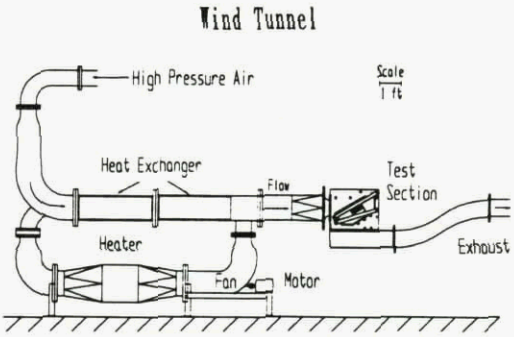


Figure 1. Virginia Tech Transonic Cascade Tunnel

### 3.2 Test Section and Cascade

The turbine blade cascade used in the facility is shown in Fig. 2. It consists of 11 aluminum turbine blades supported by two Plexiglas end walls and two aluminum endblocks. Two aluminum doors hold the endwalls in place within the test section. The doors have a rectangular opening which expose a section of the Plexiglas allowing for flow visualization techniques such as shadowgraphs to be employed in analyzing the flow and shock progression through the cascade. The blades used in the cascade are 5.08 cm (2.0 in) in span and 4.5 cm (1.77 in) aerodynamic chord and are spaced 3.81 cm (1.5 in) apart. The blade profile is designed by General Electric Aircraft Engines and has a high turning angle. Instrumentation is located in the middle (approximately midspan) of the blades in the centermost blade passage. One corner of the test section contains an opening for the insertion of a shock shaper, which introduces a moving shock(s) into the cascade (Fig. 2).

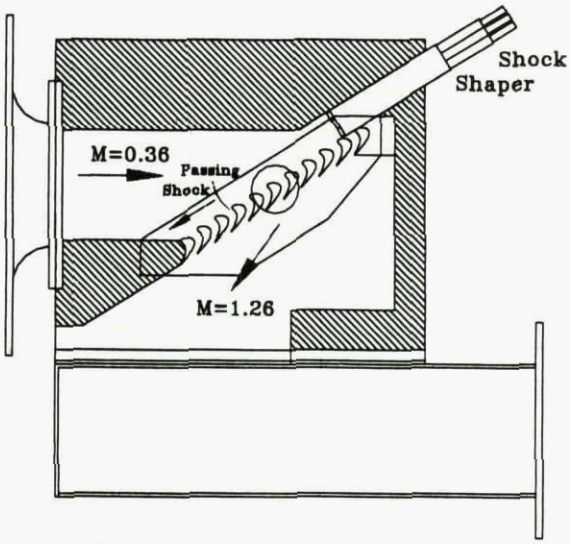


Figure 2. Cascade Test Section

### 3. 3 Shock Wave Production Set-up

The production and introduction of a moving shock into the test section is accomplished via a shock tube and shock shaper configuration[7]. The shock tube uses helium as the driver gas with an approximate driving pressure of 3.45 MPa (500 psi). A 20 mil Mylar diaphragm is used to separate the driver and driven sections. Prior to wind tunnel startup, the driver section is pressurized to approximately 1.4 MPa (200 psi). After starting the wind tunnel, the shock tube driver section is charged with additional helium until the diaphragm ruptured, sending a moving shock wave propagating through the driven section. Two lengths of flexible tubing are connected to the driven section endcap. One tube is connected to a shock shaper which introduces a shock into the test section upstream of the instrumented blade passage along the leading edge of the blades, as shown in Fig. 2. The other tube is used to trigger a Kulite pressure transducer to initiate data acquisition.

The primary purpose of the shock shaper is to change the geometry of the shock entering the test section. After traveling through tubing with a circular cross section, the shock takes on a roughly spherical shape and is undesirable for use in the test section. The shock shaper introduces the shock to a diverging passage which effectively increases the radius of curvature of the shock wave. This increase in radius of curvature is such that the test section and cascade will then be introduced to an approximately planar shock wave. The strength and speed of this shock wave closely match that of the shock emanating from the trailing edge of a transonic turbine blade in an aircraft gas turbine engine.

## 4. INSTRUMENTATION AND DATA ACQUISITION

### 4.1 Heat Flux and Pressure Measurements

Unsteady heat flux measurements in the cascade were made using Heat Flux Microsensors (HFM-7) manufactured by Vatell Corp. The sensors use 300 thermocouple pairs arranged as a thin-film differential thermopile to provide a voltage output directly proportional to the heat flux. Because the sensor is less than 2 μm thick, the frequency response is greater than 100 kHz. The sensing area for the heat flux is approximately 3.2 mm (0.125 in.) in diameter. A platinum resistance element is also provided in a separate circuit to measure the surface temperature. Both the heat flux and temperature elements are sputtered directly on an aluminum nitride substrate which has thermal properties very close to those of the aluminum blade. The sputtering process and sensor characteristics have been previously described.[8-10] The

sensor substrates were mounted in aluminum housings which were insert into the blades flush with the surface. The entire gage assembly is shown in Fig. 3.

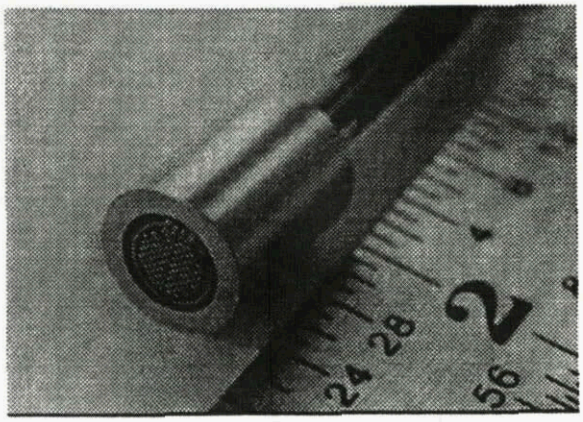

Figure 3. Heat Flux Microsensor

Several heat flux sensors were also manufactured by sputtering the same layered sensor directly on an anodized aluminum blade with the anodization layer providing electrical isolation. Depositing a sensor in this way allow measurement of heat flux with no disturbance of the flow above the blade or of the conduction heat path through the blade that might occur with an inserted sensor.

Calibration of the heat flux sensors was performed by two methods. A radiation calibration was done by the manufacturer (prior to and following experiments). This was then checked during testing by means of an in-situ calibration procedure made possible by the simultaneous surface temperature measurement. In this method, initial transient tunnel start data (from an initially isothermal blade condition) allow the heat flux signal to be mathematically converted to temperature according to a 1-D semi-infinite heat flux model. The sensitivity of the heat flux sensor is then iterated to best match the two resulting temperature signals.[10] The two calibrations showed agreement within 5 percent.

A single blade passage was instrumented with heat flux and pressure gages at 5 separate locations, 3 on the suction surface, and 2 on the pressure surface. The gage locations are shown in Fig. 4.

Unsteady blade static pressures were measured using Kulite XCQ-062-50 high-response miniature transducers. The transducers have a diameter of 1.7 mm (0.067 in). Each transducer is equipped with a B-screen which protects the internal diaphragm from being damaged by debris moving through the test section. The frequency response of the installed transducers is approximately 23 kHz. Pressure transducers were located adjacent to each HFM-7 gage location in order to obtain unsteady pressure and heat flux at a given location simultaneously.

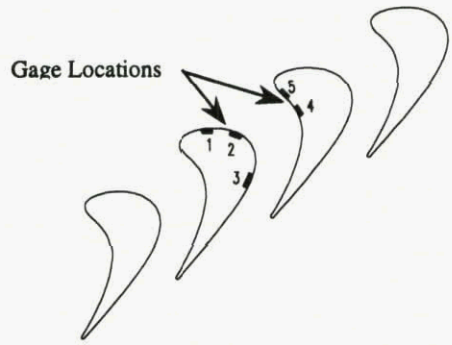


Figure 4. Heat Flux Gage Locations

**4.2 Shadowgraphs**

Spark shadowgraph flow visualization techniques were used to document the progression of shock waves through the cascade. Figure 5 shows an example of a shadowgraph taken in the cascade. Shadowgraphs were taken at different time intervals from a trigger point located upstream of the instrumented passage. The shadowgraphs were compared to the unsteady heat flux and pressure measurement results by correlating an initial peak on a given gage with a shadowgraph. Each shadowgraph has a corresponding delay time at which it was taken from the trigger point. The time axes of the unsteady heat flux and pressure traces were then transformed into the delay time frame. The traces could then be used to correlate a specific shock wave or reflection in the flow shadowgraphs to its corresponding heat flux and pressure peak.

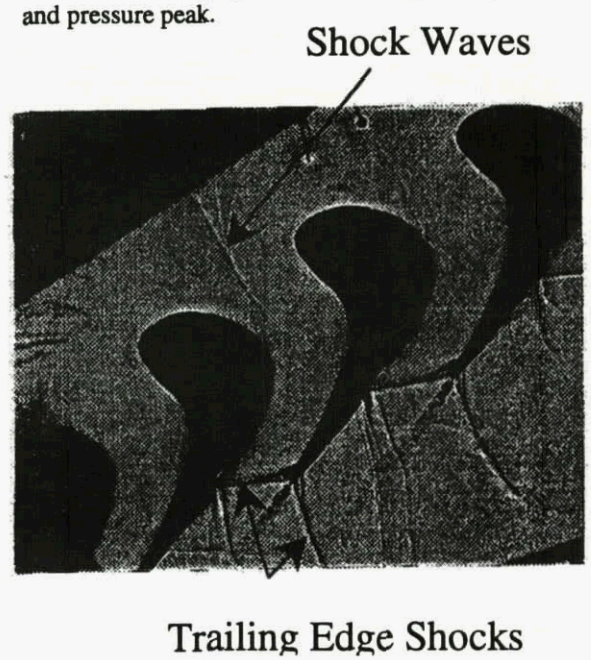


Figure 5. Spark Shadowgraph of Flow in the Cascade with a Passing Shock

### 4.3 Interferometer

An optical interferometer is an instrument designed to exploit the interference of light and the fringe patterns that result from optical path differences. The most commonly used interferometer is the Mach-Zehnder type. (See Ref. (11) for a general discussion of these instruments) Since the light source used in a Mach-Zehnder type interferometer is not coherent, it is necessary to adjust the path length difference between the reference and working beams to be less than one-tenth of a wavelength of the light.

The development of the laser introduced a source of highly coherent light permitting the interference of wavefronts which propagated along various axes. The inherent improvement in coherence length relaxed the requirement for nearly identical path lengths between the arms of interferometric systems. Figure 6 shows the basic optical components of a single-plate interferometric system. The wedge plate splits the light beam into two overlapping beams with a slight angle between them. It is the action of the wedge plate that causes fringe formation. The wedge plate is also the cause of the most distinct feature of single-plate interferograms, the presence of a "double image". Due to the light reflection off both the front and rear surfaces of the wedge plate, all objects in the test section create two separate images at the image plane. The distance between the two images is referred to as the image separation distance. The second parabolic mirror is used to focus the parallel light beams. This image can be focused onto a photographic plate or a CCD camera.

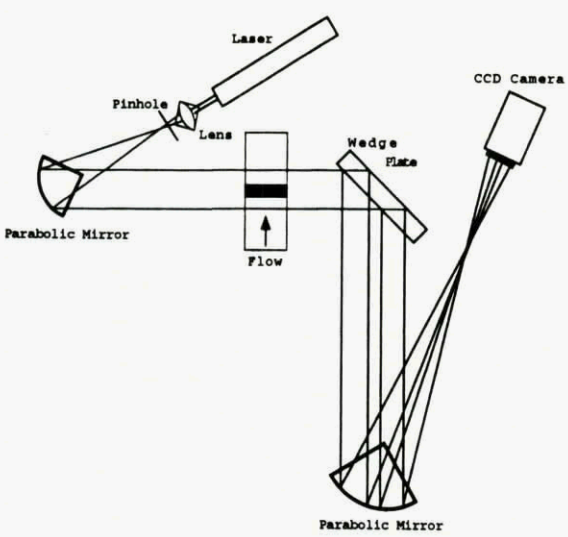


Figure 6. Basic Single-Plate Interferometric System

Some of the advantages of a single-plate interferometer over the Mach-Zehnder interferometer can now be seen. First, since the parallel beam is split only after it passes through the test section, no compensation chamber is needed. Also, since the wedge angle is fixed, there is no need for heavy vibration free mounting of the wedge plate. Furthermore, only a single wedge plate is needed, compared to the two beam splitters and two flat mirrors required for the Mach-Zehnder interferometer. Finally, and most importantly, the setup of a single-plate system is simpler. Disadvantages include lower fringe quality and more difficult data interpretation. For a single-plate interferogram a domain in the flowfield with a known density distribution will be required, however this flowfield can be chosen in a region where data acquisition is relatively easy. Details of interpreting single-plate interferograms can be found in Ref. (12).

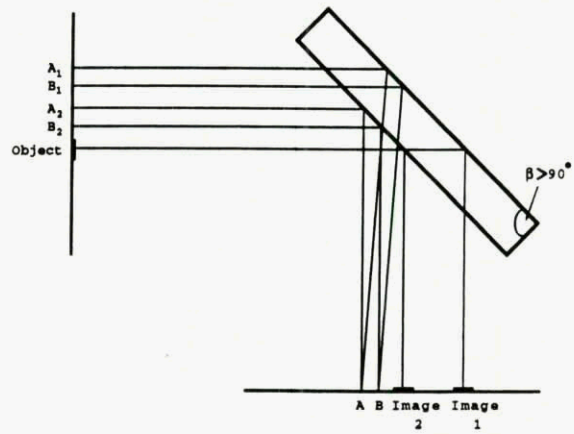


Figure 7. Light Path through Single Plate Interferometer

Figure 7 depicts the image formation for a certain orientation of the wedge plate. If one picks two points, A and B, in the interferogram, the $A_1$, $A_2$, $B_1$ and $B_2$ points can be traced back to the test section. Then, the following relationship can be written between the densities at these points:

$$(\rho_{A_1} - \rho_{B_1}) - (\rho_{A_2} - \rho_{B_2}) = -\lambda_0 / K\left(f_{AB_f} - f_{AB_n}\right)$$

where $\lambda_0$ is the wavelength of the laser light and $f_{AB}$ with subscripts $f$ and n are the number of fringes between points A and B in the interferogram with flow and no-flow, respectively. The $K$ constant is given by

$$K = \frac{Lk}{n_0 \rho_{ref}}$$

where $L$ is the span of the test section, $n_0$ is the index of refraction for ambient air, $\rho_{ref}$ is a reference density (1.252 kg/m$^3$) and $k$=3 x 10$^{-4}$.

Looking at the first equation, it is clear that if the absolute value of the density at a given point is to be found, the density has to be known at three other locations. It can further be shown that when the density is known in a band having the width of the image separation distance, d, the density can be found anywhere else in the studied flowfield.

In the unsteady flowfield of interest here, the passing shock generated by the shock tube travels through the test section at a nominal velocity of 340 m/s. Short shutter times, of the order of 0.33 μs, are needed to capture the image of the passing shock without excessive blur. This shorter shutter time requires an increase in light intensity of at least two orders of magnitude at the photographic plane. Another problem is synchronizing the shuttering of the light source with the passing of the shock. Finally, the major problem of collecting a known density field in these unsteady conditions needed to be addressed as well as the difficulty of referencing all the data together.

CCD intensifier cameras typically have nanosecond shuttering times and high gain capabilities. The CCD camera offered many advantages and simplifications. In order to produce a sequence of timed interferograms showing the passing of the shock, a triggering and synchronizing mechanism was sought. A high-frequency static pressure transducer is placed slightly upstream of the blade passage to be studied. As the shock passes, it creates a sharp pressure spike. This spike, with the addition of a time delay circuit, triggers the shuttering of the CCD camera.

Because of the large number of images to be reduced we elected to automate the fringe detection. Two $C^{++}$ codes were written to reduce the gray-scale images to density values. The pre-processing algorithm has four main functions: image stretching, low-pass filtering, adaptive binarization and line thinning. The second code performs the fringe counting and outputs the final reduced density values. See Ref. (13) for details.

The image information output from a CCD camera is in a format known as gray scale. In order to detect the fringe edges and to enhance fringes that are lost in uneven background lighting, adaptive binarization (also referred to as adaptive thresholding) must be employed. In fixed thresholding, a single gray level is set as the cutoff level. Any pixel values falling under this level are set to 0 (black). Otherwise the pixel value is set to 1 (white), producing a simple black and white image. Setting a single threshold level for the interferometric images is difficult, since the image is disturbed by uneven lighting. Thus, a threshold level that adapts itself to the local gray scale level is required. Locally adaptive binarization methods compute a threshold level for each pixel in the image on the basis of the information contained in the neighborhood of that pixel. Figure 8 shows an example of an adaptively binarized image.

Since the binarization algorithm can leave thick fringes that could complicate the fringe counting, it was necessary to process the binarized images with a line thinning algorithm. The Hilditch algorithm was chosen for its robust nature and ease of implementation. Figure 9 shows an example of a thinned image.

A detailed uncertainty analysis was undertaken and can be found in Ref. (13). The computed reference density value and overall uncertainty given by the jitter program was 2.808 +/- 0.093 (+/- 3.31%) kg/m$^3$.

Figure 8. Adaptively Binarized Interferogram

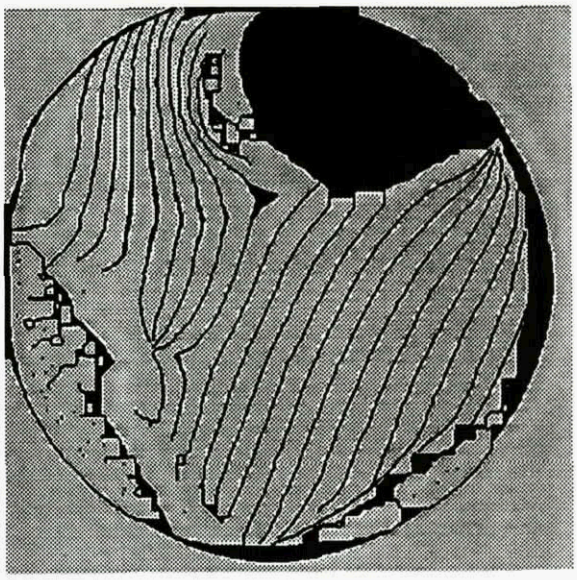

Figure 9. Thinned Interferogram of Unheated Flow

## 5. RESULTS

The relatively long run time of the VPI transonic cascade facility allows a wide variety of fluid and thermal measurements to be made. A sampling of some of the different types of results that have been achieved is presented.

Figure 10 shows heat flux and temperature data for gage location #1 during the entire test run[14]. The tunnel was started at about 9 seconds. The measured heat flux immediately increased sharply and then started to decay

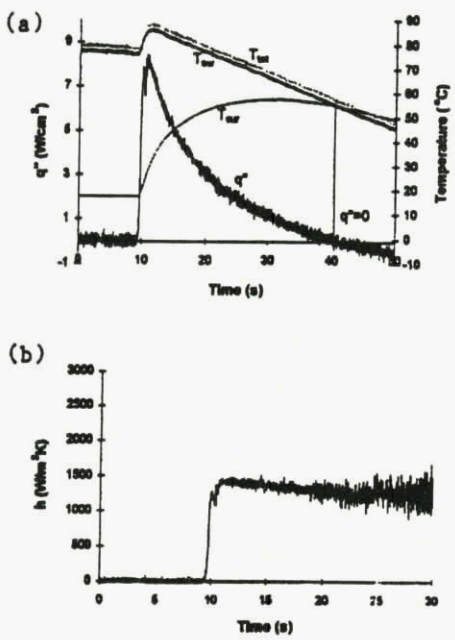


Figure 10. Time History of Heat Flux, Surface Temperature and Heat Transfer Coefficient

and crossed zero at about 40 seconds. The surface temperature ($T_{sur}$) of the blade as measured with the platinum resistance element increased to about 55 C before it started to drop after about 35 seconds into the test run. The total temperature of the tunnel ($T_{tot}$) as measured with a thermocouple placed in the plenum of the tunnel, indicated a monotonic decreasing value with time.

The adiabatic wall temperature ($T_{aw}$) was used to define the heat transfer coefficient (h)

$$h = \frac{q}{T_{aw} - T_{sur}}$$

where q is the measured heat flux. Because the flow temperature is dropping and the blade temperature is rising, a point is eventually reached when the local heat flux reaches zero. At that point the adiabatic wall temperature is measured as the local blade surface temperature. By definition this is expressed in terms of the recovery factor, r

$$T_{aw} = T_{tot} - (1 - r)\frac{U^2}{2C_p}$$

where $C_p$ is the specific heat and U is the freestream velocity above the heat flux gage. Because the freestream velocity is kept nearly constant though control of the tunnel total pressure, the last term of the above equation is assumed constant. The adiabatic wall temperature is, therefore, offset by a constant amount below the total temperature. Consequently, the entire curve for $T_{aw}$ can be determined from the measurements, as shown in Fig. 10a. Using the data from Fig. 10a, the heat transfer coefficient throughout the run can be calculated, as shown in Fig. 10b. The calculated heat transfer coefficient remains fairly constant, as expected. The unusually high fluctuating level of the heat transfer coefficient after 25 seconds is due to the fact that the quotient of q/ΔT approaches zero divided by zero.

In addition to the time-averaged heat transfer coefficients, short runs at high sampling rates (1 MHz) were used to acquire high frequency heat flux information. Simultaneous flow data was obtained directly above the heat flux gage in the turbulent freestream using miniature hot-wire probes. The streamwise velocity was correlated with the surface heat flux. Inlet turbulence fields were generated by upstream grids.

Samples of the resulting data[15] are shown in Figs. 11-13 with the hot-wire positioned 1.0 mm from the blade surface for the heat flux gage on the pressure side at location #5. The energy spectra of the velocity with three different turbulence conditions is shown in Fig. 11. The local turbulence intensity for G0 was 2.17%, for G2 was 4.57% and for G4 was 7.15%. the corresponding heat flux spectra is shown in Fig. 12. The coherence between the two signals is shown in Fig. 13. A value of one specifies complete coherence at the indicated frequency. The coherence below 10 kHz is quite substantial and indicates that the freestream turbulence events are felt all the way through the boundary layer to the surface.

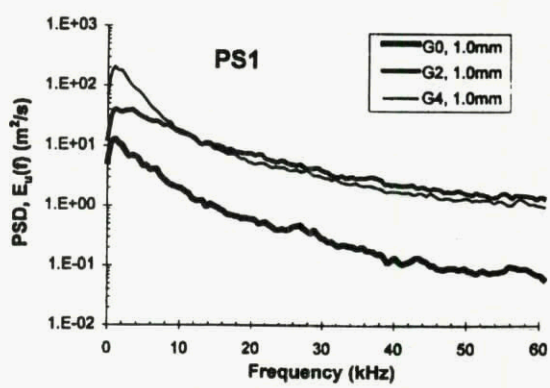


Figure 11. Velocity Energy Spectra of Flow over Gage #5 for Different Grid Turbulence.

The progression of the moving shock waves introduced into the test section was recorded with shadowgraphs triggered from pressure transducers mounted in the test section. The images were computerized and used to produce a timed sequence of the shock movement through the blade passage. This was then compared with the corresponding pressure and heat flux traces for the different gage locations. A sample of these traces is shown in Figs. 11 and 12. The initial shock wave is clearly seen as a sharp rise in both the pressure and heat flux signals. The first reflection is observed about 80 μs later. The gages farther back on the blade see stronger reflections. The importance of the fast time response of

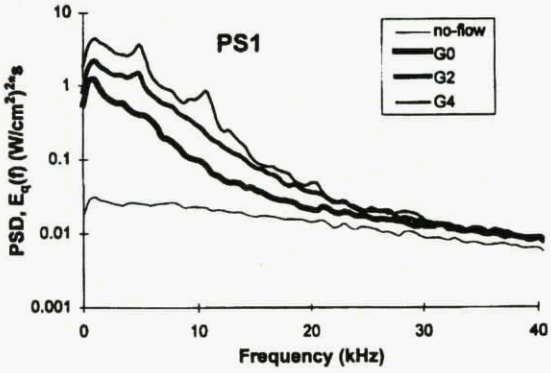


Figure 12. Heat Flux Energy Spectra at Gage #5 for Different Grid Turbulence.

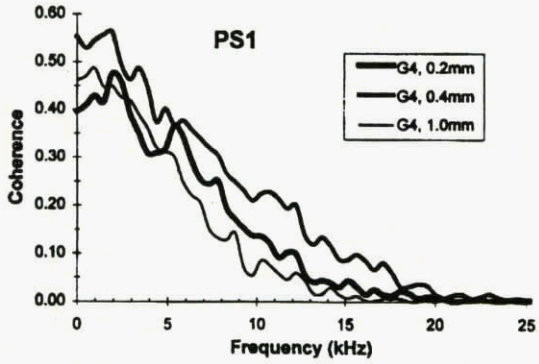


Figure 13. Coherence of Velocity and Heat Flux at Gage #5.

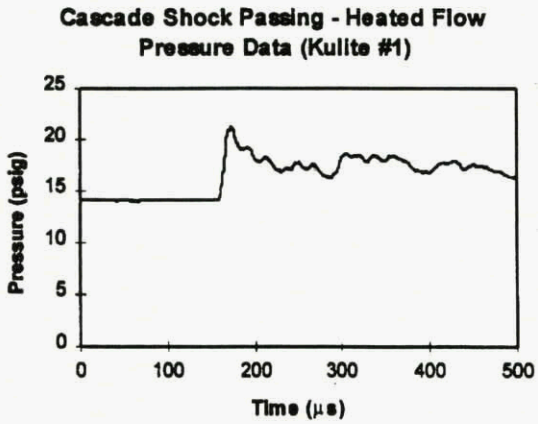


Figure 14. Sample Pressure Data for Kulite #1

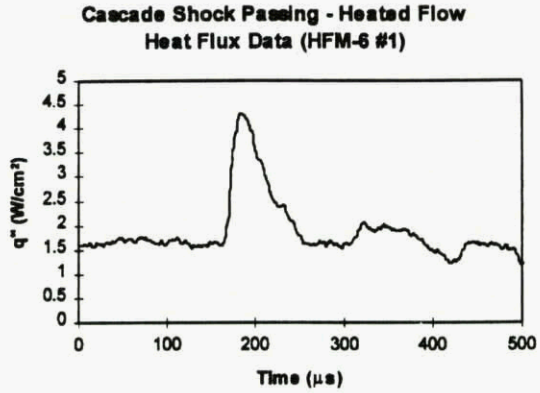


Figure 15. Sample Heat Flux Data for HFM #1

the pressure and heat flux instrumentation is apparent for capturing the details of these shock events.

Figure 16 shows a typical unsteady raw interferogram. To orient the reader, all of the raw interferograms are flipped both horizontally and vertically as a result of optical manipulation of the light path. Therefore, the bottom right of the images is upstream of the cascade and the upper left is in the blade passage. The initial shock will travel from left to right across the bottom of the images. The characteristic double image of single-plate interferograms is easily seen by examining the turbine blade found in the upper right corner of the images. The double image is most noticeable for the blades where one sees a black image and a second gray image displaced from the first.

Figure 16. Unprocessed Interferogram of Unsteady Shock Passing in the Cascade

In order to reduce the interferograms, both a no-flow (an interferogram taken without any tunnel flow) and a flow image must be captured. In a no-flow

interferogram, the density is constant, therefore, the fringes are basically straight lines. When the cascade flowfield is generated and a flow image captured, the density variations shift the fringes. This phenomena is especially noticeable near the crown and the stagnation points of the steady interferograms. Any shock waves present in the flowfield are characterized by the coalescence of a large number of fringe lines.

The raw data is converted to a density field using the procedure outlined above. A representative density field result is shown in Fig. 17, taken at a delay time of 258 μsec.,where the presence of the shock is clearly seen. In all of the density results, the approximate location of the shock is shown by a black line with arrows indicating the direction of travel. Portions of the blade are also shown for reference. As expected, the flow away from the cascade, toward the inlet is fairly uniform with a density value ranging from between 2.4 and 2.5 kg/m$^3$. Also, the decrease in density as the flow enters the blade passage corresponds to the increase in velocity experienced by the flow as it is accelerated toward sonic velocity at the throat. The density behind the shock has increased to over 2.7 kg/m$^3$. The reflection from the suction surface of the lower blade of the initial shock is also shown. The passage of the reflection appears to have reduced the flow acceleration in the blade passage near the suction side, as evidenced by the elevated densities in this region. Further results at other times during the shock passing event are available in Ref. (16).

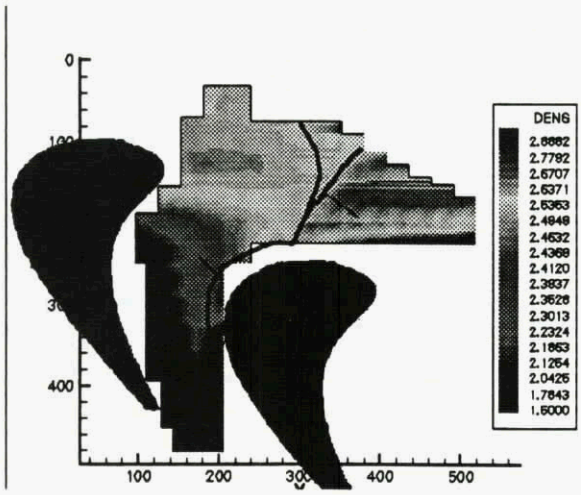


Figure 17. Unsteady Density Field Deduced from the Interferogram in Fig. 16.

## 6. CONCLUSIONS

The facility and instrumentation developed at Virginia Tech for studying the effects of time-dependent flow phenomena in a turbine cascade have been described. The components of unsteadiness from upstream rotor blades and the combustor of a gas turbine engine are modeled individually as shocks, wakes and freestream turbulence. The decomposition of the unsteadiness allows fundamental physical modeling of the effects on the flow structure and blade heat transfer. The strength and spacing of the shocks, the intensity and length-scale of the turbulence, and the wake velocity defect and turbulence can all be independently controlled.

The blow-down facility provides 30 seconds of heated flow through a stationary blade cascade that matches the Reynolds number, Mach number and temperature ratio characteristics of advanced gas turbine engines. Detailed observations are provided by spark shadowgraphs ($10^{-8}$ sec.), laser interferometry ($10^{-7}$ sec.) to obtain the instantaneous global density field, and surface pressure and heat flux measurements.

Sample results from each of the measurement techniques described have been presented to demonstrate the capabilities that have been developed for studying these complex flow phenomena.

## 7. REFERENCES

1. Fottner, L., "Review on Turbomachinery Blading Design Problems," Lecture Series AGARD-LS-167, 1989

2. Seiverding, C. H., and Cicatelli, G., "A Review of the Research on Unsteady Turbine Blade Wake Characteristics." AGARD Conference 1995.

3. Ashworth, D. A., LaGraff, J. E., Schultz, D. L., and Grindrod, K. J., "Unsteady Aerodynamic and Heat Transfer Processes in a Transonic Turbine Stage." ASME Paper 85-GT-128, 1985.

4. Doorly, D. J. and Oldfield, M. L. G., "Simulation of the Effects of Shock Wave Passing on a Turbine Rotor Blade." ASME Paper 85-GT-112, 1985.

5. Rao, K.V., Delaney, R.A. and Dunn. M.G., "Vane-blade Interaction in a Transonic Turbine, Part 1: Aerodynamics," J. Propulsion and Power, Vol. 10, No. 3, pp. 305-311, 1994.

6. Kiss, T., Schetz, J. A. and Moses, H. L. "Experimental and Numerical Study of Transonic Turbine Cascade Flow." AIAA J., Vol. 34, No. 1, pp. 104-109, 1996.

7. Doughty, R. L., Schetz, J. A. and Moses, H. L. "Multiple Shock Wave Generation for Cascade Testing." AIAA Paper 95-0305.

8. Hager, J. M., Onishi, S., Langley, L. W., and Diller, T. E., "High Temperature Heat Flux Measurements." J. Thermophysics and Heat Transfer, Vol. 7, 1993, pp. 531-534.

9. Hager, J. M., Simmons, S., Smith, D., Onishi, S., Langley, L. W., and Diller, T. E., "Experimental Performance of a Heat Flux Microsensor." J.

Engineering for Gas Turbines and Power, Vol. 113, 1991, pp. 246-250.

10. Holmberg, D.G., and Diller, T. E., "High Frequency Heat Flux Sensor Calibration and Modeling." J. Fluids Engineering, Vol. 117, pp. 659-664, December 1995.

11. Holder, D.W., North, R.J. and Wood, G.P., "Optical Methods for Examining the Flow in High-speed Wind Tunnels," AGARDograph 23, AGARD, 1956.

12. Kiss. T., "Experimental and Numerical Investigation of Transonic Turbine Cascade Flow," Ph.D. Dissertation, Virginia Polytechnic Inst. and State Univ., 1992.

13. Wesner, A.L., "An Interferometric Study of Unsteady Passing Shock Flow in a Turbine Cascade," Ph.D. Dissertation, Virginia Polytechnic Inst. and State Univ., 1996.

14. Hale, J.H., Diller, T.E. and Ng, W.F.,"Effects of a Wake on Turbine Blade Heat Transfer in a Transonic Cascade," ASME Paper No. 97-GT-130, 1997.

15. Holmberg, D.G., Ng, W.F. and Diller, T.E.,"A Frequency Domain Analysis: Turbine Leading Edge Region Heat Transfer," accepted for 1997 IMECE in Dallas, TX, Nov. 1997.

16. Wesner, A.L., Schetz, J.A. and Grabowski, H., "An Interferometric Study of Unsteady Passing Shock Flow in a Turbine Cascade," AIAA 97-2751, 1997.

Paper 40
Author J. Schetz

Q: Evans

Is the sharp jump in heat flux as a shock passes due to shock heating, shock-boundary layer interaction, or both?

A: It is difficult to separate precisely shock heating and boundary layer description effects. We have done some analysis and experiments that indicate that shock heating is the larger effect.

# Overcoats for the Improved Performance of PdCr High Temperature Thin Film Strain Gages

**O.J. Gregory, S.E. Dyer and J.D. Cooke**
Department of Chemical Engineering, 205 Crawford Hall
University of Rhode Island
Kingston, RI 02881
USA

## 1. SUMMARY

Overcoat protection schemes for thin film devices have typically focused on inhibiting the growth of native oxides formed on the sensor surface, rather than on improving the passivating nature of these native oxides. Here, thin sputtered Cr overcoats and heat treatments in varying oxygen partial pressures enhanced the passivating nature of native $Cr_2O_3$ films formed on PdCr thin film strain gages. Results of strain tests using sensors protected using this approach are presented and the implications are discussed. PdCr gages with sputtered Cr overcoats withstood 12,000 dynamic strain cycles of 1100 $\mu\varepsilon$ during 100 hours of testing at a temperature of 1000°C in air. Gage factors of 1.3 with drift rates as low as 0.1 Ω/hr were achieved for devices having a nominal resistance of approximately 100 Ω's. TCR's ranging from +550 ppm $°C^{-1}$ to +798 ppm $°C^{-1}$ were realized depending on the overcoat and thermal history. Possible mechanisms for an anomaly in the electrical characteristics of these films at 800 °C and improvements in stability due to the use of overcoats are presented.

## 2. INTRODUCTION

The reliable measurement of both static and dynamic strain at elevated temperatures is critical to the development of advanced gas turbine engines; one of the harshest environments challenging materials systems today. Engine components are subject to rigorous mechanical loading conditions, high temperatures and corrosive and/or erosive media [1,2].

The leading candidate for use as a high temperature static strain gage is based on an alloy of Pd-Cr. These alloys have excellent structural stability up to 1000 °C, form a continuous solid solution (i.e. they do not undergo any phase changes upon thermal cycling) and exhibit the desired strain versus temperature characteristics [3]. NASA has developed static strain gages based on a PdCr (87:13) alloy in both thin film and wire form which are capable of operating at temperatures up to 1000°C for limited periods of time. However, the oxidation resistance of thin film PdCr is marginal due to internal oxidation of Cr in the alloy at high temperature. Attempts to reduce the high temperature oxidation of fine PdCr wires using overcoats such as alumina and alumina with small additions of zirconia have been only moderately successful [4,5].

Historically, work in the area of improving the high temperature stability of thin films has focused on delaying the onset of oxidation via the use of overcoats. Improving the high temperature performance of thin film PdCr strain gages by enhancing the protective nature of the native oxide has not been reported to date.

Although the physical properties of thin film materials are rarely equal to the material properties in bulk form, the oxidation of bulk Cr has been widely studied and these studies have served as a useful reference point. During the oxidation of Cr a single solid oxide forms according to the equilibrium reaction:

$$2Cr(s) + 3/2O_2\,(g) = Cr_2O_3(s) \qquad (1)$$

However, under certain conditions, there are other complications that must be considered. One is the formation of volatile oxides and the other is scale buckling as a result of compressive stress development [6]. Although the formation of volatile oxides is a function of oxygen partial pressure, it is not of concern here. Of interest are the physical properties of the single passivating oxide ($Cr_2O_3$) which forms, with respect to porosity, intrinsic stress and adhesion. Since these properties have been found to be highly dependent on the ambient oxygen pressure during oxidation, an opportunity exists to tailor the properties of the oxide by varying the $O_2$ ambient. Although other authors have reported the growth of relatively strain free, adhesive, $Cr_2O_3$ scales grown from bulk Cr in 100% oxygen, to our knowledge, this approach has never been tried with thin films of PdCr or Cr [7].

*Paper presented at an AGARD PEP Symposium on "Advanced Non-Intrusive Instrumentation for Propulsion Engines", held in Brussels, Belgium, 20-24 October 1997, and published in CP-598.*

The two most important parameters governing the reliability and performance of high-temperature thin film strain gages are (1) gage factor (G) and, (2) temperature coefficient of resistance (TCR). Gage factor is defined as:

$$G = \frac{\Delta R}{R_o} * \frac{1}{\varepsilon} \qquad (2)$$

where R is the resistance of the film and ε is the strain applied to the film. For static strain gages, a constant (or baseline) reference resistance ($R_o$) is used in the calculation, while for dynamic strain, the value of interest is the peak to peak resistance value associated with the cyclic change in applied strain. TCR is defined as:

$$TCR = \frac{\Delta R}{R_o} * \frac{1}{\Delta T} \qquad (3)$$

where T is the temperature and the other parameters are as defined previously. Ideally, a strain gage will exhibit a high G and low TCR. Unfortunately, these two goals are usually found to be in competition with one another and thus trade-offs in these parameters are needed to make practical devices. Continuous metal gages exhibiting low TCR's are limited in theory and practice to G's of $2<G<3$, which have been readily attained in numerous systems, although not at the elevated temperatures researched here [8,9]. Larger gage factors can be realized via the use of semiconductor (G=100) or discontinuous metal films (G=30) [10,11]. However, the TCR and stability of these films are not acceptable for high temperature applications. Recent work using wide-bandgap (heavily doped), semiconducting oxide materials has shown considerable promise [12,13]. TCR's of these materials are lower than is typical of most semiconductors but still higher than is typical of most metal systems. A need exists for improvements in established metal gages as engine temperatures rise in the near future. As reported within, the controlled addition of those components necessary for the formation of self-passivating $Cr_2O_3$ scales grown on PdCr thin films offers possibilities for improvements in the high temperature electrical performance of PdCr thin film strain gages. These improvements demonstrate, for the first time, the suitability of PdCr thin films for use as dynamic strain gages at temperatures up to 1000 °C for extended times. The morphology of $Cr_2O_3$ grown in various partial pressures of oxygen is discussed in terms of its effect on stability and TCR.

## 3. EXPERIMENTAL

### *3.1. Substrates*

Hot isostatically pressed $Si_3N_4$ ceramics were used as the high temperature substrates since they are electrically insulating and exhibit linear-elastic mechanical properties at elevated temperatures. They are also one of the leading candidates for use in advanced aerospace technologies. Surface treatment studies and TCR tests were conducted on as-processed and machined surfaces of the $Si_3N_4$ bars measuring 49.92 mm x 4.02 mm x 3.0 mm. In practice, strain gages may be deposited on either surface. Dynamic and static strain testing required the use of specially designed $Si_3N_4$ beams that insured constant strain down the central axis of the beams, such that errors in the strain measurements could be minimized.

Treatment of surfaces prior to thin film deposition consisted of a high temperature oxidation step, 50 hours at 1200 °C, followed by 40 minutes of selective etching in a 9:1 solution of $NH_4F$ and HF acids. Etch time was determined using ellipsometry to monitor the refractive index, and hence the chemical composition, of the surface as a function of etch time. The substrates were then cleaned in acetone, methanol and DI water followed by a nitrogen blow dry and low temperature oven bake prior to film deposition.

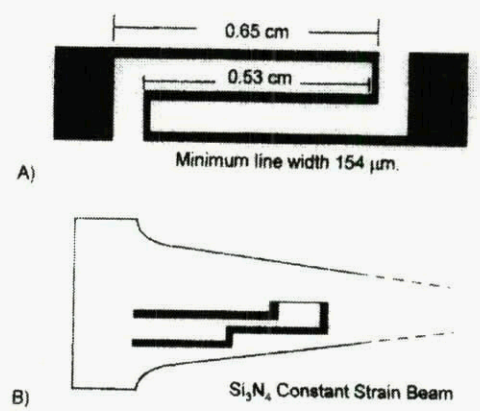


Fig. 1 (A) Plan view of TCR pattern, line widths and spacings in the active region are 154 μm, (B) plan view of high temperature strain gage pattern.

In terms of electrical and mechanical properties, parallel gap resistance welding techniques have been found to be an acceptable method of joining the bulk Pt leadout wires to the thin film Pt bond pads [14]. Welding 0.0076 cm Pt wires to the Pt bond pads and more robust 0.051 cm Pt wires to the 0.0076 cm Pt wires posed little difficulty.

*3.2. Pattern Delineation and Lead Out Wires*

Active strain gage elements were patterned using lift-off microlithography techniques. After deposition of an $Al_2O_3$ interlayer, 4 μm of positive photoresist was spin coated onto the $Si_3N_4$ substrates. Using a UV light source, the strain gage pattern was contact printed onto the photoresist coated $Si_3N_4$ substrates. By eliminating the traditional hardbake step after exposure, clean liftoff was possible after film deposition. Clean liftoff was also enhanced by sputtering the PdCr at very low pressures which aided in its anisotropic deposition. Shadow masking techniques were used for the Pt leadout films and bond pads where Pt lead wires were welded to the devices. Patterns and geometries used for TCR and dynamic strain tests at high temperature are shown in Fig. 1.

*3.3. Thin Film Deposition*

Active strain gage elements, overcoats, and interlayers were deposited at low temperature using an MRC model 822 rf sputtering system. Prior to deposition, the sputtering chamber was evacuated to a background pressure of less than 2 x $10^{-6}$ Torr at which point semiconductor grade argon was leaked into the chamber. Parameters used in sputtering the various layers are given in Table1.

**Table 1.** Thin Film Deposition Parameters. Sputter cycles of 10 minutes on and 10 minutes off for a total sputter time of 1 hour were used to deposit the PdCr films in order to avoid excessive heating of the substrate and hardbaking of the photoresist.

| Mat'l | Target Comp. | Power density (W $cm^{-2}$) | Gas Press. (mT) | Dep rate (Å $min^{-1}$) | Time (min) |
|---|---|---|---|---|---|
| $Al_2O_3$ | 100% $Al_2O_3$ | 17.69 | 8.0 | 67.0 | 75 |
| PdCr | 14% Cr | 23.88 | 3.0 | 235.0 | 60 |
| Cr | 100% Cr | 10.62 | 15.0 | 146.0 | 5 |
| Pt | 100% Pt | 32.81 | 8.0 | 200 | 240 |

*3.4. Interlayers and Overcoats*

$Al_2O_3$ interlayers served as both a means to grade the thermal expansion mismatch between the films and the substrate and as an adhesion promoter. In terms of adhesion and thermally generated stress relief, the thermal coefficient of expansion (TCE) of $Al_2O_3$ is ideal for use with the other materials in this strain gage system.

Overcoat protection focused on enhancing the passivating properties of the naturally occurring $Cr_2O_3$ films formed on pure Cr and PdCr alloys. Thin films of PdCr both with and without sputtered Cr overcoats were oxidized in varying partial pressures of oxygen. Oxidation of films in 100% oxygen ambients was conducted at a temperature of 700 °C after first densifying the films at 700 °C in nitrogen. Then, after cycling to 1000 °C in air, comparisons were made of the electrical properties and morphology of the various films. An electrical anomaly observed in some films at 800 °C was investigated by cycling the films in this region of interest (700 °C to 1000 °C) several times.

*3.5. Electrical Measurements*

Temperature coefficient of resistance (TCR) and electrical drift at temperature experiments were conducted in a Deltech tube furnace. Resistance changes as a function of time and temperature in air ambients were monitored using a Hewlett Packard 34401A multimeter, a Keithley 244 programmable constant current source, and a Keithley 7001 switch system. Currents of +/-1.0 mA were passed at regular time intervals and, using a modified Van der Pauw test structure (4 point probe technique), corresponding voltage drops were read. In this way the resistance of the gage could be determined while negating any contact effects associated with the current carrying leads. Continuous data acquisition was achieved using an IEEE 488 interface and National Instruments' LABWINDOWS software. A type J thermocouple was placed adjacent to the samples to confirm the temperature.

Longitudinal gage factors (G) were determined using a specially designed strain apparatus which induced cyclic strains of up to 1100 μstrain at 1000°C for hundreds of hours. Using constantan alloy strain gages obtained from Measurements Group, Inc., accurate to +/-0.5%, the apparatus was tested and calibrated. In addition to the instruments used for data collection outlined above, output from a linear variable differential transducer (LVDT) was integrated into the setup to monitor instantaneous levels of applied strain. The constant strain beams were alternatively loaded in tension and compression using an eccentric cam powered by a dc motor. The strain gages were ramped at a rate of

3 °C $min^{-1}$ to 1000 °C in air at which point strain testing was initiated.

## 4. RESULTS / DISCUSSION

Scanning electron microscopy (SEM) of the surfaces prior to the oxidation and etch treatment revealed three distinct morphologies on the as-processed surface: an acicular needle-like phase, a broad faced crystalline phase and an amorphous phase (Fig. 2A).

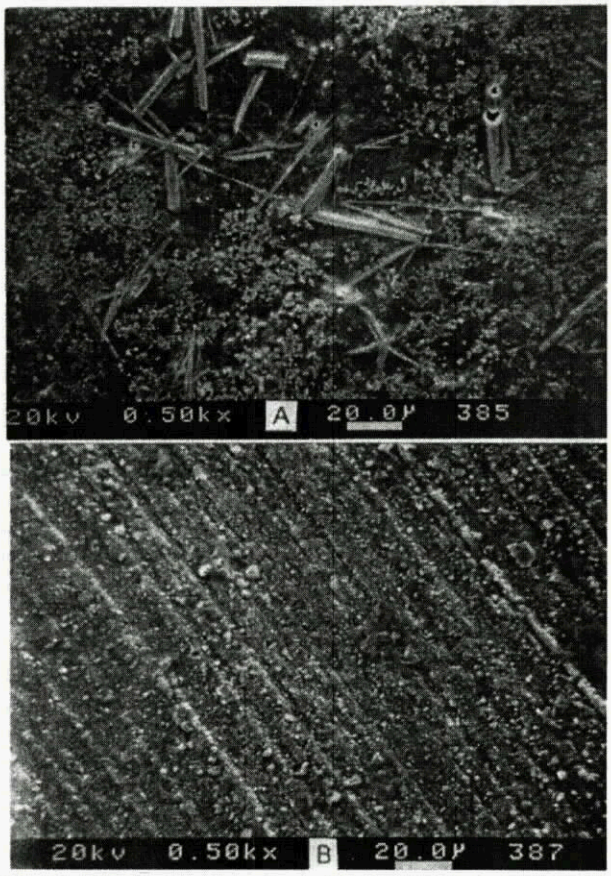


Fig. 2. SEM micrographs of $Si_3N_4$ surfaces prior to oxidation and etch surface treatment; (A) as-processed surface, (B) machined surface

Previous oxidation studies on similar hot isostatically pressed $Si_3N_4$ substrates revealed that the oxide scale generally consists of needle-like and plate-like $Y_2O_3 \bullet 2SiO_2$ crystals; needle-like or lenticular $SiO_2$ and, lastly, amorphous silica containing large amounts of impurity (additive) atoms [15,16]. In contrast, the machined surface appeared much more uniform (Fig. 2B), consisting primarily of an amorphous silica phase.

After the oxidation and etch treatment the two surfaces appear much more similar (Fig. 3A and Fig. 3B). Plate-like and amorphous phases now dominate the morphology of both surfaces. Since thin film strain gages may ultimately be deposited on either surface, one goal of the oxidation and etch treatment was to standardize the two surfaces. This was especially important since the as-received test pieces used in this research had varied thermal histories.

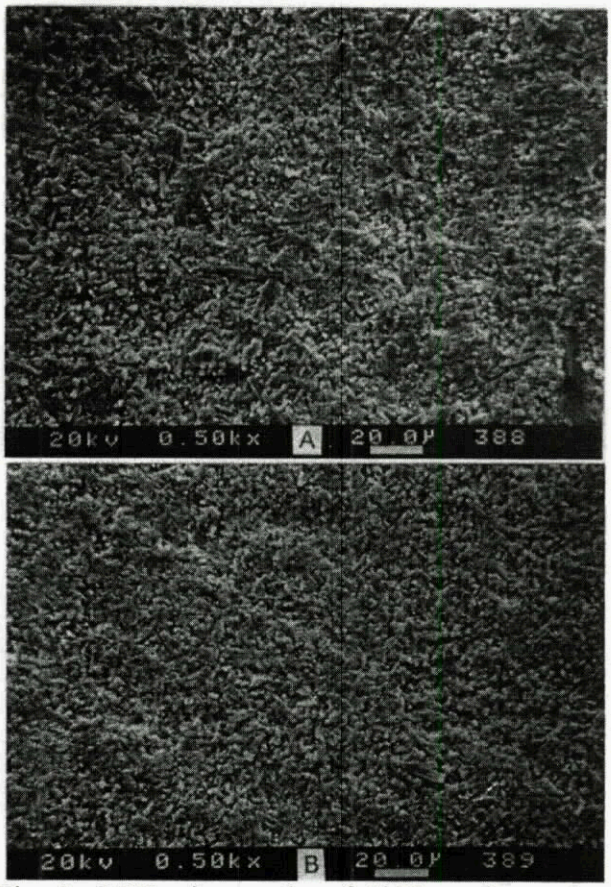


Fig. 3. SEM micrographs of $Si_3N_4$ surfaces after oxidation and etch surface treatment; (A)as-processed surface, (B) machined surface.

Ellipsometry was used to quantify the changes in chemical composition depicted in the metallographic study. After the oxidation step in the surface pre-treatment (i.e. prior to etch), ellipsometry measurements showed an index of refraction for the machined surface of 1.50, which is indicative of mostly $SiO_2$ (1.44); whereas the as-processed surface had an index of refraction of 1.90, which is more characteristic of stoichiometric $Si_3N_4$ (2.05). Excessive amounts of $SiO_2$ on the machined surface were most likely caused by the high surface temperatures attained during prior machining operations. As the ensuing etch progressed, the refractive index of the machined surface changed gradually from that of $SiO_2$ to that of $Si_3N_4$, asymtotically approaching a value of 1.88. The refractive index of the as-processed surface remained constant at approximately 1.90. As a

result of the pre-deposition oxidation and etch surface treatment, the two surfaces are chemically more similar than they were before the treatments. Etching also served to remove the $SiO_2$ layer so that a more stable silioxynitride layer was established as our starting surface. This silioxynitride layer served as an etch stop and had been previously determined to be a stable layer for $Al_2O_3$ depositions [17].

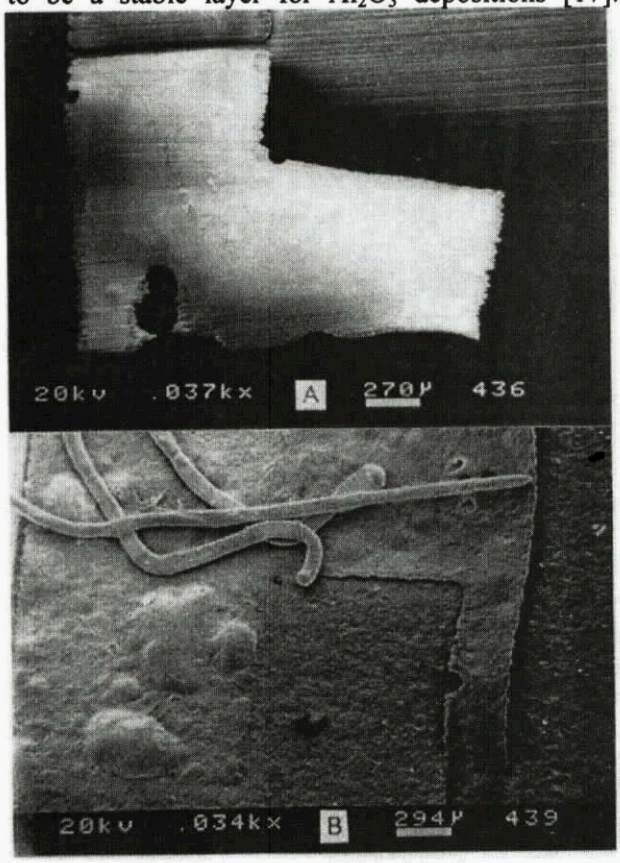


Fig. 4. SEM micrographs showing effect of surface treatment on adhesion of PdCr to $Si_3N_4$ machined surfaces. An interlayer of 5,000Å of $Al_2O_3$ was deposited in both cases; (A) untreated surface; (B) treated surface

Surface profilometry before and after implementation of the oxidation and etch process revealed a slight increase in the roughness of the machined surface. No changes were detected in the topography of the as-processed surface.

Evidence of improvements in the adhesion of PdCr films on treated surfaces (oxidized and etched) versus untreated surfaces is seen in Fig. 4. PdCr thin films were deposited onto treated and untreated machined $Si_3N_4$ surfaces with 5000 Å of $Al_2O_3$ serving as an interlayer. The films were then cycled to a temperature of 1000°C in air. PdCr films deposited onto the untreated surface (Fig. 4A) completely delaminated while those deposited onto the treated surfaces (Fig. 4B) showed characteristic signs of adhesion.

The bubbles present on the treated surface are evidence of decohesion caused by compressive stress built up during the formation of the $Cr_2O_3$ scale. In this context, the bubbles are actually signs of improved adhesion on the treated surface relative to the untreated surface. Bubbles were not observed on the untreated surfaces, since the film easily delaminated from the substrate at the onset of compressive stress development in the film, i.e. the adhesion was so poor that the bubbles did not have a chance to form. The convex shape of the delaminated film is a further sign of compression in the oxide.

Residual stress development in these PdCr alloys is due to the large molar volume increase that results from the oxidation of chromium (Pilling Bedworth Ratio of 2.07), leaving the $Cr_2O_3$ films formed on the surface in a highly compressed state [7]. The overall growth mechanism of $Cr_2O_3$ is the outward transport of Cr and inward transport of oxygen along the grain boundaries. Therefore, most of the new oxide material formed will grow within the scale along the grain boundaries. The result is large growth stresses and scale cracking and deformation [18].

The effectiveness of $Al_2O_3$ as an interlayer is seen in the SEM's of PdCr films cycled to 800°C using varying thicknesses of sputtered $Al_2O_3$ as an interlayer as seen in Fig. 5. PdCr films deposited on 1000 Å of $Al_2O_3$ had many cracks and fissures while those deposited on 5000 Å of $Al_2O_3$ showed little evidence of cracking. Alumina serves as an effective thermal expansion mismatch decoupler since its TCE is between that of $Si_3N_4$ and PdCr, aiding in stress relief during temperature cycling (see Table 2). Laminated structures are often constructed where the materials in the layup are selected to minimize thermally induced mechanical stress between the two outer layers [19].

Another reason that $Al_2O_3$ is an effective interlayer is due to the strong bond it makes to $SiO_2$. Interfacial bond strength is known to be a function of the relative free energy of formation of the respective oxides. For example, if a metal film is deposited onto an oxide, and the free energy of formation of the metal oxide is more negative than the free energy of formation of the surface oxide

onto which the metal is being deposited, the metal will reduce the surface oxide of the underlying layer and form a very strong bond at the interface [20].

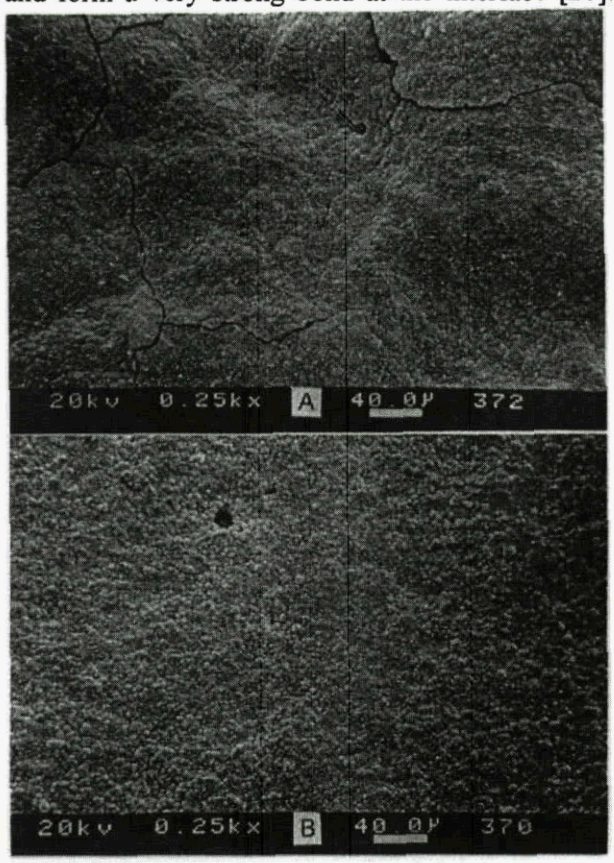


Fig. 5. SEM micrographs of PdCr films cycled to 800 °C using varying thicknesses of sputtered $Al_2O_3$ as an interlayer and thermal expansion mismatch decoupler; (A) 1000Å of $Al_2O_3$; (B) 5000Å of $Al_2O_3$

Since the free energy of formation of $Al_2O_3$ is more negative than that of $SiO_2$ a strong bond is formed when $Al_2O_3$ is deposited on $SiO_2$. Relevant thermodynamic and thermal expansion properties of the materials used in this investigation are given in Table 2.

The morphology of $Cr_2O_3$ grown in various partial pressures of oxygen from both PdCr alloy and pure Cr films is shown in Figures 6 and 7. Processing conditions include: (Fig 6A) PdCr oxidized in air, (Fig 6B) PdCr oxidized in 100% oxygen, (Fig 7A) Cr overcoats oxidized in air and, (Fig 7B) Cr overcoats oxidized in 100% oxygen.

Microstructural differences are evident between PdCr films oxidized in air (Fig. 6A) and those oxidized in 100% oxygen ambients (Fig. 6B). A dense oxide consisting of low aspect ratio

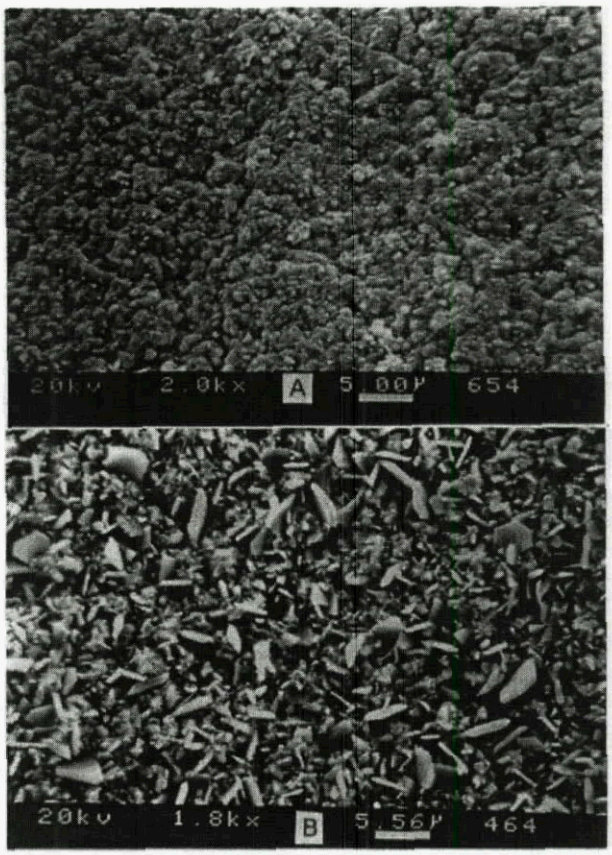


Fig. 6. SEM micrographs showing surface morphology of $Cr_2O_3$ grown in various partial pressures of oxygen from PdCr films; (A) PdCr oxidized in air and (B) PdCr oxidized in 100% oxygen.

**Table 2**: Properties of Selected Thin Film Materials [7,21,22]

| Material | Gibb's Free Energy of Formation (kcal/mole) | Thermal Expansion Coeff. ($K^{-1}$) |
|---|---|---|
| $Si_3N_4$ | ---------- | $1.8 \times 10^{-6}$ |
| $SiO_2$ | -204.7 | $4.0 \times 10^{-6}$ |
| $Al_2O_3$ | -378.1 | $6.0 \times 10^{-5}$ |
| Pd | ---------- | $2.0 \times 10^{-4}$ |
| $Cr_2O_3$ | -253.2 | $7.3 \times 10^{-6}$ |

hexagonal platelets covers the surface of the PdCr film oxidized in 100% oxygen (Fig. 6B). The platelets appear to be growing out from a background scale consisting of smaller nodules. The $Cr_2O_3$ grown in air shows no hexagonal platelets but does exhibit nodular type growths which are connected to form a continuous scale (Fig. 6A). The fissures and nodules present in the scale are typical of brittle, highly stressed oxide growth.

Additional protection was achieved by applying overcoats of Cr to the PdCr films prior to oxidation. It should be emphasized that these overcoats are only 730 Å thick whereas typical thin film overcoat schemes are on the order of 100 μm thick. $Cr_2O_3$

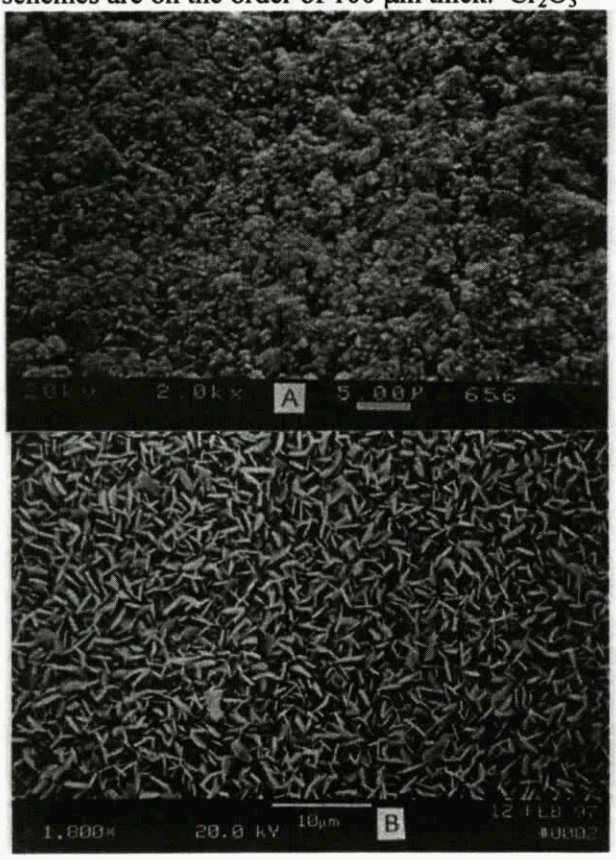


Fig. 7. SEM micrographs showing surface morphology of $Cr_2O_3$ grown in various partial pressures of oxygen from Cr films; (A) Cr oxidized in air and (B) Cr oxidized in 100% oxygen.

grown from pure Cr in air (Fig. 7A) appears similar to $Cr_2O_3$ grown from PdCr in air (Fig. 6A). A continuous nodular scale with fissures typical of $Cr_2O_3$ growth is evident. In contrast, $Cr_2O_3$ grown in 100% oxygen from Cr (Fig. 7B) displays many fine hexagonal platelets effectively covering the surface of the film. This result is similar to that achieved using PdCr and 100% oxygen (Fig. 6B) except now the platelets are more dense and do not appear to grow out of a background of $Cr_2O_3$ nodules.

The use of Cr overcoats allows a continuous passivating $Cr_2O_3$ scale to form quickly, effectively blocking the grain boundary transport of oxygen and the subsequent internal oxidation of Cr in the alloy. In addition, pure oxygen ambients stabilize the growth of hexagonal shaped platelets. The orientation of the hexagonal platelets is important since, compared to the continuous nodular scales, it may reduce the amount of scale cracking resulting from subsequent applied stresses. Stresses included here can be both those induced by the strain testing apparatus as well as those resulting from normal oxide growth. The platelets are anchored at one edge only so they are more able to accommodate the alternate bending stresses induced during strain testing, thereby sustaining the integrity of the passivating film for longer periods under harsh conditions. The second source of stress alleviated by the vertical growth of hexagonal platelets is related to the increased molar volume of $Cr_2O_3$ relative to Cr. Continuous nodular scales are constrained by the surface area of the substrate on which they grow whereas the hexagonal platelets can grow relatively strain free in the vertical direction.

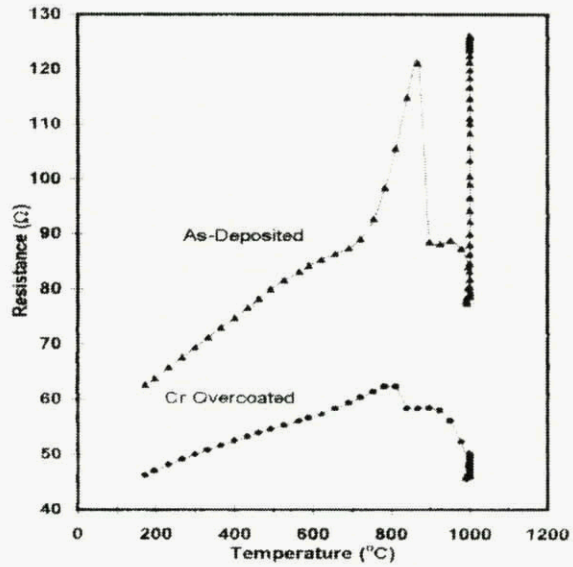


Fig. 8. Electrical resistance as a function of temperature for Cr overcoated and as-deposited PdCr strain gages cycled to 1000°C in air. The increase in resistance at 1000°C is an indication of drift during an 8.6 h hold.

Further evidence of improvements in the self-passivating nature of $Cr_2O_3$ grown on PdCr using Cr overcoats is seen in the electrical properties of these films at high temperature, as seen in Fig. 8.

Gages fabricated with and without Cr overcoats were ramped to 1000 °C in air and held for an extended period while the electrical resistance was monitored. Over the temperature range of 200 °C < T < 700 °C, the as deposited PdCr film exhibited a TCR of +798 ppm $°C^{-1}$ while the gage overcoated with Cr displayed a smaller TCR of +551 ppm $°C^{-1}$. Both gages exhibited a nearly constant TCR up to

approximately 700 °C, at which point TCR for the as-deposited PdCr gage increased sharply. A maximum in resistance was realized for both films at approximately 800 °C, followed by a sharp decrease in resistance. Over the temperature range of 800 °C < T < 1000 °C the resistance of both films decreased to levels approaching their respective starting values.

The electrical anomaly seen in Fig. 8 was accentuated by cycling the films in the temperature region of 700 °C < T < 1000 °C. As seen in Fig. 9,

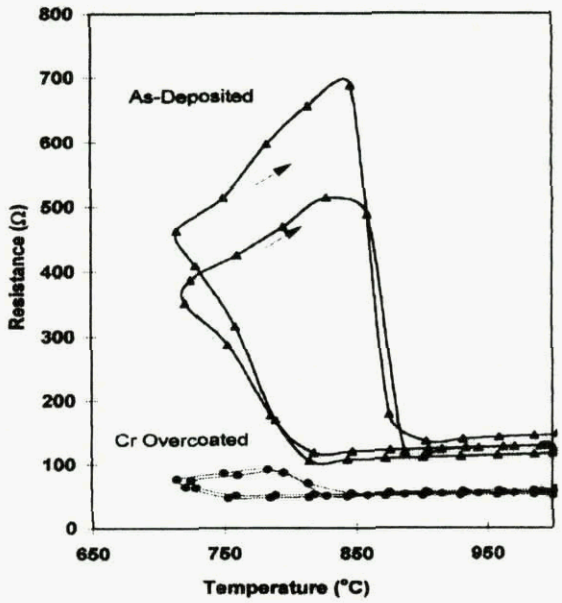


Fig. 9. Electrical instability of Cr overcoated and as-deposited PdCr strain gages in the temperature range 700°C to 850°C.

a repeatable and reproducible hysterisis loop was observed in both films. On a percentage basis, the effect observed for the unprotected film was much greater during these two cycles (Fig. 9) than in the initial cycle (Fig. 8). During the first cycle the maximum resistance of the unprotected film was 122 Ω, but increased to 500 Ω during the second cycle and 700 Ω for the third cycle.

This can be explained by the additive residual stress effects applied to the brittle $Cr_2O_3$ scale during thermal cycling, resulting in scale buckling and cracking. This led to further oxidation of the underlying PdCr and caused the upward trend in resistance. However, for the Cr protected gage, the magnitude of the electrical anomaly as a consequence of additional cycling was insignificant. For this film the maximum resistance for the first cycle was 62 Ω and increased to only 89 Ω for the second cycle and 94 Ω for the third cycle. This is further evidence of the improved protection provided by the passivating $Cr_2O_3$ grown on the pure Cr overcoat. Fig. 8 also provides additional TCR data for the temperature range of 900 °C < T < 1000 °C. In this range the as deposited PdCr film exhibited a TCR of +518 ppm $°C^{-1}$ while the gage overcoated with Cr displayed a TCR of +507 ppm/°C.

Other researchers have noted the anomaly in resistivity behavior described above in thin wire PdCr strain gages (diameter 25 μm) at approximately 800 °C. The cause was attributed to microstructural changes caused by Si and $Al_2O_3$ impurities in the drawn wire. When the wire was replaced by thin films of PdCr (10 μm) the anomaly disappeared [22]. Several phenomena may be responsible for the presence of the electrical anomaly in our PdCr thin films. Among these are impurities derived from the lift-off lithography techniques employed for pattern transfer, which are eventually introduced into the sputter chamber. The lack of a hardbake step in the processing sequence leads to outgassing of spin casting solvents, absorbed water, developer, and photo active compounds present in the resist upon exposure to vacuum. Ironically, it is this same outgassing that proved so beneficial in eliminating the film tearing usually associated with lift-off type procedures during pattern delineation. Blisters and bubbles were observed in PdCr films deposited directly over the photoresist, which is a strong indication that outgassing occurred during deposition.

Other possible explanations for the electrical anomaly seen here are: (1) the generation and relaxation of stresses due to oxide growth, (2) competing grain growth and grain boundary oxidation processes, and as discussed earlier, (3) thermal expansion coefficient mismatch between the various layers. In contrast to the 10 μm PdCr films used in other studies, our films were only 1.4 μm thick. The compressive stresses associated with $Cr_2O_3$ assures that as the oxide forms, the underlying PdCr film will be put into a state of tension, assuming that there is reasonable adherence of the metal to the oxide. These stresses may lead to changes in resistance. Stress relief as a result of crack formation in the brittle $Cr_2O_3$ may also result in resistance changes. Additionally, the processes of grain growth (decreased resistance) and

oxidation (increased resistance) may have an effect as temperatures increase.

The effect of Cr overcoat protection on the resistivity drift rates of PdCr strain gages held at a temperature of 1000 °C can be seen in Fig. 10.

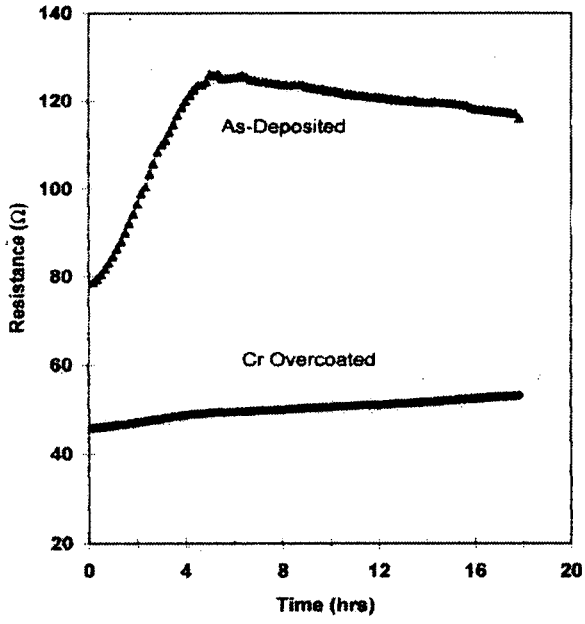


Fig. 10. Drift of Cr overcoated and as-deposited PdCr strain gages held at a temperature of 1000°C in air for 17 hr.

The first 8.6 hours of this 17.8 hour soak can also be seen in the vertical rise in resistance at 1000 °C in Fig. 8. During the first 5.2 hours of the soak, the drift of the unprotected (i.e. as-deposited) PdCr gage was 10.2 Ω $hr^{-1}$ (12.0%), after which time the drift diminished to -1.1 Ω $hr^{-1}$ (0.89%) for the remaining 12.6 hours of the test (17.8 hours total). On the other hand, the gage protected with a pure Cr overcoat exhibited almost no drift at temperature for the entire 17.8 hour test. For this gage, an initial drift of 0.44 Ω $hr^{-1}$ (0.92%) for the first 5.2 hours was followed by a drift of 0.38 Ω $hr^{-1}$ (0.76%) for the duration of the test. These results compare favorably with state of the art 10 μm thick PdCr films deposited by NASA, where drifts of 0.8 % after 17 hours at 1050 °C were observed [22]. Since our films are much thinner (1.4 μm), further improvements may be realized in terms of strain sensitivity and response.

The 5.2 hour delay in electrical stabilization of the unprotected PdCr strain gage relative to the Cr protected gage is a sign of the rate at which a continuous, protective scale of $Cr_2O_3$ forms. The films overcoated with Cr have the advantage of forming a passivating $Cr_2O_3$ layer quickly over the entire surface since many more nucleation sites are available for growth of the self-passivating oxide. $Cr_2O_3$ grown from the PdCr matrix (14% Cr) forms initially at the surface Cr sites. Since a continuous passivating film cannot form quickly on the surface, grain boundary diffusion of Cr and oxygen dominates, leading to internal oxidation of Cr and the development of large internal stresses. Overcoats of Cr minimize this effect.

During high temperature (1000 °C) dynamic strain testing in air, PdCr strain gages with Cr overcoats proved to be much more stable than those strain gages fabricated without a Cr overcoat. A typical device fabricated without the benefit of a Cr overcoat exhibited relatively high initial drift rates (77 Ω/hr) which did not diminish quickly enough to warrant further testing. On the other hand, initial drift rates of the PdCr gage overcoated with pure Cr were significantly lower and quickly decreased to negligible levels. Piezoresistive responses at selected intervals for a Cr overcoated PdCr strain gage oxidized in air are shown in Fig. 11. Piezoresistive data taken from complete I-V characteristics were sampled for ten minutes every hour over the duration of the test. Results in Figure 11 are shown after (A) 4.4 hours, (B) 25.0 hours, (C) 39.0 hours and (D) 75.0 hours of continuous dynamic strain. In the early stages of the dynamic strain measurements a drift rate 2.6 Ω $hr^{-1}$ (3.0%) was determined along with a gage factor of 1.5 (Fig. 11A).

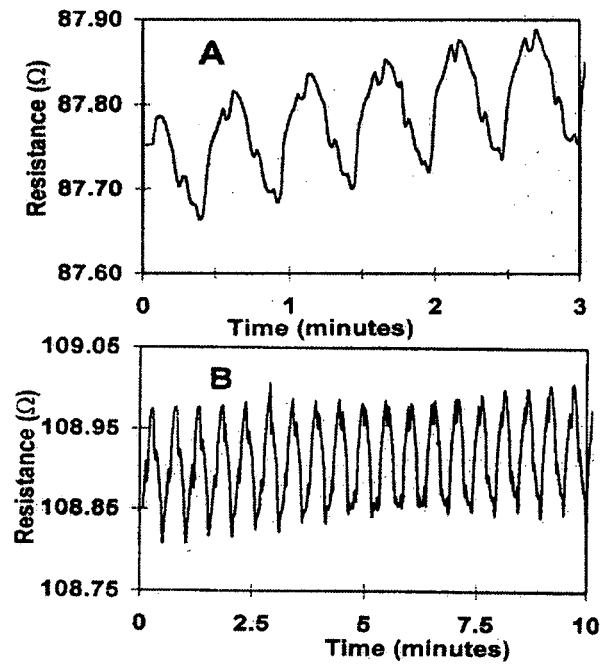

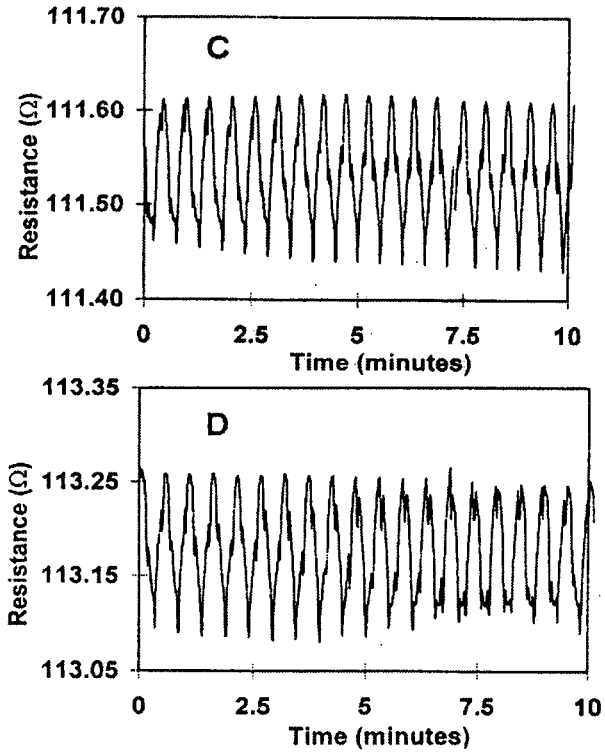


Fig. 11. Piezoresistive response of a Cr overcoated PdCr strain gage strained cyclically to 1100 microstrain at a temperature of 1000°C in air for over 100 hours; (A) after 4.4 hrs, (B) after 25 hrs, (C) after 39 hrs and, (D) after 75 hrs

As the test progressed, drift rates diminished to negligible levels and gage factors of 1.3 were established over the time interval of 25 hours to 100 hours. Overall, the PdCr strain gage protected by a passivating $Cr_2O_3$ scale grown in air from pure Cr survived 12,000 strain cycles of 1100 με over a period of 100 hours at 1000 °C.

The final stages of this study involved the testing of a PdCr strain gage overcoated with Cr and pre-oxidized in 100% oxygen ambients. Here, earlier discussion on the microstructure of $Cr_2O_3$ and its effect on gauge stability (Figs. 6 and 7), suggesting vertical, hexagonal platelets may offer better protection than continuous, nodular type growths, is shown to be valid. Using the processing steps outlined in this paper, a prototype strain gage was fabricated and tested at Allied Signal Engines at a temperature of 900 °C in air, after first oxidizing the Cr overcoat in 100% oxygen. Testing in state of the art facilities using dynamic strain cycles of 1000 με applied at 1000 Hz, resulted in a gage surviving more than 10,000,000 strain cycles [23].

## 5. CONCLUSIONS

The performance of high temperature, thin film strain gages based on PdCr has been significantly improved by enhancing the protective properties of the native $Cr_2O_3$ films formed on the surface of these sensors. By depositing sufficient Cr to form a continuous, passivating $Cr_2O_3$ scale and oxidizing under high oxygen partial pressures, positive results were realized with respect to electrical stability and robustness. Morphological studies of $Cr_2O_3$ scales grown from PdCr and Cr surfaces in varying partial pressures of oxygen have been presented and their influence on gauge performance discussed.

Based on thermodynamic/physical properties such as the relative free energies of formation and TCE, interlayers were selected and incorporated into the thin film stack which improved the adhesion of rf sputtered PdCr films and aided in their stress relief during thermal cycling. Treatments used to stabilize the surface of various $Si_3N_4$ ceramic substrates proved to enhance the stability of the sensors as well.

Ultimately, these improvements were demonstrated in the electrical response of these films at high temperature. Gage factors averaging 1.3 were measured as well as TCR's and drift rates as low as +507 ppm $°C^{-1}$ and 0.76%, respectively, for extended high temperature low frequency testing. Explanations for an electrical anomaly frequently observed in these films at a temperature of 800 °C were discussed. The performance of these films has been greatly improved to the point where, for the first time, these films are shown to warrant use as high temperature dynamic strain sensors.

## 6. ACKNOWLEDGEMENTS

The authors would like to thank NASA Lewis Research Center, Cleveland, OH and AlliedSignal Engines, Phoenix, AZ for support of this work.

## REFERENCES

1. V. DeSapio, "Advanced Structural Ceramics: Challenges to Commercializa-tion," *ChemTech*, (1993) 46-51.

2. J.T. Demasi-Marcin and D.K. Gupta, "Protective Coatings in the Gas Turbine Engine," *Surf. Coat. Technol*, 68/69 (1994) 1-9.

3. C.O. Hulls, R.S. Bailey and F.D. Lemkey, "High Temperature Static Strain Gage Alloy Development Program," *NASA Report No. CR-174833*, 1985.

4. J.F. Lei, "Influence of Rare Earth Oxide Additions on the Oxidation Behavior of PdCr Strain Gage Material, *177th Electrochemical Society Meeting*, ECS abstract 933, (1990) 90-91.

5. J.F. Lei, "A Resistance Strain Gage with Repeatable and Cancelable Apparent Strain for Use to 800°C," *NASA Report No. CR-185255*, 1990.

6. N. Birks and G.H. Meier, Introduction to High Temperature Oxidation of Metals, Edward Arnold Ltd, London, p. 81, 1983.

7. P. Kofstad, *High Temperature Corrosion*, New York: Elsevier Applied Science Publishers Ltd., 1988, p.255.

8. W.H Atkinson, M.A. Cyr and R.D. Strange, "Development of Sensors for Ceramic Components in Advanced Propulsion Systems - Phase Two," *NASA Report No. 195283*, 1994.

9. M.M. Lemcoe, "High Temperature Strain Gage Measurements to 2000°F: Can it be done?," *Sensors Expo International Conference Proceedings*, 203C-1-7, 1989.

10. M.A. Angadi, R. Whiting, R. Angadi, "The Electromechanical Properties of Thin Manganese Films," *J. Mater. Sci. Lett.*, 8 (1989) 555-558.

11. C. Li, P.J. Hesketh, and G.J. Maclay, "Thin Gold Film Strain Gauges," *J. Vac. Sci. Technol. A*, 12 (1994) 813-819.

12. S.E. Dyer, O.J. Gregory, P.S. Amons and A. Bruins Slot, "Preparation and Piezoresistive Properties of Reactively Sputtered Indium Tin Oxide Thin Films," *Thin Solid Films*, 288 (1996) 279-286.

13. O.J. Gregory, A. Bruins Slot, P.S. Amons and E.E. Crisman, "High Temperature Strain Gages Based on Reactively Sputtered AlNx Thin Films," *Surf. Coat. Technol*, 88 (1996) 78-89.

14. P. Kayser, J.C. Goderoy and L. Leca, "High-Temperature Thin-Film Strain Gages," *Sens. Actuators A*, 37-38 (1993) 328-332.

15. G. E. Aniolek, *Thin Film Sensors for High Performance Silicon Nitride Ceramics*, University of Rhode Island, Thesis, 1994.

16. G.N. Babini, A. Bellosi, P. Vincenzini, "A Diffusion Model for the Oxidation of Hot Pressed $Si_3N_4$-$Y_2O_3$-$SiO_2$ Materials," *J. Mater. Sci.*, 19 (1984) 1029-1042.

17. G.E. Aniolek and O.J. Gregory, "Thin Film Thermocouples for Advanced Ceramic Gas Turbine Engines", *Surface and Coatings Technology*, **68/69**, 70-75, 1994.

18. E.W.A. Young, J.H. Gerretsen and J.H.W. de Wit, "The Oxygen Partial Pressure Dependence of the Defect Structure of Chromium(III) Oxide, *J. Electrochem. Soc.: Solid State Science and Technology*, Sep. (1987) 2257 -2260.

19. D.G. Lamoreaux, "Thermal Expansion Decoupler," *Motorola Inc. Technical Developments*, 15 (1992) 122.

20. O.D Trapp, L.J. Lopp and R.A. Blanchard, *Semiconductor Technology Handbook*, Technology Associates, sec.8 (1993) 12.

21. D.R. Lide, *Handbook of Chemistry and Physics - Edition 71*, CRC Press, sec.5 (1990) p. 4.

22. J.F. Lei and W.D. Williams, "PdCr Based High Temperature Static Strain Gage," *AIAA 2nd International Aerospace Planes Conference*, (1990)1-7.

23. Harvey Niska, AlliedSignal, Unpublished data.

# High Temperature - Thin Film Strain Gages Based on Alloys of Indium Tin Oxide

**Otto J. Gregory, James D. Cooke and Joseph M. Bienkiewicz**
Department of Chemical Engineering, 205 Crawford Hall
University of Rhode Island
Kingston, RI 02881
USA

## 1. SUMMARY

A stable, high temperature strain gage based on reactively sputtered indium tin oxide (ITO) was demonstrated at temperatures up to 1050°C. These strain sensors exhibited relatively large, negative gage factors at room temperature and their piezoresistive response was both linear and reproducible when strained up to 700 μin/in. When cycled between compression and tension, these sensors also showed very little hysteresis, indicating excellent mechanical stability.

Thin film strain gages based on selected ITO alloys withstood more than 50,000 strain cycles of +/- 500 μin/in during 180 hours of testing in air at 1000°C, with minimal drift at temperature. Drift rates as low as 0.0009 %/hr at 1000°C were observed for ITO films that were annealed in nitrogen at 700°C prior to strain testing. These results compare favorably with state of the art 10 μm thick PdCr films deposited by NASA, where drift rates of 0.047 %/hr at 1050°C were observed [1,2]. Nitrogen annealing not only produced the lowest drift rates to date, but also produce the largest dynamic gage factors (G= -23.5).

These wide bandgap, semiconductor strain sensors also exhibited moderately low temperature coefficients of resistance (TCR) at temperatures up to 1100°C, when tested in a nitrogen ambient. A TCR of +230 ppm/°C over the temperature range 200°C<T<500°C and a TCR of -469 ppm/°C over the temperature range 600°C<T<1100°C was observed for the films tested in nitrogen. However, the resistivity behavior changed considerably when the same films were tested in oxygen ambients. A TCR of -1560 ppm/°C was obtained over the temperature range of 200°C<T<1100°C. When similar films were protected with an overcoat or when ITO films were prepared with higher oxygen contents in the plasma, two distinct TCR's were observed. At T< 800 °C, a linear TCR of -210 ppm/°C was observed and at T> 800°C, a linear TCR of -2170 ppm/°C was observed.

The combination of a moderately low TCR and a relatively large gage factor make these semiconducting oxide films promising candidates for the active strain elements in high temperature thin film strain gages, particularly in applications where static strain measurement is desired.

## 2. INTRODUCTION

A new family of high-temperature resistance strain gages, based on thin films of indium-tin oxide (ITO), is being developed to meet future materials requirements in advanced aerospace structures and propulsion systems [3,4]. An accurate measurement of both static and dynamic strain, at temperatures greater than 1000 °C, is often required when evaluating a materials durability and predicting the lifetime of aerospace propulsion systems [1,2,5-8]. Conventional resistance strain gage techniques cannot be used to measure strain in such applications, due to the intrusive nature of these devices, and problems associated with bonding the sensor elements. Thin film strain gages are deposited directly onto the surface of a component by rf sputtering techniques and, as a result, are in direct communication with the surface being deformed. They are particularly attractive in advanced propulsion systems, since they do not adversely affect gas flow over the surface of a rotating component, they have a negligible thermal mass and do not require adhesives or cements for bonding purposes [7].

Indium-tin oxide is a promising candidate for the active strain elements in high temperature thin film strain sensor applications due to its electrical and chemical stability at high temperature and its relatively large piezoresistive response. ITO solid solutions are stable in pure oxygen ambients at temperatures greater than 1500°C but can dissociate in pure nitrogen ambients at temperatures as low as 1200°C [9, 10]. The sublimation temperatures for bulk ITO ceramics in air ambients should occur somewhere in between these values, and these solid solutions should be stable at temperatures up to 1300°C.

*Paper presented at an AGARD PEP Symposium on "Advanced Non-Intrusive Instrumentation for Propulsion Engines", held in Brussels, Belgium, 20-24 October 1997, and published in CP-598.*

These thin film strain gages will not only be subjected to large mechanical strains, they will also be subjected to large thermal strains as well. Therefore, those parameters that affect the accuracy and sensitivity of the strain gage over an extended temperature range must be considered in their development. Two of these critical design parameters are the temperature coefficient of resistance (TCR) and the gage factor (G) as defined below [11, 12]

$$TCR = \frac{\Delta R / R_0}{\Delta T} \tag{1}$$

$$G = \frac{\Delta R}{R} \cdot \frac{1}{\varepsilon} \tag{2}$$

where $\varepsilon$ is strain, R is resistance, and T is temperature. The total contribution to the measured strain (fractional resistance change) for a given application is the sum of the actual mechanical strain at a given temperature and the apparent or temperature induced strain due to the TCR of the semiconductor and the differences in thermal expansion between the gage and the substrate, as shown below:

$$\Delta\varepsilon = \frac{[\Delta R / R]_\varepsilon}{G} = \frac{[(\Delta R / R)_{\varepsilon,T} - (\Delta R / R)_T]}{G} \tag{3}$$

where

$$(\Delta R / R)_T \equiv [TCR_g + (\beta_s - \beta_g)G]\Delta T \tag{4}$$

$$(\Delta R / R)_T = \alpha_g \Delta T \tag{5}$$

and where $\beta_s$ and $\beta_g$ are the coefficients of thermal expansion for the substrate and gage, respectively. From the above relationships, it is evident that the TCR should be as low as possible to avoid the need for temperature compensation [3-8]. By minimizing the thermal component of static strain (apparent strain) and maximizing the gage factor, it should be possible to maximize sensitivity and output of the sensor. If for example, an engine component experiences a 10% variation in temperature across the surface at 1000°C ($\Delta T$ = 100°C), and the strain gage has a gage factor of -20 with an accuracy of 10%, the TCR of the strain gage should be -40ppm/°C or less, if the sensor is to be used without temperature compensation, assuming there is no difference in TCE between the substrate and gage. Under these static strain conditions, a strain gage with a TCR greater than -40ppm/°C would make temperature compensation necessary.

In general, the piezoresistive response (or gage factor) of a semiconductor strain gage is the finite resistance change of the sensing element when subjected to a strain, and results from both changes in dimension of the active strain element and changes in the resistivity ($\rho$) of the active strain element [7]. The piezoresistive effect in semiconductors, given by equation (6) below, is typically 1-2 orders of magnitude greater than those observed in metals and alloys [3,4], largely due to the resistivity dependence on strain:

$$G = 1 + 2\eta + \left(\frac{d\rho}{\rho} \cdot \frac{1}{d\varepsilon}\right) \tag{6}$$

where $\eta$ is Poison's ratio and $\rho$ is the semiconductor resistivity. Specifically, the large piezoresistive effect observed in elemental semiconductors such as germanium and silicon, has been related to changes in mobility and carrier concentration as a direct result of changes in the band structure and the anisotropy of the effective mass [11-14].

In addition to the piezoresistive response, the active strain elements used in a high temperature static strain gage, should exhibit a relatively low temperature coefficient of resistance (TCR) so that the thermally induced apparent strain ($\Delta\varepsilon_T$) in equation (7) below is negligible compared to the actual applied strain. The drift rate (DR) at temperature, described by equation (8) below, should also be small compared to the applied strain, especially where testing protocols require prolonged exposure at elevated temperature.

$$\Delta\varepsilon_T = {(\Delta R / R_0)_T}/{G} \tag{7}$$

$$DR = \frac{\Delta R}{R} \frac{1}{t} \tag{8}$$

Metallic based strain gages typically have low TCR's (< 500 ppm/°C) and low gage factors (on the order of 2). Semiconductor based strain gages posses much larger gage factors but are usually limited by the relatively high TCR's (>2000 ppm/°C), associated with intrinsic semiconduction. However, heavily doped semiconductors with relatively high charge carrier concentrations can exhibit temperature independent electrical behavior,

atypical of intrinsic semiconductors. By fabricating semiconductors that exhibit saturated extrinsic behavior, the production of thermally activated charge carriers can be held to a minimum, thereby minimizing TCR.

The temperature range over which a semiconductor's conductivity is dominated by extrinsically generated charge carriers is dependent on bandgap. Thus, wide bandgap semiconductors have the greatest potential for strain gage applications, within this class of materials. Of all of the wide bandgap semiconductors, the oxide semiconductors exhibit the best stability in oxidizing ambients and thus, from this viewpoint, indium tin oxide with a bandgap of 3.5 ev has considerable potential as an active strain element.

In this paper, we report on the piezoresistive properties of ITO strain gages measured at low and high temperatures as well as the TCR and drift rates of the same films. The potential that these ITO thin films have as the active strain element in high temperature strain gages is discussed.

## 3. EXPERIMENTAL

### *3.1 Thin film deposition*

Indium-tin oxide (ITO) films were deposited by rf reactive sputtering at low temperature using an MRC model 822 sputtering system. A high density target (12.7 cm in diameter) with a nominal composition of 90 wt% $In_2O_3$ and 10 wt% $SnO_2$ was used for all depositions. Prior to deposition, the sputtering chamber was evacuated to a background pressure of less than 1 x $10^{-6}$ Torr , at which point semiconductor grade argon and oxygen were leaked into the chamber to establish a total pressure of 8 mTorr. Oxygen partial pressure was varied from 0% to 50% while an rf power density of 2.4 W/cm$^2$ was maintained during each sputtering run. Film thickness was measured using a Sloan Dektak stylus profilometer.

Patterned ITO thin films were used as the active elements for all strain measurements. High temperature electrical tests required the use of refractory substrates that are electrically insulating. For this purpose, aluminum oxide constant strain beams were cut from rectangular plates using abrassive waterjet cutting techniques. These alumina constant strain beams were then sputter-coated with 6μm of high purity alumina prior to the deposition of the active strain gages. Prior to the $Al_2O_3$ deposition, all substrates were cleaned by sonicating successively in acetone, methanol, and distilled water, followed by a dry $N_2$ blow dry. The substrates were then sputter-etched for further cleaning prior to sputtering. These high purity alumina constant strain beams were used for all high temperature piezoresistive measurements as well as TCR and drfit rate determinations.

Microlithography techniques were used to pattern all of the active strain gage elements. After depositing a 1.5-2.5 μm layer of indium tin oxide, a 4 μm thick layer of positive photoresist was spin-coated onto the films. The photoresist was then soft baked and the strain gage pattern transferred to the ITO film by contact printing. Masks containing the strain gage pattern were used in conjunction with a collimated UV light source in a Kasper aligner for the purpose of pattern transfer. After exposure and development, the ITO films were etched in concentrated hydrochloric acid to delineate the final device structure.

### *3.2 Strain Measurement*

The piezoresistive response of the ITO films were measured at low and high temperatures using a four wire method and ohmic contacts to the ITO gage materials were formed using sputtered precious metal contacts. Strain measurements were made using a cantilever bending fixture that was interfaced to a linear variable differential transducer (LVDT) to measure deflection of the beam (Figure 1).

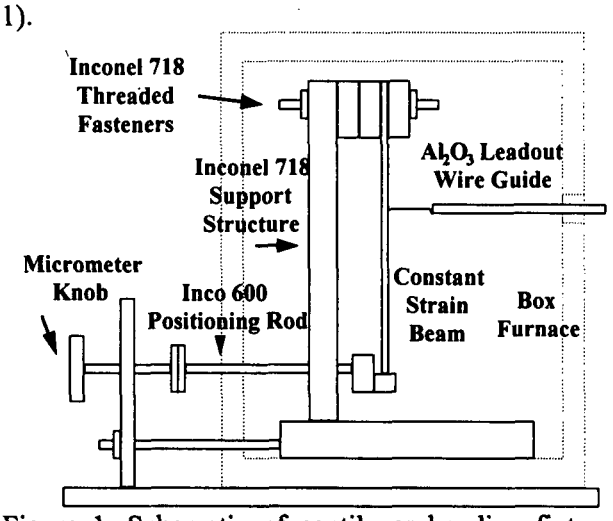


Figure 1. Schematic of cantilever bending fixture that was interfaced to a linear variable differential transducer (LVDT) to measure deflection.

Corresponding resistance changes were monitored with a Hewlett Packard 34401A multimeter and a Keithley constant current source. The LVDT output, multimeter and constant current source were interfaced to an I/O board and an IBM PC employing an IEEE 488 interface and National

Instruments LabWindows software for continuous data acquisition.

*3.3 Electrical Characteristics*

Sheet resistance of the as-deposited and annealed ITO films was measured using a four point probe technique and a hot probe was used to "type" these wide bandgap materials. TCR and drift at elevated temperatures were tested in both inert and oxidizing atmospheres. The modified van der Pauw test structure shown in Figure 2 was transferred to ITO coated substrates using the microlithography techniques described above. Thin film platinum contacts were deposited onto the ITO test structure

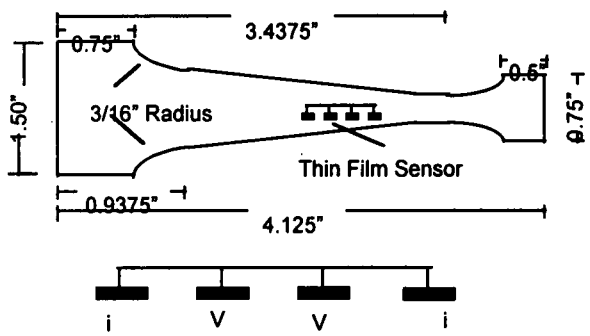


Figure 2. Constant strain beam showing location of van der Pauw test structure

by sputtering through a shadow mask that was properly aligned to the bond pads. Pt wire leads were then wire bonded to these contacts using parallel gap welding techniques. An inert atmosphere was maintained by passing semiconductor grade argon gas through a refrigeration unit operating at -40°C, and then through an oxygen getter (containing titanium turnings maintained at 400°C) to remove any residual water and oxygen. High temperature electrical measurements were made in a Deltech furnace with a 7 inch hot zone. The furnace was ramped to the desired temperature in 20°C increments and held for 15 min to establish thermal equilibrium. At specified time intervals, a complete I-V characteristic of the film was established at each temperature using a Keithley constant current source, a Hewlett Packard multimeter and an IBM PC with an IEEE 488 interface.

4. RESULTS

Large, negative gage factors were observed when the reactively sputtered ITO films were repeatedly strained in tension and compression at room temperature. When the as-deposited ITO films were strained in tension, there was a corresponding decrease in resistivity, resulting in gage factors between -6.5 and -11.4. When the films were strained in compression, there was a corresponding increase in ITO resistivity. Annealing experiments using various heat treating schedules and ambients and their effect on the electrical and optical properties of ITO are well documented in the literature [15-18]. In our case, films annealed in air exhibited gage factors between -3.83 and -9.85. A gage factor of -77.71 was achieved after annealing an ITO film in a 99.999% nitrogen ambient. This increase in gage factor was attributed to (1) the annealing of point defects which increased mobility and (2) enhanced grain growth.

Figure 3 depicts the piezoresistive response of a typical ITO strain gage based on an active film grown in a 35% oxygen plasma, along with a conventional metal foil gage. An ITO strain gage processed in a similar manner and annealed in high purity nitrogen is also shown in the figure. From this figure it can be seen that the piezoresistive response for the air annealed ITO film was both reproducible and linear up to approximately 700 microstrain (μin/in) and exhibited very little hysteresis. The piezoresistive response of the nitrogen annealed film was very large but experienced some hysteresis whereas the conventional metal strain gage exhibited a much smaller positive gage factor (G=2) with a very linear response with little or no hysteresis as might be expected. The piezoresistive responses of two

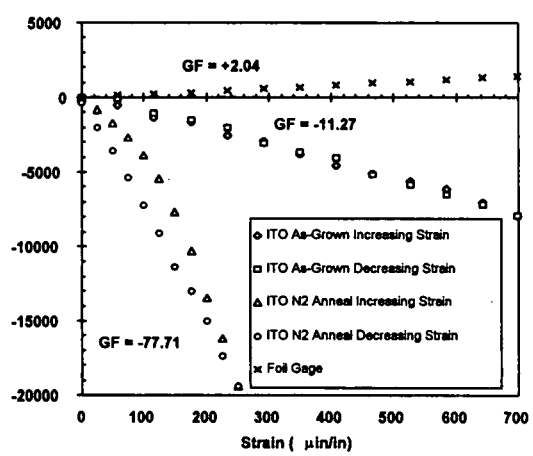


Figure 3. Piezoresistive response of various ITO strain sensors prepared in a 35% $O_2$ plasma, annealed under different conditions and tested at room temperature.

ITO strain gages, prepared with different oxygen contents in the plasma, and tested in air under static

strain conditions as a function of temperature, are shown in Fig. 4.

When ITO films were prepared with less than 5% oxygen in the plasma, the gage factor changed sign (from negative to positive) as the temperature was increased, whereas the gage factor of ITO films prepared with 30% oxygen in the plasma were large

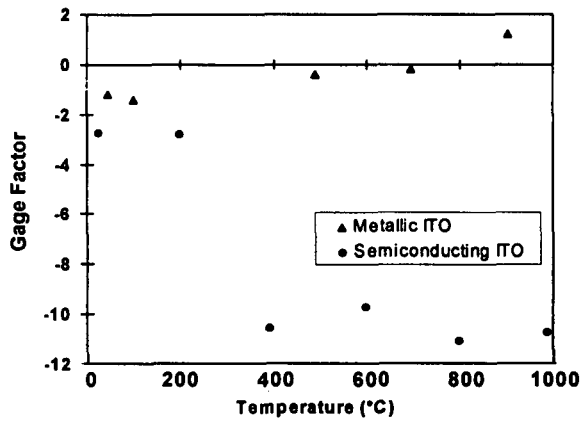


Figure 4. Gage factor as a function of temperature for two ITO films grown under very different conditions; one was grown in 5% $O_2$ and the other grown in 30% $O_2$.

and negative. At high temperature, the piezoresistive responses of the metallic ITO gages having low charge carrier concentrations and high mobilities exhibited behavior similar to that of conventional metal gages, while the ITO gages having lower mobilities and higher charge carrier concentrations approached a value of -12.0.

The piezoresistive response of the ITO films shown in Figure 4 differed considerably depending on the baseline resistivity of the as-deposited films i.e. "metal-like" or "semiconductor-like". The room temperature resistivity of the metallic ITO film was $8.1 \times 10^{-3}$ ohm cm and the room temperature resistivity of the semiconducting ITO film was $6.5 \times 10^{-2}$ ohm cm. At elevated temperatures, the piezoresistive response for the metallic ITO film was positive and the piezoresistive response for the semiconducting ITO film was negative. For the metallic ITO film, the electronic contribution to G in equation (6), i.e., the strain coefficient of resistivity term ($d\rho/\rho_o \cdot 1/d\varepsilon$), decreases with increasing temperature, as indicated by the sign change in G at temperatures > 600 °C. In contrast, the strain coefficient of resistivity term for the semiconducting ITO film increases with increasing temperature, resulting in a larger value of $|G|$. Thus, there is a marked change in the piezoresistive response of ITO, commensurate with chemical and physical property changes due to differences in the oxygen content in the plasma.

Not only did the piezoresistive properties of the ITO strain gages vary with oxygen content in the films but the baseline electrical properties varied with oxygen content, as shown in Table 1. Here, the ITO thin films exhibited reasonably high charge carrier concentrations, even though the semiconductor has a bandgap of 3.5 ev. A maximum in Hall mobility and minimum in charge carrier concentration was observed when 10% oxygen was employed in the plasma. Also, a maximum in room temperature resistivity was observed for the ITO films grown in a 10% oxygen plasma. However, this growth condition did not

| Oxygen Conc. in Plasma (%) | Carrier Conc. ($cm^{-3}$) | Hall Mobility ($cm^2$/Vsec) | Resistivity (ohm cm) |
|---|---|---|---|
| 5 | $7.14 \times 10^{19}$ | 4.4 | 0.021 |
| 5 annealed | $5.0 \times 10^{20}$ | 3.0 | 0.004 |
| 10 | $3.88 \times 10^{18}$ | 33.1 | 0.049 |
| 10 annealed | $1.10 \times 10^{20}$ | 2.8 | 0.020 |
| 20 | $1.5 \times 10^{20}$ | 3.5 | 0.011 |
| 20 annealed | $1.0 \times 10^{20}$ | 10 | 0.074 |
| 30 | $2.5 \times 10^{20}$ | 1.4 | 0.016 |
| 30 annealed | $5.0 \times 10^{20}$ | 12.0 | 0.001 |

Table 1. Electrical properties of as-deposited and annealed ITO films grown in varying oxygen partial pressures. Annealed films were heat treated in a $N_2$ ambient at 700 °C for 10 h.

result in the largest room temperature piezoresistive response, as might be expected. Instead, films with higher charge carrier concentrations and lower mobilities, corresponding to at least 30% oxygen in the plasma, yielded the largest room temperature gage factors. The piezoresistive response also depended on the annealing atmosphere and thermal history, as well. From Table 1, it can be seen that annealing of the ITO films in a nitrogen ambient for 10h increased the Hall mobility dramatically in the films with greater than 10% $O_2$, while decreasing the mobility in the films containing less than 10% $O_2$. Therefore, it is not surprising that the results shown in Figure 4, for the high temperature piezoresistive response of ITO films prepared under very different conditions, are so dramatically different.

Several ITO strain gages were tested under dynamic strain conditions in air ambients at temperatures up to 1000 °C. Figures 5, 6 and 7 show the results of an ITO strain gage prepared in a 30% $O_2$ plasma and tested dynamically in air at 1000°C. The decrease in gage factor was attributed to the oxidation of the bulk films and the surfaces of microcracks formed as a result of straining the sensor, such that the gage resistance increased. Initially, a drift rate of 0.022%/hr was observed, which decreased with time at temperature to a final value of 0.004%/hr, which is compares favorably to drift rates for PdCr thin film strain gages [3,4].

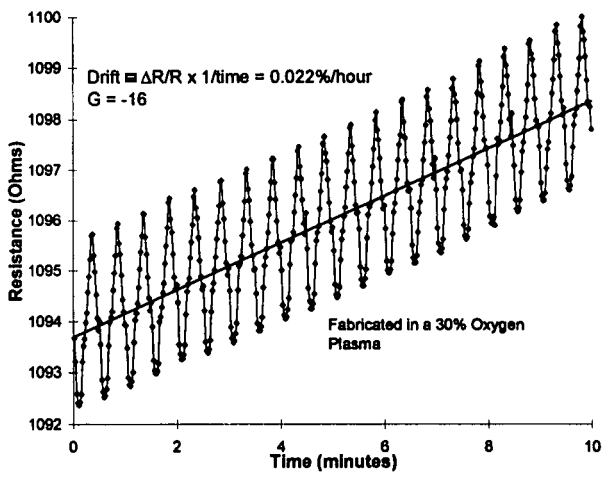


Figure 5. First 10 minutes of a dynamic strain test of an ITO sensor at 1000°C in air (ε=+/- 200 μin/in)

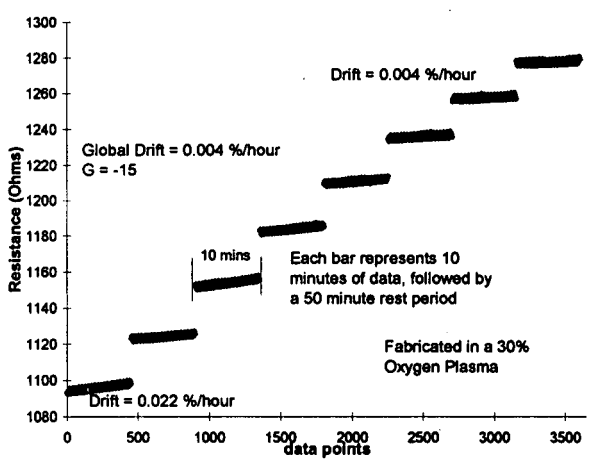


Figure 6. First 8 hours of a dynamic strain test of an ITO sensor at 1000°C in air (ε=+/- 200 μin/in)

Figure 8 shows a dynamic strain test of an as-deposited ITO strain gage grown in a 30% oxygen plasma. This gage exhibited an initial decrease in electrical resistance, followed by a monotonic increase in gage resistance with time. The initial decrease was attributed to the annealing of point defects incorporated into the film during sputtering, whereas the monotonic increase was most likely due to oxidation of the film and compensation of the oxygen vacancies, the source of the excess charge carriers. This trend was typical of all as-deposited ITO sensors tested to date, suggesting that a post deposition annealing step is warranted.

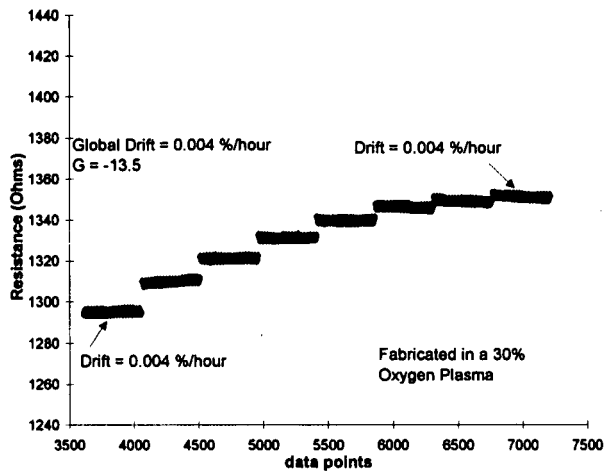


Figure 7. Hours 9 to 16 of a dynamic strain test of an ITO sensor at 1000°C in air (ε=+/- 200 μin/in)

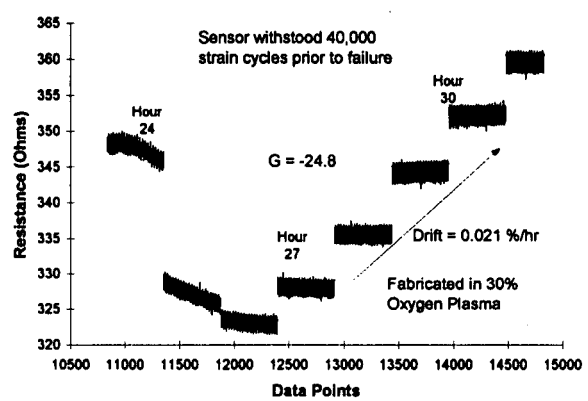


Figure 8. Hours 24 to 31 of a dynamic strain test of an ITO sensor (30 % oxygen plasma) at 1000°C in air (ε=+/- 350 μin/in)

Figures 9, 10 and 11 show the results of three ITO strain gages fabricated with 30% oxygen in the plasma and tested dynamically in air at 1000°C. The influence of different annealing atmospheres (air, oxygen, and nitrogen) on gage factor and initial drift rate of these ITO gages is evident in these figures. Nitrogen annealing produced the largest dynamic gage factor (G=-23.5) and the lowest drift rate (DR= 0.0009%/hr) of all gages tested. This effect is shown more dramatically when the drift rates of these different gages are compared over the course of a 60 h test (shown in Figure 12). A similar ITO sensor annealed in nitrogen withstood more than 50,000 strain cycles of +/- 500 μin/in

during 180 h of testing air at 1000°C, suggesting that nitrogen annealing also improves sensor lifetime.

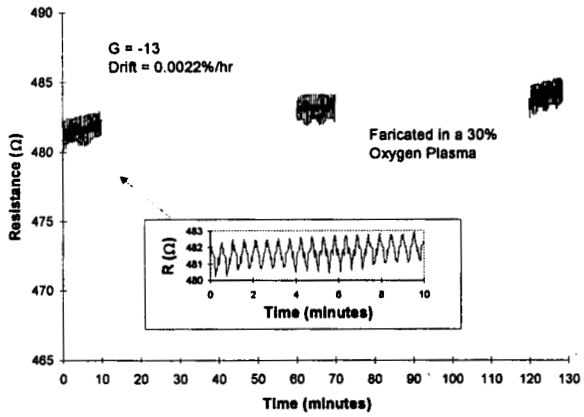


Figure 9. First 3 cycles of a dynamic strain test of an ITO sensor (30 % oxygen plasma) at 1000°C in air (ε=+/- 350 μin/in)

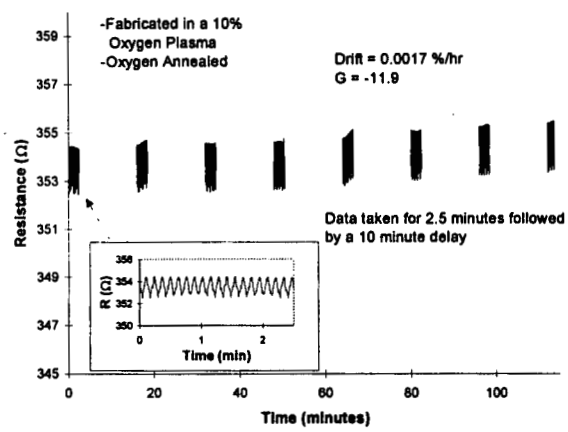


Figure 10. First 116 minutes of a dynamic strain test of an ITO sensor (10 % oxygen plasma) at 1000°C in air (ε=+/- 500 μin/in)

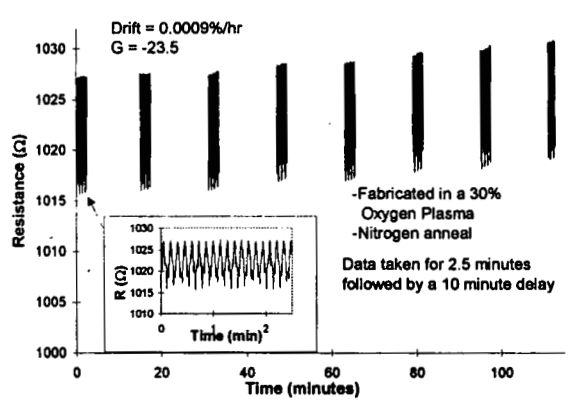


Figure 11. First 116 minutes of a dynamic strain test of an ITO sensor (30% oxygen plasma) at 1000°C in air (ε=+/- 500 μin/in)

The effect of thermal cycling on the electrical stability of an ITO thin film strain gage tested in a nitrogen ambient is shown in Figure 13. During ramp (1) of the first thermal cycle, a large positive TCR of +3600 ppm/°C was observed at temperatures up to 500°C, at which point a maximum in resistivity was observed. Upon further heating to 900°C, a large negative TCR of -2600 ppm/°C was observed and upon cooling to room temperature (ramp 2) the maximum in resistivity diminished greatly. This trend continued with subsequent thermal cycling (ramps 3-5), with the films finally approaching a positive TCR of +230 ppm/°C at T< 500°C and -469 ppm/°C at T< 900°C (ramp 6). The relatively low, negative TCR of the latter ITO film is typical of saturated extrinsic behavior, whereas, positive TCR's are more characteristic of metals and heavily doped, degenerate semiconductors.

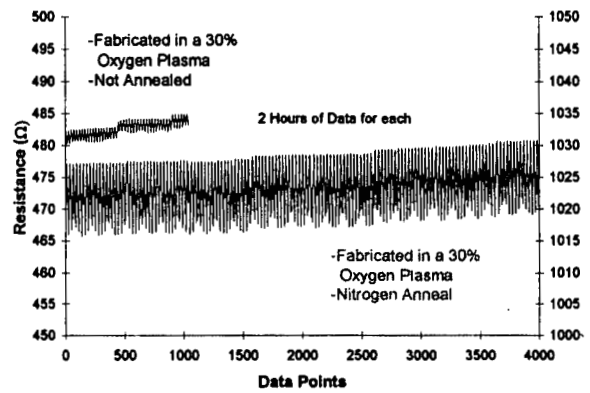


Figure 12. A comparison of two ITO sensors prepared with 30% oxygen in the plasma and tested at 1000°C in air (ε=+/- 500 μin/in). Note: different sampling rates were used in collecting the data.

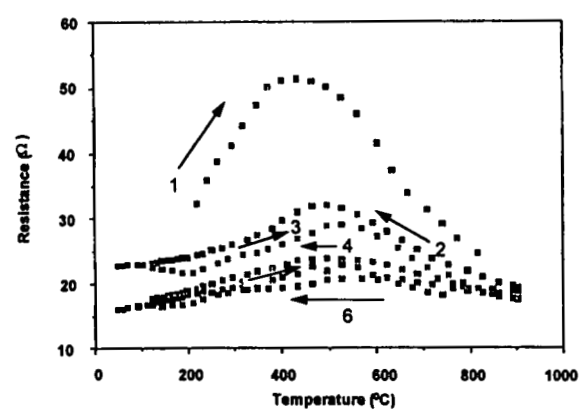


Figure 13. Electrical resistivity of an ITO strain sensor prepared in a 10% oxygen plasma and tested as a function of temperature in a nitrogen ambient.

The electrical responses of the films tested in oxygen ambients were very different than those tested in nitrogen. When compared to the response in nitrogen, the shape of the electrical resistivity vs. temperature curve and final TCR of an ITO film prepared in a 10% $O_2$ plasma and tested in oxygen remained relatively unchanged after repeated thermal cycling (Figure 14). Here, a TCR of -1560 ppm/°C was obtained over the entire temperature range of 200°C<T<1100°C. This behavior was very different from that of the ITO films prepared in a 30% $O_2$ plasma. Figure 15 shows the electrical response and final TCR of an ITO film prepared in a 30% $O_2$ plasma and tested in oxygen. Here, two very different TCR's were observed, depending on temperature, suggesting that there are two different thermally activated charge carriers responsible for the overall conductivity of these ITO films. A TCR of -210 ppm/°C was observed over the temperature range 130°C<T<600°C and a TCR of -2170 ppm/°C was observed over the temperature range 700°C<T<1100°C. ITO films prepared in a 30% $O_2$ plasma exhibited the lowest TCR of all films tested to date. Oxidation effects on the resistivity of the ITO films tested in an oxygen ambient are also evident in Figure 15. At low temperatures (130 °C <T<700°C), the slope of the resistivity-temperature curves is increasing with number of thermal cycles. Thus, repeated thermal cycling tended to increase the TCR from -210ppm/°C to levels approaching -1560 ppm/°C, which corresponds to the activation energy associated with intrinsic behavior. Since ITO is a relatively wide bandgap semiconductor, ($E_g$=3.5 ev), it is most likely that a shallow impurity is responsible for the low temperature (saturated extrinsic) electrical behavior. At higher temperatures, the thermally generated charge carriers dominate and the behavior is more typical of an intrinsic semiconductor. Since the largest high temperature piezoresistive responses were also realized with ITO films prepared in a 30% oxygen plasma, it appears that films made with these higher oxygen contents are ideally suited for high temperature strain applications where large gage factors and thermal stability are desired.

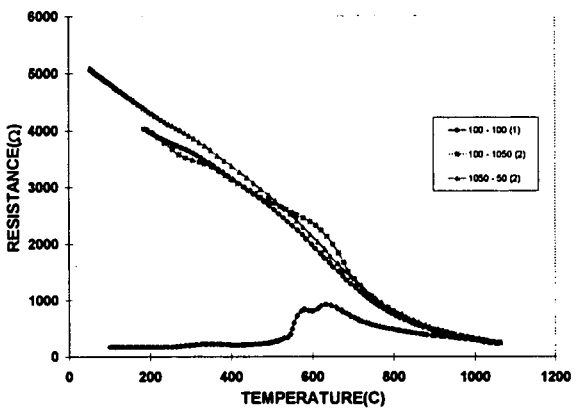


Figure 14. Electrical resistivity of an ITO strain sensor prepared in a 10% oxygen plasma and tested as a function of temperature in air.

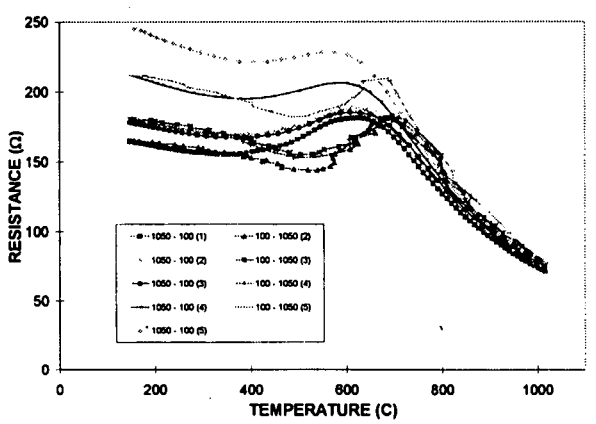


Figure 15. Electrical resistivity of an ITO strain sensor prepared in a 30% oxygen plasma and tested as a function of temperature in air.

Wide bandgap semiconductors (intrinsic semiconductors) typically exhibit a large negative TCR while most heavily doped semiconductors and metals exhibit much smaller TCR's. When ITO films were prepared in a 10% oxygen plasma and subsequently protected with a sputtered overcoat to prevent further oxidation of the underlying material and compensation of the excess charge carriers, the electrical behavior shown in Figure 16 resulted. This behavior was very similar to that shown in Figure 15 for an ITO sensor prepared in a 30% oxygen plasma without an overcoat. In Figure 16, TCR's on the order of -430 ppm/°C and -1760 ppm/°C were observed over the temperature ranges of 150°C<T<600°C and 800°C<T<1100°C, respectively. In this particular case as before, the ITO sensor exhibited two types of semiconducting behavior suggesting that there are two different thermally activated charge carriers responsible for the overall conductivity of these ITO films. It is most likely that a shallow impurity was responsible for the low temperature electrical behavior of these films and that the high temperature electrical behavior was dominated by thermally generated charge carriers. If the onset of the higher activation energy charge carrier responsible for conduction in the temperature range 800°C<T<1100°C can be delayed to yet higher temperatures, a more stable high temperature strain gage would result.

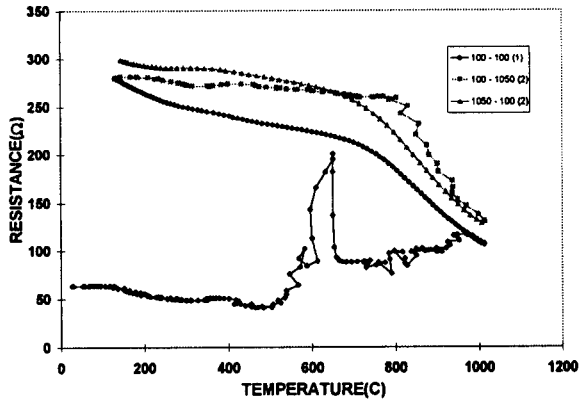


Figure 16. Electrical resistivity of an ITO strain sensor prepared in a 10% oxygen plasma and tested as a function of temperature in air. The sensor was overcoated with an protective layer prior to testing.

Complete I-V characteristics were established at each temperature interval (20°C intervals) during thermal cycling. The I-V trace at each temperature was linear and passed through the origin. This suggests that the platinum films used for metallization and interconnection purposes formed reasonable ohmic contacts with the ITO films over an extended temperature range. The fact that there was no apparent rectification behavior at these higher temperatures implies that no barrier height was formed and that no interfacial reactions or displacement reactions occurred.

## 5. CONCLUSIONS

A stable, high temperature thin film strain gage based on reactively sputtered ITO was demonstrated at temperatures up to 1050°C. The active ITO strain elements in these gages exhibited relatively large room temperature gage factors, compared to conventional metal based strain gages (G as large as -77.7, depending upon deposition conditions and post deposition annealing treatments). The piezoresistive response of these sensors was both linear and reproducible when strained up to 700 μin/in. A large, negative piezoresistive response was observed for all ITO films; ie when the films were strained in tension, there was a corresponding decrease in ITO resistivity, and when strained in compression, there was a corresponding increase in ITO resistivity. Since all ITO films tested n-type by hot probe, it was not surprising that the resulting gage factors were negative. This result is consistent with other n-type semiconductors such as silicon, which also exhibits a large negative piezoresistive response. The ITO films also showed very little hysteresis when cycled between compression and tension, indicating excellent mechanical stability.

The ITO strain sensors also exhibited a moderately low temperature coefficient of resistance (TCR) at temperatures up to 1100°C, when tested in a nitrogen ambient. A TCR of +230 ppm/°C over the temperature range 200°C<T<500°C and a TCR of -469 ppm/°C over the temperature range 600°C<T<1100°C was observed for the films tested in nitrogen. However, the resistivity behavior changed considerably when the same films were tested in oxygen ambients. These same films exhibited two different TCR's, depending on temperature; a relatively low negative TCR (-210 ppm/°C) for T<800°C, and a relatively high negative TCR (-2170 ppm/°C) for T>800°C. The transition from low to high TCR was independent of the number of thermal cycles, but typically occurred at 800°C. The combination of a moderately low TCR and relatively large gage factor makes these ITO films promising candidates for the active strain elements in high temperature thin film strain gages, particularly in applications where temperature compensation is usually required.

Strain test results in our laboratory indicate that refractory, semiconducting oxides such as ITO are particularly well suited for applications where the measurement of strain in air ambients is desired at temperatures greater than 1000°C. Thin film strain gages based on selected ITO alloys withstood more than 50,000 strain cycles of +/-500 μin/in during 180 hours of testing in air at 1000°C, with minimal drift at temperature. Drift rates as low as 0.0009%/hr at 1000°C were observed for ITO films that were annealed in nitrogen at 700°C prior to strain testing. These results compare favorably with state of the art 10 μm thick PdCr films deposited by NASA, where drift rates of 0.047%/hr at 1050°C were observed [1,2]. Nitrogen annealing not only produced the lowest drift rates to date (DR=0.0009%/hr), but also produced strain sensors with the largest dynamic gage factors (G=-23.5) and longest lifetimes.

## 6. ACKNOWLEDGEMENTS

The authors would like to thank NASA Lewis Research Center, Cleveland, OH for support of this work under NASA Grant NAG3-1428. The authors would also like to thank Dr. Lawrence Matus of the NASA Lewis Research Center for the Hall measurements.

## 7. REFERENCES


1. Jih-Fen Lei, "A Resistance Strain Gage with Repeatable and Cancelable Apparent Strain for Use to 800°C", NASA Report No. CR-185256, 1990.

2. Jih-Fen Lei, "Development and Characterization of PdCr Temperature-Compensated Wire Resistance Strain Gage". NASA Contract Report No. CR-185135, 1989.

3. O.J. Gregory, S.E. Dyer, P.S. Amons and A. Bruins Slot, "Characteristics of A Reactively Sputtered Indium Tin Oxide Thin Film Strain Gage for Use at Elevated Temperatures", MRS Symposium Proceedings, 1995 Fall Meeting, Boston MA, Vol. 403, p.597-602, 1996.

4. S.E. Dyer, O.J. Gregory, P.S. Amons and A. Bruins Slot, "Preparation and Piezoresistive Properties of Sputtered ITO Thin Films", Thin Solid Films, 288, p.279-286, 1996.

5. W.H. Atkinson, M.A. Cyr and R.D. Strange, "Development of Sensors for Ceramic Components in Advanced Propulsion Systems", NASA Report No. 195283, 1994.

6. M. M. Lemcoe, "High-Temperature Strain Gage Measurements to 2000°F: Can it be done?", Sensors Expo International Conference Proceedings, p. 203C-1-7, 1989.

7. G.R. Witt, "The Electromechanical Properties of Thin Films and the Thin Film Strain Gauge", Thin Solid Films, 22,p.133-156, 1974.

8. P. Kayser, J.C. Goderoy and L. Leca, "High-Temperature Thin Film Strain Gauges", Sensors and Actuators, 37-38, p. 328-332, (1993).

9. N. Nadaud, M. Nanot and P. Boch, "Sintering and Electrical Properties of Titania and Zirconia Containing $In_2O_3$-$SnO_2$ (ITO) Ceramics", J. American Ceramic Society, 77, No. 3, p. 843-846, (1994).

10. J.H.W. DeWit, "The High Temperature Behavior of $In_2O_3$", J. Solid State Chemistry, 13, p. 192-200, (1975).

11. G.L. Bir and G.E. Pikus, Symmetry and Strain Induced Effects in Semiconductors, Holsted Press, New York., 1974, p.369.

12. Patricia A. Beck, Bert A. Auld, and Ki-Soo Kim, "Silicon Sensors as Process Monitoring Devices", Res Nondestr Eval, 5, p. 71-93, (1993).

13. Charles S. Smith, "Piezoresistance Effect in Germanium and Silicon", Physical Review, 94 (1), p. 42-49.

14. A. Garcia-Alonso, J. Garcia, E. Castono, I. Obieta and F.J. Gracia, "Strain Sensitivity and Temperature Influence on Sputtered Thin Films for Piezoresistive Sensors", Sensors and Actuators A, 37-38, p. 784-789, (1993).

15. J.R. Bellingham, A.P. Mackenzie, and W.A. Phillips, "Precise Measurements of Oxygen Content: Oxygen Vacancies in Transparent Conducting Indium Oxide Films", Applied Physics Letters, 58.22, p. 2506-2508, (1991).

16. K. L. Chopra, S. Major and K. Pandya, "Transparent Conductors-A Status Review", Thin Solid Films, 102, p. 1-46, (1983).

17.Yuzo Shigesato, Satoru Takaki, and Takeshi Haranoh, "Electrical and Structural Properties of Low Resistivity Tin-Doped Indium Oxide Films", J. Applied Physics, 71 (7), p. 3356-3364, (1992).

18. A.J. Steckl and G. Mohammed, "The Effect of Ambient Atmosphere in the Annealing of Indium Tin Oxide Films", J. Applied Physics, 51 (7), p. 3890-3895, (1980).

Paper 42
Author: Gregory

Q: Pink

What was the hysteresis below 700°C?

A: There was no hysteresis below 700°C for the PdCr thin film strain gauge.

Q: de Wolf

Could you indicate the physical size of your ITO strain gauge shown for instance in figure 2?

A: The physical size of an active ITO strain gauge is approximately 1.5 cm x 2mm x 2 micrometres. These dimensions are not the smallest that we can fabricate and if so desired, the length and width could be reduced by one order of magnitude. These dimensions can be changed to suit the final resistance of the gauge, given that the thickness is fixed at about 2 micrometres.

Q: Loftus

Would you advocate abandoning PdCr based on these results?

A: PdCr is a well characterised, well behaved thin film strain gauge. We are trying to push this gauge to its limit in terms of operating temperatures. So the answer is that over the short term we would not abandon PdCr. However, as the useful operating temperature of PdCr is exceeded, we expect ITO and materials similar to it to take us beyond the capability of PdCr.

Q: What is the variation of characteristics from sample to sample?

The ITO strain gauges are prepared by reactive sputtering so control of the sputtering gas composition and pressure is critical. The variation in gauges made in the same sputtering run is less than 5% but the variation from run to run can be as much as 15 % depending on specifics of the process parameters used to make the films.

# OPTICAL DIAGNOSTICS FOR CRYOGENIC LIQUID PROPELLANTS COMBUSTION

L. Vingert, M. Habiballah, P. Gicquel, E. Brisson - ONERA, BP 72, F-92322 Châtillon, France
S. Candel, G. Herding, R. Snyder, P. Scouflaire, C. Rolon - CNRS/EM2C/ECP, 92295 Chatenay Malaba
D. Stepowski, A. Cessou, R. Bazile, P. Colin, S. Guerre - CNRS/CORIA/Rouen, BP 72, 92322 Châtillon
M. Péalat, F. Grisch, P. Bouchardy - ONERA

## Abstract

Detailed experimental studies of cryogenic propellant combustion are needed to improve design and optimization of high performance liquid rocket engines. A test facility called MASCOTTE has been built up by ONERA to study elementary processes (atomization, droplet vaporization, turbulent combustion...) that are involved in the combustion of liquid oxygen (LOX) and gaseous hydrogen ($GH_2$). This article reports results from experiments carried-out on MASCOTTE under a consortium of laboratories and manufacturers associating ONERA, CNRS, CNES and SEP, on the jet flame issued from a single coaxial injector. This device fed with liquid oxygen and gaseous hydrogen is placed in a chamber equipped with quartz windows. The spray and the flame are observed with a set of optical methods: high speed cinematography, light emission from OH radicals, laser induced fluorescence of OH and $O_2$, elastic scattering from the LOX jet. These techniques are used to obtain images of the spray and of the flame zone. It is then possible to deduce the flame location with respect to the liquid jet from simultaneous elastic scattering of the LOX jet and LIF of OH measurements or from average emission images treated with Abel's transform. The images obtained by exciting the fluorescence of $O_2$ provide complementary information on the flame shape and they may be used to estimate the local reaction rate. Quantitative temperature measurements based on Coherent Anti-Stokes Raman Scattering from $H_2$ and LOX droplets size and velocity measurements by means of a Phase Doppler Particle Analyzer give additional clues on the spray and the combustion zone.

## Nomenclature

| | |
|---|---|
| $d$ | injector diameter |
| $D_o$ | initial droplet diameter |
| $D_{10}$, $D_{32}$ | arithmetic mean, Sauter mean diameter |
| $Da_c$, $Da_v$ | Damköhler numbers |
| $J$ | momentum flux ratio |
| $L$ | combustor length |
| $M$ | mixture ratio |
| $\dot{m}$ | mass flow rate |
| $p$ | pressure |
| $Re$ | Reynolds number |
| $t$ | time |
| $T$ | temperature |
| $V$ | velocity |
| $We$ | Weber number |
| $x$, $r$ | axial, radial distance |
| $X$ | mole fraction |
| $\lambda_{eff}$ | evaporation constant |
| $\lambda$ | wave length |
| $\rho$ | density |
| $\sigma$ | surface tension |
| $\omega$ | frequency |

## 1. Introduction

### *Overall context and objectives*

The low cost development of liquid rocket engines, which must be more and more performing and reliable, is still a big challenge for the manufacturers. Standard practice in the design of such space propulsion systems has mostly relied on accumulated know-how, and trial and error methodologies. More recently, computational tools have been progressively introduced in the design process but have not replaced testing. Combustion in rocket motors working with both liquid oxygen and hydrogen at high pressure (up to 20 MPa) is so complex that its computation cannot be carried-out without extensive validation of numerical models, based on detailed investigation of elementary processes (atomization, droplet vaporization, turbulent combustion...) in well controlled configurations and nevertheless representative operating conditions. The main objective of the present research program has been to generate a fundamental understanding of the spray characteristics and combustion mechanisms, and to develop an experimental database providing guidelines for computer modeling.

Results reported in this article were gathered by different teams working in cooperative research program on combustion in liquid rocket motors. This collaboration is sponsored by CNES and SEP and involves ONERA and CNRS. Experiments are carried-out on the MASCOTTE facility operated by ONERA. Selected samples of results and related interpretations are presented. The structures of the spray and of the flame in the near field of the coaxial injector are specifically considered. Additional information may be found in other references: on coaxial jets atomization in Ledoux et al.[1], Gicquel et al.[2], on flame structure in Herding et al.[3,4,5], Snyder et al.[6], Guerre et al.[7], Cessou et al.[8], on CARS measurements in Grisch et al.[9], on optical diagnostics applicable to cryogenic combustion in Brummund et al.[10] Other references to previous literature may be found in these articles.

This article begins with a brief review of the fundamental mechanisms controlling cryogenic flames. The MASCOTTE experimental facility is described in Section II. Section III deals with atomization studies, Section IV with OH imaging, Section V with gaseous $O_2$ Laser Induced Fluorescence and Section VI with $H_2$-CARS thermometry.

### *Qualitative description of cryogenic combustion*

In standard applications of cryogenic combustion, reactants are introduced in the chamber through coaxial injectors. Liquid oxygen generally flows in the inner tube at low speed while gaseous hydrogen is fed by the outer annular duct. In standard devices the central tube is set in recess with respect to the exhaust plane. In some devices a certain amount of swirl is also communicated to the liquid oxygen stream. In the present case we only consider flush mounted LOX and hydrogen ducts and there is no swirl. Cryogenic combustion involves a variety of coupled physical and chemical processes which are summarized schematically in Fig. 1.

Atomization starts at the confluence of the liquid and gaseous streams. The liquid core size diminishes progressively

*Paper presented at an AGARD PEP Symposium on "Advanced Non-Intrusive Instrumentation for Propulsion Engines", held in Brussels, Belgium, 20-24 October 1997, and published in CP-598.*

as the spray is formed. Initial LOX ligaments are torn away by the high speed hydrogen stream. The ligaments break into finer droplets which may be still too large to sustain the shearing stresses associated to the velocity difference between the gaseous and liquid phase. This leads to secondary atomization. The droplets vaporize and the gaseous oxygen and hydrogen react in a highly turbulent flowfield.
While these processes are closely coupled one may sort out some controlling factors. It is first concluded from experiments on atomization in coaxial jets by Hopfinger and Lasheras[11] that the jet break-up is sensitive to the gas to liquid momentum flux ratio $J$ and that the droplet size is set by the relative Weber number $We$ which compares aerodynamic forces to surface tension.

$$J = \frac{\rho_g V_g^2}{\rho_l V_l^2} \qquad We = \frac{\rho_g (V_g - V_l)^2 d_l}{\sigma}$$

The Reynolds numbers of gaseous hydrogen and liquid oxygen define the initial states of flow. If these numbers are sufficiently large the two propellant streams are turbulent and the break-up of the liquid jet depends mainly on the momentum flux ratio $J$. This ratio controls the stripping of the liquid core and sets the core length. Studies carried-out by Hopfinger and Villermaux[12] indicate that the core length is inversely proportional to $J^{1/2}$. The size of the droplets formed by the primary and secondary atomization is then determined to a great extent by the Weber number.
Processes of vaporization, mixing and combustion may be characterized by their three characteristic times $t_v$, $t_m$ and $t_c$, which define two Damköhler numbers, a chemical reaction Damköhler number $Da_c$ which compares the mixing time to the chemical time and a vaporization Damköhler number $Da_v$ which compares the mixing time to the vaporization time. Estimates of these numbers (see for example Snyder et al.[6]) indicate that the chemical Damköhler number is always much larger than unity while the vaporization Damköhler number is generally lower than unity. It is then concluded that vaporization of the liquid droplet controls the combustion process. If the droplets produced by atomization are too large, their typical time will be excessive and the droplets might even escape the combustion chamber without being fully vaporized (see Section III). The large chemical Damköhler number indicates that combustion will take place in thin reactive layers and that the regime of combustion will be of the "flamelet" type.
Some straightforward calculations[6] may be carried-out to estimate the ratio of the interdroplet distance to the droplet diameter. One finds that the spray formed after jet break-up is quite dense with droplets separated from each other by less than 10 mean diameters. Under these circumstances the regime will be dominated by external group combustion whereby the flame is established as an outer layer surrounding the spray.

## 2. The MASCOTTE test facility

### *Definition, operating domain*

The MASCOTTE cryogenic combustion test facility was developed by ONERA to study elementary processes which are involved in the combustion of cryogenic propellants, namely liquid oxygen (LOX) and gaseous hydrogen ($GH_2$). MASCOTTE is aimed at feeding a single element combustor with actual propellants. Three successive versions of this test facility were built up:
- in the first step (V01), only low chamber pressures (< 10 bar) and use of hydrogen at room temperature were allowed;
- in the second version (V02), a heat exchanger was implemented in the hydrogen line in order to cool hydrogen down to about 100 K. This permitted to increase the maximum flow rate of $GH_2$ at low pressure with subsonic flow at the injector exit;
- the third improvement (V03) is aimed at reaching supercritical pressures in the combustor and at increasing the maximum LOX flow rate from 100 g/s to 400 g/s.

Research teams from different laboratories belonging to CNRS and ONERA, regrouped in a joint research program (GDR) managed by CNES and SEP, may run experiments on MASCOTTE, with following objectives: improve the knowledge and the modeling of physical phenomena, provide experimental results for computer code validation, improve and assess diagnostic techniques (especially optical diagnostics). These may be later used in more severe conditions, i.e. higher pressures and flow rates on the P8 test facility at DLR/Lampoldshausen.
The MASCOTTE project started in 1991. The civil engineering, the fluid storage and feedlines were achieved in 1992 ; the electrical systems and computerization, as well as the level 0 and 1 acceptance tests, in 1993. The first fire tests at atmospheric pressure (level 2 acceptance) were run in January 1994. V02 upgrading was achieved in fall 1995 and V03 in spring 1997. As the experiments reported here did not involve the use of V03, this latter version will not be further described here after.

As can be seen on the sketch of MASCOTTE V02 (Fig. 2), the 180 l LOX tank is pressurized with helium, rather than nitrogen, to minimize pollution of the liquid with dissolved gas. In the Ariane 4 cryogenic stage H10, the LOX tank is actually pressurized with helium, as well as in the Ariane 5 EPC. In the MASCOTTE facility, the LOX issued from the tank traverses a liquid nitrogen heat exchanger and reaches a temperature of 80 K to avoid vaporization and cavitation problems in the line and two phase flow in the injector. During the initial chilling down phase of the line, the course of the oxygen is diverted to a heat exchanger where it is vaporized before it is evacuated into the atmosphere. An additional liquid nitrogen line is aimed at cooling the injection head of the combustor as well as the part of the LOX line between the derivation and the injector.
The definition of the hydrogen line is classical. The storage is constituted of 2 containers of 28 bottles pressurized at 200 bars, each container representing 252 $m^3$ of hydrogen in normal conditions. The flow rate is regulated by means of a sonic throat. The change from V01 to V02 consisted of implementing a heat exchanger in the high pressure section of the hydrogen line (upstream of the sonic throat). The hydrogen temperature can be cooled down from room temperature to 100 K. The mass flow rate specification for the device is 100 g/s of hydrogen. To keep the hydrogen at 100 K, the whole line downstream of the heat exchanger is immersed in a liquid nitrogen flow.
Besides the main fluids (LOX and $GH_2$), additional fluids are available for different purposes on the bench :
- gaseous nitrogen is the auxiliary fluid aimed at operating the pneumatic and relief valves, it is also used to pressurize the liquid nitrogen tank and may be injected in the chamber at the nozzle entrance to drive the pressure independently from the combustion (at low pressure) or to help cooling the nozzle;
- gaseous helium is used to pressurize the LOX and to cool the internal face of the combustion chamber windows;
- a high pressure water circuit is used to cool the nozzle;
- liquid nitrogen is used to cool the injection head and the main lines downstream the heat exchangers as well as to feed this exchangers.

Versions V01 and V02 of MASCOTTE permit to reach a pressure of 10 bar in the combustion chamber.
The specified hydrogen mass flow rate range for V01 was 5 to 20 g/s of gaseous hydrogen at room temperature, when operating at atmospheric pressure in the combustion cham-

ber. The upper limit corresponds to the sonic limit (i.e. *Mach*=1) at the injector exit, because the flow must remain subsonic in the injector to be representative of a rocket coaxial injector. For V02 and V03 this limit is of course a function of the injector geometry, of the hydrogen injection temperature and of the chamber pressure. The actual upper limit of hydrogen flow rate, that the test bench could deliver, is related to the pressure of the storage (maximum 200 bar) and to the cross section of the sonic throat implemented in the line. With the current storage of 500 $m^3$, the maximum available flow rate of hydrogen would be approximately 75 g/s. The actual lower limit corresponds to the lowest upstream pressure for which the throat becomes sonic.
On the LOX side, the inner diameter of the line is 10 mm. The maximum mass flow rate corresponding to a velocity of 5 m/s in such a line would be approximately 450 g/s, while the specified ranges were: 20 to 100 g/s of liquid oxygen for V01 and V02 and 20 to 400 g/s for V03. Actually, it is very difficult to stabilize a mass flow rate lower than 40 g/s with a calibrated orifice upstream the injector.

### *Choice of reference points*

Similarity between low pressure experiments and high pressure rocket chamber operation is not easy to assure. Among the many possible scaling rules one may however choose to conserve the gas to liquid momentum ratio which essentially controls jet break-up and atomization. This choice is based on cold flow tests reported by Hopfinger and Lasheras[11] and by older correlations derived for shear coaxial injectors. The operating mass flow rates of LOX and $GH_2$ are chosen to preserve the momentum flux ratio at the different operating pressures. This in turn induces changes in the mixture ratio. Such variations are however admissible if the chemical Damköhler $Da_c$ lies in the proper range, a condition which is well satisfied as $Da_c$ is much greater than unity for global mixture ratios exceeding 2 ($M > 2$).
To choose some reference points suitable for all the test campaigns involving different optical diagnostic techniques, the operation domains of MASCOTTE at atmospheric pressure (combustor without nozzle) or around 10 bar (combustor with a 15 mm throat diameter nozzle) have been plotted in Figs. 3 and 4. On each diagram one can find the available flow rates limits for both fluids, the mixture ratio limits, total injected mass flow rate contours $\dot{m}_t$ (Fig. 3) or pressure contours (Fig. 4) as well as $J$ isovalues contours.
Two reference points A and C have been chosen for the MASCOTTE V01 test bench at atmospheric pressure. For both of them, the LOX mass flow rate is 50 g/s. Changing from A to C, the mixture ratio $M$ is increased from 3.3 to 5, while the $J$ ratio is approximately divided by 2. When running the bench at 10 bar or with cold hydrogen (V02), or for non reactive flow simulation tests, equivalent operating points have been defined by keeping the LOX mass flow rate and the $J$ ratio roughly constant. To achieve this, the injector had to be changed by reducing the hydrogen annulus outer diameter $d_G$. Tests conditions corresponding to operation at 1 and 10 bar are summarized in table 1.

*Table 1 : MASCOTTE operating points*

| Point | $p$ bar | $T_{GH2}$ K | $\dot{m}_{LOX}$ g/s | $\dot{m}_{GH2}$ g/s | $V_{LOX}$ m/s | $V_{GH2}$ m/S | $M$ | $J$ |
|---|---|---|---|---|---|---|---|---|
| A | 1 | 289 | 50 | 15.0 | 2.23 | 893 | 3.3 | 13.4 |
| C | 1 | 289 | 50 | 10.0 | 2.23 | 628 | 5.0 | 6.3 |
| A-10 | 10 | 289 | 50 | 23.7 | 2.23 | 308 | 2.1 | 14.5 |
| C-10 | 10 | 289 | 50 | 15.8 | 2.23 | 207 | 3.2 | 6.5 |
| D'-5 | 5 | 289 | 40 | 11.2 | 1.78 | 292 | 3.6 | 10.2 |
| C'-8 | 8 | 289 | 50 | 9.5 | 2.23 | 163 | 5.3 | 3.2 |
| Fl | 1 | 94 | 50 | 9.5 | 2.23 | 419 | 5.3 | 8.1 |

Results shown in this article generally correspond to points A and C, but some data collected for C' at 8 bar, D' at 5 bar and Fl (cooled hydrogen injection) are also given.

### *The combustion chamber*

The combustion chamber is designed for 30 s of operation at atmospheric pressure, for a maximum total mass flow rate of 120 g/s at a mixture ratio $M = \dot{m}_{LOX}/\dot{m}_{GH2}$ of 6. This test duration is reduced to 20 s at 10 bar. It may be fired 6 to 10 times in a day, with 5 to 10 minutes between two successive runs. The chamber section is square with an inner dimension of 50 mm. The stainless steel structure holds two lateral fused silica windows (100 mm long and 50 mm high). The window internal face is cooled by a gaseous helium film. Upper and lower windows, 100 mm long but only 10 mm wide, are used for laser sheet transmission. Fig. 5 gives a sketch of the combustor. It is constituted of different interchangeable modules, which permit visualizations of the whole combustion chamber by placing the transparent module at different longitudinal positions (Fig. 6). The nozzle is made of graphite. A water cooled copper nozzle is also available as shown in Fig. 2. The combustor has been run more than 1000 times (including 30 seconds runs at atmospheric pressure and 20 seconds runs at 10 bar). In these tests, the LOX mass flow rate was varied from 40 to 90 g/s and the $GH_2$ mass flow rate from 10 to 30 g/s.

## 3. Atomization studies

This section presents a test campaign mainly focused on the LOX droplets size analysis. First, to provide preliminary information on the fluid dynamics of the LOX core breaking process, a visualization technique using a stroboscopic laser sheet associated with a high speed camera (2000 frames/s) was used. After those initial visualizations, the main objective of this work consisted of measuring LOX droplets size and velocity on the axial flow, in order to get a good mapping of the spray characteristics around the LOX core. A PDPA system with one component of velocity was used for those measurements.
The two experimental investigations give a good qualitative (by visualization) and quantitative (by Phase Doppler technique) description of the LOX spray in terms of atomization and vaporization processes in hot fire conditions. Three different zones have been detected: near the post tip, a first atomization zone; downstream, a relative long ligaments zone; and, finally, a well-defined droplets spray.
Looking at the droplet size evolution along the combustion chamber also provides some information on the vaporization process.

### *Visualization experiment*

The first step, aimed at providing preliminary information of LOX core break up process and at localizing the atomization zone was achieved by means of a visualization technique using a stroboscopic laser sheet associated with a high speed camera. The laser sheet was formed by a stroboscopic copper laser beam (at $\lambda$ = 510.6 nm: green) focused through a cylindrical and a spherical lens. This sheet was 70 mm wide and about 1 mm thick near the chamber axis. The strobe frequency was 2 kHz and the pulse time duration about 40 ns. A high speed 16 mm movie camera (NAC E-10) was used in association with black and white high speed sensibility movie film (500 ISO). This camera was used at 2000 frames/s. An optical pick-up synchronized images with the strobe frequency. The scattering light of LOX was then recorded to get the liquid structure in good conditions.
Four operating conditions have been investigated during this test campaign, namely points A and C of table 1 at 1 and 10 bar. Two kinds of images were recorded during these

visualization tests. First, the phenomena were recorded without any filter to reject the luminous flame light (Fig. 7). Those images permitted to get the structures of both the luminous flame and the liquid inside the reaction zone. In a second configuration, a bandpass filter, centered at the wavelength of the laser beam around 510 nm, was fitted in front of the camera lens. In this configuration only the scattered light of the liquid structure was visualized (Fig. 8).
A first analysis of the recorded movies permitted to determine where the LOX core was too dense to perform Phase Doppler Particle Analyzer measurements. This result was useful to establish a test plan for the spray characterization. Another interesting information was the comparison between results at 1 and 10 bar. At 1 MPa the flame emission was clearly detectable in the near blue spectral region while it was not at atmospheric pressure. This is only a qualitative information and spectroscopic measurements are planned to get complementary information on the spectral emission of the flame.
We have also digitized a sequence of about 50 frames of one condition (point C, atmospheric pressure) with Kodak high resolution digital camera (2048x2048), and made an analysis of a sequence of 20 frames to follow some liquid structures to estimate their velocity in the combustion chamber. A good correlation was observed between those measurements and the mean droplet velocity obtained with the PDPA at the same location in combustion chamber.
Finally, we made a zoom on a precise zone of a picture to follow the secondary atomization process: the breakup of a ligament in single droplets (spherical or not).

### *Atomization and vaporization results and analysis*

After the initial visualization tests described above, the main objective of this study consisted in measuring LOX droplet sizes and velocities under hot fire conditions with the AEROMETRICS PDPA and describing the atomization and vaporization zone by a fine mapping of those measurements around the LOX core.
The laser emission is an Helium Neon of 15 mW nominal power. The laser beam is focused into the test chamber by a 1000 mm transmitter lens. The receiver system is situated in the forward direction, at 30° off-axis, to collect the scattered light with a 500 mm standard lens. A red bandpass filter is placed in front of the three detectors behind the receiver lens. This configuration is the AEROMETRICS commercial one-component system. The PDPA complete theory has been described and explained in Bachalo and Houser[13]. In our experiment, due to limited access, it would have been very difficult to have a good collecting angle through the windows without the following specific optical arrangement: the transmitter and the receiver are placed on both sides of the combustor, with a 15° angle. The LOX refractive index was chosen at 1.221.
At atmospheric pressure, 55 tests at point A and 52 at point C were performed. Seven radial profiles have been explored along the flow axis, and as close as possible to the LOX post tip. Those profiles ranged from $x/d = 4$ (where $d$ stands for the LOX post inner diameter) out of the axis because of the presence of the LOX core, until $x/d = 36$. An additional measurement was also performed downstream of the combustion chamber exit at $x/d = 72.4$, which showed the presence of LOX droplets at a relatively far distance from the injector. Fig. 9 shows an example of histograms for points A and C at $x/d = 36$ and $r/d = 0$ (that is to say on the axis).
Only two radial profiles have been performed at 1 Mpa, one very close to the coaxial injector, with $x/d = 4$ and another at $x/d = 16$. Here, like at atmospheric pressure, a measurement outside of the combustion chamber, after the throat, showed that no droplet existed at a distance of $x/d = 83.6$.
This spray analysis with the PDPA provided radial and axial profiles of droplets size and axial velocity. A relatively good description of the spray under hot fire conditions has been done at atmospheric pressure, qualitatively with visualization and quantitatively with droplets size and velocity measurements, for two operating conditions corresponding to two mixture and momentum ratios. A global sketch of the spray is presented in Fig. 10. However this "artistic drawing" is only a mean representation of all the spray phenomena inside the combustion chamber, and, as it can be seen on the pictures from the visualization tests, the instantaneous spray structures, obtained with a resolution time of 40 ns, look very different.
The better atomization is obtained in condition A. This can be seen on mean sizes and velocities and is easily detectable in Fig. 11 showing the radial variations of $D_{32}$ and mean velocity. However in each case (A and C), we saw a *first atomization zone* near the injector outlet, where a droplets spray coexists with the liquid core (intact liquid jet) flowing out of the LOX post. This zone extends from $x/d = 0$ to almost $x/d = 8$. In this zone droplets are measured out of the center line in a short area between $r/d = 1$ and $r/d = 2$. No measurement is possible for $r/d < 1$, and no liquid objects are detected for $r/d > 2$. A second zone appears downstream of this well defined fine spray and LOX core: it looks like a big *ligaments and droplets* region, where the validation rate is very low (less than 30%). This zone extends from $x/d = 10$ to $x/d \geq 20$. Further downstream we find a better *atomization and vaporization area* (with validation above 60%) but where the particles are still relatively large. This analysis has been confirmed by complementary information given by other measurements performed on the same combustor (see following sections).
Comparisons between results at atmospheric pressure and at 1MPa in two cases (A and C) show that the size values are similar. This result seems to confirm that the momentum flux ratio $J$ and the Weber number actually are similarity parameter of major importance for the atomization process, since they are the only dimensionless numbers which were kept constant when increasing the pressure in the combustor.
We compared the evaporation time $t_v = (D_o)^2 / \lambda_{eff}$, defined by A.H. Lefebvre[14] which accounts for both preheating and convective effects on a droplet moving in a flow, to the resident time $t_r = L / Vg$ of a droplet in the combustor. We obtained for point A at atmospheric pressure: $t_r = 5.82$ ms and $t_v = 6.21$ ms. Through this result we can notice that resident and evaporation times have similar values, and we confirm the fact that droplets can survive far from the injector outlet. Droplets with a diameter over 200 µm can cross the whole length of the combustion chamber and reach the exit (in tests at atmospheric pressure).
Finally we compared empirical correlations issued from different references on coaxial injectors investigations[15, 16, 17] to our experimental diameter values.
Applying the equation of ref.15, obtained with water and air, we have respectively for case A and C: $D_{32A} = 45$ µm and $D_{32C} = 71$µm. The equation of ref.16, with an other water and air coaxial configuration, gives : $D_{32A} = 151$ µm and $D_{32C} = 210$ µm and finally with the equation of ref. 17, established for liquid wax and air, the results would be : $D_{32A} = 16$ µm and $D_{32C} = 21$ µm . Each of the three results obtained with the Phase Doppler system (near injector region, ligament zone, downstream region) may be predicted with one of the above correlations.

## 4. OH radical imaging

### *Diagnostics review*

Emission of OH radicals may be used to locate regions of intense combustion. Radiation from OH takes place in the

near UV range between 306 and 320 nm (Dieke[18]). Emission bands are clearly separated from those of oxygen and water. Detection is achieved with an intensified CCD camera (featuring 578x384 pixels with 12 bits depth) equipped with a Nikon 105 mm f=4.5 UV objective. A UG-5 glass filter blocks radiation above 400 nm and two WG 305 filters suppress radiation below 283 nm while passing 306 and 320 nm where chemiluminescence is observed. The camera is placed on one side of the combustor at right angles with respect to the axis (Fig. 12). Emission images provide the instantaneous signal integrated over the line of sight (i.e. over a line orthogonal to the axial direction). It is not possible to deduce the local values from an observation under a single viewing angle. However, the instantaneous images may be averaged and the resulting data may be processed through an Abel transform to determine the mean volumetric light intensity distribution[5]. This tape of numerical tomography is suitable if the flame is axisymmetric and if self absorption of the light radiated by the flame is not too large.

Direct illumination of liquid-gas interfaces produces elastic light scattering (ELS), the detection of which may be used to locate the liquid phase and more specifically determine the distance of LOX jet break-up. A laser sheet is used as incident light while the scattered radiation is recorded with a CCD camera placed at right angles (Fig. 12).

Fluorescence of OH radicals is being used extensively in combustion experiments to characterize reactive layers in flames. The pumping laser wavelength is most commonly tuned to the $Q_1$ branch of the rotational level $J'' = 6$ transition $A^2\Sigma(v' = 1) \leftarrow X^2\pi(v'' = 0)$ at 283.92 nm. The choice of the $J'' = 6$ level minimizes the temperature dependence of the fluorescence signal. For moderate laser intensities the regime is linear and it may then be shown that the fluorescence signal is proportional to the number density of OH molecules. In practical applications, it is convenient to detect off-resonance light radiation. The shift between the pumping wavelength and the LIF signal allows separation of the useful signal from other radiations. This is particularly important here because the liquid oxygen jet and spray produce an intense scattered signal at the pumping wavelength. The laser pulse is generated by a Nd:YAG pumped dye laser (Continuum Powerlight and ND6000). Typical pulse energies using R590 dye and a BBO doubling crystal were 30 mJ for a pulse duration of 20 ns. Fluorescence is detected by a gated intensified CCD camera (578x384 pixels with 12 bits depth) equipped with one UG-5 glass filter and four WG-305 filters which eliminate most of the scattered light (Fig. 12). The exposure time is 50 ns, images are acquired at 10 Hz. Some Raman signal originating from the liquid phase (at 296 nm) may still be present in the detected signal but its level is lower than that of the LIF signal (see Snyder et al.[6] for more details on the set-up and on the interpretation of the detected signals).

In some experiments two cameras were employed to obtain simultaneous images of the LOX jet (using ELS) and of the flame (using LIF). After correction for orientation and scaling the images were combined to locate the flame with respect to the liquid phase. This simultaneous imaging method is also useful in evaluating possible crosstalk between light scattering and LIF

### *Emission, ELS and OH-PLIF imaging results*

Systematic experiments carried-out on the MASCOTTE facility have provided a large data base of images for a set of operating conditions. Some of these data are already described in Snyder et al.[6] and Herding et al.[3-5]. A selection of images is included in this subsection. In the emission images included in Fig. 13, the injector geometry is shown to scale and the complete height of the chamber is displayed. It is important to remember that the signal detected by the camera is integrated over the line of sight and it is therefore not possible to determine the precise nature of the patterns appearing in these pictures. It is however clear that radiation from OH starts right at the injector lips. The reactive layer is nearly cylindrical initially and expands further downstream. The boundary of emission images move away from the axis and the flame fills the central portion of the chamber.

Laser induced fluorescence images (Fig. 14) show some distinct features. The LIF signal is already quite strong at the injector and the level does not change notably downstream. A highly corrugated layer of intense fluorescence is observed in the lower part of the picture while the upper trace of LIF fades out. The signal does not quite vanish in the LOX core indicating that some parasitic signal (probably Raman scattering at 296 nm) is also detected by the camera. The presence or absence of LIF signals on the upper side of the chamber may be interpreted by considering the quality of LOX core disintegration and atomization. If this process is delayed, the laser sheet crosses the LOX jet without much distortion and produces OH fluorescence. This is the case in the injector vicinity. If the jet breaks up and produces a dense spray of droplets, the beam is scattered effectively and cannot produce fluorescence from the upper flame sheet. This explains why the LIF signal is in general much stronger in the lower side of the chamber which is illuminated by the unperturbed laser sheet.

Combined LIF and ELS images are displayed in Fig. 15. These pictures show that the LIF signal is distinct from the scattered light. Near the injector the LIF and ELS signals are quite close indicating that the flame develops in the near vicinity of the LOX core. The previous data clearly indicate that reaction begins near the injection plane and that the reactive layer is than relatively smooth initially and highly corrugated after jet break-up. The flame expands away from the axis when the spray is formed at few diameters from the injection plane.

This general picture is confirmed by the data deduced from the Abel transformed average emission images. Fig. 16 gives the emission transformed images for operating condition A at 10 bar (very similar features are observed for point C). The mean volumetric distributions deduced by numerical inversion indicate that the mean flame begins at the LOX tube lip. The mean flame is initially a thin, nearly cylindrical, surface which expands downstream into a thick shell surrounding the gaseous oxygen and LOX spray formed after jet break-up. The volumetric OH emission intensity is spread over a region of finite thickness. Further downstream, the mean flame becomes annular. The inner and outer diameters of the flame volume slowly decrease with axial distance as the oxygen convected in the central region is being consumed.

## 5. Planar Laser Induced Fluorescence of $O_2$

### *Principle*

Planar laser induced fluorescence of $O_2$ is a well suited tool for investigations of cryogenic jet flames owing to its very high sensitivity at elevated temperature. It is practically insensitive to collisional quenching up to 15 bar as the fluorescence yield is dominated by predissociation. At a given temperature the fluorescence intensity is directly proportional to the oxygen concentration and to the local laser irradiance in the control volume. The effective absorption cross section of a broadband argon-fluoride laser and the fluorescence efficiency are strongly increasing with the oxygen temperature Lee and Hanson[19]. As a drawback to this useful feature the local effective irradiance is progressively attenuated as the laser progresses in hot oxygen. Complex iterative techniques involving both temperature and concentration are usually required to correct this decay.

In the present configuration where $O_2$ is inside the flame the laser irradiance will not be altered when reaching the reaction zone in which the hot and weak amount of $O_2$ about the stoichiometric surface can be detected with a maximal sensitivity. This reverse configuration (compared to the standard case where oxidizer is diffusing from the outside ambient air) is a key point of the detection technique which allows restoration of the flame surface (Guerre et al.[7]).

The same general layout than for OH imaging is used with following components. The pulsed radiation ($\lambda$ =193 nm, $\Delta\lambda$ = 0.7 nm, $W$ =170 mJ/15 ns, $f$ =10 Hz) of an ArF laser (Lambda Physik LPX 100) is focused into a vertical light sheet (30 mm high x 800 µm thick) passing through the jet axis. The fluorescence is imaged at 90° onto a gated intensified CCD camera (Proxitronic, $\Delta t_{gate}$ = 50 ns) with a 105 mm f/4.5 UV objective lens equipped with a high pass filter ($T_r$(193nm) = $10^{-8}$, $T_r$(220nm) = 0.4) rejecting the parasitic elastic light at the laser wavelength. The video signal is digitized by a frame grabber board (512x512 pixels on 8 bits) connected to a PC.

With the ArF excimer laser $O_2$ is excited through the Schumann-Runge system ($B^3\Sigma_u^- - X^3\Sigma_g^-$) Within the laser wavelength extend, four vibrational bands of $O_2$ are present :

$$(v' = 0) \leftarrow (v'' = 4)\ ,\ (v' = 1) \leftarrow (v'' = 7)\ ,$$

$$(v' = 2) \leftarrow (v'' = 10)\ ,\ (v' = 3) \leftarrow (v'' = 14)$$

which are hot bands. In our configuration excitation with ArF excimer laser sheet allows to map gaseous oxygen above 800 K.

### *Laser induced fluorescence of $GO_2$ results*

Laser induced fluorescence of gaseous oxygen has been used to map the instantaneous flame and to investigate the influence of pressure and temperature of the fast hydrogen coflow on the flame front structure. The emphasis was put on the oxygen consumption within the flame, thus eleven operating conditions were explored keeping the mixture ratio constant with hydrogen injected at 300 K (under 1 and 8 bar) and with hydrogen at 80 K (at 1 bar). Fig. 17 shows an example of single shot fluorescence image of $O_2$ for point C at 1 bar.

This image indicates that the flame is attached to the injector lips as already observed in OH spontaneous emission and OH-LIF images.

Statistical analysis has been performed by processing 200 images for each operating condition to obtain the probability distribution of the flame location. A map of this distribution is presented in Fig. 18 for three different operating conditions with the same flow rates, two with $H_2$ at 300 K at 1 and 8 bar (cases C and C'-8 respectively) and one with $H_2$ at 95 K at 1 bar (case F1). Dimensionless numbers are outlined in Table 1. In case C the probability distribution has a large dissymetry which is reduced in case C'-8 where the pressure was higher. In case F1 with cold hydrogen the distribution is nearly symmetric but the flame surface is more divergent.

## 6. Coherent Anti-Stokes Raman Spectroscopy

### *Principle*

Studies carried-out during the last 15 years indicate that broadband Coherent Anti-Stokes Raman Spectroscopy (CARS) has the appropriate temporal and spatial resolutions for measurements in turbulent combustion systems. Its use in cryogenic combustion is however quite challenging. CARS is observed when three waves of frequencies $\omega_0$, $\omega_1$ and $\omega_2$ pass through a gas mixture (for example Eckbreth[20]). If the frequency difference $\omega_1$ - $\omega_2$ is close to the Raman-active vibrational frequency $\omega_p$ of a molecular component of the gas, an intense beam with frequency $\omega_3 = \omega_0 + (\omega_1 - \omega_2)$ will be generated in the forward direction of the incident waves. The two coherent incident waves $\omega_1$ and $\omega_2$ force the molecules to oscillate in phase at the frequency $\omega_1 - \omega_2$. Then the $\omega_0$ radiation is scattered off by molecules whose polarizability is modulated by the oscillation. A new coherent wave is thus created at the frequency $\omega_3 = \omega_0 + (\omega_1 - \omega_2)$ called the anti-Stokes frequency. The same wave is often used to pump and probe the molecular oscillation ($\omega_0 = \omega_1$), the anti-Stokes frequency is then given by $\omega_3 = \omega_1 + (\omega_1 - \omega_2)$. A CARS spectrum, i.e. the energy of the anti-Stokes pulses as a function of the frequency difference $\omega_1 - \omega_2$ allows both the chemical and the temperature analysis of the gas mixture. It is created by a single laser pulse exciting one or more molecular species of the gas mixture using a broad-spectral-bandwidth $\omega_2$ laser and detecting the resulting anti-Stokes beam with a CCD detector set up at the output of a spectrometer. The shape and the amplitude of a spectrum depend on the temperature and the density of the species respectively. While the shape is not disturbed by thermally-induced refractive index gradients affecting the beams when they pass through a turbulent medium, the amplitude is often reduced because the beams fail to cross in the prescribed probe volume. As a consequence, the first goal of CARS tests conducted on MASCOTTE focused on thermometry, using $H_2$ that is the major diatomic species present in the gas flow. The CARS setup (see Magre et al.[21]) consists of an ensemble including the two lasers, their associated optics and a detection part divided into a reference and a measuring channels. An optical bench of 150X50 $cm^2$ holds the two lasers. The $\omega_1$ beam is the doubled-frequency output of a Nd:YAG laser chain composed of a single-mode $Q$ switched oscillator followed by an amplifier. It is partly used to pump a dye laser chain (dye: LDS 698) which emits the broad $\omega_2$ spectrum. The $\omega_2$ bandwidth is 100 $cm^{-1}$ (FWHM) and the central wavelength is 683 nm. At the output of the emitter bench, the $\omega_1$ beam has already been split in two parallel beams and one of them is overlapped with the $\omega_2$ beam (planar BOXCARS arrangement). The energy/pulse of the beams are 30 mJ for each of the $\omega_1$ beams and 2 mJ for the $\omega_2$ beam. All beams are horizontally polarized. The beams are focused first in a 1 atm pressure slow flow of argon where a weak CARS signal is created to monitor the fluctuations of direction and of pulse energy of the $\omega_1$ and $\omega_2$ lasers and of the spectral shape of the $\omega_2$ laser. Then, that reference signal is split-off and the laser beams pass to the MASCOTTE facility where they are refocused in the chamber (Fig. 19). Three pairs of 25 mm-diameter 8mm-thick optical windows have been especially installed on the top and bottom of the burner replacing the long and narrow ones used for the LIF laser sheet. The windows are 400-700 nm A.R. coated on their external surface and they are recessed from the chamber by 30 mm to lengthen the distance between the windows and the laser focus in order to avoid laser damages. The CARS beams are focused using a 140-mm-focal-length achromat yielding a 0.9 mm-long and 40 µm diameter probe volume. Reference and sample CARS spectra are then dispersed in two separate spectrometers and detected with intensified 532-photodiode arrays. The spectral dispersion is 0.25 $cm^{-1}$/diode and the resolution is 1.6 $cm^{-1}$ (FWHM). The rate of data acquisition is 5 Hz.

Instantaneous temperature measurements are deduced from single shot CARS spectra of $H_2$ which present the singularity to have a spectrum of isolated $Q$-rotational lines. At atmospheric pressure, collisional broadening is negligible

and all the lines are in the Doppler regime. Consequently, the temperature are deduced by plotting the amplitudes of the $Q(1)$ to $Q(5)$ or $Q(7)$ in a Boltzmann diagram. The error bar of an instantaneous temperature is the uncertainty given by the least square fitting routine and reflects the accuracy of the complete apparatus including the data processing. To illustrate the capability of the setup, an experiment is performed by feeding the MASCOTTE chamber with a mixture of 10% $H_2$ and 90 % Ar. The uncertainty of the instantaneous temperatures is of the order of 10 K and the temperature averaged from 150 Boltzmann plots is 296 K with a standard deviation of 10 K. When the pressure increases, collisional processes become important and Raman linewidths of the $Q$-branch transitions of $H_2$ exhibit a well-known contraction according to an effect first analyzed by Dicke[22]. The effect, which is often termed "Dicke" or "motional" narrowing, is due to a reduction of the Doppler contribution to the total line broadening with increasing collision frequency. The decrease in Doppler broadening results from a coherent averaging of frequencies within the normal Doppler line profile, induced by velocity-changing collisions that conserve vibrational phase. If the frequency of velocity-changing collisions is greater than that of dephasing collisions, sub-Doppler total linewidths can result. The resulting profile of the $Q$-rotational line is a generalized Galatry profile where the characteristic parameters are the collisional linewidth, the Doppler linewidth and the effective frequency of velocity-changing collisions $\beta = kT/mD$ where $D$ is the optical diffusion coefficient. For the MASCOTTE experiment, the presence of $H_2O$ and $O_2$, two other possible collisional partners for $H_2$, contribute significantly to the $H_2$ relaxation processes and consequently, also change the CARS spectral shape. $H_2O$ has to be taken into account precisely because of its abundance in the combustion products and the efficiency of its collision with $H_2$. On the contrary, the effect of $O_2$ is merged with those of $H_2$ because the collisional behavior of $H_2$ and $O_2$ are similar. Values of the pressure-broadening coefficients for $H_2$-$H_2$ and $H_2$-$H_2O$ collisions are those measured and modeled by Berger and Robert (unpublished). These parameters, obtained experimentally in the temperature range 300 K- 1200 K, are extrapolated in order to predict the $H_2$ spectra at temperatures up to 3000 K. Temperatures are deduced by fitting the experimental spectra with the theoretical ones calculated for different temperatures and for different molar fractions of $H_2$ and $H_2O$. The fitting technique used is a simple least squares where the error function is given by

$$F = w_j\left[I_j^{exp} - I_j^{theo}(T, X_{H2}, X_{H2O})\right]^2$$

where $I_j$ is the signal intensity of the $j$-th rotational $Q$-line and $w_j$ is a statistical weight characteristic of the magnitude of the lines. $X_{H2}$, and $X_{H2O}$ are the molar fractions of $H_2$ and $H_2O$ with $X_H = 1 - X_{H2O}$ by assumption.

### *Temperature measurements results*

The CARS measurements correspond to four experimental conditions previously used during the LIF campaign (A and C at 1 and 10 bar).

At atmospheric pressure, the measurements are carried-out at four axial locations from the injector exit (between 80 and 250 mm) by placing the combustor modules with and without optical ports as necessary. In each axial section, the measurement points are located between the input window and the injector axis in order to reduce the disturbances affecting the beams before they reach the probe volume. An ensemble of 150 instantaneous temperature measurements are recorded during each run with an uncertainty of 50 to 100 K which is 5 to 10 times more than the value obtained during the demonstration experiment. However the temperature fluctuations induced by turbulent combustion exceed by far this uncertainty. The measurements also show no evidence of a temperature evolution during the run indicating that the process is stationary and that it may be characterized by histograms, mean values and standard deviations. Thus, Fig. 20 shows typical data obtained at different positions displayed with a temperature step of 100 K matching the apparatus uncertainty. The temperature distributions display the degree of burnout which depends primarily on the mixing of $H_2$ and $O_2$. Depending on the measurement locations, the validation percentage, defined as the ratio between the number of spectra successfully processed and the total number of laser pulses, ranges between 0 and 100 %. Data processing fails when the experimental signals are too weak reflecting either low instantaneous $H_2$ mole fraction within the probe volume or imperfect beam crossing due to large refractive index gradients present in the chamber. Preliminary experiments devoted to probing $H_2O$ and $O_2$ indicate that CARS signals could be obtained at positions where the validation rates for $H_2$ are too low. For $r <$ 10 mm, the validation percentage is low whatever the distance from the injector because of a slow mixing of the $O_2$ axial flow with the surrounding $H_2$ flow. The mean temperature increases downstream (Fig. 21) while the standard deviation decreases slightly when the excess of $H_2$ is reduced (condition C). Results show that the combustion is not complete at $x$ = 250 mm when the burner operates at atmospheric pressure, which is confirmed by the fact that LOX droplets detected by the PDPA leave the combustor.

At a pressure of 10 bar the combustor runs during 15 s yielding 75 CARS data samples. Measurements correspond to sections located between 10 and 410 mm from the injector exit. Fig. 22 shows the radial profiles of the mean temperature and the standard deviation of temperature at $x$ = 10 mm close to the injector. No CARS signal is detected at $r$ = 0 mm indicating that hydrogen is never present in the liquid oxygen core flow. The mean temperature increases with radial distance reaching 600 K at $r$ = 20 mm (condition C-10). This result indicates that hot gases formed downstream recirculate in this region. The temperature is slightly lower (by about 50 K) for operating conditions A. The temperature standard deviation decreases with the radial distance from 120 K at $r$ = 5 mm to 70 K at $r$ = 20 mm while the validation percentage increases from 0. The high validation rate and the low standard deviation mean that the recirculation zone is relatively homogeneous. In contrast the low validation percentage and the large temperature standard deviation recorded at $r$ = 5 mm show the presence of a zone where the $H_2$ mole fraction and temperature fluctuate, demonstrating the presence of an unsteady mixing layer between the inner oxygen jet and the surrounding hydrogen flow.

For the two operating conditions, radial mean temperature profiles are nearly identical. For instance, Fig. 23 shows the data recorded at three axial positions for the condition A (10 bar). The mean temperature profiles are relatively flat. The temperatures reach 2400 K with a standard deviation of about 600 K due mainly to random fluctuations induced by the turbulent flow. At $x$ = 180 and $x$ = 250 mm, the validation rate increases as the measurement point approaches the wall. In contrast at $x$ = 410 mm, the validation rate, nearly 50 % is quite independent of the radial position.

## 7. Discussion and conclusion

The structure of cryogenic two-phase reactive flows is investigated in this article. High speed cinematography and Phase Doppler measurements provide information on the spray structure, while OH imaging, O2 Laser Induced Fluorescence and $H_2$-CARS thermometry are used to analyze the flame.

In this particular case of a single shear coaxial injector placed in a square chamber and for the range of parameters investigated, three successive zones may be identified in the spray : a first atomization zone near the injector outlet

(between $x/d = 0$ and $x/d = 8$), where a droplets spray coexists with the liquid core flowing out of the LOX post, a second zone of ligaments and droplets from $x/d = 10$ to $x/d \geq 20$ and further downstream a better atomization and vaporization area.

The flame is stabilized in the vicinity of the LOX tube and takes the shape of a "shell". As indicated by the OH-PLIF images, the instantaneous reactive layer is thin and highly corrugated.

The reactive sheet is initially in contact with the LOX jet and expands further downstream. The Abel transformed emission images show that reaction takes place in a finite region surrounding the liquid jet, and later the gaseous oxygen and LOX spray. Temperature is initially stratified in the radial direction and becomes more homogeneous further downstream after intense mixing

The sharpness of the oxygen fluorescence maps support the expected assumption that oxygen-hydrogen combustion rate is higher than turbulent mixing rate in the cryogenic jet flame. This finding is also corroborated by the fact that the flame is always attached (or nearly attached) to the lips of the coaxial injector. It is then expected that two phase calculations and modeling based on diffusion flamelet structures can apply to this situation.

Statistics of flame location obtained from $O_2$-LIF show that in the near field the wrinkling and flapping of the flame are low and increase with downstream locations in agreement with the data obtained with OH-LIF and OH emission imaging.

CARS thermometry results lead to the following conclusions:

- The mean temperatures are higher (by about 300 K) than the adiabatic temperature calculated with a mixture ratio $M = 2.1$. Since the measurements require a strong CARS $H_2$ spectrum, there exists a potential for biasing the mean temperature; and it is expected that such biasing, when present, will be most significant in the region where the validation rate will be weak. Moreover, the precise knowledge of the collisional linewidths at high temperature may also induce an additional bias.
- At $x = 180$ mm, the mean temperature has leveled-off, indicating that intense mixing takes place in the turbulent flame.
- At $x = 180$ mm and $x = 250$ mm and close to the axis, the low validation rates indicate that the hydrogen mole fraction is quite low near the inner flow. In contrast at the chamber exhaust ($x = 410$ mm), a validation rate of about 60 % for all radial positions tends to indicate that the flow is more homogeneous.

A final comparison between the mean temperature axial profiles at $r = 15$ mm recorded at 1 and 10 bar (Fig. 24) indicates that heat is released more quickly at the higher pressure.

## Acknowledgments

This work was supported by SEP and CNES.. Technical help provided by A. Mouthon and R. Barraud (ONERA) is gratefully acknowledged.

## References

[1]Ledoux, M., Caré, I., Micci, M., Glogowski, M., Vingert, L., and Gicquel, P., "Atomization of Coaxial-Jet Injectors," *Proceedings of the 2nd International Symposium on Liquid Rocket Propulsion*, Chatillon, France, 1995.

[2]Gicquel, P., Brisson, E., and Vingert, L., "Experimental investigation of a LOX spray under hot fire conditions," *Proc. of the 7th International Conference on Liquid Atomization*, Seoul, Korea, August 1997.

[3]Herding, G., Snyder, R., Souflaire, P., Rolon, C. and Candel, S., "Emission and laser induced fluorescence imaging of cryogenic propellant combustion," *Proc. of the Conference on Propulsive Flow in Space Transportation Systems* , Bordeaux, France, CNES, July 1995.

[4]Herding, G., Snyder, R., Scouflaire, P., Rolon, C. and Candel, S., "Flame stabilization in cryogenic propellant combustion," *26th Symposium (International) on Combustion*, The Combustion Institute, Pittsburgh, 1996.

[5]Herding, G., Snyder, R., Rolon, C. and Candel, S., "Investigation of cryogenic propellant flames using computerized tomography of OH emission images," *Submitted to Journal of Propulsion and Power*, 1997.

[6]Snyder, R., Herding, G., Rolon, C. and Candel, S., "Analysis of flame patterns in cryogenic propellant combustion," *Combustion Science and Technology*, Vol. 124 1997.

[7]Guerre, S., Bazile, R. and Stepowski, D., "Conditioned dissipation and average consumption maps in a turbulent non-premixed flame using planar laser induced fluorescence of 02," *26th Symposium (International) on Combustion*, The Combustion Institute, Pittsburgh, 1996.

[8]Cessou, A., Colin, P., Vingert, L., Habiballah, M., and Stepowski, D., "Fluorescence induite par plan laser du dioxygène dans une flamme diphasique turbulente oxygène liquide/hydrogène gazeux," *Journée d'Etudes de la Société Française des Thermiciens*, Toulouse, Mai 1997.

[9]Grisch, F., Bouchardy, P., and Péalat, M., "Mesures de température par Diffusion Raman Anti-Stokes Cohérente à pression atmosphérique sur le banc Mascotte", *5ème Colloque GDR Moteurs-Fusées*, Paris, France, Octobre 1995.

[10]Brummund, U., Cessou, A., Oschwald, M., Vogel, A., Grish, F., Bouchardy, P., Péalat, M., Vingert, L., Habiballah, M., Snyder, R., Herding, G., Scouflaire, P., Rolon, C. and Candel, S., "Laser diagnostics for cryogenic propellant Combustion Studies," *Proc. of the 2nd International Symposium on Liquid Rocket Propulsion*, Chatillon, France, 1995.

[11]Hopfinger, E. and Lasheras, J. C., "Breakup of a water jet in high velocity co-flowing air," *Proc. of the 6th International Conference on Liquid Atomization*, Rouen, France, edited by A. J. Yule and C. Dumouchel, Begell House, New York, 1994.

[12]Villermaux, E, "Mixing and spray formation in coaxial jets", *Proc. of the 3rd International symposium on Space Propulsion*, Beijing, China, August 1997.

[13]Bachalo, W.D., and Houser, M.J., "Phase Doppler spray Analyzer for simultaneous measurements of drop size and velocity, " *Optical Engineering*, volume 23, N°5, 1984.

[14]Lefebvre, A.H. "Droplet evaporation," *Atomization and sprays*, N. Chigier (ed.), chap. 8, an Hemisphere Publishing Corporation, 1989.

[15]Nukiyama, S., and Tanasawa, Y. "Experiments on the atomization of liquids in an air stream," *Trans. Soc. Mech. Eng. Jpn.*, vol.5, N°18, pp.62-67, 1939.

[16]Lorenzetto, E.G., and Lefebvre, A.H., "Measurements of drops size on a plain jet airblast atomizer," *AIAA journal*, vol. 2, N° 3, pp. 583-585, 1964.

[17]Kim, K.Y., and Marchal, W.R., "Drop size distributions from pneumatic atomizers," *Journal of Am. Inst. Chem. Eng.*, vol.17, N° 3, pp. 575-584, 1971.

[18]Dieke, G. H., and Crosswhite, H. M., "The ultraviolet bands of OH: fundamental data," *Journal of Quantitative Spectroscopy and Radiative Transfer*, Vol. 2 , 1962, pp. 97-199.

[19]Lee, M. P., and Hanson, R. K., "Calculations of 02 absorption and fluorescence at elevated temperatures for a broadband Argon-Fluoride laser source at 193 nm," *Journal of Quantitative Spectroscopy and Radiative Transfer*, Vol. 36 , 1986, pp. 425-440.

[20]Eckbreth, A. C. ,"Laser diagnostics for combustion temperature and species," *Abacus Press*, Cambridge, 1988.

[21]Magre, P., Moreau, P., Collin, G., Borghi, R., and Péalat, M., *Combustion and Flame*, Vol. 71, 1988, pp. 147-153.

[22]Dicke, R. H., *Physical Review*, Vol. 89 , 1953, pp. 472.

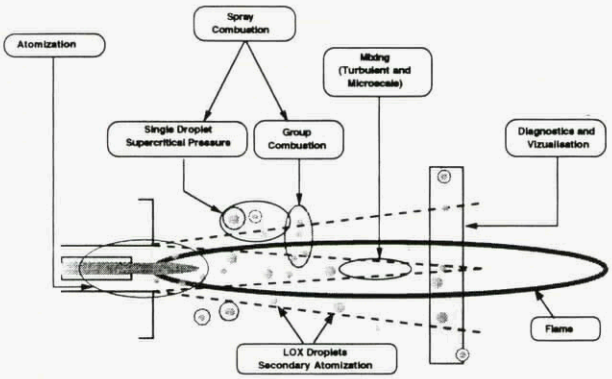


Fig. 1 : Main mechanisms of coaxial jet cryogenic flame

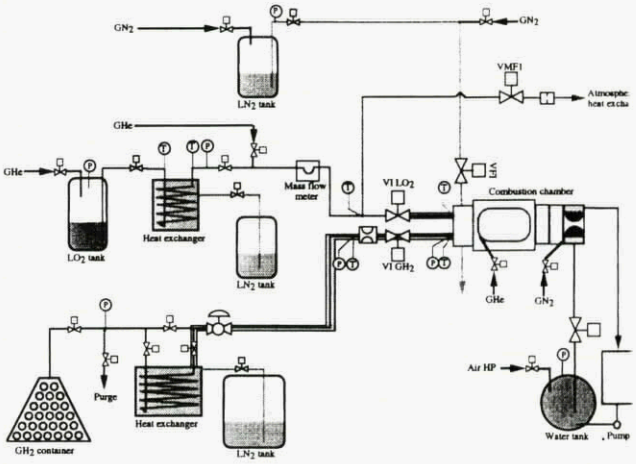


Fig. 2 : General layout of MASCOTTE version V02

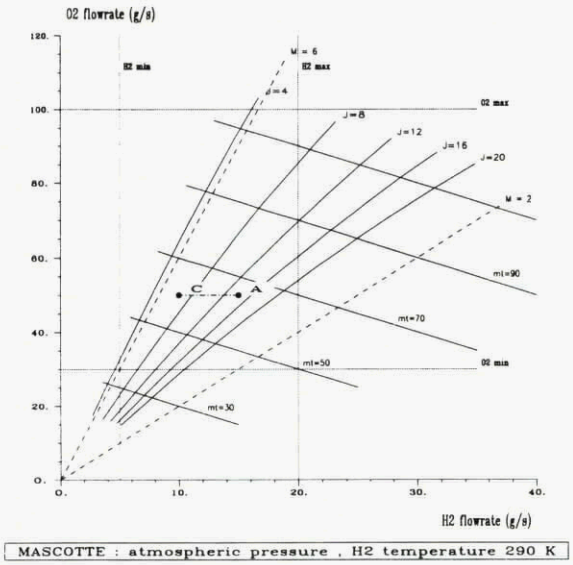


Fig. 3 : Operation domain of MASCOTTE at 1 bar

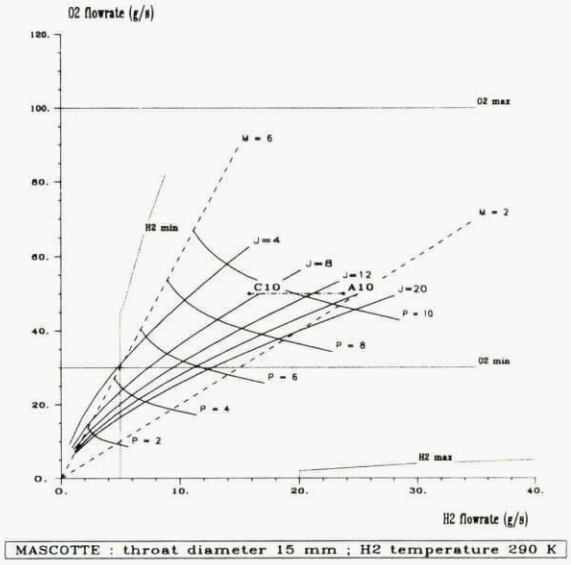


Fig. 4 : Operation domain of MASCOTTE around 10 bar

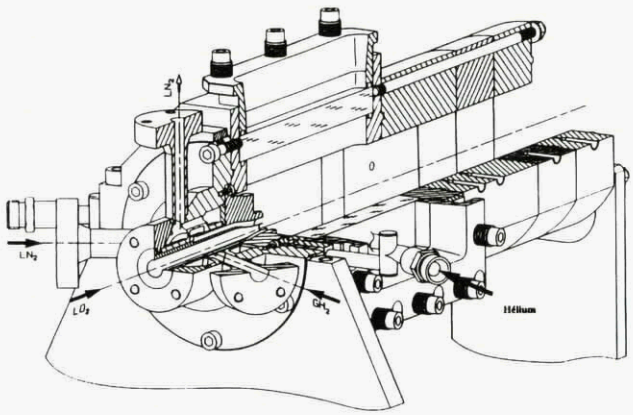


Fig. 5 : Sketch of the MASCOTTE combustor

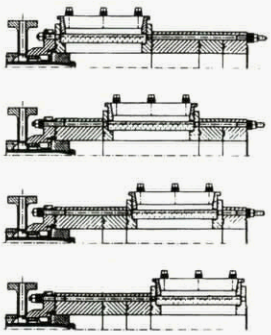

Fig. 6 : Different positions of the visualization module

Fig. 7 : Visualization of both flame and liquid jet

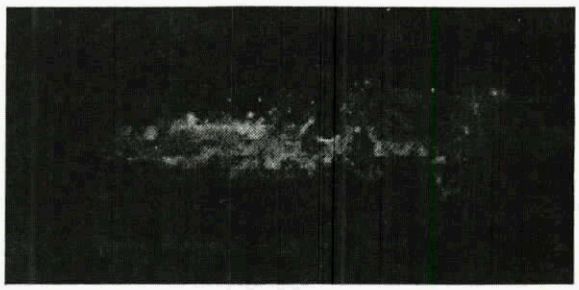

Fig. 8 : Visualization of liquid jet alone

A - 1bar
x/d = 36 r/d = 2.4
Validation = 51 %
D10 = 52.5 µm
D32 = 71.0 µm
V mean = 44.8 m/s
V RMS = 9.7

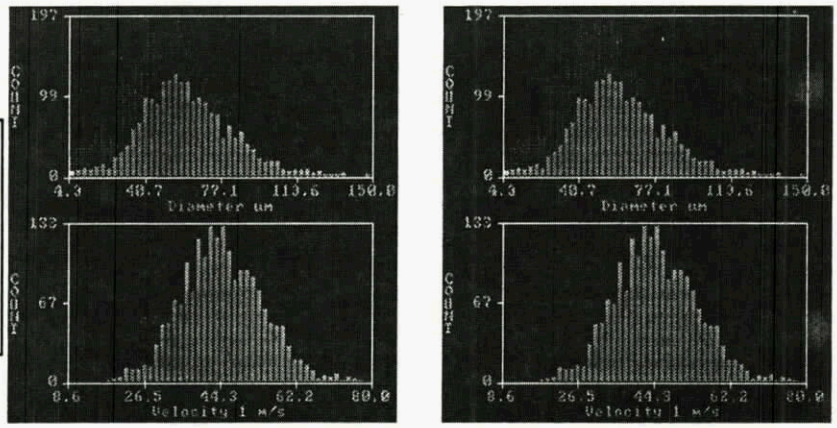


C - 1 bar
x/d = 36 r/d = 1
Validation = 60 %
D10 = 47.0 µm
D32 = 68.7 µm
V mean = 32.1 m/s
V RMS = 7.8

Fig. 9 : Example of size and velocity histograms

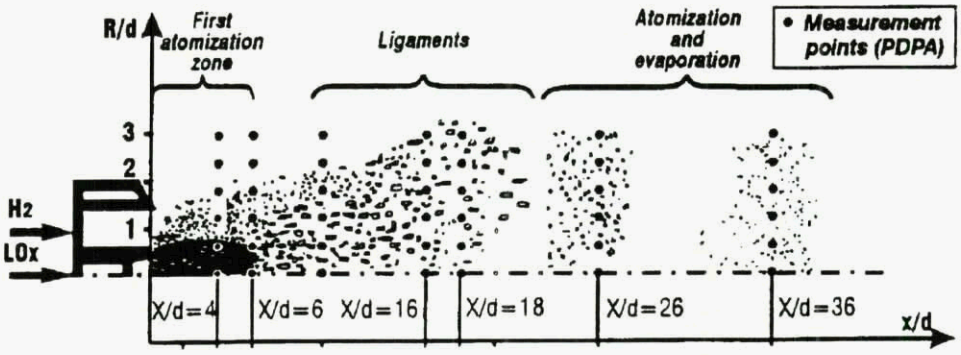


Fig. 10 : Qualitative description of the mean structures of the spray

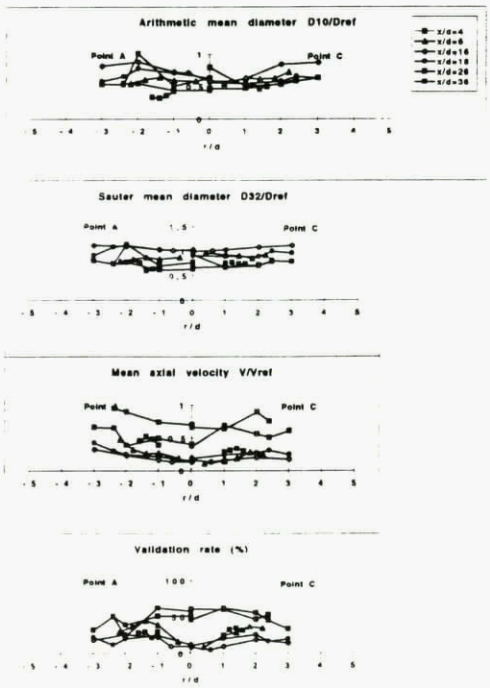


Fig. 11 : Radial variations of spray characteristics

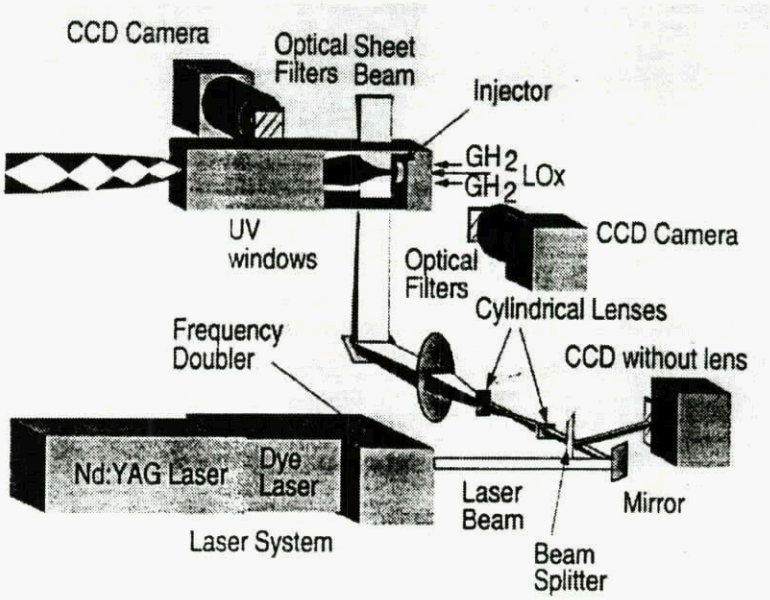


Fig. 12 : General layout of laser and detection optics for emission, ELS and LIF imaging

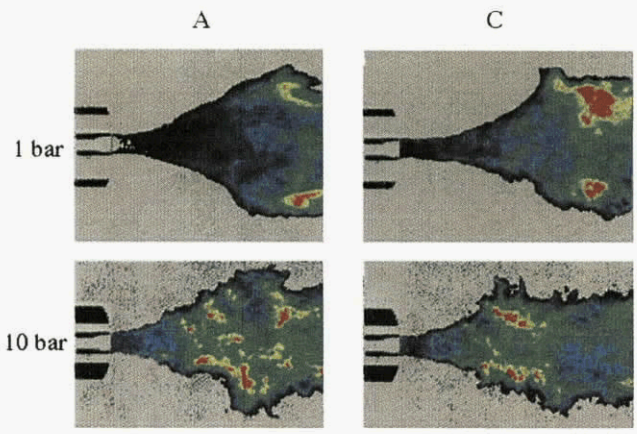


Fig. 13 : Typical emission images of OH in the UV range

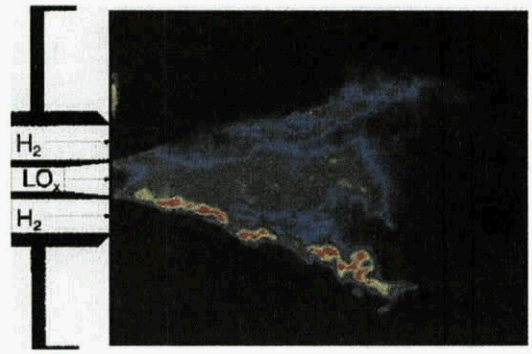


Fig. 14 : Typical OH-LIF image
The laser sheet is transmitted into the combustor from below

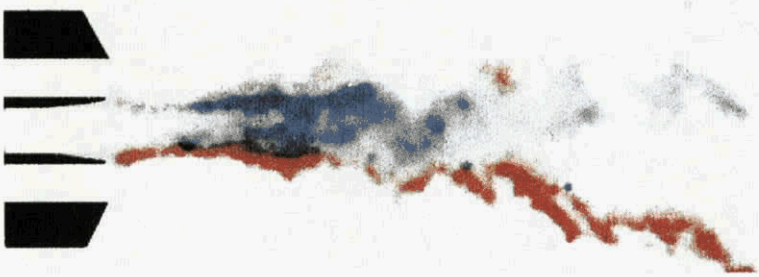

Fig. 15 : Simultaneous detection of OH-LIF (red) and ELS (blue)

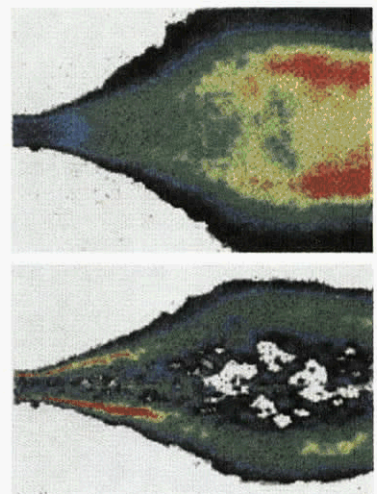

Fig. 16 : Average and Abel transformed OH emission image

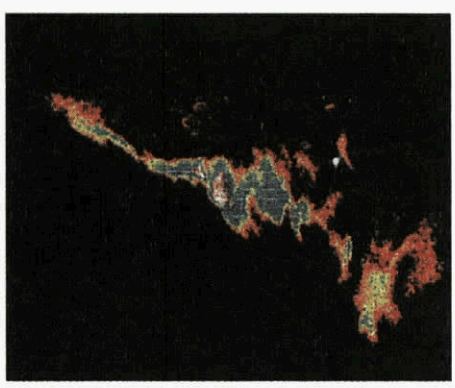

Fig. 17 : Typical $O_2$-LIF image.
The laser sheet is transmitted into the combustor from below

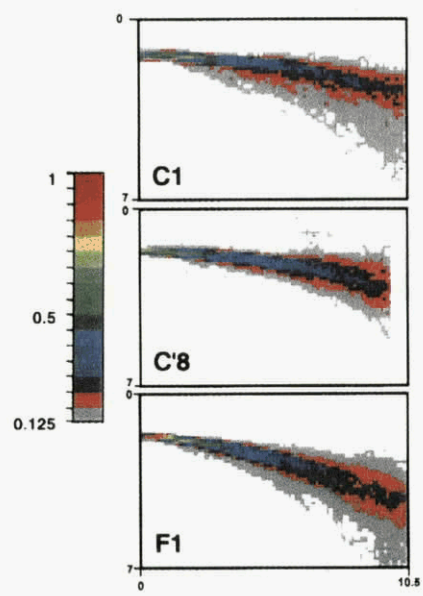


Fig. 18 : Probability distribution of flame location
for conditions C, C'-8 and F1

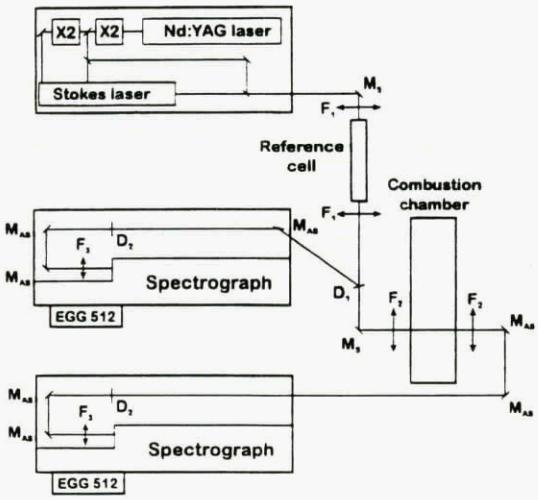


Fig. 19 : Sketch of CARS optical arrangement.
MS and MAS are high reflectance mirrors for 530-700 nm and 400-530 nm. D1 and D2 are dichroic filters. F1, F2 and F3 are 500, 140 and 250 mm focal length achromats.

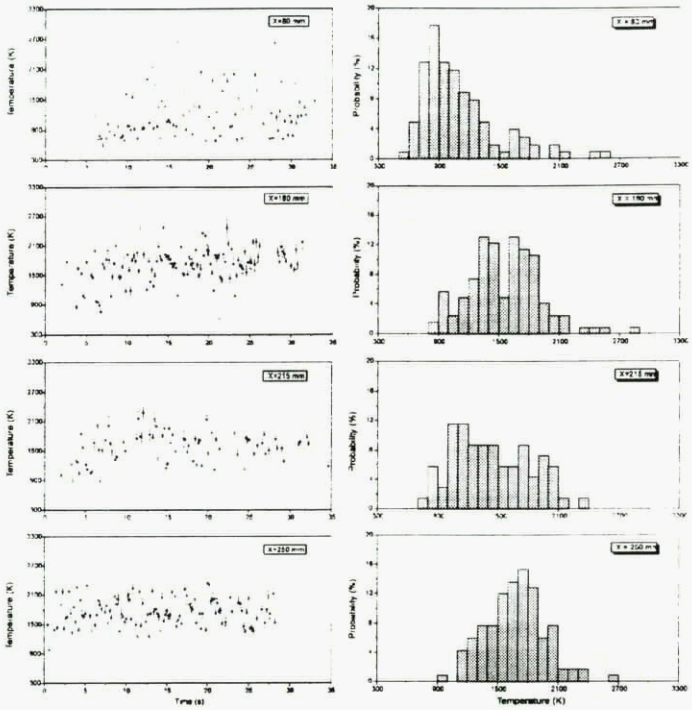

Fig. 20 : CARS temperature measurements :
time evolution and histograms for single-shot spectra.
Operating point C at 1 bar. Radial position r = 20 mm.

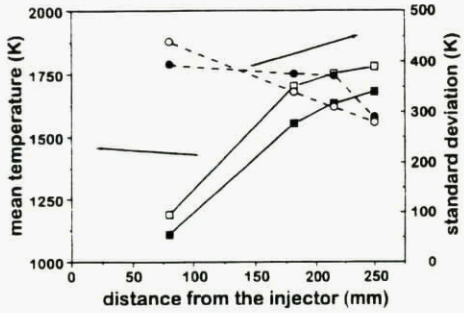


Fig. 21 : Mean temperature (squares) and standard deviation (circles) for points A (black) and C (open symbols), 1 bar. Radial position r = 20 mm.

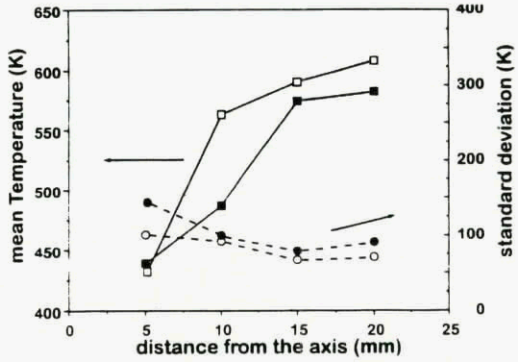


Fig. 22 : Mean temperature (squares) and standard deviation (circles) for points A (black) and C (open symbols), 10 bar. Axial position x = 10 mm.

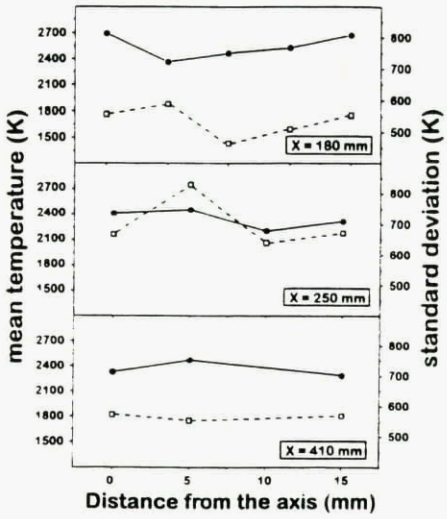


Fig. 23 : Mean temperature (circles) and standard deviation (squares) for point A at 10 bar.

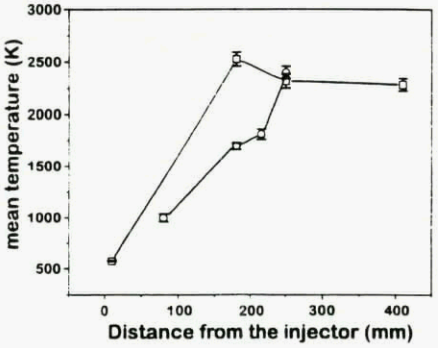


Fig. 24 : Mean temperature profiles for point A at 1 bar (circles) and 10 bar (squares). Radial position 15 mm.

# A Quantitative 2D Density Measuring System Using UV Rayleigh Scattering at an Atmospheric Wind Tunnel

**C. Jakiel, K. Fiedler, O. Sieber**
Universität der Bundeswehr
Hamburg, FB Maschinenbau
Laboratorium für Strömungsmaschinen, Holstenhofweg 85
D-22043 Hamburg
Germany

## Summary

An optical density measuring system based on Rayleigh scattering was installed in an atmospheric wind tunnel. The system monitors the scattered light induced by a laser sheet irradiating the flow field behind a plane VKI-1 turbine cascade. The measuring procedure needing very short time is based on a relative measurement. This paper presents a brief summary of fundamentals, the experimental setup, and the measurement principles. As experimental result plane density distributions at different blade heights are given for subsonic and transonic flow. The experimental data is compared to results of a three-dimensional Navier-Stokes calculation.

## 1 Introduction

The application of cascade flow simulation represents an important instrument for the design of efficient turbomachinery components. While developing a simulation program qualitative and quantitative measurements are used for validating. Because of increasing need of flow simulation under real conditions, i.e., three-dimensional, compressible, viscid, turbulent and possibly by shock waves affected, the expectations with respect to the capabilities of the programs are increasing, and thus likewise on the measurements. Beside the aim of validating, exact measurements with high information content are desired for basic investigation on flow characteristics in order to better understand gas flow in general. Therefore, special information is needed, e.g., on boundary layer design, on the mixing process between jet and wake or on the structure of shock and expansion waves. At this point conventional measuring systems often have limits, especially a too low resolution in many cases. Additionally, when using pneumatic probes the disturbance of the flow causes inaccuracies, especially close to surfaces and in supersonic flows. Because of these reasons, presently more and more non-intrusive optical measuring systems are applied.

Rayleigh scattering is an optical method for receiving density information from a transparent gas media. It is well proven and often applied for fluid mechanics investigations, e.g., studying the mixing processes in gas jets[1,2] or obtaining information on shock wave and boundary layer structures[3,4].

For expanding the application of Rayleigh scattering technique a measurement system was installed at the atmospheric wind tunnel of the Laboratory for Turbomachinery in order to measure density fields behind a plane turbine cascade. The system monitors the scattered light induced by a laser sheet irradiating the test section. Because of scattering at air molecules, supplementary tracer particles are not required, which offers an additional advantage compared to several other optical measuring techniques. The employed measurement procedure, based on relative measurement, allows to receive the density distribution quantitatively.

## 2 Rayleigh Scattering

The phenomenon of Rayleigh scattering belongs to the group of elastic scattering processes. This means that Rayleigh scattering is a process without a permanent exchange of energy between light and matter, but with change of light direction. So the frequency of scattered light is equal to the frequency of incident light.

The intensity of Rayleigh scattered light can be described by a fundamental correlation, if the following simplifications are assumed:

- The gas atoms and gas molecules are considered as dielectric spheres with a diameter, that is smaller than the wavelength of the incident light. Therefore, the electric field can be regarded as constant over the sphere.
- The test section is irradiated in one direction with monochromatic and linearly polarized light. The scattered light is linearly polarized as well.
- The particles are randomly spread in the measuring volume.
- Multiple scattering is neglected, i.e., light that has been scattered at one particle will not be scattered at another particle.
- The distance to the observer is large compared with the dimensions of the observed scattering volume.

*Paper presented at an AGARD PEP Symposium on "Advanced Non-Intrusive Instrumentation for Propulsion Engines", held in Brussels, Belgium, 20-24 October 1997, and published in CP-598.*

With these assumptions the Rayleigh scattering intensity of all air molecules in the measuring volume is obtained by

$$I = \sigma \frac{\overline{N}}{r^2} I_0 . \qquad (1)$$

Thus, the intensity of the detected light $I$ depends on the Rayleigh scattering cross section $\sigma$, the number of particles $\overline{N}$, the distance to the measuring volume $r$, and on the intensity of the incident laser light $I_0$.[5] The Rayleigh scattering cross section is the theoretical effective plane for the incident photons, which is unequal to the geometrical cross section. The effective cross section is highly dependent on the characteristics of the particles and on the frequency of the incident radiation. As the Rayleigh cross section increases with the fourth power of frequency, the use of light sources with high frequency is recommendable to get large scattering intensities.

Although $\sigma$ of air depends on pressure, temperature and composition of air[6] the effective cross section can be assumed as constant for the conditions being found in the wind tunnel utilized for these experiments.[5] It is obvious that the constant composition of air in the test section is a basic requirement.

## 3 Experimental Setup

All experiments were performed in an atmospheric wind tunnel for plane cascades (Fig. 1). The wind tunnel is supplied with ambient air, which passes through a dust filter prior to being compressed by a centrifugal compressor. If pressure ratios higher than 2.0 or mass flows greater than 18 kg/s are required, a second compressor is used additionally. The total temperature of the compressed air is kept constant by water cooling. This air supply design allows a steady-state testing of subsonic and supersonic flow in the wind tunnel without time limits. After entering the moderation chamber, where the total temperature, the total pressure, and the humidity are measured, the air is led to the test section. Within the test section the blades are mounted with fixed geometrical parameters in a changing frame forming the endwalls of the flow channel and containing measuring apertures. For the measurements described herein the dimensions of the inlet flow channel were 300 mm x 100 mm, allowing the installation of a cascade of 12 blades.

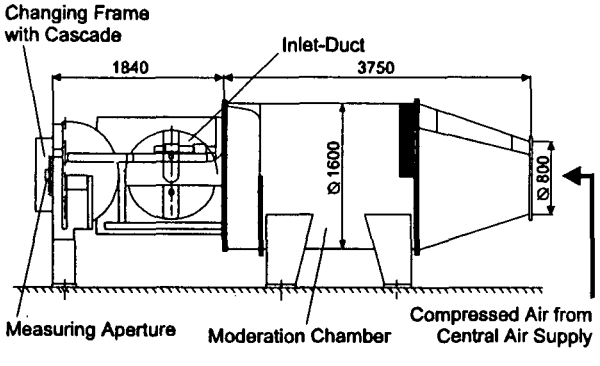


**Fig. 1: Wind tunnel for plane cascades.**

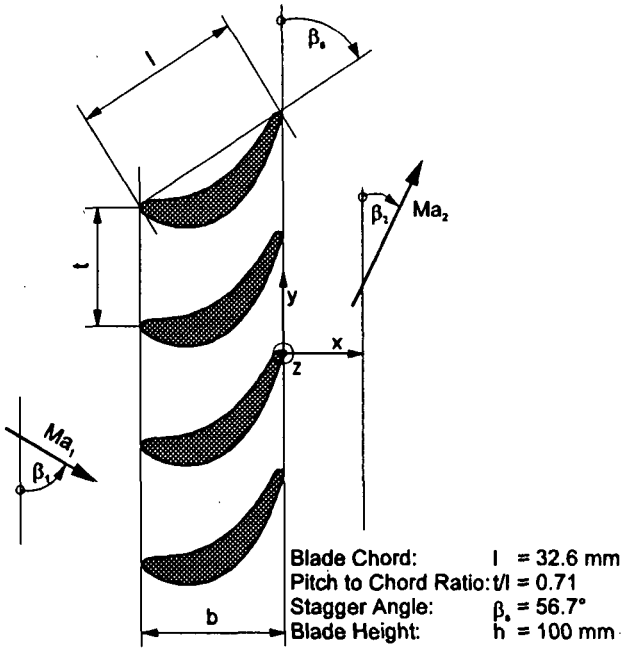


**Fig. 2: VKI-1 cascade geometry.**

The cascade used is of the type VKI-1 (see Fig. 2), which is typical for a cooled gas turbine rotor blade section designed for transonic flow. It was proposed for comparisons of experimental and computational results by the Von Karman Institute (VKI) in 1973.[7] Since then it has been investigated intensively by experiments as well as in flow calculations.

An excimer laser (Lambda-Physik LPX 110i), modified with a polarizer, is employed as light source. The ArF laser works in the deep UV at 193 nm. This high frequency yields Rayleigh signals stronger by one to two orders of magnitude compared to lasers working in the visible range.

The emitted Rayleigh light is imaged by a 12-bit intensified charge-coupled device (ICCD) camera (LaVision) via an UV-light-sensitive lens (UV-Nikkor 105 mm, f/4.5). The cooled CCD chip has a spatial resolution of 384 x 286 pixels. A 486 personal computer with special purpose software (LaVision) controls the complete system, i.e., it synchronizes laser and imaging system, and it records and stores the images. A pre-evaluation of the acquired CCD images is also possible with this software.

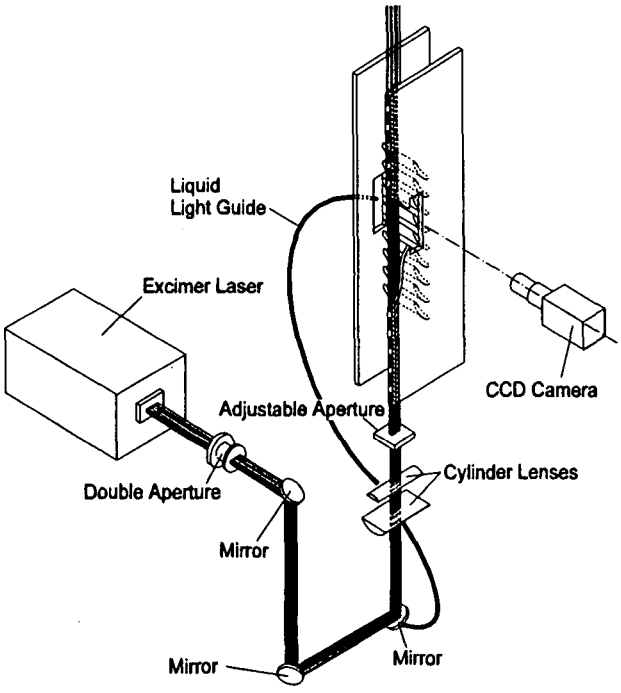


**Fig. 3: Optical Setup.**

The arrangement used for beam positioning is shown in Fig. 3. The laser beam is blanked out by a double aperture directly after emerging. With the help of three mirrors the beam is positioned to the direction parallel to the endwalls and parallel to the trailing edge plane. Two cylinder lenses focus the laser beam to reduce the thickness under 0.5 mm at a width of about 20 mm. With these dimensions the area of measurement can be considered as a plane. At least one adjustable aperture is used to suppress direct irradiation of the trailing edges and to fix the sheet cross section as a rectangle. All optical components are mounted on a base frame via translation stages. This arrangement allows varying the laser beam position in $z$-direction within a range of 45% of blade height without rebuilding and re-aligning. The distance to the trailing edge plane was chosen as small as possible and fixed for this study.

The position of the laser beam relative to the blades and the extension of the evaluation range, both in the $x$-$y$-plane, are determined with optical aids. The uncertainty of position and extension is smaller than 1.5% according to the pitch. The position in $z$-direction is fixed by the translation stages with a maximum deviation of 0.5 % according to the blade height.

To make precise monitoring of the beam energy possible, some laser light is cut off at the third mirror and, after transformation to longer wavelength, led through a liquid light guide. The transformation is necessary, because the lightwave guide is transparent for wavelengths longer than $\lambda$ = 260 nm. The second exit of the light pipe is fixed opposite to the measuring window, so that the camera can image the transmitted energy signal while taking the images (see Fig. 4). It was proved by experiments that the recorded energy signals show a linear dependence on the laser output energy within the range of possible beam energy fluctuations of maximum +/- 5% from pulse to pulse.[5]

Figure 4 schematically shows the camera view. The opening in the endwall allows optical access to the measuring volume and the nearby trailing edges of the blades. The laser beam can be seen radiating through the measuring volume parallel to the trailing edges. As mentioned before, the energy monitor output is also part of the image. Since no open apertures are allowed in order to properly guide the flow, the Rayleigh scattered light reaches the camera through a silica glass window with an optimized transmission rate at 193 nm. The material for the background insert was selected to minimize direct reflections of scattered light to the camera. We found this silica glass very suitable, because influence of the surface on the recorded intensities was smallest when using this window. To reduce the influence of light scattered outside the test section, the laser beam was covered as far as possible.

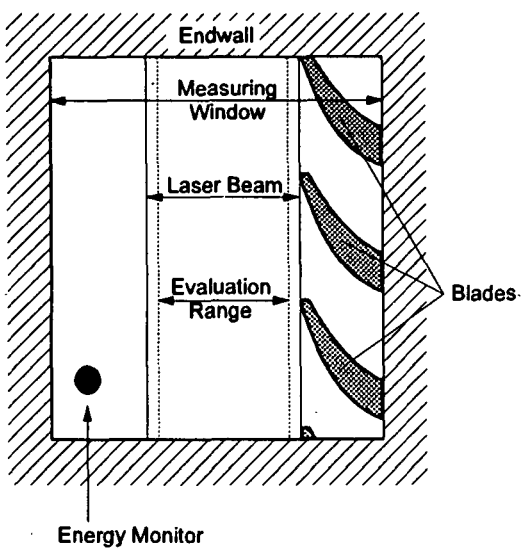


**Fig. 4: Camera view.**

## 4 Measurement Principles

When imaging Rayleigh scattering signals, the recorded value for each pixel $(x, y)$ can be described by

$$S(x,y) = c(x,y) \cdot I_0(x,y) \cdot \sigma \cdot \overline{N}(x,y), \quad (2)$$

with the constant value $c$, which contains all spatially dependent but constant parameters such as distance to the measuring plane and characteristics of the optical equipment. Equation (2) does not contain the share of possible stray light, because it can be assumed as small compared to the Rayleigh signal. This assumption is legitimate, because scattered light reflected at the background plane and from outside the test section could be minimized (see preceding section), and no significant stray light from other surfaces, e.g., the blades, could be detected. With the composition of air staying constant and the number of molecules

$\overline{N}(x,y)$ being proportional to the density $\rho(x, y)$, Eq. (2) can be rewritten as

$$S(x,y) = K(x,y)\cdot\rho(x,y). \quad (3)$$

The evaluation of the Rayleigh scattering signals is based on a relative measurement, because with this kind of evaluation potential sources of error, such as incident light inhomogenities and spatially dependent sensitivity of the imaging optics, can be eliminated. Therefore, first a wind-on image is taken, i.e., during wind tunnel operation. The recorded signals contain the information on density variation given by

$$S_1(x,y) = K(x,y)\cdot\rho_1(x,y). \quad (4)$$

Additionally, a wind-off image is taken under standard conditions, i.e., across the whole field of view the density has to be on the same level and exactly known:

$$S_0(x,y) = K(x,y)\cdot\rho_0. \quad (5)$$

It should be noted that the air filling the test section during wind-off imaging has passed the same way as the air at wind-on imaging, and thus the composition of air is the same in both parts of the measurement. The pixelwise division of the two signals yields a ratio for each pixel, which is proportional to the local density in the flow field:

$$F_1(x,y) = \frac{S_1(x,y)}{S_0(x,y)} = \frac{\rho_1(x,y)}{\rho_0}. \quad (6)$$

After this, the density field is determined qualitatively, and the potential sources of errors, such as the aforementioned beam aberrations or optical setup characteristics, are eliminated, if they are stationary and on the same level in both pictures.

This easy measurement procedure (6) presupposes identical laser light energy $I_0$ while taking the wind-on and the wind-off image. If this can not be achieved, the energy level has to be known exactly in order to be able calibrating the density ratio $F_1(x, y)$. Because the beam energy fluctuates from pulse to pulse and decreases during the operation due to limited lifetime of the laser gases, an energy monitor is used as described earlier. Since the energy monitor output is part of the recorded image (see Fig. 4), an average value of the energy monitor signal is calculated from both the wind-on image ($\varnothing EM_1$) and the wind-off image ($\varnothing EM_0$). Now a calibration of the density ratio $F_1(x, y)$ is possible:

$$F_{1,c}(x,y) = F_1(x,y)\frac{\varnothing EM_0}{\varnothing EM_1}. \quad (7)$$

Without taking the laser energy into consideration, the average values of the density ratio deviate up to 6% from their mean value although they were measured at the same flow conditions. But with energy monitor calibration the deviation can be reduced to less than 1%. It should be noted, that this calibration has no influence on the qualitative result, because the whole density field is converted with a constant ratio. Usually the ratio $\varnothing EM_0/\varnothing EM_1$ varies from 0.94 to 1.02.

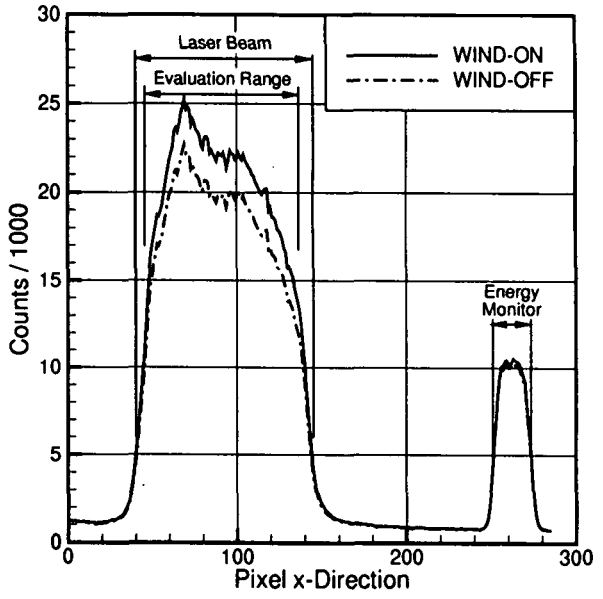


**Fig. 5: Intensity distribution in *x*-direction**

Figure 5 shows a typical intensity profile of the measuring volume and of the energy monitor. The differences in density between the wind-on and the wind-off image can bee seen as distances between the two profiles within the range of the laser beam. Likewise, these two profiles with similar behavior elucidate the necessity of a relative measurement, since the intensity differences caused by the density variation are smaller than the differences caused by the beam inhomogenities. The intensities in the area of the energy monitor are about two times inferior to the Rayleigh scattering intensities in this case, but they are one order of magnitude higher than the signals from the areas not being evaluated. Thus, a clear distinction of the areas is possible. It can be seen clearly that the evaluation range has to be smaller than the width of the laser beam, because the laser intensities decline rapidly at the lateral borders of the beam, and so the signal-to-noise ratio is too low in these areas.

Simultaneously to recording the wind-off image, the pressure and the temperature in the testing room are measured for calculating the density $\rho_0$, which is constant across the whole field of view. With this the density field at wind tunnel operation is determined qualitatively and quantitatively:

$$\rho_1(x,y) = F_{1,c}(x,y)\cdot\rho_0. \quad (8)$$

In these experiments, altogether 2500 laser shots were summed up for both wind-on and wind-off images. This number basically is yielded from 50 shots summed up on chip. The intensities of 10 of these bursts were read out, added by software, and stored on hard disk. This process needing about 20 seconds was completed five times without breaks. The result of averaging these five data sets yields the information of the density field.

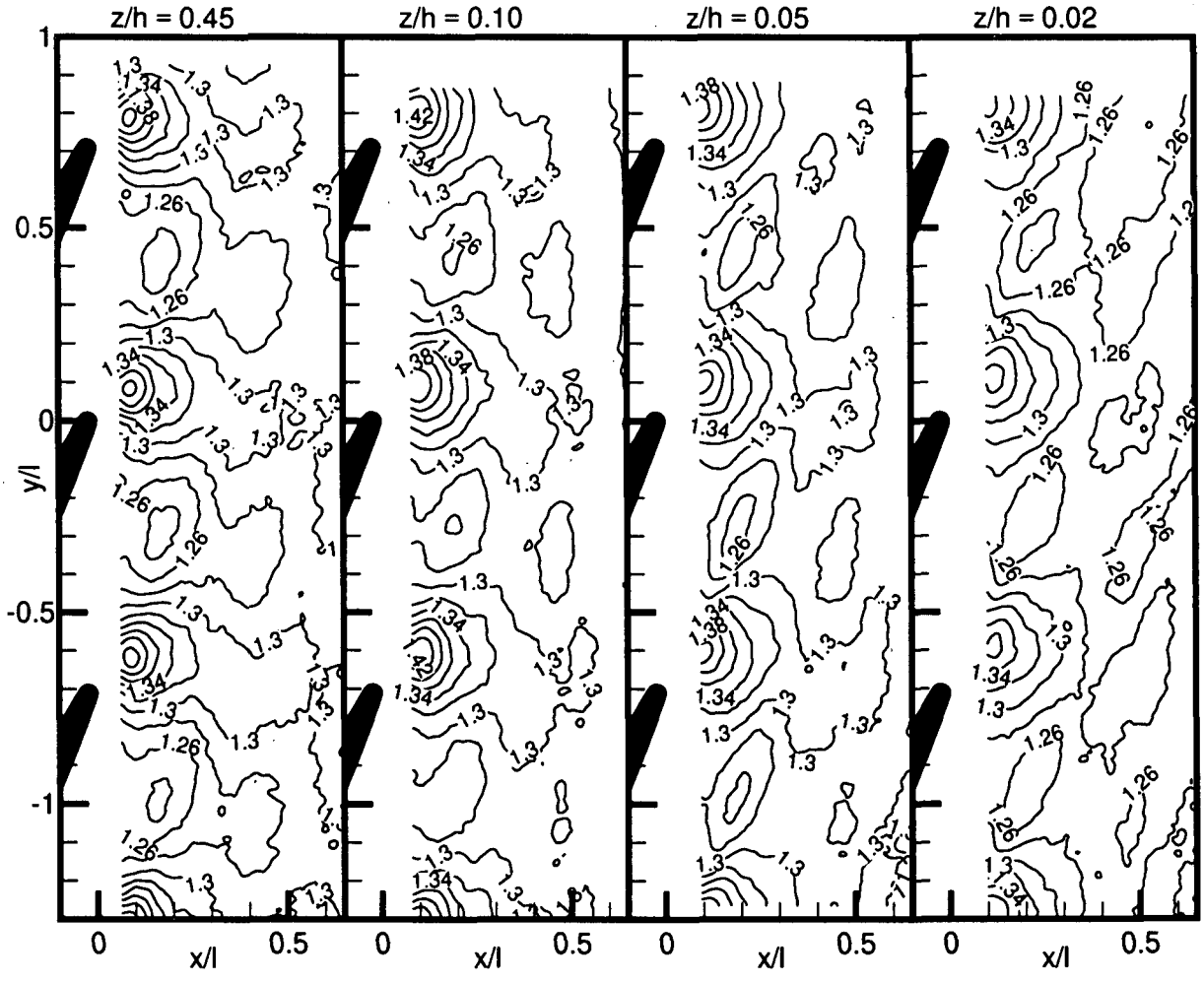


**Fig. 6: Measured density fields [kg/m³] at $Ma_{2is}$ = 0.90.**

A statistical evaluation of the five single sets increases the opportunity of detecting errors such as unusual laser energy fluctuations or Mie particles. With this measurement procedure it is also proved that photon shot noise is not the limiting factor for density accuracy.

## 5 System Capabilities and Limits

Since its installation the measuring system was intensively tested to determine reproducibility, sensitivity and conditions limiting the field of application.[5,8] These measurements showed that density differences lower 1% according to the ambient density can be distinguished, i.e., even at low Mach numbers as $Ma_{2is}$ = 0.75 usable results can be achieved with a very good reproducibility. The uncertainty in reproducibility amounts to a maximum of +/- 1.5%, which includes all system uncertainties, as for example energy monitoring or determining $\rho_0$.

As mentioned before the measurement procedure presupposes stray light being small compared to the Rayleigh signal. When measurements are accomplished near to surfaces the intensities of laser light reflected directly or scattered light reflected may increase and make the neglect of stray light no more tenable. This problem is intensified, when movement of the optical background occurs between wind-on and wind-off conditions due to the flow force. In this case even smaller stray light intensities than without movement can falsify the results. So a well-considered arrangement and choice of surface materials and the minimization of cascade movement are important requirements for high quality results. Referring to these conditions the wind tunnel construction was reinforced, and the studies in the 3D flow field were accomplished between front endwall and midspan.

When ambient air is used for Rayleigh scattering investigations, the possibility of another elastic scattering process has to be taken into consideration. This process, called Mie scattering, is caused by particles, like dust or aerosols, which are much larger than gas molecules, so that the assumptions of Rayleigh scattering are not fulfilled. Additionally in atmospheric wind tunnels Mie scattering can be effected by water or ice particles, which are produced by condensation at high expansion ratios, e.g., as needed for transonic flow. The Mie particles yield higher scattering signals, due to the very much enlarged scattering cross section, which falsifies the results or in the worst case prevents

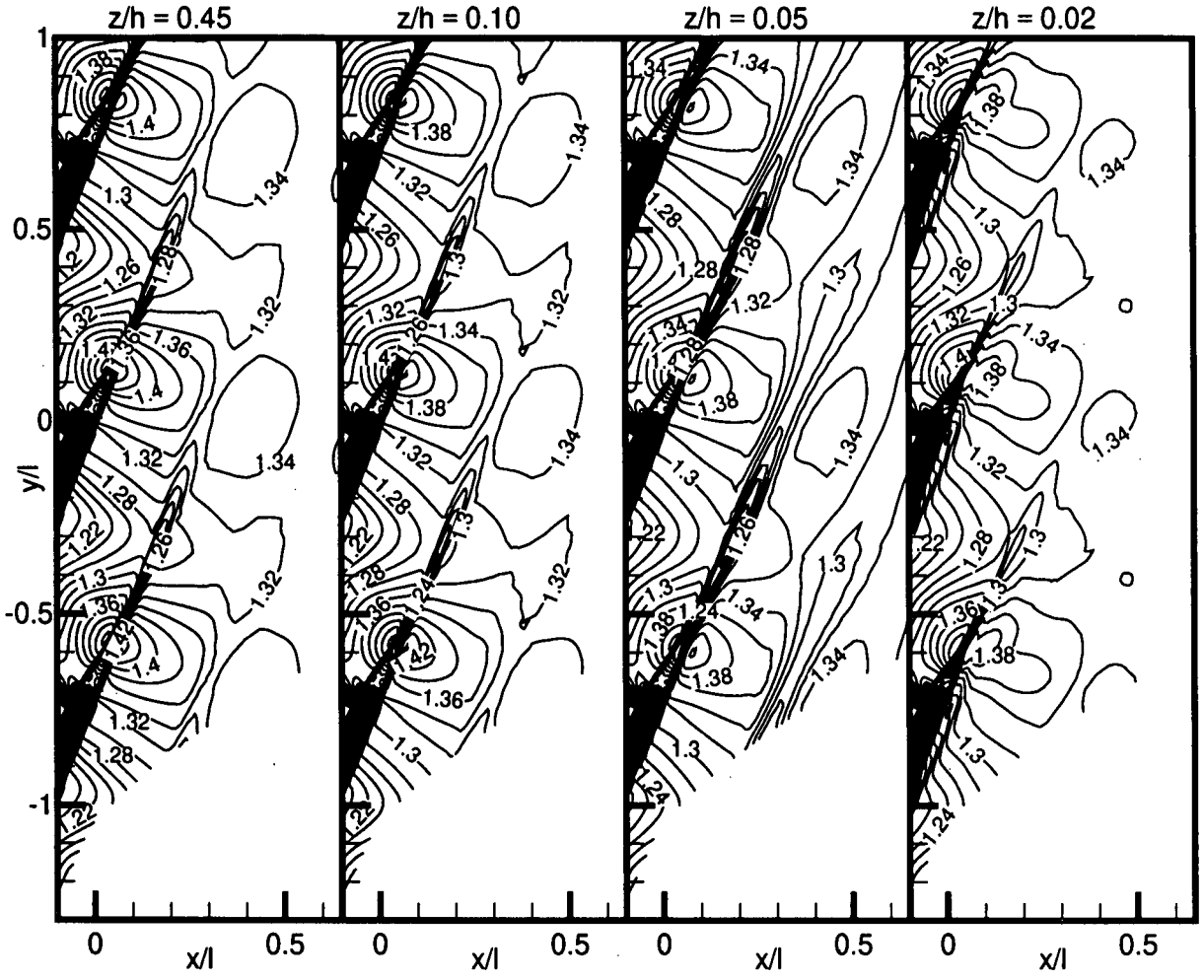


**Fig. 7: Calculated density fields [kg/m³] at $Ma_{2is}$ = 0.90.**

evaluation due to local saturation on the CCD chip. Because of this, the outlet Mach number in all experiments was chosen sufficiently low so that condensation did not occur, depending on the humidity of the ambient air and on the inlet temperature level. In general the highest achievable Mach number is $Ma_{2is}$ = 0.75 in summer and $Ma_{2is}$ = 1.05 on cold dry winter days, but which are very rare. Even though the air is led through a dust filter, very few small particles may reach the measuring area. But it is ensured that there are fewer particles effecting Mie scattering than the limit Schweiger[9] established for neglecting Mie scattering in Rayleigh experiments.

## 6 Results

Figure 6 shows the results obtained from a Rayleigh scattering experiment at the isentropic outlet Mach number $Ma_{2is}$ = 0.90. Four positions in $z$-direction were chosen from the range between front endwall and midspan.

In all cases the density fields of the three measured flow channels correspond very well. The non-periodicities between the flow channels are insignificant, they are caused by small manufacturing inaccuracies of the cascade.

In midspan the range between trailing edges and $x/l$ = 0.3 contains a distinctive density distribution. This is mainly caused on the one hand by a pressure maximum, positioned downstream directly behind the trailing edge, and on the other hand by temperature gradients due to jet and wake. Behind $x/l$ = 0.3 the flow gets well-balanced, just small density variations are visible. Approaching the endwall only small changes can be made out until $z/h$ = 0.05. But in this position it is already recognizable, that the static temperature begins having more influence on the density distribution. With further approaching this develops more clearly. At $z/h$ = 0.02 the density generally becomes lower, since the higher losses near to the endwall cause higher temperatures.

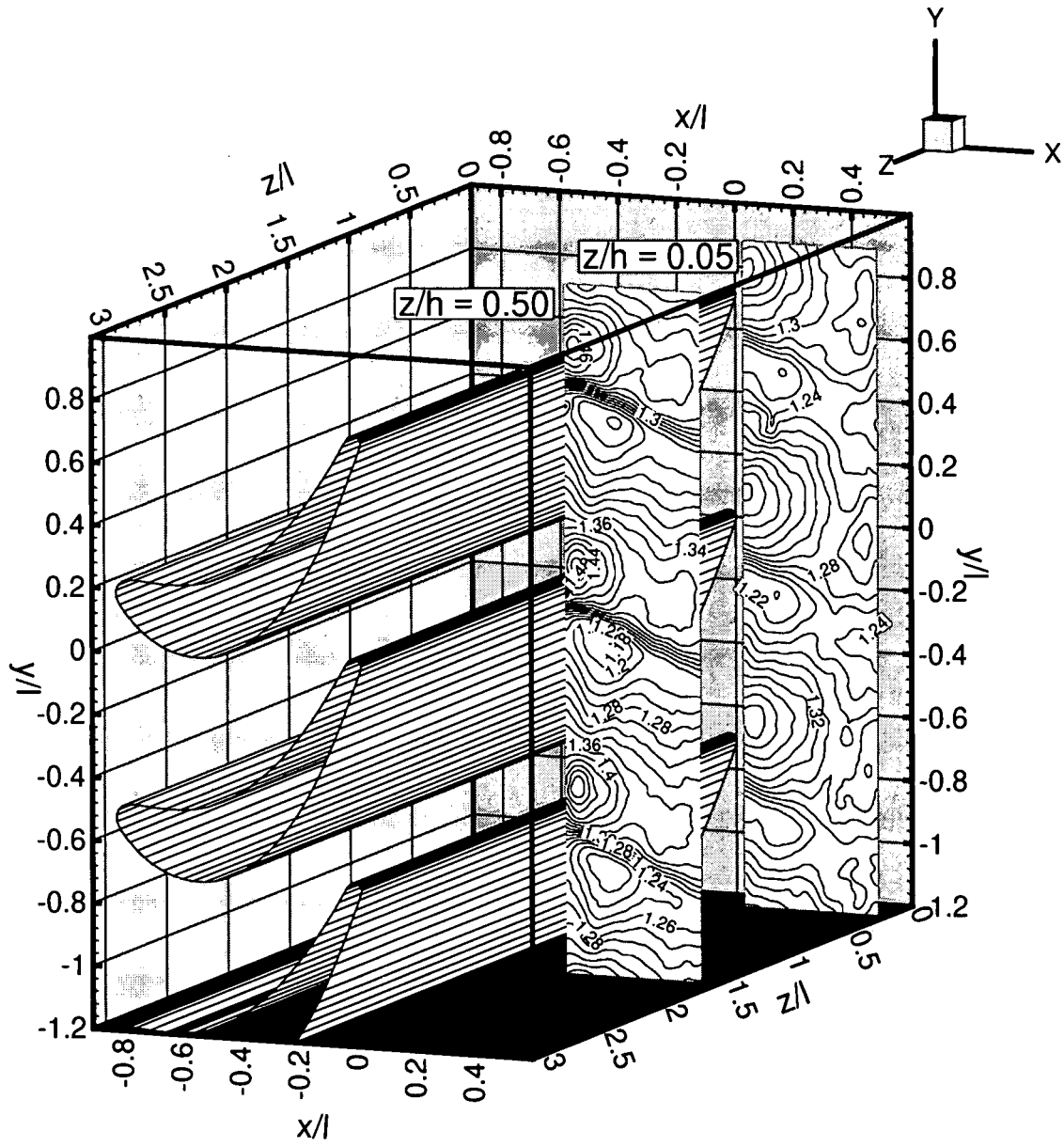


**Fig. 8: Measured density fields [kg/m³] at $Ma_{2is}$ = 1.00.**

Figure 7 displays the corresponding results of a 3D calculation. The employed simulation program uses Navier-Stokes equations, complemented by the Baldwin-Lomax turbulence model.[10] The numerical results show the wakes much more distinctive and spatial restricted, but this cannot be proved true by the experiments. Outside the wakes a qualitatively good agreement with the measurement can be seen. Approaching the endwall very few changes are recognizable. The more marked and longer visible wakes at $z/h$ = 0.05 are one remarkable change. They are caused by boundary layer material rolled up to a discrete vortex, which expands the plane wake at this $z$-position. A computed increase of losses due to endwall boundary layer is not visible even at $z/h$ = 0.02, it begins nearer to the endwall than measured. These differences in qualitative information may have the following reasons. First there might be an inadequate modeling of the mixing of wake and isentropic flow in the program. This was discussed intensively in former experimental and numerical investigation of the plane flow in midspan.[5] This can also be noticed here for the mixing of lossless material and high-loss material from secondary flows. Furthermore, differences in obtaining the density distributions are possible, because the real complicate thermal conduction through blades and endwalls could not be considered by the calculation, and few other parameters could not fit exactly. These reasons should also explain the generally slightly higher density values of the simulation.

To demonstrate additionally the usefulness of the Rayleigh scattering system for obtaining flow characteristics Fig. 8 partly shows the measured density distribution at $Ma_{2is}$ = 1.00. The shock wave can be seen very clearly in midspan, the structure develops as

it is expected for transonic turbine cascades.[11] The shock wave crosses the wake and hardly widens up to the end of the evaluation area at $x/l$ = 0.6. Near the endwall the shock wave dissolves and the density field differs qualitatively and quantitatively from midspan plane because of secondary flow effects.

## 7 Conclusions

The optical measuring system used in this study allows the quantitative measurement of high resolution density fields behind cascades. The measurements can be accomplished in a very short time and with a very good reproducibility. The measurement system is suitable for investigating transonic and supersonic flow characteristics, because neither probes disturb the flow field nor tracer particles are needed for the Rayleigh scattering process. But the sensitivity also allows measurements in subsonic flow. The results show that the combination of density fields from different blade heights affords an insight into the three-dimensional flow field behind the plane turbine cascade. Next aim concerning this system is the realization of measurements within the passage. Further adjusting and optimization, in preparation and under testing at present, will make the system available for these measurements.

## 8 References


[1] Escoda, M. C., Long, M. B., "Rayleigh Scattering Measurements of the Gas Concentration Field in Turbulent Jets," *AIAA Journal*, Vol. 21, No. 1, 1983, pp. 81-84.

[2] Shirinzadeh, B., Hillard, M. E., Jeffrey Balla, R., Waitz, I. A., Anders, J. B. Exton, R. J., "Planar Rayleigh scattering results in helium-air mixing experiments in a Mach-6 wind tunnel," *Applied Optics*, Vol. 31, No. 30, 1992, pp. 6529-6534.

[3] Smith, M., Smits, A., Miles, R., "Compressible Boundary-Layer Density Cross Sections by UV Rayleigh Scattering," *Optics Letters*, Vol. 14, No. 17, 1989, pp. 916-918.

[4] Miles, R., Lempert, W., "Two-Dimensional Measurement of Density, Velocity and Temperature in Turbulent High-Speed Air Flows by UV Rayleigh Scattering," *Applied Physics B*, Vol. 51, 1990, pp. 1-7.

[5] Sieber, O., "Quantitative Dichtefeldmessung mit Rayleigh-Streulicht am Laufschaufelprofil VKI-1 und Vergleich mit einer numerischen Simulation," Vol. 301, *Fortschrittsberichte VDI Reihe 7*, VDI-Verlag, Düsseldorf, Germany, 1996.

[6] Allen, C.W., "Astrophysical Quantities," The Athlone Press, London, 1973.

[7] Sieverding, C. H., "The Turbine Blade Definition," *VKI Lecture Series 59*, Transonic Flows in Turbomachinery, May 1973.

[8] Miebach, F., "Beitrag zur dreidimensionalen Dichtemessung am ebenen Gitterwindkanal mit Rayleigh-Streulicht," Report, Laboratorium für Strömungsmaschinen, Universität der Bundeswehr Hamburg, Germany, 1996.

[9] Schweiger, G., "Lokale Dichtemessung in verdünnten Gasen mit Hilfe der Laserlichtstreuung," Deutsche Forschungs- und Versuchsanstalt für Luft- und Raumfahrt, Forschungsbericht 73-83, Porz-Wahn, Germany, 1973.

[10] Schöll, E., "Ein dreidimensionales Rechenverfahren für reibungsbehaftete Strömungen in Schaufelreihen von Turbomaschinen," Vol. 287, *Fortschrittsberichte VDI Reihe 7*, VDI-Verlag, Düsseldorf, Germany, 1996.

[11] Sieverding, C. H., "Experimental Data on Two Transonic Turbine Blade Sections and Comparison with Various Theoretical Methods," *VKI Lecture Series 59*, Transonic Flows in Turbomachinery, May 1973.

Paper 45
Author: Jackiel

Q: Ainsworth

In order to take the technique forward to inter-passage measurements, what particular challenges are faced?

A: The main challenges for inter-passage measurements are :

- The cascade movement has to be reduced even more than for measurements behind cascades.
- A suitable set-up has to be developed and tested with respect to the stray light problem. It has also to be found which dimensions of the laser beam are usable, and which illuminated areas are suitable for evaluation.

Q: Sieverding

Your measurements show time averaged density distribution. Do you see possibilities to extend this technique for taking instantaneous recordings of the density distribution?

A: For instantaneous recordings of density distribution a one-laser-shot-measurement is required. We tested a measurement with one laser shot, but the influence of noise was the same order as the local density gradients, so only some distinctive density structures like the position of the wake could be found qualitatively. Here a large increase of incident laser energy in the measurement area might be a possibility for improving the results.

# Particle Image Velocimetry Measurements from the Stator-Rotor Interaction Region of a High Pressure Transonic Turbine Stage at the DERA Isentropic Light Piston Facility

by

**K S Chana and N Healey**
DERA Propulsion Department
170 Building, Pyestock
Farnborough, Hants, GU14 0LS, UK

**P J Bryanston-Cross**
Optical Engineering Laboratory
Department of Engineering
Warwick University
Coventry CV4 7AL, UK

## 1. Summary

In high pressure turbines the flow in the stator-rotor interaction region is highly complex with periodic and random unsteady effects generated as the stator wakes impinge on the rotor blades. Measuring the flow in this region is difficult with conventional instrumentation, further complicated in a short duration facility. This paper discusses the application of particle image velocimetry to this region of flow and, outlines the technological advances made recently to demonstrate the technique in the short duration Isentropic Light Piston Facility (ILPF) at DERA Pyestock.

A series of measurements have been made in the stator passage and the stator-rotor gap region of the MT1 high pressure turbine stage, in the ILPF. The measurements have been made at full engine-representative flow conditions and provide an instantaneous quantitative whole field visualisation of this unsteady flow region. The measured velocity field is compared with computational fluid dynamics (CFD) predictions obtained using a three-dimensional viscous flow slover.

Theses measurements are thought to be the first to be made in a rotating transonic facility.

## 2. Introduction

The stator-rotor gap regions of turbomachinery blade rows are dominated by complex three-dimensional viscous flows, generated by the successive interactions of stationary and rotating blade rows. A large proportion of the loss within the turbomachine is generated in this region; however, these regions are not well modelled by current design and analysis methods.

Experimental investigation of the flow within the stator-rotor region of turbomachines is complicated, because conventional probes capable of measuring unsteady flows are physically large and hence disturb the flow path. PIV (particle image velocimetry), however, offers an alternative non-intrusive whole field measuring technique to resolve the flow magnitude and direction in a particular plane.

This paper presents velocity data gathered at mid-span in the stator-rotor region of the MT1 turbine stage for a number of rotor blade positions; additionally some data have been obtained in the stator passage.

## 3. Test facility and the MT1 turbine stage

The PIV measurements reported in this paper were acquired in the DERA Isentropic Light Piston Facility (ILPF). The ILPF is a short duration wind tunnel for testing full aeroengine size high-pressure turbine stages. A schematic of the facility is shown in Figure 1. The operating principles of this type of facility were first described by Jones et al (1973). The main components of the ILPF are: i) the pump tube containing a light-weight free piston, ii) a fast acting valve, iii) the turbine stage and iv) the turbobrake. Prior to a run the piston is positioned at the upstream end of the pump tube and the fast acting valve is closed. The pump tube is then filled to a predetermined pressure, whilst the working section is evacuated, and the turbine assembly is spun up to the desired speed. To start a run, high pressure air is introduced behind the piston causing it to move forward and compress the air in front. This compression is nearly isentropic, thereby heating the test gas. When the desired pressure and temperature are reached, the fast acting valve is allowed to open, and a steady flow of air is passed through the turbine stage. The run time of the facility can be varied from approximately 400ms to 2 seconds depending on the conditions required.

The turbine module is shown in Figure 2. A unique feature of this unit is the aerodynamic turbobrake which absorbs the energy produced by the turbine, so that the rotational speed is maintained nearly constant throughout the run. The turbobrake and the turbine are mounted on a common shaft supported on two sets of oil lubricated bearings. The shaft is hollow in order to house electronic circuit boards to condition signals from instrumented rotor blades.

The pressure ratio across the stage is set by the second throat at exit from the stage. This is an annular variable area device which maintains axisymmetry in the exhaust flow, and since it is choked it also isolates the turbine from disturbances originating downstream. The performance of the turbobrake is controlled using blockage rings which reduce the exit flow. Fine tuning is achieved by adjusting the amount of flow which by-passes the turbobrake.

The ILPF is capable of matching all the non-dimensional parameters relevant to turbine fluid mechanics and heat transfer for modern advanced aircraft engines.

The MT1 turbine is an unshrouded, high-pressure research turbine relevant to future civil aircraft applications. The stage has 32 ngvs and 60 rotor blades.

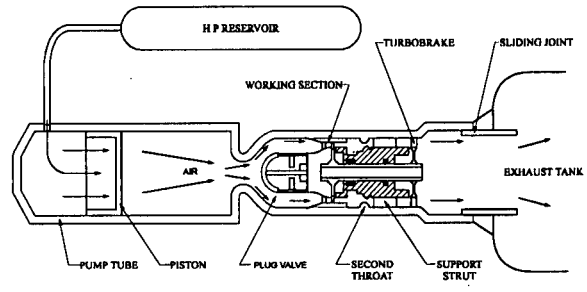


Figure 1. Schematic of Isentropic Light Piston Facility (ILPF)

*Paper presented at an AGARD PEP Symposium on "Advanced Non-Intrusive Instrumentation for Propulsion Engines", held in Brussels, Belgium, 20-24 October 1997, and published in CP-598.*

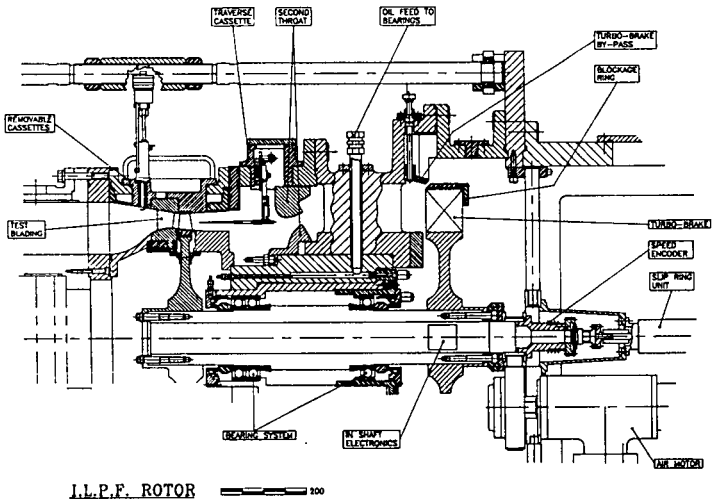


Figure 2. Cross section of the ILPF turbine working section

## 4. Particle image velocimetry measuring technique

The development of optical measurement methods for transonic flow is relatively recent and has been strongly coupled with that of the available laser and computing technology. Conventional development has led to the construction of a number of optical systems velocimeters such as LDV and L2F (laser two focus) which are only capable of making single point measurements in a flow field. Little attention has been paid, mainly because of the data storage and processing overheads, to the photographic and video measurement ability to capture a whole field of data instantaneously.

The PIV measurements show that it is now possible to make instantaneous whole field quantitative measurements of a transient transonic flow within an industrial environment. In order to perform PIV in an engine representative environment a number of technological advances have been made. The PIV system was based upon the use of digital cameras coupled to a fibre optic delivery system. Extensive post-processing software has also been evolved to extract data of a suitable quality for aerodynamic measurement.

## 5. Experimental system

The Experimental system used in this work is a development of that used previously to measure the flow at the trailing edge region of an annular cascade in the ILPF (Funes-Gallanzi, 1994).

The laser light source was a Lumonics HLS series Nd/YAG 200mJ pulse laser. With a beam diameter of about 5 mm. The laser is capable of providing two pulses of 10ns duration and from 40ns to 100ms in separation. It also has the ability, though not explored in these experiments to provide a third pulse.

The laser can be pulsed continuously by its own internal clock at pre-set repetition rates or controlled by an external trigger signal. Normally the internal firing mode was used in the setup stage of the experiment in which the laser was fired at 12.5 Hz in an open lasing condition for the optics alignment. For the external trigger mode, the laser was put in a standby state; when a -15 volts pulse was applied to the external trigger the laser fired. The laser then recharged to prepare for the next pulse. For reasons of precision, timing control of the laser firing and the signal conditioning of the external trigger, a Laser Firing System (LFS) was used as a buffering interface between the external triggering source and the laser itself.

Fibre optic delivery system

For this test series two types of laser light sheet delivery systems were demonstrated. The first was a fibre optic delivery system developed at Heriot-Watt University. A fibre optic delivery system has several advantages over a conventional "rigid optical system"; i) it allows for an independent construction and test of the whole optical system prior to the experiment and ii) it has the ability to deliver laser light in a more flexible and safer manner.

The fibre optic system consists of 3 main sections (see figure 3). They are the de-launch (input), launch (output) and the optical fibre bundle sections.

The specification of the fibre optics is listed below:

The number of optical fibres used in each bundle - 19
The type of optical fibre used - multi mode step index
The core diameter of the optical fibre - 100 mm
The numerical aperture (NA) of the de-launch section - 0.1
The numerical aperture (NA) of the launch section - 0.05
The length of the optical fibre bundle - 2m

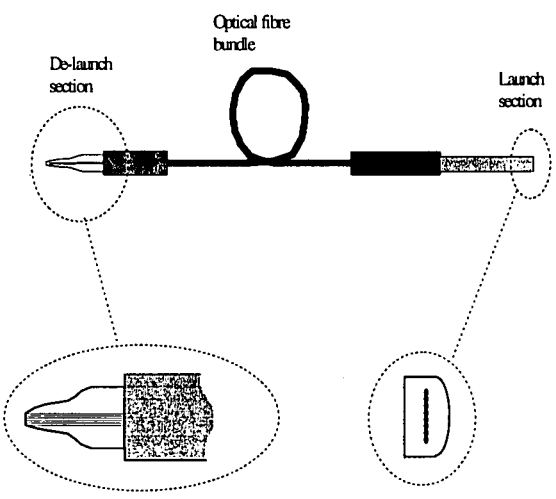


Figure 3. Fibre delivery system

In the de-launch head, the face of each individual optical fibre was polished and then the fibres were bonded together to form a round bundle. The de-launch head was carefully mounted in a hollow steel cylinder for rigidity. A transparent plastic cladding was used to interface the extension of the de-launch bundle to the hollow steel cylinder which provides a support medium. At the launch head, the face of each individual optical fibre was polished and bonded side-by-side forming a 'sheet' like structure. This "optical fibre sheet" was then carefully glued into a hollow D section brass rod to form a rigid head for mounting within the optical probe.

A flexible non-transparent plastic cladding was used to shield the optical fibre bundle body. This cladding was bonded permanently to the metal support of the de-launch and launch heads.

The fibre optic system was successful in delivering a good quality laser beam of the required power. However, after a number of test runs and set-up trials a significant reduction in the power delivery was detected. This was caused by overheating of the fibre ends which resulted in a decline in their optical properties. In consequence a rigid optics set-up was designed and used for the remaining runs.

Rigid optics delivery

In the new system, the laser beam had to be directed in the optical probe from a remote source. This was achieved using adjustable dielectric mirrors, replacing the original fibre optics, and mounted on the rotor module and the optical working section.

Optical probe

Both the fibre optic and the rigid optics approach shared the same method of optical entry, via a 10mm diameter optical probe arrangement, fitted to the ILPF cassette system (see optical working section). The laser light sheet was produced by fitting the optical probes with a combination of normal optical lenses to shape the laser light beam. The two delivery systems required very different laser beam shaping optics. The primary requirement for the probe, used with the fibre optic delivery system, was to relay the pre-formed light sheet on to the mirror at the end of the probe (figure 4a). This was achieved with a positive spherical lens, which was essentially the equivalent of a zoom lens. For the rigid optics delivery system, a more conventional approach was adopted where the laser beam was collimated at entry to the optical probe using a 'weak' positive lens. The beam was then projected through a positive cylindrical lens and a negative cylindrical lens to form the light sheet (figure 4b). Once the probes were fitted to the optical working section they could be moved in the radial direction and rotated to position the laser light sheet.

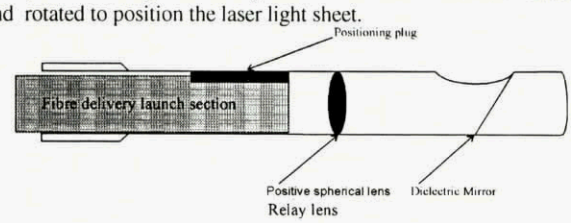


Figure 4a. Optical probe for fibre delivery system

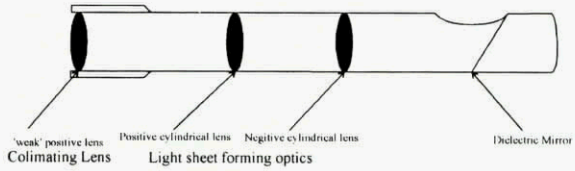


Figure 4b. Optical probe for rigid optics delivery system

Optical working section

A Perspex test cassette was machined at the Osney Laboratories Oxford to provide an optical window, see Figure 5a and 5b. The thickness of the window was 12mm, to minimise aberrations and astigmatism, and kept constant without compromising the casing annulus shape. The window allows optical access from upstream of the nozzle guide vane to downstream of the rotor trailing edge. The laser light sheet entry into the working section was achieved using two stator blades, which were machined internally and fitted with glass windows in the pressure and suction sides as shown in Figure 6. A 10mm hole was drilled through the leading edge of each stator vane to take the optical probes. The probes create a sheet of laser light (15mm x 0.2mm) which is projected into the flow field, between the stator blades and along the flow direction. This allowed the positioning of two light sheets creating a complete coverage of the region of interest.

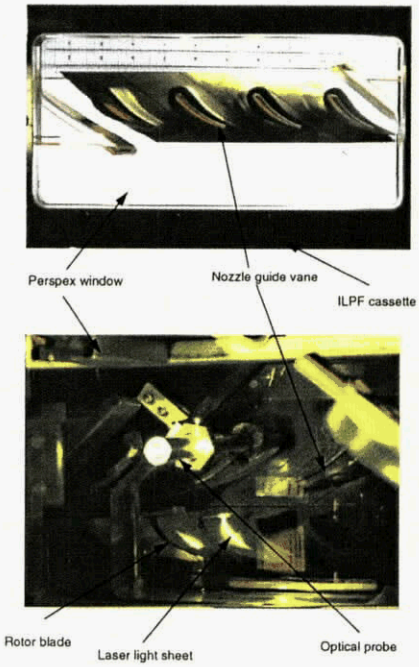


Figure 5a and 5b. ILPF Optical cassette

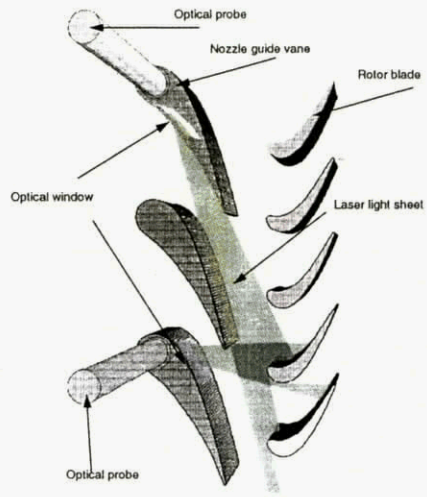


Figure 6. Schematic of stator vanes fitted with optical windows

Seeding

Polystyrene particles of 0.45μm diameter suspended in water were used to seed the flow. A TSI6000 six-jet atomiser was used to inject seeding into the ILPF pump tube prior to pressuring it to the pre-run level. During the seeding stage, all six jets of the TSI atomiser were used and the seeding time was about 20 minutes.

System changes

A major change was introduced to enhance the optical imaging system compared with that used previously. A Charge Coupled Device (CCD) based video camera was used to replace conventional wet film. The main drive towards this approach has been the rapid data access achieved at the end of a test run with a video system. This has the advantage of allowing the PIV system to be reviewed between tests. The images were captured in real-time at 25Hz. The camera was modified to separate the CCD part from the conditioning electronics (remote-head operation) so that the camera could be accommodated in the limited space available on the facility. The camera assembly with lens and the fibre optic probes were mounted directly on to the optical working section.

## 6. Image processing

The principle of the image processing system is particle tracking, using a direct spatial digital processing method the basis of which was laid down by Goss (1989). The particle image-displacement was determined by applying the following processes to the image; i) discrimination between background noise and particle information was made using an algorithm which interrogated the image for packets of information that were larger than the possible particle size (performed on the number of pixels used to define a particle) and ii) potential pairing was carried out by effectively fitting two radii around each identified particle, an inner radius which corresponded to the particle moving with the minimum expected velocity and an outer radius for the maximum expected velocity. The existence of a particle pair within this band yields a velocity vector. The presence of a third or additional particles in the sweep area invalidates the pairing.

To optimise the processing method three further issues were considered. Firstly, the particle image was required to have a clearly defined Gaussian profile to allow identification of the peak as the particle centre. Secondly an average distance between particle pairs of 10 pixels was needed to ensure an accurate velocity estimate. Finally, the image was set to cover the maximum area of interaction between the stator and the rotor blades.

The seeding was optimised to give an average of 1 particle-pair per $mm^2$

The precision with which the particle centre can be evaluated was the main aspect of the processing algorithm. The accuracy of locating the centroid, relative to the displacement within the particle pairs and the correctness of the pairing determined the accuracy of each velocity vector. The accuracy of the centroid position depended on the algorithm used and quality of the particle image profile. The characteristics defining the profile quality are: diameter of the particle image; peak intensity; mean and standard deviation of the noise signal; level of distortions (astigmatism and saturation). The particle diameter is determined by the magnification and numerical aperture of the lens, the incident light intensity and image exposure. The noise level depends on the background scattered light, the pixel size of the digital camera and the general electronic noise in the system. Three algorithms have been developed for estimating the position and displacement of the particles. The simplest is known as the centre of mass approach. In this method the intensity of the particle image is weighted and used to calculate the equivalent centre of gravity. This approach is computationally quick, with an accuracy in the region of 1/4 of a pixel. An alternative strategy is to cross-correlate between a pair of images. This increases the accuracy to approximately 1/8th. A third approach calculates the centre of the particle based upon a two-dimensional Gaussian fit. This method is computationally time consuming, but provides both a particle centre estimation to better than 1/10th of a pixel and also differentiates between genuine particle data and background noise. For the data presented in this paper the majority of the images have been calculated using the centre of mass approach. Typically for an average distance between particles of 9 pixels, the velocity error is estimated to be within 4%. However, for selected stator wake images, where a low noise, high image quality was possible, the two dimensional Gaussian fit was applied, giving an estimated velocity accuracy of 2%. It should be noted that although alternative methods of processing claim a higher velocity average, such as the correlation approach described by Adrian (1985). This approach inevitably performs a spatial average of a bigger area. It also takes an average of the velocity variations within the flow.

## 7. Calibration of the images

For the calibration of the image a test target, mounted on the rotor blades at the position of the light sheet, was used. The grid size was 20 lines/inch in both horizontal and vertical directions. The magnification was calculated by extracting one line from a test image and measuring the distance in pixels between two adjacent grid lines. For a better accuracy, the average distance for several lines was taken with an overall calibration error smaller than 0.5%. Figure 7 shows the stator reference image and the chosen regions for the calibration evaluation.

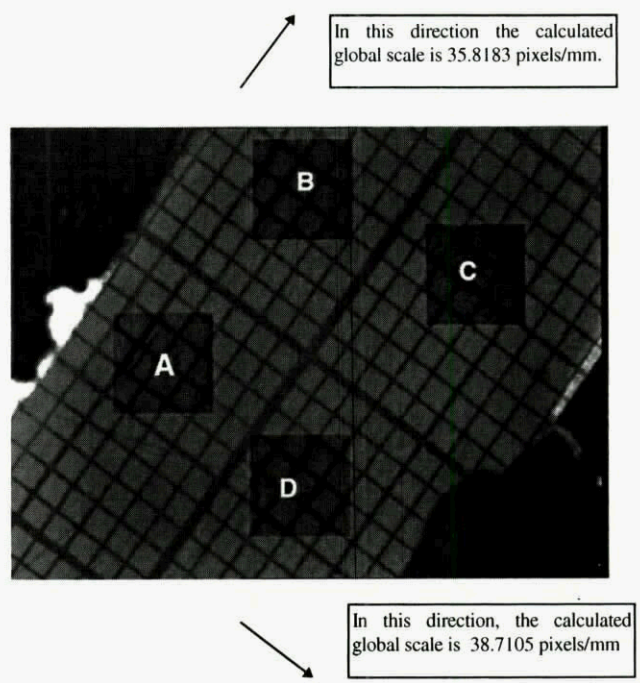


Figure 7. Calibration image

## 8. Results

Figure 8 shows an example of a PIV image taken in the stator-rotor region with the rotor blade visible in the image. Particle image pairs can be clearly identified. The bright area to the right of the image is glare from the rotor blade, caused by the laser light sheet as it comes into contact with the blade (it varies from image to image depending on the position of the rotor blade).

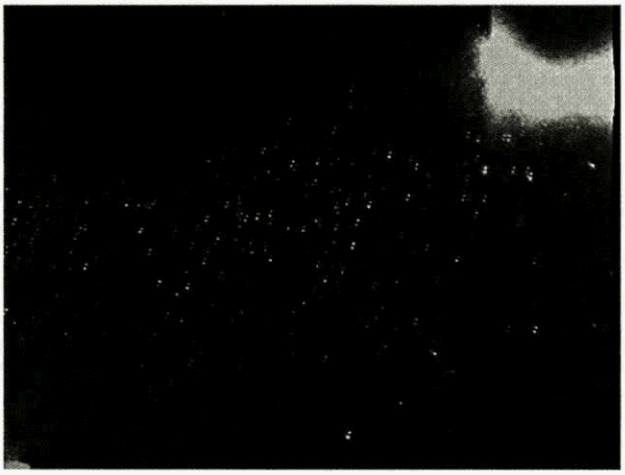

Figure 8. PIV image

A typical instantaneous image processed for velocity using the procedure outlined above is shown in Figure 9. The number of velocity vectors extracted from each image depends on the amount of glare produced by the rotor and ngv, and varies from around 100 for images with high glare to 500 for images with almost no glare. For comparison purposes contour plots of the velocity magnitude are required. In order to do this the data are fitted with an un-structured grid using simple triangulation where the data points form the nodes of the triangles. Bi-linear interpolates are then obtained at the centroids of the triangles. Additional division of the original triangulation is carried out using Delanuay's method to provide the contouring routine with a higher point density.

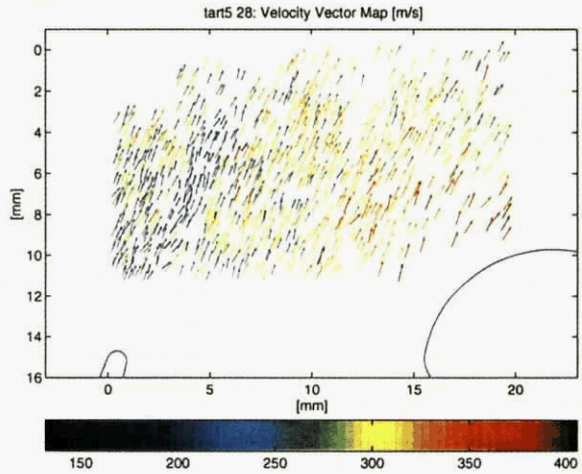


Figure 9. Measured instantaneous velocity (m/s)

Each run of the facility produces about 35 PIV images during the 2 second run time, of which 20 to 25 are usable. The density of data per image can be increased by combining additional images with a similar rotor position, allowing the periodic features to be examined. This procedure tends to average out the random variations and has been undertaken for many different rotor positions to form a sequence showing how the Mach number distribution varies, as the rotor moves past the ngv. The plots in Figure 10a to 10e show 5 images taken from such a sequence. The velocity data obtained from the PIV images and the measured inlet total temperature have been used to obtain the Mach number. The steady flow energy conservation relationship was applied to determine the local static temperature and acoustic speed.

$$T_0 = T + \frac{u^2}{2C_p}$$

Where $T_0$ is the stage inlet total temperature, T is the local static temperature, u is the local velocity and $C_p$ the specific heat.

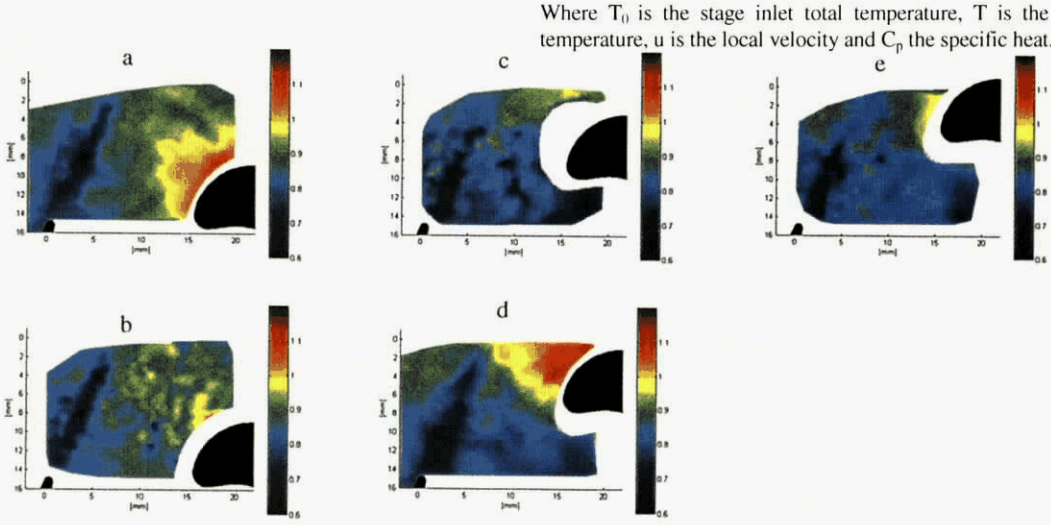


Figure 10. Measured Mach number distribution for various rotor positions

The validity of the steady flow relationship is expected to deteriorate for positions close to the rotor and within the rotor blade passage. In mitigation however, the resulting errors in Mach number vary only as the square root of static temperature and only a small amount of data exist within the rotor passage region.

PIV data from within the stator passage have been assembled together with data taken in the stator-rotor region for comparison purposes in Figure 11a. This shows many flow features expected in turbomachinery, for example the wake generated by the trailing edge of the stator, and the higher velocities experienced as the flow accelerates around the rotor suction surface crown. Figure 11b shows a Mach number distribution predicted by a viscous three-dimensional time marching programme (TRANScode, Calvert 1997), the calculation was performed for the ngv alone and contains no rotor information. The measured inlet total pressure and an average ngv hub exit static pressure were imposed as boundary conditions (the average exit static pressure was evaluated using measurements taken across an ngv pitch with the rotor present). The results presented from both the experiment and the CFD calculation are in the absolute frame of reference. Comparison of the ngv passage Mach number levels shows very good agreement; the ngv wake results also show good overall agreement although the wake is less mixed out in the prediction. In the experimental results, the wake immediately downstream of the ngv trailing edge is not as well defined. This effect is not real but is caused by the sparsity of data in this region. Seeding this low velocity region was difficult; similarly data close to the rotor blade crown was sparse because of glare problems mentioned earlier.

The prediction also shows a second wake from the neighbouring ngv emerging to the right of the plot; it is obscured in the experimental data by the presence of the rotor.

A two-dimensional unsteady prediction has also been performed for the MT1 turbine stage using the UNSFLO code (Giles, 1993). In this case the prediction included a rotor and the boundary conditions were set by matching the rig inlet total pressure and the rotor exit static pressure at the hub. The pressure division between the stator and rotor depends on the viscous flow modelling within both blade rows. Figure 12 shows the predicted Mach number distribution for a rotor position close to that of the experiment. The main flow features are generally well modelled. The ngv passage acceleration, near the suction side (A), is higher than both the experiment and the TRANScode prediction. This is probably a result of the pressure drop across the blade rows not being correctly distributed, due to imperfections in the viscous modelling. Nonetheless, the acceleration around the rotor suction surface crown and the ngv wake regions are in good agreement with the experiment; the CFD is more highly resolved in the rotor crown region and captures the fast changing flow field. The ngv wake is less mixed out than the experimental results suggest. This is not surprising as the CFD solution is a hybrid calculation and has two grids associated with it. The stators and rotors have an 'O' grid for the viscous layer, which interfaces with a more regular 'H' grid within which the computation is inviscid. The wake of the ngv falls mostly outside the viscous grid, hence the Euler solution within the 'H' mesh does not model the wake dissipation.

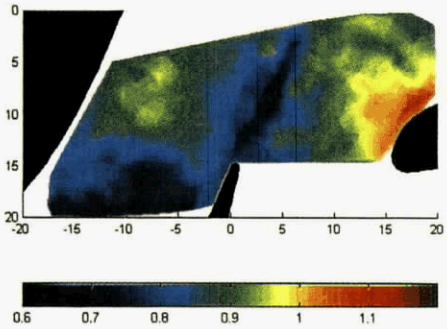


Figure 11a. Measured Mach number distribution

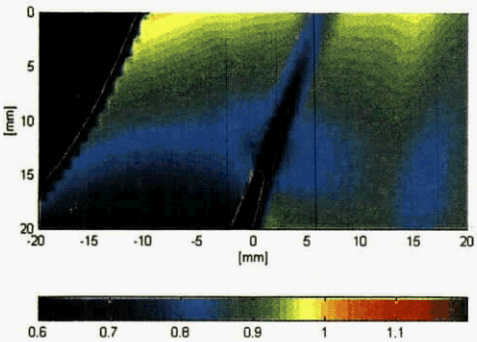


Figure 11b Predicted Mach number distribution using TRANScode

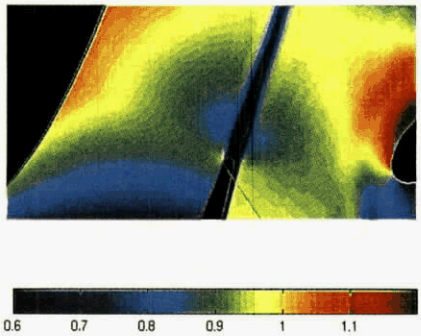


Figure 12. Predicted Mach number distribution using the UNSFLO code

Figure 13a and 13b show similar measured and predicted results for a different rotor position. The results are broadly similar to those already discussed but the rotor crown acceleration is possibly better resolved.

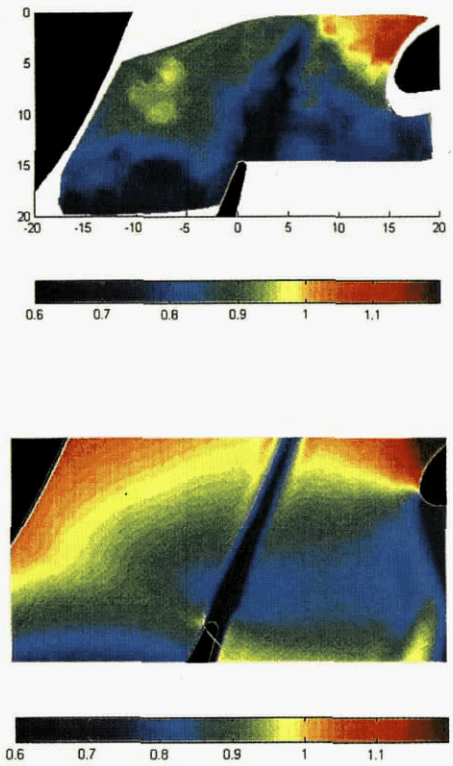


Figure 13b Predicted Mach number distribution using the UNSFLO code

## 9. Conclusions

The PIV system has been successfully modified to include a CCD video camera, enabling the data to be viewed within the turn around time of the ILPF facility. The processing software has also been enhanced to allow a more accurate assessment of the flow field. An accuracy of between 2 to 4% can be obtained depending on the processing method chosen. Laser light sheet reflections from the rotor blades have reduced the number of useful particle pairs available, and further work will investigate better coatings to reduce such glare.

The fibre delivery system has advantages compared with the rigid optics system used in the current study. However further development of the fibre bundle would be required to achieve a satisfactory operational life.

The results reported here have demonstrated the ability of PIV to allow measurements to be taken in turbomachinery flows where it is almost impossible to use conventional instrumentation. The data have been obtained at engine representative conditions for various rotor positions, with a rotor speed of 8200 rpm.

Comparison of PIV data with CFD calculations has shown good agreement in both the ngv passage and the stator-rotor region for two rotor positions.

## 10. Acknowledgements

The assistance of S J Anderson, W J Corbett, W K lee, M Burnett, D D Udrea and J Ackerman in the acquisition and presentation of data contained in this report is gratefully acknowledged. Thanks are also due to G C Smith for the prediction work.

## 11. References

1. Adrian, R. and Yao, C., 1985, "Pulse laser technique application to liquid and gaseous flows and the scattering power of seed materials". Applied Optics. Vol 24 No1

2. Calvert, W.J. at al, 1997, "Evaluation of a 3D Viscous Code for Turbomachinery Flows" ASME Paper 97-GT-078

3. Funes-Gallanzi, M., Bryanston-Cross, P.J. and Chana, K.S., 1994, "Wake region measurements of a highly loaded three-dimensional nozzle guide vane tested at DRA Pyestock using particle image velocimetry". ASME Paper 94-GT-349

4. Giles, M. B., 1993, "Validation of a numerical method for unsteady flow calculation", ASME Journal of Turbomachinery, Vol. 115, pp. 110-117

5. Goss, L.P. et al, 1989, "A novel technique for blade-to-blade velocity measurements in a turbine cascade", AIAA/ASME/SAE/ASEE 25th Joint Propulsion Conference, Monterrey CA July 10-12,

6. Jones, T.V., Schultz, D.L. and Hendley, A.D., 1973, "On the flow in an isentropic light piston tunnel", MOD (Proc. Exec.) Aeronautical Research Council, R & M. No 371

(c) British Crown Copyright 1997/DERA

Published with the permission of the controller of Her Britannic Majesty's Office.

Paper 46
Author: Chana

Q: Eisenlohr

How do you account for the measurement of a decelerating flow in an area where one expects, and the CFD shows, an accelerating flow?

A: The small area where the decelerating flow is seen is where the earlier vector plot shows a reduced density of data. Hence the deceleration is not likely to be real. To improve on this one could inspect other similar images to increase the point density here.

Q: Weigand

1. Did you also compare the directions of the velocity vectors?
2. Do you have provisions in your current PIV-system to discriminate reverse of the flow direction?

A :
1. The direction of the velocity vectors has not been compared yet, but we are hoping to do this soon.
2. The current PIV system does not discriminate for flow direction. However, we have recently purchased a new CCD camera, which is a cross-correlation camera with 2 CCD chips. This will permit flow direction evaluation.

# The Unsteady Structure of Simulated Turbine Film Cooling Flows from PIV

Richard B. Rivir
Aero Propulsion and Power Directorate, Wright Laboratory/POTT
Wright-Patterson Air Force Base, OH 45433 - 7251, USA

Sivaram P. Gogineni and Larry P. Goss
Innovative Scientific Solutions Inc., 2786 Indian Ripple Road
Beavercreek, OH 45430, USA

David J. Pestian
University of Dayton Research Institute
Dayton, OH 45469, USA

## 1. SUMMARY

Unsteady turbine film cooling flows are subjected to free stream disturbances which exceed those of a fully turbulent boundary layer. Hot wires, cold wires, and thermocouples have in the past been used to obtain local, time resolved point measurements of velocity, temperature and mixing. The structure of the flow and its interaction with free stream structures remains largely hidden. Two-color, double pulsed, PIV (Particle Image Velocimetry) was used to investigate simulated turbine film-cooling flows with high free stream turbulence and wake passing. High resolution (3000x2000 pixels), instantaneous, velocity distributions obtained by CCD camera have been compared against those obtained from 35mm film digitized at 2700 ppi resulted in realizations with similar spatial resolution. Averages of 1 to 30 instantaneous PIV velocity measurements have been compared against simulated turbine film cooling flow velocity profiles measured by hot wire. The resulting PIV velocity profile measurements were mostly within the envelope of the mean and rms velocity measurements of the hot wire. The PIV images allow instantaneous estimates of the shear layer development, vertical cooling jet film spread, turning, and interactions with the free stream turbulence. Instantaneous vorticity, and dissipation distributions have also been obtained. The lateral jet spread of the film at the wall was measured with liquid crystals and thermocouples and compared with the vertical PIV spread. The centerline vertical film jet spread, turning angle, and shear layer growth has been characterized from the PIV realizations as a function of blowing ratio, Reynolds number, periodic forcing amplitude, frequency, and free stream turbulence.

## NOMENCLATURE

| | |
|---|---|
| A | Film foot print with Tu or forcing, ($cm^2$) |
| $A_o$ | Film foot print with Tu =1% ($cm^2$) |
| $c_\tau$ | Constant f (accuracy of software determination of particle displacement, 1-10%) |
| $d_\tau$ | Recorded image diameter (mm) |
| d | Film-cooling-hole diameter (1.905 cm) |
| DVR | Dynamic Velocity Range = $M_o\ \Delta p_{max}/\ c_\tau\ d_\tau$ |
| $M_o$ | Magnification factor |
| $\Delta p_{max}$ | Maximum velocity displacement (μm) |
| R | coolant blowing (mass-flux) ratio ($\rho_c U_o/\rho_f U_f$) |
| Re | Reynolds number based on film-cooling-hole diameter |
| Tu | Turbulence intensity (u'/U) |
| U | Mean local streamwise velocity (m/s) |
| x | Streamwise distance measured from the downstream lip of the injection hole (cm) |
| y | Vertical distance from the injection surface (cm) |
| f | Forcing frequency (Hz) |
| ω | Vorticity, 1/2((V/(x-(U/(y) (1/s) |
| Ω | Reduced frequency (free stream velocity/coolant-hole diameter/oscillation frequency, U/d f) |

## 2. INTRODUCTION

PIV has been explored as an initial step for the measurement of unsteady flow phenomena associated with the film cooling of turbine components. Recent trends in aircraft gas-turbine combustor designs have resulted in short, high-temperature combustors which produce highly turbulent exit flows. These flows are further complicated by stator wake interactions, non steady passage vortices, end wall horseshoe vortices, along with non-steady up stream cooling flows. As the exit temperature of the combustors is raised to increase engine-cycle efficiency, effective film cooling of the turbine components downstream of the combustor becomes increasingly important. Modeling of turbine film cooling flows computationally requires extensive meshes and intersection of meshes of different densities such that experimental verification of film effectiveness and heat transfer coefficient is still required for code verification. The instantaneous

*Paper presented at an AGARD PEP Symposium on "Advanced Non-Intrusive Instrumentation for Propulsion Engines", held in Brussels, Belgium, 20-24 October 1997, and published in CP-598.*

realizations of velocity obtainable from PIV can provide a detailed understanding of many of these unsteady flow features.

Bons et al. (1994, 1995) investigated the effect of unsteadiness and high free stream turbulence on film-cooling effectiveness using physical probes including hot wires and thermocouples. Physical probes, however, are hampered by their intrusive nature, limited spatial resolution from point wise measurements, and spatial averaging over sparse arrays of measurement points. Liquid Crystals and IR measurements have been made of the surface temperature distributions but quantitative simultaneous spatially and temporally resolved measurements of the film flow are still lacking. This study provides instantaneous realizations of the film cooling hole centerline vector flow fields for a range of conditions encountered in turbine flows and summarizes results from several of our current PIV investigations of turbine film cooling flows.

## 3. EXPERIMENTAL SETUP AND PROCEDURES

### 3.1 Facility description

The open-loop film-cooling wind tunnel, as shown in figure 1, has been described in detail by Bons et al. (1994, 1995). The main flow passes through a conditioning plenum containing perforated plates, honeycomb, screens, and a circular-to-rectangular transition nozzle. Downstream of the transition nozzle, at the film cooling station, free stream turbulence levels of 0.7% (± 0.05) can be achieved, with velocity and temperature profiles uniform to within 1%. A single row of 1.905-cm film-cooling holes at an injection angle of 35 deg. to the primary flow was investigated. The length-to-diameter ratio of the film-cooling holes evaluated was 2.4. The ratio of integral turbulence scale to film-hole diameter is in the range 2.88 - 4.23, depending on the turbulence level and turbulence generation mechanism. The ratio of momentum thickness to hole diameter typically is 0.05. The ratio of micro scale to film-hole diameter is in the range 0.1 - 0.39. The ratio of temperature or density of the film flow to primary flow is typically, 1.07 - 1.09. The variation in blowing ratios (R = 0.5 - 1.5) is achieved by varying the ratio of the film flow velocity to the primary flow velocity. For simulation of the vane-wake effects, the film cooling jet flow is modulated with a speaker located in the side wall of the coolant supply plenum at an appropriate reduced frequency $\Omega$.

### 3.2 Range of Experimental Parameters Investigated

Film-cooling air is injected through rows of typically 0.5 - 0.8 mm diameter holes in the blade surface. The jet injection hole was scaled up by a factor of 35 to study the flow characteristics of a turbine-blade film-cooling hole. The cooling air is supplied from the compressor exit bleed flow and is maintained at essentially constant pressure. Typical engine Reynolds numbers for film cooling holes are in the range of 20,000. The Reynolds numbers (Re - based on the coolant-hole diameter of 1.905 cm) which were investigated for the unforced flow in this investigation were 10,000, 20,000 and 40,000. The effect of free stream turbulence was investigated for turbulence levels of 1%, 6%, 12% and 17% for the blowing ratios of 0.5, 0.7, 1.0, and 1.5 at a Reynolds number of 20,000. The effect of Reynolds numbers of the film at 10,000, 20,000, and 40,000 was investigated for blowing ratios of 0.5, 0.7, 1.0, and 1.5 at turbulence levels of 1% and 17%. The two-color PIV technique was used to examine the region around the film-cooling hole for 3 diameters downstream, to document the penetration of the film jet into the free stream, to determine the shear-layer characteristics, and to determine the film jet spread.

The effect of vane wake on rotor film cooling flow was simulated by periodic forcing of the film-cooling flows at the typical rotor blade passing reduced frequency $\Omega$. Phase-locked measurements at 45-deg. increments of the periodic film forcing for free stream turbulence levels (Tu) of 1 and 17% were obtained for frequencies of 5 and 20 Hz.

### 3.3 Two-color PIV System

PIV has been used for a number of years to measure velocity distributions in planar cross sections of aerodynamic flow fields (Adrian 1991, Lourenco et al. 1989). The two-color PIV system uses color for temporal marking of the seed particles in the flow field which also results in higher data yields and signal-to-noise levels than are attainable with single color systems by eliminating any uncertainty in particle direction. The green (532-nm) laser output from a frequency-doubled Nd:YAG laser and the red (640-nm) laser output from a Nd:YAG-pumped dye laser (DCM dye) are combined by a dichroic beam splitter and directed through sheet-forming optics. The laser-sheet energy is typically 20 mJ/pulse, with a sheet thickness of < 1 mm at the test section. The temporal delay between the two lasers is dependent upon the flow velocity, optical magnification, and interrogation spot size. It is set at ~ 12 μs for a Re = 20,000 film flow velocity. A 105-mm micro lens with an f-number of 5.6 was used to record the images. The same lens was used for CCD and the 35mm film realizations.

The implementation and selection of the seeding is an important factor in PIV measurements in complex three-dimensional flows. The seed particles must be small (typically < 1 (μm) to track accelerations in the fluid effectively. In the present experiment sub-micron size particles are introduced into the film cooling flow in the film plenum.

One of the problems in the use of film for mean PIV measurements is the inability to maintain the absolute coordinates of the recorded features during the digitization process while multiple frames are averaged. This occurs because the film cannot be consistently loaded into the film-scanner to the degree required for reproducibility. This problem is eliminated when using a digital color CCD since no film digitization is required. The high-resolution Kodak DCS 460 CCD system extends two-color PIV by recording the color images onto a single high-resolution color CCD camera, thus eliminating the processing time and subsequent digitization time of color film and the complexities associated with conventional image-shifting techniques. The DCS 460 has 3060 x 2036 pixels, with each pixel being 9 $\mu m^2$. The CCD camera has a built-in 12-bit analog-to-digital converter for

increased dynamic range and a frame rate of 1 frame/sec. It also features a PC-MCIA storage drive which delivers about 26 exposures, with each PIV image occupying ~ 6 Mbytes. The color response of the DCS 460 CCD array is accomplished by overlaying the individual pixels of the camera with a series of red, green, and blue color filters. The chosen green and red laser wavelengths were situated near the peak of the transmission of the green and red camera filters, respectively. Because the camera was built to respond, as a human eye to color, most of the pixels are green-sensitive. The relative percentages of green, blue, and red pixels are 50%, 25%, and 25% respectively. The distribution of the red and blue pixels is random for minimizing straight-edge effects. The output from the camera controller to the computer is a 24-bit RGB tiff image; thus, the 12-bit A/D camera output must be mapped into three 8-bit colors, each having a spatial resolution equivalent to the chip size (3060 x 2036). This is accomplished through proprietary software developed by Kodak which involves some form of interpolation to increase the spatial resolution of the camera. Because of the proprietary nature of this interpolation software, it was not known how the resulting resolution of the color camera would compare with 35 mm film or if it would be useful for accurate PIV measurements. The CCD camera allowed on line optimization of the seed density and intensity of the sheet illumination.

The software for data reduction uses the correlation of 5-8 particles to compute the velocity vector at a single point. The cross-correlation technique is based on intensity maps of the red and green images of scattered light. The intensity distributions of the red and green images r(x,y) and g(x,y) and their corresponding Fourier transforms are R(a,b) and G(a,b). The two-dimensional cross-correlation function

$$h(x,y) = \int_R \int_R r(\alpha,\beta)\, g(x+\alpha, y+\beta)\, d\alpha\, d\beta$$

$$= F^{-1}[F(r(x,y))\, F(g^*(x,y))]$$

$$= F^{-1}[R(\alpha,\beta)\, G^*(\alpha,\beta)] \qquad (1)$$

is employed to determine the magnitude and direction of the average velocity over the interrogation area. Note that unlike processing methodologies that are based on auto correlation, the direction of the velocity vectors is uniquely determined.

The correlation function (1) is calculated over small segments (interrogation domains) of the PIV image. In order to process the digitized PIV image, it is dissected into small sub regions. The dimensions of each interrogation domain depend on the particle density, estimated local velocity gradients, particle image size, and the desired spatial resolution. The maximum displacement of each particle must be less than half of the interrogation spot. In the present experiments, the interrogation domain measures 64 x 64 pixels and corresponds to 1.4 x 1.4 mm area in the measured flow. In order to enhance the overall resolution, the interrogation domains are overlapped by one-half the domain size. The peak of the correlation map calculated by Eq. (1) corresponds to the average velocity within the interrogation spot. An intensity weighted peak searching routine is used to determine the exact location of the peak to a sub-pixel accuracy. The number of particle pairs that are necessary to ensure a desirable signal to noise ratio is reduced to four or five pairs when this cross-correlation analysis is employed.

### 3.4 PIV Calibration

A comparison of the resolution and accuracy of 35 mm film against the CCD camera was performed using a disk rotating at a constant rpm. The measurement of the rotating velocity vector is illustrated in figure 2a and the calibrations obtained for film and CCD are compared in figure 2b illustrating that similar accuracy and resolution is achieved for film and CCD (Gogineni et al. 1996a). Figure 2a also illustrates the direction resolving capability of this configuration. Since the PIV measurements are instantaneous realizations, some sort of averaging is required to compare against mean and rms hot wire measurements. Figure 3a illustrates a film boundary layer comparison of 30 PIV realizations and a hot wire traverse of the same flow. The bars indicate the spread in an average of 5, 10, 20, and 30 PIV realizations at each data point for unforced flow conditions (x/d = 1, Re = 20,000, R = 0.7, and Tu = 1, (Gogineni et al. 1996d). The wide scatter is due to the high Reynolds number, high turbulence levels, and the large-scale turbulent structures of the film-cooling flow. Since only the film-cooling flow was seeded in this experiment, the velocities obtained in the interface region of the unseeded high-speed free stream and the seeded slower-speed film-cooling flow would be expected to deviate from those obtained with a hot-wire probe which cannot distinguish between the two flows. The rms fluctuation was measured at a constant flow condition, and the results show that the rms deviation approaches 20% as the number of samples is increased. The PIV images do however represent the instantaneous flow structures with fidelity. In the present experiment 30 images is of course not sufficient for accurate determination of the mean velocity and rms velocities.

Gogineni et al. (1997) has examined the sensitivity of particle size to the accuracy of the mean and rms errors for a variable particle size as well as the variable displacement error for a fixed particle size. A particle size which records as 2.5 - 4 pixels results in an rms error of 0.017 to 0.06 pixels in position. A fixed particle size of 4 pixels results in an error of 2.5% at a 2 pixel pair displacement and 1.3% at a 20 pixel pair displacement as is illustrated by the plot of this relationship in figure 3b. Adrain's (1996) Dynamic Velocity Range (DVR) for the Kodak CCD camera results in a useful range of velocity measurement of nearly 70 for this configuration.

## 4. RESULTS AND APPLICATION OF PIV TO SIMULATED TURBINE FILM COOLING FLOWS

Turbine-blade film cooling takes place in a very hostile, unsteady environment where velocity and temperature disturbances exceed 20%. The free stream and film cooling boundary layer wall conditions in these flows exceed those encountered in classical fully turbulent boundary layers. Parameters of interest in this problem include jet spread or film

effectiveness, R, Re, Tu, and Ω. Accurate modeling of these flows has proved difficult due to the high level of unsteadiness. Nominally 10 - 30 instantaneous images were obtained for a given flow condition to capture the essence of the flow features.

**4.1 Liquid Crystal and Thermocouple Measurements of Mean Jet Spread and Film Effectiveness**

Liquid crystals were also use to measure wall surface temperatures allowing calculation of η, and h. Figure 4 shows liquid crystal measured temperature contours on the wall for turbulence intensities of 1%, 6%, 11%, and 17%. The green liquid crystal line is nominally 0.4°C wide. Figure 4 shows an increased spread angle with Tu for the same constant temperature contour. The film has virtually disappeared by a x/d = 6 in figure 4. Figure 5 shows the spread half angle of the film coolant obtained by digitizing the temperature contours of figure 4. Figure 5 indicates the film spread angle to be nearly linear with Tu.

Direct measurement of the film cooling effectiveness was obtained from thermocouples on the adiabatic test section wall. An array of 84 thermocouples provided the wall surface temperature distribution. Figure 6 illustrates the centerline film cooling effectiveness measurements for Tu=0.9% 6.5%, 11.5%, and 17%. These measurements, which extended to large values of x/d, indicated a 50% attenuation in effectiveness over the low turbulence case at x/d=6, and an attenuation of 70% at x/d=22.

The liquid crystal measured lateral jet spread, figure 4, is compared with the measured thermocouple centerline vertical attenuation or spread, figure 5, in Table 1 at x/d = 6.7. Table 1 indicates similar jet spreads with turbulence from the two measurements

**Table 1 Comparison of Film Spread to Tu=1% Spread Area**

| Tu in % | Ao/A Liquid Crystal | Ao/A Cl thermocouple |
|---|---|---|
| 6 | 0.76 | 0.75 |
| 12 | 0.60 | 0.67 |
| 17 | 0.44 | 0.44 |

The film cooling effectiveness drops rapidly as the pair of counter rotating vortices, formed by the interaction of the free stream horseshoe vortex with the film jet, pull free stream fluid under the film and the center of the film flow lifts off the surface. The free stream contributes significantly to the rapid mixing out of the coolant temperature. The cylindrical film hole results in symmetric spread with the maximum film effectiveness moving away from the wall as a result of the vertical lifting of the film.

**4.2 PIV Measurements**

The two-color PIV technique was used to measure the penetration of the film jet, the shear-layer characteristics (scale, frequency and angle of spread), vorticity, and the jet spread angles. Figure 7 compares centerline flows from PIV realizations at Re = 20,000 as the turbulence level is increased from 1% to 17%. One can see that increasing the turbulence from 1% to 17% more than doubles the vertical film spread for R = 0.7. The resulting vector velocity fields are shown below the corresponding PIV realization in figure 7. The slope of the shear layer over the film cooling hole and after the film cooling hole in figure 7 indicates different interactions take place over and after the film hole with the primary flow.

The resulting angles of the film coolant flow have been plotted in figure 8 for R=0.5, 0.7, 1.0, 1.5, and Tu=1, 6, 12, 17% (Gogineni et al. 1996b). Figure 8 shows a linear relationship between the jet-exit slopes with both Tu and R, for R < 1.0. Different slopes of the linear relationship are observed for the spread angle over and after the film hole. There is a decrease in jet spread for R=1.5, however, the spread angle remains appreciable. Increased jet spread results in more rapid mixing out of the film cooling flow.

Figure 9a illustrates CCD images obtained at a Reynolds number of 40,000, at free stream Tu levels of 1% and 17% for R = 0.7 and 1.5. The increase in Re has proportionally increased the frequency or reduced the scale of the shear layer over the film cooling hole, while after the film hole the blowing ratio and the free stream turbulence control the shear layer scales or frequency. When Tu was increased from 1 to 17% for R = 0.7, no appreciable change was observed in the eddy sizes in the shear layer after the film-cooling hole. A significant change however took place at Re=40,000 for R = 1.5. When R was increased from 0.7 to 1.5 at a free stream Tu level of 17%, the roll-up frequency for the shear layer after the film-cooling hole decreases. In the shear layer over the film hole, a second parallel shear layer can be detected (figure 9a, which may be associated with a separation from the back side entrance of the film-cooling hole. When R < 1.0, it is observed that the shear-layer roll up is the reverse of what would normally be expected. This reverse roll up is attributed to the film-cooling wall boundary layer.

Figure 9b shows the vorticity distribution Γ, computed by central differencing of the velocity field. The solid lines indicate positive vorticity, and the dashed lines indicate negative vorticity. As expected, high values of vorticity are found in the shear layer and in the film layer at lower R. When R is increased to 1.5 and Tu to 17%, the vorticity is concentrated in the shear layer far from the surface. The vorticity distribution from the CCD data showed a significant improvement over that from the 35-mm, film data. This can be attributed to the presence of the more valid vectors and on line optimization of seeding and laser sheet intensity.

**4.3 Periodically Forced Film Measurements**

The passage of the stator-wake was simulated by periodic forcing of the film-cooling flow at the appropriate reduced frequency, Ω. Scaling up the film cooling holes on a turbine blade results in frequencies of interest for these simulated film cooling flows in the range of 5 to 50 Hz. The average η and average h resulting from periodically forced disturbances at 5, 10, and 20 Hz was compared to that from random turbulence in

Bons et al., 1995 using thermocouples with either a constant heat flux surface or an adiabatic wall. The mean film cooling effectiveness at large x/d (>20) from the adiabatic wall measurements shows that the attenuation was the same for a periodically forced film flow as that of continuous free stream turbulence of the same amplitude. Adiabatic wall measurements of these flows forced at 5, 10, and 20 Hz showed little difference between the 10 and 20 Hz cases A preferential amplification of a low forcing frequency (5 Hz) was observed near the film hole so 5 and 20 Hz cases were chosen for the PIV investigation .

PIV was used to examine the flow field for film flows forced at 5 and 20 Hz for preferential frequency response, flow structure, interaction with the free stream, and jet spread angle. PIV exposures were phase locked to the film-coolant driving frequency, and data recorded at phase-angle increments of 45 degrees of the forcing cycle (Gogineni et al. 1996c). The blowing ratios of 0.5, 0.7, 1.0, and 1.5 were investigated at a Reynolds number of 20,000. Figure 10 shows a typical double-exposed PIV image and the corresponding instantaneous velocity distribution at a phase angle of 180 degrees for R = 0.5, Re = 20,000, and Tu = 17% with periodic forcing at 5 Hz and 20 Hz. These realizations illustrate the double shear layer at the leading edge of the film hole, a reverse roll up of the shear layer, the two characteristic scales (one over the film hole and one after the film hole), and a preferential amplification of the low forcing frequency (this amplification was also observed with hot wire measurements).

It was previously indicated that jet spread (angle of the film) was indicative of the mixed film temperature. The film flow angles for the shear layers and the film jet were obtained from the instantaneous PIV realizations. Typical results for the phase locked spread angle over the film cooling hole and after the film cooling hole are summarized in figures 11 and 12. According to these results free stream turbulence of 17% contributed very little additional spread to the periodically forced flow. Periodic forcing of the film cooling flow resulted in forced film flows with twice the forcing frequency and average spread angles which were between those observed for the 1% and 17% free stream turbulence cases. Although the amplitude of the forced with or without Tu versus the 17% continuous case are similar, the average instantaneous spread angle for the periodically forced with or without Tu film is 57% less than the 17% continuous free stream case. An average of the phase averaged measurements should of course be investigated to see if this could be used to reduce film cooling mass flows. Table 2 presents the average spread angles for the periodically forced flows for both frequencies. A comparison of the forced PHI2 and 17% spread angles with the 1% PIV spread angle indicates Ao/A ratios of 0.70 and 0.36 respectively which are found to be similar but slightly less than the lateral spread Ao/A ratios obtained from liquid crystal and thermocouple measurements. Near the film cooling hole (<3 diameters) the forced 1% flow is spread at approximately half the 17% spread angle from the PIV realizations.

**Table 2 Mean Spread Angles x/d<3**

| Spread Angle | Blowing Ratio | Forced Tu=1% | Tu= 1% | Tu=17% |
|---|---|---|---|---|
| Mean PHI 1 | 0.5 | 29.5 | | |
| | 0.7 | 34.3 | 22.2 | 29.2 |
| | 1.0 | 39 | | |
| Mean PHI 2 | 0.5 | 9.3 | | |
| | 0.7 | 12.4 | 8.7 | 22.9 |
| | 1.0 | 13.1 | | |

## 5. CONCLUSIONS

Short l/d film cooling holes significantly affect the flow by virtue of the film tube wall boundary layer. This film wall boundary layer remains a dominant driver in the development of the film coolant flow as evidenced by the reverse roll up seen in PIV realizations.

Turbine film cooling data from 35-mm film after digitization and from a 3060 x 2036 pixel CCD camera have been compared and found to have similar spatial resolutions. The CCD allowed optimization of seeding and laser-sheet intensity which resulted in higher vector densities. Hot-wire data and the average of more than 20 PIV frames at x/d = 1 agreed favorably for these highly unsteady flows; however, direct use of mean values for these flows would require an average of more than the 30 samples used in this investigation.

Free stream turbulence of 17% results in attenuation of the cooling effectiveness by 50% at x/d=6 and a 70% reduction at x/d=22. A linear relationship was observed between the instantaneous spread angle of the film, blowing ratio, and continuous free stream turbulence intensity. Periodic forcing and continuous free stream unsteadiness produce similar vertical jet spread at large x/d. The film jet spread angle, at small x/d, for periodic forcing with or with out free stream turbulence is 57% less than continuous free stream turbulence. Periodic forcing exhibited film fluctuations at twice the forcing frequency. The film shear layer is dominated by Reynolds number over the hole and by blowing ratio and free stream turbulence after the hole.

PIV has proved to be extremely useful in obtaining additional information on the structure of turbine film-cooling flows such as jet spread, shear-layer growth, and shear-layer frequency. PIV also allows the computation of realizations of vorticity and dissipation for direct comparison with CFD data

## ACKNOWLEDGMENT

This work was performed under partial sponsorship of the Air Force Office of Scientific Research Project 2307BW, with Dr. James McMichael as program manager.

## REFERENCES


1. Adrain, R. J., 1991, "Particle Imaging Techniques for Experimental Fluid Mechanics," Annual Review of Fluid Mechanics, Vol 23 pp. 261-304.
2. Adrain, R. J., 1996, "Strategies for Imaging Flow Fields with PIV," AIAA 96-198, 27th AIAA Fluid Dynamics Conference, New Orleans, LA.
3. Bons, J., MacArthur, C., and Rivir, R., 1994, "The Effect of High Freestream Turbulence on Film Cooling Effectiveness," ASME 94-GT-51, 39th International Gas Turbine and Aeroengine Congress and Exposition, The Hague, Netherlands.
4. Bons, J., Rivir, R., Mac Arthur, C., and Pestian, D., 1995, "The Effect of Unsteadiness on Film Cooling Effectiveness," AIAA 95-0306, 33rd Aerospace Sciences Meeting and Exhibit, Reno NV.
5. Gogineni, S., Trump, D., Goss, L., Rivir, R., and Pestian, D., 1996a," High Resolution Digital Two-color PIV (D2CPIV) and Its Application to High Freestream Turbulent Flows," 8th International Symposium on Applications of Laser Techniques to Fluid Mechanics, Lisbon, Portugal.
6. Gogineni, S., Rivir, R., Pestian, D., and Goss, L., 1996b, "PIV Measurements of Flat Plate Film Cooling Flows with High Free Stream Turbulence," AIAA 96-0617, 34th Aerospace Sciences Meeting and Exhibit, Reno NV.
7. Gogineni, S., Trump, D., Pestian, D., and Rivir, R., 1996c, "PIV Measurements of Periodically Forced Flat Plate Film Cooling Flows with High Free Stream Turbulence," 1996 ASME International Gas Turbine and Aeroengine Congress/Users Symposium and Exposition, Birmingham, UK. ASME 96-GT-236.
8. Gogineni, S., Rivir, R., Goss L., and Pestian, D., 1996d, "PIV Technology for Simulated Turbine Film Cooling Flows," The 6th International Symposium on Flow Modeling and Turbulence Measurements, Tallahassee FL.
9. Gogineni, S., Trump, D., Goss, L., Rivir, R., and Pestian, D., 1997, "High Resolution Digital Two-color Digital PIV Employing a Single CCD Camera," Experiments in Fluids, Revision in Progress.
10. Lorenco, L. M., Krothapalli, A., and Smith, C. A., "Particle Image Velocimetry, Advances in Fluid Mechanics Measurements, (M. Gad-el-Hak, ed.) Springer-Verlag, Berlin, pp. 127-199.


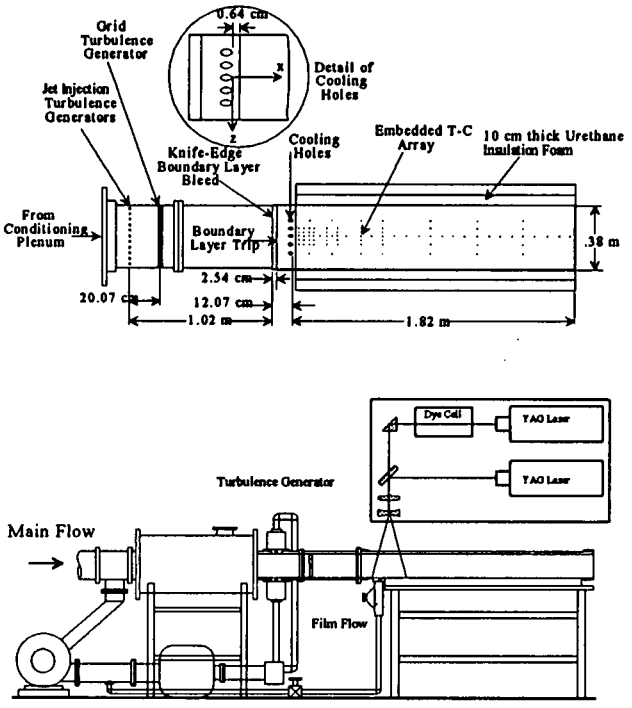


**Figure 1. Schematic of the High Turbulence Film Cooling Facility with 2 Color PIV.**

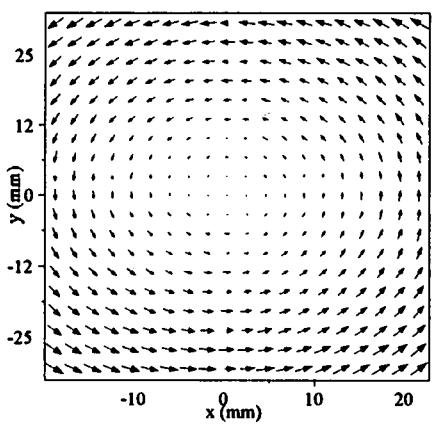


**Figure 2a. Rotating Calibration Disk Velocity Vectors.**

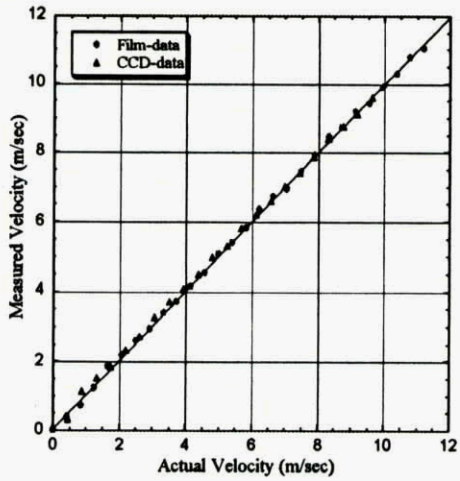


**Figure 2b. Comparison of CCD and 35 mm Velocity Calibration.**

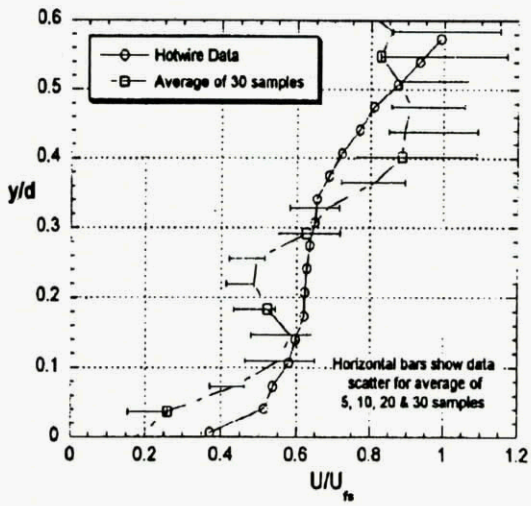


**Figure 3a. Comparison of Hot Wire and PIV Velocity Profiles.**

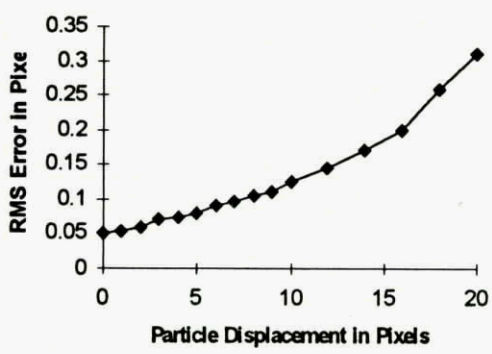


**Figure 3b. RMS Error for Particle Displacement in Pixels**

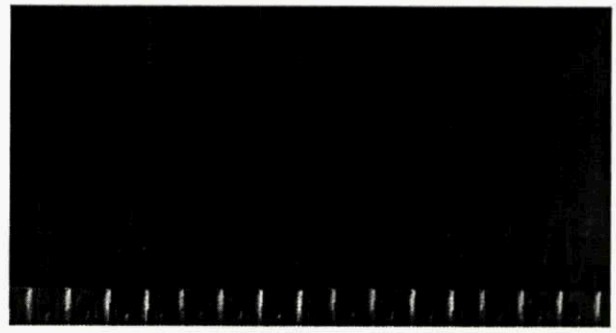

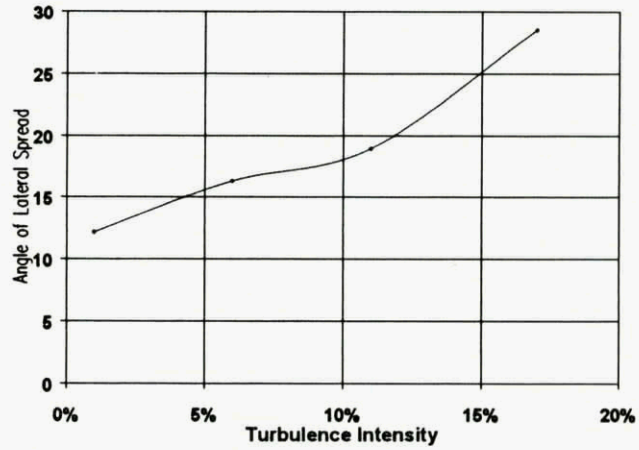


**Figure 5. Liquid Crystal Measured Spread Angle at x/d=6.7, Due to Tu=1%, 6%, 11%, 17%.**

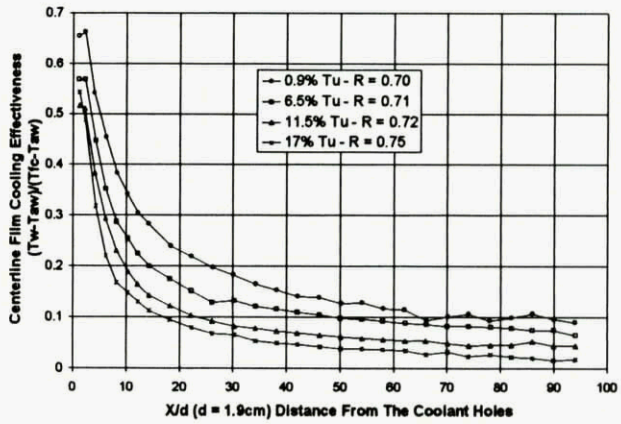


**Figure 6. Centerline Film Cooling Effectiveness vs. x/d from Adiabatic Wall, Re=19,000, z/d=0.**

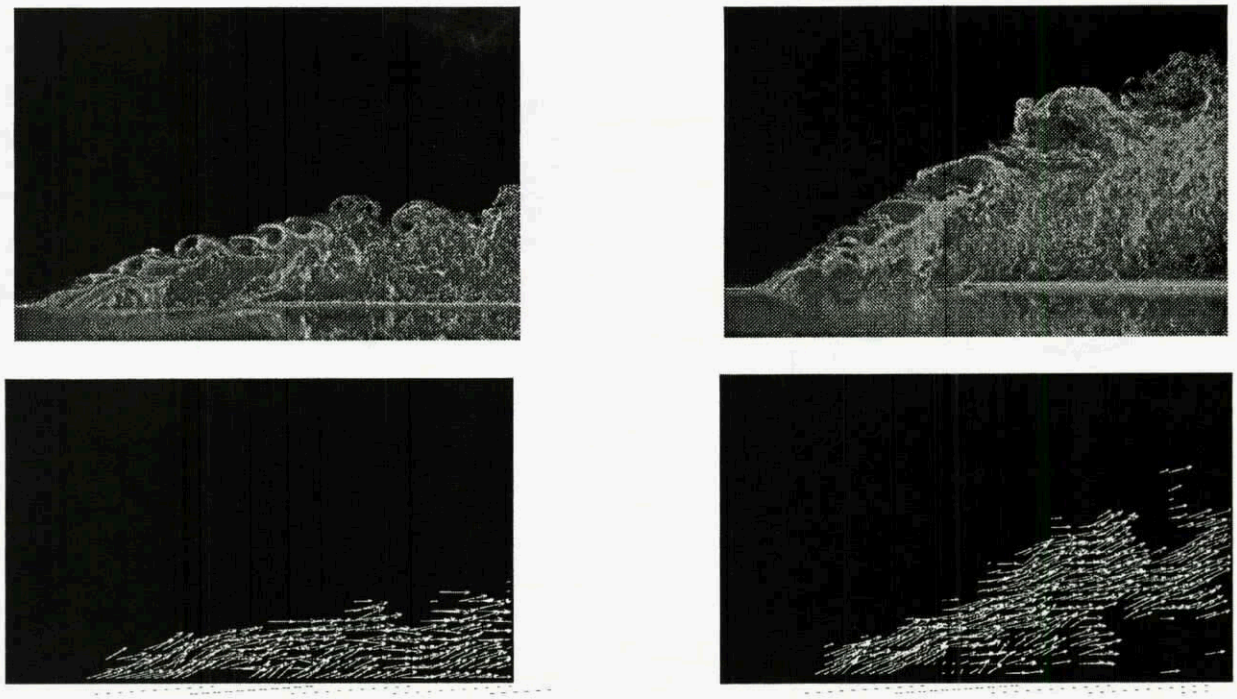

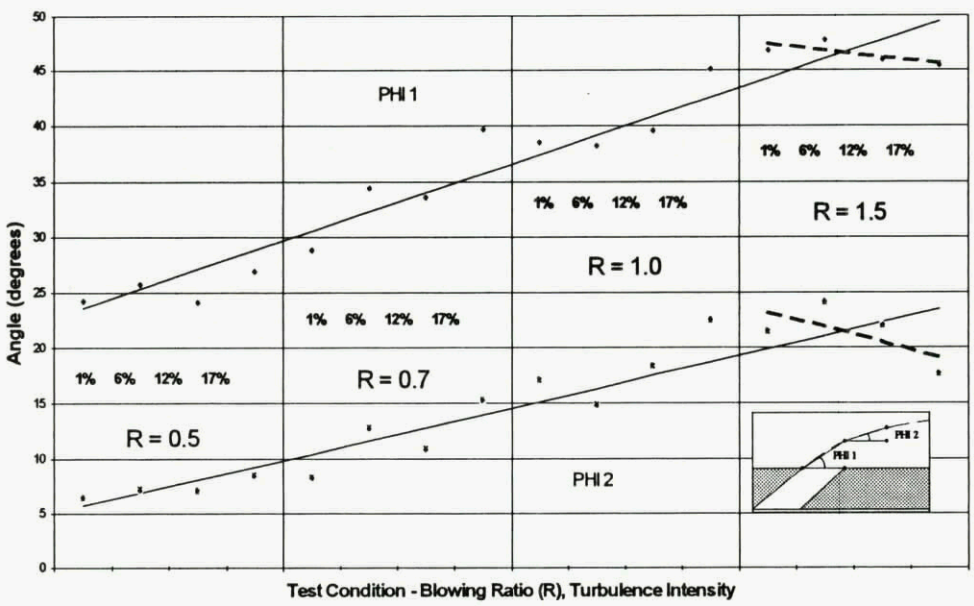


**Figure 8. Film Cooling Spread Angles with Tu and Blowing Ratio, Re=20,000.**

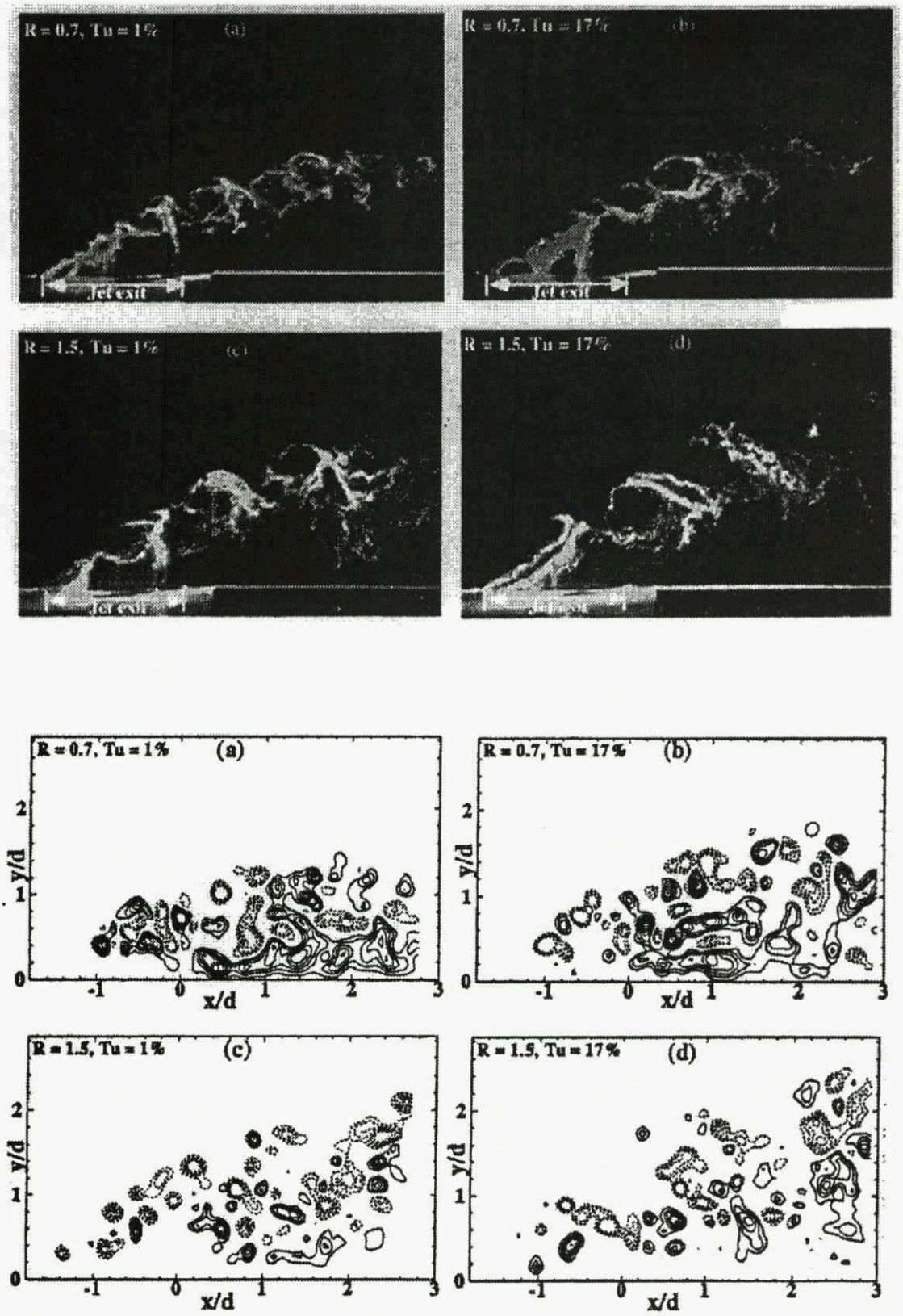


**Figure 9b. Instantaneous Vorticity Distribution (Re = 40,000)**

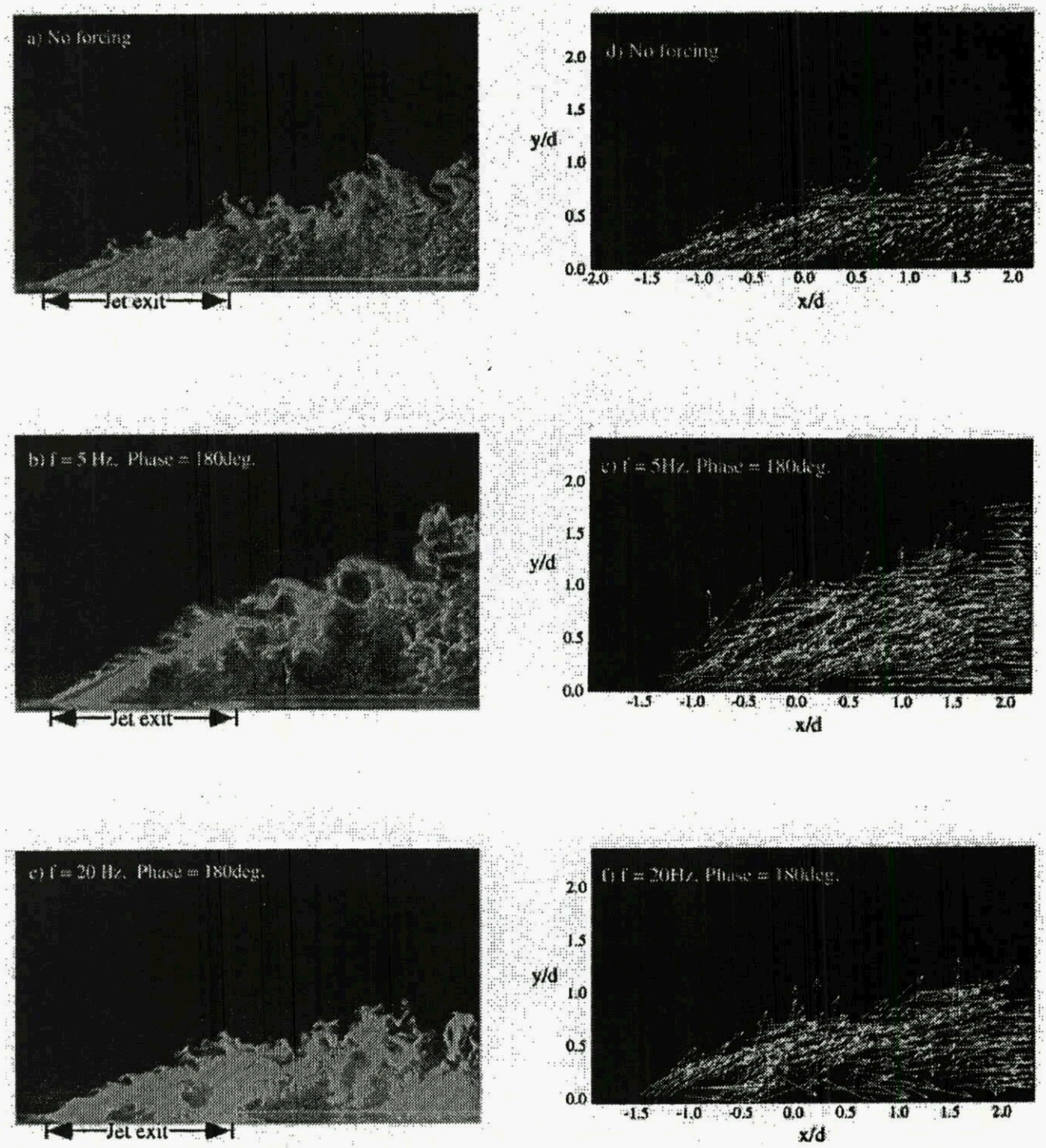


Double Exposed PIV Images

Instantaneous Velocity Distribution

**Figure 10. Periodically Forced Film Cooling Flows**
**R = 0.5, Tu = 17%, Re = 20, 000**

In the following paragraph the intensity distribution inside the beam splitting domain will be derived.
The intensity distribution inside the laser beam can be described by the gaussian function:

$$I(r) = I_0 \cdot e^{-2\cdot(\frac{r}{r_0})^2} \qquad (6.)$$

The geometry of the laser beam as well as the gaussian function suggest a computation in polar co-ordinates, whereas the integration domain (see figure 5) is more easily described in Cartesian co-ordinates.

$$I(x,y) = I_0 \cdot e^{-2\cdot\frac{x^2+y^2}{r_0^2}} \qquad (7.)$$

Integration limits:

$x_A = 0$

$x_B = \sqrt{r_0^2 - y^2}$

$y_A = r_0 \cdot \cos(\frac{\alpha}{2})$

$y_B = r_0$

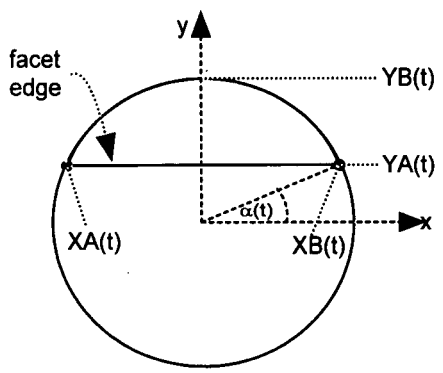


**Figure 5 Geometry of integration domain**

The intensity distribution is integrated in two circle segments, making use of the vertical symmetry.

$\beta = \frac{\alpha}{2}$ will be used for shortening.

$$P(\beta,r_0) = 2\cdot I_0 \int_{y=r_0\cos(\beta)}^{r_0} [\int_{x=0}^{\sqrt{r_0^2-y^2}} e^{-\frac{2}{r_0^2}x^2} dx]\cdot e^{-\frac{2}{r_0^2}y^2} dy \qquad (8.)$$

Since the gaussian function does not have a primitive, it has to be integrated numerically at this point. The result of the integration is the so called *error-function* erf (x).

$$\int_0^x e^{-x^2} dx = \frac{\sqrt{\pi}}{2} \cdot erf(x)$$

With the substitution $u = \frac{\sqrt{2}}{r_0} \cdot x$ the integration can be simplified to:

$$\int_{x_A}^{x_B} e^{-\frac{2}{r_0^2}} dx = \frac{r_0}{\sqrt{2}} \int_{u_A}^{u_B} e^{-u^2} du = \frac{r_0}{\sqrt{2}} \cdot \frac{\sqrt{\pi}}{2} \cdot erf(u)|_{u_B}^{u_A} \qquad (9.)$$

The new integration-limits apply to:

$u_A = 0$

$u_B = \sqrt{2\cdot[1-(\frac{y}{r_0})^2]}$

After insertion of the limits and with erf (0) = 0:

$$\int_{x=0}^{\sqrt{r_0^2-y^2}} e^{-\frac{2}{r_0^2}x^2} dx$$

$$= \frac{\sqrt{\pi}}{2\cdot\sqrt{2}} r_0 \cdot erf\{\sqrt{2\cdot[1-(\frac{y}{r_0})^2]}\}$$

At the end it has to be integrated about the ordinate:

$$P(\beta,r_0) = \sqrt{\frac{\pi}{2}} r_0 I_0$$

$$\cdot \int_{y=r_0\cos\beta}^{r_0} erf\{\sqrt{2[1-(\frac{y}{r_0})^2]}\}\cdot e^{-\frac{2}{r_0^2}y^2} dy \qquad (10.)$$

For the numerical calculation of this integral a ten point Gauß-Legendre algorithm has been used (see Press et al.[7], chapter 4).

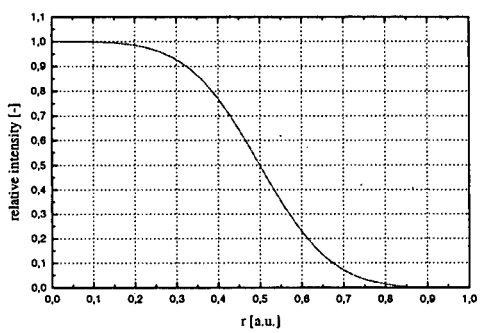


**Figure 6 Intensity decay in beam splitting domain**

Figure 6 demonstrates the rapid intensity decay within the beam splitting domain. The curve is normalised to unity.

However, light sheets generated by polygon mirrors are still of a higher quality than those generated by cylindrical lenses. Another positive aspect is the fact that the beam can be deflected with a very high frequency (in experiments up to 16 kHz were adjusted), thus allowing time resolved measurements even with cw lasers.

### 2.1.2 Galvanometer Scanner

The most attractive scanning method is galvanometer scanning. A mirror, mounted on a shaft, is driven by a magnetic field. The field can be controlled by an arbitrary command signal with the restrictions not to trespass the maximum amplitude nor frequency. The aperture angle is controlled by the signal amplitude, whereas the frequency equals that of the command signal. The maximum frequency lies in the order of several hundred Hertz, depending on the mirror inertia. In the experiments an assembly with a maximum frequency of 170 Hz was used.
The most attractive feature is the fact that the command signal can be prescribed, enabling the control of the remaining time in the probe volume.
The mirror position $\varphi$ is related to the command signal by

$$\varphi(t) = A \cdot U(t) \qquad (11.)$$

where A is an arbitrary constant, depending on the mirror driving unit. The mirror scan frequency $\omega_M$ can be expressed as

$$\omega_M = A \cdot \frac{dU(t)}{dt} \qquad (12.)$$

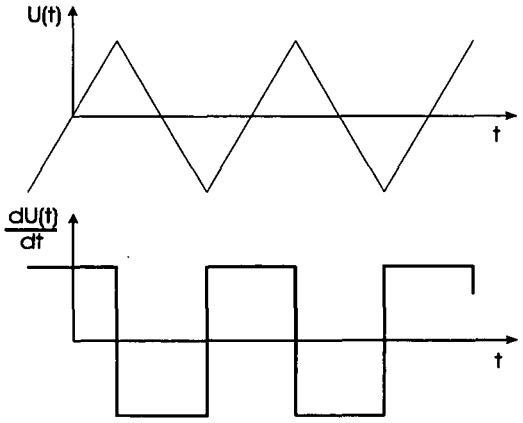


**Figure 7 Galvo Scanner Command Signal**

If the command signal is a saw tooth (see figure 7), the $\cos^2$-distribution will turn out with the same reason as in the case of the polygon mirror. The command signal has to be modified in order to achieve a constant scan velocity over the whole light sheet expanse and therefore a constant light intensity.
Any signal generator can be used, but the specific advantage of galvo scanners can only be experienced with programmable signal generators.
Another payoff is the fact that the sheet height can be adjusted to the optical arrangement by simply varying the command signal amplitude. In the experiments the maximum beam deflection was $\pm 30°$.
Equation (4.) only holds, if inertial effects can be neglected. Whenever the galvo scanner works in the proximity of the frequency limit, inertial effects in the turning points will become dominant. For this case an autocalibration routine has been setup, compensating for delays in the turning points.

## 2.2 Reflection suppression

Whenever the light sheet method is applied in turbo machines, the problem of surface reflections arises, by which the measurement accuracy is vigorously influenced. Reflected light is in general several orders of magnitude more intense than the light scattered by particles. If reflections cannot be omitted, there is a possibility to suppress them. One technique is to cover the reflecting material with a thin sheet of fluorescent painting. The first author has created this paint by mixing the laser dye rhodamine 610 in ethanol having strong absorption bands for argon ion lines.
The next step is to place the appropriate laser line filter in front of the camera, cutting all wavelength but the laser line. When the light touches the painted surface, the reflections will be wavelength shifted and thus filtered by the laser line filter.

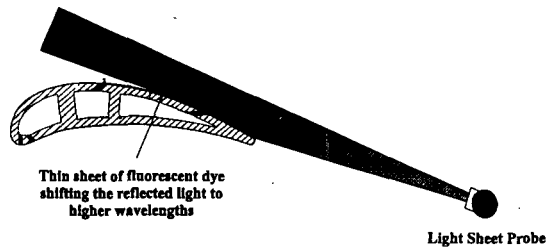


**Figure 8 Reflection suppression by fluorescent paint**

Another wide spread suppression technique is the use of black or soot painting. In figure 10a it can be seen that the decision if to use fluorescent paint, is strongly angular dependant.

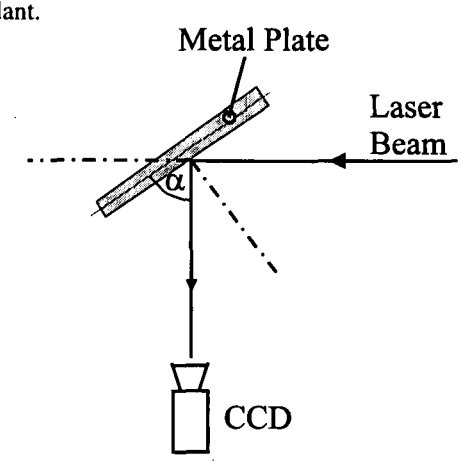


**Figure 9 Experimental Setup**

The study has been carried out with a metal plate, covered with 3 different surfaces (see figure 9). The first was the blank metal, the second was a soot painting and the third was the fluorescent paint. The laser beam as well as the camera were mounted stationary. While turning the plate, the scattered signal was recorded by the ccd. It turned out that for large angles $\alpha$ soot painting is recommended.

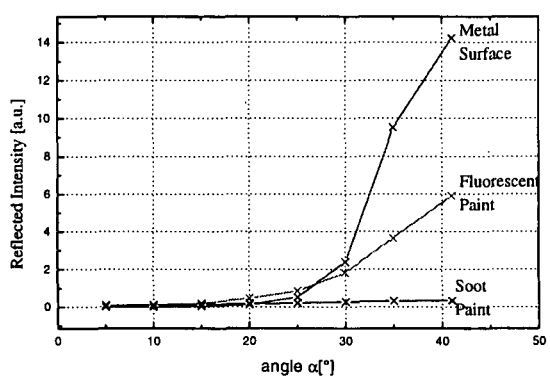


**Figure 10a Angular dependance of reflection suppression**

As can be seen in figure 10b, there exists a break even point when $\alpha$ equals 40°.

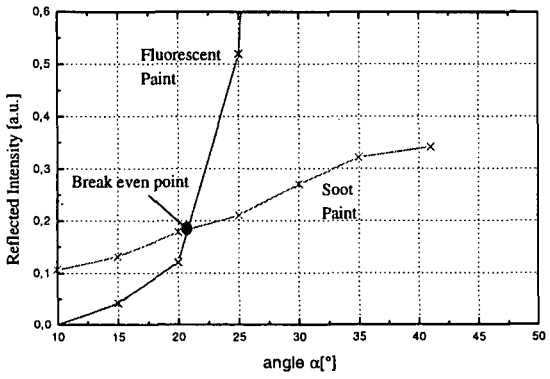


**Figure 10b Break even point in suppression efficiency**

When turning to smaller angles, the filtering capacity of the fluorescent paint turns out to be nearly 100% whereas the efficiency of the soot suppression remains nearly unchanged.
In light sheet experiments, the reflection angle $\alpha$ is very small in general. Therefore fluorescent paint is recommended.

### 2.3 Optimum particle diameter

Particles used in marker nephelometry should meet the following requirements:

1. particles should be small in order to follow the flow
2. the imaginary part of the index of refraction should be zero, yielding absorption free scattering

The scattering efficiency increases with increasing particle diameter. From the viewpoint of signal to noise ratio larger particle diameters are preferred, leading to the search of a compromise between flow following and signal intensity.

Three different domains can be distinguished:

1. Rayleigh Scattering
2. Mie Scattering
3. Geometrical Optics

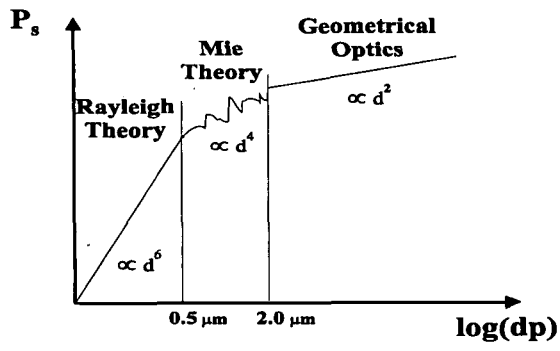


**Figure 11 Scattering Theories**

The fact that in the diameter range of the Mie theory the scattering cross section is very irregular but approximately proportional to the fourth power and in geometrical optics to the square of the diameter, leads to the conclusion that an optimum diameter must exist for maximum scattering efficiency from a given fluid volume, since the particle volume increases with the third power of $d_p$.

If a given fluid volume is atomised, it is supposed for computational convenience that all $N$ particles possess the same diameter $d_p$. The whole fluid volume will than be the sum over all particle volumes:

$$V = N \cdot \frac{\pi}{6} \cdot d_p^3 \qquad (11.)$$

The scattered light primarily depends on the particle diameter and on the viewing angle. In general, the collecting optics are placed normal to the light sheet. For the a viewing angle range from 85° to 95° the following approximation holds for $\lambda = 514.5nm$:

$$c_{sca} = a_0 \cdot d_p^{\,a_1 + a_2 \log(d_p)} \qquad (12.)$$

with:

$a_0 = 0.0608649 \mu m^2$
$a_1 = 2.263$
$a_2 = -1.376$

This approximation was received by performing a Mie computation, using the algorithm given in Bohren [4].
With $I_L$ as the laser intensity and $c_{sca}$ as the scattering cross section, the total scattering power will be:

$$P = I_L \cdot c_{sca}(d_p) \cdot N \qquad (13.)$$

The maximum scattering power from a given fluid volume can now be estimated by differentiating equation (13.) with respect to $d_p$.

$\frac{dP}{d(d_p)} \overset{!}{=} 0$, yielding an optimum diameter of

$$d_{opt} = 1.85 \mu m.$$

i.e. particles with a diameter of $d_{opt}$ have the highest scattering efficiency for a given fluid volume.

### 2.4 POLARISATION

Laser light is highly polarised. In general argon ion lasers are specified with a polarisation ratio of at least 100:1. Theoretically, Mie scattered light conserves the polarisation property of the incident beam. But this is only true for ideal dipole scatterers (see figure 12).

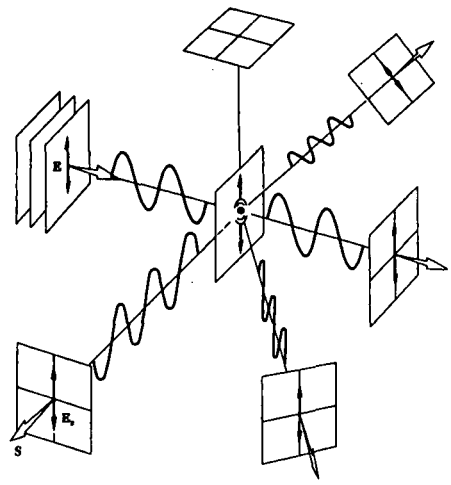

**Figure 12 Conservation of polarisation in scattering process (taken from Hecht [8])**

In practical applications there is usually a range of particle diameters more or less narrow, depending of the quality of the particle generator. But even a particle ensemble will conserve polarisation at least partly.
Polarisation influences the intensity in the vertical direction of the light sheet. Experiments have shown that the influence is rather small compared to the influence of the scattering direction. It turned out that the maximum difference between parallel and vertical polarisation was in the order of 10 % (see figure 13 for experimental results).

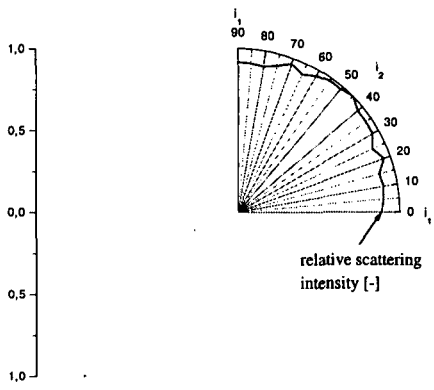


**Figure 13 Influence of polarisation on the scattered intensity**

Although it is possible to correct the image numerically by correlating with reference images, it is recommended to prevent the polarisation effect by introducing a $\lambda/4$-plate into the beam path.
If mounted properly, this should prevent any polarisation influence in the raw image.

## 2.5 Extinction, a further error source

Whenever light is scattered by particles, the incident light will be attenuated. This effect, called *extinction* comprises absorption and scattering. The loss of intensity along a line can be formalised by the Lambert-Beer-law in differential form:

$$dI(x) = -(\sigma_{abs} + \sigma_{sca}) \cdot c(x) \cdot I(x) dx \qquad (14.)$$

with $\sigma_{abs}$ as absorption coefficient and $\sigma_{sca}$ as scattering coefficient. Supposing $\sigma_{abs} = 0$ and constant concentration in the field $c \neq f(x)$ yields the well known Lambert-Beer law in integral form:

$$I(x) = I_0 \cdot e^{-\sigma x} \qquad (15.)$$

i.e. in the case of homogeneous particle distribution the intensity decay is of exponential type.
The first author has implemented a technique to compensate the extinction effect for arbitrary particle distributions.
The basis of the correction algorithm is a so called *shooting method.* Other methods- such as relaxation can also be used but as mention Press et al. [7] shooting should be preferred, if the convergence property is satisfying.
Equation (14.) denotes a first order ordinary differential equation. In case such an equation has to fulfil boundary conditions at more than one point, the problem is called a *two point boundary value problem.*
In the case of light sheet measurements the boundary conditions are given by the laser intensity on both sides of the probe volume.
Shooting means starting from the left boundary and integrating the differential equation until the right boundary is reached (see figure 14).

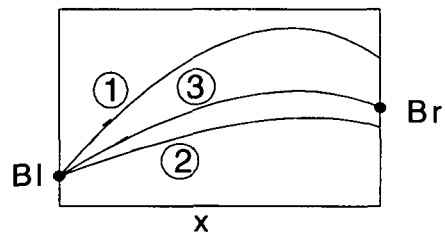


**Figure 14 Shooting Method**

### 2.6.1 Implementation of a correction algorithm

It is necessary to measure the integral extinction along each line in the image. This means that apart from the flow image there must be a second camera or line array saving the intensity profile.
This knowledge must be correlated with the content of the mixing image. The algorithm will be explained for a single line. Each line in the image must be treated alike.
The first step is the choice of an appropriate starting vector.

$$c_0(x) = \frac{gv(x)}{\max(gv(x))} \qquad (16.)$$

gv(x) are the extracted grey values from the flow image. $c_0(x)$ is already the required start vector, with a definition range between 0 and 1. In a first step the local intensity of the laser beam must be computed. Therefore the local concentrations as well as the intensity at both boundaries are required. The start vector for local laser intensity is set arbitrarily to a value of 100.
The measurement volume is divided into cells where each cell has the size of a pixel.
As the laser beam enters the chamber, it will be attenuated progressively in each cell. The degree of attenuation

depends on the local particle concentration. Equation (14.) can be discretised by:

$$I_{i+1} = I_i - k \cdot c_i \cdot I_i \qquad (17.)$$

The free parameter k has to be assigned an arbitrary starting value and will be changed inside the iteration algorithm (see figure 15).

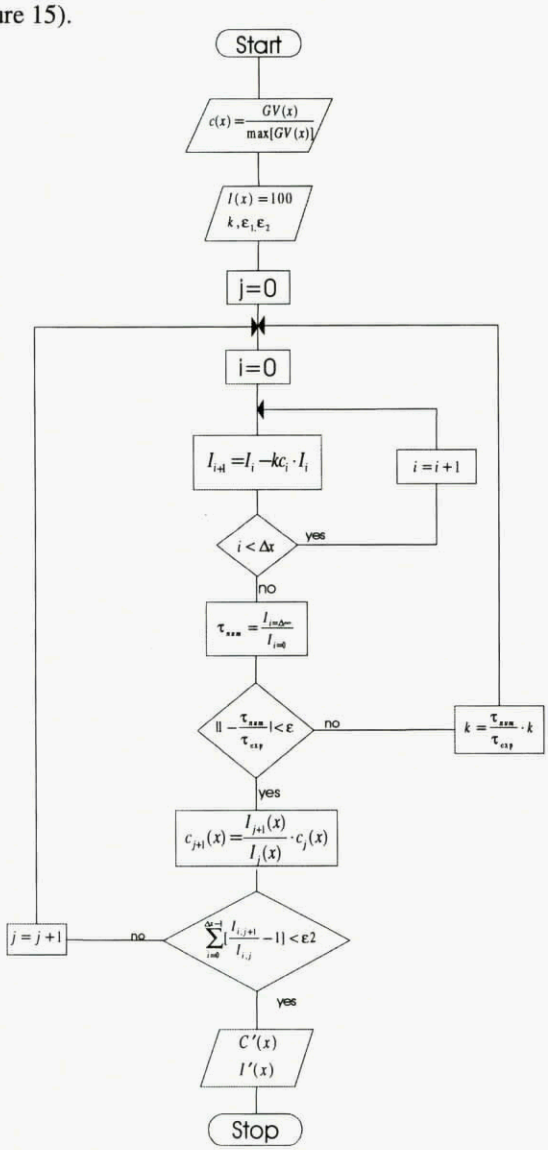


**Figure 15 Shooting method, flow chart**

The local concentrations $c_i$ are taken from the starting vector $c_0(x)$. With eq. (17.) the new intensity vector is defined. The intensity at the right boundary is $I_L$. Now, the numerical transmission $\tau_{num}$ can be computed.

$$\tau_{num} = \frac{I_L}{I_0} \qquad (18.)$$

If the numerical transmission is higher than the transmission in the experiment (case 1 in figure 14), the free parameter k has to be reassigned in a way that after the next iteration numerical and experimental transmission will lie closer together.

Therefore a *score function* is introduced by

$$k_{j+1} = \frac{\tau_{num}}{\tau_{\exp}} \cdot k_j \qquad (19.)$$

where j is the iteration step.

The parameter k is altered, until

$$\left|1 - \frac{\tau_{num}}{\tau_{\exp}}\right| < \varepsilon_1 \qquad (20.)$$

If this is done, the concentration vector c(x) can be reassigned by

$$c_{i,j+1} = \frac{I_{i,j+1}}{I_{i,j}} c_{i,j} \qquad (21.)$$

i represents the spatial co-ordinate, whereas j is the iteration index. Now, the concentration vector is changed and a new intensity vector I(x) can be computed, using eq. (17.). In general, eq. (20) will no longer hold after the iteration so that a new iteration of k becomes necessary.

If the method converges, neither the intensities nor the concentrations will change after a few iterations. At that time, the concentration values are corrected for extinction influence.

### 2.6.2 A priori estimation of the free parameter k

Parametric studies have turned out that an a priori estimation of the free parameter k is possible, if one knows the overall length of the measurement volume as well as the integral transmission:

$$k_0 = (-0.29 + 2.335 \cdot e^{-\frac{\tau - 0.09685}{0.46241}}) \cdot \Delta x^{-1} \qquad (22.)$$

$\Delta x$ has to be given in pixel units.

### 2.6.3 Convergence criteria

The method converges rapidly with an upper limitation of 80% extinction. This amount should never be reached in the pure scattering experiment, but the shooting method could also be used, if one wanted to correct images with a high degree of absorption ($\sigma_{abs} >> 0$), where extinction is a predominant problem.

As will be shown in figure 21, extinction never occurs without an effect called *secondary* or *multiple scattering*. This is why experiments with a high degree of extinction but without multiple scattering cannot be executed.

### 2.6.4 Testing with synthetic images

In order to test the potential of the shooting method, synthetic images have been computed, based on known concentration distributions. It could be demonstrated that a quasi perfect restoration could be obtained after a couple of iterations.

Two different test images have been examined:

1. homogeneous concentration distribution
2. 3 separated gaussian peaks with the same amplitude

In the first case of homogeneous concentration distribution, the Lambert-Beer law (15.) can be applied in integral form.

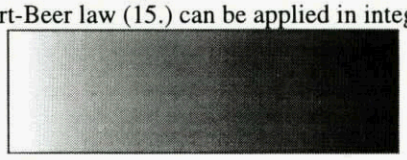

**Figure 16 Test image, exponential decay**

Figure 16 shows the test image. An integral extinction value of 50% was chosen.

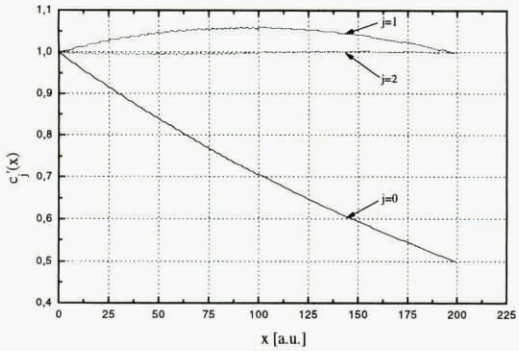


**Figure 17 Correction of exponential attenuation**

Figure 17 shows the correction process. j=0 shows a horizontal profile at iteration step 0 (raw image). After the first iteration (j=1) the corrected concentration distribution is symmetric. The estimate for the maximum amplitude is 6% too large. After the second iteration (j=2) the corrected concentration already equals the real concentration distribution, being supposed uniform.

The second test case is far more challenging, thus showing very good results.
Three equally spaced gaussian peaks are supplied in the test image, shown in figure 18.

**Figure 18 Test image**

The amplitude of the underlying concentration is equal for all peaks.

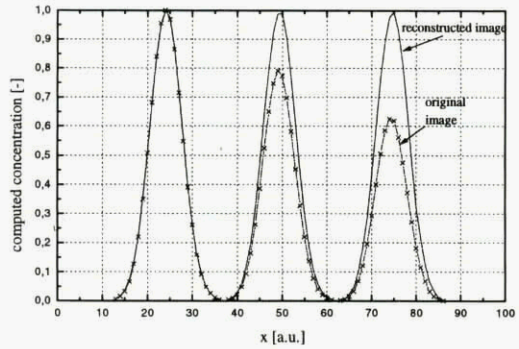


**Figure 19 Correction of 3 equally spaced gaussian intensity peaks**

From figure 19 can be deduced that the concentration distribution has been reconstructed completely.
Figure 20 shows the reconstructed image.

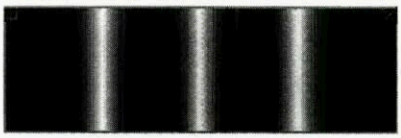

**Figure 20 Reconstructed image**

Applying the correction algorithm to the experimental data leads- depending on the seeding density- to a significant increase of the measurement accuracy.

## 2.7 Multiple Scattering

The most challenging difficulty in scattering experiments is the correction of secondary scattering effects.
Secondary scattering denotes the facts that particles can be light sources for adjacent particles. This effect is concentration dependant. The existence of multiple scattering has been proved in a number of experiments.

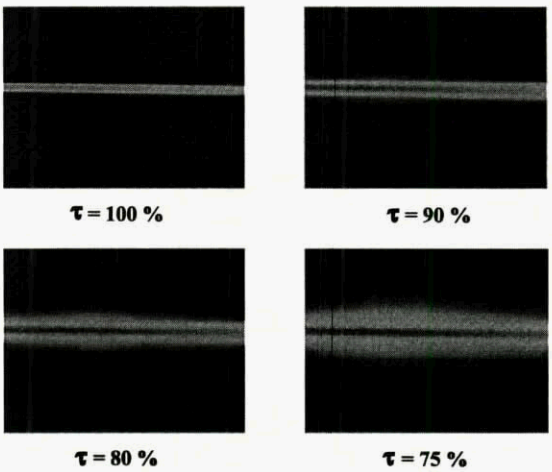


**Figure 21 Multiple Scattering Corona around Stationary Laser Beam**

Figure 21 shows a stationary laser beam in a laboratory combustion chamber with homogeneous seeding. The incident beam entered the plane on the left side and left after a total distance of 15 cm. On the outlet side the transmission ratio $\tau$ was measured by a photo diode.
The chamber was seeded with four different particle loads. In the upper left image no extinction could be measured. The beam was thin. For the following experiments the seeding was intensified successively. On the upper right image the overall extinction was 10 % and a small increase in the beam thickness can be recognised. In the lower column both images show an increase in radial direction. But this expansion is not constant along the beam. In the first quarter of the path the expansion increases, due to the strong secondary scattering in forward direction. After reaching the maximum diameter the expansion decreases, caused by the coexisting extinction effect on the centreline.

Another experiment is shown in figure 22. The image shows a cross section of a jet in crossflow, 2d downstream of the injection. The light sheet was obscured at two points by a light stop with a diameter of 4 mm.

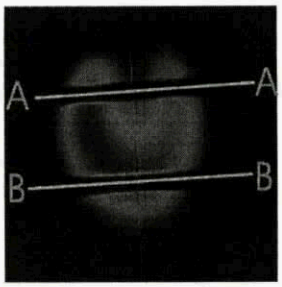


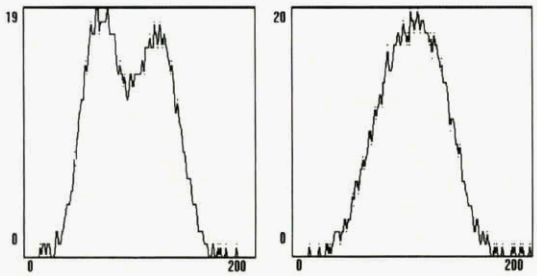


Intensity Profile A-A  Intensity Profile B-B

**Figure 22 Multiple Scattering**

Under the assumption that secondary scattering effects can be neglected, the intensity profiles A-A and B-B can only show the camera dark current. At least the signal must not be correlated to the surrounding medium.
Even though, the profiles show a highly correlated signal compared to the surrounding medium. The amplitude of the peak in the dark zone can used as an estimate for the influence of MS. The maximum intensity in the proximity of the dark zone was about 200 counts. This equals a maximum influence of 10% under realistic conditions.

A number of different methods have been examined for the correction of multiple scattering, however none of them has revealed satisfying results, yet. However, in spite of this uncorrected error source all the other optimisations lead to a maximum measurement error of less than 10%.

## 3. APPLICATION IN AN RQL COMBUSTION CHAMBER

First concentration measurements with the light sheet method were carried out in the mentioned RQL combustion chamber under atmospheric, non-preheated condition. Only the secondary flow was seeded. Figure 23 shows the upper section of the quench-region of the combustion chamber, where three rows of secondary air jet holes are prepared for quick downmixing. . The axial sheet was positioned parallel to the flow direction.

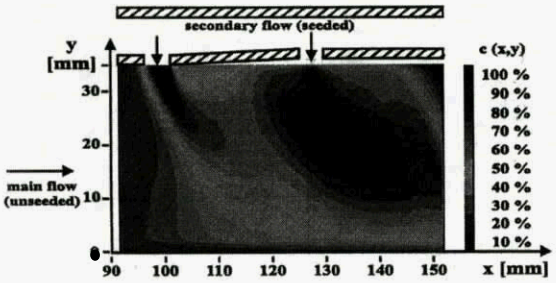


**Figure 22 Isothermal Mixing in RQL chamber**

The core of the jets of the first and the third row of secondary air jets can be seen clearly. The penetration of the secondary air jets is strong enough to ensure a satisfactory mixing in the whole quench zone.
Considering that this result could be collected in a very short time, the light sheet method has proven its qualification for development tests and is at this time used as a tool for the optimisation of mixing configurations for combustors.

## CONCLUSION

A light sheet method for quantitative concentration measurements has been treated. Optimisation methods have been developed. Laboratory experiments have indicated that the measurement accuracy at the present stage is less than 10% the largest part of which is due to the multiple scattering phenomenon. The actual research is focused on testing correction algorithms.
Experimental results from Griebel [1] and [2] showed a good agreement between mixing behaviour in the reacting and non-reacting experiment, indicating that the light sheet method is an appropriate tools for the pre-design of modern combustion chambers.

## ACKKNOWLEDGEMENTS
Mr. Thomas Schmidt, Fachhochschule Köln, is gratefully acknowledged for his programming support.

## REFERENCES

[1] **P. Griebel**: Untersuchung zur schadstoffarmen atmosphärischen Verbrennung in einem Fett-Mager-Brennkammersektor für Flugtriebwerke
Doctoral Thesis Ruhr-Universität Bochum, to be published

[2] **P.Griebel, M.Fischer, E.Magens, H.Nannen, A.Winandy, A.Chrysostomou, U.Meier, W.Stricker**: Experimental investigation of an atmospheric rectangular rich quench lean combustor sector for aeroengines, ASME 97-GT-146, 1997.

[3] **H.C.van de Hulst**: Light Scattering by Small Particles, Chapman and Hall, 1957

[4] **C.F.Bohren, D.R.Huffman**: Absorption and Scattering of Light by Small Particles, John Wiley and Sons, 1983

[5] **M.Kerker**: The scattering of light and other electromagnetic radiation, Academic Press, 1969

[6] **B.Ruck**: Lasermethoden in der Strömungsmeßtechnik, AT-Fachverlag, Stuttgart,
1990

[7] **W.H.Press, S.A.Teukolsky, W.T.Vetterling and B.P.Flannery**: Numerical Recipes in C, chapter 17

[8] **E.Hecht**: Optik, Addison-Wesley, chapter 8

Paper 48
Author: Voigt

Q: Wernet

Does the particle size affect the location of the minimum in the extinction/multiple scattering plots that you showed ?

A: I tried to show the 4 dominant influencing parameters separately. The diagram that you ask for is the line profile that appears, when you consider only the scattering direction. In this diagram the minimum strongly depends on the particle diameter. In the laboratory I measured that the minimum appeared at approximately 110°, although in general one expects the minimum to appear at 90°. However the multiple scattering effect also depends on the particle diameters, since its influence is proportional to the angular intensity distribution (phase function).

In the plane which is perpendicular to the aforementioned, the polarisation state has to be taken into account.

Q: Wernet

The sample graph that you showed in your talk had a long path of the light sheet through the seeded fluid. For the case that you showed, it would appear that the light sheet intensity does not change significantly across the actual measurement region.

Would it be possible to adjust particle size so that the change in intensity of the light sheet is minimised across the actual measurement region?

A: If I want to correct the flow field image for beam attenuation, I have to record the whole flow field, starting at the point where the beam enters the measurement volume and including the location where the beam leaves the measurement volume. The whole path that undergoes extinction has to be taken into account.

# Application of Two-Color Digital PIV for Turbomachinery Flows

**S. Gogineni, J. Estevadeordal, B. Sarka, and L. Goss**
Innovative Scientific Solutions Inc.
2786 Indian Ripple Road
Dayton, OH 45440-3638, USA

**W. Copenhaver**
Aero Propulsion and Power Directorate
WL/POTF, Bldg 18
Wright Laboratory, 1950 Fifth Street
Wright-Patterson AFB, OH 45433, USA

## ABSTRACT
The potential application of a Two-Color Digital-Particle-Image-Velocimetry (DPIV) system to turbomachinery-type flows was evaluated. This system records double-exposed color images onto a single CCD sensor (3060 x 2036 pixel) and eliminates the photographic-film processing time and subsequent digitization time as well as the complexities associated with conventional image-shifting techniques. The system was calibrated using simulated known displacements and gradients and was applied to the flowfield in a 20-in.-dia. axial fan. DPIV implementation issues such as optical access, seeding strategies, and blade-passage synchronization related to turbomachinery flows were explored. Instantaneous velocity measurements were made at different spanwise locations. These measurements provided instantaneous information on the blade wake region, the flow separation off the blades, and the interaction between successive blades and also allowed a greater understanding of the impact of these phenomena on turbomachinery performance.

## 1. INTRODUCTION
Future Air Force missions will require air-breathing engines to operate at twice their current thrust-to-weight capabilities. The turbomachinery components of these engines establish the ability of the engine to generate thrust and also account for the greatest percentage of weight in the engine. To meet the thrust-to-weight goals, turbomachinery weight must be reduced and performance increased by the use of thinner or even hollow blades, increased loading, increased tip speeds (flow Mach number), and decreased blade-row spacing. These factors individually cause increases in flowfield unsteadiness and in conjunction create significant design challenges.

Although turbomachinery performance is governed by *unsteady* fluid flows, steady design methods are currently being used to develop turbomachinery, with the lack of basic knowledge being compensated by extensive empirical correlations. Advanced laser-based diagnostic techniques are very useful for providing quantitative evidence of unsteady effects on the blade-passage scale, for identifying the relative importance of length and time scales of unsteady-flow phenomena in turbomachinery, and for providing future improvements in technology based on the recognition of unsteady phenomena. Two pointwise velocimetry techniques that have been applied to compressor research are Laser Transit Anemometry (LTA) and Laser Doppler Velocimetry (LDV). However, issues associated with low data rates (long run times), slow mapping due to the pointwise nature of these techniques, and measurement uncertainties associated with unsteady flowfields make these methods difficult to apply outside of the basic-research environment. Particle Image Velocimetry (PIV), an instantaneous two-dimensional planar velocimetry technique, offers the potential to investigate the effect of unsteady flowfields on blade loading, blade structural response, loss production, wake transport, wake attenuation, wake-induced boundary-layer transition, and flow separation if the obstacles to its application in a transonic turbomachine can be overcome.

PIV has been used for a number of years to measure velocity distributions in planar cross sections of aerodynamic flowfields.[1] One of the difficulties involved in implementing this technique is the 180-deg. directional ambiguity which results from the inability to determine the temporal sequence of the particle pairs. Several techniques have been developed to resolve this ambiguity; most involve imposing a shift between consecutive image exposures by means of scanning or rotating mirrors, pulse tagging, calcite crystals, or polarizing beam splitters. Recently, cross-correlation cameras were introduced to resolve the directional ambiguity. In early experimental approaches involving the PIV technique, the particle images were recorded on photographic film. However, this type of recording is time-consuming because of the need to wet-process the film before digitization and subsequent computer processing. For the high-cost turbomachinery test environment, wet-processing makes PIV prohibitive. In most cases tests cannot be repeated at a later time after wet-processing reveals incomplete data. This disadvantage can be overcome by recording the particle images directly onto a two-dimensional CCD array. This approach has been recognized by several investigators and successfully applied to a wide variety of flows.

Extension of the two-color PIV technique to include CCD cameras has been hampered in the past by the lack of commercially available, high-resolution, color CCD camera systems. Because of recent developments in high-resolution color CCD cameras, the difficulty in utilizing them for two-color PIV has significantly decreased. The two-color DPIV system[2] implemented in the present experiment records the color images onto a single, high-resolution (3060 x 2036 pixel), color CCD sensor and has the following advantages: 1) the processing time and subsequent digitization time of color film are eliminated as are the complexities associated with conventional image-shifting techniques, 2) higher data yields and signal-to-noise levels are attainable, and 3) the method is suitable for harsh test environments. This new technique was successfully applied to a wide variety of flows (e.g., periodically forced flat-plate film-cooling flows with high freestream turbulence,[3] supersonic turbulent boundary layers involving pressure gradients,[4] non-circular coaxial jets,[5] and vortex-flame interactions[6]). The results demonstrated the resolution necessary for exploring the flow features in complex flowfields.

*Paper presented at an AGARD PEP Symposium on "Advanced Non-Intrusive Instrumentation for Propulsion Engines", held in Brussels, Belgium, 20-24 October 1997, and published in CP-598.*

Several investigators have explored the application of various types of PIV techniques to unsteady flowfields in rotating machines.[7-11] In the present paper we describe the potential application of two-color digital PIV for turbomachinery flows. As a test case a 20-in.-dia. axial fan was used to explore some of the challenges of turbomachinery flow measurement and to capture salient flow features such as the blade wake region and the interaction between flows from successive blades. The two-color digital PIV system was calibrated using simulated known displacements and gradients. In addition, a detailed uncertainty analysis of the two-color DPIV system was conducted using the numerical simulations.

## 2. DPIV IMPLEMENTATION ISSUES RELATED TO TURBOMACHINERY FLOWS

Some of the issues involved in implementing the PIV technique for turbomachinery flows are 1) optical access, 2) seeding strategies, 3) minimization of surface glare, 4) blade-passage synchronization, and 5) measurement-frame positioning.

### 2.1 Optical Access

Careful consideration must be given to the need of considerable optical access (transmitter and receiver portions) for a PIV instrument and possible interference with the aerodynamic and aeromechanic performance of the test apparatus. The transmitter must deliver the laser light sheet to the area being studied--typically, in embedded stages, between the rotor blades and perpendicular to the receiver optics. Because the rotor blades are staggered, the laser light sheet must enter the rotor at an angle. Figure 1 shows a generic rotor-blade setup. Several options are available for introduction of the laser light sheet into the rotor casing.

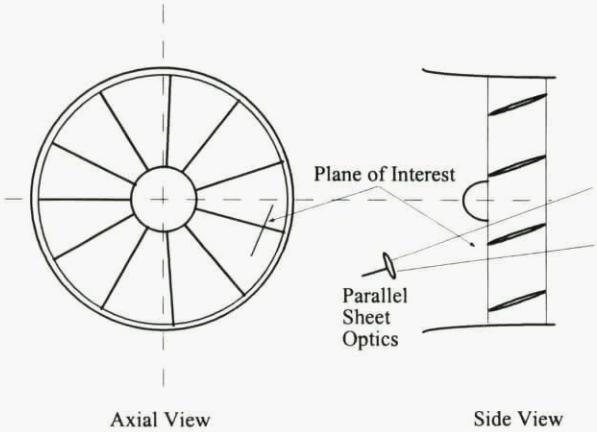


Fig. 1 Schematic of the generic rotor-blade setup.

A uniform-intensity, parallel light sheet that illuminates an entire blade passage requires a combination of lenses having a diameter approximately equal to the distance between adjacent rotor blades. This lens arrangement should be placed far upstream of the rotor to ensure minimum contamination of the flowfield.[12] This approach would not be possible for a turbomachinery blade row that has other blade rows upstream and downstream of it. A second approach would be to use an expanding-beam or fan approach to illuminate the passage between adjacent blades. This approach permits the use of substantially smaller optics that can be built into a fiber-optic delivery system and inserted between blade rows. The drawback of this system is that the fanning light sheet formed from these optics illuminates not only the passage between adjacent blades but also the blades themselves. This can lead to excessive glare which can significantly hamper attempts to make measurements near the blade surface. Brendel[12] suggested that a scanning wand be employed. This rotating prism coupled to a fiber-optic delivery system would deliver the light sheet in the desired area without having it hit the blade surfaces. This approach, however, requires the use of a continuous-wave (cw) laser for formation of the scanning light sheet. With the small-size particles required in the PIV technique for tracking the flow, a scanning cw laser would be impractical. The optimum solution to this problem would be to use a fiber-optic-based fanning light sheet in conjunction with high-powered lasers and to take steps to minimize the effects of glare.

Anderson et al.[13] demonstrated the possibility of providing a fiber-optic-based laser-beam delivery system from Nd:YAG lasers. They used several individual fibers (bundles) rather than a single fiber for the transmission of high-peak-power pulses (> 20 mJ) from Q-switched and frequency-doubled Nd:YAG lasers. This system significantly reduced the compromise that takes place between the maximum transmittable power and the quality of the output beam. This type of fiber-optic-based laser-sheet delivery system, although not required for this study, can be employed in either upstream or downstream locations between blade rows or, in the case of highly curved blades, in both locations.

### 2.2 Seeding Strategies

For successful measurements in complex high-speed unsteady air flows, selection and implementation of the proper seeding strategy is a major factor. The seeding particles must be extremely small (typically < 1 μm) for tracking accelerations in the fluid (air) effectively and avoiding the consequences of viscous and inertia forces. These particles must also be efficient light scatterers to ensure exposure of the recording media. Minimization of particle agglomeration and assurance of uniform distribution are also important factors in seed-particle selection. The flammability of the seeding material and the risk of exposure of personnel to hazardous concentrations of the seeding particles must also be assessed. Another important factor is the cost and availability of the seeding material. The amount of seeding required in high-mass-flow facilities limits the choice to materials available in large quantities at low cost.

One possible method of seeding in turbomachinery applications is a smoke arrangement normally used in theatrical presentations. In this system the particles are produced when pressurized fluid passes through a heat exchanger where it is heated to a temperature near its vaporization point. The heated and pressurized liquid is discharged through a nozzle, causing it to vaporize as the pressure drops. As the vapor mixes with cooler ambient air, an aerosol or fog consisting of very fine particles is created. Tisserant and Breugelsmans[9] implemented this type of system and noted that there is a tendency for the particles to condense onto the blade surface and produce an oil film that smears onto the window under the action of centrifugal forces. This led to their use of a shutter system to protect the receiver window. They also examined incense smoke consisting of solid particles; however, its production requires a combustion process and generates strong odors as well as nicotine oil which causes coalescence. This coalescence affects the particle-size distribution because larger particles are generated; thus, seeding with glycerin particles is preferred. Bryanston-Cross and Epstein[8] evaluated the type

of seeding particles for turbomachinery applications and concluded that gonish particles with a particle distribution of 200 - 400 nm dia. are suitable for use in high-temperature environments. Although styrene particles with 500 nm dia. showed no agglomeration, they melted at temperatures > 100° C. For the present study particles generated from a mixture of glycerin and water were chosen for seeding.

### 2.3 Minimization of Surface Glare

Excessive glare that can significantly hamper attempts to make measurements near the blade surface can be minimized using the following approaches. The first approach involves shifting the particle-scattering wavelength away from the laser wavelength using fluorescing dyes. Rhodamine 640 added to the glycerin liquid, when excited with a Nd:YAG laser (532 nm), will fluoresce at ~ 610 nm. A wavelength shift would allow the use of a simple bandpass filter to reject scattering at the laser wavelength. The short fluorescence lifetime of the laser dye will minimize blurring effects, and its high quantum efficiency will result in strong signal levels. The second approach is to coat preformed alumina or titanium-dioxide particles with a concentrated Rhodamine 640-ethanol solution. When dried, the coated particles could be used for wavelength-shifted DPIV. This may be necessary to minimize coating effects associated with the glycerin seeding technique. The third and most simple approach chosen for this study is to coat the blade surfaces with black paint. Although this approach does not completely eliminate the problem, it does minimize the surface-glare influences.

### 2.4 Blade-Passage Synchronization

For making successful measurements in turbomachinery applications, the DPIV instrumentation must be synchronized with the compressor-blade position. In conventional PIV methods the camera shutter is synchronized with the laser pulses to assure that both exposures are captured on the image. For turbomachinery applications this process must be phase locked with the blade passage. For this study blade-passage synchronization was achieved with a diode laser and a photodiode. The photodiode senses dropout in the diode laser signal when the blade blocks the beam. This signal dropout is used as the trigger for the DPIV system. For this study no attempt was made to capture a specific blade passage. This would require additional information on blade location relative to the shaft rotational position. For high-speed turbomachinery, blade-passage frequencies are as high as 20 kHz (50-μs period). In these situations, synchronization of all components must be controlled at levels of 5 μs or less. For this study the blade-passage frequency was on the order of 2 kHz, requiring synchronization accuracy of 50 μs.

### 2.5 Measurement-Frame Positioning

For turbomachinery applications, velocity data obtained within the blade passage is typically resolved in the rotating-blade reference frame. For pointwise measurements, as with LDV, this requires only that the radial location of the "probe volume" be known to ascertain radial sheets of relative velocity data. Since radius is required to determine the blade relative velocity, pointwise measurements made on a constant radius lend themselves to vectorial conversion to the relative frame. Since DPIV measurements are made on a flat (not constant-radius) plane and the blade relative motion is not constant along the plane in the blade pitchwise direction, care must be taken to ensure that the plane is tangent to a chosen minimum radius of interest. If assurances are made that the plane is parallel to the axial centerline of the turbomachine then the blade relative motion can be assumed to be constant along the plane in the axial direction.

## 3. EXPERIMENTAL SETUP AND PROCEDURES

### 3.1 Experimental Facility

The schematic of the experimental facility is shown in Fig. 2. A rectangular box (8 ft. x 4 ft. x 4 ft.) was fabricated for the settling chamber. This box contains honeycomb and coarse and fine screes for flow management. The settling chamber and the fan duct were connected via a convergent section.

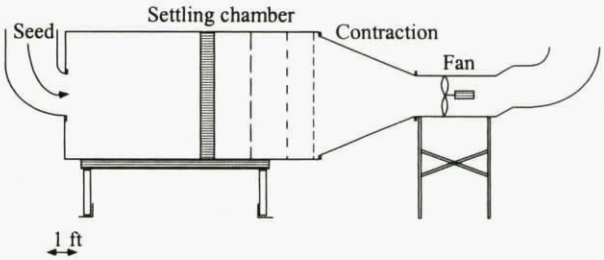


Fig. 2 Schematic of the experimental facility.

A commercially available 20-in.-dia.-duct axial fan was considered for the investigation, and the original fan was replaced with an automotive engine-cooling fan [Fig. 3(a)]. This fan has 11 equally spaced forward-swept blades, and the shape of each blade is an airfoil having a bulbous leading edge. The tip radius is 9.92 in., and the hub radius is 3.64 in. The blades are made from injection-molded nylon and the hub from aluminum. The axial deflection of this fan is < 0.3 in. at 2500 rpm. Both the transmitting and receiving windows [Figs. 3(b) and 3(a)] were made of Plexiglas. High-impact 0.25-in.-thick polycarbonate sheet was used for making these accesses. Both windows were preformed to match the radius of the test section and clamped with an aluminum frame formed to the same radius. This port was made sufficiently large for visualizing the flow from blade to blade and the wake from the blade trailing edge. Instantaneous velocity measurements were made at three spanwise locations [closer to the hub, tip location, and between hub and tip location]; results are presented only for the tip and the mid-region locations. The laser system and the CCD camera were

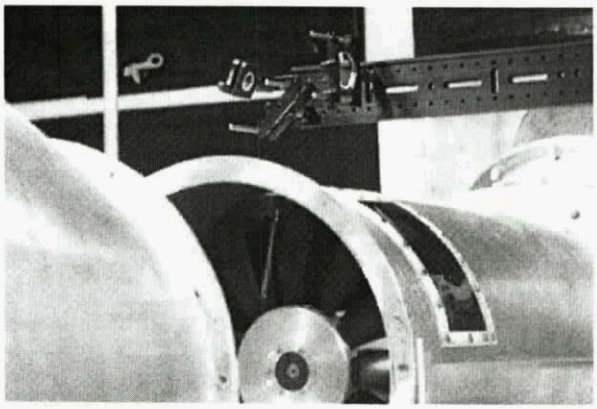

Fig. 3(a) Photograph of the 20-in.-dia. axial fan.

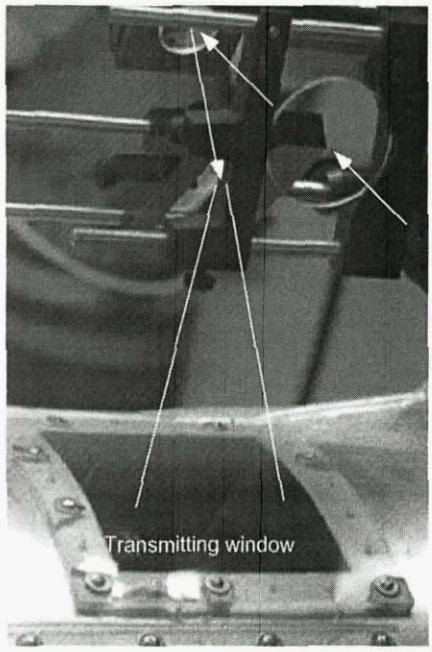


Fig. 3(b) Photograph of the transmitting window.

synchronized to the blade position for eliminating double-image and uncaptured-image problems.

### 3.2 Two-Color DPIV System

The two-color DPIV system (Fig. 4) uses color for temporal marking of the seed particles in the flowfield. The green (532-nm) laser output from a frequency-doubled Nd:YAG laser and the red (640-nm) laser output from a Nd:YAG-pumped dye laser are combined by a dichroic beam splitter and directed through sheet-forming optics. The laser-sheet energy is typically 60 mJ/pulse, with a thickness of ~ 1 mm at the test section. The temporal delay between the two lasers is a function of the gas velocity, optical magnification, and interrogation spot size. In the present experiment, the time delay between the two lasers was set at 20 μsec. The flow is seeded with sub-micron size particles generated from a mixture of glycerin and water. The scattering from these seed particles is recorded on a CCD sensor.

CCD sensors are inherently monochromatic, which means that the individual photosites cannot distinguish the color of the light. For capturing color on the CCD sensor, digital-camera designers have developed a number of schemes.[14] One of the simplest approaches is to mount an RGB filter wheel in front of a monochromatic sensor and make three sequential exposures, one for each color. In this case, all photosites on the sensor capture red-, green-, or blue-image data during the appropriate exposure. This method produces very true colors, but it requires three exposures. Another method employs three separate full-frame CCDs, each coated with a filter to make it red-, green-, or blue-specific. A beam splitter inside the camera divides incoming images into three copies, one aimed at each CCD. This type of camera delivers high-resolution, good-quality color rendering; however, it is costly and bulky.

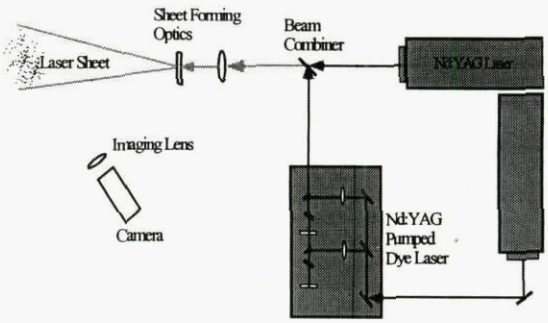


Fig. 4 Schematic of the two-color DPIV system.

For overcoming the above disadvantages, Kodak developed a unique single-chip camera (the one used in the present investigation) which has a resolution of 3060 x 2036 pixels and has the ability to capture all three colors with a single, full-frame CCD (Model DCS 460c). This is accomplished by coating each camera element (pixel) with either a red-, green-, or blue-color filter. Because the green color yields the best measure of brightness to the human eye, the green pixels make up 50% of the camera sensor. The remaining 50% is equally divided between red and blue pixels. Achieving a full 3060 x 2036 RGB image requires a multi-step process in which red, green, and blue pixels are interpolated. The camera image when recorded is digitized at 12 bits, but to save diskspace the image is automatically compressed to 8 bits before storage. The first step in the interpolation process is to decompress the image back to 12 bits. This is accomplished using a gray-scale response curve. Next, a pattern correction of the camera image is undertaken to account for variations in pixel-to-pixel sensitivity formed in the manufacturing process. The pattern-correction file is unique to each camera and is supplied by Kodak. Because green captures the luminance levels that can translate across to red and blue planes for the human eye, the green interpolation is carried out first, followed by the red and blue. Software for the decompression of the Kodak camera image before processing has been successfully developed by ISSI. The software subdivides the image into strips corresponding to the image width and the interrogation region height. The strip is expanded, processed, and then discarded, eliminating the need for large computer memory during analysis.

One of the first problems encountered with the Kodak RGB images was the apparent bleedthrough of the green component into the surrounding red and blue components. While this may be an important feature in the reproduction of human eye performance, it has an undesired effect in PIV images. Before the decompression routines were developed in-house, a cross-talk factor was employed during data analysis that allowed the user to selectively subtract portions of the green image from the red or blue images. While this feature was effective, it was apparent, after examination of Kodak's interpolation routines, that the source of the problem was the interpolation software rather than the camera. To correct for this problem, the in-house decompression (interpolation software) was written in such a way that the green component was not added to the average pixel value. The immediate result was that the apparent green cross-talk disappeared, and subtraction of a portion of the green image from the red during data analysis was no longer necessary.

### 3.3 Data Analysis

Once the PIV image has been captured and digitized, the velocity field is obtained using a cross-correlation technique. The present cross-correlation technique is based on intensity maps of the red and green images of the scattered light. Consider the intensity distributions of the red and green images, r(x,y) and g(x,y), and their corresponding Fourier transforms, $R(\alpha,\beta)$ and $G(\alpha,\beta)$. The two-dimensional cross-correlation function

$$\begin{aligned} h(x,y) &= \int_R \int_R r(\alpha,\beta)\, g(x+\alpha,y+\beta)\, d\alpha\, d\beta \\ &= F^{-1}\,[F(r(x,y))\, F(g^*(x,y))] \\ &= F^{-1}\,[R(\alpha,\beta)\, G^*(\alpha,\beta)] \end{aligned} \qquad (1)$$

is employed to determine the magnitude and direction of the average velocity over the interrogation area. (Note that unlike in processing methodologies based on autocorrelation, the direction of the velocity vectors is uniquely determined.)

The correlation function is calculated over small segments (interrogation domains) of the PIV image. The dimensions of each interrogation domain are dependent on particle density, estimated local velocity gradients, particle-image size, and desired spatial resolution. The maximum displacement of each particle must be less than one-half the interrogation spot. In the present experiments, the interrogation domain measured 128 x 128 pixels, corresponding to 1.88 x 1.88 mm in the measured flow. For enhancing the overall resolution, the interrogation domains are overlapped by one-half the domain size. The peak of the correlation map corresponds to the average velocity displacement within the interrogation spot. An intensity-weighted peak-searching routine is used to determine the exact location of the peak to sub-pixel accuracy. The number of particle pairs normally necessary to ensure a desirable signal-to-noise ratio is reduced to four or five pairs when the cross-correlation analysis is employed.

### 3.4 Uncertainty Analysis

Because the color sensor is divided into different red, green, and blue sensors, the standard analysis to determine instrument uncertainties must be extended. Figure 5 displays the arrangement of the color sensor. The full-field red, green, and blue images of a scene are not captured with this detector, as would be the case with a three-sensor color camera, and, thus, errors in particle position and velocity can occur. The objective of this work was to identify these errors to ensure that the camera was operated in a manner which would minimize them.

In order to assess the errors associated with the Kodak color camera, numerical simulations of the camera were undertaken. In the first simulation, a particle was positioned in an image at a known location and a gray image (simulating the information the camera records) constructed. The gray image was then processed using the decompression software employed for data analysis and a three-component RGB image generated. From the RGB image, the location of the particle was determined using the same peak-finding software employed in the PIV analysis routines. The difference in the locations of the simulated and measured particle positions as a function of particle-image size is shown in Fig. 6. The three curves in this figure correspond to the cases where 1) the pixels are all the same color, 2) the particle is of green color only, and 3) the particle is either red or blue in color. The curves in this figure correspond to the largest error encountered as the particle position is varied

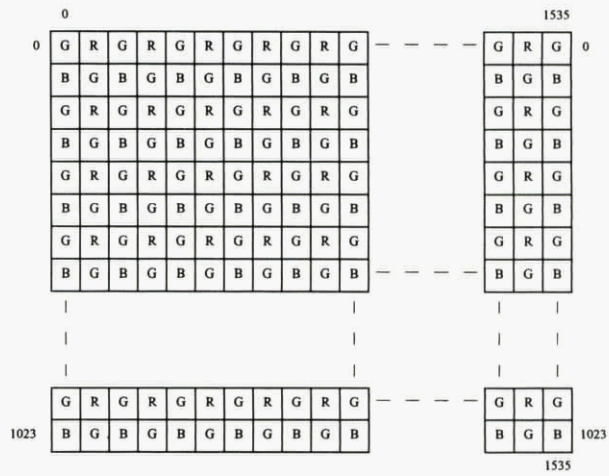


Fig. 5 Color-image pixel grid for Kodak camera.

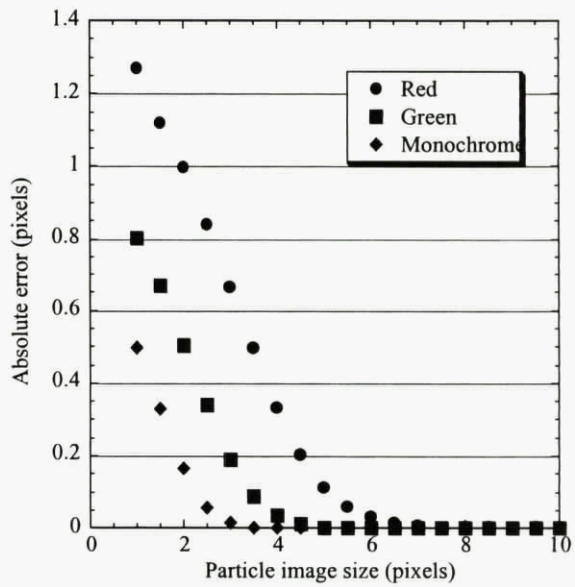


Fig. 6 Particle positions as a function of particle image size.

over pixels in both the x and the y direction. This error usually occurs when the particle is located between sensor elements. As can be seen from Fig. 6, even in the case of a monochrome sensor, the particle-image size must be larger than the pixel size to ensure error-free measurements. For this simulation the particle image is of Gaussian shape, with diameter equal to the 0.025 value of the Gaussian wings which corresponds to the first zero of an Airy distribution. In the green-color case of the Kodak camera, the particle-image diameter must be greater than 3 pixels to ensure an acceptable error in particle location, while it must be larger than 4 pixels for the red-pixel case. Figure 6 represents the maximum error which occurs when the particle is positioned at a fixed location on the sensor. For assessing the errors associated with a random particle field, a second series of simulations which employed the existing PIV analysis software was undertaken.

In the second simulation, a random particle field of constant-number, -displacement, and -image size was generated and analyzed with the PIV software. The associated mean and rms errors of the particle-pair displacements were determined as a function of particle image size and displacement. The results of this simulation are shown in Figs. 7(a-c). The instrumental rms for a fixed particle displacement [see Fig. 7(a)] increases as the particle-image size decreases but is tolerable with an image size above 2.5 pixels. Figure 7(b) displays the instrumental rms for a fixed particle-image size (4 pixels) with a variable particle-pair displacement. The magnitude of the rms increases with displacement, whereas the relative rms decreases with displacement (2.5% at 2 pixels and 1.3% at 20 pixels). Figure 7(c) shows the error of the simulated-to-measured mean displacements as a function of particle displacement for a fixed particle-image size (4 pixels). Note the systematic error of ~ 0.035 pixels which is relatively constant with particle displacement. This error is small and should not significantly impact the experimental results.

The above simulations indicated that the particle image size is critical to minimizing the instrument contribution to the velocity rms and that the recorded size should be at least 2.5 - 5 pixels to ensure acceptable errors. The chromatic correction of most lenses does not allow the widely separated green, red, and blue colors to focus at the same settings; therefore, it is best to focus the green and allow the red and blue to be slightly defocused, thus ensuring a larger image size for the red and blue particles.

From the simulation results discussed above, the dynamic velocity range and the dynamic spatial range of the camera can be calculated. Adrian[15] defines the dynamic velocity range (DVR) as the ratio of the maximum velocity to the minimum resolvable velocity which is given by

$$DVR = \frac{u_{\max}}{\sigma_u} = \frac{M_0 \Delta x_{p\max}}{c_\tau d_\tau} \qquad (2)$$

where $M_0$ is the magnification factor, $\Delta x_{pmax}$ is the maximum velocity displacement, $c_\tau$ is a constant that depends on the ability of the analysis software to determine the displacement (1 - 10%), and $d_\tau$ is the recorded-image diameter. In the case of the Kodak color camera, the maximum velocity would correspond to a pixel displacement of 20 pixels for a 64 x 64 interrogation spot size, resulting in an rms uncertainty of 0.3 pixels [see Fig. 7(b)] or a DVR of 67. This is approximately one-half the expected DVR of a 2k x 2k monochrome camera which is strictly due to the lower density of red and blue pixels. The dynamic spatial range (DSR) is defined as the ratio of the largest resolvable length scale to the smallest resolvable length scale and is given by

$$DSR = \frac{l_x}{\Delta x_{p\max}} = \frac{L_x / M_0}{\Delta x_{p\max}} \qquad (3)$$

where $L_x$ is the format of the recording medium (3060 x 2036). If the smallest camera dimension is divided by the maximum displacement (20 pixels), the result is a DSR of 100 which is the same as that of a 2k x 2k monochrome camera.

Thus, it can be argued that while the DVR of the Kodak color camera is less than that of the equivalent monochrome camera, the instrument is still capable of nearly a 70-fold

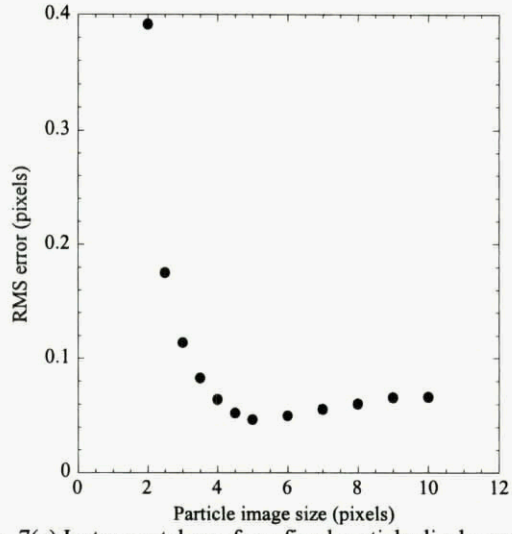

Fig. 7(a) Instrumental rms for a fixed particle displacement.

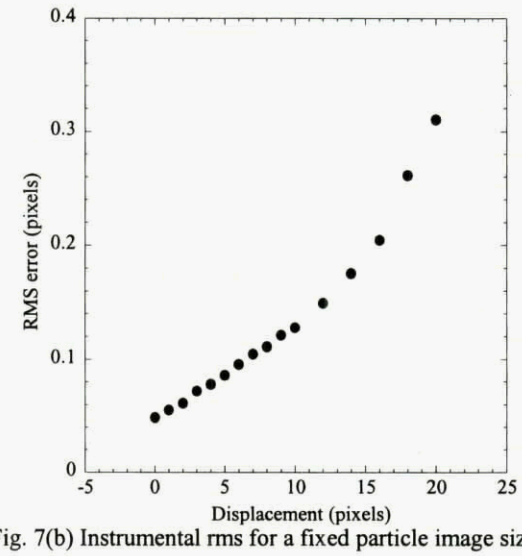

Fig. 7(b) Instrumental rms for a fixed particle image size.

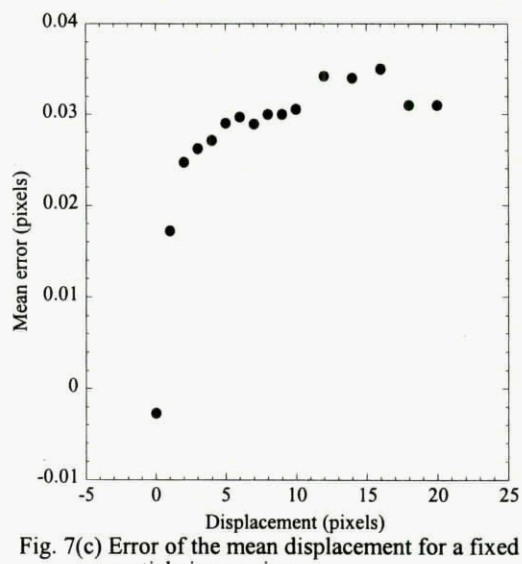

Fig. 7(c) Error of the mean displacement for a fixed particle image size.

velocity range. Considering the 3k x 2k recording capabilities of the Kodak color camera and the simple removal of directional ambiguity that color allows, the Kodak 460 DCS camera is a good compromise for obtaining high-quality, high-resolution PIV images.

## 4. RESULTS AND DISCUSSION

For understanding complex flow phenomena in low-speed turbomachinery flows, several laser-sheet/haze flow-visualization pictures were obtained at different spanwise locations of the blade. Figures 8(a) and 8(b) are typical photographs, representing mid-region (r = 6.75 in.) and tip-region (r = 9 in.) locations. In the mid-region [Fig. 8(a)], parallel trailing-edge wake structures emanating from the suction side of different blades can be seen. These structures are very organized and do not significantly interact with each other. However, closer to the tip-region location [Fig. 8(b)], complex interaction occurs among the trailing-edge wake structure from the suction side of the blade, the flow structure from the pressure side of the same blade, and the trailing-edge wake structure from another blade. This interaction is persistent and was observed in many visualizations obtained with the present experimental configuration. The flow structure from the pressure side of the surface is currently under investigation. From the above sample visualizations, a small region near the trailing edge (shown by a rectangular box) was chosen for obtaining quantitative information such as velocity and vorticity.

Figure 9(a) contains a typical double-exposed, two-color DPIV image of the axial fan when the illumination plane was nominally 9 in. from the hub center. For clarity, the axis direction of rotation and the intersection of the laser sheet and blade suction surface are indicated in the figure. The image is oriented such that the horizontal direction represents the fan axial direction, beginning just upstream of the rotor trailing edge, while the vertical direction represents the fan pitchwise direction. The image is not tangent to the circumference of the rotor but is slightly tilted, resulting in a varying radial location for the vertical direction. Minimal changes are expected in the flowfield over the radius variation. This figure shows the instantaneous flow structures near the exit of the rotor. A region of separated flow can be seen near the blade trailing edge at the suction surface; this results in a fairly large trailing-edge wake. The instantaneous absolute-velocity distribution associated with the DPIV image is shown in Figure 9(b).

The blade wake is clearly evidenced by the region of varying-direction velocity vectors behind the rotor. Downstream of the wake region, the fluid exits with considerable swirl in the directions of rotation. The high-swirl flow exists in the region previously identified as the complex-flow-structure region shown in Figure 9(a). Aft of these flow structures, a small amount of swirl still exists. Figure 9(c) represents the relative flowfield. In general, the relative velocity near the blade surface follows the contour of the blade, as expected. The blade wake region, where the velocity vectors vary about the mean relative direction, can be clearly seen in this representation. It appears that the wake region originates from the blade suction surface since the vectors deviate from the blade contour there. This wake region is also present in the relative-velocity representation [Fig. 10(b)] where the blade is captured in another position in the frame. Figures 10(a) and 10(b) clearly demonstrate the complexity of the flowfield in the tip region of this blade row. The data suggest that tip gap flows influence the absolute velocity field, creating regions of high swirl in the blade passage and just aft of the blade row.

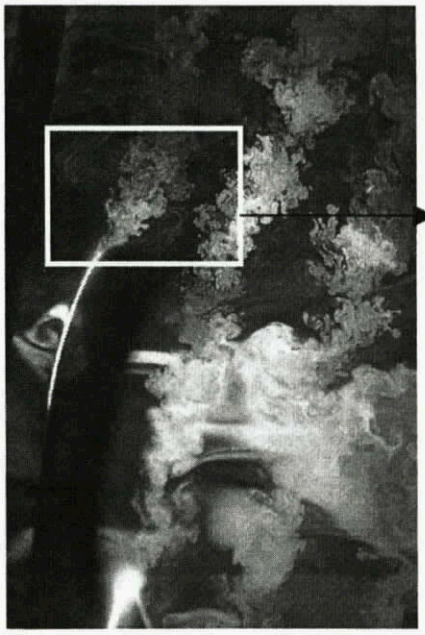


Fig. 8(a) Trailing-edge wake structures in the mid-region location.

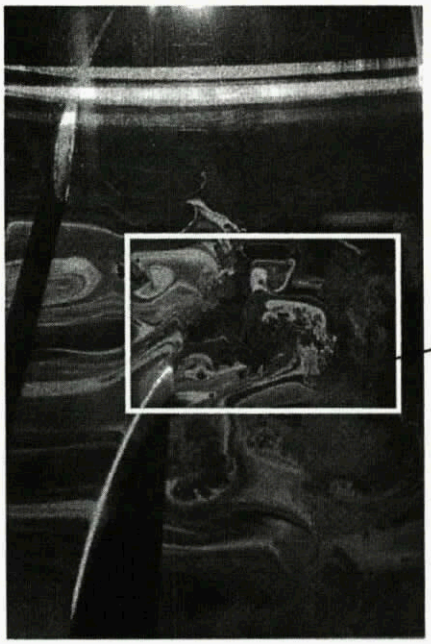


Fig. 8(b) Complex interaction of the trailing-edge flow structures in the tip-region location.

Figure 11 shows the flowfield at the same spanwise location for on operating speed of 1200 rpm. In this figure the absolute velocity is nominally 21 m/sec, while the relative velocity is 43 m/sec. Figures 11(a) and 11(b) indicate that the influence of the wake fluids extends farther downstream than in the lower speed case. Also, the region of disturbed flow can be seen more clearly. Again, it is possible that this region is influenced considerably by the tip-clearance vortex

Fig. 9(a) Double-exposed PIV image (1.77 in. x 1.18 in.) (plane 9 in. from hub center).

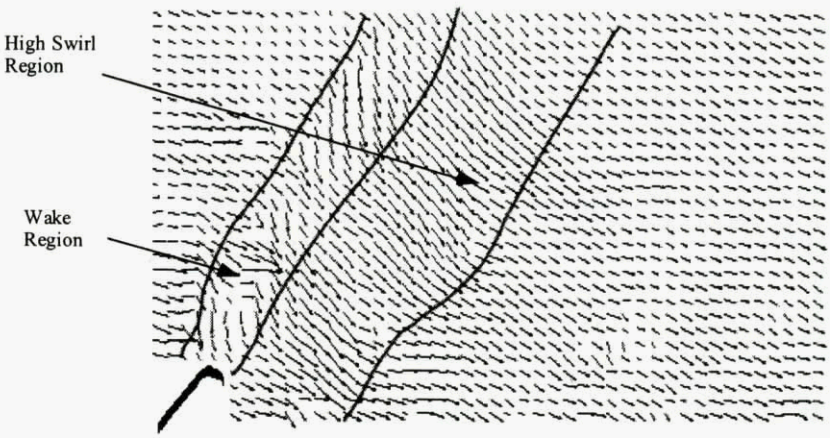


Fig. 9(b) Instantaneous absolute-velocity distribution.

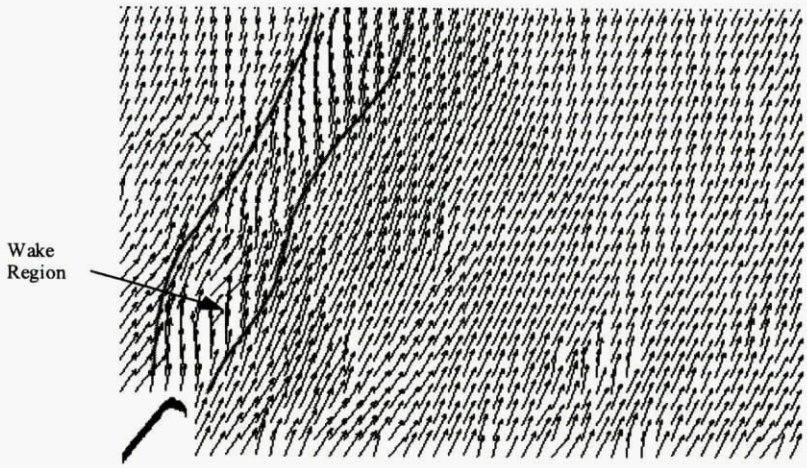


Fig. 9(c) Instantaneous relative-velocity distribution.

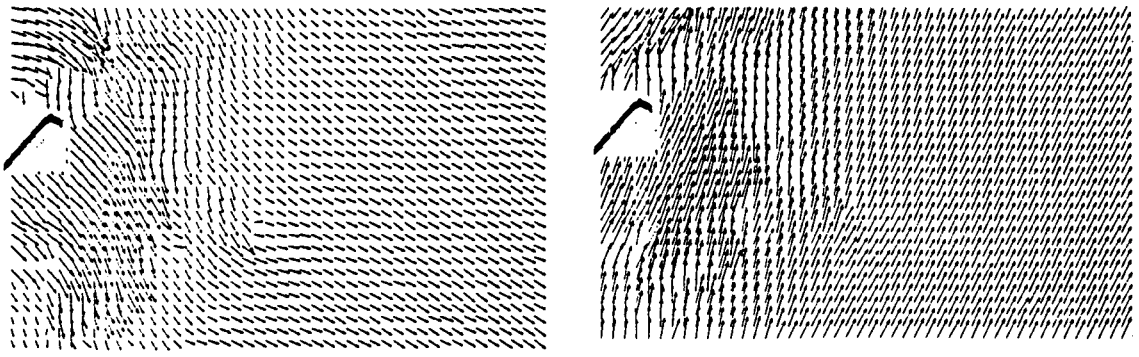

a) b)

Fig. 10 Instantaneous velocity distribution (plane 9 in. from hub center, 622 rpm);
a) absolute velocity, (b) relative velocity.

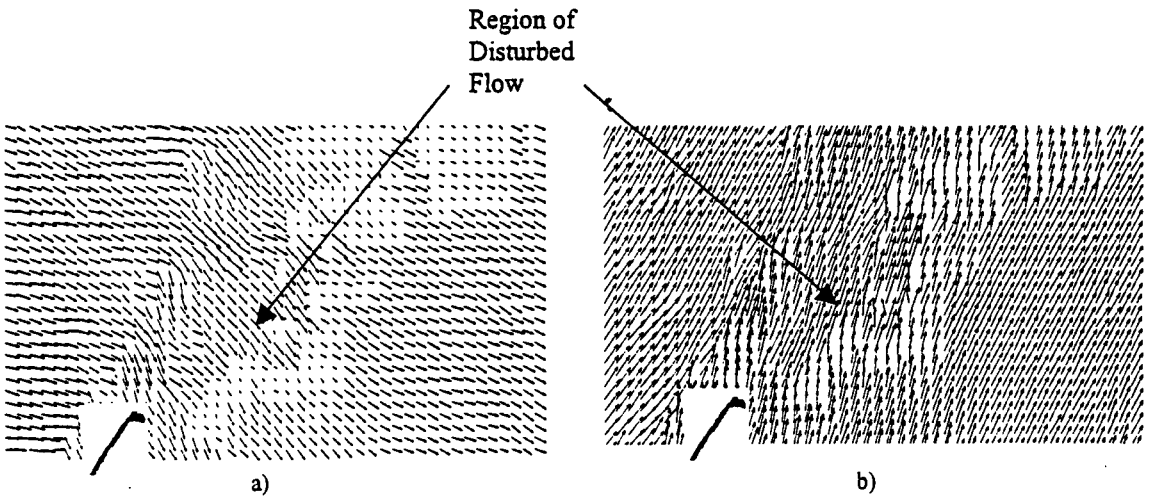


a) b)

Fig. 11 Instantaneous velocity distribution (plane 9 in. from hub center, 1200 rpm);
a) absolute velocity, (b) relative velocity

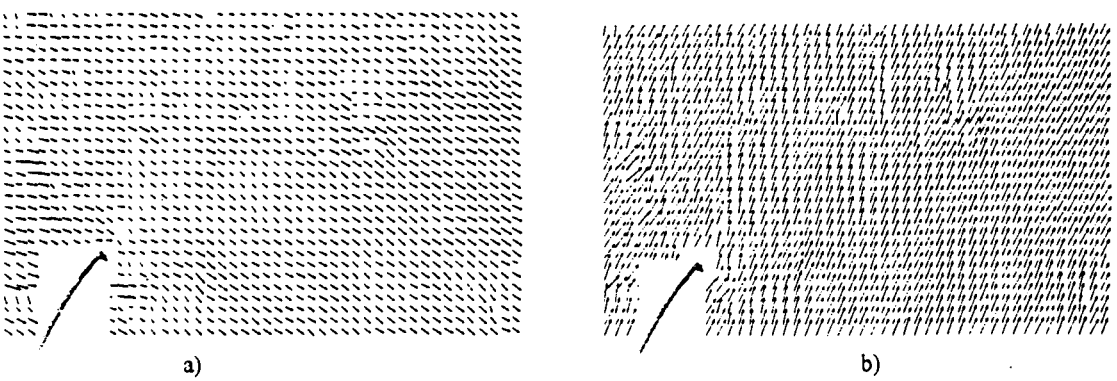

a) b)

Fig. 12 Instantaneous velocity distribution (plane 6.5 in.. from hub center, 622 rpm);
a) absolute velocity, (b) relative velocity.

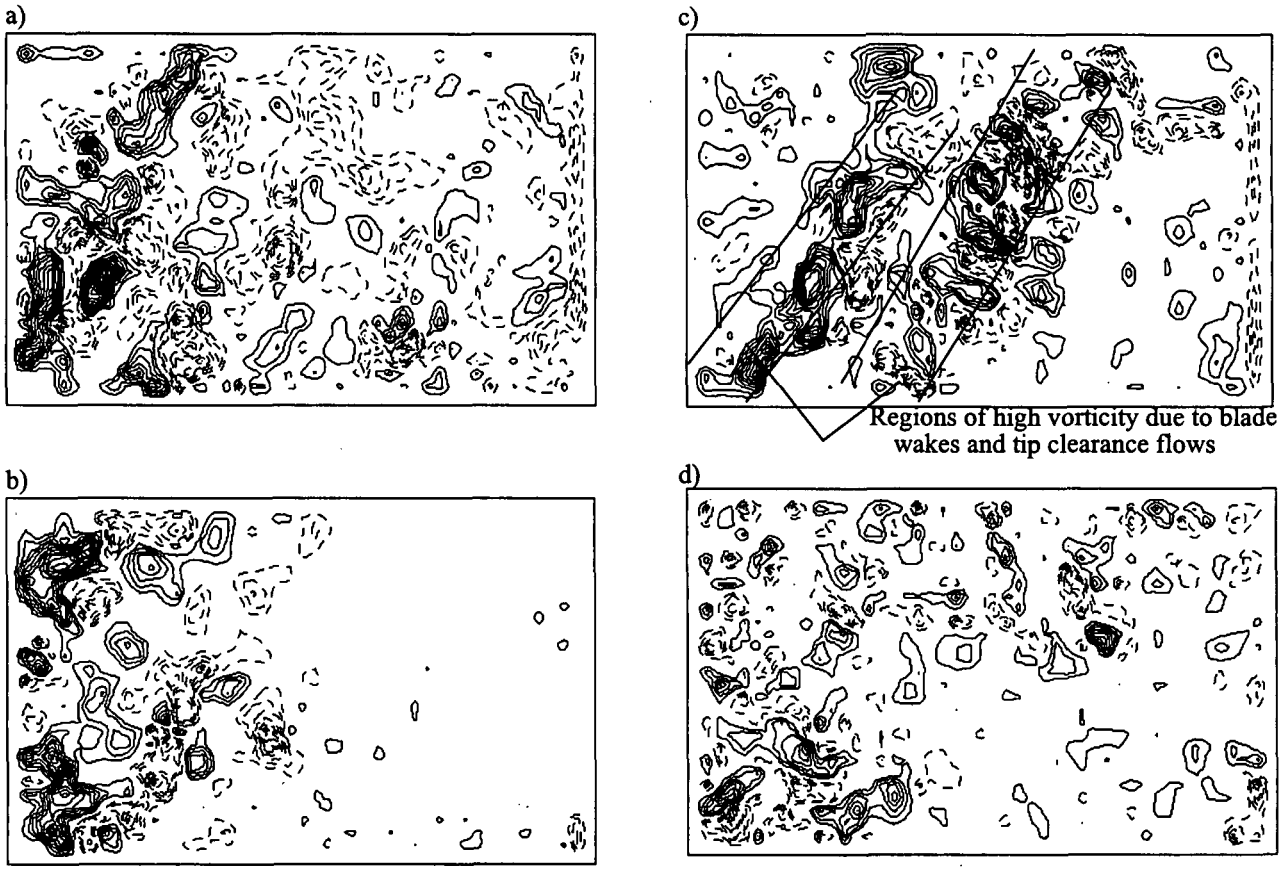


Fig. 13 Vorticity contours corresponding to Figs. 9-12: a) R = 9 in. (Fig. 9); $-0.807 \times 10^3 < \omega < 1.211 \times 10^3$, $\Delta\omega = 0.1 \times 10^3$; b) R = 9 in. (Fig. 10); $-0.639 \times 10^3 < \omega < 0.942 \times 10^3$, $\Delta\omega = 0.067 \times 10^3$; c) R = 9 in. (Fig. 11, 1200 rpm); $-0.766 \times 10^3 < \omega < 0.730 \times 10^3$, $\Delta\omega = 0.134 \times 10^3$; d) R = 6.75 in. (Fig. 12); $-0.375 \times 10^3 < \omega < 0.357 \times 10^3$; $\Delta\omega = 0.045 \times 10^3$. Values are normalized by rotational velocity $(mxs)^{-1}$.

from the leading-edge region of an adjacent blade. The viewing window does not allow confirmation of this hypothesis. However, Figure 12 clearly indicates a reduction in the region of disturbed flow for a midspan location (r = 6.75 in.) where gap flows have minimal influence. These results at the mid-span location are for the 622-rpm operating condition and, therefore, are best compared with Fig. 9 results for the tip location. At this location the flowfield is fairly well behaved.

The vorticity distributions corresponding to Figs. 9 - 12 are shown in Fig. 13. These distributions were obtained by central differencing the instantaneous velocity field. The solid and dashed lines correspond to positive and negative vorticity, respectively. The vortical structures in these figures clearly demonstrate the complexities of the flowfield in the wake and high-swirl regions. Two regions of high vorticity, aligned with the blade-stagger angle, can be seen in Figs. 13(a), (b), and (c), all of which contain measurement results obtained at the tip region of the compressor. The clearest of the three, Fig. 13(b), is for the higher speed test case.

## 5. SUMMARY

A two-color Digital Particle Image Velocimetry (DPIV) system employing a single-chip CCD color sensor was developed and implemented to investigate the flowfield in a low-speed axial fan. This system eliminated the photographic-film processing time and the subsequent digitization time as well as the complexities associated with conventional image-shifting techniques. Errors associated with the digital color camera were assessed using numerical simulations. The results indicated that the particle-image size is critical in minimizing the instrument contribution to the velocity rms and that the recorded size should be at least 2.5 - 5 pixels to ensure acceptable errors.

DPIV implementation issues such as optical access, seeding strategies, and blade-passage synchronization related to turbomachinery flows were explored, and instantaneous velocity measurements were made at different spanwise locations. These measurements along with the vorticity computations provided information on the spanwise variations of the blade wake region, suggesting increased complexity of wakes near the tip. These measurements aid our understanding of complex turbomachinery flows.

Future work will concentrate on the development of a fiber-optic laser-beam delivery system, software for improving vorticity computation from the velocity field and computing the pressure field, and strategies for surface-glare minimization. This improved system will be used in the Compressor Aero Research Laboratory (Wright-Patterson Air Force Base) transonic compressor to investigate the effect of unsteady flowfields on blade loading, blade structural response, loss production, wake transport, wake attenuation, wake-induced boundary-layer transition, and flow separation.

**ACKNOWLEDGMENTS**
The authors wish to acknowledge Darryl Trump of ISSI and Dr. M. Brendel of ITT (Dayton) for their help with the experimental setup. The authors would also like to acknowledge Wright Laboratory (Contract No. F33615-97-C-2710) for support of this work and M. Whitaker of ISSI for editorial comments.

**REFERENCES**

[1]Adrian, R. J., "Particle Imaging Techniques for Experimental Fluid Mechanics," *Ann. Rev. Fluid Mech.*, Vol. 23, 1991, pp. 261-304.

[2]Gogineni, S., Trump, D., Goss, L., Rivir, R., and Pestian, D., "High Resolution Digital Two-Color PIV and Its Application to High Freestream Turbulent Flows," Proc. 8th International Symposium on Applications of Laser Techniques to Fluid Mechanics, Lisbon, Portugal, July 8-11, 1996, pp. 18.2.1 - 18.2.8.

[3]Gogineni, S., Trump, D., Rivir, R., and Pestian, D., "PIV Measurements of Periodically Forced Flat Plate Film Cooling Flows with High Free Stream Turbulence," International Gas Turbine and Aeroengine Congress and Exhibition, Birmingham, UK, June 10-13, 1996 (ASME Paper 95-GT-236).

[4]Gogineni, S., Goss, L., Glawe, D., Bowersox, R., and Wier, R., "Digital Two-Color PIV and Flow Visualization Studies for Complex Supersonic Flows," ASME Fluids Engineering Division Summer Meeting, Vancouver, B. C., Canada, June 22-26, 1997 (ASME Paper FEDSM 97-3092).

[5]Bitting, J., Gogineni, S., Nikitopoulos, D., and Gutmark, E., "Visualization of Non-Circular Coaxial Nozzle Flow Structure," 50th APS/DFS Annual Meeting, San Francisco, CA, November 23-25, 1997.

[6]Gogineni, S., Hancock, R., Schauer, F., and Lucht, R., "Phase-Resolved DPIV Investigation of Vortex-Flame Interactions in Hydrogen Jet Diffusion Flames," 50th APS/DFS Annual Meeting, San Francisco, CA, November 23-25, 1997.

[7]Paone, N., Riethmuller, M. L., and Van den Braembussche, R. A., "Application of Particle Image Displacement Velocimetry to a Centrifugal Pump," 4th International Symposium on Applications of Laser Techniques to Fluid Mechanics, Lisbon, Portugal, July 11-14, 1988.

[8]Bryanston-Cross, P. J., and Epstein, A., "The Application of Sub-Micron Particle Visualization for PIV at Transonic and Supersonic Speeds," *Prog. Aero. Sci.*, Vol. 27, 1990, pp. 237 - 265.

[9]Tisserant, D., and Breugelsmans, A. E., "Rotor Blade-to-Blade Measurements Using PIV," IGTI Turbo Expo, Houston, Texas, July 1995 (ASME Paper 95-99).

[10]Wernet, M. P., "PIV for Turbomachinery Applications," Conference on Optical Technology in Fluid, Thermal, and Combustion Flow III (Society of Photo-Optical Instrumentation Engineers), San Diego, CA, July 27 - August 1, 1997 (NASA TM 107525).

[11]Gogineni, S., Goss, L., W. Copenhaver., and Gorrell, S., "Development of Digital Two-Color PIV for Turbomachinery Applications," 35th Aerospace Sciences Meeting and Exhibit, Reno, NV, January 6-10, 1997 (AIAA 97-0494).

[12]Brendel, M., "Optical Considerations for a Flow Visualization Method Applicable to Transonic Compressor Rotors," Final Report, Contract No. F33615-90-C-2086, Subcontract S-246-022-001 (Universal Energy Systems, Dayton, OH, September 1993).

[13]Anderson , D. J., Jones, J. D. C., Easson, W. J., and Greated, C. A., "Fiber-Optic Bundle Delivery System for High Peak Power Laser Particle Image Velocimetry Illumination," *Rev. Sci. Instrum.*, Vol. 67, No. 8, 1996, pp. 2675 - 2679.

[14]Kodak Digital and Applied Imaging" (Eastman Kodak Company, Rochester, NY, 1997).

[15]Adrian, R., "Strategies for Imaging Flowfields with PIV," 27th AIAA Fluid Dynamics Conference, New Orleans, LA, June 17-20, 1996 (AIAA Paper 96-1988).

Paper 49
Author: Gogineni

Q: Broichhausen

The measurements in a high pressure compressor are very challenging. Have you an idea already about the arrangement to realise optical access?

A: The ideal optical transmitter for a high pressure compressor is a fibre optic Nd:YAG based laser sheet delivery system. Our company has initiated this research, and is planning to design this system. Until that time, the effective way to generate the sheet is by using the periscope approach as described by Dr Wernet of NASA Lewis (USA) and Prof Epstein of MIT (USA).

Q: Edmonds

Have you estimated the particle concentration in the measurement region?

A: The particle concentration in the measurement region is of the order of 8-10 particle pairs over a 1mm x 1mm interrogation window.

Q: Fabry

What is the accuracy of the velocity vectors?

A: The errors involved are of the order of 1-3 % on the full scale range.

Q: Fabry

What is the resolution (in pixels and mm) and what is the overlap?

A: Resolution is 68 pixels/mm and overlap is 50% in the interrogation window.

# Recent progress in whole-field non-intrusive measurements of 3-D velocity vectors and particle size.

C.S. Moraitis,
Systelligence Consultants and Research associates*
D. Tisserant, F.A.E. Breugelmans
von Karman Institute For Fluid Dynamics†
72 Chaussée de Waterloo,
B-1640, Rhôde St.-Genèse, Belgium

## 1 SUMMARY

Recent success in the implementation of particle image velocimetry (PIV) as a useful two-dimensional technique has encouraged efforts to develop three-dimensional non-intrusive methods. Holography appears to be a suitable technique to image three-dimensional flows seeded with small particles.
A novel technique to process double or multiple exposure holograms has been developed during the last four years. Information about velocity and particle size is obtained by using an optical/digital processing technique. The interference pattern due to light-waves emanating from particles images is imaged and then processed digitally. Applicability of the concept is first demonstrated by processing a double-exposed hologram of a synthetic particle field submitted to a known displacement. For different ratios between the depth (out-of-plane) displacement-component and the lateral (in-plane) one, results are discussed. They show that the accuracy is strongly related to the choice of the digital processing parameters, especially the number of fringes which are contained in the interference pattern.
Additional benchmarking of the technique has been carried out by applying it to a real flow of which velocity and direction are well known. Therefore, a jet flow facility with adjustable yaw and pitch angle has been designed. Various flow configurations have been investigated. At present state of work, processing result have to be improved. The diffraction halo of the particle images is so small that a limited number of fringes are available at the output of the optical processing part. Thus results of the digital processing algorithm are affected by a large uncertainty.

## 2 INTRODUCTION

Development of the Particle Image Velocimetry (PIV) technique over the last decade has resulted in its successful application to many laboratory and industrial flows investigations ([1], [2], [3], [4] , [5]). This technique provides whole-field two-dimensional unsteady velocity distribution and recently efforts have been produced to extend the concept to three-dimensional (3D) flow analysis. Since holography had been used long before the appearance of PIV as an imaging technique for particle fields, it is quite natural to attempt the extraction of 3D velocity information from the analysis of particle holograhic records [6], [7]. The major feature of that recording media is the 3D reconstruction of the particle field image. The velocity vector is determined by the measurement of the three displacement components between two images of the same particle recorded at two different times.
Besides the adaptation of two-dimensional analysis technique (stereo-scopic method [8], scanning laser sheet technique [9]) to the determination of the three velocity components, an original optical processing scheme is proposed in 1992 by Moraitis [10]. This scheme relies on the probing of in-line double-exposure holographic records by a relatively narrow laser beam resulting in the reconstruction of only a narrow pencil within the initial flow field. The lateral dimension of this pencil is given by the lateral dimension of the probing beam. The selection of an axial position within this pencil, a process referred as depth discrimination, is accomplished by a pinhole aperture. Particles images reconstructed in the vicinity of the aperture produce waves which contribute to a final interference pattern, while any others are strongly attenuated. Thus the output of the optical processor is an interference pattern from double or multiple images of particles which lay close to a given point upon recording. Every such interference pattern corresponds to a single velocity vector of the flow field.
The whole concept was formalized mathematically by Moraitis in 1992. Its applicability was demonstrated using computer-generated holograms. However further efforts have been required since then to develop a reliable and universal processing algorithm for the analysis of the optical processor output. Experimental validation of the technique has been carried out using holographic records of an artificial particle distribution which was submitted to a known displacement between exposures. The next step of the practical verification is the application of that concept to the measurement of velocity in the potential core of a round jet whose direction can be adjusted in space.

## 3 THEORETICAL BACKGROUND.

### 3.1 Mathematical description of the processing scheme.

Moraitis [10] had established that the output of the optical processor in the case of double-exposure holograms reads :

$$I(x,y) = \frac{M^2\beta^2 d^2}{x^2+y^2} J_1^2\left(\frac{\pi d\sqrt{x^2+y^2}}{M\lambda_2 f}\right) \cos^2\left[\pi\left(\frac{x\Delta x + y\Delta y}{M\lambda_2 f} + \frac{\lambda_1 \Delta z}{M^2\lambda_2^2 f^2}(x^2+y^2)\right)\right] \quad (1)$$

where

* Skoufa 92,38 334 VOLOS, Greece.
† Steenweg op Waterloo 72, 1640 Sint-Genesius-Rode, Belgium.

*Paper presented at an AGARD PEP Symposium on "Advanced Non-Intrusive Instrumentation for Propulsion Engines", held in Brussels, Belgium, 20-24 October 1997, and published in CP-598.*

- M is the magnification of the optical processor.
- $\lambda_1$ is the recording laser wavelength.
- $\lambda_2$ is the reconstruction laser wavelength.
- $\Delta$x is the displacement of the particle between exposures along the x-axis.
- $\Delta$y is the displacement of the particle between exposures along the y-axis.
- $\Delta$z is the displacement of the particle between exposures along the z-axis.
- $f$ is the focal length of the first lens of the optical processor.
- d is the actual particle size.
- $\beta$ is a constant depending on the holographic emulsion.

Equation (1) is the product of two fluctuating terms and a constant. Both terms contain different items of informations : the Bessel function envelope depends on particle size while the cosine-squared term contains only velocity (displacement-component) information. Therefore if the particle size is sought, modulations due to the cosine squared term have to be eliminated by a low pass filtering of the whole digital image. If the spatial cut-off frequency of the filter is sufficiently low, the filtering of the image results in a bright spot whose diameter is inversely proportional to the particle size. Of course some sort of calibration might be required if the background intensity of the image is so high that it is difficult to locate accurately the first zero of the Bessel function envelope.
As it concerns the determination of the displacement component, the two-dimensional Fourier transformation of a pattern expressed by equation (1) could be used. Transformation of the Bessel function envelope results in the convolution of two cylinder functions in the frequency domain and give rise to a kernel whose spatial extent equals

$$\frac{d}{M\lambda_2 f} \tag{2}$$

While the cosine squared term gives rise to a term which reads

$$2\exp\left(j\pi\frac{M\lambda_2 f}{2\lambda_1\Delta z}(\xi\,\Delta x+\eta\,\Delta y)\right)$$
$$\cos\left[\pi\frac{M^2\lambda_2^2 f^2}{2\lambda_1\Delta z}\left(\xi^2+\eta^2+\frac{(\Delta x)^2+(\Delta y)^2}{M^2\lambda_2^2 f^2}\right)\right] \tag{3}$$

The spatial period of this term for $\xi$=$\eta$=0 reads

$$\left(\frac{4\lambda_1\Delta z}{M^2\lambda_2^2 f^2}\right)^{\frac{1}{2}} \tag{4}$$

If the spatial extent (2) of the convolution kernel is considerably narrow compared to the spatial period (4) i.e., if

$$d << 2\sqrt{\lambda_1\Delta z} \tag{5}$$

the convolution kernel has no detectable effect on the result of the Fourier transform and can be ignored. In this case one can consider with reasonable accuracy that the Fourier transform of (1) is equal to (3). Then, since expression (3) is digitally computed, the modulus and argument can be processed separately. The argument $\phi$ of expression (3) reads

$$\phi=\pi\frac{M\lambda_2 f}{2\lambda_1\Delta z}(\xi\,\Delta x+\eta\,\Delta y) \tag{6}$$

Loci of zero argument describe a family of straight lines in the $(\xi.,\eta)$ space. The slope of this set of lines is related to coefficients $\frac{\Delta x}{\Delta z}$ and $\frac{\Delta y}{\Delta z}$.
The modulus of the expression (3) reads

$$A=\cos\pi\left[\frac{M^2\lambda_2^2 f^2}{2\lambda_1\Delta z}\left(\xi^2+\eta^2+\frac{(\Delta x)^2+(\Delta y)^2}{M^2\lambda_2^2 f^2}\right)\right] \tag{7}$$

Loci of zero modulus describe a set of concentric circles. The analysis of this set of circles as a digital pattern can lead to the determination of circle radii which depend on $\Delta z$ and on ratios evaluated upon the processing of the argument of (3). This processing scheme had original favors from authors [10] because fast algorithms for two-dimensional Fourier transform were already existing and the implementation of analyzing tools for the modulus and argument of expression (3) were rather straightforward. But the condition expressed by equation (5) limits the domain of applicability in terms of particles size or magnitude of $\Delta z$ displacement component. Therefore, an alternative processing scheme was developed. This new scheme relies on the geometric features of the interference pattern described by equation (1).
If one examines expression (1) carefully, it becomes obvious that the cosine-squared term in (1) will give rise to bright fringes when its argument equals an integer multiple of $\pi$ radians i.e. when,

$$\left[\left(\frac{x\Delta x+y\Delta y}{M\lambda_2 f}+\frac{\lambda_1\Delta z}{M^2\lambda_2^2 f^2}(x^2+y^2)\right)\right]=k$$
$$k=\pm 0,1,2,\ldots \tag{8}$$

which is equivalent to,

$$\left(x+\frac{M\lambda_2 f}{2\lambda_1}\frac{\Delta x}{\Delta z}\right)^2+\left(y+\frac{M\lambda_2 f}{2\lambda_1}\frac{\Delta y}{\Delta z}\right)^2=$$
$$\frac{M^2\lambda_2^2 f^2}{\lambda_1\Delta z}\left(\frac{(\Delta x)^2+(\Delta y)^2}{4\lambda_1\Delta z}+k\right)$$
$$k=\pm 0,1,2,\ldots \tag{9}$$

Equation (9) represents a family of concentric circles. Rather than analyzing the complete pattern one can rely on lines or columns of the image. The location of all intensity maxima along a line or a column is performed with a peak-finding algorithm. It is based on the sign variation of the first derivative of the intensity distribution. Then one can set up a system of equations which consists of as many equations as the number of detected peaks in the signal described by the left-hand side of equation (8). Considering that maxima are located in abscissa $x=x_1$,$x=x_2$,$x=x_3$ and $x=x_4$ of a horizontal line described by $y=y_1$. Those coordinates satisfy the following system of equations,

$$\begin{aligned}
\mu x_1\Delta x+\mu y_1\Delta y+\ & \nu(x_1^2+y_1^2)\Delta z-k=0\\
\mu x_2\Delta x+\mu y_1\Delta y+\ & \nu(x_2^2+y_1^2)\Delta z-k=1\\
\mu x_3\Delta x+\mu y_1\Delta y+\ & \nu(x_3^2+y_1^2)\Delta z-k=2\\
\mu x_4\Delta x+\mu y_1\Delta y+\ & \nu(x_4^2+y_1^2)\Delta z-k=3
\end{aligned} \tag{10}$$

where $\mu=1/(M\lambda_2 f)$ and $\nu=\lambda_1\mu^2$. $\Delta$x, $\Delta$y, $\Delta$z and k are the unknowns of the system which is solved by the singular value decomposition method [11].
The processing algorithm is rather simple and robust. It can be applied to vertical or horizontal line so that the computation time is reduced.

### 3.2 Limitations of the technique.

When the practical implementation of the technique has been carried out, some limitations appears. Some of them are relevant to the holographic technique itself whereas others are entailed to the processing algorithm.
As for two dimensional PIV applications, seeding concentration is an important parameter. Uniformity of the particle distribution is necessary to achieve a good velocity field resolution since measurements are conditioned by the particle presence. On the other hand, a too high concentration will result in a loss of images quality. Holographic film are actually recording the interference of the light diffracted by the object and a reference light beam which is not affected by the object. In the case of particle field recording, each particle is an object. Therefore if the concentration of particles is too high, multiple interferences will be generated by the light diffracted by different sources. Then images can not be reconstructed or if they are, the speckle noise level will make difficult any observation. However recent studies [12] as well as our own experience tend to suggest that if optical hologram reconstruction results in particle images of acceptable quality, then there is no fundamental reason why those images shall not form the diffraction pattern which constitutes the very essence of our processing scheme. It means that if particle density is too high for the success of the optical processing scheme, it is already far too high for recording a hologram at all.
As already mentioned in the previous section by equation (5), particle size can have a decisive effect on the algorithm which can be used for the analysis of the optical processor output. Furthermore, the fringe pattern which carries velocity information modulates the diffraction halo of which spatial extent depends on the particle size. If we assume that at least three fringes must be visible for the success of the image analysis, the following condition should be satisfied,

$$\left[\frac{(\Delta x)^2 + (\Delta y)^2}{(\Delta z)^2}\right] < \frac{2.44\lambda_1}{d} \qquad (11)$$

Since the right-hand-side of (11) is less than unity in most cases, the most severe limitation of the technique is that the depth displacement must be larger than the lateral displacement.
Limitations of the digital processing algorithm are mainly due to the accuracy which affects the identification of intensity maxima position in the initial signal. Presence of Speckle noise introduces localized intensity maxima that might be confused with maxima pertaining to the interference pattern. Therefore, some preliminary low-pass filtering of the original image is applied before the peak detection process begins. In addition to the low-pass filter, some criteria were defined to decide if the maxima is pertaining to the interference pattern or not. A level of intensity ratio between two successive peaks is imposed, as well as a minimum separation distance. Also to be accepted, maxima should reach a threshold level. Values of those criteria are defined by analyzing some samples of optical processor output for a given hologram. A general calibration procedure is not yet defined.

## 4 OPTICAL/DIGITAL PROCESSOR IMPLEMENTATION.

### 4.1 Optical processing hardware.

Figure 1 is a schematic representation of the processing hardware set-up. The optical part of the processor consists of three distinct components, namely the illuminating (i.e. reconstructing optics), the probing stage and the receiving (i.e. processing) optics. As shown on figure 1, the illuminating optics consists of a low power (30 mW) He-Ne laser complemented by a beam expander. Typically, the diameter of the re-illumination area is equal to 30 mm since only a small part of the holographic plate must be illuminated at a time. The size of the re-illumination area is mainly dictated by the intensity of light which provides a well contrasted interference pattern at the output of the processor. The choice of a He-Ne laser (wavelength equal to 632 nm) is imposed by the nature of light which is used upon holographic recording. A Ruby laser is currently used and it has a wavelength equal to 694 nm. In order to limit the aberration appearing upon the reconstruction of the particle-field image, the reconstruction light wavelength should be as close as possible to the one used upon recording.
The probing stage is a computer controlled X-Y-Z translation stage carrying the holographic plate undergoing processing by means of a plate holder. The real image of the flow is formed between the probing stage and the receiving optics.

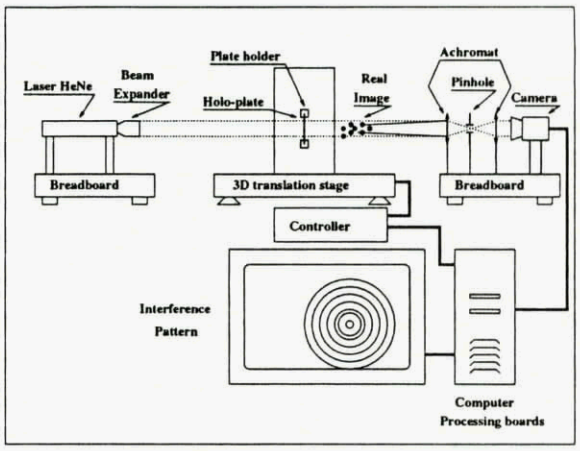


Fig. 1 : Optical processing bench for particle holograms recording.

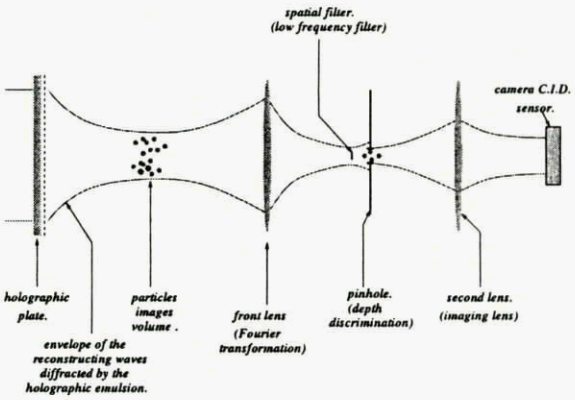


Fig. 2 : Optical processor unit.

The receiving optics are sketched on figure 2. The first achromatic lens of the optical processor images the flow field in such a way that the probe volume is imaged in the vicinity of a narrow (200-800 $\mu$m) aperture (pinhole). Simultaneously this lens acts as a Fourier transform lens

yielding a Fourier plane somewhere between itself and the pinhole. The second achromatic lens images this Fourier plane directly onto the charge injection device (CID) array of the camera. However because of the presence of the pinhole, only those components of the optically formed Fourier transform which give rise to particle images in the vicinity of the aperture contribute to the formation of the interference pattern seen by the camera. Hence the aperture accomplishes simultaneously the selection of the lateral position of the probe volume and the depth discrimination. Rather than moving the aperture the holographic plate is moved instead to vary the position of the probe volume.

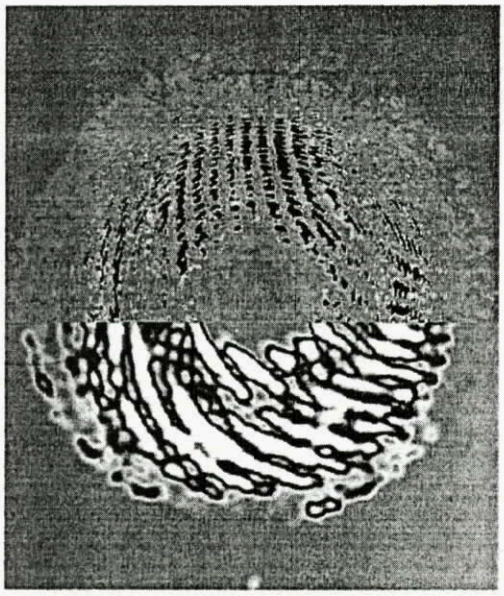

Fig. 3 : Optical processor output : (top)original signal (bottom)filtered signal.

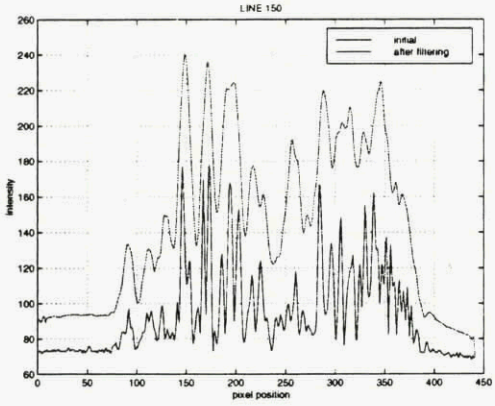


Fig. 4 : Intensity distribution along a line of optical processor output.

The digitization of the interference pattern is carried out with a CIDTEC CID2250 CID camera. Its resolution is 512 by 512 physically square pixels covering an area of 7.68 by 7.68 mm. The selection of a CID camera was dictated by the broad range of intensities present in the subject to digitization (interference pattern). The very high intensity of the zero-frequency spot would have given rise to extensive image blurring if a CCD camera were used instead. Furthermore, the processing algorithm relies on informations contained in a spatially limited area of the interference pattern. Acquisition of only the pixels contained in such limited areas instead of grabbing complete 512 by 512 pixel images allows image acquisition and image processing to proceed at higher throughput rates. The digitized image is acquired by a Data Translation DT3851 frame grabber which enables the image display on the computer's VGA monitor.
In order to speed up digital processing operations, an Ariel DSP-C40 Cyclops processor board (operating at 40 Mflops) is currently implemented. It will receive images data over the DT-Connect port and accomplishes all the subsequent processing.

## 4.2 Digital processing algorithm.

Different steps of the processing are presented on figures 3 and 4. Figure 3 is the digital image obtained by optical processing of a computer-generated hologram. The upper part of the picture corresponds to the initial signal whereas the bottom has been modified by low-pass filtering. Observation of the original part of the image shows a rather complex pattern mixed with random noise. Fringes are not clearly visible. Therefore we need to improve the digital pattern before analyzing it.
The filtering of the image is done by using a fitting polynomial interpolation slipping on the image to smooth it. Actually, each point of the initial image row (or column) is replaced by a value computed with a second order polynomial that fits surrounding points. This technique is quite efficient and does not introduce any shift in the peak intensity position which is essential for our purpose. Figure 4 shows the noise reduction capability of the filtering process by representing simultaneously filtered and non-filtered intensity distribution along a line. The research of intensity peak loci is then carried out on several lines or columns.
The evaluation of the theoretical uncertainties affecting the digital processing is done with the assumption that maxima position are determined with an uncertainty of 1 camera pixel. Numerical simulation of the optical signal was done with equation (1) for a lateral displacement $\Delta x = 50$ or $100$ $\mu$m and a ratio $\frac{\Delta z}{\Delta f}$ ranging from 0 to 6. The number of intensity peaks used upon processing was imposed in order to check its influence on the uncertainty value.

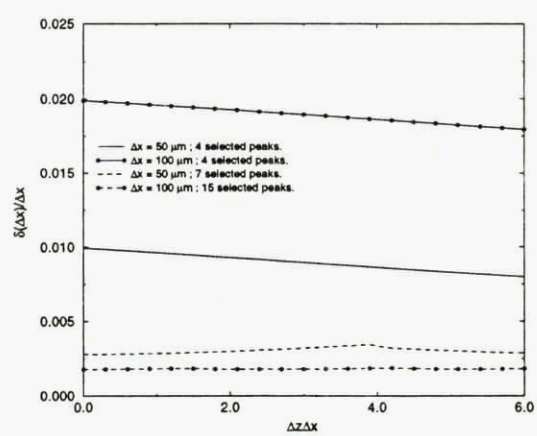


Fig. 5 : Relative uncertainty affecting the measurement of in-plane displacement component $\Delta$x.

Figures 5 and 6 are graphical presentations of the relative uncertainty affecting the determination of the in-plane

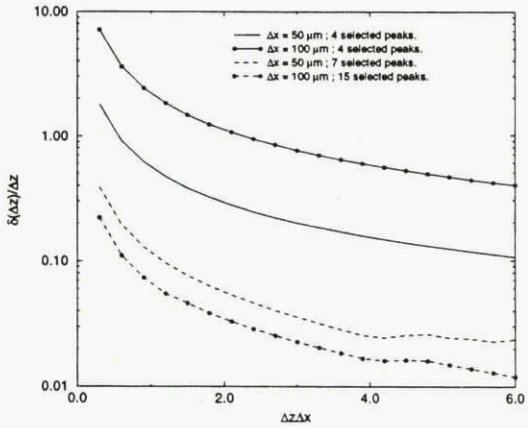


Fig. 6 : Relative uncertainty affecting the measurement of in-plane displacement component $\Delta z$.

and out-of-plane displacement component with respect to parameters mentioned above. A first observation is that increasing the number of peaks improves the relative uncertainty. Secondly, the determination of the lateral displacement component is less affected by the uncertainty than the evaluation of the out-of-plane component.
Since signals were simulated, errors between imposed conditions and processing results are negligible in all cases. Nevertheless, uncertainty distribution gives the propensity for error to propagate because of the addition of background noise inherent to any practical optical application.

# 5 EXPERIMENTAL VALIDATION.

## 5.1 Benchmarking of the optical processor.

The holographic recording technique has been discussed by many authors in the literature [13], [14]. The basic principle is that one actually records on a frame the interference between a reference light beam and the light diffracted by the object. The generation of constructive interference is only possible when a coherent light source is used. In most of holographic applications the initial light beam is split in two part, one being used to build the reference beam while the other illuminates the object. Upon reconstruction the developed hologram should be illuminated with a light beam similar to the reference one. Then light is diffracted by the holographic emulsion and gives rise to a virtual and a real object image.
When micro-objects are recorded, it is possible to use a specific set-up which requires a single beam. If the presence of small objects in the reference beam path are not disturbing it too much, it is still possible to get constructive interferences between the portion of light which is diffracted by micro-objects and the non-disturbed part of it. This kind of set-up is called in-line holography or Gabor's holography. Royer [15] demonstrated practically that this set-up was suitable to record relatively small objects. That technique is very simple and optical aberrations are limited.
As it is sketched on figure 7, in-line holography was utilized to record holograms of an artificial particle distribution which was submitted to a known displacement. That particle field was obtained by deposing a solution of talc particles on a glass plate. Once the solvent is evaporated, particles adhere on the plate. Particles diameter range goes from 15 $\mu$m to 25 $\mu$m which makes them suitable for in-line recording. The recording distance was fixed at 58 mm.

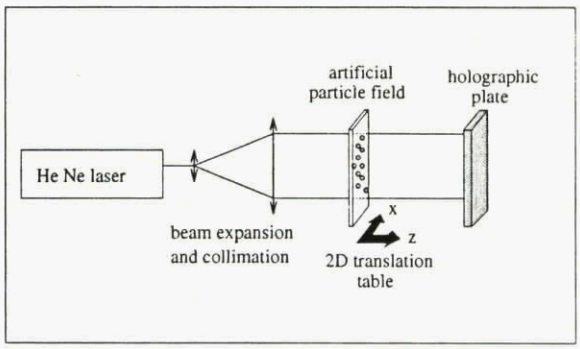


Fig. 7 : In-line holographic recording set-up for artificial particle field.

Double-exposure holograms are generated by recording two successive illuminations of the glass support. Between both illuminations, the glass plate is moved and the displacement is carefully measured. A collimated He-Ne laser beam is used as a light source.
In order to check the validity of the theoretical development reported in previous chapter, hologram recording are carried out with different displacement conditions. The varying parameter is the ratio between in-plane (defined by directions x and y) and the out-of-plane (along z-axis) displacement components. Imposed ratios $\gamma_x = \frac{\Delta z}{\Delta x}$ are 0, 4 and 6.
Before bringing us quantitative results, the optical processing allows one to observe the evolution of the final interference pattern in a function of the ratio $\gamma_x$. When $\gamma_x = 0$, the optical processor output is a set of straight fringes like in the case of two-dimensional PIV data processing. This observation is confirmed by considering $\Delta z = 0$ in equation (8). By increasing the ratio $\gamma_x$, the curvature of the observed fringes increases also. From equation (9), we note that the radius of curvature is inversely proportional to ratios $\gamma_x$ and $\gamma_y = \frac{\Delta z}{\Delta y}$.

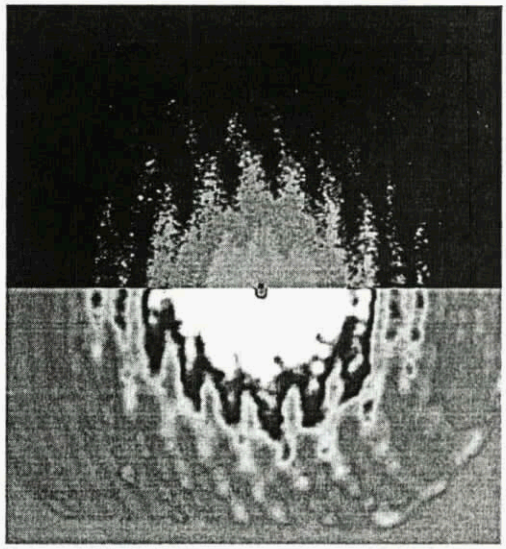

Fig. 8 : Optical processor output for $\frac{\Delta z}{\Delta x}$ =6 and $\Delta x$ = 36.8 $\mu$m: (top)original signal (bottom)filtered signal.

Figure 8 is an example of fringes pattern obtained when

| $\Delta$x ($\mu$m) | $\gamma_x$ | $\gamma_y$ | $\epsilon_x$ (%) | $\epsilon_y$ (%) | $\epsilon_z$ (%) |
|---|---|---|---|---|---|
| 176 | 0 | 0 | 2.3 | - | - |
| 35.8 | 4 | 0 | 1.1 | - | 4.2 |
| 36.8 | 6 | 0 | 2.1 | - | 4.3 |

Table 1 : Errors associated to processing.

$\gamma_x$ = 6 and $\gamma_y$=0. Bottom part of the image plane has been low-pass filtered. Fringes are curved towards the right side. The distance between them is decreasing from right to left. This variation of space between consecutive intensity maxima is mainly containing information about the out-of-plane (depth) displacement component.
Parameters pertaining to the imposed displacement ($\Delta$x, $\gamma_x$, $\gamma_y$) as well as relative errors ($\epsilon_x$, $\epsilon_y$ and $\epsilon_z$ respective to x, y and z directions) between measurement and real values are given in table 1. Processing is based on the detection of at least 7 peaks. Largest error is 4.3 % of the measured displacement while minimum relative error is 1.1 %. Those values can be reduced by improving the peak detection algorithm. Implementation of a sub-pixel interpolation scheme to refine the determination of peaks position could improved the resolution of the algorithm which is now limited by the pixel size.

## 5.2 Application to a real flow.

### 5.2.1 Description of the facility.

Experiments with a simple flow test case have a double purpose : on one hand, they are useful to optimize the holographic recording of micron flow-tracers and thus prepare more complex applications. On the other hand, they allows one to test the validity and the strength of the processing technique in real flow application.
Hologram recording are carried out in the potential core of a round jet flow. The test-facility is sketched on figure 9. It has two degrees of freedom in rotation. Therefore it is possible to modify the flow direction with accuracy by adjusting the desired yaw ($\alpha$) and pitch ($\beta$) angles. In the potential core, the turbulence level is limited. So we can assume that both velocity and direction of the flow are well defined. The nozzle diameter is 80 mm and the velocity range extends up to 40 m/s. Flow is seeded downstream with glycerine-smoke particles which are introduced through a Venturi.

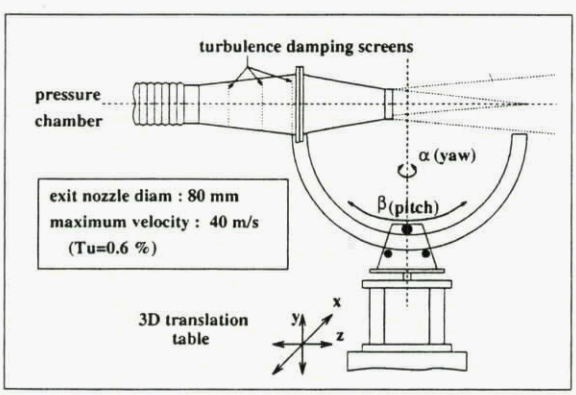


Fig. 9 : Calibration jet-flow facility.

The design of the holographic recording set-up (sketched on figure 10) is based on investigations of Royer [15]. Since the particle size is very small, it is not possible to use the original in-line set-up as it was used upon the benchmarking procedure. Now it is necessary to illuminate the portion of flow field with a high intensity laser beam coherent with the reference beam. The energy of those beams should be balanced so that the amount of light scattered by flow tracers is equal to the intensity of the reference beam in order to produce constructive interference on the holographic plate. The ratio of intensity per surface unit between the auxiliary illumination beam and the reference beam is ranging from $5^4$ to $8^4$. The balance of intensity was done by adjusting the position of a polarizer placed in the reference beam path. The laser source is a Ruby laser (wavelength = 694.3 nm) delivering 400 mJ per pulse. The flow velocity was fixed at 15 m/s and the time delay between both exposures was set at 10 $\mu$s. Depending on the flow configuration (because of geometrical constraints), the recording distance extends from 50 mm to 65 mm.

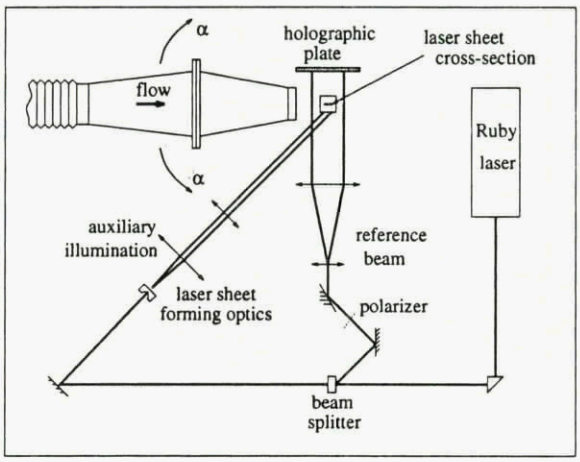


Fig. 10 : Recording set-up in the jet-flow.

### 5.2.2 Discussion of results.

During the first experiment, our investigations are restricted to two-dimensional flow configurations in order to optimize the recording conditions. A typical fringes pattern obtained with the optical processor is sketched on figure 11. The flow pitch-angle was set at 36 degrees. Like in classical Fourier analysis of two-dimensional PIV image, we observe a set of straight fringes. This pattern is processed by using auto-correlation technique and our digital processing algorithm. Respective measurements of the velocity are 15.2 m/s and 15.44 m/s, whereas evaluation of the pitch angle are 33.74 and 32.5 degrees. The agreement between results of both processing techniques is good and thus validate our processing method.
Figure 12 is an interference pattern obtained from a flow having a yaw angle equal to 67.5 m/s and a negative pitch angle of 5. degrees. It leads to a 3-D flow configuration with $\gamma_x$=2.4 and $\gamma_y$=-10.5 . Fringes are slightly curved but Speckle noise and saturation of the central part of the CID sensor by the light intensity reduce the number of visible fringes. The noise makes the detection of the fringes position difficult. Therefore results are processed in a restricted area located in the left-side of the pattern. The horizontal and out-of-plane velocity component are respectively measured to be equal to 9.35 m/s and 22.5 m/s. Those values are quite larger than the imposed flow velocity, although the ratio between the measurements is matching the imposed ratio $\gamma_x$. The spatial period of

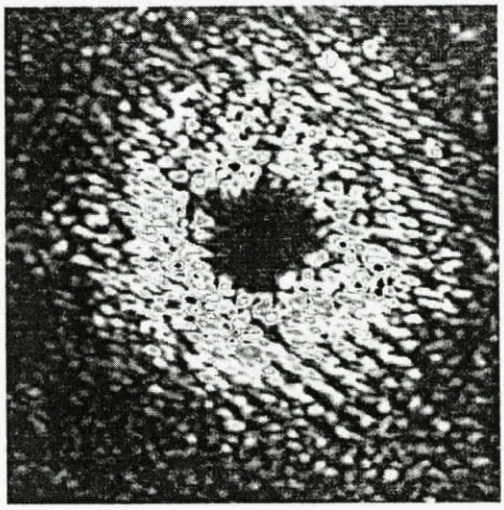

Fig. 11 : Example of fringes pattern from two-dimensional flow test-case.

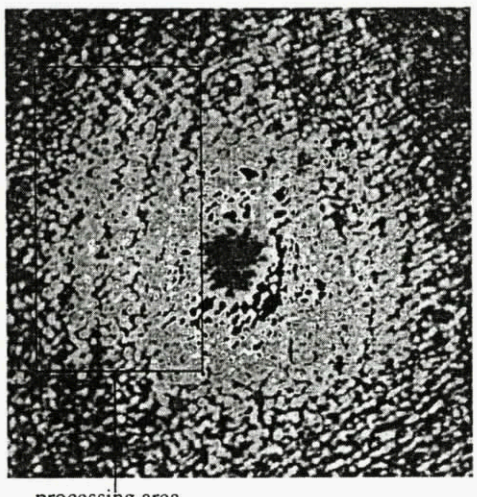


Fig. 12 : Example of fringes pattern from three-dimensional flow test-case : $\frac{\Delta z}{\Delta x}$=2.4 and $\frac{\Delta z}{\Delta y}$=10.5

the fringes in the processing area is computed by Fourier transformation and it gives rise to a value of the horizontal velocity component equal to 10.5 m/s. At the present state of development, one can only explain differences between imposed conditions and measurements by the fact that the processing is done with a limited number of fringes. This limited information does not allow one to compute accurately the horizontal displacement. It is nevertheless possible to measure the ratio $\gamma_x$ because the fringes curvature is well defined. But this curvature is not enough strong to enable the accurate measurement of the vertical velocity component.

## 6 CONCLUSION.

The use of holographic particle records for three-dimensional velocimetry is proposed. The extraction of velocity information is based on the digital processing of the optical Fourier transformation of the particle-field image. When experiments are carried out with a synthetic planar particle field, the results confirm theoretical expectations and demonstrate the validity of the technique. In the case of applications to real flows, optical noise and the size of flow tracers makes the obtaining of satisfactory results more difficult. In particular the size of the particle diffraction-halo limits the number of "visible" fringes and thus leads to more inaccurate results.
This processing technique is still in the early stages of its development. Further refinement of the noise removal algorithm and intensity peak finding should improve the quality of results. As concerns the improvement of the accuracy despite the limited number of observable fringes, an artificial decrease in the radius of curvature of the fringes (which is equivalent to an increase of the depth displacement component by moving the holographic plate between each recording exposure) can give rise to better results. This technical refinement is currently being studied by numerical and practical simulations.

## ACKNOWLEDGMENTS

This work is sponsored by the European Union, contract MATI-CT930033 of their "Measurement and Testing" research program and involves collaboration with the University of Edinburgh (United Kingdom), DANTEC Measurement Technology (Denmark) and the French-German research Institute "Saint-Louis". Many thanks to Laurent DUBOIS who carried out most of the experimental work.

## REFERENCES

[1] Paone N., Riethmuller M.L., and Van den Braembussche R.A. Experimental investigation of the flow in the vaneless diffuser of a centrifugal pump by pidv. *Exp. in Fluids*, Vol.7, No. 6:371–378., 1989.

[2] Liu Z-C., Landreth C.C., Adrian R.J., and Hanratty T.J. High resolution measurement of turbulent structure in a channel with particle image velocimetry. *Exp. in Fluids*, Vol.10, No. 6:301–312., 1991.

[3] Raffel M., Seelhorst U., Willert C., Vollmers H., Buetefisch K.A., and Kompenhans J. Measurement of vortical structures on a helicopter rotor model in a wind tunnel by LDV and PIV. *Heighth International Symposium on Applications of Laser Techniques to Fluid Mechanics*, Lisbon, Portugal, Vol.1, Paper 14.3, 1996.

[4] Chana K.S., Matthews I.W., Bryanston-Cross P.J., and Funnes-Gallanzi M. Intra-blade quantitative transonic flow measurements at the DRA pyestock isentropic light piston facility using piv. *11th Symp. on Measuring Techniques for Transonic and Supersonic Flow in Cascades and Turbomachines*, München, Germany, Paper 20., 1992.

[5] Tisserant D. and Breugelmans F.A.E. Rotor blade-to-blade measurements using particle image velocimetry. *Journal of Turbomachinery - ASME Transactions*, Vol.119, No. 2:176–181., 1997.

[6] Trolinger J.D. Particle field holography,. *Optical Engineering,*, Vol.14, No.5, 1975.

[7] Royer H. Holographic velocimetry of submicron particles. *Optics communications*, Vol.20, No.1, 1977.

[8] Hinsch K.D., Hinrichs H., Roshop A., and Dreesen F. Holographic and stereoscopic advances in 3D PIV. *ASME FED*, Vol.148:33–36., 1993.

[9] Hinrichs H. and Hinsch K.D. Multiple light sheet particle holography for 3d velocimetry. *Seventh International Symposium on Applications of Laser Techniques to Fluid Mechanics*, Lisbon, Portugal, Vol.2, Paper 26.2, 1994.

[10] Moraitis C.S.M. Optical processing of holographic particles records. PhD thesis, Physics Laboratory I, Technical University of Denmark, 1992.

[11] Press H.W., Flannery B.P., Teukolsky S.A., and Vetterling W.T. Numerical recipes in C: The Art of Scientific Computing. Cambridge University Press, 1988.

[12] Meng H. and Hussain F. In-line recording and off-axis viewing technique for holographic particle velocimetry. Applied Optics, Vol.34, No. 1:1827–1840., 1995.

[13] Collier R.J., Burckhardt C.B., and Lin L.H. *Optical holography*. Academic Press, 1971.

[14] Royer H. La microholographie. Technical report, ISL report 128/89, French-German Institute of Saint-Louis, 1989.

[15] Royer H. Montages particuliers pour l'holographie des micro-particules. Technical report, ISL report 118/76, French-German Institute of Saint-Louis, 1976.

# Demonstration of PIV in a Transonic Compressor

**Mark P. Wernet**
National Aeronautics and Space Administration
Lewis Research Center, MS 77-1, 21000 Brookpark Road
Cleveland, OH 44135, USA

## 1. SUMMARY

Particle Imaging Velocimetry (PIV) is a powerful measurement technique which can be used as an alternative or complementary approach to Laser Doppler Velocimetry (LDV) in a wide range of research applications. PIV data are measured simultaneously at multiple points in space, which enables the investigation of the non-stationary spatial structures typically encountered in turbomachinery. Many of the same issues encountered in the application of LDV techniques to rotating machinery apply in the application of PIV. Preliminary results from the successful application of the standard 2-D PIV technique to a transonic axial compressor are presented. The lessons learned from the application of the 2-D PIV technique will serve as the basis for applying 3-component PIV techniques to turbomachinery.

## 2. INTRODUCTION

Recent advances are leading to the emergence of PIV as a powerful velocity measurement technique which can be used as an alternative or complementary approach to LDV in a wide range of research applications. Refined data processing techniques and continuous increases in computational power have made PIV a more widely available and practical measurement technique. Stereo viewing optical configurations provide planar 3-component velocity measurements, which further enhances the usefulness of the PIV technique in turbomachinery applications. For a general overview of the various implementations of the PIV technique see Adrian, 1986 and Grant, 1997. PIV is a planar measurement technique wherein a pulsed laser light sheet is used to illuminate a flow field seeded with tracer particles small enough to accurately follow the flow. The positions of the particles are recorded on either photographic film or digital CCD cameras at each instant the light sheet is pulsed. In high-speed flows, pulsed Nd:YAG lasers are required to provide sufficient light energy (~100mJ/pulse) in a short time interval (<10 nsec) to record an unblurred image of the particles entrained in the flow. The data processing consists of either determining the average displacement of the particles over a small interrogation region in the image or the individual particle displacements between pulses of the light sheet. Knowledge of the time interval between light sheet pulses then permits computation of the flow velocity. Different data processing schemes are employed depending on the number of exposures per frame and the seed particle concentration (Keane and Adrian, 1993, Wernet, 1995). While each technique has some inherent benefits, the appropriate choice depends on the characteristics of the flow and recorded image constraints.

Turbomachines are used in a wide variety of engineering applications for power generation, pumping and aeropropulsion. The need to reduce acquisition and operating costs of aeropropulsion systems drives the effort to improve propulsion system performance. Improving the efficiency in turbomachines requires understanding the flow phenomena occurring within rotating machinery. Detailed investigation of flow fields within rotating machinery have been performed using Laser Doppler Velocimetry (LDV) for the last 25 years. LDV measurements are time and ensemble averaged over all of the blade passages in a rotating machine (Strazisar, 1986, O'Rourke and Artt, 1994, Skoch et al., 1997). Since the current state of the art in computational design tools deals with time averaged flow in turbomachinery blade rows (Ucer, 1994), LDV results are well suited for comparison to CFD predictions of the averaged flow fields. While a series of instantaneous spatial velocity measurements obtained using PIV can be averaged together to compute the time-mean flow field, individual PIV images enable the study of non-stationary spatial flow structures, making PIV a very powerful diagnostic for the study of unsteady flow phenomena.

Numerous researchers have employed various PIV techniques to study the unsteady flows in rotating machines. Paone et al., 1988, used PIV to make blade-to-blade plane velocity measurements in a centrifugal compressor. Although not a rotating machine application, Bryanston-Cross et al, 1992 described photographic PIV measurements obtained in a transonic turbine cascade rig. The light sheet illumination was introduced via an 8.0 mm diameter hollow turbulence generating bar which was already part of the experimental rig. Post et al., 1991 also discuss PIV measurements in a turbine cascade using photographic film. In this work color film was employed and the light sheet pulses were of two distinct wavelengths, which then permitted cross-correlation data reduction of the electronically digitized photographs. Cogineni and Goss, 1997 have described a two color digital PIV

*Paper presented at an AGARD PEP Symposium on "Advanced Non-Intrusive Instrumentation for Propulsion Engines", held in Brussels, Belgium, 20-24 October 1997, and published in CP-598.*

technique which should be applicable to turbomachinery applications. A high resolution (3000x2000 pixel) single CCD sensor color camera is employed to record the particle images at two instances in time on a single CCD image frame using red and green illumination pulses. Shepherd et al, 1994 used photographic PIV to study the flows inside both centrifugal and axial fans. The test setups employed water as the working fluid and hence were restricted to low rotational speeds. Tisserant and Breugelmans, 1997 used a digital PIV technique to measure the flow field in a subsonic (30-70 m/s, 3000-6000rpm) axial fan. They noted that an optical periscope type probe (similar to that used by Bryanston-Cross, et al 1992) is required for introducing the light sheet into the flow and that out-of-plane velocities are sometimes significant, causing a loss of correlation of the in-plane velocities. Rothlübbers et al, 1996, used digital PIV to study the flow in a radial pump. Low seed particle concentrations were identified as not suitable for rotating machine studies, where high spatial resolution measurements are required. Oldenburg and Pap, 1996, used a digital PIV setup to investigate the flow field in the impeller and volute of a centrifugal pump. The lab scale facility used water as the working fluid and a transparent impeller.

The application of PIV to turbomachinery at NASA Lewis Research Center (LeRC) is a two stage program wherein 2-D PIV is initially applied to resolve issues regarding optical access, light sheet delivery and flow seeding. In the second phase of the program, a stereo viewing optical system employing tilted CCD sensor planes which satisfy the Scheimpflug condition will be used to acquire planar, 3-component velocity measurements. The stereo viewing planar, 3-component PIV technique utilizing Fuzzy inference for maximized data recovery has been previously demonstrated in a supersonic nozzle flow at LeRC (Wernet, 1996).

In this work we discuss the successful application of digital PIV to a transonic compressor. Measurements have been obtained in a single stage 50.8 cm diameter transonic axial compressor facility at LeRC. The measurements were obtained using upstream illumination of the blade-to-blade rotor passage at a rotational speed of 17,150 rpm and also using downstream illumination at a rotational speed of 13,800 rpm. A special optical periscope probe was used to generate and introduce the light sheet into the flow. A brief description of the optical setup and some preliminary results are presented. Techniques for averaging together PIV velocity vector maps with spurious vectors are also presented and discussed. The averaged measurements illustrate that PIV yields high accuracy velocity vector maps in much less time than traditional LDV techniques.

## 3. OPTICAL ACCESS AND LIGHT SHEET DELIVERY

Obtaining optical access to the flow field is never a trivial issue in rotating machine applications since the casing through which the measurements are to be made is cylindrical. Ideally, the optical access port will permit the collection of light scattered from particulates in the flow without significantly disturbing the flow. The LeRC transonic compressor facility has a large optical access port which is curved to match the radius of curvature of the compressor casing. Backscatter LDV systems are reasonably well suited for the single optical access port typically encountered in turbomachinery applications. However, the standard PIV technique requires that the light scattered by the particles traversing the light sheet be collected at 90° from the plane of the light sheet. Hence, the light sheet must be introduced either upstream or downstream from the optical access port used for scattered light collection and directed along the flow direction. Care must be taken to insure that the light sheet optics do not disturb the stream tube feeding the blade passage under study. If the propagation direction of the light sheet is aligned with the stagger angle of the blades and the optics are located sufficiently far upstream or downstream, then the flow in the measurement region will not be disturbed.

A very compact light sheet delivery system was constructed using a periscope type configuration as shown in figure 1a. The pulsed Nd:YAG beam is directed down the bore of the tube which contains light sheet forming optics and a 90° turning mirror. The periscope probe has an outside diameter of 12.7 mm and utilizes 8 mm diameter optics (200 mm focal length spherical and -25 mm focal length cylindrical lenses) to form the Nd:YAG laser beam into a laser sheet. The light sheet exits the probe through a window which keeps the optics inside the probe protected from contamination by seed material. An implementation of this NASA designed and constructed probe is shown in operation in figure 1b. The small diameter periscope probe is inserted through the compressor casing upstream of the measurement location, see figure 1c. Moving the probe in and out through the casing changes the spanwise location of the illumination plane. In order to align the propagation direction of the light sheet along the blade stagger angle, the light sheet probe is inserted below the horizontal rig centerline. This insertion location also ensures that the light sheet probe does not disturb the flow upstream of the actual measurement location. The mounting base which attaches the probe to the casing is designed so that the light sheet generating probe is oriented horizontally, even though the entrance point through the rig casing window is below the horizontal centerline of the rig. Maintaining a horizontal entry ensures that the plane of

the light sheet will remain parallel with the axis of the compressor, simplifying the recording system requirements. Figure 1d shows a photograph of the PIV system installation in the compressor rig. Downstream illumination is being used in this configuration. The Nd:YAG laser is observed in the lower left corner of the picture along with an articulated arm which extends from the laser over to the light sheet probe. The light sheet illumination can be seen in the compressor blade rows and the PIV camera is mounted next to the rig.

In the periscope probe configuration, directing the pulsed laser beam down the bore of the periscope tube is extremely challenging. An articulated light arm with mirror joints was used to easily and reliably direct the beam down the bore of the probe, see figure 1c and d. Articulated light arms for Nd:YAG laser beam delivery are commercially available from several commercial PIV vendors and permit the full energy range of the laser to be used (200 mJ/pulse at 532 nm). Use of the light arm simplifies the coupling of the Nd:YAG beam to the periscope and also adds an increased level of safety to the installation since the beam is entirely enclosed when outside of the compressor casing. The light sheet delivery probe depicted in figure 1a has been successfully used by the author to deliver 125 mJ pulsed illumination into the compressor facility.

## 4. SEEDING

A uniform and sufficiently high concentration of flow seeding is the most critical element in any PIV experiment. If the number of particles recorded on the CCD image frame is too low, then correlation techniques cannot be applied, although particle tracking could still be utilized. As discussed previously, particle tracking does not typically provide a sufficient density of measurements necessary to adequately characterize the complex flows encountered in turbomachinery (Rothlübbers et al, 1996). However, provided the particle concentration is sufficiently high to support correlation computations particle tracking can be combined with the correlation technique results to provide high spatial resolution velocity estimates (Keane and Adrian, 1993, Wernet, 1995).

The global facility seeding system developed for use in laser anemometry measurement programs in the transonic compressor facility was inadequate for PIV measurements. A sample calculation reveals the inadequacy. An LDV experiment utilizing a probe volume that is 100 μm in diameter by 500 μm long to measure a 200 m/s flow may achieve a data rate of 2KHz. This measurement rate is obtained by using a seed particle concentration of 0.2 particles/mm$^3$. Conversely, in a digital PIV experiment where the field of view is 50×50 mm (yielding a spatial resolution of about 50 μm/pixel), the light sheet thickness is 1 mm, and the interrogation region size is 32×32 pixels, the required seed particle concentration to ensure that there are 15 particles per interrogation region(or 15 particle pairs for double exposure image capture) is 6 particles/mm$^3$. Hence, the seeding requirements for PIV are more than an order of magnitude higher than that required for LDV.

Global seeding of a large scale facility with high mass flow rates for PIV measurements is impractical. Instead, the seed material must be introduced locally near the measurement plane. For transonic flows, sub-micron particles are required for accurately following the flow. A multiple jet atomizing seeding system employing smoke juice and producing particles with a nominal diameter of 0.7 μm seeds the flow field via a small diameter tube through the compressor casing. Locating the seed injection tube many tube diameters ( > 70) upstream of the measurement station provided sufficient seed particle concentrations for correlation processing of the collected PIV images while adding negligible disturbance to the measurement region.

## 5. IMAGE ACQUSITION AND PROCESSING

The primary factors influencing the choice of image acquisition and processing techniques for the LeRC turbomachinery application are: efficiency of rig run time; maximum flexibility in image manipulation and storage; and optimal data processing. Although photographic film offers the highest spatial resolution image measurements, electronic image acquisition has several advantages such as: enabling cross-correlation processing; real time feedback of the flow seeding conditions; optimization of the laser inter-pulse timing; image focusing; on-line assessment of flare light from blade surfaces and simplified data archiving and storage (image files instead of photographic film). A judicious choice of the camera field of view can result in acceptable levels of spatial resolution. CCD cameras with 1000×1000 pixel sensors can image a 50×50 mm field of view with 50 μm/pixel resolution. Assuming 64×64 pixel processing subregions with 50% overlap, the resulting velocity vector grid will have approximately 1.6 mm spatial resolution. In cases where larger fields of view are required and/or high resolution CCD imagers are not available, photographic film may be the only acceptable choice.

Another advantage to using electronic image capture in PIV image acquisition has to do with correction of the images from window distortions. In many cases the optical access ports used to record the PIV image data are curved to match the inside diameter of the turbomachine casing. Image capture through these curved windows results in image distortion. By

recording a reference image of a calibration target with a Cartesian grid of points, a set of image warping coefficients can be computed to correct for the effects of the window distortion. The image warping is readily applied to the digital imagery, but is not so straightforward when photographic recording is used.

Submicron particles are required to faithfully follow the flow in transonic machinery. Although the spatial resolution of the optical system is much larger than the actual geometric image of the particle on the CCD sensor, the diffraction effects of the optical system may produce effective particle images which are much larger (Adrian, 1986). For example, using an f/30 optical recording system operating at a magnification of 0.16 and illumination wavelength of 0.532 μm, would yield 45 μm diameter diffracted particle images for 0.7 μm particles. The diffracted particle images are on the order of the pixel size and hence will result in a minimal correlation peak centroid estimation error, (Wernet and Pline, 1993)

Cross-correlation data reduction is the optimal data reduction technique for PIV since it offers directionally resolved velocity vectors, no self correlation peak and hence no restriction on the minimum particle displacement between exposures (the relative accuracy of the velocity measurements is inversely proportional to the displacement between exposures, therefore a reasonable displacement is desirable). To facilitate cross-correlation data processing, a pair of single exposure image frames are required. Refinement of the "frame-straddling" technique first demonstrated by Wernet, 1991 has led to the development of commercial PIV cameras which permit a pair of image frames to be acquired with a very small inter-frame period (<1 μsec). The cameras employed are standard RS-170, 60 fields/sec video cameras or high resolution full frame CCD imagers running at 30 frames/sec. Using the frame-straddling technique, both camera systems offer inter-frame exposure intervals of 1/30 sec down to < 1 μsec.

Flare light reaching the CCD camera can cause significant amounts of blooming, leaving large areas of the imaged field useless. Aligning the light sheet along the blade stagger angle minimizes the intersection area of the light sheet with the blade surface, hence, significantly reducing the amount of surface flare light. Painting the rotor hub and blades black also significantly improves the signal to noise ratio in the recorded images. Some flare light from the blade surfaces is desirable for referencing since it marks the position of the blade leading edge/surface in the recorded images. When all else fails, black tape can be placed on the optical access port window to block flare light caused by the light sheet hitting the blade surfaces.

Recently available commercial PIV systems provide user friendly software interfaces and have made the technique close to "turn key". The main benefit of these commercial PIV systems stems from their ability to provide real-time, or very nearly real-time velocity vector maps from the acquired imagery by using electronic cameras and fast data processing. The electronic image acquisition and real-time processing of the acquired imagery provides immediate feedback to the experimenter on the quality and uniformity of the flow seeding, the appropriateness of the selected inter-pulse exposure interval and laser power level. Once the experimental parameters have been fine-tuned the data acquisition system can be configured to rapidly acquire a series of data sets so that average flow properties can be computed.

For the acquisition of images from facilities with high overhead costs, PIV systems which allow fast acquisition and storing of the acquired digital images are most desirable. Fast processing of the data is not important once the experimental parameters have been optimized; however, archiving the original image data is extremely important. The processing parameters selected during the initial setup may not prove to be the best settings for achieving the maximum information recovery from the raw PIV images. Archiving all of the raw image data permits the investigation of spurious results in the processed vector fields. Without the raw image files there is no way to discern the real cause of spurious vectors. Additional image processing steps may be required to maximize information recovery in regions of the image where noise levels are high, or particle concentrations are low. The application of combined correlation/particle tracking data processing strategies are usually performed off-line due to the longer processing times and steps involved. Finally, future improvements in data processing algorithms and techniques may permit better data extraction. For all of these reasons, storing the original image files is desirable and may save the expense of having to rerun the experimental tests.

## 6. AVERAGING VELOCITY VECTOR MAPS

Each PIV measurement realization is spatially averaged and the accuracy of the average particle displacement estimate across the interrogation region depends on several factors: the particle seed density in the fluid must be high enough so that on the order of 15 particles are recorded in each interrogation region; the tracer particles must be sufficiently small so that the particles accurately follow the flow; and the recorded particle images should be small in order to minimize the error in estimating the particle displacement peak (Wernet and Pline, 1993). When these criteria are satisfied, PIV estimates on the order of a few percent are obtained (Adrian, 1986). Averaging the results from several

hundred image frames will lower these errors, yielding accuracies which are comparable to those obtainable with LDV, and yet the total acquisition time for the PIV data is nearly an order of magnitude shorter.

One of the advantages of PIV over traditional point averaging techniques such as LDV is that both the instantaneous and average flow field properties can be examined. The sequence of instantaneous PIV images that are acquired must be combined to compute the average flow field quantities. This would be a straight forward process if all of the PIV images were uniformly seeded and of good quality. However, while the seed density is generally reasonably uniform, some image frames are acquired with sparse or non-uniform seeding. When processed, these images will yield velocity vector maps which are incomplete or have spurious vectors where the seed density is inadequate for proper correlation processing. These spurious vectors will have a detrimental effect on the computed mean flow properties, and therefore a procedure for judiciously removing them must be used.

The procedure devised for computing the mean flow quantities from a series of processed PIV image velocity vector maps utilizes both hard velocity cutoff limits and an automated procedure for identifying outliers. The high and low velocity cutoff limits set by the user are applied and then the mean and standard deviation are computed at each grid point in the velocity vector map. The automated procedure for removing outliers is based on Chauvenet's criterion, (Taylor, 1982) in which the probability of occurrence of a given point deviating from the mean is computed. The main assumption here is that the parent velocity distribution is Gaussian. The number of standard deviations that a given point lies from the mean is first computed. Then the probability that a given point should deviate from the mean by this many standard deviations is computed from the error integral and multiplied by the number of points in the distribution. If the computed probability is less than a preset level then the point is removed. This technique may not be appropriate in instances where the parent distribution is not Gaussian, such as in the vicinity of a shock where the distribution of velocity measurements may be bimodal. An advantage of this technique is that it relies on the computed mean flow properties over several independent image frames to discriminate spurious vectors. In a single instantaneous PIV image acquisition, other criteria such as the ratio of the correlation peak to the first noise peak must be used, which can mistakenly remove good data points from the image maps. Other techniques for validation of the instantaneous velocity vector maps exist (Wernet, 1995), however, none of these techniques were used to process the measurements presented here.

## 7. EXPERIMENT

The facility used in the study is a 50.8 cm diameter, single stage axial compressor with a design speed of 17,188 rpm and a mass flow rate of 20.19 kg/s. The rotor has 36 blades with a span of 75 mm at the leading edge and 56 mm at the trailing edge. The blade stagger angle is 41° at the hub and 61° at the tip. The casing is fitted with a large optical access window (200×100 mm) which is molded to the complex contour of the casing. The glass thickness is 3 mm and produces a very small amount of optical distortion. None of the optical distortion effects will be considered here.

The seeding was provided by a 6 jet atomizer (producing 0.7 μm diameter particles using Rosco's smoke juice) which injected seed through a 6 mm diameter seeding probe located approximately 80 probe diameters upstream of the rotor. The seeding probe position could be adjusted radially to provide seed in the plane of illumination. The light sheet was introduced into the rig via a LeRC-designed and built optical periscope probe depicted in figure 1a. The probe was inserted through the casing at two locations: at a circumferential position 45° below the rig centerline and approximately 200 mm upstream of the rotor; and also at 45° above the rig centerline and 240 mm downstream of the rotor. The inclination angle of the light sheet roughly matched the blade stagger angle at both mid span for the upstream illumination case and near the blade tip for the downstream illumination setup. The light sheet generated by the probe was approximately 45 mm wide and 1 mm thick at the measurement location. A commercial articulated light arm was used to couple the light from a dual cavity Nd:YAG laser system to the periscope probe. The Nd:YAG light sheet pulse energy was approximately 125 mJ/pulse. A schematic representation of the optical system implementation in the compressor rig is depicted in figure 1c.

Commercial PIV system software running on a PC was used to collect and analyze the data. No array processing hardware was required. A 1000×1000 pixel cross-correlation CCD camera utilizing frame-straddling was used to acquire pairs of single exposure images. An adjustable electronic delay triggered from a once-per-rev signal on the rotor was used to trigger image acquisition and laser firing to record PIV data from a selected blade passage on the rotor wheel. The camera image acquisition and laser firing were all software controlled via a commercial synchronizer. Correlation processing was used to initially verify that sufficient seed particles were present and that the appropriate laser inter-pulse timing had been selected. After the PIV experimental parameters were determined, raw PIV images were acquired directly into the PC's memory and then saved directly to disk without processing the images. Correlation processing of the images was performed off-

line after the experiment was completed. The image acquisition rate was 10 frame pairs/sec (limited by the Nd:YAG laser repetition rate) and the time to store each image to disk was approximately 1 second. This data acquisition mode minimized the rig run time and offered maximum flexibility in the selection of the appropriate post processing of the acquired images.

## 8. RESULTS AND DISCUSSION

For the upstream illumination case the camera image scale factor was 56 μm/pixel, yielding a 56x56 mm field of view, and the inter-frame time was 2.67 μs. The light sheet illumination covered most of a blade passage in the circumferential direction at a passage height of 46 mm from the hub (70% span). The plane of the light sheet intersected the lower blade at constant radius, but was slightly inclined along the pressure surface of the upper blade. The compressor was operated at 17,150 rpm and a mass flow rate of 20.14 kg/s, yielding a pressure ratio of 1.86. The flow velocity upstream of the rotor is 190 m/s and the blade speed at the measurement plane is 390 m/s. The flow direction is from left to right and the rotational direction is from top to bottom. A single exposure raw PIV image is shown in figure 2a and a processed instantaneous velocity vector map in figure 2b. Figure 2a shows the relative positions of the blades and the level of particulate seeding. Tape has been placed on the windows to reduce the flare light scattered off of the blade surfaces. The blade profiles at the measurement plane location are shown in figures 2b-d. The vectors in figure 2b are shown in the relative frame (wheel speed has been added) and are scaled in proportion to velocity vector magnitude and also gray scale coded by vector magnitude. The correlation subregion size was 64x64 pixels (3.6x3.6 mm subregions) with 50% overlap. Spurious vectors located around the blade surfaces and in the periphery of the image have been removed. No interpolation or data filling has been applied. Figure 2c shows the average velocity vector map from a 110 frame average of processed velocity vector maps. Under these rig operating conditions a strong shock forms off the upper blade leading edge and spans the blade passage. The position of the blade-to-blade plane shock is readily observed by the sharp drop in vector magnitude within the blade passage (light to dark shading). A bow wave also forms off of each blade extending outward (up and to the left) from each blade leading edge. The bow wave from both the lower and upper blades are observed in the left portion of the image. There is also a significant change in velocity magnitude across the bow waves as indicated by the change in gray scale shading. The average velocity vector map in figure 2c is smoother and has more filled in areas than the instantaneous vector map shown in figure 2b. Figure 2d shows the relative standard deviation for the frame averaged data shown in figure 2c. The magnitudes of the relative standard deviations for each velocity vector in the average vector map are denoted by gray scaled dots. The relative standard deviations shown in figure 2d are on the order of 5% for most of the measurements. Larger standard deviations are observed where shocks exist in the flow due to the large velocity gradients in these regions.

The computed relative standard deviations contain the effects of flow turbulence, the measurement errors of the PIV technique, the errors in the once-per-rev trigger signal and any particle seeding variations or particle lag effects. Since the expected flow turbulence is on the order of 2-3%, the low relative standard deviations shown here are believed to result mostly from the flow turbulence. The expected measurement errors from the PIV technique were previously discussed and are believed on the order of a few percent for the instantaneous PIV images, and on the order of 1% for the 110 frame average shown here. The contribution to the measured relative standard deviations arising from errors in the once-per-rev signal timing are expected to be less than 1%. The remaining particle lag errors arising from non-uniform particle seeding are also assumed to be less than 1%. Accounting for the contribution of all of these error sources agrees with the observed relative standard deviations.

Previous LDV measurements (Strazisar, 1997) acquired in the same facility under similar conditions will be used to assess the quality and accuracy of the averaged PIV data. The vertical line inside the blade profiles in figure 2c indicates the 20% chord position along the blade at 70% span. Figure 3a and 3b show the relative Mach number versus % pitch measurements obtained using PIV and LDV, respectively. The LDV measurements were obtained at a higher sampling density across the blade pitch (200 points) and are closer to the blade surfaces than the PIV measurements (17 points). Both systems show the blade-to-blade shock occurring at approximately 65% pitch. Both sets of measurements show the shock spanning about 15% of pitch. Figures 3c and 3d show the absolute flow angle versus % pitch measurements obtained using PIV and LDV. Again the measurements between the two techniques are in very good agreement, spanning essentially the same range and exhibiting similar features.

For the downstream illumination case the camera image scale factor was 53 μm/pixel, yielding roughly a 53x53 mm field of view. The light sheet illumination covered most of a blade passage in the circumferential direction at a passage height of 50 mm from the hub at the blade trailing edge and 70 mm from the hub at the blade leading edge (nominally 91% span). Figures 4a and b show the velocity vector maps and relative standard deviations from both a 40 frame and 50 frame average

of processed PIV images. The inter-frame acquisition times were 2.67 μs and 1.53 μs, respectively. The correlation subregion size was again 64x64 pixels with 50% overlap. For these measurements the compressor was operated at 13,800 rpm and a mass flow rate of 15.4 kg/s, yielding a pressure ratio of 1.58. The blade speed at the measurement plane is 345 m/s. The vector magnitudes in figure 4a and b are again coded by length and gray scale and the standard deviations in figures 4c and d are coded by gray scale. The location and existence of the blade wake is easily identified by the low velocity region aligned with the blade. The width of the wake appears to be approximately 5 vectors across, which corresponds to a physical width of 8 mm. The location of the blade wakes in the instantaneous images were wider and randomly meandered about. Again as in the upstream rotor illumination case, the relative standard deviations are generally on the order of 5% throughout most of the image, becoming larger mainly in the blade wake region.

There are some slight differences in the velocity vector magnitudes shown in figures 4a and b. The location of the blade wake and velocity magnitude within the blade wake are essentially identical. However, the velocity vectors above and below the blade wake are of differing magnitudes and do not exhibit the same uniformity. This lack of uniformity may stem from: the unequal number of frames averaged together in the two cases; insufficient number of frames averaged in both instances; or a significant out-of-plane velocity component. The uniformity and similarity of the relative standard deviations obtained in figures 4c and d suggest that the differences in the velocity vector maps is not caused by a lack of a sufficient number of frames used to compute the averages. The upstream measurement results show that the PIV data are of high quality and have low measurement error. For these downstream illumination images there may be significant tip clearance flow near the blade tips, which manifests itself as an out-of-plane or radial velocity component. The data in figure 4b was obtained using a shorter inter-frame time and hence, should be less sensitive to the radial velocity component. The measurements in figure 4a may be biased to higher velocities since the out-of-plane velocity component may cause a loss of correlation or velocity bias due to the longer inter-frame acquisition time. No definite conclusions can be drawn from these images, however, they do emphasize the importance of measuring all three velocity components in the complex flows encountered in turbomachinery in order to unambiguously characterize the flow.

## 9. SUMMARY

Recent advances are leading to the emergence of Particle Imaging Velocimetry as a powerful velocity measurement technique which can be used as an alternative or complementary approach to LDV in a wide range of research applications. Commercial PIV processors have matured to the point where they have simplified the data acquisition and reduction of PIV imagery to a "turn key" operation. Successful PIV measurements have been obtained in a transonic compressor yielding both instantaneous snapshots and time averaged velocity vector maps of the complex turbomachinery flow. Techniques were demonstrated for averaging velocity vector maps which contain spurious vectors resulting from varying amounts of particulate seeding in the captured images. The preliminary results shown here and compared with previous LDV measurements prove that the PIV technique yields fast and accurate velocity information. The average velocity vector maps obtained here in just a matter of minutes have previously taken a factor of 6 longer to obtain via LDV in similar facilities. The PIV results show clear evidence of the blade wakes. The instantaneous vector maps show the meandering nature of the blade wakes while the averaged images show the spatial extent of the disturbance. The PIV measurement errors have been shown to be less than variations caused by the flow turbulence. The nominal relative standard deviation in the PIV measurements were shown to be roughly 5%, except near shocks or in the blade wake regions.

The study of the complex flow fields encountered in turbomachinery necessitates the use of 3-component velocity measurements to fully resolve the flow field features. On the road to development of a 3-component measurement capability we have demonstrated a 2-D PIV measurement program in a transonic compressor. Future work will concentrate on extending the 2-D PIV technique to obtain planar 3-component velocity measurements in high-speed turbomachinery using a two camera, stereo viewing arrangement.

## ACKNOWLEDGEMENTS

I would like to thank Mr. Dave Williams and Mr. Barry Piendl for their support in operation of the transonic compressor facility and Dr. Anthony Strazisar for useful discussions on transonic compressor fluid mechanics. I would also like to Thank Mr. W. T. John for fabricating the light sheet probe and assisting in the installation of the PIV system.

## 10. REFERENCES


Adrian, R. J., "Multi-Point Optical Measurements of Simultaneous Vectors in Unsteady Flow - A Review", *Int. J. of Heat and Fluid Flow*, Vol 7, pp 127-145, 1986.

Bryanston-Cross, P. J., Towers, C. E., Judge, T. R., Towers, D. P., Harasgama, S. P., Hopwood, S. T., "The Application of Particle Image Velocimetry (PIV) in a Short-Duration Transonic Annular Turbine Cascade", *ASME J. of Turbomachinery*, Vol. 114, pp 504-509, April 1992.

Cogineni, S., Goss, L., Copenhaver, W., Gorrell, S., "Development of Digital Two-Color PIV for Turbomachinery Applications", *AIAA 35th Aerospace Sciences Meeting*, AIAA-97-0494, January 6-10, Reno NV, 1997.

Keane, R.D., Adrian, R.J., "Prospects for Super-Resolution with Particle Image Velocimetry", *SPIE Conference on Optical Diagnostics in Fluid and Thermal Flow*, Vol 2005, San Diego, CA, pp 283-293, July 14-16, 1993

Grant, I., "Particle Imaging Velocimetry: a Review", *Proc. Instn Mech Engrs*, Vol 211, Part C, pp 55-76, 1997.

Oldenburg, M. and Pap, E., "Velocity Measurement in the Impeller and in the Volute of a Centrifugal Pump by Particle Image Displacement Velocimetry", *Eighth International Symposium on Applications of Laser Techniques to Fluid Mechanics*, Lisbon, Portugal, July 8-11, pp 8.2.1-8.2.5, 1996.

O'Rourke, M. J. and Artt, D. W., "Considerations Involving the Application of the Laser Doppler Velocimetry Technique to Fluid Measurements Within a Radial Inflow Turbocharger Rotor", *Seventh International Symposium on Applications of Laser Techniques to Fluid Mechanics*, Lisbon, Portugal, July 11-14, pp 3.1.1-3.1.5, 1994.

Paone, N., Riethmuller, M. L., Van den Braembussche, R. A., "Application of Particle Image Displacement Velocimetry to a Centrifugal Pump", *Fourth International Symposium on Applications of Laser Techniques to Fluid Mechanics*, Lisbon, Portugal, July 11-14, pp 6, 1988.

Post, M. E., Goss, L. P., Brainard, L. F., "Two-Color Particle Imaging Velocimetry in a Turbine Cascade", *Proceedings of the AIAA Aerospace Sciences Mtg*, AIAA 91-0274, Jan 7-10, 1991.

Rothlübbers, C., Scheffler, T., Orglmeister, R., Siekmann, H., "Particle Tracking Velocimetry Measurements in a Radial Pump with Particle Pair Detection Using the Hough Transform", *Eighth International Symposium on Applications of Laser Techniques to Fluid Mechanics*, Lisbon, Portugal, July 8-11, pp 8.6.1-8.6.6, 1996.

Shepherd, I. C., La Fontaine, R. F., Welch, L. W., Downie, R. J., "Velocity Measurement in Fan Rotors Using Particle Imaging Velocimetry", *ASME Conference on Laser Anemometry - 1994: Advances and Applications*, Vol. 191, pp 179-183, 1994.

Skoch, G. J., Prahst, P. S., Wernet, M. P., Wood, J. R., Strazisar, A. J., "Laser Anemometer Measurements of the Flow Field in a 4:1 Pressure Ratio Centrifugal Impeller", ASME 97-GT-342, June 1997.

Strazisar, A.J., "Laser Fringe Anemometry for Aero Engine Components", in AGARD CP-399, Advanced Instrumentation for Aero Engine Components, 1986.

Strazisar, A.J., Personal Communication, 1997.

Taylor, J. R., An Introduction to Error Analysis, University Science Books, Oxford University Press, Mill Valley, CA, 1982.

Tisserant, D. and Breugelmans, F. A. E., "Rotor Blade-to-Blade Measurements Using Particle Image Velocimetry", *ASME J. of Turbomachinery*, Vol. 119, pp 176-181, April 1997.

Ucer, A., Editor, "Turbomachinery Design Using CFD", AGARD Lecture Series 195, May, 1994.

Wernet, M. P., "Particle Displacement Tracking Applied to Air Flows", *Fourth International Conference on Laser Anemometry*, Cleveland, OH, pp 327-335, August 5-9, 1991.

Wernet, M. P., Pline, A., "Particle Displacement Tracking Technique and Cramer-Rao Lower Bound Error in Centroid Estimates From CCD Imagery", *Experiments in Fluids* **15**, 295-307, 1993.

Wernet, M. P., "Fuzzy Inference Enhanced Information Recovery from Digital PIV Using Cross-Correlation Combined with Particle Tracking", *SPIE Conference on Optical Diagnostics in Fluid and Thermal Flow*, Vol. 2546, July 9-14, 1995.

Wernet, M. P., "Stereo Viewing 3-Component, Planar PIV Utilizing Fuzzy Inference", AIAA-96-2268, June 17-20, 1996.

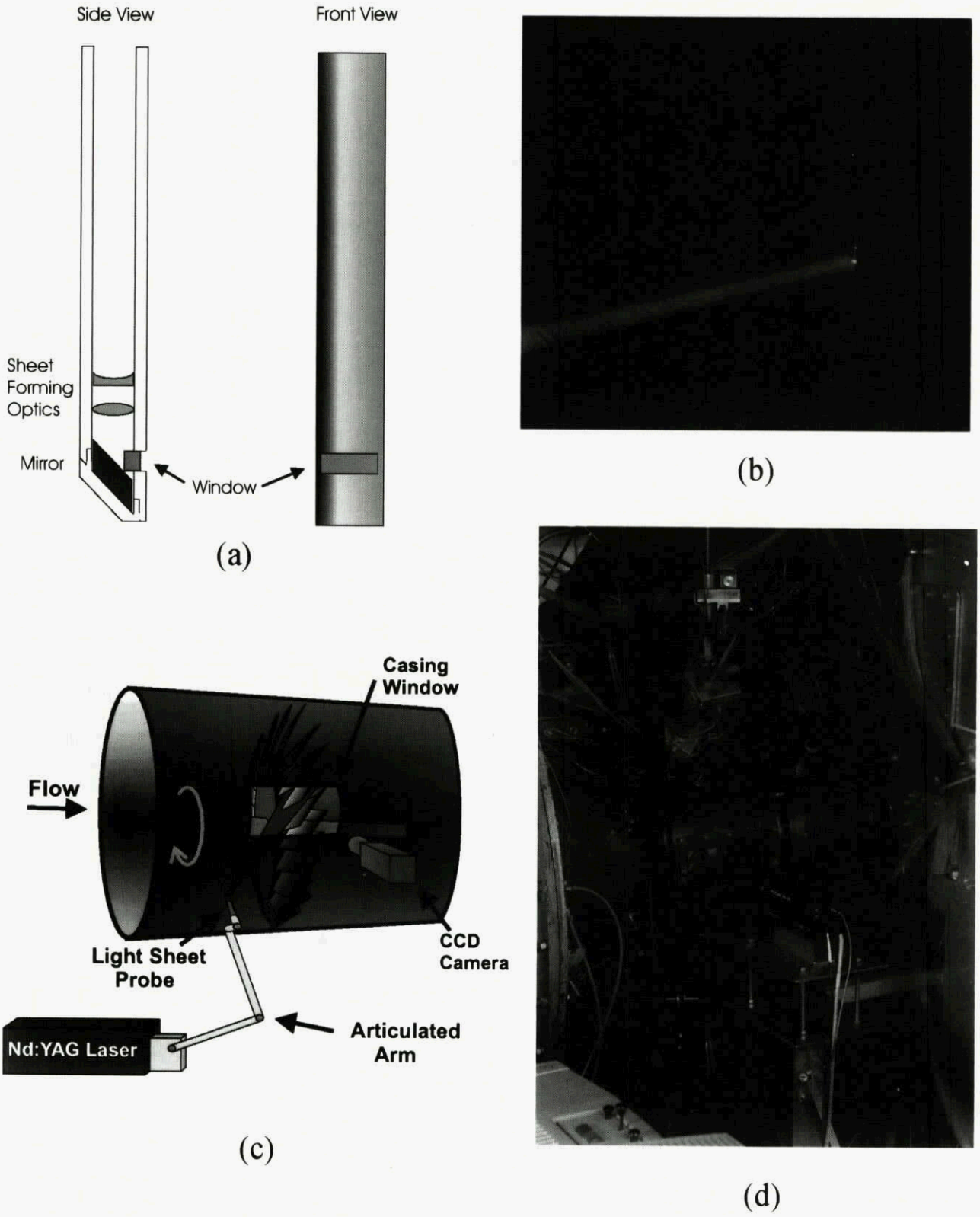


Figure 1: a) Cut away view of the light sheet periscope probe showing lenses, mirror and exit window;
b) Picture of light sheet probe in operation where the light sheet emerges from the probe horizontally;
c) Diagram indicating light sheet insertion into compressor rig, location of casing window and CCD camera;
d) PIV system installation, note laser in lower left corner and articulated armconnecting to probe (upper right).

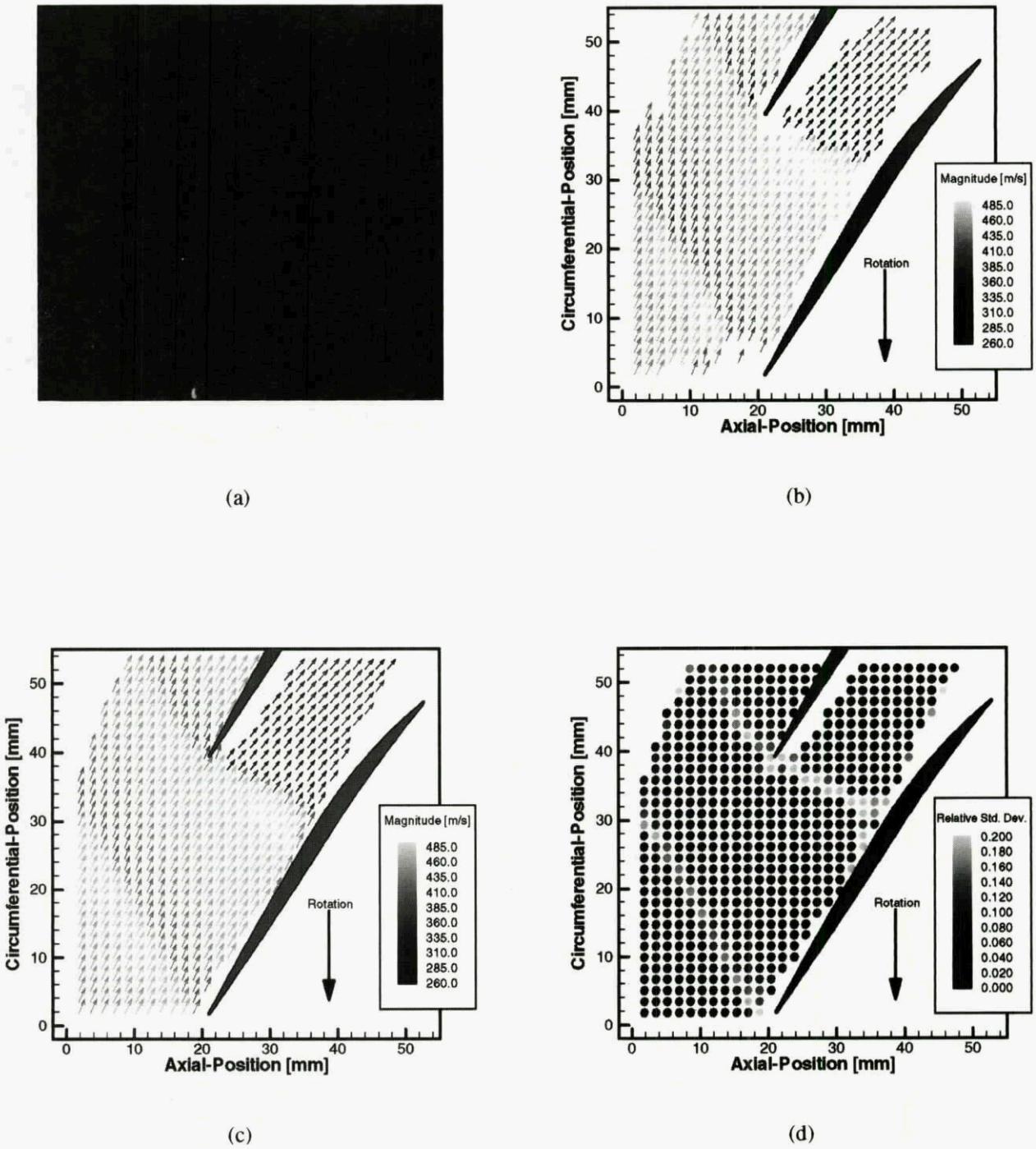


Figure 2: a) Raw single exposure CCD camera image of seed particles in compressor flow, tape has been placed on the casing window over the blades to block surface flare light; b) Instantaneous PIV image of the particle field shown in (a); c) Average of 110 processed vector maps; d) Relative standard deviation of the 110 frame average shown in (c).

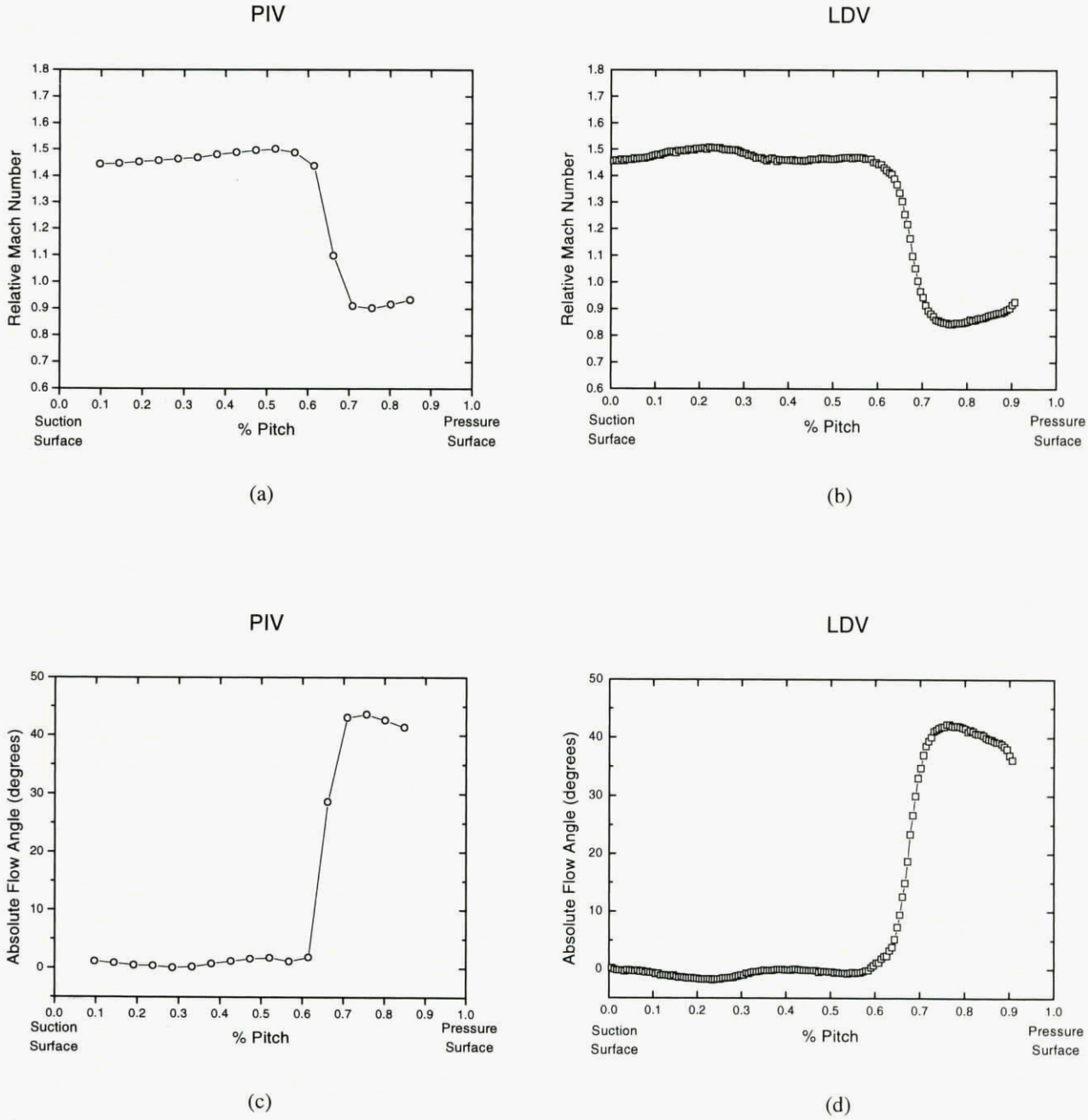


Figure 3: Comparison of PIV and LDV measurements at 20% chord for the velocity vector maps shown in figure 2. Mach number versus % Pitch for PIV (a) and LDV (b); Flow angle versus % Pitch for PIV (c) and LDV (d).

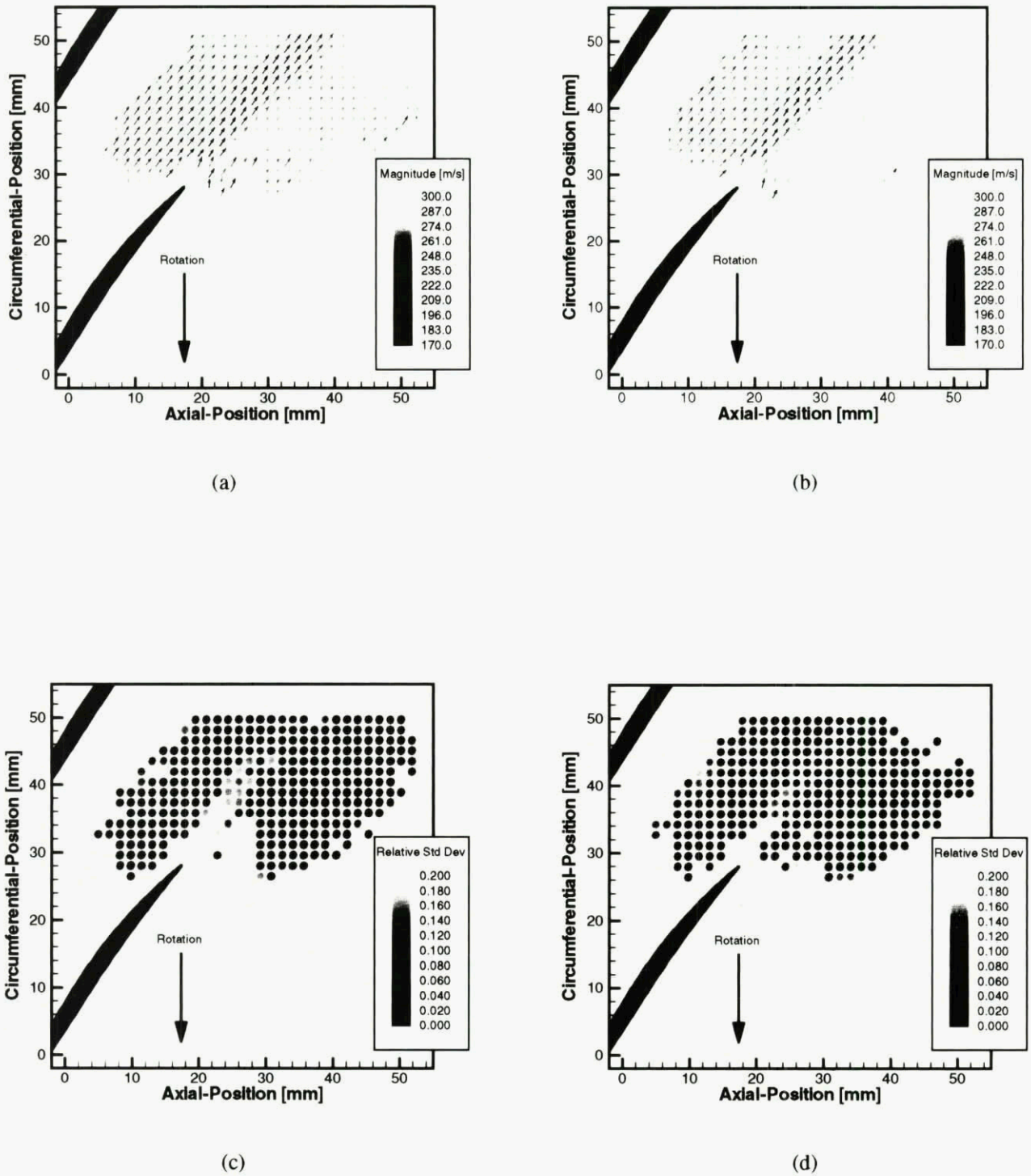


Figure 4a: Downstream illumination showing blade wakes from the average of 40 images and inter-frame time of 2.6 μs, b) same conditions as in 4a, except 50 images have been averaged and the inter-frame time is 1.53 μs; c&d) relative standard deviations for the velocity vector plot shown in figure 4a & b.

Paper 51
Author: Wernet

Q: Chana

Have you studied the issue of what minimum camera angles are required for the stereoscope approach, in order to achieve an adequate accuracy of the third componenty of velocity?

A: Yes, the error in the out of plane measurement is inversely proportional to the sine of the coupling angle between the two cameras. The optimal coupling angle is 90° for minimum error in the out-of-plane component of velocity. Nominally the out of plane error is $\sqrt{2}$ to 3 times as large as the in-plane velocity component.

Q: Chana

Do you believe that such angles can be achieved in turbomachinery, bearing in mind that window access will always be limited?

A: We have two unique facilities at NASA Lewis with large optical access ports (100mm x 100mm). Certainly not all facilities are so equipped and therefore will not permit the necessary optical access for stereoscopic PIV.

Q: Edmonds

How did you design a seeding probe to mix seed without disturbing the flow field?

A: The seeding probe was a 6.3 mm diameter tube bent at a right angle through which the atomised seed material was introduced to the flow. The tube could be adjusted radially to place the seed in the plane of the light sheet and also rotated to place the seed stream at the appropriate circumferential position in the compressor.

Q: Edmonds

You claim that in 10 minutes you could measure 100 average images with a 2% confidence, with seed density of 6 particles/mm$^3$, also that LDV would require 1-2 hours . With such a seed density would the LDV system not be able to measure the flow to the same resolution in less that 1 hour?

A: The numbers that I quoted in the presentation are very conservative. In reality the time to acquire and save an image is approximately 1.2 seconds. To acquire and save 100 image pairs would require 240 seconds or 4 minutes. However, the main point to be made is that PIV measures the instantaneous planar velocity field, allowing the researcher to study non-stationary flow phenomena. PIV data are not meant to replace LDA data, but instead to complement them. The average measurements were presented only to provide a comparison to LDA measurements, not to replace them. The main point is that PIV is an instantaneous technique.

# Applications of Three Dimensional Doppler Global Velocimetry to Turbo Machinery and Wind Tunnel Flows

**I. Roehle, R. Schodl**
German Aerospace Research Establishment (DLR)
Institute for Propulsion Technologie
Postfach 90 60 58
Linder Höhe
D-51140 Köln
Germany

## Abstract

Doppler Global Velocimetry is an imaging anemometer. A DGV system optimised for time averaged three component velocity measurements was designed and set up. The first application of the system was the investigation of the flow field of a swirl spray nozzle in a cylindrical casing. The flow field in the whole volume of the combustor was measured.

The DGV System was also applied to investigate the wake region of a car model in a wind tunnel. An arrangement with three light sheets was chosen. The 3D-DGV results are in a good agreement with 3D-LDA measurements of the same flow.

3D-DGV measurements were carried out inside the model of the inlet of a fighter aircraft. A flexible endoscope was used to overcome the serious problems of the optical excess of this fully capsuled flow.

## Introduction

The spatially resolved measurement of flow velocities is of great importance for experimental studies in the field of energetics, aeronautics and astronautics. Experimental data is needed to validate and improve numerical codes and to analyse unknown flow phenomena. Typical objects of investigation are for example jet engine or rocket engine components such as combustion chambers, engine inlets or propulsion nozzles.

Quite often only nonintrusive, optical techniques are applicable to such objects. Point techniques like Laser Doppler, Phase Doppler and Laser-2-Focus Anemometry are very accurate and have reached a high level of development. However the detailed analysis of three dimensional flows is rather time consuming, since numerous measurements at different locations are needed, therefore these techniques are rarely applied to research facilities with either short run times or high operational costs.

Light sheet techniques, especially Particle Image Velocimetry (PIV) are capable of measuring velocity fields at one instant of time and are therefore in principle better suited to analyse 3D-flow structures. However to obtain the mean flow velocity with PIV, a large series of pictures need to be taken and processed, which is also time consuming. Aside from this, the 3D-capability of this technique is still restricted and PIV also requires quite proper experimental conditions.

A new technique, known under the name of Doppler Global Velocimetry (DGV), has, at least in principle, more convenient features. DGV measures all three components of the flow vector in the light sheet plane. DGV is fast concerning acquisition and processing (nearly on-line) and it is also applicable to rough experimental conditions. DGV was first presented in 1990 [1] and 1991 [2],[3]. The published results indicate that the DGV technique fulfils the mentioned requirements, however, it's measurement accuracy has not yet been examined.

This report describes the DGV system which was set up by the Institute for Propulsion Technology and the experimental experiences which were gained in practical applications. An accuracy analysis is still under preparation.

## Principle of Doppler Global Velocimetry

Like LDA or PIV, DGV also measures the velocity of tracer particles which have to be added to the flow. With one orientation of the laser light sheet and one direction of observation, one component of the flow velocity is measured.

DGV takes advantage of the fact, that the frequency of the scattered light is shifted in frequency due to the Doppler effect:

$$\Delta\nu=\nu-\nu_0 \qquad (1)$$

$\nu_0$ : Laser frequency
$\nu$ : Scattered light frequency
$\Delta\nu$ : Doppler shift

This shift depends on the particle velocity $\vec{V}$, the light sheet direction $\vec{l}$ and the direction of observation $\vec{o}$:

$$\Delta\nu = \nu_o \frac{\left(\vec{o}-\vec{l}\right)}{c}\vec{\mathbf{V}} \qquad (2)$$

The first basic idea of DGV is to measure the scattered light frequency $\nu$ by transmitting the scattered light through an iodine cell (Figure 2). Iodine has strong absorption lines, which are used as a frequency to transmission converter. These lines interfere for example with the 514 nm line of the $Ar^+$-Laser as well as the 532 nm line of the frequency doubled YAG-Laser. Consider the frequency $\nu$ to be on the slope of one absorption line (Figure 3). Then $\nu$ can be determined by measuring the iodine cell transmission of the scattered light. Therefore two detectors are required to measure the light intensity

*Paper presented at an AGARD PEP Symposium on "Advanced Non-Intrusive Instrumentation for Propulsion Engines", held in Brussels, Belgium, 20-24 October 1997, and published in CP-598.*

before and after the cell. To do this the transmission profile T(ν) of the iodine cell must be known.

The laser frequency $\nu_0$ must be known and stabilised precisely, so that the Doppler shift $\Delta\nu$ can be calculated according to equation (1).

With equation (2), one component of the vector $\vec{V}$ can be calculated. It is the component in the direction of $\vec{o}-\vec{l}$, the bisector of the angle formed by the direction of the laser light and the direction of observation (Figure 1).

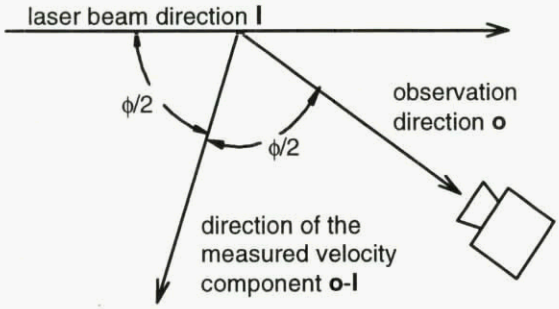


Figure 1: Direction of the measured velocity component depending on the laser light direction and the direction of observation.

The second basic idea of DGV is to use two CCD-cameras as detectors, both watching the same section of a laser light sheet (Figure 3). By pixel wise division of the two pictures and further post processing a map of one velocity component in the light sheet is obtained. Depending on the type of laser (cw or pulsed), the result is either a time averaged or frozen velocity picture.
The second and the third velocity components are measured by changing the arrangement of the optical setup.

There are two alternative ways to accomplish this:

- With one light sheet direction and three synchronised camera systems in different positions which simultaneously capture momentary pictures, the momentary 3D-velocity distribution can be obtained. Such a configuration is needed to investigate instationary 3D-flow structures [4].
- The second alternative is to use only one camera system in a fixed position and three light sheets with different orientations. The three pictures of the three light sheets have to be taken one after the other, with the consequence that this method is restricted to stationary flows only.

The second method is well suited for long exposure times of the camera system. By working with long exposure times, the turbulent velocity fluctuations are integrated in each pixel of the camera chip. In this way the fluctuations are averaged and the result is a picture of the mean velocity distribution. Since the exposure times are in the order of several seconds, even the low light sheet intensities achieved with an $Ar^+$-Laser give sufficient illumination of the DGV pictures.
The second method is also simpler, concerning set-up and handling, while the long integration times allow a sparser seeding.

Because of these advantages, and with special regards to the experimental applications, the second method was chosen for the set-up described next.

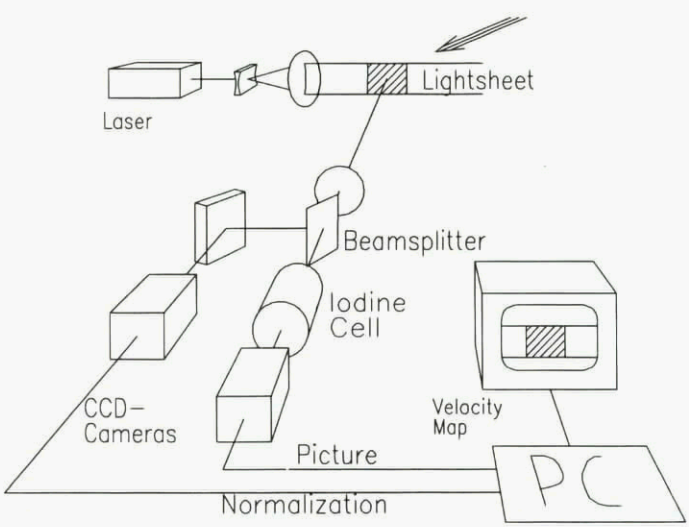


Figure 2: The Doppler Global Velocimetry set-up.

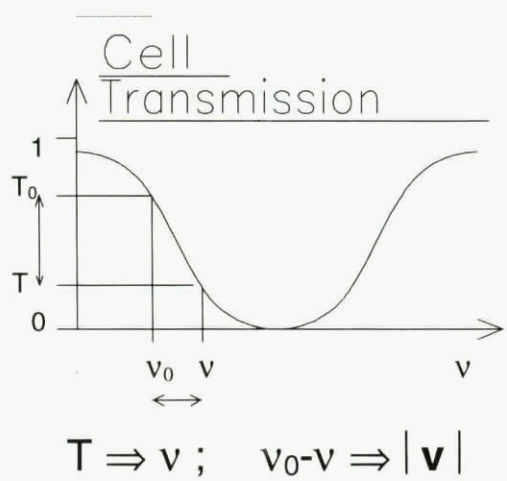


Figure 3: Transmission profile of the iodine cell.

## The Highlights of DGV

- DGV gives velocity pictures.
- The technique is nearly on-line because of the fast data acquisition and the fast and simple post processing.
- DGV does not need to detect single particles. That means that very small particles like dust or soot with very good flow following behaviour can also be used. The optical access does not need to be brilliant. Windows for example do not have to have optical quality, but may have slightly uneven or curved surfaces. Endoscopes can also be used to solve more serious access problems.

## DGV-System Set-up

The DGV-system consists of the following components: the laser with frequency stabilisation, light sheet generating optics, camera system and digital image acquisition and processing devices. These components will be briefly described in the following paragraphs. More detailed and basic information is given in [5],[6].

## The laser & frequency control

A Lexel 5 Watt $Ar^+$ -Laser with Etalon was used (single mode 1 W). To carry out accurate DGV measurements, the frequency of the laser has to be stabilised. The following example gives an estimation of the required stability: If the camera system is looking at the light sheet under an angle of 90° the measured component is pointing along the bisector of this angle, 45° to the light sheet. A resolution of 1 m/s of this component equals to a frequency shift of $\Delta\nu$ = 2.7 MHz.

The frequency drifts of a commercially available $Ar^+$-Laser are far too big to resolve this small frequency difference. Because of this it was necessary to enhance the frequency stability of the laser. Therefore the rear mirror of the resonator was placed on a piezo translator to rapidly change the length of the resonator. The etalon was stabilised by an external temperature control.

The frequency $\nu_0$ is measured with a calibrated reference iodine cell or alternatively and even more accurate with the hyperfine structure of iodine [5],[6]. A controller unit stabilises $\nu_0$ by controlling the piezo translator and the etalon temperature.

This control system has the following specifications:

- The precision of the reproducible adjustable laser frequency is $\pm$ 1 MHz.
- The fast frequency fluctuations can be suppressed with the same precision.
- The laser can be continuously tuned along the frequency range of 2 GHz in the region of the iodine line, which makes a calibration of the iodine cell possible.

Because of the enhancement of the frequency stability the remaining laser dependent errors of the velocity measurement are reduced to less than 0.5 m/s in regards to the example mentioned above.

## Light Sheet generation

To generate the light sheet the laser beam is guided through a fibre to a light sheet box which contains all the optics. The height of the light sheet and the distance of the waist can both be adjusted. The maximum height is 140 mm, the waist is smaller than 1 mm with hardly any practical limits to the waist distance. Because of the separation of laser and the optic, the alignment of the laser light sheet relative to the object of investigation is quite simple.

The light sheet optics are also optimised for long exposure times. The light sheet has a flat top-hat intensity profile, generated by a scanning technique with a modulation frequency of 10 to 20 Hz. A top-hat profile minimises the intensity dynamics in the measured picture with positive influence on the measurement accuracy. Three light sheet boxes are available to establish the three light sheets. An opto-mechanical switch is used to direct the light to either one of the light sheet boxes.

## The DGV-camera system

The performance of the camera system equals in principle the setup in Figure 2. One collecting lens generates an intermediate picture, which is transferred by a transfer lens to the chips of the two cameras. A non polarising beam spliter plate is used to reduce polarisation influences. A laser line filter reduces ambient light. A pair of 12-Bit cooled slow scan CCD cameras are used because of their good signal to noise ratio (SNR) and their linear sensitivity characteristics. Normal video CCD cameras usually do not have a SNR better than 100 ($\cong$ 7 Bit) and show nonlinear behaviour for high intensities.

By cooling the chip of the slow scan camera long exposure times of several seconds are possible without integrating too much dark current. Therefore they are the ideal choice for this DGV-System which is optimised for time averaged measurements performed by long exposure times.

In order to get identical pictures from both cameras, the cameras are mounted on micro positioning devices to allow precise alignment. An additional software alignment currently is not applied but may further enhance the quality of the measurement. Figure 4 shows a photograph of the camera system.

The iodine cell is made from quartz glass, evacuated and filled with a small iodine crystal. The cell is placed in a temperature controlled oven. At a certain temperature all the iodine is evaporated (in our case 57°C), so that the gas density remains constant at temperatures exceeding this level. In this way an easy density stabilisation is achieved.

The calibration curve $T(\nu)$ of the cell is obtained by linear scanning of the laser and at the same time measuring the cell's transmission The cell temperature is fixed and can be reproduced in the experiment.

From this data set a software look up table is generated for calibrating the DGV pictures. The images are acquired and stored with a PC-based system.

This system also accomplishes the post processing, which includes:

- Background subtraction (ambient light and laser reflexes)
- Division of the content of the two pictures
- Pixel specific sensitivity correction
- The mapping $T \rightarrow \nu$ (T) : Look up table
- The mapping $\nu \rightarrow \nu$ ($\nu$) : Equation (2)
- Combination of three one component measurements to one 3D-measurement
- Vector or false colour representation of the results
- Generation of data files readable with other software (if needed)

A further point - not yet developed - will be the picture alignment by software and dewarping of the pictures.

The whole post processing takes about 30 seconds and can be started immediately after the DGV pictures are taken. In this way the technique is nearly on-line. The final measurement error of the ensemble of laser and camera result in a velocity uncertainty of ±1 m/s.

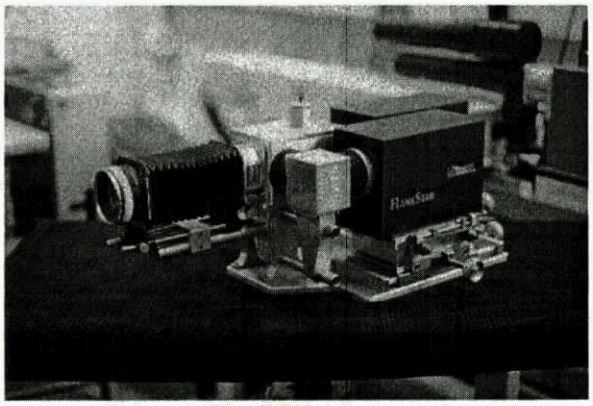

Figure 4: The DGV-camera system.

## DGV in the Flow of a Swirler

The flow field of a fuel atomisation nozzle was investigated. Such nozzles are an important component of combustion chambers of jet engines. Two circular air flows pass two swirl generators and are combined in the exit of the nozzle. In this way a recirculating flow with strong shear stresses is generated. These shear stresses atomise the fuel film tearing off the atomisation lip of the nozzle. The fuel injector is placed in the center of the nozzle but is not used in the experiment.

The atomisation nozzle has a outlet diameter of 11 mm. It was operated under atmospheric pressure with a pressure drop of 30 mbar and was inserted in a tube with a diameter of 54 mm. The 3D-flow field in the pipe downstream the nozzle was investigated. Figure 5 shows the experimental arrangement. A slit in the tube at the light sheet location avoids measurement disturbances, caused by reflections. Therefore the windows, which are needed to avoid flow leakage, are recessed from the inner wall. The light sheet and camera location was fixed. The nozzle was moved to change the axial position of the measurement.

The direction of the velocity component $v_{xr}$ measured with the setup is also indicated in Figure 5. The other two velocity components needed to determine the 3D-vector could be measured by two further DGV-pictures taken with two other light sheets overlapping at the same location, with the light sheet direction rotated 120° and 240° around the pipe axis. However these two additional measurements are unnecessary, because of the cylindrical symmetry of the flow. The resulting measurement pictures equal the first velocity picture apart from a respective rotation around the pipe axis. This means that in a flow with cylindrical symmetry only one DGV-picture is sufficient to describe the 3D-flow. The other two components can be generated in the computer. Of course this simplified method may only be applied to measure mean values. The instantaneous flow distribution never shows any symmetry because of turbulent fluctuations.

The presented experiment has got a cylindrical symmetry and only the time averaged flow field is of interest. Therefore the DGV-system optimised for the measurement of mean flow velocities was used to analyse the flow field.

The light sheet illuminated the whole cross section. The Laser power was 300 mW. The air was seeded with glycerine particles with an average diameter of 0.2 µm. The particle density was so low that, with the flow switched on, the scattered light could hardly be seen by the eye. To achieve sufficient image quality, an exposure time from 1 to 5 seconds was needed. This time is sufficient to integrate the turbulent velocity fluctuations.

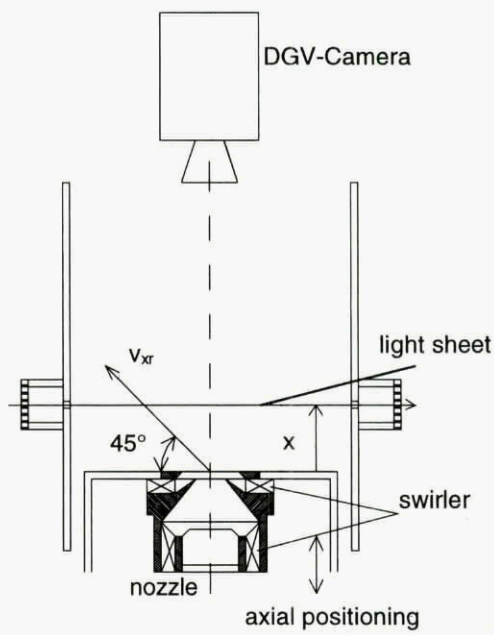


Figure 5: Set-up for DGV measurements in the flow field of a swirl nozzle.

## Results of the swirler measurements

The result of a DGV-measurement at a certain axial position x is shown in Figure 6. The upper part shows the image of the camera behind the iodine cell and the lower part the picture of the reference camera. First the background light is subtracted, then the pictures are divided and the divided picture is corrected in accordance with the pixel specific sensitivity differences. Then, by the use of the calibration function T(ν) and with regards to the geometry of the optical arrangement, the distribution of the velocity component $v_{xr}$ is obtained (Figure 7).

In the next step the user marks the symmetry centre of the picture and the computer calculates the two other velocity pictures by turning the resultant picture 120° and 240° around the symmetry centre. These three pictures are combined to a 3D-vector field which is shown in Figure 8.

The components in the light sheet are represented by a vector plot and the axial component is represented by a so called „luminescence plot".

This result is obtained after about 30 seconds, the measurement takes 5 seconds, the post processing requires 25 seconds.

The full volumetric flow field can be acquired within a few minutes by stepwise changing the axial position of the light sheet. As an example, Figure 9a shows the vector field in the plane along the tube axis. Figure 9b shows the distribution of the circumferential velocity.

The pictures indicate quite clearly how fast the swirl flow in the tube is smoothed. Secondary flow structures can be observed, especially the recirculation torus in the corners at the bottom of the tube and the axial recirculation. Both effects are very important for the combustion because they are needed to stabilise the flame.

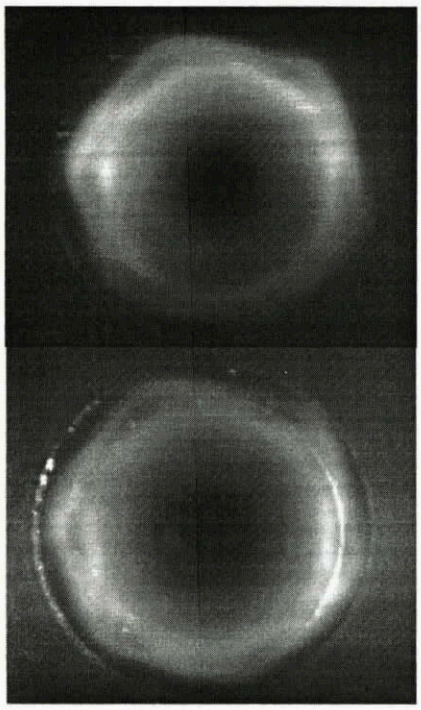

Figure 6: Signal and reference DGV picture

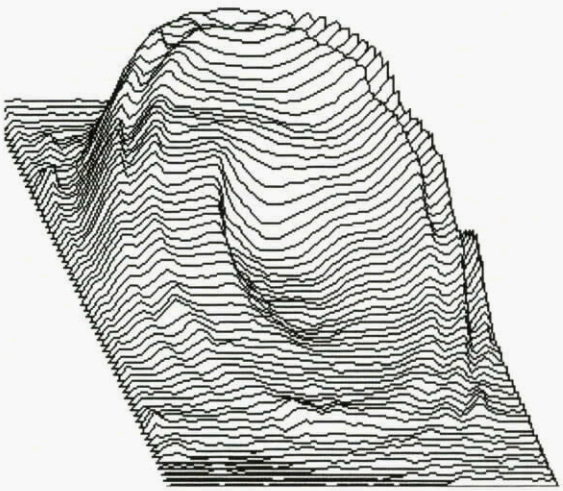

Figure 7: Result of a DGV-measurement. The distribution of one velocity component.

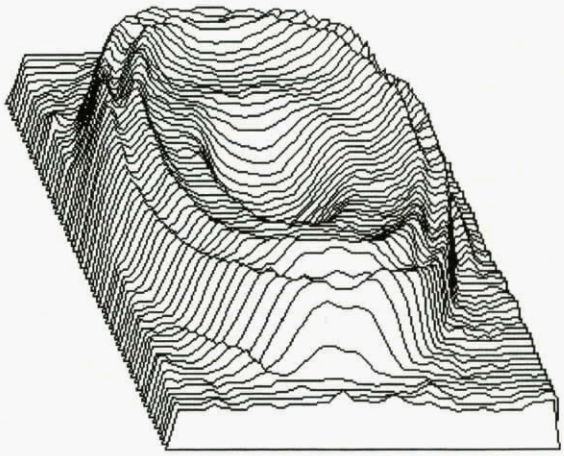

Axial component

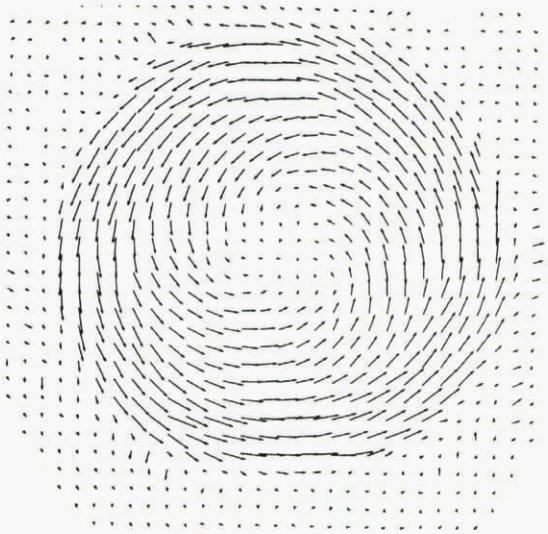

Flow vectors in the light sheet plane

Figure 8: 3D-velocity distribution of the flow 2 mm above the swirl nozzle.

These results show, that this method is an excellent tool for fast analysis of complex flow fields. The resolution is between 1 and 2 m/s, since the smallest vectors which still make sense have a length of 1.5 m/s.

Reliable statements concerning the accuracy of DGV are not yet possible. Among many other potential error sources [4], we assume that reflections of the laser, reflections of the scattered light and multi-scattering may affect the accuracy as well as high turbulence in combination with non linearity of the iodine line and inhomogeneous seeding causing non linear averaging.

If such error sources can be avoided, the absolute accuracy can be estimated to be at least smaller than 5m/s. This was proven by a first comparison of the DGV results of the swirler with LDA-measurements at the same location.

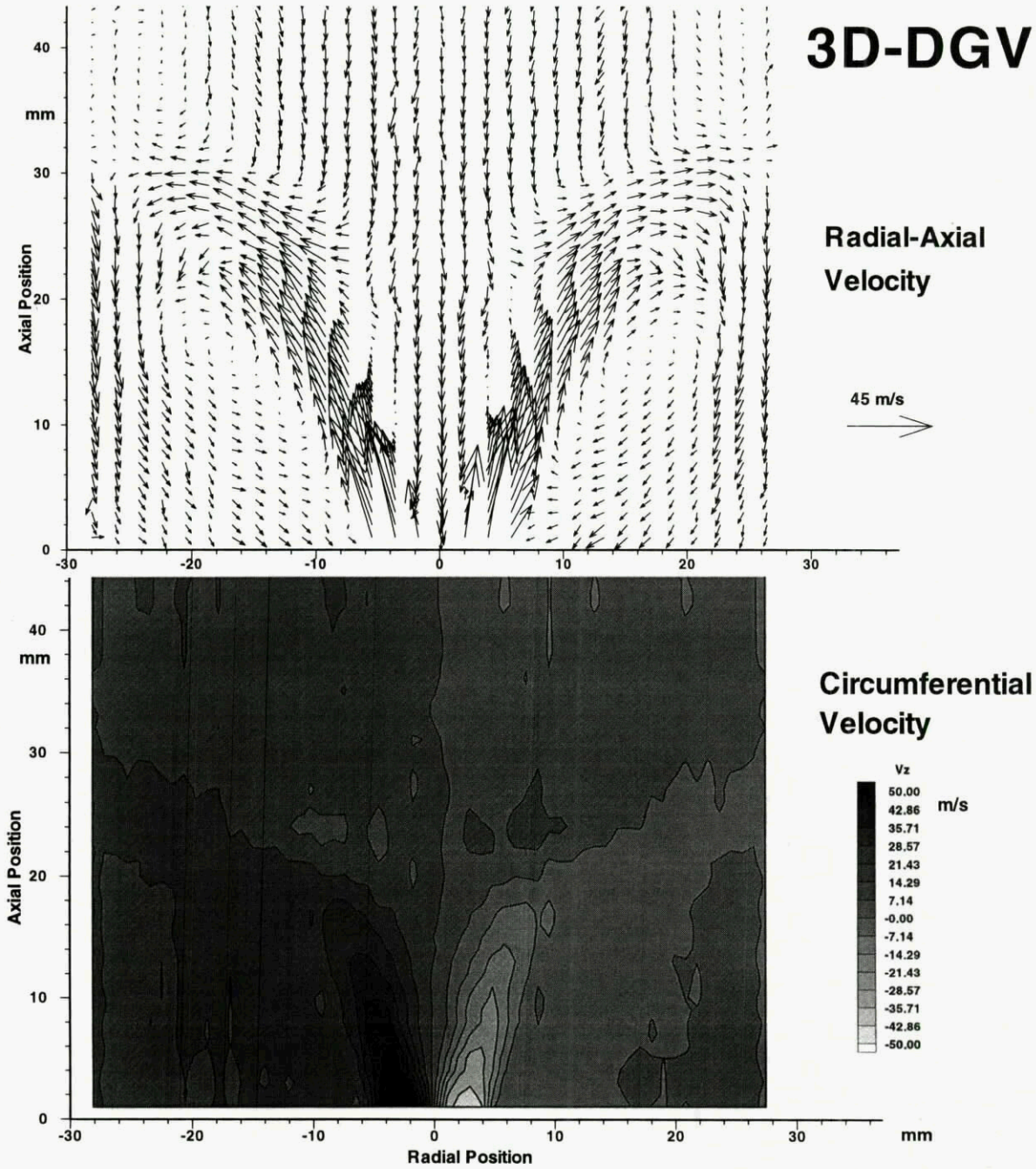


Figure 9 (a,b): Flow field of the fuel spray nozzle.

## DGV measurements in the wake region of a car model

Car designers have to pay special attention to aerodynamic properties such as drag, lift and side forces, aerodynamic noise and dirt deposition.
The design procedure is an iterative experimental process. The shape of a clay car model (typical scale 1:5 or 1:4) is stepwise optimised by a series of short wind tunnel tests. The purpose of each test is to examine the aerodynamic effect of the last variations of the model. To evaluate the actual performance of the model, force balance measurements, stream line seeding and wool tuft visualisation are used in the first place.
The power of these classic techniques is not always sufficient. The force balance gives only a few integrated values that cannot be directly related to a certain flow phenomena. Stream line seeding and wool tufts only work up to Reynolds numbers which represent a velocity of 6 km/h of the full size car.

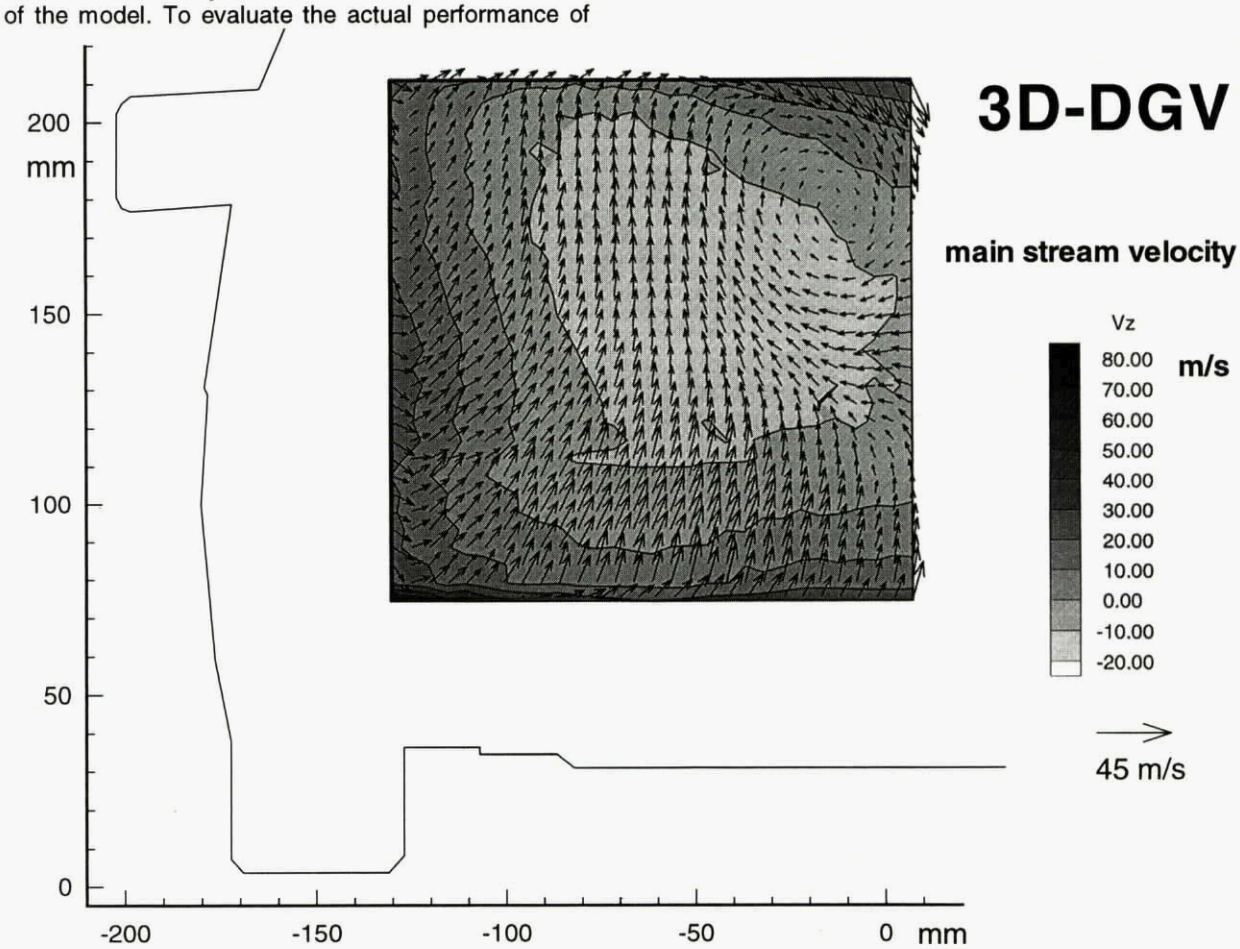


Figure 10: 3D-DGV measurement in the wake region of a car model. (Acquisition time :30 seconds)

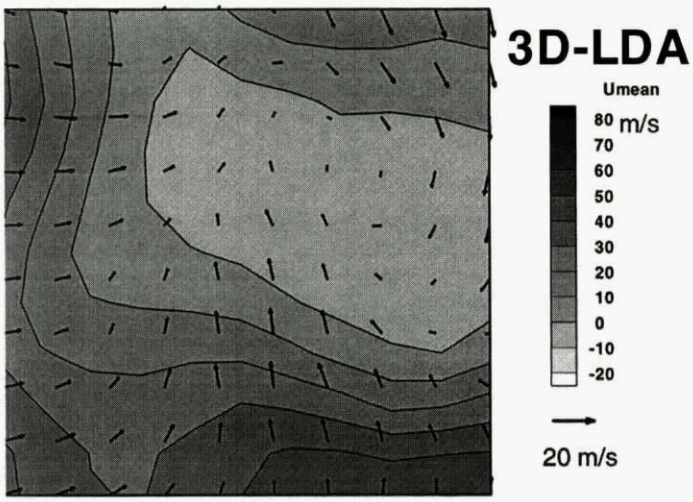


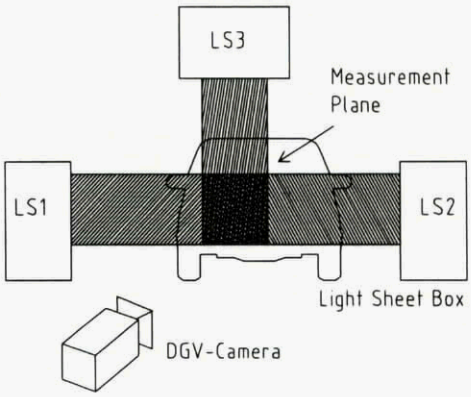


Figure 11 (a,b): 3D-LDA measurements at the location of the DGV measurements in Figure 10. (Acquisition time: approximately 2 hours)

DGV-set-up in the Wind tunnel

To measure flow structures at realistic Reynolds numbers, LDA measurements can generally be carried out, but it takes at least 10 seconds to 2 minutes to measure only one LDA point. The reason for this is, that it is necessary to integrate the low frequency turbulent fluctuations. Therefore LDA can not be constantly used to support the aerodynamic optimisation process of the car model, but will only be applied to some exemplary test cases. This demonstrates that there is still the need for another technique. This technique might be DGV, because it enables quick 3D-measurement within less than 30 seconds in quite a large plane in the flow with no restrictions to the Reynolds number.

The DGV system was used to investigate the wake region of an experimental 1:5 car model in a 1.8m x 1.3m low speed wind tunnel at Mercedes Benz in Sindelfingen/Stuttgart. The light sheet boxes were installed left, right and above the open test section (Figure 11b), illuminating a plane perpendicular to the main flow direction 150 mm behind the model. The model had a length of 800 mm. This plane was observed from down-stream the flow. It had a size of 140 x 140 $mm^2$. The free stream velocity was 50 m/s. A fog generator placed in the settling chamber was used for seeding the flow.

A sequential 3D-DGV measurement was carried out. The exposure time for each picture pair was ten seconds, so that the final results were obtained after one minute, 30 seconds taken by the image acquisition and another 30 seconds for the post processing. The power in the light sheet was 150 mW.

## Results of the car measurements

Figure 10 shows the DGV results. A recirculation zone with a vortex was observed, which is a typical structure in the wake region of a car. The main stream velocity component increased twards the top, bottom and left side of the measurement region because of the influence of the free stream. These results are in good agreement with 3D-LDA data of the same flow at the same location (Figure 11 a) [7].

- The vortices are detected at approximately the same location.
- The shape of the isolines are similar.
- The amplitudes of the recirculation are around minus 20m/s concerning both, the DGV and the LDA measurements.

Obviously the data density of the DGV measurement is much higher since it is an imaging technique. Therefor smaller structures like the recirculation vortex are observed more clearly. The LDA picture took approximately 2 hours acquisition time, which is very long compared to the DGV-acquisition time of only 30 seconds.

A detailed comparison between the LDA and DGV results was not possible, because the model was not placed at exactly the same position in the test section and the boundary layer suction was not switched on during the DGV measurement. Especially the wake region of the car is very sensitive to such small changes of the aerodynamic boundary conditions, so this may be an explanation for the differences of the LDA and DGV data.

An important observation was, that a lot of care had to be taken concerning the homogeneity of the seeding, in order to avoid biasing caused by correlated fluctuations of seeding density and velocity. This effect is generally well known in wind tunnel research. Homogeneous seeding also helps to keep the images in the dynamic range of the camera.

## DGV Measurements in the Model of an DASA-Engine Inlet

The flow inside a model of an engine inlet was investigated with DGV. The experiments carried out were aimed to evaluate in how far DGV measurements could be a helpful tool for the development of an engine inlet.

The engine inlet of a fighter aircraft is usually curved and long compared to it's diameter. Therefor the flow inside shows typical pipe flow phenomena which have to be examined and quantified in order to ensure a sufficient air supply of the turbo engine. Velocity inhomogenities such as the vorticity and the loss of total pressure have to be measured as a function of the mass flux and angle of attack of the air plane.

The set-up is shown in Figure 12. A Seeding box with a blower and the fog generator inside was used generate a homogenous seeding. The seeded air was sagged in the inlet. The inlet was mounted on a so called optical module, which was used to investigate the flow at the exit of the inlet e.g. at the interface plane to the turbo engine. A glass ring serves as a window for the three light sheets. A stem with a mirror and a flexible endoscope is placed further down stream watching the light sheet. The endoscope transfers the image to the camera system. The mass flow rate and the stationary pressures at the wall near the light sheet were measured with pressure probes.

The three light sheet boxes generated three light sheets forming an angle of 120°. For each measurement three pictures were taken, each with an exposure time of 5 seconds.

The inlet was blocked on one side to simulate an aerodynamic disturbance causing strong secondary structures. Figure 13 shows the result of a measurement. A strong vortex was measured. The distribution of the axial velocity was measured as well and is represented by grey values.

The axial velocities were used to determine the mass flow rate, the mach number, the total pressure distribution. Important design parameters were derived from this data, such as the total pressure loss, the total pressure distortion and the vortisity angle.

The results were compared to Laser-2-Focus measurements and to measurements with pressure probes. The results were promising. Therefor the technique will be applied on a model in a wind tunnel next. A detailed comparison will be published.

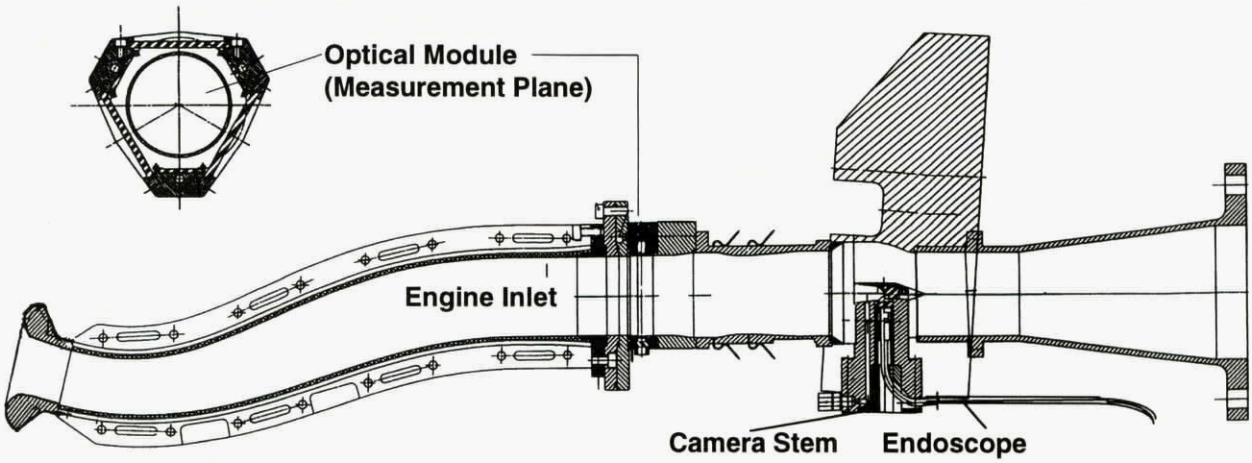


Figure 12: DASA-engineinlet (one side was blocked), optical module, camera stem and endoscope

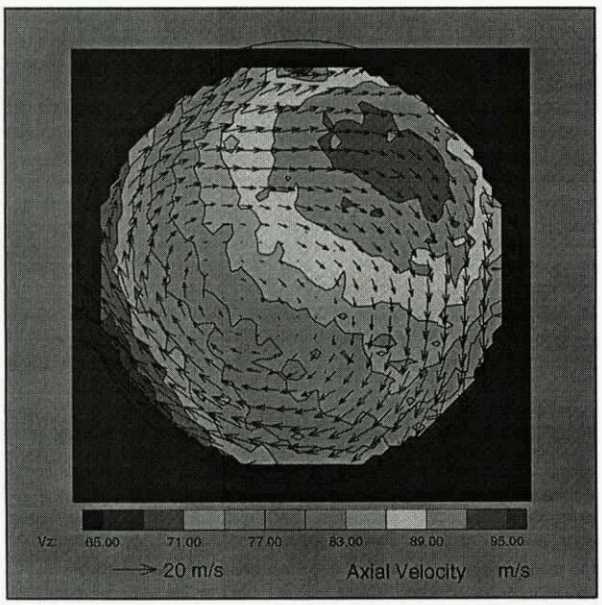


Figure 13: Flow field in the optical module

It should be stressed that these are the first imaging velocimetry experiments using a flexible endoscope. This is an important characteristic of DGV since in this way, DGV can also be applied to flows with pour optical excess.

## Outlook

Because of the encouraging results of the swirler and the wind tunnel experiment, continuation of the development of the DGV-System is intended. The system will be applied to investigate turbomachinery components in the first place.

On the one hand, emphasis will be kept on sequential time averaged measurement with long exposure times and on the other hand, a pulsed, diode pumped YAG-laser is in preparation as a powerful and narrowband light source to visualise instationary flow structures and to enable measurements in flames.

## Summary

With the aim of studying the capabilities of a new measurement technique called DGV, a measurement system was set up. The most important components were optimised with regards to accurate mean values. The 3D-flow field of a atomisation swirl nozzle was investigated as well as the 3D-flow structure in one plane in the wake region of a car model. The results show that this technique is very practical, when a quick general look to a flow is needed.

DGV is an important addition to the established velocimetry techniques. It is suitable as an analysing device for aerodynamic development; a tool the car and aircraft industry for example are already looking for.

## References

[1] H. Komine: „System for measuring velocity field of fluid flow utilising a laser-doppler spectral image converter ",US Patent 4 919 536, 1990.

[2] J.F. Meyers, H. Komine: „Doppler Global Velocimetry - A New Way to Look at Velocity", ASME Fourth International Conference on Laser Anemometry, Cleveland Ohio, August. 1991.

[3] R.B. Miles: „Instantaneous Velocity Field and Background Suppression by Filtered Raleigh Scattering", AIAA paper, No. AIAA-91-0357, 1991.

[4] J.F. Meyers: „Evolution of Doppler Global Velocimetry Date Processing", Proceeding, Eighth International Symposium on Applications of Laser Techniques to Fluid Mechanics", Lisbon, 8-11 Julie, 1996

[5] I. Röhle, R. Schodl: „Laser-Doppler-Velocimetry auf der Basis frequenzselektiver Absorption", Diplomarbeit, DLR interner Bericht Nr. IB-325-8-93, 1993.

[6] I. Röhle, R.Schodl: „Evaluation of the Accuracy of the Doppler Global Technique", Proceeding. Optical Methods and Data Processing in Heat and Fluid Flow, London 14/15 April, pp. 155-161, 1994.

[7] J. Schmitt: LDA measurements in the wake region of a car model, Private communication, Mercedes Benz Sindelfingen, 1994.

[8] I.Röhle: „Three Dimensional Doppler Global Velocimetry in the Flow of a Fuel Spray Nozzle and in the Wake Region of a Car", Flow Measurement and Instrumentation, Elsevier Science Ltd, 1997,Oxford.

Paper 52
Author: Roehle

Q: When operating the DGV it acquires much information in a short time. However, the tuning of the laser and filter is very critical for DGV as far as I know. How much time do you need in practice to tune the laser and the filter and can you comment on the criticality? Does the tuning determine the uncertainty for DGV measurements?

A: Before the DGV measurement starts, the laser is tuned until the desired frequency is reached. The duration of this tuning process depends on the range the laser frequency has to be tuned. In general a tuning velocity of about 2 MHz/s to 4MHz/s is feasible. Usually one misses the desired frequency, by setting the etalon temperature, by a few hundred MHz, so that the operation point is reached after one to two minutes. The laser is then stabilised to this frequency.

This process has only got to be performed once. After that the DGV system is ready to measure without time limitation and without any further tuning of the laser, so that a lot of pictures can be acquired oneafter the other.

The critical question is in how far the laser frequency is kept constant with the time. The best accuracy we ever reached was +-1MHz in the laboratory. Under test rig conditions we are definately less accurate. We never investigated this but I hope we can reduce the frequency fluctuations of the laser to less than + 4 MHz (= + 2m/s).
It should be pointed out only the component perpendicular to the light sheet plane is effected by an offset in the laser frequency. The components in the light sheet are only effected, when the laser frequency changes during the acquisition of the three pictures.

Another critical point is being able to tune the laser linearly. This is not important during the DGV experiment, but when we calibrate the iodine cell. We achieve a good linearity by locking the laser frequency to an external interferometer which can be tuned linearly. Of course this calibration is not performed before each experiment, but only once in the laboratory. Thanks to the high quality of the iodine cells this calibration does not change over months or even years.

Because of this the iodine cell (e.g. the filter) does not cause big uncertainties. As explained in the paper we stabilised the vapour density by fully evaporating the iodine crystal. In this way the cell profile was always quite reproducible.

The heating of the cell takes about half an hour before the experiment.

Q: Weigand

Maybe, you can give us an idea of the accuracy of DGV data results of comparison with LDA - or other velocimetry measurements?

A: We once compared point DGV measurements with L2F measurements in a free jet. The accuracy was +- 3m/s. This was in good agreement with theoretical estimations.

The velocity resolution however is better. The smallest vectors in the presented results have a length of only 1m/s so the resolution should be of this magnitude.

The presented LDA and DGV measurement in the wake region of the Mercedes should not be compared in detail because the aerodynamic boundary conditions were not fully alike. Especially the way the seeding is introduced to a wind tunnel flow has in general strong influence on laser anemometry results. Since DGV needed a more dense seeding a different seeding generator was used which distributed the particles in a different way than the generator for the LDA measurements. A wind tunnel experiment like this is not well suited for accuracy analysis.

# REPORT DOCUMENTATION PAGE

| 1. Recipient's Reference | 2. Originator's Reference | 3. Further Reference | 4. Security Classification of Document |
|---|---|---|---|
| | AGARD-CP-598 | ISBN 92-836-0055-X | UNCLASSIFIED/ UNLIMITED |

**5. Originator**

Advisory Group for Aerospace Research and Development
North Atlantic Treaty Organization
7 rue Ancelle, 92200 Neuilly-sur-Seine, France

**6. Title**

Advanced Non-Intrusive Instrumentation for Propulsion Engines

**7. Presented at/sponsored by**

The Propulsion and Energetics Panel (PEP) 90th Symposium,
held in Brussels, Belgium, 20-24 October 1997.

| 8. Author(s)/Editor(s) | 9. Date |
|---|---|
| Multiple | May 1998 |

| 10. Author's/Editor's Address | 11. Pages |
|---|---|
| Multiple | 550 |

**12. Distribution Statement**

There are no restrictions on the distribution of this document. Information about the availability of this and other AGARD unclassified publications is given on the back cover.

**13. Keywords/Descriptors**

| | | |
|---|---|---|
| Propulsion | Lasers | Laser anemometers |
| Neutron diffraction | Instruments | Raman spectroscopy |
| Vibration | Measurement | Paints |
| Interferometers | Turbomachinery | Pressure sensors |
| Speckle | Gas turbine engines | Fluorescence |
| Temperature | Exhaust emissions | Thin films |
| Ceramics | Absorption | Combustion |
| Composite materials | Infrared radiation | Turbine Blades |
| Holography | Laser doppler velocimetry | Design |
| Flames | | |

**14. Abstract**


Changes in engine technology such as higher temperatures, higher tip speeds, new metal/composite/ceramic materials together with radical changes in design philosophy will require amongst other prerequisites the ability to measure and to monitor key internal gas and structural characteristics. The symposium papers presented non-intrusive measurement and analysis technologies in the following categories:

— Laser Point Measurements (11)

— Absorption and Infrared Techniques (4)

— Paints - Surface Sensors (6)

— Laser Induced Fluorescence (6)

— Mechanical (7)

— Films (5)

Laser Planar Measurement (9)

and a Keynote Address

AGARD

NATO OTAN

7 RUE ANCELLE • 92200 NEUILLY-SUR-SEINE

FRANCE

Télécopie 0(1)55.61.22.99 • Télex 610 176

**DIFFUSION DES PUBLICATIONS**

**AGARD NON CLASSIFIEES**

L'AGARD détient un stock limité de certaines de ses publications récentes. Celles-ci pourront éventuellement être obtenus sous forme de copie papier. Pour de plus amples renseignements concernant l'achat de ces ouvrages, adressez-vous à l'AGARD par lettre ou par télécopie à l'adresse indiquée ci-dessus. *Veuillez ne pas téléphoner.*

Des exemplaires supplémentaires peuvent parfois être obtenus auprès des centres de diffusion nationaux indiqués ci-dessous. Si vous souhaitez recevoir toutes les publications de l'AGARD, ou simplement celles qui concernent certains Panels, vous pouvez demander d'être inclus sur la liste d'envoi de l'un de ces centres.

Les publications de l'AGARD sont en vente auprès des agences de vente indiquées ci-dessous, sous forme de photocopie ou de microfiche. Certains originaux peuvent également être obtenus auprès de CASI.

## CENTRES DE DIFFUSION NATIONAUX

**ALLEMAGNE**
Fachinformationszentrum Karlsruhe
D-76344 Eggenstein-Leopoldshafen 2

**BELGIQUE**
Coordonnateur AGARD - VSL
Etat-major de la Force aérienne
Quartier Reine Elisabeth
Rue d'Evere, B-1140 Bruxelles

**CANADA**
Directeur - Gestion de l'information
(Recherche et développement) - DRDGI 3
Ministère de la Défense nationale
Ottawa, Ontario K1A 0K2

**DANEMARK**
Danish Defence Research Establishment
Ryvangs Allé 1
P.O. Box 2715
DK-2100 Copenhagen Ø

**ESPAGNE**
INTA (AGARD Publications)
Carretera de Torrejón a Ajalvir, Pk.4
28850 Torrejón de Ardoz - Madrid

**ETATS-UNIS**
NASA Center for AeroSpace Information (CASI)
Parkway Center, 7121 Standard Drive
Hanover, MD 21076

**FRANCE**
O.N.E.R.A. (Direction)
29, Avenue de la Division Leclerc
92322 Châtillon Cedex

**GRECE**
Hellenic Air Force
Air War College
Scientific and Technical Library
Dekelia Air Force Base
Dekelia, Athens TGA 1010

**ISLANDE**
Director of Aviation
c/o Flugrad
Reykjavik

**ITALIE**
Aeronautica Militare
Ufficio Stralcio AGARD
Aeroporto Pratica di Mare
00040 Pomezia (Roma)

**LUXEMBOURG**
*Voir* Belgique

**NORVEGE**
Norwegian Defence Research Establishment
Attn: Biblioteket
P.O. Box 25
N-2007 Kjeller

**PAYS-BAS**
Netherlands Delegation to AGARD
National Aerospace Laboratory NLR
P.O. Box 90502
1006 BM Amsterdam

**PORTUGAL**
Estado Maior da Força Aérea
SDFA - Centro de Documentação
Alfragide
P-2720 Amadora

**ROYAUME-UNI**
Defence Research Information Centre
Kentigern House
65 Brown Street
Glasgow G2 8EX

**TURQUIE**
Millî Savunma Başkanliği (MSB)
ARGE Dairesi Başkanliği (MSB)
06650 Bakanliklar - Ankara

## AGENCES DE VENTE

**NASA Center for AeroSpace Information (CASI)**
Parkway Center, 7121 Standard Drive
Hanover, MD 21076
Etats-Unis

**The British Library Document Supply Division**
Boston Spa, Wetherby
West Yorkshire LS23 7BQ
Royaume-Uni

Les demandes de microfiches ou de photocopies de documents AGARD (y compris les demandes faites auprès du CASI) doivent comporter la dénomination AGARD, ainsi que le numéro de série d'AGARD (par exemple AGARD-AG-315). Des informations analogues, telles que le titre et la date de publication sont souhaitables. Veuiller noter qu'il y a lieu de spécifier AGARD-R-nnn et AGARD-AR-nnn lors de la commande des rapports AGARD et des rapports consultatifs AGARD respectivement. Des références bibliographiques complètes ainsi que des résumés des publications AGARD figurent dans les journaux suivants:

**Scientific and Technical Aerospace Reports (STAR)**
STAR peut être consulté en ligne au localisateur de ressources uniformes (URL) suivant:
http://www.sti.nasa.gov/Pubs/star/Star.html
STAR est édité par CASI dans le cadre du programme NASA d'information scientifique et technique (STI)
STI Program Office, MS 157A
NASA Langley Research Center
Hampton, Virginia 23681-0001
Etats-Unis

**Government Reports Announcements & Index (GRA&I)**
publié par le National Technical Information Service
Springfield
Virginia 2216
Etats-Unis
(accessible également en mode interactif dans la base de données bibliographiques en ligne du NTIS, et sur CD-ROM)

*Imprimé par le Groupe Communication Canada Inc.*
*(membre de la Corporation St-Joseph)*
*45, boul. Sacré-Cœur, Hull (Québec), Canada K1A 0S7*

REGISTRY
18 JUN 1998
DRIC

AGARD

NATO OTAN

7 RUE ANCELLE • 92200 NEUILLY-SUR-SEINE

FRANCE

Telefax 0(1)55.61.22.99 • Telex 610 176

UNLIMITED

## DISTRIBUTION OF UNCLASSIFIED AGARD PUBLICATIONS

AGARD holds limited quantities of some of its recent publications, and these may be available for purchase in hard copy form. For more information, write or send a telefax to the address given above. *Please do not telephone.*

Further copies are sometimes available from the National Distribution Centres listed below. If you wish to receive all AGARD publications, or just those relating to one or more specific AGARD Panels, they may be willing to include you (or your organisation) in their distribution.

AGARD publications may be purchased from the Sales Agencies listed below, in photocopy or microfiche form. Original copies of some publications may be available from CASI.

### NATIONAL DISTRIBUTION CENTRES

**BELGIUM**
Coordonnateur AGARD - VSL
Etat-major de la Force aérienne
Quartier Reine Elisabeth
Rue d'Evere, B-1140 Bruxelles

**CANADA**
Director Research & Development
Information Management - DRDIM 3
Dept of National Defence
Ottawa, Ontario K1A 0K2

**DENMARK**
Danish Defence Research Establishment
Ryvangs Allé 1
P.O. Box 2715
DK-2100 Copenhagen Ø

**FRANCE**
O.N.E.R.A. (Direction)
29 Avenue de la Division Leclerc
92322 Châtillon Cedex

**GERMANY**
Fachinformationszentrum Karlsruhe
D-76344 Eggenstein-Leopoldshafen 2

**GREECE**
Hellenic Air Force
Air War College
Scientific and Technical Library
Dekelia Air Force Base
Dekelia, Athens TGA 1010

**ICELAND**
Director of Aviation
c/o Flugrad
Reykjavik

**ITALY**
Aeronautica Militare
Ufficio Stralcio AGARD
Aeroporto Pratica di Mare
00040 Pomezia (Roma)

**LUXEMBOURG**
*See* Belgium

**NETHERLANDS**
Netherlands Delegation to AGARD
National Aerospace Laboratory, NLR
P.O. Box 90502
1006 BM Amsterdam

**NORWAY**
Norwegian Defence Research Establishment
Attn: Biblioteket
P.O. Box 25
N-2007 Kjeller

**PORTUGAL**
Estado Maior da Força Aérea
SDFA - Centro de Documentação
Alfragide
P-2720 Amadora

**SPAIN**
INTA (AGARD Publications)
Carretera de Torrejón a Ajalvir, Pk.4
28850 Torrejón de Ardoz - Madrid

**TURKEY**
Millî Savunma Başkanliği (MSB)
ARGE Dairesi Başkanliği (MSB)
06650 Bakanliklar - Ankara

**UNITED KINGDOM**
Defence Research Information Centre
Kentigern House
65 Brown Street
Glasgow G2 8EX

**UNITED STATES**
NASA Center for AeroSpace Information (CASI)
Parkway Center, 7121 Standard Drive
Hanover, MD 21076

### SALES AGENCIES

**NASA Center for AeroSpace Information (CASI)**
Parkway Center, 7121 Standard Drive
Hanover, MD 21076
United States

**The British Library Document Supply Centre**
Boston Spa, Wetherby
West Yorkshire LS23 7BQ
United Kingdom

Requests for microfiches or photocopies of AGARD documents (including requests to CASI) should include the word 'AGARD' and the AGARD serial number (for example AGARD-AG-315). Collateral information such as title and publication date is desirable. Note that AGARD Reports and Advisory Reports should be specified as AGARD-R-nnn and AGARD-AR-nnn, respectively. Full bibliographical references and abstracts of AGARD publications are given in the following journals:

**Scientific and Technical Aerospace Reports (STAR)**
STAR is available on-line at the following uniform resource locator:
http://www.sti.nasa.gov/Pubs/star/Star.html
STAR is publis
and Technical I
STI Program O
NASA Langley
Hampton, Virgi
United States

**Government Reports Announcements & Index (GRA&I)**
published by the National Technical Information Service
Springfield
Virginia 22161

NTIS Bibliographic

*351956++P+UL*

(A Corporation Company)
45 Sacré-C da K1A 0S7

UNLIMITED

ISBN 92-836-0055-X